CARBON NANOTUBES APPLICATIONS ON ELECTRON DEVICES

Edited by **Jose Mauricio Marulanda**

INTECHWEB.ORG

Carbon Nanotubes Applications on Electron Devices
Edited by Jose Mauricio Marulanda

Published by InTech
Janeza Trdine 9, 51000 Rijeka, Croatia

Publishing Process Manager Viktorija Zgela
Technical Editor Teodora Smiljanic
Cover Designer Jan Hyrat
Image Copyright fenghui, 2010. Used under license from Shutterstock.com

First published July, 2011
Printed in Croatia

A free online edition of this book is available at www.intechopen.com
Additional hard copies can be obtained from orders@intechweb.org

Carbon Nanotubes Applications on Electron Devices, Edited by Jose Mauricio Marulanda
p. cm.
ISBN 978-953-307-496-2

Contents

Preface

Carbon nanotubes (CNTs), discovered in 1991, have been a subject of intensive research for a wide range of applications. Carbon nanotubes have emerged as the main target of many researchers around the world in pursue to the next nanoscale device. CNTs are one-dimensional (1D) graphene sheets rolled into a tubular form and due to their exceptional electrical and mechanical properties, the possible application in a wide spectrum of electron devices is certainly the focus of future research generations. This book provides excellent review on the techniques for fabrication aimed to specific applications for current technology. A tremendous amount of work is presented on different modeling and simulation based on the applied semiconductor physics of carbon nanotubes.

In the past decades, although carbon nanotubes have undergone massive research, considering the success of silicon, it has, nonetheless, been difficult to appreciate the potential influence of carbon nanotubes in current technology. The main objective of this book is therefore to give a wide variety of possible applications of carbon nanotubes in many industries related to electron device technology. This should allow the user to better appreciate the potential of these innovating nanometer sized materials.

Readers of this book should have a good background on electron devices and semiconductor device physics as this book presents excellent results on possible device applications of carbon nanotubes.

This book has been outlined as follows: it begins with a very interesting analysis on the synthesis and properties as well as fabrication techniques. This is followed by a study on different models and simulations performed on carbon nanotubes. Lastly, the book presents a significant amount of work on different devices and applications available to current technology.

A list of the chapters is given below. It is recommended to the reader to go over the following brief descriptions, as they provide an excellent preview on the material and results of the book's chapters.

Chapter 1. Carbon Nanotube Synthesis
This chapter provides information on the versatility of carbon element, which allows the forming of more than 50% of known chemical compounds. The procedures most commonly used include: arc discharge, laser ablation and catalytic decomposition of carbon-containing compounds over catalyst: the so-called chemical vapour deposition (CVD) techniques on a flat substrate.

Chapter 2. Syntheses and Electronic Applications of Helical Carbon Nanofibers
This chapter describes the history, classification, synthesis, and application of HCNFs. It mainly introduces research results that are compared with the literature. The problems that still remain in the CVD growth and the future researches of HCNFs are discussed.

Chapter 3. Synthesis and Properties of the Arrays of Magnetically Functionalized Carbon Nanotubes
The purpose of this chapter is to summarize actual results regarding synthesis of multiwall carbon nanotubes, particularly, magnetically functionalized multiwall carbon nanotubes (MFCNTs), with the use of iron nanoparticles as growth catalyst and complex analysis of their crystal structure, composition, and magnetic properties as a function of peculiarities of synthesis procedure.

Chapter 4. Characterizing Multi Walled Carbon Nanotube Synthesis for Field Emission Applications
This chapter's effort focuses on the growth of multi-walled carbon nanotubes for field emission. The potential applications being considered require that the CNT synthesis method be compatible with conventional substrate materials, chiefly silicon, and micro-fabrication processes to allow integration with conventional electronic devices.

Chapter 5. Microwave Assisted Preparation of Carbon Nanotubes with Versatile Functionality
In this chapter, the awareness of the particular microwave absorbing properties of CNTs and their different behavior, with respect to typical organic compounds, create a possibility for the preparation of a wide range of new materials useful in assorted fields, including telecommunications, biomedical applications, and illumination technologies. Following the examples discussed in this chapter, it is clear that the potential of microwave development in the 21st century is considerable.

Chapter 6. Implantable Electrodes with Carbon Nanotube Coatings
This chapter will discuss the use of CNTs as active coatings for implantable neural electrodes (NEs). It begins with the background and motivation behind NEs and it then discusses a few examples of electrical stimulation and recording used in treating or ameliorating various nervous disorders.

Chapter 7. Carbon Nanotube Fabrication: Patent Analysis
In this chapter, patent bibliometric analysis and patent network analysis are used to analyze patents for CNT fabrication. The goal is to find the overall relationship among

the patents in the patent network and grasp the key technology of CNT fabrication. Finally, suggestions on future directions and trends of CNT fabrication based on the results of analysis are presented.

Chapter 8. Modeling of Carbon Nanotube Field Effect Transistors
This chapter starts with a brief summary of progress in CNTFET technology (planar and coaxial CNTFET). It is followed then by a description on the simulation approach used, the non-equilibrium Green function. Numerical simulations are used to discuss some key issues in device physics such as ballistic transport, transport with scattering and current-voltage characteristics of CNTFET.

Chapter 9. Functionalization Methods of Carbon Nanotubes and Its Applications
In this chapter, the applications of carbon nanotubes as functional materials in the region of biosensing, fuel cells, medical treatment, and so on, especially in the region of thermal conductivity are summarized. There is a belief that the researchers can, with the content of this chapter, gain deeper insight into the study field of carbon nanotubes.

Chapter 10. Nanodesign and Simulation Toward Nanoelectronic Devices
This chapter will show how design nanoelectronic component embodied with interesting device characteristics can be achieved, especially rectifying diodes. This chapter shows how a simple strategy for designing nanoelectronic diodes is creating CNT heterojunction and controlling their electronic structure.

Chapter 11. Low Frequency Noise Spectroscopy at Nanoscale: Carbon Nanotube Materials and Devices
This chapter describes noise properties of carbon nanotube based materials and devices. After a brief introduction on peculiarities of transport and noise properties of CNTs, this chapter introduces main noise components and theoretical models of the flicker noise directly related to conductivity of the materials. Furtheron, a review on the noise properties of individual CNT-based structures, which are considered to be the best from a nanoscale fundamental studies point of view, is presented.

Chapter 12. High Frequency Properties of Carbon Nanotubes and Their Electromagnetic Wave Absorption Properties
In this chapter, there is a great discussion on the static magnetic properties of MWCNTs and SWCNTs, as well as their electromagnetic wave properties. This chapter ends with a study on the doping effect of MWCNTs on the electromagnetic properties of NiCoZn spinel ferrites.

Chapter 13. Application of Carbon Nanotubes to Mirror Actuators for Space Laser Communications
This chapter studies the potential of the polymer actuators to be used in the optical terminals. For the study, a scenario in which an optical ground station and a satellite in a low earth orbit carry out laser communications is assumed. The angular operations of

the movable parts to track the communicating counter object are estimated. By using this sample, the angular operation characteristics of the actuator are investigated.

Chapter 14. Sonophysically Exfoliated Individual Multi-Walled Carbon Nanotubes in Water Solution and Their Straight Forward Route to Flexible Transparent Conductive Films
In this chapter, the authors proposed to create a sonophysically-exfoliated method with the aid of surfactants or polymers that produce homogeneous MWCNTs–water solutions. Significantly, the resulting suspensions of water-soluble MWCNTs were homogeneous and the MWCNTs were uniformly dispersed for at least two years; neither sedimentation nor aggregation of nanotubes was observed.

Chapter 15. Application of Multi-Walled Carbon Nanotubes for Innovation in Advanced Refractories
In this chapter, CNTs are introduced into refractories to improve their mechanical properties and thermal conductivity, such as Al_2O_3-C refractories for slide gates and carbon blocks for blast furnaces in iron and steel making industry.

Chapter 16. Carbon Nanotube Based Photonic Devices: Applications in Nonlinear Optics
This chapter starts with the description of the physical mechanisms that are accountable for the exceptional optical properties of carbon nanotubes (CNTs). Various methods for fabrication and the potential applications of CNTs in optical switching devices are presented. In addition there is an extensive discussion in the future of CNT-based photonic devices in the context of becoming an integral part in the fast developing fiber laser technology.

Chapter 17. Carbon Nanotube Industrial Applications
In this chapter, PVA is selected as substrate and mixed-acid and hydrogen peroxide modified carbon nanotube as filler. The carboxylation products are then subjected to characteristic analysis to learn the effect of reaction condition on the carboxylation degree of CNTs. This chapter, for the first time, provides investigation into the effect of carboxylation method on carbon nanotube structure and property.

Chapter 18. Carbon Nanotube Nanofluidics
This chapter introduces and provides an overview on Carbon Nanotube Nanofluidics with three focal areas: water transport, gas transport and ionic liquid transport. Carbon Nanotube Nanofluidics can be defined as both a discipline and a research area that pertain to mass transport under nanoscale confinement given by CNT. In this chapter, it is shown how nanoscale mass transport phenomena takes place inside CNT.

Chapter 19. Carbon Nanotubes Based Radiation Detectors
In this chapter, the possibility to use carbon nanotubes in designing new radiation detectors is discussed. First, a proof of the possibility to employ electronic signals produced inside CNTs is given by discussing the condition where nanotubes are deposited on sapphire that is passive both from the optical and the electronic point of view. Then, the possibility to exploit carbon nanotubes in combination with other materials like silicon is presented.

Chapter 20. Carbon Nanotubes in Passive RF Applications
The aim of this chapter is to introduce to the reader with an updated view for the problems of electromagnetic field interaction with carbon nanotube with emphasis on the possible passive RF applications. This chapter also presents possible applications of carbon nanotubes based on their absorbing properties in microwave frequencies.

Chapter 21. Chemically Modified Carbon Nanotubes: Characterization and Their Applications
In this chapter, the modification routes are presented and mainly classified into two types namely surface modification and bulk modification. The surface modification includes electrochemically-induced method, polymer grafting and metal nanoparticle deposition. The bulk modifications include chemical reduction of diazonium salts using hypophosphorous acid as a reducing agent, which is a thermally activated covalent, microwave assisted and ball milling modification.

Chapter 22. Laser Patterning of Carbon Nanotubes Thin Films and Their Applications
This chapter reports a new low-temperature method for fabricating thin film MWNTs on a polycarbonate substrate based on the laser peeling method. This method can fabricate a film with varying MWNTs concentrations straightforwardly. The fabricated sparsely networked MWNTs thin film are shown to exhibit the feature of sufficient outcrop tube tips on the film surface.

Acknowledgments
I would like to express my thankfulness to the authors of the chapters in this book for their excellent contributions in their areas of expertise and for the efforts invested in the publication of their work. I am positively sure that the material published in this book will be of a great help and genuinely appreciated by students, professors, and researchers all around the world.

Jose Mauricio Marulanda
The Editor

Part 1

Synthesis and Properties

1

Carbon Nanotubes Synthesis

Eba Medjo Rolant
University of Yaoundé I, Faculty of Science,
Republic of Cameroon

1. Introduction

Carbon is the most important element of the periodic classification for human Being. It is known since prehistoric times in form of diamond. Many centuries after, the graphitic form is discovered and used. The other forms completing the traditional forms of carbon, carbynes and amorphous carbons are recently known. The history of modern Carbon Science started more than a hundred years ago, and continues to expand rapidly. In the earlier years of the decade 1890, Hughes and Chambers were studied carbon fibers and filaments. Half century later, reports in hollow of carbon fibers were published, presenting the structures as being composed of many finer threads and twisted, with thickness varying from 10 to 200 nanometers. At that time the demand of improved mechanic properties of carbon materials by space and aerospace industry, led to real progress in production and characterization of carbon based materials.

In the 1970 and 1980 decades, sustained investigations have led to many techniques of synthesis of carbon materials (Baird et al, 1971; Dresselhaus et al, 1988), many methods of characterization and of course an important number of novel carbon allotropes, with a generic name of *carbon nanostructures* (CNSs). The first discovered carbon nanostructure, is the fullerene in 1985, the second is the carbon nanotube (CNT) in 1991 by Sumio Iijima of the NEC, Japan (Iijima, 1991). Nowadays, there is a plethora of carbon nanostructures. Among these novel nanostructures, carbon nanotube exhibits unique physical and chemical properties. It is promising to revolutionize several fields of fundamental science and contribute as major component of nanotechnology. It can be used in composite materials or in individual functional element of nanodevices such as: hydrogen storage, nanomanipulation, medical usages and nanoporous membranes. Besides the attractive aspects of carbon nanotubes, their synthesis techniques are complex compared to other materials used in different domains of technology and different existing methods of synthesizing. These methods lead to CNTs with sometimes an important quantity of impurities incorporated, encapsulated or adsorbed, whose amount and types depend on techniques and parameters of synthesis.

This chapter provides information in the versatility of carbon element, allowing him to form more than 50% of known chemical compounds. There is a considerable amount of literature on the study of carbon nanotubes grown by varieties of synthesis techniques. The procedures most commonly used include: arc discharge, laser ablation and catalytic decomposition of carbon-containing compounds over catalyst: the so-called chemical vapour deposition (CVD) techniques on a flat substrate (Dresselhaus & Endo, 2001). This

last method has attracted much attention due to the fact that it appears to be a promising technique for the production process at relatively low cost and mass quantities. It has become the most popular technique of CNTs synthesis and can lead to a controlled growth of the CNTs by varying operating parameters such as gas mixture, temperature, pressure and catalyst.

2. Carbon hybridization

In the nature, there are some pure materials that have striking different properties even made of the same atoms, carbon is one of them. Found in abundance in the universe, in the sun, in the stars, the comets and in the atmosphere, carbon is also the basic component of all organic matter. It is found everywhere from the graphite in a pencil, to the soot in a chimney. Two very popular materials: graphite and diamond could not be more different. Both are made of carbon atoms linked through strong bonds. Natural carbon exists in two isotopic forms, ^{12}C and ^{13}C. The nucleus of the abundant isotope of carbon ^{12}C is composed of six protons and six neutrons. Neutral carbon atom is tetravalent and has totally six electrons with four of them occupying the outer orbit. Therefore, the electronic configuration of the carbon atom at fundamental state is $1s^2 2s^2 2p_x^1 2p_y^1 2p_z^0$ and does not explain several bonds of carbon structures. According to organic chemistry, one of the two $2s$ electrons is promoted to $2p_z$ orbital. So the electronic wave functions for the four weakly bound electrons can mix each others, thereby changing the occupation of the $2s$ and $2p$ orbitals, since the energy difference between the lower $2s$ and the upper $2p$ levels is low compared to the binding energy in the chemical bonds. This mixing of atomic orbitals is called *hybridization*. In carbon atom, three possible hybridizations occur denoted sp, sp^2 and sp^3.

In the sp hybridization, there is linear combination of $2s$ orbital and one of the three $2p$ orbitals, $2p_x$ for example. From these two atomic orbitals, two equivalent orbitals are formed, called *hybridized orbitals* and, are expressed by linear combinations of $|2s\rangle$ and $|2p_x\rangle$ as illustrated in Fig. 1, and denoted $|sp_a\rangle$ and $|sp_b\rangle$.

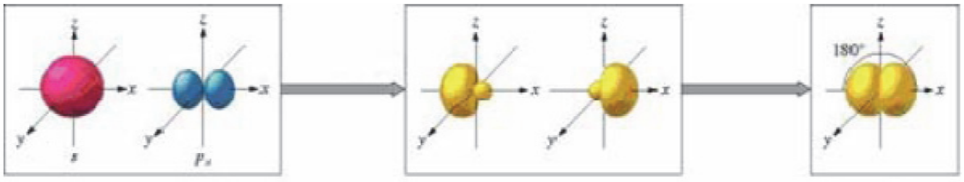

Fig. 1. *Sp* hybridization and form of resulting structure orbitals of carbon atom

In the sp^2 hybridization, three atomic orbitals are involved. The $2s$ and two of $2p$ orbitals, for example $2p_x$ and $2p_y$, are mixed. The three obtained hybridized orbitals are in the same plane and form three σ bonds in molecules. The resulting structure is planar. The hybrid atomic orbitals obtained have large amplitude in the directions of the three nearest neighbour atoms. These three directions are denoted by a trigonal bonding, as shown in Fig. 2.

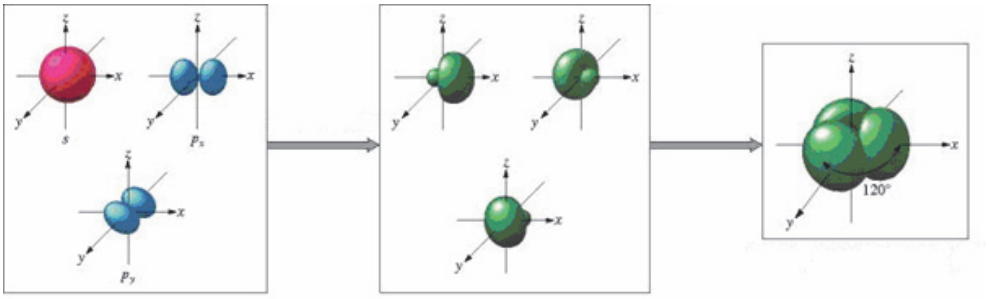

Fig. 2. Illustration of sp^2 hybridization and resulting structure.

The carbon atom provides a sp^3 hybridization through its tetragonal bonding to four nearest neighbour atoms which have the maximum spatial magnitude from each other as graphically presented in Fig. 3. The four directions of tetrahedral bonds from the carbon can be selected as (1,1,1), (-1,-1,1), (-1,1,-1) and (1,-1,1). In order to make elongated wave functions to these directions, the $2s$ orbital and the three $2p$ orbitals are mixed, forming a sp^3 hybridization.

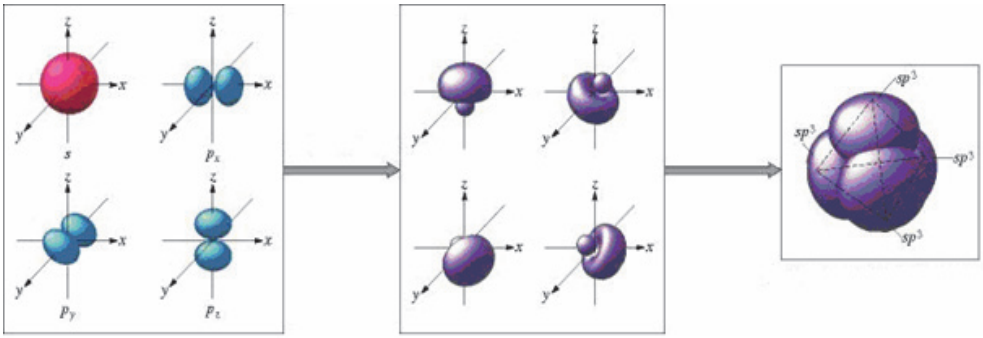

Fig. 3. Illustration of sp^3 hybridization and resulting structure.

3. Carbon allotropes

Carbon is known as the king of chemical elements owing to its versatility and diversity in all fields. It is known to form nearly ten millions different compounds. Carbon holds the sixth place in the list of abundance in Universe. First of all, life is based on carbon. Secondly, the several allotropic forms of carbon have very peculiar and interesting properties. It is known in form of diamond earlier and has been prized for centuries as a gemstone of exceptional beauty, brilliance and lustre. In the form of graphite, it is used since the middle of the 15th century as a writing material. A graphitic basal plane or a graphene layer can be defined as an hexagonal network of covalently bonded carbon atoms or a single two-dimensional (2D) layer of three-dimensional (3D) graphite. The compounds of pure carbon have two *traditional allotropes* known since thousands of years or centuries. They are: diamond, a hard and colourless solid of carbon atoms sp^3

hybridized, and graphite soft and black solid with sp^2 atoms hybridization. The other pure carbon allotropes of this group are the carbynes and the amorphous carbons. The forms discovered from 1985 to now are carbon nanostructures.

3.1 Traditional forms of carbon

3.1.1 Diamond

Diamond always comes on top when compared to any other material. It has been the hardest known substance till the recent two decades and is inert to chemical corrosion and can withstand compressive forces and radiations. Diamond is transparent to visible light, X-rays, ultraviolet radiations and much of the infrared spectrum. It conducts heat better than any other material. Fig. 4 bellow shows an image of diamond by electron microscope.

Fig. 4. Diamond's electron micrograph

At room temperature, it has the highest thermal conductivity than any solid (Dolmatov, 2001). These impeccable qualities arise from the elemental nature of carbon and its bonding structure. In diamond, each carbon atom is covalently single bonded to four other carbon atoms by strong σ bonds. Diamond is now produced by CVD. In this low-pressure technique, artificially produced diamonds have less impurities and crystalline defects, and are affordable and accessible for use in science and industry. Naturally occurring diamond is almost always found in the crystalline form with a purely cubic orientation of sp^3 bonded carbon atoms as illustrated in Fig. 5, while synthetic diamond is a randomly mixture of cubic and hexagonal lattices. In special conditions, carbon crystallizes in *lonsdaleite,* which is a form similar to diamond but with hexagonal structure.

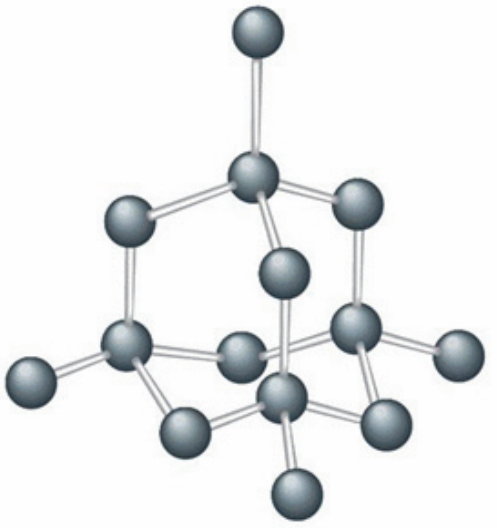

Fig. 5. Cubic structure of natural diamond

3.1.2 Graphite

Graphite is a highly anisotropic solid. Structurally, its interplanar spacing (3.35 Å) is quite large compared to the in plane interatomic spacing (1.42 Å). Physically, its stiffness along the plane is quite large because of strong σ bonds and in the perpendicular direction; it is weak because of the Van der Waal's forces. The planes can be cleaved easily making graphite quite a soft material. Also electronically it is anisotropic, because of π and π^* bands overlap. This has metallic conductivity along the plane and semi-conducting perpendicular to the plane.

The anisotropy in conductivity is about 10^3. The sp^2 hybridization forms a planar structure. It is made of strong fibers composed of series of stacked parallel layers as shown in Fig. 6. It is black and lustrous, optically opaque, unaffected by weathering. Its greasy friction-resistant properties allow for applications in lubricating oils and greases, dry-film lubricants, batteries, conductive coatings, electrical brushes, carbon additives and paints. The graphite is the most stable form of pure carbon structures, stacked with an offset between neighbouring sheets of 1/2 of a lattice constant in an A-B-A-B layering. The sheets are separated by a larger distance (3.35 Ä) and interact weakly with a mixture of covalent and Van der Waals bonding that gives graphite strong lubricating properties, as pieces of graphite planes can glide along each other almost frictionless. The weak bonding of graphite in the perpendicular direction to the planes (Pierson, 1993) makes the synthesis of monocrystalline graphite almost impossible since the planes can shift with respect to each other, and they can also rotate. This gives the so-called *turbostatic graphite*, which has very crystalline planes, but with orientational disorder between them. The best commercial graphite is highly-oriented pyrolitic graphite (HOPG) which has a reduced disorder, but still remains polycrystalline. The theoretical interest in being able to play with true monocrystals of graphite is immense (Novoselov et al., 2004; Bunch et al., 2005).

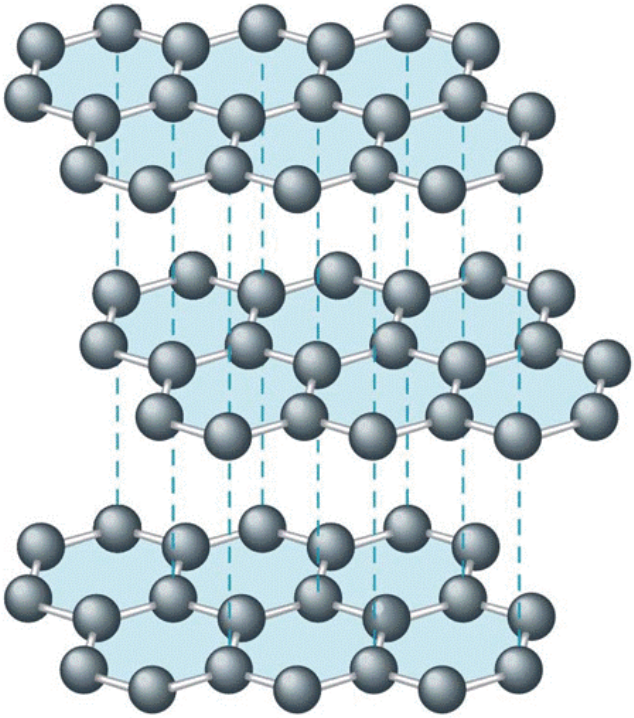

Fig. 6. Hexagonal structure of Graphite in an A-B-A-B layering

3.1.3 Carbynes

Linear chains of carbons which have sp bonding or *carbynes* have been subject to intensive research for many years (Heimann et al., 1999). These carbon structures are stable at high temperature and pressure. *sp* carbon chains can present:

a. alternating single and triple bonds; *the polyyne*, with the following chemical structure

$$\left[-C\equiv C-C\equiv C-\right]n$$

b. only double bonds; *the polycumulene*, chemically structured as follow

$$\left[=C=C=C=C=\right]n \text{ with } n>10 \text{ (Heimann et al., 1983).}$$

Theoretical calculations suggest that polycumulenes are less stable than polyynes (Heimann et al., 1983). Both species are characterized by an extremely high reactivity with oxygen, hydrogen and a strong tendency to interchain cross linking (Heimann et al., 1999), thus rendering the direct observation of a pure carbyne-assembled solid is still a major challenge. Carbynes are silver-white coloured and are found in meteoritic carbon deposits, where they are mixed with graphite particles. Synthetic carbynes have also been prepared by sublimation of pyrolytic graphite. They are formed during very rapid solidification of liquid

carbon, near the surface of the solidified droplets formed upon solidification. In the solid form, carbynes have a hardness intermediate between diamond and graphite.

3.1.4 Amorphous carbons

The amorphous carbons or free reactive carbons are carbon allotropes that do not have any crystalline structure. Scientific research on amorphous forms of carbon has found importance in recent decades owing to its rich underlying physics and tremendous applications. The widely known forms of amorphous carbons are: black of carbon, carbon fibers, porous carbon, glassy carbon, diamond like carbon (DLC) and pyrocarbon. Amorphous carbons (*a*-C) and diamond-like carbon (*ta*-C or DLC) solids are characterized by a large varieties of types and properties that stem from combinations of principally two hybridized forms of carbon sp^2 and sp^3. The properties of amorphous carbon films depend on the parameters used during deposition. One of the most common ways to characterize amorphous carbons is through the ratio of sp^2 to sp^3 hybrid bonds present in the material. Amorphous carbons are usually applied as coatings to other materials.

3.2 Carbon nanostructures

3.2.1 Fullerenes

Fullerenes are molecules consisting of carbon sheets of hybridized sp^2, forming a closed sphere structure. These spherical structures are built up out of hexagons and pentagons. The fullerene's formation is based on the introduction of pentagonal, heptagonal or other kind of "defect" rings between the hexagonal rings of the graphene sheets, which favour a higher curvature of the sheet. Each fullerene, by definition, consists of 12 pentagons (Fig. 7), since a sphere containing *n* hexagons cannot be closed otherwise according to Euler's theorem.

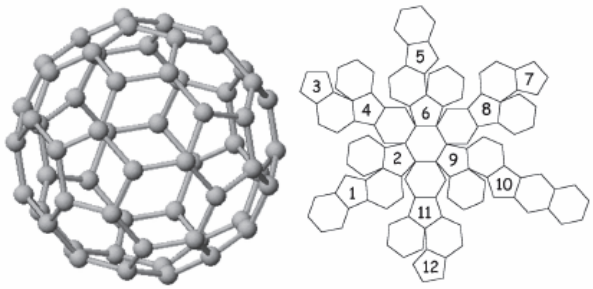

Fig. 7. Fullerene C_{60}. The necessary twelve pentagons to fulfil Euler theorem are numbered

C_{60} is made of 20 hexagons and 12 pentagons. Each carbon atom is at the intersection of two hexagons and one pentagon. When compared to planar graphene, the introduction of a pentagon gives a positive curvature to the surface. Euler's rules dictate that to create a closed surface, we need a total "curvature charge" of 12 (Hamon et al., 2001). As a result, all the simple fullerenes will have the same number of pentagons, 12, and differ only by the number of hexagons inserted between them. The extreme small fullerene C_{20} is too curved to be stable, as are the other intermediate fullerenes before C_{60}. C_{60} defines the "isolated

pentagon" rule: all pentagons in a stable fullerene must be surrounded by hexagons. The smallest sphere fulfilling these conditions is C_{60}.

This molecule, consisting of sixty carbon atoms, forms a perfect **"soccer ball"** structure. Due to its similarity to the domed houses dreamed up by the architect Buckminster-Fuller, the molecules were named *Buckminster fullerenes or fullerenes* in short. New and larger shapes were discovered as shown in Fig. 8, with 70, 76, 82, 84… carbon atoms (Kroto, 1987), and even more. Sometimes fullerenes fit together concentrically forming bucky onions (Mordkovich et al., 2002).

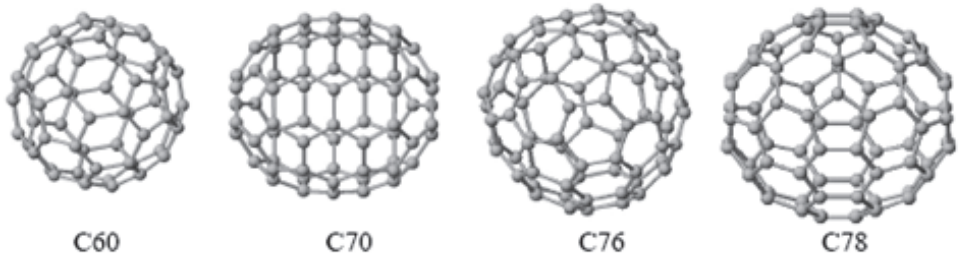

Fig. 8. Some fullerenes.

3.2.2 Carbon nanofibers

Carbon nanofibers (CNFs) are conical structures that have diameters varying from a few to hundreds of nanometers and lengths ranging from less than a micron to millimeters. The internal structure of carbon nanofibers varies and is comprised of different arrangements of modified graphene sheets. In general, CNFs have a structure which is a mixture of aligned graphene planes as well as a bamboolike or cup-stacked structure, previously ascribed to herringbonelike structure, in other words a nanofiber consists of stacked curved graphite layers that form cones or "cups" (Krishnan et al., 1997; Melechko et al., 2005). Currently there is no strict classification of nanofiber structures. The main distinguishing characteristic of nanofibers from nanotubes is the stacking of graphene sheets of varying shapes. Defining α as an angle between the fiber axis and the graphene sheet near the sidewall surface, nanofiber with $\alpha = 0$ is a special case in which, one or more graphene layers form cylinders that run the full length of the nanostructure. This arrangement, with its closed and semi-infinite surface results in extraordinary properties that made this type of nanofiber known to the world as a carbon nanotube.

3.2.3 Carbon nanotubes

In 1991, Sumio Iijima discovered (Iijima, 1991) yet another fascinating form of carbon, in the soot recovered from the discharge of an electrical arc between graphite electrodes. He found ultra-thin tubules of carbon: the carbon nanotube. Since this period, countless papers on carbon nanotubes, their properties, and applications have appeared and generated great interest for future applications based on their field emission and electronic transport properties, their high mechanical strength and chemical properties (Hueczko, 2002; Meyyappan et al., 2003). Carbon nanotubes can be described as cylindrically shaped molecules formed of rolled up single or multilayer sheets of graphitic planes presented on

Fig. 9. In other words, it can be considered as an infinite strip cut out of a graphene sheet and rolled up along the direction perpendicular to the strip. Geometrically, CNTs have one of the highest aspect ratio of any object in nature. Their length can exceed several millimeters for diameters around ten nanometers. The characteristics of a carbon nanotube, and the position of every atom in it, can be determined by just two integers. All what is needed, it is the circumference of the tube, which joins the two equivalent atoms along the circumference. These will be superimposed once the strip is rolled up.

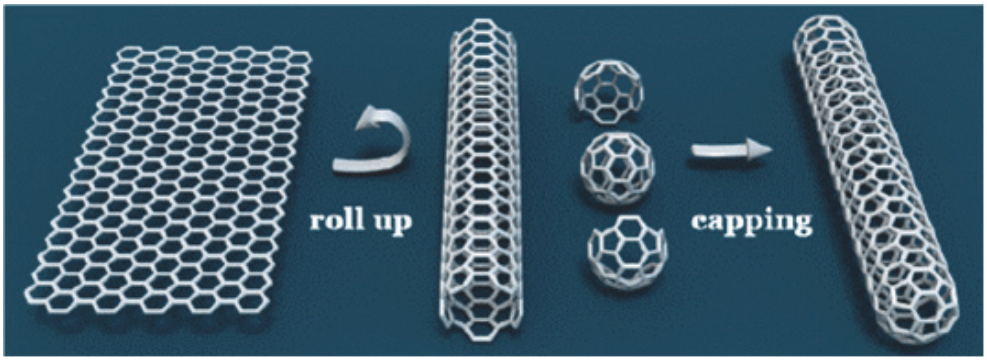

Fig. 9. SWCNT capped with half of a C_{60} fullerene molecule.

The vector between the two graphene's atoms $\vec{C}_h$, called the chiral vector is part of the 2 dimension (2D) crystalline lattice, and denoted by the two integer indices, n and m called *Hamada integers* (Hamada et al., 1992). If $\vec{u}$ and $\vec{v}$ are the lattice vectors of a 2D graphene plane as schemed in Fig. 9, the chiral or helicity vector is expressed by:

$$\vec{C}_h = n\vec{u} + m\vec{v} \tag{1}$$

The circumference of the tube L is the length of $\vec{C}_h$ and is expressed by:

$$L = a_{C-C}\sqrt{3(n^2 + m^2 + nm)} \tag{2}$$

Experimentally, for an inter-atomic distance $a_{C\text{-}C} = 1,44$ Å, the diameter of the tube is

$$D_t = \frac{L}{\pi} = \frac{a_{C-C}\sqrt{3(n^2 + m^2 + nm)}}{\pi} \tag{3}$$

Here a is the in-plane lattice constant, equal to about $a = 2,49$ Å
Various types of carbon nanotubes are characterized by their respective chiral angles θ

$$\begin{cases} \sin\theta = \dfrac{\sqrt{3m}}{2\sqrt{n^2 + m^2 + nm}} \\ \cos\theta = \dfrac{2n + m}{2\sqrt{n^2 + m^2 + nm}} \end{cases} \tag{4}$$

θ is so that $0 \le \theta \le 30°$.

The determination of (*n, m*) and other physical properties, in order to establish correlations and use theoretical models, is still a hot topic of research. CNTs are much smaller than most of the vapour-grown carbon fibers (VGCFs) that have been studied for many years, but the smallest VGCFs often closely resemble to CNTs in their external morphology. However, CNTs are clearly distinguished from VGCFs by the fact that a perfect CNT is a single crystalline grain, and even a defective CNT is a single crystal in cross section, except where the defect occurs. The simplest termination is a hemispherical cap formed by a half of fullerene. General rules have described the topology of the termination as a function of the Hamada indices (*n, m*). The prototypical example is shown in Fig. 9, but CNTs can also be open ended. According to the integers *n* and *m*, CNTs can be metallic, if *n-m* is a multiple of 3, and semiconductor otherwise.

The exceptional low-dimensionality and symmetry of carbon nanotubes are at the origin of their spectacular physical properties governed by quantum effects. A carbon nanotube can be one of three types, depending on the orientation along which the graphitic planes are folded. When the value of θ is, respectively, 0°, 30° or takes any intermediary value, a nanotube is respectively called zigzag, armchair or chiral as illustrated in Fig. 10 bellow.

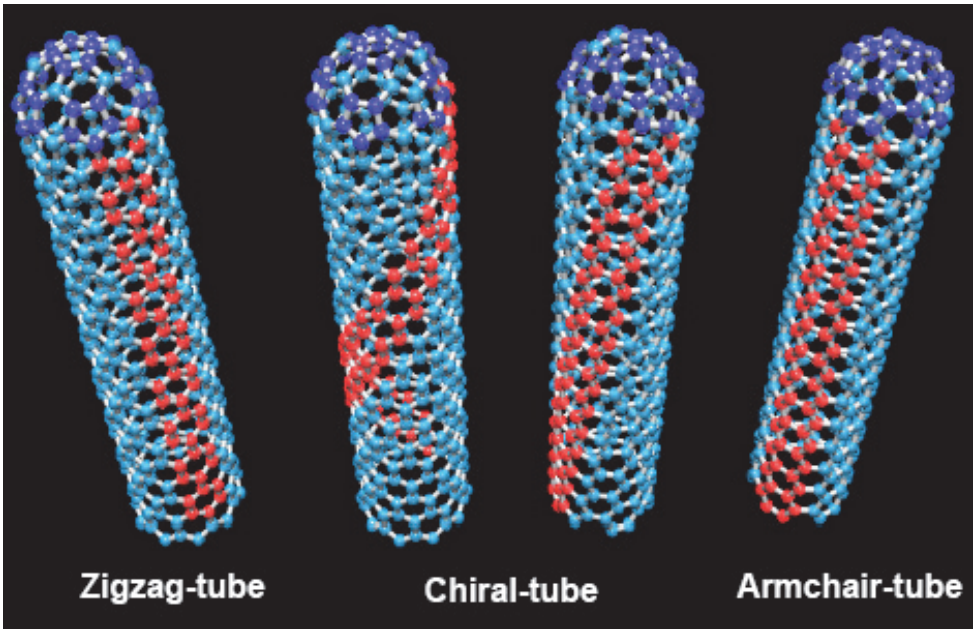

Fig. 10. Possible vectors specified by the pairs of integers (n, m) for general carbon nanotubes including armchair, zigzag, and chiral.

Two types of CNTs can be distinguished; single walled carbon nanotubes (SWCNTs) and multi-walled carbon nanotubes (MWCNTs) as seen in Fig. 11. They can have different properties one another.

Typical outer diameters are approximately 1-6 nm for SWCNT and 6-100 nm for MWCNT. MWCNT can be rolled up with their graphene layers concentric or spiral.

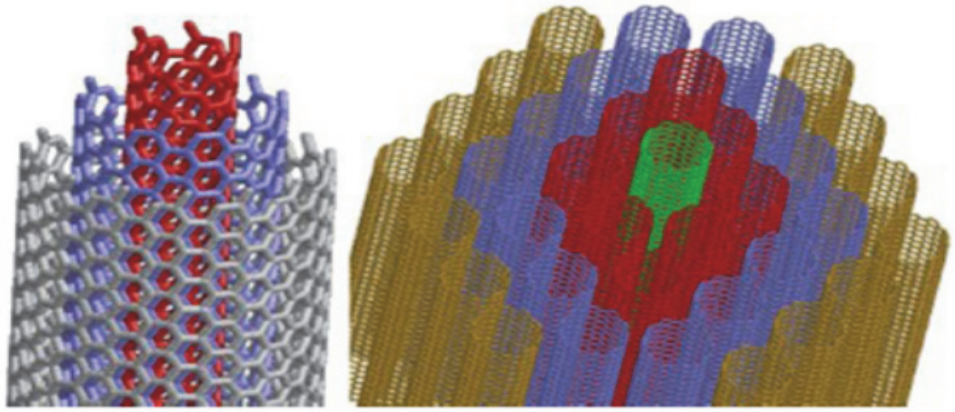

Fig. 11. Different kinds of CNTs with regard to the number of walls: (a) SWCNT and (b) MWCNT.

3.2.4 Other carbon nanostructures

There are nowadays a plethora of carbon nanostructures. Among them, one can mention:

- The Single walled carbon nanohorns (SWNHs): they are typically constituted by tubes of about 2 to 5 nm of diameter and 30 to 50 nm long, which associate with each others to give rise to round-shaped aggregates of 100 nm of diameter. Their large surface areas and inner nanospaces are of great importance since they ensure a great affinity, for example, with organic electron donors. They are especially good for hydrogen storage and electric field emission.
- The Carbon nanosheets (CNs), they are known as field emission source for high emission.
- The Carbon nanoporous are carbon "balls" often linked together as granular electuary waiver some holes between which shows an amorphous structure. Their images reveal nanopores distribution all around the carbon nanoporous balls.
- The Carbon nanoparticles (CNPs) which are characterized by an average diameter of 80 nanometers. They have in general catalyst particles encapsulated in.
- The Carbon nanobuds (CNBs): they are carbon nanostructures in which fullerenes are covalently attached to outer sidewall of CNTs. It is a hybrid material with useful properties, both of fullerenes' and CNTs'. CNBs have been found to be exceptionally good for field emitter.

4. Synthesis of carbon nanotubes by chemical vapour deposition CVD

Many applications as electronics' need CNTs with high density, high quality, and good alignment as prerequisites, because these qualities lead to stable parameters of the devices. And that is why special efforts are done in synthesized techniques since decades. Most of the existing models for the catalytic CVD growth of nanotubes are based on a mechanism formulated several years before the official CNTs discovery (1991), proposed by Baker (Baker et al.,1972), The CNSs growth method using a direct current plasma and hot

filaments-enhanced catalytic chemical vapour deposition process has been fully described by Cojocaru (Cojocaru, 2003). Chemical vapour deposition can produce larger quantities of CNSs. CVD of hydrocarbons over metallic catalysts yields the carbon nanotubes and other carbon filaments with diameter changed from 1 to 100 nm depending on the synthesis operating parameters as temperature, kind and size of catalyst (Ivanov et al., 1994). A reactant gas containing carbon is inserted into a vacuum chamber at a given temperature between 600 and 1000 K. In the presence of an appropriate transition metal (TM) catalyst, the gas is decomposed and, in the convenient conditions of temperature and pressure, the carbon can feed the growth of CNSs. Nanostructures grown by CVD are usually not straight and contain some defects.
There are many variants of CVD. We present the one known as Hot Filament Plasma Enhanced Catalytical Chemical Vapour Deposition (HF PE CCVD).

4.1 Substrate preparation

The substrate is prepared by the deposition of a SiO_2 layer (thickness 8 nm) by a Distributed Electron Cyclotron Resonance (DECR) plasma process on a Si(100) sample (Sb n-doped with ρ = 3 mΩ.cm; size 8.5 x 6 x 0.245 mm^3). SiO_2 is evaporated on Si(100) for two main reasons: it is a protective barrier layer that prevents the formation of transition metal silicide through direct interaction with silicon, and SiO_2 is a non-wetting substrate that is convenient for transition metal (TM) diffusion and aggregation. However the thickness of the SiO_2 layer must be thin enough to allow electron conduction through tunnelling for field emission measurements. This sample SiO_2/Si(100) is then transferred into a stainless steel Ultra High Vacuum (UHV) preparation chamber (base vacuum 10^{-10} mbar) where TM consisting of Co or Fe or a mixture of them is evaporated without air removal. TM is evaporated with an OMICRON EFM3 effusive source at a pressure within 7-10.10^{-10} mbar on the sample heated at 925 $\pm$ 20 K during 30 min. The flux rate at 973 K is estimated to 0.025 nm of equivalent layer per minute from an in situ X-ray photoemission spectroscopy (XPS) analysis. In other cases the transition metal is deposited by sputtering (Cojocaru & Le Normand, 2006).

4.2 CNTs growth by the DC HF CCVD

After the catalyst evaporation on the substrate, the whole is further transferred into an UHV CVD chamber for the growth of the carbon nanotubes and nanostructures in general at base pressure lower than 10^{-9} mbar (Fig. 12). The gas mixture 100 sccm (Standard cubic centimetres per minute) C_2H_2:H_2:NH_3 is thermally activated by hot filaments up to a power P_f around 150 W and kinetic energy-activated by polarisation between tantalum grid electrodes with the cathode grid in front of the sample at V_p = -300 $\pm$ 10 V. The discharge is ignited and stabilized by the electron emission of the hot filaments. This ensured a high concentration of ionic species as well as activated radicals in front of the sample. A small additional negative extraction voltage of about V_e = 10 V is applied to the sample, which allowed withdrawing a controlled current of ionic species onto the sample (I_e), with extraction power $P_e = I_e * V_e$. The temperature which value is 973 K is controlled and regulated by an independent infrared heater set on the rear side of the sample. A Pt/PtRh thermocouple is contacted the rear side of the sample during the temperature rise. This thermocouple is switched off when the polarisation is started. The contact is then used to

monitor the electric current onto the sample due to the discharge. The sequences of deposition are the following: the sample is first heated under vacuum (10 K/min, 573 K, 10 min). Then the temperature is risen to 973 K (10 K/min; 40 min) in a H_2 atmosphere at 15 mbar. The main growth parameters are shown on Table 1.
The Acetylene and ammonia were introduced. Subsequently the primary discharge and the extraction discharge onto the sample are adjusted to the desired values. The extraction current I_e is set constant throughout the deposition process.
To stop the CNSs growth, the acetylene, the polarisation, the filaments and finally the hydrogen feed through are subsequently switched off. The growth mechanism of CNSs (CNTs, CNFs) occurs cleanly in a process constituting in three steps (Figs 13 & 14):

a. the adsorption and the decomposition of hydrocarbon species such as CH_4, C_2H_4, C_2H_2,
b. the diffusion of carbon through metallic particles and,
c. the extrusion for obtaining the graphitic walls.

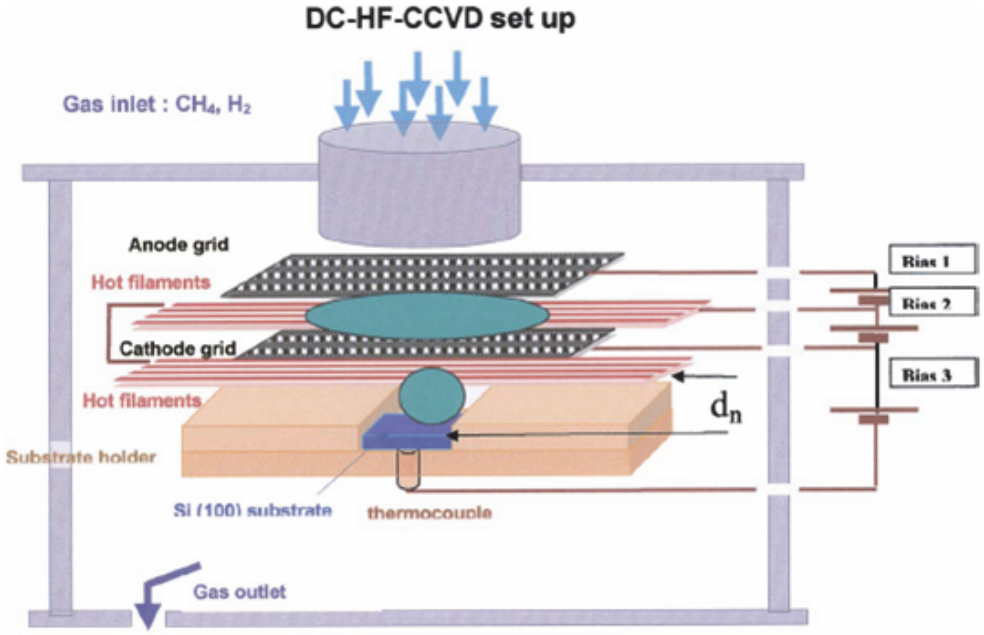

Fig. 12. Representation of the DC HF CCVD system, the distance d_n between the substrate and the bottom of couple filaments is defined. The primary plasma between the cathode and the anode and the extraction plasma above the substrate are displayed in full.

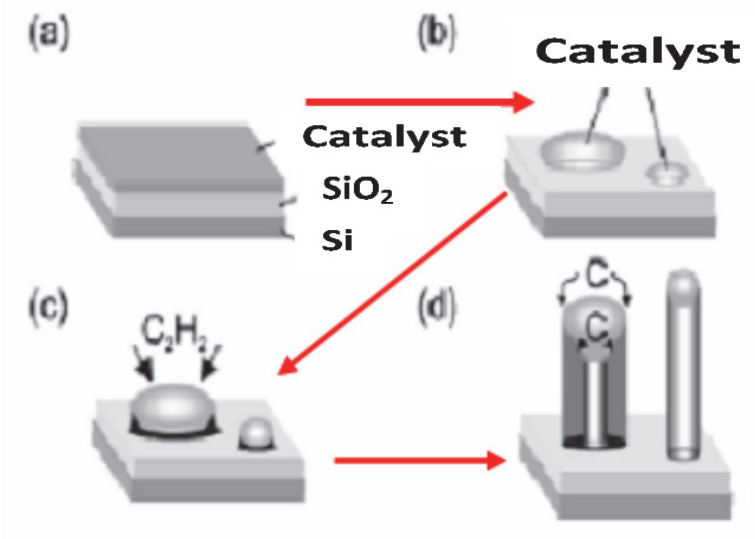

Fig. 13. Representation of the growth mechanism in DC HF CCVD process. (a) is the substrate consisting in silicon, silicon dioxide and catalyst (Co), (b) formation of calyst particles, (c) diffusion of carbon through catalyst particles (d) formation of graphitic walls.

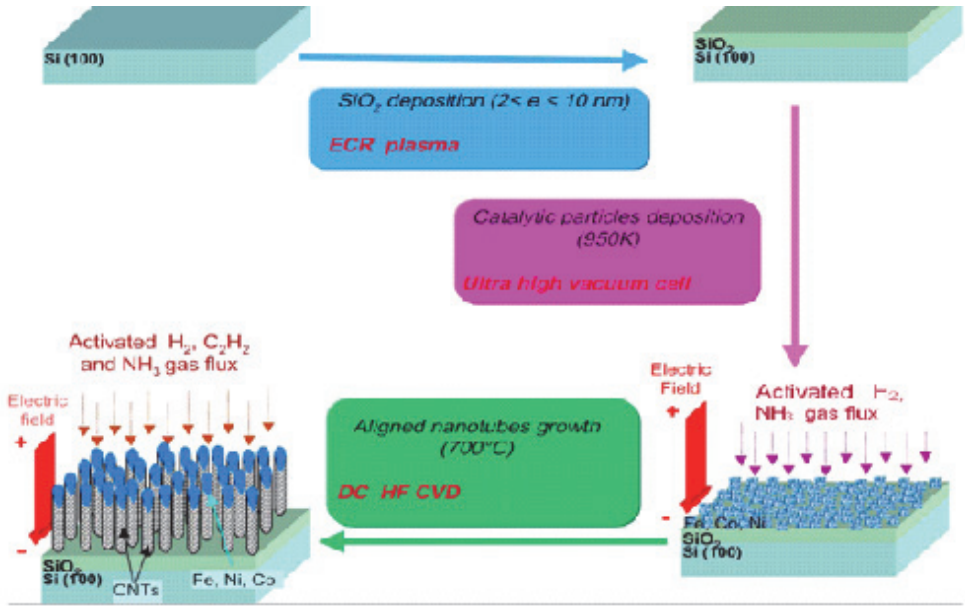

Fig. 14. Sketch of the steps of substrate preparation and CNTs growth in HF PE CCVD.

According to the nature of the hydrocarbon, the mode of deposition of the catalyst as well as the pressure of the gas mixture, the temperature, the hot filaments power and the plasma power, different carbon nanostructures are allowed to grow as shown in Table 2 (Eba Medjo et al., 2009a). The growth process starts after the substrate elaboration and proceeds in the vacuum chamber: The first step is thermal reduction that occurs at temperature between 30 and 700° C.

NH_3 (%)	0	1	3
Temperature substrate (K)	973	973	973
C_2H_2 +NH_3+H_2 (sccm)	100	100	100
C_2H_2 (%)	20	20	20
p (mbar)	15	15	15
t (minutes)	15	15	15
Activation power of the filaments (W) [Temperature of the filaments (K)]	150 [2100]	150 [2100]	150 [2100]
d_n (mm) Substrate-Filaments distance	5	5	5
V^*_p (V) DC activation	310	300	295
I_p* (mA) DC activation	3.75	11	16
V_e** (V) extraction	10	10	10
I_e** (mA) extraction	2	2	2

Table 1. Main experimental growth parameters of PE HF CCVD

Sample	Catalyst	TM deposition Process	**Carbon Nanostructure**	TM/Si	P_f (W)	P_e (mW)	Pressure (mbars)	T (K)
I Nanot24	Co	Sputtering	**CNFs (graphene // substrate)**	/	150	10	15	973
II Nanot29	Co	Sputtering	**CNTs (poorly oriented)**	/	150	30	15	973
III Nanot30	Co	Evaporation	**CNFs (graphene ⊥ substrate)**	0.33	150	30	15	973
IV Nanot31	Co	Evaporation	**CNTs**	0.87	150	30	15	973
V Nanot36	Co	Evaporation	**CNPs**	/	100	20	15	973
VI Nanot42	Co	Evaporation	**CNTs (highly oriented)**	/	145	20	15	1083
VII FLN1	Co	Evaporation	**CNTs (medium oriented)**	/	140	20	15	973
VIII FLN2	Co-Fe	Evaporation	**CNTs (highly oriented)**	/	140	20	15	973
IX FLN4	Co	Evaporation	**CNWs**	/	140	20	5	973

Table 2. Carbon nanostructures grown on SiO_2(5nm)/Si(100) substrate and main preparation characteristics. Other conditions are: 100 sccm C_2H_2:H_2:NH_3 with relative content 20:79:1, filaments- substrate distance is 5mm; gas flow: 100 sccm.

At this step, the plasma is not yet activated. The formation of TM particles begins. The second step is the catalyst reduction. It takes place at 700°C under the hot filaments thermal activation. With the activated gas flux of H_2 and NH_3, particles are formed. The HF PE CCVD system, the different steps of substrate preparation and CNSs growth are presented in figs 12, 13 and 14 (Cojocaru, 2003; Eba Medjo et al., 2009b). The last step is the growth of the CNSs after the addition of the acetylene and ammonia gas always. From the technologic point of view, CNTs synthesis aims to optimize field emission and implies the optimization of CNTs films growth in forms of bulk aligned and oriented perpendicularly on a plane substrate. To satisfy these requirements, methods of synthesis by chemical vapour deposition enhanced catalytically by using plasma and hot filaments are considered to be the most versatile. The presence of TM (Fe, Co, Ni) as catalysts spread on the substrate allows controlling local nucleation deeply for oriented CNTs.

The choice of transition metals is due to the metal-carbon diagram phase. In the range of temperatures used (700-1200°C), carbon has a finite solubility in these metals, favour the formation of metal-carbon solid solution, segregation and further precipitation (Helveg et al., 2004). Preparation of metallic particles distribution (size, orientation, density…) is a crucial step of the overview process because the density and the size of TM particles control the size and the distribution of CNTs. To obtain a uniform spatial distribution of TM particles, a proceeding of metal evaporation *in situ* under ultra vacuum under and lower temperature on SiO_2/Si(100) has been performed (Fig. 14).

5. Other carbon nanotubes synthesis methods

5.1 Arc discharge

The arc discharge method, initially used for producing fullerenes, is the most common and perhaps easiest way to produce CNTs as it is rather simple (Iijima, 1991). The most perfect multiwall carbon nanotubes are produced using the arc-discharge evaporation of graphite in an inert atmosphere (Ebbesen & Ajayan, 1992). Arc discharge apparatus is presented in the following figure (Fig. 15).

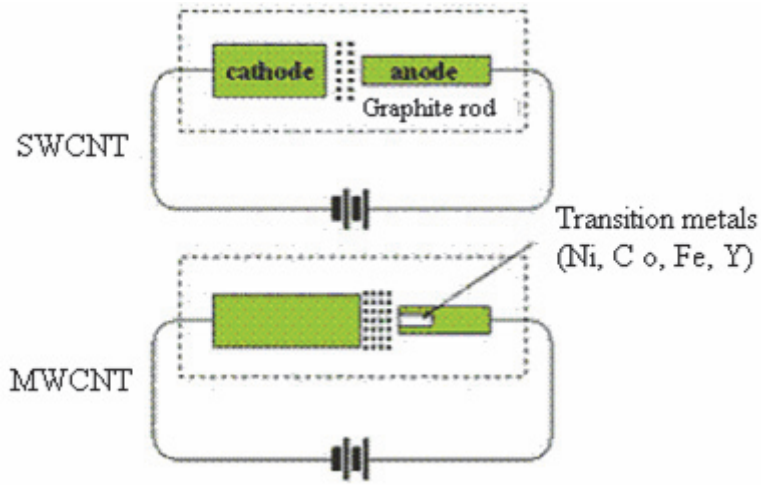

Fig. 15. Schematic diagram of Arc discharge apparatus.

However, it is a technique that produces a complex mixture of components and requires further purification to separate the CNSs from the soot and the residual catalytic metals present in the crude product. This method creates CNSs through arc-vaporization of two carbon rods placed end to end, separated by approximately 1 mm, in an enclosure that is usually filled with inert gas at low pressure. According to recent investigations, it is also possible to create CNSs with the arc method in liquid nitrogen. A direct current of 50 to 100 A, driven by a potential difference of approximately 20 V, creates a high temperature discharge between the two electrodes. The discharge vaporizes the surface of one of the carbon electrodes, and forms a small rod-shaped deposit on the other electrode.

5.2 Plasma arcing

This method was the first for producing CNTs in reasonable quantities. It consists of applying an electric current across two carbonaceous electrodes in an inert gas atmosphere. It involves the evaporation of one electrode as cations followed by deposition at the other electrode. This plasma-based process is analogous to the more familiar electroplating process in a liquid medium. CNTs are formed by plasma arcing of carbonaceous materials, particularly graphite. The fullerenes appear in the soot that is formed, while the CNTs are deposited on the arcing in the presence of cobalt with a 3% or greater concentration. However, when cobalt is added as a catalyst, the nature of the product changes. The mechanism by which cobalt changes this process is still unclear.

5.3 Ball milling

Essentially, this method consists of placing graphite powder into a stainless steel container along with four hardened steel balls. The container is purged, and argon is introduced. The milling is carried out at room temperature for up to 150 hours. Following milling, the powder is annealed under an inert gas flow at temperatures of 1400 °C for six hours. The mechanism of this process is not well known, but it is thought that the ball milling process forms nanostructures nuclei, and the annealing process activates carbon nanotubes growth.

5.4 Laser ablation or laser vaporization

Laser ablation near the surface of the target creates an almost continuous inflow of hot carbon atoms and ions, into the experimental chamber. The shock wave generated by each pulse rapidly decelerates in the ambient gas atmosphere and further propagation of hot atoms proceeds by diffusion, finally forming a mixture of carbon and filling gas with some average density and temperature. The density and temperature of this mixture change with the distance from the target. Depending on the masses of ablated atoms and the atoms of the filling gas, the processes of energy exchange will occur at different rates. If the masses of colliding atoms are comparable, the carbon can lose a significant part of its energy in a single collision. Hence, efficient energy equilibration occurs after several collisions: the carbon vapour is cooling down and the argon gas is heating up.

On the basis of kinetic considerations, the following scenario for carbon nanotubes formation in a carbon-argon mixture created by high repetition rate laser ablation has been suggested. Initially, the chamber gas is at ambient temperature. The continuous inflow of hot carbon increases the temperature in the mixture. When the carbon vapour temperature and the number density reach the level where the probability of carbon-carbon attachment becomes significant, the formation of carbon nanotubes begins. The carbon consumption rate during

this formation process significantly exceeds the evaporation rate due to laser ablation. Therefore, the carbon density rapidly decreases to the value where the formation process terminates. Thus, the ablation rate, target parameters, pressure and the ambient gas determine the formation time, and accordingly, the size of the nanotubes. This technique produces CNTs of almost as high quality as arc discharge. The temperatures reached are included in the range of 1200 to 2000 K, which explains the residual difference in graphitization.

6. Carbon nanotubes contamination

Fig. 16 shows two CNTs XANES spectra with drastic differences. If the defects like: topological defects in the grapgene sheets (the occurrence of pentagons and heptagons), the sp^3 hybridized carbons atoms and incomplete bonding that have slight changes that can be neglected, are not taken into account, it is observed that some features present in Fig. 16 (a) are not found in Fig. 16 (b), especially peaks K and L, and are replaced by P, P′ and P″ (Eba Medjo et al, 2009a).

These new peaks are not intrinsic to CNTs. They are the result of contamination which can be considered as accidental adsorption of atoms, molecules or radical compounds, in agreement with SEM and TEM analysis, where it is not found bundles of CNTs as it may be, according to literature. Among the reasons of the presence of non-intrinsic features in XANES spectra is the presence of TM particles as proved by SEM and TEM. Actually, it is known that the features attributed to the so-called free-electron-like interlayer (FELI) states in the graphite and other carbon nanostructures are also due to contamination (Kuznetsova et al., 2001). The peaks P, P′ and P″ are assigned to adsorbed potassium atoms according to features parameters (Sasaki, 1984; Eba Medjo et al., 2009a). The samples are constituted of different kinds of CNSs. Their behaviour with those contaminants is of great importance and helps to distinguish them. XANES spectra of those samples present many differences. When analyzing unannealed spectra, some of them do not display P, P′ and P′′ features. In Fig. 16, the comparison of chemical inertness of unannealed samples shows an important difference.

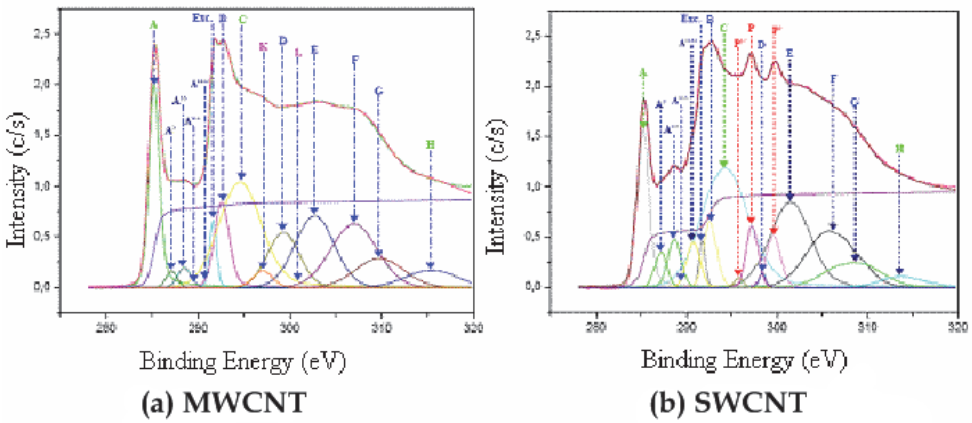

Fig. 16. CNTs experimental and calculated superimposed XANES spectra at grazing incidence from unannealed samples: (a) without potassium contamination, (b) with potassium contamination.

In (a) there is no potassium contamination, while in (b), the intensity of potassium peaks is considerable. The spectrum (a) belongs to MWCNT which is not chemically as reactive as SWCNT (b) with a great reactivity and can easily establish chemical bond. The chemical inertness is important for CNSs that gain less sp^3 character during their growth or the curvature, in other words, those with a great diameter or small curvature. The comparison of XANES spectra of unannealed samples shows another important difference. This difference is due once more to the varying behaviour of carbon nanostructures samples in presence of contaminants. Fig. 16 (a) presents less contamination of potassium than Fig. 16 (b). In the typical case of CNTs, when the outer diameter is important, the CNTs are less chemically active and therefore are not favoured to establish chemical bonds. The adsorption contribution to the signal is observed at the contaminants adsorbed region in the free-electron-like interlayer states band, when no previous annealing of the sample is realized before recording the spectra (Kuznetsova et al., 2001).

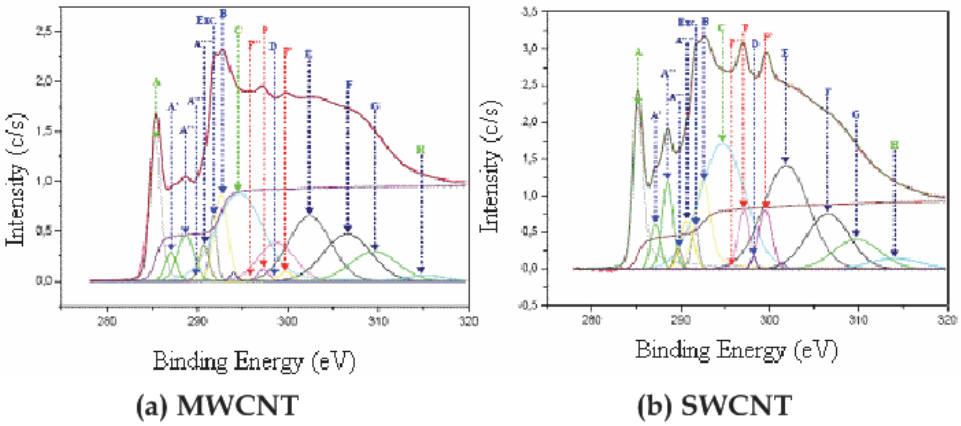

Fig. 17. Contaminated CNTs experimental and calculated superimposed XANES spectra at normal incidence from annealed (550°C) samples: (a) sample is sensitive to thermal annealing; (b) sample is less sensitive to thermal treatment.

But the sensitivity to thermal treatment is not uniformed for each sample, as shown in Fig. 17. The sample in Fig. 17 (a) is more sensitive to thermal annealing than the one whose XANES spectrum is presented in Fig. 17 (b). This difference is assigned to the curvature effect, which is relative to the outer diameter and the sp^2 / sp^3 ratio of the CNT. The contamination is due to atomic, radical or molecular adsorption of many species present or formed during synthesis phase, such as oxygen (O); water (H_2O) and TM. The spectral features P, P′ and P′′ are assigned to potassium (K) along with the IP of K, L…levels of the element. This potassium present in samples might come from the beam line on the synchrotron station.

7. Carbon nanotubes characterization

Because of contamination and defects occurring during synthesis phases and the possibility to obtain many kinds of CNSs, it is basic to characterize each nanostructure synthesized.

Characterization helps to avoid false results, confusions or wrong conclusions concerning nanostructures and their properties, and of course their applications. There are many techniques of CNSs characterization. The most utilize are electron microscopy which is a powerful technique in the sense that, it can be directly correlated to the atomic-scale microstructure of the carbon nanostructure with its physical properties, thus providing a characterization of the morphology and the nanostructure (Somani & Umeno, 2007).
Raman spectroscopy is also used to identify the hybridization of carbon atoms in each of the carbon nanostructures obtained. So this spectroscopy is very important in the characterization of CNSs. XAS recorded on the carbon K-edge is a powerful tool to provide chemically-selective information on the local environment around carbon in solid materials, like diamond, amorphous carbons nitride, amorphous graphitic carbon and CNSs (Eba Medjo et al., 2009a). The technique is also suitable to probe the adsorption of functional organic molecules with information both on the distance and the orientation of bonds (Kuznetsova et al., 2001; Eba Medjo et al., 2009b). This property is due to the angular dependence of the absorption transitions. The angular dependence has been reported on graphite since a long time (Rosenberg et al., 1986) and the analysis has been further refined both on an experimental and a theoretical points of view. The π^* antibonding state corresponds to the out-of-plane bonds in the sp^2 bonding configuration and exhibits strong polarization dependence. According to the absorption process, the signal is maximum when the direction of the electric field of the incident light matches the direction of unfilled orbitals.
The CNSs obtained are of four kinds. When the catalyst is prepared by sputtering and the plasma power rather low, the CNFs can grow with graphene sheets axis parallel to the surface. Strong adhesion of the catalyst to the substrate and low energy ions can explain this mode of growth. Carbon nanoparticules (CNPs) are prepared when the power of the hot filaments is low. The growth of graphene layer seems impossible. The ammonia introduced in gas mixture during the synthesis has three concentrations, which are 0, 1 and 3% respectively. The acetylene concentration remained at 20%. Hydrogen is the third and last gas in the mixture. The activation power of the filaments is 150 W and yields the filaments temperature of 2100 K. The distance d_n between the substrate and the bottom couple of filaments is 5 mm. Under these synthesis conditions it is possible to control the nature of the carbon nanostructures synthesized in agreement with literature (Cojocaru & Le Normand, 2006). The four types of CNSs obtained are, according to SEM images (Table 1):

- Carbon nanowalls (CNWs),
- Carbon nanoparticules,
- Carbon nanofibers, with graphene sheet parallel and perpendicular to the substrate respectively and,
- Carbon nanotubes, with poor, medium and high orientation, respectively (Eba Medjo, 2011).

Within the medium value of the plasma power (Table 2), as shown with SEM study, carbon nanotubes are yet grown. Transmission electron microscope is employed to improve the characterization of the nanostructures by SEM. These samples however display different mutual orientations. The highly oriented films are obtained under optimized conditions and poorly and medium oriented films are also obtained, showing more defects. One of the very important observations is that each carbon nanostructure grown has TM nanoparticles at its top. One observes, TM particles inside tubules, on tubes walls coming from growth process by VLS (Vapour, Liquid and Solid) mode (Helveg et al., 2004). TEM observations show at the same time that the surface of the nanotubes exhibits an amorphous structure due to wall surface defects.

The outer diameters of the CNTs are directly determined from TEM images with high accuracy. Thus the mean outer diameter is 15 nanometers the smallest being 6 nm corresponding surely to SWCNTs or to a few number of walls. The upper values, may account for outer diameters of MWCNTs. The analysis of TEM images leads to extensive values of length, varying from 100 to 400 nanometers. The density of nanotubes spreads also in a very large range. It ranges between 350 to 1000 µm. Fig. 18 (c) shows CNTs completely detached from the substrate with catalyst particles on one end, and the graphitic end of attachment to the substrate. Unfortunately, TEM images of CNTs do not give the opportunity to determine the exact number of walls of each sample of CNTs.

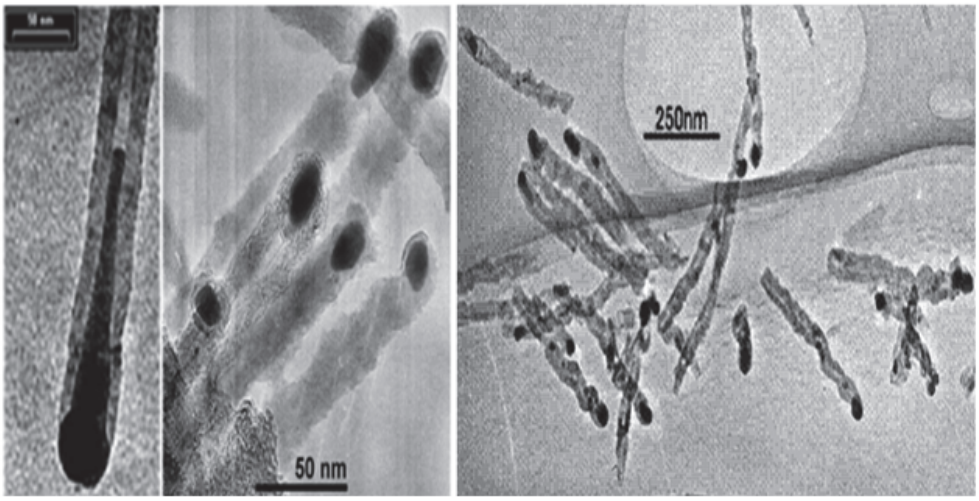

(a) (b) (c)

Fig. 18. CNTs TEM images with TM particles inserted at one end: (a) CNT highly oriented, (b) CNTs medium oriented and (c) CNTs sample synthesized with 1% of NH_3. The two ends of each CNT are well observed detached from the substrate. One end has graphitic structure (half fullerene) and the other has a TM particle inserted in the tube.

This deficiency is the result maybe of defects mutually aligned CNTs of different densities are obtained, depending on the ammonia concentration in the reactive gas mixture. A perfect CNT is an abstraction, because the hexagonal structure sp^2 forms layers with different types of alterations as shown in literature. These alterations can come from the growth mode, from the deposit on a substrate, or they can be the result of a heat or chemical treatment (Ebbesen & Takada, 1995). An important consequence of these defects on surface morphology that needs to be pointed out is the roughness of CNTs surface.

The defects are in general very important because they can modify the electronic properties of the nanostructure, and so, can be seen as a feature that can influence nanostructures applications. Generally, a defective site has a high chemical reactivity, in other words, this site is chemical reactions favoured (Eba Medjo et al., 2009a). Thus CNTs with poor orientation and those many defects are not appropriate for applications in field emission devices, but can have other important applications like chemical functionalization. In most cases, TEM investigations and seldom in SEM's, it is shown that the catalyst metal particles

are attached to the nanostructures top end Fig. 18, or found inside or at last in the sidewalls. According to the aimed applications, the presence of ultrafine cobalt or cobalt/iron nanoparticles of various diameters at the top of CNTs can have negative effect. In particular in the case of emission of electrons or electric field, the particles need to be carried off. Thus, the purification of nanostructures needs to be one of crucial parts of synthesis process. TEM gives direct insight into the structure of carbon nanomaterials and can help to identify the material or the phase correctly. Without observations by TEM, one may lead to wrong or incorrect conclusions.

It is the most important and most reliable technique for correctly identifying the nature and the form of carbon nanomaterials, in spite of the fact that the information that can be extracted is not straight-forward, since the preparation of TEM samples may mask observation of the nanostructures of lower size, or the possibility of the projection of artefacts. TEM has become useful for *in situ* microscopy, for observing dynamic processes at the nanoscale measurements which directly correlate physical properties with structures, holographic imaging of electric and magnetic fields, quantitative chemical mapping at subnanometer resolution and for ultra-high resolution imaging.

CNTs main features at normal incidence for FLN1_OE56					
Peak Names	Peaks	Binding energy (eV)	Kinetic energy (eV)	Intensity (c/s)	Final-state band and Brillouin-zone
A	285.50	285.20	1199.20	3.55	π_0 near Q
A′	286.53	287.14	1197.26	0.24	free-electron-like interlayer states + adsorption
A″	288.40	288.50	1195.90	0.40	free-electron-like interlayer states + adsorption
A‴	288.70	/	/	/	free-electron-like interlayer states + adsorption
A⁗	290.70	/	/	/	free-electron-like interlayer states + adsorption
C-H Exc.	291.76	291.65	1192.75	0.68	Exciton
B	292.65	292.57	1191.83	1.93	σ_1, σ_2: $\Gamma \rightarrow Q$
C	295.50	294.50	1189.90	6.54	π_0 or π_1 near Γ
D	297.80	297.06	1187.34	0.45	σ_3–σ_6: $Q \rightarrow P$
E	303.50	302.70	1181.70	3.83	σ_7 near Q
F	307.50	306.97	1177.42	4.00	σ_9 near Q
G	308.50	309.75	1174.65	1.90	/
H	316.50	315.40	1169.00	1.20	π_4 near Q
I	329.00	329.00	/	/	/
J	333.00	333.00	/	/	/
K	295.40	297.05	1187.35	0.00	π_0 or π_1 near Γ
L	301.85	299.30	1185.10	2.40	σ_6–σ_7: near Q
R = (A+C+H+K)/ (B+D+E+F+G+L) = 0,778					$R=(\pi/\sigma)_{tot}$

Table 3. Main features' parameters for CNTs XANES spectrum none contaminated by potassium at normal incidence from FLN1_OE56.

The assignment of main features of the XANES spectra of CNTs at normal incidence is given by Table 3 and Table 4, with CNTs samples none potassium-contaminated and potassium-contaminated respectively.

Annealed and potassium-contaminated CNTs at normal incidence Nanot29_OE36					
Peaks Names	Peaks	Binding energy (eV)	Kinetic energy (eV)	Intensity (c/s)	Final-state band and Brillouin-zone
A	285.50	285.20	1199.20	4.75	π_0 near Q
A′	286.53	287.31	1197.09	1.66	free-electron-like interlayer states + adsorption
A″	288.40	288.67	1195.73	2.12	free-electron-like interlayer states + adsorption
A‴	288.70	289.68	1194.72	0.03	free-electron-like interlayer states + adsorption
A⁗	290.70	290.35	1194.05	2.10	free-electron-like interlayer states + adsorption
C-H Exc.	291.76	291.64	1192.76	0.73	Exciton
B	292.65	292.40	1192.00	3.03	σ_1, σ_2: $\Gamma \rightarrow Q$
C	295.50	294.67	1189.73	14.40	π_0 or π_1 near Γ
D	297.80	298.30	1186.10	0.35	/
P″	297.51	296.20	1188.20	0.17	Potassium L_2 level
E	303.50	301.85	1182.55	9.45	σ_7 near Q
F	307.50	306.54	1177.86	5.78	σ_9 near Q
G	308.50	310.00	1174.40	2.60	/
H	316.50	314.30	1170.10	1.08	π_4 near Q
I	329.00	329.00	/	/	/
J	333.00	333.00	/	/	/
P	296.60	297.20	1187.20	1.16	Potassium L_2, L_3 level
P′	299.62	299.37	1184.78	1.83	Potassium L_2-L_1 levels
$R = (A+C+H+P'')/(B+D+E+F+G) = 0.962$					$R=(\pi/\sigma)_{tot}$

Table 4. Main features' parameters for annealed and potassium-contaminated CNTs samples XANES spectrum at normal incidence.

Understanding the growth mode of CNTs is among the imperatives in their characterization and can lead to the growth modelling. Two dominant growth modes are observed in SEM and TEM images, the tip growth mode and the base growth mode. In tip growth mode, the transition metal nanoparticle catalyzing the growth remains at the top. The adhesive forces between the substrate and the catalyst nanoparticles seem typically too small and the

particles are lifted up as the CNTs grow. The process takes place till the temperature is upper, before the cooling.

When the adhesive forces between the catalyst TM particles and the substrate are very important, the catalyst nanoparticles are not lifted up by the growing CNT during the growth process. The TM particles remain at the bottom of the CNT. The parameters of each kind of growth mode have yet to be clarified, because the nature of the growth mode, whether tip or base, is basic for the knowledge and the choice of the growth mechanism aiming the way of various applications.

In the light of the XANES and HOPG spectra used as a starting point model, a prior annealing of the samples prevents the increase of intensity in the free-electron-like interlayer states region of the spectra, clarifying that these features are not intrinsic. The use of the OTP for CNTs, the parameter $R(\alpha)$, deduced from the fitting of the carbon K-edge X-ray absorption spectra by the ratio of the intensity of π -type features over σ -type features' one, is defined to determine more quantitatively the respective contributions of the σ^* and π^* transitions at incidence angle α, is dual and completes electron microscopy characterization.

The parameter $R(\alpha)$ is expressed by the relation below:

$$R(a) = \frac{A + C + H + K}{B + D + E + F + G + L} \tag{5}$$

where A, B, C… are the main peaks assigned in the XANES spectrum of CNTs, or

$$R(a) = \frac{\sum \pi}{\sum \sigma} \tag{6}$$

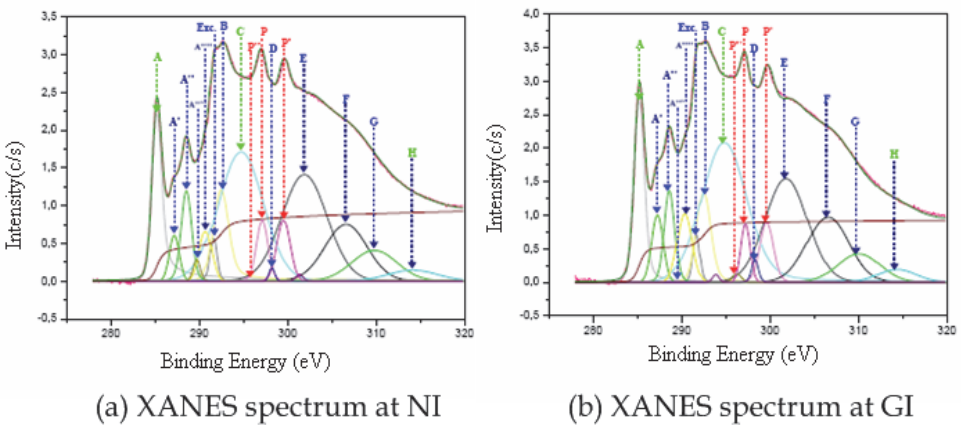

(a) XANES spectrum at NI (b) XANES spectrum at GI

Fig. 19. Potassium contaminated CNTs experimental and calculated superimposed XANES spectra at normal incidence (NI) and at grazing incidence (GI).

The OTP can first of all give information about the orientation of the CNTs relatively to the substrate plan (Eba Medjo et al., 2009b). It can moreover inform about the contamination and by the way lead to quantitative properties of CNTs, as the ability to functionalization,

the curvature and of course the number of walls (SWCNTs or MWCNTs) and chemical inertness (Eba Medjo et al., 2009a). As a general trend, the $R(\alpha)$ parameter values at normal incidence are greater than those at grazing incidence for CNTs contrary to those of the HOPG. The obtained CNTs are classified in three groups according to its values according to Table 5:

- Those with poor orientation,
- The other with medium range orientation,
- The last group which is formed of high oriented nanostructures.

For poorly oriented CNTs, the discrepancy between the two values (NI and GI) is too small. It increases towards high oriented CNTs according to Table 5 bellow.

CNTs	CNTs1	CNTs2	CNTs3
NI	0.778	0.962	0.975
GI	0.732	0.883	0.665
ΔR	0.046	0.079	0.310
Observation	Poor Oriented	Medium Oriented	High Oriented

Table 5. The values of $R(\alpha)$ of three samples of CNTs. The discrepancy of these values at normal incidence (NI) and grazing incidence (GI) allows the classification of CNTs in: poor, medium and high oriented.

The comparison of XANES spectra of unannealed samples and annealed ones shows an important difference due to the variation of the behaviour of carbon nanostructures samples in presence of contaminants.

When the outer diameter is important (MWCNTs), the CNTs are less chemically reactive and therefore, are not favoured to establish chemical bonds. But when the outer diameter is too small (SWCNTs), the chemical reactivity is very important, and such CNST are appropriate for functionalization.

The adsorption contribution to the signal of the contaminants in the free-electron-like interlayer states region is observed when no previous annealing of the sample is realized. This absorption contribution is important at normal incident than at grazing incidence. But the sensitivity to thermal treatment is not uniform for each sample. The difference is assigned to the curvature effect which is relative to the outer diameter and the sp^2 / sp^3 ratio of each CNT type. These results elucidate that the CVD is one of the best techniques for synthesis of the CNSs for multiple purposes till date.

8. Single walled carbon nanotubes functionalization

The functionalization of carbon nanotubes in general and single wall carbon nanotubes in particular is among the very actively discussed topics in nanoscience, because of the planned modification of properties is believed to open towards nanotechnology applications. Among the proposed applications closed to technical realization, recent developments of reliable methods for the functionalization of the SWCNTs provide an additional impetus to extend the scope of their application spectrum (Kuzmany et al, 2004). On top of their properties, SWCNTs possess high mechanical and chemical stability. This latter property is certainly advantageous from an application point of view. This attribute imposes chemical modification schemes, whereby new functions can be implemented that

cannot otherwise be acquired by pristine nanotubes, and lead to the development of methods allowing selective and controlled functionalization. For most applications SWCNTs require functionalization, such as changing some of the graphite properties to make nanotubes soluble in different media, or attaching different radicals or even inorganic particles (Hirsch, 2002) for future utilization.

Functionalization methods of carbon nanotubes can be divided into two major groups:

- Endohedral functionalization which consist to fill SWCNTs with some colloidal suspensions. It can be done by exploiting the phenomenon of spontaneous penetration or by wet chemistry method of filling nanotubes (Pederson & Broughton, 1992). SWCNTs are also filled by fullerenes. Sometimes, polymerization of fullerenes is done inside the SWCNTs.
- Exohedral chemical functionalization: its purpose is to attach covalently functional groups (-COOH for example) or metals in the outer walls of SWCNTs to make it soluble in different media. This kind of functionalization can be done via the main source of reactivity of the nanotubes which are: the curvature induce effect, the defects (misalignment) and the ends or the capping fullerene hemispheres. Among the most popular class of functionalization of nanotubes is the noncovalent exohedral functionalization, by wrapping SWCNTs in peptides or polymers for example.

There are various ways to functionalize SWCNT. Any functionalization of pristine CNTs is made to change properties such as inertness, solubility, conductivity, magnetism, etc., thus making nanotubes applicable for different purposes. So functionalization of functional groups creates new class of carbon nanomaterials with new properties. In principle functionalization is possible from the inside of the nanotubes and on the side-walls. It will help to separate metallic SWCNTs to semiconducting ones. This separation is of basic important in the fabrication of Carbon nanotube field effect transistor (CNTFET). Fig. 20 shows functionalization of SWCNT trough oxidation.

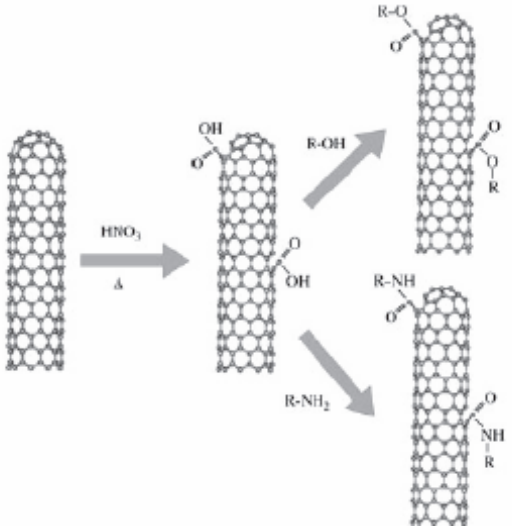

Fig. 20. Schematic representation of CNTs functionalization through oxidation followed by the esterification or amidization of the carboxyl groups

9. Single walled carbon nanotubes dopage

Carbon nanotube structure derives from bidimensional structure of the graphene and has the possibility to pass from the semiconductor state with modulable gap, to metallic state by adjusting only the diameter. This is a unique property of SWCNT. A SWCNT can act as either a conductor or a semiconductor, depending on the angle of the atom arrangement along the tube. A simple method to determine if a carbon nanotube is metallic or semiconducting is to consider its indices (*n, m*). The nanotube is metallic if *n*=*m* or *n*-*m*=3*i*, where *i* is an integer. Otherwise, the tube is semiconducting. In general SWCNT needs to be doped for efficient used in transistor. Dopage consists on feeling in any pure or intrinsic structure generally semiconductor, impurities (atoms) to change his behavior behalf electrons. The structure gives then easily, electrons than usual and is called *donor* or *n type* structure, or it receives easily electrons than usual and is called *acceptor* or *p type* structure. CNTs used in transistors are often doped. SWCNTs synthesized are naturally p type semiconductors, in the other hand, their induce charges are positive (holes). This phenomenon is explained by many theories. The most common is that of charge transfer from CNT to the electrode with the relative low Fermi level. Another explanation is that CNTs are doped by atoms and radical compounds present or formed during the synthesis, the gases absorption or the purification processes (Dang, 2008).
There are many ways to dope CNTs in order to obtain n type CNTs semiconductor. One consists on the exposure of the CNTs to electron donors like alkalis. However, the use of potassium or oxygen in CNTs dopage has induced phenomena. The easiest way of n type dopage is to anneale p type or natural synthesized CNTs.

10. Single walled carbon nanotubes transistors

Carbon nanotube field effect transistors utilize semiconducting single-wall CNTs to assemble electronic devices similar to MOSFETs. An individual semiconductor SWCNT is used as a channel of the transistor between the drain and the source as illustrated in Fig. 21 and Fig. 22. This has been experimentally investigated for the first time by Tans and co-workers in the year 1998 (Tans et al., 1998). Since this period, the performance of these transistors is increasing and equalizes the best silicon transistors. Then carbon nanotubes transistors seem to be among serious nanodevices promising to replace MOSFET transistors in near future. The band gap is known to be inversely proportional to the tube diameter *d* as shown by Tomanek and Enbody (Tomanek & Enbody, 2002) in the relation (7) bellow:

$$E_g = \frac{0.9k}{d} \tag{7}$$

where k is a constant. In electronic devices, it is necessary to have an important E_g corresponding to a lower d to eliminate the excessive production of charges thermal holders. However, a low E_g gives rise to an important current.
Thus an appropriate choice of diameter is convenient. At 300 K temperature, standard values of bandgap are: 1.12 eV for silicon, O.67 eV for germanium and 1.43 eV for GaAs. For a given E_g , d can be determined and of course (n, m) *Hamada integers* (Hamada et al., 1992) according to relation (1). Two mechanisms of contact between metal (source/drain) and semiconducting SWCNT interface lead to two types of carbon nanotubes field effect transistors.

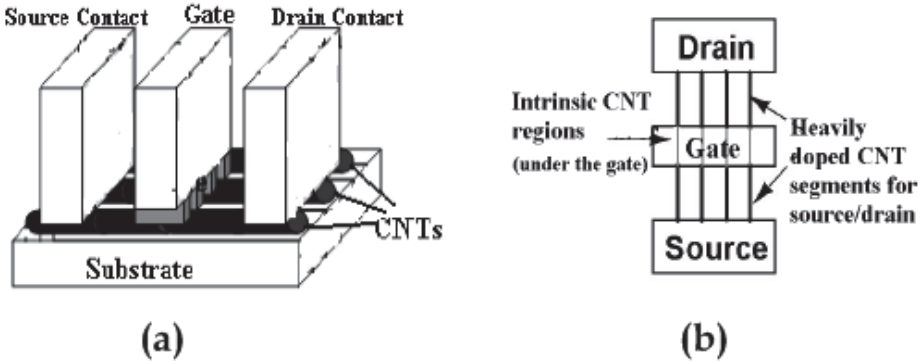

Fig. 21. Schematic diagram of carbon nanotube transistor: (b) cross section view; (a) top view

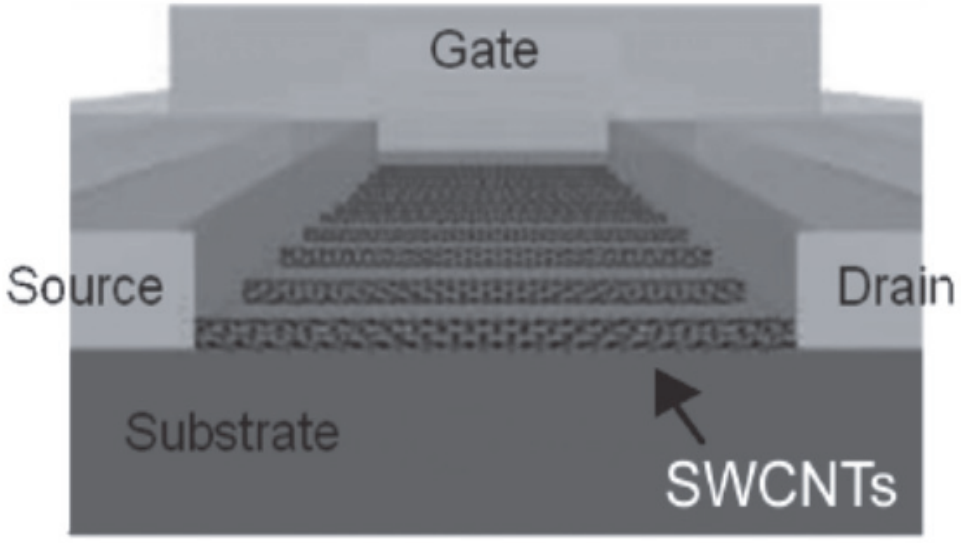

Fig. 22. The SWCNTs serve as the channels between the source and the drain in multichannel CNTFET.

The first type is the Schottky barrier CNTFET (SB-CNTFET) or Schottky type. It is the one with the contacts operated by modulating the transmission coefficient of the Schottky barriers at the contacts or junctions between the metals (drain and source) and the SWCNT. The Schottky barrier is an energy barrier for carriers' transport, which is often a severe limitation for devices. In semiconductor devices, this problem is generally avoided by replacing metal junctions with heavily doped regions of the semiconductor. However, nanotube devices have generally relied on direct metal-semiconductor interfaces. Nonetheless, good device performance can be obtained. The reason is that the Schottky barrier represents a much less severe limitation for CNTFETs than for conventional FETs, due to the quasi-one-dimensional (1D) of the SWCNT. A carbon nanotube transistor operates as unconventional Schottky barrier transistors in which transistor action occurs primarily by varying the contact resistance rather than the channel conductance. There is not alteration of the resistivity of the channel. The Schottky barriers preclude charges to cross the junction at low gate voltage. Applying positive voltages than the gate voltage, the N type device suppresses the Schottky barrier and consequently increases the holes injection at the drain. The SB-CNTFET has consequently a high ambipolar characteristic.
The second type is the C-CNTFET consisting of an intrinsic SWCNT with ends doped, one n type doped and another p doped. It is obtained by modulating the upper level of bandgap of the SWCNT. When the gate voltage is applied to the silicon back gate, the Schottky barriers are controlled or suppressed. Thus the CNTFET has an unipolar characteristic as a standard or conventional MOSFET. C-CNTFET helps to overcome the SB-CNTFET limitations like un-increasing miniaturization, which stops the enhancement of performance. According to their geometry, CNTFETs are classified into two types. The first one is the back-gate CNTFET proposed for the first time by Tans et.al. Fig. 23 presents the coaxially gated carbon nanotube transistor. This model is done to improve electrostatic coupling between the SWCNT and the gate.

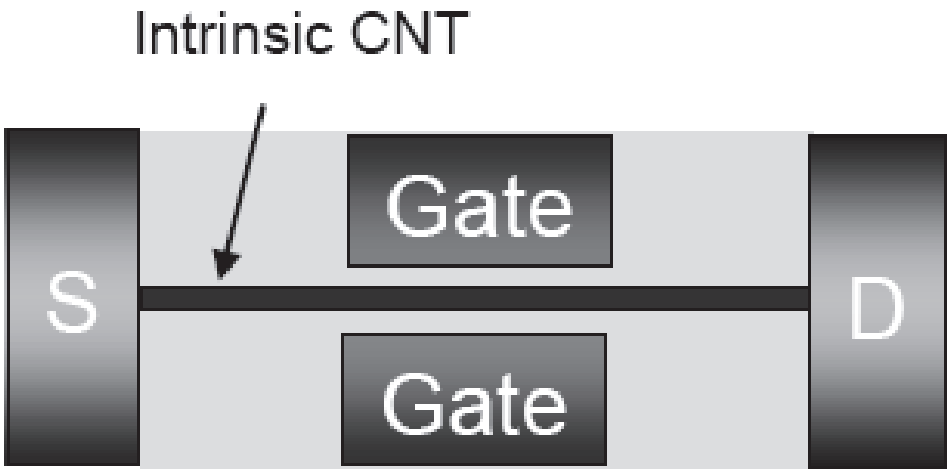

Fig. 23. Wrap-around gate CNTFET with an intrinsic SWCNT monochannel.

In this structure a single SWCNT is used to bridge two noble metal electrodes on an oxidized silicon wafer; the SWCNT plays the role of channel and the metal electrodes act as source and drain. The heavily doped silicon wafer itself behaves as the back gate. The other one is the top gate CNTFET with gate placed over the CNT.
In contrast to conventional Si MOSFETs with source and drain contacts oppositely doped compared to the channel, CNTFETs usually have metal contacts. In interface between a metal and a SWCNT, a Schottky barrier (SB) is formed. If a metal and a semiconductor are joined and the Fermi level in the semiconductor is higher in energy than that in the metal, electrons move from the semiconductor into the metal leaving a positive background of ionized atoms. Electrons continue to be transported across the interface until the Fermi levels of the two systems have equilibrated. A SB for holes (electrons) arises due to the mismatch between the Fermi level of the metal and the valence (conduction) band of the semiconductor.
The main transport mechanisms in a metal-semiconductor contact are thermionic emission over the Schottky barriers (tunneling through the SB and recombination and generation). The barrier thickness can be reduced by increasing the electric field close to the interface by for example, increasing the doping of the semiconductor. The tunneling current is also larger in a reversed biased compared to a forward biased SB due to the thinner barrier. The measurements of the SB heights as a function of SWCNT diameter confirm that large SWCNTs diameter have to be used to obtain CNTFETs with negligible SBs. However, even though large diameter SWCNTs have the additional benefit of a high mobility (Zhou et al, 2005) their small band gaps lead to high off state currents resulting in a trade-off between switching speed and leakage current. The I_{on} over I_{off} ratio still very low compared to theoretical, this seems to be the result of the fact that SWCNTs used are a mixture of semiconductor and metallic. Towards this goal, the semiconducting tubes are now rendered non-conductive by application of an appropriate gate voltage prior to the electrochemical modification. The FETs fabricated in this manner are found to display favourable holes mobilities and a high ratio approaching 106 between the current in the ON and OFF state. However, the results show that the SB decreases with increasing SWCNT diameter, an effect which is attributed to the decrease in band gap. In addition, the measurements indicate that a SWCNT diameter larger than 2 nm is needed to obtain a SB height close to zero for a palladium (Pd) contacted SWCNT in vacuum. The Schottky barrier height is given by the relation (8) bellow:

$$\Phi_{SBh} = \varphi_{SWCNT} - \varphi_m - \frac{E_g}{2} \tag{8}$$

where $\varphi_{SWCNT} = 5.0eV$ is the SWCNT work function,
$\varphi_m = 5.12eV$ is the metal (Pd) work function and E_g gived by equation (7). The relation enhancement leads to the effective Schottky barrier height.
For many electronic applications it is of great importance to have CNTs that exhibit uniform electrical properties. The fabrication of CNTFET requires exclusively semiconducting nanotubes. At present there exists no synthesis technique that allows for a reliable control over the electrical properties of synthesized nanotubes. The raw material of SWCNTs constitutes a mixture of metallic and semiconducting single walled carbon nanotubes.

11. Conclusion

Among chemical elements with impressive number of allotropes is found the carbon. These allotropes are divided in two groups: the traditionals and the carbon nanostructures. This last group is led by carbon nanotubes characterize by unique properties allowing numerous applications and have emerged as main building blocks in nanotechnology. A large part of the success of the MOSFET transistor is due to the fact that it can be scaled to increasingly smaller dimensions, which results in higher performance. Though this trend still continues, bulk MOSFET will soon reach its limiting size. For this reason, the semiconductor industry is looking for different materials and devices to integrate with the current silicon-based technology and in the long run, possibly replace it. The carbon nanotube field effect transistor is one among the most promising alternatives due to its superior electrical properties. Among the obstacles encountered in the use of CNTFET is a well-known phenomenon occurring under a vacuum environment or with a top gate oxide and top gate electrode, the undesirable ambipolarity in Schottky barrier (Martel *et al*, 2008). CNT-based CMOS technology is realized by suppressing the ambipolar regions of the CNTFETs with p- or n-type doping (Bachtold et al, 2001). Doping of CNTs with p or n-type to remove ambipolarity is still great challenge. The poor understanding of the most important factors that affect SB formation in metal-CNT interface junction stems from the difficulty in using many of the techniques available for bulk materials to perform measurements on SBs in nanoscale contacts. Carbon nanotubes are nowadays commonly used in laboratories due to their commercial availability in large quantities.

But some properties of CNTs and their applications have not yet fulfilled the expectations, while others are still object of intensive exploration. In addition, effective purification methods can ensure a reasonable quality of the samples. The recently developed chemical and electrochemical functionalization schemes have significantly extended the application spectrum of CNTs. However, the actual challenge still remains the reaching complete control in their synthesis to selectively obtain isolated SWCNTs as well as bundles, to control their location and orientation, and to synthesize complex and organized networks of arrays of CNTs directly on large substrates suitable for applications.

12. Acknowledgements

The author would like grateful acknowledge Mr. Abega, J. C. of the rectorate of University of Yaounde I, for his helpful advices and his logistical assistance. He thanks on the same time Dr Ben-Boli, G. H. the main responsible of the Nuclear Physics laboratory of Physics department, Faculty of Science, University of Yaounde I, Pr Mane Mane J and Dr Tiodjio Sendja, B. for many helpful discussions.

13. References

Bachtold, A., Hadley, P., Nakanishi, T. & Dekker, C., Logic circuits with carbon nanotubes transistors, *Science, 2001*, *294*, 1317

Baird, T., Fryer, J. R. & Grant, B., Carbon formation on iron and steel foils by hydrogen pyrolysis reactions at 700° C, *Carbon* 12, 591, 1974

Baker, R. T. K., Barber, M. A., Harris, P. S., Feates, F. S. & Waite, R. J., Nucleation and Growth of carbon deposits from the nickel catalyzed decomposition of acetylene, *J. Catalysis,* 26, 51, 1972

Bunch, S., Yaish, Y., Brink, M., Bolotin, K. & McEuen, P. L., Coulomb oscillations and hall effect in quasi-2D graphite quantum dots, *Nano Letters,* 5, 287, 2005

Cojocaru, C S & Le Normand, F, On the role of activation mode in the plasma and hot filament enhanced catalytic chemical vapour deposition of vertically aligned carbon nanotubes, *Thin Solid Films*, 515 53, 2006

Cojocaru, C. S., Synthèse contrôlée CCVD des films de nanostructures orientées de carbon, *Thesis*, Université Louis Pasteur, Strasbourg I, 2003

Dang, T. T., Portes logiques à base de CNTFETs –Dispersion des caractéristiques et tolérance aux défauts ; *Thesis*, Institut Polytechnique de Grenoble, 2008

Dresselhaus, M. S., Dresselhau,s G., Sugihara, K., Spain, I. L. & Goldberg, H. A., *Graphite Fibers and Filament*s, Springer-Verlag, Berlin, 1988

Dolmatov, V. Y., Detonation synthesis ultrqdispersed diamond: properties and applications, *Russ. Chem. Re*V., 70, 607, 2001

Eba Medjo, R., Thiodjio Sendja, B., Mane Mane, J. & Owono Ateba, P., A study of carbon nanotube contamination by XANES spectroscopy, *Phys. Scr*. 80, 045601, 2009

Eba Medjo, R., Thiodjio Sendja, B., Mane Mane, J. & Owono Ateba, P., XAS study of the orientation of oriented carbon nanotubes films, *Phys. Scr*. 80, 055602, 2009

Eba Medjo, R., Structural and morphological characterization of carbon nanostructures synthesized by chemical vapour deposition using spectroscopic techniques and electron microscopies, *Thesis*, University of Yaounde I, 2011

Ebbesen, T. W. & Ajayan, P.M., Large-scale synthesis of carbon nanotubes, *Nature,* 358, 220-222, 1992

Ebbesen T. W. & Takada T., Topological and sp^3 defect structures in nanotubes, *Carbon,* 33, 973, 1995

Hamada, N., Sawada, S. & Oshiyama, A., "New One-Dimensional Conductors: Graphitic Microtubules", Phys. Rev. Lett. 68, 1579 1992

Hamon, A. L., Contribution à l'étude des nanotubes: structure et contraste en microscopie électronique, enchevètrements et comportement mécanique, *Thesis*, Ecole Centrale de Paris, 2001

Heimann, R. B., Kleiman, J. & Salansky, N. M., A unified structural approach to linear carbon polytupes, *Nature*,306 , 164, 1983

Heimann, R. B., Evsyukov, S. E. & Kavan, L., *Carbyne and Carbynoid Structures*, Kluwer Academic Press, Dordrecht, 1999

Helveg, S., Lopez-Cartes, C., Sehested, J., Hansen, P., Clausen, B., Rostrop-Nielson, J., Ablid-Pedersen, F. & Norskov, Atomic-scale imaging of carbon nanofibre growth, *Nature*, 427, 426, 2004

Hirsch, A., Functionalization of single-walled carbon nanotubes, *Angewandte Chemie-International Edition* 41 (11), 1853-1859, 2002

Hueczko, A., Vertically aligned carbon nanofibers and related structures, *Appl. Phys. A*., 74, 617, 2002

Iijima, S., Helical microtubules of graphitic carbon, Nature, 354, 56, 1991

Ivanov, V., Nagy, J.B., Lambin, Ph., Lucas, A., Zhang, X.B., Zhang, X.F., Bernaerts ,D., Van Tendeloo, G., Amelinckx, S. & Van Landuyt, J., Carbon nanotubes production by catalytic pyrolysis of benwene, *Chem. Phys. Lett.* 223, 329, 1994

Krishnan, A., Dujardin, E., Treacy, M. M. J., Hugdahl, J., Lynum, S. & Ebbesen, T. W., Graphytic cones and the nucleation of curved carbon surfaces, *Nature*, 388, 451, 1997

Kroto, H. W., The stability of Fullerene Cn (n= 24, 28, 32, 50, 60 and 70), *Nature*, 329, 529, 1987

Kuzmany, H., Kukovecz, A., Simona, F., Holzweber, M., Kramberger, Ch. & Pichler, T., "Functionalization of carbon nanotubes", *Synthetic Metals*, 141 113–122, 2004

Kuznetsova, A., Popova, I., Yates, J. T., Bronikowski, M. J., Huffman, C. B., Liu, J., Smalley, R. E., Hwu, H. H. & Chen, J. G. G., Oxygen-containing functional groups on single-wall carbon nanotubes: NEXAFS and vibrational spectroscopic studies, *Journal of the American Chemical Society* 123 (43), 10699-10704, 2001

Martel, R., Derycke, V., Lavoie, C., Appenzeller, J., Chan, K., Tersoff, J., & Avouris, P., "Ambipolar Electrical Transport in Semiconducting Single-Wall Carbon Nanotubes," *Phys. Rev. Lett.* 87, 256805, 2001

Melechko, A. V., Merkulov, V. I., McKnigh,t T. E., Guillorn, M. A., Klein, K. L., Lowndes D. H. & Simpson, M. L., Vertically aligned carbon nanofibers and related structures: Controlled synthesis and directed assembly, *J. Appl. Phys*., 97, 041301, 2005.

Meyyappan, M., Delzeit, L., Cassell, A. & Hash, D., Carbon nanotube growth by PECVD: a review, *Plasma Sources Science and Technology*., 12, 205, 2003

Mordkovich, V. Z., Shiratori, Y., Hiraoka, H. & Takeuchi, Y., Synthesis of multishell fullerenes by laser vaporization of composite carbon targets, *Physics of the Solid State*, 44, 4, 603, 2002

Novoselov, K., Geim, A. K., Morozov, S. V., Jiang, D., Zhang, Y., Dubonos, S. V., Grigorieva, I. V. & Firsov, A.A., Electric field effect in atomically thin carbon films. *Science*, 306(5696), 666, 2004

Pederson, M. R. & Broughton, J. Q., Nanocapillarity in Fullerene Tubules, *Physical Review Letters,* 69 (18), 2689-2692, 1992

Pierson, H. O., *Handbook of carbon, graphite, diamond and fullerenes*, *Processing and Applications*. (William Andrew Publishing/Noyes, New Jersey, 1993

Rosenberg, R. A., Love, P. J. & Rehn, V., Polarization-dependant C(K) near-edge X-ray absorption fine structure of graphite, *Phys. Rev. B* 33, 4034, 1986

Sasaki S., KEK, National Laboratory for High Energy, Physics, *Report*, 83, 22 1984

Somani, P. R. & Umeno, M., *Modern Research and Educational Topics in Microscopy*, ed. Mendez-VilasA & Diaz J., Formatex Vol. 2, 634-642, 2007

Stanford University, CNFET Model website,http://nano.stanford.edu/model.php/id=23

Svensson J., Carbon Nanotube Transistors: Nanotube Growth, Contact Properties and Novel Devices, *Thesis,* University of Gothenburg, Göteborg, 2010

Tans, S.J., Verschueren, A.R.M. & C. Dekker, "Room-temperature transistor based on a single carbon nanotube", *Nature*, Vol.393, pp.49–52, 1998

Tomanek, D. & Enbody, R.J.; "Science and Application of Nanotubes", *Fundamental Materials Research*, 2002

Zhou, X., Park, J.-Y., Huang, S., Liu, J., & McEuen, P. L., Band structure, phonon scattering, and the performance limit of single-walled carbon nanotube transistors. *Phys. Rev. Lett.*, 95(14), 146805, 2005.

2

Syntheses and Electronic Applications of Helical Carbon Nanofibres

Yoshiyuki Suda, Hirofumi Takikawa and Hideto Tanoue
Toyohashi University of Technology
Japan

1. Introduction

Helical carbon nanofibre (HCNF) is spiral-shaped carbon nanofibre (CNF) with coil and fibre diameters in the range of 20—1000 nm and 5—400 nm, respectively. The unique three-dimensional structure of HCNFs induces a lot of researches to apply HNCFs to electrical and electronic engineering as well as mechanical engineering. Carbon nanotubes (CNTs) were first discovered in the soot produced by an arc discharge and laser ablation has been one of the most reliable methods to prepare high-quality CNTs. On the other hand, HCNFs has been almost entirely grown by chemical vapour deposition (CVD) using hydrocarbon feedstock gases. In this chapter, we describe the history, classification, synthesis, and application of HCNFs. We mainly introduce our research results including the latest topics, comparing with the other group's work. The problems that still remain in the CVD growth and the future researches of HCNFs we intend are also discussed.

2. History of HCNFs

In 1953, Davis et al. have found minute vermicular growths of carbon through the experimental work on the deposition of carbon in the brickwork of blast furnaces (Davis et al., 1953). In 1955, Hofer et al. reported the growth of carbon filaments with fibre diameters of 10 to 200 nm. They used the catalytic deposition technique of carbon from carbon monoxide by the following disproportionation reaction.

$$2CO \rightarrow C + CO_2 \quad (1)$$

At atmosphere pressure, the reaction takes place between 300 and 800°C. They used Ni, Co, and Fe as a catalyst and a combustion tube with an electric furnace for the carbon growth. Carbon filaments grew on all of the catalysts at 390°C, and the deposits on Fe were single solid strands. They also found that the filaments were extended in two directions from central catalyst particles (Hofer et al., 1955).

Boehm intended to find a continuous process of carbon filaments by feeding metal carbonyl into a CO stream before it passed a heated tube. He introduced $Ni(CO)_4$- or $Fe(CO)_5$-containing CO (80%)/H_2 (20%) gas mixture into the heated zone of a heat-resistant glass tube with an electric furnace at temperatures of 550—770°C. When $Fe(CO)_5$ was used, the

usual fibril with twisted strands was grown at 600—650°C. In an electron microscopy observation, he found that twisted filaments very often form double or even triple helices (Boehm, 1973).

Though the CO disproportionation reaction is a reliable method to synthesize carbon filaments including commercially-available CNTs (http://www.unidym.com/), it is highly deleterious in several industrial processes (Hofer et al., 1955). Baker et al. developed the catalytic decomposition of C_2H_2 gas over catalyst surfaces and studied the effect of Sn on the growth of filaments from the Fe/C_2H_2 system. In this system, significant deposit growth of carbon filaments was only observed at temperatures above 800°C with Sn-coated Fe foils in a 665-Pa C_2H_2. They found that the filaments were nearly all spirals with a constant pitch and the Fe/Sn alloy worked to form spiral filaments. On pure iron, deposits grew at temperatures as low as 650°C; however, it became autolytically poisoned after a few minutes. The growth still continued on Fe/Sn after more than 2 h, and poisoning was never observed (Baker et al., 1975).

Motojima et al. have grown regularly coiled carbon filaments by the catalytic pyrolysis of C_2H_2 at 350–750°C using Ni plate and powder as a catalyst (Motojima et al., 1990). His group also succeeded to grow very regularly coiled spring-like fibres of Si_3N_4 from a gas mixture of Si_2Cl_6, NH_3, and H_2 at 1200°C on a graphite substrate on which an iron impurity was painted (Motojima et al., 1989). These results show that various types of helical nanofibres including HCNFs can be grown if the suitable combination of catalyst and source gas is found.

These findings were published prior to the discovery of multi-walled CNTs (MWCNTs) (Iijima, 1991) and single-walled CNTs (SWCNTs), (Iijima & Ichihashi, 1993). CNTs consist of concentrically rolled-up graphitic layers and have relatively smaller dimensions than CNFs (Saito et al., 1998). CNTs were discovered in the soot produced by an arc discharge, and arc discharge and laser ablation of catalyst metals-containing graphite rod have been excellent methods to synthesize high-quality SWCNTs (Journet et al., 1997), (Thess et al., 1996). In 1998, growth of SWCNTs by CVD was successfully realized by Kong et al. (Kong et al., 1998) and subsequently CVD has become a dominant technique in the CNT research and development. Concurrently with the development of SWCNT synthesis by CVD, very thin HCNF which has a hollow structure with several concentric graphitic layers were formed by Ivanov et al. (Ivanov et al., 1994). This structure is called multi-walled carbon nanocoil (MWCNC) and described in Section 7.

Zhang of the Prof. Nakayama's group intended to fabricate HCNFs in high yield and tried to deposit Fe on indium-tin-oxide (ITO) substrate instead of Fe/Sn system. They successfully grew HCNFs using C_2H_2/He gas mixture at 700°C. It is noted that more than 95% of carbon deposits grew helically on the ITO substrate (Zhang et al., 2000).

Takikawa et al. used a hot-filament CVD apparatus to enhance the carbon deposition efficiency and to lower growth temperature (550—600°C), Cu as a substrate, and C_2H_4 as a carbon feedstock gas. HCNF with an inner diameter (called carbon nanocoil, CNC) grew on Ni-coated Cu substrate at 550°C, and HCNF without an inner diameter (called carbon nanotwist, CNTw) grew on Zn-coated Cu substrate at 600°C. It was the first time that Zn (or ZnO_x) was found to be a possible catalyst for HCNFs growth (Takikawa et al., 2000). Hereafter, a lot of catalyst combinations for the growth of HCNFs have been reported, as explained in Section 4.3.

3. Classification

Figure 1 shows scanning electron microscopy (SEM) micrographs of HCNFs. HCNFs can be categorized into three types by the inner diameter and fibre cross section: (1) carbon nanocoil (CNC) which has a spiral spring shape with an inner diameter; (2) carbon nanotwist (CNTw) which has a twisted shape without an inner diameter; and (3) multi-walled carbon nanocoil (MWCNC) whose diameter is typically smaller than 50 nm with a hollow structure of concentric graphitic layers. Both CNTw and CNC have angular and round types. MWCNC is typically the round type.
See more information about the classifications of HCNFs, carbon microcoil (CMC) which has a coil diameter ≥ 1 μm, and coiled CNT in the following review papers (Motojima & Chen 2004), (Hanus & Harris 2010).

4. Experimental

4.1 CVD apparatus for HCNF growth

Here we introduce a CVD apparatus for HCNF growth in our laboratory. The apparatus consist of a quartz tube (45 mm inner diameter and 500 mm long), an electric furnace, and gas supply system. The quartz tube and electric furnace are horizontally arranged. Catalyst for HCNF growth, which is deposited on substrate or supported on mesoporous materials is placed in the centre of the quartz tube and heated up to a desired temperature (typically ≤ 800°C) under the flow of dilute gas (He or N_2). Hydrocarbon feedstock gas (C_2H_2 or C_2H_4) is added to the dilute gas when HCNF is grown. Flow rates of the gases are controlled with a mass flow controller. The exhaust gas through the quartz tube is firstly collected into the bubbler tube and then evacuated.

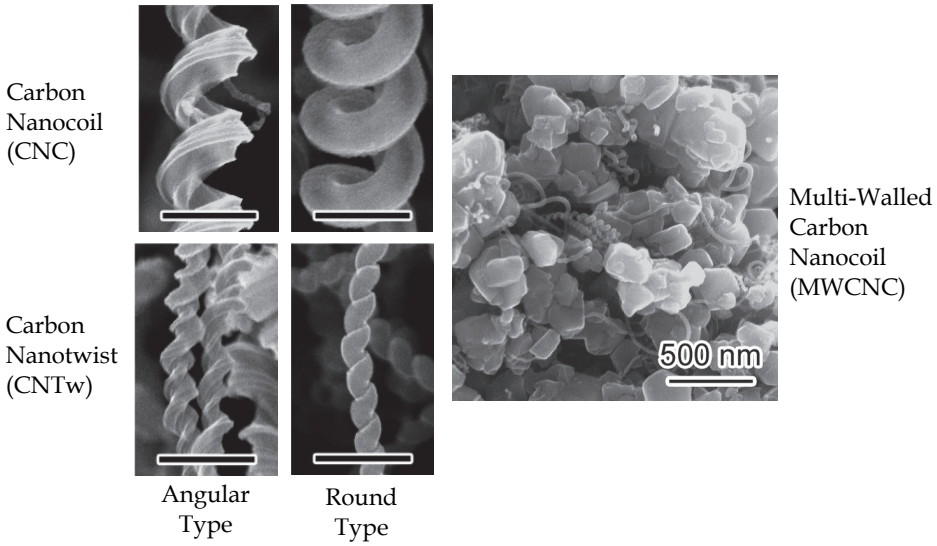

Fig. 1. SEM micrographs of HCNFs. Scale bar: 500 nm.

4.2 Development of automatic CVD system for mass production

Based on the experimental results of HCNF growth using the CVD apparatus, Prof. Takikawa developed an automatic CVD system with a consecutive substrate transfer mechanism for mass production of HCNFs (Hosokawa et al., 2007). Schematic of the CVD system is shown in Figure 2. The system is composed of substrate loading chamber, transfer chamber, process reactor with electric furnace, and cooling chamber. Two gate valves separate the loading, transfer, and cooling chambers. No separation exists between the transfer chamber and the process reactor. All chambers are made of stainless steel, except a perpendicularly placed process reactor (quartz tube, 94 mm inner diameter). A substrate cassette containing up to 8 substrates of 70 mm in diameter is placed in the loading chamber. Each substrate is then transferred from the cassette to the process reactor by the cassette-elevator robot-arm, horizontal robot-arm, and vertical robot-arm. After the reaction, the substrate is transferred to the cooling stage in the cooling chamber. The cooling stage has a rotary actuator, and the substrate is dropped to the bottom of the collection pot after sufficient cooling. This procedure is controlled by a sequencer, and the substrates are one by one transferred and treated while keeping the furnace temperature in the process condition.

4.3 Catalyst preparation

In CVD process, catalyst is needed to synthesis carbon nanomaterials including CNFs, HCNFs, CNTs, and graphene. (Jong & Geus 2000), (Motojima & Chen 2004), (Hanus & Harris 2010), (Kumar & Ando 2010), (Yu et al., 2008) Multi-walled CNTs and carbon nanoparticles can be formed from vaporised carbon in arc discharge or laser ablation. Metals that dissolve carbon are usually used as a catalyst of carbon nanomaterials. As stated in Section 2, Baker found the effect of binary-catalyst on HCNF growth, and then various combinations of binary-catalysts for HCNF growth have been found, e.g. Fe/ITO (Zhang et al., 2000), Fe/SnO_2 (Chen et al., 2004), (Xu et al., 2005), Fe/Sn (Hokshin et al., 2007), Fe-based

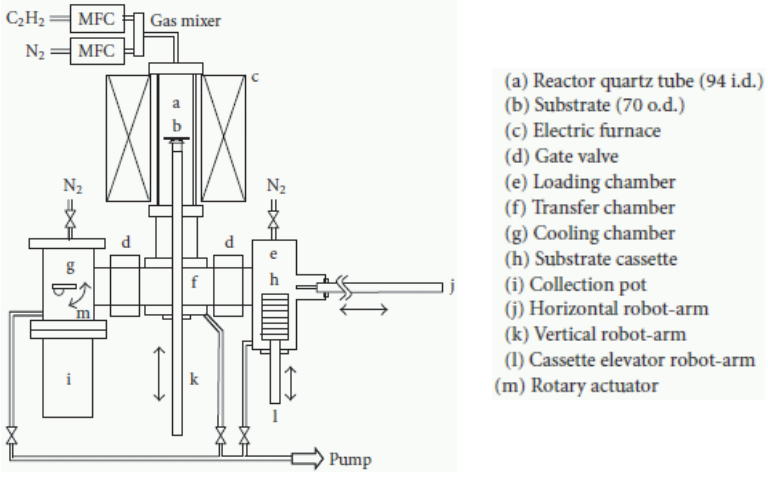

Fig. 2. Schematic diagram of automatic CVD system with a consecutive substrate transfer mechanism. (Hosokawa et al., 2007)

alloys (Fe-Cr-Mn-Mo, Fe-Cr-Ni-Mo (SUS513), Fe-Ni-Cr-Mo-Mn-Sn) (Yang et al., 2004), (Yang et al., 2005), Ni/SnO_2 (Hosokawa et al., 2007), Ni/Sn (Yokota et al., 2010), Cu-(Ni, Cr, Ti or Zn) (Takikawa et al., 2000), and Ni/Cu (Katsumata et al., 2004).
According to our experimental results, it is possible to grow CNC and CNTw selectively by the combination of binary catalyst; CNC is synthesized by Fe-based catalyst, and CNTw synthesized by Ni-based catalyst. In this chapter, the results of HCNF growths by Fe/Sn and Ni/Sn catalysts are mainly introduced. Fe and Ni are well-known to dissolve carbon, whereas Sn cannot dissolve carbon.

4.4 HCNF growth conditions

The CVD conditions used in our study are listed in Table 1. It does not make much sense to determine "the best" condition because CVD condition strongly depends on CVD apparatus, dimension of the chamber and type and amount of the catalysts. Here we introduce commonly-used CVD conditions. The feedstock gas mainly used was C_2H_2 and diluted with He or N_2 gas. The temperature range was broad, 400—800°C because catalytic decomposition of C_2H_2 takes place even below 400°C. Optimum temperatures for the growth of CNC and CNTw were determined through the number of growth experiments using our apparatus. The reaction time was set to mostly 10 min. During this time period, growth of CNF is constant. Various types of catalysts were tried and their results were described in each section.

Feedstock gas (flow rate)	Dilute gas (flow rate)	Temp.	Reaction time
C_2H_2 (50—350 ml/min)	He (400—1000 ml/min) N_2 (1000—1400 ml/min)	400—800°C	10—30 min
Catalyst	Substrate	Reference	
Ni, Zn	Cu	Takikawa et al., 2000	
Ni/Cu, NiO/CuO	Quartz	Katsumata et al., 2004	
Fe/SnO_2	Quartz	Xu et al., 2005	
Ni/SnO_2	Graphite	Hosokawa et al., 2007 Hosokawa et al., 2008	
Fe/Sn, Ni/Sn	Graphite	Yokota et al., 2010	
Fe/Sn	Zeolite	Yokota et al., 2011	

Table 1. CVD conditions for HCNF growth.

4.5 Characterisation

After the reaction, the carbon deposit was weighed using an analytical balance. For the as-grown carbon deposit mixed with the catalyst, the carbon deposition rate was calculated as follows:

$$\text{Deposition rate of carbon} = \{(W_{tot} - W_{cat})/W_{cat}\}/\text{time} \quad (2)$$

where W_{tot} is the total weight of the catalyst and the carbon deposit, W_{cat} is the weight of the catalyst, and time is the duration of C_2H_2 introduction. Therefore, the deposition rate reveals the carbon yield per unit weight of the catalyst per unit time.

The carbon deposit was observed using a field emission scanning electron microscope (FE-SEM) (S-4500II, Hitachi), an energy dispersive X-ray analyser (EDX) (DX-4, Phillips) and transmission electron microscopes (TEM) (JEM-2010 and JEM-2100F, JEOL). The deposit was then evaluated based on its HCNF purity estimated from several visual fields in the SEM micrographs. The fibre diameters, the coil diameters and the coil pitches of HCNFs were also measured on the SEM micrographs.
The field emission properties of HCNFs were measured in a vacuum chamber and the apparatus used is described in Section 8.

5. Quantity synthesis of HCNFs

5.1 Parametric study on growth of carbon nanocoil

5.1.1 Effects of catalyst composition

In order to determine the optimum composition of the Fe/Sn catalyst, the Fe percentage over the total weight of Fe and SnO_2 was adjusted from 0 to 100% at steps of 10%. The catalytic performance of every combination was evaluated based on the deposition rate and the SEM micrograph of carbon deposits under identical conditions. The reaction was carried out at 700ºC for 10 min with flow rates of C_2H_2 and He at 180 and 420 ml/min, respectively. Figure 3 shows that the carbon deposition rate increases with the Fe percentage. There are no significant depositions on pure Fe and pure SnO_2. With the catalysts having Fe percentages between 60 and 90%, carbon deposition rates saturate to approximately 4 min^{-1}. This means that 40 times of carbon materials were deposited on one portion of catalyst in 10 min under the given process conditions.

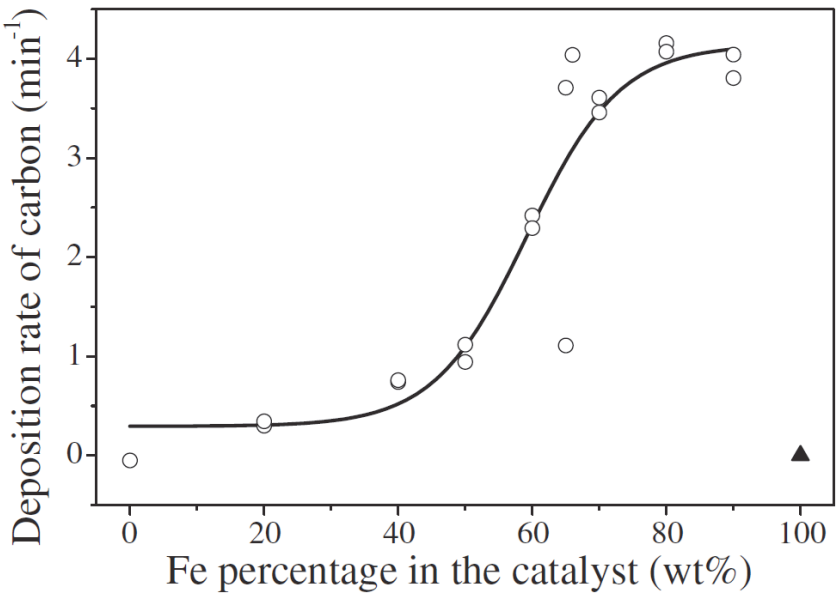

Fig. 3. Deposition rates of carbon materials on the composition of the catalyst. Pyrolysis of C_2H_2 was carried out on 10 mg mixture of Fe and SnO_2 at 700ºC for 10 min with the flow rates of C_2H_2 and He gases of 180 and 420 ml/min, respectively. (Xu et al., 2005)

Figure 4 shows SEM micrographs of carbon materials deposited on catalysts of various compositions. On the catalyst with 20% Fe, as shown in (a), no significant carbon deposition can be observed. On the catalysts with 40%, 50%, and 60% Fe in (b), (c), and (d), respectively, twisted fibres dominate the visual fields of the micrographs. On the catalysts of 67% (e), 70% (f), and 80% (g) Fe, CNCs are found to be the main components of the deposits, the fibre diameters of the CNCs grown from the catalyst with 67% Fe are distributed from 50 nm to 300 nm. CNC percentages lessen with further increase of the Fe ratio, and CNCs can rarely be found among the short fibres grown from the catalyst with 90% Fe. From the micrographs, we also notice that fibre diameters tend to become smaller with increasing SnO_2 ratio. These results reveal that CNC selectivity is solely dependent on catalyst composition and that the optimum combination of the catalyst with high CNC selectivity as well as carbon deposition activity lies within a rather narrow range.

5.1.2 Influences of reaction temperature

Because the catalyst with 67 wt% Fe in a mixture with SnO_2 gave the highest selectivity for CNC formation as well as the highest deposition yield under the given experimental conditions, it was chosen for the optimisation of reaction temperature from 400 to 800°C. Carbon yield and CNC selectivity at different temperatures were evaluated after a reaction of 30% C_2H_2 in a mixture with He for 10 min.

Figure 5 presents carbon deposition rates at different reaction temperatures. At temperatures below 675°C, the carbon deposition rate increases with temperature. On the contrary, carbon deposition rate decreases with rising temperature > 725°C. The optimum temperatures for obtaining high carbon yields lie in the range between 625 and 725°C.

Similar optimum temperatures were also reported for other catalyst systems such as iron carbide doped with tin monoxide (Hernadi et al., 2002), Fe-coated ITO (Zhang et al., 2000), and Sn-coated Fe foil. (Baker et al., 1975)

Figure 6 shows SEM micrographs of carbon deposits formed on the catalyst at different reaction temperatures. At 500°C, as shown in (a), small amounts of amorphous carbon are observed on the catalyst particles. At 600°C in (b), carbon nanofibres (CNFs) and CNCs are found to be mixed with the amorphous carbon. With increasing reaction temperature, the amount of amorphous carbon decreases and CNC selectivity increases steadily until 700°C. Further elevation of the temperature results in the decrease of CNC selectivity and the increase of CNF yield. At 700°C (e), CNCs with a broad coil diameter distributions ranging from as thin as 10 nm to as thick as 600 nm are formed at high selectivity.

These results reveal that CNC selectivity is very sensitive to reaction temperature, and that 700°C is the optimum temperature for both CNC selectivity and carbon deposition rate under the given experimental conditions.

5.1.3 Effects of helium gas addition

To optimise gas composition for CNC formation, the flow rates of He and C_2H_2 were regulated at 400–1000 and 50–300 ml/min, respectively. The catalyst with an Fe percentage of 67% and the reaction temperature of 700°C were fixed for each batch. Carbon yield and CNC selectivity at different gas compositions were evaluated after the reaction for 10 min.

Figure 7 shows the plot of the carbon deposition rate versus the partial pressure of C_2H_2 gas in a mixture with He gas. When the partial pressure of the C_2H_2 gas rises from 0.1 to 0.2, carbon deposition rate attains to a maximum, and decreases with further increase of the partial pressure of the C_2H_2 gas beyond 0.3. The carbon deposition rate maximizes when the partial pressure of the C_2H_2 gas is between 0.2 and 0.3.

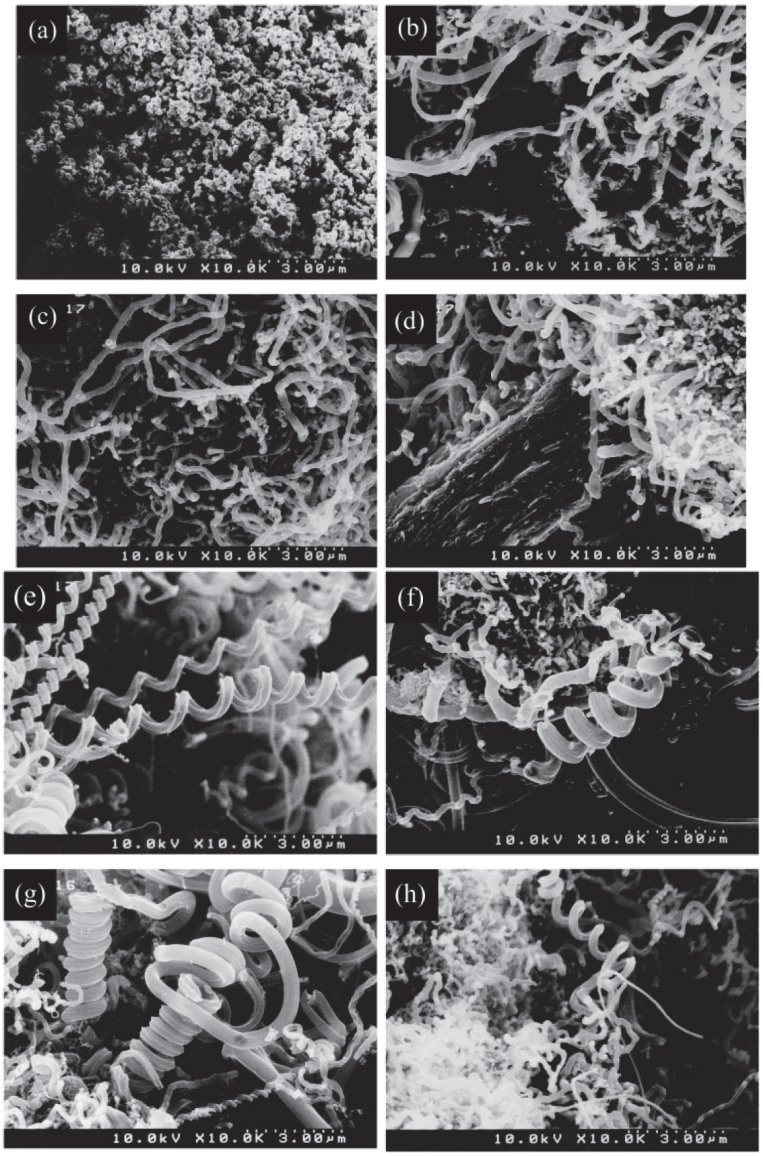

Fig. 4. SEM micrographs of carbon materials deposited on the catalysts with various weight percentage of Fe: (a) 20%, (b) 40%, (c) 50%, (d) 60%, (e) 67%, (f) 70%, (g) 80%, and (h) 100% in the mixture with SnO_2. The reaction conditions are the same as those in the case of Fig. 3. (Xu et al., 2005)

Figure 8 shows the dependence of CNC selectivity on the partial pressure of the C_2H_2 gas in the gas mixture with He gas. Although data were greatly scattered, there exists a maximum for the selectivity of CNC between 0.16 and 0.24. The average selectivity of CNC obtained under these optimum conditions is approximately 55%.

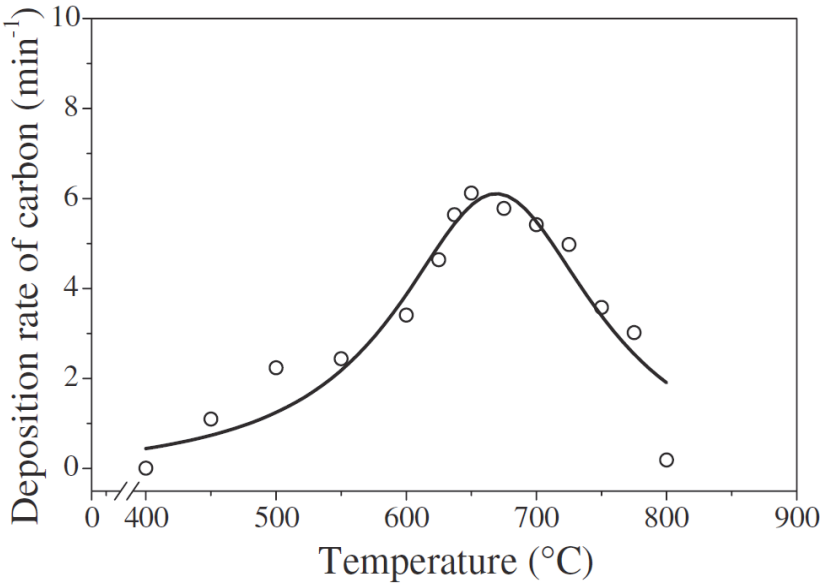

Fig. 5. Deposition rates of carbon materials at different reaction temperatures. Pyrolysis of C_2H_2 was carried out on 10 mg mixture of Fe and SnO_2 of 2 to 1 weight ratio for 10 min with the flow rates of C_2H_2 and He gases of 180 and 420 ml/min, respectively. (Xu et al., 2005)

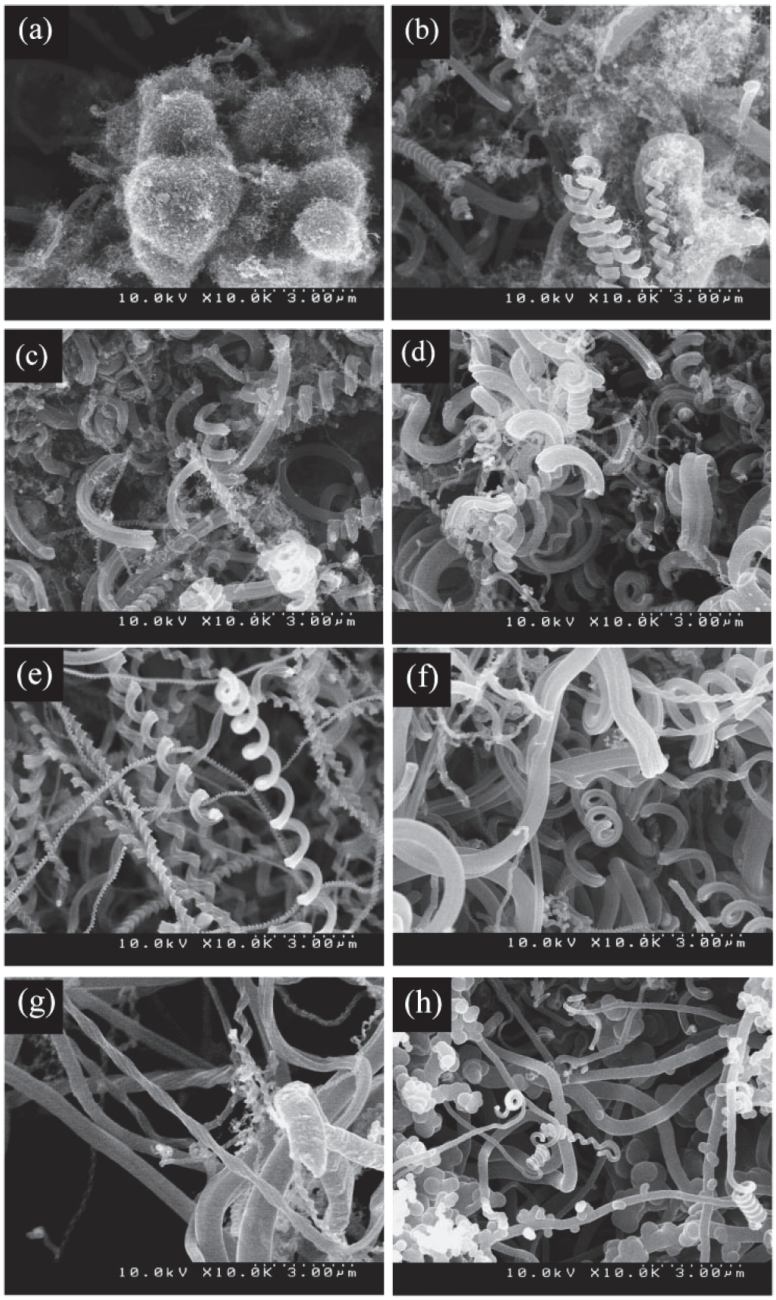

Fig. 6. SEM micrographs of the carbon materials deposited on the catalysts at the temperatures of (a) 500°C, (b) 600°C, (c) 650°C, (d) 675°C, (e) 700°C, (f) 725°C, (g) 750°C, and (h) 800°C. (Xu et al., 2005)

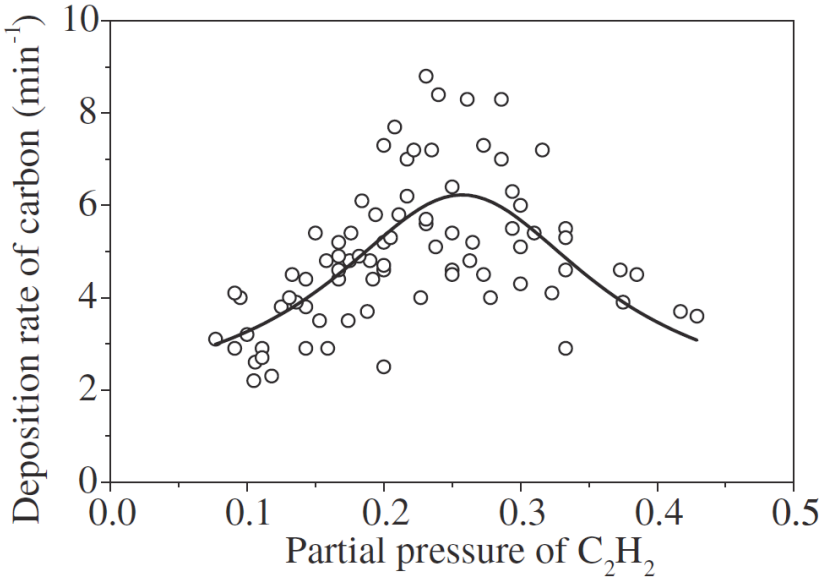

Fig. 7. Deposition rates of carbon materials at different reaction temperatures. Pyrolysis of C_2H_2 was carried out on 10 mg mixture of Fe and SnO_2 of 2 to 1 weight ratio for 10 min with the flow rates of C_2H_2 and He gases of 180 and 420 ml/min, respectively. (Xu et al., 2005)

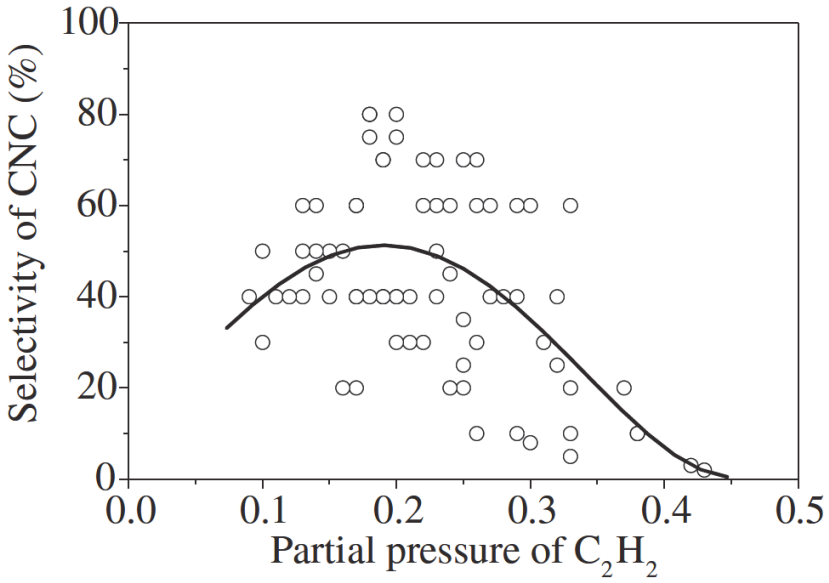

Fig. 8. Selectivity of CNCs plotted with partial pressure of C_2H_2 in a mixture with He gas. The process conditions are the same as those in the case of Fig. 7. (Xu et al., 2005)

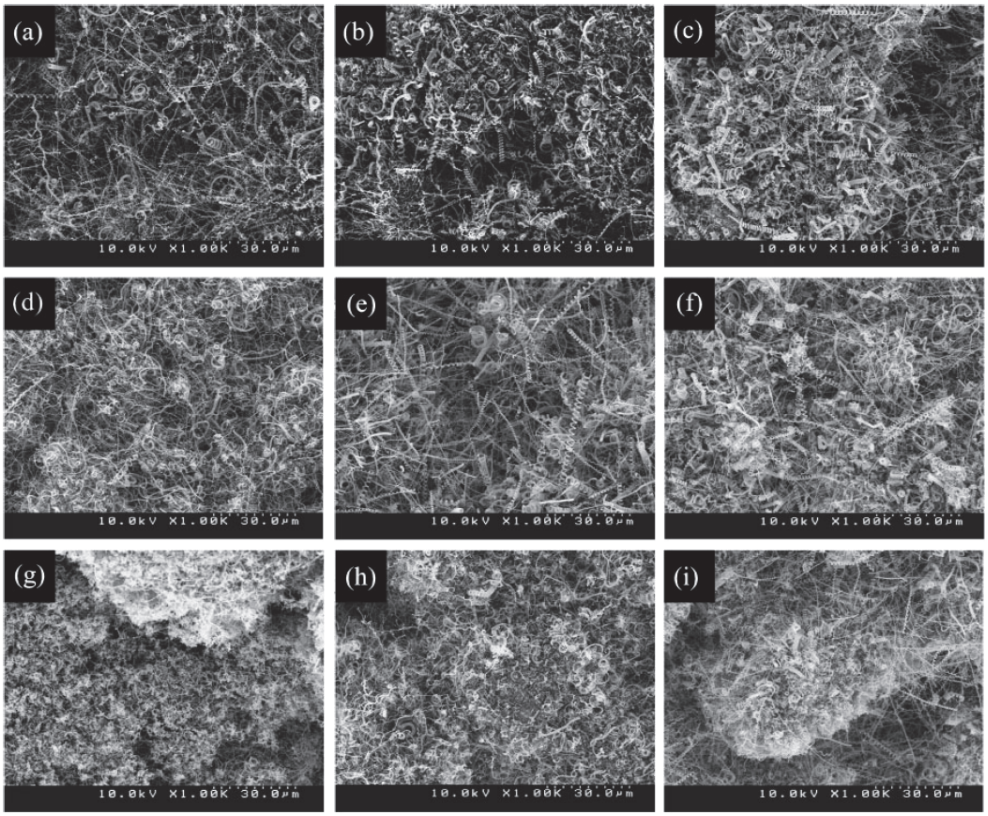

Fig. 9. SEM micrographs of the carbon deposited in C_2H_2/He gas mixtures of (a) 100/400, (b) 100/700, (c) 100/1000, (d) 150/400, (e) 150/700, (f) 150/1000, (g) 300/400, (h) 300/700, and (i) 300/1000. The CVD conditions are the same as those in Fig. 7. (Xu et al., 2005)

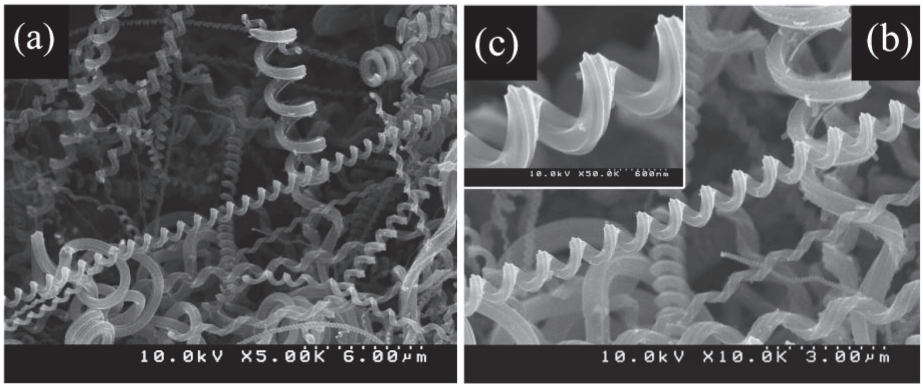

Fig. 10. SEM micrographs of carbon deposits under the optimum condition at (a) low, (b) middle and (c) high magnification. (Xu et al., 2005)

Figure 9 shows SEM micrographs of carbon deposits at gas compositions of 100 ml/min C_2H_2 gas in the mixture with (a) 400, (b) 700, and (c) 1000 ml/min He, those of carbon deposits with 150 ml/min C_2H_2 gas in the mixture with (d) 400, (e) 700, and (f) 1000 ml/min He, and those of carbon deposits with 300 ml/min C_2H_2 gas in the mixture with (g) 400, (h) 700, and (i) 1000 ml/min He. Higher CNC selectivity is observed on the diagonal line from upper left (a) through (e) to the lower right (i), and their C_2H_2 gas partial pressures are 0.20, 0.18, and 0.23, respectively. While keeping the flow of C_2H_2 gas at 100 ml/min, increasing the flow of He gas up to 700 and 1000 ml/min leads to the formation of more fibres and tightly compacted CMCs. In the case of the flow of 300 ml/min C_2H_2 gas and 400 ml/min He gas, numerous carbon particles can be observed instead of CNCs, CNFs or CMCs.

5.1.4 CNCs deposited under optimum conditions

After systematical optimisation of process conditions to obtain high yield as well as high purity of CNC, the best combination is confirmed to be Fe/SnO_2 catalyst of 2/1 in weight, reaction temperature of 700°C, and C_2H_2/He flow of 150/700 ml/min. CNCs deposited under optimum conditions were characterised in detail with FE-SEM.

Under the optimum conditions, the average selectivity of CNCs is approximately 80%, and the average deposition rate is approximately 5.5 min^{-1}. Figure 10 shows SEM micrographs of CNCs deposited under the optimum condition. From the micrograph with lower magnification, CNCs with different pitches and diameters can be observed, the pitches for the same coil are almost the same, the axes of CNCs are quite straight, and the longest CNCs are over 50 μm. By measuring 200 CNCs in the micrographs, the average pitch and diameter of the CNCs are found to be 750 and 750 nm, respectively and the average diameter of CNC fibre is estimated to be 350 nm.

5.2 Parametric study on growth of carbon nanotwist

In this section, parametric study on growth of carbon nanotwist (CNTw) reported by Katsumata et al. is introduced. The CVD apparatus with a NiCr alloy hot-filament was used to synthesize CNFs. Two methods were employed for preparing the catalyst-coated substrate. The first method was shielded cathodic arc deposition. (Takikawa et al., 1998) This method is a type of physical vapour deposition (PVD), in which the ions emitted from the cathode spot of vacuum arc discharge plasma are plated on the substrate. The second method was the sol-gel drop-coat method. Commercial sol-gel solutions for NiO and CuO coating, containing 3 wt% of Ni and Cu, were ultrasonically mixed. Then the mixed solution was dropped from a pipette on the substrate and dried at 200°C on a hot plate.

5.2.1 Ni/Cu multi-layer PVD-coated film catalyst

In this experiment, the flow rate of the source gas was 180 ml/min and the process time was 20 min. SEM and TEM micrographs of the deposited products under a different gas source and with/without hot-filament (HF) assist are shown in Figures 11 and 12, respectively.

When C_2H_2 gas was used without HF assist, as shown in Figures 11(a) and 12(a), CNC was synthesized. When C_2H_2 gas was used with HF assist, as shown in Figures 11(b) and 12(b), a rope-like fibre consisting of two to four fibres twisted together, called carbon nanorope (CNR), was synthesized. The CNR always had a catalyst particle at the top of the fibre. The TEM micrograph indicated the shape of the comparably fat trunk at the centre with thinner skin around the trunk. When C_2H_4 gas was used without HF assist, cocoon-like products

were obtained, as shown in Figure 11(c). When C_2H_4 gas was used with HF assist, as shown in Figures 11(d) and 12(c), CNTw was synthesized. The outer diameters of CNC and CNTw were thinner than that of CNR. These results indicate that a Ni/Cu catalyst provides various shapes of HCNFs depending on process conditions.
Figure 13 shows the result of EDX analysis of CNTw. It was found that the major deposition material was C, although the catalyst was composed of Ni and Cu, with the amount of Cu in the catalyst higher than that of Ni.

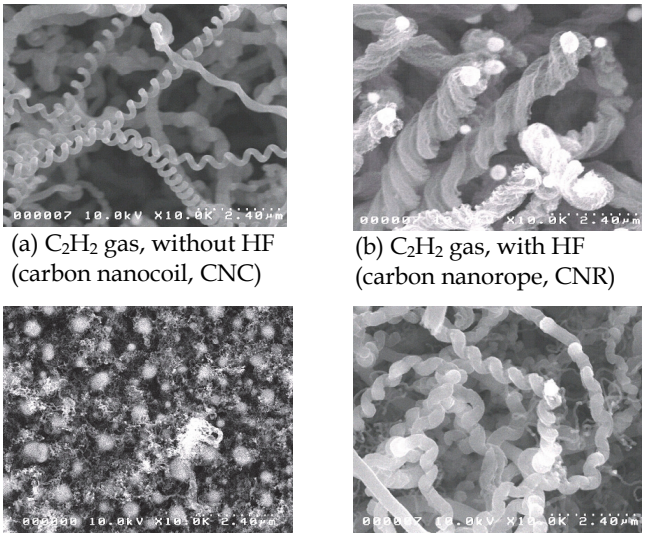

(a) C_2H_2 gas, without HF (carbon nanocoil, CNC)

(b) C_2H_2 gas, with HF (carbon nanorope, CNR)

(c) C_2H_4 gas, without HF

(d) C_2H_4 gas, with HF (carbon nanotwist, CNTw)

Fig. 11. SEM micrographs of various HCNFs prepared with Ni/Cu multi-layer PVD-coated film catalyst. HF: hot-filament assist. (Katsumata et al., 2004)

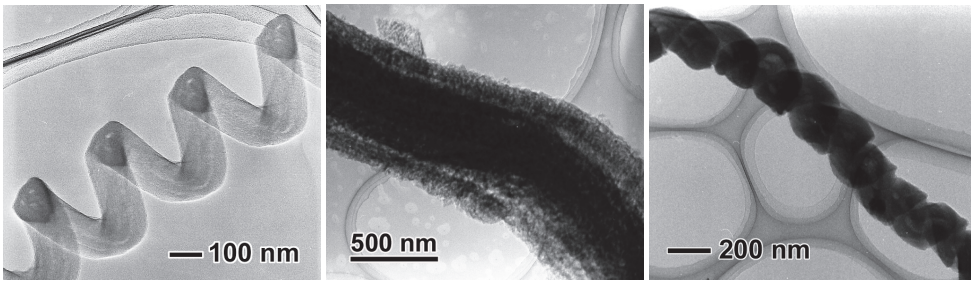

(a) CNC (b) CNR (c) CNTw

Fig. 12. TEM micrographs of various HCNFs prepared with Ni/Cu multi-layer PVD-coated film catalyst. (Katsumata et al., 2004)

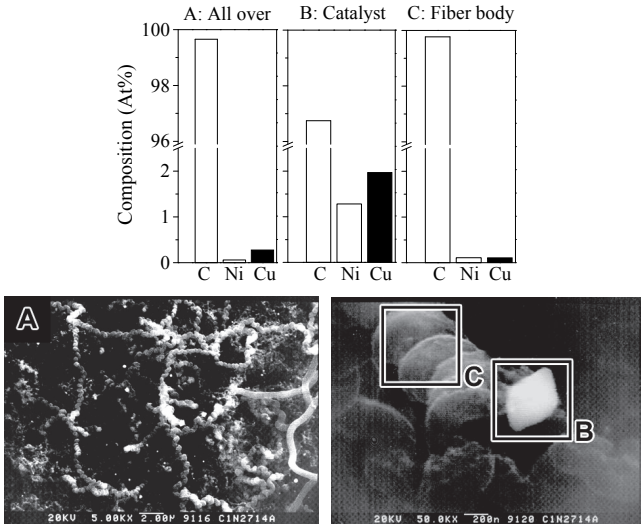

Fig. 13. EDX analysis of CNTw and SEM micrographs of analysis positions. (Katsumata et al., 2004).

5.2.2 Ni/Cu mixture sol-gel film catalyst

In this experiment, C_2H_2 gas was used as a carbon feedstock and a hot-filament was not used. The deposition time was 10 min.

Figure 14 shows the dependence of the NiO/CuO ratio on the carbon yield rate processed at 650ºC with a C_2H_2 flow rate of 180 ml/min. The range where the HCNF was obtained is indicated in the figure. When the amount of NiO was larger than that of CuO, the deposition amount was larger, although the product was mostly CNFs without helicity. When the NiO amount was lower, the deposition amount was smaller and the product was mostly HCNFs. The optimum NiO/CuO composition ratio for HCNF synthesis was in the range of 4/6—1/9 and the optimum was 2/8. This ratio is very close to a previous report indicating that the ratio of Ni/Cu=3/7 provides the HCNFs in the CVD process with C_2H_4. (Kim et al., 1992)

Figure 15 shows the temperature dependence of the carbon yield rate. The NiO/CuO ratio was 2/8. When the temperature was 500—600ºC, which was the optimum, the HCNF product yield as well as the carbon yield rate was high, and the fibre diameter was 80—100 nm. When the temperature was higher than 600ºC, the carbon yield was lower, the HCNF yield was low, and the HCNFs were thick (200—300 nm diameter). When the temperature was lower than 500ºC, the carbon yield was lower and the HCNF yield was low. The temperature obtained in the present work was lower than the optimum temperature of 600—700ºC for Ni/Cu catalyst and C_2H_4 feedstock gas. (Kim et al., 1992) This implies that C_2H_2, which is readily to thermally decomposed, is adequate for the lower temperature process.

The influence of the flow rate of the C_2H_2 source gas on the carbon yield rate is shown in Figure 16. When the C_2H_2 gas flow rate was lower than 100 ml/min, carbon yield was low and the product was a CNF without helicity. When the flow rate was 125—180 ml/min, the HCNF

yield as well as the carbon yield rate was high. When the flow rate was higher, the carbon yield was also high though a HCNF was not obtained. In this experiment, most HCNFs grown were CNTw. Figure 17 is a micrograph of CNTws prepared in the optimum condition.

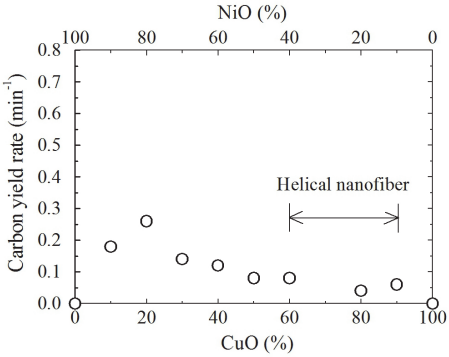

Fig. 14. Dependence of NiO/CuO catalyst composition rate on carbon yield rate. Process temeperature, 650°C; C_2H_2 flow rate, 180 ml/min. (Katsumata et al., 2004)

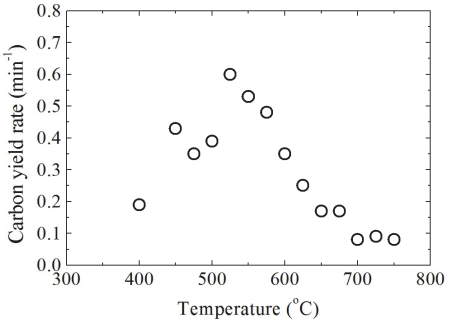

Fig. 15. Dependence of process temperature on carbon yield rate. NiO/CuO ratio, 2/8; C_2H_2 flow rate, 180 ml/min. (Katsumata et al., 2004)

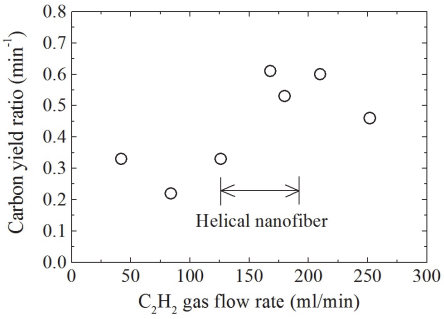

Fig. 16. Dependence of source gas flow rate on carbon yield rate. NiO/CuO ratio, 2/8; process temperature, 550°C. (Katsumata et al., 2004)

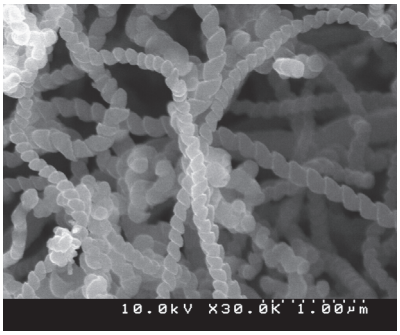

Fig. 17. CNTw obtained at optimum conditions. NiO/CuO ratio, 2/8; process temperature, 550°C; C_2H_2 flow rate, 160 ml/min. (Katsumata et al., 2004)

5.3 Increase of the CNTw production rate by an automatic CVD system

In this section, the results by an automatic CVD system that the production rate of CNTw increased up to 5400 times, compared with the conventional CVD system are shown. (Hosokawa et al., 2007) The automatic CVD system is described in detail in Section 4.2. The detail of CNTw growth conditions is indicated in each of the figure caption.

The synthesized carbon nanomaterials were observed by a compact digital camera and an FE-SEM, as shown in Figure 18. In case of the direct film-growth CNTw on Ti-coated glass, the CNTw yield in carbonaceous product was almost 100%, and no other shape of carbonaceous material was found. The overview morphology of the film was quite uniform. The weight of the catalyst coated on the substrate was 0.7mg. The film thickness was approximately 4 μm for 30-minute process time. The weight of the film was 1.3 mg, evaluated from the weight change of the substrate before and after CNTw growth. Thus, the

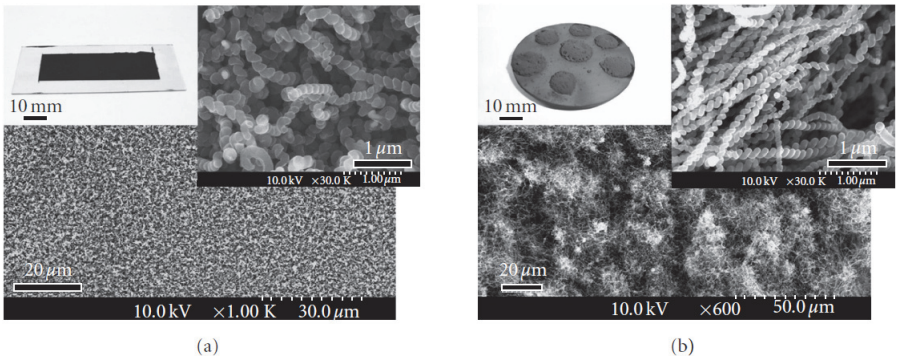

Fig. 18. Photograph and SEM micrograph of CNTw. (a) Direct film-growth of CNTw on Ti-coated glass substrate. Ni/Cu/In_2O_3 catalyst was used. The flow rates of C_2H_2: 80 ml/min; He: 420 ml/min; reaction temperature: 470°C. (b) Powdery CNTw synthesized in automatic CVD system on graphite substrate. Ni/SnO_2 catalyst was used. The flow rates of C_2H_2: 350 ml/min; N_2: 1400 ml/min; reaction temperature: 470°C. Upper left, overall view; upper right, high-magnification SEM; lower, low-magnification SEM, respectively. (Hosokawa et al., 2007)

synthesis ratio of CNTw against the catalyst in weight, indicating the production efficiency on catalyst, was approximately 1.9, and the production rate was approximately 0.5 mg/h.
As shown in Figure 18(b), the product of CNTw synthesized from Ni/SnO_2 catalyst formed a softly-swollen dome shape on the substrate. So far, when 8 substrates were consecutively processed, approximately 6 g of CNTw was produced in 3 hours. In average, 900 mg CNTw was produced on 1 substrate by 36 mg of catalyst. Thus, the production rate was approximately 2,700 mg/h, and productivity of powdery CNTw was 5,400 times, compared with direct film-growth. The grown CNTw was easily scraped off the substrate and the powdery form CNTw was obtained. Yield of CNTw shape material in the carbonaceous product was almost 100%. The synthesis ratio of CNTw against the catalyst in weight was approximately 25. The fibre diameter of powdery CNTw was found to be thinner (average 90 nm) than that of the direct film growth CNTw (average 150 nm).

6. Analyses of HCNFs structure and their growth mechanism

6.1 Splitting and flattening of HCNFs

In this section, the experimental result that CNC was found to show a drastic shape change, splitting and flattening when HCNFs were acidified in a 30% hydrogen peroxide solution. (Yokota et al., 2010) The HCNF growth condition is indicated in each of the figure caption.

6.1.1 Experimental details

HCNFs were prepared with a CVD system, as previously reported. (Takikawa et al., 2000), (Katsumata et al., 2004) The substrate was a graphite plate (25×25 mm, thickness 3 mm) placed at the reactor centre. A liquid-state mixed catalyst was dropped on to the substrate, then dried to solidify at 200°C for 10 min in air and the Fe/Sn or Ni/Sn catalyst was formed. The source gas used was C_2H_2 (150 ml/min) and the dilute gas was N_2 (1000 ml/min). The other conditions were as follows: the reaction temperature was 700°C (Xu et al., 2005) using the Fe/Sn catalyst for CNC synthesis and 550°C using the Ni/Sn catalyst for CNTw synthesis. The growth time was 10 min for each reaction.
50 mg of as-prepared HCNF was treated in a flask with 10 ml of a 30% hydrogen peroxide solution under reflux. The treatment temperature was varied from 20 to 200°C for 1 h. The treatment time was 30–150 min at 100°C and 15–90 min at 140°C. After the treatment, the acid-treated HCNF was extracted from the solution by suction filtration and subsequently dried at 120°C for 1 h on a hotplate.

6.1.2 Synthesis of HCNFs acid-treated

Figure 19 shows the surface images of as-prepared CNCs and CNTws. By careful observation, as-prepared CNCs and CNTws were found to be categorized into angular- and round-types according to their fibre cross-sections (see Figure 1). The Ni–Sn catalyzed reaction produces only the round-type CNTw. However, the Fe–Sn catalyzed reaction produces the other three types simultaneously; round and angular-type CNCs and the angular-type CNTw. The typical yield of CNCs in the products prepared using the Fe–Sn catalyst was 30–40% as determined from the SEM observations. The content ratio of HCNFs was > 90%, < 10% and < 1% for the angular-type CNCs, angular-type CNTws and round type CNCs, respectively.

6.1.3 Acid treatment results

SEM micrographs of the four types of CNCs and CNTws after acid treatment are shown in Figure 20. The shape of the angular-type CNC was found to change dramatically. While the angular-type CNC was split and flattened, the round-type CNC was also split but not significantly flattened. As for the angular-type CNTw, the fibre surface was slightly edged. The shape of the round-type CNTw was unaffected by the treatment.

The weight loss and shape change of CNCs by acid treatment for 1 h were evaluated. (Yokota et al., 2010) The weight decreased as the temperature was increased. Furthermore, the weight decreased dramatically at 80–120ºC. The weight loss was due to the carbon oxidation reaction. The release of carbon dioxide was confirmed by the observation that limewater became cloudy by the gas generated during the acid treatment. Therefore, these results indicate that etching of CNCs and dissolution of amorphous carbon progressed when the oxidation reaction proceeded at temperatures above 80ºC. The saturation of weight loss was observed over 140ºC and this was caused by the boiling of the hydrogen peroxide solution (i.e., boiling point of 141ºC). The CNC shape did not change between 20 and 60ºC. CNCs were split into a few pieces over 100ºC. The weight loss as a function of treatment time for reaction temperatures of 100 and 140ºC was also evaluated. (Yokota et al., 2010) As the treatment time increased, the shape change became significant. The weight loss reached saturation at 100ºC when the reaction time was > 120 min, whereas at 140ºC, saturation was reached after 45 min. At saturation, the weight difference due to the different temperatures was ~48% at 100ºC and ~38% at 140ºC.

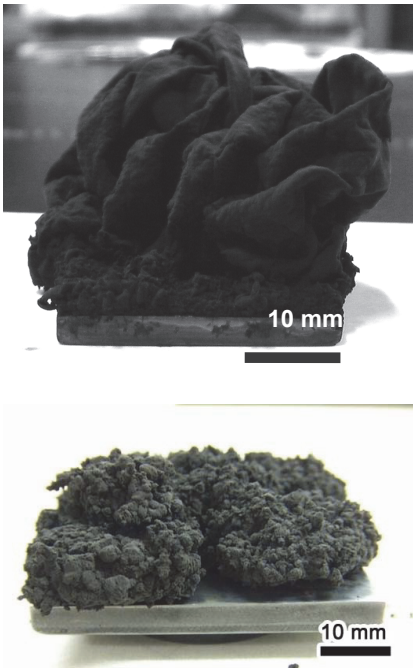

Fig. 19. Images of as-grown HCNFs synthesized by CVD. (a) CNCs using the Fe/Sn catalyst and (b) CNTws using the Fe/Sn catalyst.

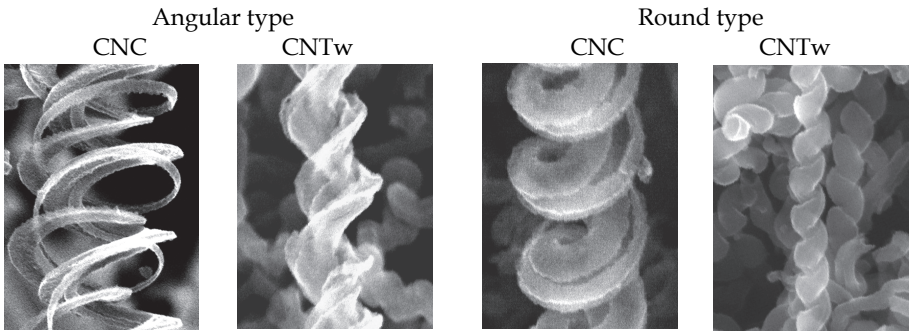

Fig. 20. SEM micrographs of four types of HCNFs after the acid treatment.

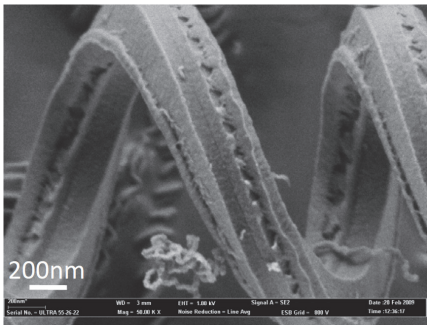

Fig. 21. SEM micrograph of CNC by the FE-SEM with a low acceleration voltage. Courtesy of Dr. Hamanaka at JFCC.

As previously described, the structures of most HCNFs prepared with an Fe-based catalyst are not uniform in the radial direction of the fibre. (Chen et al., 2004), (Xu et al., 2005), (Zhang et al., 2000), (Pan et al., 2002), (Yang et al., 2005) In other words, there are high and low density regions inside the fibre. Figure 21 shows a micrograph of angular-type CNC by the FE-SEM with a low acceleration voltage. Difference in the surface structure of CNC is clearly observed. This non-uniformity continues along the length of the fibre. The low density part, which is bonded to the high density parts, is considered to initially dissolve by acid treatment while the high density parts remain and appear as flattened CNCs.

6.2 Analysis of the CNC structure by 3D-TEM

To analyse the CNC structure, electron tomography of the as-grown and acid-treated CNCs was obtained using a TEM tomography system (JEOL, TEMography). (Yokota et al., 2010) The TEM images of the samples were serially recorded at tilt angles from 60 to −60° degrees with a 1° step size (i.e., total of 120 images). The CNC position in each image was aligned precisely.

Figure 22 shows a TEM micrograph of CNC before acid treatment. The transmission image of an as-grown CNC showed contrasting density in the fibre. In contrast, the flattened CNC after acid treatment showed a uniform contrast. An SEM observation showed that the

number of the fibres after acid treatment was dependent on the CNC shape. Figure 23 shows that the CNC split into three fibres.

The 3D image of CNCs was taken by electron tomography. The cross-sectional image showed that there is a shadow present inside the CNCs. This shadow was seen from the images sliced in the x, y and z directions. This shadow indicates the existence of a cavity inside the CNC. These results show that the structure of the CNC has a hollow centre. The flattened CNC after acid treatment showed that three helical fibres were in parallel. The cross-sectional observation showed that each fibre was separated and their diameter was approximately a quarter of the as-grown CNC.

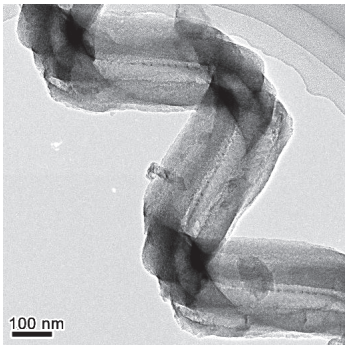

Fig. 22. TEM micrograph of as-grown CNC.

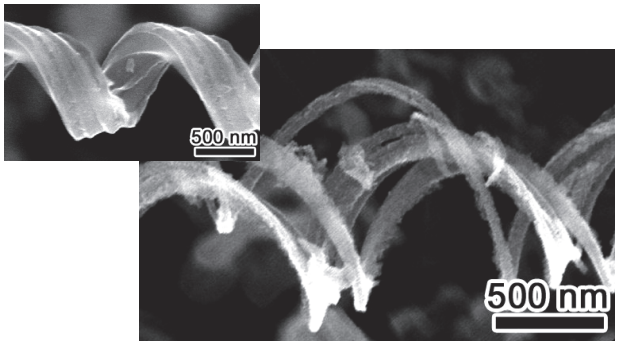

Fig. 23. The CNC splits into three fibres.

6.3 HCNFs growth mechanism

6.3.1 General mechanism for growth of carbon fibres

Baker et al. postulated a bulk-diffusion model of carbon through catalyst particles. (Baker et al., 1972) In this mechanism, hydrocarbon gas decomposes on exposed surfaces of catalyst particles into hydrogen and carbon. Because this reaction is exothermic, a temperature gradient is believed to exist through a catalyst particle. The dissociated carbon dissolves into the surface of the heated catalyst particle and diffuses to its cold tail. Since the solubility of carbon in a catalyst particle is temperature dependent, excess carbon precipitates out to

form carbon filaments with the same diameter as that of the catalyst particle. The bulk diffusion is believed to be the limiting step of the process.
Another model of CNF formation has been demonstrated by Rodriguez et al. (Rodriguez, 1993), (Rodriguez et al., 1995) In this model, catalyst particles are characterised as tiny crystals with various facets. Hydrocarbon decomposes at one face, and carbon in the form of a graphite layer precipitates at another face. Catalyst composition and crystallinity dominate the structure of deposited fibres. For example, herringbone structure was formed from Fe–Cu (7/3) catalyst in C_2H_4–H_2 (4/1) gas mixture, whereas the stacked structure was predominant due to the reaction of CO–H_2 (4/1) on Fe-based catalyst. Hydrogen is important in CNF formation, because it acts as the terminator of dangling bonds at edges of stacked graphite platelets. (Nolan et al., 1995) The concept of a spatial velocity was introduced to explain the growth of wavy and helical nanotubes. The mismatch between extrusion velocities of different faces of a catalyst particle results in the deformation of carbon deposits. (Fonseca et al., 1996), (Fonseca et al., 1995), (Amelinckx et al., 1994)
In spite of the differences between these models, it is commonly accepted that hydrocarbon precursors dissociate on catalyst particles, and the formed carbon species dissolve into catalyst particles and recombine to form carbon filaments. This general mechanism suggests that the fibre diameter is dominated by the particle size of the catalyst, the carbon structure is determined by the crystallinity of the catalyst, and the filament shapes, such as tubular, helical, or wavy, are related to the surface anisotropy or composition of the catalyst.

6.3.2 Interpretation of temperature effects

Generally, below room temperature, acetylene is adsorbed molecularly with its C–C axis parallel to the catalyst surface. (Hung & Bernasek, 1995) The thermal pyrolysis may follow several routes depending on the initial coverage and catalyst activity. Acetylene adsorbs on a clean Fe (100) surface by sp^3 hybridization. At lower exposure (< 0.2 layer), C_2H_2 decomposes to form CH and CCH at –20°C. At higher exposure (> 0.2 layer), C_2H_2 partially dehydrogenates to form CH, CCH and $CHCH_2$ at the adsorption temperature of –173°C. When the surface is warmed to 120°C, a CCH_2 species is formed by the dehydrogenation of $CHCH_2$. (Hung & Bernasek, 1995) This means that acetylene adsorption on Fe is a self-initiative process and the activation energy of C_2H_2 decomposition is fairly low. However, at high temperature, C_2H_2 adsorption will result in a rather low coverage on catalyst.
In the kinetic study of the growth of CNTs on γ-Fe metal from acetylene, the activation energy was deduced, from an Arrhenius plot, to be 142 kJ/mol. (Baker, 1989) This value is close to the activation energy for carbon diffusion in bulk metal, 148 kJ/mol. (Smithells, 1992) This suggests that the bulk diffusion of carbon would be the rate-limiting step. (Lee et al., 2003) Since the solubility of carbon in a metal is also temperature dependent, temperature elevation will accumulate the dissolution as well as the diffusion of carbon in the catalyst particles. Therefore, an enhanced deposition rate of carbon is to be expected.
Unfortunately, the experimental results do not coincide with the above prediction. There must have been other factors affected by temperature. These factors include hydrocarbon adsorption on the catalyst, catalyst deactivation, and gas phase reactions of hydrocarbon. Since adsorption, pyrolysis of C_2H_2, and precipitation of carbon are all exothermic processes, (Bell & Shustorovich, 1990) the increase of temperature shifts the reaction equilibrium to the precursor side and results in less total conversion.

The optimum temperature for both the selectivity and the deposition rate of CNCs is around 700°C under the given experimental conditions. Noting that the eutectic point where austenite, ferrite and cementite coexist in the Fe–C phase diagram is at 723°C, phase changes accompanying transportation and precipitation of carbon is postulated to be a key in carbon fibre formation. (Qin, 1997)

6.3.3 Mechanism involving gas reaction

When hydrogen was used as the dilution gas in the pyrolysis of methane in an inductively coupled plasma reactor, CNFs were produced. However, replacing hydrogen with argon favours the production of MWCNTs. (Delzeit et al., 2002) Atomic hydrogen as well as hydrogen molecule acts as a terminator of dangling bonds on the edges of graphite platelets. Furthermore, because of the reaction of hydrogen with the carbon deposit, hydrogen is also believed to be helpful for avoiding the deactivation of the catalyst.

Xu and Pacey decomposed acetylene in a flow system between 584 and 697°C under pressures between 27 and 127 Torr. An induction period for the formation of vinylacetylene and benzene was observed, which was considered to be crucial evidence of a free radical mechanism. (Xu and Pacey, 2001) Although they suggested that two C_2H_2 molecules were involved in the initial reaction, collisions between C_2H_2 and He are considered to be the main happening in our system because of the high addition of a large amount of He gas.

7. Synthesis of multi-walled CNC (MWCNC)

In this section, the experimental result that thin CNC with a fibre diameter of < 50 nm was synthesized by CVD using Fe/Sn catalyst supported on zeolite is introduced. (Yokota et al., 2011) TEM observation revealed that more than 90% of the CNCs obtained were multi-walled CNCs (MWCNCs), and the remainder was columnar CNCs without a hollow structure. Three-dimensional images of an MWCNC with Au nanoparticles on its surface were reconstructed by electron tomography and confirmed that the MWCNC had a three-dimensional helical shape. The HCNF growth condition is indicated in each of the figure caption.

7.1 Experimental details

Thin CNCs were synthesized using a catalytic CVD method and Fe/Sn catalyst supported on Y-type zeolite (Tosoh, HSZ-390HUA). The process of supporting metals on zeolite is as follows. Fe and Sn powders with a weight ratio of 3/2 were dissolved in dilute hydrochloric acid solution and mixed with the zeolite powder in the solution. The total weight of Fe and Sn in the solution was 5 wt%. The mixed solution was then sonicated for 10 min and dried at 110°C for 20 h. A 10 mg quantity of the zeolite with Fe/Sn catalyst on a quartz boat was placed in a quartz reactor tube. The tube was substituted with N_2 (1000 ml/min) and heated to desired reaction temperatures (650–750°C) for 1 h. When the reactor reached the desired temperature, C_2H_2 gas was added in the tube as a source gas for 10 min while keeping the N_2 flow. The flow rate of C_2H_2 was varied between 50 and 300 ml/min.

7.2 SEM and TEM observation of MWCNCs

Figure 24 shows SEM micrographs of zeolite with carbon fibres synthesized by CVD at 700°C. The flow rates of C_2H_2 were (a) 50 ml/min and (b) 150 ml/min, respectively. The

CNC fibre diameters obtained by C_2H_2 flow rates of 50 ml/min and 150 ml/min were measured to be ≈20 and ≈30 nm, respectively. It seems that the fibre diameter thickened with increasing C_2H_2 flow rate. The fibre cross-section of thin CNCs is round without angles and differs from that of previously obtained CNCs synthesized by Fe microparticles with Sn solution, which had a reported fibre diameter of at least 120 nm. (Zhang et al., 2000), (Yokota et al., 2010) Fe/Sn catalyst nanoparticles were formed on zeolite which has a mesoporous structure with pore size of 0.4–0.8 nm. CNCs were observed only on the zeolite surface. It seems reasonable that the Fe/Sn nanoparticle on zeolite synthesized the thin CNC.

Figure 25 shows TEM micrographs of thin CNCs synthesized with 50 ml/min C_2H_2 flow. More than 90% of the thin CNCs obtained were multi-walled CNCs (MWCNCs). The striped pattern of the multiple layers and the hollow structure were observed clearly. Bamboo-like CNCs having a graphitic layer in the hollow and MWCNCs containing a nanoparticle in the hollow were observed. The particle encapsulated in an MWCNC was confirmed to be an Fe nanoparticle without Sn using an EDX spectroscope equipped with a TEM. Columnar CNCs that did not have hollows but having diameters almost the same as that of the MWCNCs were also observed. The number of MWCNCs, bamboo-like MWCNCs, nanoparticle-containing MWCNCs and columnar CNCs were 21, 2, 3 and 3 respectively in the sample. In addition, the coil diameter of columnar CNCs was smaller than that of the MWCNCs, indicating that the form of columnar CNCs resembles that of CNTw. (Hosokawa et al., 2008), (Yokota et al., 2010), (Takikawa et al., 2000) To our knowledge, the columnar CNCs have not been previously reported though there are reports of MWCNCs. (Kanada et al., 2008), (Lu et al., 2004), (Yang et al., 2003)

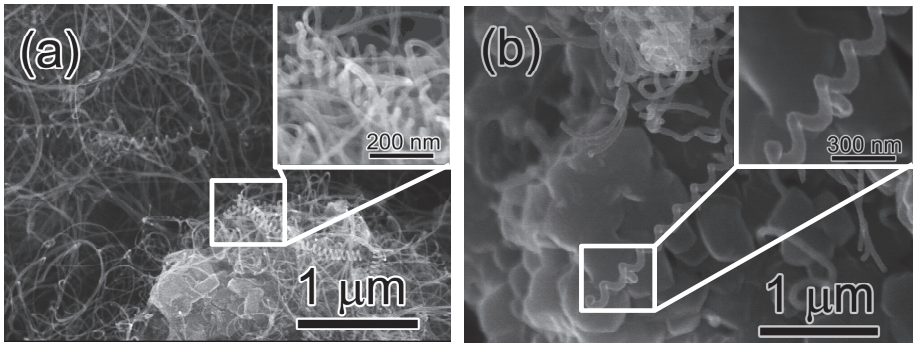

Fig. 24. SEM micrographs of thin CNCs synthesized by Fe/Sn catalyst supported on zeolite at 700ºC. C_2H_2 flow rates were (a) 50 and (b) 150 ml/min.

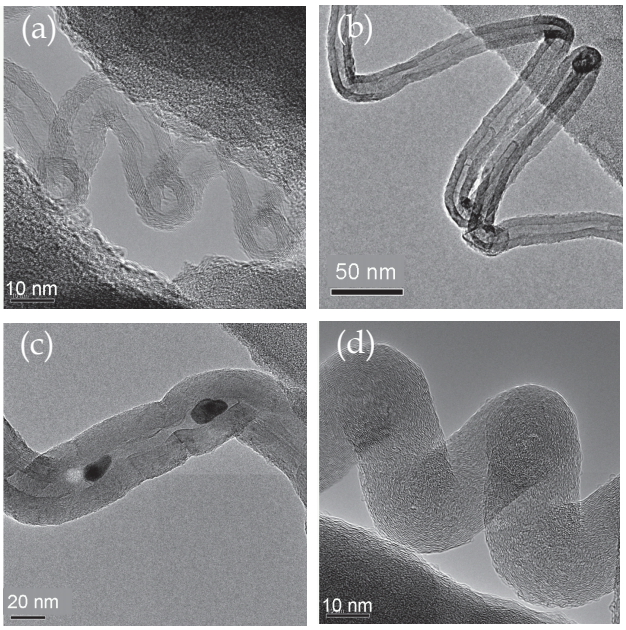

Fig. 25. TEM micrographs of thin CNCs. (a) A MWCNC with hollow and graphitic layer structures. (b) Bamboo-like CNC. (c) CNC containing an Fe nanoparticle in the tube. (d) Columnar CNC. The columnar CNC included concentric graphitic layers with spacing of ≈0.34 nm. (Yokota et al., 2011)

The fibre and coil diameters of thin CNCs were measured from the TEM micrographs. The coil diameter is determined as the outer diameter of the CNC. The number of samples analysed was 29, and coil diameters could be measured for 23 of the 29 CNCs. The average fibre and coil diameters of thin CNCs were 15±5 nm and 50±20 nm, respectively.

Kanada et al. reported that the fibre diameters of MWCNCs were less than 25 nm and the coil diameter was 54±20 nm. (Kanada et al., 2008) These dimensions are similar to our results. The number of graphitic layers of MWCNCs and coil pitches were evaluated to be 10–30 and 25–200 nm, respectively. The fibre and coil diameters of the thin CNCs in this study were as small as 1/10 those for previously obtained CNCs. (Yokota et al., 2010) Note that the structures of CNCs changed from an amorphous structure to a multi-walled graphitic layer as the CNC diameter became small. It was reported that most thin CNCs with fibre diameter less than 50 nm had graphite structure. (Kanada et al., 2008), (Lu et al., 2004), (Yang et al., 2003) When the fibre diameter of CNF became small, the fibre formed the multi-walled structure. The change of CNC structure appeared similarly in the reduction of CNF diameter. The structure change from amorphous to graphitic implies the enhancement of the electrical characteristics of CNCs. It was reported that the electrical resistivity of "graphitic" CNF (≈10^{-6} Ωm) (Melechko et al., 2005) was lower than that of "amorphous" carbon micro coil (≈10^{-4} Ωm). (Kajihara et al., 2005)

As the flow rate increased, the amount of carbon deposit, which does not include the mass of metals and zeolite, increased and the fibre became thick, as shown in Figure 24. When the acetylene flow rate and reaction time were 50 ml/min and 10 min, respectively, the amount of carbon in an acetylene molecule was about 0.5 g. The weight of carbon deposits was about 1–2 mg, and about 0.2–0.4% of carbon was deposited from acetylene. The temperature was varied from 650°C to 750°C while keeping the C_2H_2 flow rate at 50 ml/min. The carbon deposit was highest (2 mg) at 650°C and gradually decreased with temperature. However, most of the deposit was CNFs, and CNCs could not be found at 650°C. CNCs were observed at temperatures of at least 700°C. The coil pitch of CNCs grown at 750°C was longer than that of CNCs grown at 700°C. These results suggest that the C_2H_2 flow rate influences not only the yield of MWCNCs in the carbon deposit but also the fibre diameter and CNC structure.

7.3 3D-TEM analysis of the MWCNC structure and future subject

Electron tomography of the MWCNC was performed using a TEM tomography system. Reconstruction of 3D image for the MWCNC has been hardly done because there is almost no "marker" on the surface to recognize the rotation of an MWCNC. In this analysis, Au nanoparticles were deposited on MWCNCs by ion sputtering. This helped us recognize the rotation when the tilt angle was changed.

Figure 26(a) shows a TEM micrograph of an MWCNC with Au nanoparticles. The diameters of Au nanoparticles ranged 1–10 nm. This suggests that MWCNCs are applicable as a support material of nanoparticles. Figure 26(b) shows a reconstructed 3D image of an MWCNC with Au nanoparticles. From the 3D image, it is confirmed clearly that the MWCNC had a helical shape with a left-hand helix.

Problems still remain in raising the ratio of the MWCNCs to CNTs from 10%. A possible explanation for this experimental observation with SEM is that Fe and Sn nanoparticles were independently supported on different pores of a zeolite. In TEM observation, most MWCNCs did not contain catalyst particles on the end or inside the tube; the catalyst particles inside the tube that we could find contained less than 0.1 wt% Sn.

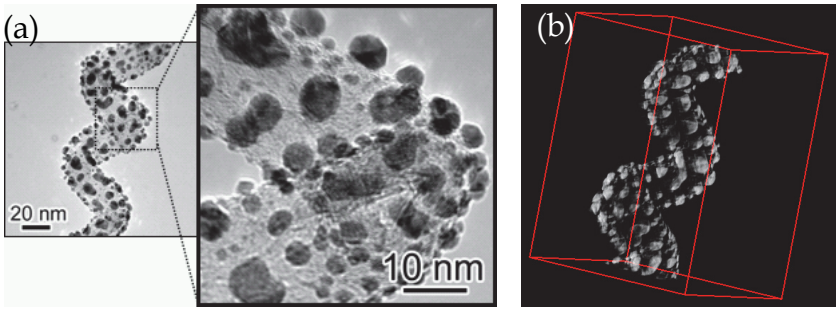

Fig. 26. Electron tomography of an MWCNC. (a) TEM micrograph of the MWCNC coated with Au nanoparticles. (b) Volume rendering image of the reconstructed MWCNC 3D image of (a). These images show that the MWCNC had a helical shape with a left-hand helix.

8. Application

In this section, we introduce an application of HCNF to field emission device. CNTw is used as an electron emitter and mixed with a binder and printed on Si substrate. We have shown that dielectric barrier discharge treatment made CNTws stand up. The field emission property was enhanced by the upright CNTws. (Hosokawa et al., 2008) The detail of experimental conditions is indicated in each of the figure caption.

8.1 Fabrication of CNTw field emitter

CNTw was synthesized by catalytic CVD. (Katsumata et al., 2004), (Hosokawa et al., 2007) The CNTws grown were mixed with an organic binder composed of ethyl cellulose in a mortar and the CNTw paste was made. The mixture ratio by weight of CNTw and binder was 7/93. The CNTw paste was screen-printed on a Si substrate measuring 5mm×40mm, and a dot pattern of CNTw film (dot size = 100 μm × 100 μm, spacing =100 μm) was formed. The CNTw film was calcined in an electric furnace at 120°C for 2 h or 400°C for 1 h. (Lee et al., 2006) The film thickness after the calcination was 3 μm. To measure the field emission property, Zn : ZnO phosphor was used as an anode, and the anode area, gap distance and pressure were 0.1 cm^2 (ϕ3.6 mm), 100 mm and 10^{-4} Pa, respectively.

8.2 Stand-up treatment

The CNTw emitter was treated by a dielectric barrier discharge (DBD) apparatus as shown in Figure 27. A quartz plate was glued on both electrode surfaces and DBD was generated between the plates (Xu, 2001). In He gas, the glow discharge was uniformly generated ('glow mode'), whereas DBD was seen in N_2 ('filament mode'). In this study, both modes were applied to the CNTw emitter. The emitter was placed on the grounded electrode and treated by generating a discharge on the substrate surface (Figure 28). The following treatment conditions were commonly used: the gap distance (distance from the emitter surface to the upper electrode) = 1 mm, discharge frequency = 30 kHz, pulse duration = 2.0 μs and gas flow rate = 2000 ml/min. For 'glow mode,' He gas was used, and an electric field of 4.4 kV/mm was applied for 30 s. On the other hand, N_2 gas was used and an electric field of 6.8 kV/mm was applied for 'filament mode.' The treatment time was varied from 0 to 180 s. The filaments between the electrodes move randomly while the discharge is sustained. Therefore, it is possible to treat the whole area of the substrate uniformly if the size of the substrate is smaller than that of the dielectric plate.

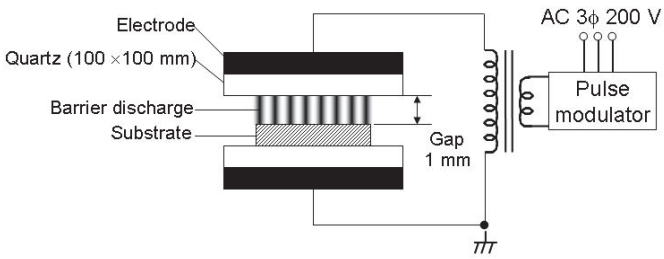

Fig. 27. Schematic of dielectric barrier discharge (DBD) apparatus. (Hosokawa et al., 2008)

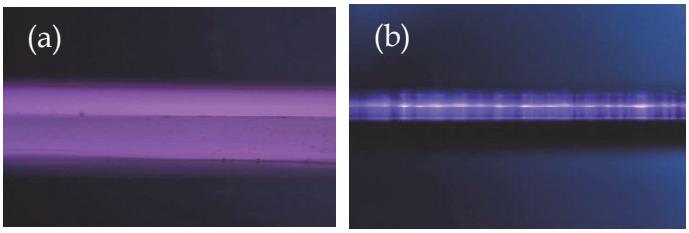

Fig. 28. Photographs of stand-up treatment by (*a*) 'glow mode' and (*b*) 'filament mode.' (Hosokawa et al., 2008)

8.3 Making CNTws stand up

Figure 29 shows an SEM micrograph of the emitter treated by 'glow mode.' The surface does not seem changed by 'glow mode' treatment, and CNTws remain tangled and heaped on the substrate. On the other hand, by 'filament mode' treatment, the CNTws were made to stand vertically from the substrate, as shown in Figure 30. For a treatment time ≥ 30 s, flocculated CNTws are not seen any more, and it is confirmed that 3–5 CNTws are upright at 5 μm intervals on the emitter treated for 30 and 60 s. Their length from the substrate surface became shorter due to etching as the treatment time increased. The great difference in the treatment results between the 'glow' and 'filament' modes is clearly shown in Figures 29 and 30. To explain this, the orientation forces applied to CNTws in each mode are illustrated in Figure 31. The electric field is almost uniform in the vertical direction from the substrate in the 'glow mode' (Figure 31(a)) and Coulomb force:

$$F = qE, \tag{3}$$

where q is the electric charge on CNTws; E the electric field only acts on CNTws. On the other hand, in the 'filament mode,' a non-uniform electric field is generated between the electrodes, and not only the Coulomb force but also the gradient force

$$F = \frac{1}{2} grad\left(E^2 \rho_m \frac{\partial \varepsilon}{\partial \rho_m} \right), \tag{4}$$

where ε is the permittivity of CNTw; ρ_m the density of CNTw acts on CNTws in the direction in which the electric field strength is increasing. (Stratton, 1941) The gradient force in the 'filament mode' is larger than the Coulomb force since the gradient force is proportional to the gradient of the product of permittivity and electric field squared. Consequently, CNTws could be raised by the gradient force in the 'filament mode.'

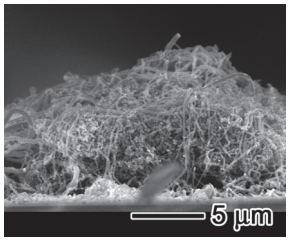

Fig. 29. SEM micrograph of the emitter treated by 'glow mode.' (Hosokawa et al., 2008)

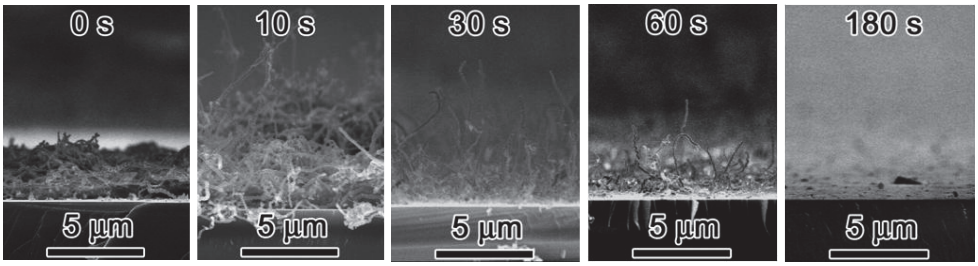

Fig. 30. SEM micrographs of the emitter treated by 'filament mode' at different treatment times. (Hosokawa et al., 2008)

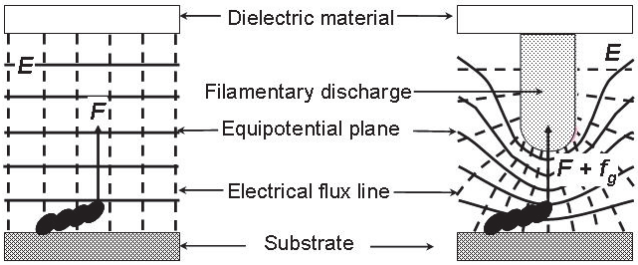

Fig. 31. Schematic illustrations of orientation force on CNTw: (a) uniform electric field in 'glow mode,' (b) non-uniform electric field in 'filament mode.' (Hosokawa et al., 2008)

8.4 Field emission property

Figure 32 shows the field emission properties of the CNTw emitter treated by the 'filament mode' and emission pattern at a maximum current. Before the treatment, a spark easily occurred at a low electric field. The treatment made the field emission current higher. The field emission properties of the emitter at different treatment times are listed in Table 2. With emitter treatment for 10 s, the emission site is not uniformly distributed as shown in Figure 32. By the 30 s treatment, the emission is not concentrated but uniformly spread and the field emission properties are greatly enhanced. The ratio of the emitting area of the sample treated for 30 s to the phosphor surface reached 57% though that of the untreated sample was 2% only. As shown in Table 2, the length of CNTws was also gradually decreased and the distribution of CNTw length was narrowed due to etching with an increase in treatment time. This indicates that the treatment by 'filament mode' serves to flatten the emitter tips as well as make them stand up. However, the number of CNTws by the 60 s treatment was decreased and it made the field emission virtually impossible. Field emission did not occur from the 180 s treated emitter because mostly CNTws were removed. Also, we tried to treat the emitters composed of conductive/nonconductive whiskers and CNTs by the 'filament mode' and confirmed that the conductive whiskers were made to stand up. The CNTs were easily removed just after the ignition of DBD. A possible explanation for this is that the diameter of CNTs used was much thinner (~10 nm) than that of CNTws. Therefore, this stand-up treatment by DBD would be suitable for thick CNFs.

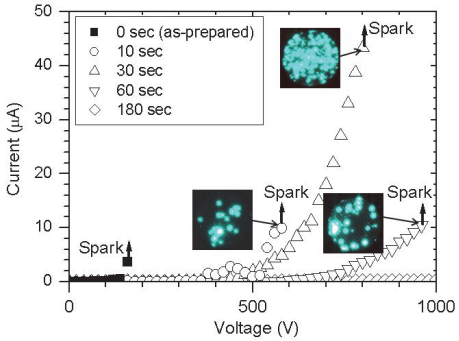

Fig. 32. Field emission property of the CNTw emitter treated by 'filament mode' at different treatment times. Inset photos show the emission pattern from each CNTw emitter. (Hosokawa et al., 2008)

Treatment time (s)	Threshold electric field for field emission current = 1 μA (V/μm)	Maximum current density (mA/cm²)	CNTw length (μm)
0	1.5	0.037 (at 160 V)	5—10
10	5.2	0.098 (at 580 V)	5—10
30	4.6	0.433 (at 800 V)	3.6—5.4
60	7.0	0.105 (at 960 V)	1—3
180	Not measured	0.003 (at 1000 V)	0

Table 2. Field emission property of the CNTw emitter at different treatment times. As for the untreated CNTws, we measured the length of powdery CNTws before fabricating the emitter. (Hosokawa et al., 2008)

9. Conclusion

We have shown that HCNFs are grown by CVD and that their dimension and types can be controlled by binary catalysts and CVD conditions. There are many possible HCNF applications to a wide area of nanoelectronics and nanomechanics industries. An example of HCNF application as an electron field emitter was introduced in this chapter. We have been trying to apply HCNF as a catalyst support in fuel cell and such a new application case is expected to appear.

10. Acknowledgements

We would like to thank to our collaborator: Mr. H. Ue of Tokai Carbon Co., Ltd., Mr. K. Shimizu of Shonan Plastic Mfg. Co., Ltd., and Mr. Y. Umeda of Toho Gas Co., Ltd. for their support. We also thank to our students: Mr. Y. Hosokawa, Mr. M. Yokota, Mr. K. Takimoto, Ms. L.S. Ling, Mr. Y. Sugioka, and Mr. Y. Ishii for their experimental work. The technical support for microscopy observation by Dr. T. Hamanaka of Japan Fine Ceramics Center (JFCC) and Mr. K. Muramoto of Toyohashi University of Technology is greatly

acknowledged. This work has been partly supported by the Research Project of the Venture Business Laboratory from Toyohashi University of Technology (Toyohashi Tech); Global COE Program "Frontier of Intelligent Sensing" from the Ministry of Education, Culture, Sport, Science and Technology (MEXT); Core University Programs (JSPS-CAS program in the field of "Plasma and Nuclear Fusion") from The Japan Society for the Promotion of Science (JSPS); Grant-in-Aid for Young Scientists (B) from MEXT; Toukai Foundation for Technology; Research Foundation for Materials Science; Chubu Science and Technology Center; and CASIO Science Promotion Foundation.

11. References

Amelinckx, S.; Zhang, X.B.; Bernaerts, D.; Zhang, X.F.; Ivanov, V. & Nagy, J.B. (1994). A Formation Mechanism for Catalytically Grown Helix-Shaped Graphite Nanotubes, *Science*, Vol.265, No.5172, (July 1994), pp. 635-639, ISSN 0036-8075

Baker, R.T.K.; Barber, M.A.; Harris, P.S.; Feates, F.S. & Waite, R.J. (1972). Nucleation and Growth of Carbon Deposits from the Nickel Catalyzed Decomposition of Acetylene, *Journal of Catalysis*, Vol.26, No.1, (July 1972), pp. 51-62, ISSN 0021-9517

Baker, R.T.K.; Harris, P.S. & Terry, S. (1975). Unique Form of Filamentous Carbon. *Nature*, Vol.253, No.5486, (January 1975), pp. 37-39, ISSN 0028-0836

Baker, R.T.K. (1989). Catalytic Growth of Carbon Filaments, *Carbon*, Vol.27, No.3, (1989), pp. 315-323, ISSN 0008-6223

Bell, A.T. & Shustorovich, E. (1990). Analysis of the Thermochemistry of C_2 Hydrocarbons on Transition Metal Surfaces Using a Refined BOC-MP Approach, *Surface Science*, Vol.235, Nos.2-3, (September 1990), pp. 343-350, ISSN 0039-6028

Boehm, H.P. (1973). Carbon from Carbon Monoxide Disproportionation on Nickel and Iron Catalysts: Morphological Studies and Possible Growth Mechanism. *Carbon*, Vol.11, No.6, (December 1973), pp. 583-590, ISSN 0008-6223

Chen, B.; Fujimura, Y.; Katsumata, T.; Takikawa, H.; Hibi, Y.; Sakakibara, T. & Itoh, S. (2004). Effect of Multi-Catalysts on Carbon Nanofiber Synthesis in CVD, *Transactions of the Materials Research Society of Japan*, Vol.29, No.2, (March 2004), pp. 559-562

Davis, W.R.; Slawson, R.J. & Rigby, G.R. (1953). An Unusual Form of Carbon. *Nature*, Vol.171, No.4356, (April 1953), p. 756, ISSN 0028-0836

Delzeit, L.; McAninch, I.; Cruden, B.A.; Hash, D.; Chen, B.; Han, J. & Meyyappan, M. (2002). Growth of Multiwall Carbon Nanotubes in an Inductively Coupled Plasma Reactor, *Journal of Applied Physics*, Vol.91, No.9, (May 2002), pp. 6027-6033, ISSN 0021-8979

Fonseca, A.; Hernadi, K.; Nagy, J.B.; Lambin, Ph. & Lucas, A.A. (1995). Model Structure of Perfectly Graphitizable Coiled Carbon Nanotubes, *Carbon*, Vol.33, No.12, (1995), pp. 1759-1775, ISSN 0008-6223

Fonseca, A.; Hernadi, K.; Nagy, J.B.; Lambin, Ph. & Lucas, A.A. (1996). Growth Mechanism of Coiled Carbon Nanotubes, *Synthetic Metals*, Vol.77, Nos.1-3, (February 1996), pp. 235-242, ISSN 0379-6779

Hanus, M.J. & Harris, A.T. (2010). Synthesis, Characterisation and Applications of Coiled Carbon Nanotubes, *The Journal of Nanoscience and Nanotechnology*, Vol.10, No.4, (April 2010), pp. 2261–2283, ISSN 1533-4880

Hernadi, K.; Fonseca, A.; Nagy, J.B.; Fudala, A.; Bernaerts, D. & Kiricsi, I. (2002). Catalytic Production of Carbon Nanofibers over Iron Carbide Doped with Sn^{2+}, *Applied Catalysis A*, Vol.228, Nos.1-2, (March 2002), pp. 103-113, ISSN 0926-860X

Hofer, L.J.E.; Sterling, E. & McCartney, J.T. (1955). Structure of the Carbon Deposited from Carbon Monoxide on Iron, Cobalt and Nickel. *The Journal of Physical Chemistry*, Vol.59, No.11, (November 1955), pp. 1153-1155, ISSN 0022-3654

Hokshin, S.; Pan, L. & Nakayama, Y. (2007). Diameter Control of Carbon Nanocoils by the Catalyst of Organic Metals, *Japanese Journal of Applied Physics*, Vol.46, No.8A, (August 2007), pp. 5383-5385, ISSN 0021-4922

Hosokawa, Y.; Shiki, H.; Shinohara, Y.; Yokota, M.; Takikawa, H.; Ina, T.; Okada, F.; Fujimura, Y.; Yamaura, T.; Itoh, S.; Miura, K. & Yoshikawa, K. (2007). Preparation of Powdery Carbon Nanotwist and Application to Printed Field Emitter, *Research Letters in Materials Science*, Vol.2007, (2007), 59167, ISSN 1687-6822

Hosokawa, Y.; Shinohara, Y.; Yokota, M.; Shiki, H.; Suda, Y.; Oke, S.; Takikawa, H.; Ina, T.; Morioki, M.; Fujimura, Y.; Yamaura, T.; Itoh, S. & Miura, K. (2008). Filament discharge enhances field emission properties by making twisted carbon nanofibres stand up, *Journal of Physics D: Applied Physics*, Vol.41, No.20 (October 2008) 205418, ISSN 0022-3727

Hung, W.H. & Bernasek, S.L. (1995). Adsorption and Decomposition of Ethylene and Acetylene on Fe(100), *Surface Science*, Vol.339, No.3, (October 1995), pp. 272-290, ISSN 0039-6028

Iijima, S. (1991). Helical Mircotubules of Graphitic Carbon. *Nature*, Vol.354, No.6348, (November 1991), pp. 56-58, ISSN 0028-0836

Iijima, S. & Ichihashi, T. (1993). Single-Shell Carbon Nanotubes of 1-nm Diameter. *Nature*, Vol.363, No.6430, (June 1993), pp. 603-605, ISSN 0028-0836

Ivanov, V.; Nagy, J.B.; Lambin, Ph.; Lucas, A.; Zhang, X.B.; Zhang, X.F.; Bernaerts, D.; Van Tendeloo, G.; Amelinckx, S. & Van Landuyt, J. (1994). The Study of Carbon Nanotubules Produced by Catalytic Method. *Chemical Physics Letters*, Vol.223, No.4, (June 1994), pp. 329-335, ISSN 0009-2614

Jong, K.P.D. & Geus, J.W. (2000). Carbon Nanofibres: Catalytic Synthesis and Applications, *Catalysis Reviews –Science and Engineering*, Vol.42, No.4, (2000), pp. 481-510, ISSN 0161-4940

Journet, C.; Maser, W.K.; Bernier, P.; Loiseau, A.; Lamyde la Chapelle, M.; Lefrant, S.; Deniard, P.; Leek, R. & Fischerk, J.E. (1997). Large-Scale Production of Single-Walled Carbon Nanotubes by the Electric-Arc Technique. *Nature*, Vol.388, No.6644, (August 1997), pp. 756-758, ISSN 0028-0836

Kanada, R.; Pan, L.; Akita, S.; Okazaki, N.; Hirahara, K. & Nakayama, Y. (2008). Synthesis of Multiwalled Carbon Nanocoils Using Codeposited Thin Film of Fe–Sn as Catalyst, *Japanese Journal of Applied Physics*, Vol.47, No.4 (April 2008), pp. 1949-1951, ISSN 0021-4922

Kajihara, Y.; Hihara, T.; Sumiyama, K. & Motojima, S. (2005). Electrical Resistivity of Carbon Micro Coil Measured by a Multi-Probe Unit Installed in a Scanning Electron Microscope, *Japanese Journal of Applied Physics*, Vol.44, No.9A (September 2005), pp. 6867-6869, ISSN 0021-4922

Katsumata, T.; Fujimura, Y.; Nagayama, M.; Tabata, H.; Takikawa, H.; Hibi, Y.; Sakakibara, T. & Itoh, S. (2004). Synthesis of Twisted Carbon Nanofiber by Catalytic CVD Method, *Transactions of the Materials Research Society of Japan*, Vol.29, No.2, (March 2004), pp. 501-504

Kim, M.S.; Rodriguez, N.M. & Baker, R.T.K. (1992). The Role of Interfacial Phenomena in the Structure of Carbon Deposits, *Journal of Catalysis*, Vol.134, No.1, (March 1992), pp. 253-268, ISSN 0021-9517

Kong, J.; Cassell, A.M. & Dai, H. (1998). Chemical Vapor Deposition of Methane for Single-Walled Carbon Nanotubes. *Chemical Physics Letters*, Vol.292, Nos.4-6, (August 1998), pp. 567–574, ISSN 0009-2614

Kumar, M. & Ando, Y. (2010). Chemical Vapor Deposition of Carbon Nanotubes: A Review on Growth Mechanism and Mass Production, *The Journal of Nanoscience and Nanotechnology*, Vol.10, No.6, (June 2010), pp. 3739-3758, ISSN 1533-4880

Lee, H.J.; Lee, Y.D.; Moon, S.I.; Cho, W.S.; Lee, Y.H.; Kim, J.K.; Hwang, S.W. & Ju, B.K. (2006). Enhanced surface morphologies of screen-printed carbon nanotube films by heat treatment and their field-emission properties, *Carbon*, Vol.44, No.13 (November 2006), pp. 2625–2630, ISSN 0008-6223

Lee, Y.T.; Kim, N.S.; Park, J.; Han, J.B.; Choi, Y.S.; Ryu, H. & Lee, H.J. (2003). Temperature-Dependent Growth of Carbon Nanotubes by Pyrolysis of Ferrocene and Acetylene in the Range between 700 and 1000°C, *Chemical Physics Letters*, Vol.372, Nos.5-6, (May 2003), pp. 853-859, ISSN 0009-2614

Lu, M.; Liu, W.; Guo, X. & Li, H. (2004). Coiled Carbon Nanotubes Growth via Reduced-Pressure Catalytic Chemical Vapor Deposition, *Carbon*, Vol.42, No.4 (2004), pp. 805-811, ISSN 0008-6223

Melechko, A.V.; Merkulov, V.I.; McKnight, T.E.; Guillorn, M.A.; Klein, K.L.; Lowndes, D.H. & Simpson, M.L. (2005). Vertically Aligned Carbon Nanofibers and Related Structures: Controlled Synthesis and Directed Assembly, *Journal of Applied Physics*, Vol.97, No.4 (February 2005), 041301, ISSN 0021-8979

Motojima, S.; Ueno, S.; Hattori, T. & Goto, K. (1989). Growth of Regularly Coiled Spring-Like Fibers of Si_3N_4 by Iron Impurity-Activated Chemical Vapor Deposition. *Applied Physics Letters*, Vol.54, No.11, (March 1989), pp. 1001-1003, ISSN 0003-6951

Motojima, S.; Kawaguchi, M.; Nozaki, K. & Iwanaga, H. (1990). Growth of Regularly Coiled Carbon Filaments by Ni Catalyzed Pyrolysis of Acetylene, and Their Morphology and Extension Characteristics. *Applied Physics Letters*, Vol.56, No.4, (January 1990), pp. 321-323, ISSN 0003-6951

Motojima, S. & Chen, X. (2004). Nanohelical/Sprial Materials, In: *Encyclopedia of Nanoscience and Nanotechnology*, Nalwa, H. S., (Ed.), Vol.6, pp. 775-794, American Science Publishers, ISBN 1-58883-001-2, Stevenson Ranch, California, USA

Nolan, P.E.; Schabel, M.J.; Lynch, D.C. & Cutler, A.H. (1995). Hydrogen Control of Carbon Deposit Morphology, *Carbon*, Vol.33, No.1, (1995), pp. 79-85, ISSN 0008-6223

Pan, L.; Zhang, M. & Nakayama, Y. (2002). Growth Mechanism of Carbon Nanocoils, *Journal of Applied Physics*, Vol.91, No.12, (June 2002), pp. 10058-10061, ISSN 0021-8979

Qin, L.C. (1997). CVD Synthesis of Carbon Nanotubes, *Journal of Materials Science Letters*, Vol.16, (1997), pp. 457-459, ISSN 1573-4811

Rodriguez, N.M. (1993). A Review of Catalytically Grown Carbon Nanofibers, *Journal of Materials Research*, Vol.8, No.12, (December 1993), pp. 3233-3250, ISSN 0884-2914

Rodriguez, N.M.; Chambers, A. & Baker, R.T.K. (1995). Catalytic Engineering of Carbon Nanostructures, *Langmuir*, Vol.11, No.10, (October 1995), pp. 3862-3866, ISSN 0743-7463

Saito, R.; Dresselhaus, G. & Dresselhaus, M.S. (1998). *Physical Properties of Carbon Nanotube*, Imperial College Press, ISBN 978-1860942235, London, UK

Smithells, C.J. (1992). *Smithells Metals Reference Book*, Brandes, E.A. & Brook, G.B., (Eds.), Butterworth-Heinemann, ISBN 978-0750675093, London, UK

Stratton, J.A. (1941). *Electromagnetic Theory*, McGraw-Hill, ISBN 978-0070621503, New York/London

Takikawa, H.; Shinsako, K. & Sakakibara, T. (1998). TiN/Ti Film Formation by Vacuum Arc Deposition with Droplet Shield Plate, *Thin Solid Films*, Vol.316, Nos.1-2, (March 1998), pp. 73-78, ISSN 0040-6090

Takikawa, H.; Yatsuki, M.; Miyano, R.; Nagayama, M.; Sakakibara, T.; Itoh, S. & Ando, Y. (2000). Amorphous Carbon Fibrilliform Nanomaterials Prepared by Chemical Vapor Deposition, *Japanese Journal of Applied Physics*, Vol.39, No.9A, (September 2000), pp. 5177-5179, ISSN 0021-4922

Thess, A.; Lee, R.; Nikolaev, P.; Dai, H.; Petit, P.; Robert, J.; Xu, C.; Lee, Y.H.; Kim, S.G.; Rinzler, A.G.; Colbert, D.T.; Scuseria, G.E.; Tománek, D.; Fischer, J.E.; & Smalley, R.E. (1996). Crystalline Ropes of Metallic Carbon Nanotubes. *Science*, Vol.273, No.5274, (July 1996), pp. 483-487, ISSN 0036-8075

Xu, G.; Chen, B.; Shiki, H.; Katsumata, T.; Takikawa, H.; Sakakibara, T.; Itoh, S. & Ina, T. (2005). Parametric Study on Growth of Carbon Nanocoil by Catalytic Chemical Vapor Deposition, *Japanese Journal of Applied Physics*, Vol.44, No.4A, (April 2005), pp. 1569-1576, ISSN 0021-4922

Xu, X. (2001). Dielectric barrier discharge—properties and applications, *Thin Solid Films*, Vol.390, Nos.1-2 (June 2001), pp. 237–242, ISSN 0040-6090

Xu, X. & Pacey, P.D. (2001). An Induction Period in the Pyrolysis of Acetylene, *Physical Chemistry Chemical Physics*, Vol.3, No.14, (2001), pp. 2836-2844, ISSN 1463-9076

Yang, S.; Chen, X. & Motojima, S. (2004). Morphology of the Growth Tip of Carbon Microcoils/Nanocoils, *Diamond and Related Materials*, Vol.13, Nos.11-12, (November-December 2004), pp. 2152-2155, ISSN 0925-9635

Yang, S.; Chen, X., Motojima, S. & Ichihara, M. (2005). Morphology and Microstructure of Spring-Like Carbon Micro-Coils/Nano-Coils Prepared by Catalytic Pyrolysis of Acetylene Using Fe-Containing Alloy Catalysts, *Carbon*, Vol.43, No.4, (2005), pp. 827-834, ISSN 0008-6223

Yang, Y.; Hu, Z.; Lu, Y.N. & Chen, Y. (2003). Growth of Carbon Nanotubes with Metal-Loading Mesoporous Molecular Sieves Catalysts, *Materials Chemistry and Physics*, Vol.82, No.2 (November 2003), pp. 440-443, ISSN 0254-0584

Yokota, M.; Shinohara, Y.; Kawabata, T.; Takimoto, K.; Suda, Y.; Oke, S.; Takikawa, H.; Fujimura, Y.; Yamaura, T.; Itoh, S.; Miura, K. & Morioki, M. (2010). Splitting and Flattening of Helical Carbon Nanofibers by Acid Treatment, *The Journal of Nanoscience and Nanotechnology*, Vol.10, No.6, (June 2010), pp. 3910-3914, ISSN 1533-4880

Yokota, M.; Suda, Y.; Takikawa, H.; Ue, H.; Shimizu, K. & Umeda, Y. (2011). Structural Analysis of Multi-Walled Carbon Nanocoils Synthesized with Fe-Sn Catalyst Supported on Zeolite, *The Journal of Nanoscience and Nanotechnology*, Vol.11, No.3 (March 2011), pp. 2344-2348, ISSN 1533-4880

Yu, Q., Lian, J., Siriponglert, S., Li, H., Chen, Y.P. & Pei, S.-S. (2008). Graphene Segregated on Ni Surfaces and Transferred to Insulators, *Applied Physics Letters*, Vol.93, No.11, (September 2008), 113103, ISSN 0003-6951

Zhang, M.; Nakayama, Y. & Pan, L. (2000). Synthesis of Carbon Tubule Nanocoils in High Yield Using Iron-Coated Indium Tin Oxide as Catalyst, *Japanese Journal of Applied Physics*, Vol.39, No.12A, (December 2000), pp. L1242-L1244, ISSN 0021-4922

3

Synthesis and Properties of the Arrays of Magnetically Functionalized Carbon Nanotubes

Vladimir Labunov[1], Alena Prudnikava[1], Kazimir Yanushkevich[2],
Aleksander Basaev[3], Alexander Danilyuk[1],
Yulia Fedotova[4] and Boris Shulitskii[1]
[1]*Belarussian State University of Informatics and Radioelectronics,*
[2]*Institute of Solid-State and Semiconductor Physics NASB,*
[3]*Scientific and Manufacturing Complex "Technological Centre," Moscow Institute of Electronic Technology,*
[4]*National Scientific and Educational Centre of Particle and High-Energy Physics BSU,*
[1,2,4]*Belarus,*
[3]*Russia*

1. Introduction

Carbon nanotubes (CNTs) are carbon molecules with a unique combination of specific mechanical, electrical, emission, optical and chemical properties. Over the last fifteen years, these objects have not ceased to amaze with regularly revealed new effects and applications (Harris, 2002).

A substantial step forward in the development of nanotechnologies is the use of carbon nanotubes filled with nanoparticles consisting of different materials. The resulting nanocomposites exhibit properties of both encapsulated and encapsulating materials with promising synergetic effects. This leads to a considerable additional contribution to the potentialities of their use in microelectronic and nanoelectronic devices (Labunov & Shulitski, 2005). One of the promising directions in this field is the investigation of the properties of carbon nanotubes combined with magnetic materials (Labunov, 2006), because there arises a possibility of synthesizing magnetically functionalized carbon nanotubes, in particular, multiwall carbon nanotubes filled with ferromagnetic nanoparticles.

Nanostructuring of a massive magnetic material substantially affects its magnetic properties. For example, the coercive force decreases, while the magnetic permittivity and the saturation magnetization increase with a decrease in the grain size to 40–20 nm. This effect is enhanced in the case of very small grain sizes (of the order of one domain). As a consequence, the magnetic vectors of atoms in an external magnetic field are identically oriented within a grain, thus eliminating losses through the domain walls and neighboring domains with different magnetization directions. Materials with grains of this size can have no hysteresis and possess superparamagnetic properties. When single-domain ferromagnetic nanoparticles are embedded in a nonmagnetic matrix, this matrix weakens the magnetic interaction between nanoparticles and, hence, decreases the magnetic field required to reorient their magnetic moments. Such nanocomposites are

characterized by a giant magnetoresistance. This has opened up new possibilities for their practical applications, for example, in sensitive elements of magnetometers and magnetic read heads.
Therefore, considerable progress can be made, for example, in increasing the capacity of magnetic read– write devices owing to the use of magnetically functionalized carbon nanotubes prepared by filling of carbon nanotubes with ferromagnetic nanoparticles. In this case, the particle size can be small enough to represent a single domain and the carbon nanotube walls serve as nonmagnetic separating regions between nanoparticles.
The purpose of present review is to summarize actual results regarding synthesis of multiwall carbon nanotubes, particularly, magnetically functionalized multiwall carbon nanotubes (MFCNT), with the use of iron nanoparticles as growth catalyst and complex analysis of their crystal structure, composition, and magnetic properties as a function of peculiarities of synthesis procedure.

2. Preparation of carbon nanotubes

Generally, there are several techniques for introducing a material into carbon nanotube cavities (Harris, 2002). One of the techniques is conventional evaporation of carbon in an arc discharge with the use of an anode containing the material that should be encapsulated. For the most part, this technique is applicable to materials that can "survive" under extreme conditions of electric arc discharge. The second technique consists in chemically opening the ends of closed nanotubes, followed by introducing a filler compound inside nanotubes due to the capillary effect. This method proved to be better than the first technique and can be used for incorporating fillers from melts (liquid phases) and even in the case of biological molecules. The third technique involves the synthesis of carbon nanotubes through the high-temperature pyrolysis of liquid hydrocarbons in a mixture with a volatile catalyst, providing the growth of carbon nanotubes. Catalyst nanoparticles, deposited on a substrate, initiate the growth of carbon nanotubes. Moreover, during growth they are embedded in carbon nanotubes over their entire length and even occupy the ends of the nanotubes. Consequently, this technique is most appropriate for obtaining MFCNT. It is this technique that was used in our work for preparing multiwall carbon nanotubes filled with particles of iron, which is the most widely used magnetic compound among the triad of iron, cobalt, and nickel. Carbon nanotubes were synthesized by high-temperature pyrolysis of liquid hydrocarbon *p*-xylene C_8H_{10} in a mixture with volatile ferrocene $[Fe(C_2H_5)_2]$ as a catalyst at atmospheric pressure with the use of argon as a gas carrier on the surface of silicon substrates [KDB 20 (100)] in a tubular quartz reactor specially designed for these purposes (Labunov, 2005). The samples for investigations were prepared under conditions of predominant growth of carbon nanotubes on the Si substrates with thermal oxide SiO_2 (0.6 μm) (Labunov et al., 2006). Ferrocene concentration c_x in p-xylene equaled 0,5, 5 and 10 %, the mixture injection rate into the reactor zone was 1 ml/min, the temperature was 775-875 °C, the argon flow rate was 100 cm^3/min, and the reaction time varied in the range 1-5 min. Under these synthesis conditions, carbon nanotube arrays were formed either on the silicon substrates or reactor walls.

3. Morphology, structure and composition of magnetically functionalized carbon nanotubes synthesized by injection CVD method

3.1 Variety of CNTs morphologies studied with transmission electron microscopy

Transmission microscopy study of CNTs synthesized by injection CVD technique revealed variety of morphologies of multiwalled CNTs, filled with particles of different Fe phases.

Fig. 1 shows typical images demonstrating formation of nanocomposites at the ends of CNTs. One should classify four main variants of metallic filler inside CNTs: at the very end of closed CNT (1), at some distance from closed end (2), nanocomposite emerges from opened CNT (3) and CNT with opened and unfilled ends (4). As evidenced from Fig. 1 all CNTs are multiwalled with diameter of 10-20 nm and should be classified as thin-walled CNTs because diameter is larger then the wall thickness. The majority of filler phase has a spherical form with the aspect ratio (length to diameter) ~5:1 - 8:1.

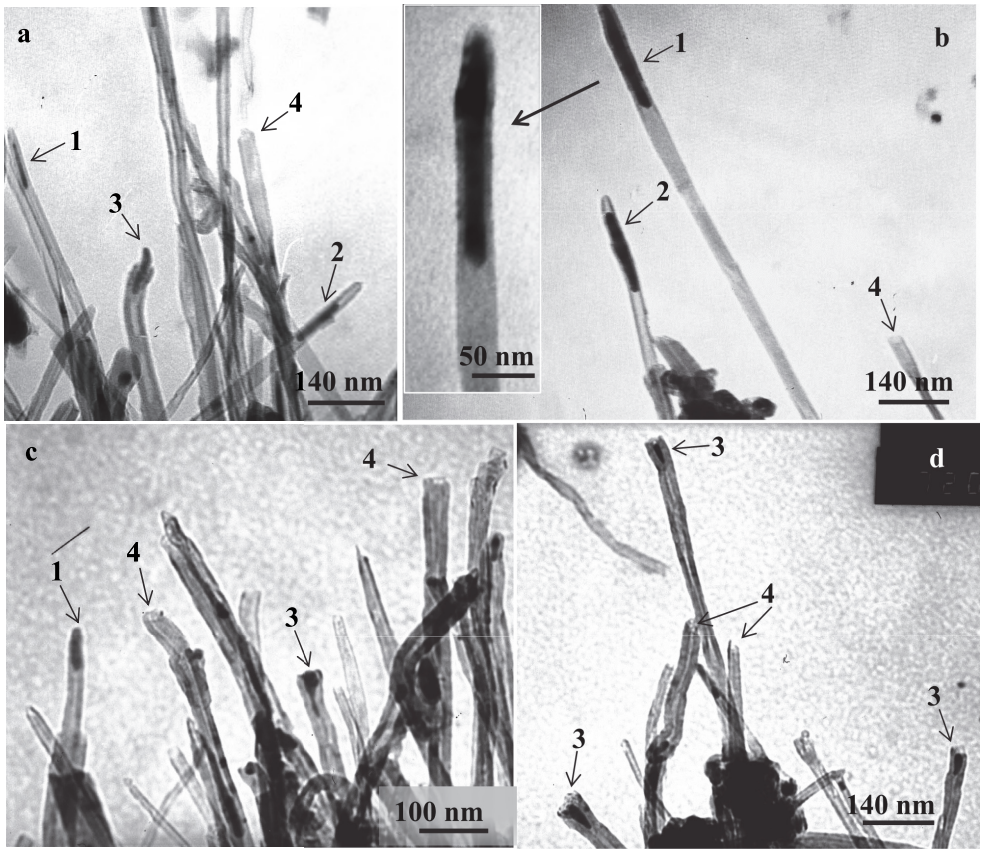

Fig. 1. TEM images of CNTs with the various geometries types of nanocomposites formed on the CNTs ends: at the very end of closed CNT (1), at some distance from closed end (2), nanocomposite emerges from opened CNT (3) and CNT with opened and unfilled ends (4).

The most typical CNT arrays morphology is presented in Fig. 2.
Microscopic image usually reveal multiwall CNTs of different shape and morphology: with unfilled channel (1), with channel filled with composite of prolonged spherical form (2); with particles of spherical form composite separated with internal walls in channel (3). Diameter of these CNTs ranged within 20-30 nm at channel diameter of 7-10 nm, i.e. they should be classified as thin-walled CNTs. Diameter of precipitations, particularly of spherical form (2), is higher so that they "swell" the channel.

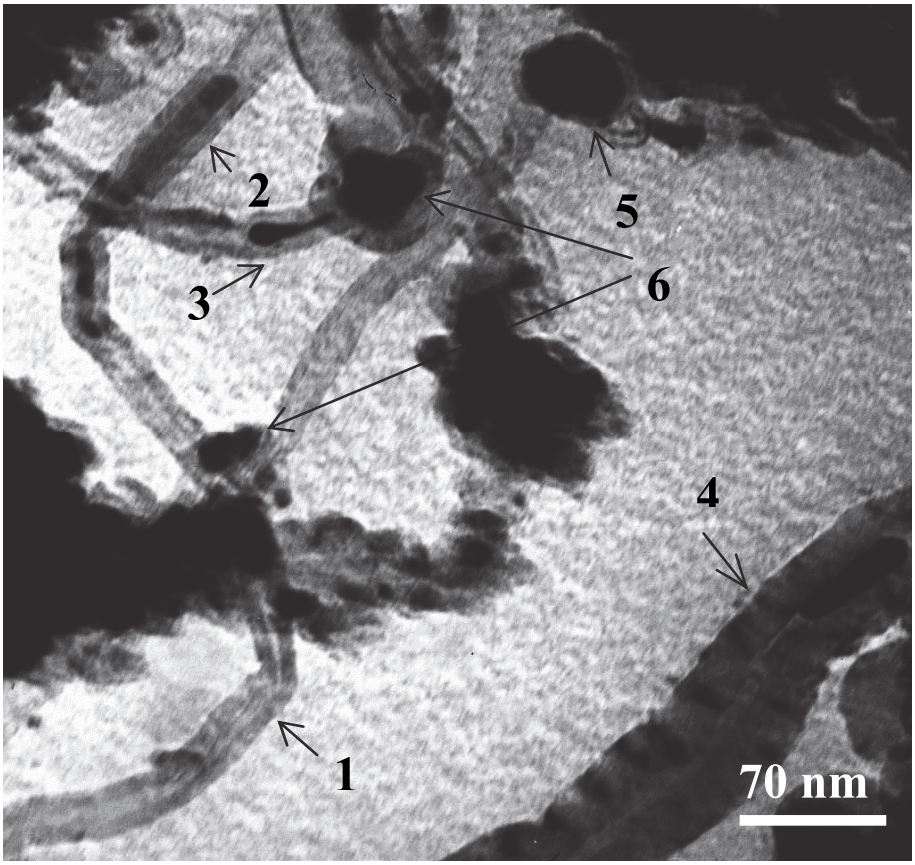

Fig. 2. The most typical morphology of multiwall CNT arrays: thin-walled - (1) with unfilled channel; (2) with channel filled with composite of prolonged spherical form; (3) with particles of spherical form composite separated with internal walls in channel; (4) thick-walled; (5) capsules; (6) obcordate form.

One should particularly consider multiwall CNTs (4) of large diameter (50-70 nm) with narrow channel (7-10 nm). Such CNTs should be classified as thick-walled. The peculiar feature of these nanotubes is that they possess nanocomposite inclusions not only inside the channel but also inside the walls (dark inclusions perpendicular to the films). Precipitation of nanocomposite filler inside walls of CNTs most probably resulted in the increase of their thickness. In so doing, multiwall CNTs should be divided into thin-walled and thick-walled CNTs. One more class of nanocomposite filler is particles incapsulated inside carbon shell (5). Unique obcordate form of nanocomposie is precipitated on the junction of two nanotubes (6). Obviously, such capsules are incorporated into the CNTs edges. Furthermore, such capsules evidence the tip-growth mechanism of CNts growth (Li, 2000).
Variants of above mentioned structures and morphology of CNTs are shown in details in Fig. 3. Different examples of CNTs, filled with nanocomposite particles with high aspect ratio, have been shown. Such particular form of inclusions support anisotropy of CNTs

magnetic properties in parallel and perpendicular directions and could be applied in magnetic recording media (Pull, 2005). Fig.3a shows thin-walled CNT with filler of variable thickness, which length equals approximately 2/3 of CNT length (1). Thick-walled «compound» CNT (2), containing areas of different thickness: channel and walls of one of them is filled with nanoparticles, the second part is thinner with empty channel, and third part –approximately up to 2/3 filled with composite. The inset in Fig.3a presents CNT with channel completely filled with composite. Combination of thin-walled CNT with channel almost completely filled with composite and capsule «fixed» on its edge is shown in Fig. 3b. Fig. 3c clearly revealed obcordate structure of CNT within the junction of two thick-walled CNTs. Channel of one of the nanotubes is filled with composite while second is empty. Simultaneously, walls of both CNts contain nanocomposite. Fig. 3b clarifies the origin of obcordate structure of CNT – it is formed due to the merging of two capsules from different structures.

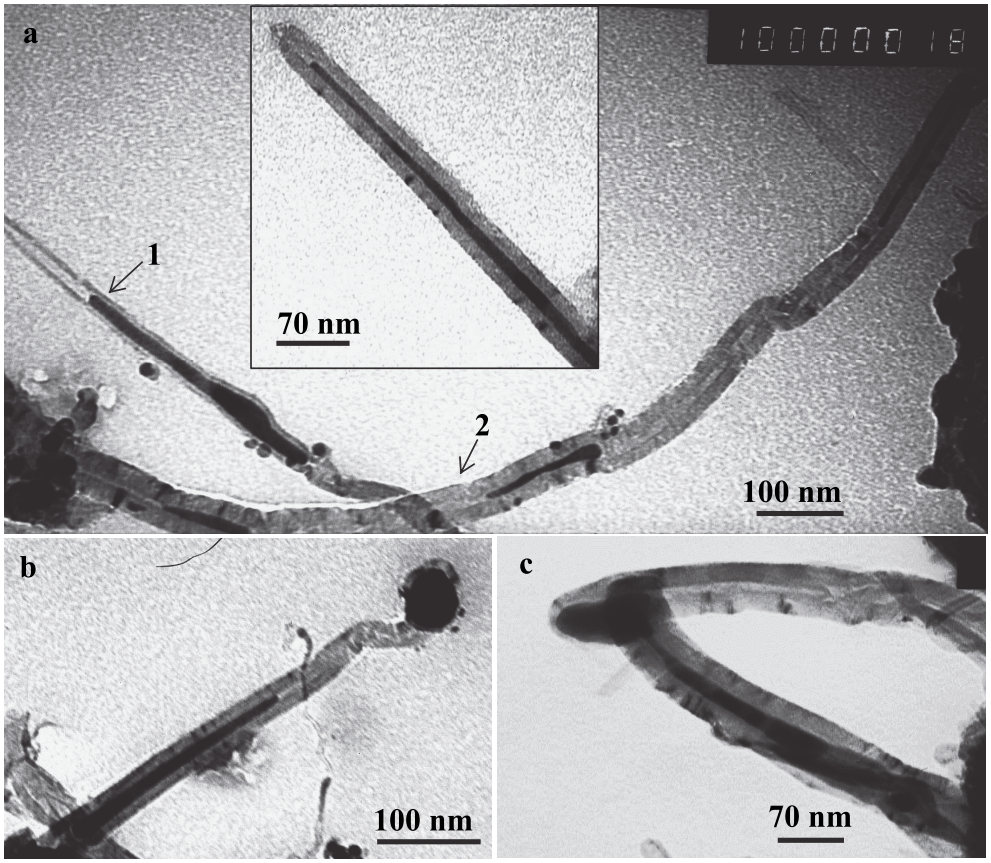

Fig. 3. Details of CNTs morphologies shown in Fig.2, with strong filling of channels: (a) separate CNTs; (b) combination of thin-walled CNTs and capsule; (c) obcordate–like form within the junction of two thick-walled CNTs.

Variety of structures and geometries of CNTs are not limited with incorporation of filler inside channel or wall of nanotubes or carbon capsules. Filler could also be located outside of the tubes – on their walls both thin- and thick-walled. Fig. 4 shows micrographs of thin-walled CNTs with nanocomposite formed outside of their walls.

As evidenced from Fig. 4, nanocomposite is located in the form of balls on the outer side of walls in CNTs. When particles are of relatively large size (20-30 nm) it is clearly seen that they are incapsulated inside the shell constituting short nanotubes, formed on the surface of the basic CNT (2). When size of particles is small (3-5 nm) just dark spots are seen (1). Possible, these particles are incapsulated as well, but in this case carbon shells cannot be clearly observed in transmission microscopy image due to their very small thickness.

Fig. 5 presents micrographs of thick-walled CNTs of different kinds: Fig. 5a – separate nanotube, Fig. 5b – combination of CNT and capsule, «fixed» on its edge (such a combination seem to be quite usual). As evidenced from Figs. 5 a and b, nanocomposite filler is located inside nanotubes and capsules (1), inside the walls (2) and on the surface of walls (3), where nanotubes are seen as incapsulated balls. Fig. 7a shows that, similarly to the case of thin-walled CNTs, balls of filler inside short nanotube is formed on the surface of basic nanotube (3). It is quite possible that all composite nanoparticles are incorporate on the nanotubes surface in such a way. However, many of them located in unfavorable configuration against electron beam in microscope so, that their ideal configuration could not be recognized. On the other hand, the majority of nanocomposite particles, located on the walls surfaces, possess disordered form (4).

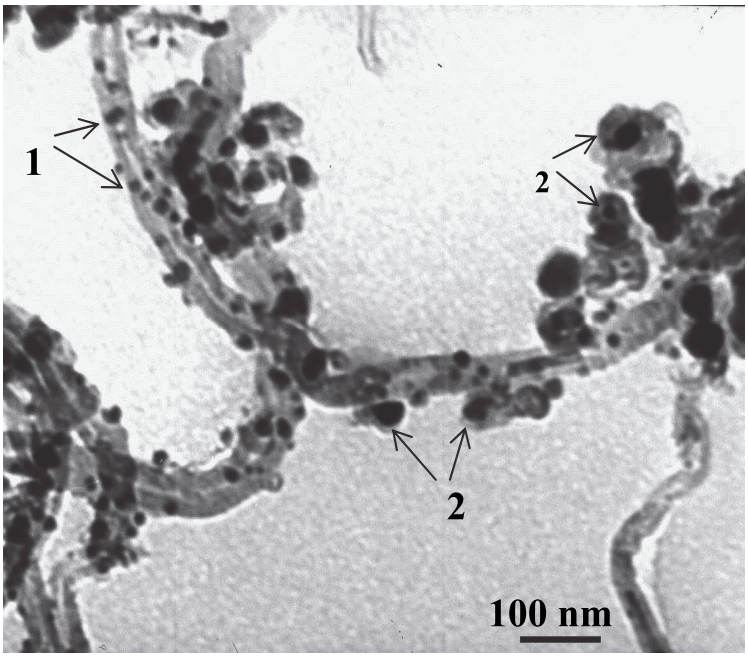

Fig. 4. Thin-walled CNTs with nanocomposite formed on the outside parts of their walls: (1) dark balls of small size (3-5 nm); (2) balls of relatively large size (20-30 nm) inside the shell of short nanotubes.

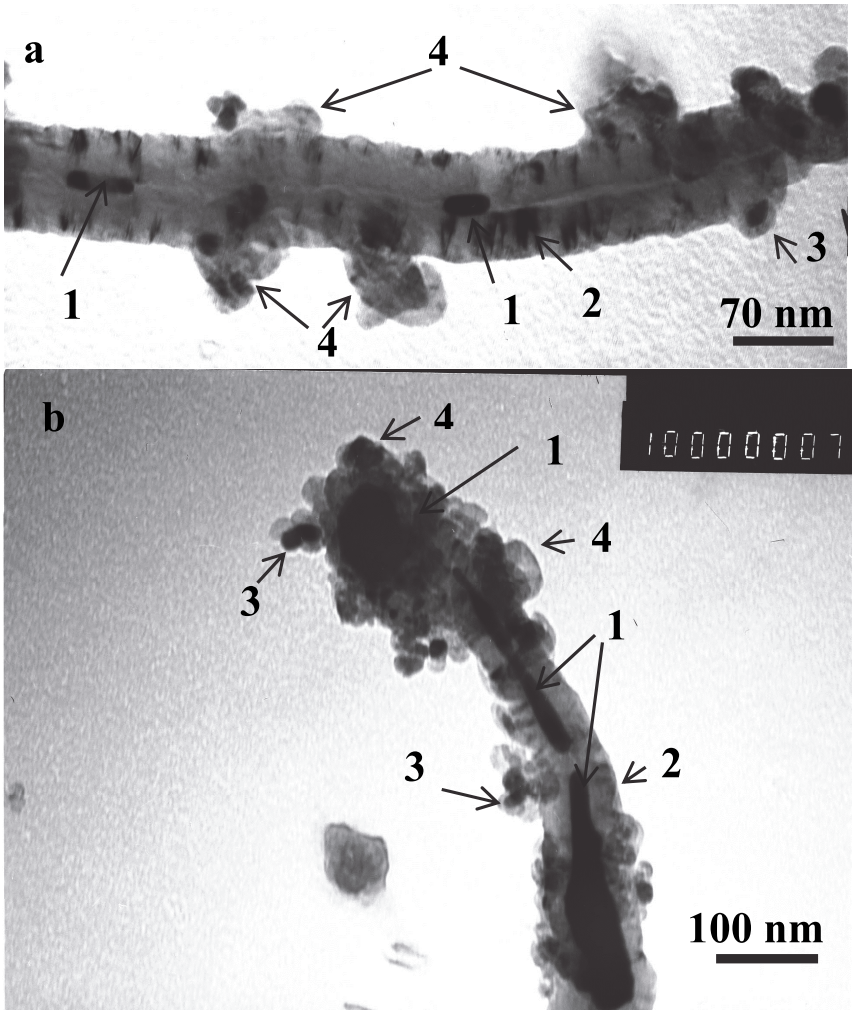

Fig. 5. Thick-walled CNTs - (a) separate nanotube; (b) combination of nanotube and capsule. Nanocomposite is located: (1) – inside the channel, (2) – inside the walls, (3) – on the surface of walls in the from of balls incapsulated inside short nanotubes, and (4) – in disordered form.

3.2 Effects of synthesis on Si substrate and on the walls of a quartz reactor

Comparative study of the morphology and composition of carbon nanotubes synthesized on Si substrate and on the walls of a quartz reactor has been performed on samples containing c_x = 10 %. The external appearance of the carbon nanotube arrays is shown in Fig. 6. It can be seen from Fig. 6 that the array of vertically aligned close-packed carbon nanotubes is formed under the abovementioned synthesis conditions. Bright inclusions against the dark background of the array cleavage wall (Fig. 6a) and the array surface are characteristics of the image. The carbon nanotubes located at the center of the array cleavage wall are shown

in Fig. 6b. It can be seen that the carbon nanotubes are broken and bent. The bending of the carbon nanotubes can suggest that, in the array, there are internal stresses, which lead to deformation of nanotubes after cleavage. Bright inclusions are clearly seen at the ends of broken carbon nanotubes. This indicates the presence of metal-containing particles. Rather long bright arc regions in the image of the nanotube array can result from illumination upon focusing of the electron beam of the microscope. Since metal-containing segments of nanotubes are observed at the center of the height of the array, we can assume that they are also located inside the carbon nanotubes along their entire length. As can be seen from Fig. 6c, disordered nanostructures of different configurations are formed at the array surface. This phenomenon is typical of the synthesis for carbon nanotubes through the high-temperature pyrolysis of liquid hydrocarbons in a mixture with a volatile catalyst. At the instant of completion of pyrolysis synthesis, the synthesis conditions change abruptly, deviate from optimum, and prevent orientated growth of carbon nanotubes. The presence of bright regions in the image of the array surface also indicates that metal-containing nanoparticles are contained at the surface.

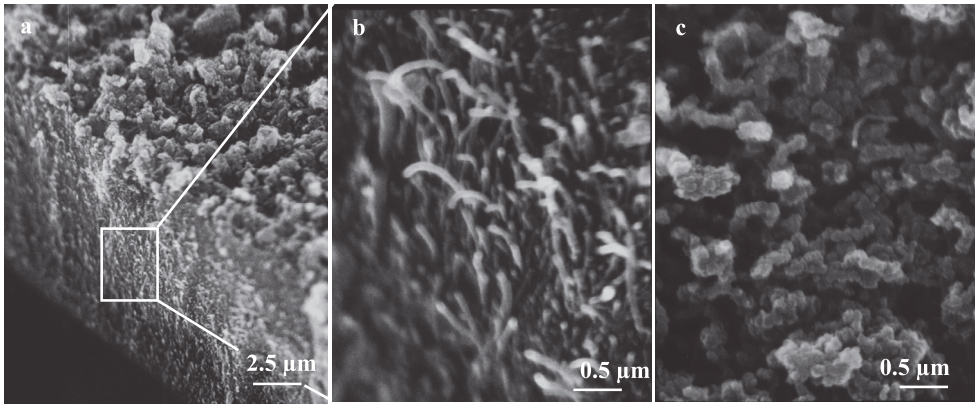

Fig. 6. Images of carbon nanotubes synthesized on Si substrate and on the walls of a quartz reactor: (a) axonometric view of carbon nanotube arrays (vertical wall of array cleavage and array surface), low magnification; (b) vertical wall of array; and (c) carbon nanotube array surface, high magnification.

To identify phase composition of carbon nanotubes synthesized on the Si substrates and formed at the walls of the quartz reactor XRD analysis was performed at room temperature. The X-ray diffraction data (Cu *K* radiation) were collected by point sampling with an angle step of $\Delta 2\theta = 0.03°$. The exposure time per each angle point was $\Delta\tau = 5$ s. The X-ray diffraction patterns of the carbon nanotubes of both types are depicted in Fig. 7. For the carbon nanotubes synthesized on the silicon substrate, the X-ray diffraction pattern (Fig. 7a) in the angle range $5^\circ \le 2\theta \le 30^\circ$ contains a set of low-intensity reflections that can be assigned to amorphous carbon in the composition of the soot and graphite.

The X-ray diffraction pattern in the angle range $5^\circ \le 2\theta \le 80^\circ$ involves high-intensity reflection (400) from the Si substrate a series of low-intensity reflections that can be used for determining the composition of the composite under investigation. Somewhat unexpectedly, the identification of the X-ray diffraction patterns revealed that Fe_3C cementite is the main component of carbon nanotubes. The reflections indexed as (112), (201), (211), (122), (004),

(222), and (313) for Fe_3C cementite (Lipson & Steeple, 1970) are clearly seen in the X-ray diffraction pattern. Iron in the form of the (110) and (200) reflections and the Fe_5C_2 carbide in the form of the (021) (Lipson & Steeple, 1970) reflection manifest themselves in the X-ray diffraction pattern. The carbon nanotubes deposited on the reactor walls were mechanically separated from the walls in the form of a powdered material. The X-ray powder diffraction pattern of the carbon nanotube powder (Fig. 7b) contains a halo of amorphized carbon at small angles 2θ and a pronounced (111) reflection of graphite with a rhombohedral structure (ICDD card no. 75-2078, PCPDFWIN) (JCPDS, 1998). This structure is characteristic of carbon nanotubes. At larger angles, the X-ray powder diffraction pattern exhibits a series of lines corresponding to the Fe_3C, Fe, and Fe_5C_2 phases, the intensities of which are considerably higher than those of lines shown in Fig. 7a. Analysis of the X-ray powder diffraction pattern in Fig. 2b also demonstrates that the Fe_3C cementite with an orthorhombic structure (space group Pbnm) dominates over the other components in the sample under investigation. A comparison between the areas of the reflections (with allowance made for the overlapping reflections) shows that the Fe_3C content in the composite with respect to the Fe and Fe_5C_2 contents is more than 90 %. By using the techniques for identifying the orthorhombic structure and its quadratic form (Lipson & Steeple, 1970)

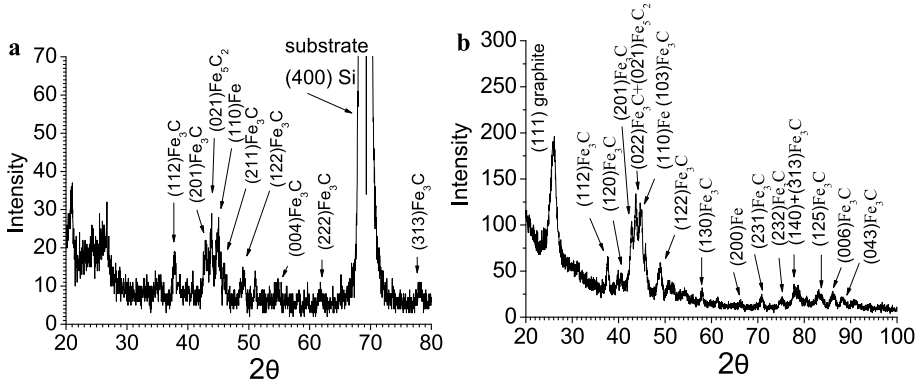

Fig. 7. XRD patterns of carbon nanotubes: (a) synthesized on Si substrates and (b) on quartz reactor walls.

$$\sin^2\theta_{\lambda kl} = \frac{\lambda^2}{4a^2}h^2 + \frac{\lambda^2}{4b^2}k^2 + \frac{\lambda^2}{4c^2}l^2 \tag{1}$$

the unit cell parameters of the Fe_3C phase in the carbon nanotubes were determined. It should be noted that the numbers of the reflections corresponding to the Fe_3C phase in the X-ray diffraction patterns in Figs. 7a and 7b are sufficient for this purpose. The calculated unit cell parameters are as follows: a=0.452 nm, b=0.508 nm, and c=0.672 nm. This is in good agreement with the corresponding unit cell parameters a = 4.518 Å, b = 5.069 Å, and c = 6.736 Å available in the ICDD database (card nos. 76-1877 and 75-0910, PCPDFWIN) (JCPDS, 1998) for the polycrystalline compound Fe_3C.

The results are undeniably of theoretical and practical interest. The dominance of the Fe_3C cementite in the composition of the carbon nanotubes indicates that, during their growth, Fe catalyst particles are not only embedded in the carbon nanotube, they also interact with the

nanotube with the formation of the stable compound Fe_3C, which in the massive polycrystalline form possesses pronounced ferromagnetic properties. From the practical viewpoint, this will make it possible to use magnetically functionalized carbon nanotubes for fabricating reliable microelectronic and nanoelectronic devices resistant to external actions.

Further investigation of carbon nanotubes has been performed by transmission electron microscopy. For this purpose, the carbon nanotubes were dispersed on a carbon microgrid of a high-resolution electron microscope. The experimental results are presented in Fig. 8.

It is known that electron diffraction patterns of carbon nanotubes, especially when they are obtained for multiwall nanotubes, are difficult to interpret (Pull, 2005). However, qualitative analysis of the electron diffraction patterns of the samples under investigation (Fig. 8a) demonstrates a good correlation with the X-ray diffraction data. The halo associated with the amorphized carbon is rather pronounced. The electron diffraction pattern contains (002) and (004) reflections of the graphite. Possibly, these reflections overlap with the (002) and (004) reflections of the cementite (PDF no. 76-1877). This is the most real situation, because, according to the contrast, all inclusions in nanotubes are nanocrystals and, hence, should also be characterized by point reflections. Moreover, it is clear that a coherent interface $(002)_{graphite}$ II $(002)_{Fe3C}$ should occur between the graphite and the carbide. As regards ring reflections, they can be associated with the graphite. Furthermore, the weak reflections (110) and (211) attributed to the iron particles are observed in the electron diffraction pattern. The image of the array of misoriented carbon nanotubes is displayed in Fig. 8b. It can be seen from this figure that a large number of black dots and horizontally located nanotubes occur in the image. The black dots can correspond either to filler particles at the ends of the nanotubes located perpendicular to the substrate or to magnetic nanoparticles encapsulated by carbon. It is evident that filler nanoparticles are characterized by a considerable size dispersion. It should be noted that the size of encapsulated particles exceeds their size in nanotubes and is in the range ~40–50 nm. The diameter of the nanotubes located in the horizontal plane varies from ~5 to ~40 nm. The original images in which it is possible to see both nanotubes and nanocapsules are displayed in Figs. 8c and 8d. It can be seen from these figures that the nanotubes are multiwall and their outside diameter varies from ~20 to ~40 nm. The diameter of filler nanoparticles is smaller and ranges from ~5 to ~20 nm. The two nanotubes and a dumbbell-like nanocapsule are clearly seen in Fig. 8c. One of the nanotubes has an empty channel, and the other nanotube is filled with oval nanoparticles (~5–20 nm in diameter) separated by walls. A carbon nanotube array fragment also involving two nanotubes and a nanocapsule is shown in Fig. 8d. In this case, too, one nanotube has an empty channel and the neighboring nanotube contains elongated nanoparticles ~5 nm in diameter and ~80 nm in length.

Therefore, investigations of carbon nanotubes by transmission electron microscopy permitted us to determine the ranges of the nanotube and filler particle sizes. It was established that filler inclusions in the carbon nanotubes have different configurations and different sizes and are differently embedded in the nanotubes. Analysis of the electron microscope images demonstrated that the outside diameters of multiwall carbon nanotubes and filler particles (located inside nanotubes) are characterized by large size dispersion. Moreover, it was revealed that the samples contain an insignificant number of single-wall carbon nanotubes.

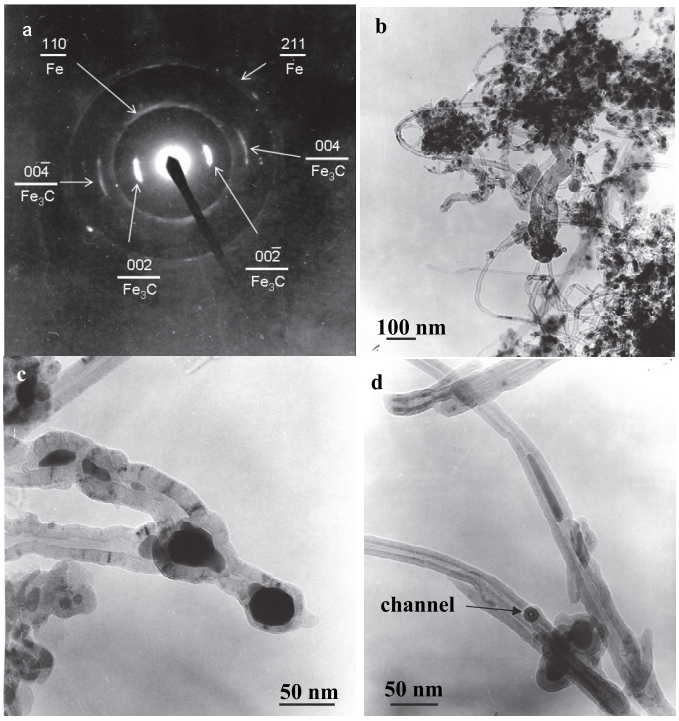

Fig. 8. Electron microscopic data: (a) electron diffraction pattern, (b) general view of disordered carbon nanotube array, and (c, d) fragments of two nanotubes and a nanocapsule.

3.3 Effects of catalyst concentrations during injection CVD synthesis

Typical TEM images of CNTs synthesized at various concentrations of ferrocene c_x in the feeding solution are presented in fig.9: (a) 0.5 %; (b, c) 5 %; (d) 10 %. It is seen, that CNTs are multi-wall. Their outer diameters vary from ~20 to ~80 nm. The diameters of the nanoparticles inside CNTs are smaller and reach ~30 nm. It is worthy to note that all the CNT arrays synthesized by us (with 0.5 %, 5 %, and 10 % of ferrocene) are composed of nanotubes with the inclusions of all the types represented in Fig. 9 (a-d), but the inclusion shapes shown in Fig. 9 (a) are more typical for 0.5 %-samples, in Fig. 9 (b) - for 5 %-samples and in Fig. 9 (c, d) - for 10 %-samples.

The XRD data (Cu$K\alpha$ radiation) performed at room temperature were collected by point sampling with an angle step of $\Delta 2\theta$=0.03°. The exposure time per each angle point was $\Delta\tau$=5 s. The XRD patterns of the CNTs of three types are depicted in Fig. 10 (a, b, c). All the XRD patterns contain a halo of amorphous carbon at small angles 2θ and a pronounced (111) reflection of graphite with a rhombohedral structure (ICDD card no. 75-2078, PCPDFWIN) (JCPDS, 1998). This structure is characteristic of carbon nanotubes. At larger angles, the X-ray powder diffraction pattern exhibits a series of lines corresponding to the F_3C, α-Fe and Fe_5C_2 phases. Analysis of the X-ray powder diffraction data demonstrates that the F_3C cementite with an orthorhombic structure (space group Pbnm) dominates over the other

components in the samples under investigation. A comparison between the areas of the reflections (with allowance made for the overlapping reflections) shows that the F_3C content in the composite with respect to the α-Fe and Fe_5C_2 contents is more than 90%. The calculated in our previous work unit cell parameters are as follows: a = 0.452 nm, b = 0.508 nm and c = 0.672 nm (Basaev, 2008).

Comparing figures 10 a, b and c one can conclude that the higher is the catalyst concentration in the feeding solution, the higher will be the content of Fe_3C and α-Fe phases in the MFCNTs filler. The XRD pattern corresponding to 10 %-specimen contains not only the most intense reflex (110) of α-Fe at $2\theta \approx 44.7^o$, but also a sufficiently remote the second by the intensity reflex of pristine Fe (211) at $2\theta \approx 82.4^o$. As the concentration c_x increases, the intensity of the carbide phase reflexes also increases not only at small angles, but also at sufficiently large angles 2θ.

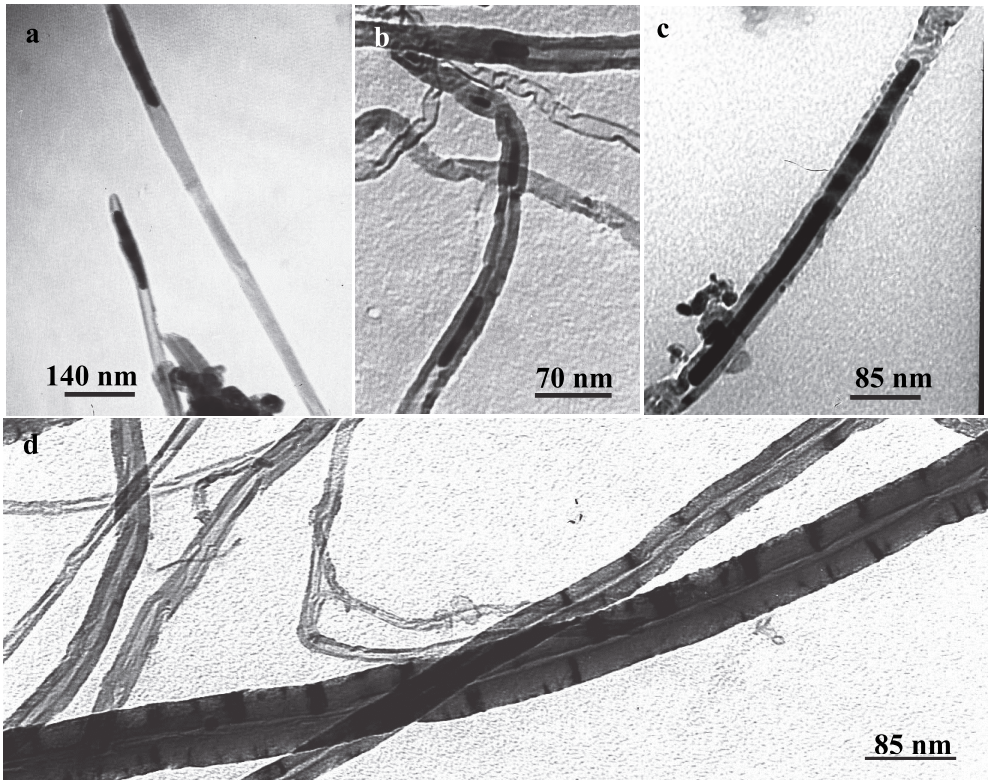

Fig. 9. Typical TEM images of CNTs synthesized at various concentrations of ferrocene in the feeding solution: (a) 0.5 %; (b) 5 %; (c, d) 10 %.

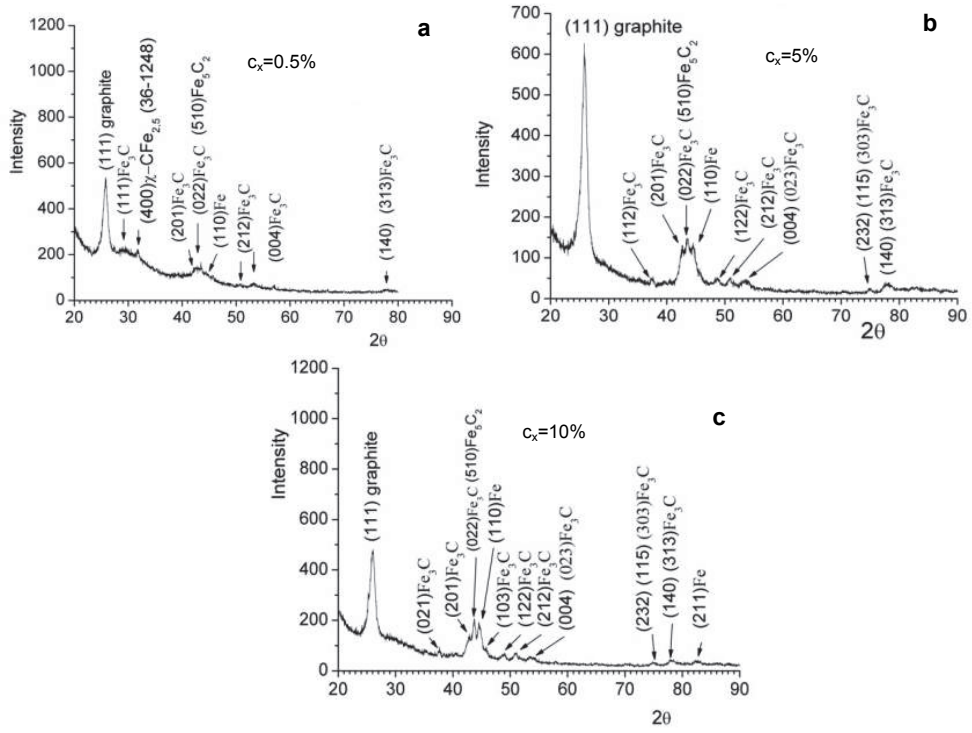

Fig. 10. XRD patterns of the powdered CNTs synthesized at various concentrations c_x of ferrocene in the feeding solution: (a) 0.5 %, (b) 5 %, and (c) 10 %.

4. Magnetic properties of CNT arrays synthesized by the injection CVD method at various catalyst concentrations

The specific magnetization of the synthesized MFCNTs was measured by the static ponderomotive method (Chechernikov, 1969). The dependences $\sigma(T)$ were obtained in the temperature range 78 K ≤ T < 600 K in the magnetic field H = 0.86 T (the magnetic field gradient across a sample region $\Delta Z \approx$ 3.0 cm was $dH_Z/dx \approx 0.16$ T cm^{-1}). The temperature dependences $\sigma(T)$ were measured upon heating of the samples from liquid-nitrogen temperature. The temperature dependence $\sigma(T)$ upon heating in the temperature range 78 K≤T<1100 K that clearly reflects a sequence of manifestations of all magnetic phases of the filler in CNTs and a variation in their specific magnetization with an increase in the temperature was demonstrated by us in (Basaev et al., 2008).

The dependences σ (T) for the nanotube powders under investigation are plotted in Fig. 11 (a-c). The anomalous point in the dependence $\sigma(T)$ corresponds to the Curie point T_C ~ 480 K for cementite Fe_3C (Chikazumi, 1980).

According to this data, the increase of ferrocene content in the feeding solution leads to the increase of the specific magnetization of the CNT array both at liquid-nitrogen temperature and in the whole temperature range while the magnetic order of Fe_3C exists (up to its Curie

point, T_C ~480 K). Noteworthy, the specific magnetization increases also at the temperatures higher T_C for Fe_3C: from ~0.6 A m²/kg for c_x= 0.5 % to ~4.5 A m²/kg for c_x= 10 %. This phenomenon could be only explained by the presence of bigger amount of the magnetic filler inside the nanotubes formed at higher catalyst concentrations. Noticeably, the character of $\sigma(T)$ curve for 0.5 % differs from 5 % and 10 %: it has an almost horizontal plateau up to 300 K, but the curves corresponding to the other two samples do not.

We conducted some theoretical investigations and estimated that the obtained experimental dependence of the specific magnetization of the sample with c_x=10 % in the temperature range of 80-300 K satisfies Bloch law:

$$M(T) = M(0)[1 - BT^{3/2} - CT^{5/2}], \tag{2}$$

and at temperatures 300-480 K it corresponds to Stoner law:

$$M(T) = M(0)[1 - (T / T_C)^2]^{1/2}, \tag{3}$$

where $M(0)$ is saturation magnetization at zero temperature, T_C is Curie temperature of Fe_3C, B=1.65·10^{-5} K$^{-3/2}$, C~10^{-8} K$^{-5/2}$.

The temperature dependence of magnetization of the sample with c_x=5% also correspond to Bloch law, but in the temperature range of 80-450 K. Here the Bloch constant B=6.1·10^{-5} K$^{-3/2}$. Taking into account that the magnetization of 10 %-sample is three times the magnetization of 5 %-sample (Fig. 12-13), the exchange constant which characterizes the exchange interaction in case of c_x=10% is less than when c_x=5%. The observed weakening of the exchange interaction is natural property of the films consisting of ultra thin magnetic layers, and can relate both to dimensional effect and the consequence of decreasing of the effective magnetic momentum of Fe atoms. The thickness of the interface where CNT change the electronic structure of Fe varies from 1 nm to 2-5 nm. The essential changes in the $\sigma(T)$ dependence occur when the thickness of magnetic inclusions is smaller than the doubled thickness of the interface, i.e. when the interfaces of the inclusions overlap (Komogortsev et al., 2007).

The Fe inclusions as their sizes decrease can retain their magnetic properties up to thicknesses of 2-3 nm. Their magnetic properties can degrade significantly at large sizes, when, for example, they contact the interlayer material, so the average atomic magnetic moment decreases and the exchange interaction become weaker. This effect spreads into the depth of 2-5 nm and, probably, can be related to the interlayer stirring which leads to changes in the electronic structure of Fe localized on the surface interfaces (Varnakov et al., 2007).

The hysteresis loops of the samples, obtained at 0.5 % of ferrocene in the feeding solution (c_x = 0.5 %) at low temperatures (10 K) showed diamagnetic nature of the material what might be caused by the insufficient sensitivity of the equipment. Taken at different temperatures, the hysteresis loops of non oriented blocks of MFCNT arrays synthesized at c_x = 5 % and c_x = 10 % are presented in Fig. 12 and Fig. 13, correspondingly. All the curves are symmetrical. In 5 %-sample (Fig. 5) the hysteresis loop area decreases with increasing the temperature.

In 10 %-sample (Fig. 13), on the contrary, as the temperature increases the hysteresis loop area slightly increases. As a result, with increasing the temperature the taken from the loops coercivity H_c decreases for the sample with c_x = 5 %, but slightly increases (for ~35 mT=0.35 kOe at 287 K comparing with 10 K) for 10%-sample. The residual magnetization M_r and the

saturation magnetization M_s decrease with increasing the temperature for both samples. At that, the M_r and M_s values of 10%-sample are higher than that of 5%-sample in the whole temperature range. In particular, the difference ΔM_r reaches ~0.1 emu/g at 10 K, ~0.09 emu/g at 287 K, and the difference ΔM_s ~0.22 emu/g at 10 K, ~0.20 emu/g at 287 K. However, coercivity $H_c(c_x$=10%) smaller than $H_c(c_x$=5 %), especially at low temperatures when difference between them reaches ~0.73 kOe (0.073 T) at 10 K.

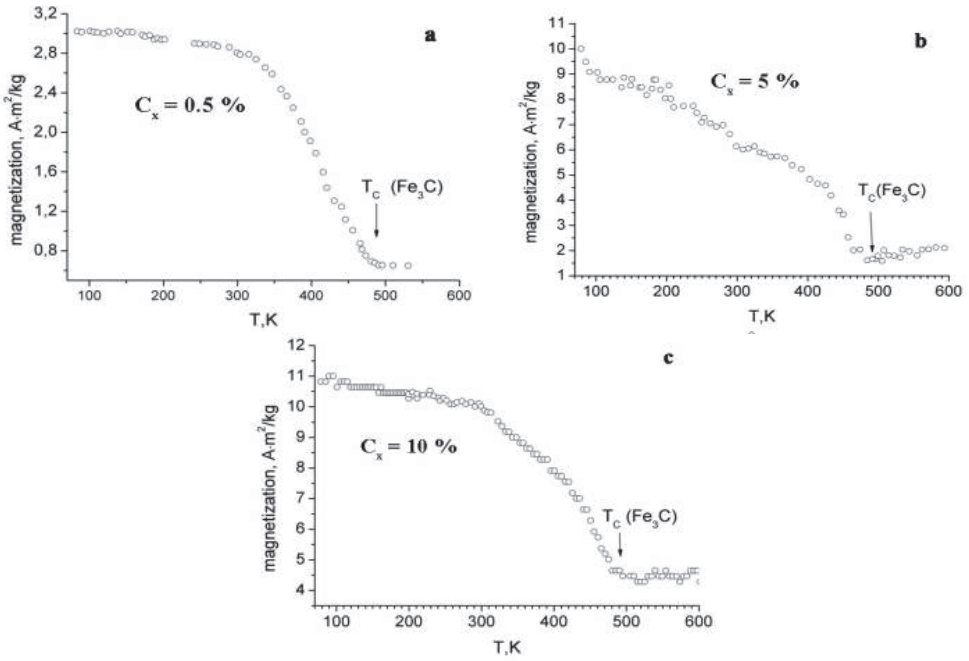

Fig. 11. Temperature dependences σ = *f*(*T*) in heating for powder CNTs synthesized at various concentrations of ferrocene c_x in the feeding solution: (a) 0.5%, (b) 5%, and (c) 10%

The facts that the saturation magnetization of 10%-sample is approximately three times the magnetization of 5 % - sample and the coercive force is smaller can be explained by the higher concentration of magnetic inclusions in that sample. This also might be one of the reasons H_c (c_x=10 %) < H_c (c_x=5 %) at low temperatures. One can assume that in the sample with c_x=5% the particles with smaller dimensions prevail, and for them M_s is lower and H_c is higher than in 10 %-sample.

In a general case, the coercive force is proportional to anisotropy and in inverse proportion to specific magnetization. For composites its value can be calculated using the effective anisotropy constant $H_C = 2K_{eff} / M_S$. For MFCNTs K_{eff} value can be estimated by the shape anisotropy (Vas'kovskiya et al., 2007). This implies, taking into consideration the experimental data, that in 5%-samples the decrease of anisotropy occurs faster as the temperature increases in comparison with the decrease of magnetization. In that case it means that the concentration of the nanoparticles of spherical or ellipsoidal shapes dominates. For these particles the temperature fluctuations lead to spontaneous

magnetization more effectively in comparison with, for example, the particles of elongated shape. As a consequence, the effective anisotropy decreases as temperature increases. On the contrary, in 10 %-samples where the coercive force does not decrease with increasing the temperature the particles of elongated shape predominate (or their increased concentration exists). For elongated particles the energy of anisotropy is considerable, and the temperature fluctuations have not significant influence on spontaneous magnetization.
Thus, in case of c_x= 10 % we have conservation of the shape anisotropy with increasing the temperature to 300 K, what can be related to an increase of the concentration of elongated particles. For that type of particles the increase of thermal fluctuations with increasing the temperature does not result in the loss of the shape anisotropy value, as in case of spherical ones or similar ellipsoids. In addition, the origination of bridges between the particles causing the generation of the domain boundaries, as well as particle sticking which closes magnetic fluxes, may influence the effective coercive force.

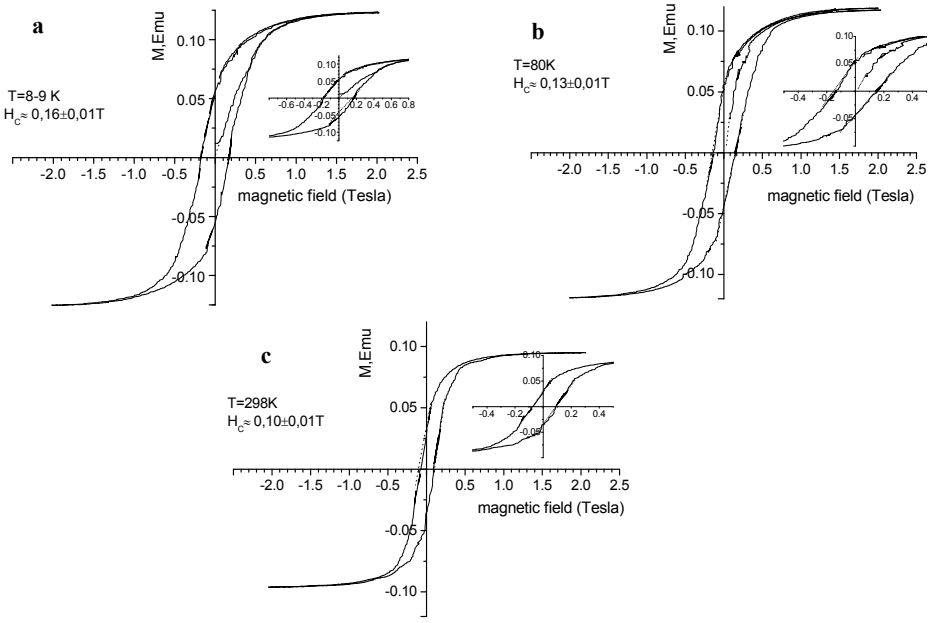

Fig. 12. The hysteresis loops of the non-oriented blocks of MFCNT arrays obtained at 5 % of ferrocene in the feeding solution taken at temperatures: (a) T = 8 K, (b) T = 80 K, (c) T=298.

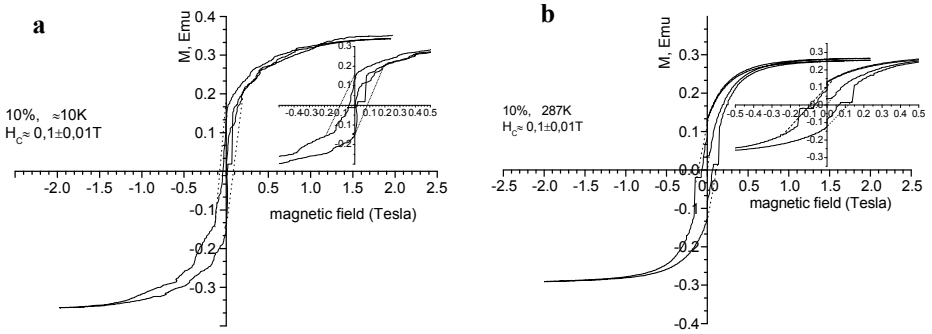

Fig. 13. The hysteresis loops of the non oriented blocks of MFCNT arrays obtained at 10 % of ferrocene in the feeding solution taken at temperatures: (a) T = 10 K, (b) T = 287 K.

5. Model of magnetic structure in Fe_3C nanoparticles

Magnetic structure of individual nanoparticles of various magnetic materials is the subject of numerous theoretical and experimental investigations (Chernavskij, 2002; Cowburn, 1999, 2002; Hollinger et al, 2003; Guslienko & Novosad, 2004; Kondorsky, 1952, 1979; Kravchuk et al., 2007; Kravchuk & Sheka, 2007; Ross et al., 2002; Usov & Peschanyj, 1994).

Nanodisk may reveal either homogeneous or vortex state dependently on its size (radii R and thickness L) as well as on the direction of magnetic field. Magnetization in direction perpendicular to the cross-section of nanodisk means homogeneous perpendicular z-state. In the case when magnetization is parallel to the cross-section of nanodisk – this is in-plane state. When size of nanodisk exceeds correspondent exchange length R_0, configuration of magnetic field tends to overcome the formation of poles on the surface. It resulted in magnetic moments torsion and formation of vortex structure.

In accordance with (Hollinger et al., 2003) the magnetic vortex state of the disk has a fourfold topological degeneracy, since in principle one can measure (and flip) independently both the vorticity of the state and the central polarization (+/-) of the vortex; i.e. one has 2 bit per dot for a 'vortex-state disk', instead of only 1 bit for 'single-domain disk'.

In our theoretical model homogeneous magnetic state of nanodisk is described in continuous approximation applying de-magnetization coefficients.

Vortex structure is characterized with exchange energy normalized per $\pi R^2 L M_S^2$ value (Kravchuk, 2007; Guslienko & Novosad, 2004):

$$w_{ex} = (R / R_0)^2 \int_0^1 d\rho\rho \left[\left(\frac{d\theta}{d\rho} \right)^2 + \frac{\sin^2 \theta}{\rho^2} \right], \tag{4}$$

and magnetostatic energy:

$$w_m = \frac{4\pi}{\beta} \int_0^\infty \left(\int_0^1 \cos\theta(\rho) J_0(\rho x) d\rho \right)^2 [1 - \exp(-\beta x)] dx \,, \tag{5}$$

where $\beta = L / R$, $J_0(z)$ – zero-order Bessel function of the first kind, ρ – polar radius in-plane of the disk, θ(ρ) – angle, characterizing magnetization, M_S – saturation magnetization of nanodisk material.

Euler equation, that minimize total magnetic energy of nanodisk $w_v = w_{ex} + w_m$, possess integral-differentiate form (Guslienko & Novosad, 2004):

$$\frac{d^2\theta(\rho)}{d\rho^2} + \frac{1}{\rho}\frac{d\theta(\rho)}{d\rho} - \frac{\cos\theta(\rho)\sin\theta(\rho)}{\rho^2} = \left(\frac{R}{R_0}\right)^2 \sin\theta(\rho)\int_0^1 \rho'\cos\theta(\rho')g(\rho,\rho',\beta)d\rho', \tag{6}$$

where magnetostatic kernel equals:

$$g(\rho,\rho',\beta) = -\frac{4\pi}{\beta}\int_0^\infty [1-\exp(-\beta x)]J_0(\rho x)J_0(\rho' x)dx \tag{7}$$

It is the authors opinion (Guslienko & Novosad, 2004; Kravchuk et al., 2007; Kravchuk & Sheka, 2007) that equation (6), that could be solved with function $\theta(\rho)$, should be analyzed only approximately. Our analysis shows that elimination of improper kernel integral (7) is possible by application of integral transformations. The first kernel term (4) is transformed using integral Bessel - Hankel transform (Ditkin & Prudnikov, 1961). It will draw to the relationship:

$$g_1(\rho,\rho') = -\frac{4\pi}{\beta}\int_0^\infty J_0(\rho x)J_0(\rho' x)dx = -\frac{4\pi}{\beta}\frac{1}{(\rho+\rho')\Gamma(1)}F\left(\frac{1}{2};\frac{1}{2};1;\frac{4\rho\rho'}{(\rho+\rho')^2}\right), \tag{8}$$

where Γ - gamma-function; F – hypergeometric function of ½, ½, 1 parameters and argument $v = 4\rho\rho'(\rho+\rho')^{-2}$. Applying integral Laplace transform (Ditkin & Prudnikov, 1961) to the second term in (7), we receive the relationship:

$$g_2(\rho,\rho',\beta) = -\frac{4\pi}{\beta}\int_0^\infty \exp(-\beta t)J_0(\rho t)J_0(\rho' t)dt = -\frac{4\pi}{\beta}\left(\frac{1}{\pi\sqrt{\rho\rho'}}Q_{-\frac{1}{2}}\left(\frac{\beta^2+\rho^2+\rho'^2}{2\rho\rho'}\right)\right), \tag{9}$$

where $Q_{-1/2}(x)$ - Legandre spherical function of the second kind of the parameter -½, that is defined using hypergeometric function (Ditkin & Prudnikov, 1961; Gradshtein & Ryzhik, 1971). In so doing,

$$g_2(\rho,\rho',\beta) = -\frac{4\pi}{\beta}\frac{1}{\sqrt{\beta^2+\rho^2+\rho'^2}}F\left(\frac{3}{4};\frac{1}{4};1;\left(\frac{2\rho\rho'}{\beta^2+\rho^2+\rho'^2}\right)^2\right) \tag{10}$$

Obtained relationships (11), (13) allow exact calculation of the function (10). The advantage of applied hypergeometric functions is the absence of improper integrals as well as simplicity and universality of calculations.

Next, equation (6) is transformed to equation containing linear integral term by substitution of desired function $u(\rho) = \cos\theta(\rho)$ and substitution $1-u^2 = 1-4z^2 = f(z)$. Consequently we obtain equation

$$\left(\frac{d^2z}{d\rho^2}\right)-\frac{f_z'(z)}{f(z)}\left(\frac{dz}{d\rho}\right)^2+\frac{1}{\rho}\left(\frac{dz}{d\rho}\right)+\frac{1}{2}f(z)U(\rho)=0\,, \tag{11}$$

where

$$U(\rho)=\left(\frac{u}{\rho^2}+(R/R_0)^2\int_0^1 u(\rho')\rho' g(\beta,\rho,\rho')d\rho'\right), \tag{12}$$

with boundary conditions: $z(0)=1/2,\ dz/d\rho_{\rho=0}=0$.

The solution of non-linear equation (11), in accordance with (Kamkr, 1971), corresponds to the solution of first term $(dz/d\rho)=f(z)\omega(\rho)$, where function $\omega(\rho)$ is defined with linear first term equation $(d\omega/d\rho)+(\omega/\rho)+(1/2)U(\rho)=0$. After integration we obtain the relationship:

$$u(\rho)=\frac{C_1\rho^{4C_2}Y(\rho)-1}{C_1\rho^{4C_2}Y(\rho)+1}\,, \tag{13}$$

where $Y(\rho)=\exp\left(-2\ln\rho\int\rho U(\rho)d\rho+2\int\rho\ln(\rho)U(\rho)d\rho\right)$, C_1, C_2 - constants.

Deduced system of equations (12), (13) for calculation of vortex magnetization distribution in nanodisk contains linear Fredholm equation of the second kind (12) and the expression, combining functions $u(\rho)$ and $U(\rho)$.

Basing on the obtained system of equations (10)-(12) calculations of vortex magnetization distribution in Fe_3C nanodisks 5 to 100 nm in size has been performed. Calculation results were compared with the results, obtained for permalloy using OOMMF software for micromagnetic modeling (The object oriented micromagnetic framework. http://math.nist.gov/oommf/). It has been shown that vortex magnetization distribution is well approximated with the function

$$u_f(\rho)=\frac{C_1-C_2\rho^2-C_3\rho^3}{C_1+C_4\rho^2+C_5\rho^3}\,, \tag{14}$$

where $C_{(1\text{-}5)}$ – constant values, depending on nanodisk's size.

It is established, basing on performed calculations that Gaussian distribution commonly applied as probe function for approximation of magnetization vortex, draw to the significant error and could be used only for description of kernel vortex. Simultaneously, $uf(\rho)$ function practically satisfies the equation (6) in the whole range of radii R and nanodisk thicknesses L. Calculated distributions of vortex magnetization for different radii and thicknesses in Fe_3C nanodisks are presented in Fig. 14. It is shown that an increase of L draw to the increase of the radii of vortex kernel in accordance with the relationship $L^{1/p}$ (p=3.6-4.0), while an increase of R resulted in the proportional decrease of the kernel vortex radii. The size of vortex changed similarly.

Calculated diagram of basic magnetic states in cylindrical Fe_3C nanoparticles for the radii-height plane evidences that exchange length for Fe_3C nanoparticles ranges within 6-8 nm, see Fig. 15. The important conclusion is that within applied approximation vortex state of Fe_3C nanodisks with one central vortex is stable for radii values of 8-16 nm and thickness of 12-80 nm. These results together with well-established thermal stability make Fe_3C

nanoparticles very prospective for application in modern recording media with recording density about 1 Tbit/inch[2].

Proposed model was also applied for consideration of temperature dependencies of the crossover between vortex and homogeneous z-state in the temperature range 300-470 K. It is shown in Fig. 16 that temperature increase supports the crossover from the vortex to homogeneous z-state. At constant values of nanoparticles radii and height temperature growth draw to the increased radii and vortex size. Such peculiar dependencies originate from growing exchange length with temperature.

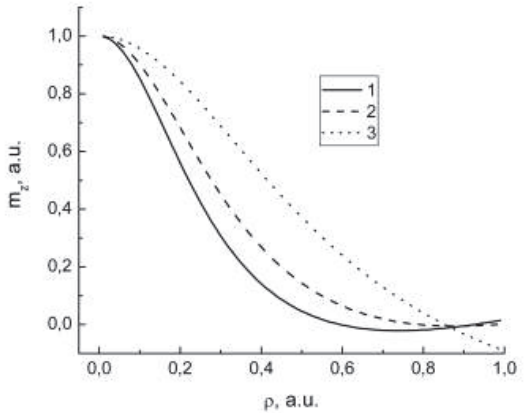

Fig. 14. Distribution of vortex magnetization in Fe_3C nanodisks at β =3.0: $r=R/R_0$=2.5 (curve 1); r=2.0 (2); r=1.2 (3).

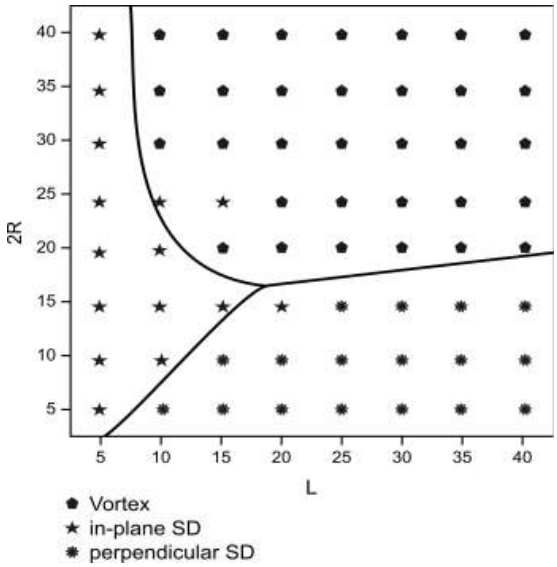

Fig. 15. Diagram of crossovers between different magnetic states for nanodisks (SD) of Fe_3C (analytic and micromagnetic simulation, nm)

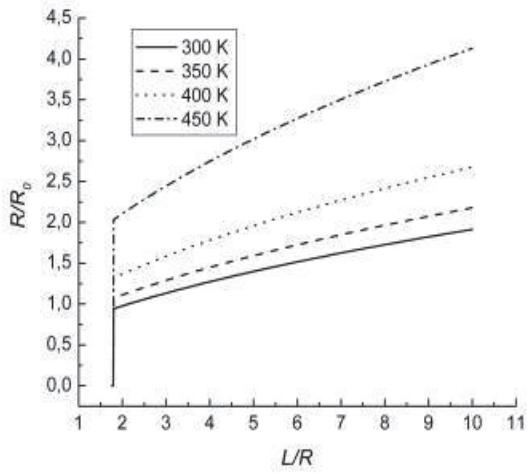

Fig. 16. Temperature dependencies of the radius R which defines the crossover between the vortex and the homogeneous perpendicular z-state for Fe_3C.

6. Local ^{57}Fe states in carbon nanotubes synthesized by injection CVD method

6.1 Effect of ferrocene concentration c_x

In the present experiment local ^{57}Fe states in MFCNTs were studied by application of Mössbauer spectroscopy as a function of the ferrocene concentration c_x (1 %, 5 % and 10 %) in samples sintered at temperature in the reaction zone T equaled 875°C. The process duration time t was 1 min. The cooling rate of the synthesized MFCNT arrays was determined by the natural cooling down rate of the heating furnace. The injection rate of the feeding solution into the reaction zone v=1 ml·min^{-1} and Ar flow rate v_{Ar}=100 cm^3 ·min^{-1} were provided in all the experiments considered below.

Recorded RT Mössbauer spectra are presented in fig. 17 (a-c), correspondingly. The best fitting of the spectra was performed in assumption of four different subspectra, i.e. singlet C, quadrupole doublet D and two magnetic sextets S_1 and S_2. Hyperfine parameters of the subspectra are summarized in table 1.

The parameters of singlet C and sextet S_2 are characteristic of fcc γ-Fe and bcc α-Fe, correspondingly. Spectra fitting confirmed (see table 1) that γ-Fe phase, existing at 860 °C in accordance with Fe-C phase diagram, was detected also during the cooling process at all c_x and partially transformed into ferromagnetic α-Fe, Fe_3C and antiferromagnetic FeC_2 phases. It is to admit that the contribution of γ-Fe nanoparticles was quite significant (between 20 % and 31 %). It means that by "quenching" process draw to the formation of thermodynamically stable at ambient conditions γ-Fe phase. The relative contribution of γ-Fe and α-Fe phases for 5% and 10% samples is almost the same, but for 1% is comparably higher. Sextet S_1, should be assigned to the cementite phase Fe_3C in strong correlation with X-ray diffraction data (Basaev et al., 2008). It is important to note the presence of nonmagnetic FeC_2 phase characterized with quadrupole doublet D. The relationship between Fe_3C and FeC_2 phase's contributions revealed the dependency on c_x, in the samples.

In fact, Fe_3C contribution increased with c_x, at the expense of FeC_2. Particularly, at the applied conditions of synthesis Fe_3C content is growing up from 21 % at c_x=1 % up to its higher value 54 % at c_x=10 %.

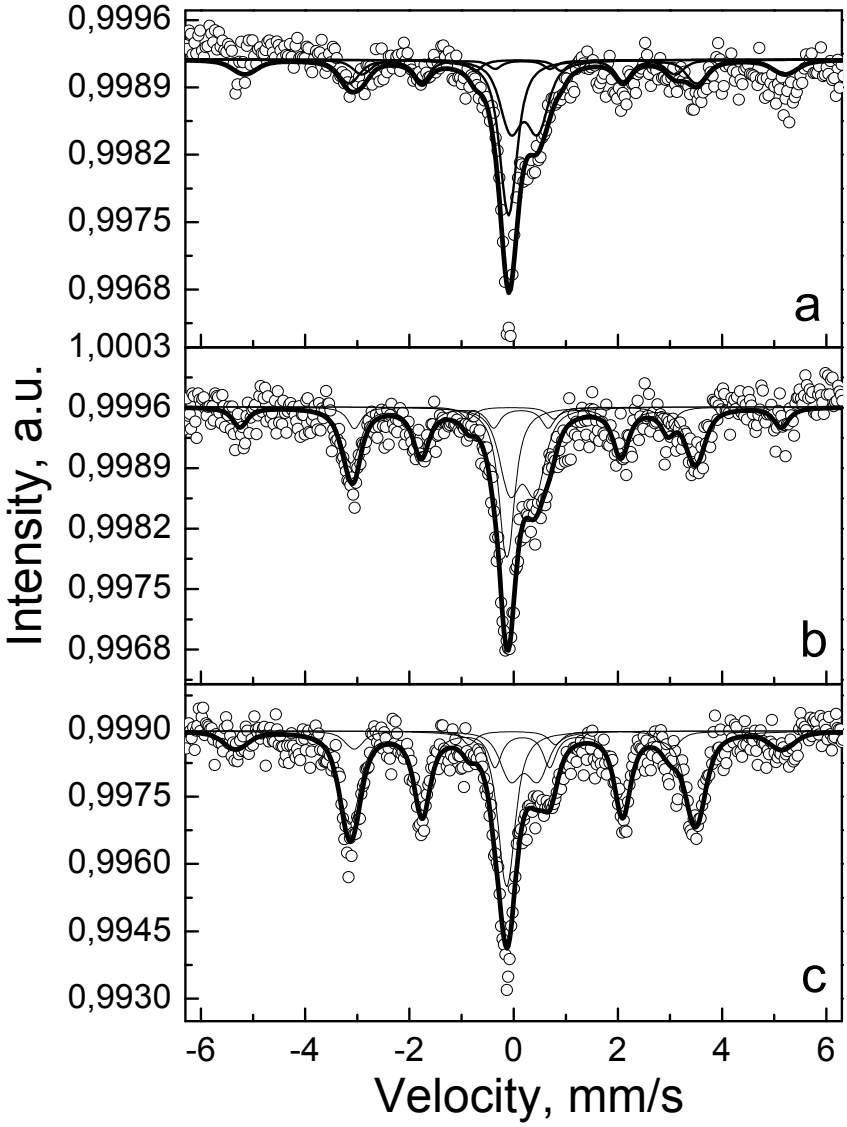

Fig. 17. Mössbauer spectra of MFCNTs synthesized at c_x=1 % (a), c_x =5 % (b) and c_x =10 % (d) (t=1 min, T= 875 ºC, natural cooling down rate of the reactor).

c_x , %	Subspectrum	δ, mm·s^{-1}	ΔE, mm·s^{-1}	H_{eff}, T	Contribution	Phase
1	Singlet C	-0,10	0	-	31	γ-Fe
	Doublet D	0,2	0,52	-	31	FeC_2
	Sextet S_1	0,17	0	20,7	21	Fe_3C
	Sextet S_2	0,06	-0,03	32,2	17	α-Fe
5	Singlet C	-0,13	-0,11	-	21	γ-Fe
	Doublet D	0,17	0,48	-	28	FeC_2
	Sextet S_1	0,16	0,02	20,5	37	Fe_3C
	Sextet S_2	-0,05	0	32,3	14	α-Fe
10	Singlet C	-0,13	0	-	20	γ-Fe
	Doublet D	0,20	0,52	-	13	FeC_2
	Sextet S_1	0,17	0	20,6	54	Fe_3C
	Sextet S_2	-0,06	-0,03	32,6	13	α-Fe

Table 1. Hyperfine parameters of the spectra of MFCNTs synthesized with different concentrations c_x of the feeding solution; δ – isomer shift, ΔE – quadrupole spitting, H_{eff} – hyperfine magnetic field (T=875°C, t=1 min, slow cooling rate)

6.2 Effect of cooling rate

In the second experiment Mössbauer spectroscopy was applied to investigate influence of cooling rate during MFCNTs synthesis c_x=10 %, T=825 °C, t=4 min. The cooling methods for this case were different: either slow realized by natural cooling down rate, or fast, using Ar stream of 450 cm^3·min^{-1} and immediate extracting of the CNT samples out of the reactor.

Actually, absence of noticeable changes in phase composition was also detected by Mössbauer investigation (fig. 18). Hyperfine parameters extracted by fitting of Mössbauer spectra are presented in the table 2. According to the table 2, as in a case of table 1, Mössbauer spectra could be fitted with four subspectra characterizing γ-Fe, α-Fe, Fe_3C and FeC_2 phases. For the both samples the contribution of cementite is the largest, ~ 82%, and their hyperfine parameters coincide within the error. There is a little difference in contributions of α-Fe subspectra. In the slow-cooled sample 8 % of α-Fe was formed whereas in the fast-cooled one - 6 %. Besides, the width of spectral line of the last sample is larger than that of the first one, evidencing that slow cooling gives better crystallization of α-Fe. Apart from the described above magnetic subspectra two nonmagnetic components – singlet corresponding to γ-Fe and doublet belonging to FeC_2 – were detected. The doublets possess similar hyperfine parameters and almost the same relative contributions in the both samples. The γ-Fe contribution was a little bit higher in the fast-cooled sample (see table 2).

As compared to our results presented in table 1, where the concentration of the feeding solution was the same (c_x=10%), the contribution of Fe-containing phases was different: Fe_3C ~80 % instead of ~50 % (see table 1). In our previous paper [28] the content of cementite phase was even higher (~ 90%). The specific feature of these experiments is the duration of CNT synthesis process: 1 min (for samples described in table 1); 4 min (for samples described in table 2), and 5 min for samples considered in (Basaev et al., 2008). Therefore, the duration of the synthesis process strongly influences the contribution of iron-containing phases, i.e. the higher is the duration, the higher the content of Fe_3C phase will be. It is evident that for the obtaining the maximum amount of Fe_3C phase the process duration of 5 min. is optimal in our experiments. According to (Wei et al., 2006), in the case when the process duration exceeds 20 min., the annealing of Fe is going on, that can lead to the

decomposition of even thermodynamically stable Fe_3C. CNTs destruction and its morphology deterioration take place. External and internal diameters of CNTs and distance between them are enlarging up to 50 %, branching is appearing and number of spherical shape Fe particles is increasing.

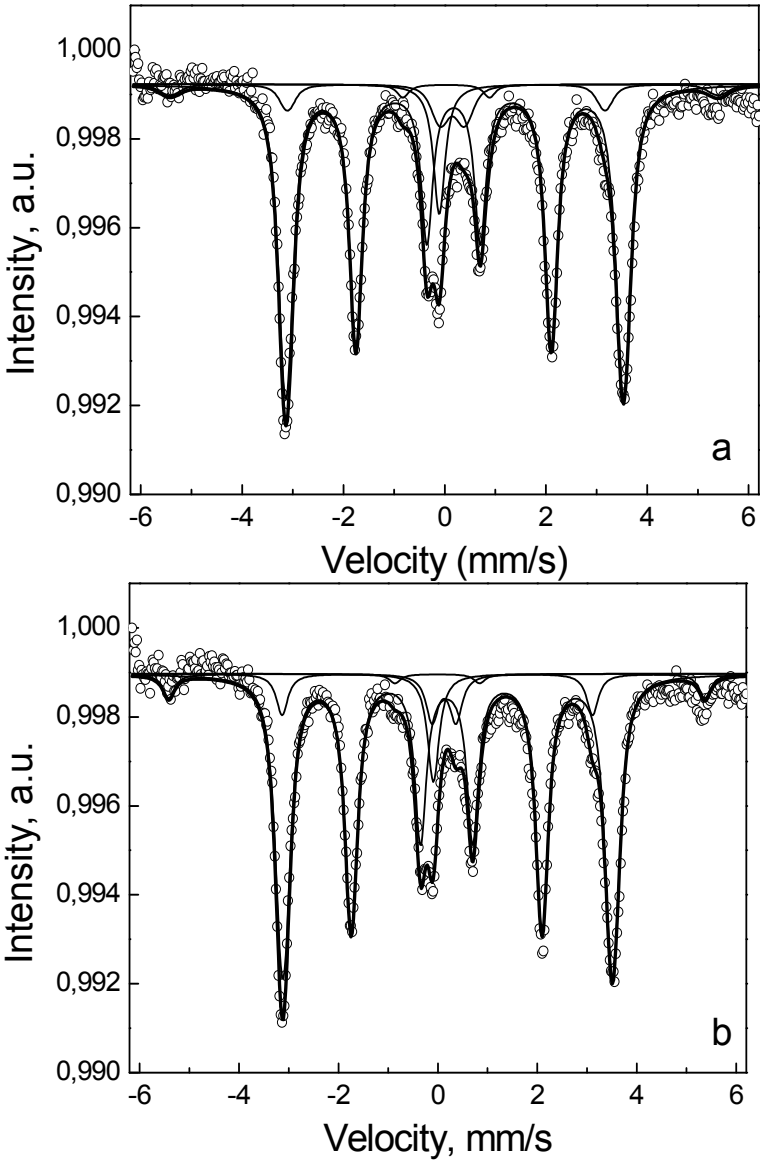

Fig. 18. Mössbauer spectra of MFCNTs synthesized at c_x=10 % t=3.5 min, T= 825 ºC after fast (a) and slow (b) cooling down rates of the synthesis equipment

Cooling	Subspectrum	δ, mm·s^{-1}	ΔE, mm·s^{-1}	H_{eff}, T	Contribution	Phase
fast	Singlet C	-0,11	0	-	7	γ-Fe
	Doublet D	0,15	0,48	-	5	FeC_2
	Sextet S_1	0,18	-0,02	20,7	82	Fe_3C
	Sextet S_2	0,01	0,01	33,6	6	α-Fe
slow	Singlet C	-0,09	0	-	6	γ-Fe
	Doublet D	0,12	0,48	-	5	FeC_2
	Sextet S_1	0,19	0,01	20,6	81	Fe_3C
	Sextet S_2	-0,02	-0,01	33,5	8	α-Fe

Table 2. Hyperfine parameters of the spectra of MFCNTs after fast and slow cooling down rates; δ – isomer shift, ΔE – quadrupole spitting, H_{eff} – hyperfine magnetic field (c_x=10 %, T=825 °C, t=4 min)

6.3 Effect of synthesis temperature

The Mössbauer spectra of the MFCNTs synthesized at two different temperatures, 775 °C and 875 °C, using c_x=1 %; t=4 min and at fast cooling of the furnace after their synthesis are shown in fig. 19.

It is noteworthy that TEM investigations (not shown) did not reveal any new peculiarities in a way the magnetic particles fill nanotubes. Mössbauer spectra of these samples revealed very different phase contributions of Fe-containing phases for two applied synthesized temperatures. As evidenced from the Table 3 summarizing the hyperfine parameters of the corresponding spectra at T=775°C γ-Fe phase was not detected, that is in agreement with the phase diagram of Fe-C. The content of Fe_3C at this temperature is ~60 %, even higher than at c_x=10 % with t=1min (table 1). One should note that at T=775 °C there is very low content of α-Fe phase (only 4 %), and contribution of Fe carbides definitely dominates. It means that at this relatively low temperature the process of γ-Fe phase transformation into other Fe-containing phases was not detected and α-Fe, Fe_3C and FeC_2 phases are directly created during the synthesis process. Large amount of carbides testifies their stability as compared to α-Fe.

Temperature during synthesis, °C	Subspectrum	δ, mm·s^{-1}	ΔE, mm·s^{-1}	H_{eff}, T	Contribution	Phase
875	Singlet C	-0,10	0	-	31	γ-Fe
	Doublet D	0,2	0,52	-	31	FeC_2
	Sextet S_1	0,17	0	20,7	21	Fe_3C
	Sextet S_2	0,06	-0,03	32,2	17	α-Fe
775	Doublet D	0,17	0,50	-	36	FeC_2
	Sextet S_1	0,18	0,02	20,8	60	Fe_3C
	Sextet S_2	0,09	0,15	33,9	4	α-Fe

Table 3. Hyperfine parameters of the spectra of MFCNTs synthesized at 775 °C and 875 °C; δ – isomeric shift, ΔE – quadrupole spitting, H_{eff} – hyperfine magnetic field (c_x =0,5%, t=4min, fast cooling)

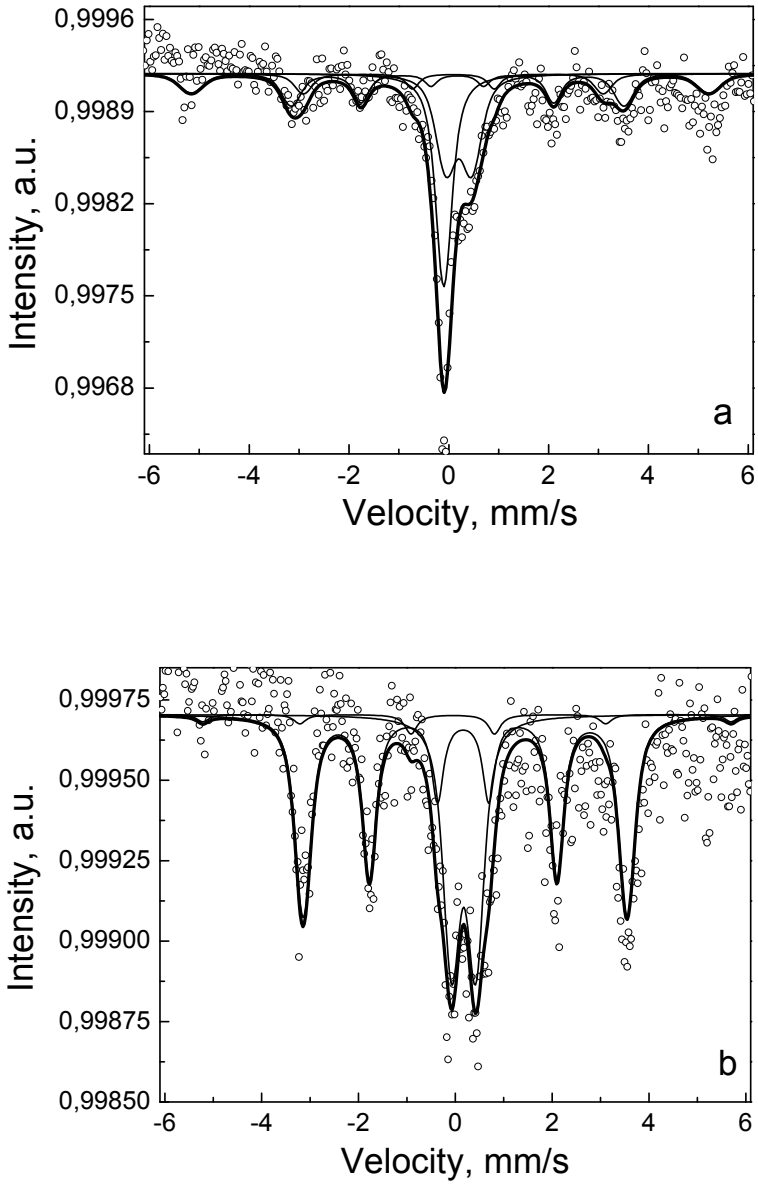

Fig. 19. Mössbauer spectra of the MFCNTs synthesized at two different temperatures, 875°C and 775°C (c_x=1%, t=4 min, fast cooling down rate of the furnace)

7. The influence of electron irradiation on the magnetic properties of carbon nanotubes filled with Fe-phases composite

It is well established that application of CNTs filled with ferromagnetic material as sensors for magnetic scanning probe microscopy, for spintronics devices, high-density magnetic memory materials, biomedicine etc. revealed important requirements to their stability during interaction with electron beams. Lots of theoretical and experimental studies have been conducted on the interaction of electrons with the carbon atoms of the shells of pristine CNTs leading to changes of mechanical, electronic and, correspondingly, electrical properties (Banhart, 1999; Vijayaraghavan et al., 2005; Zhang & Iijima, 2000). However, not many results address the influence of electron irradiation on CNTs filled with the magnetic component. With this respect, we studied the electron irradiation effect on the structure, composition and magnetic properties of CNTs filled with Fe_3C mostly (amount of α-Fe, Fe_5C_2 is negligible).

CNT arrays have been synthesized by the high temperature pyrolysis of the xylene/ferrocene (feeding) solution at atmospheric pressure. Ar was used as a gas-career. The concrete regime of CNT arrays synthesis was chosen as following: the ferrocene concentration c_x in the feeding solution was 0.5%, 5% and 10%, its injection rate into the reaction zone was 1 ml min^{-1}, temperature in the reaction zone was 870°C, and the argon flow rate was 100 cm^3 min^{-1}. The process duration time was 5 minutes. The cooling rate of the synthesized CNTs was determined by the natural cooling down rate of the heating furnace. At these conditions the dense vertically aligned CNT arrays filled with the magnetic Fe-contained nanocomposite were formed at the walls of tubular type quartz reactor. As it was shown previously, the filler inside CNTs represents ~90% of Fe_3C and ~10% of α-Fe and Fe_5C_2 (Basaev et al., 2008). CNTs were mechanically removed from the reactor walls for the exposure to electron irradiation and further investigations.

CNTs were irradiated at room temperature with a dose of 10^{15} cm^{-2} using an electron accelerator.

Typical structures of CNTs synthesized using 10%-feeding solution (i.e. c_x=10%) before and after the electron irradiation are presented in figure 20. TEM investigations showed that the structure of CNT shells in general looks unchanged after the electron irradiation. However, those CNTs filled with the magnetic nanocomposite appear to have absolutely different morphology from it was before (figure 20 a,b). The cylinder-shaped filler nanowires located in CNT channels under e-irradiation were transformed into the ball-shaped particles (figure 20 b). The structure of CNT itself was visibly modified also in this area, i.e. the channel inside CNT almost disappeared, the CNT shell became defective. Such transformations might be caused by a pressure buildup within a nanotube in the process of irradiation which leads to tube collapsing and, correspondingly, filler nanowire squeezing and its final break up (Sun et al., 2006). The observed splitting of the filler particles must certainly influence the magnetic properties of CNTs.

The $\sigma(T)$ dependences were obtained in the temperature range 78 K ≤ T < 600 K in the magnetic field H = 0.86 T in the cooling and heating modes. The $\sigma(T)$ dependences measured upon heating of the CNTs samples with different concentration of ferrocene in the feeding solution before and after electron irradiation are shown in figure 21 (a-c). The anomalous point in the dependence $\sigma(T)$ corresponds to the Curie point T_C ~ 480 K for cementite Fe_3C (Basaev, 2008).

One can observe the decrease of the specific magnetization of the irradiated CNTs both at liquid-nitrogen temperature and in the whole temperature range, what is most probably governed by the structural point defects occurred during the electron irradiation. In figure 22 the dependences $\sigma(T)$ of the irradiated CNTs measured both in the heating and cooling modes in a temperature range $700 \div 800\ K \leq T < 100 \div 300\ K$ are shown. It is seen that $\sigma(T)$ curve measured upon cooling lies well above another measured upon heating. It means that as the samples were heated during the first circle of $\sigma(T)$ measurements the radiation defects were annealed what resulted in the increase of the specific magnetization which aimed to reach the primary measured values of non-radiated samples. These measurements confirm the fact that the decrease of magnetization of CNTs is governed by the point structural defects created during electron irradiation.

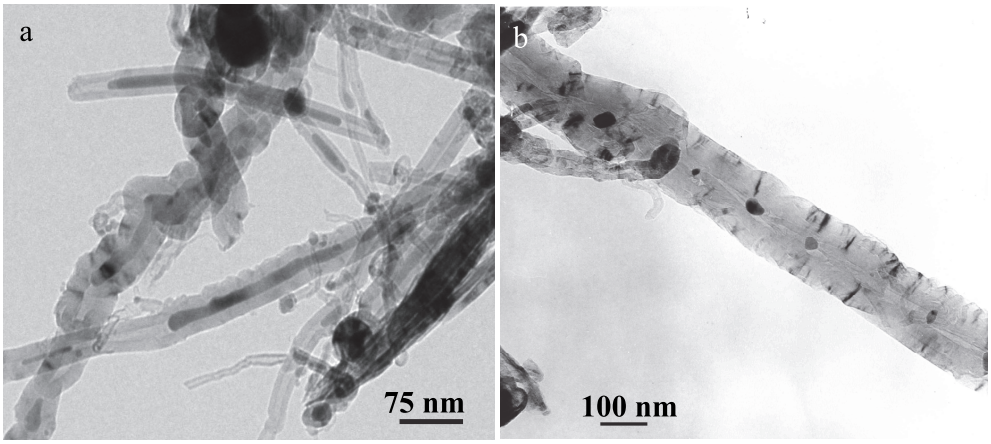

Fig. 20. Typical TEM views of CNTs synthesized using 10%-feeding solution: (a) before and (b) after the electron irradiation.

The comparison of the ratio "signal-background" in the X-ray spectra taken on the CNT specimens synthesized at c_x=10% before and after the e-irradiation with the dose of 10^{15} cm^{-2} (figure 23) revealed the decrease of integral intensity of X-ray reflexes in the angle range $20° < 2\theta < 30°$ corresponding to crystalline state of the carbon composing CNTs. This can be explained by the generation of point defects in the crystal structure caused by Coulomb interaction of incident electrons with the atom nuclei and electron shells of target material. Point defects, such as Frenkel pairs, in contrast to dislocations, do not result in enormous changes of the phase state of material, but just unit cell deformations (Shalayev, 1967). In the angle range $40° < 2\theta < 55°$ which characterizes the Fe_3C and α-Fe the intensity decrease is less pronounced. The integral intensity of the reflexes at large angles in the range $74° < 2\theta < 85°$ before and after the irradiation remains almost the same what is in agreement with (Lipson & Steeple, 1972) since the large angle reflexes are not sensitive to small structure deformations in polycrystals. There wasn't found any new reflexes after the exposure to electron irradiation, so we can fearlessly conclude that the used doses resulted only in crystal structure distortion of the C-Fe_3C-α-Fe-Fe_5C_2 composite.

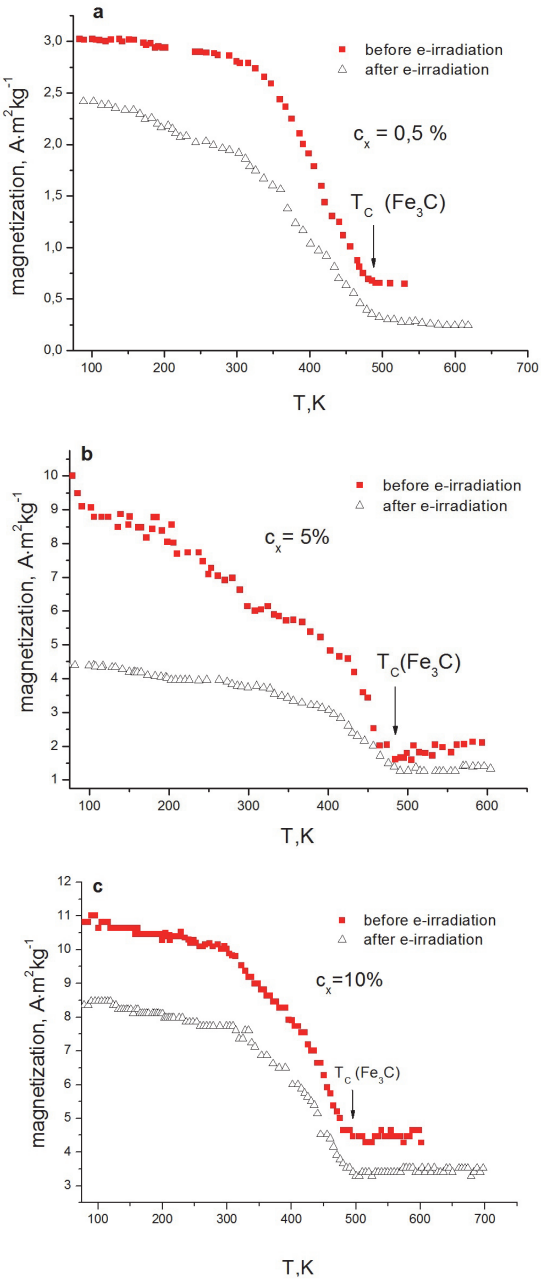

Fig. 21. Temperature dependences $\sigma=f(T)$ of CNTs synthesized using various concentrations of ferrocene in the feeding solution c_x before and after the electron irradiation measured in the heating mode: (a) c_x=0.5%, (b) c_x=5%, (c) c_x=10%.

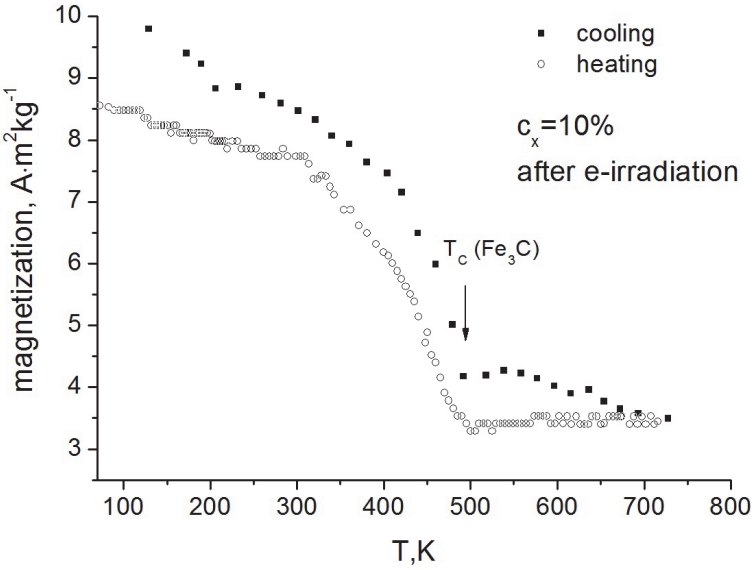

Fig. 22. Temperature dependences $\sigma=f(T)$ of the irradiated CNTs measured in the heating and cooling modes.

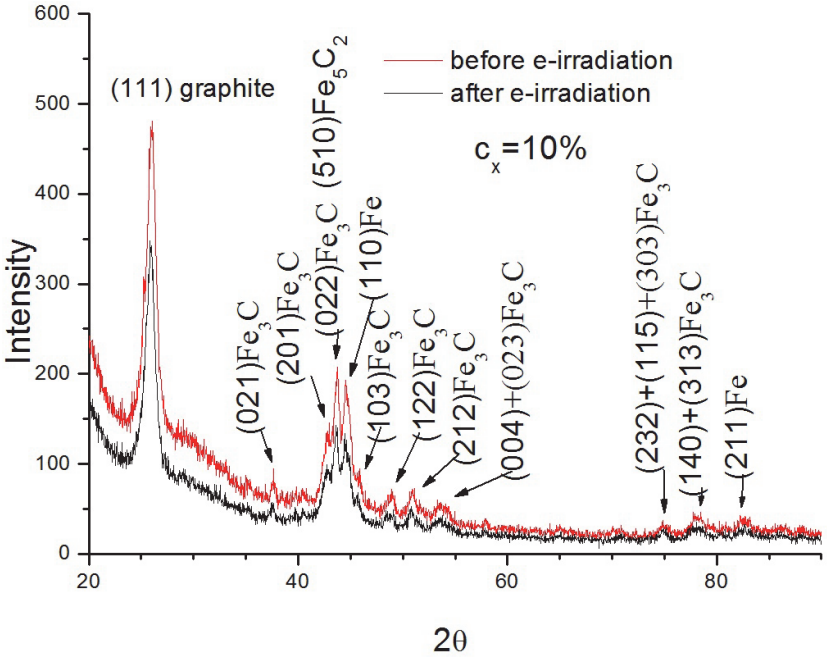

Fig. 23. X-ray diffraction patterns of powder-like nanotube arrays synthesized at 10% of ferrocene in the feeding solution before and after e-irradiation.

8. Acknowledgements

Financial support from State Program for Scientific Research "Functional materials, nanomaterials", project 2.4.12 is gratefully acknowledged.

9. Conclusions

Magnetically functionalized multiwall carbon nanotubes (MFCNT) were synthesized by the high-temperature pyrolysis of liquid hydrocarbon p-xylene C_8H_{10} in a mixture with a volatile catalyst, namely, ferrocene $Fe(C_5H_5)_2$, on the surface of silicon substrates in a quartz reactor. Under the synthesis conditions used in the experiment, arrays of vertically aligned nanotubes are formed on the silicon substrates and reactor walls.

Using different experimental methods it is established that carbon nanotubes of both types exhibit identical properties and represent a complex nanocomposite, C–Fe_3C–Fe_5C_2–Fe. The analysis of the results of X-ray diffraction results, measurements of the specific magnetization, and Mössbauer spectroscopy demonstrated that the Fe_3C content in the filler of the carbon nanotubes is approximately 90%. The unit cell parameters for the structure of the Fe_3C phase in the nanotubes were determined to be a = 0.452 nm, b = 0.508 nm, and c = 0.672 nm. An analysis of the temperature dependences of the specific magnetization $\sigma = f(T)$ demonstrates that, in the temperature range 78 K ≤ T ≤ 1060 K, the magnetic properties of the nanotubes under investigation are governed by the properties of iron carbides (in the form of Fe_3C and Fe_5C_2) and iron. It is revealed that synthesized carbon nanotubes possess reversible magnetic properties in the temperature range 78 K ≤ T ≤ 720 K. The effective magnetic fields on ^{57}Fe nuclei in the composition of the filler components were determined. It was revealed that a certain number of filler particles in the carbon nanotubes possess superparamagnetic properties.

The influence of the catalyst concentration (1%, 5%, and 10%) in the feeding solution on the magnetic properties of the CNT arrays was investigated. X-ray diffraction analysis revealed that the higher the catalyst concentration in feeding solution is, the higher is the content of Fe_3C and Fe phases in the CNTs filler. An analysis of the temperature dependences of the specific magnetization $\sigma=f(T)$ showed that the specific magnetization increases as the ferrocene concentration increases. The temperature dependencies of the specific magnetization demonstrated its higher values for 10%-specimens both lower and higher Curie point of Fe_3C. The anisotropy of the specific magnetization measured perpendicular ($\sigma_\perp$) or parallel ($\sigma_{//}$) to the surface of CNT array inheres in our samples. It was found that $\sigma_\perp > \sigma_{//}$ and both values are higher for the sample prepared at higher concentrations of ferrocene.

The phase composition of magnetic filler located inside of multi-wall MFCNTs was determined be using Mössbauer Spectroscopy. MFCNTs were obtained by the injection CVD method using ferrocene-xylene solution at various conditions (i.e. the ferrocene concentration c_x (0.5%, 5%, and 10%) in the feeding solution, slow or fast cooling down rates of the synthesis reactor, temperature of the reaction zone during synthesis), which may influence the magnetic properties of MFCNTs owing to different contribution of Fe phases. SEM and TEM methods were used to investigate the morphology and structure of the synthesized material. It was shown that Fe_3C phase formation is favorable at relatively low temperatures (775 ^oC) during CNT synthesis, long duration of the CNT growth process, as well as at high content of the catalyst in the feeding solution.

Model of the magnetic structure of cylindrical nanoparticles of cementite Fe_3C was developed. Systems of equations for calculation of the vortex magnetization of the nanoparticles were obtained within continuum approach based on Euler equation minimizing total energy of the cylinder. The temperature effect on single domain size, equal to 6-8 nm at 300 K is also considered. It was shown, that as temperature increases from 300 to 450 K, the single domain size for cementite increases in 2.16 times, and to 470 K – in 3.4 times. The magnetic structure of the cylindrical cementite nanoparticles encapsulated into the carbon nanotubes has been studied in the absence of magnetic field depending on its size in the temperature range of 300-470 K using continuous approximation. The distribution of the magnetization in the cementite nanocylinders has been calculated considering the uniaxial crystallographic anisotropy. The vortex magnetization has been simulated using the rational fractional functions which ensure the required accuracy of the calculations and allow determining the vortex size correctly. It has been shown that the geometrical parameters of the nanoparticles and the temperature are the main factors influencing the transitions between the vortex and homogeneous states. The temperature dependence of the transition between the vortex state and the homogeneous z-state in the temperature range of 300-470 K has been calculated. It has been revealed that the rise in the temperature leads to the vortex size enlarging and promotes the transition from the vortex to either homogeneous or planar states, depending on the size of nanocylinder. The reverse transfers are banned, since the single-domain length increases as the temperature rises.

10. References

Basaev, A.S., Bokhonov, B.B., Demidenko, O.F., Labunov, V.A., Makovetskii, G.I., Prudnikova, E.L., Reznev, A.A., Saurov, A.N., Fedosyuk, V.M., Fedotova, Yu.A., Shulitskii, B.G. & Yanushkevich, K.I. (2008). Synthesis and Properties of Magnetically Functionalized Carbon Nanotubes, *Nanotechnologies in Russia*, Vol. 3, pp. 184–190

Banhart, F. (1999). Irradiation effects in carbon nanostructures, *Rep. Prog. Phys.*, Vol. 62, pp. 1181-1221.

Chechernikov, V. I. (1969). *Magnetic Measurements*, Moscow State University, Moscow (in Russian)

Chikazumi, S. (1980). *Physics of Ferromagnetism, Magnetic Properties of Materials*, Syokabo, Tokyo

Chernavskij, P.A. (2002). New in magnetic methods of investigations of metal-deposited catalysts, *Russian Chemical Journal*, Vol. XLVI, No 3, pp. 19-30 (in Russian)

Cowburn, R.P., Koltsov, D.K., Adeyeye, A.O. & Welland, M.E. (1999). Single-Domain Circular Nanomagnets, *Physical Review Letters*, Vol. 83, No.5, pp. 1042-1045

Cowburn, R.P. (2002). Magnetic nanodots for device applications, *J. Magnetism and Magnetic Materials*, Vol 242-245, Part 1, pp. 505-511

Ditkin, V.A., Prudnikov, A.P. (1961). *Integral transformations and operational calculus*, Fizmatgiz, Moscow (in Russian)

Gradshtein, I.S, Ryzhik, I.M. (1971). *Tables of integrals, sums, series and multiplications*, Nauka, Moscow

Guslienko, K.Yu., Novosad, V. (2004).Vortex state stability in soft magnetic cylindrical nanodots, *J. Applied Physics*, Vol. 96, No. 8, pp. 4451-4455

Harris, P. J. F. (2002). *Carbon Nanotubes and Related Structures*, Cambridge University Press, Cambridge

Hollinger, R., Killinger, A. & Krey, U. (2003). Statics and fast dynamics of nanomagnets with vortex structure, *J. Magnetism and Magnetic Materials*, Vol. 261, pp. 178-189

Joint Committee on Powder Diffraction Standards—International Centre for Diffraction Data (JCPDS—ICDD), PCPDFWIN, Version 2.00, 1998

Kamke, R. (1971). Manual on ordinary differential equations, Nauka, Moscow

Komogortsev, S. V., Iskhakov, R. S., Balaev, A. D., Kudashov, A. G., Okotrub, A. V. & Smirnov, S. I. (2007). Magnetic properties of Fe_3C ferromagnetic nanoparticles encapsulated in carbon nanotubes, *Physics of the Solid State*, Vol. 49, pp. 734-738

Kondorsky, E.I. (1952). To the theory of single-domain particles, *Reports of Academy of Sciences USSR*, Vol. 82, No 3, pp. 365-367 (in Russian)

Kondorsky, E.I. (1979). On the stability of certain magnetic modes in fine ferromagnetic particles, *IEEE Transactions on Magnetics*, Vol. 15, No.5, pp. 1209-1214

Kravchuk, V.P., Sheka, D.D. & Gaididei, Yu.B. (2007). Equilibrium magnetization structures in ferromagnetic nanorings, *J. Magnetism and Magnetic Materials*, Vol. 310, pp.116-125

Kravchuk, V.P., Sheka, D.D. (2007). Thin ferromagnetic nanodisk in out-of-plane magnetic field, *Solid State Physics*, Vol. 49, No 10, pp. 1834-1841 (in Russian)

Labunov, V. A., Shulitski, V. G. (2005). Nonrestricted Large Area of Vertically Aligned Carbon Nanotubes, *Proceedings of the III Russian–Japanese Seminar "Advanced Technological Processes, Materials, and Equipment for Production of Solid-State Electronics Elements and Nanomaterials MISiS–ULVAC"*, Moscow, Russia, April 11–12, 2005

Labunov, V. A., Shulitski, B. G. & Prudnikava, E. L. (2006). High-Efficiency Method of Selective CNT Arrays growth on the Metal/Dielectric/Semiconductor Substrates for FEDs Application, *Digest of Technical Papers of the International Symposium, Seminar and Exhibition (SID-2006)*, San Francisco, United States, June 4–9, 2006.

Li, De-Ch., Dai, L., Huang, Sh., Mau, A. W.H. & Wang, Zh. L. (2000). Structure and growth of aligned carbon nanotube films by pyrolysis. *Chem. Phys. Lett.*, Vol. 316, pp. 349-355

Lipson, H., Steeple, H. (1970). *Interpretation of X-ray Powder Diffraction Patterns*, Macmillan, London

Lipson, G., Steeple, H. (1972). *Interpretation of powder X-ray spectra*, Mir, Moscow (in Russian)

Pul, Ch. (2005). *Nanotechnologies*, Technosfera, Moscow (in Russian)

Ross, C.A., Hwang, M. & Shima, M. et al. (2002). Micromagnetic behavior of electrodeposited cylinder arrays, *Physical Review B*, Vol. 65, pp. 144417(1)-(8)

Shalayev, A.M. (1967). *Interaction of ionizing radiation with metals and alloys*, Atomizdat, Moscow (in Russian)

Sun, L., Banhart, F., Krasheninnikov, A., Rodriguez-Manzo, J.A., Terrones, M. & Ajayan, P. (2006). Carbon nanotubes as high-pressure cylinders and nano-extruders, *Science*, Vol. 312, pp. 1199-1205

Usov, N.A., Peschanyj, S.E. (1994). Vortex distribution of magnetization in thin ferromagnetic cylinder, *The Physics of Metals and Metallography*, Vol. 78, pp. 13-24 (in Russian)

Varnakov, S.N., Bartolomé, J., Sesé, J. Ovchinnikov, S.G., Komogortsev, S.V., Parshin A.S. & Bondarenko, G.V. (2007). Size effects and magnetization of (Fe/Si) n multilayer film nanostructures, *Physics of the Solid State*, Vol. 49, pp. 1470-1475

Vas'kovskiya, V.O., Patrin, G. S., Velikanov, D. A., Svalov, A. V., Savin, P. A., Yuvchenko, A. A. & Shchegoleva, N. N. (2007). Magnetism of Co layers in a Co/Si multilayer film, *Physics of the Solid State*, Vol. 49, pp.302-307

Vijayaraghavan, A., Kanzaki, K., Suzuki, S., Kobayashi, Y., Inokawa, H., Ono, Y., Kar, S. & Ajayan, P.M. (2005). Metal-semiconductor transition in single-walled carbon nanotubes induced by low-energy electron irradiation, *Nano Lett.*, Vol.5, pp. 1575-1578.

Wei, B., Shima, M., Pati, R., Nayak, S. K., Singh, D.J., Ma, R., Li, Y., Bando, Y., Nasu, S. & Ajayan, P. M. (2006). Room-Temperature Ferromagnetism in Doped Face-Centered Cubic Fe Nanoparticles, *Small*, Vol.2, pp. 804–809

Zhang, Y., Iijima, S. (2000). Microstructural evolution of single-walled carbon nanotubes under electron irradiation, *Philos. Mag. Lett.*, Vol.80, pp. 427-433

4

Characterizing Multi-Walled Carbon Nanotube Synthesis for Field Emission Applications

Benjamin L. Crossley[1], Nathan E. Glauvitz[1], Betty T. Quinton[2],
Ronald A. Coutu[1], Jr. and Peter J. Collins[1]
[1]*Air Force Institute of Technology*
[2]*Air Force Research Laboratory*
USA

1. Introduction

The first evidence of carbon nanotubes comes from transmission electron microscope (TEM) micrographs published by Radushkevich in 1952 in the Russian Journal of Physical Chemistry (Radushkevich, 1952). However, without the capability to reliably produce, characterize, or use these carbon nanotubes little was done besides document their existence until 1991. Iijima effectively rediscovered or introduced carbon nanotubes to the scientific community as a by-product of an electric arc discharge method of synthesizing C60 fullerenes (Iijima, 1991). Since Iijima published his seminal article in Nature identifying multi-walled carbon nanotubes (MWCNT) in 1991, followed by the more significant discovery of single-walled carbon nanotubes (SWCNT) in 1993, research into the properties and applications of carbon nanotubes has flourished. In 1995, only four years after carbon nanotubes were introduced to the scientific community by Iijima, de Heer *et al* demonstrated the field emission capabilities of carbon nanotubes with the fabrication of a small electron gun using multi-walled carbon nanotubes (de Heer, 1995). CNTs have many unique physical and electrical properties making them ideal candidates for field emission sources. There are many potential applications for CNT based field emission devices ranging from flat panel displays to charge neutralization for electric propulsion on satellites. This research effort focuses on the growth of multi-walled carbon nanotubes for field emission. The potential applications being considered require that the CNT synthesis method be compatible with conventional substrate materials, chiefly silicon, and micro-frabrication processes to allow integration with conventional electronic devices. Of the many documented CNT synthesis methods, Chemical vapor deposition (CVD) synthesis occurs at low enough temperatures to facilitate silicon substrates. For this particular study two CVD processes, thermal chemical vapor deposition (T-CVD) and microwave plasma enhanced chemical vapor deposition (MPE-CVD), are used to produce MWCNT films or carpets.

The CNT growth process begins with substrate preparation. Each silicon substrate is first coated with a barrier layer of titanium or chrome. This thin film acts as an adhesion layer and as a diffusion barrier. It also facilitates the cathode connection to the CNTs during field emission tests. CNT growth via any CVD method requires a catalyst for the carbon atoms to nucleate around. The transition metals Fe, Ni, Co, and alloys composed of one or more of these elements have proven effective as catalyst materials. For this effort, only

sputtered Ni and Fe are considered for catalyst layers. The catalyst layer must be granulated into nanoparticles to facilitate CNT synthesis. The catalyst is broken into nanoparticles by high temperature annealing treatment in the T-CVD process and by a hydrogen plasma treatment in the MPE-CVD process. Both methods are carried out *in situ* and are followed immediately by the CNT synthesis process. The catalyst material, barrier layer, granulation and synthesis processes are varied and the resulting CNTs are tested for field emission.

Characterizing each step of the synthesis process and comparing the field emission capabilities of the resulting CNTs as the parameters are changed leads to a fabrication process optimized for field emission applications. The first step in characterizing each synthesis process is using scanning electron microscopy (SEM) to determine the size and spacing of the granulated nanoparticles after the annealing or hydrogen plasma pretreatment of the catalyst material. After CNT synthesis, the carbon nanotubes are characterized physically via Raman spectroscopy and SEM imagery. Raman spectroscopy provides a method to determine the quality of the CNTs. SEM micrographs are used to determine CNT areal density, presence of amorphous carbon, and CNT physical characteristics such as diameter, length, and alignment.

Next the field emission properties of the CNTs are characterized to include turn-on electric field strength, maximum current density at a fixed electric field strength, current density versus electric field strength relationship, and Fowler-Nordheim plot. Field emission tests are performed in a diode configuration under high vacuum. The CNTs are grounded and act as the cathode. The anode is a copper collector plate located above the CNTs. The anode is swept across a positive voltage range. The field emission current is measured through the anode and the current density is calculated using the area of the sample under test. The current density vs. electric field relationship is collected as the anode voltage is swept across the voltage range and displayed in a corresponding graph. The Fowler-Nordheim plot is derived from the Fowler-Nordheim model for field emission from a flat metal plate in a vacuum and provides evidence the recorded current density is the result of field emission as opposed to thermionic emission.

All the CNT characterization and field emission data is collected and relationships between the quality of the CNT carpet growth and the resulting field emission properties are defined. Due to the results of another research effort that indicate a carbon buffer layer may facilitate CNT growth, the effects of an additional carbon buffer layer between the barrier and the catalyst on CNT quality and field emission is also reported. Finally, the barrier/catalyst combination that makes the best field emission source is determined.

2. Synthesis of carbon nanotubes

Since Iijima recognized carbon nanotubes as a by-product of the arc discharge synthesis of fullerenes, the method has been refined for the fabrication of carbon nanotubes. There are three main carbon nanotube fabrication categories that have since been developed:

- Arc discharge synthesis
- Laser ablation synthesis
- Thermal synthesis.

Efforts to produce higher quality, larger quantities, and improve control have yielded a myriad of fabrication methods within each of these categories. The basic physics involved in each fabrication method defines the category.

2.1 Arc discharge

Arc discharge synthesis was the first synthesis method used to reliably produce both MWCNTs and SWCNTs (Bhushan, 2007). Arc discharge or electric arc discharge synthesis is accomplished by generating plasma between two graphite electrodes using a low voltage, high current power supply. The process occurs in an inert atmosphere of He or Ar with pressures ranging from 100 to 1000 torr (O'Connell, 2006). The plasma contains vaporized carbon from the electrodes which then forms carbon nanotubes as it is deposited on the cathode and other areas of the reactor. SWCNTs can only be produced with the addition of a metal catalyst, usually added to the anode via a small hole where a catalyst/graphite powder mixture is placed. CNTs produced using the arc discharge synthesis method require purification before use due to carbon soot and fullerene by-products.

2.2 Laser ablation

Laser ablation or laser vaporization, as the name implies, uses a continuous-wave or pulsed-wave laser to vaporize a graphite or catalyst metal infused composite graphite target. The process occurs in a quartz furnace at 1200° C with a constant flow of inert gas, He or Ar (Tanaka et al, 1999). Vaporized graphite creates a plume with nanoparticles of the metal catalyst which facilitate the growth of SWCNTs. The plume containing the carbon nanotubes and various by-products is swept through the furnace by the inert gas and collected via condensation on a cooled copper (Cu) collector. Again, the presence of carbon by-products makes purification necessary.

2.3 Thermal synthesis

Thermal synthesis is a broad category of synthesis methods that rely on thermal energy to produce CNTs. Included in this category is plasma enhanced chemical vapor deposition (PE-CVD), which is a hybrid of plasma based and thermal based synthesis. Due to the wide variety of options and precise control offered by thermal synthesis, chiefly chemical vapor deposition methods; this category has received the most attention from researchers and has yielded the most promising results for controlled CNT fabrication.

CVD in its essence is passing a volatile precursor across a heated substrate to facilitate the deposition of thin films. CVD as a synthesis method could be considered a broad category by itself due to the vast number of variations of this simple process that are available. Two CVD methods, thermal CVD and microwave plasma enhanced CVD, are described below along with the detailed recipes used for CNT synthesis.

All CVD methods require a metal catalyst nanoparticle to facilitate the growth of CNTs. It has been shown that the diameter of the resulting CNTs corresponds to the diameter of the catalyst nanoparticle (Wong et al, 2005). The transition metals Fe, Ni, Co, and alloys composed of one or more of these transition metals are the primary catalyst materials. There are a number of methods for depositing the catalyst on the substrate many of which can be easily patterned making it possible to grow CNT arrays at desired locations. Common methods include soaking or spin coating the substrate with Fe, Co, or Mo nitrate oracetate salt and then drying the sample. Sputtering or evaporating a thin layer of catalyst material on the substrate and then subsequently breaking up the catalyst into nanoparticles using a pretreatment consisting either of a high temperature anneal or exposure to a H_2 plasma followed by CNT growth by introducing the carbon feedstock gas. This method has been used extensively and a correlation between the deposited layer thickness and resulting

CNT diameters, thicker layers result in larger diameters, has been documented (Garg et al, 2008; Terranova et al, 2006). The pretreatment time and power, however, must be determined for any given thickness. Contrary to the relationship between catalyst layer thickness and CNT diameter a longer pretreatment time does not always result in smaller particle sizes. Recently, Amana *et al*. reported that due to Ostwald ripening, pretreatment for too long will result in a lower CNT yield (Amama et al, 2009). Ostwald ripening is a phenomenon related to strain energy that results in small particles shrinking and disappearing over time while large particles increase in size. The Ostwald ripening effect was also documented in a study of MPE-CVD pretreatment of Ni catalyst where an increase in the H_2 plasma pretreatment from 5 to 7 minutes resulted in an increase in nanoparticle size from 25 nm to 40 nm (Crossley et al, 2010).

2.3.1 Thermal chemical vapor deposition

Thermal CVD is the simplest method of chemical vapor deposition. A T-CVD system, as shown in Fig. 1, consists of a furnace, feedstock gasses, and a vacuum pump. Resistive heaters or furnaces operate at temperatures ranging from 500° C to 1200° C in T-CVD systems. A substrate or target with Fe, Ni, Co, or an alloy of these three transition metals on the surface is placed in the furnace. An anneal in a non-volatile gas can be performed to form the necessary nanoparticles from thin films of the above mentioned catalyst materials. A carbon feedstock gas such as methane (CH_4) or carbon monoxide (CO) for SWCNT growth or acetylene (C_2H_2), ethylene (C_2H_4), or benzene (C_6H_6) for MWCNT is flowed across the target substrate (Geckelar & Rosenburg, 2006). The gas reacts with the catalytic nanoparticles to produce carbon nanotubes.

CVD synthesis occurs at relatively low temperatures that allow conventional substrates to be used, opening up opportunities for integration of CNTs with conventional electronics, optoelectronics, and other applications. With the proper growth conditions, pure CNTs can be produced with yield rates as high as 99% (O'Connell, 2006). Thus no purification or post processing is necessary unless the catalyst metal must be removed.

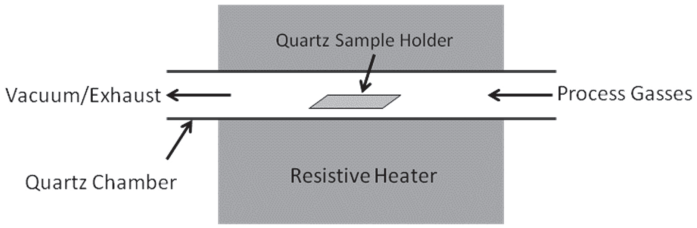

Fig. 1. Thermal chemical vapor deposition system.

2.3.2 T-CVD process

The quartz chamber and samples are prepared for growth by evacuating the chamber down to less than 10 mTorr for 15 minutes; after which an Ar+H_2 mix (95% + 5%) is flowed through the chamber to remove unwanted contaminates. The chamber is then evacuated again for an additional 15 minutes. Now that the samples and chamber are prepared, the Ar+H_2 gas mix is flowed while the chamber pressure is stabilized at approximately 90 Torr for the remainder of the entire process. The sample is anealed at 750° C to form iron nano-

islands necessary for CNT synthesis. Next, the growth phase begins with the introduction of the carbon feedstock, in this case an $Ar+C_2H_2$ (90% + 10%) mix, into the chamber. Growth times ranged from 2 - 20 minutes, resulting in MWCNTs measuring from 5 – 30 µm in length. The growth phase is followed by a short clean phase with $Ar+H_2$ flow while the chamber temperature is maintained at 750° C. This removes any weakly bonded residual surface carbon contamination from the sample. Finally, the chamber is cooled to room temperature over a 45-60 minute period with a constant flow of the $Ar+H_2$ mixture.

2.3.3 Plasma enhanced chemical vapor deposition

Plasma Enhanced Chemical Vapor Deposition uses energy from H_2 plasma generated from a DC, radio frequency (RF), or microwave power supply, to break down the carbon feedstock gas and facilitate CNT growth at lower temperatures and pressures than simple thermal CVD. Vertically aligned MWCNTs grown on a silicon substrate at temperatures below 330° C by microwave plasma enhanced CVD have been documented (Terranova et al, 2006). Typical substrate temperatures range from 400° C to 900° C. PE-CVD systems are capable of growing both SWCNTs and MWCNTs; more importantly these CNTs can be patterned, vertically aligned, and grown on a variety of substrates.

A MPE-CVD system is shown in Fig. 2. Microwave power, up to 1 kW, is transmitted from the generator through a wave guide to a microwave coupler that emits the radiation via the antenna into the CVD chamber. If conditions are correct, the resulting plasma will be centered over the substrate and allow for CNT growth over large areas, >10 cm^2. The CNT growth and plasma formation are dependent upon a number of controllable variables: the microwave power, chamber pressure, gas composition, gas flow, and substrate temperature. The ability to precisely control so many of the growth parameters is the key reason that PE-CVD has become the most researched synthesis method.

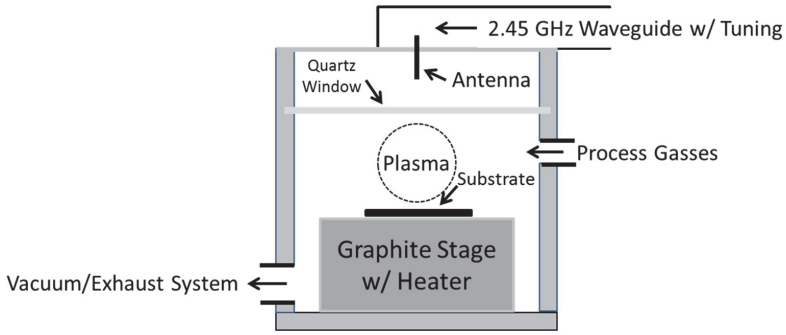

Fig. 2. Microwave plasma enhanced chemical vapor deposition system.

The pretreatment and growth process, as indicated above, are also dependent upon the gas composition, flow rate, and pressure. PE-CVD systems use relatively low pressures ranging from 10 – 300 Torr. Lower pressures reduce the presence of residual gasses allowing for more process control. Flow rates depend upon the chamber pressure and gas composition, but recipes reported in the literature range between 100 sccm and 400 sccm total gas flow rate. The gas flow rate and location of the gas inlet can affect the plasma location within the chamber, so an effective flow rate tends to be system specific.

Gas composition can also vary greatly from process to process. Typical pretreatment recipes consist of pure H_2, or some combination of H_2 and Ar. However, recent studies have indicated trace amounts, < 1%, of water (H_2O) or nitrogen (N_2) can significantly improve pretreatment effects resulting in greater density and smaller diameter catalyst particles (Amama et al, 2009; Chang et al, 2008). During growth, the gas composition can be even more complex consisting of a carbon feedstock such as, but not limited to, CO, CH_4, or C_2H_4, diluted in H_2, Ar, N_2, He, or some combination. Many different working compositions are possible, but the carbon feedstock gas should be greater than 6% of the gas mixture to provide enough carbon stock for CNT growth (Nessim et al, 2008). Gas compositions usually contain between 10% and 40% feedstock gas. Amorphous carbon, a common unwanted by-product, is more reactive than CNTs which has led to the use of trace amounts of oxidizers such as oxygen (O_2), H_2O, and hydroxide (OH) and the use of ethanol (C_2H_5OH) as a feedstock gas with very promising results (O'Connell, 2006).

2.3.4 MPE CVD process

The first step in the MWCNT growth process employed for the MPE-CVD system is removing as many potential contaminants as possible. After a substrate is loaded, the chamber is evacuated below 10 mTorr. Then the graphite stage and substrate are heated to 400° C in a hydrogen atmosphere of approximately 15 Torr. Once the system has reached a steady state, a catalyst pretreatment phase breaks up the catalyst layer into the nano-islands necessary for CNT growth. Pretreatment phase exposes the catalyst layer to a H_2 plasma induced by 400 W of microwave power for 5 minutes. The microwave power is terminated at the end of the pretreatment phase and the temperature increased to 650° C while maintaining the same gas flow and pressure. The growth phase occurs for 2 minutes at 650° C, with a hydrogen and methane (CH_4) mix, and 1000 W of microwave power. A 2 minute growth results in MWCNTs approximately 2 μm in length. The hydrogen flow and chamber pressure are maintained to facilitate cooling back to room temperature.

2.4 Carbon nanotube growth mechanisms

Carbon nanotube growth occurs in one of two places and via one of two methods at each location. The type of growth, gas phase or substrate, depends upon the location of the catalyst particle. When the catalyst and CNT formation occur in the chamber atmosphere, it is gas phase growth. Substrate growth is more common and the type of growth applied in this study. It occurs when the catalyst is deposited on the substrate. Both types of CNT growth rely on either surface carbon diffusion or bulk carbon diffusion as the actual growth mechanism.

Surface carbon diffusion is thought to be the growth mechanism for low temperature synthesis methods. The metal catalyst remains solid throughout the growth process and the "cracked" carbon from the feedstock gas diffuses around the particle surface. The carbon nanotube nucleates around the side of the metal particle. Since there is an abundant source of carbon from the feedstock gas, carbon continues to break down on the catalyst, diffuse around the particle, and facilitate nanotube growth (O'Connell, 2006).

In bulk carbon diffusion the catalyst can be either a solid or liquid nano-droplet depending on the transition metal and process temperature. The "cracked" carbon feedstock gas is dissolved by the catalyst until saturation at which point a carbon nanotube forms on the outer surface. This is a vapor – liquid – solid transition, where the feed stock gas is broken down into a hydrocarbon vapor, then forms a metal-carbon liquid when dissolved by the catalyst, and finally transitions to a crystalline carbon solid in the form of a nanotube.

Substrate growth through surface carbon diffusion is the most likely growth type and mechanism for CVD methods. This stems from the goals of most CVD growth methods which is to keep the temperature low to facilitate more substrate options and the use of deposited catalysts for controlled growth. Regardless of the growth mechanism substrate growth can occur at either end of the nanotube. If the stiction of the catalyst particle to the substrate is sufficiently large the particle will stay adhered to the substrate and the CNT will form by base growth. Tip growth occurs when the catalyst particle has insufficient stiction. In this case, the CNT adheres to the substrate and the catalyst forms the tip of the growing CNT. Fig. 3 illustrates both substrate growth conditions. While both base and tip growth can be observed with SWCNT and MWCNT fabrication, tip growth is dominant in MWCNTs and base growth is dominant in SWCNTs. This is largely due to the forces exercised on the catalyst nanoparticle at the time of growth; SWCNTs cannot overcome the stiction of the catalyst while typically MWCNTs can. Base growth in MWCNTs is often observed if the catalyst nanoparticles are patterned or formed as a function of deposition as these particles have a significantly higher stiction than nanoparticles formed by a granulation process. Tip growth is expected for all cases in this effort due to the catalyst pretreatment methods used to create the nanoparticle nucleation sites.

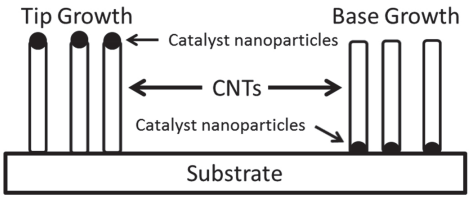

Fig. 3. Carbon nanotube tip and base growth from a substrate.

In theory, CNT growth should be capable of continuous growth as long as the feedstock carbon gas is supplied. In reality, there are a number of conditions that can occur and impede or prematurely terminate the growth process. Growth can only occur at the catalyst; base growth can be slowed and even stopped due to slow or loss of diffusion of carbon down to the nanoparticle. The carbon feedstock gas can supply an over abundance of carbon causing the deposition of amorphous carbon which then coats the catalyst and subsequently impedes and ultimately stops CNT growth. Occasionally, the catalyst can form graphitic shells instead of a carbon nanotube which will block access to more carbon ending the growth process. These are causes of poor growth conditions and can usually be avoided by appropriately adjusting the growth parameters.

3. Carbon nanotube field emission

CNTs have many unique properties ideal for field emission such as narrow diameters, high aspect ratios, high temperature stability, good conductivity, and structural strength. Carbon nanotubes make excellent electron emitters, not because of a low work function, but due to the extremely high local electric field that forms at the small diameter tips. Single walled CNTs have diameters from 0.6 nm to 1.4 nm and multi-walled CNTs can range from 12 nm to more than 100 nm in diameter. Both types of CNTs can range from tens of nanometers to microns and even millimeters in length resulting in incredible aspect ratios. The resulting

focus of the electric field at the tips of the CNTs is often referred to as the electric field enhancement factor. Previous research as summarized by Bonard *et al* has shown multi-walled CNTs to be more robust emitters than single walled CNTs (Bonard et al, 2001). Thus, only multi-walled CNTs are grown in this field emission effort. While the conductivity of single walled CNTs can be metallic or semiconducting depending on the nanotube structure, all multi-walled CNTs are considered metallic conductors because some of the nested nanotubes making up the multi-wall CNT will be metallic. This makes attempts to control or consider the chirality or type of CNTs grown unneccessary; another benefit of using MWCNTs for field emission instead of SWCNTs.

Potential commercial applications are the driving forces behind CNT field emission research. Different applications lead to different requirements, however, there are a few figures of merit that can be used to assess the relative quality of a CNT emitter. Current density is the value most often given when reporting results of CNT field emission research. Current density without knowing the associated electric field is of little use. The area used to calculate current density is also important. The current density from a single CNT can be remarkably high, basing the potential emission from an array of nanotubes on a single CNT has led to current density predictions as unfathomably high as 10^7 A/cm^2 (Zhu et al, 1999). But, due to screening effects, getting every CNT in a large area to emit electrons has proven to be a much more difficult task making current density measuremtents of individual CNTs useless in predicting the field emission from large areas of CNTs.

Other important parameters that aid in comparing results are the turn-on field, E_{to}; the electric field enhancement factor, β; and the total current density at a high electric field strength. The turn on field, much like diodes and transistors, is the field required to achieve a given current density. A current density of 1 μA/cm^2 is used to determine E_{to}. The enhancement factor is a measure of the increase in the localized electric field at the CNT emission site compared to the macro electric field of the system. An explanation and the method of calculating β from measured data is detailed below in Section 3.2.

CNT field emission is achieved with a diode configuration, shown in Fig. 4, where the CNTs act as the cathode emitters and a copper collector plate serves as the anode. The diode configuration is often used for its simplicity and to characterize the field emission properties of unpatterned CNT carpets. Field emission using this configuration often requires high voltages to establish the necessary electric fields, due to the relatively large distance, *d*, between cathode and anode.

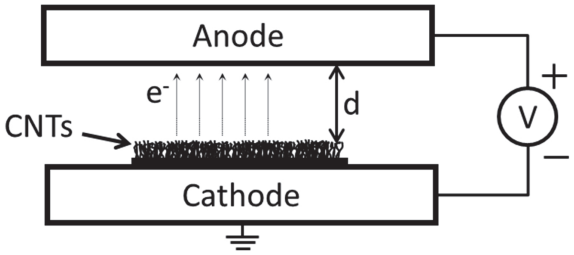

Fig. 4. Diode configured field emission schematic.

In his seminal publication, de Heer estimated a mere 0.1 % of the total CNTs were emitting (de Heer et al, 1995). They concluded only a tiny fraction of CNTs was sharp enough to be

efficient emitters. Since then, the phenomenon has been attributed to electrostatic screening effects (Leonard, 2008). As the number of CNTs in the emission area increases the space between them decreases limiting the electric field penetration around the CNTs. This limited field penetration, in turn, reduces the localized electric field enhancment significantly. 2D electrostatic simulations of field penetration between CNTs, visualized in Fig. 5, resulted in a 60% reduction in the localized electric field of nanotubes separated by 50 nm compared to a single CNT (Crossley et al, 2009). A uniform dense growth of CNTs effectively becomes the equivalent of a flat surface negating many of the advantages carbon nanotubes offer as a field emission source. Many optimized separation distances have been proposed for ideal CNT field emission ranging from a separation equal to the CNT height to a separation 5 times the CNT height, however it is widely accepted that some separation is necessary to reduce screening effects for efficient field emission (Nilsson et al, 2000; Smith & Silva, 2009; Suh et al, 2002). When unpatterned CNT carpets are grown, as is the case for this current study, the process of granulating the catalyst layer can be adjusted to affect the resulting nano-particles size and areal density. Both of which can have significant effects on field emission properties.

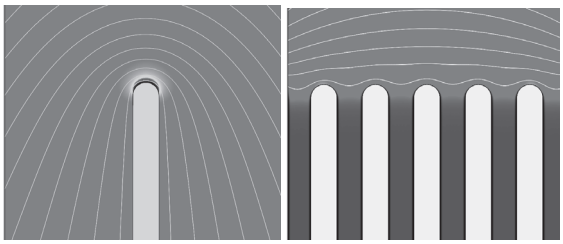

Fig. 5. Electrostatic field penetration for (a) Single CNT and (b) CNTs with 50 nm spacing.

3.2 Fowler-Nordheim plot and field enhancement

The Fowler-Nordheim (FN) model describes the current or current density obtained from electrons tunneling through a metal-vacuum potential barrier at 0 K. Other conditions for the Fowler-Nordheim model include tunneling from a flat metal surface; the metal or emitter is modeled as a free electron gas; and the potential barrier height is independent of the applied voltage (Leonard, 2008). Although the actual potential barrier is a combination of the image force potential and the external force potential; a simplifying triangular barrier, shown in Fig. 6, is adequate for the approximations used to derive the Fowler-Nordheim plot.

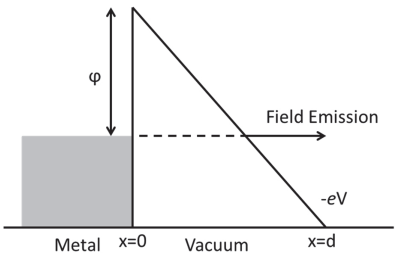

Fig. 6. Fowler-Nordheim triangular potential barrier approximation.

The simplified FN equation for current density from field emission is shown below.

$$J = \frac{aF^2}{t^2(y)\varphi} e^{\left(\frac{-b\varphi^{3/2}}{F}\upsilon(y)\right)} \tag{1}$$

Where current density, J, is in A/cm^2, a and b are constants of 1.54 x 10^{-6} AV^{-2}eV and 6.83 x 10^7 eV$^{-3/2}$Vcm^{-1}, $t(y)$ and $\upsilon(y)$ are tabulated functions, F is the applied electric field, and φ is the work function. The function $t(y)$ is close to and so often set equal to unity. The Nordheim function, $\upsilon(y)$, varies significantly; however, in what is considered an improper or gross simplification $\upsilon(y)$ is also commonly set to unity (Paulini et al, 1993).

The applied field is adjusted to account for the sharp tip of carbon nanotubes by including a field enhancement factor β. The field enhancement factor takes into account the microscopic or localized field at the emitter tip. Electric field lines concentrate at the area of small radius of curvature resulting in much higher localized field potentials. The applied field F, is considered a uniform field such as between two parallel plates and is defined defined as:

$$F = \frac{V}{d} \tag{2}$$

where V is the applied voltage and d is the separation distance as shown in Fig. 6. The inclusion of the enhancement factor gives the localized field shown in Equation (3).

$$F_{Local} = \frac{\beta V}{d} \tag{3}$$

Field enhancement for field emitting CNTs has a wide range of reported values from 1000 to 8000 and even as high as 26000 (Chhoker et al, 2007; Seelaboyina et al, 2008). Issues with determining field enhancement will be discussed below.

Including the simplifications mentioned above, the field enhancement factor, and converting from current density to current by including the total emission area the following FN current relationship is obtained:

$$I \approx \frac{aS\beta V^2}{d^2\varphi} e^{\left(\frac{-bd\varphi^{3/2}}{\beta V}\right)} \tag{4}$$

where S is the emitting surface area in cm^2. By dividing by V^2 and taking the natural log Equation (4) takes the form:

$$\ln\left(\frac{I}{V^2}\right) \approx -\frac{bd\varphi^{\frac{3}{2}}}{\beta V} + \ln\left(\frac{Sa\beta^2}{d^2\varphi}\right) \tag{5}$$

Equation (5) is easily recognized as the equation of a line for $\ln(I/V^2)$ as a function of $1/V$. Thus, FN field emission can be shown if a line results from plotting measurements of emission current as a function of the applied voltage in the form $\ln(I/V^2)$ versus $1/V$. This is often referred to as a Fowler-Nordheim plot--see Fig. 7 as an example--and is used to demonstrate field emission as opposed to thermionic emission.

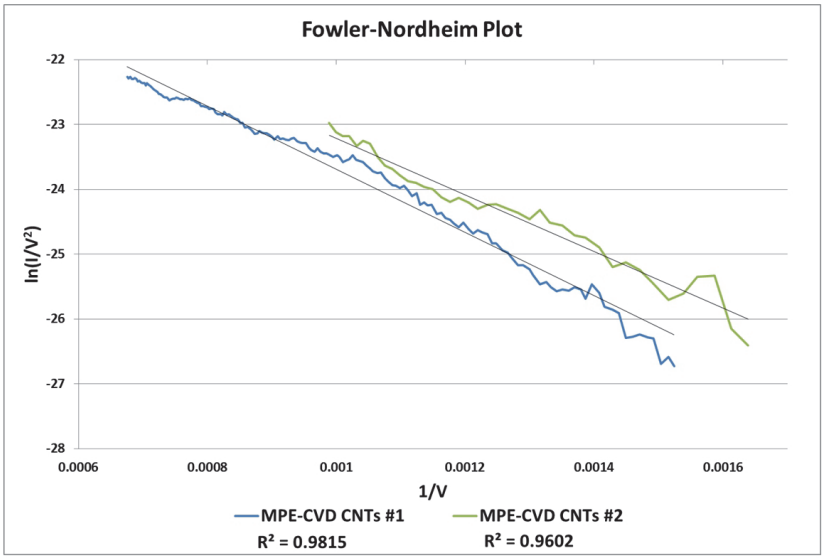

Fig. 7. Fowler-Nordheim Plot of MPE-CVD grown CNT samples with linear trendline.

The slope of the FN plot, given in Equation (6), can be used to determine the field enhancement factor, β. There is one caveat to this method of calculating the enhancement factor: the work function of the CNTs must also be known. There have been several methods employed to measure the work function of CNTs. Ultraviolet photoemission spectroscopy was used to measure the work function of SWCNT bundles at 4.8 eV, while other reported values have ranged from 4.3 eV to 5.7 eV (Suzuki et al, 2000). Xu *et al* used a transmission electron microscope with a unique tungsten needle sample holder to measure the work function of individual MWCNTs grown via MPE-CVD. The measurements indicated differences in the physical structure at the tube tips caused variations in the work functions from 4.51 eV to 4.78 eV (Xu et al, 2005). Only MWCNTs are considered in this study as well, so a work function of 4.65 eV is used in all calculations. Thus, for MWCNT samples #1 and #2 shown in Fig. 7 the resulting field enhancement factors are 2390 and 3460 respectively. A higher β is indicative of more efficient field emission. The increased localized electric field results in field emission at lower applied voltages.

$$m = \frac{bd\varphi^{\frac{3}{2}}}{\beta} \tag{6}$$

With all the assumptions and simplifications listed, it is obvious the FN model is not accurate for field emission from CNT tips. However, many experimental and theoretical efforts to develop an accurate model have yet to produce a conclusive result; while the FN relationship given above has been proven experimentally to be a good fit for I-V characteristics of CNT emitters of all kinds (Leonard, 2008). The sheer number of methods and processes used to achieve emission and the often seemingly contradictory results of different research efforts have made a functional model for electron emission from carbon nanotubes a difficult and elusive task.

4. Substrate preparation

A low resistivity Si substrate is prepared by first depositing a barrier layer and then the catalyst material. A low resistivity barrier layer provides an adhesion layer, electric contact, and diffusion barrier preventing the formation of silicides. Previous research has indicated that the barrier layer material can significantly affect the granulation process (Crossley et al, 2010). Thus, the barrier material and thickness can have significant effects on CNT growth. Studies show that barriers such as silicon dioxide and aluminum oxide produce high yields of CNTs, but due to their insulating nature they were not considered for use as barrier layers in this study. Instead conductive barriers of titanium and chromium that meet all the above barrier layer requirements were used. One set of wafers had a 20 nm layer of sputtered amorphous carbon deposited on the barrier layers to determine if the carbon layer would promote more uniform CNT growth and limit possible adverse effects caused by different thicknesses and types of barrier materials. Silicon wafers were sputtered with Ti or Cr barriers of 25 nm and 100 nm followed by iron catalyst layers of 2 nm and 10 nm. The 100 nm thick barriers were used to provide better electrical conduction for field emission and further micro-fabrication processes planned for future research. Two catalyst thicknesses were used because there is a strong correlation between the thickness of the catalyst layer, the size of the nano-particles after granulation, and the diameter of the resulting CNTs (Crossley et al, 2010; Wong et al, 2005). All wafers prepared as described above were used in the T-CVD process. CNTs grown by MPE-CVD used a 20 nm titanium barrier with a 10 nm nickel catalyst layer determined through a previous research effort (Crossley et al, 2010).

5. Results

Identical sets of samples cleaved from wafers prepared as described in Section 4 were processed in two separate manners. The first set of samples was only processed through the granulation of the catalyst, the anneal for T-CVD and the hydrogen plasma pretreatment for MPE-CVD described in Sections 2.3.2 and 2.3.4 respectively. The samples were cooled, removed, and the resulting nano-islands imaged by SEM. Due to the anneal temperature and required cooling time the nano-islands imaged will not be identical to the samples which proceed directly from anneal to CNT growth. However, analysing the size and areal density of the catalyst nano-islands provides a good indication of the resulting diameter and density of CNTs.

The second set of samples was processed through both granulation and growth phases of each CVD method. The resulting multi-walled CNT carpets were characterized by Raman spectroscopy and imaged by SEM to determine their quality. After this characterization of CNT quality, the field emission properties of the CNT carpets were measured in a custom built field emission test chamber. Correlating the field emission properties with CNT characterization provided insight into what properties of the CNT carpets are key to making the most efficient and effective field emission devices.

5.1 CNT characterization

Raman spectroscopy is the first step in characterizing the CNT carpet samples. Raman spectroscopy is a light scattering technique where an excitation laser is focused on the material of interest and the interaction of the light photon with the material results in a

small amount of light scattering at a slightly different frequency. This slight shift in frequency is called a Raman shift and provides a unique finger print of the material. Raman spectroscopy has been used for decades to identify carbon materials; and more recently has been shown capable of providing a myriad of information about carbon nanotubes such as doping, defects, diameter, chirality, and curvature (Dresselhaus et al, 2010).

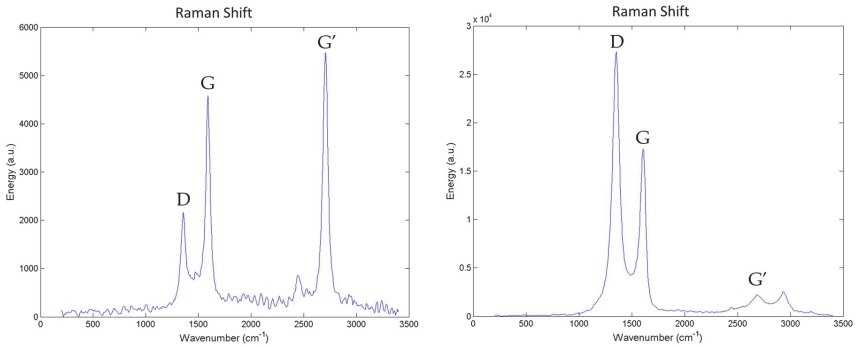

(a) (b)

Fig. 8. Raman shift with D, G, and G′ peaks labeled; (a) good quality or low defect MWCNTs grown by T-CVD and (b) poor quality or defect prone MWCNTs grown by MPE-CVD.

Raman spectroscopy was performed using a 532 nm green excitation laser. CNTs have a Raman shift with three primary peaks of interest, D-band, G-band, and G′-band, that can be used to determine the CNT carpet quality (DiLeo et al, 2007). The G-band peak is located at approximately 1580 cm^{-1} and is a result of ordered C--C bonds, indicative of defect free graphene and carbon nanotubes. The D-band, approximately 1350 cm^{-1}, is a disorder induced peak caused by defects in the carbon structure. A relative determination of CNT quality can be found by comparing the ratio of the D-band intensity (I_D) over the G-band intensity (I_G). The G′-band, approximately 2700 cm^{-1}, is dispersive but it is the result of a double resonance process and is also very prevalent in Raman shift data for graphene. DiLeo *et al* propose that in MWCNTs disorder or defects will reduce this double resonance process decreasing the G′ peak intensity providing a more accurate indication of CNT quality from the ratio of the G′ peak intensity ($I_{G'}$) over I_D (DiLeo et al, 2007). The ratio, $I_{G'}/I_G$, was also recorded to determine any correlation with field emission properties. Raman spectroscopy by itself does not provide a complete picture of carbon nanotube quality. SEM images are also necessary to determine the areal density, presence of amorphous carbon, and physical characteristics of the CNTs.

Fig. 8 (a) shows the Raman shift of T-CVD grown CNTs from 10 nm of Fe catalyst on a 100 nm Ti barrier with the D, G, and G′ peaks labelled. The I_D/I_G and $I_{G'}/I_D$ ratios, 0.47 and 2.52 respectively, represent the best quality MWCNTs of all the different catalyst/barrier combinations considered. Fig. 8 (b) is the Raman shift of MWCNTs grown by MPE-CVD and as is common for CNTs grown in this manner the D peak intensity is much greater than the G peak. The high D peak intensity is from first order dispersion effects caused by defects in the CNTs. These same defects prevent the secondary double resonance dispersion effects that cause the G′ peak, which is correspondingly low. With I_D/I_G and $I_{G'}/I_D$ ratios of

1.58 and 0.1, these MWCNTs are the poorest quality of all the different catalyst/barrier combinations considered for both growth methods, T-CVD and MPE-CVD. However, as mentioned above, Raman spectroscopy provides a relative measure of the quality of the CNTs, but SEM imagery is required to complete the characterization of the CNTs.

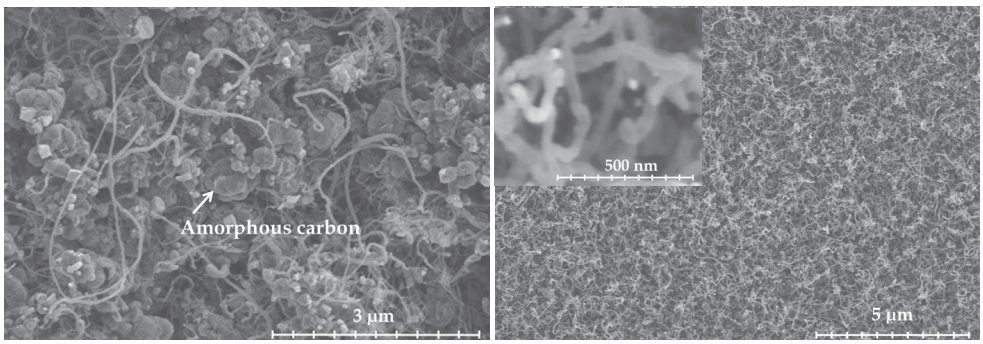

(a) (b)

Fig. 9. SEM micrograph of MWCNT growth by (a) T-CVD from 10 nm Fe catalyst on a 100 nm Ti barrier and (b) MPE-CVD from 10 nm Ni catalyst on a 20 nm Ti barrier.

SEM micrographs of the above two samples, the highest and lowest quality CNT samples per Raman spectroscopy, are shown in Fig. 9. The T-CVD sample in Fig 9 (a) has sparse CNT growth with large amounts of amorphous carbon deposited on the substrate surface. Also, the diameter of the CNTs varies widely from ~20 – 100 nm. While the CNTs that are present may have few defects, the overall quality of the CNT carpet is poor due to the low areal density, amorphous carbon deposits, and diverse diameters. The MPE-CVD sample in Fig. 9 (b) is a dense CNT carpet with no visible amorphous carbon deposits and much more uniform CNT diameters at approximately 50 nm and lengths of 1 – 2 μm. The 500 nm scale inset shows a close up view of the MWCNTs. The bright spots at the CNT ends are caused by catalyst particles that facilitated tip growth and now form a cap or plug at the CNT tip. These CNTs are riddled with growth defects, but the CNT carpet is much better quality than the sparse growth in Fig. 9 (a).

Table 1 below lists the Raman shift intensity ratios and SEM based qualitative assessment of CNT growth for all catalyst/barrier combinations. The chrome barrier of both 25 and 100 nm thicknesses performed poorly. Two combinations, Cr-100/Fe-2 nm and Cr-100/C-20/Fe-2 nm, did not grow CNTs. In Fig. 10 the SEM micrograph of the catalyst after the anneal and growth process revealed poor granulation with the expected nano-islands spanning hundreds of nanometers instead of the desired 25 - 50 nm. The Cr-100/Fe- 13 nm sample grew a sparse CNT carpet with CNT diameters in excess of 100 nm putting them closer to carbon fibers rather than carbon nanotubes. The addition of 20 nm of carbon improved the anneal process. The Cr-100/C-20/Fe-10 nm sample showed an improvement over the Cr-100/Fe-10 nm sample in both D/G and G′/D intensity ratios and the CNT diameters were reduced to less than 100 nm.

The 25 nm chrome samples had poor overall CNT carpets. The Cr-25/Fe-10 nm sample was almost identical to the Ti-100/Fe-10 nm sample shown in Fig. 9 (a), sparse growth of low defect CNTs with large deposits of amorphous carbon. The addition of 20 nm of carbon had little effect, improving the Raman shift intensity ratios slightly in the Cr-25/C-20/Fe-2 nm

case and making the D/G and G′/D intensity ratios slightly worse for the Cr-25/C-20/Fe-10 nm case. In both cases there was no appreciable difference in the SEM micrographs between the carbon and no carbon buffer layer combinations.

Barrier Layer Type & Thickness (nm)		Catalyst (nm)	D/G	G'/G	G'/D	Areal Density	Overall Growth
Chrome	100	13	0.69	0.82	1.20	Low	Poor
	100	2	No CNT Growth				
	25	10	0.48	1.11	2.31	Low	Poor
	25	2	0.88	0.72	0.82	Medium	Poor
Chrome & Carbon	100 & 20	10	0.60	1.09	1.82	Medium	Good
	100 & 20	2	No CNT Growth				
	25 & 20	10	0.54	1.19	2.19	Low	Poor
	25 & 20	2	0.81	0.89	1.10	Medium	Poor
Titanium	100	10	0.47	1.19	2.53	Low	Poor
	100	2	0.56	0.95	1.71	Low	Poor
	25	10	0.48	0.99	2.06	Medium	Good
	25	2	0.90	0.86	0.96	Medium	Good
Titanium & Carbon	25 & 20	10	0.48	1.09	2.26	Low	Poor
	25 & 20	2	1.09	0.69	0.63	Medium	Poor
MPE-CVD #1	Ti 20	Ni 10	1.26	0.20	0.16	High	Good
MPE-CVD #2	Ti 20	Ni 10	1.58	0.15	0.09	High	Good

Table 1. Raman shift peak intensity ratios and SEM based qualitative assessment of CNT growth for all catalyst/barrier combinations.

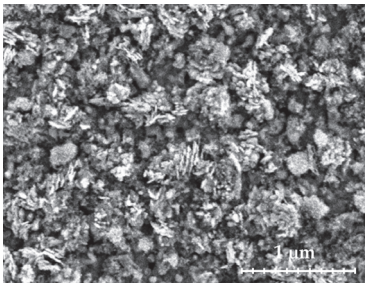

Fig. 10. SEM micrograph of the Cr-100 nm/Fe-20 nm sample after anneal and growth processes.

All titanium barrier combinations produced CNT carpets; although the 100 nm titanium samples had anneal issues that resulted in low defect CNTs with poor overall CNT carpet growth as discussed above and shown in Fig. 9 (a). The 25 nm titanium barrier proved most effective for growing MWCNT carpets. The Ti-25/Fe-10 nm sample, shown in Fig. 11, produced a medium to high density, low defect CNT carpet with little to no amorphous carbon and fairly uniform diameters. The Ti-25/Fe-2 nm carpet had a lower areal density with more CNT defects as evidenced by the Raman shift ratios. Adding the carbon thin film

had little effect on the Raman shift characteristics and made the overall CNT carpets less dense with more amorphous carbon deposits; for the Ti-25/C-20/Fe-10 nm case the amount of amorphous carbon was significantly increased.

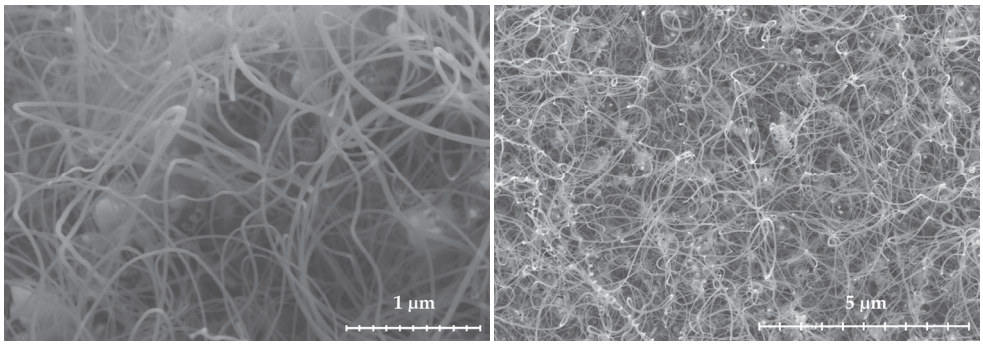

Fig. 11. SEM micrographs of CNT carpet grown by T-CVD on Ti-25/Fe-10 nm sample.

Using thermal CVD, the 25 nm Ti is clearly the most effective barrier with the Ti-25/Fe-10 nm sample producing the cleanest, defect free CNT carpets out of all the barrier/catalyst combinations. The 100 nm Ti and both Cr barrier thicknesses have different thermal properties that will require extensive study to determine an appropriate anneal process for each barrier/catalyst combination to achieve catalyst nano-islands conducive to CNT synthesis. The addition of sputtered carbon as a buffer between the barrier and the catalyst did not reduce the effects of changes to the barrier, but rather added another change to the thermal properties during the anneal process. The addition of carbon on the chrome barrier improved the anneal process and subsequent CNT growth. However, the carbon layer degraded the overall quality of the CNT carpet growth when added to the Ti barrier.

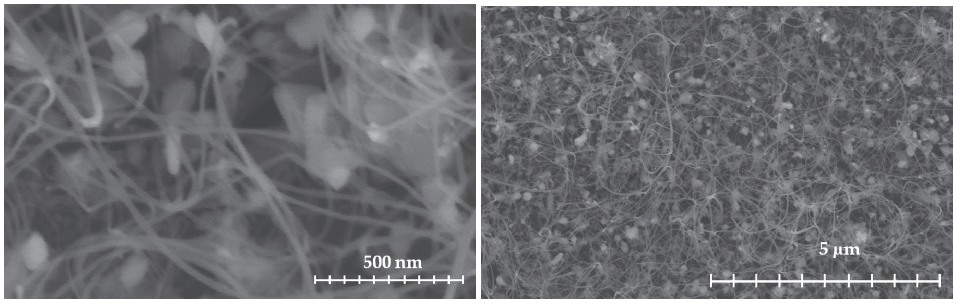

Fig. 12. SEM micrographs of CNTs grown by T-CVD for 2 minutes on Ti-25/Fe-10 nm.

The MPE-CVD grown CNT carpets are defect prone, but have no discernable amorphous carbon and have the highest areal density. MPE-CVD also offers precise control of the CNT growth conditions in the MPE-CVD process making it possible to achieve CNT carpets with uniform lengths. The CNT carpets of the two samples considered are approximately 2 μm in length. The short length is necessary for future integration into gated field emission devices. The T-CVD process does not have as much control over the growth conditions of the CNTs. Fig. 12 shows a Ti-25/Fe-10 nm sample with a CNT carpet from a 2 minute

growth. The CNTs are less dense than the 20 minute growth shown in Fig. 11, but still are in excess of 10 µm in length with many exceeding 15 µm. Integration of CNTs grown by T-CVD into gated field emission devices is unlikely until the lack of uniformity and control of the CNT lengths is resolved.

5.2 Field emission

After CNT characterization with Raman spectroscopy and SEM imagery, the CNT carpets were tested for field emission in a diode configured test chamber similar to the schematic shown in Fig. 4. The chamber is evacuated to less than $1x10^{-6}$ torr before field emission testing. The total current is measured on both the supply and ground side of the device under test to detect any potential leakage currents. A complete test run consists of increasing the extraction voltage in 10 V increments, equates to ~0.05 V/µm, from zero up to a preset voltage. At each voltage, after a pause for the system to reach a steady state, 100 measurements are taken at 0.01 s intervals and averaged before proceeding to the next voltage increment. After reaching the preset voltage, the process is reversed and measurements are taken as the voltage steps back down to zero. The initial preset voltage is 700 V or ~3 V/µm. However, if at any point during the test damage occurs to the CNTs, determined by visual arching at the CNT carpet or by sudden current spikes, the test is immediately terminated and the highest voltage measured is recorded as the maximum for the device under test. If a device is tested to 700 V with little or no field emission measured, the set voltage is increased for further testing. The system maximum voltage is 5000 V or ~23 V/µm. The highest electric field applied for this effort was 5.34 V/µm. Increasing the electric field strength too far damages the CNTs and causes permanent degradation in field emission performance.

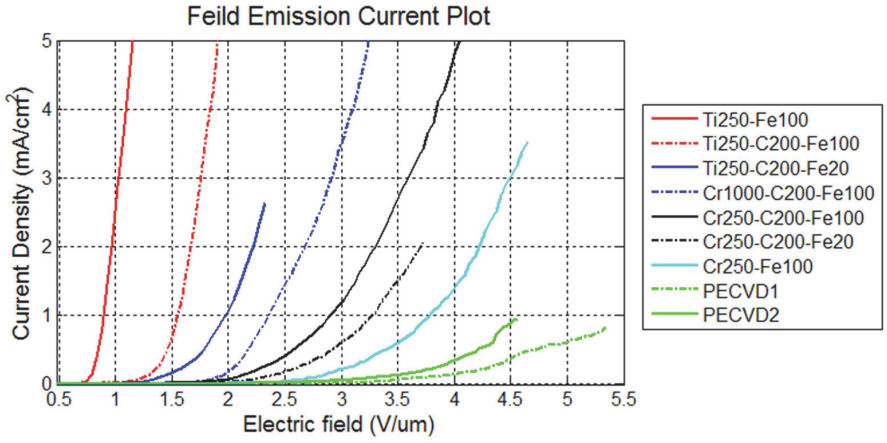

Fig. 13. Field emission current density plot for selected samples from Table 2.

The collected field emission data displayed in Fig. 13 visually identifies the strong field emission performers. The measurements are collected as current and matching voltage. The total field emission area is determined by measuring the sample area under the collector plate during the field emission tests using a set of precision callipers. The electric field is calculated simply by dividing the applied voltage by the distance, d, between the device

under test and the collector plate (d = 215 μm). The field emission vs electric field plot should be an exponentially increasing curve if field emission is the current source. All of the samples shown in Fig. 13 demonstrate this exponential trait. The Ti-25/Fe-10 nm sample identified in Section 5.1 as the best overall CNT carpet sample clearly stands out as the best performer. The field emission test results are used to determine field emission properties or metrics for each sample. The turn-on electric field is the electric field strength required for a sample to reach a current density of 1 μA/cm^2. As described above, the maximum current density achieved without damaging the CNT carpet and the corresponding electric field was also collected. The raw current vs voltage data was used to create Fowler-Nordheim Plots, $\ln(I/V^2)$ versus $1/V$, for each sample as derived in Section 3.2. A linear Fowler-Nordheim plot is indicative of field emission. The Fowler-Nordheim plots for selected samples are contained in Fig. 14. Least squares linear regression was used to determine the slope, m, of the linear plots so the field enhancement factor, β, could be calculated using (7).

$$\beta = \frac{bd\phi^{\frac{3}{2}}}{m} \tag{7}$$

Where b = 6.83 x 10^7 eV$^{-3/2}$Vcm^{-1}, d = 2.15x10^{-4} cm, and φ = 4.65 eV. All the field emission metrics are listed for each processed barrier/catalyst combination in Table 2.

As mentioned above, the Ti-25/Fe-10 nm sample immediately jumps out as the best field emission source with the highest β, lowest turn-on electric field, and the highest total current density with the lowest electric field. Excellent field emission from the CNT carpet with the best qualities is a reassuring result. However, the improvement in field emission from adding the carbon buffer to the chrome barrier is astounding. The Cr-100/Fe-13 nm sample had extremely large diameter CNTs to the point of being considered carbon fiber more than carbon nanotubes. The field emission from these samples was also poor with a total current density of only 0.13 mA/cm^2.

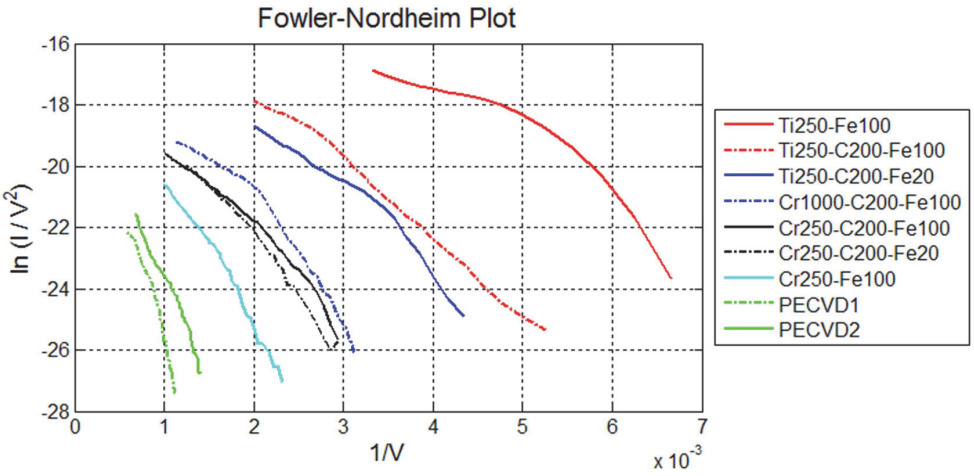

Fig. 14. Fowler-Nordheim plot for selected samples from Table 2.

The Cr-100/C-20/Fe-10 nm sample on the other hand demonstrated a 30% reduction in turn-on voltage and a 100x increase in maximum current density. The same is true for the 25 nm chrome barrier layers. While the addition of the carbon buffer did not have a significant effect on the characteristics of the CNT carpets showing moderate improvement in the Raman shift for the Cr-25/C-20/Fe-2 nm sample and a moderate degradation for the other sample, the improvements to the field emission properties are striking. Both samples saw a 20% reduction in turn-on electric field strength, 2.5x and 6x increases in maximum current density, and corresponding increases in the field enhancement factor. The carbon buffer layer clearly has a positive interaction with the chrome barrier that enhances field emission.

Much like the results on the CNT characteristics, the carbon buffer on the 25 nm titanium barrier layer degraded the field emission properties to include lower field enhancement factors, higher turn-on electric fields, and lower maximum current densities. The maximum current density between the Ti-25/Fe-2 nm and Ti-25/C-20/Fe-2 nm samples decreases from 9.25 mA/cm^2 to 2.63 mA/cm^2 at essentially the same electric field strength. As clearly as the carbon buffer improved the field emission properties of the chrome barrier samples, it degraded the field emission properties of the titanium barrier samples.

Barrier Layer Type & Thickness (nm)		Catalyst (nm)	Beta	Turn-on E-field (V/μm)	Max Current Density (mA/cm^2)	Max E-field (V/μm)
Chrome	100	13	4660	2.09	0.13	3.72
	100	2	No CNT Growth			
	25	10	3110	2	3.52	4.65
	25	2	3630	1.95	0.34	4.19
Chrome & Carbon	100 & 20	10	4870	1.49	12.30	4.14
	100 & 20	2	No CNT Growth			
	25 & 20	10	5430	1.58	8.71	4.65
	25 & 20	2	4150	1.58	2.05	3.72
Titanium	100	10	6780	1.63	0.30	3.26
	100	2	3130	2.23	3.99	5.12
	25	10	8640	0.70	13.34	1.40
	25	2	8020	0.93	9.25	2.37
Titanium & Carbon	25 & 20	10	6070	0.88	12.94	2.33
	25 & 20	2	6130	1.07	2.63	2.33
MPE-CVD #1	Ti 20	Ni 10	2390	2.78	0.82	5.34
MPE-CVD #2	Ti 20	Ni 10	3460	2.22	0.95	4.56

Table 2. Field emission data for all combinations of barrier/catalyst samples.

Field emission from the MPE-CVD samples does not compare well with the T-CVD samples. The MPE-CVD carbon nanotubes have a much higher areal density and are much shorter in length at 2 μm. Both of these factors increase screening effects reducing field emission. The controlled growth using MPE-CVD makes patterned and gated or triode configured field emission devices more feasible.

6. Conclusion

In this phase of a continuing research effort to develop CNT field emission devices, a study of the effects of Ni and Fe catalyst layers deposited on Ti and Cr diffusion barriers has been used to determine an optimum combination for effective field emission from CNTs produced via both T-CVD and MPE-CVD. As expected, thicker catalyst layers resulted in larger nano-particles after the anneal or pretreatment granulation process causing more amorphous carbon deposits as shown in SEM images. Raman spectroscopy was used to characterize the quality of the CNTs. The G'/G ratio was calculated as another possible metric that could relate Raman shift characteristics to field emission. Since no relationship was evident and there is no evidence that the G'/G ratio is helpful in determining CNT quality, the G'/G ratio was determined to be an unnecessary calculation for future endeavors.

This study showed that sputtered Fe catalyst films on thin barrier layers (25 nm) of Ti facilitate excellent CNT growth by T-CVD with superior CNT field emission properties, specifically, lower turn-on electric fields and much higher field emission current densities than any other combination of barrier and catalyst via either growth method. There was not a clear correlation between CNT quality as determined by Raman spectroscopy and CNT field emission. This is attributed to the effects CNT areal density has on field emission. When the areal density is extremely high, such as with the CNT carpets grown by MPE-CVD, screening effects impede field emission. When the CNT growth is sparse, the lack of field emission sources or CNTs impedes field emission. The best field emission was achieved by the Ti-25/Fe-100 sample which had both good Raman shift characteristics and qualitatively good or medium areal density.

The addition of a carbon buffer layer between chrome diffusion barriers and the catalyst layer showed some potential for improving the quality of CNT growth and increased field emission dramatically. The lack of CNT synthesis with thicker barrier layers was attributed to poor or at least different thermal properties of the thicker metallic barrier which impeded the granulation process resulting in incomplete separation of the catalyst nanoparticles shown through SEM micrographs. The lack of good quality CNT carpet growth from any of the Cr barrier samples, which are often used successfully in CNT synthesis, is a result of the significant impact different barrier layers have on the granulation and growth processes. Any changes to the barrier or catalyst will require the development of a specific growth recipe.

While the most successful field emission results were achieved with samples produced by T-CVD, the MPE-CVD process allows better control and uniformity of the CNT lengths. The shorter length and high areal density of the MPE-CVD CNTs increasing screening effects is the primary cause of the lower field emission performance. However, this same control makes integration into electronic devices possible where the less controllable growth of the T-CVD process would potentially fail. Using the controllability of the MPE-CVD process gated CNT arrays are being fabricated to achieve field emission at lower voltages.

Future research will focus on the interactions of the carbon buffer layer with the catalyst and barrier to determine the mechanism or process that drives the field emission improvements seen with the chrome barrier samples but not the titanium barrier samples. The T-CVD process will be refined to allow more control over the length and areal density of the CNTs for integration into gated devices.

7. Acknowledgment

The authors would like to thank the Air Force Research Laboratory (AFRL) Propulsion Directorate for the use of their resources and facilities, especially the MPE-CVD and T-CVD systems. The authors appreciate the technical support and access to cleanroom equipment provided by the AFRL Sensors branch RYD. As always the research would not be possible without the dedicated work of AFIT's own cleanroom support, Rick Patton and Rich Johnston.

Disclaimer: The views expressed in this article are those of the authors and do not reflect the official policy or position of the United States Air Force, Department of Defense, or the U.S. Government.

8. References

Amama, P., Pint, C., McJilton, L., Kim, S., Stach, E., Murray, T., et al. (2009). Role of water in super growth of single-walled carbon nanotube carpets. *Nano Letters*, Vol. 9, No. 1, pp. 44-49.

Bhushan, B. (Ed.). (2007). Springer Handbook of Nanotechnology, Springer, ISBN 3-540-01218-4, Verlag, Germany.

Bonard, J., Kind, H., Stöckli, T., & Nilsson, L. (2001). Field emission from carbon nanotubes: The first five years. *Solid-State Electronics*, Vol. 45, No. 6, pp. 893-914.

Chang, S., Lin, T., Li, T., & Huang, S. (2008). Carbon nanotubes grown from nickel catalyst pretreated with H2/N2 plasma. *Microelectronics Journal*, Vol. 39, No. 12, pp. 1572-1575.

Chhoker, S., Srivastava, S., & Vankar, V. (2007). Field emission properties of carbon nanostructures: A review, *Proceedings of International Workshop on Physics of Semiconductor Devices*, ISBN 978-1-4244-1728-5, Mumbai, December 2007.

Crossley, B., Kossler, M., Coutu Jr., R., Starman, L., & Collins, P., (2010). Effects of hydrogen pretreatment on physical-vapor-deposited nickel catalyst for multi-walled carbon nanotube growth. *Journal of Nanophotonics*, Vol. 4, No. 1, pp. 049502-049502-6.

Crossley, B., Kossler, M., Starman, L., Coutu Jr., R., & Collins, P., (2009). Optimization of carbon nanotube field emission arrays. *Proceedings of COMSOL Conf.,* Vol. 6288, Boston, MA, October 2009.

DiLeo, R., Landi, B., & Raffaelle, R., (2007). Purity assessment of multiwalled carbon nanotubes by Raman spectroscopy. *Journal of Applied Physics*, Vol. 101, No. 6, pp. 064307-064307-6.

Dresselhaus, M. S., Ado J., Hofman, M., Dresselhaus G., & Saito, R., (2010). Perspectives on Carbon Nanotubes and Graphene Raman Spectroscopy, *Nano Letters*, Vol. 10, No. 3, pp. 751-758.

Fursey, G. (2005). *Field Emission in Vacuum Microelectronics*. Kluwer Academic/Plenum Publishers, ISBN 0-3064-7450-6, New York.

Garg, R., Kim, S., Hash, D., Gore, J., & Fisher, T. (2008). Effects of feed gas composition and catalyst thickness on carbon nanotube and nanofiber synthesis by plasma enhanced chemical vapor deposition. *Journal of Nanoscience and Nanotechnology*, Vol. 8, No. 6, pp. 3068-3076.

Geckelar K., & Rosenburg E. (2006). *Functional Nanomaterials*. American Scientific Publishers, ISBN 1-5888-3067-5, California.

Heer, W. A. d., Chatelain, A., & Ugarte, D. (1995). A carbon nanotube field-emission electron source. *Science*, Vol. 270, No. 5239, pp. 1179-1180.

Iijima, S., (1991). Helical Microtubules of Graphitic Carbon, Nature, Vol 354, November 1991, pp. 56-58, ISSN 0028-0836.

Leonard, F. (2008). *The Physics of Carbon Nanotube Devices*. William Andrew, ISBN 978-0-8155-1573-9, Norwich, NY.

Nessim, G., Hart, A., Kim, J., Acquaviva, D., Oh, j., Morgan, C., et al. (2008). Tuning of vertically-aligned carbon nanotube diameter and areal density through catalyst pre-treatment. *Nano Letters*, Vol. 8, No. 11, pp. 3587-3593.

Nilsson, L., Groening, O., Emmenegger, C., Kuettel, O., Schaller, E., Schlapbach, L., et al. (2000). Scanning field emission from patterned carbon nanotube films. *Applied Physics Letters*, Vol. 76, No. 15, pp. 2071-2073.

O'Connell, M. (2006). *Carbon Nanotubes: Properties and Applications*. CRC Press, ISBN 0-8493-2748-2, Boca Raton, FL.

Paulini, J., Klein, T., & Simon, G. (1993). Thermo-field Emission and the Nottingham Effect. *Journal of Physics D: Applied Physics*, Vol. 26, No. 8, 1310-1315.

Radushkevich, L., Lukyanovich, V. (1952). O structure ugleroda, obrazujucegosja pri termiceskom razlozenii okisi ugleroda na zeleznom kontakte. *Zurn. Fisic. Chim.*, Vol. 26, pp. 88-95, Available from:<http://carbon.phys.msu.ru/publications/1952-radushkevich-lukyanovich.pdf >.

Seelaboyina, R., Boddepalli, S., Noh, K., Jeon, M., & Choi, W. (2008). Enhanced field emission from aligned multistage carbon nanotube emitter arrays. *Nanotechnology*, Vol. 19, No. 6, pp. 65605-65609.

Smith, R., & Silva, S. (2009). Maximizing the electron field emission performance of carbon nanotube arrays. *Applied Physics Letters*, Vol. 94, No. 13, pp. 133104-133104-3.

Suh, J., Jeong, K., Lee, J., & Han, H. (2002). Study of the field-screening effect of highly ordered carbon nanotube arrays. *Applied Physics Letters*, Vol. 80, No. 13, pp. 2392-2394.

Suzuki, S., Bower, C., Watanabe, Y., & Zhou, O. (2000). Work functions and valence band states of pristine and cs-intercalated single-walled carbon nanotube bundles. *Applied Physics Letters*, Vol. 76, No. 26, pp. 4007-4009.

Tanaka, K., Yamabe, T., & Fukui, K. (1999). *The Science and Technology of Carbon Nanotubes*. Elsevier, ISBN 0-0804-2696-4, New York, NY.

Terranova, M., Sessa, V., & Rossi, M. (2006). The world of carbon nanotubes: An overview of CVD growth methodologies. *Chemical Vapor Deposition*, Vol. 12, No. 6, pp. 315-325.

Wong, Y., Kang, W., Davidson, J., Hofmeister, W., Wei, S., & Huang, J. (2005). Device characterization of carbon nanotubes field emitters in diode and triode configurations. *Diamond & Related Materials*, Vol. 14, No. 3, pp. 697-703.

Xu, Z., Bai, X., Wang, E., & Wang, Z. (2005). Field emission of individual carbon nanotube with in situ tip image and real work function. *Applied Physics Letters*, Vol. 87, No. 16, pp. 163106-163106-3.

Zhu, W., Bower, C., Zhou, O., Kochanski, G., & Jun, S. (1999). Large current density from carbon nanotube field emitters. *Applied Physics Letters*, Vol. 75, No. 6, pp. 873-875.

5

Microwave-Assisted Preparation of Carbon Nanotubes with Versatile Functionality

Yong-Chien Ling and Archana Deokar
Department of Chemistry, National Tsing Hua University
Taiwan

1. Introduction

Since the accidental discovery of carbon nanotubes (CNTs) during the synthesis of fullerene by Iijima (Iijima 1991), tremendous research has been done on CNTs. CNTs are under intense investigation owing to their spectacular mechanical and electrical properties (Vazquez, Georgakilas, and Prato 2002). Many ways are currently available for the production of CNTs, which include arc-discharge (Journet et al. 1997), pulsed laser vaporization (Kokai et al. 2000), chemical vapor deposition (Campos-Delgado et al. 2010). However, commercial applications of CNTs have been inhibited by the lack of large-scale production of purified CNTs. Moreover, the intrinsic Vander Waals attraction of CNTs towards each other leads easily to entangle agglomerates, which results in their insolubility in most of organic and aqueous solvents.

One of the most powerful approaches to improve CNT solubility is the covalent functionalization of their side walls and tips (Tasis et al. 2006). A wide variety of reactions have been described, most of them employing the conventional chemical techniques, such as refluxing and/or sonication in organic solvents or mineral acids, often making use of high temperature and/or pressure (Hu et al. 2003), long reaction time (Holzinger et al. 2003), or highly reactive species (Brunetti et al. 2007). With the aim of optimizing a multiple funcitonalization approach, many research groups have developed new synthetic strategies to produce multifunctional CNTs avoiding the use of long reaction time, toxic solvent, and extreme condition. Vazquez and coworkers described that 1,3-dipolar cycloaddition of azomethineylides can readily occur on CNTs (Brunetti et al. 2007). However, a severe limitation of this process is the great amount of the DMF and the lengthy time (five days) needed to complete this reaction.

Recently, a microwave-assisted synthesis is enabling technology that has been extensively used in organic synthesis (Dallinger and Kappe 2007; Brunetti et al. 2007; Nuchter et al. 2004). Microwave-assisted modification of CNTs is non-invasive, simple, fast, environmentally friendly, and clean method as compared to traditional methods. Usually, the use of the microwave facilitates and accelerates reactions, often improving relative yields. In case of microwave-assisted functionalization of CNTs, microwave irradiation of CNT reduces the reaction time and gives rise to products with higher degrees of functionalization than those obtained by the conventional thermal methods (Vazquez and Prato 2009). Interestingly, Liu and coworkers (Liu, Zubiri et al. 2007) suggest a competitive effect of microwave irradiation that both promotes functionalization and removes some

functional groups that are initially present. On the other hand, Vazquez and coworkers show that a solvent-free technique combined with microwave irradiation produces functionalized nanotubes in just 1 h of reaction, paving the way to large scale production of functionalization (Brunetti et al. 2007).

2. Carbon nanotube and microwave interaction

CNT exhibit impressive potentials in many applications such as electrical interconnects, (Kreupl et al. 2004; Li et al. 2003) thermal interface materials, (Biercuk et al. 2002; Liu et al. 2004) high-performance fibers, (Koziol et al. 2007; Vigolo et al. 2000), environmental monitoring (Lee, Sun, and Ling 2009; Lee et al. 2010), and health & biotechnology (Ghule et al. 2007) so on. Although the theoretical intrinsic electrical, thermal, and mechanical properties of an individual CNT are extraordinary, synthesized CNTs in reality are far from being defect-free. Lin and coworkers developed an ultrafast microwave annealing process to reduce the defect density in vertically aligned CNTs. The as-annealed CNTs showed dramatic improvement in thermal stability, mechanical properties, and electrical conductivity (Lin et al. 2010). Thus, microwave opens the door for the defect-free modification or functionalization of CNTs for various possible applications mentioned above.

2.1 Mechanism of the carbon nanotube-microwave interaction

Commercially available CNTs contains different impurities such as amorphous carbon and metallic nanoparticles; which are factors to be considered in order to explain the strong microwave absorptions observed. Microwave irradiation may cause heating by two main factors: (1) dipolar polarization and (2) conduction (joule heating) (MacKenzie, Dunens, and Harris 2009). The presence of impurities that are electrically conductive, such as metal or carbon, could support the mechanism based on conduction heating. According to this mechanism, microwaves do not heat the material immediately; rather motion of the electrons is induced by electric field, causing sample heating. In this way, Joule heating induced by the metal catalyst particles should generate localized superheating (Wadhawan, Garrett, and Perez 2003). The behavior of amorphous carbon and graphite impurities under the microwave irradiation is less controversial; extended π-system permits conductivity (and thus joule heating) to enable localized heating. However, another potential source of localized superheating should be considered, namely, the generation of gas plasma from absorbed gases (particularly H_2) in CNTs, under the microwave irradiation, which has been reported in some cases (Imholt et al. 2003). A simple model was proposed by Ye and coworkers (Ye et al. 2006), to explain microwave-induced heating of CNTs, through transformation of electromagnetic energy into mechanical vibrations. Within this model, CNTs subjected to microwave irradiation undergoes ultraheating due to a transverse parametric resonance, which arises from the polarization of CNTs in the microwave field. For impure CNTs, Joule heating occurs because imperfections and impurities damp the transverse vibration mode. The same authors claim that, in a dense and viscous local environment, CNTs will not vibrate. Therefore, there is neither transverse resonance not Joule effect thus no heating, which would explain the different results of absorption, in the presence of solvents or under dry conditions, observed by other groups (Vazquez and Prato 2009). Fig. 1 represents schematic of CNTs interaction with microwaves (Lobach et al. 2002; Liu, Gao et al. 2007; Lee et al. 2010; Chajara et al. 2010).

Various methods for purifying CNTs have been reported, including chemical oxidation, thermal oxidation, filtration (Bandow et al. 1997), and chromatography. These methods can be divided into two groups, namely destructive and non-destructive; both are time-consuming and have high thermal budgets. Microwave-assisted heating has been proven to be an efficient method for the purification of CNTs in every aspect.

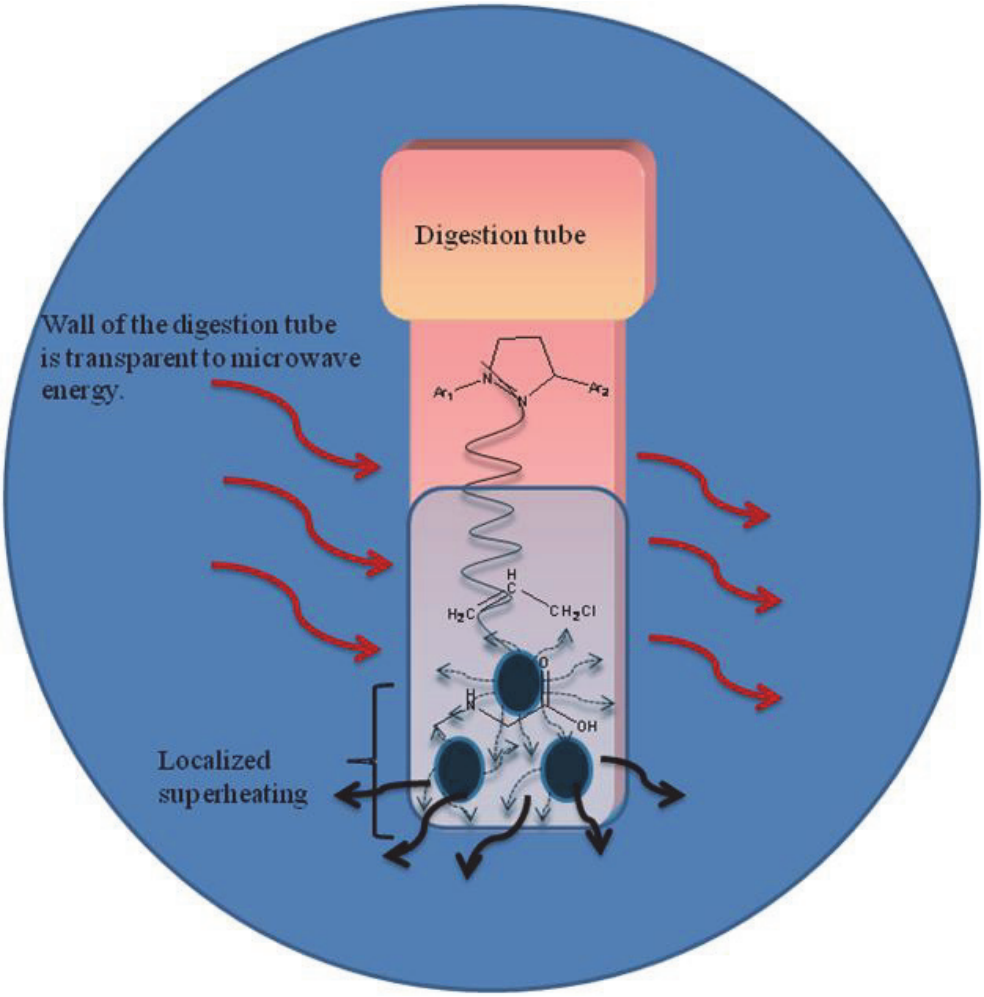

Fig. 1. Schematic of sample heating by microwave

2.2 Microwave-assisted purification of carbon nanotubes

Microwave-assisted purification demonstrates significant efficiency improvements over traditional acid reflux with minimal carbon nanotube damage under optimized conditions (MacKenzie, Dunens, and Harris 2009). Table 1 represents the comparison of solution based traditional purification processes with microwave based purification method.

Method	Reagents used (Vol.)	Temp.	Time period	References
Chemical method (Refluxing)	3 M HNO_3 (60 ml)	120°C	16 hr	(Lobach et al. 2002)
Thermal oxidation	O_2 or Air	500-800°C	40-60 min	(Liu, Gao et al. 2007)
Microwave-assisted purification (With solvent)	15.8 M HNO_3 (5 ml)	120-180°C	30 min	(Lee et al. 2010)
Solvent free microwave-assisted purification	null	100-150°C	5 min	(Chajara et al. 2010)

Table 1. Comparison of the traditional purification methods and the microwave-assisted purification method.

Microwave based method consumes less time, with high sample throughput, small reagent volume, reliable control over amenable temperature and pressure than traditional purification methods. The dispersion of CNTs is the most important issue for CNTs applications. Fig. 2 demonstrates the effect of microwave temperature on the dispersion of the CNTs, we can clearly observe pristine and 100°C heated CNTs appears to settle at the bottom (Fig. 2a and 2b); Whereas, 10 and 30 min, 140°C microwave heated CNTs are well dispersed in the water (Fig. 2c and 2d).

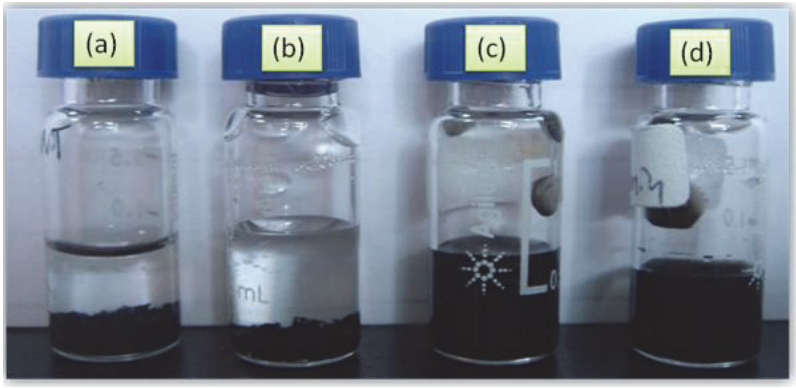

Fig. 2. Microwave-assisted acidification of CNTs: effect of temperature on dispersion of CNTs (a) pristine CNTs, (b) microwave treated CNTs at 100°C for 30 min, (c) at 140°C for 10 min, (d) for 30 min.

Ko.et.al.(Ko et al. 2004) carried out the microwave-assisted purification of multiwall carbon nanotubes (MWNTs) in a closed vessel at 180°C for 30 min in the presence of 20 % hydrogen peroxide and compared efficiency with nitric acid (Fig. 3). This figure indicates that the oxidation power of the reagent is the influencing parameter for microwave-assisted

purification, especially at higher temperatures. Fig. 3 demonstrates that hydrogen peroxide is a more favourable purification agent than the nitric acid. This observation implies that the oxidizing power of hydrogen peroxide toward the decomposition of such defects as amorphous carbon and metal particles is higher than that of nitric acid over a range of temperatures. The gravimetric results demonstrate that the former exhibits better efficiency for removing defects than the latter one. Fig. 4 displays the effect of the purification temperature on the weight loss and plots of derivative thermogravimetric analysis curves as a function of temperature. We can observe that prior to purification the samples undergo two significant weight losses at 195 and 550°C; whereas the samples after purification with hydrogen peroxide exhibit only one significant weight loss temperature. The derivative thermogravimetry curves after purification at 140 and 180°C each display a sharp peak near 520°C. In contrast, after purification at 200°C a broad peak appears in the range 525–575°C. Fig. 4(a) illustrates the first weight loss arises from the combustion of carbonaceous defects in air at ca. 195°C. As the temperature of the thermogravimetric analysis system exceeds 400°C, the nanotube samples begin to decompose in the air and do not fully evaporate until the temperature reaches 650°C. Obviously, the broad peak in the derivative thermogravimetry plot in Fig. 4(d) originates from partial and unsymmetrical decomposition of the nanotubes in the presence of hydrogen peroxide when microwave heating at 200°C.

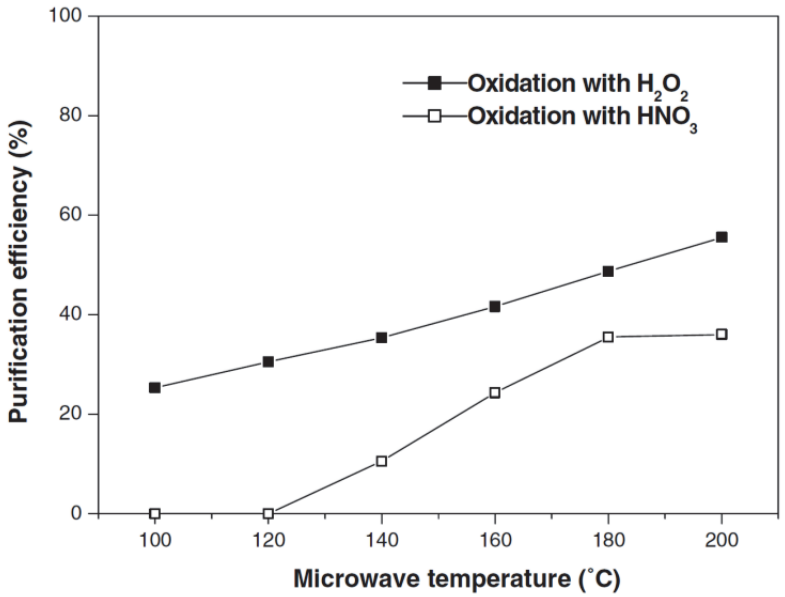

Fig. 3. Effects of temperature and reagent (hydrogen peroxide or nitric acid) on the efficiency of the microwave-assisted purification of nanotubes, as measured by the gravimetric method. Reproduced with permission from ref (Ko et al. 2004) Copyright 2004 Elsevier.

On the other hand, Grennberg (Chajara et al. 2010) and coworkers recently reported reagent -free microwave based method which concurs "green" for the purification of MWNTs as it is extremely faster, with significantly less damage to CNTs, and with less waste compared to previously reported processes.

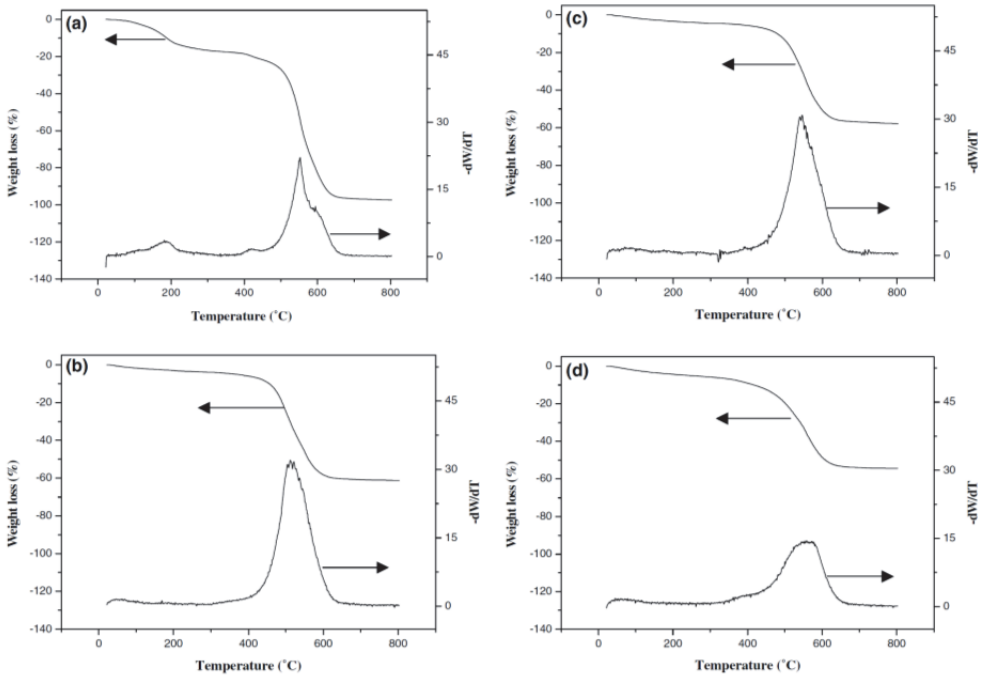

Fig. 4. Thermogravimetric analyses of samples of nanotube purified with hydrogen peroxide at different microwave temperatures. (a) Before purification. After heating at: (b) 140, (c) 180, and (d) 200°C. Reproduced with permission from ref (Ko et al. 2004) Copyright 2004 Elsevier.

Reagent-free microwave-assisted purification yields very pure CNTs within a few min of heating and a simple filtration without the involvement of acidic/oxidative reagents. According to thermogravimetric analysis, Raman and IR spectroscopy, as well as scanning and transmission electron microscopy, the process yields pure nanotubes with a low degree of defects.

The purification is efficient for as-produced and post-synthesis treated CNTs. Morphological observations (Fig. 5) suggests that thermal delaminating of treated non-CNT carbon from CNT is the key step, which attenuated by solubilization of amorphous carbon, preventing re-aggregation. Non-CNT matrix that surrounds the as-received CNTs (Fig. 5a) is transformed into irregularly-shaped amorphous carbon recovered from the filtrate (Fig. 5c and 5d), and the individual MWNTs become more individualized (Fig. 5b). In order to explore the scope of the method, purification protocol has been applied to MWNTs. The left panel in Fig. 6 shows the Raman spectra of the as-received MWNTs, microwave-purified MWNTs (one cycle), and of the filtrate containing the impurities. The D-band was found at 1352 cm^{-1}, the G-band at 1578 cm^{-1} and the G′-band at 2708 cm^{-1}. The only significant difference between the untreated MWNTs sample and the microwave-purified sample was a decrease in the intensity of the D-band. The D/G ratio was ~0.8 for the as-received sample and ~0.7 for the sample treated once. This is as expected with a decrease in the amount of amorphous carbon in the purified sample. The purification protocol could be repeated several times with fresh solvent, resulting in an increasing purity of the CNT material, However repeating the purification protocol more than twice resulted in some damage to

the MWNTs, as was evident by the small relative increase of the D band intensity (Fig. 6, right panel), but to a very low degree compared to conventional oxidative processes.

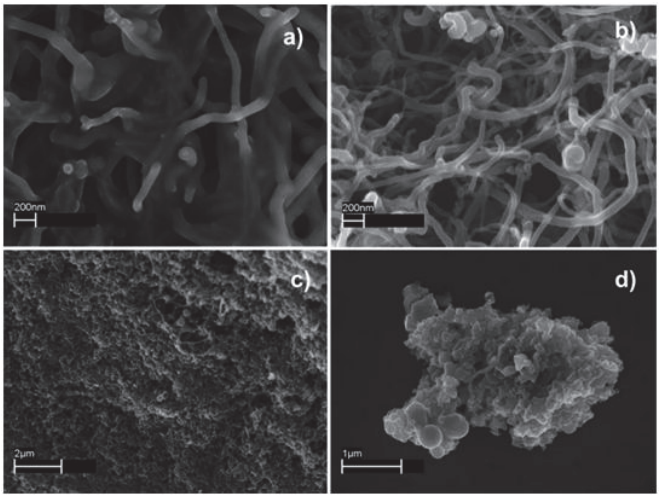

Fig. 5. SEM images of (a) as-received MWNTs (the MWNTs are covered with amorphous carbon), (b) purified MWNTs (two cycles) (the MWNTs are no longer covered with amorphous carbon and appear as individual tubes), (c) filtrate (the image shows amorphous carbon and a few MWNTs) and (d) filtrate with aggregates of amorphous carbon. Reproduced with permission from ref (Chajara et al. 2010) Copyright 2010 Royal Society of Chemistry.

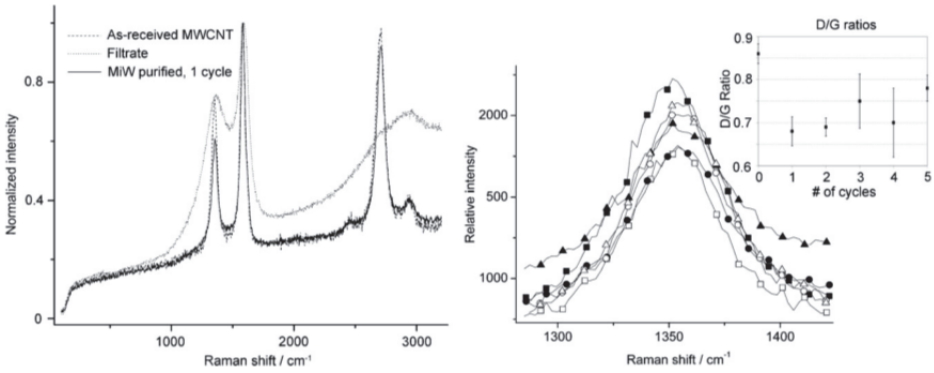

Fig. 6. Raman spectra of the MWNTs (normalized to the G-band). Left panel: as-received MWNTs (dashed line), microwave-purified (MiW) MWNTs (one cycle in CH_2Cl_2) (-), filtrate (--). Right panel: expansion of the D-band region of MWNTs treated for 1–5 cycles in CH_2Cl_2: ■ As-received MWNTs, □ MiW purified (one cycle), ● MiW purified (two cycles), ○ MiW purified (three cycles), ▲ MiW purified (four cycles), and △ MiW purified (five cycles) (spectra are normalized to the G-band). The inset shows the D/G ratio for the material treated 1–5 times (based on three measurements per sample). Error bars indicate standard deviations. Reproduced with permission from ref (Chajara et al. 2010) Copyright 2010 Royal Society of Chemistry.

3. Covalent functionalization of carbon nanotube sidewall

Microwave-assisted synthesis has become an important tool for chemists for rapid organic and inorganic synthesis. A huge number of research papers have appeared over the last decades on the application of microwave technology in organic synthesis (Delgado et al. 2004; Wang, Iqbal, and Mitra 2005; Brunetti et al. 2008). Some major advantages over classical thermal methods are spectacular decrease in reaction time, improved conversion, clean product formation, and wide scope for the development of new reaction conditions.

3.1 Microwave-assisted synthesis of CNTs/organic based nanocomopsites by microwave method

For instance, Brunetti and coworkers (Brunetti et al. 2007) have described a solvent-free technique combined with microwave irradiation, which provides a fundamentally different approach when considering the chemistry of CNTs. In the absence of solvents, CNTs absorb the radiation directly and it is possible to take full advantage of the strong microwave absorption typical of pristine nanotubes. Moreover, solvent-free conditions pave the way to green protocols and large-scale functionalization. The method has been applied to produce multifunctionalized CNTs using a combination of two different addition reactions: the 1,3-dipolar cycloaddition of azomethine ylides and the addition of diazonium salts, both *via* a simple, fast, and environmentally friendly method (Fig. 7). The reaction can be followed by Raman spectroscopy, which shows the increase of the D-band (~1300 cm^{-1}, sp^3 carbons) at the expense of the G-band (~1600 cm^{-1}, sp^2 carbons).The extremely high temperature observed in the absence of solvent might permit the functionalization of CNTs using new types of reaction that do not work under classical reflux heating (Vazquez and Prato 2009).

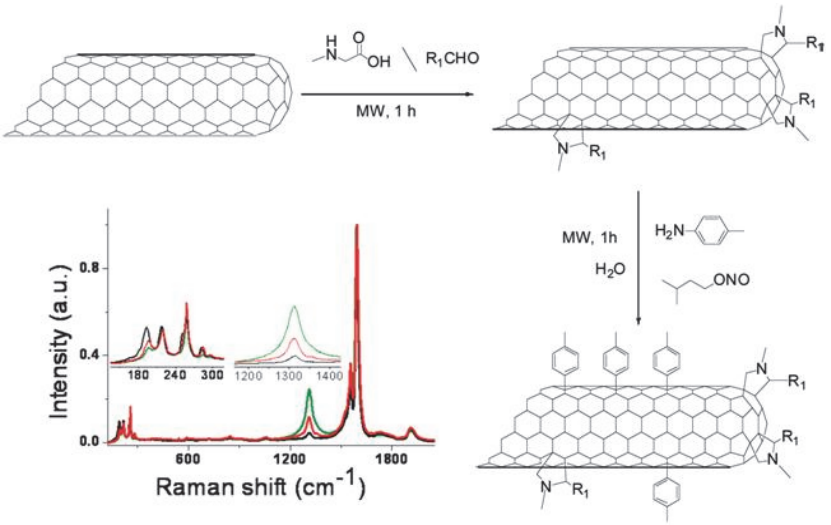

Fig. 7. Microwave-assisted double functionalization of SWNTs: Raman spectra (Exc: 633 nm) of pristine SWNTs (black line), SWNTs functionalized by 1,3-dipolar cycloaddition (red line), and doubly functionalized SWNTs (green line). Reproduced with permission from ref (Vazquez and Prato 2009) Copyright 2009 American Chemical Society.

Using similar approach, a solvent-free microwave-assisted method has also been employed for the covalent functionalization of carbon nanohorns based on the Bingel reaction (Economopoulos et al. 2009) and 1,3-dipolar cycloaddition of azomethineylides (Brunetti et al. 2008).

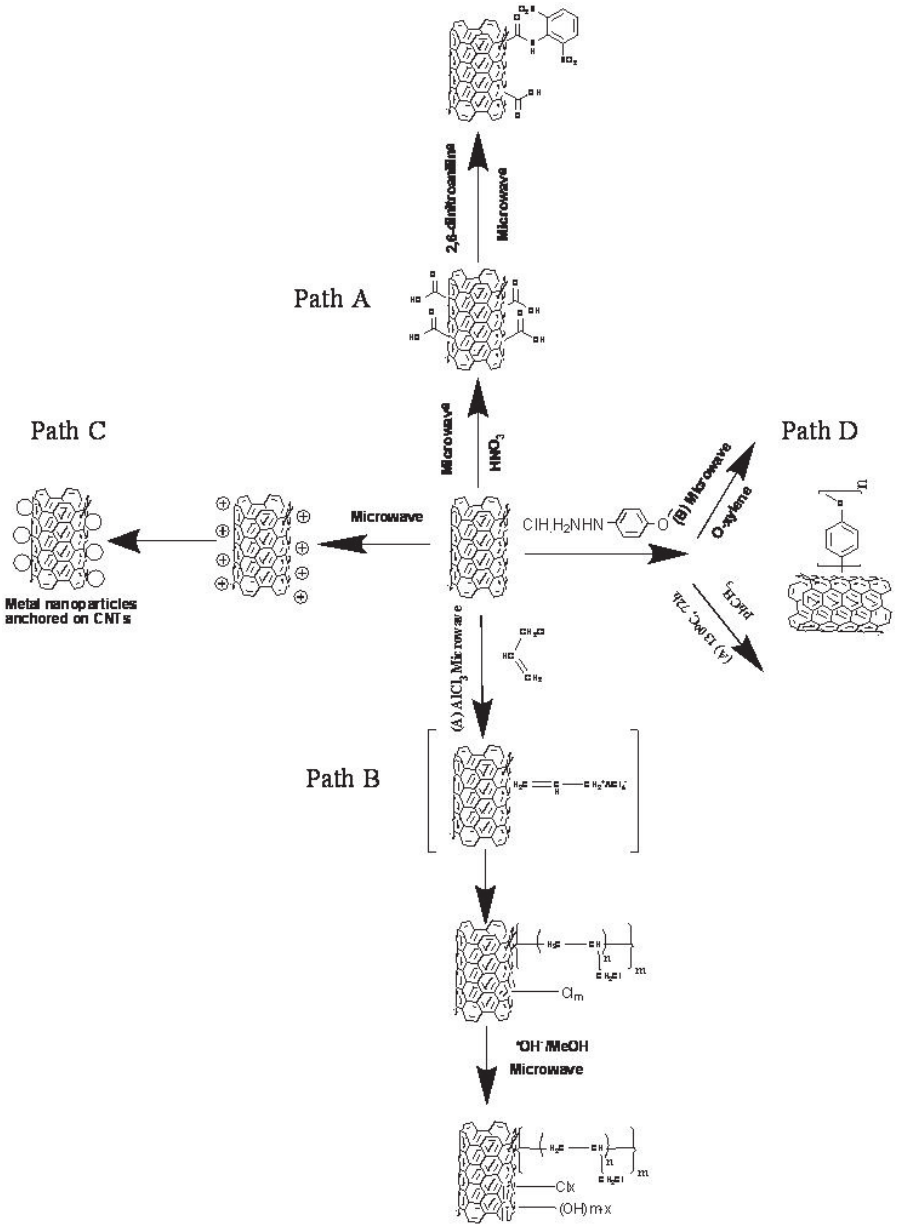

Fig. 8. Schematic representation of various covalent functionlization reactions of carbon nanotube sidewall.

3.1.1 Microwave-assisted radical functionalization of single-wall carbon nanotubes

Liu and coworkers compared the efficiencies of two methods for functionalizing single wall carbon nanotubes (SWNTs) through a radical addition of 4-methoxyphenylhydrazine hydrochloride by a classical thermally activated procedure and via a microwave-assisted method. (Path D in Fig. 8) represents the reaction scheme by either classical (a) or microwave method (b) to yield the same product. The experimental signatures of sample functionalized by the classical and microwave methods are quite comparable. With a similar yield of functionalization, the microwave-assisted reaction is far more rapid with an optimal time of around 5 min. This represents a vast reduction in reaction time which for the classical method is often measured in days (Liu, Zubiri et al. 2007).

On the other hand, Tian (Tian et al. 2009) and coworkers have demonstrated a highly efficient approach to prepare the polymer-grafted SWNTs by electrophilic addition with 3-chloropropane based on microwave technique (path B in Fig. 8). In the presence of $AlCl_3$, 3-choloropropene initially was turned into cation $CH_2=CH_2-CH^+$, which underwent an electrophilic addition to form oligomers. Thus, 3-cholropropene would be attached to the surface of SWNTs in the form of the polymer chains and –Cl groups, and the Cl^- atoms could be substituted by OH^- groups after the hydrolysis with alkaline methanol. The attachment of the hydroxyl groups opens the way to further derivatize SWNTs, and the polymer chains enhance the interaction between modified SWNTs and more polymer molecule chains.

With the combination of different characterization techniques Wang and coworkers (Wang, Iqbal, and Mitra 2005) proved that pristine SWNTs can be covalently functionalized, where the reaction time is reduced to the order of minute.

Two model reactions, namely amidation and 1,3-cycloaddition of SWNTs were carried out successfully in relatively short times using a microwave reactor. The 1-3 dipolar cycloaddition of SWNTs was carried out in 15 min under microwave irradiation. (Please insert Fig. 3 after the above mentioned description)

3.2 Microwave-assisted synthesis of CNTs-based hybrid materials

Modifying the CNT surface with desired functional groups is an important step for creating CNT-based hybrid structures and has been used to assemble CNTs and separate CNTs with different structures (Raghuveer et al. 2006). Raghuveer and coworkers describe an eco-friendly approach of using microwaves to rapidly functionalize MWNTs with carboxyl, carbonyl, hydroxyl, and allyl termini, without the use of aggressive oxidants (e.g., HNO_3) or ultrasonication. We also adapt this method to derivatize CNTs with nanoparticles synthesized in situ by metal-ion reduction during functionalization, all in a single processing step. This approach offers a new way for efficiently creating hybrid nanostructures. Using similar kind of approach we have synthesized gold nanoparticles coated MWNTs for the adsorption of sulfur compounds as shown in Fig. 8 (path C). Morphological observations illustrates the gold nanoparticles are uniformly anchored onto MWNTs and after the modification still preserved the structure of CNTs (Fig. 9).

Another interesting application of microwave-assisted fabrication is CNT AFM (atomic force microscopy) tips (Druzhinina, Hoeppener, and Schubert 2010). A new, fast, alternative approach for the fabrication of CNT AFM tips is reported. Thereby, the tube material is grown on the apex of an AFM tip by utilizing microwave irradiation and selective heating of the catalyst. The deposition of the catalyst material could be further improved by utilizing particle picking approaches, e.g., by force vs. distance curve recording, to further increase

the controllability of the presented approach. Reaction time as short as three min allowed the fabrication of CNT AFM tips in a highly efficient process. This method demonstrates a promising approach toward a cheaper, faster, and straightforward synthesis of CNT AFM tips as shown in Fig. 10.

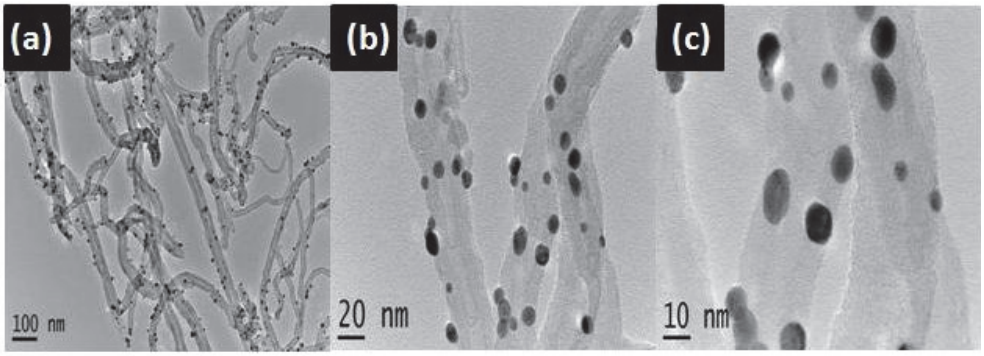

Fig. 9. (a) Low- and (b, c) high magnification micrographs illustrating the decoration of MWNTs with 3-10 nm diameter Au nanoparticles. Note that hollow of the tubes remain intact, indicating that the overall structure of the CNTs are preserved.

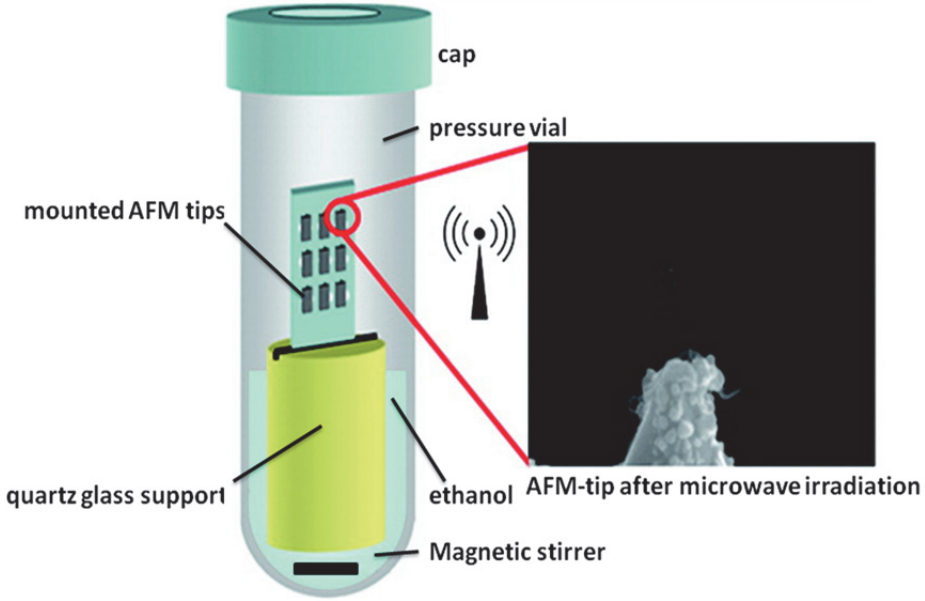

Fig. 10. Quartz glass pressure vial with mounted AFM cantilevers, support, and liquid ethanol reservoir. Morphology of AFM tip after microwave irradiation. Reproduced with permission from ref (Druzhinina, Hoeppener, and Schubert 2010) Copyright 2010 American Chemical Society.

We have carried out microwave-assisted acidification of CNTs, as the first step towards the synthesis of CNTs-based hybrid materials. Various experimental parameters for microwave acidification (e.g. heating temperature and time period of microwave, various types and amounts of oxidative reagent) were investigated. The synthesized hybrid material was used as a gas adsorbent, consisting of magnetic iron-oxide nanoparticles (MINPs) and CNTs (Lee et al. 2010). These hybrid materials were resulted from the electrostatic interaction between MINPs and the surface of microwave-assisted acidified MWNTs as shown in Fig. 11. As compared to traditional Tenax GR adsorbent, our hybrid material shows promising lower detection limit and larger breakthrough volume (Fig. 12 and Table 2).
On the other hand, Chen (Chen et al. 2009) and coworkers have reported microwave-assisted solid state grafting of MWNTs in polyurethane composite, exhibiting excellent optical limiting properties. Wallace (Zhang et al. 2010) research team has synthesized Pt/CNTs based nanocomposite electrocatalyst for proton-exchange membrane fuel cells by using microwave-assisted heating of functionalized SWNTs. Catalytic performance was found to be superior to Pt NPs supported by raw CNTs or by carbon black prepared under the identical condition.

Fig. 11. Synthesis of MWNTs based gas adsorbent.

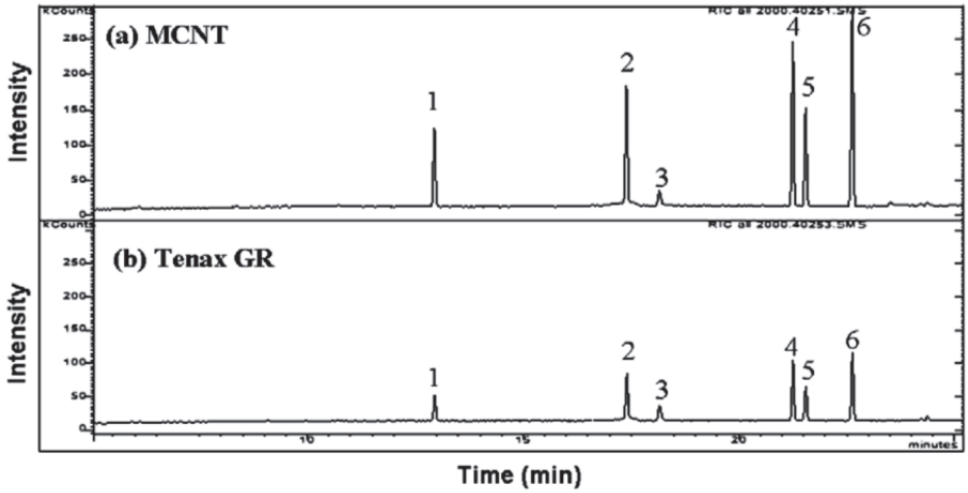

Fig. 12. The total ion chromatogram of BTEXS obtained using (a) 50-mg MWNTs, and (b) 200-mg Tenax GR adsorbent at a sampling rate of 80 mL min^{-1}. Peak identity: (1) benzene, (2) toluene, (3) impurity from thermal desorption device, (4) ethyl benzene, (5) xylene, and (6) styrene. Reproduced with permission from ref (Lee et al. 2010) Copyright 2010 Elsevier.

Compound	Break through volume (BTV)		Detection limit (DL)	
	MWNTs	Tenax GR	MWNTs	Tenax GR
Benzene	100	20	0.7	7.7
Toluene	>100	40	0.9	9.1
Ethyl benzene	>100	40	0.8	8.0
Xylene	>100	40	0.7	7.9
Styrene	>100	40	0.8	8.5

a. BTV: Lg^{-1}
b. DL: ppbv
c. 50-mg amount

Table 2. Adsorption efficiency of MWNTs nanocomposites over commercially available Tenax GR. Reproduced with permission from ref (Lee et al. 2010) Copyright 2010 Elsevier.

4. Summary and future perspectives

For the past decade, despite of the tremendous growth on microwave-driven synthesis, still there are plenty of rooms at the bottom. Microwave is non-invasive, simple, fast, environmentally friendly, and clean processing method as compared to traditional thermal methods. Microwave-assisted method offers excellent reproducibility and avoids all tedious process involved with synthesis of CNTs based nanocomposites by traditional synthesis methods. By controlling the preferential microwave absorption of different types of tubes, it is possible to obtain samples consisting primarily of semiconducting nanotubes, which is critical for many applications. In addition, the extremely high temperature observed, in the absence of solvent, might activate the reactivity of CNTs, permitting their modification in new kinds of reactions that do not work under classical reflux heating. The awareness of the particular microwave absorbing properties of CNTs and their different behavior with respect to typical organic compounds should open the door to the preparation of a wide range of new materials useful in assorted fields, including telecommunications, biomedical applications, and illumination technologies. From the examples discussed here, it is clear that the potential of microwave is worthwhile for the growth of 21st century, however to setup the large-scale microwave for industrial production commands further research and engineering work.

5. References

Bandow, S., A. M. Rao, K. A. Williams, A. Thess, R. E. Smalley, and P. C. Eklund. 1997. Purification of single-wall carbon nanotubes by microfiltration. *Journal of Physical Chemistry B* 101 (44):8839-8842.

Biercuk, M. J., M. C. Llaguno, M. Radosavljevic, J. K. Hyun, A. T. Johnson, and J. E. Fischer. 2002. Carbon nanotube composites for thermal management. *Applied Physics Letters* 80 (15):2767-2769.

Brunetti, F. G., M. A. Herrero, J. D. Munoz, A. Diaz-Ortiz, J. Alfonsi, M. Meneghetti, M. Prato, and E. Vazquez. 2008. Microwave-induced multiple functionalization of carbon nanotubes. *Journal of the American Chemical Society* 130 (25):8094-8100.

Brunetti, F. G., M. A. Herrero, J. D. M. Munoz, S. Giordani, A. Diaz-Ortiz, S. Filippone, G. Ruaro, M. Meneghetti, M. Prato, and E. Vazquez. 2007. Reversible microwave-assisted cycloaddition of aziridines to carbon nanotubes. *Journal of the American Chemical Society* 129 (47):14580-14581.

Campos-Delgado, J., I. O. Maciel, D. A. Cullen, D. J. Smith, A. Jorio, M. A. Pimenta, H. Terrones, and M. Terrones. 2010. Chemical Vapor Deposition Synthesis of N-, P-, and Si-Doped Single-Walled Carbon Nanotubes. *Acs Nano* 4 (3):1696-1702.

Chajara, K., C. H. Andersson, J. Lu, E. Widenkvist, and H. Grennberg. 2010. The reagent-free, microwave-assisted purification of carbon nanotubes. *New Journal of Chemistry* 34 (10):2275-2280.

Chen, Y. H., V. S. Muthukumar, Y. B. Wang, C. Li, S. S. Krishnan, S. S. S. Sai, K. Venkataramaniah, and S. Mitra. 2009. Microwave-assisted solid-state grafting of multi-walled carbon nanotubes on polyurethane for the synthesis of a composite with optical limiting properties. *Journal of Materials Chemistry* 19 (36):6568-6572.

Dallinger, D., and C. O. Kappe. 2007. Microwave-assisted synthesis in water as solvent. *Chemical Reviews* 107 (6):2563-2591.

Delgado, J. L., P. de la Cruz, F. Langa, A. Urbina, J. Casado, and J. T. L. Navarrete. 2004. Microwave-assisted sidewall functionalization of single-wall carbon nanotubes by Diels-Alder cycloaddition. *Chemical Communications* 15:1734-1735.

Druzhinina, T. S., S. Hoeppener, and U. S. Schubert. 2010. Microwave-Assisted Fabrication of Carbon Nanotube AFM Tips. *Nano Letters* 10 (10):4009-4012.

Economopoulos, S. P., G. Pagona, M. Yudasaka, S. Iijima, and N. Tagmatarchis. 2009. Solvent-free microwave-assisted Bingel reaction in carbon nanohorns. *Journal of Materials Chemistry* 19 (39):7326-7331.

Ghule, A. V., K. M. Kathir, T. K. S. Kumar, S. H. Tzing, J. Y. Chang, C. Yu, and Y. C. Ling. 2007. Carbon nanotubes prevent 2,2,2 trifluoroethanol induced aggregation of protein. *Carbon* 45 (7):1586-1589.

Holzinger, M., J. Abraha, P. Whelan, R. Graupner, L. Ley, F. Hennrich, M. Kappes, and A. Hirsch. 2003. Functionalization of single-walled carbon nanotubes with (R-)oxycarbonyl nitrenes. *Journal of the American Chemical Society* 125 (28):8566-8580.

Hu, H., B. Zhao, M. A. Hamon, K. Kamaras, M. E. Itkis, and R. C. Haddon. 2003. Sidewall functionalization of single-walled carbon nanotubes by addition of dichlorocarbene. *Journal of the American Chemical Society* 125 (48):14893-14900.

Iijima, S. 1991. Helical Microtubules of Graphitic Carbon. *Nature* 354 (6348):56-58.

Imholt, T. J., C. A. Dyke, B. Hasslacher, J. M. Perez, D. W. Price, J. A. Roberts, J. B. Scott, A. Wadhawan, Z. Ye, and J. M. Tour. 2003. Nanotubes in microwave fields: Light emission, intense heat, outgassing, and reconstruction. *Chemistry of Materials* 15 (21):3969-3970.

Journet, C., W. K. Maser, P. Bernier, A. Loiseau, M. L. delaChapelle, S. Lefrant, P. Deniard, R. Lee, and J. E. Fischer. 1997. Large-scale production of single-walled carbon nanotubes by the electric-arc technique. *Nature* 388 (6644):756-758.

Ko, C. J., C. Y. Lee, F. H. Ko, H. L. Chen, and T. C. Chu. 2004. Highly efficient microwave-assisted purification of multiwalled carbon nanotubes. *Microelectronic Engineering* 73-74:570-577.

Kokai, F., K. Takahashi, D. Kasuya, T. Ichihashi, M. Yudasaka, and S. Iijima. 2000. Synthesis of single-wall carbon nanotubes by millisecond-pulsed CO_2 laser vaporization at room temperature. *Chemical Physics Letters* 332 (5-6):449-454.

Koziol, K., J. Vilatela, A. Moisala, M. Motta, P. Cunniff, M. Sennett, and A. Windle. 2007. High-performance carbon nanotube fiber. *Science* 318 (5858):1892-1895.

Kreupl, F., A. P. Graham, M. Liebau, G. S. Duesberg, R. Seidel, and E. Unger. 2004. Carbon nanotubes for interconnect applications. *Ieee International Electron Devices Meeting 2004, Technical Digest*:683-686.

Lee, P. L., Y. K. Chiu, Y. C. Sun, and Y. C. Ling. 2010. Synthesis of a hybrid material consisting of magnetic iron-oxide nanoparticles and carbon nanotubes as a gas adsorbent. *Carbon* 48 (5):1397-1404.

Lee, P. L., Y. C. Sun, and Y. C. Ling. 2009. Magnetic nano-adsorbent integrated with lab-on-valve system for trace analysis of multiple heavy metals. *Journal of Analytical Atomic Spectrometry* 24 (3):320-327.

Li, J., Q. Ye, A. Cassell, H. T. Ng, R. Stevens, J. Han, and M. Meyyappan. 2003. Bottom-up approach for carbon nanotube interconnects. *Applied Physics Letters* 82 (15):2491-2493.

Lin, W., K. S. Moon, S. J. Zhang, Y. Ding, J. T. Shang, M. X. Chen, and C. P. Wong. 2010. Microwave Makes Carbon Nanotubes Less Defective. *Acs Nano* 4 (3):1716-1722.

Liu, C. H., H. Huang, Y. Wu, and S. S. Fan. 2004. Thermal conductivity improvement of silicone elastomer with carbon nanotube loading. *Applied Physics Letters* 84 (21):4248-4250.

Liu, J., M. R. I. Zubiri, B. Vigolo, M. Dossot, Y. Fort, J. J. Ehrhardt, and E. Mcrae. 2007. Efficient microwave-assisted radical functionalization of single-wall carbon nanotubes. *Carbon* 45 (4):885-891.

Liu, Y. Q., L. Gao, J. Sun, S. Zheng, L. Q. Jiang, Y. Wang, H. Kajiura, Y. M. Li, and K. Noda. 2007. A multi-step strategy for cutting and purification of single-walled carbon nanotubes. *Carbon* 45 (10):1972-1978.

Lobach, A. S., N. G. Spitsina, S. V. Terekhov, and E. D. Obraztsova. 2002. Comparative analysis of various methods of purification of single-walled carbon nanotubes. *Physics of the Solid State* 44 (3):475-477.

MacKenzie, K., O. Dunens, and A. T. Harris. 2009. A review of carbon nanotube purification by microwave assisted acid digestion. *Separation and Purification Technology* 66 (2):209-222.

Nuchter, M., B. Ondruschka, W. Bonrath, and A. Gum. 2004. Microwave assisted synthesis - a critical technology overview. *Green Chemistry* 6 (2):128-141.

Peng, H. Q., L. B. Alemany, J. L. Margrave, and V. N. Khabashesku. 2003. Sidewall carboxylic acid functionalization of single-walled carbon nanotubes. *Journal of the American Chemical Society* 125 (49):15174-15182.

Pompeo, F., and D. E. Resasco. 2002. Water solubilization of single-walled carbon nanotubes by functionalization with glucosarnine. *Nano Letters* 2 (4):369-373.

Raghuveer, M. S., S. Agrawal, N. Bishop, and G. Ramanath. 2006. Microwave-assisted single-step functionalization and in situ derivatization of carbon nanotubes with gold nanoparticles. *Chemistry of Materials* 18 (6):1390-1393.

Tasis, D., N. Tagmatarchis, A. Bianco, and M. Prato. 2006. Chemistry of carbon nanotubes. *Chemical Reviews* 106 (3):1105-1136.

Tian, R., X. B. Wang, Y. Xu, S. Q. Li, L. Wan, M. J. Li, and J. Cheng. 2009. Microwave-assisted functionalization of single-walled carbon nanotubes with 3-chloropropene. *Journal of Nanoparticle Research* 11 (5):1201-1208.

Vazquez, E., V. Georgakilas, and M. Prato. 2002. Microwave-assisted purification of HIPCO carbon nanotubes. *Chemical Communications* 20:2308-2309.

Vazquez, E., and M. Prato. 2009. Carbon Nanotubes and Microwaves: Interactions, Responses, and Applications. *Acs Nano* 3 (12):3819-3824.

Vigolo, B., A. Penicaud, C. Coulon, C. Sauder, R. Pailler, C. Journet, P. Bernier, and P. Poulin. 2000. Macroscopic fibers and ribbons of oriented carbon nanotubes. *Science* 290 (5495):1331-1334.

Wadhawan, A., D. Garrett, and J. M. Perez. 2003. Nanoparticle-assisted microwave absorption by single-wall carbon nanotubes. *Applied Physics Letters* 83 (13):2683-2685.

Wang, Y. B., Z. Iqbal, and S. Mitra. 2005. Microwave-induced rapid chemical functionalization of single-walled carbon nanotubes. *Carbon* 43 (5):1015-1020.

Ye, Z., W. D. Deering, A. Krokhin, and J. A. Roberts. 2006. Microwave absorption by an array of carbon nanotubes: A phenomenological model. *Physical Review B* 74 (7):-.

Zhang, W. M., J. Chen, G. F. Swiegers, Z. F. Ma, and G. G. Wallace. 2010. Microwave-assisted synthesis of Pt/CNT nanocomposite electrocatalysts for PEM fuel cells. *Nanoscale* 2 (2):282-286.

6

Implantable Electrodes with Carbon Nanotube Coatings

Saugandhika Minnikanti and Nathalia Peixoto
George Mason University
United States of America

1. Introduction

Carbon nanotubes (CNTs), discovered in 1950 (Monthioux & Kuznetsov, 2006; Radushkevich & Luk'yanovich 1952) and rediscovered in 1993 (Iijima & Ichihashi, 1993), came into the limelight as a promising next generation material for standard electronics, computers and aerospace industries. Its ballistic conductance, chemically inert nature (Niyogi et al., 2002), nano size (Ajayan 1999) and ease of chemical functionalization (Shim et al., 2002; Sinnott, 2002) opened the doors for it to become an important biomaterial (Malarkey & Parpura, 2007). The diameter of the nanotubes is of particular interest to neuroscientists: they are of the same order as neuronal processes. The interface of sub-cellular compartments with a material of that same size spawns numerous new ideas. This facilitates an interaction at a molecular level, imperative in the formation of "functional neuronal circuits"(Lee & Parpura, 2009), was one of the possibilities considered early on. CNTs could be functionalized with one or more bioactive molecules (Mattson et al., 2000). The molecular control of neuronal architecture at focal microdomains seemed possible now. This promoted the candidacy of CNTs out of the variety of available nanomaterials, and onto the main neuroscience stage (Pancrazio, 2008).

In this chapter we will discuss the use of CNTs as active coatings for implantable neural electrodes (NEs). We begin with the background and motivation behind NEs, discussing a few examples of electrical stimulation and recording used in treating or ameliorating various nervous disorders. There are various techniques for the evaluation of electrode performance. The two most important are cyclic voltammetry and electrochemical impedance spectroscopy. These techniques are the focus of a section which includes robustness and reliability in neural electrodes. The rationale behind using CNT as a NE coating is discussed next. It throws light on the properties that make them unique. We describe the figures of merit of CNTs with respect to the development and requirements necessary for designing stimulating electrodes. The problems associated with using CNTs fabrication and manipulation are also discussed with the objective of establishing an appropriate view of the challenges faced when using and handling this material. A discussion on CNTs and neuronal interactions then follows. We will limit our approach to a subset of studies relevant to using CNTs as a conductive substrate to stimulate and record

from neuronal cell lines, which we call "neurocompatibilty". Various techniques have been devised to deposit CNTs on substrates for biological interaction. The following section consists of methods mentioned in the literature to deposit CNTs specifically as an electrically active neural interface and characterization results. This is followed by overview of *in vivo* studies conducted using CNTs as electrodes to stimulate and record from the nervous system. We will conclude this chapter with the current limitations and future investigations of CNTs as NEs.

2. Background and motivation

Luigi Galvani was a pioneering scientist who opened the doorway of using electrical stimulation on excitable tissue. He showed, in his famous experiment in 1780 on a frog, that muscle could contract as a result of electrical stimulation. This work led Galvani to propose that electricity is secreted in the brain and thus distributes itself from nerves to muscles (Parent, 2004). His work paved the way for the development of modern electrophysiology. His nephew Aldini, in 1803, at the Royal College of Surgeons, applied an electric shock to the corpse of a criminal. The results were theatrical. In his own words "when the rods were applied to Foster's mouth and ear, the jaw began to quiver, the adjoining muscles were horribly contorted, and the left eye actually opened" (Parent, 2004). This famous experiment led to the idea that electricity can restore life; from then on neural and muscular tissues became the focus of research on controllable electrical stimuli to induce activity. Technological advancements such as, cathode ray oscilloscope, micro-wires, and galvanometer later in the 19th and 20th centuries helped in understanding the structure and functions of excitable tissues such as neuronal and skeletal, cardiac, and smooth muscles. Nowadays long-term electrical stimulation is used to treat different neurological and muscular disorders(Bhatt, 2001). From the 20th century on neurologists have been using electrical stimulation to identify specific sites in the brain. Today electrical stimulation of relevant brain regions to alleviate symptoms of certain neurological disorders is available clinically.

Electrical stimulation is used to treat various kinds of disorders, from pacing the heart (through pacemakers) to bladder control. Electrical stimulation is delivered to its targets through electrodes. Here we will focus on electrical stimulation of the nervous system, more specifically of the central nervous system. With the exception of transcranial direct stimulation, applied from outside the skull (a non-invasive technique), electrical stimulation of the nervous system requires implantable electrodes. We focus here on those applications: brain stimulation by means of electricity delivered via microwires or microelectrodes that are inserted in the brain.

One of the popular treatments of Parkinson's disease is deep brain stimulation (DBS), where microelectrodes are placed in regions of the brain called thalamus, sub-thalamic nucleus, and globus pallidus (Vitek, 2002). Electric stimulation is applied to prevent tremor and other involuntary movements. The exact mechanisms of deep brain stimulation are still not clear, although there are many models proposing sometimes controversial mechanisms of action (Vitek, 2002). In order to restore functional vision, microelectrode arrays have been implanted over the visual cortex (Wyatt & Rizzo, 1996). Cochlear implants also use microelectrodes that restore hearing of patients by

stimulating specific regions of the auditory nerve (Wilson et al., 1991). Lastly, electrical stimulation is used to treat neurological disorders such as drug resistant depression (Mayberg et al., 2005), Tourette's syndrome (Servello et al., 2008), and epilepsy (Velasco et al., 1995).

Neural recordings are helpful in at least two applications: brain-computer interfaces and rehabilitation. For example, patients with movement disorders due to the failure in the connection between the cerebral motor system and muscles caused by injury, stroke, or degenerative disorders could benefit from recording electrodes. This missing or damaged links can be restored by recording the intent from the cerebral motor system and using those signals to control a prosthetic device. On another application, recording electrodes may also help deciding on stimulation protocols for an already implanted DBS electrode system. This will be highly beneficial when developing an adaptive and patient-tailored, closed loop system.

2.1 Invasive electrical interfacing with body

There are invasive and non-invasive methods for electrical stimulation and recording. An ideal invasive electrode used for stimulation or recording should be small, so that there is minimal tissue damage, and it should have enough recording sites for monitoring many neurons simultaneously. These electrodes can be made of various metal substrates such as platinum or medical grade stainless steel.

The electrode is the interface between the body and the prosthetic device used for electrophysiological research. One side is the metal electrode attached to an electrical circuit: here electrons are the charge carriers. The second side is the physiological medium (electrolyte) where charge is carried by ions. The fundamental process occurring at the electrode-electrolyte interface is charge transduction between electrons of the metallic electrode and ions of the electrolytic species. The two basic mechanisms of charge transfer at the electrode-electrolyte interface are faradaic and non-faradaic, as briefly discussed below. For more detailed descriptions of types of electrodes, we refer the reader to electrochemical textbooks (Bard & Faulkner, 2006; Varma & Selman, 1991).

2.1.1 Faradaic charge transfer

Here reduction and oxidation of chemical species in the electrolyte take place during electron transfer to and from the electrode. During reduction an electron is added to the chemical species and this occurs when the electrode is driven to negative potentials. In oxidation, removal of an electron from the chemical species occurs when the electrode is driven to a positive potential in reference to the solution (figure 1). This mechanism injects redox products in solution. In a reversible charge transfer the redox species injected into the electrolytic media are recovered at the electrode surface when the direction of current is reversed. A typical example of a Faradaic charge transfer is the process at the surface of silver-silver chloride electrodes.

2.1.2 Non-faradaic charge transfer

Charge redistribution can also occur by charging and discharging of the double layer present at the electrode-electrolyte interface. The double layer acts like a capacitor, with the

metallic electrode as one plate and the other being the electrolyte/tissue (Guyton & Hambrecht, 1974). Ions from the electrolyte either move towards or away from electrode depending on its charge. This process doesn't involve actual electron transfer between the electrode and the electrolytic species.

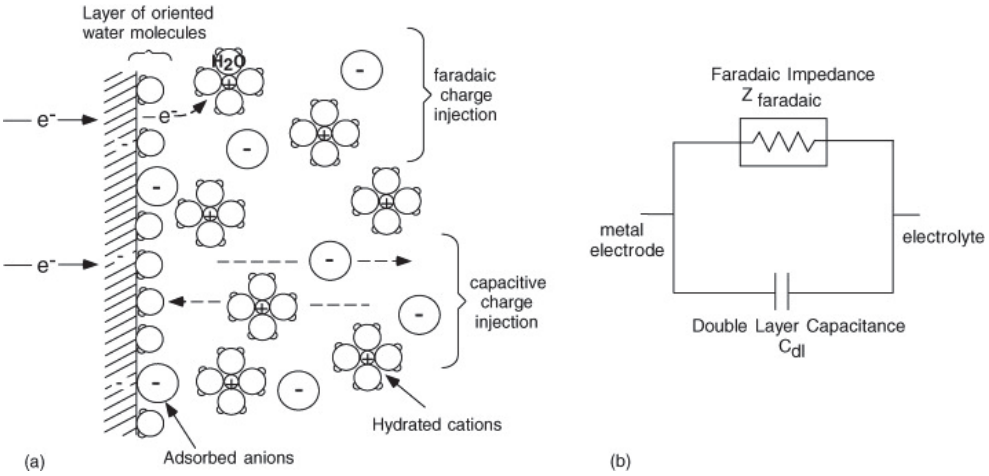

Fig. 1. Schematic of faradaic and non-faradaic (capacitive) charge transfer at the electrode-electrolyte interface. Reprinted with permission from (Merrill et al., 2005) . Copyright (2005) Elsevier.

Usually, the charge presented by a conventional metallic electrode through a stimulus pulse is above the holding capacity of the double layer. Thus, the charge transfer contribution of the electrochemical faradaic mechanism dominates the capacitive non-faradaic mechanism (Guyton & Hambrecht, 1974).

3. Electrode characterization

Electrode characterization is carried out in order to understand the nature of the electrode performance when it is exposed to biological tissue. Properties of particular interest are the charge injection level, electrochemical and structural properties, corrosion levels, and the potential window. There are various techniques involved in measuring or characterizing each of these. For example, structural characterization can be done using scanning electron microscopy (SEM), tunneling electron microscopy, and atomic force microscopy to study the surface morphology of the electrode. Similarly, there are various methods for electrochemical characterization. In controlled current methods a constant current is passed between a pair of electrodes in an electrochemical cell and the voltage of the working electrode is measured at the same time (Sawyer & Roberts, 1974a). There are various types of control potential methods: chronopotentiometry, chronoamperometry, and chronocoulometry. In controlled potential methods the voltage between the electrodes is kept constant and the current flowing in the electrochemical cell is monitored (Sawyer & Roberts, 1974b). Controlled potential coulometry techniques, linear sweep and cyclic

voltammetry (CV) experiments are a few examples of controlled potential methods. Controlled current methods are used evaluate the diffusion coefficients, rates of electrode processes, adsorption parameters, and rates of coupled chemical reactions occurring at the electrode surface within the supporting electrolyte (Sawyer & Roberts, 1974a). Linear sweep voltammetry evaluates the mechanism, kinetics and thermodynamics of the chemical reactions. Cyclic voltammetry (CV) is a derivative of linear sweep voltammetry, which captures both the oxidation and reduction cycle of the system. The last method we will discuss is electrochemical impedance spectroscopy (EIS), which investigates the interfacial reaction mechanisms and is essential to evaluate depositions (Macdonald, 1991). There are many other techniques described in detail in the literature (Bard & Faulkner, 2006; Varma & Selman, 1991).

3.1 Electrochemical characterization

The most important methods for biological electrodes are CV and EIS. CV measures the maximum charge that the electrode can deliver. This information is essential in evaluating electrodes used for electrical stimulation of tissue. EIS not only shows the voltage-current behavior of the electrode in the electrolyte but it provides information on the way the impedance of an electrode varies for a chosen frequency range. This data is essential because both high and low frequency stimulation of tissue are performed to study and treat various disorders. The two methods, CV and EIS, are discussed below.

3.1.1 Cylic voltammetry

CV is an electrochemical method where the potential of a working electrode is varied with time in a triangular waveform (figure 2). The current through the electrochemical cell is measured during the complete cycle of forward and reverse sweep rates (Crow, 1994). The potential is varied at sweep rate ranging from 10 mV/s to about 1000 V/s and the respective current is recorded as a function of potential. While the potential is varied, the surface of the electrode becomes sufficiently negative or positive,a solution species may gain or transfer electrons to and fro from the electrode surface. This movement of electrons generates current in the electrode circuitry. The reaction at the electrode surface varies from reduction, oxidation or none (Evans et al., 1983) and depends on the electrode potential. In a completely reversible system, species reduced in the forward scan of each cycle are re-oxidized during the reverse scan.

CV is useful in chemical research that provides an interpretable format regarding the electrochemical processes characterizing the electrode-electrolyte interface. (Sawyer & Roberts, 1974b). The integrated area of the CV of any electrode is equal to its charge storage capacity (CSC). To understand the curve, first assume that the electrolyte contains a species O; R is its reduced form and its reducing potential is E0. Initially, non faradaic currents will flow as the electrode potential is greater than the reduction potential. As the electrode potential approaches its reducing potential, reduction begins and the faradaic current is established. When the electrode potential crosses the reducing potential, most of the O species is reduced to R. As the potential is reversed and crosses the reducing potential most of the R species oxidized to O and anodic current flows. As the surface concentration decreases, a limit sets on oxidation and reduction of the electrolytic species, followed by the depletion effect (Bard & Faulkner, 2006). This shows up as the oxidation (Op) and reduction peaks (Rp) (figure 2C).

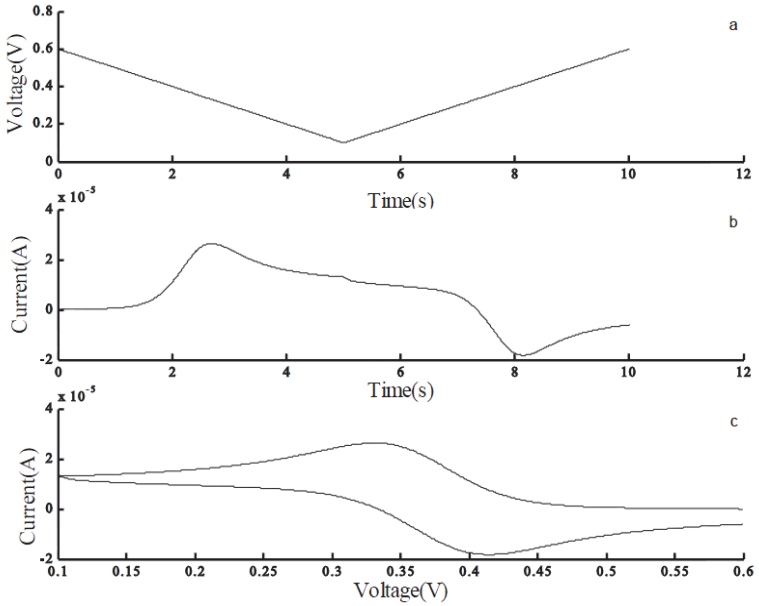

Fig. 2. (A) Applied voltage, (B) Measured current, (C) CV, combining (A) and (B).

3.1.2 Electrochemical impedance spectroscopy

The current-voltage behavior at the interface due to faradaic, non-faradaic and electronic components is described by impedance (Stieglitz, 2004) , measured through EIS. In this technique the system response is measured for a small amplitude, periodic AC signal spanned across a range of frequencies (Lasia, 1999). As the input and output signals are alternating current (AC) the impedance measure is complex. The real part is resistive and the imaginary part is the capacitive nature of the electrode. Nyquist and Bode plots are common graphical representations of complex impedance.

4. Requirements for successful neural electrodes

As in any engineering project, the design of robust electrodes for implantation entails careful analysis. The requirements should be stated with the goal in mind of a successful ten or twenty year lifetime: electrodes need to be functional during that whole period, either as recording or as stimulating devices. This is no easy task: mechanical, electrical, and biochemical constraints come into play (Merrill et al., 2005). A short description on the requirements for a neural electrode (NE) with a brief discussion of each figure of merit from the perspective of CNT electrodes follows.

4.1 The importance of impedance

Implanting an electrode in the brain wounds nearby tissue by severing capillaries, thus causing anoxia, and consequentially also neuronal and glial death (Perry 1994; Polikov et al., 2005). This trauma activates cellular mechanisms that aim at maintaining homeostasis

(Anderson, 2004). The insertion damage activates central nervous system macrophages which immediately secrete members of IL-1 (interleukin-1) family and other pro-inflammatory cytokines and chemokines. These in turn promote astrogliosis (Perry, 1994). Astrogliosis leads to reactive glial scar tissue formation, which has been shown, through histopathological techniques, to extend over weeks to years (Griffith & Humphrey 2006; Polikov et al., 2005). The reactive gliosis creates an insulating layer around the electrode, thus increasing the apparent impedance to the tissue. The take home message, from an inflammatory perspective, is that inserting a foreign body into the brain has multiple consequences, one of which is the formation of a shield around it. This is relevant in the design of an implantable electrode because an insulating layer around an electrode would mean no passage of direct current between the conductive material and the biological tissue.
The main target for a NE, as the name indicates, are neurons. Spatial proximity to neurons determines how well the signal is transferred. The common analogy that helps visualize the relevance of this spatial variable is a microphone in a football stadium: if a reporter is interviewing a player after a game, and the microphone is next to his mouth, one can hear his comments. Were that microphone five feet away, we would hear the roar from the audience, and if he screamed we could tell whether he was speaking or not, but we could never hear the words out of his mouth. When recording from neurons in the brain, the cells immediately around the electrode will be heard (recorded from) loud and clear. If there is a "space" (either physical space or an insulating layer) between the electrode and the cell, we lose signal. This would decrease their efficiency in recording low voltages and would require higher voltages/current to deliver the same amount of charge for stimulation. This would be harmful to the tissue. Thus electrodes having lower impedance can compensate for the rise in impedance *in vivo.*
CNT walls consist of hexagonal network of carbon atoms that are sp2 bonded. The electrons thus are delocalized and mobile inside and outside the nanotube channel. This renders them with a high electrical conductivity, on the order of 10^8 $\Omega^{-1}m^{-1}$ (Baxendale, 2003). Coatings of functionalized and non-functionalized CNTs decrease the apparent electrode impedance measured. Thus a high signal-to-noise ratio (SNR) can be maintained while measuring small (micro Volts) neuronal signals from the extracellular space.

4.2 Mechanical integrity

The electrode material should maintain its mechanical integrity, which means that the material should not bend, delaminate, or break when passing through tissue. It should withstand movement between the electrode and the tissue after implantation. The material should not degrade if placed in an electrolyte medium for extended periods, under physiological conditions. CNTs are known to be one of the strongest materials that can be manufactured, with a Young's modulus of a single carbon nanotube exceeding 1TPa, about five times stronger than steel (Treacy et al., 1996). Despite this fact, CNTs are very flexible. Molecular dynamic techniques have helped to demonstrate that nanotubes restore back to their formal shape on removal of mechanical stress (Salvetat et al., 1999). This shows that CNTs are mechanically strong as well as flexible. This property of high strength and flexibility is essential in the design of penetrating electrodes. Compromises must be met however if the CNT is used merely as the last coating on a substrate: the mechanical characteristics of the substrate will obviously influence the integrity of the electrode.

4.3 Charge delivery and electrical stability

An electrode should be able to deliver sufficient charge through the double layer formed at the electrode-tissue interface to elicit an action potential. The charge delivered should be at a low electrode potential to prevent water electrolysis and damage the tissue. For any electrode there is a reversible charge injection limit i.e., the total amount of charge that an electrode can deliver before the electrode potential reaches the water electrolysis potential. Therefore, the reversible CSC of an electrode material should be high enough to deliver sufficient charge before irreversible reactions initiate. The reversible CSC depends upon the electrode material, electrolytic species, and on the stimulation parameters. Even if the electrode material is biocompatible the faradaic reaction byproducts must not be toxic to the tissue. Also these redox byproducts should not cause damage to the electrode itself.

The entangled matrix of CNTs over a substrate and the hollow inner channel of a nanotube help in transportation of ions but also enhances the double layer effects (Fang et al., 2006). This is helpful because by increasing the effective area or accessible layer that contributes to double layer we can deliver the required amount of charge by keeping the size of the electrode small, a necessity of biological electrodes. Such bioelectrodes have large surface area making CNTs ideal materials even for energy storage (Du & Pan, 2006). Research has shown that charge transfer of pure CNT in an electrolytic medium is mostly non-Faradaic (Barisci et al., 2000). This type of charge transfer doesn't allow the formation of oxidation and reduction species. CNTs are often functionalised and co-deposited with other materials over electrodes. This could induce redox reactions and thus may lead to faradaic charge transfer (Barisci et al., 2000).

Neurons and electrically excitable cells have been successfully recorded from and stimulated via CNT substrates. CNT-neuronal interaction has resulted in enhanced efficiency in signal transmission (Mazzatenta et al., 2007), efficient stimulation (Gheith et al., 2006; Liopo et al., 2006; Lovat et al., 2005) , and recordings with high SNR (Keefer et al., 2008).

4.4 Water window

The potential window is defined as the voltage range above which irreversible electrochemical reactions take place. This is commonly used to evaluate the quality of the electrode material. One could test electrode materials in any solution of interest. However, in the case of a biological electrode the working potential window should be well within the water window limits. The reason for that is the presence of water in biological tissue. A water window is defined as the potential region between the oxidation of water to form oxygen and the reduction of water to form hydrogen.

Due to its "well defined graphitic structure" , CNTs have a wide working potential (Hue et al., 2004) making it possible to work well within the water window limit. Figure 3 shows electrodes being cycled in phosphate buffered saline, inside and outside of the water window. The extremely high currents are indicative of irreversible reactions taking place at the interface.

4.5 Surface topography

Surface topography can influence the growth and orientation of neurons in culture. Surfaces having nanofeatures have been shown to influence cell attachment and can be used to navigate cells to a specific region on the silicon substrate. (Craighead et al., 1998). CNT electrodes can be used to position and form stable networks due to the stable and strong

physical interactions between the neurons and the CNTs. (Sorkin et al., 2009). The neurons move towards CNT covered surfaces and single neurons move particularly towards the CNT surfaces (Galvan-Garcia et al., 2007).

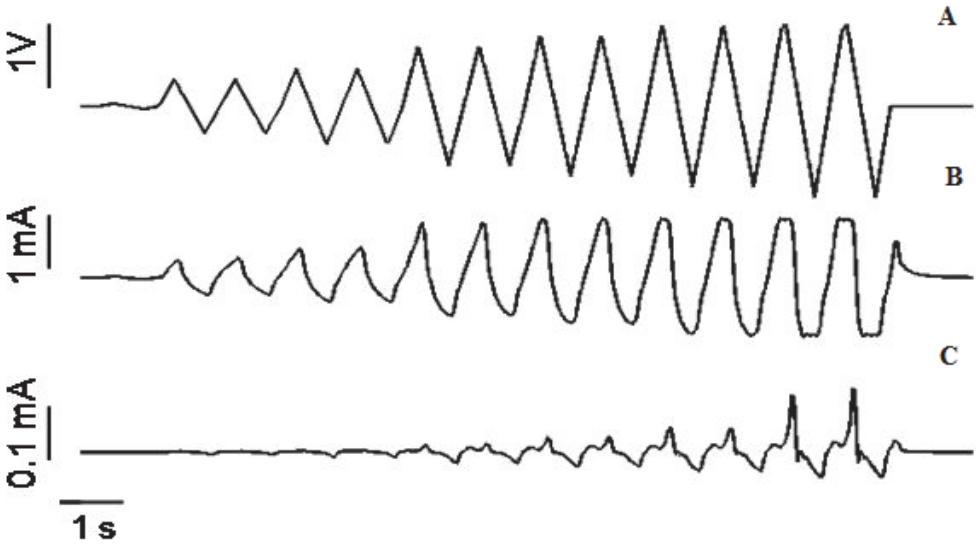

Fig. 3. Voltage controlled stimulation can drive electrodes outside the safe region determined by the water window. Stimulation sequence with 1 Hz triangular waveform, two periods per setting; amplitude of stimulus increases from 0.5 V to 0.7 V, then 1.1; 1.3; 1.5; 1.7 V. (A) Stimulation voltage, measured versus silver/silver chloride pellet in solution. (B) Current through iridium oxide film electrode, with 1 mA scale. During the 1.7 V peak stimulation, current through the iridium oxide is clipped due to amplifier saturation (amplitude higher than 1 mA). (C) Current through MWCNT electrode. Scale bar is 100 µA. Oxidation peaks are typical of non-reversible reactions at the electrode surface.

4.6 Biocompatibilty

The electrode surface, which contacts the biological tissue, should be biocompatible. Biocompatible means that the material will not induce toxic effects once in contact with the body. Another important quality of the material should be to not cause excessive immune response. Once an electrode is implanted it will be treated as a foreign material by the body, but the material should not impact the immune system dramatically (Polikov et al., 2005). This kind of response would reduce the electrode charge delivery capacity and recording sensitivity (Williams et al., 2007). Biocompatibility of CNTs is highly dependent on their mode of production, size, purification chemical functionalization, dose, and type of administration (systemic etc) (Ciofani et al., 2010; Nayagam et al., 2011). However, CNT surfaces are chemically inert (Niyogi et al., 2002) and can be modified by various functional groups to tailor them for a specific biological function.

As a substrate for neural implants CNTs seem to be bio- and neuro-compatible (see section 5 of this chapter) as they allow for neuronal growth and differentiation**.** CNTs as substrates for neuronal growth were first explored by Mattson et al in 2000. Since then studies on neuronal growth and interactions with CNTs have increased tremendously. CNTs tend to create an effective anchoring site for neurons and glial cell differentiation (Jang et al., 2010; Sorkin et al., 2009).
CNT coated surfaces are neuro-adhesive in *in vitro* scenarios (Galvan-Garcia et al., 2007). We believe this is an indication of a more generalized, also *in vivo,* behavior: certain kinds of CNT perform well when implanted in any excitable tissue. For example, immobilized multi-walled-walled CNT (MWCNT) arrays were implanted in male guinea pig muscles (Nayagam et al., 2011). The immobile CNTs presented with an insignificant host response while the dislodged CNTs were phagocytosed. The CNT arrays showed a minimal level of surface fouling. These results are very encouraging for further developing neural electrodes.

4.7 Issues associated with CNTs as neural electrodes

Although CNTs are promising, there are limiting factors when using it as electrode material for biological purposes. Pristine CNTs are inherently hydrophobic materials (Yang et al., 2007). Their surface are made of non-polar graphitic basal plane and hence most of this high surface area doesn't contribute to charge transfer in an aqueous media (Wang et al., 2006). Hence, surface modification of nanotubes is imperative to make them hydrophilic (Lacerda et al., 2006). Organic solvents render CNT surfaces hydrophilic and thus are used as a treatment technique. These solvents might be trapped between porous nanotubes or inside them even after extensive treatment for solvent removal (Wang et al., 2006).
The bioavailabilty of metallic catalysts used to grow CNTs might also contribute to harm the tissue (Guo et al., 2007). Thus harsh purification methods need to be employed to remove metal catalysts (Fe, Ni) (Hu et al., 2003). The current techniques of making CNTs are limited in the sense that both metallic and semiconducting nanotubes are produced together as bundles (Krupke et al., 2003). The conductivity of metallic CNT is higher than the semiconductor CNT. Therefore, it is highly desirable to coat NEs with purely metallic CNTs.
Owing to their nanoscale geometry, CNTs can interact with and modulate ionic channel behavior, which in turn impacts neuronal characteristics potentially in the long term. For example, single-walled CNTs blocked ion fluxes through potassium ion channels expressed in CHO cells (Park et al., 2003). The authors speculated that the CNTs blocked the channel pore and thus influenced ionic permeability through the membrane. Significant increase in cytoplasmic calcium ions after neurons were depolarized via single-walled CNT (SWCNT) was also reported (Ni et al., 2005). Carboxyl (COOH)-terminated MWCNTs interacted like an antagonist towards three kinds of potassium channels expressed on undifferentiated PC12 cells (Xu et al., 2009). PC12 cells are rat adrenal derived cells that exhibit a distinct neuronal phenotype (Wood et al., 1993), for example voltage-activated inward currents and action potentials (APs). It was speculated that the inhibitory effect on PC12 cells was due to CNTs physically interacting with amino-acid residues of the channel pore. The reduction of calcium and potassium currents by CNTs further demonstrates the impact of carbon nanotube on neuronal physiology (Jakubek et al., 2009; Xu et al., 2009). However, in all of these studies the cell lines were exposed to CNTs that were dispersed in the cell media and available for immediate cellular uptake. As a coating for neural electrode this kind of cellular uptake will not take place if the CNT forms a stable and robust coating during the lifetime of the implant.

5. Neurocompatibility

Biocompatibility, low impedance, and high charge delivery capacity are some of the necessary conditions for successful implantable materials, as we discussed above. These are however not sufficient conditions for neural implants. Neurons could for example grow on substrates and be affected in subtle ways, not immediately perceptible through electrochemical analyses. Here we discuss methods and results that address the more specific problem of "neurocompatibility". This concerns the morphological and electrophysiological characteristics of neurons when exposed to CNT substrates. Most of the results in this area have been obtained in culture and compared against previously established controls. Cell cultures, we argue, are a reasonable experimental model to demonstrate neurocompatibility, as they can be repeated with no loss in generalization.

5.1 Viability and morphology of neurons interacting with CNT substrates

The first results on the interaction of cultured neurons with CNT coated substrates were somewhat controversial: rat hippocampal neurons did not thrive when growing on CNT substrates. This was confirmed by two independent studies: the first (Mattson et al., 2000) admitted some compatibility but also showed long-term (8 days) decreased branching of neuronal processes, while the second (Hu et al., 2004) demonstrated, with quantitative growth cone measurements, that neurite growth in cultured rodent hippocampal cells was different than in control dishes. Similar results were shown for SWCNT substrates and NG108 neuroblastoma (cultured) cells, wherein the cells differentiated but at a reduced rate when compared to tissue-treated polystyrene controls (Liopo et al., 2006).

These early results may have been due to the CNT substrate preparation: highly purified CNTs sheets or yarns were later shown to be conducive to neuronal attachment (Galvan-Garcia et al., 2007). Extension of processes was also comparable to neurons grown on control substrates. Conductivity of the CNT substrate also seemed to matter in terms of neurite outgrowth (Malarkey et al., 2009). Only a small range of conductivities of SWNT-PEG (poly-ethylene-glycol) substrates supported neuronal growth and processes extension. Hippocampal neurons grown on vertically aligned MWCNTs arrays were healthy and growth was comparable to control cultures on plastic Petri dishes (Wang et al., 2006). Successful neuronal growth and interaction with CNTs has now been demonstrated by several groups and their neurocompatibility was confirmed (Ben-Jacob & Hanein 2008; Keefer et al., 2008; Khraiche et al. 2009; Lovat et al. 2005; Lobo et al. 2008).

CNTs present an effective and consistent anchoring site for neuronal attachment and development, and for glial cell differentiation (Jang et al., 2010; Sorkin et al., 2009). CNT coated surfaces are neuro-adhesive in *in vitro* applications (Galvan-Garcia et al., 2007; Lobo et al. 2008). Skillfully designed studies have shown CNT electrodes can be used to position and form stable networks due to mechanically intact contacts between the neurons and the CNTs. The neurons move toward CNT covered surfaces and single neurons position themselves on CNT surfaces. A reasonable hypothesis for the greater affinity of neurons to move specifically towards CNTs coated sites is the higher polylysine adsorption on CNTs. This translates into a more friendly (also more hydrophilic) surface on the CNT than in adjacent areas. The second hypothesis, not necessarily contrary to the first, poses that the nano-mesh structure of the deposited CNTs simulates the structure of the extracellular matrix (ECM). Our current understanding of the electro-mechanical-chemical coupling is very poor. The neuronal affinity to CNTs may be due to the varied nature of CNT production, deposition technique, orientation, and various functionalization ligands.

5.2 Electrical properties of cells impacted by CNT

Neuronal cell cultures grown on SWCNT coated glass substrates showed increased synaptic activity and consequently also increased excitability when compared to control glass substrates. The increase in neuronal activity could be due to a "bidirectional electrotonic current transfer, redistributing the charge along the surface of the membrane" (Lovat et al., 2005). Other studies have also shown that cultured cells on SWCNT substrates maintained their electrohysiological responses comparable to control dishes (Lovat et al., 2005; Mazzenta et al., 2007). However, Cellot et al (2009) demonstrated the presence of an additional somatic membrane depolarization following several action potentials in a burst. An after-depolarization occurs indirectly due to dendritic calcium electrogenesis. This phenomenon is commonly observed during backpropagating action potentials.

"Intimate contacts" were reported between hippocampal neurons and the SWCNTs; this was demonstrated through scanning electron microscope images. These intimate contacts were believed to create a physical channel, which would electrically couple nanotubes to neurons, forming a sort of short-circuit. This short-circuit would ultimately lead to the after-depolarization (Cellot et al., 2009).

Once neurons are plated in primary cell cultures, they extend neuronal processes and make synapses, provided the media is appropriately replenished, and the pH and temperature kept constant (at 7.4 and around 37°C). After 5 to 7 days *in vitro* (DIV) electrophysiological (spontaneous or stimulated) activity can be recorded, and action potentials are the traditional unit of measure in such cultures (Van Pelt et al., 2004). The same electrophysiological signature signal can be measured earlier, around DIV 4, when neurons are exposed to CNT-arrays. Even more interesting, the spontaneous activity increases continously until DIV 7, which is significantly different from the control cultures (Khraiche et al., 2009).

5.3 Stimulation and recording *in vitro* via CNT substrates

Experimental results with CNT-based substrates for stimulating and recording from neuronal cells have been very encouraging. CNT-neuronal interaction has resulted in increased efficiency for signal transmission (Mazzatenta et al., 2007), efficient stimulation (Gheith et al., 2006; Liopo et al., 2006; Lovat et al., 2005), and recordings with high signal-to-noise ratio (SNR) (Keefer et al., 2008 Sauter-Starace et al. 2009)**.** SWCNTs were the first CNTs tested for electrical stimulation of neurons (Liopo et al. 2006). Here dorsal root ganglion neurons were stimulated with SWCNTs deposited on glass coverslips. Another study to test the interaction of cells with carbon nanotubes involved deposition of multilayers of (PAA–/SWCNT+) (PAA: poly(acrylic acid)) on a glass slide. Electrical connections were made with ITO (indium-tin-oxide) strips contacting the SWCNT layer (Gheith et al., 2006) (figure 4). The membrane currents were measured by whole-cell patch clamp. Both of these studies reported fast inward transmembrane currents caused by ionic movement through voltage-gated sodium channels.

CNTs were also used to modify the active surface of MEAs which were then used to stimulate and record from neurons. Vertically aligned CNTs were also used to stimulate embryonic rat hippocampal neurons (Wang et al., 2006). In this case, stimulation current pulses were applied through MWCNT pillars. The evoked APs were optically identified by measuring variance in intracellular calcium using Fluo-4, a calcium indicator. Later, vertically aligned CNTs were embedded in parylene-C to create a flexible MEA (Lin et al., 2009). The flexible CNT-MEAs were able to successfully record spontaneous spikes from the crayfish nerve cord. Ben Jacob et

al (2008) used planar CNTs-MEAs to record from and stimulate neuronal cell lines. APs generated by ganglion cells were recorded by SWCNT- MEAs in greater proportion when compared to geometrically identical Pt-MEAs (Gabriel et al., 2009). CNT probes developed to interface with neurons both intracellularly and extracellularly were comparable in performance to traditionally used glass electrodes with silver/silver chloride wires (Yeh et al., 2009). Steam plasma treatment made MWCNT MEAs hydrophillic (Chen et al., 2010) and were then used to record extracellular APs from a neural cell from crayfish.

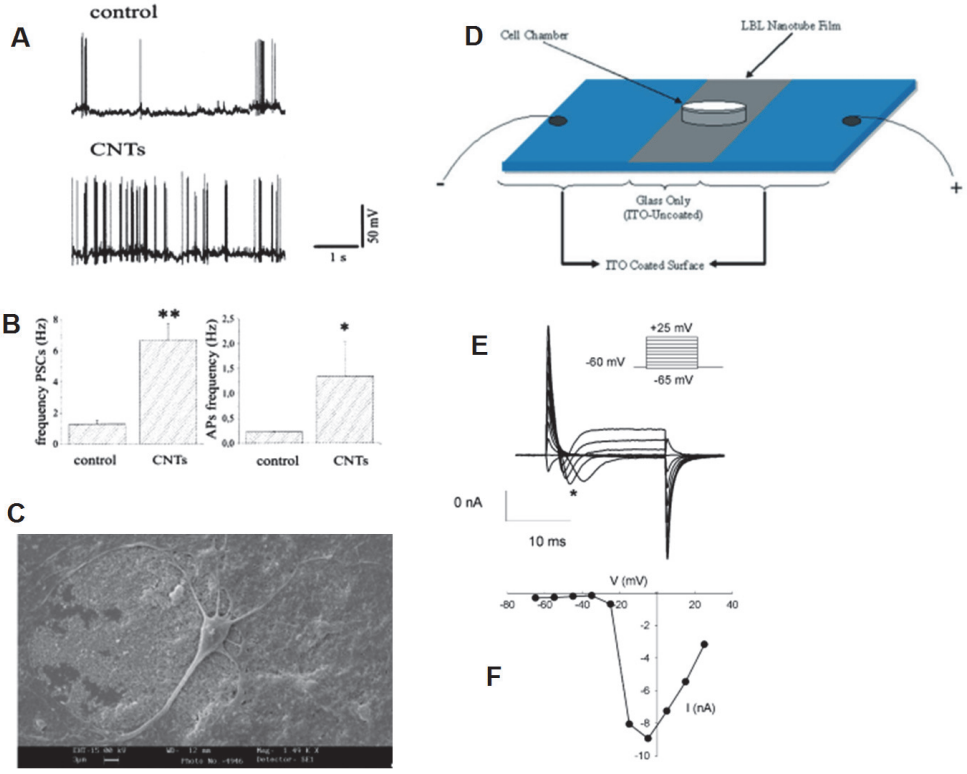

Fig. 4. (A) Spontaneous firing activity recorded in current clamp mode from cultured hippocampal neurons. The activity is enhanced on CNT substrate in comparison to control. (B) Increase in PSCs as well as APs frequency on CNT substrates is shown in a histogram plot. (C) SEM images of neonatal hippocampal neuron after 8 days in culture on coated MWCNT surface on a peptide-free glass. (D) Illustration of the setup used for stimulating a cell in culture via a SWCNT layer. (E) Ionic currents were recorded in the whole-cell voltage-clamp while a (inset) 10 mV increment stimulation protocol was applied through the pipette. (F) Plot of peak inward currents from (E) as a function of stimulation voltage. (A-C) Reprinted with permission from (Lovat et al., 2005), copyright (2005) American Chemical Society. (D-F) Reprinted with permission from (Gheith et al, 2006), copyright (2006) Wiley.

Efforts to demonstrate neurocompatibility of CNT substrates have yielded great results: in summary, cells can be successfully cultured on carbon nanotubes with no damage to their morphology or impairment to their electrophysiological activity. On the contrary: these preliminary efforts have generated questions that point to other modes of interaction between cells and CNTs. We argue that this interface holds many more open questions that can only be addressed through detailed experimental investigations.

6. CNT deposition methods

CNT films coated on neural interfaces have been produced by solvent evaporation, electrochemical deposition, chemical vapor deposition (CVD), layer-by-layer assembly, and electrophoresis. Different groups have used the same techniques with variations in several parameters, either in terms of using a different functionalized group, dispersing solution, co-deposition material material, or substrate. Examples of each method used to fabricate an implantable neural electrode as discussed below For every technique described, the background questions are how straightforward the deposition or growth is, which impacts cost, and how biocompatible the resulting electrode surface and bioavailable species are.

6.1 Chemical vapor deposition

In CVD a hydrocarbon gas provides with carbon atoms that grow on seeded metallic catalysts (Cassell et al., 1999). These catalytic metals are seeded onto metallic tracks realized on a substrate through standard microfabrication techniques; for example, using standard UV photolithography, electron-beam evaporation, and resist lift-off techniques. The substrates are usually silicon, silicon dioxide, quartz and metallic, or any other microfabrication-compatible substrate. The whole setup is then placed in a quartz tube, maintained at atmospheric pressure in a flow furnace. The hydrocarbon gas mixture is passed over the quartz at high temperatures (500°C to 1000°C). The gas catalytically decomposes over the metal particles (iron or nickel) at these temperatures. CNTs are formed on the catalyst layer. The size, geometry, location, quantity, and quality of yield is dependent on the support layer as well as on the metal catalyst (Cassell et al., 1999).

Recently, CVD was used to grow CNTs on penetrating microelectrodes. The tips of commercially available platinum-tungsten wires were electroplated with nickel via potentiostatic electrodeposition. Standard CVD process was used to grow CNTs on the micro electrode surface (Ansaldo et al., 2011) (figure 5(A,B)). An increase in CSC and decrease in impedance was reported for CVD-CNT electrodes. A similar CVD technique was used to grow CNTs vertically on MEAs (Wang et al., 2006) (figure 5(G,H,I)).

6.2 Electrochemical

Electrochemical deposition can be used to co-deposit CNTs with metals, conductive, and non-conductive polymers. The deposition of a conductive coating onto an electrode is achieved by putting a charged species on the electrode to be coated. The electrode is immersed into a solution containing oppositely charged desired species to be deposited. The electric current drives the counter ions to the electrode, oxidizing and reducing the desired species on the electrode surface. Co-deposition CNTs serves two purposes: enhancing the conductivity by lowering impedance and larger interacting surface area by increasing porosity. This in turn boosts the CSC and decreases the impedance. Electrochemical deposition can be used to coat variety of substrates and geometrical shapes.

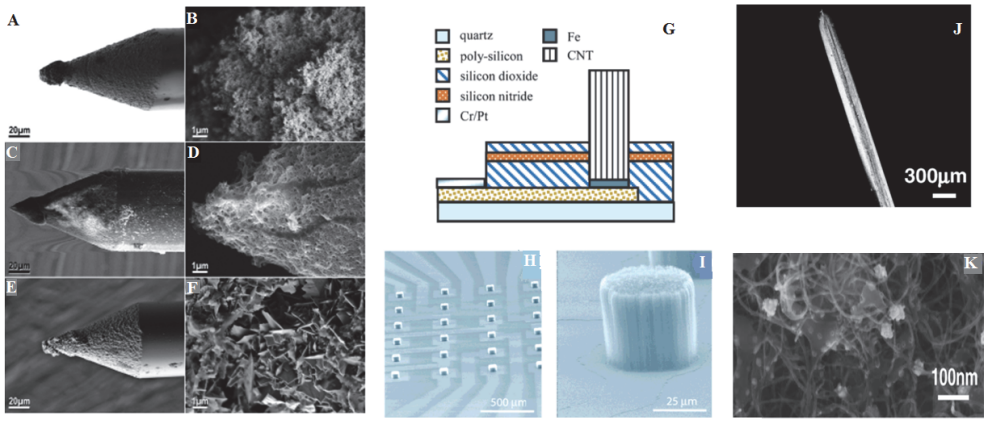

Fig. 5. SEM images reveals the morphology of (A,B) CNT-CVD, (C,D) Poly-pyrrole-CNT, (E,F) Gold-CNT coated penetrating microelectrodes. (G) Schematic of microelectrode array (MEA); (H) array of microelectrodes; (I) one microelectrode with forest-like CNTs extending vertically outside the plane of the MEA. (J) SEM image of stainless steel electrode after MWCNT deposition. (K) SEM image at higher magnification. Homogeneous random entangled arrangement of MWCNT over the metal substrate is observed, which increases the effective area of the electrode. (A-F) Reprinted with permission from (Ansaldo et al., 2011), copyright (2011) American Chemical Society. (G-I) Reprinted with permission from (Wang et al., 2005), copyright (2005) American Chemical Society. (J,K) Reprinted with permission from (Minnikanti et al., 2009), copyright (2009) Institute of Physics.

Keefer et al (2008) coated MEAs and penetrating wire electrodes with three different electrochemical CNT deposition methods using voltage controlled methods. The three coatings differed in functionalization and preparation methods. For all coatings, experimental results showed an increase in the charge storage capacity and a decrease in impedance when compared to bare wire electrodes. The morphology of the obtained surfaces, depending on the coating, is dramatically different. Figure 5 (A-F) shows examples of nanorough surfaces and of nanoporous surfaces (Ansaldo et al., 2011).

6.3 Electrophoresis

Electrophoresis is used in our laboratory to deposit CNTs onto metallic substrates (stainless steel and gold). Electrophoretic deposition (EPD) occurs due to the movement of charged particles in a suspension under the influence of an applied electric field. In the case of CNT EPD, the applied field deforms the particle double layer distortion and causes particle coagulation on the substrate. The coagulation is derived from the Derjaguin-Landau-Verwey-Overbeek (DLWVO) theory and is governed by London-Van der Waals forces (Sarkar & Nicholson, 1996). For each set of EPD experiments, a DC voltage of approximately 2V is applied between a bare stainless steel electrode (anode) and a bare gold electrode (cathode). The distance between the two electrodes needs to be kept at 1 mm or less in order for the deposition to take place during the first five to ten minutes. The field used in our experiments yields a stable cohesion of MWCNTs (figure

5(J,K)) onto metallic substrates (Boccaccini et al., 2006), (Minnikanti et al., 2009). The modulus of impedance of the bare stainless steel electrode decreases by two orders of magnitude for most of the frequencies tested. The cathodic charge storage capacity (CSCc) of bare electrodes significantly increases after MWCNT deposition, for example in one case the CSCc increased from 2.18 $\mu C/mm^2$ to 7.15 $\mu C/mm^2$ after deposition. Electrodes can be aged (for months) by exposing them to air, but they still maintain high CSCc. Some CNT-coated electrodes show oxygen uptake and further enhance their charge delivery capacity during the aging process.

EPD is a versatile procedure. While the results may be extremely sensitive to deposition parameters, factorial design of experiments can be applied in order to find an optimum deposition protocol, depending on substrate and CNT solution desired. In particular for NEs, water based dispersions are preferred. They can be used in EPD, thus reducing the presence of harsh toxic chemicals in the final implantable electrode. Further steps are commonly taken to improve adhesion, as for example microwave heating (Su et al., 2010).

6.4 Layer-by-layer assembly

Layer–by-layer assembly is the alternate adsorption of charged poly-ions on a substrate to create a thin coating. Each adsorption step leads to the formation of a monolayer poly-ion species. Poly-ions are formed after a poly-electrolyte dissociates in an aqueous solution. Jan et al (2009) used MWCNTs in poly(sodium styrene sulfonate) (PSS) and Poly vinyl alcohol (PVA) as alternate adsorption layers. The substrate used was a 400 μm diameter ball electrode made of platinum-iridium (Pt-Ir). The deposition process consisted of alternately immersing in each solution, followed by a rinse with deionized water and dried using an air jet. PVA/MWCNT coated electrodes decreased the impedance and increased the CSC of the Pt-Ir. Also, a higher CSC was reported for the PVA/MWCNT electrodes in comparison to polyethylenedioxythiophene and iridium oxide having identical thickness (Jan et al., 2009). Others have also reported using this method to deposit CNT on glass coverslips to grow and stimulate neuronal cultures (Gheith et al., 2006). This method can be used on arbitrarily shaped objects. This technique offers simplicity and flexibility. A variety of structures can be coated with thickness controlled at a nanoscale level.

6.5 Solvents and sprays

These two techniques have been used to deposit CNTs on planar substrates. A traditional substrate here is a glass coverslip. Using external electrical connections to these substrates neuronal cultures can be stimulated. These techniques have not been used to coat implantable NEs, as adhesion and long term stability haven't been characterized yet.

6.5.1 Solvent

This method involves dispersing CNTs in organic solvents. CNTs are deposited onto substrates as thin films as the organic solvent evaporates. Lovat et al (2005) suspended functionalised MWCNTs in DMF and then deposited the solution as drops via a pipette on top of the glass coverslips. MWCNTs attached to the glass surface as the solvent evaporated. The advantage of this method is that it is economical and operates at room temperature and pressure.

6.5.2 Spray

Compressed air can break down an aqueous media into a fine layer of deposited mist on a heated substrate. The heat causes the aqueous portion of the deposited mist to evaporate and thus leaves a thin continuous film. The deposition thickness is dependent on the flow rate of the solution and speed at which the nozzle moves towards the substrate. Malarkey et al (2009) deposited CNTs on glass coverslips by spraying an aqueous media of SWCNT-PEG using an airbrush. The SWCNT-coverslips were heated to 160° C to form uniform films (Malarkey et al., 2009). The advantages include economical, flexible procedure and the usage of aqueous based solutions.

7. CNT coated implants: *in vivo* studies

The ultimate test of an implantable electrode is the experimental demonstration of charge transfer after surgery. Hopefully many months later, that same electrode will still transfer charge to and from the central nervous system, without significant inflammation or mechanical disruption to the tissue: this will be the *litmus* test for that material. Throughout this chapter we have taken the reader across a wide field: we have touched on electrochemistry, principles of charge transfer, biocompatibility, mechanical and electrical requirements for electrodes, and methods for deposition of CNTs onto conductive and non-conductive substrates. We have attempted to present an unbiased description of the available literature in the field of neural interfaces mediated by CNTs, and have pulled insights from adjacent fields which, we believe, impact the engineering of such electrodes.

We turn now to the *litmus* test mentioned above: a deft insertion, seamless integration with the central nervous system, and then the electronic and ionic flow across the electrode-tissue interface is the objective of these CNT-coated electrodes. The first time a CNT electrode was used in an animal, chronically implanted, as a recording electrode was in 2008. Keefer et al (2008) reported the successful recording of local field potentials (LFPs) via MWCNT electrodes in two different animal models. LFPs are defined as the combined extracellular activity from multiple neurons. Two types of electrochemically deposited MWCNT electrodes were implanted in the motor cortex of anesthetized rats: MWCNT-Au-tungsten wire stereotrode, and MWCNT/Ppy-modified stainless steel electrodes. Both MWCNT and control electrodes recorded neural activity from a common source. However, single neuron spikes measured via MWCNT electrodes had larger amplitude and those electrodes (MWCNT) presented greater sensitivity for detecting neuronal activity.

MWCNT coatings using covalent chemistry were also investigated by that same research group (Keefer et al., 2008). The acyl-chloride modified nanotubes were covalently attached to amine-coated stainless steel electrodes. These electrodes along with control (uncoated electrodes) were implanted in the V4 region visual cortex of a monkey. The measured LFP traces (figure 6(A,B)) for both electrodes show a strong temporal correlation, aindicative of a common origin of the measured signal. Here also the measured spike amplitude of the MWCNT-coated electrode was larger than in controls. Power spectra analysis shows that the MWCNT electrode data had more power in the frequency range of 1-300 Hz. Inspection of the surface morphology of explanted MWCNT electrodes revealed mechanical stability even after penetrating through the dura matter.

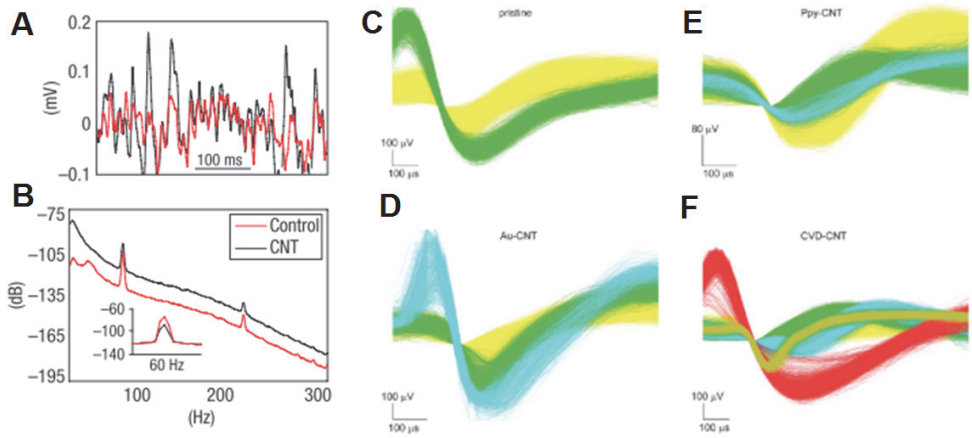

Fig. 6. (A) LFP traces. (B) Power spectral density (PSD) analysis from CNT coated compared with control electrodes. PSD with 60-Hz line noise subtracted. The LFP amplitude and average power is greater with lower 50 Hz for CNT electrodes in comparison to controls. Inset: PSD with 60-Hz line noise subtracted .(C-F) Single unit activity from an acute session, using non-coated (pristine) and coated (Ppy,Au,CVD)-CNT electrodes. Sorted units are color coded, each representing one neuron. (A-B) Reprinted with permission from (Keefer et al, 2008), copyright (2008) Nature, (C-F) Reprinted with permission from (Ansaldo et al, 2011), copyright (2011) American Chemical Society.

Ansaldo et al (2011) recorded intracortical neuronal activity in rat cortex with three types of CNT coated electrodes and compared it to a control electrode. Quartz-insulated platinum/tungsten wires with CVD grown CNT coatings (CVD-CNT), PPy-CNT and Au-CNT nano composites were used as electrodes. This group is the first to record single unit neural signal *in vivo* via CVD deposited CNTs on microelectrodes in animal models (figure 6(C-F)). The impedance of the CNT electrodes did not change significantly before of after the recordings. The authors conclude that the CVD deposited CNT is the best electrode in terms of robustness, but the use of high quantities of nickel will prevent the chronic use of these electrodes.

Our group developed electrophoretically deposited MWCNT electrodes, with the explicit requirement of wide frequency stimulation of deep brain structures (Minnikanti et al., 2010). We conducted acute implants in the rodent hippocampus to evaluate the *in vivo* performance of the MWCNT electrodes, and to compare that performance with the *in vitro* results. *In vivo* and *In vitro* (phosphate buffered saline, pH 7.4) analysis follows the same regime, with *in vitro* tests done both prior and subsequently to implanting the electrode. The analysis consisted of 30 CV cycles (50 mV/s, -0.7 V to 0.7 V) followed by an EIS cycle (5 mHz to 50 kHz, 10 mVpp). The developed MWCNT electrodes maintained their CSCc and impedance *in vivo* (figure 7). EIS performed *in vitro* and *in vivo* showed that the impedance modulus was not significantly affected when electrodes are implanted in deep brain structures (figure 7). This behavior is unlike that observed in traditional electrodes, where the charge decreases, and the impedance increases, during and after implantation.

We also investigated the immediate response to low-frequency stimulation by evaluating the transcriptional levels of IL-1β and TLR2 using reverse-transcriptase polymerase chain

reaction (RT-PCR). Two key molecules involved in the signaling cascades for inflammatory responses to damage in the CNS are the receptor TLR2 (Owens et al., 2005) and the pro-inflammatory cytokine IL-1β (Rothwell et al., 2000). IL-1β was upregulated as part of the inflammatory response to low-frequency stimulation, but TLR2 did not significantly increase in stimulated tissue when compared to controls. The inflammatory molecules initially active at the electrode–nervous tissue interface did not increase the impedance of MWCNT electrodes. Our investigation of the surface morphology post-implantantion shows that the MWCNT mesh withstands implantation. This is indicative of the robustness of the adhesion of nanotube film to the stainless steel surface and of the successful implant and extraction procedures used during the implant.

Tissue reaction determines the viability of a material as an implant material. A recent study, the first of its kind, investigated the chronic (12 weeks) response of muscle to implanted aligned carbon nanotubes (ACNTs) (Nayagam et al., 2011). Although not implanted in CNS, this study is highly relevant as it tests immoblized MWCNT arrays and not freely floating MWCNTs. Male guinea pigs were implanted with ACNT/SIBS (poly[styrene-b-isobutylene-b-styrene]) arrays. Two controls were used: SIBS sheets coated with stannous octoate as an internal positive control and poly-tetra-fluoro-ethylene as a negative controls. Histopathology was performed in order to assess the host response to controls as well as to the CNT material. The immobile CNTs did not elicit a significantly different host response when compared to controls. However, dislodged CNTs elicited an immune response and were phagocytosed. Also the immobile ACNTs had low levels of surface fouling. These results are encouraging towards the usage of CNTs as implantable electrodes and emphasizes on the necessity of a stable CNT deposition.

A chronic study involved implanting electrochemically co-deposited PPy/SWCNT on platinum wire electrodes in rat brains for 6 weeks (Lu et al., 2010). Bare platinum wires were used as controls. Tissue response was conducted by characterizing the expression of GFAP and NeuN immunostaining around the implant site. GFAP is a specific marker of astrocytes and NeuN reflects neuronal densities. Higher GFAP expression is indicative of elevated inflammatory processes. GFAP expression was lower for the coated electrode in comparison to the bare electrode. The neuronal density was higher as well as the neurons surrounding the implant were larger in comparison to bare electrode, signifying better neuronal survival. However, it has been shown that low impedance and high charge PPy-CNT coatings degrade when subjected to extensive periods of standard clinical stimulation pulses (Ansaldo et al., 2011). Thus the improved performance of co-depositing CNTs may be lost due to the instability of PPy.

Flexible CNTs MEAs were implanted in the motor region of a non-human primate (Sauter-Starace et al., 2009) for a chronic study. The MEAs consisted of polyimide support with alternate titanium nitride (TiN) and CNT electrodes. CNTs were deposited by CVD process. ECoG signals were recorded over the period of one year. The power spectra of recorded activity shows that CNT electrodes sensed greater amount of signal than the TiN electrodes. Absence of acute reactive gliosis covering the MEAs was reported.

A CNT-NE was recently used as interface with the nervous system of an insect (Tsang et al., 2010). The authors microfabricated flexible neuroprosthetic probes (FNPs) with CNT-Au nanocomposites. The FNPs were a part of a telemetry system interfacing with the insect's CNS. The implant was successfully tested in adult as well as in pupal stage moths. The applied stimulation via CNT-FNPs was able to force an unbound flying insect to turn.

In vitro experiments recreate a limited environment faced by a NE. Thus acute and chronic *in vivo* studies are crucial for evaluating the true performance of a NE. Although few *in vivo* studies have been conducted for CNT based recording and stimulating NEs, so far they show promising results. Collectively, these studies encourage the use of CNTs for the development of neuroprosthetic devices as long as they are immobilized. More chronic studies need to be performed before the judgment is passed on the performance and effect of CNT-based implantable NEs.

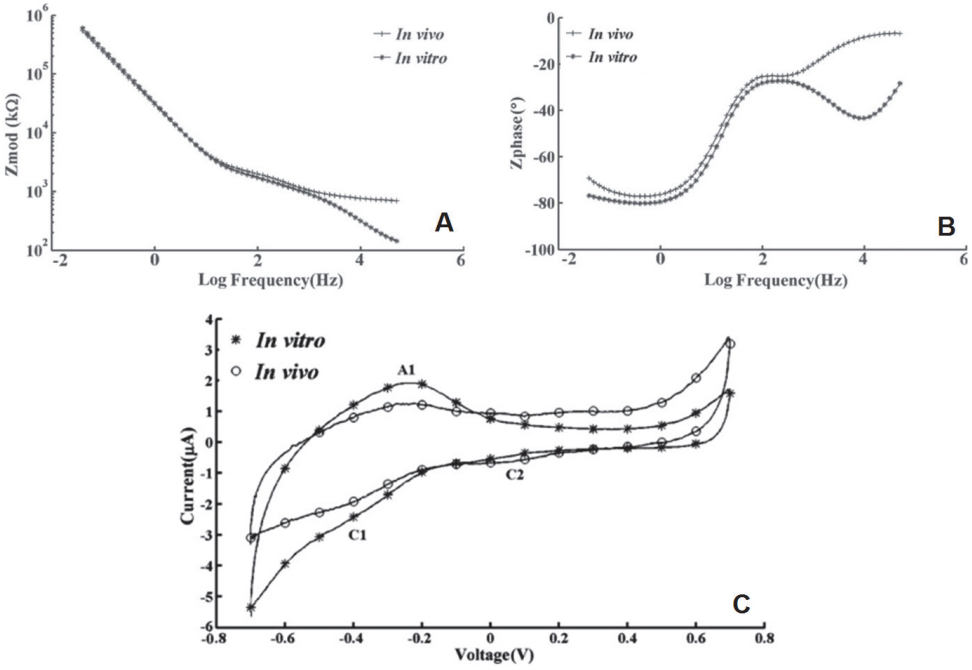

Fig. 7. Bode plots comparing (A) impedance modulus and (B) impedance phase (C) CV of a single bare stainless steel electrode (◦) to a MWCNT electrode (+). Measurements use a three electrode setup in PBS (pH 7.4) solution with Ag/AgCl as the reference electrode and platinum foil as a counter electrode. Lowering of impedance is observed over the measured frequency range. For the bare stainless steel electrode, CSCc = 0.488 mC cm^{-2} ; for the MWCNT-coated electrode, CSCc = 0.996 mC cm^{-2}. Reprinted with permission from (Minnikanti et al., 2010). Copyright (2010) Institue of Physics.

8. Conclusions

Current NE substrates used clinically are metallic (Greenberg & Rezai, 2003). In the past few years, issues with the processibility of conductive polymeric materials were overcome, and they became viable alternatives to metal electrodes (Cui & Zhou, 2007; Cui et al., 2001; Richardson-Burns et al., 2007). However, stability of conductive polymers is questionable (Ansaldo et al., 2011; Peixoto et al., 2009). CNTs, with their distinctive properties, can improve the performance of NE, as a coating over the metallic electrodes (Minnikanti et al., 2010) or when electrochemically co-deposited with conductive polymers (Keefer et al., 2008).

Over a decade ago the first CNT-neuronal experiment was performed (Mattson et al., 2000). Still, the true nature of the CNT-neuron interface remains an open question. Certain unique interface features offer an edge over current NE materials. Interaction with CNTs rearranges the charge along the membrane surface to increases neuronal excitability (Lovat et al., 2005). This could be particularly useful for NEs. If passive contact increased the excitability of neurons *in vivo* this would reduce the required charge to stimulate neurons. The enhanced cell adhesive property of CNTs may present an improved tissue–electrode interaction. This may reduce the need for the adhesion promoting layer, for example laminin or polylysine. Recently simulation results of stimulating the brain using a CNT based optically activated stimulator was presented (Mohy-Ud-Din et al., 2010). The idea was to use the implantable CNT stimulator that transduces light into electrical current. Unlike the traditional opto-genetic approach, in this case the genetic modification of neurons is not necessary.

Electrodes based on MWCNTs and deposited through electrophoresis were developed in our lab and presented a very interesting observation not related to the CSC, but to the preservation of the underlying substrate electrochemistry (Minnikanti et al., 2009). We have tested the same deposition method with different substrates, and all of them kept their characteristic reduction-oxidation peaks upon MWCNT deposition. Those CNT electrodes present an interesting *in vivo* behavior: they maintained their CSC *in vivo* and *in vitro* in acute scenarios (Minnikanti et al., 2010). The inflammatory response from the tissue hinders the charge transfer in acute and chronic situations. Tracking of inflammatory response *in vivo* is of importance if the objective of the implant is charge transfer. We have demonstrated that certain inflammatory molecules, initially active at the electrode-nervous tissue interface, do not prevent charge transfer neither increase the impedance of MWCNT electrodes in acute implants (Minnikanti et al., 2010). This effect of molecular interaction occurring at the interface of MWCNTs and neural tissue needs to be further investigated. This will help identify the key molecules in this unique behavior and thus create a model for testing the potential of any material as a neural implant or electrode.

Characterization of the CNT-neuron interface, at least electrically, has been focused on using SWCNTs as substrates (Gheith et al., 2006; Liopo et al., 2006; Mazzatenta et al., 2007). Many other aspects need to be investigated such as interacting protein conformational changes, variation in depolarization or hyperpolarization, and protein expression and adhesion when in contact with CNTs. Care needs to be taken before correlating or extrapolating the data. CNTs show promise as a next generation neuroprostheitc material. These are diamonds in raw waiting to be polished the *right* way.

9. References

Ajayan, P.M., 1999. Nanotubes from Carbon. *Chemical Reviews*, 99(7), 1787-1800.

Anderson, J., 2004. Inflammation, Wound Healing, and the Foreign Body Response. In B. D. Ratner, ed. *Biomaterials science: an introduction to materials in medicine*, ISBN 9780125824637 Academic Press.

Ansaldo, A., Castagnola, E., Maggiolini, E., Fadiga, L., & Ricci, D., 2011. Superior Electrochemical Performance of Carbon Nanotubes Directly Grown on Sharp Microelectrodes. *ACS Nano, 5(3),2206-2214.*

Bard, A.J. & Faulkner, L.R., 2006. *Electrochemical methods: fundamentals and applications*, ISBN 8126508078 A1bazaar.

Barisci, J.N., Wallace, G.G. & Baughman, R.H., 2000. Electrochemical studies of single-wall carbon nanotubes in aqueous solutions. *Journal of Electroanalytical Chemistry*, 488(2), 92-98.

Baxendale, M., 2003. Biomolecular applications of carbon nanotubes. *IEE Proceedings Nanobiotechnology,* 150 (1), 3-8.

Ben-Jacob, E. & Hanein, Y., 2008. Carbon nanotube micro-electrodes for neuronal interfacing. *Journal of Materials Chemistry*, 18(43), 5181–5186.

Bhatt, J., 2001. Electrical stimulation in medical sciences: from basic to applied. *Journal of Applied Basic Medical Sciences*, 3(3), 49-51.

Boccaccini, A.R., Cho, J., Roether, J.A., Thomas, B.J.C., Minay, E.J., & Shaffer, M.S.P., 2006. Electrophoretic deposition of carbon nanotubes. *Carbon* 44 (15), 3149-3160.

Cassell, A.M., Raymakers, J.A., Kong, J., & Dai, H., 1999. Large Scale CVD Synthesis of Single-Walled Carbon Nanotubes. *The Journal of Physical Chemistry B* 103 (31), 6484-6492.

Cellot, G., Cilia, E., Cipollone, S., Rancic, V., Sucapane, A., Silvia Giordani, S., & Gambazzi, L., 2009. Carbon nanotubes might improve neuronal performance by favouring electrical shortcuts. *Nature Nanotechnology,* 4 (2), 126-133.

Chen, C.H., Su, H.C., Chuang, S.C., Yen, S.J., Chen, Y.C., Lee, Y.T., Chen, H., Yew, T.R., Chang, Y.C., Yeh, S.R., & Yao, D.J., 2010. Hydrophilic modification of neural microelectrode arrays based on multi-walled carbon nanotubes. *Nanotechnology,* 21 (48), 485501.

Ciofani, G., Raffa, V., Vittorio, O., Cuschieri, A., Pizzorusso, T., Costa, M., & Bardi, G., 2010. In vitro and in vivo biocompatibility testing of functionalized carbon nanotubes. *Methods in Molecular Biology (Clifton, N.J.)*, 625, 67-83.

Craighead, H.G., Turner, S.W., Davis, R.C., James, C., Perez, A.M., St. John, P.M., Isaacson, M.S., Kam, L., Shain, W., & Turner, J.N., & Banker, G., 1998. Chemical and topographical surface modification for control of central nervous system cell adhesion. *Biomedical Microdevices*, 1 (1), 49–64.

Crow, D.R., 1994. *Principles and applications of electrochemistry*, ISBN 0748743782 , CRC.

Cui, X.T., Lee, V.A., Raphael, Y., Wiler, J.A., Hetke, J.F., Anderson, D.J., & Martin, D.C., 2001. Surface modification of neural recording electrodes with conducting polymer/biomolecule blends. *Journal of biomedical materials research* 56 (2), 261–272.

Cui, X.T. & Zhou, D.D., 2007. Poly (3, 4-ethylenedioxythiophene) for chronic neural stimulation. *IEEE Transactions on Neural Systems and Rehabilitation Engineering,* 15 (4), 502–508.

Du, C. & Pan, N., 2006. High power density supercapacitor electrodes of carbon nanotube films by electrophoretic deposition. *Nanotechnology*, 17(21), 5314-5318.

Evans, D.H., O'Connell, K.M., Petersen, R.A., & Kelly, M.J., 1983. Cyclic voltammetry. *Journal of Chemical Education* 60 (4), 290.

Fang, W.C., Huang, J.H., Chen, L.C., Su, Y.O., Chen, K.H., & Sun, C.L., 2006. Carbon Nanotubes Grown Directly on Ti Electrodes and Enhancement of Their Electrochemical Properties by Nitric Acid Treatment. *Electrochemical and Solid-State Letters*, 9 (1), A5-A8.

Gabriel, G., Gómez, R., Bongard, M., Benito, N., Fernández, E., & Villa, R., 2009. Easily made single-walled carbon nanotube surface microelectrodes for neuronal applications. *Biosensors and Bioelectronics* 24 (7), 1942-1948.

Galvan-Garcia, P., Keefer, E.W., Yang, F., Zhang, M., Fang, S., Zakhidov, A.A., Baughman, R.H., & Romero, M.I., 2007. Robust cell migration and neuronal growth on pristine

carbon nanotube sheets and yarns. *Journal of Biomaterials Science, Polymer Edition*, 18 (10), 1245–1261.

Gheith, M.K., Pappas, T.C., Liopo, A.V., Sinani, V.A., Shim, B.S., Motamedi, M., Wicksted, J.P., & Kotov, N.A., 2006. Stimulation of Neural Cells by Lateral Currents in Conductive Layer-by-Layer Films of Single-Walled Carbon Nanotubes. *Advanced Materials,* 18 (22), 2975-2979.

Greenberg, B.D. & Rezai, A.R., 2003. Mechanisms and the current state of deep brain stimulation in neuropsychiatry. *CNS spectrums*, 8, 522–528.

Griffith, R.W. & Humphrey, D.R., 2006. Long-term gliosis around chronically implanted platinum electrodes in the Rhesus macaque motor cortex. *Neuroscience Letters*, 406(1-2), 81-86.

Guo, L., Morris, D.G., Liu, X., Vaslet, C., Hurt, R.H., & Kane, A.B., 2007. Iron Bioavailability and Redox Activity in Diverse Carbon Nanotube Samples. *Chemistry of Materials,* 19(14), 3472-3478.

Guyton, D.L. & Terry Hambrecht, F., 1974. Theory and design of capacitor electrodes for chronic stimulation. *Medical & Biological Engineering*, 12(5), 613-620.

Hu, C.G, Wang, W.L., Liao, K.J., Liu, G.B., & Wang, Y.T., 2004. Systematic investigation on the properties of carbon nanotube electrodes with different chemical treatments. *Journal of Physics and Chemistry of Solids* 65 (10), 1731-1736.

Hu, H., Ni, Y., Montana, V., Haddon, R.C., & Parpura, V., 2004. Chemically Functionalized Carbon Nanotubes as Substrates for Neuronal Growth. *Nano Letters,* 4 (3), 507-511.

Hu, H., Zhao, B., Itkis, M.E., & Haddon, R.C., 2003. Nitric Acid Purification of Single-Walled Carbon Nanotubes. *The Journal of Physical Chemistry B,* 107 (50), 13838-13842.

Iijima, S. & Ichihashi, T., 1993. Single-shell carbon nanotubes of 1-nm diameter. *Nature*, 363(6430), 603-605.

Jakubek, L.M., Marangoudakis, S., Raingo, J., Liu, X., Lipscombe, D., & Hurt, R.H., 2009. The inhibition of neuronal calcium ion channels by trace levels of yttrium released from carbon nanotubes. *Biomaterials* ,30 (31), 6351-6357.

Jan, E., Hendricks, J.L., Husaini, V., Richardson-Burns, S.M., Sereno, A., Martin, D.C., & Kotov, N.A., 2009. Layered Carbon Nanotube-Polyelectrolyte Electrodes Outperform Traditional Neural Interface Materials. *Nano Letters,* 9 (12), 4012-4018.

Jang, M.J., Namgung, S., Hong, S., & Nam, Y., 2010. Directional neurite growth using carbon nanotube patterned substrates as a biomimetic cue. *Nanotechnology,* 21 (23), 235102.

Keefer, E.W., Botterman, B.R., Romero, M.I., Rossi, A.F., and Gross, G.W., 2008. Carbon nanotube coating improves neuronal recordings. *Nature Nanotechnology,* 3 (7), 434-439.

Khraiche, M.L., Jackson, N., & Muthuswamy, J. 2009. Early onset of electrical activity in developing neurons cultured on carbon nanotube immobilized microelectrodes. *Conference Proceedings: Annual International Conference of the IEEE Engineering in Medicine and Biology Society,* 777-780.

Krupke, R., Hennrich, F., Löhneysen, H, & Kappes, M.M., 2003. Separation of Metallic from Semiconducting Single-Walled Carbon Nanotubes. Science, 301 (5631), 344 -347.

Lasia, A., 1999. Electrochemical impedance spectroscopy and its applications. *Modern aspects of electrochemistry*, 32, 143–248.

Lee, W. & Parpura, V., 2009. Chapter 6 - Carbon nanotubes as substrates/scaffolds for neural cell growth. *Progress in Brain Research*, 180, 110-125.

Lin, C.M., Lee, Y.T., Yeh, S.R., & Fang, W., 2009. Flexible carbon nanotubes electrode for neural recording. *Biosensors and Bioelectronics,* 24 (9), 2791-2797.

Liopo, A.V., Stewart, M.P., Hudson, J., Tour, J.M., & Pappas, T.C., 2006. Biocompatibility of Native and Functionalized Single-Walled Carbon Nanotubes for Neuronal Interface. Journal of Nanoscience and Nanotechnology, 6, 1365-1374.

Lobo, A.O., Antunes, E.F., Machado, A.H.A, Pacheco-Soares, C., Trava-Airoldi, V.J., & Corat, E.J., 2008. Cell viability and adhesion on as grown multi-wall carbon nanotube films. *Materials Science and Engineering: C,* 28 (2), 264-269.

Lovat, V., Pantarotto, D., Lagostena, L., Cacciari, B., Grandolfo, M., Righi, M., Spalluto, G., Prato, M., and Ballerini, L., 2005. Carbon Nanotube Substrates Boost Neuronal Electrical Signaling. *Nano Letters*, 5 (6), 1107-1110.

Lu, Y., Li, T., Zhao, X., Li, M., Cao, Y., Yang, H., & Duan, Y.Y., 2010. Electrodeposited polypyrrole/carbon nanotubes composite films electrodes for neural interfaces. *Biomaterials*, 13(19), 5169-5181.

Macdonald, J.R. 1991. Application of Electrochemical Impedance Spectroscopy in Electrochemistry and Corrosion Science. In R. Varma & J. R. Selman, eds. *Techniques for characterization of electrodes and electrochemical processes*, ISBN 0471824992, Wiley.

Malarkey, E.B., Fisher, K.A., Bekyarova, E., Liu, W., Haddon, R.C., & Parpura, V., 2009. Conductive Single-Walled Carbon Nanotube Substrates Modulate Neuronal Growth. Nano Letters, 9 (1), 264-268.

Malarkey, E.B. & Parpura, V., 2007. Applications of Carbon Nanotubes in Neurobiology. *Neurodegenerative Diseases*, 4(4), 292-299.

Mattson, M., Haddon, R. & Rao, A., 2000. Molecular functionalization of carbon nanotubes and use as substrates for neuronal growth. *Journal of Molecular Neuroscience*, 14(3), 175-182.

Mayberg, H.S., Lozano, A.M., Voon,V., McNeely, H.E., Seminowicz, D., Hamani, C., Schwalb, J.M., & Kennedy, S.H., 2005. Deep Brain Stimulation for Treatment-Resistant Depression. *Neuron,* 45 (5), 651-660.

Mazzatenta, A., Giugliano, M., Campidelli, S., Gambazzi, L., Businaro, L., Markram, H., Prato, M., & Ballerini, L., 2007. Interfacing Neurons with Carbon Nanotubes: Electrical Signal Transfer and Synaptic Stimulation in Cultured Brain Circuits. *Journal of Neuroscience,* 27 (26), 6931-6936.

Merrill, D.R., Bikson, M. & Jefferys, J.G., 2005. Electrical stimulation of excitable tissue: design of efficacious and safe protocols. *Journal of Neuroscience Methods*, 141(2), 171-198.

Minnikanti, S., Pereira, M. G.A.G, Jaraiedi, S., Jackson, K., Costa-Neto, C.M., Li, Q., & Peixoto, N., 2010. In vivo electrochemical characterization and inflammatory response of multiwalled carbon nanotube-based electrodes in rat hippocampus. *Journal of neural engineering,* 7(1), 016002.

Minnikanti, S., Skeath, P. & Peixoto, N., 2009. Electrochemical characterization of multi-walled carbon nanotube coated electrodes for biological applications. *Carbon*, 47(3), 884-893.

Mohy-Ud-Din, Z., Woo, S.H., Kim, J.H., & Cho, J.H., 2010. Optoelectronic stimulation of the brain using carbon nanotubes. *Annals of Biomedical Engineering,* 38 (11), 3500-3508.

Monthioux, M. & Kuznetsov, V.L., 2006. Who should be given the credit for the discovery of carbon nanotubes? *Carbon*, 44(9), 1621–1623.

Nayagam, D. A. X., Williams, R.A., Chen, J., Magee, K.A., Irwin, J., Tan, J., Innis, P., et al. 2011. Biocompatibility of Immobilized Aligned Carbon Nanotubes. *Small*, 7(8), 1035-1042.

Ni, Y., Hu, H., Malarkey, E.B., Zhao, B., Montana, V., Haddon, R.C., & Parpura, V., 2005. Chemically Functionalized Water Soluble Single-Walled Carbon Nanotubes

Modulate Neurite Outgrowth. *Journal of Nanoscience and Nanotechnology,* 5, 1707-1712.

Niyogi, S., Hamon, M.A., Hu, H., Zhao, B., Bhowmik, P., Sen, R., Itkis, M.E., & Haddon, R.C., 2002. Chemistry of Single-Walled Carbon Nanotubes. *Accounts of Chemical Research* 35 (12), 1105-1113.

Owens, T., Babcock, A.A., Milward, J.M., & Toft-Hansen, H., 2005. Cytokine and chemokine inter-regulation in the inflamed or injured CNS. *Brain Research Reviews*, 48(2), 178-184.

Pancrazio, J. J., 2008. Neural interfaces at the nanoscale. *Nanomedicine,* 3 (6), 823-830.

Parent, A., 2004. Giovanni Aldini: From animal electricity to human brain stimulation. *The Canadian Journal of Neurological Sciences*, 31(4), 576–584.

Park, K.H., Chhowalla, M., Iqbal, Z., & Sesti, F., 2003. Single-walled Carbon Nanotubes Are a New Class of Ion Channel Blockers. *Journal of Biological Chemistry*, 278 (50), 50212 - 50216.

Peixoto, N., Jackson, K., Samiyi, R., & Minnikanti, S., 2009. Charge Storage: Stability measures in implantable electrodes. In *Annual International Conference of the IEEE, Engineering in Medicine and Biology Society, 2009*, pp. 658-661.

Perry, V.H., 1994. *Macrophages and the nervous system*, ISBN 1570590443, RG Landes.

Polikov, V.S., Tresco, P.A. & Reichert, W.M., 2005. Response of brain tissue to chronically implanted neural electrodes. *Journal of Neuroscience Methods*, 148(1), 1-18.

Radushkevich, L.V. & Luk'yanovich, V.M., 1952. Structure of the carbon produced in the thermal decomposition of carbon monoxide on an iron catalyst. *Zhur. Fizicheskoj Himii*, 26(1), 88–95.

Richardson-Burns, S. M, Hendricks, J.L., Foster, B., Povlich, L.K., Kim, D.H., & Martin, D.C., 2007. Polymerization of the conducting polymer poly (3, 4-ethylenedioxythiophene)(PEDOT) around living neural cells. *Biomaterials*, 28 (8), 1539–1552.

Rothwell, N.J. & Luheshi, G.N., 2000. Interleukin 1 in the brain: biology, pathology and therapeutic target. *Trends in Neurosciences*, 23(12), 618-625.

Salvetat, J.P., Bonard, J.M., Thomson, N.H., Kulik, A.J., Forr, L., Benoit, W., & Zuppiroli, L., 1999. Mechanical properties of carbon nanotubes. *Applied Physics A: Materials Science & Processing*, 69 (3), 255-260.

Sarkar, P. & Nicholson, P.S., 1996. Electrophoretic Deposition (EPD): Mechanisms, Kinetics, and Application to Ceramics. *Journal of the American Ceramic Society*, 79(8), 1987-2002.

Sauter-Starace, F., Bibari, O., Berger, F., Caillat, P., & Benabid, A.L., 2009. ECoG recordings of a non-human primate using carbon nanotubes electrodes on a flexible polyimide implant. In *4th International IEEE/EMBS Conference on Neural Engineering* , 112-115.

Sawyer, D.T. & Roberts, J.L., 1974a. Controlled Current Methods. In *Experimental electrochemistry for chemists*. ISBN 9780471755609, Wiley, p. 394.

Sawyer, D.T. & Roberts, J.L., 1974b. Controlled Potential Methods. In *Experimental electrochemistry for chemists*. ISBN 9780471755609, Wiley, p. 340.

Servello, D., Porta, M., Sassi, M., Brambilla, A., & Robertson, M.M., 2008. Deep brain stimulation in 18 patients with severe Gilles de la Tourette syndrome refractory to treatment: the surgery and stimulation. *Journal of Neurology, Neurosurgery & Psychiatry* 79 (2), 136 -142.

Shim, M., Kam, N.W.S., Chen, R.J., Li, Y., & Dai, H., 2002. Functionalization of Carbon Nanotubes for Biocompatibility and Biomolecular Recognition. *Nano Letters,* 2 (4), 285-288.

Sinnott, S.B., 2002. Chemical functionalization of carbon nanotubes. *Journal of Nanoscience and Nanotechnology*, 2(2), 113–123.

Sorkin, R., Greenbaum, A., David-Pur, M., Anava, S., Ayali, A., Ben-Jacob, E., & Hanein, Y., 2009. Process entanglement as a neuronal anchorage mechanism to rough surfaces. *Nanotechnology,* 20 (1), 015101.

Stieglitz,T., 2004. Electrode Materials for Recording and Stimulation. In K. W. Horch & G. S. Dhillon, eds. *Neuroprosthetics theory and practice*. ISBN 9812380221 ,World Scientific Pub Co Inc.

Su, H.C., Chen, C.H., Chen, Y.C., Yao, D.J., Chen, H., Chang, Y.C., & Yew, T.R., 2010. Improving the adhesion of carbon nanotubes to a substrate using microwave treatment. *Carbon,* 48 (3), 805-812.

Treacy, M.M.J., Ebbesen, T.W. & Gibson, J.M., 1996. Exceptionally high Young's modulus observed for individual carbon nanotubes. *Nature*, 381(6584), 678-680.

Levine, R.B., & Voldman, J., 2010. Remote control of a cyborg moth using carbon nanotube-enhanced flexible neuroprosthetic probe. In *IEEE 23rd International Conference on Micro Electro Mechanical Systems (MEMS),* 39–42.

Van Pelt, J., Corner, M.A., Wolters, P.S., Rutten, W.L.C., & Ramakers, G.J.A., 2004. Longterm stability and developmental changes in spontaneous network burst firing patterns in dissociated rat cerebral cortex cell cultures on multielectrode arrays. *Neuroscience Letters* 361, (1-3), 86-89.

Varma, R. & Selman, J.R., 1991. *Techniques for characterization of electrodes and electrochemical processes*, ISBN 0471824992 , Wiley.

Velasco, F., Velasco, M., Velasco, A.L., Jimenez, F., Marquez, I, & Rise, M., 1995. Electrical Stimulation of the Centromedian Thalamic Nucleus in Control of Seizures: Long-Term Studies. *Epilepsia* 36 (1), 63-71.

Vitek, J.L., 2002. Mechanisms of deep brain stimulation: Excitation or inhibition. *Movement Disorders*, 17(S3), S69-S72.

Wang, K, Fishman, H.A., Dai, H., & Harris, J.S., 2006. Neural Stimulation with a Carbon Nanotube Microelectrode Array. *Nano Letters,* 6 (9), 2043-2048.

Williams, J.C., Hippensteel, J.A., Dilgen, J., Shain, W., & Kipke, D.R., 2007. Complex impedance spectroscopy for monitoring tissue responses to inserted neural implants. *Journal of Neural Engineering* 4 (4), 410-423.

Wilson, B.S., Finley, C.C., Lawson, D.T., Wolford, R.D., Eddington, D.K., & Rabinowitz, W.M., 1991. Better speech recognition with cochlear implants. *Nature,* 352 (6332), 236-238

Wood, K.W., Qi, H., D'Arcangelo, G., Armstrong, R.C., Roberts, T.M., & Halegoua, S., 1993. The cytoplasmic raf oncogene induces a neuronal phenotype in PC12 cells: a potential role for cellular raf kinases in neuronal growth factor signal transduction. *Proceedings of the National Academy of Sciences of the United States of America* 90 (11), 5016 -5020.

Wyatt, J. & Rizzo, J., 1996. Ocular implants for the blind. *Spectrum, IEEE,* 33(5), 47-53.

Xu, H., Bai, J., Meng, J., Hao, W., Xu, H., & Cao, J.M., 2009. Multi-walled carbon nanotubes suppress potassium channel activities in PC12 cells. *Nanotechnology,* 20 (28), 285102.

Yang, W., Thordarson, P., Gooding, J.J., Ringer, S.P., & Braet, F., 2007. Carbon nanotubes for biological and biomedical applications. *Nanotechnology,* 18 (41), 412001.

Yeh, S.R., Chen, Y.C., Su, H.C., Yew, T.R., Kao, H.H., Lee, Y.T., Liu, T.A., et al., 2009. Interfacing Neurons both Extracellularly and Intracellularly Using Carbon−Nanotube Probes with Long-Term Endurance. *Langmuir,* 25 (13), 7718-7724.

7

Carbon Nanotube Fabrication: Patent Analysis

Pao-Long Chang, Chao-Chan Wu and Hoang-Jyh Leu
Feng Chia University
Taiwan

1. Introduction

Patent documents contain important results of research and development. These documents have long been recognized as a very rich and potentially fruitful source of data for the study of innovation and technological change (Choi et al., 2007). Patent analysis is a valuable method that transfers patent documents into systematic and useful information. The information is helpful to evaluate technological development, monitor technological trends, manage R&D process, and make technological strategies (Chang et al., 2010). In general, patent bibliometric analysis is most commonly used to implement patent analysis (Narin, 1994). Bibliometric data that include such information as patent number, country, inventor, assignee, date of application, and so forth in patents are used to analyze the development and distribution of the patented technology. Furthermore, patent network analysis is an advanced technique of patent analysis suggested by Yoon & Park (2004). This method shows the overall relationship among all patents being studied as a visual network. Researchers can comprehend the overall structure intuitively and identify the influential patents in the patent network.

In the field of nanotechnology, carbon nanotubes (CNTs) possess important roles and technological key factor (Kuusi & Meyer, 2007). CNTs are composed of grapheme sheets rolled into seamless hollow cylinders with diameters within 50 nm. The fabrication of nanotubes is not a difficult task, since they can be found also in common environments such as the flame of a candle. But it is very difficult to control their size, orientation and structure, in order to be able to use them for technological tasks. In 1991, multi-wall nanotubes (MWNTs) were firstly discovered in a carbonaceous stalagmite-like deposit by Iijima (1991), which was the by-product of the fullerene growth process on the electrode. Then, single-wall nanotubes (SWNTs) were discovered in 1993 during the course of synthesizing carbon nanocapsules filled with magnetic fine metal particles (Fe, Co, Ni) (Iijima & Ichihashi, 1993; Bethune et al., 1993). The commonly manufacturing processes of CNTs contain different types of manufacturing technology such as arc-discharge, laser ablation, and chemical vapor deposition (CVD). Arc-discharge and laser ablation methods for the growth of CNTs have been actively pursued in the past ten years. Both methods involve the condensation of carbon atoms generated from evaporation of solid carbon sources. The temperatures involved in these methods are close to the melting temperature of graphite, 3000-4000^{o}C. Recent interest in CVD nanotube growth is also due to the idea that aligned and ordered CNT structures can be grown on surfaces with control that is not possible with arc-discharge or laser ablation techniques.

From recent research, CNTs have been demonstrated to possess remarkable mechanical, electronic and thermal properties with providing strong, light and high toughness traits. On mechanical properties, CNTs have high perfection in their structures and highest modulus of all known materials (Treacy et al., 1996). On electronic properties, CNTs are either metallic or semimetallic depending on the geometry (Saito et al., 1992). On thermal properties, thermal conductivity of CNTs is about twice as high as diamond (Thostenson et al., 2001). Due to these ideal properties, CNTs exhibit unique physical and chemical characteristics as being revolutionary advanced materials. Furthermore, CNTs have been proposed as new materials for single-molecular transistors, catalyst supports, electron field emitters in panel displays, molecular-filtration membranes, gas and electrochemical energy storages, energy-absorbing materials, and scanning probe microscope tips (Kuusi & Meyer, 2007).

Several studies have successfully revealed the use of patent analysis to analyze the development of nanotechnology (Hullmann, 2007; Wong et al., 2007; Chang et al., 2010). Recently, a great deal of attention is being paid to CNTs which represent novel and popular nanomaterials. CNTs have many extraordinary properties and different kinds of applications. Even though CNTs have many advantages and potential, currently some technical bottlenecks need to be solved. Therefore, it is necessary to monitor the current states and the future trends of the emerging technology before the next stage of technological development. This study implements patent analysis to explore the technological states and trends of CNTs in order to assist researchers in executing and managing technology for CNT fabrication.

In this study, patent bibliometric analysis and patent network analysis are used to analyze patents for CNT fabrication. First, we use patent bibliometric analysis to analyze bibliometric data in the patent documents for finding the developmental path of CNT fabrication and its current states. Then, we draw a network graph of the patents regarding CNT fabrication by using patent network analysis. We seek to find the overall relationship among the patents in the patent network and grasp the key technology of CNT fabrication. Finally, we suggest future directions and trends of CNT fabrication based on the results of analyses.

2. Methodologies

2.1 Data collection

The data of patent documents in the field of CNT fabrication were collected from the U.S. Patent and Trademark Office (USPTO) database available at www.uspto.gov. The search was made by looking for the code "carbon nanotube" or "CNT" in the titles of patent documents in recent ten years. Five experts in the area of CNT then reviewed the search results and eliminated the irrelevant ones. 97 patents issued from 2001 to 2010 were collected. The data set contains patents from U.S. Patent No. 6,331,690 to U.S. Patent No. 7,854,991. However, because the patent numbers are too long to be usable for patent analysis, the patents were sorted by issue date and labeled with serial numbers from 1 to 97, with number one being the oldest patent.

2.2 Patent bibliometric analysis

Patent bibliometric analysis is a research method utilizing bibliometrics to perform patent information analysis in order to evaluate technological activities (Narin, 1994). Bibliometric data such as patent number, document type, date of issue, country, title, inventor, assignee,

international patent classification, date of application, and so forth in patent documents are analyzed (Gupta & Pangannaya, 2000). Hence, the researcher can perform statistical calculations on the chosen set of bibliometric data to analyze the development and distribution of the patented technology. In this study, patent bibliometric analysis would be used to analyze 97 patents about CNT fabrication to uncover the developmental path and current states of CNT fabrication

2.3 Patent network analysis

Network analysis attempts to describe the structure of interactions (edges) between actors (nodes). Actors are the given entities in the network. The relationship among actors and the location of individual actors in the network provide rich information and assist the researcher in comprehending the overall structure of the network (Wasserman & Faust, 1994).

In recent, Yoon & Park (2004) used the concept of network analysis in patent analysis, and suggested patent network analysis. Particularly, Chang et al. (2010) applied this method to analyze the technological trends of carbon nanotube field emission display (CNT-FED) technology. This method uses the frequency of keywords occurrence in patent documents as the input base to produce a visual patent network. The relations among patents represent edges in the patent network while individual patents represent nodes. Patent network analysis visually displays all the relationship among the patents and assists the researcher in intuitively understanding the entire structure of the patent database. In addition, because network analysis uses several patent keywords as its input, this method is capable of detecting the internal structure of patent network and thereby produces useful results.

Patent network analysis uses two mathematical tools to present the information from the patent network, namely graph and quantitative technique. Graph can visually display the structure of a set of patents by generating a patent network. However, if too many patents are involved or a wide variety of patent relationship exits, graph will become too complicated to show the exact relationship among the patents. In this case, the indexes calculated from quantitative technique can clearly show the information on the patent network.

Following patent bibliometric analysis, patent network analysis would be used to examine the overall relationship among the patents about CNT fabrication and to find out the key patents. Primarily, this study adopts the below steps to graph the patent network:

Step 1. Technical experts select the relevant patent keywords based on the substance and characteristics of the patented technologies.

Step 2. Calculating the frequency of keywords occurrence in patent documents and integrate the data into keyword vectors. The keyword vectors from patent 1 to patent m are as follows:

$$\begin{aligned} &\text{Patent 1:} \quad (k_{11}, k_{12}, k_{13}, \cdots, k_{1n}) \\ &\text{Patent 2:} \quad (k_{21}, k_{22}, k_{23}, \cdots, k_{2n}) \\ &\qquad \vdots \quad \vdots \\ &\text{Patent } m\text{:} \quad (k_{m1}, k_{m2}, k_{m3}, \cdots, k_{mn}) \end{aligned} \tag{1}$$

For example, in the document of patent 1, the first keyword occur k_{11} times, the second keyword occur k_{12} times and so on as above.

Step 3. Utilizing Euclidian distance to calculate the distance between the patents and to establish the relationship among patents. If keyword vectors of patent *i* and patent *j* are defined as $(k_{i1}, k_{i2}, \cdots, k_{in})$ and $(k_{j1}, k_{j2}, \cdots, k_{jn})$ respectively, the Euclidian distance value (E_{ij}^d) between the two vectors is computed as follows:

$$E_{ij}^d = \sqrt{(k_{i1} - k_{j1})^2 + (k_{i2} - k_{j2})^2 + \cdots + (k_{in} - k_{jn})^2} \tag{2}$$

Step 4. Euclidian distance matrix (E^d matrix) is composed of all Euclidian distance values among all vectors. However, the E^d matrix must be dichotomized in order to graph the patent network. It is necessary to transform the real values of E^d matrix into standardized values from 0 to 1 for dichotomizing in the next step.

$$E_{ij}^s = \frac{E_{ij}^d}{Max(E_{ij}^d, i = 1, \cdots, m\ ; j = 1, \cdots, m)} \tag{3}$$

The E^d matrix is interpreted as dividing the all values of E^d matrix by the maximum value of E^d matrix. The all values of E^s matrix are from 0 to 1.

Step 5. The cell of the E^s matrix must be a binary transformation, comprising 0s and 1s if it is to exceed the cut-off value *p*:

$$I_{ij} = \begin{cases} 1, & \text{if } E_{ij}^s < p \\ 0, & \text{if } E_{ij}^s \geq p \end{cases} \tag{4}$$

The *I* matrix includes binary value where I_{ij} equals 1 if patent *i* is strongly connected with patent *j*. I_{ij} equals 0 if patent *i* is weakly connected with patent *j* or not at all connected. That is, if the E^s value is smaller than the cut-off value *p*, the connectivity between patent *i* and patent *j* is regarded as strong and the I_{ij} value is set to 1. Otherwise, the connectivity is considered weak and the I_{ij} value is set to 0. The determination of cut-off value is a task of trial-and-error. The researcher has to select a reasonable cut-off value so that the structure of the network becomes clearly visible. Then, the *I* matrix can be employed to develop a patent network.

Subsequently, the quantitative technique which contains two indexes can be utilized to examine the structure of the patent network. The first index that finds out the relatively important patents in the patent network is technology centrality index (TCI):

$$TCI_i = \frac{C_i}{n-1} \tag{5}$$

$C_i = \sum r$, *r*: ties of patent *i*

where n denote the number of patents. TCI of a patent network is interpreted as the ratio of the number of tied links to all n-1 other patents. It measures the relative importance of a subject patent by calculating the density of its linkage with other patents. That is, the higher the TCI, the greater the impact on other patents. TCI can be used to identify the influential patents in the field of the technology being studied. Moreover, detailed information on these influential patents needs to be obtained. Technological and strategic implication can be deduced from the information as well.

Moreover, the second index called technology cycle time (TCT) index can be used to measure the trends of technological progress in overall network. Let T_i be the application date of patent i, and the formula for calculating TCT index of patent i is shown below:

$$TCT_i = \underset{j}{Median} \left\{ \left| T_i - T_j \right| \right\} \tag{6}$$

where patent j and patent i are connected. It is defined as the median value of age gaps between subject patent and other connected patents. Shorter cycle time reflects faster technology progress; longer cycle time reflects slower technology progress. Thus, patents relating to a rapidly progressing technology should have a smaller TCT index than patents relating to a slowly progressing technology. The changing trends of technological advancement can be detected through calculating TCT index.

3. Results of patent bibliometric analysis

The bibliometric techniques were used to analyze the status of technological development for CNT fabrication in this study. Looking at the different aspects of patenting activities such as growth in patents, country analysis, assignee analysis, co-inventors analysis, and productivity of inventors; the main goal of this investigation is to comprehend the developmental path and current states of CNT fabrication.

3.1 Growth in patents

Figure 1 indicates the growth in the number of patents in the field of CNT fabrication. The earliest patent was issued in 2001 among the collected 97 patents. The patenting activity is mostly presented from 2007 to 2010 by the issue dates, and the majority of patents are filed from 2003 to 2006 by the application dates. In general, it takes about 2-4 years to move from patent application to patent issue. Either the date of issue or application shows that CNT fabrication is still attracting much interest in nanotechnology after 2000. This is confirmed by the fact that Sumio Iijima of the NEC Laboratory in Japan reported the first observation of MWNTs in 1991. After that, significant research efforts in efficient and high-yield CNT growth methods were continually described. The success in CNT growth has led to the CNT related patents. Nevertheless, the number of patent application decreased after 2007, the reason for the phenomenon may be due to the basic science issues needed to be understood and technological bottlenecks needed to be overcome. Currently, the main bottleneck in CNT fabrication is probably one of the main issues either to develop a mass production process or to control growth in order to obtain well-designed nanotube structure. If the trouble is solved, the growth can be expected for the patents and products.

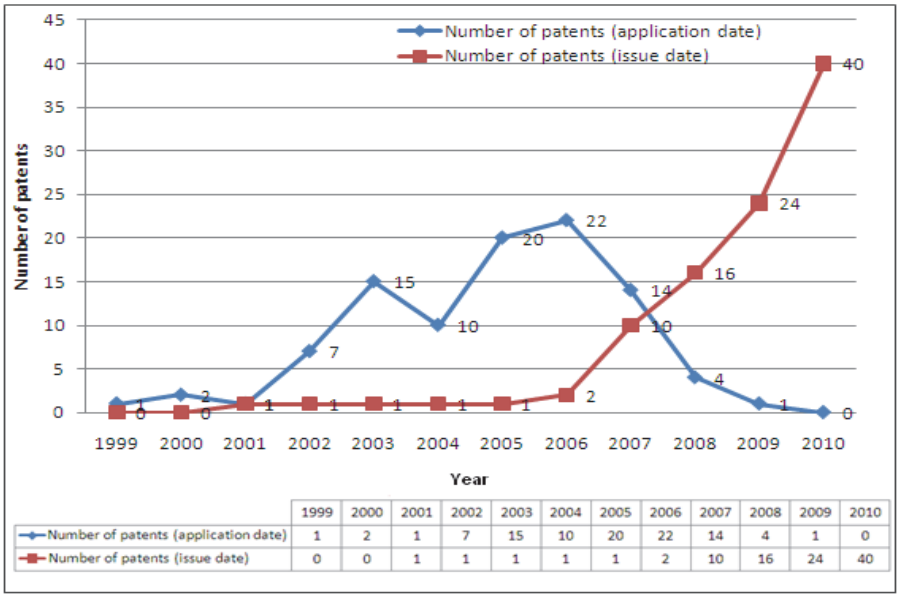

Fig. 1. Growth in patents

3.2 Country analysis

Figure 2 shows the distribution of patenting activity in different countries. USA is the most active in patents for the field of CNT fabrication. This result confirms the fact that USA owns

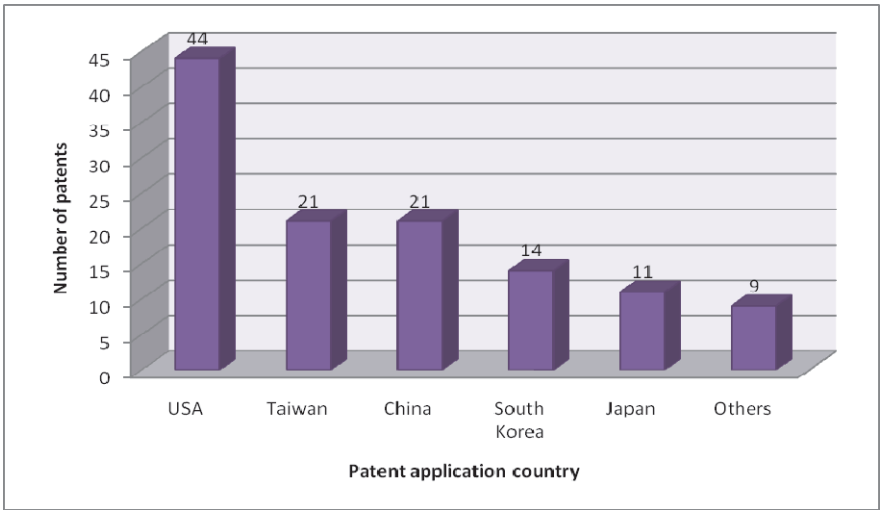

Note: There is discrepancy between "total number of all patents of all countries" and "total number of all patents" because 23 patents were filed by two countries at the same time.

Fig. 2. Country analysis

the leading status in material science of nanotechnology. In fact, the systematic study of carbon filaments of very small diameters came from the discovery of fullerenes (C_{60}) by Harold Kroto, Richard Smalley, Robert Curl, and coworkers at Rice University, USA before 1991. Of course, a great deal of progress has been made in characterizing and understanding the unique properties of CNT in USA since the Iijima's discovery in 1991. In addition, the other countries in figure 2 are Taiwan, China, South Korea and Japan according to the number of patents. This phenomenon means that these Asian countries attach great importance to CNT fabrication research.

3.3 Assignee analysis

Figure 3 provides the patenting activity of assignees ranging from corporations, academic institutes, R&D institutes, government institutes, consortiums of corporations and academic institutes, and individual. The data indicate that corporations are the most active assignees which own 51 patents and occupy 52.58%; the second are consortiums of corporations and academic institutes which own 19 patents and occupy 19.59%; the third are academic institutes which own 17 patents and occupy 17.53%. In fact, CNTs arouse great interest in the research community because of their strange electronic properties, and this interest continues as other remarkable properties are discovered and promised for practical applications develop by industrials. Because the CNT fabrication belongs to the highly interesting material, not only corporations but also academic institutes play important role in assignee for CNT related basic research.

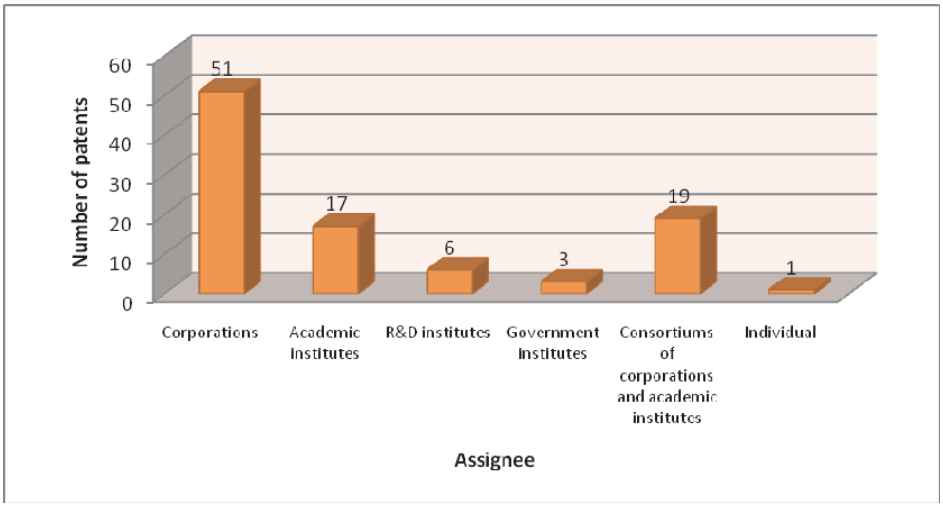

Fig. 3. Assignee analysis

This study further analyzes each assignee to find out the active assignees in CNT fabrication. In the corporate assignees, Samsung from South Korea is the most active company in the field of CNT fabrication. The second active corporations are Intel and IBM from USA as well as NEC from Japan. In fact, these companies possess the important status in the field of nanotechnology, and all of them take CNT fabrication seriously at this moment. In the academic institutes, most of patents were applied from several universities

in USA. This confirms that academic institutes in USA play the important roles in CNT basic research. In the R&D institutes, the Industrial Technology Research Institute (ITRI) from Taiwan is the most active assignee. ITRI is the main R&D institutes in Taiwan, and the manufacturing technology of CNT is one of their developmental directions in applications of field emission displays (FEDs). In the government institutes, the three assignees are from USA, and all these patents are produced from USA government subsidy plan.
Among all consortiums of corporations and academic institutes, there are 18 patents were filed jointly by Hon Hai Precision Company in Taiwan and Tsinghua University in China. This cooperation shows that the two assignees have grasped the critical technologies in CNT fabrication and these technologies were expected to create the marketable product in the future. For the individual, the only one patent was filed by inventor Cheol-Jin Lee.

3.4 Co-inventors analysis

Figure 4 shows the pattern of co-inventorship in the field of CNT fabrication. Among all 97 patents, only 15 patents are from single inventors, and the other 82 patents are from co-inventors. More than half of all patents are from two or three inventors. The remaining patents come from four or more inventors. The highest number of inventors for one patent is 9 persons. Thus, it is clear that research in CNT related project is most frequently done by teamwork.

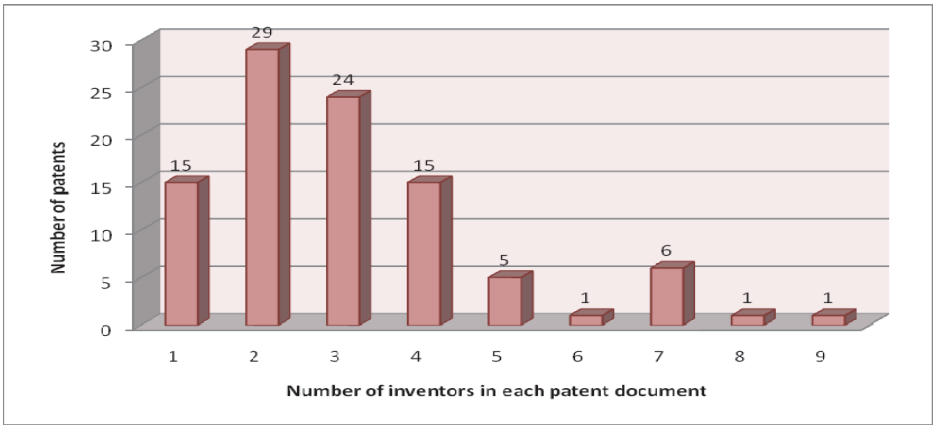

Fig. 4. Co-inventors analysis

3.5 Productivity of inventors

This section further analyzes the total number of patents owned by each inventor. In other words, the productivity of inventors in the patents of CNT fabrication was evaluated. Figure 5 demonstrates the information on the productivity of inventors. There are totally 210 inventors in all collected patents. Among these inventors, 174 inventors produced only one patent each. The inventors owning only one patent consist of 82.86% of all inventors. Only 14 inventors produced more than two patents each, and they occupy 6.67% of all inventors. Further, the most productive inventor produced a maximum number of seventeen patents, and the inventor is Shou-Shan Fan from Tsinghua University in China. The second most productive inventor is Liang Liu from Tsinghua

University in China, who produced eleven patents. The analytical result means that the high productivity of inventors is concentrated on a few inventors although there are many inventors in the field of CNT fabrication.

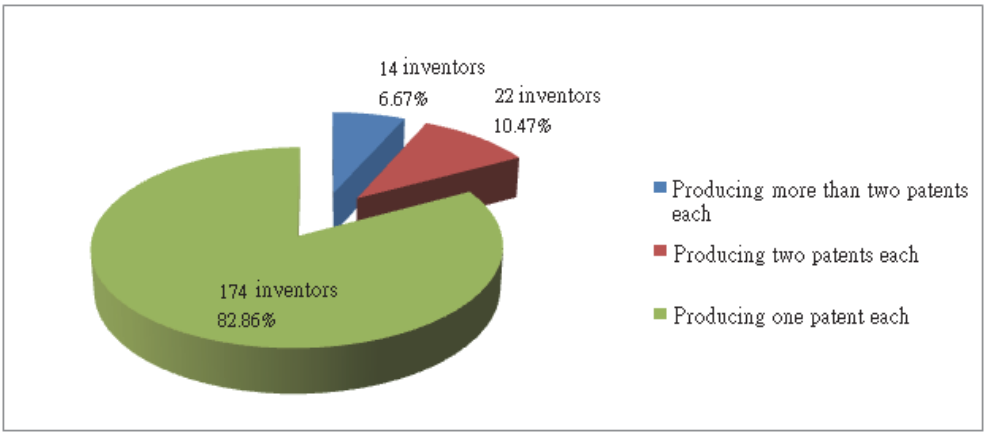

Fig. 5. Productivity of inventors

4. Results of patent network analysis

In order to obtain more information from patent documents, patent network analysis was used to further analyze the overall structures among the 97 patents regarding CNT fabrication. On the basis of five steps in the section of methodology, the representative patent keywords with important technical feature were adopted for producing the patent network. A total of 17 keywords were selected in step 1, including "chemical vapor deposition", "arc discharge", "laser", "catalyst", "substrate", "array", "evaporation", "pattern", "purification", "amorphous", "voltage", "derivatized", "helium", "crystalline", "gas", "current" and "modified", and the cut-off value p=0.18 was chosen in step 5. In the following section, the structural features of patent network were described and discussed in depth.

Figure 6 demonstrates the overall patent network in terms of connectivity. This network analysis divides all the 97 patents into two sets, an interconnected set and an isolated set. The interconnected set represents the critical key point of overall patent network, including 85 patents and the relationship among these patents. It provides much information in the fabrication and application of CNT based materials. From these inventions, the processes for CNT fabrication can be classified according to their manufacturing technologies, such as arc-discharge, laser ablation, chemical vapor deposition, and novel synthesis for functional CNTs. Nevertheless, there are still 12 patents in the isolated set. Among these patent documents, their main inventions are also claim for controlling CNT growth through the unique apparatus, system, method or process. However, these progresses don't meet the recent mainstream tendency, their originality is not ready to establish in present production level. Moreover, their improvements don't well fit the major technological trends and recent industry requirements in CNT applications, so they are excluded from the network through this patent network analysis.

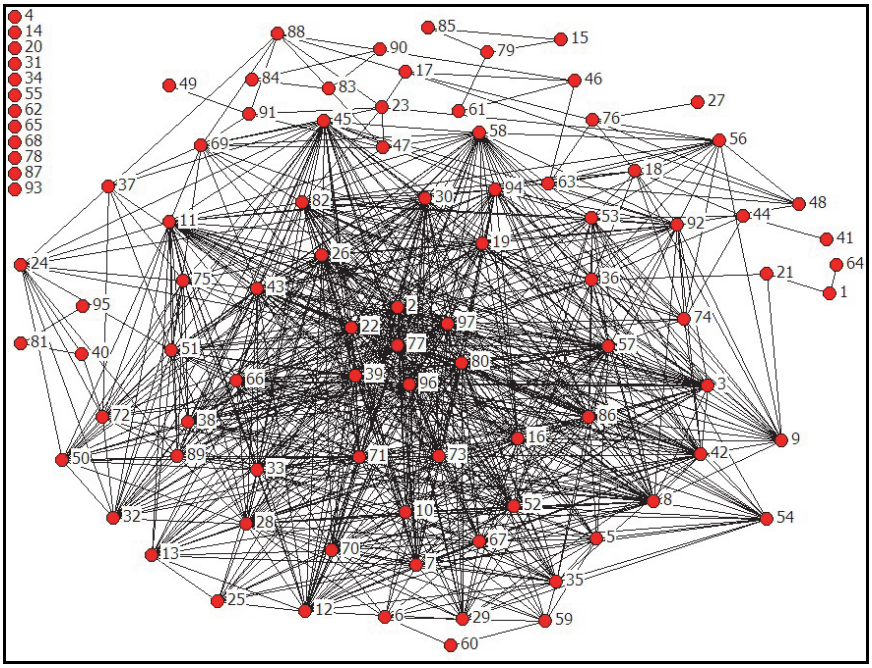

Fig. 6. Patent network of CNT fabrication

4.1 Quantitative analysis of patent network: TCI method

From this patent network, it can be observed that several patents close mutual linkages intuitively. As intuitive identification in the visual network, these patents are located in the central area of the patent network and possessed close relationship. They may represent the core technology in the field of CNT fabrication and application. Furthermore, the TCI method is used to identify the relatively important patent in this patent network. There are seven patents with higher TCI values above 0.42, including patent numbered 77, 97, 96, 2, 39, 80 and 22. Table 1 shows these relatively important patents in the patent network with higher TCI values, and far ahead of other patents. Through the visual patent network and TCI values, we can find out the relatively important patents. These patents represent the core technologies and the developing trends in CNT fabrication and application. We discuss the detailed meanings further as follows.

Patent number (real patent number)	TCI value
77 (U.S. Patent No. 7,744,843)	0.4896
97 (U.S. Patent No. 7,854,991)	0.4688
96 (U.S. Patent No. 7,851,064)	0.4479
2 (U.S. Patent No. 6,401,526)	0.4479
39 (U.S. Patent No. 7,514,116)	0.4375
80 (U.S. Patent No. 7,763,230)	0.4375
22 (U.S. Patent No. 7,374,793)	0.4271

Table 1. TCI values of the relatively important patents

From the above table, these seven patents with higher TCI values are further classified according to their titles, abstracts and claims of the patent documents. A reasonable explanation is expanded as below. The patent numbered 77 is the most important patent with a highest TCI value. This invention is to provide a method for synthesizing SWNTs which comprise extracting metals from carbide by halogen treatment at ambient or low pressure. Accordingly, this novel technology provides a method for the bulk synthesis of carbon nanotubes from metal carbides. The nanotube nucleation and growth occur upon the conversion of carbides into carbon without any catalyst. Thus, bulk nanotube powders, free-standing nanotube films, and thin layers of carbon nanotubes can be easily grown on SiC single crystals, polycrystalline carbide ceramics and particulate substrates. This convenient method is significant and useful for the further applications.

Furthermore, the patent with second order of TCI value is numbered 97. This invention has an object to provide carbon nanotubes and aligned single-walled carbon nanotube bulk structures with high purity and high specific surface area from CVD production process. In previous experience, the growth of the carbon nanotubes by the existent CVD method involved a problem that the activity lifetime of the metal catalyst was short, the activity was degraded in several seconds, and the growth rate of the carbon nanotube was not under best condition, which hindered the productivity. Thus, this patent has been proposed a method of controlling the activity of the iron catalyst and the growth of the carbon nanotube by a novel production process and apparatus. Based on this technique, various application uses can be attained such as for heat dissipation materials, heat conductors, electric conductors, optical devices, reinforcing materials, electrode materials, batteries, capacitors or super capacitors, electron emission devices, adsorbents, gas storages and so on. Accordingly, the CVD based production process for the growth of MWNTs is also important. The patent numbered 80 on the sixth order of TCI value reveals a useful process for the formation of all types of fullerenes, and in particular yields MWNTs with low defect density and controllable weight percent of metal impurity atoms. The advance in a wide range of nanotechnology applications depend critically on the availability of suitable starting materials, fabricating methods, or producing apparatus. In the case of applications and products using CNTs, the critical issues are freedom from defects and attaining low levels of impurities. Both problems are related to growth conditions and parameters, they have been virtually impossible to control the defect densities and impurity levels of fullerenes in previous research.

From the viewpoint of commercial applications, the semiconductor devices and the microelectronic elements are both the integral parts in global high-tech industries. The patents with the order of third, fifth and seventh are numbered 96, 39 and 22, they are all related to apply CNTs as role materials in semiconductor and microelectronic devices. According to recent results of scientific researches, CNTs are nanoscale high-aspect-ratio cylinders consisting of hexagonal rings of carbon atoms that may assume either a semiconducting electronic state or a conducting electronic state. The availability of CNTs and the cost of their synthesis is a primary issue hindering their introduction in various potential mass-produced end products, especially in IC industrials. Therefore, the conventional method for synthesizing carbon nanotubes is to deposit a layer of catalyst material on a substrate, which may be patterned to form an array of small dots that operate as seed areas for CVD growth using a carbonaceous precursor in FET device applications. Otherwise, the CNTs produced from CVD processes can be also applied to conductive

patterns in microelectronic fields using CNT pastes to reinforce printed and applied paste-based metal wires. Such printed wires may be used in a wide range of electric circuits or metallic interconnections and the CNTs provide superior electrical and thermal conductivities, higher current densities, and remarkably improved strength compared to metal wires printed without CNT reinforcement.

Finally, the last patent within above table 1 is numbered 2. Unlike the previous six patents, its application date is earlier than the year of 2000. This reveals that this patent plays an important role in the early stage of CNT based research, and it still has influences in recent years. This invention relates generally to SWNT probe-tips for the atomic probe microscopy by direct synthesis method. The growth of SWNT tips involves dip coating silicon pyramids with a liquid phase catalyst followed by CVD using methane. The interactions between the silicon pyramidal surface and the nanotube ensure proper SWNT orientation. Production of large scale arrays of nanotube probe-tips using contact printing and controllably shortening nanotubes in an inert discharge are also mentioned.

From this patent network analysis, TCI can help us to realize the technological trends in the field of CNT fabrication and application. The full potential of CNTs for applications will be realized until the growth of nanotubes can be optimized and well-controlled. Real-world applications of CNTs require either large quantities of bulk materials or device integration in scaled-up fashions. Therefore, the front seven patents in TCI analysis reveal that fabrication and application of CNTs have the same importance in the future. The researchers work for different goals should pay the same attention in these two areas. For materials such as composites and hydrogen storage, it is desired to obtain high quality CNTs at the kilogram or ton level using growth methods that are simple, efficient and inexpensive. For devices such as CNT based electronics, scale-up will unavoidably rely on self-assembly or controlled growth strategies on surfaces combined with microfabrication techniques. Significant work has been carried out in recent years to tackle these issues.

Nevertheless, many challenges remain in the nanotube growth area after TCI analysis. First, an efficient growth approach to structurally perfect nanotubes at large scales is still lacking. Second, growing defect-free nanotubes continuously to macroscopic lengths has been difficult. Third, control over nanotube growth on surfaces should be gained in order to obtain large-scale ordered nanowire structures. Finally, there is still a seemingly formidable task of controlling the chirality of single-walled CNTs by any existing growth method. In this way, development of functional devices based on CNTs will surely have a significant impact on present and future technology needs.

4.2 Quantitative analysis of patent network: TCT method

TCT index reflects the trends of technological progress. The short TCT represents faster technology progress, but long TCT has the opposite result. The changing trends of technological progress in CNT fabrication and application should be monitored by this analysis. In this study, we calculate the median of age gaps between each subject patent and other connected patents in the whole patent network. TCT value varies from 0.37 to 5.65 years in this patent network, which shows the different rates of technological innovation in the synthesis and use of CNTs. Table 2 shows the front eight patents which own the shorter TCT index values (less than 1 year) and lists the front ten patents with long TCT index values (more than 3 years).

Short TCT group		Long TCT group	
Patent number (real number)	index value	Patent number (real number)	index value
85 (U.S. Patent No. 7,781,017)	0.37	47 (U.S. Patent No. 7,585,584)	3.08
49 (U.S. Patent No. 7,597,869)	0.62	18 (U.S. Patent No. 7,338,648)	3.16
79 (U.S. Patent No. 7,744,958)	0.70	72 (U.S. Patent No. 7,728,947)	3.18
91 (U.S. Patent No. 7,820,245)	0.73	7 (U.S. Patent No. 7,160,530)	3.20
15 (U.S. Patent No. 7,291,319)	0.73	81 (U.S. Patent No. 7,767,275)	3.41
23 (U.S. Patent No. 7,394,192)	0.76	46 (U.S. Patent No. 7,582,507)	3.48
11 (U.S. Patent No. 7,268,077)	0.94	6 (U.S. Patent No. 7,078,007)	3.57
71 (U.S. Patent No. 7,728,497)	0.99	3 (U.S. Patent No. 6,743,408)	3.78
		40 (U.S. Patent No. 7,531,156)	5.19
		2 (U.S. Patent No. 6,401,526)	5.65

Table 2. Short and long TCT index values of some patents

4.2.1 Short TCT

From the result of TCT index, the patents which have short TCT are related to the fabrication and utilization of CNTs for further industrial applications, and this index can provide the speed of technological innovation in this patent network. The patents with short value are numbered 85, 49, 79, 91, 15, 23, 11 and 71 which can be divided into three groups including CNT production, CNT based devices, and CNT based emitters.

The patents numbered 49 and 91 are classified into CNT production. From the discoveries of researches, the CNTs have excellent electrical, magnetic, nonlinear optical, thermal, and mechanical properties, such as possessing a high Young's modulus, a high elastic modulus, and a low density. Depending on their length, diameter, and mode of spiraling, the CNTs can exhibit metallic or semiconductor properties. They are widely used in a variety of diverse fields, such as nanometer-scale electronics, materials science, biological science, and chemistry. At present, methods for producing carbon nanotubes include an arc discharge method, a laser ablation method, and a CVD method. The CVD method generally uses transition metals or oxides as a catalyst to grow CNTs at high temperature by decomposition of carbon-containing reactive gas. Compared with the other two methods, the CVD method is superior in operational simplicity, low cost, and mass production, therefore the CVD method has become widely used. A typical CVD method for producing CNTs includes the steps of (1) providing a substrate coated with a catalyst layer on a surface; (2) putting the substrate in a reaction device; (3) heating the reaction device; (4) introducing a carbon-containing reactive gas and thereby growing CNTs on the substrate. However, when using a typical method to produce CNTs after about 5 to 30 minutes, the rate of precipitation of carbon is greater than that of diffusion of carbon. Thus, the catalyst particles become blocked by accumulation of the decomposed carbon of the carbon-containing reactive gas. Therefore, the CNTs stop growing at a short length.

In addition to above mention, another four patents regarding CNT based devices own the shorter TCT values (numbered 85, 79, 15 and 11). These inventions relate to methods for making devices from substrates by CVD processes. At present, the CNT based devices from CVD methods already have a wide range of applications, but the CNT based devices fabricated by arc discharge or laser ablation can not be directly use for applications. The process control is needed over the building and organization of nanotube-based architectures. Normally, the orientation of growing nanotubes is controlled for the purpose of achieving rectilinear and parallel CNTs with each other, and the CVD method can help to align along a

linear direction and extend perpendicularly from the substrates. Even though there are many devices prepared from CVD based methods, most of the synthesis methods suffer from a lack of control over the size and shape of the nanotubes. Some methods of CNT production lead to mixtures of SWNTs and MWNTs. Other methods result in production of nanotubes with variations in nanotube shape and size, leading to a lack of control over the properties of the resulting nanotubes. From above analysis, the scientists and researchers should pay their attention to this matter for improving the technology progress. This shows that a larger proportion of the CNT based subjects, which need to be promoted in both academia and industrial, is of immediate relevance for the inventive activity leading to patents in this field.
Finally, the other two patents with short TCT (numbered 23 and 71) are related with aligned CNTs as electrode emission source to improve applications. The electron emission devices are displays that create images by emitting light by having phosphors in a phosphor layer of an anode plate collide with electrons emitted from electron emission sources of a cathode under an electric field generated when a voltage is applied to the anode and the cathode. The CNTs with good electron conductivity have properties such as a good field enhancement effect, low work function, good field emission property, low driving voltage, and an ability to be fabricated over a large area. Therefore, CNTs are good electron emission sources for electron emission devices. Recent interests in these inventions provide CNTs which exhibit good characteristics due to small differences in CVD process and apparatus.
According to above mentions, the result of TCT index with lower value can effectively reflect the present technological trends, and the CNT production, CNT based devices, and CNT based emitters are really the most popular subjects in industrial applications of CNTs.

4.2.2 Long TCT

In addition to the patents with short TCT index value, the front ten patents with long TCT index value are also listed for further discussion. These ten patents are numbered 47, 18, 72, 7, 81, 46, 6, 3, 40 and 2. From the contents of these patents, they are still related to the CNT fabrication and application through CVD processes, but these inventions focus on the controlling synthesis of CNTs for the specific situations uses or applications. Since the first observation of CNTs, the subjects of patent documents can be classified according to their subjects, such as synthesis method, growth mechanism, chemical/physical property, theoretical prediction, and potential applications. Nevertheless, the patents with long cycle time indicate the subjects are not in popular demand or with narrow utility in this analysis. Their subjects are relative mature and useful without further progress, and this situation indicates these inventions could not be easily replaced and overtaken.
The patents numbered 18, 81, 6 and 40 describe the CNT synthesis through the different core techniques. The technological importance in CNT fabrication processes is including of low temperature synthesis, self vertical alignment, nanoparticle based synthesis, and organic liquid based catalysis growth. The technical advantages of these four patents are designed to produce CNTs with controlled shape, diameter, wall thickness, length, orientation, and location of growth. Although these patents are filed and applied for a period of time, their main invention is still the critical factor for the controlling synthesis of CNT on a substrate. For this reason, it is very reasonable for these four patents owning the long TCT index value. But there are still some problems needed to be solved in the future, the final goal of these inventions is applied for the industrial applications.
Furthermore, the patents numbered 47, 72, 7, 46, 3 and 2 also describe the CNT fabrication regarding the controlling synthesis of CNT onto various templates for applications, such as

fuel cell electrodes, LCD devices, hydrogen storage devices, electronic transistors, AFM tweezers and so on. Specifically, vertical alignment has been an important objective due to the technological requirements for applications in above fields. Until now, there is still no more effective solution which can manipulate CNTs for mass production. Because these techniques are still difficult to control and labor intensive, in situ aligning of nanotubes during growth onto the porous substrates including foam, felt, mesh and membrane have been attempted. However, the reactions and the synthesis of these materials in novel combinations with varying substrates or coatings cannot be easily achieved. Therefore, the techniques of making above structures are always disclosed as patents with longer TCT.
Even if it is important for creating a new fabrication process for CNT, a new method is very difficult to establish in recent years. All researchers are moving their resources to create the application of CNT related products. Therefore, TCT will become longer and longer for the fabrication process research. This phenomenon may further indicate that the TCT index can monitor the changing trends of technological advancement for fabrication and application of CNT. And the TCT index value can quickly point out that the object in mind for CNT materials is modified the CNT structure to improve the whole process of device production.

5. Conclusions

In this study, patent bibliometric analysis and patent network analysis were both used to monitor the states and the trends of CNT fabrication. These analyses not only can assist researchers in understanding the developmental states of CNT fabrication, but also can help them to quickly grasp the technological trends for CNT fabrication. Moreover, the results of this study fully demonstrate the critical technologies of CNTs and provide suggestions regarding future technological development.
For all the analytical results of this study, first, the main growth methods of producing CNT are classified for laser ablation, arc-discharge, and CVD methods. Although the CNT material was observed from the year of 1991, the fabrication process is still attracting much attention after 2000. The key technology of CNT fabrication is finding the way to produce CNTs in higher yields, high purity, well conformation, and better quality by CVD process, and the growth of nanotube materials in bulk was also mentioned.
Second, the patent network graph was obtained from the keywords of CNT related patents. A major portion of patents in the center of network graph can be obviously distinguished, and it seems to reflect the actually technological trends. It represents the truth that major purpose of CNT production is in the field of CNT fabrication and application. The similar result was found in TCI and TCT measurements. The CVD process plays an important role for manufacturing CNT based devices in industrial field. Therefore, it is without doubt that patent documents are a valuable resource of technical and commercial knowledge. The potential, market demand, and future direction of patent data can be easily realized from this analysis.
Third, this study reveals the critical technologies for growing the CNT materials generally fallen into two categories: (1) enhancing the characteristic of CNT with various methods, and (2) producing CNT by CVD method on various substrates for applications. Some of these inventions could become real marketable applications in the near future, but others need further modification and optimization. Moreover, there still remains a strong need for better control in purifying and manipulating CNTs, and the development of functional devices or structures based on CNTs will surely have a significant impact on future technology needs.
From this analysis result, the advantage of CNTs makes them of potential use in controlling synthesis of nanoscale structures, which play an important role in the field of nanotechnology

engineering. Up to the present, it is not really possible yet to grow CNTs in an ambient condition for mass production. Even if there have been some successes in growing CNTs through tuning the conditions and apparatuses by trial and error, the general challenges for developing CNTs still focus on growing stable and functional materials. Furthermore, another challenge is in the manipulation of CNTs. The operational skill of CNT related materials is still in the infancy, and it relies strongly on the powerful tools of manipulating CNT structures at the atomic scale. This will become a major challenge in the near future, among several others.

6. Acknowledgement

We are grateful for the financial support from the National Science Council in Taiwan (Grand No. NSC 97-2221-E-035-068-MY3).

7. References

Bethune, D. S.; Klang, C. H.; de Vries, M. S.; Gorman, G. ; Savoy, R.; Vazquez, J. & Beyers, R. (1993). Cobalt-catalyzed growth of carbon nanotubes with single-atomic-layer walls. *Nature,* Vol. 363, No. 6430, pp. 605-607.

Chang, P. L.; Wu, C. C. & Leu, H. J. (2010). Using patent analyses to monitor the technological trends in an emerging field of technology: a case of carbon nanotube field emission display. *Scientometrics,* Vol. 82, No. 1, pp. 5-19.

Choi, C.; Kim, S. & Park, Y. (2007). A patent-based cross impact analysis for quantitative estimation of technological impact: the case of information and communication technology. *Technological Forecasting and Social Change,* Vol. 74, No. 8, pp. 1296-1314.

Gupta, V. K. & Pangannaya, N. B. (2000). Carbon nanotubes: bibliometric analysis of patents. *World Patent Information,* Vol. 22, No. 3, pp. 185-189.

Hullmann, A. (2007). Measuring and assessing the development of nanotechnology. *Scientometrics,* Vol. 70, No. 3, pp. 739-758.

Iijima, S. & Ichihashi, T. (1993). Single-shell carbon nanotubes of 1-nm diameter. *Nature,* Vol. 363, No. 6430, pp. 603-605.

Iijima, S. (1991). Helical microtubules of graphitic carbon. *Nature,* Vol. 354, No. 6348, pp. 56-58.

Kuusi, O. & Meyer, M. (2007). Anticipating technological breakthroughs: Using bibliographic coupling to explore the nanotubes paradigm. *Scientometrics,* Vol. 70, No. 3, pp. 759-777.

Narin, F. (1994). Patent bibliometrics. *Scientometrics,* Vol. 30, No. 1, pp. 147-155.

Saito, R.; Fujita, M.; Dresselhaus, G. & Dresselhaus, M. S. (1992). Electronic structure of chiral grapheme tubules. *Applied Physics Letters,* Vol. 60, No. 18, pp. 2204-2206.

Thostenson, E. T.; Ren, Z. F. & Chou, T. W. (2001). Advances in the science and technology of carbon nanotubes and their composites: a review. *Composites Science and Technology,* Vol. 61, No. 13, pp. 1899-1912.

Treacy, M. M. J.; Ebbesen, T. W. & Gibson, J. M. (1996). Exceptionally high Young's modulus observed for individual carbon nanotubes. *Nature,* Vol. 381, No. 6584, pp. 678-680.

Wasserman, S. & Faust, K. (1994). *Social Network Analysis: Methods and Application*, Cambridge University Press, ISBN: 0-521-38707-8, Cambridge, UK.

Wong, P. K.; Ho, Y. P. & Chan, C. K. (2007). Internationalization and evolution of application areas of an emerging technology: The case of nanotechnology. *Scientometrics,* Vol. 70, No. 3, pp. 715-737.

Yoon, B. & Park, Y. (2004). A text-mining-based patent network: analytical tool for high-technology trend. *Journal of high technology management research,* Vol. 15, No. 1, pp. 37-50.

Part 2

Modeling and Simulation

8

Modeling of Carbon Nanotube Field Effect Transistors

Dinh Sy Hien
HCM City University of Natural Sciences, Vietnam

1. Introduction

Since the discovery of carbon nanotubes (CNTs) by Iijima in 1991 [1], significant progress has been achieved for both understanding the fundamental properties and exploring possible engineering applications. The possible application for nanoelectronic devices has been extensively explored since the demonstration of the first carbon nanotube transistors (CNTFETs) in 1998 [2]. Carbon nanotubes are attractive for nanoelectronic applications due to its excellent electric properties. In a nanotube, low bias transport can be nearly ballistic across distances of several hundred nanometers. The conduction and valence bands are symmetric, which is advantageous for complementary applications. The bandstructure is direct, which enables optical emission, and finally, CNTs are highly resistant to electromigration.

Significant efforts have devoted to understand how a carbon nanotube transistor operates and to improve the transistor performance [3, 4]. It has been demonstrated that most CNTFETs to date operates like non-conventional Schottky barrier transistors [5, 6], which results in quite different device and scaling behaviors from the MOSFET-like transistors. Important techniques for significantly improving the transistor performance, including the aggressively scaling of the nanotube channel, integration of thin high-κ gate dielectric insulator [7], use of excellent source-drain metal contacts [8], and demonstration of the self-align techniques, have been successfully developed. Very recently, a nanotube transistor, which integrates ultra-short channel, thin high-κ top gate insulator, excellent Pd source-drain contacts is demonstrated using a self-align technique [9]. Promising transistor performance exceeding the state-of-the-art Si MOSFETs is achieved. The transistor has a near-ballistic source-drain conductance of $0.5 \times e^2 / h$ and delivers a current of 20 μA at $|V_G-V_T| \sim 1$ V. In this work, numerical simulations are developed to explain experiments, to understand how the transistor operates and what controls the performance, and to explore the approaches to improve the transistor performance. New simulation approaches are necessary for a carbon nanotube transistor because it operates quite different from Si transistors. The carbon nanotube channel is a quasi-one-dimensional conductor, which has fundamentally different carrier transport properties from the Si MOSFET channel. It has been demonstrated that treating the Schottky barriers at the metal/CNT interface and near-ballistic transport in the channel are important for correctly modeling the transistor. The CNT channel is a cylindrical semiconductor with a ~1 nm diameter, which means the electrostatic behavior of the transistor is quite different from Si MOSFETs with a 2D electron

gas. All carbon bonds are well satisfied at the carbon nanotube surface, which results in a different semiconductor/oxide interface. Furthermore, the phonon vibration modes and carrier scattering mechanisms are quite different in carbon nanotubes, which results in different roles of phonon scattering in CNTFETs. In this work, we developed physical simulation approaches to treat CNTFETs. We will show that our understanding of the carrier transport, electrostatics, and interracial properties seem to be sufficient to describe the behavior of the recently demonstrated short-channel CNTFETs.

This work is organized as follows. In section II, we start with a brief summary of progress in CNTFET technology. This discussion is intended to provide background of carbon nanotube, CNTFET technology. As our understanding of CNTFET device physics has evolved, an ability to model and simulate them has also been developed. Fabrication of CNTFET is discussed in section III. This section is intended to introduce progress in CNTFET fabrication. Section IV briefly describing the simulation approach that we use. In this section, we present non-equilibrium Green function method that commonly used for modeling and simulation in nano-scale devices. In section V, these numerical simulations are used to discuss some key issues in device physics such as ballistic transport, transport with scattering, current-voltage characteristics of CNTFET.

2. Carbon nanotube and CNTFET

2.1 Structure of CNT and CNTFET

Carbon nanotube (CNT) was discovered by Ijima in 1991 [1]. Since then, CNTs have been a leading candidate in continued improvement of the performance, speed and density of integrated circuits.

CNT can be viewed conceptually as graphene (a single atomic layer of graphite) sheets rolled up into concentric cylinders. The number of sheets is the number of walls and thus CNTs fall into two categories: single-wall CNTs (Figure 1a) and multi-wall CNTs (Figure 1b). There are currently three methods to synthesize CNTs: arc discharge, laser ablation and chemical vapor deposition (CVD).

The atomic structure of a single-walled CNT is conveniently explained in terms of two vectors C_h and T. T is called translational vector, it defines the direction of CNT axis. C_h is called chiral vector, representing the circumference of a CNT. Two carbon atoms crystallographically equivalent to each other were placed together according to: $C_h = n.\ \mathbf{a_1} + m.\ \mathbf{a_2}$, where $\mathbf{a_1}$ and $\mathbf{a_2}$ are the unit vectors of 2D graphene sheet (Figure 1c). (n, m) indices determine the diameter and chirality of CNTs.

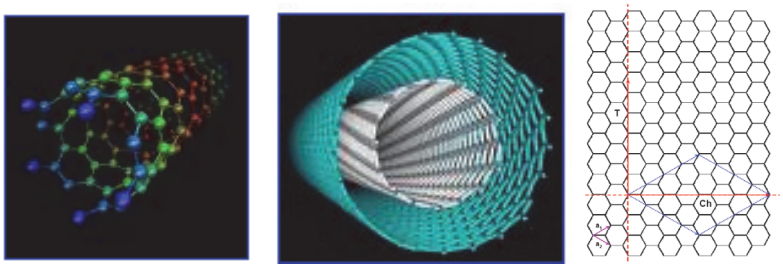

(a) (b) (c)

Fig. 1. a) Single-walled carbon nanotube, b) multi-wall CNT, c) form of a single walled CNT from a graphene sheet.

Theoretical studies have shown that a single-walled CNT can be either metallic or semiconducting depending on its chirality and diameter. (n, m) nanotubes with n = m (arm-chair) are metallic; for n – m ≠ 3 × integer, the nanotubes are semiconducting with band gap proportional to 1/d. For n – m = 3 × integer, the nanotubes would be quasi-semiconducting with a small band gap proportional to $1/d^2$. The sensitivity of electrical properties on structural parameters in unique for CNTs, which opens up numerous opportunities in nanotube systems. The diameter of the zigzag nanotube, d is [7]

$$d = \frac{n\sqrt{3}a_{cc}}{\pi} \tag{1}$$

where a_{cc} = 0.142 nm is the carbon-carbon bond length in graphene. The diameter dependence on n in (16,0), (19,0), and (22,0) zigzag CNTs, which are in the experimentally useful diameter range (1.2 - 1.8 nm), can be listed in the table 1.

Type of zigzag CNTs	(16,0)	(19,0)	(22,0)
Diameter (nm)	1.25	1.50	1.70
Bandgap energy (eV)	0.67	0.56	0.49

Table 1. Parameters of semiconducting CNTs.

First of all, single-walled CNT are 1 D quantum systems and the two-terminal conductance is given by Landauer Buttiker formalism as: $G_c = (N.\ e^2/h) \times T$, where N is the number of conduction channels in parallel, T is transmission coefficient, and h is Plank constant, 6.625×10^{-34} J.s. For a single-walled CNT the band structure gives rise to two propagating channels and taking into account the additional spin quanta of electrons, there are four "channel" in total. Therefore, N = 4 and $G_c = (4e^2/h) \times T$, corresponding to a two-terminal resistance $R_C = 1/G_c = (h/4e^2) \times (1/T)$. In addition, the scattering of charge carriers along the length of CNTs results in a Drude-like resistance, $R_D \propto L_{CNT}$, where L_{CNT} is the length of CNT. Thus, the total resistance of a single-walled CNT contacted by metal leads on both ends is sum of these two contributions: $R_{tot} = R_C + R_D$.

If the contact is perfect (T = 1) and CNT is scattering free, charge carriers can move through the nanotube ballistically, we have $R_{tot} = R_C = h/4e^2 \approx 6.5\ k\Omega = R_0$. Usually, R_{tot} and R_C are greater than R_0 because T is less than one due to the reflection of charge carriers at the imperfect metal/CNT interface. R_{tot} even greater when there exists energy barriers at the metal/CNT interface, namely, Schottky barriers when CNTs are semiconducting. Schottky barriers have been a long standing problem for silicon and other conventional semiconductors. This problem is circumvented by replacing metal leads with heavy doping in conventional semiconductor industry. However, doping CNTs with nanoscale spatial resolution would be a formidable challenge. Recently, R_{tot} approaching R_0 has been observed for semiconducting CNT by Javey et al. at room temperature [8]. Further group reported a mobility of 79000 $cm^2/V.s$ measured from a semiconducting CNT [9]. This value exceeds those for all known semiconductors. Furthermore, the strong covalent bands give CNTs high mechanical strength and thermal stability and enormous charge carrying capacity. Current density as high as 10^9 A/cm^2 has been reported [10].

2.2 Carbon nanotube field effect transistors

CNTFET is a three-terminal device consisting of a semiconducting nanotube bringing two contacts (source and drain), and acting as a carrier channel, which is turned on or off electrically via the third contact (gate). Presently, there are several types of CNTFETs have been fabricated, but CNTFET geometries may be grouped in two major categories: planar and coaxial CNTFET, whether planar or coaxial, relies on simple principles, while being governed by additional phenomena such as 1D density of states (DOS), ballistic transport, and phonon scattering.

Planar CNTFETs (Figure 2a) constitute the majority of devices fabricated to date, mostly due to their relative simplicity and moderate compatibility with existing manufacturing technologies. The coaxial geometry (Figure 2b) maximizes the capacitive coupling between the gate electrode and the nanotube surface, thereby inducing more channel charge at a given bias than other geometries. This improved coupling is desirable in mitigating the short-channel effects that plague technologies like CMOS as they downside device features. The key device dimensions are: the gate inner radius, R_g, and thickness, t_g; the nanotube radius, R_t, and length L_t; the insulator thickness $t_{ins}= R_g-R_t$; the end-contact radius, t_c (the source and drain may sometimes be of different sizes), and length, L_c; and the gate-underlap L_u.

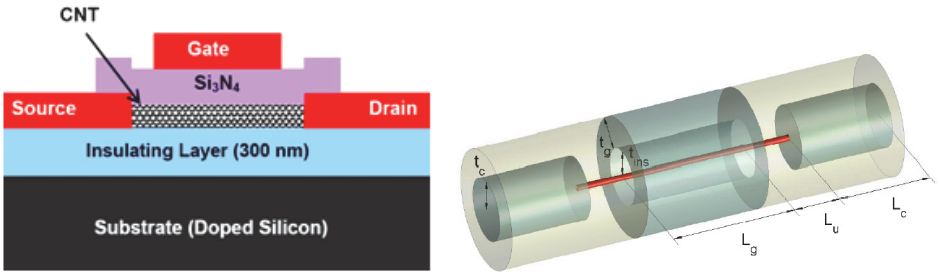

(a) (b)

Fig. 2. Structures of CNTFETs: a) planar, b) coaxial.

Manufacturing issues will ultimately play a decisive role in any future CNT electronic technology. Our focus here, however, is on the physics of CNT devices - specifically the CNTFET. It is still too early to tell what role CNTFETs will play in electronic systems of the future, but they provide us with a specific context in which to develop technology and understand transport, contacts, interfaces, etc.; which are likely to be important for CNT electronics in general. It is appropriate, however, to say a few words about where CNTFET technology stands today. Early CNTFETs were fabricated using nanotubes synthesized by a laser ablation process using nickel-cobalt catalysts [11]. The nanotubes were then suspended in a solvent and dispersed on an oxidized silicon wafer with predefined metal contact pads. The result was a random distribution of CNTs with some that bridged the contacts. Subsequently, catalytic chemical vapor deposition (CVD) methods were developed to grow CNTs on predefined catalyst islands [12]. The nanotubes thus fabricated are rooted in the catalyst islands and grow in random directions on the wafer with some terminating on

another island creating bridges. CVD techniques provide more control over device fabrication and have led to rapid progress in device performance.

CNTFETs are typically p-type devices that operate as so-called Schottky barrier (SB) transistors. The p-type characteristics have been attributed to the alignment of source-drain metal Fermi level near the valence band of the CNTs rather than to background doping or charges [5]. The holes in the channel are electrostatically induced by applying a negative gate voltage. Transistor action occurs because the gate modulates the SB width for hole tunneling near metal-CNT contact [5, 6]. While early transistors used gold (Au) as contact metals, significant performance improvements were obtained by using palladium contacts instead, which seem to eliminate the Schottky barrier for holes and produce near-ballistic operation [6]. However, other metals such as cobalt (Co) and titanium (Ti) are still being employed for high performance CNTFETs.

Early CNTFETs were fabricated on oxidized silicon substrates with a back-gated geometry and a thick SiO_2 layer that resulted in poor gate control of drain current [13, 14]. The use of a top-gated geometry produced immediate performance improvements [16]. Wind et al. deposited a thin dielectric layer (15-20 nm) on top of CNTs, and lithographically defined metal electrodes for gating and contacts. A transconductance ($g_m = dI_{ds}/dV_{gs} \mid_{Vds}$) of 3.25 μS and subthreshold swing ($S = ln(10)\ [dV_{gs}/d(ln(I_{ds}))]$) of 130 mV/decade were obtained, which was a significant improvement in device performance [16]. Later, the incorporation of high-κ dielectrics in a top-gated structure produced even better device characteristics [18]. Javey et al. employed a high-κ ZrO_2 (κ ~ 25) gate dielectric with a thickness of ~ 8 nm and obtained $g_m \approx 12$ μS and $S \approx 70$ mV/decade [18]. Although not always with top-gated geometry, other groups have also reported the use of high-κ dielectrics such as HfO_2 (κ ~ 11), TiO_2 (κ ~ 40-90), $SrTiO_3$ (κ ~ 175), and even electrolyte gating mechanisms for attaining improved performances [19, 20, 21, 22, 23]. In the case of electrolyte gating, Siddon et al. have reported $S \approx 62$ mV/decade which is very close to the theoretical limit of 60 mV/decade [23]. All of these devices appear to operate as CNT MSDFETs, some with essentially no barrier and others with rather large (half bandgap) barriers.

The possibility of ballistic operation of CNTFETs has been a topic of great interest. Since there are no dangling bonds in CNTs, surface scattering can be expected to be negligible. Back-scattering by acoustic phonons is suppressed by symmetry arguments related to the CNT bandstructure [24, 25] and by the reduction in phase space for one-dimensional conductors. The result is that mean-free-paths of several hundred nanometers are commonly observed [24, 26]. Under high bias, however, optical or zone boundary phonons may be emitted, and the mfps decrease substantially. Yao et al. showed that for long metallic CNTs, the current saturates at about 25 μA per nanotube [24]. They showed that the high-field current is limited by the emission of optical or zone boundary phonons with $\hbar\omega_0 \approx 200$ meV and that the high-field mfp is ~ 10 nm. Yao's results suggest that for short nanotubes, comparable in length to the mfp, the current should exceed 25 μA per nanotube. This expectation was confirmed by Park et al [27] and Javey et al, [26] who both showed that the current increases above 25 μA when the length of the nanotube is less than several mfps long. By analyzing their data, both Park and Javey extracted an mfp of ~10 – 15 nm, which was consistent with the value extracted by Yao for long nanotubes. The mfps deduced from these experiments are considerably shorter than the values of 50 nm or so, which are estimated from the expected electron-phonon coupling strength [24, 27]. Although these

results are for metallic nanotubes, similar effects are expected for semiconducting nanotubes and CNTFETs. For a tube much shorter than the mfp, carrier transport in the tube is quasi-ballistic, and the tube resistance is nearly length-independent. In contrast, a tube much longer than the mfp behaves like a classical resistor, in the sense that the resistance is proportional to the tube length.

Several recent improvements to CNTFET design collectively incorporate various techniques that have been developed during the past few years. For instance, Javey et al. reported a self-aligned top gate structure that uses the catalytic CVD method for CNT growth, a thin HfO_2 top gate dielectric ~ 50 nm in length and self-aligned palladium source-drain contacts [28]. A transconductance of 30 μS, subthreshold swing of 110 mV/decade, and a saturation current of ~25 μA at a power supply of V_{DD}~1 V were obtained [28]. Novel CNTFET device structures that enable high current operation and high integration densities have also been reported [29]. These devices are all of the metal source-drain (MSDFET) variety, but it is recognized that the use of a metal source will limit the drain current (unless the SB is sufficiently negative). Although progress in CNTFETs has been rapid, there are still many issues to address. The potential for digital logic [30, 31] was demonstrated early on. Techniques that modify the behavior of the nanotube from p-type to n-type have been implemented, which allowed their use in complementary CMOS logic. Following this, Derycke et al. demonstrated an inverter structure based on nanotubes [30]. Other nanotube based elementary digital logic gates with high gain and high I_{on}/I_{off} ratios, such as a NOR gate, a ring oscillator and an SRAM cell, have also been implemented [31].

With respect to RF performance, measurements [32, 34] and modeling [35] have both been initiated to assess performance potential. Experimental work includes that of Frank and Appenzeller, [32, 33] who developed a technique to circumvent the low-current-drive problem of CNTFETs to place a lower bound on the frequency response. Li et al. [34] measured the microwave reflection coefficient from a load comprised of a nanotube and a matching circuit and demonstrated transistor operation at 2.6 GHz. In terms of modeling, Burke [35, 36] has suggested an RF circuit model for a metallic nanotube, and emphasized the importance of both quantum capacitance and kinetic inductance. More recently, Burke used a standard formula, along with estimated and measured values for the parameters, to predict the unity-current-gain frequency (f_T) of CNTFETs, and suggested the f_T would be given by 80 GHz divided by the tube length in microns [$f_T = 80\ GHz / L(in\ \mu m)$].

A pressing issue that limits logic and RF device performance has to do with contacts. Good contacts to the valence band are achieved by using palladium. The barrier height is approximately zero for relatively large diameter nanotubes (D ~ 1.7 nm). Achieving small barrier contacts to the small diameter nanotubes that will be necessary for room temperature operation (D ~ 1 nm) is a key challenge, as is also achieving good, low barrier, contacts to the conduction band. CNT MOSFETs, however, are expected to deliver significantly better performance than MSDFETs, and recent progress on stable, heavy doping of CNTs is encouraging [37, 38]. For many applications, high currents are needed, so innovative structures that place several CNTs in parallel will be required. If these problems can be addressed, manufacturing challenges will move to the forefront. The key challenges are control of chirality and development of low temperature growth processes to allow CNTFETs to be placed at low cost on CMOS substrates.

3. Fabrication of CNTFET

Following the discussion on the properties of carbon nanotubes, we now give an overview of an important application and the topic of this work: the carbon nanotube field effect transistor. This three-terminal device consists of a semiconducting nanotube bridging two contacts (source and drain) and acting as a carrier channel, which is turned on or electrostatically via the third contact (gate). Presently, there are various groups pursuing the fabrication of such devices in several variations, achieving increasing success in pushing performance limits, while encountering myriad problems, as expected for any technology in its infancy. While the ease of manufacturing has improved significantly since their first conception in 1998, CNTFETs still have a long way to go before large-scale integration and commercial use become viable. Furthermore, as these transistors evolve at every research step, the specifics of their workings become clearer, and given that the aim of this work is to present a working model of CNTFETs, it is reassuring to see some of the findings presented herein being proven by recently released experimental data.

As regards the CNTFET's principle of operation, we briefly introduce two distinct methods by which the behavior of these devices can be explained. Primarily, the typical CNTFET is a Schottky-barrier device, *i.e.*, one whose performance is determined by contact resistance rather than channel conductance, owing to the presence of tunneling barriers at both or either of the source and drain contacts. These barriers occur due to Fermi-level alignment at the metal-semiconductor junction, and are further modulated by any band bending imposed by the gate electrostatics. Moreover, in some devices, the work-function-induced barriers at the end contacts can be made virtually transparent either by selecting an appropriate metallization or by electrostatically forcing via a separate virtual-gate terminal. These devices, sometimes labeled as bulk-modulated transistors, operate differently in that a thicker (non-tunneling) barrier, between the source contact and the mid-length region of the device, is modulated by the gate-source voltage. This operation is akin to that of a ballistic MOSFET, and effectively amounts to a channel modulation, by the gate, of a barrier to thermionically-emitted carriers, injected ballistically from the end contacts. We now provide a brief description of typical CNTFET geometries, which are grouped in two major categories, planar and coaxial. The specifics of nanotube growth and transistor fabrication issues, albeit of tremendous importance for this emerging field of nanoscale transistors, are beyond the scope of this work.

3.1 Planar devices

Planar CNTFETs constitute the majority of devices fabricated to date, mostly due to their relative simplicity and moderate compatibility with existing manufacturing technologies. The nanotube and the metallic source-drain contacts are arranged on an insulated substrate, with either the nanotube being draped over the pre-patterned contacts, or with the contacts being patterned over the nanotube. In the latter case, the nanotubes are usually dispersed in a solution and transferred to a substrate containing pre-arranged electrodes; transistors are formed by trial and error. Manipulation of an individual nanotube has also been achieved by using the tip of an atomic force microscope (AFM) to nudge it around the substrate; due to its strong, but flexible, covalent bonds, this is possible to do without damaging the molecule. In the case where the electrodes are placed over the tube, manipulation of the CNT is not required and alignment markers, pre-arranged on the substrate, allow accurate positioning of the contacts once the nanotube is located via examination by a scanning

tunneling microscope (STM). The gate electrode is almost always on the back side of the insulated substrate, or alternatively is patterned on top of an oxide-covered nanotube.
The first CNTFET devices were reported in 1998, and involved the simplest possible fabrication. They consisted of highly-doped Si back gates, coated with thick SiO_2, and patterned source-drain metal contacts, either using Au or Pt, as shown in figure 3A [13, 14]. Experimentations with different metals such as Ti, Ni, Al, and Pd have since been carried out by several groups, primarily to manipulate the work function difference between the end contacts and the nanotube. Subsequent work also produced a device that replaced the back gate with an electrode placed over the substrate, perpendicular to the source and drain contacts, as illustrated in figure 3B [15]. Here, the nanotube was separated from this gate electrode by a thin insulating layer of Al_2O_3, with the source-drain electrode strips placed over the tube ends for reduced contact resistance.

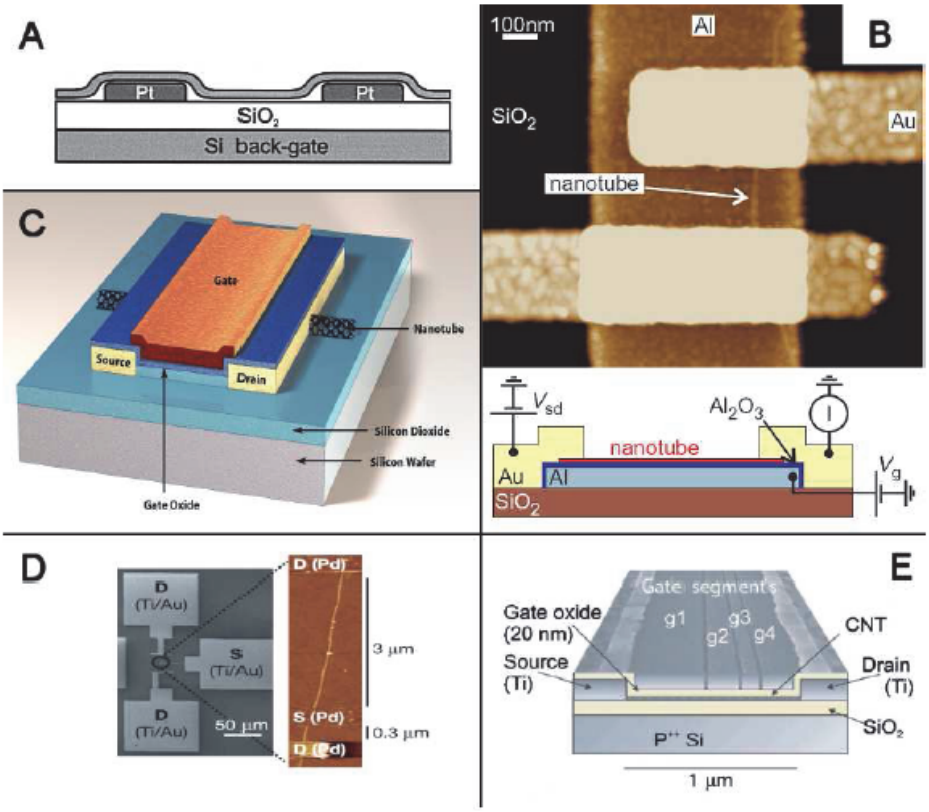

Fig. 3. Examples of planar CNTFETs: (A) Ref. [13], (B) Ref. [15], (C) Ref. [16], (D) Ref. [9], and (E) Ref. [19].

Figure 3C shows a further improvement in CNTFETs through the placement of the gate electrode over the semiconducting nanotube, thus improving the channel electrostatics via the thin gate oxide [16]. Moreover, the Ti source-drain metalizations in this device form

titanium carbide abrupt junctions with the nanotube, yielding increased conductance [17]. Another attempt to obtain better gate electrostatics involved materials with high dielectric constants, such as zirconia (ZnO_2) and hafnia (HfO_2), being used as gate insulators [18].
Figure 3D illustrates a device built with Pd source-drain contacts in order to exploit the sensitivity of this material's work function to hydrogen [9].
A multi-gate device, as shown in figure 3E, has recently been reported, whereby parallel top gates are used to independently control the electrostatics of different sections of the channel, thus facilitating a study of the transport characteristics of the nanotube channel [19]. More recently, a device with excellent DC characteristics was fabricated with Pd end contacts, Al gate, and hafnia for the insulator [10].
Most recently, a local gated carbon nanotube field effect transistor, as shown in figure 4, has been reported [42]. The approach is based on directed assembly of individual single wall carbon nanotube from dichloroethane via AC dielectrophoresis onto pre-patterned source and drain electrodes with a local aluminium gate in the middle. Local gated CNTFET devices display superior performance compared to global back gate with on-off ratios greater than 10^4 and maximum subthreshold swings of 170 mV/decade.

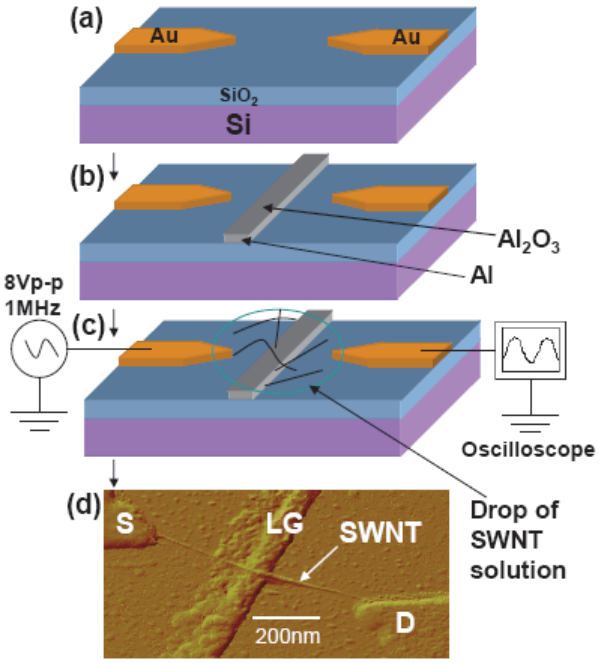

Fig. 4. Fabrication of local gated CNTFET: a) Source-Drain electrodes of 1 μm separation are patterned on heavily doped Si/SiO_2 substrates (250 nm thick oxide layer), b) Local Al gate electrodes are patterned using EBL and a 2-3 nm thick Al_2O_3 is created by oxygen plasma treatment, c) DEP assembly of CNT. An AC voltage of 8 Vp-p is applied for 1-2 seconds to the source electrode with a function generator, d) resulting AFM image of a device showing nanotubes are assembled at the tips [42].

3.2 Coaxial devices

Although yet to be fabricated in its ideal form, coaxial devices are of special interest because their geometry allows for better electrostatics than their planar counterparts. Capitalizing on the inherent cylindrical shape of nanotubes, these devices would exhibit wrap-around gates that maximize capacitive coupling between the gate electrode and the nanotube channel.

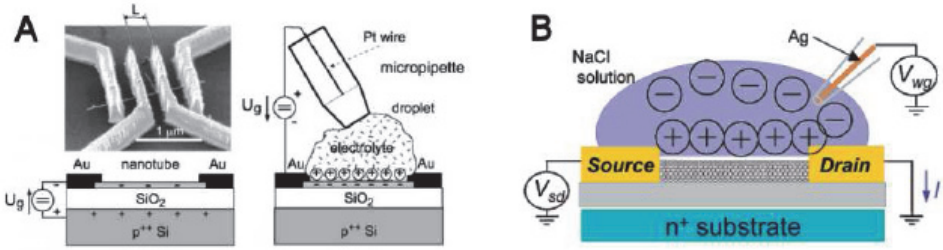

Fig. 5. Examples of electrolyte-gated CNTFETs: (A) Ref. [39], (B) Ref. [40].

Presently, the closest approximation to this geometry has been the development of electrolyte-gated devices. Kruger et al. reported the first such device, shown in figure 5A, using a multi-wall nanotube for the channel [39]. Two gates can be activated: a highly-doped Si back gate similar to planar devices; and an electrolyte gate, formed by a droplet of $LiClO_4$ electrolyte contacted by a thin platinum wire.

Figure 5B illustrates an improved version of this device, this time using single-wall carbon nanotubes and NaCl for the electrolyte, and yielding current-voltage characteristics that match those of modern Si MOSFETs [40]. Alternative structures for CNT devices that place the tube vertically with respect to the substrate have already been used for field-emission applications. Coaxial CNTFETs could perhaps be fashioned by placing nanotubes inside the cavities of a porous material such as alumina, surrounding them by an electrolyte solution for gating of individual devices.

Carbon nanotube transistors are not, however, the only devices in which an increased channel coupling is being sought. Other Si technologies, such as the FinFET and the tri-gate MOSFET are presently attempting to do this, and "wrap-gated" InAs-nanowire transistors have already been successfully prototyped [41].

Before we describe simulations and device physics of CNTFETs, we examine a key issue, numerical simulation technique that commonly used in modeling of nanoscale devices, non-equilibrium Green function method (NEGF).

4. Non-equilibrium Green function method

A number of groups have reported modeling and simulation studies of CNTFETs [43-48]. Our intent in this section is not to review that works. Instead, we briefly describe the techniques we currently use to simulate CNTFETs, because the results of our simulations will be used in section V to illustrate key features of CNTFET device physics.

Detailed treatment of carbon nanotube electronics requires an atomistic description of the nanotube along with a quantum-mechanical treatment of electron transport. For ballistic transport, we self-consistently solve the Poisson and Schrödinger equations using the non-equilibrium Green's function (NEGF) formalism [49]. Electron-phonon scattering does occur

under modest bias [26] and can be simulated by semi-classical, so-called Monte Carlo techniques, but scattering has a rather small role on the dc performance of CNTFETs with a channel length less than 100 nm.

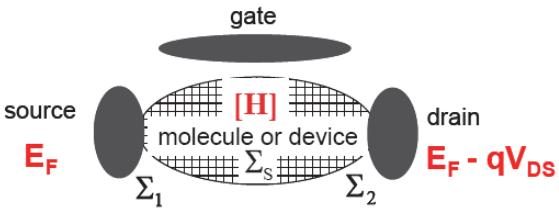

Fig. 6. A generic transistor comprised of a device channel connected to source and drain contacts. The source-drain current is modulated by a third electrode, the gate. The quantities involved in NEGF formalism are also shown.

To correctly treat transport in carbon nanotube transistors, we need to include quantum mechanical tunneling through the Schottky barriers at the metal-nanotube contacts, and quantum tunneling and reflection at the barriers within the nanotube channel. The non-equilibrium Green's function (NEGF) formalism provides a sound approach to describe ballistic and dissipative quantum transport. Figure 6 describes the essence of the technique and the key parameters of the formalism. We describe the device by using an effective mass Hamiltonian $H = -\left(\hbar^2 / 2m^*\right)\nabla^2 + U(r)$ and using the method of finite differences. The approach begins by identifying a suitable basis set and Hamiltonian matrix for the isolated channel. The self-consistent potential, which is a part of the Hamiltonian matrix, is included in the diagonal components of **H**, which is an N x N matrix where N is the total number of orbitals in the simulation domain (i.e. the number per carbon atom times the number of carbon atoms in the channel). The second step is to compute the so-called self-energy matrices, Σ_1, Σ_2, and Σ_S, which describe how the channel couples to the source and drain contacts, and to the scattering process. For example, only ballistic transport is treated, we assume that $\Sigma_S = 0$, while transport with scattering, $\Sigma_S \neq 0$. The third step is to compute the retarded Green's function. The retarded Green's function for the device in matrix form is given by

$$G(E) = [(E + i\eta^+)I - H - \Sigma(E)]^{-1} \tag{2}$$

where η^+ is an infinitesimal positive value, and I is the identity matrix.
The self-energy contains contributions from all mechanisms of relaxation, which are the source and drain electrodes, and from scattering:

$$\Sigma(E) = \Sigma_1(E) + \Sigma_2(E) + \Sigma_S(E) \tag{3}$$

Note that, in (2), the self-energy functions are, in general, energy dependent. The density matrix given by

$$[\rho] = \int_{-\infty}^{+\infty} \frac{dE}{2\pi} \left\{ \left[A_1(E)\right] f_1(E) + \left[A_2(E)\right] f_2(E) \right\} \tag{4}$$

where $A_{1,2}(E)$ are spectrum functions given by

$$A_1(E) = G\Gamma_1 G^+, A_2(E) = G\Gamma_2 G^+ \tag{5}$$

where level broadening can be defined as follows:

$$G_{1,2}(E) = i[S(E) - S^+(E)] \tag{6}$$

where $\Sigma^+(E)$ represents the Hermitian conjugate of $\Sigma(E)$ matrix defined by (2).
$f_{1,2}(E)$ are the Fermi distribution functions in the source and drain contacts, respectively. The Fermi distribution functions are given by

$$f_{1,2}(E) = \frac{1}{1 + \exp\left(E - \mu_{1,2}\right)/kT} \tag{7}$$

Once we apply a drain-source bias, V_{DS}, the Fermi energies in the source and drain contacts denoted by μ_1 and μ_2 will separate as follows

$$\mu_1 = E_f + \left(eV_{DS}/2\right) \text{ and } \mu_2 = E_f - \left(eV_{DS}/2\right) \tag{8}$$

The current flows from source to drain can be defined by

$$I = \frac{4e}{\hbar}\int_{-\infty}^{+\infty}\frac{dE}{2\pi}T(E)\left[f_1(E) - f_2(E)\right] \tag{9}$$

With the transmission coefficient T(E) given by

$$T(E) = \text{Trace}\left[G_1(E)G(E)G_2G^+(E)\right] \tag{10}$$

In the next section, we will use numerical simulations to discuss the physics of CNTFETs.

5. Simulations of CNTFET

In this section we summarize versions of simulators on nanoelectronics devices such as NEMO-VN1, and NEMO-VN2 that are developed by our research group for demonstrations. Especially, here we have focused on simulation results of CNTFETs. The reader can refer to [50, 51] for more detail.

5.1 NEMO-VN1 [52]

The dimensional scaling of CMOS device and process technology will become much more difficult as the industry approaches 10 nm around year 2020 and will eventually reach asymptotic end according to the International Technology Roadmap for Semiconductor for emerging research devices (2005). Beyond this period of traditional CMOS it may be possible to continue functional scaling by integrating an alternative electronic device on to a silicon platform. These alternative electronic devices in the future include 1D structures (such as CNTs and compound semiconductor nanowires), RTDs, SET, molecular and spin devices, all of which are discussed in ref. [52].

Despite these exciting possibilities, nanoelectronic devices are still in their relative infancy. The expense and difficulty of device fabrication precludes simply building and testing vast arrays of quantum devices. To focus efficiently on the best design, engineers need a tool that predicts electronic characteristics as a function of the device geometry and composition. In the more scientific mode, such a simulator would greatly enhance the understanding of quantum effects that drive the transport process and provide a means to investigate new device concepts.
Even conventional devices require a correction for quantum effects associated with the smaller device features. MOS devices, for example, exhibit electron confinement effects in the inversion layer. This phenomenon is a function of decreasing oxide thickness rather than the overall size of the device. Quantum effects become important as the oxide layer thickness decreases below 2 nm, which will soon be a standard for manufactured integrated circuits. Problems of this nature will become more prevalent as device geometries continue to shrink.
Nanoelectronic device modeling requires a fundamental quantum-mechanical approach. Many forms of quantum correction to classical electronic device models have been proposed or implemented. These include MOSFET-specific quantum corrections and generic quantum corrections to the drift-diffusion, hydrodynamic, and Boltzmann transport equation models. Therefore, the semiconductor industry needs a new fully quantum-mechanically based TCAD (technology computer aided design) tool [52].
To address this problem, we developed a general purpose quantum device simulator called NEMO-VN1 (NanoElectronic MOdeling in Vietnam). NEMO-VN1 can simulate a wide variety of nanoelectronic devices, including Quantum Dot (QD), Resonant Tunneling Diode (RTD), Resonant Tunneling Transistor (RTT), Single Electron Transistor (SET), Molecular FET (MFET), Carbon Nanotube Field Effect Transistor (CNTFET), Spin FET (SPINFET). It has a collection of models that allow user to trade off between calculation speed and accuracy. NEMO-VN1 also includes a graphic user interface (GUI) of Matlab that enables parameter entry, calculation control, display of calculation results, and in-situ data analysis methods.
In the next section, we review the capabilities of NEMO-VN1 and give example of typical NEMO-VN1 simulations.

5.1.1 NEMO-VN1 GUI

Another important goal of the NEMO-VN1 project was to make a user-friendly simulator that provides as much control as possible over every aspect of the simulation. Flexibility and ease of use are difficult to achieve simultaneously, but given the complexity of quantum device simulations became clear that both criteria were vital to program success. Consequently, graphic user interface (GUI) development was major part of the NEMO-VN1 program.

5.1.2 Main screen

NEMO-VN1 has a rich variety of simulation models, while this provides the maximum flexibility in term of applicability to different types of devices and test conditions. The problem is that NEMO-VN1 requires over 100 simulation parameters. Traditional device simulators force the users to familiarize themselves with all available simulation parameters and ensure that they are set correctly. To minimize this burden for the users, NEMO-VN1 uses a hierarchical approach to input and displays simulation parameter values. The top level of this hierarchy specifies the highest level option (type of device). Subsequent levels contain more detailed options such as current-voltage characteristics of devices, types of material, size of devices, size of barriers, temperature, colors, etc.

The main screen shown in Figure 7a is the central location where the user controls the NEMO-VN1 simulation. From Main Screen, the user can choose various types of quantum device simulations by clicking the mouse pointer on component items (left top corner). In this manner, the user can quickly enter the device list with minimum of typing. Double clicking the left mouse pointer on each item in the device list initiates the selection of models which is used to calculate the current voltage characteristics (Figure 7b).

(a) (b)

Fig. 7. a) The NEMO-VN1 main screen. File of components contains a device list. b) Pressing left mouse pointer on "components" displays a list of simulation quantum devices.

5.1.3 NEMO-VN1 simulation

In the course of the NEMO-VN1 program, we have simulated QD, QWi, QWe, RTD, RTT, SET, CNTFET, MFET, and SPINFET. As example, in the following sections, we consider current voltage characteristics of CNTFET.

5.1.4 CNTFET's simulation

The algorithm for the calculation of drain current in the model can be described as follows. Because of the small size of these devices, and the near one-dimensional nature of charge transport within them, CNTFET's modeling demands a rigorous quantum-mechanical basis. This is achieved in this model by using non-equilibrium Green's function method to compute transport of the electron and hole charges in nanotubes, and by using the Landauer Equation to compute the drain current. The model of CNTFET is displayed in Figure 8a. Current voltage characteristics are shown in Figure 8b.

The current voltage curve can be divided into two regions: linear and saturation. Drain current in the linear region of planar CNTFET can be described as follows:

$$I_d = \frac{W}{L}\mu C_{ox}[(V_{gs} - V_T)V_{ds} - \frac{V_{ds}^2}{2}] \tag{11}$$

or

$$I_d = K_n\left[2\left(V_{gs} - V_T\right)V_{ds} - V_{ds}^2\right] \tag{12}$$

where K_n is conductance of CNTFET, W is the width of CNTFET, L is the length of CNTFET, μ is mobility of carriers, C_{ox} is oxide gate capacitance.

We can also obtain saturation current of CNTFET by replacing $V_{ds(sat)} = V_{gs} - V_T$. Then the expression of saturation current of CNTFET can be written:

$$I_{d(sat)} = K_n\left(V_{gs} - V_T\right)^2 \tag{13}$$

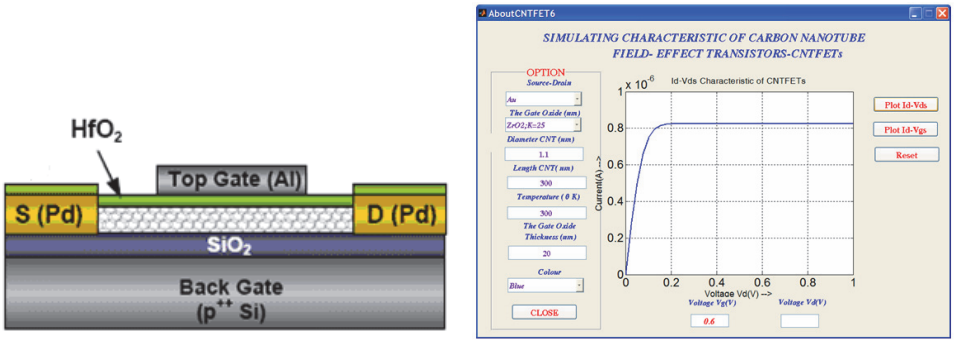

(a) (b)

Fig. 8. a) The model of CNTFET, b) NEMO-VN1 plots current voltage characteristics for CNTFET. Current is measured as a function of drain voltage at 300 K. For this device, source-drain of CNTFET is made of Au, the diameter of CNT is 1.1 nm, the length of CNT is 300 nm, the gate thickness is 20 nm

The drain I-V characteristics in 3D are shown in Figure 9. The parameters used in 3D simulation are drain current-voltage characteristics and temperature. Drain I-V characteristics exhibited dependence of saturation drain current (ON-current) on temperature. When CNTFET is cooled, drain saturation currents were lightly decreased.

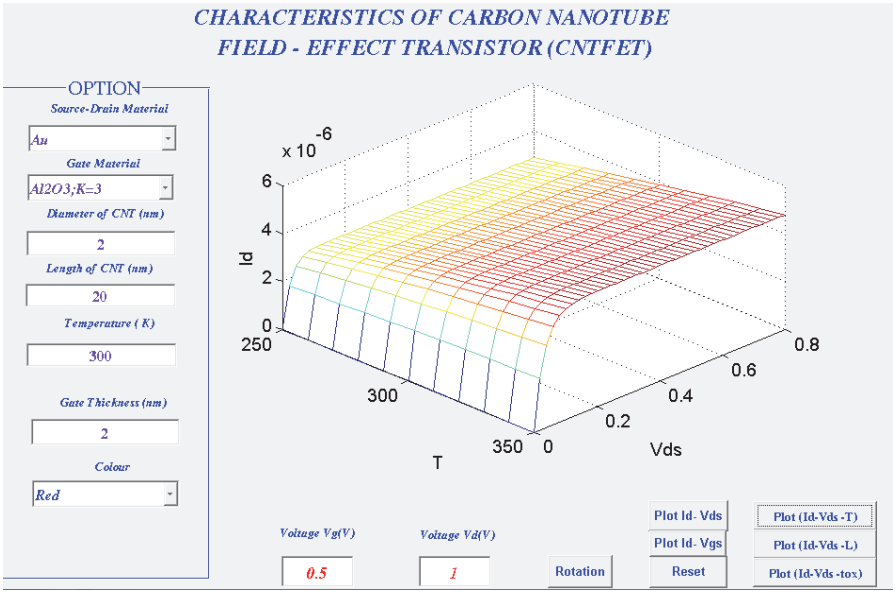

Fig. 9. Drain current-voltage characteristics in 3D. When CNTFET is cooled, its saturation drain currents are lightly decreased.

Drain current-voltage characteristics in 3D exhibited dependence of saturation currents on CNTFET length, L are shown in figure 10. Tendency of saturation currents is decreased, when CNTFET length is increased. We found that in the range of CNTFET length from 10 nm to 15 nm, ON-currents lightly changed.

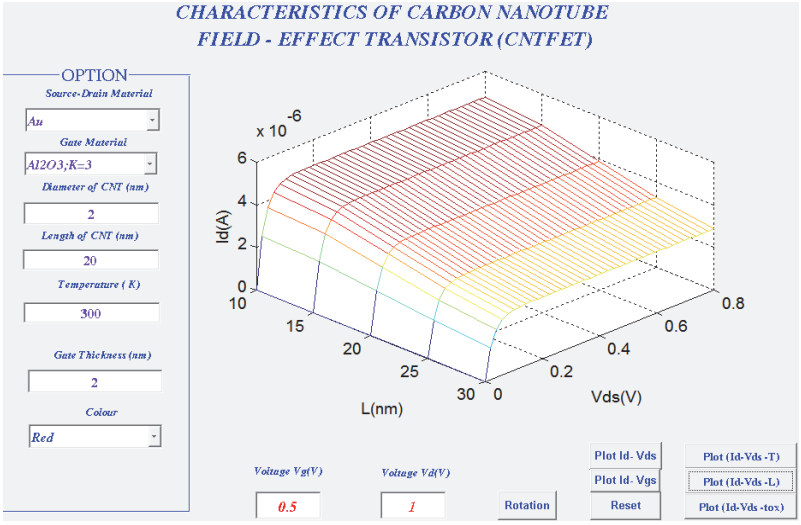

Fig. 10. Drain current-voltage characteristics in 3D exhibited dependence of saturation drain currents on CNTFET length.

Drain current-voltage characteristics in 3D exhibited dependence of saturation current on the gate thickness of CNTFET, t_{ox} are shown in figure 11.

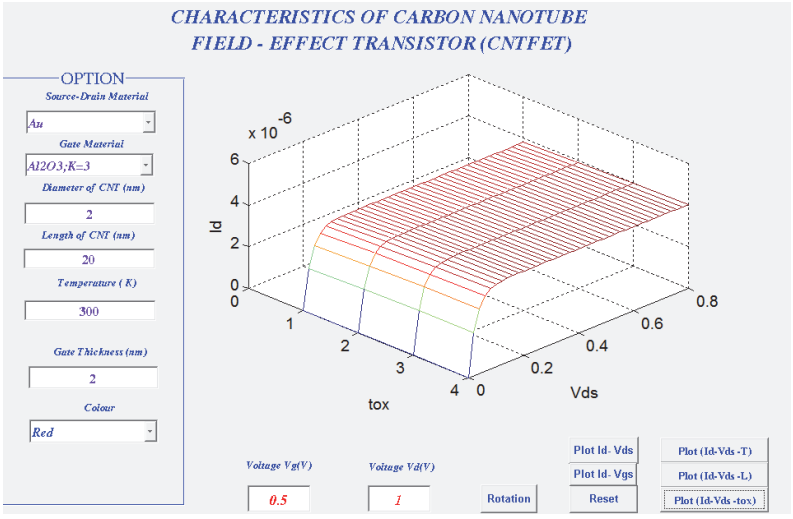

Fig. 11. Drain current-voltage characteristics in 3D exhibited dependence of saturation drain currents on the gate thickness of CNTFET.

The current voltage curve can be divided into two regions: linear and saturation. Drain current in the linear region of coaxial CNTFET can be described as follows:

$$I_d = \mu C_{ox}[(V_{gs} - V_T)V_{ds} - \frac{V_{ds}^2}{2}] \tag{14}$$

or

$$I_d = K_n\left[2\left(V_{gs} - V_T\right)V_{ds} - V_{ds}^2\right] \tag{15}$$

where K_n is conductance of CNTFET, μ is mobility of carriers, C_{ox} is gate capacitance.
In the coaxial CNTFET,

$$C_{ox} = 2\pi R_g L_g k\varepsilon_0 \left(\lg\frac{R_g}{R_t}\right)^{-1} \tag{16}$$

where k is relative dielectric constant, ε_0 is dielectric constant in vacuum, 8.85×10^{-14}Fcm^{-2}.
We can also obtain saturation current of coaxial CNTFET by replacing $V_{ds(sat)} = V_{gs} - V_T$. Then the expression of saturation current of CNTFET can be written:

$$I_{d(sat)} = K_n\left(V_{gs} - V_T\right)^2 \tag{17}$$

The drain I-V characteristics in 2D are shown in figure 12. The saturation current at V_{GS} = 0.5 V is around 6 μA.

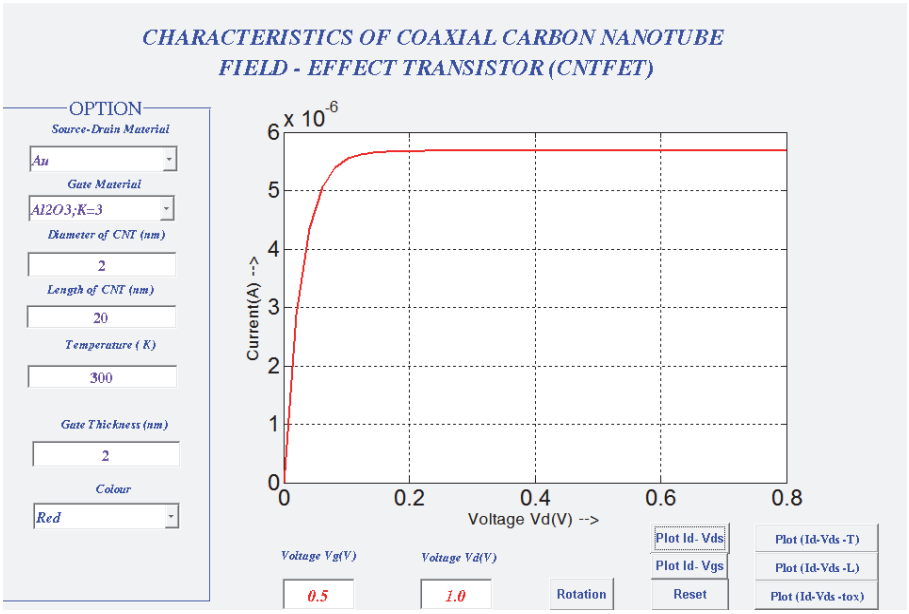

Fig. 12. Drain current-voltage characteristics of coaxial CNTFET.

The drain I-V characteristics in 3D are shown in figure 13. The parameters used in 3D simulation were drain current-voltage characteristics and temperature. Drain I-V characteristics exhibited dependence of saturation drain current on temperature. When CNTFET is cooled, saturation currents were lightly decreased.

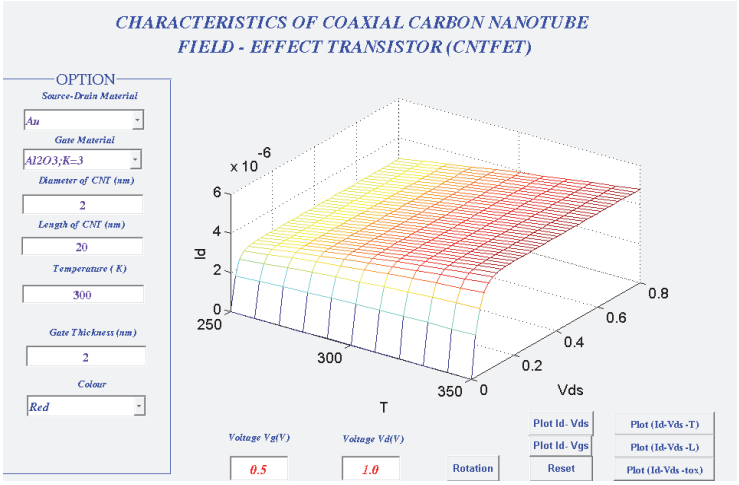

Fig. 13. Drain current-voltage characteristics in 3D. When CNTFET is cooled, its saturation drain currents were lightly decreased.

Drain current-voltage characteristics in 3D exhibited dependence of saturation currents on CNTFET length, L are shown in figure 14. Tendency of saturation currents is decreased, when CNTFET length is increased. We have also found that in the case of coaxial CNTFET, ON-currents in the range of the length, L from 10 nm to 15 nm is lightly decreased.

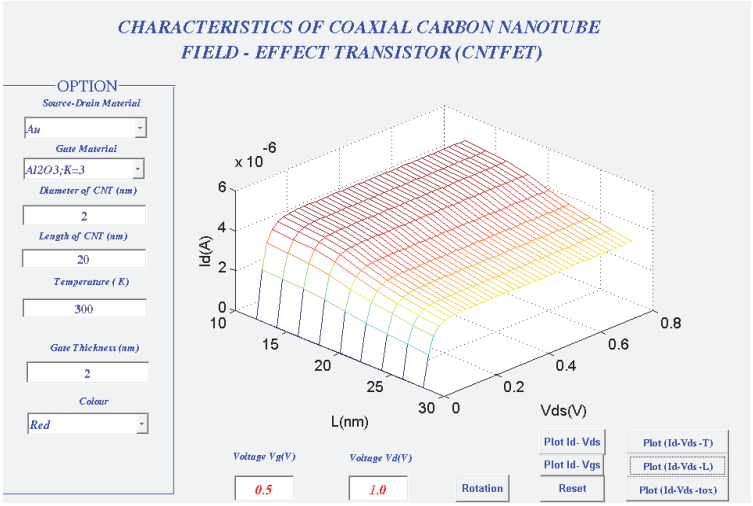

Fig. 14. Drain current-voltage characteristics in 3D exhibited dependence of saturation drain currents on CNTFET length.

5.2 NEMO-VN2 [53]

The quantum device simulator – NEMO-VN2 focuses on carbon nanotube FET (CNTFET). CNTFETs have been studied in recent years as potential alternatives to CMOS devices because of their compelling properties. Studies of phonon scattering in CNTs and its influence in CNTFET have focused on metallic tubes or on long semiconducting tubes. Phonon scattering in short channel CNTFETs, which is important for nanoelectronic applications, remains unexplored. In this work the non-equilibrium Green's function (NEGF) is used to perform a comprehensive study of CNT transistors. The program has been written by using graphic user interface (GUI) of Matlab. We find that the effect of scattering on current-voltage characteristics of CNTFET is significant. The degradation of drain current due to scattering has been observed. Some typical simulation results have been presented for illustration.

5.2.1 Simulation results of CNTFETs

The main goal of the NEMO-VN2 project was to make a user-friendly simulator that provides as much control as possible over every aspect of the simulation. Flexibility and ease of use are difficult to achieve simultaneously, but given the complexity of quantum device simulations became clear that both criteria were vital to program success. Consequently, graphic user interface (GUI) development was major part of the NEMO-VN2 program.

NEMO-VN2 has a rich variety of simulation models, while this provides the maximum flexibility in term of applicability to types of different devices and test conditions. The problem is that NEMO-VN2 requires over 100 simulation parameters. Traditional device simulators force the users to familiarize themselves with all available simulation parameters and ensure that they are set correctly. To minimize this burden for the users, NEMO-VN2 uses a hierarchical approach to input and displays simulation parameter values. The top level of this hierarchy specifies the highest level option (nanodevices). Subsequent levels contain more detailed options such as current-voltage characteristics of devices, types of material, size of devices, size of barriers, temperature, colours, etc.

The main screen shown in figure 15a is the central location where the user controls the NEMO-VN2 simulation. From main screen, the user can choose various types of quantum device simulations by clicking the left mouse pointer on the submenu of nanodevices (in the left top corner). In this manner, the user can quickly enter the device list and hot keys with minimum of typing. Clicking the left mouse pointer on each item in the device list or using hot keys initiates the selection of models which is used to calculate the current voltage characteristics (figure 15b).

In the course of the NEMO-VN2 program, we have simulated all of emerging nanodevices such as RTD, RTT, SET, planar CNTFET, coaxial CNTFET, molecular FET, and SPINFET. Here, as an example, we study the effects of phonon scattering on the planar and coaxial CNTFET characteristics. We compare their characteristics under ballistic and that with phonon scattering. The device parameters are used for the simulations are as follows: source-drain material of Au, length of CNTFET, L = 20 nm, diameter of CNT, d = 1.5 nm, zigzag, gate material of Al_2O_3, gate thickness, t_{ox} = 2 nm, temperature under simulation, T = 300 K.

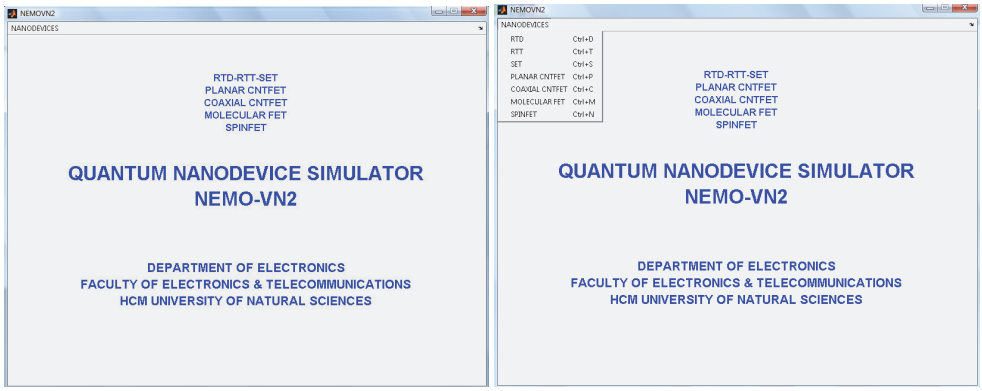

(a) (b)

Fig. 15. a) The NEMO-VN2 main screen, b) pressing left mouse pointer on "NANODEVICES" displays a list of simulation quantum devices.

Figure 16 compares the I_{DS}-V_{DS} results for two types of planar and coaxial CNTFETs having the length of 20 nm under ballistic transport and that with phonon scattering. It is shown that scattering can have an appreciable affect on the ON-current. At V_{GS} = 0.7 V, in the planar and coaxial CNTFETs, the ON-current is reduced by 9% due to the phonon scattering. It can be noted that when the gate voltage is increased the saturated drain current gradually increased.

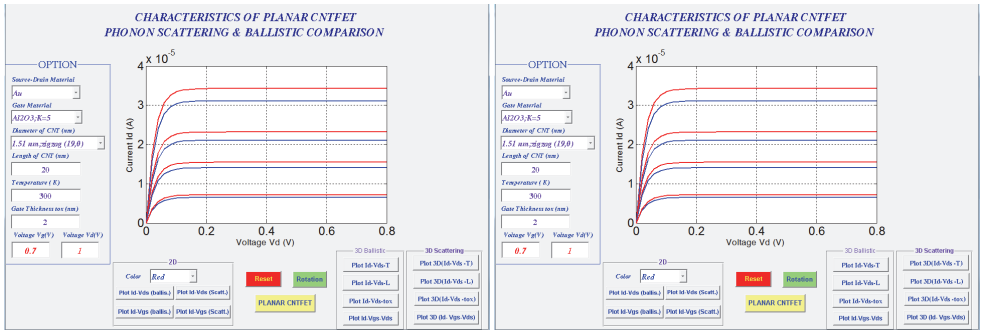

a) b)

Fig. 16. I_{DS}-V_{DS} characteristics of a) planar and b) coaxial CNTFETs having the length of 20 nm under ballistic transport (red colour), with scattering (green colour) at various gate biases in the range from 0.4 to 0.7 V in the step of 0.1 V. The bottom and top curves are at the gate voltages of 0.4 V and 0.7 V, respectively.

Figure 17 shows I_{DS}-V_{GS} characteristics of planar and coaxial CNTFETs. When the gate voltage is small, the drain current is gradually increased. When the gate voltage is greater than V_{GS} = 0.3 V, the drain current is exponentially increased.

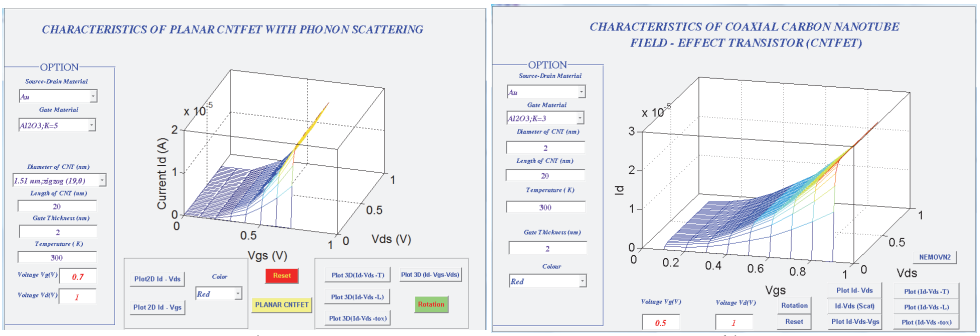

a) b)

Fig. 17. Three dimensional simulations of I_{DS}-V_{GS} characteristics of CNTFETs having the length of 20 nm: a) planar, b) coaxial.

Figure 18 compares the length dependence of I_{DS}-V_{DS} results for the (19,0) CNTFETs under phonon scattering. The ON-current at V_{GS} = 0.7 V is reduced when the length is changed by 15, 10, 5, 2.5 nm. In figure 18a, it is also shown that the impact of phonon scattering in planar CNTFET increases for shorter length tubes at high voltage bias. It should be noted that ON-current strongly depends on reducing the length of CNTFET. At high gate voltage bias ON-current of CNTFET having length of 15 nm is by 30 μA, when length of CNTFET reduced to 2.5 nm ON-current is by 8 pA. In figure 18b, it is also shown that the impact of phonon scattering in coaxial CNTFET. ON - current increases for shorter length tubes at high voltage bias. It should be noted that ON-current strongly depends on reducing the length of CNTFET. At high gate voltage bias ON-current of the coaxial CNTFET having length of 15 nm is by 9 μA, when length of CNTFET reduced to 2.5 nm ON-current is by 150 nA.

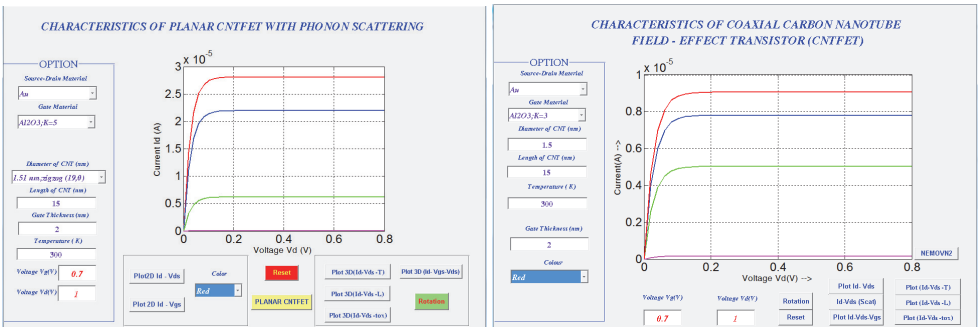

a) b)

Fig. 18. The length dependence of I_{DS}-V_{DS} results for the (19,0) CNTFETs under phonon scattering: a) planar CNTFETs; b) coaxial CNTFETs. The lengths of CNTFETs are of 15, 10, 5, 2.5 nm from top to bottom curves.

Figure 19a compares the diameter dependence of the I_{DS}-V_{DS} results of the impact of phonon scattering in planar CNTFET having the length of 15 nm. It is shown that ON-currents at V_{GS} = 0.7 V increase by 8, 11, 14 μA when diameters of CNT increase by 1.25, 1.5, 1.7 nm, respectively. In figure 19a, it notes that the impact of phonon scattering in CNTFET decreases for larger diameter tubes.

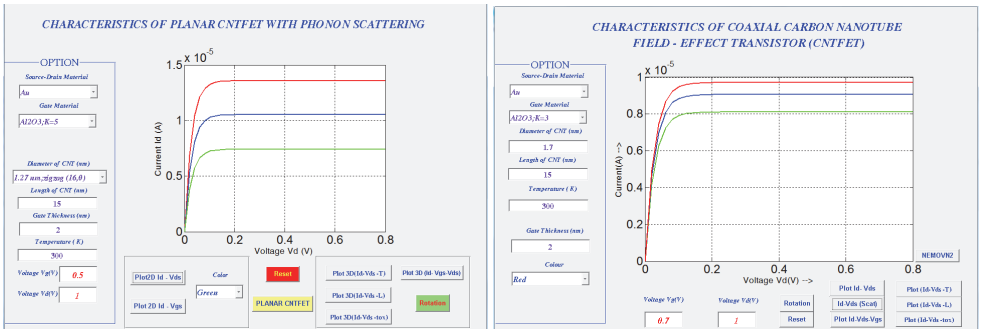

a) b)

Fig. 19. The diameter dependence of I_{DS}-V_{DS} characteristics at V_{GS} = 0.7 V in CNTFET having the length of 15 nm under scattering: a) in planar CNTFET ON-current increase by 8, 11, 14 μA when diameters of CNT increase by 1.25, 1.5, 1.7 nm, respectively, b) in coaxial CNTFET under scattering, ON-currents increase by 8.0, 9.0, 9.5 μA when diameters of CNT increase by 1.25, 1.5, 1.7 nm, respectively.

Figure 19b compares the diameter dependence of the I_{DS}-V_{DS} results of the impact of phonon scattering in coaxial CNTFET of 15 nm length. It is shown that I_{DS}-V_{DS} results at V_{GS} = 0.7 V increase by 8.0, 9.0, 9.5 μA when diameters of CNT increase by 1.25, 1.5, 1.7 nm, respectively. In figure 19b, it is also shown that the impact of phonon scattering in CNTFET decreases for larger diameter tubes.

6. Conclusion

Carbon nanotube field-effect transistors are interesting devices with potentially important applications in nanoelectronics. In this work, we have summarized the current status of the field in terms of fabrication technology and device physics. The rate of progress in CNTFET technology and in the understanding of their device physics has been very rapid. Although uncertainties remain, the dc performance of field-effect transistors can now be explained. During the next few years, we expect to see increased work on other devices, for example, high-speed transistors, optoelectronics devices, and bio-sensors. We are sure to learn a good deal of interesting new device physics in the process and may even discover important technological applications.

7. References

[1] S. Iijima, Helical Microtubules of Graphitic Carbon, *Nature*, Vol. 354, pp. 56-58, 1991.

[2] S. J. Tans, A. R. M. Verschueren, and C. Dekker, Room-temperature transistor based on a single carbon nanotube, *Nature*, Vol. 393, pp. 49-52, 1998.

[3] P. Avouris, J. Appenzeller, R. Martel, and S. J. Wind, Carbon nanotube electronics, *Proceedings of the IEEE*, Vol. 91, pp. 1772-1784, 2003.

[4] P. L. McEuen, M. S. Fuhrer, and H. K. Park, Single-walled carbon nanotube electronics, *IEEE Transactions on Nanotechnology*, Vol. 1, pp. 78-85, 2002.

[5] S. Heinze, J. Tersoff, R. Martel, V. Derycke, J. Appenzeller, and P. Avouris, Carbon nanotubes as Schottky barrier transistors, *Physical Review Letters*, Vol. 89, pp.106801.1-106801.4, 2002.

[6] J. Guo, S. Datta, and M. Lundstrom, A numerical study of scaling issues for Schottky-Barrier carbon nanotube transistors, *IEEE Transactions on Electron Devices*, Vol. 51, pp. 172-177, 2004.

[7] R. Saito, G. Dresselhaus, and M. S. Dresselhau, *Physical Property of Carbon Nanotubes*, Imperial Colledge Press, London, U.K, 1998.

[8] S. J. Wind, J. Appenzeller, R. Martel, V. Derycke, and P. Avouris, Fabrication and electrical characterization of top gate single-wall carbon nanotube field-effect transistors, *Journal of Vacuum Science & Technology B*, Vol. 20, pp. 2798-2801, 2002.

[9] A. Javey, J. Guo, Q. Wang, M. Lundstrom, and H. J. Dai, Ballistic carbon nanotube field-effect transistors, *Nature*, Vol. 424, pp. 654-657, 2003.

[10] A. Javey, J. Guo, D. B. Farmer, Q. Wang, E. Yenilmez, R. G. Gordon, M. Lundstrom, and H. Dai, Self-aligned ballistic molecular transistors and parallel nanotube arrays, *Nano. Lett.*, Vol. 4, No. 7, pp. 1319-1320, 2004.

[11] A. Thess, R. Lee, P. Nikolaev, H. Dai, P. Petit, J. Robert, C. Xu, Y. H. Lee, S. G. Kim, A. G. Rinzler, D. T. Colbert, G. E. Scuseria, D. Tomanek, J. E. Fischer, and R. E. Smalley, Crystalline ropes of metallic carbon nanotubes, *Science*, Vol. 273, pp. 483-487, 1996.

[12] J. Kong, H. T. Soh, A. M. Cassell, C. F. Quate, and H. Dai, Synthesis of individual single-walled carbon nanotubes on patterned silicon wafers, *Nature*, Vol. 395, pp. 878-881, 1998.

[13] Sander J. Tans, Alwin R. M. Verschueren, and Cees Dekker, Room-temperature transistor based on a single carbon nanotube, *Nature*, Vol. 393, pp. 49-52, 1998.

[14] R. Martel, T. Schmidt, H. R. Shea, T. Hertel, and Ph. Avouris, Single- and multi-wall carbon nanotube field-effect transistors, *Appl. Phys. Lett.*, Vol. 73, No. 17, pp. 2447-2449, 1998.

[15] Adrian Bachtold, Peter Hadley, Takeshi Nakanishi, and Cees Dekker, "Logic circuits with carbon nanotube transistors," *Science*, Vol. 294, pp. 1317-1320, 2001.

[16] S. J. Wind, J. Appenzeller, R. Martel, V. Derycke, and Ph. Avouris, Vertical scaling of carbon nanotube field-effect transistors using top gate electrodes, *Appl. Phys. Lett.*, Vol. 80, No. 20, pp. 3817-3819, 2002.

[17] R. Martel, V. Derycke, C. Lavoie, J. Appenzeller, K. K. Chan, J. Tersof, and Ph. Avouris, Ambipolar electrical transport in semiconducting single-wall carbon nanotubes, *Phys. Rev. Lett.*, Vol. 87, No. 25, pp. 256805-1-256805-4, 2001.

[18] Ali Javey, Hyoungsub Kim, Markus Brink, QianWang, Ant Ural, Jing Guo, Paul McIntyre, Paul McEuen, Mark Lundstrom, and Hongjie Dai, High-k dielectrics for advanced carbon-nanotube transistors and logic gates, *Nature Mater.*, Vol. 1, pp. 241-246, 2002.

[19] S. J. Wind, J. Appenzeller, and Ph. Avouris, Lateral scaling in carbon-nanotube field-effect transistors, *Phys. Rev. Lett.*, Vol. 91, No. 5, 058301-1-058301-4, 2003.

[20] J. Appenzeller, J. Knoch, V. Derycke, R. Martel, S. Wind, and P. Avouris, Field-modulated carrier transport in carbon nanotube transistors, *Physical Review Letters*, Vol. 89, No. 12, 126801, 2002.

[21] B. M. Kim, T. Brintlinger, E. Cobas, M. S. Fuhrer, H. M. Zheng, Z. Yu, R. Droopad, J. Ramdani, and K. Eisenbeiser, High-performance carbon nanotube transistors on $SrTiO_3$/Si substrates, *Applied Physics Letters*, Vol. 84, pp. 1946-1948, 2004.

[22] S. Rosenblatt, Y. Yaish, J. Park, J. Gore, V. Sazonova, and P. L. McEuen, High performance electrolyte gated carbon nanotube transistors, *Nano Letters*, Vol. 2, pp. 869-872, 2002.

[23] G. P. Siddons, D. Merchin, J. H. Back, J. K. Jeong, and M. Shim, Highly efficient Gating and doping of carbon nanotubes with polymer electrolytes, *Nano Letters*, Vol. 4, pp. 927-931, 2004.

[24] Z. Yao, C. L. Kane, and C. Dekker, High-field electrical transport in single-wall carbon nanotubes, *Physical Review Letters*, Vol. 84, pp. 2941-2944, 2000.

[25] T. Ando, H. Matsumura, and T. Nakanishi, Theory of ballistic transport in Carbon Nanotubes, *Physica B*, Vol. 323, pp. 44, 2002.

[26] A. Javey, J. Guo, M. Paulsson, Q. Wang, D. Mann, M. Lundstrom, and H. J. Dai, High-field quasiballistic transport in short carbon nanotubes, *Physical Review Letters*, Vol. 92, 106804, 2004.

[27] J. Y. Park, S. Rosenblatt, Y. Yaish, V. Sazonova, H. Ustunel, S. Braig, T. A. Arias, P. W. Brouwer, and P. L. McEuen, Electron-phonon scattering in metallic single-walled carbon nanotubes, *Nano Letters*, Vol. 4, pp. 517-520, 2004.

[28] A. Javey, J. Guo, D. B. Farmer, Q. Wang, E. Yenilmez, R. G. Gordon, M. Lundstrom, and H. Dai, Self-aligned ballistic molecular transistors and parallel nanotube arrays, *Nano Letters*, Vol. 4, pp. 1319-1322, 2004.

[29] R. Seidel, A. P. Graham, E. Unger, G. S. Duesberg, M. Liebau, W. Steinhoegl, F. Kreupl, and W. Hoenlein, High-current nanotube transistors, *Nano Letters*, Vol. 4, pp. 831-834, 2004.

[30] V. Derycke, R. Martel, J. Appenzeller, and P. Avouris, Carbon nanotube inter- and intramolecular logic gates, *Nano Letters*, Vol. 1, pp. 453-456, 2001.

[31] A. Bachtold, P. Hadley, T. Nakanishi, and C. Dekker, Logic circuits with carbon nanotube transistors, *Science*, Vol. 294, pp. 1317-1320, 2001.

[32] D. J. Frank and J. Appenzeller, High-frequency response in carbon nanotube field-effect transistors, *IEEE Electron Device Letters*, Vol. 25, pp. 34-36, January 2004.

[43] J. Appenzeller and D. J. Frank, Frequency dependent characterization of transport properties in carbon nanotube transistors, *Applied Physics Letters*, Vol. 84, pp. 1771-1773, 2004.

[34] S. D. Li, Z. Yu, S. F. Yen, W. C. Tang, and P. J. Burke, Carbon nanotube transistor operation at 2.6 GHz, *Nano Letters*, Vol. 4, pp. 753-756, 2004.

[35] P.J. Burke, Luttinger Liquid theory as a model of the gigahertz electrical properties of carbon nanotubes, *IEEE Transactions on Nanotechnology,* Vol.2, No.1, pp. 129-144, Sept. 2002.

[36] P.J. Burke, An RF circuit model for carbon nanotubes, *IEEE Transactions on Nanotechnology,* Vol.2, No.1, pp. 55-58, March. 2003.

[37] M. Radosavljevic, J. Appenzeller, Ph. Avouris, and J. Knoch, High performance of potassium n-doped carbon nanotube field-effect transistor, *Applied Physics Letters*, Vol. 84, No. 18, pp. 3693-3695, 2004.

[38] A. Javey, R. Tu, D. B. Farmer, J. Guo, R. G. Gordon, and H. Dai, High performance n-type carbon nanotube field-effect transistors with chemically doped contacts, *Nano Letters*, Vol.5, No. 2, pp.345-348, 2005.

[39] M. Kruger, M. R. Buitelaar, T. Nussbaumer, C. Schonenberger, and L. Forro, Electrochemical carbon nanotube field-effect transistor, *Appl. Phys. Lett.*, Vol. 78, No. 9, 1291-1293, 2001.

[40] Sami Rosenblatt, Yuval Yaish, Jiwoong Park, Jeff Gore, Vera Sazonova, and Paul L. McEuen, High performance electrolyte gated carbon nanotube transistors, *Nano Lett.*, Vol. 2, No. 8, pp. 869-872, 2002.

[41] Lars-Erik Wernersson, Tomas Bryllert, Erik Lund, and Lars Samuelson, Wrap-gated InAs nanowire field-effect transistor, *IEDM Tech. Digest*, 273-276, 2005.

[42] Paul Stokes and Saiful I. Khondaker, Local gated single-walled carbon nanotube field effect transistors assembled by AC dielectrophoresis, *Nanotechnology*, Vol. 49, 175202, 2008.

[43] D.L. John, L.C. Castro, J.P. Clifford and D.L. Pulfrey, Electrostatics of coaxial schottky-barrier nanotube field-effect transistors, *IEEE Trans. Nanotech.*, Vol. 2, 175-180, 2003.

[44] G. Pennington and N. Goldsman, Semi-classical transport and phonon scattering on electrons in semiconducting carbon nanotubes, Phys. Rev. B, 68, 045426, 2003.

[45] K. Alam and R. Lake, Performance of 2 nm gate length carbon nanotube field-effect transistors with source-drain underlaps, *Appl. Phys. Lett.*, Vol. 87, pp. 073104, 2005.

[46] A. Verma, M. Z. Kauser, and P. P. Ruden, Ensemble Monte Carlo transport simulations for semiconducting carbon nanotubes, *J. Appl. Phys.*, Vol. 97, pp. 114319, 2005.

[47] T. S. Xia, L. R. Register, and S. K. Banerjee, Calculations and applications of the complex band structure for carbon nanotube field-effect transistors, *Phys. Rev. B*, Vol. 70, pp. 045332, 2004.

[48] A. Svizhenko and M. P. Anantram, Effect of scattering and contacts on current and electrostatics in carbon nanotubes, *Phys. Rev. B.*, Vol. 72, pp. 085430, 2005.

[49] S. Datta, Q*uantum transport: atom to transistor*, Cambridge University Press, Cambridge, UK, 2005.

[50] Dinh Sy Hien, Dinh Viet Nga, Nguyen Thi Luong, Thi Tran Anh Tuan, Modeling of planar carbon nanotube field effect transistor and three dimensional simulations of current-voltage characteristics, *Journal of Physics*, Vol. 187, 012049, UK (8pp), 2009.

[51] Dinh Sy Hien, Nguyen Thi Luong, Thi Tran Anh Tuan, 3D simulation of coaxial carbon nanotube field effect transistor, *Journal of Physics*, Vol. 187, 012061, UK (8pp), 2009.

[52] Dinh Sy Hien, Nguyen Thi Luong, Le Hoang Minh, Tran Tien Phuc, Pham Thanh Trung, Bui An Dong, Huynh Lam Thu Thao, Nguyen Van Le Thanh, Thi Tran Anh Tuan, Huynh Hoang Trung, Nguyen Thi Thanh Nhan, Dinh Viet Nga, Development of quantum device simulator, NEMO-VN1, *Journal of Physics*, Vol. 187, 012088, 2009.

[53] Dinh Sy Hien, Development of quantum device simulator, NEMO-VN2, *Proceedings of fifth IEEE international symposium on electronic design, test and applications, DELTA 2010*, 13-15 January 2010, Ho Chi Minh City, pp. 170-173, 2010.

9

Functionalization Methods of Carbon Nanotubes and Its Applications

Lifei Chen, Huaqing Xie and Wei Yu
School of Urban Development and Environmental Engineering,
Shanghai Second Polytechnic University,
Shanghai,
China

1. Introduction

In 1991 Iijima [Iijima, 1991] presented transmission electron microscopy observations of elongated and concentric layered microtubules made of carbon atoms, nowadays which were called carbon nanotubes (CNTs). In order to understand the structure of a carbon nanotube, it can be first imagined as a rolled up sheet of graphene with planar-hexagonal arrangement of carbon atoms distributed in a honeycomb lattice. CNTs are classified into single-walled carbon nanotube, double-walled carbon nanotube, and multi-walled carbon nanotube according to the rolling layers of graphene sheets. Several techniques for producing CNTs have been established and all of them have advantages as well as disadvantages. Usually being applied methods are high temperature techniques, namely arc discharge [Bystrzejewski et al., 2008; Sun et al., 2007] and laser ablation [Rüummeli et al., 2007], as well as chemical vapor deposition (CVD) with its most common variants [Ayala et al., 2008; Nikolaev et al., 1999]. CNTs possess unique electronic, chemical, and mechanical properties that make them leading materials for a variety of potential applications. But the outer wall of pristine CNTs is, in principle, conceived as chemically inert. This is not always desirable for applications and for this reason. One of the most promising routes to overcome this difficulty is to functionalize CNT. Functionalization extends their properties and consequently their application potential. Hence understanding their functionalization is crucial for fully exploiting their potential. Researchers have developed some effective methods to functionalize CNT surfaces such as covalent modification or noncovalent approaches including polymer wrapping, biomolecule binding, and metal ion binding. Other functionalization routes which have been thought to make them chemically active in the past few years, including chemical and solid-phase or hydro-mechanochemical method will also be introuduced in details in the following contributions. The advantages and shortcomings of every functionalization method will be showed clearly. At the same time some characterization methods for CNTs will be also refered. In the last part of this chapter the applications of carbon nanotubes as functional materials in the fields of biosensing, fuel cells, medical treatment, and so on, especially in the field of thermal conductivity are summarized. It is our hope that all the content of this chapter can supply helps to the researchers in the study of carbon nanotubes.

2. Functionalization

2.1 Noncovalent functionalization of carbon nanotubes

CNTs are usually functionalized by harsh oxidative processes, such as refluxing in the mixture of HNO_3 and H_2SO_4 to generate defects on the sidewalls and tube tips, those defects can serve as anchor groups for functionalization and/or can provide sites for the coordination chemistry [Li et al., 2007]. However, such oxidation method usually reduces the electrical conductivity and corrosion resistance of CNTs due to the introduction of a large number of defects. Therefore, development of a better and more effective functionalization method that can not only introduce high density and homogeneous surface functional groups but also has little or no structural damage to CNTs remains a major challenge. Recently, noncovalent functionalization of CNTs has attracted particular attention because it does not induce any structural transformation and secondary structure.

2.2.1 Polymer functionalization of multi-walled carbon nanotubes

Polyaniline, polypyrrole, polythiophene and their derivatives have been considered as promising materials for supercapacitors [Woo et al., 2008], electrochemical sensor [Waghuley et al., 2008], modification agent [Mohana Reddy et al., 2009] and so on due to the existence of various oxidation structures, electrically conducting polymers. Among them, conducting polypyrrole has been the focus of a great deal of research for catalytic materials application in recent years because its superior properties including high electric conductivity, high specific capacitance and good chemical and thermal stability, especially facile synthesis and environmentally friendly. Zhao et al [Zhao et al., 2010] reported a simple chemical polymerization of pyrrole monomer on Multi-walled CNTs (MWNTs) without addition any oxidants at room temperature. This method avoids the requirement of lower temperature and the introduction of lots of impurity ions from the oxidants used during the chemical oxidative polymerization of the pyrrole monomer. Furthermore, such treatment could preserve the integrity and the electronic structure of MWNTs.

Poly ethylene glycol (PEG) have been one of the most preferred synthetic molecular species for various purposes in bio-related applications owing to its non-toxicity as well as its good solubility under various physiological conditions. From many earlier studies Lee et al [Lee et al., 2007] found that molecules containing aromatic moieties are adsorbed onto the graphite surface more strongly than molecules composed only of aliphatic components, owing to π–π interaction between the graphite surface and the aromatic component of amphiphilic molecule involving both the van der Waals interaction and the electrostatic interaction. Using amphiphilic molecules to functionalize CNT surfaces has been recognized as one of the most useful approaches to improve the dispersion of CNTs in aqueous media. Using this approach, the solubility of CNTs can be greatly enhanced by anchoring hydrophobic segments on the surfaces of CNTs, where hydrophilic segments are orientated toward the aqueous phase. Recently, several groups reported on the solubilization of single-walled CNTs (SWNTs) in water using amphiphilic building blocks such as block copolymers, lipids, and surfactants [Balavoine et al., 1999]. Park [Park et al., 2007] described a noncovalent process for surface functionalization of SWNTs using amphiphilic diblock copolymer (PEtOz-PCL), consisting of hydrophilic PEtOz and hydrophobic PCL, with remarkably enhanced solubility particularly in aqueous media. The PEtOz block on the nanotube surface provides possibility to further controlled assembly and also can be utilized as a template for the formation of Au nanoparticles on the surface of SWNT.

Using polymer chains to 'wrap' CNTs is a versatile and effective way for CNT functionalization. In particular, block copolymers (BCPs) may provide a series of attractive noncovalent wrapping and decoration for the functionalization of CNTs. These approaches can be driven by distinct interactions between CNTs and polymers including p-stacking, electrostatic interactions, and decoration of CNTs with micelles [Zou et al., 2008; Kang et al., 2003]. One block of the BCPs forms a close interaction with CNTs, while the other block(s) provide the dispersibility and chemical compatibility to the CNTs [Szleifer &Yerushalmi-Rozen, 2005]. More attractively, the intriguing ability of BCPs to self-assemble into ordered nanostructures brings researchers an ideal nanoscale template for CNT alignment control, and can be utilized further for fabrication of functional hybrid materials and functional devices including flexible field emission display panels. Recently, Li et al [Li et al., 2005; Li et al., 2006] decorated CNTs using controlled crystallization of homopolymers such as poly(ethylene) (PE) and nylon-66. The heteroepitaxial growth of crystalline polymers on CNT surfaces provides a new way in noncovalent methods for Wang et al [Wang et al., 2010] to decorate BCP on CNTs via a controlled polymer crystallization method. This method not only provides a noncovalent technique for BCP decoration on CNT surfaces, but also provides a promising approach to the uniform dispersion of CNTs in selective microdomains of BCPs and controlled alignment of CNTs in BCP ordered nanostructures. Sluzarenko et al [Sluzarenko et al., 2006] presented a versatile method for the preparation of dispersed nanotubes using polystyrene-b-polyisoprene diblock copolymers in different selective organic solvents. Stable dispersions have been obtained in polar (DMF) and nonpolar (heptane) media depending on the selectivity of the diblock copolymers. The direct interaction between the nanotubes and the different blocks is not the most important parameter for stabilization. The driving force seems to be the selectivity of the solvent toward the block copolymer and the block copolymer ratio. Zhang [Zhang et al., 2006] have investigated the effect of melt mixing on the interaction between multi-walled carbon nanotubes (MWNTs) and polystyrene (PS) matrix. They found that the interaction between pristine MWNTs and PS in solution was exist but not strong enough to allow MWNTs to be soluble in solvent.

Among the noncovalent functionalization, due to absence of reactive groups in the functionalized CNTs, the interfacial interaction between CNTs and epoxy is weak. Li [Li et al., 2008] reported the non-covalent functionalization of MWNTs by using 2- aminoethanol ($H_2NCH_2CH_2OH$) in the presence of sodium hydroxide and the application for conductive composites with higher conductivity. The introduced amine group is expected to react with epoxide group from epoxy prepolymer to improve the interfacial interaction between MWNTs and epoxy matrix leading to efficient MWNTs dispersion.

Good solubility of inherently insoluble CNTs in organic solvents has been achieved through surface modification with various homopolymers and/or block copolymers, either covalently such as surface-targeted grafting or in situ polymerization, or noncovalently. Liu et al [Liu et al., 2006] reported on a simple, nondestructive method to noncovalently modify MWNTs with a graft polymer synthesized in laboratory, polystyrene-g-(glycidyl methacrylate-co-styrene) (PS-g-(GMA-co-St)). The noncovalent modification strategy is based on the affinity of the PS main chains to the surfaces of pristine MWNTs (p-MWNTs), and the modified MWNTs can be solubilized in a wide variety of polar and nonpolar organic solvents at the same time.

2.2.2 Aromatic small-molecule-based noncovalent functionalization

The traditional noncovalent methods usually suffer from some disadvantages, such as the low loadings in solutions, the specific complex and synthetic reagents for the functionalization, and a long period of sonication. Hu [Hu et al., 2006] et al presented a new noncovalent approach for the dissolution and the surface modification of SWNTs by a commercially available diazo dye, Congo red (the molecular structural formula is shown in Fig. 1). The stability of solubilized SWNTs + CR were observed for more than two months, and should be realized by the the π-stacking interaction between the sidewall and Congo red.

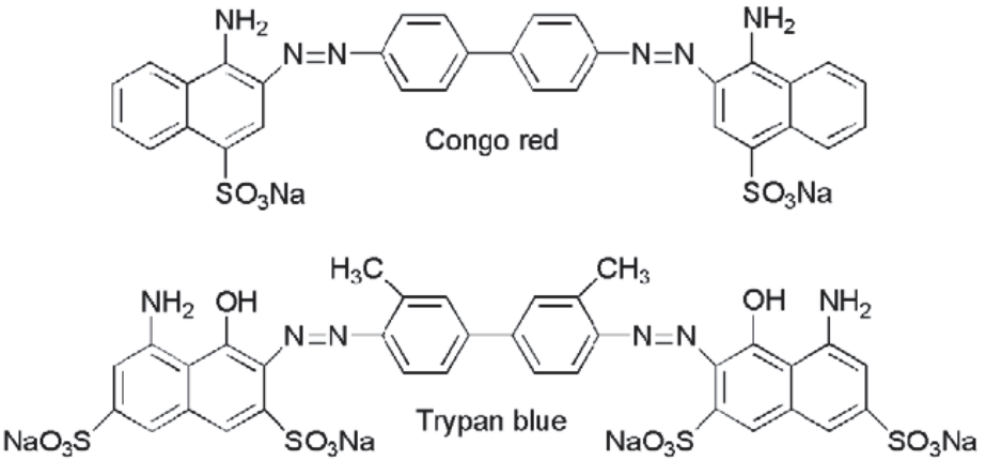

Fig. 1. Molecular structures of Congo red and trypan blue

Among chemical modification, chemical doping and physical treatments, modifying the nanotube surface using aromatic moieties through noncovalent interaction is a very attractive one. Noncovalent functionalization to the CNT not only is a much simpler method compared with covalent functionalization but also has the advantage of preserving nanotube's sp^2 structure, thus the electronic properties [Tournus et al., 2005; Lu et al., 2006]. Though noncovalent sidewall functionalization of CNTs using aromatics molecules has shown many exciting potentials, there has been very few systematic studies on their interaction mechanism. Herein, Liu et al [Liu et al., 2008] systematically studied the noncovalent functionalization of MWNTs by using a series of aromatic organic dyes (Scheme 1) with different structural characteristics. These molecules can be classified into three different categories based on their morphologies and also can be classified into three groups according to their loaded charges in protonic solvents. They found that molecular geometry and charge play the key roles for the dye–MWNTs interactions. The molecules with planar structures and high charge load are favored for the adsorption.

Zhang et al [Zhang et al., 2004] studied the functionalization of SWNTs with electroactive inorganic compounds: Prussian blue (PB) and investigated the molecular interactions between them. They also found that π–π stacking interaction coupled with ionic interaction exist between SWNTs and PB.

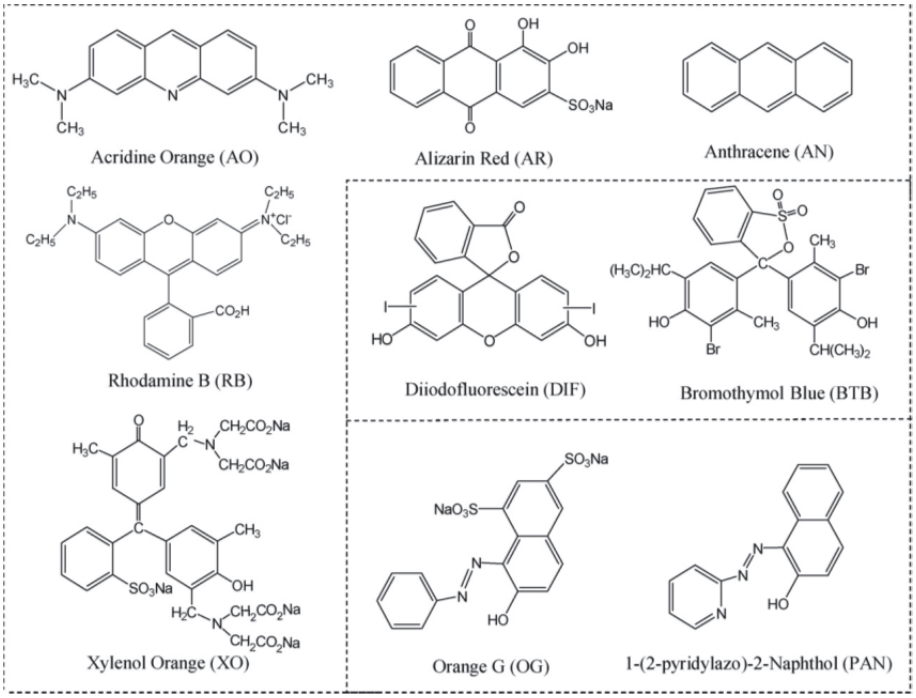

Scheme 1. Structures and names of the used dye molecules

2.2.3 Bio-molecule-based noncovalent functionalization

The potential use of CNTs in biorelated areas has prompted many researchers to investigate the functionalisation of CNTs with biological macromolecules such as proteins and oligosaccharide [Baker et al., 2002; Chen et al., 2001]. Noncovalent functionalization of CNTs with bio-macromolecules, such as DNA and proteins is an additional potential strategy to prepare new bioelectronic nanomaterials [Bale et al., 2007; Chen et al., 2001], which could take advantage of the molecular recognition properties of the bound biomolecules. Wei et al. found that a hydrophobic protein called PANHS can be utilized for controlled noncovalent functionalization of MWNTs and at the same time can be used to control the assembly of AuNPs after binding AuNPs onto the proteins [Wei et al., 2010]. They also investigated the formation of MWNT–AuNP hybrids by incubating protein-protected AuNPs with PANHS functionalized MWNTs, as introduced in Fig 2. They found that proteins, as an intermediate that can react with both MWNTs and AuNPs, play a significant role for mediating the assembly of AuNPs and formation of different hybrids based on MWNTs.

The effectiveness of dispersing and purifying carbon soot using biopolymers (e.g., proteins or DNA) has been studied extensively. Dieckmann et al. [Dieckmann et al., 2003] used non-specific binding of a-helix amphiphilic peptide to assist in dispersing CNTs in aqueous media. The hydrophobic region of the peptide interacted with the aromatic surface of the CNT, while the hydrophilic face promoted self-assembly through peptide-peptide interactions. Zheng et al. [Zheng et al., 2003] demonstrated that the ssDNA self-assembled

into a helical structure around individual tubes in such a way that the electrostatics of the DNA–CNT hybrid depends on the tube diameter and electronic properties. Zhong et al [Zhong et al., 2009] applied X-ray absorption near edge structure (XANES) spectroscopy to investigate the adsorption mechanism of streptavidin proteins onto SWNTs and found that due to the presence of a hydrophobic pocket (of proteins) and a hydrophobic surface (of SWNTs), the C=O protein bonds are affected by the corresponding aromatic structure of SWNTs and an interface interaction occurs, leading to small but relevant structural distortions.

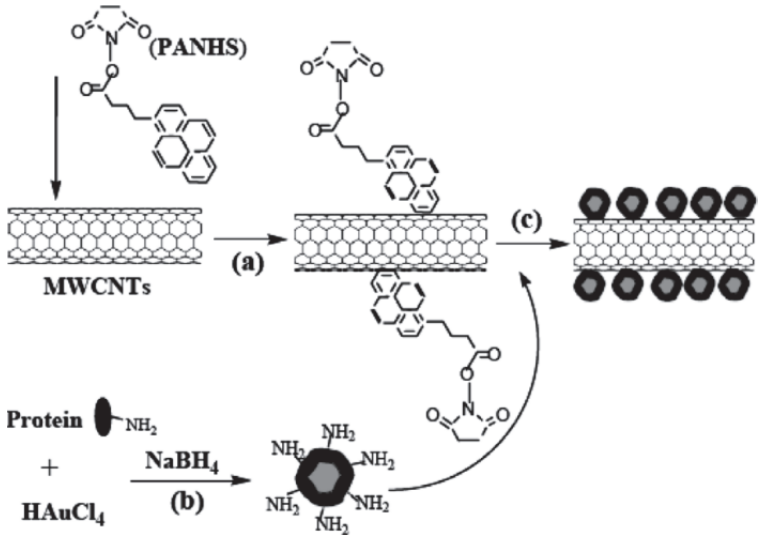

Fig. 2. Model representation for the protein-mediated formation of MWNT–AuNP hybrids. (a) Functionalization of MWNTs with PANHS. (b) Preparation of protein-protected AuNPs. (c) Self-assembly of protein-protected AuNPs on MWNTs by the nucleophilic substitution of NHS group with primary and secondary amines on the surface of protein.

Xue et al [Xue et al., 2011] previous work focused on functionalized MWNTs with arginine–glycine–aspartic acid–serine peptide for cell capture. Dynamic change in the glycosylation status on carcinoma cell surfaces has been considered to play important roles in oncogenic transformation, cell differentiation, and metastasis. Hydrophobins are small proteins (~100 amino acids) that play various roles in fungal physiology related to surface phenomena, such as adhesion, formation of surface layers, and lowering of surface tension [van Wetter et al., 2000]. The remarkable property of hydrophobins is that they have both hydrophobic and hydrophilic parts which make them easy to self-assemble at various interfaces to form polymeric amphipathic membranes and effect the reversal of the surfaces wettability. However, in contrast to these surfactants, surface activity depends on a conformational change of the molecules during assembly rather than on a diffusion-limited adsorption to the interface. Utilization of the properties of hydrophobins in applications such as coatings, emulsion stabilization, and separation technologies has been discussed [Hektor & Scholtmeijer, 2005]. Recently, the ability of hydrophobins to improve the dispersibility of hydrophobic particles in water [Kurppa et al., 2007] has been demonstrated. In addition, the

protein presents numerous reactive groups such as hydroxyls, amines, thiols, and carboxylic acids which provide sites for further surface modification of the CNTs.

Graphite is composed of layers, which form the infinite extension of the polyacene structure. It shows affinity towards acromatics due to its 2D structure with conjugated π bonds. In addition, incorporation of graphite into the polymer matrix can effectively modify the polymer chain packing. Considering the superior properties such as high flexibility, low mass density, and the effective π–π stacking interaction between CNT and aromatic compounds [Zhao et al., 2003], CNT with 1D structure and considerable nanochannels is speculated to be excellent candidate for substituting or complementing conventional nanofillers in the fabrication of nanocomposite pervaporation membranes [Sung et al., 2004; Moniruzzaman et al., 2006]. However, two issues have to be solved in order to fully explore the potential of CNTs. One is the serious aggregation of CNTs leading to difficulties in their manipulation and incorporation into polymeric matrixes [Delozier et al., 2006]. Another is the strong hydrophobicity leading to significant decrease of membrane selectivity. Hydrophilic modification seems a promising and feasible solution. Therefore, chitosan (CS) with distinct hydrophilicity due to the existence of high proportion amino and hydroxyl groups is introduced in Peng et al [Peng et al., 2007] studies. They remarkably improved the dispersion and solubility behavior of CNT through substantial wrapping of chitosan utilizing the emulsifying capacity of chitosan, and the unique solubility behavior of chitosan.

Remarkable properties for biological applications can be obtained due to unique structure of DNA. DNA has been shown to interact with CNTs and wrap onto single-walled carbon nanotubes (SWNTs) for their dispersion and DNA transportation [Lustig et al., 2005; Liu et al., 2007]. DNA-coated carbon nanotube (DNA–CNT) solutions are stable for months at room temperature [Ming et al., 2007]. Many applications for the DNA–CNT system are being explored, including biosensors, DNA transporters, and field effect transistors. The advantages of most of the studies on DNA-stabilized nanotubes have been based on sonication treatment for SWCTs functionalization. According to this, Li [Li et al., 2009] and his coworkers reported a simple method based on sonication treatment to obtain supramolecular adduct of DNA–MWNT composites. It is found that DNA is an effective dispersant for MWNTs and that these dispersions are very stable. The products were characterized scanning electron microscopy (SEM) and the result is shown in Fig 3. SEM image showed that MWNTs were dispersed sufficiently and covered entirely with DNA. Raman measurements confirmed that the interaction between DNA and MWNTs was realized by the strong π–π interactions between the backbones of DNA and the surface of carbon nanotubes.

2.3 Covalent functionalization of carbon nanotubes

Two main strategies including covalent functionalization of the CNT surface with solvophilic molecules and non-covalent surface coating by amphiphilic molecules such as low molecular weight surfactants and polymeric amphiphiles have been proved to prevent the undesirable inter-tube aggregation in solvent. The former has been recognized as an effective means for solubilization or stable dispersion of CNTs, though often gives rise to a severe disruption of π-networks of the CNTs, and thereby leads to possible losses in their mechanical and electrical properties of pristine CNTs [Peng & Cho 2000]. Besides, the covalent functionalization of CNT surface, one of the typical example being the carboxylation of CNTs, usually requires tedious reaction process under strong acidic conditions. These disadvantages are circumvented by utilizing amphiphilic molecules whose solvophobic molecular.

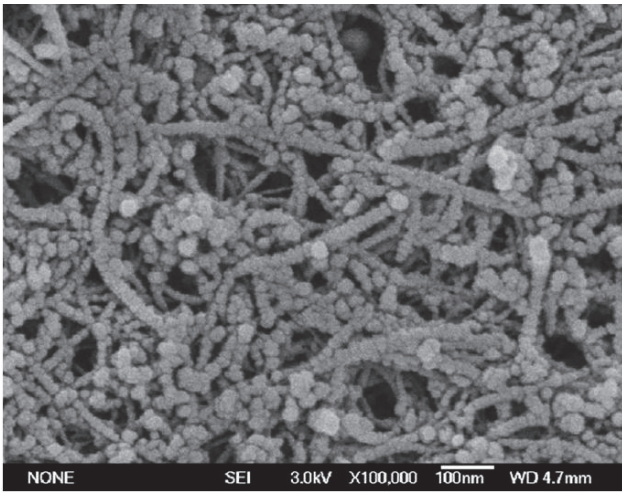

Fig. 3. SEM image of DNA–MWCNT composites with 0.5 wt% DNA.

It has been proved that the CNTs can cross the cell membranes easily and to deliver the peptides, proteins, nucleic acids, and medical drug into cells [Bianco et al., 2005 & Wu et al., 2005]. To realize these applications, biomolecules, such as proteins and DNAs, must be bound to CNTs. The biomolecules can be connected to CNTs via noncovalent or covalent bonding. Williams et al.[Williams et al., 2002] developed a method to couple SWNTs covalently to peptide nucleic acid (PNA, an uncharged DNA analogue) and to hybridize these macromolecular wires with complementary DNA. It was found that DNA attachment occurs predominantly at or near the nanotube ends. Maruyama et al.[Maruyama et al., 2007] reported the attachment of protein molecules to f-MWNTs in an aqueous buffer solution. A chemical reaction using carbodi-imide forms chemical bonds between open-ended tips of MWNTs and protein molecules. In another study, f-MWNTs were attached to the protein via diimide activated amidation [Huang et al., 2002]. And bovine serum albumin (BSA) proteins can be covalently attached to SWNTs and MWNTs via diimide-activated amidation under ambient conditions, while the overwhelming majority (f=90%) of the protein species in the nanotube–BSA conjugates remain bioactive. Hazani et al. [Hazani et al., 2003] have covalently modified SWNTs with DNA and found that the SWNT–DNA adducts hybridize selectively with complementary strands with minimal nonspecific interactions with noncomplementary sequences. Baker et al. [Baker et al., 2002] covalently attached DNA onto SWNTs to develop a DNA biosensor. The good stability, accessibility, and selectivity, however, will be achieved through covalent bonding because of its capability to control the location of the biomolecule, improve stability, accessibility, and selectivity, and reduce leaching. Awasthi et al [Awasthi et al., 2009] reported the preparation of amino f-MWNTs and attachment of biomolecules [e.g. bovine serum albumin (BSA) protein and DNA] to the amino f-MWNTs. The MWNTs have been prepared by spray pyrolysis method and then functionalized with amino group.

Yang et al [Yang et al., 2010] have provided a green method to functionalize CNTs, which avoided the problems of environmental pollution, equipment corrosion, and health hazard causing by both strong acids and organic solvents. This method was shown in Fig 4. Initially, hydroxyl groups were covalently attached to the surface of MWNTs by one step

free radical addition of 4,4′-azobis(4-cyanopentanol) (ACP) in water. Poly(ε-caprolactone)-grafted MWNTs (MWNT-g-PCL) was then synthesized by in situ ring-opening polymerization of ε- caprolactone in the presence of MWNT–OH in room temperature ionic liquids (RTILs). The hydroxyl-functionalized CNTs are commonly obtained by three steps in turn [Zeng et al., 2006], including oxidation in strong acids, acylation in thionyl chloride, and esterification in organic solvents. Herein, only a one-step process for MWNT–OH is required to perform in water. More importantly, RTILs may provide environmentally benign "green" alternatives to volatile organic solvents for chemical synthesis due to their low volatility, non-flammability and high thermal stability [Greaves & Drummond, 2008]. Their works about the functionalization of CNTs using water and RTILs as the reaction media appears relatively facile and green in comparison with the one previously reported in strong acids and organic solvents.

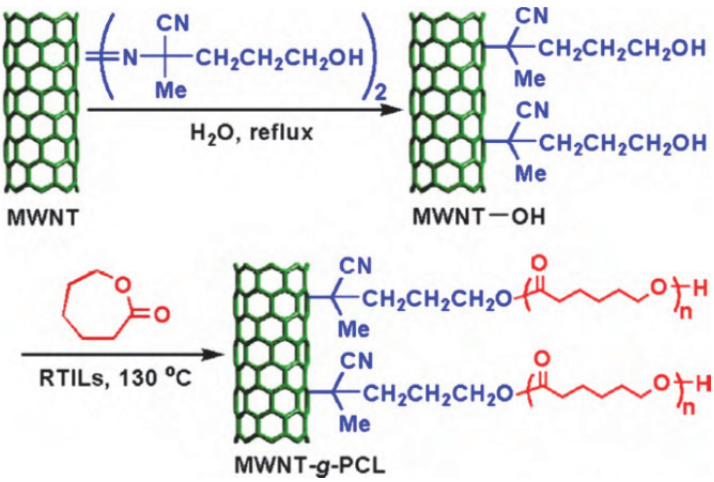

Fig. 4. Schematic representation for covalent attachment of hydroxyl groups to MWNTs by free radical addition of 4,4′-azobis(4-cyanopentanol) in water and subsequent surface-initiated ring-opening polymerization of ε-caprolactone in room temperature ionic liquids (RTILs).

Chemical functionalization is an essential prerequisite in order to get uniform properties of the CNT-polymer composites and avoided serious concerns of reproducibility in their electrical, mechanical and thermal behavior caused by segregation and non-uniform mixing behavior. Chemical method is rather easy for their wide use in medical and biological applications since these functional groups provide necessary sites for covalent or non-covalent coupling of SWNTs. Many reactions are required to be carried out over long period of time. For example, for carboxylation or hydroxylation, the reaction mixture is typically refluxed in concentrated HNO_3 or acid mixture for 10–50 h, which is a tedious and time consuming process. To avoid this time consuming carboxylation of SWNTs, recently Wang et al. [Wang et al., 2006] have demonstrated a rapid functionalization using microwave (MW) radiation in presence of concentrated acid mixture under pressure.

Conjugated polymers are a novel class of semiconductors, and have been found to have wide applications in many areas, such as organic light emitting diodes for flat panel

displays, photovoltaic cells for solar energy conversion, thin-film transistors, and chemical sensors [McQuade et al., 2000]. It has arose the researchers great interest to combine the advantages of carbon nanotubes and conjugated polymers. Xu et al [Xu et al., 2007] reported an effective method to prepare the above mentioned novel structure and expected that this kind of novel hybrid structures could be used to fabricate efficient organic solar cells. Through covalent bond connected to the MWNTs, the fluorescence of polyfluorenes was completely quenched by the MWNTs, indicating a fast photo-induced electron transfer from polyfluorenes to MWNTs.

CNTs incorporated inside a matrix have been expected to improve the properties of the polymeric materials including electrical conductivity, mechanical enhancement, and so on. Many strategies to improve their compatibility with a polymer matrix have been provided including surfactant molecules or wrapping polymers which can be used as mixing mediators. Covalent functionalization procedures are sometimes used in order to reduce the interfacial energy between CNT walls and solvent, monomers or polymers. By using this way grafting functional groups on the CNT surface can be chosen to be polymer-compatible, thus increasing the CNTpolymer matrix interactions, though the grafted groups can alterate the CNT structure in the case of high levels of functionalization. Vigolo et al [Vigolo et al., 2009] proposed a multistep procedure to covalently functionalize SWNTs. This chemical procedure is based on the direct attack of the sp2 carbon on the CNT surface through a free radical process. This allows having a certain control of the yield of functionalization without the introduction of a large number of defects. Moreover, C–C bond can be created directly on the CNT surface, which is efficient enough to modify the surface properties of the CNTs but preserve their structural integrity, though the yield of functionalization is relatively low.

2.4 Other functionalization of carbon nanotubes

One of the methods of chemical surface modification of carbon nanotubes is to use nitric acid (HNO_3). It also has been performed over distinct carbon materials like activated carbons, carbon xerogels, graphite or ordered mesoporous carbons. The introduction of oxygen-containing groups on the surface of CNTs enhances their solubility in aqueous or organic solvents and reduces the van der Waals interactions between different CNTs, promoting the separation of nanotube bundles into individual tubes. Studies about seeking for the effect of chemical oxidation on SWNT structure, show that functionalization by means of HNO_3 causes the tube caps open but basically retain their pristine electronic and mechanical properties. No significant defects are additionally produced, thus the chemical modification mostly occurs at the opened caps and at the already existing defects along the sidewall of SWNTs [Balasubramanian & Burghard, 2005]. As the HNO_3 is used at very high concentrations using boiling methods high density of oxygen-containing groups can be introduced efficiently. Marques et al [Marques et al., 2010] have developed a methodology to tailor the introduction of oxygenated functionalities using the same HNO_3 hydrothermal oxidation procedure. Kim et al. [Kim et al., 2006] have chemically treated carbon nanotubes using a mixture of H_2SO_4 and HNO_3. The effects of acid treatment methods on the diameter dependent length separation of single walled carbon nanotubes were investigated. They found that smaller diameter nanotubes were preferentially shortened by the acid treatment process and migrated farther from the original sample well during the gel electrophoresis. This technique can provide a preparative, scalable method for separating nanotubes by length and diameter. Chiang et al [Chiang et al., 2011] also have investigated the influence of

treatment duration on multi-walled carbon nanotubes functionalized by H_2SO_4/HNO_3 oxidation. They found that if the samples were oxidized for two days they will had the most abundant surface -COOH and the highest oxidation resistance. The oxidation mechanism of MWNTs in mild H_2SO_4/HNO_3 mixture was proposed, which was a successive and iterative process, including the initial attack on active sites, and next the hexagon electrophilic attack generating new defects and introducing more oxygen, and then the tubes becoming thinner and shorter.

Modification of carbon nanotubes by KOH or NaOH is a well-known method. MWNTs were modified by KOH in order to obtain high surface area with micropores. The adsorption-desorption isotherms of N_2 was applied to characterize the modified MWNTs. It was found that the specific surface area of MWNTs increases with increasing modification temperature of MWNTs, on the other hand, the average pore width decreases [Lee et al., 2005]. The capacity of hydrogen storage onto the KOH modified CNTs can be improved under ambient pressure and at moderate temperature [Chen & Huang, 2007].

Raymundo-Piñero et al. [Raymundo-Piñero et al., 2005] obtained new information on the mechanism of porosity development during chemical activation by KOH and NaOH using various multiwalled nanotubes (MWNTs) of different structural organization. They show that NaOH is only effective with disordered materials whereas KOH is effective whatever the structural order. The nanotubular morphology is completely destroyed if the precursor reacted with KOH is in poor order, whereas it is preserved when NaOH is used. The morphology for the more ordered materials remains unchanged with both reactants. If KOH was used to activate the MWNTs a large concentration of defects in the nanotubes walls will generate. The differences found between KOH and NaOH during activation are related with an additional intercalation step of metallic K or Na produced during the redox reactions. It is shown that metallic K has the ability to be intercalated in all materials in contrast with Na which can only intercalate in the very disorganised ones.

Another reported method to functionalize SWNTs is solid-phase mechanochemical reaction in which potassium hydroxide (KOH) reacted with SWNTs and hydroxyl groups were added directly onto the surfaces of SWNTs at room temperature [Pan et al., 2003]. However, when this technique was applied in treating MWNTs, the reactants (KOH and CNTs) agglomerated severely and could not mix equably. Our groups have presented a new way to modify the surfaces of pristine multi-walled carbon nanotubes (PCNTs) in a large scale production. We named this method as wet-mechanochemical reaction, in which PCNTs react with KOH in ethanol solvent at room temperature under mechanical milling. Compared with solid-phase mechanochemical reaction, the wet-mechanochemical reaction, in addition to involving highly reactive centers generated by the mechanical energy imparted to the reaction system, makes materials contact effectively. Furthermore, compared with the CNTs from the acid treatment, the physical properties of the CNTs from the wet-mechanochemical reaction, such as the thermal conductivity applied in the nanofluids, will suffer minor effect [Chen et al., 2008a]. This method was successfully applied to functionalize SWNTs and double-walled carbon nanotubes (DWNTs). SWNTs and DWNTs with optimized aspect ratio can be obtained by adjusting the ball milling parameters [Chen & Xie, 2010]. Mechanical ball milling following concentrated acid treatment is an effective means to obtain relatively straight CNTs with hydrophilic groups and an appropriate length distribution. The obtained CNTs wan used to prepare water and silicon oil based nanofluids, which has the optimized thermal conductivity enhancement.

3. Methods for CNT characterization

Morphology of CNTs can be characterized by transmission electron microscopy (TEM) or scanning electron microscopy (SEM). The former one can give the structures of CNT walls, and the latter can exhibit the CNT outside sketch. UV-vis scanning spectra can be used to examine the fuctionalized CNTs to check the stability of the complex covalently attached to the CNTs and possible leaching of the complex. FT-IR spectroscopy can show that which kinds of groups are introduced on the CNT surfaces. X-ray diffraction (XRD) patterns of MWNTs can prove that if the modified MWNTs still have the same cylinder wall structure as raw MWNTs and inter-planner spacing of all samples remains the same. The mass loss given by the thermogravimetric analysis (TGA) also can show which groups grow on the CNT surfaces. Evidence for the modification of MWNTs coming from the XPS spectrum can reveal the surface chemical state, and can be used to calculate the content of elements on surface of MWNTs by area of each element. The weight content of elements can indicate the presence of groups [Salavati-Niasari & Bazarganipour, 2008].

4. Applications of carbon nanotubes as functional materials

The possibility to combine the remarkable specificity and parallel processing of biomolecules with carbon nanotubes has attracted considerable attention for several types of applications, including the creation of new types of biosensors, the fabrication of drug or vaccine delivery devices, medical treatment, and so on. Furthermore, the functionalized carbon nanotubes can be also used in fuel cells, and in the field of thermal management.

Pantarotto et al. [Pantarotto et al., 2003] has shown that peptide–carbon nanotube complexes can enhance the immune (antibody) response against the peptides with no detectable cross-reactivity to the carbon nanotubes. It has shown that the functionalized carbon nanotubes can cross cell membranes accumulate in the cytoplasm without being toxic for the cell. Zeng et al [Zeng et al., 2007] have successfully prepared novel CNT nano-composites by grafting poly(amidoamine) (PAMAM) with CNTs. The GOx and HRP immobilized CNT-PAMAM based on the functional CNTs was synthesized. The bi-enzymatic CNT-PAMAM nano-composites are highly dispersible in water and show very promising applications in the fabrication of mediator-free bi-enzymatic biosensors for sensitive detection of glucose. The GOx and HRP immobilized CNT-PAMAM shows excellent performance for glucose sensing.

MWNTs can be fuctionalized using tetrahydrofuran solvent. THF is an oxygen-containing heterocycle with five-membered rings. The electronegativity difference between carbon and oxygen makes the C–O bond moderately polar. Thus THF is a polar and aprotic solvent and has a sterically accessible oxygen atom. In chloroplantic acid solution THF could be protonated. Thus, $PtCl_6^{2-}$ and Sn^{4+} ions would be attracted to the sterically accessible oxygen atoms in THF by electrostatic self-assembly. Pt and binary PtSn nanoparticles can be synthesized on THF-functionalized MWNTs with high dispersion and uniform distribution due to their importance for the electrooxidation reactions of methanol and ethanol in low temperature fuel cells. PtSn/MWNTs show significantly lower onset potential and higher oxidation current densities toward the CO and ethanol electrooxidation as compared with pure Pt/MWNTs and conventional Pt/C catalysts. The results demonstrated the effectiveness of the THF-functionalized MWNTs as the catalyst supports in the development of highly dispersed Pt and Pt-based electrocatalysts for low temperature fuel cells [Wang et al., 2010]. CNTs have been increasingly considered as an

advanced metal catalyst support for proton exchange membrane fuel cells (PEMFCs), owing to their outstanding physical and mechanical characteristics [Saha & Kundu, 2010]. Multi-walled carbon nanotubes have been functionalized by oxidation in acid medium and used as support for the incorporation of Pt nanoparticles. The Pt nanoparticles supported on the MWNTs subjected to the most severe functionalization treatment gives the best cathode electrode for PEMFC applications, even exceeding the performance of commercial Pt/C commercial catalysts as the cathode electrode in a proton-exchange membrane fuel cell [Hernández-Fernández et al., 2010]. CNTs also can be effectively functionalized by intermittent microwave heating (IMH)-assisted HF/H_2O_2 solution treatment. Pt supported on CNTs-HF/H_2O_2 (Pt/CNTs-HF/H_2O_2) has an average particle size of 2.8 nm, smaller than that for Pt supported on CNTs treated by other methods. Pt/CNTs-HF/H_2O_2 electrocatalysts display a high electrochemical surface area, high Pt utilization efficiency, a superior electrocatalytic and mass activity for the O_2 reduction reaction (ORR) with respect to other catalyst samples. The obtained Pt/CNTs-HF/H_2O_2 would be excellent electrocatalyst supports of fuel cells [Yin et al., 2009]. Reddy and Ramaprabhu [Reddy & Ramaprabhu, 2007] have designed and developed a metal hydride-based hydrogen storage device. For the first time, good quality of MWNTs have been synthesized by pyrolysis of acetylene over hydrogen decrepitated alloy hydride catalyst. Pt-supported MWNTs (Pt/MWNTs) electrocatalysts have been prepared by chemical reduction method using functionalized MWNTs. Fabrications of a fuel cell stack and a planar configured microfuel cell have been done using membrane electrode assembly prepared with Pt/MWNTs electrocatalyst and Nafion 1135 membrane.

MWNTs have very high thermal conductivity, which make it excellent candidate to prepare thermal conductivity enhanced nanofluids. In our previous study, we developed some methods for preparing MWNT contained nanofluids. The nanofluids have the features of high thermal conductivity, long term stability, and surfactant-free. Briefly the present steps involved in the preparation of MWNT nanofluids include: (1) disentangle the nanotube aggregates and introduce hydrophilic functional groups on the surface of the nanotubes by mechanochemical reaction and (2) disperse the chemically treated MWNTs into a base fluid. Potassium hydroxide has been used to modify the surfaces of MWNTs. Distilled water (DW), ethylene glycol (EG), and glycerol (Gly) were used as base fluids. The aggregates and entanglements of PCNTs have been broken after chemical treatment. MWNTs were cut short by the intensive mechanical forces during the ball milling process. Thermal conductivity measurements revealed that the thermal conductivity enhancement reaches up to 17.5% at a volume fraction of 0.01 for an ethylene glycol based nanofluid and the temperature variation has no obvious effects on the thermal conductivity enhancement for the as prepared nanofluids [Chen et al., 2008b]. Surfactant-free nanofluids containing double- and single-walled carbon nanotubes were also obtained by using the same method. Study found that aspect ratios of the SWNTs and DWNTs could be tailored by adjusting the ball milling parameters. Chemical surface effects of CNTs play the main roles in improving the thermal conductivity enhancement with the increase of temperature. CNTs with smaller diameters offer more contribution to the thermal conductivity enhancement of CNT water-based nanofluids compared with the CNTs with larger diameters. Thermal conductivity enhancement also has close relation to the initial heat transfer performance of the CNTs [Chen & Xie, 2010a]. Another method was also applied in which MWNTs were treated by concentrated acid combined with mechanical ball mill technology. The treated multi-walled carbon nanotubes (TCNTs) with functionalized surfaces and controlled morphologies were

used to prepare silicon oil based nanofluids by using hexamethyldisiloxane as dispersant. Thermal conductivity results of the obtained nanofluids show that the collective effects, involving straightness ratio, aspect ratio, and aggregation of TCNTs, play a key role in the thermal conductivity of CNT nanofluids. This study suggests that the thermal characteristics of nanofluids might be manipulated by means of controlling the morphology of the additions, which also provide a promising way to conduct investigation on the mechanism of heat transfer in nanofluids [Chen & Xie, 2009]. Furthermore, stable homogeneous nanofluids of MWNTs were prepared by using gemini cationic surfactant trimethylene-1,3-bis (dodecyldimethyl ammonium bromide), abbreviated as 12-3-12,2Br−1, as dispersing agents. At relatively low temperatures the superfluous surfactant molecules form stable layer or column micelles, making an increase in the viscosity of nanofluids. Only 0.6 wt% gemini surfactant used to obtain 0.5 wt%MWNTdispersions. The dispersions show no MWNTs precipitation for at least 5 weeks [Chen et al., 2008c]. Another research shows that higher concentration of cationic gemini surfactant is a negative factor in improving the thermal conductivity of nanofluids. Increase of spacer chain length of cationic Gemini surfactant gives rise to the sediment of MWNTs in the nanofluids, resulting in decrease of thermal conductivity enhancement of MWNT nanofluids [Chen & Xie, 2010b].

5. Conclusion

Many potential applications of carbon nanotubes often need them to be prior purified and functionalized. Some effective methods to functionalize carbon nanotube surfaces including covalent modification, noncovalent approaches, chemical and solid-phase, hydro-mechanochemical method, and so on have been summarized. The advantages and shortcomings of the functionalization method were also showed clarified. At the same time some characterization ways for carbon nanotubes were refered. In the last part of this chapter the applications of carbon nanotubes as functional materials in the fields of biosensing, fuel cells, medical treatment, and so on, especially in the field of thermal management are summarized. It is our hope that all the content of this chapter can supply helps to the researchers in the field of carbon nanotubes.

6. Acknowledgments

This work was supported by the Program for Professor of Special Appointment (Eastern Scholar) at Shanghai Institutions of Higher Learning, and the Program for New Century Excellent Talents in University (NCET-10-883).

7. References

Ayala, P., Grüuneis, A., Kramberger, C., Grimm, D., Engelhard, R., Rüummeli, M.H., Schumann, J., Kaltofen, R., Büuchner, B., Schaman, C., Kuzmany, H., Gemming, T., Barreiro, A., & Pichler, T. (2008). Cyclohexane triggers staged growth of pure and vertically aligned single wall carbon nanotubes. *Chemical Physics Letters*, Vol. 454, No. 4-6,(March 2008), pp.332-336, ISSN 0009-2614

Baker,S.E., Cai, W., Lasseter, T.L., Weidkamp, K.P., & Hamers, R.J. (2002). Covalently bonded adducts of deoxyribonucleic acid (DNA) oligonucleotides with single-wall

carbon nanotubes Synthesis and hybridization. *Nano letters*, Vol.2, No.12,(October 2002), pp.1413-1417, ISSN 1530-6984

Balasubramanian, K., & Burghard, M. (2005). Chemically functionalized carbon nanotubes. *Small*, Vol.1,(January 2005), pp.180-192, ISSN 1613-6810

Bale, S.S., Asuri, P., Karajanagi, S.S., Dordick, J.S., & Kane, R.S. (2007). Protein directed formation of silver nanoparticles on carbon nanotubes. Advanced Materials, Vol.19, No.20, (October 2007), pp. 3167-3170, ISSN 1521-4095

Bianco, A., Kostarelos, K., & Prato, M. (2005). Applications of carbon nanotubes in drug delivery. *Current Opinion in Chemical Biology*, Vol. 9,No.6, (December 2005), pp.674-679, ISSN 1367-5931

Bystrzejewski, M., Rümmeli, M.H., Lange, H., Huczko, A., Baranowski, P., Gemming, T., & Pichler, T. (2008). Single-walled carbon nanotubes synthesis a direct comparison of laser ablation and carbon arc routes. *Journal of Nanoscience and Nanotechnology*, Vol.8, No.1, (January 2008), pp.6178-6186(9), ISSN 1550-7033

Chen, C.H., & Huang, C.C. (2007). Hydrogen storage byKOH-modified multi-walled carbon nanotubes. I*nternational Journal of Hydrogen Energy,* Vol.32, No.2, (February 2007), pp.237-246, ISSN 0360-3199

Chen, L.F., Xie, H.Q., Li, Y., & Yu, W. (2008a) Surface ChemicalModification of Multiwalled Carbon Nanotubes by aWet-Mechanochemical Reaction. J*ournal of Nanomaterials*, Article ID 783981, 5 pages

Chen, L.F., & Xie, H.Q. (2010a). Surfactant-free nanofluids containing double- and single-walled carbon nanotubes functionalized by a wet-mechanochemical reaction. T*hermochimica Acta*, Vol.497, No.1-2, (October 2007), pp. 67-71, ISSN 0040-6031

Chen, L.F., & Xie, H.Q. (2009). Silicon oil based multiwalled carbon nanotubes nanofluid with optimized hermal conductivity enhancement. *Colloids and Surfaces A*, Vol.352, No.1-3, (December 2009), pp.136-140, ISSN 0927-7757

Chen, L.F., Xie, H.Q., Li, Y., & Yu, W. (2008b). Nanofluids containing carbon nanotubes treated by mechanochemical reaction. *Thermochimica Acta*, (October 2008),Vol.477, No.1-2, pp.21–24, ISSN 0040-6031

Chen, L.F., Xie, H.Q., Li, Y., & Yu, W. (2008c). Applications of cationic gemini surfactant in preparing multi-walled carbon nanotube contained nanofluids. *Colloids and Surfaces A*,

Vol.330, No.2-3,(December 2008), pp.176–179, ISSN 0927-7757

Chen, L.F., & Xie, H.Q. (2010b). Properties of carbon nanotube nanofluids stabilized by cationic gemini surfactant. *Thermochimica Acta*, Vol. 50, No. 1-2, (July 2010), pp.62–66, ISSN 0040-6031

Chiang, Y.C., Lin, W.H, & Chang, Y.C. (2011). The influence of treatment duration on multi-walled carbon nanotubes functionalized by H2SO4/HNO3 oxidation. *Applied Surface Science*, Vol.257, No.6, (Junauary 2011), pp. 2401-2410, ISSN 0169-4332

Angiolini, L., Benelli, T., Giorgini, L.,& Salatelli, E.(2006). Optically active photochromic polymers with three-arm star structure by atom transfer radical polymerization, Macromolecules, Vol.39, No.5,(May 2006), pp. 3731–3737, ISSN 0024-9297

Greaves, T.L., & Drummond, C.J. (2008). Protic Ionic Liquids Properties and Applications. *Chemical Reviews*., Vol.108, No.1,(December 2007), pp. 206-237, ISSN 0009-2665

Hazani, M., Naaman, R., Hennrich, F., & Kappes, M.M. (2003). Confocal fluorescence imaging of DNA-functionalized carbon nanotubes, *Nano letters*, Vol.3, No.2, (December 2002), pp.153-155, ISSN 1530-6984

Hektor, H.J., & Scholtmeijer, K., (2005). Hydrophobins proteins with potential. *Current Opinion in Biotechnology*, Vol.16, No.4, (August 2005), pp.434-439, ISSN 1367-5931

Hernández-Fernández, P., Montiel, M., Ocón, P., Gómez de la Fuente, J.L., García-Rodríguez, S., Rojas, S., & Fierro, J.L.G. (2010). Functionalization of multi-walled carbon nanotubes and application as supports for electrocatalysts in proton-exchange membrane fuel cell. *Applied Catalysis B Environmental*, Vol.99, No.1-2,(August 2010), pp. 343-352, ISSN 0926-3373

Hu, C.G., Chen, Z.L., Shen, A.G., Shen, X.C., Li, J., & Hu, S.S. (2006). Water-soluble single-walled carbon nanotubes via noncovalent functionalization by a rigid, planar and conjugated diazo dye. *Carbon*, Vol.44, No.3, (March 2006), pp. 428-434, ISSN 0008-6223

Huang, W., Taylor, S., & Fu, K. (2002). Attaching proteins to carbon nanotubes via diimide activated amidation. *Nano letters*, Vol.2, No.4,(March 2002), pp.311-314, ISSN 1530-6984

Iijima, S. (1991) Helical microtubules of graphitic carbon. *Nature*, Vol. 354, (November 1991), pp. 56-58.

Kim, Y., Lee, D., Oh, Y., Choi, J., & Baik, S. (2006). The effects of acid treatment methods on the diameter dependent length separation of single walled carbon nanotubes. *Synthetic Metals*, Vol.156, No.16-17, (August 2006), pp.999-1003, ISSN 0379-6779

Lee Mohana Reddy, A., & Ramaprabhu, S. (2007). Design and fabrication of carbon nanotube-based microfuel cell and fuel cell stack coupled with hydrogen storage device. *International Journal of Hydrogen Energy*, Vol.32, No.17, (December 2007), pp.4272-4278, ISSN 0360-3199

Lee, S.M., Lee, S.C., Jung J.H., & Kim, H.J. (2005). Pore characterization of multi-walled carbon nanotubes modified by KOH. *Chemical Physics Letters*, Vol.416, No.4-6, (December 2005), pp.251-255, ISSN 0009-2614

Li, C.Y., Li, L.Y., Cai, W.W., Kodjie, S.L., & Tenneti, K.K. (2005). Nanohybrid Shish-kebabs periodically functionalized carbon nanotubes. *Advanced Materials,*Vol.17, No.9, (May 2005), pp.1198–202, ISSN 1521-4095

Li, L., & Xing, Y. (2007). Pt−Ru Nanoparticles Supported on Carbon Nanotubes as Methanol Fuel Cell Catalysts. *Journal of Physical Chemistry C,* Vol.111, No.6, (January 2007), pp. 2803-2808, ISSN 1932-7447

Li ,L.Y., Li, C.Y., & Ni, C.Y. (2006). Polymer crystallization-driven, periodic patterning on carbon nanotubes. *Journal of the American Chemical Society*, Vol.128, No.5, (January 2006) pp.1692-1699, ISSN 0002-7863

Li, X., Wong, S.Y., Tjiu, W.C., Lyons, B.P., Oh, S.A., & He, C.B. (2008). Non-covalent functionalization of multi walled carbon nanotubes and their application for conductive composites. *Carbon*, Vol.46, No.5, (April 2008), pp.829-831, ISSN 0008-6223

Li, Z.Z., Wu, Z.Y., & Li, K. (2009). The high dispersion of DNA–multiwalled carbon nanotubes and their properties. *Analytical Biochemistry*, Vol. 387, No.2, (April 2009), pp.267-270, ISSN 0003-2697

Liu, C.H., Li, J.J., Zhang, H.L., Li, B.R., & Guo, Y. (2008). Structure dependent interaction between organic dyes and carbon nanotubes. *Colloids and Surfaces A*, Vol.313-314, No.1, (February 2008), pp.9-12, ISSN 0927-7757

Liu, Y.T., Zhao, W., Huang, Z.Y., Gao, Y.F., Xie, X.M., Wang, X.H., & Ye, X.Y. (2006). Noncovalent surface modification of carbon nanotubes for solubility in organic solvents. *Letters to the Editor / Carbon*, Vol.44, No.8, (July 2006), pp.1613-1616, ISSN 0008-6223

Liu, Z., Winters, M., Holodniy, M., Dai, H.J. (2007). siRNA delivery into human T cells and primary cells with carbon-nanotube transporters, *Angewandte Chemie International Edition*, Vol.46, No.12,(March 2007), pp.2023-2027,ISSN 1521-3773

Lu, Y., Bangsaruntip, S., Wang, X., Zhang, L., Nishi, Y., & Dai, H. (2006). DNA functionalization of carbon nanotubes for ultrathin atomic layer deposition of high kappa dielectrics for nanotube transistors with 60 mV/decade switching, *Journal of the American Chemical Society,* Vol.128, No.11, (March 2006), pp.3518-3519, ISSN 0002-7863

Lustig, S.R., Jagota, A., Khripin, C., & Zheng, M. (2005). Theory of structure-based carbon nanotube separations by ion-exchange chromatography of DNA/CNT hybrids, *Journal of Physical Chemistry B,* Vol.109, No.7,(January 2005), pp.2559-2566, ISSN 1520-6106

Marques, R.R.N., Machado, B.F., Faria, J.L., & Silva, A.M.T. (2010). Controlled generation of oxygen functionalities on the surface of Single-Walled Carbon Nanotubes by HNO3 hydrothermal oxidation. *Carbon*, Vol.48, No.5,(April 2010), pp.1515-1523, ISSN 0008-6223

Maruyama, H., Yoshimura, S. H., & Akita, S. (2007). Covalent attachment of protein to the tip of a multiwalled carbon nanotube without sidewall decoration. *Journal of Applied Physics*, Vol.102, No.9, (November 2007), pp. 094701-094705,ISSN 0021-8979

McQuade, D.T., Pullen, A.E., & Swager, T.M. (2000). Conjugated Polymer-Based Chemical Sensors.*Chemical Reviews*, Vol.100, No.7, (June 2000), pp.2537-2574, ISSN 0009-2665

Mohana Reddy, A.L., Rajalakshmi, N., & Ramaprabhu, S. (2008). Cobalt-polypyrrole-multiwalled carbon nanotube catalysts for hydrogen and alcohol fuel cells. *Carbon*, Vol.46, No.1, (January 2008), pp. 2-11, ISSN 0008-6223

Moniruzzaman, M., &Winey, K.I. (2006). Polymer nanocomposites containing carbon nanotubes. *Macromolecules*, Vol. 39, No.16, (July 2006), pp.5194-5205, ISSN 0024-9297

Moulton, S. E., Minett, A.I., Murphy, R., Ryan, K.P., McCarthy, D., Coleman, J.N., Blau, W.J., & Wallace, G.G. (2005). Biomolecules as selective dispersants for carbon nanotubes. *Carbon*, Vol. 43, No.9,(August 2005), pp.1879-1884, ISSN 0008-6223

Nikolaev, P., Bronikowski, M.J., Bradley, R.K., Rohmund, F., Colbert, D.T., Smith, K.A., & Smalley, R.E. (1999). Gas-phase catalytic growth of single-walled carbon nanotubes from carbon monoxide. *Chemical Physics Letters*, Vol.313, No. 1-2,(November 1999), pp. 91-97, ISSN 0009-2614

Pan, H. L., Liu, L. Q., Guo, Z. X., Dai, L. M., Zhang, F.S., & Zhu, D. B. (2003). Carbon Nanotubols from Mechanochemical Reaction. *Nano letters,* Vol.3, No.1, (November 2002), pp. 29–32, ISSN 1530-6984

Pantarotto, D., Partidos, C.D., Graff, R., Hoebeke, J., Briand, J.P., & Prato, M. (2003). Synthesis, structural characterization, and immunological properties of carbon nanotubes functionalized with peptides. *Journal of the American Chemical Society*, Vol.125, No.20, (April 2003), pp. 6160-6164, ISSN 0002-7863

Park, C., Lee, S., Lee, J.H., Lim, J., Lee, S.C., Park, M., Lee, S. S., Kim, J., Park, C.R., & Kim. C. (2007). Controlled assembly of carbon nanotubes encapsulated with amphiphilic block copolymer. *Carbon*, Vol.45, No.10,(September 2007), pp.2072-2078, ISSN 0008-6223

Peng, F.B., Pan, F.S., Sun, H.L., Lu, L.Y., & Jiang, Z.Y. (2007). Novel nanocomposite pervaporation membranes composed of poly(vinyl alcohol) and chitosan-wrapped carbon nanotube. *Journal of Membrane Science*, Vol.300, No.1-3,(August 2007), pp.13-19, ISSN 0376-7388

Peng, S., & Cho, K. (2000). Chemical control of nanotube electronics. *Nanotechnology*, Vol.11, No.2, (June 2000), pp.57-60, ISSN 0957-4484

Raymundo-Piñero, E., Azaïs ,P., Cacciaguerra, T., Cazorla-Amoró s, D., Linares-Solano, A., & Béguin, F. (2005). KOH and NaOH activation mechanisms of multiwalled carbon nanotubes with different structural organization. *Carbon*, Vol.43, No.4, (April 2005) pp.786-795, ISSN 0008-6223

Rümmeli, M.H., Kramberger, C., Loeffler, M., Jost, O.,Bystrzejewski, M., Grueneis, A., Gemming, T., Pompe, W., Buechner, B., & Pichler, T. (2007). Catalyst volume to surface area constraints for nucleating carbon nanotubes. *Journal of Physical Chemistry B*, Vol. 111, No. 28, (June 2007),pp. 8234-8241, ISSN 1520-6106

Saha, M.S., & Kundu, A. (2010). Functionalizing carbon nanotubes for proton exchange membrane fuel cells Electrode. *Journal of Power Sources*, Vol.195, No.19, (October 2010), pp.6255-6261, ISSN 0378-7753

Salavati-Niasari, M., & Bazarganipour, M. (2008). Covalent functionalization of multi-wall carbon nanotubes (MWNTs) by nickel(II) Schiff-base complex Synthesis, characterization and liquid phase oxidation of phenol with hydrogen peroxide. *Applied Surface Science*, Vol.255, No.5, (December 2008),pp.2963-2970, ISSN 0169-4332

Sluzarenko, N., Heurtefeu, B., Maugey, M., Zakri, C., Poulin, P., & Lecommandoux, S. (2006). Diblock copolymer stabilization of multi-wall carbon nanotubes in organic solvents and their use in composites. *Carbon*, Vol.44, No.15, (December 2006), pp.3207-3212, ISSN 0008-6223

Sun, X., Bao,W., Lv,Y., Deng, J., & Wang, X. (2007). Synthesis of high quality singlewalled carbon nanotubes by arc discharge method in large scale. *Material Letter*, Vol. 61, No. 18, (July 2007), pp. 3956-3958, ISSN 0167-577X

Sung, J.H., Kim, H.S., Jin, H.-J., Choi, H.J., & Chin, I.-J. (2004). Nanofibrous membranes prepared by multiwalled carbon nanotube/poly(methylmethacrylate) composites, *Macromolecules*, Vol.37, No.26, (December 2004), pp.9899-9902, ISSN 0024-9297

Szleifer, I., & Yerushalmi-Rozen, R. (2005). Polymers and carbon nanotubes – dimensionality, interactions and nanotechnology. *Polymer*, Vol.46, No.19,(September 2005), pp.7803-7818, ISSN 0032-3861

Thess, A., Lee, R., Nikolaev, P., Dai, H., Petit, P., Robert, J., Xu, C., Lee, Y.H., Kim, S.G., Tournus, F., Latil, S., Heggie, M.I., & Charlier, J.C. (2005). π-stacking interaction between carbon nanotubes and organic molecules. *Physical Review B Condensed Matter,* Vol.72, (August 2005), pp. 075431, ISSN 1098-0121

van Wetter, M.A., WÖten, H.A.B., & Wessels, J.G.H. (2000). SC3 and SC4 hydrophobins have distinct roles in formation of aerial structures in dikaryons of Schizophyllum commune. *Molecular Microbiology*, Vol.36, No.1, (January 2000), pp. 201-210, ISBN 978-0-12-677530-3

Vigolo, B., Mamane, V., Valsaque, F., Ha Le, T.N., Thabit, J., Ghanbaja, J., Aranda, L., Fort, Y., & McRae, E. (2009). Evidence of sidewall covalent functionalization of single-walled carbon nanotubes and its advantages for composite processing. *Carbon*, Vol.47, No.2, (February 2009), pp.411-419, ISSN 0008-6223

Waghuley, S.A., Yenorkar, S.M., Yawale, S.S., & Yawale, S.P. (2008). Application of chemically synthesized conducting polymer-polypyrrole as a carbon dioxide gas sensor. *Sensors and Actuators, B*, Vol.128, No.2, (January 2008), pp.366-373, ISSN 0925-4005

Wang, W.R., Xie, X.M., &Ye, X.Y. (2010). Crystallization induced block copolymer decoration on carbon nanotubes. *Carbon*, Vol.48, No.5,(April 2010), pp.1680-1683, ISSN 0008-6223

Wang, X. S., Wang, H.C., Huang, Y.J., Zhao, Z.X., Qin, X., Wang, Y.Y., Miao, Z.Y., Chen,Q., & Qiao, M.Q. (2010). Noncovalently functionalized multi-wall carbon nanotubes in aqueous solution using the hydrophobin HFBI and their electroanalytical application. *Biosensors and Bioelectronics*, Vol.26, No.3, (November 2010), pp.1104-1108, ISSN 09565663

Wang, Y., Iqbal, Z., & Mitra, S. (2006). Rapidly Functionalized, Water-Dispersed Carbon Nanotubes at High Concentration. *Journal of the American Chemical Society*, Vol.128, No.1, (December 2005), pp.95–99, ISSN 0002-7863

Wei, G., Pan, C.J., Reichert, J., & Jandt ,K.D. (2010). Controlled assembly of protein-protected gold nanoparticles on noncovalent functionalized carbon nanotubes. *Carbon*, Vol.48, No.3, (January 2011), pp.645-653, ISSN 0008-6223

Williams, K. A., Veenhuizen, P. T. M., & de la Torre, B.G.R. (2002). Nanotechnology Carbon nanotubes with DNA recognition. *Nature*,Vol.420, (December 2002), pp.761-761

Woo, S.-W., Dokko, K., & Kanamura, K. (2008). Composite electrode composed of bimodal porous carbon and polypyrrole for electrochemical capacitors . *Journal of Power Sources*, Vol.185, No.2, (December 2008), pp.1589-1593, ISSN 0378-7753

Wu, W., Wieckowski, S., & Pastorin, G. (2005). Targeted delivery of amphotericin B to cells by using functionalized carbon nanotubes. *Angewandte Chemie International Edition*, Vol.44,No.39,(October 2005), pp.6358-6362,ISSN 1521-3773

Xu, G.D., Zhu, B., Han, Y., & Bo, Z.S. (2007). Covalent functionalization of multi-walled carbon nanotube surfaces by conjugated polyfluorenes. *Polymer*, Vol. 48, No. 26,(December 2007), pp. 7510-7515, ISSN 0032-3861

Xue, Y.D., Bao, L., Xiao, X.R., Ding, L., Lei, J.P., & Ju. H.X. (2011). Noncovalent functionalization of carbon nanotubes with lectin for label-free dynamic monitoring of cell-surface glycan expression. *Analytical Biochemistry*, Vol.410, No.1, (March 2011), pp.92-97, ISSN 0003-2697

Yang, Y.K., Qiu, S.Q. He, C.G., He, W.J., Yu, L.J., & Xie, X.L. (2010). Green chemical functionalization of multiwalled carbon nanotubes with polyin ionic liquids. *Applied Surface Science*, Vol.257, No. 3, (November 2010), pp. 1010-1014, ISSN 0169-4332

Yin, S.B., Shen, P.K., Song, S.Q., & Jiang, S.P. (2009), Functionalization of carbon nanotubes by an effective intermittent microwave heating-assisted HF/H2O2 treatment for electrocatalyst support of fuel cells. E*lectrochimica Acta*, Vol.54, No.27, (November 2009),pp.6954-6958, ISSN 0013-4686

Zhao, Y. C., Yang, X.L., Tian,J.N., Wang, F.Y., & Zhan, L. (2010). A facile and novel approach toward synthetic polypyrrole oligomers functionalization of multi-walled carbon nanotubes as PtRu catalyst support for methanol electro-oxidation. J*ournal of Power Sources,* Vol.195, No.15, (August 2010), pp. 4634-4640, ISSN 0378-7753

Zeng, H., Gao, C., & Yan, D. (2006). Poly(ε-caprolactone)-Functionalized Carbon Nanotubes and Their Biodegradation Properties. *Advanced Functional Materials,* Vol.16, No.6,(February 2006), pp. 812-818, ISSN 1616-3028

Zeng, Y.L., Huang, Y.F., Jiang, J.H., Zhang, X.B., Tang, C.R., Shen, G.L., & Yu, R.Q. (2007). Functionalization of multi-walled carbon nanotubes with poly(amidoamine) dendrimer for mediator-free glucose biosensor. *Electrochemistry Communications*, Vol.9, No.1, (January 2007) pp.185-190, ISSN 388-2481

Zhang, Y.J., Wen, Y., Liu, Y., Li, D., & Li, J.H. (2004). Functionalization of single-walled carbon nanotubes with Prussian blue. *Electrochemistry Communications*, Vol.6, No.11, (November 2004), pp.1180-1184, ISSN 1388-2481

Zhang, Z.N., Zhang, J., Chen, P., Zhang, B.Q., He, J.S., & Hu, G.H. (2006). Enhanced interactions between multi-walled carbon nanotubes and polystyrene induced by melt mixing. *Carbon*, Vol.44, No.4, (April 2006), pp.692-698, ISSN 0008-6223

Zhao, J., Lu, J.P., Han, J., & Yang, C.-K. (2003). Noncovalent functionalization of carbon nanotubes by aromatic organic molecules, *Applied Physics Letters,* Vol.82, No.21 (April 2003), pp.3746-3748, ISSN 0003-6951

Zheng, M., Jagota, A., Semke, E.D., Diner, B.A., McLean, R.S., & Lustig, S.R. (2003). DNA-assisted dispersion and separation of carbon nanotubes. *Nature-Materials*, Vol.2, No.5, (April 2003), pp. 338-342

Zhong, J., Song, L., Meng, J., Gao, B., Chu, W.S., Xu, H.Y., Luo, Y., Guo, J.H., Marcelli, A., Xie, S.S., & Wu. Z.Y. (2009). Bio–nano interaction of proteins adsorbed on single-walled carbon nanotubes. *Carbon*, Vol.47, No.4, (April 2009)pp.967-973, ISSN 0008-6223

Zou, J.H., Liu, L.W., Chen, H., Khondaker, S.I., McCullough, R.D., & Huo, Q. (2008). Dispersion of pristine carbon nanotubes using conjugated block copolymers. *Advanced Materials,* Vol.20, No.11, (June 2008), pp.2055-2060, ISSN 1521-4095

10

Nanodesign and Simulation Toward Nanoelectronic Devices

Sang Uck Lee[1] and Yoshiyuki Kawazoe[2]
[1]*Corporate R&D / LG Chem. Research Park*
[2]*Institute for Materials Research, Tohoku University*
[1]*Korea*
[2]*Japan*

1. Introduction

The low-dimensional allotropes of carbon have drawn much attention in a multitude of fields owing to their outstanding fundamental properties and potential for applications. Interest in such systems has branched out from carbon fullerenes and carbon nanotubes (CNTs) toward other novel carbon nanomaterials such as graphitic onions, cones, nanohorns, nanohelices, nanobarrels, and graphene. All of these unique carbon nanomaterials show promising capabilities for applications in electronic devices.

Especially, CNT has the potential to make the process of development of electronics comprehensible to us as well as conquering many of the size limitations of the circuits with possible applications in integrated circuits and energy conservation. It is believed that CNT-electronics shares the potential, together with Biotechnology and Artificial Intelligence to improve current devices. Such advances can then be used to solve problems not possible in present. Conductive and high-strength composites; energy conversion and energy storage devices; sensors; field emission displays and radiation sources; hydrogen storage media; and nanometer-sized semiconductor devices, probes, and interconnects are some of the many potential applications based on carbon nanotubes. Some of these applications are now realized in products. Others are demonstrated in early to advanced devices.

In the field of electronics, experiments over the past several years have given researchers hope that wires and functional devices tens of nanometres or smaller in size could be made from such low-dimensional materials and incorporated into electronic circuits that work far faster and on much less power than those existing today. In the long term, the most valuable applications will take further advantage of the unique electronic properties of low-dimensional materials. Surrounded by such anticipation, the advancement of techniques for characterizing and manipulating of individual molecules and the availability of first-principles methods to describe electron tunneling through atomic chains or single molecules have facilitated the development of a variety of electronic devices, attesting to the potential utility of these molecules in nanoelectronic device architectures.

Few possible applications of CNT in electronics are discussed below:

Carbon nanotube field-effect transistors (CN-FETs): CNT is one of the candidates for a quantum wire for the molecular-FET. Multi-channel carbon nanotube field-effect transistors (CNFETs) have been realized by depositing a large number of CNTs onto a metallic back gate. This work clearly demonstrates that CN-FETs are promising components for high-

frequency (HF) applications. Recently, several works have been reported on the CNTs for FETs and CNT-logic applications.

Transistors: IBM has made CN-FET resembling to conventional MOSFET having conductional channel beneath the gate electrodes separated by a thin dielectric. The top gate devices exhibited excellent electrical characteristics, including steep sub-threshold slope and high transconductance at low voltages by reducing the gate-to-channel separation. Furthermore, the IBM scientists were able to fabricate both hole (p-type) and electron (n-type) transistors. The top-gate design allows independent gating of each transistor, making it possible to generate CMOS (complementary metaloxide semiconductor) circuits that have a simpler design and consume less power. The nanotube devices in this case outperformed the prototype silicon transistor.

Logic circuits: The first inter-molecular logic circuit has been created by IBM. The circuit is a voltage inverter made by using two nanotube field-effect transistors.

Diodes: A nanotube formed by joining nanotubes of two different diameters end to end can act as a diode, suggesting the possibility of constructing electronic computer circuits entirely out of nanotubes. A "p–n junction" is simulated along the single-walled carbon nanotube channel using two separate gates close to the source and drain of the CNTFET, respectively. The Schottky barrier field-effect transistor mechanism-based calculations of the current–voltage characteristics of the double-gated CNTFET show a good rectification performance of the p–n junction.

As like the applications, CNTs have been evinced as the material of future which will assist in extending the Moore's law, which says that number of transistors per integrated circuit doubles every 18 months, and it has been the guiding principle for the semiconductor industry for over 30 years. The prime driving force in nanoelectronic industry is due to the continual miniaturization of electronic devices.

However, it will be progressively difficult to continue downscaling at this rate, as quantum tunneling, interconnect delays, gate oxide reliability, and excessive power dissipation, among other factors, start hampering the performance of such devices. While some of these issues can, in principle, be handled by improving device design, packaging, processing, and channel mobilities, the rapidly increasing cost of fabrication motivates exploration of entirely new paradigms, such as novel architectures and new channel materials. One promising direction involves replacing the "top-down" lithographic approach with a "bottom-up" synthetic chemical approach of assembling nanodevices and circuits directly from their molecular constituents. Molecules are naturally small, and their abilities of selective recognition and binding can lead to cheap fabrication using self-assembly. In addition, they offer tenability through synthetic chemistry and control of their transport properties due to their conformational flexibility.

In the case of CNTs, significant progress has been reported regarding synthesis, functionalization, and control of the electronic properties. Insertion into and doping of CNTs are steps toward nanotube functionalization, possibly opening pathways to the creation of nanoelectronic devices, to the synthesis of heteronanotubes, and to the application of CNTs in many fields of science. However, their use as building blocks for nanoelectronic devices has not yet been fully realized due to lack of control of the reactivity of the outer CNT walls and of the basic electronic structure.

Therefore, for electronics applications, it is very desirable to modify the electronic structure of CNT to obtain a metallic or a *p*- and *n*-type semiconducting behavior. Many attempts at

this direction have been reported. The energy gap can be adjusted by changing the chemical composition. For instance, boron and nitrogen atoms are among the atoms most conveniently used as dopants of CNTs, since they have atomic sizes similar to that of carbon, a property that provides them with a strong probability of entering into the carbonaceous lattice. In addition, it has also been experimentally and theoretically reported that the doping of CNTs with nitrogen atoms tailors the electronic structure of the nanotube by introducing donor states near the Fermi level with additionally localized nonbonding states of lone pair electrons, which brings about an enhancement of electron conduction of semiconducting CNTs at low temperature. Even though it is possible to functionalize and control the electronic properties of CNT through chemical doping, fine tuning of doping concentration remains very difficult. Another method for CNT electronic structure engineering is non-covalent modification, i.e. encapsulation. Recently, air-stable amphoteric doping on CNTs has been realized by encapsulating organic molecules inside CNTs and it has been found that the carrier type and concentration in CNT can easily be controlled by tuning the electron affinity (EA) and ionization potential (IP) of the encapsulated molecules. Compared to previously investigated metal atoms or fullerenes encapsulated CNTs, there are many advantages in using an organic molecule encapsulation. Organic molecules are typically stable in air, simple to synthesize, and abundant. They have already been used to adjust the CNT band structure.

In this chapter, I will show how we can design nanoelectronic component embodied with interesting device characteristics, especially rectifying diodes. Simple strategy for designing nanoelectronic diodes is creating CNT heterojunction and controlling their electronic structure. In view of incorporating CNTs into real operational nanodevices, CNT-based intramolecular junctions were proposed early on. As mentioned before, a diode electronic component has been realized by joining nanotubes of two different diameters end to end. Both theoretical and experimental studies of such nanojunctions are full of promise. The junctions can be designed through various conceivable linkages within one-dimensional morphologies, such as a direct covalent bond, organic or metallic linkages, and even spacing. Such formation of one-dimensional heterojunctions has led to materials with unique properties and multiple functionalities not realized in single-component structures that are useful for a wide range of applications.

Especially, I will introduce how we can design and simulate conventional three types of diodes, Zener-, Schottky-, and Esaki-type diodes. I will introduce that the CNT junctions with chemical or physical doping, and organic linkages open the door to the design nanoelectronic components embodied with unique electron transport characteristics as nanoelectronic devices. The designed nanoelectronic components will give an insight into the design and implementation of various electronic logic functions based on CNTs for applications in the field of nanoelectronics.

2. Theoretical methodology

Remarkable progress in the molecular(nano) electronics has been made in the last few years, as researchers have developed ways of growing, addressing, imaging, manipulating, and measuring small groups of molecules connecting metal leads. Several prototype devices such as conducting wires, insulating linkages, rectifiers, switches, and transistors have been demonstrated. In parallel, there has been significant theoretical activity toward developing the description of nonequilibrium transport through molecules.

Transport through a molecule under bias is essentially a nonequilibrium, quantum kinetic problem. Contacting a molecule with two leads effectively "opens up" the system, replacing the discrete molecular energy levels with a continuous density of states and establishing a common electrochemical potential and a band lineup between the contacts and the molecule. Under bias, the two contact electrochemical potentials split, and the molecule, in its bid to establish equilibrium with both contacts, is driven strongly out of equilibrium. Current flow thus requires a formal treatment of nonequilibrium transport, through a suitable wave function (scattering theory) or Green's function technique. The Keldysh–Kadanoff–Baym nonequilibrium Green's function (NEGF) formalism gives us a rigorous theoretical basis for describing quantum transport through such a system at an atomistic level.

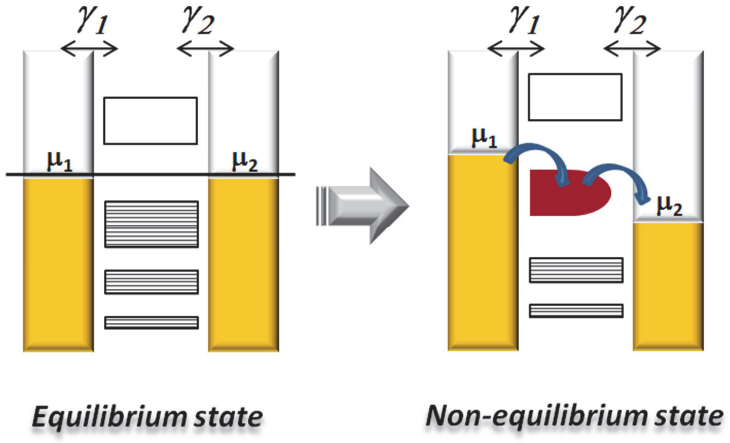

Fig. 1. Electron flow under applied bias.

This approach has been proven to be a powerful tool for studying electron-transport phenomena in nanodevices, and it provides a link between electron transport, first-principles electronic structure theory, and qualitative molecular orbital theory.

A typical simulation procedure consists of self-consistently coupling an electronic structure calculation with a suitable transport solver. Transport involves a nonequilibrium, open-boundary problem. We formally partition this problem into an active device and semi-infinite contacts that add or remove charges from it. The device energy levels and electrostatics are described by a Hamiltonian and a self-consistent potential, respectively, while the semi-infinite self-energy matrices with complex eigenvalues. Starting from an initial guess for the device density matrix described in a suitable basis set, we calculate the self-consistent potential, which, added with the device Hamiltonian, generates the device Fock matrix. The Fock matrix, together with the contact self-energies, determines the nonequilibrium Green's function that describes the causal response of the device to a unit excitation. The NEGF formalism gives us exact prescriptions thereafter for recomputing the nonequilibrium density matrix and current density, including the effects of many-body interactions and scattering within the device. The great advantage of this method is its generality: within the same framework, we can describe transport through various materials such as molecules, silicon transistors, nanowires, nanotubes, spintronic devices, and quantum dots.

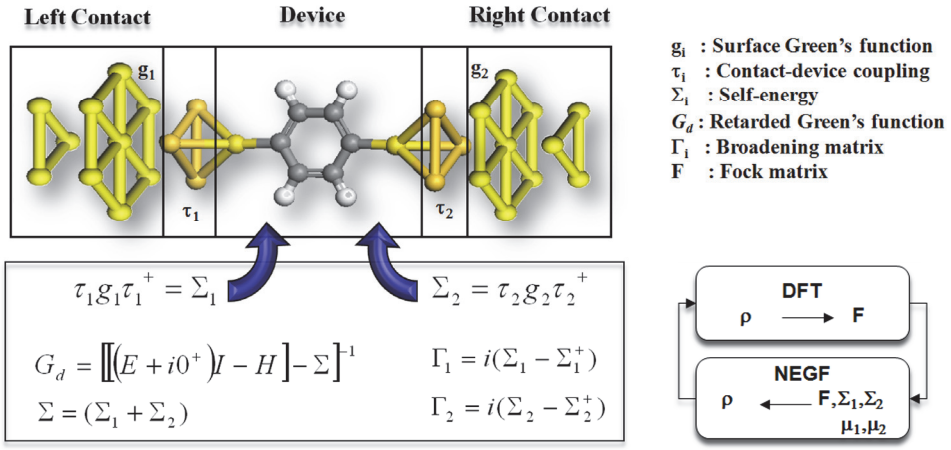

Fig. 2. Schematic of the nonequilibrium Green's function (NEGF) approach combined with density functional theory (DFT).

In the NEGF approach introduced above, the surface Green's functions describing semi-infinite electrodes attached to the defined device part from the left and right sides are derived using the Hamiltonian and overlap matrices corresponding to each CNT contact. The Green's function in this study is given by

$$G = \left(E^{+}S - F - \Sigma_1 - \Sigma_2\right)^{-1} \tag{1}$$

Here E^{+} denotes the energy plus an infinitesimal imaginary part (usually 10^{-5} or 10^{-6}), and S and F are the overlap and Fock matrices of the scattering part and $\Sigma_{1,2}$ is the self-energy matrix of the left and right electrode contacts, respectively. An applied bias leads to two different contact chemical potentials, $\mu_{1,2} = E_f \mp eV/2$. The current through the scattering part is calculated by integrating the transmission coefficient within the bias window ($\mu_1 - \mu_2$) around the Fermi level.

$$I = (2e/h)\int_{-\infty}^{\infty} dE\, T(E,V)\left(f_1(E-\mu_1) - f_2(E-\mu_2)\right) \tag{2}$$

where the $f_{1,2}$ are the Fermi functions with electrochemical potential $\mu_{1,2}$

$$f_{1,2}(E) = \left(1 + \exp\left[\frac{E-\mu_{1,2}}{k_B T}\right]\right)^{-1} \tag{3}$$

T(E) is the transmission coefficient between two electrodes derived from the Hamiltonian and the self-energies of electrodes:

$$T(E) = Tr\left[\Gamma_1 G \Gamma_2 G^{+}\right] \tag{4}$$

3. Designing nanoelectronic diodes

3.1 Conventional diodes

In electronics, a diode is a two-terminal electronic component that conducts electric current in only one direction. The term usually refers to a semiconductor diode, the most common type today. The most common function of a diode is to allow an electric current to pass in one direction (called the diode's forward direction) while blocking current in the opposite direction (the reverse direction). A semiconductor diode's behavior in a circuit is given by its current–voltage characteristic, or *I*–*V* graph. The shape of the curve is determined by the transport of charge carriers through the so-called depletion layer or depletion region that exists at the *p*-*n* junction between differing semiconductors. When a *p*-*n* junction is first created, conduction band (mobile) electrons from the *n*-doped region diffuse into the p-doped region where there is a large population of holes (vacant places for electrons) with which the electrons "recombine". When a mobile electron recombines with a hole, both hole and electron vanish, leaving behind an immobile positively charged donor (dopant) on the *n*-side and negatively charged acceptor (dopant) on the p-side. The region around the *p*-*n* junction becomes depleted of charge carriers and thus behaves as an insulator.

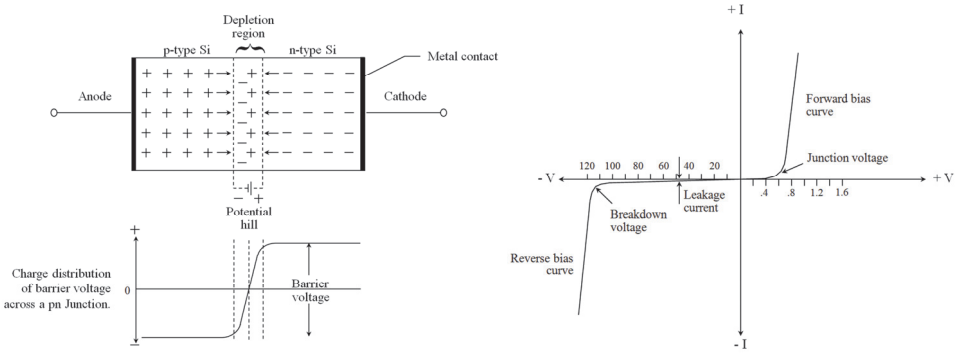

Fig. 3. *p*-*n* junction diode and *I*–*V* characteristics.

This unidirectional behavior is called rectification, and is used to convert alternating current to direct current, and to extract modulation from radio signals in radio receivers. However, diodes can have more complicated behavior than this simple on-off action. This is due to their complex non-linear electrical characteristics, which can be tailored by varying the construction of their *p*-*n* junction. These are exploited in special purpose diodes that perform many different functions. For example, specialized diodes are used to regulate voltage (Zener diodes), to generate radio frequency oscillations (Esaki diodes), to generate high speed response (Schottky diodes), to produce light (light emitting diodes (LED)), and to generate current (photodiode).

3.2 Designing strategy for nanoelectronic diodes

It has become clear through many studies that electron transport characteristics are influenced by the intrinsic properties of molecules, including their length, conformation, energy gap between the highest occupied molecular orbital (HOMO) and lowest unoccupied molecular orbital (LUMO), and the alignment of molecular levels relative to the

Fermi level of the contact. It has been demonstrated that the conductance of molecules can be controlled by the position of individual molecular levels. Therefore, the controlling the alignment of energy levels relative to the Fermi level of the contact allow us to design molecular scale devices using several building blocks such as carbon nonotubes.
Therefore, the strategy for designing nanoelectronic diodes is based on the control of the intrinsic properties, i.e. the electronic structure, of CNT by creating CNT junctions with organic linkages and chemical or physical doping. In this section, I will introduce four CNT junctions having Zener-, Schottky-, and Esaki-type diode characteristics.

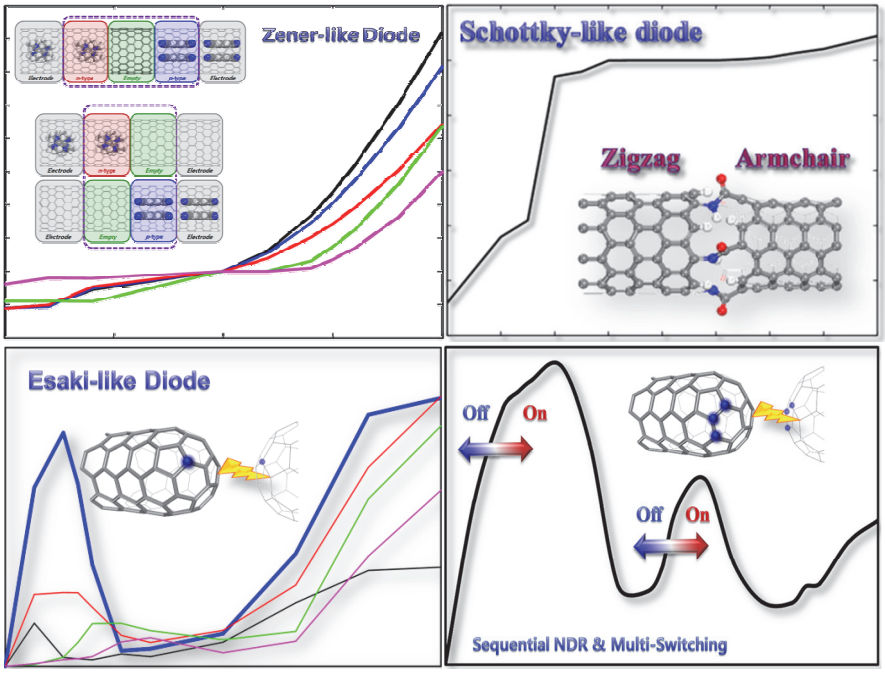

Fig. 4. Designed Zener-, Schottky-, and Esaki-type diodes.

3.3 Pure CNT

Detailed knowledge of the electron transport characteristics of pristine CNTs, both metallic (armchair) and semiconducting (zigzag) CNTs is a necessary requirement for investigating the designed CNT heterojunctions. Current–voltage (*I*–*V*) characteristics and bias dependence of the transmission curves, T(E,V), of the pure CNTs are shown in Figure 5. *I*–*V* curves and T(E,V) plots show the intrinsic characteristics of each CNT with the white dotted lines indicating the bias window. The current is calculated by integrating the transmission coefficient within the bias window around the Fermi level. In fact, only the low-bias *I*–*V* characteristics can be reasonably well reproduced by the equilibrium transmission characteristics, T(E,V = 0). However, the deviation in both the magnitude and the peak position of transmission becomes significant at a large bias as can be seen from the shift of the peak near the Fermi level by the applied bias voltage. Hence, the evaluation of T(E,V) is very important to reveal unique features of the systems investigated herein.

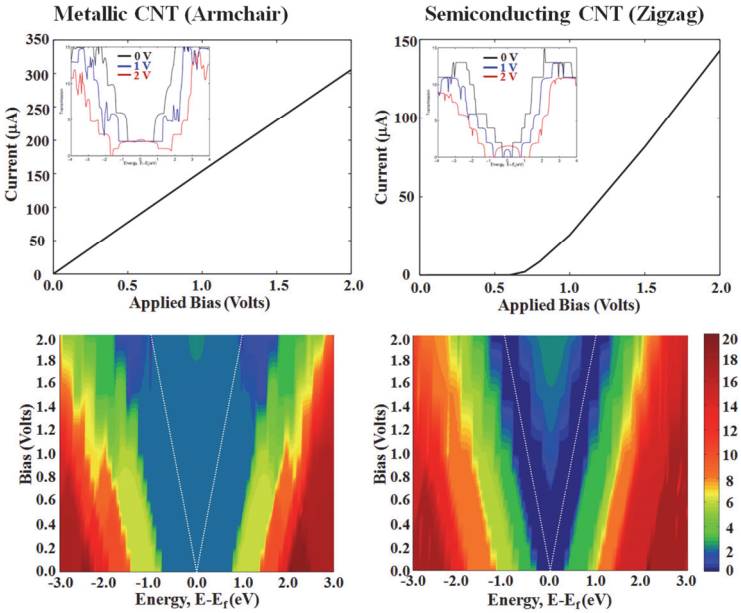

Fig. 5. *I–V* curves and bias dependence of the transmission curves, T(E,V), calculated at every 0.2 bias voltage for metallic and semiconducting pure carbon nanotube. T(E,V) curves at 0.0, 1.0, and 2.0 V are shown in the inset. Dotted white lines indicate the range of current integration around the Fermi level.

The pure metallic CNT has two open conduction channels near the Fermi level at all applied bias ranges and shows a linear *I–V* curve. On the other hand, the pure semiconducting CNT has a band-gap that increases according to the applied bias voltage near the Fermi level. However, when the applied bias voltage reaches a certain bias voltage, 0.8 V in this model, a new transmission peak appears near the Fermi level, which significantly contributes to the electron transport and current.

3.4 Zener-like diode: Organic molecules encapsulation & charge transfer

One-dimensional carbon nanotube (CNT) junctions can be designed by encapsulating *p*- and *n*-type organic molecules into CNTs with electrophilic tetracyano–p–quinodimethane (TCNQ) and nucleophilic tetrakis(dimethylamino)ethylene (TDAE) molecules, where the charge transfer play an important role in determining the electron transport characteristics and lead to materials with unique properties, *p-n* junction diode, *i.e.* Zener-like diode.

The operational device characteristics of organic molecules encapsulated CNT junctions originate from distinct response of intrinsic transmission peaks of pure CNTs and the distinctive response is determined by the manner of the charge transfer. The charge transfer between CNT and doped organic molecules causes lateral shift of the transmission peaks, and the charge transfer between the encapsulated organic molecules cause vertical shift of the transmission peaks. Therefore, by controlling the charge transfer, *i.e.* the electron affinity (EA) and ionization potential (IP) of the encapsulated molecules, we can finely tune the operational device characteristics.

3.4.1 Modeling

Each tetracyano–p–quinodimethane (TCNQ) and nucleophilic tetrakis(dimethylamino) ethylene (TDAE) molecules molecule is encapsulated in carbon nanotubes (13,0) and (17,0) (CNT13 and CNT17), as shown in Figure 6. Encapsulated organic molecules are separated by 4.342 Å or 4.480 Å for TCNQ and 5.675 Å for TDAE at periodic boundary condition with 12.780 Å of z-axis cell size. In the case of TCNQ molecule, we considered parallel(P) and tilted(T) stacking patterns at CNT17 due to a large diameter. So, we denote the designed models as "CNTa–b_c", where "a", "b", and "c" respectively mean the size of zigzag CNT, encapsulated organic molecule, and stacking pattern.

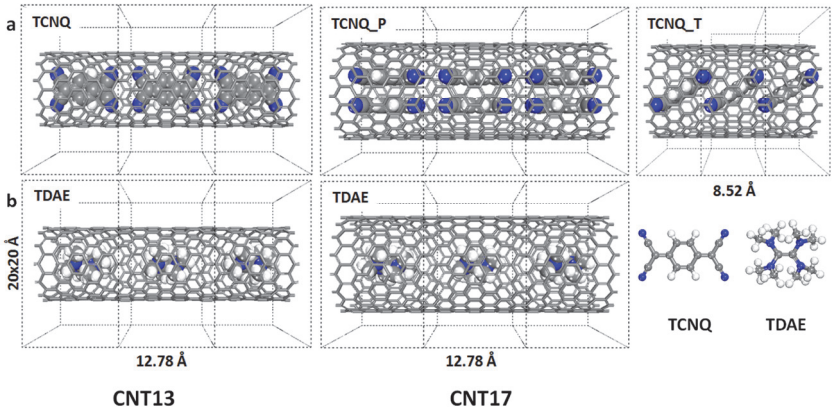

Fig. 6. Schematic of (a) TCNQ or (b) TDAE encapsulated carbon nanotubes (13,0) and (17,0) (CNT13 and CNT17). In the case of TCNQ molecule, parallel(P) and tilted(T) stacking patterns are considered at CNT17.

3.4.2 Electron transport characteristics of TCNQ and TDAE encapsulated CNTs

When we encapsulate TCNQ and TDAE molecules into the semiconducting CNTs, the charge transfer between organic molecule and CNT affects the band structures of CNT. But the change of band structures is opposite each other because TCNQ and TDAE have different electrostatic features, electrophilic and nucleophilic. The electronic band structures of TCNQ and TDAE encapsulated CNT17s, pure CNT17 and organic molecules are shown in Figure 7.

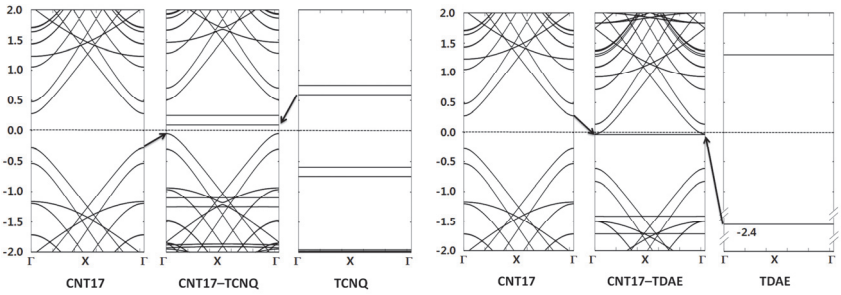

Fig. 7. Electronic band structures of TCNQ and TDAE encapsulated CNT17s, and pure CNT17 and organic molecules (TCNQ and TDAE).

The flat bands near the Fermi level are derived from the lowest unoccupied molecular orbital (LUMO) states of TCNQ, and the highest occupied molecular orbital (HOMO) states of TDAE, where each LUMO and HOMO creates acceptor and donor states in the gap of CNT. The band structures shift up and down by doping of TCNQ and TDAE, respectively. The band in CNT17-TDAE closely lies in the top of the CNT valence band, which induces charge transfer from CNT to TCNQ. The higher-lying band in CNT17-TDAE, however, overlaps with the bottom of the CNT conduction band. The bands are partially filled, indicative of effective electron transfer from TDAE to CNT. It is seen that the relatively large change of HOMO level in TDAE is derived from the large charge transfer, that is the doping effect of *n*-type encapsulated organic molecule is more significant than that of *p*-type one.

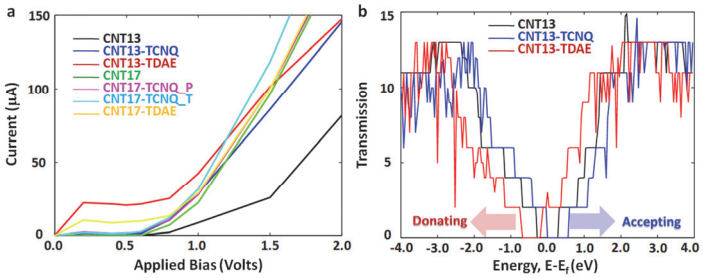

Fig. 8. (a) I–V curves and (b) the transmission curves, T(E,V=0), of TCNQ or TDAE encapsulated CNTs, "CNTa–b_c", where "a", "b", and "c" respectively mean the size of zigzag CNT, encapsulated organic molecule, and stacking pattern.

Let us now discuss the electron transport characteristics of *p*- and *n*-type doped CNTs. Current–voltage (*I*–*V*) and equilibrium transmission, T(E,V = 0), and bias dependence of the transmission curves, T(E,V), of TCNQ and TDAE encapsulated CNTs are compared to the pure CNT13 and CNT17 as shown in Figure 8. The pure semiconducting CNTs (CNT13 and CNT17) have a band-gap that increases according to the applied bias voltage near the Fermi level. So, pure semiconducting CNTs do not have current under low bias voltage. However, when the applied bias voltage reaches a certain voltage (~0.6 V), a new transmission peak appears near the Fermi level, which significantly contributes to the electron transport and current as shown in Figure 8.

TCNQ encapsulated CNTs show similar current behavior with pure semiconducting CNTs regardless of parallel or tilted conformation. There is almost no current until 0.6 V, beyond which the current starts to increase. In contrast TCNQ encapsulated CNTs, the change of energy level is larger for TDAE encapsulated CNTs and the direction of shift of transmission peak is opposite, moreover transmission peak crosses over the Fermi level and enters into the bias window as seen in Figure 8(b). Therefore, TDAE encapsulated CNTs have very small currents when applied bias is smaller than a critical bias voltage (~0.8 V), above which the current begins to increase owing to a new transmission peak within the bias window. Furthermore, this new transmission peak increases with increasing applied bias. It is seen that the *I*–*V* characteristic of TDAE encapsulated CNTs show varistor-like behavior (i.e., a resistor with a significantly nonohmic current–voltage characteristic) because the amplitude and number of conducting channels, which are located in the integration window, are constant for a large range of applied voltages (from ~0.0 to ~0.8 V) The varistors are often used to protect circuits against excessive voltage.

Accordingly, it is worth mentioning that the effect of non-covalent doping essentially originates from the shift of the transmission peaks. The charge transfer between CNT and doped organic molecules causes lateral shift of the transmission peaks, shift left or shift right, which gives different behavior under the applied bias voltages. And the shift can be controlled by tuning the electron affinity (EA) and ionization potential (IP) of the encapsulated molecules.

3.4.3 Electron transport characteristics of p-n junctions with TCNQ and TDAE encapsulated CNTs

We have investigated the operational device characteristics of the organic molecules encapsulated CNT *p-n* junctions, as shown in Figure 9. We incorporated empty region between *n*-type CNT17-TDAE and *p*-type CNT17-TCNQ with the distance of "d", in order to reduce direct interaction between doped organic molecules (Junction 1-3). In addition, we considered CNT *p-n* junctions composed of only one type of CNT, p- or n-type, and pure semiconducting CNT (CNT17) (Junction4 and 5), where CNT17 acts as both an electron acceptor and electron donor according to the dopant of counterpart. Scattering region and electrode are defined as shown in Figure 9.

Figure 10 shows the *I–V* characteristics of the organic molecules encapsulated CNT *p-n* junctions, where all designed junctions display completely non-linear and asymmetric *I–V* curves and provide rectifying behaviors regardless of the type of junction with a large current under forward bias while almost no current under reverse bias, resembling that of a conventional Zener diode . The current rises for a positive bias applied to the left electrode. The rectifying behavior can be understood by the induced electric field between the left *n*-

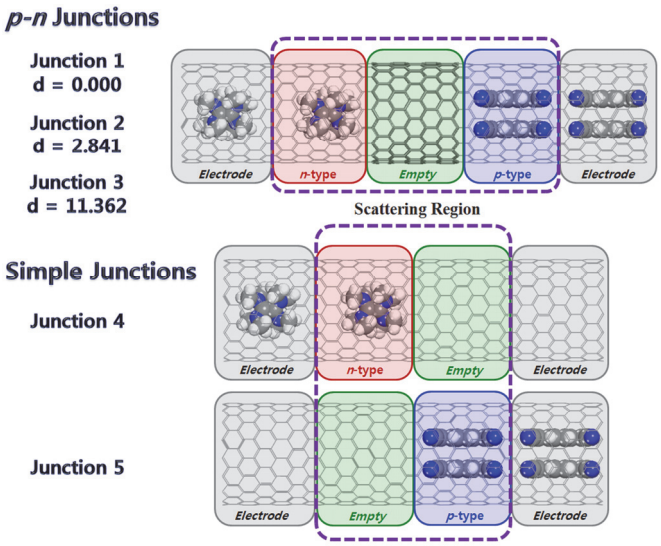

Fig. 9. Schematic of the TDAE and TCNQ encapsulated p-n junctions. Junction1, Junction2 and Junction3 contain *n*-type TDAE and *p*-type TCNQ molecules, and empty region is inserted between them with the cell size of "d". Junction4 and Junction5 have only *n*-type TDAE or *p*-type TCNQ respectively. Scattering regions are denoted by dotted box.

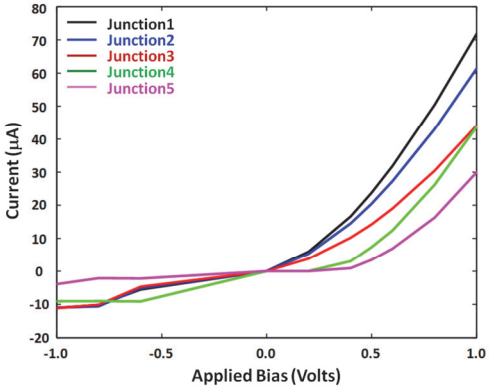

Fig. 10. *I–V* characteristics of TDAE and TCNQ encapsulated CNT *p-n* junctions

type CNT17-TDAE to the right *p*-type CNT17-TCNQ. Because the encapsulated TCNQ and TDAE molecules are electrophilic and nucleophilic, electric field is induced by charge transfer between them, and the direction is from the left n-type CNT17-TDAE to *p*-type CNT17-TCNQ. If the direction of the electric field is the same to the direction of the electron flow under a forward, it has current. But, under reverse bias (negative bias), the electric field acts as a potential barrier of the electron flow. Therefore, the rectifying behavior is determined by the orientation of the electric field arising from the charge transfer between *p*- and *n*-type doped CNTs. Furthermore, the difference of rectifying ability among the designed junctions implies the role of the charge transfer and induced electric field.

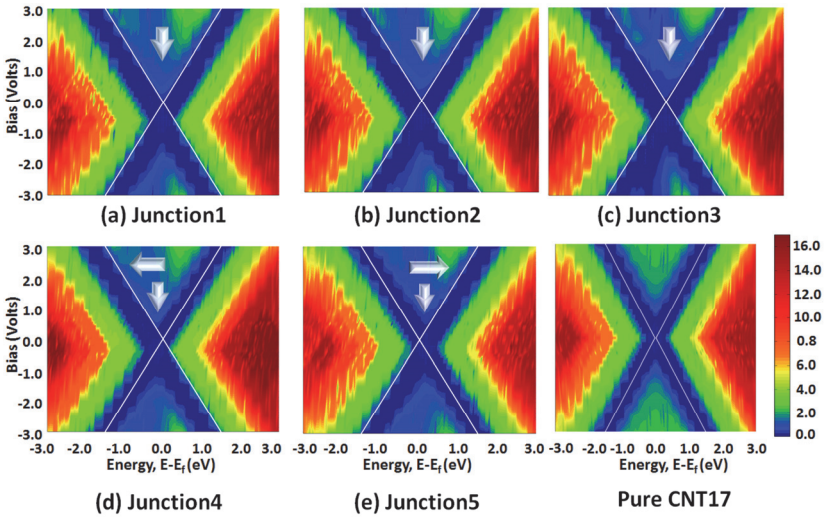

Fig. 11. Bias dependence of the transmission curves, T(E,V), calculated at every 0.2 bias voltage for the TDAE and TCNQ encapsulated CNT p-n junctions compared to that of pure CNT17: (a) Junction1, (b) Junction2, (c) Junction3, (d) Junction4, and (e) Junction5. White arrows point out the shift of transmission peaks compared to that of pure CNT17. White lines indicate the range of current integration around the Fermi level.

Junction1-3 show the decrease of current with increasing the size of empty region under forward bias (positive bias), and Junction4 and 5 have smaller current because the large empty region or absence of one type of dopant molecule suppresses a charge transfer between *p*-and *n*-type CNTs.
In previous section, we have mentioned that lateral shift of the transmission peaks is seen for the TDAE or TCNQ encapsulated CNTs according to the dopants. In contrast, vertical shift of the transmission peaks is also seen the organic molecules encapsulated p-n junctions by charge transfer between encapsulated n-type and *p*-type molecules, as seen in Figure 11. The designed CNT *p*-*n* junctions show significant shift of the transmission peaks to negative bias region, i.e. shift down, as indicated by white arrow, in comparison to the symmetric behavior of pure CNT17, which leads the designed CNT *p*-*n* junctions to have rectifying behavior. Weak rectifying behavior and weak current of Junction4 and 5 can be explained by weak vertical shift of the transmission peaks, furthermore, the inherent effect of organic molecule encapsulation, lateral shift of transmission peaks, is seen, because they have only one type of dopant molecules. So, we can address that the rectifying behavior originate from asymmetric vertical shift of the transmission peaks, and which induced by the charge transfer between the encapsulated organic molecules, TDAE and TCNQ. And the shift also can be controlled by tuning EA and IP of the encapsulated molecules.
It is concluded, that the effect of non-covalent doping and the rectifying behavior essentially originates from the shift of the transmission peaks through charge transfer between the CNT and different types of dopants. Therefore, we can realize conventional Zener-like diode using the organic molecule encapsulated CNT junctions.

3.5 Schottky-like diode: Organic linkage & dipole moment

One-dimensional carbon nanotube (CNT) junctions with peptide linkages can be designed, where the incorporation of peptide linkages and their associated dipole moments play an important role in determining the electron transport characteristics and lead to materials with unique properties, such as Schottky-like behavior.
The incorporation of peptide linkages gives rise to the suppression of current and the effects are more significant for metallic CNTs than for semiconducting CNTs. Furthermore, the electron transport characteristics of the designed junctions depend on the direction of the dipole moment associated to the peptide linkages, which brings about asymmetric I–V behavior.

3.5.1 Modeling

The carbon nanotube models used in this study are metallic (armchair (5,5)) and semiconducting (zigzag (10,0)) CNTs. The intramolecular heterojunctions are assembled with two CNT units and five peptide linkages, shown in Figure 12. When less than five covalent linkages are employed or the chemical bridges are asymmetrically distributed around the CNT mouths, the conformational flexibility of the resulting model junctions increases considerably.
Figure 12 shows the investigated intramolecular heterojunctions composed of metallic and semiconducting CNTs, and peptide linkage. SM1 and SM2 indicate semiconductor/metal, and metal/semiconductor junctions with peptide linkages, respectively. The SM1 and SM2 junctions are distinguished by the asymmetric peptide linkage composed of C=O and N–H bonds. In the SM1 junction, the C=O and N–H bonds are, correspondingly, connected to the metallic and semiconducting CNTs and vice versa in the SM2 junction.

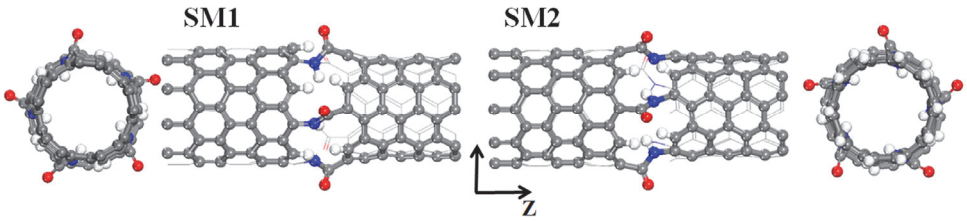

Fig. 12. Optimized structures of four carbon nanotube intramolecular heterojunctions with peptide linkages, SM1, and SM2.

3.5.2 Electron transport characteristics

Figure 13 shows the *I*–*V* characteristics of intramolecular heterojunctions, SM1, and SM2. The directions of their dipole moments are oriented from the C=O bond to the N–H bond. Therefore, the direction of the dipole moment can be either the same or opposite with respect to the direction of the applied bias; each positive and negative applied bias correspondingly gives parallel or anti-parallel alignment with the direction of the dipole moment vector.

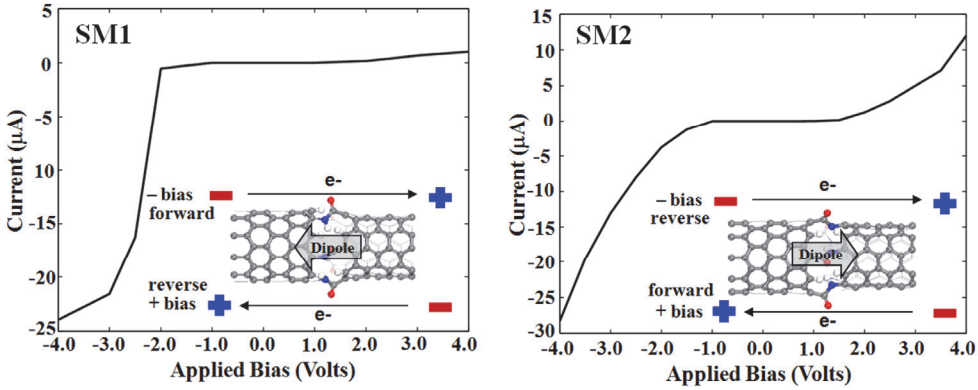

Fig. 13. I–V curves of four carbon nanotube intramolecular heterojunctions, SM1, and SM2. The directions of forward and reverse bias, electron flow, and dipole moment are indicated in the inset.

Junctions made by CNTs with different chiralites evoke unique properties and multiple functionalities. Indeed, the metal and semiconductor junction with a positive barrier height has a pronounced rectifying behavior, as in a typical Schottky diode. The difference in the electronic structures and screening properties of metallic and semiconducting CNTs gives rise to different band-bending profiles and, subsequently, a Schottky barrier at the junction interface, which explains the rectifying behavior across the junction. A large current exists under forward bias, while almost no current exists under reverse bias. In Figure 13, the SM1 junction displays a completely non-linear and asymmetric *I*–*V* curve, resembling that of a Schottky diode. The current rises sharply above a threshold voltage, -2.0 V, for a negative

bias applied to the left semiconducting CNT. There is a small increase in current for reverse bias.

The difference between the SM1 and SM2 junctions results from the connecting way between peptide linkages and CNT electrodes. In other words, the orientation of the dipole moment arising from the peptide linkages plays an important role in the resulting Schottky-like behavior. In the SM1 junction, the C=O and N–H bonds are correspondingly connected to the metallic and semiconducting CNTs, respectively, which sets up the direction of the dipole moment vector from the metallic CNT to the semiconducting CNT. Therefore, the charge transfer is induced from the semiconducting CNT to the metallic CNT, where the direction of the charge transfer is the same to the direction of the electron flow under a forward bias of the Schottky diode. It means that the SM1 junction resembles an *n*-type Schottky diode. In contrast, the SM2 junction resembles the p-type one. Accordingly, it can be explained why Schottky-like behavior is observed in our SM1 junction but not in the SM2 junction. In addition, the large dipole moment associated to the SM2 junction (7.21 Debye) also intensifies the symmetric *I*– *V* characteristics because a reverse bias is aligned parallel to the dipole moment vector, resulting in an increase of current. Under a reverse bias, the change of current is much larger in the SM2 junction than in the SM1 junction, as seen in Figure 13.

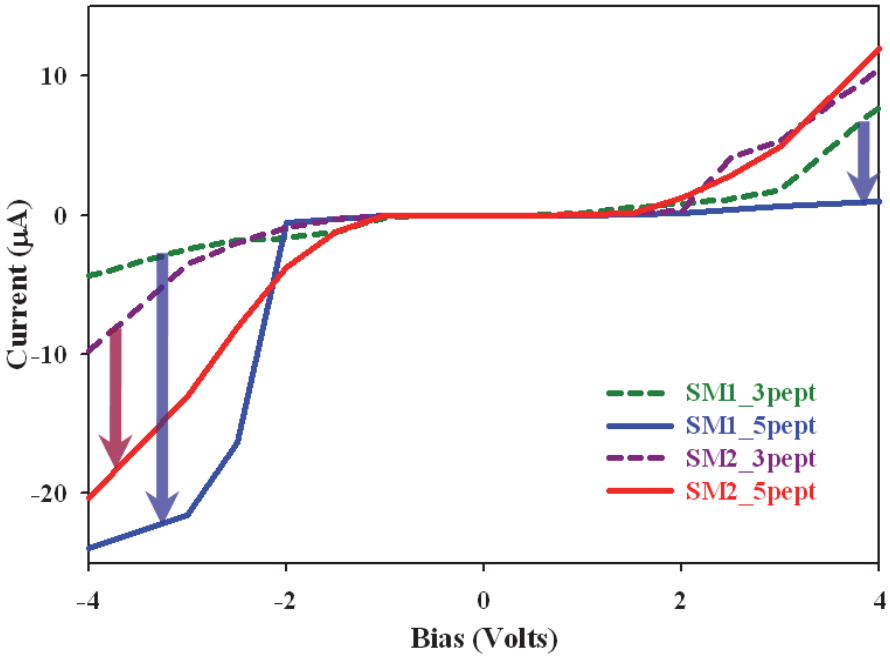

Fig. 14. *I*–*V* curves of SM1 and SM2 junctions at the different number of peptide linkages.

We have investigated the effects of the number of peptide linkage on the electron transport characteristics of the SM1 and SM2 junctions to clarify the effect of the dipole moment to the Schottky barrier and rectifying behavior. In Figure 14, it is seen that the tunneling current of the SM1 junction is suppressed at the reverse biases (positive biases) by increasing the number of peptide linkages, which reveals the dependence of the Schottky barrier on the

dipole moment. In contrast, there is no significant dipole dependence at the SM2 junction. The increase of the tunneling current of both the SM1 and SM2 junctions at the negative biases originates from the increase of tunneling channels when the number of linkages increases from three to five peptides.
Based on these results, we can prove that the Schotkky barrier is basically induced by the intrinsic nature of the pure semiconducting–metallic CNT junctions; afterwards the induced Schotkky barrier can be controlled at the SM1 junction by varying the dipole moment through the number of incorporated peptide linkages, whereas the effect of the dipole moment is not significant at the SM2 junction.

3.6 Esaki-like diode / multi-switching: Chemical doping & donor state

One-dimensional carbon nanotube (CNT) junctions with two single- (or multi-)nitrogen-doped (N-doped) capped carbon nanotubes (CNTs) facing one another can be designed, where the modification of the molecular orbitals by the N-dopants generates a conducting channel in the designed CNT junctions, inducing a negative differential resistance (NDR) behavior, which is a characteristic feature of the Esaki-like diode, that is, tunneling diode. And by controlling doping level, NDR based multi-switching behaviour can be achieved.
The NDR behavior significantly depends on the N-doping site and the facing conformations of the N-doped capped CNT junctions. Furthermore, a clear interpretation is presented for the NDR behavior by a rigid shift model of the HOMO- and LUMO-filtered energy levels in the left and right electrodes under the applied biases.

3.6.1 Modeling

The front end of the N-doped capped CNT(5,5) and CNT(9,0) is closed with a hemisphere of fullerene and the carbon atoms on the other end are passivated with hydrogen atoms. Then nitrogen atom is substituted at the cap or sidewall region as denoted by letters in Figure 15(a). In order to provide the device part of the two-probe system (contact–device–contact), that is, N-doped capped CNT junctions, saturated hydrogen atoms are detached from the optimized N-doped capped CNT(5,5) and CNT(9,0) and the modified structure is replicated so as to face one another with the proper distance, as shown in Figure 15(a). The distances between two facing N-doped capped CNTs are referred to as the distance of the fullerene dimer because the designed CNTs have a hemisphere of fullerene as a cap. Then the left and right sides of the CNT junctions are connected to appropriate semi-infinite CNT electrodes with the same chiralities of the CNT junctions.
In the single-N-doped capped CNT junctions, we consider four different conformations depending on the chirality of the CNTs (armchair(5,5) and zigzag(9,0)) and the spatial arrangement of the nitrogen atoms in the designed CNT junctions. Because of the distinct cap structures of the armchair(5,5) and zigzag(9,0) CNTs, pentagon- and hexagon-facing conformations are possible for the CNT(5,5) and CNT(9,0), respectively. In addition, both pentagon- and hexagon-facing conformations have the eclipsed and staggered conformations owing to the spatial arrangement of the N-dopants.
In addition, the designed multi-N-doped capped CNT junctions are considered, which are b-site_multi-N-doped CNT junctions according to the number of doped nitrogen atoms and their conformations compared to that of single-N-doped capped CNT(5,5) junction, **55b**. In

the multi-N-doped capped CNT junctions, only eclipsed arrangement of armchair(5,5) CNT junctions are considered. Whole designed geometries are depicted in the Figure 15(b).

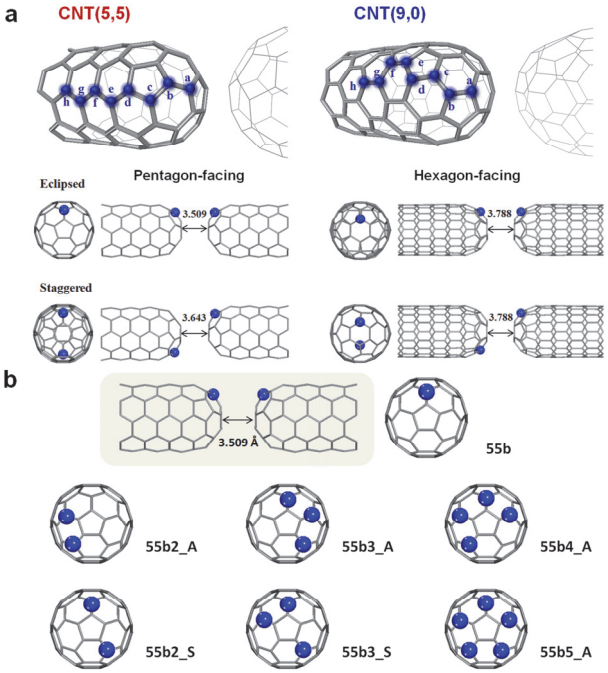

Fig. 15. (a) Schematic of the two facing single-N-doped capped carbon nanotubes (CNTs) in different conformations according to the chirality of the CNTs (armchair(5,5) and zigzag(9,0)) and the spatial arrangement of the nitrogen dopants; pentagon- or hexagon-facing and eclipsed or staggered conformations. The notations of **55xE** and **90xS** mean that **x** is nitrogen doping site and **E** and **S** mean eclipsed and staggered. The letters (**a – h**) indicate the atomic sites for replacing carbon with nitrogen atoms. (b) Schematic of the two facing multi-N-doped capped carbon nanotubes according to the number of doped nitrogen atoms and their conformations compared to that of single-N-doped capped CNT(5,5) junction, **55b**. Models of have nitrogen atoms at only **"b"** doping site (b-site_multi-N-doped CNTs).

3.6.2 Electron transport characteristics

Current–voltage (*I–V*) characteristics of the single-N-doped capped CNT(5,5) and CNT (9,0) junctions at the eclipsed and staggered conformations, respectively, are compared to the pure capped CNT junction as shown in Figure 16. The **55xE** and **90xS** notations mean that **x** is the single-N-doping site and **E** and **S** are eclipsed and staggered, respectively. The remarkable feature emerging from the *I–V* characteristics of the N-doped CNT junctions is that the tunneling current between two single-N-doped capped CNTs is dramatically increased by N-doping and a negative differential resistance (NDR) is observed. The NDR is a typical feature of the Esaki-like diode, that is, tunneling diode. In the eclipsed conformation of the single-N-doped capped CNT(5,5) junctions, a sharp current peak appears at an applied bias range of 0.0V<V<0.8 V, while the current is very low around the 1.0V<V<1.5V applied bias range.

Furthermore, it is seen that the height of the sharp current peak (I_{peak}) and the peak position (V_{peak}) strongly depend on the N-doping site. The V_{peak} gradually moves up to higher bias range when the doping site is changed from cap to sidewall: **55aE** is 0.2, **55bE** is 0.4, **55cE** is 0.5, **55dE** is 0.8, **55eE** is 0.8, and **55fE** is 1.0 V. And the **55bE** junction has a maximum I_{peak} value, 11.73μA, which is considerably larger as compared to that of other junctions. In addition, the **55bE** junction has the largest peak-tovalley ratio (PVR), 15.03. The PVR value of the **55bE** junction is more than twice the PVR value of the typical solid-state Esaki-diode, that is, GaAs/AlGaAs diode. In contrast to the dependence on the N-doping site, there is no significant difference of the I–V characteristics between two eclipsed and staggered conformations. Both conformations show that the NDR behavior and the current peak and PVR value depend on the single-N-doping site in the same way. Such features of the *I–V* characteristics are also seen in the single-N-doped capped CNT(9,0) junctions, however the tunnelling current is significantly suppressed as compared to that of the single-N-doped capped CNT(5,5) junctions. This reveals that electron transport characteristics strongly depend on the facing conformation induced by the chirality of the CNT without regard for the eclipsed or staggered conformations. The pentagon-facing conformation of CNT(5,5) junctions provides a large tunnelling current as compared to the hexagon-facing conformation of CNT(9,0). In addition, it is found that the observed NDR behavior is strongly dependent on the N-doping site.

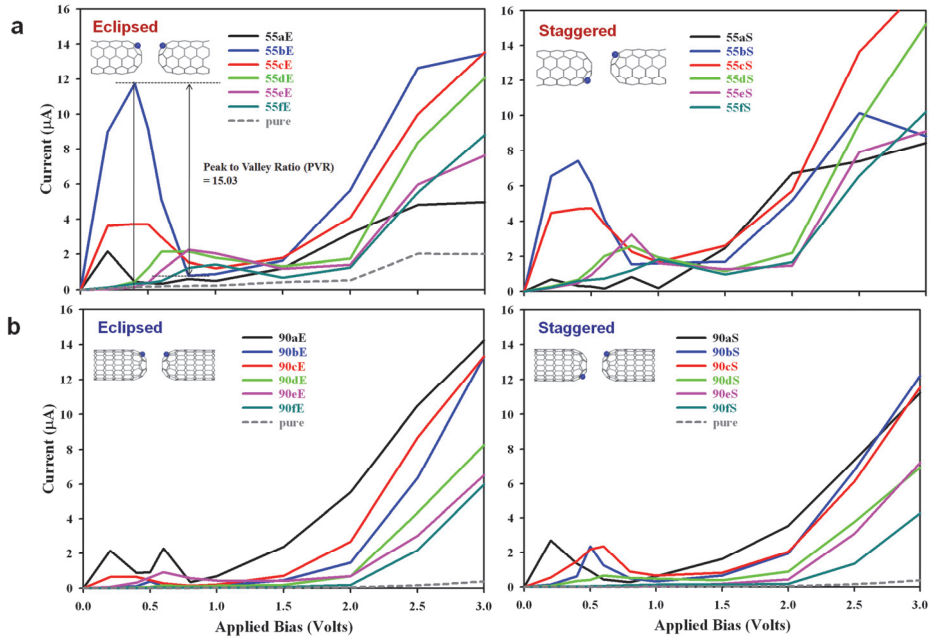

Fig. 16. a) *I–V* curves of the N-doped capped (a) CNT(5,5) and (b) CNT(9,0) junctions in the eclipsed and staggered conformations, respectively, as compared to the pure capped CNT junctions. The nitrogen atom is substituted at the **a**, **b**, **c**, **d**, **e**, and **f** doping sites, which are denoted by **55(90)a**, **55(90)b**, **55(90)c**, **55(90)d**, **55(90)e**, and **55(90)f**. The structures of junction PVRs are shown in the inset.

Therefore, we have increased the number of doped nitrogen atoms at **b** site, b-site_multi-N-doped CNT(5,5) junctions, in order to investigate how NDR behavior response the number of doped nitrogen atoms. *I*–*V* characteristics of the multi-N-doped capped CNT junctions are compared to that of the single-N-doped CNT(5,5), **55b**, and pure CNT(5,5) junctions, as shown in Figure 17.

The remarkable feature emerging from the *I*–*V* characteristics is that the tunneling current is dramatically increased by nitrogen doping and a negative differential resistance (NDR) is observed compared to that of pure CNT(5,5) junction. In comparison of the *I*–*V* characteristics of the multi-N-doped CNT junctions to that of **55b** junction, it is seen that the NDR behavior is conserved or reinforced, and the tunneling current is enhanced by addition of nitrogen atoms. The trend is strong for b-site_multi-N-doped CNT junctions rather than for multi-site_multi-N-doped CNT junctions. But the trendency is not so for all junctions, because the NDR behavior disappears at **55b3_S** and **55b5_A** junctions. And it is seen the conformational dependency, in which the junctions having aggregated conformation have enhanced current, while separated conformation gives suppressed current. The difference is clearly seen at **55b2** and **55b3** junctions, where the aggregated conformation (**55b2_A** and **55b3_A**) reinforces the current and NDR behavior, while separated conformation (**55b2_S** and **55b3_S**) suppresses the current and NDR behaviour.

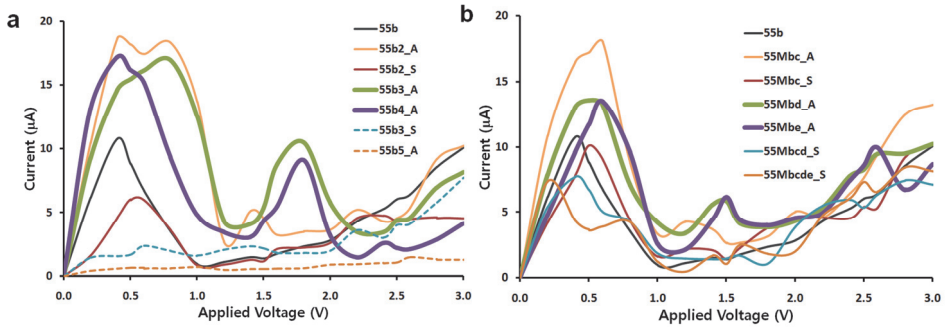

Fig. 17. (a) *I*–*V* curves of the multi-N-doped capped CNT(5,5) junctions compared to those of the single-N-doped capped CNT(5,5), and **55b**.

The *I*–*V* curve shows relatively large peak-to-valley ratio (PVR), > 4, although the height of the sharp current peak and the peak position (V_{peak}) depend on designed junctions. The remarkable feature emerging from the results is sequential NDR behavior is induced by additional nitrogen atoms and the feature depends on the confromation, aggregated or separated. In b-site_multi-N-doped CNT junctions, **55b2_A**, **55b3_A** and **55b4_A** junctions of aggregated conformation, have another new sharp current peak at 1.5 V < V < 2.0 V applied bias range (V_{peak2}) and current valley at 2.0 V < V < 2.5 V applied bias range ($V_{valley2}$). Beside, in the case of multi-site_multi-N-doped CNT junctions, weak new current peak is seen for **55b2_A**, **55Mbd_A**, and **55Mbe_A**. Among the multi-N-doped capped CNT junctions, **55b3_A** and **55b4_A** junctions provide clear sequential NDR behavior. The observed sequential NDR behavior can be used for successive switching process in which each switching occurs at different times when the bias current is gradually increased as describe in Figure 18.

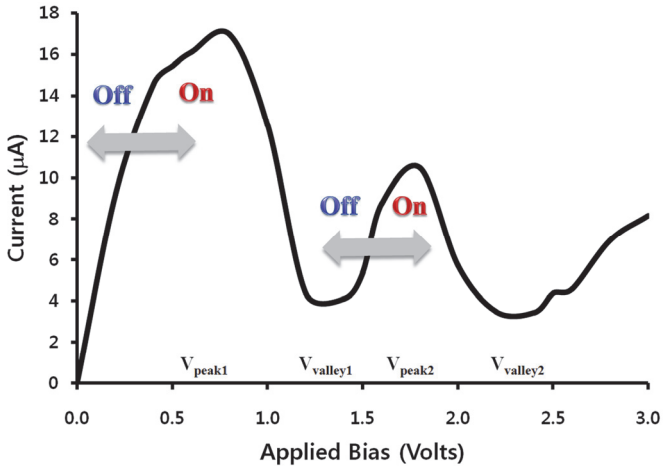

Fig. 18. Multi-switching behavior of the multi-N-doped capped CNT(5,5) junction, **55b3_A**.

3.6.3 The role of the nitrogen dopants for the NDR behavior

Such distinguishable electron transport characteristics usually originate from the intrinsic nature of the molecule, such as the molecular energy level alignment with respect to the Fermi level and their response to the applied bias voltage. In this work, a new option is the doping of CNTs with nitrogen atoms, which tailors the electronic structure of the nanotube. Nitrogen has a profound effect on the structural arrangement and electronic properties of the CNTs, such as a strong donor state near the Fermi level. It has been shown theoretically that a small amount of dopant can drastically modify the electronic transport properties of the tube. For zigzag semiconducting CNTs, doping with a single nitrogen impurity increases current flow, whereas doped metallic CNTs with boron or nitrogen atoms produce quasibound impurity states of a definite parity and reduces the conductance via resonant backscattering. Although we designed 1D heterojunctions with two N-doped capped CNTs compared to the use of open-ended CNTs previously reported, the N-dopants correspondingly affect the electron transport characteristics of the N-doped capped CNT junctions, which are enhancement of tunneling current and appearance of NDR behavior through new conducting channels.

So, in advance we have investigated the molecular orbitals of one side of the designed junctions. If the molecular orbitals are well delocalized and contribute to the cap region, they can facilitate electron conduction between the linked CNTs. In Figure 19, it can be seen that the doped nitrogen atom enhances the contribution of the molecular orbitals at the cap region, especially the majority-spin HOMO-1 and minority-spin HOMO. In addition, the majority-spin LUMO and LUMO+1, and minority-spin LUMO+1 and LUMO+2 orbitals expand into the sidewall region from the cap region. Accordingly, in the N-doped capped CNT(5,5), two groups of energy levels (HOMOs and LUMOs) generate the HOMO filtered energy levels (HFEL) and the LUMO filtered energy levels (LFEL) through coupling with the semi-infinite CNT electrode. However, when the nitrogen is doped at the sidewall region (f doping site) instead at the cap region (**b** doping site), the enhancement on the cap region is weak, which is revealed as a low tunneling current and small I_{peak} value.

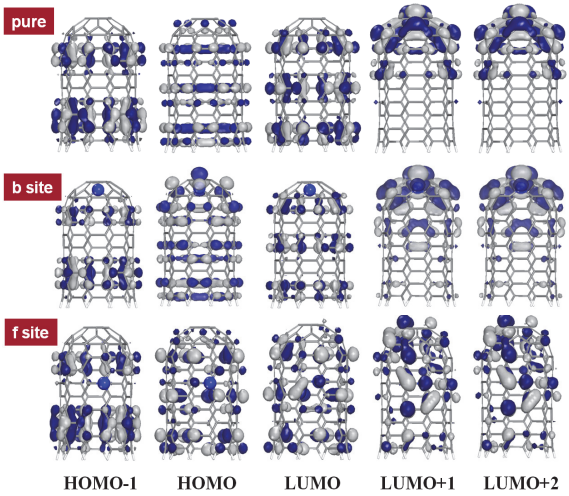

Fig. 19. Molecular orbitals of the pure and N-doped capped CNT(5,5) **b** and **f** doping sites.

Therefore, the NDR behavior in the N-doped capped CNT junctions can be interpreted by a rigid shift model of the LFEL and HFEL in the left and right electrodes under the applied biases (Figure 20). Under the applied biases, the alignment between LFEL and HFEL of each electrode gradually increases until V_{peak} due to the fact that the applied bias leads to two different contact chemical potentials. When the applied bias reaches V_{peak}, HFEL and LFEL of each electrode are well-aligned and a peak appears in the *I*–*V* curve. At V_{valley}, the tunneling current becomes low because of mismatching between the HFEL and LFEL of each electrode. However, at the higher bias voltage, the alignment between the LFEL (HFEL) and CFEL (VFEL) (conduction and valence filtered energy levels, respectively) of each electrode takes place again and the tunneling current increases.

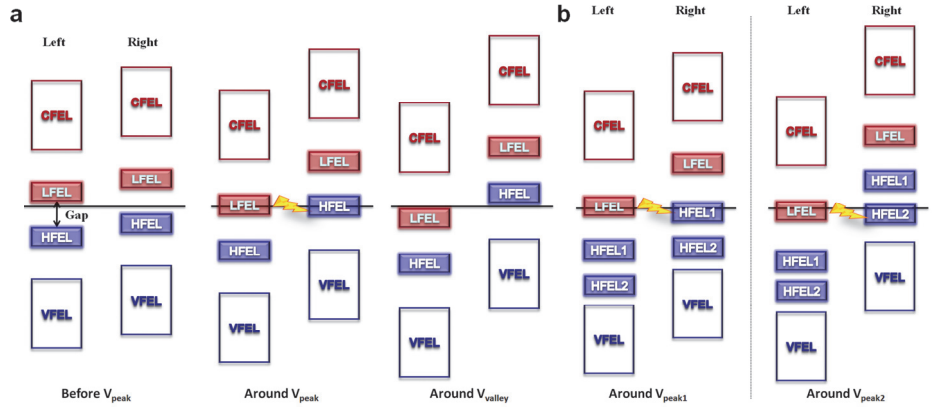

Fig. 20. Diagram of the relative shift of the energy levels in the left and right (a) single- and (b)multi-N-doped capped CNTs under applied biases around V_{peak}.

It is concluded, that the doped nitrogen atom plays an important role in the electron transport characteristics of the designed CNT junctions by modifying their molecular orbitals so as to have the NDR behavior. Therefore, we can realize conventional Esaki-like diode using the N-doped capped CNT junctions.

4. Conclusion

It has been shown how we can design nanoelectronic component embodied with interesting device characteristics, especially rectifying diodes. Simple strategy for designing nanoelectronic diodes is creating carbon nanotube (CNT) junction and controlling their electronic structure. Several types of one-dimensional CNT junctions can be designed by organic linkages and chemical or physical doping. Each designed CNT junction show unique electron transport characteristics, Zener-, Schottky-, and Esaki-like diode.

The charge transfer between CNT and encapsulated organic molecules causes lateral shift of the transmission peaks, and the charge transfer between the encapsulated organic molecules cause vertical shift of the transmission peaks. Therefore, by controlling the charge transfer, *i.e.* the electron affinity (EA) and ionization potential (IP) of the encapsulated molecules, we can finely tune the operational device characteristics.

We could know that the tunneling barrier can be controlled by the strength of dipole moment. Therefore, the rectifying behavior of Schottky-like diode can be obtained by incorporating the peptide linkages to the metallic/semiconducting CNT junctions, where the direction of the dipole moment plays an important role in the determination of the rectifying behavior.

Finally, we showed that the doped nitrogen atoms modify the molecular orbitals so as to generate a conducting channel in the designed CNT junctions by inducing a negative differential resistance (NDR) behavior, which is a characteristic feature of the Esaki-like diode, i.e. tunneling diode. And by controlling doping level, NDR based multi-switching behaviour can be achieved.

It is concluded that the designed CNT junctions open the door to the design of nanoelectronic components embodied with interesting device characteristics. We believe that the results will give an insight into the design and implementation of various electronic logic functions based on CNTs for applications in the field of nanoelectronics.

5. Acknowledgment

The authors sincerely thank the crew of the Center for Computational Materials Science of the Institute of Materials Research, Tohoku University, for their continuous support of supercomputing facilities.The authors are very thankful for the support of the CREST headed by Prof. Motoko Kotani.

6. References

Aviram, A.; Ratner, M.A. (1974). *Chemical Physics Letters*, Vol. 29, No.2, (November 1974), pp.277-283, ISSN 0009-2614

Dekker, C. (1999). Physics Today, Vol.52, (May 1999), pp.22-28, ISSN 0031-9228

Misewich, J. A.; Martel, R.; Avouris, Ph.; Tsang, J. C.; Heinze, S.; Tersoff, J. (2000). *Science*, Vol.300, No.2, (May 2000), pp.783-786, ISSN 0036-8075

Joachim, C.; Gimzewski, J. K.; Aviram, A. (2000). *Nature*, Vol.408, No.30, (November 2000), pp.541-548, ISSN 0028-0836

Tseng, G. Y.; Ellenbogen, J.C. (2001). *Science*, Vol.294, No.9, (November 2001), pp.1293-129, ISSN 0036-8075

Kwok, K. S.; Ellenbogen, J. C. (2002). *Materials Today*, Vol.5, No.2, (February 2002), pp.28-37, ISSN 1369-7021

Lee, S. U.; Belosludov, R. V.; Mizuseki, H.; Kawazoe, Y. (2011). *Nanoscale*, Vol.3, No.4, (April 2011), pp.1773-1779, ISSN 0306-0012

Brandbyge, M.; Mozos, J. L.; Ordejón, P.; Taylor, J.; Stokbro, K. (2002). *Physical Review B*, Vol.65, No.16, (March 2002), pp.165401-17, ISSN 1098-0121

Mozos, J. L.; Ordejo´n, P.; Brandbyge, M.; Taylor, J.; Stokbro, K. (2002). *Nanotechnology*, Vol.13, No.3, (March 2002), pp.346-351, ISSN 1550-7033

Avouris, Ph. (2002). *Account of Chemical Research*, Vol.35, No.12, (July 2002), pp.1026-1034, ISSN 1520-4898

Takenobu, T.; Takano, T.; Shiraishi, M.; Murakami, Y.; Ata, M.; Kataura, H.; Achiba, Y.; Iwasa, Y. (2003). *Nature Materials*, Vol.2, (October 2003), pp.683-688, ISSN 1476-1122

Zhou, O.; Shimoda, H.; Gao, B.; Oh, S.; Fleming, L.; Yue, G. (2002). *Account of Chemical Research*, Vol.35, No.12, (November 2002), pp.1043-1053, ISSN 1520-4898

Liu, Y.; Guo, H. (2004). *Physical Review B*, Vol.69, No.11, (March 2004), pp.115401-6, ISSN 1098-0121

Son, Y. W.; Ihm, J.; Cohen, M. L.; Louie, S. G.; Choi, H. J. (2005). *Physical Review Letters*, Vol. 95, No.21, (November 2005), pp.216602-4, ISSN 0031-9007

García-Suárez, V. M.; Ferrer, J.; Lambert, C. L. (2006). *Physical Review Letters*, Vol. 96, No.10, (March 2006), pp.106804-4, ISSN 0031-9007

Chen, Z., Appenzeller, J.; Lin, Y.-M.; Sippel-Oakley, J.; Rinzler, A. G.; Tang, J.; Wind, S.; Solomon, P.; Avouris, Ph. (2006). *Science*, Vol.311, No.24, (March 2006), pp.1735, ISSN 0036-8075

Zhu, W.; Kaxiras, E. (2006). *Nano Letters*, Vol.6, No.7, (June 2006), pp.1425-1419, ISSN 1530-6984

Balzani, V.; Credi, A.; Venturi, M. (2007). *Nano Today*, Vol.2, No.2, (April 2007), pp.18-25, ISSN 1748-0132;

Pichler, T. (2007). *Nature Materials*, Vol.6, (May 2007), pp.332-333, ISSN 1476-1122

Khazaei, M.; Lee, S. U.; Pichierri, F.; Kawazoe, Y. (2007). *Journal of Physical Chemistry C*, Vol.111, No.33, (August 2007), pp.12175-12180

Lee, S. U.; Belosludov, R. V.; Mizuseki, H.; Kawazoe, Y. (2007). *Journal of Physical Chemistry C*, Vol.111, No.42, (October 2007), pp.15397-15403, ISSN 1542-3050

Sumpter, B. G.; Meunier, V.; Herrera, J. M. R.; Silva, E. C.; Cullen, D. A.; Terrones, H.; Smith, D. J.; Terrones, M. (2007). *ACS Nano*, Vol.1, No.4, (November 2007), pp.369-375, ISSN 1936-0851

Mizuseki, H.; Belosludov, R. V.; Uehara, T.; Lee, S. U.; Kawazoe, Y. (2008). *Journal of Korean Physical Society*, Vol.52, No.4, (April 2008), pp.1197-1201, ISSN 1976-8524

Khazaei, M.; Lee, S. U.; Pichierri, F.; Kawazoe, Y. (2008). *ACS Nano*, Vol.2, No.5, (May 2008), pp.939-943, ISSN 1936-0851

Lee, S. U.; Belosludov, R. V.; Mizuseki, H.; Kawazoe, Y. (2008). *Small*, Vol.4, No.7, (July 2008), pp.962-969, ISSN 1613-6829

Lee, S. U.; Khazaei, M.; Pichierri, F.; Kawazoe, Y. (2008). *Physical Chemistry Chemical Physics*, Vol.10, No.34, (July 2008), pp.5225-5231, ISSN 1463-9076

Lee, S. U.; Belosludov, R. V.; Mizuseki, H.; Kawazoe, Y. (2009). *Small*, Vol.5, No.15, (April 2009), pp.1769-1775, ISSN 1613-6829

Lee, S. U.; Mizuseki, H.; Kawazoe, Y. (2010). *Physical Chemistry Chemical Physics*, Vol.12, No.37, (June 2010), pp.11763-11769, ISSN 1463-9076

Lee, S. U.; Mizuseki, H.; Kawazoe, Y. (2010). *Nanoscale*, Vol.2, No.12, (July 2010), pp.2758-2764, ISSN 0306-0012

Lee, S. U.; Belosludov, R. V.; Mizuseki, H.; Kawazoe, Y. (2011). *Nanoscale*, Vol.3, No.4, (Feb 2011), pp. 1773-1779, ISSN 0306-0012

11

Low-Frequency Noise Spectroscopy at Nanoscale: Carbon Nanotube Materials and Devices

Svetlana Vitusevich[1] and Ferdinand Gasparyan[2]
[1]*Institute of Bio- and Nanosystems,Forschungszentrum Jülich,*
[2]*Department of Physics of Semiconductors & Microelectronics,*
Yerevan State University,
[1]*Germany*
[2]*Armenia*

1. Introduction

This section presents brief description of peculiarities of carbon materials and advantages of noise spectsroscopy for the study of unique carbon nanotubes (CNT) materials and devices. In general, carbon is truly an extraordinary material with physical structures spanning three dimensional (3D) graphite, two-dimensional (2D) graphene and zero-dimensional (0D) buckyballs or buckminster fullerine spheres. It is not surprising that the structural characteristics of carbon thus yield band diagrams displaying a diverse array of physical properties. When a 2D graphene sheet is rolled into a cylinder, a one-dimensional (1D) or quasi-1D form of carbon results, namely CNTs, which have been one of the most extensively studied materials since their discovery. A single rolled-up sheet of graphene results in a single-walled nanotube (SWNT) with a typical diameter of 1 – 2 nm. The rolling direction is characterized by a chiral index (n,m). Achiral zigzag $(n,0)$ and armchair (n,n) CNTs are distinguished from the rest (chiral CNTs). Armchair tubes are always metallic, while zigzag tubes can be semiconducting or metallic (Reich et al., 2004).
Multi-walled nanotubes (MWNTs) consist of concentric cylinders with an interlayer spacing of 0.3 – 0.4 nm, and diameters that are at least an order of magnitude larger than SWNTs, between 10 – 30 nm. CNTs have high elastic modulus, strength, show efficient conductivity of heat, exhibit high thermal and chemical stability, flexibility, low mass density, and unique electrical properties (metallic conductivity and semiconductivity) which makes them excellent candidates for nano-devices and polymer composite materials (Sánchez-Pomales et al., 2010; Service, 1998). At the same time the CNTs are extremely difficult to manage due to their low solubility in both aqueous and organic solvents, which restrict the extent of their applications. Therefore one of the main challenges is the need for the development of new functionalization chemistries that can increase the solubility of CNTs without altering their CNTs properties. Transport in the CNTs of molecular SW- and MWNT-field-effect transistors (FETs) is dominated by holes and, at room temperature, it appears to be diffusive (Martel et al., 1998). Using the gate electrode, the conductance of a SWNT-FET is modulated

by more than 5 orders of magnitude. An analysis of the transfer characteristics of the FETs suggests that the CNTs have a higher carrier density than graphite and a hole mobility comparable to heavily p-doped silicon. Large-diameter MWNTs show typically no gate effect, but structural deformations can modify their electronic structure sufficiently to allow FET behavior.

Carbon nanotubes are perfect candidates for advanced nanoelectronic devices, and they have demonstrated great potential in a wide range of applications, such as FETs (Tans et al., 1998; Martel et al., 1998), elementary logic circuits (Bachtold et al., 2001; Liu et al., 2001), chemical and bio-sensors (Collins et al., 2000; Kong et al., 2000; Nguyen et al., 2002; Snow et al., 2005), hydrogen storage (Dillon et al., 1997; Yao et al., 2010), robust noise modulators for nonlinear systems (Kawahara et al., 2010).

While the noise is usually regarded as an undesirable property for applications, the fluctuation phenomenon in itself contains important information about the material and may be utilized as a valuable probe to characterize nanostructures. Nanotube based devices have been shown to exhibit very significant current fluctuations in the low-frequency (LF) regime (Collins et al., 2000), which may present serious limitations for device performance and applicability, e.g., the threshold voltage of a transistor and the detection sensitivity of a several type sensors. Excess noise above the unavoidable thermal Nyquist level, is a recognized barrier to practical, nanometer scale devices since it usually increases dramatically as dimensions shrink (Hooge, 1969). This large value of excess noise is not surprising and shows that the electrical current in nanotubes is transmitted through surface atoms and is easily perturbed by local charge fluctuations. The magnitude of this noise is an important consideration in assessing the potential of CNTs for electronic and sensor applications. Investigations of SWNT devices show that devices with similar resistances but with different sizes exhibit a systematic variation in the magnitude of $1/f$ -noise (Snow et al., 2004). In particular, it is observe that the level of $1/f$-noise in large-area devices is significantly less than the level of noise in small-area devices of comparable resistance.

Both equilibrium and nonequilibrium fluctuations of a particular atom's location, for example, gain importance as conduction paths reduced to atomic dimensions. CNTs, being covalently bonded materials, might be less susceptible to such fluctuations. Furthermore, the strong carbon–carbon bonds which form the CNT should not be subject to electromigration or defect propagation, two of the most important noise mechanisms in standard metal films and wires (Dutta & Horn, 1981). Since nanomaterials have been used for transport studies it has been frequently observed that their electrical characteristics showed substantial LF current fluctuations. In the case of CNTs those fluctuations classified as $1/f$ -type (Collins et al., 2000; Roschier et al., 2001; Snow et al, 2004; Ishigami et al., 2006; Lin et al 2006; Liu et al., 2006a, 2006b).

The first studies of CNT devices have shown that the $1/f$ -noise is much more pronounced than in conventional bulk devices and this may seriously limit the potential of CNTs for applications in electronics. Later some of the investigations demonstrated a very promising noise level at a very small current regime. The noise characteristics may be used to reveal important information concerning transport phenomena of CNT based devices in different conditions and regimes.

In-depth LF noise studies of CNT transistors and resistors can identify device imperfections such as charge trapping centers along the CNT as well as its interface with gate oxide. Large amplitudes of LF noise increase the minimum detectable signal

magnitude at low frequencies. There are reports on electronic LF noise in a metallic CNT (Fischer et al., 1997; Singh & Ghosh, 2008), CNT ropes (Collins et al., 2000; Roche et al., 2002), networks (Collins et al., 2000; Snow et al, 2004; Lin et al 2006), individual s-CNTs (Ishigami et al., 2006).

Usually CNT structures are fabricated in a FET configuration to study their transport properties. Despite the progress in CNT- FET technology, transport phenomena are still under debate. Noise spectroscopy is a powerful method for studying the transport properties, performance and reliability of material and devices, including FETs based on CNTs. It should be noted that many standard material characterization methods such as the utilization of the Hall effect, measurements of the photoconductivity and the capacitance-voltage characteristics became ineffective for nanoscaled materials and devices. At the same time, noise spectroscopy is an even more sensitive method for studying the influence of scaling on objects down to the nanoscale. Usually LF excess noise, which is registered above the thermal Nyquist noise level, increases as the dimensions shrink. The main factor in conventional materials is an increased surface-to-volume ratio due to defect surface states which are usually closer to the conducting channel.

In this review we describe noise properties of carbon nanotube based materials and devices. After brief introduction in peculiarities of transport and noise properties of CNTs we describe main noise components and theoretical models of the flicker noise directly related with conductivity of the materials. Then we review noise properties of individual CNT-based structures, which are considered to be the best from a nanoscale fundamental studies point of view. They have a cylindrically perfectly ordered shape almost without defects in the structure. We will show that the noise characteristics of CNTs are competitive to conventional materials, but many new features of transport can be revealed as a result of the nanoscale sizes of the nanotube. These objects are good for the modeling of the physical properties of any new kind of materials at the nanoscale. Then we will continue to describe the properties of carbon nanotube thin films. These structures, tunable at the nanoscale but still exhibiting quasi-bulk properties, are promising since they are flexible for different kinds of applications such as high-speed or impedance matched devices. In spite of the progress in their production technology the noise level is still high due to the excess noise produced as a result of fluctuations in the tube-tube junctions. Next we will describe noise properties in parallel aligned nanotube channels. The structures demonstrated reduced noise properties. We will discuss our efforts to improve the properties of the CNT-FETs using gamma radiation treatment. Our analysis shows that the difference in output characteristics of the FETs before and after small doses of gamma radiation treatment is due to a reduced contribution to the total current parallel to the nanotube resistance. It should be emphasized that the transconductance of the CNT-FETs and level of noise did not change strongly after the treatment with a dose of $1x10^4$ Gy and $2x10^4$ Gy. Moreover our results show that active gamma-radiation treatment can improve the transport and noise properties of CNT-FETs at a small optimal dose. The radiation treatment was found to decrease the influence of parasitic conduction channels on transport characteristics of the device. The Hooge parameters obtained are comparable to typical values obtained for conventional semiconductors. After that we will briefly give an overview on results of transport studies on CNT-based structures using shot noise. Finally we will draw the main conclusions and give a short outlook for the potential of noise spectroscopy as the basis for novel technology development.

2. Theoretical predictions of noise properties

This chapter presents the peculiarities and possibilities of Noise Spectroscopy (NS) for study CNT materials and devices at nanoscale. Usually quality and reliability of various electronic devices are correlated with their LF noise. The basic idea of NS is to treat the correlation links present in sequences of different irregularities, such as several interfaces, tube-tube junctions, spikes, "jumps", and discontinuities in derivatives of different orders, on all levels of the spatiotemporal hierarchy of the system under study as main information carriers. The tools to extract and analyze the information are power spectra or noise spectral density (NSD). Generally, several types of noise components can be separately analysed in solid state materials and devices. The components are following: the thermal noise, shot noise and excess noise (Ziel, 1986). The latter may be represented by random telegraph signal noise, generation-recombination noise, as well as the 1/f -type flicker noise dependent on physical origin of the processes in the system.

- Thermal noise, also known as Nyquist one, is result of random Brownian motion of the charge carriers in a resistor R at definite temperature T, shows independent on frequency, f, spectral power: $S_V = 4kTR$, where $k = 1.38 \times 10^{-23}$ J K^{-1} is the Boltzman constant. R can be found from measured I-V characteristic of the resistor as $R = dV/dI$, where V is the applied voltage, I is the current through the sample. The spectral density does not dependent on the current through the resistor and on material of the resistor. At the same time it can be used to analyse the effective electron temperature.
- Shot noise, which is also white in nature, arises from discrete transport characteristic of charge carrier, e: $S_V = 2eI$. Usually the shot noise became registered at low temperature, when the thermal noise is decreased and statistical fluctuations due to finite number of particles can be detected.
- Random telegraph signal (RTS) noise consists of sudden step-like fluctuations in time caused by transitions between two or more levels. Two level RTS caused by single defect results in Lorentzian noise spectrum.
- Generation-Recombination (G-R) noise is result of individual trapping-detrapping process of charge carriers to and from the traps with spectral density for definite G-R component described by Lorentzian spectrum: $S_V(\omega) \propto \tau \Big/ \left[1+(\omega\tau)^2\right]$, where τ is the time constant of process (carrier lifetime, etc), $\omega = 2\pi f$.
- Flicker noise or 1/f -noise named due to characteristic spectral density dependence on frequency: $S_V(f) \propto 1 \Big/ f^{\gamma}$, where γ is nearly 1 as for metallic as well as semiconductor carbon nanotubes. It is now established that 1/f-noise is characteristic of any kind of system, starting from single molecule to biological, physical, chemical systems and other system, including music, finance, and economy areas of research. This noise component involves a number of fluctuation processes with a time constant distribution composing 1/f dependence in noise spectra.

Usually noise spectra of FETs measured at room temperature can be described by three noise components. Fig. 1 shows typical noise spectrum, describing summarized noise, shown in red, as $S_V(f) = flicker + (generation - recombination) + thermal$:

$$S_V(f) = \frac{A}{f^{\alpha}} + \sum_i \frac{B_i}{1+(2\pi f \tau_i)^2} + 4\mathrm{k}TR\,, \tag{1}$$

where, A is the amplitude of 1/f -noise at $f = 1$ Hz, τ_i is the time constant i-component of the G-R -process, B_i is the amplitude of i-component of the G-R noise.
In this review we concentrate on flicker noise as dominant type of low-frequency fluctuations in carbon nanotube materials and devices at room temperature. In addition, this type of noise is directly related with conductivity of the structure. In this respect the noise is the most important as characteristic of transport regimes in the channel of the structure. Knowledge of the noise characteristics is important to characterize performance of nanotube based devices. Various researchers have predicted both large and small levels of 1/f -noise in CNT transistors. From one point of view, the strong carbon–carbon bonds in a CNT should reduce the amount of ion motion, which is a suspected source of 1/f -noise in other systems (Dutta & Horn, 1981). However, in CNTs every atom being a surface atom, and are thus susceptible to the influence of adsorbents (Collins et al., 2000). Additionally, due to the 1D electronic structure of the CNT, a local defect must globally affect the current.

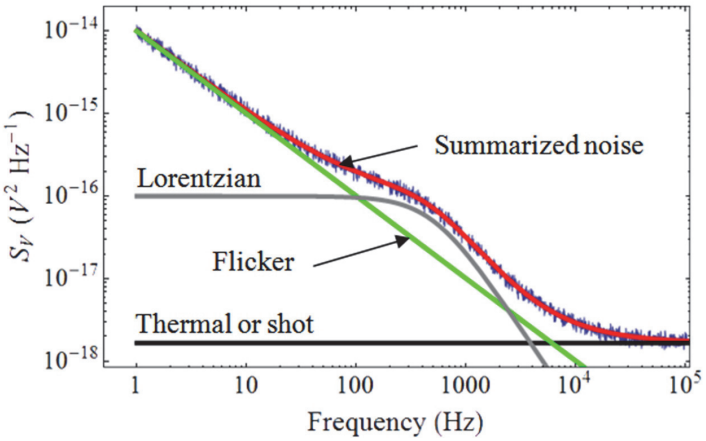

Fig. 1. Typical noise spectrum, measured at room temperature. Three noise components allow to describe LF noise spectra, S_V : flicker, G-R and thermal. It should be noted that the shot noise became registered at low temperature, when the thermal noise is decreased.

It is now accepted that 1/f -noise is produced by fluctuations of sample conductance. In general, if diffusive transport is assumed, the conductance σ is proportional to both carrier mobility, μ , and carrier concentration, n :

$$\sigma = e\mu n \,. \tag{2}$$

Therefore both components, n as well as μ , including their changes under the influence of external charge phenomena can contribute to 1/f -noise. The contribution of such a component can be studied dependent on the operation regime, different kinds of external influence, the surrounding conditions, the contact to chemo- and biomolecules, including label-free identification at the single molecule level.
There are mainly two major theories for 1/f -noise in these devices (Vandamme et al., 1994):

i. McWhorter theory of number (Δn) fluctuations,
ii. Hooge theory of mobility ($\Delta\mu$) fluctuations.

The main physical difference between these two cases is the origin of the flicker noise. McWhorter theory predicts flicker noise to be a result of number fluctuations (Δn) of charge trapping by tunneling processes in surface or interface states (McWhorter, 1957). Later thermally activated processes were suggested by Dutta and Horn for explanation of 1/f noise as a result of fluctuations of time constant τ (Dutta et al., 1981). The temperature dependence of the noise is different for tunneling and thermally activated processes, therefore such models can be separately applied. F.N. Hooge proposed that 1/f -noise is not a surface effect and it is essentially a bulk phenomenon as a result of bulk carriers mobility fluctuations ($\Delta\mu$) due to lattice scattering (Hooge, 1969; Hooge et al., 1981). Investigating metal films he found an empirical relation for 1/f -noise in form:

$$S_i = \frac{\alpha_H I^2}{fN}, \tag{3}$$

where α_H is the Hooge's constant, related to the quality of the sample and defines the level of the low-frequency noise, which is dominated by the flicker noise; N is the total number of free carriers. However, Weissman later emphasized that flicker noise extending to very low-frequencies should have a long-term memory for the fluctuation process (Weissman, 1988). The question how lattice scattering provides a memory effect in the noise taking into account that the mean life time of the carriers is in the picoseconds range is still open. The model also can not explain the cases of deviation of the frequency exponent from unity. Therefore, to describe the noise peculiarities, a combination and modification of both models number (Δn) and mobility ($\Delta\mu$) applicable for many types of conventional FETs and other semiconductor devices are proposed (Hung et al., 1990; Mannik et al., 2008; Mihaila, 2004; Gasparyan et al., 2010). By studying the gate voltage dependence of the noise associated with source-drain current, the contributions coming from fluctuations of n and fluctuations of μ can be separated (Ghibaudo & Boutchacha, 2002). Models based on mobility fluctuations predict that α_H is independent of gate voltage, V_g, while $\alpha_H \propto 1/|V_g - V_{th}|$ in models based on number fluctuations (Vandamme et al., 1994). Here V_{th} is the threshold voltage. Such as, in the linear regime, $1/A \propto |V_g - V_{th}|$ if noise is due to mobility fluctuations and $1/A \propto |V_g - V_{th}|^2$ if noise is due to number fluctuations. In the case, when the amplitude is inversely proportional to the device length the noise is a property of the length-dependent resistance of the CNT and not the electronic contacts.

The ratio of electronic noise to device signal is expected to increase with decreasing size and is thus of concern in nanoscale devices. In addition, surface adsorbents (Hedouin & Rous, 2000) are expected to have increased influence on electronic noise as the surface to volume ratio increases. Hooge model suggests that noise is caused by independent scattering events of charge carriers, which lead to $1/N$ dependence (Hooge, 1969, 1994; Hooge et al., 1981). Tersoff has proposed an alternative model that assumes that the SWNT-FET is affected by random fluctuation of charge in its environment (Tersoff, 2007). In this "charge-noise model"

$$S_I \propto \left(\frac{dI}{dV_g}\right)^2, \quad A \propto \left(\frac{d\ln I}{dV_g}\right)^2. \tag{4}$$

The charge fluctuation noise model modified for the system of p-$Si/SiO_2/Ta_2O_5$/dendrimer/single-walled CNT/electrolyte bio-chemical sensors successfully used for the explanation of noise peculiarities (Gasparyan et al., 2011b).
The expected noise immunity of a covalently bonded system is in competition with the increased relative importance of individual atomic fluctuations in nanometer-sized junctions. This size scaling is incorporated in Hooge's empirical law:

$$S_I = A\frac{I^\beta}{f^\gamma}, \tag{5}$$

which expresses the excess noise magnitude as :

$$A = \frac{\alpha_H}{N}, \tag{6}$$

$\alpha_H = 0.002$ is a constant at T= 300K for most bulk metallic systems, and even extends to the $N = 1$ case at the tip of a scanning tunneling microscope. Dependence $\alpha(T)$ can vary as a result of sample preparation, material, defect density, and other effects (Hooge, 1994), therefore the temperature dependence of the Hooge factor may provide insight into the physical origin of the flicker noise.

3. Noise spectroscopy of transport phenomena of individual carbon nanotube FETs

Individual carbon nanotube FETs (Fig. 2) are the best modeling objects for study how noise and transport characteristics change at moving to real nanoscale ballistic devices. If the channel of the device is short compared to the inelastic scattering length, then wave properties with definite transmission factor describe the transport in quantum channel. At the same time the influence of contact interface properties is increased and most of the FETs operate as Schottky barrier (SB) devices. Moreover in CNT metal induced gap states are far less effective in pinning the Fremi level at nanotube-metal contact (Leonard et al., 2000) due to 1D geometry. The barrier height at interface between CNT and metal contact is strongly affected by the local work function of the interface materials and the device properties can be effectively tuned by external environment. As a result CNT FETs demonstrate unexpected behavior different from conventional planar devices (Heinze et al., 2003). The dependence of current NSD S_I (or A) on gate voltage (Lin et al., 2006; Ishigami et al., 2006; Briman et al., 2006), CNT length (Ishigami et al., 2006), the substrate on which the SWNT rests (Lin et al., 2007) has been discussed. The majority of these studies compare experimentally measured noise magnitudes in SWNT-FETs (Collins et al., 2000; Ishigami et al., 2006; Lin et al., 2007; Appenzeller et al., 2007) to the empirical Hooge model. It is shown that Hooge's empirical rule adequately describes the LF noise in semiconductor CNT-FETs with $\alpha_H = (9.3 \pm 0.4) \times 10^{-3}$ (Ishigami et al., 2006).

3.1 Investigation of influence of contact interfaces

In general, a detailed understanding of influence of contact interface on the noise properties is needed to optimize the signal-to-noise ratio (SNR) across the full operating range of the

FET. There are two main types of CNT-FETs that are being currently studied, differing by their current injection methods. CNT-FETs can be fabricated with Ohmic or Schottky contacts. The type of the contact determines the dominant mechanism of current transport and device output characteristics. CNT-FETs are mainly divided into Schottky barrier CNT-FETs (SBCNT-FETs) with metallic electrodes which form Schottky contacts and metal-oxide-semiconductor field-effect transistor (MOSFET)-like CNT-FETs with doped CNT electrodes which form Ohmic contacts. In SB-CNT-FETs, tunneling of electrons and holes from the potential barriers at the source and drain junctions constitutes the current (Tersoff, 2007). The barrier width is modulated by the application of gate voltage, and thus, the transconductance of the device is dependent on the gate voltage (Raychowdhury et al., 2006). A typical structure and the distribution of the potential energy on the channel are shown in Fig. 3. The gate voltage makes the barriers near the source/drain thinner and increases the tunneling current. A typical structure of the MOSFET-like CNT-FETs with 20 nm doped sections and its energy band diagram is shown in Fig. 4.

One of the important aspects of NT transistors is the ambipolarity or unipolarity of their current-voltage characteristics. SB-CNT-FETs exhibit strong ambipolar behavior. For high enough gate voltages the tunneling probability of electrons through the source Schottky barrier in the conduction band is high and for the low and negative gate voltages, a Schottky barrier is formed at the drain in valence band and tunneling of holes increases the current. The energy bands for low and high gate voltages and the Schottky barriers are shown in Fig. 3. However for MOSFET-like CNT-FETs only positive gate voltages because of lowering the barrier in the channel increase the current. The energy bands for low and high gate voltages and the potential barrier in the channel are shown in Fig. 4.

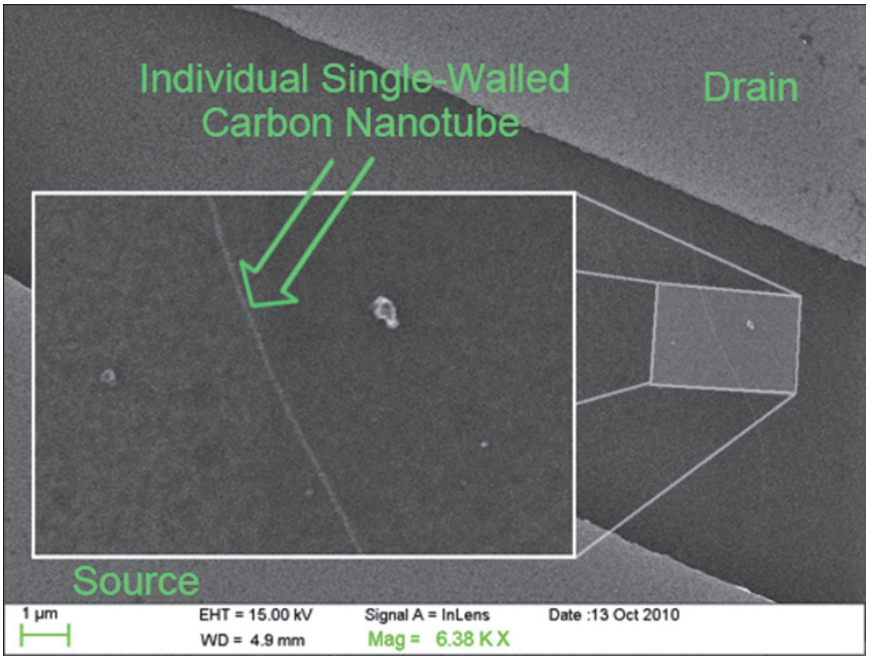

Fig. 2. SEM image of typical a CNT-FET with back gate

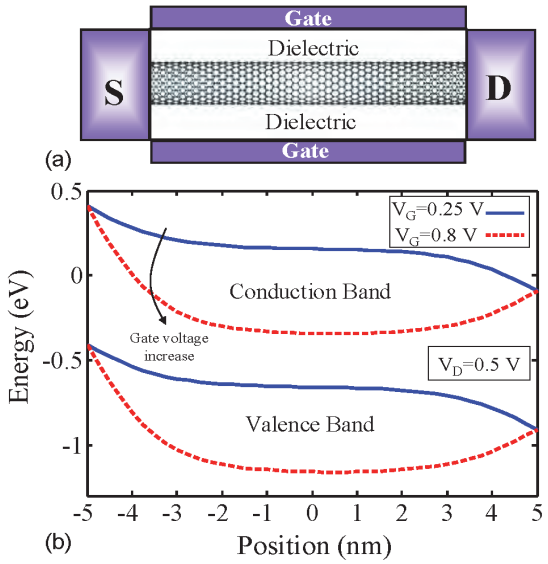

Fig. 3. Schottky Barrier CNTFET, a) 2D cross section of the coaxial structure with intrinsic CNT as the channel and metal source/drain contacts, b) Energy band diagram. The metal Fermi level is taken to be at the midgap of the CNT (Kordrostami et al., 2010).

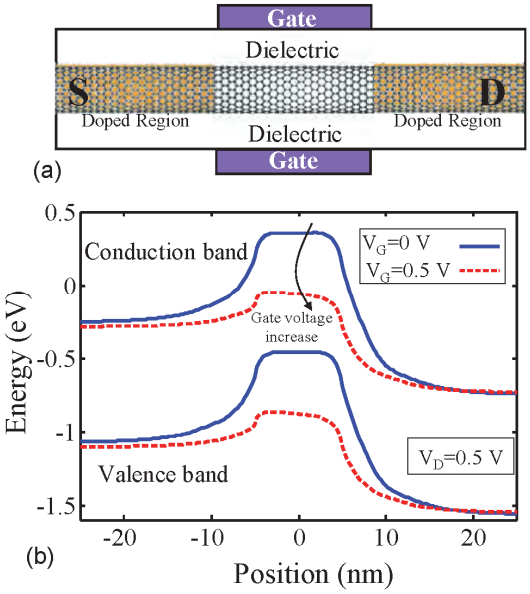

Fig. 4. MOSFET-like CNTFET, a) 2D cross section of the coaxial structure with intrinsic CNT as the channel and doped CNT sections as source/drain contacts, b) Energy band diagram (Kordrostami, et al., 2010).

Several studies suggest that CNT-FETs as Schottky-barrier transistors have a very large contact resistance at low bias related to a tunneling barrier which can be tuned with the gate voltage (Heinze et al., 2002). The results demonstrate that the device characteristics can be radically improved by tailoring the contact geometry. The charge redistribution through the interface, associated with the physics of band bending and its resulting depletion layers, and the possible occurrence of metal-induced gap states are expected to depend strongly on the relative positions of the Fermi level and band edges of the metal and CNT in contact (Tersoff, 1984). It has been shown in particular that various scaling laws, such as the length of the depletion layer as a function of doping fraction or the interface dipole, differ significantly in 1D from their 3D analogs (Heinze et al., 2005). Influence of doping on transport properties of electronic devices on the base of CNTs discussed by Charlier (Charlier et al., 2007). To demonstrate the N dependence and to evaluate the influence of scattering on the 1/f -noise of NTs, in (Collins et al., 2000) fabricated two SB-CNT-FETs with very different channel lengths: $L \approx 500$ nm and 7 μm, which are denoted as short (S) and long (L) devices, respectively. To eliminate device-to-device variations, the two CNT-FETs are fabricated using one, single, long semiconducting CNT and share a common electrode as the source. The ratio of the noise amplitude $A_S/A_L \approx 10$ of the two devices is comparable to the inverse of the corresponding length ratio $L_S/L_L = 14$, consistent with $A \propto 1/N (\propto 1/L)$ behavior. Taking into account this length dependence, the CNT-FET resistance can be expressed as

$$R = R_{SB} + R_{diff} = R_{SB} + R_0 \frac{L}{\lambda}, \quad R_0 \equiv \frac{h}{4e^2}, \tag{7}$$

where λ is the electron mean-free-path in the CNT and R_{SB} and R_{diff} are the resistance contributions due to the contact Schottky barriers and the scattering within the CNT channel, respectively, R_0 is the theoretical tube resistance at the ballistic limit $(\sim 6.5\text{k}\Omega)$. Although it has been suggested that the 1/f -noise in bulk materials is induced by scattering with surface or/and bulk phonons (Mihaila, 2004; Gasparyan et al., 2010; Asriyan & Gasparyan, 2004; Asriyan et al., 2004; Melkonyan et al., 2003, 2005a, 2005b, 2006, 2007) and the same may be true for CNTs (Gasparyan et al., 2009, 2011; Mihaila, 2002) the agreement between A_S/A_L and L_S/L_L is striking and suggests that α_H in CNFETs is not substantially influenced by the presence of acoustic phonon scattering in the long channel device.

The noise amplitude of the CNT devices is related to the resistance of the device. A/R has been found to be varied from 10^{-11} to 10^{-9} for both metallic and semiconductor SWNT devices (Vijayaraghavan et al., 2006). While the current fluctuation generated by each trapping–detrapping centre takes the form of random telegraph signal (Liu et al., 2005), the superposition of such RTS noises with a wide distribution of switching time constants yields the 1/f -noise spectrum. A RTS appears at a smaller absolute gate bias for a larger absolute drain-source bias in a CNT transistor (Roschier et al., 2001). The noise mechanism is attributed to a defect located in the drain side of the Schottky barrier CNT transistor with Ti/Au as contact material. It is noted that room temperature RTS is presented for both metallic and semiconductor CNT. By studying CNT devices with various diameters and contact metals, it is show that the ON-currents of CNFETs are governed by the heights of

the Schottky barriers at the metal/CNT interfaces. The current fluctuations are dominated by 1/f -noise at low-frequencies and correlate with the number of transport carriers in the device regardless of contact metal (Lin et al., 2007).

Sources of flicker noise in CNT-FET passivated using a high quality atomic layer deposited HfO_2 gate oxide have been reported (Kim et al., 2010). The measured 1/f -noise of the device stems from superposition of the excess noise in the Schottky barrier contacts and charge trapping – detrapping at CNT/oxide interface. Based on these results, a model for LF-noise in CNT-FETs is proposed and dominant mechanisms responsible for 1/f -noise in various device operation modes are discussed. Referring to energy-band diagrams Kim and co-authors roughly categorize the mechanism of carrier transport of the top-gate transistor as a function of biasing condition into two regimes (Kim et al., 2010):

i. Schottky barrier modulation regime: in this regime carriers are controlled by the Schottky barriers between drain/CNT and source/CNT contacts. As the drain bias is increased, the Schottky barriers become thinner and help carriers to move into the channel by thermionic emission process. In this case the 1/f -noise is proportional to the square of drain current.
ii. Gate modulation regime: under small drain/source bias the depletion regions of the CNT due to Schottky barriers are short. Carriers that pass from contacts to the channel by thermionic emission are well-controlled by the height of the energy-band and are thus controlled by the gate voltage. Long CNT-FETs show gate modulation under a larger drain/source bias. The 1/f -noise of the FETs, mainly affected by the gate bias, is dominated by charge trapping-detrapping phenomena.

By examining devices with different switching mechanisms, carrier types, and channel lengths, it is shown that the 1/f -fluctuation level is correlated to the total number of transport carriers present in the system. However, the 1/f -noise level per carrier is not larger than that of most bulk conventional semiconductors, e.g., Si.

Study that evaluates the 1/f -noise in a ballistic, 1D system, i.e., an semiconductor CNT, as a function of metal contact material and sample geometry in a FET layout and in nanoscale ballistic transistors presented in (Appenzeller et al., 2007; Lin et al., 2007). The distance between the source and drain electrode is around $L = 600$ nm for transistors. The 1/f -noise amplitude is obtained using $A = S_I f / I^2$. Based on experimental results presented in (Lee et al., 2006) $A_n = 10^{-10} R_0 / L$ were used for the 1/f -noise amplitude of individual NTs (L is the length and expressed in microns, $R_0 = 6.5\,\mathrm{k}\Omega$ is the minimum resistance in the absence of disorder). Based on experimental data a relationship $A_n = a r_n$ was assumed with $a = 10^{-10}\,\Omega^{-1}$. The simulation results clearly indicate that $A/R \sim L^{\alpha}$ is a strong function of device length with a critical exponent $\alpha = -1.3$ (for $8 < L < 20$ μm).

Investigations of LF current fluctuations of nanodevices consisting of one single semiconducting NT demonstrate that the noise amplitude A also increases monotonically with the device resistance R, with an A/R ratio that lies between 2×10^{-10} and $2 \times 10^{-9}\,\Omega^{-1}$ (Lin et al., 2006). Results of (Lin et al., 2006) present strong evidence that the gate-dependent 1/f -noise observed in CNTs for 1D systems exhibiting quasi-ballistic transport behavior is modulated by the total number of transport carriers in the channel, and the fluctuation mechanism is independent of the carrier type, i.e., electrons or holes. Furthermore, the 1/f -noise parameter determined for the CNT-FETs that consist of unpurified CNTs is quite comparable to the value observed in most bulk systems.

Hence, the noise of CNT-FETs with short channel length will be more related to the contact geometry. This should be taken into account for developing CNT-FETs with ohmic contacts.

3.2 Dielectric-nanotube interaction and hysteresis phenomena

Charge trapping in the gate oxide n-FETs may cause LF-noise and threshold shifts (Wang et al., 2007). The 1/f -noise characteristics in such devices are determined by extrinsic factors arising from ambient conditions rather than by intrinsic properties of the CNT or the necessary interfaces (i.e. CNT – oxide interface and Schottky barrier contacts). Avalanche injection into oxide traps result in the hysteresis effect in the I-V characteristics of the CNT-FETs and allows the device to function as a non volatile memory cell (Radosalvljevic et al., 2002). There are mainly two major sources for 1/f -noise in these devices (Kim et al., 2010): the excess noise in Pd – CNT Schottky barrier leading to G – R noise in the space-charge region including metal – CNT interface and charge trapping – detrapping phenomena at the CNT/oxide interface. Under a small drain bias, the Schottky barriers do not influence the transport and carriers are modulated by local gate-biasing similar to a MOSFET in linear/triode regime. Current fluctuation in this mode of operation is due to trapping/detrapping processes involving interface traps and trapped charges in the oxide layer. According to Hooge' s empirical law, the 1/f-current noise amplitude can be written as following.

In the linear region current NSD is modeled as:

$$S_I(f) = \frac{\alpha_H e \mu_{eff}}{f L^2} V_{sd} g_m (V_{sg} + V_{th}) \ , \tag{8}$$

in the saturation regime

$$S_I(f) = \frac{4\alpha_H e g_m^2 \mu_{eff}}{9 f C_g L} \frac{V_{sg} + V_{th}}{1 + \lambda V_{sd}} \ , \tag{9}$$

where $C_g L(V_{sg} + V_{th})/e \equiv N$ is the total number of carriers in CNT-FET channel, C_g is the gate capacitance per unit length, L is the gate length, V_{sg} is the gate bias voltage, V_{th} is the threshold voltage, V_{sd} is the source/drain bias voltage, λ is the channel length modulation parameter, μ_{eff} is the effective carrier mobility.

The trapping–detrapping of carriers in the oxide changes the number of carriers in the channel and also varies the surface potential along the CNT. For the intramolecular CNT-FET the 1/f -noise spectral density has been measured for individual CNTs as a function of the direct current (DC) I_{DC} at room temperature. At $I_{DC} = 0$, the voltage noise is white and equals the expected value for thermal noise $4kRT = 2.1 \times 10^{-16}$ V²/Hz of the CNT, where $R = 12.6$ kΩ for this device (Postma et al., 2001). With increasing current, additional noise appears which exhibits 1/f -dependence. These two noise powers appear to add incoherently, i.e.

$$S_V = 4kTR + \frac{A V_{DC}^2}{f} . \tag{10}$$

The frequency dependence of the noise reveals two types of LF noise spectra. For the first type the noise spectrum is strictly 1/f. For the second type a minor deviation from 1/f - dependence can be due to RTS often present in nanotube FETs (Liu et al., 2006b; 2006c; 2008). It is generated by the trapping-detrapping of carriers by tunneling into traps in the SiO_2. Therefore the RTS provides a way to probe the tunneling density of states of the CNT itself. Observed deviation can be well explained by the addition of a generation-recombination noise term which adequately describes RTS,

$$S_I = \frac{AI^2}{f} + \frac{BI^2}{1+(f/f_0)^2}, \tag{11}$$

where f_0 is the characteristic frequency for the G-R noise. For the case of mobility fluctuations, Hooge's empirical rule (see Eq. (5)) states that the noise coefficient A is given by Eq. (6). Since the total number of carriers in the system $N = C_g L\left|V_g - V_{th}\right|/e$ in a one dimensional FET in the on state, the abovementioned equation may be rewritten as

$$\frac{1}{A} = \frac{C_g L\left|V_g - V_{th}\right|}{e\alpha_H}, \tag{12}$$

where C_g is the gate capacitance per length (Yao et al., 2002), V_d, V_g and V_{th} are the drain voltage, gate voltage, and device threshold voltage, respectively. The amplitude of 1/f - noise is inversely proportional to $\left|V_g - V_{th}\right|$ indicating mobility fluctuations and ruling out number fluctuations as the cause.

The carrier traps in the oxide (Javey et al., 2003) change the effective gate potential by modifying the threshold voltage of the transistor. Effect of single trapped charges in a CNT-FET is determined: a single charge can shift and even rescale the entire transfer characteristic of the device (Kim et al., 2008). This can explain both the large RTS noise and the large variations between nominally identical devices. It is examined the dependence on both the thickness and dielectric constant of the gate dielectric, suggesting routes to reduce electrical noise. A correlated RTS is observed from the interaction of two individual defects in a CNT transistor (Wang et al., 2007). It is shown that the amplitude fluctuation of one defect significantly depends on the state of the other defect.

For the back gated CNT-FET, it is shown that source-drain current at fixed gate potential can drift in time due to significant nanotube-substrate interactions (Fuhrer et al., 2002; Radosalvljevic et al., 2002). Such drift can introduce LF noise components greater than those from the CNTs themselves. In (Liu et al., 2006a; 2006b; 2008) a correlated RTS is observed from the interaction of two individual defects in a CNT. It is shown that the amplitude fluctuation of one defect significantly depends on the state of the other defect. Moreover, statistics of the correlated switchings is shown to deviate from the ideal Poisson process. Physics of this RTS correlation is attributed to the fact that the two defects are located closer than the sum of their Fermi-Thomas screening lengths. The switching of resistance between two discrete values, known as RTS noise, was observed in individual carbon SWNT (Jhang et al., 2005). The RTS noise has been studied as a function of bias-voltage and gate-voltage as well as temperature. By analyzing the features of the RTS noise, authors identify three different types of RTS noise existing in the SWNT

related systems. While the RTS noise can be generated by the various charge traps in the vicinity of the SWNTs, the RTS noise for metallic SWNTs is mainly due to reversible defect motions between two metastable states, activated by inelastic scattering with electrons. It is shown that the 1/f-noise in single CNT-FETs is strongly dependent on temperature between 1.2 and 300 K (Tobias et al., 2008).

The physical mechanism of the RTSs observed in the single-walled CNT-FETs was explained to be due to the hopping/tunneling of carriers between the conducting channels of the SWNTs and the defect levels (Liu et al., 2006b). The defects were hole-type Coulomb repulsive centers located near the valance band of the SWNTs in the energy space and at the interface and/or several nanometers underneath SWNT in the real space. The contribution of the current fluctuations is mainly due to mobility modulation, and the large amplitude of the RTSs is analyzed to be due to the small diameters of the SWNTs. The only known way to reduce $1/f^{\gamma}$ -noise is achieved by using a free standing CNT as an island (Roschier et al., 2001).

Tobias and coauthors used Hooge's relation simply as an empirical rule for characterizing the magnitude of the noise by a single (temperature dependent) parameter $\alpha(T)$ (Tobias et al., 2008). Experiments showed that $\alpha(T = 300\text{K})$ is the same for CNTs from 1 to 30 μm long, and indicate that the fluctuating resistance responsible for the 1/f-noise is indeed from the length-dependent diffusive resistance of the CNT channel, not the contact resistance. Investigated samples are made using chemical vapor deposition grown CNTs, and contain single CNTs contacted by Pd/Nb leads. The devices were above a layer of 400 nm of thermally grown SiO_2 with a heavily doped Si substrate to allow for back gating of the devices down to cryogenic temperatures. Here were presented data from two devices taken in a gas flow helium cryostat, with temperatures ranging from 1.2 to 300 K. Device 1 has a diameter 1.4 nm, and device 2 has a diameter of 1.9 nm. The devices each have a length of 3 μm. The number of carriers is determined by assuming that the device is in the linear regime. This gives the number of carriers to be linearly proportional to the gate voltage: $N = C_g \left| V_g - V_{th} \right| / e$, where C_g is the capacitance of the CNT to the gate electrode, V_g is the gate voltage, V_{th} is the threshold voltage. The gate capacitance is determined by modeling the CNT as a wire over a two dimensional plane: $C_g = 2\pi\varepsilon\varepsilon_0 L / \ln(4h/d)$, where ε_0 is the dielectric constant, $\varepsilon = 2.45$ is the average of the dielectric constants of vacuum and SiO_2, h is the dielectric thickness, L is the length of the tube, and d is the CNT diameter. Spectrum of noise from a CNT-FET at a bias voltage shown on linear-linear scale (main panel) and log-log scale (inset) shown in the Fig. 5. The value of the Hooge parameter $\alpha(T)$ can then be determined from the slope of the $\langle 1/A \rangle$ versus V_g plot, which is equal to $C_g / e\alpha(T)$. Note that extraction of $\alpha(T)$ in is insensitive to changes in carrier number caused by, e.g., changes in the threshold voltage with temperature. Authors discussed the peak in $D(E)$ at $E \sim 0.4$ eV and argue that this feature, i.e., the broad peak that ranges from -0.2 to 0.6 eV, is responsible for the majority of the room temperature noise. The low-energy behavior of $D(E) \sim 1/E$ corresponds to an approximately temperature independent Hooge parameter. Thus, the rise of the Hooge parameter by a factor of ~20 from low temperature to room temperature is due entirely to the broad peak in $D(E)$ around 0.4 eV. The characteristic energy scale allows to rule out some possibilities for the source of the noise. The energy scale is comparable to the band gap (~0.5 and ~0.37 eV for devices 1 and 2, respectively)

and, therefore, one can rule out electronic excitations (e.g., defect ionization, etc.) within the CNT itself as the major noise source; such mechanisms should have characteristic energies less than or equal to half the band gap. Temperature dependence of the Hooge parameter for both CNT devices was presented in Fig. 6.

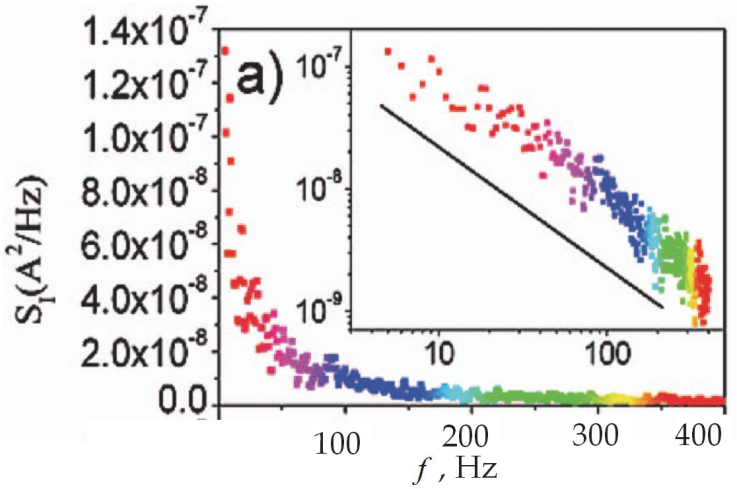

Fig. 5. Spectrum of 1/f -noise for a CNT FET at a bias voltage of 100 mV with each frequency point color coded a gate voltage of −8V, and a T=150 K, shown on linear-linear scale (main panel) and log-log scale (inset). The solid line in the inset indicates a slope of −1 (Tobias et al., 2008).

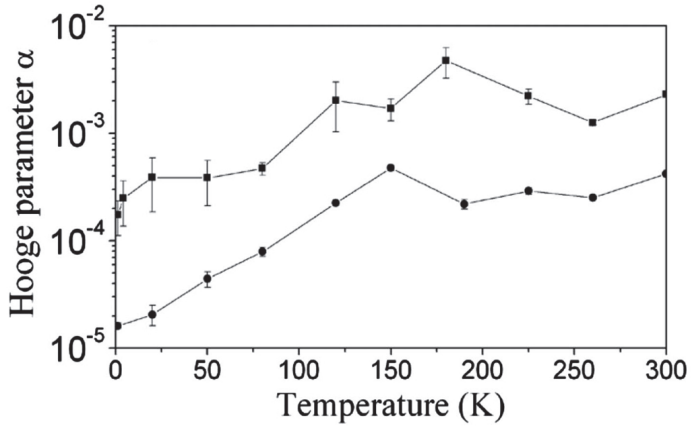

Fig. 6. (a) $\alpha(T)$ dependence for both CNT devices. The data points are calculated using data shown in Fig. 5. The significant upward trend between 1.2 K and about 150 K is seen in both samples. Filled squares and circles correspond to device 1 and device 2, respectively (Tobias et al., 2008).

Authors used the model of Dutta & Horn (Dutta & Horn, 1981) to extract the distribution of activation energies of the fluctuators $D(E)$, which shows two features: a rise at low energy with no characteristic energy scale, and a peak at energy of order 0.4 eV. The magnitude of the peak energy rules out physisorbed gas molecules with low binding energy, and electronic excitations or structural fluctuations of the CNT itself, as sources of room temperature noise. The gate voltage dependence of the noise additionally rules out potential fluctuations resulting from charge trapping and detrapping in the gate dielectric. The likely sources of the noise are the motion of defects in the gate dielectric or at the CNT-dielectric interface, or possibly strongly physisorbed (binding energy ~0.4 eV) species on the CNT or dielectric surface. The dependence of the noise on the reciprocal of the number of carriers in the sample is taken as evidence that the 1/f -noise originates in the bulk rather than on the surface; since N scales with volume Ω, the noise power $S_I \propto 1/\Omega$. However in a 1D system such as CNTs, N is proportional to the length of the system; no useful distinction can be made between the surface area and the volume, hence no distinction between surface and bulk origins of the noise can be made from the N dependence.

The 1/f -noise amplitude is reduced by about one order of magnitude when the NT is suspended, suggesting that the 1/f- noise is dominated by the trapped charges in the oxide (Lin et al., 2007a). The authors study the electrical noise of CNT lying on the substrate and when being suspended by measuring the current fluctuations at a DC bias. In CNT devices, the LF current fluctuation is dominated by the 1/f-noise, which is proportional to the square of the DC current and can be expressed by Eq. (5), with $\beta = 2$ and $\gamma = 1$. Before the etching, the current power spectra of these devices all exhibit the f^{-1} dependence with similar A values of 6×10^{-5}, 6×10^{-5}, and 8×10^{-5} for devices 1, 2, and 3, respectively. After the etching, the suspended CNT devices, 1 and 3, both show a significantly reduced 1/f -noise level with A of 1.2×10^{-5} and 1×10^{-5}, respectively. In contrast, the device 2 possesses the same 1/f -noise level after the process.

These results unambiguously confirm that the oxide substrate is one of sources of 1/f -noise in SWNT devices and provides insight into schemes to reduce the 1/f -noise in CNT devices.

3.3 Different CNT surroundings and the noise fluctuations in the channel

LF noise amplitude and frequency behavior are very sensitive to surrounding environment and to devices work conditions. It is found that the signal-to-noise ratio (SNR) is gate-potential dependent for liquid-gated SWNT transistors. The SNR is lowest in the ON-state where additional contributions to the noise lead to a decrease in the SNR by up to a factor of 5 for bare devices (Heller et al., 2009).

LF noise measurements have been performed on a single-walled CNT connected by Ti/Au electrodes. It has been found that the 1/f -noise decreases when the measurements are undertaken under vacuum and when the CNT is partially degassed, showing a correlation between the fluctuation inducing the 1/f -noise and the presence of gases (Soliveres et al., 2006). It was shown that the 1/f -noise sources are located at the metal/NT contacts and that parameter A appears to be proportional to the sample resistance by a proportionality factor close 10^{-11} Ohm^{-1}. Authors note that result $A = 1.0\times10^{-11}R$ may seem surprising as the transport is ballistic in individual CNTs and diffusive in films or mats. It was also shown that when the device is under vacuum, the effects of gases are reduced and A decreases.

Ambient gases can be considered to be at the origin of the fluctuations leading to the 1/f -noise. Excess noise with a slope different from unity can be explained by a superposition of a few Lorentzians and of the 1/f -noise. The change in slope with respect to temperature is thus explained by the variation of trap activities. Lorentzians are associated to defects or strongly bounded molecules remaining on the CNT surface. Results (Postma et al., 2001; Tarkiainen et al., 2005) have shown A to be dependent on resistance of individual CNTs. In particular, the 1/f-noise level of CNTs was found to barely vary, within a factor of two, in different gas environments at room temperature (Kingrey et al., 2006).

LF-noise measurements on individual single-walled CNT transistors exhibiting ambipolar characteristics with a polymer electrolyte as gate medium have been performed. LF-noise can be monitored in both p- and n-channel operation of the same CNT under the same chemical environment. 1/f -noise in the p-channel of polymer electrolyte gated CNT transistor is similar to that of back gate operation. However, most devices exhibit significantly larger noise amplitude in the n-channel operation that has a distinct dependence on the threshold voltage. A nonuniform energy distribution of carrier trapping/scattering sites is considered to explain these observations (Back et al., 2008).

As reported in the literature (Liu et al., 2006a; Collins et al., 2000; Lin et al., 2006), unpassivated CNT transistors show high amplitudes of LF-noise. This is mainly due to the fact that the CNT is exposed to various environmental factors, such as water molecule (Bradley et al.; 2003), mobile ions (Fuhrer et al., 2002). Chan with co-workers (Chan et al., 2010) studied the effect of electron beam exposure on CNT-FETs. The authors found that trapped charges induce the barrier along the channel, and transport is dominated by the tunneling events across this barrier. Results of noise measurements demonstrate a transition from 1/f -noise described by $S_I = AI^2/f$ to shot noise with $S_I = 2eI$ noise behavior with one order of magnitude increased noise amplitude above 1 kHz frequency. These noise investigations allow also following transport transformation from dominated by normal diffusive processes to transport dominated by tunneling events, respectively.

The 1/f -noise in individual semiconducting CNT in a FET configuration has been measured also in ultrahigh vacuum and following exposure to air (Ishigami et al., 2006). In this case the amplitude of the normalized current NSD is independent of source-drain current and inversely proportional to gate voltage, to channel length, and therefore to carrier number, indicating that the noise is due to mobility rather than number fluctuations. Hooge's constant for is found to be $(9.3\pm0.4)\times10^{-3}$. The magnitude of the 1/f -noise is substantially decreased by exposing the devices to air. The gate-voltage and channel-length dependence of the amplitude of the 1/f -noise is consistent with Hooge's empirical rule for noise caused by mobility fluctuations and not by number fluctuations (Ishigami et al., 2006). It was found that the 1/f -noise decreases when the same devices are subsequently measured in air. In the linear I-V regime, 1/f -noise changed according Eq. (5), with $\beta = 2$ and $\gamma = 1$. In experiment is typically found $S_I \propto I^{2\pm0.1}$.

Unique transport dynamics has been registered in current noise of CNT-FETs fabricated on B-doped Si substrate (Chan et al., 2009). It is shown that different molecules create different, resolvable traps that are detectable in the current noise. Therefore "receptor" states may be engineered along a nanotube that electrostatically couple to noncovalently bound targets for detection with ultrahigh specificity.

In (Mannik et al., 2008) was collected a reliable set of experimental data to analyse the mechanism responsible for the LF noise in liquid-gated SWNT-FETs and its scaling with the length of the nanotube channel down to nanometer scale. SWNTs were grown by CVD onto Si wavers with a 500 nm thick SiO_2 layer. SWNT diameters were 2.0 nm and contacted with Au top electrodes with a 2.0 nm underlayer of Cr. Channel length was below 100 nm. Authors registered that the ionic strength of the surrounding electrolyte has a minimal effect on the noise magnitude in SWNT-FETs. The results show that the gate dependence of the noise amplitude provides strong evidence for proposed charge-noise model (Tersoff, 2007). Charge noise dominates the noise of SWNT-FETs in the subthreshold region, commonly used for sensor applications. It is emphasized two properties of N that hold irrespective of the ballistic or diffusive nature of electronic transport in SWNTs:

i. N, and thus $S_I(1\text{Hz})/I^2$, as a function of liquid-gate voltage follows an exponential law in the subthreshold region with the same exponential slope as the source-drain current (Tersoff, 2007), and
ii. N scales with the channel length as $N \propto L$ at fixed gate voltage.

Comparison shows that the Hooge model fails to describe the experimental data. It is noted that all devices yield remarkably comparable A values that are quite independent of the channel length, except for the shortest device in the subthreshold region. It is concluded also that the charge-noise model presents an accurate description of experimental data in the threshold regime of SWNT-FETs. The level of charge-noise is higher for SWNT-FETs with short CNT lengths. It appears that

$$S_I(1\text{Hz}) \propto S_{input}\left(\frac{dI_{sd}}{dV_{\text{lg}}}\right)^2, \tag{13}$$

and $S_{input} \propto 1/L$. Here V_{lg} is the electrolyte potential. This dependence explained as follows. In the charge-noise model the voltage fluctuations of the gate, described to be proportional to constant S_{input}, are the result of charge fluctuations, S_q. These fluctuations couple to the SWNT-FET through some effective gate capacitance, C_{gate} so that

$$S_{input} = \left(\frac{dV_{\text{lg}}}{dq}\right)^2 S_q = \left(\frac{1}{C_{gate}}\right)^2 S_q . \tag{14}$$

The effective gate capacitance scales as $C_{gate} \propto L$ and is presumably dominated by the quantum capacitance (Rossenblatt et al., 2002). In the other hand, a homogeneous distribution of independent charge fluctuations along the length of the SWNT leads to $S_q \propto L$. Combining these dependencies for C_{gate} and S_q gives $S_{input} \propto 1/L$. This dependence also excludes that charge fluctuations in the SWNT-metal contacts are the dominating source of noise. Tersoff has proposed to include an extra term in the noise expression similar to the Hooge model

$$S_I = S_{input}\left(\frac{dI}{dV_{\text{lg}}}\right)^2 + AI^2 . \tag{15}$$

Moreover, it has been shown that for a single-protein adsorption event the SNR is proportional to $\frac{1}{C_g}\frac{dI}{dV_{lg}}\frac{1}{\sqrt{S_I}}$, which scales as $L^{-1/2}$. Therefore, the shortest channel length should be used to detect the single molecule event. However, for the case of increased sensitivity to the lowest analyte concentrations, a longer channel length should be used, taking into account that the total number of analyte molecules on the CNT is proportional to the length. In the latter case, the SNR is scaled with the length as $L^{1/2}$.
Thus a CNT as a one-atom-thick crystal layer is strongly sensitive to the surface conditions, therefore transport phenomena and noise properties of CNTs can be used for the development of chemo- and biosensors and indentification of individual molecules.

4. Noise peculiarities in carbon nanotube thin films

4.1 Advantages and disadvantages of CNT networks

The CNT networks may maintain the unusual electronic and sensors properties of individual SWNTs. They allow constructing devices of arbitrary size using conventional microfabrication technologies and improved impedance matching that is especially important for high-frequency device applications. The intertubes barriers and defects, length of the individual CNTs in the assemblies as well as contact geometry play an essential role in the electrical transport properties of the CNT arrays. Therefore different charge transport mechanisms can be observed in the arrays of CNTs: metallic conductivity, variable range hopping (VRH), weak localization (WL), and fluctuation induced tunneling. Combination of various mechanisms is possible as well. Electronic and transport properties of CNTs and mechanisms responsible for the charge transport in CNTs assemblies detailed presented by Charlier and Ksenevich with co-authors (Charlier et al., 2007; Ksenevich et al., 2010). Current noise can be used to study cross-correlation processes in carbon nanotubes networks to detect statistical correlations in quantum transport. Noise is more sensitive to percolation transport in networks than resistivity and provides important fundamental insights into physics of percolation transport in CNTs networks and films. At the same time tube-tube junctions in the networks may result in increasing flicker noise level, as will be shown below in section 4.3.
Transformation of 1/f -noise behavior from the case of single CNT to the case of crossing CNTs was studied by Collins for the SWNT (Collins et al.,2000) and Quacha for the MWNT (Quacha et al., 2002). The room temperature noise characteristics of SWNTs in different configurations, ranging from isolated individual tubes to 2D ''films'' and 3D ''mats'' of randomly interconnected CNT assemblies were studied in (Collins et al., 2000). It is finding that all SWNT samples, irrespective of the contact electrode or tube connectivity configuration, display similar excessive 1/f -noise which cannot be explained within the idealized context of covalently bonded metallic wires. Fig. 7 depicts the noise power at different bias currents measured across an isolated, single SWNT. At zero bias current, the noise was flat and agreed with the thermal Nyquist level $S_V = 4kTR$ (dashed line). At finite bias currents excess noise is observed. After subtracting the thermal baseline, the excess noise varies as $1/f^{\gamma}$, with $\gamma = 1.06 \pm 0.02$ for all bias currents within the linear-response regime. A bias current dependence of the form I^{β} is found, with $\beta = 1.99 \pm 0.4$. To characterize the absolute amplitude of the excess noise the voltage (current) noise power S_V (S_I) expressed as Eq. (5) and:

$$S_V = A\frac{V^2}{f^\gamma}, \tag{16}$$

where $A = 1.0 \times 10^{-11} R$ at $\gamma = 1.06$, R is the resistance.
Estimating for the SWNT of Fig. 7 $N \sim 10^4$ atom using Eq.(6) gives $\alpha_H = 0.2$ for SWNTs, in sharp disagreement with Hooge's law. In semiconductors and very small metal whiskers, where surface and impurity fluctuations can dominate typical bulk effects, α_H may be substantially larger than 0.002. The large value of α_H observed in the first experimental studies for SWNT similarly suggests that surface fluctuations play an important role, a result not totally unexpected if one considers that every atom that constitutes a SWNT is a surface atom. Parameter A scales with R can also be illuminated by Hooge's law. Combining $A = 10^{-11} R$ with Hooge's law gives $A = \alpha_H / N = 10^{-11} R$, whereby the number of carriers N is simply proportional to the sample conductance $G = R^{-1}$. From a qualitative point of view, this relationship merely reflects that both N and G depend on the number of parallel, conducting SWNTs in the sample.
A linear increase of noise level with resistance can be understood if the samples consist of several parallel conduction channels. In this case the resistance is inversely proportional to the number of channels M, while 1/f -noise spectral density, according to Hooge's empirical formula scales as $\propto 1/N$, where number of free charge carriers proportional to system size (Hooge, 1969, 1994; Hooge et al., 1981). As $N \propto M$, it follows that $S_I \propto R$. This reasoning applies to a selection of samples, in which the conductivity is determined by the number of parallel conduction paths. On the contrary one would expect the resistance to be directly proportional to sample length L, as well as $N \propto L$, which would give $S_I \propto 1/R$. Such dependence is not observed.

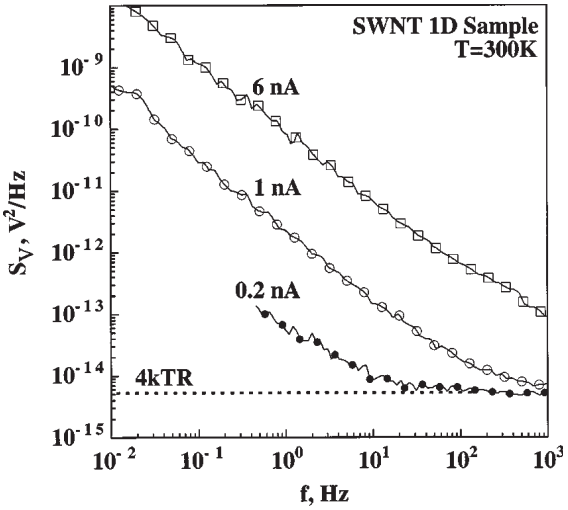

Fig. 7. $S_V(f)$ dependence for a single SWNT, for three values of applied bias current. The SWNT has a two probe resistance of 335 kΩ (Collins et al., 2000).

Carbon composite resistors considered unsuitable for most low-noise circuitry, have excess noise amplitudes between 10^{-15} and 10^{-13} (for $R \le 1\text{k}\Omega$). Carbon fibers with resistances $\le 1\text{k}\Omega$ show similar noise magnitudes. Hence, 1/f-noise in SWNT conductors is four to ten orders of magnitude larger than that observed in more conventional conductors. Very low 1/f -noise, $A \approx 10^{-13}$ was recorded for a thick rope of SWNTs (Roche et al., 2002).

For low crossing MWNT $S_V \propto V^{1.56}$ (Ouacha et al., 2002). Note, that for an individual MWNT $S_V \propto V^{1.02}$. Fig. 8 shows the voltage noise density as a function of frequency, at a bias voltage of $V = 0.1$ V for 1MWNT and 2MWNT. It is found $\beta = 1.98$ for 1MW and 2.63 for 2MWNT. For 1MW, γ ranges between 0.96 and 1.14 with an average value of 1.04, this implies that the excess noise found in 1MW is consistently 1/f -like. Similar values, i.e., γ close to unity was found for iron-filled MWNTs (Roumiantsev et al., 2001). Actually, this type of noise is found in a wide variety of systems (Hooge, 1969) and the form expressed by Eq. (5) and Eq. (16) indicates that the origin of the measured noise is conductance fluctuations. However, for the 2MWNT sample a different behavior is observed, i.e., γ is found between 1.49 and 1.63, with an average value of 1.56. A value of 1.5 for γ suggests a diffusion process between two different media. The sample 2MWNT consists of two crossing multiwalled CNTs, hence a CNT–CNT junction is formed. According to authors diffusion of carriers between the CNTs occurs and is responsible for the noise observed in 2MWNT. However, other mechanisms may also contribute to the 2MWNT noise, such as the forces between the two crossing CNTs which have consequences on the geometric structure of the CNTs. It is found that the noise in 2MWNT at higher frequencies is very close to the shot noise, which suggests the presence of an electrical barrier at the CNT–CNT junction (Ouacha et al., 2002).

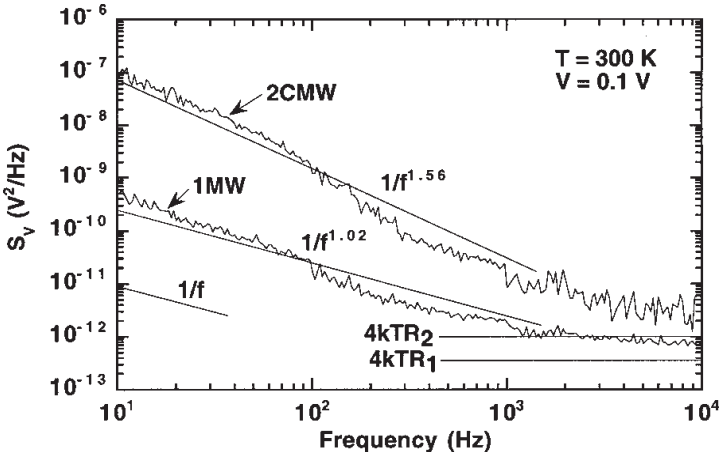

Fig. 8. Voltage noise power S_V as a function of frequency (Ouacha et al., 2002).

Peculiarities of noise have been registered in ultralow-power alcohol vapor sensors using MWCNTs (Sin et al, 2007). Unlike other types of noise, such as thermal noise or shot noise, which are not material-specific properties, parameter A in Eq. (16) generally reflects the sample quality and, most importantly, increases with decreasing device size.

For metallic CNTs, the noise amplitude A is roughly proportional to the device resistance R (Collins et al., 2000). In semiconducting CNTs, A is further modulated by the gate voltage that varies the device resistance, showing an experimental dependence $A \propto 1/N$, where N is the number of atoms or carriers in the system. High quality metal films tend to have values of A as small as 10^{-19}, with values increasing to 10^{-17} for thin films with strong grain boundary effects. At a very large current, $I = 0.1$ mA, $A \approx 10^{-10}$ has been observed for a MWNT, but that value is not likely to extrapolate well down to low currents (Vajtai et al., 2002).

Recently, another interesting effect have been demonstrated in CNT network using noise spectroscopy. Thin film network of CNT-FETs allows novel functionality – fluctuation enhanced sensing (FES) for detection of N_2O, CO, H_2S and H_2O vapor have been demonstrated (Haspel et al., 2008). The FES method is capable of increasing the chemical selectivity of carbon nanotube sensor, when using the amplitudes of the acquired power spectral density as sensor signal. Electrical noise can also help pulse-train signal detection at the nanolevel for various types of threshold units represented by carbon nanotubes (Lee et al., 2006). Small amount of noise allows enhancing the nanotube detector's performance on subthreshould level using stochastic resonance effect. Such noise-enhanced signal processing at the nanolevel promises applications to signal detection in wideband communication systems, biological and artificial neural networks.

4.2 Tube-tube junction noise and collective phenomena

Large noise coefficients obtained for CNT-FETs suggested that CNT–CNT junctions, not the CNTs themselves, are the dominant source of $1/f$ -noise in the composite paper (Imam et al., 2010; Tanaka et al., 2010). Electrical transport and noise in semiconducting CNTs is investigated in (Raychaudhuri, 2002). By studying CNT devices with various diameters and contact metals, it is show that the ON-currents of CNFETs are governed by the heights of the Schottky barriers at the metal/CNT interfaces. The current fluctuations are dominated by $1/f$ -noise at LF and correlate with the number of transport carriers in the device regardless of contact metal. The noise characteristics of randomly networked single-walled CNTs are studied with FETs in (Tersoff, 2007). Fluctuation-induced tunneling conductivity model was proposed for disordered heterogeneous systems on the contrary to the systems with hopping charge carrier transport between localized sites. Different types of CNTs arrays with existing electrical barriers can be also considered as heterogeneously disordered systems. Therefore this model was used for describing the temperature dependence of conductivity of single-walled CNTs fibers and networks. Sangwan with co-authors demonstrated that suspended carbon nanotube network shows ambipolar transport behavior with negligible hysteresis (Sangwan et al., 2008). The Hooge's constant of the suspended CNT-FETs is about 20 times lower (2.5×10^{-3}) than for control CNT-FETs on SiO_2.

Beyond the fundamental interest in understanding the transport properties of 1D system, the integration of CNTs in electronic devices such as FETs raise the question of the contact resistance, that is, the ability for electrons to jump from a metallic electrode, used as the source or drain, onto the CNT. In particular, in contrast to the predictions of quantized conductance obtained for clean infinite systems, for a CNT/electrode contact a lowering of the transmission across the interface systematically obtained. As first analyzed by Chico and co-workers (Chico, et al., 1996), even for the most favorable case, i.e., for an intramolecular CNT based heterojunction, the symmetry mismatch between incoming and outgoing

electronic states yields a transmission probability lower than 1. Intramolecular junctions have been experimentally observed by scanning tunneling microscope (Odom et al., 2002). The reduction of transmission at the interface is general to all realistic nanoscale junctions between a CNT and a metallic electrode, or other interface geometries leading to different charge injection capabilities.

Detailed analysis is performed with the parameters of number of mobile carriers and mobility in the different environment. This shows that the change in the number of mobile carriers resulting in the mobility change due to adsorption and desorption of gas molecules (mostly oxygen molecules) to the tube surface is a key factor in the 1/f -noise level for CNT network transistors (Kim et al., 2008). In order to avoid additional LF noise contribution from SiO_2-CNT interactions, the measurements were carried out in conducting liquid and 1/f -noise in CNT-FETs as a function of gate potential (Briman et al., 2006). The measured LF-noise for CNT/cellulose composite paper exhibited 1/f-characteristics and can be explained by Hooge's empirical law (5). The reduction in the intertube electrical transport barrier and decreasing of noise was found after thermal annealing of SWNT films (Lu et al., 2008). The noise spectra can be described by $S_V = AV^2/f$ with A decreased by 80% after annealing to value of 5.64×10^{-12}.

Kim and co-authors in 2007 studied noise properties in ballistic SWNT and obtained power law dependence at low bias voltages. The measurements demonstrate that noise studies are powerful method for collective phenomena study for the case of a Tomonage-Luttinger Liquid interaction effects in the SWNT devices.

4.3 Noise as sensitive tool for percolation

From a microscopic point of view, two charge transport mechanisms occur in the films: the transport along CNT themselves and the transport between crossed CNTs. Considering the large mean free path in CNTs and the weak coupling between CNTs, Soliveres and co-authors assume that the contacts between CNTs dominate the transport through the film (Soliveres et al., 2009). From a macroscopic point of view, the CNT film is modeled as a percolation network. Percolation networks have electrical properties that vary rapidly at the vicinity of the percolation threshold and follow power laws related to the density of CNTs. The conductivity and noise coefficient A were measured for the different densities. These two quantities follow power laws with critical exponent t_c for the conductivity and k for the noise, as expected in percolation processes.

$$A \propto \left(\frac{RS}{L}\right)^{w}, \tag{17}$$

where $w = k/t_c$, R is the film resistance, S is the section area.

Based on the experimental results in (Briman, et al., 2006) it is concluded that the number of carrier fluctuations is the source of the 1/f -noise. In (Akabane & Miwa, 2009) the resistance fluctuation of CNTs in vacuum low temperature with laser irradiation is measured and the origin of mobility fluctuation is suggested.

Behavior of the 1/f -noise scaling is observed in percolating systems (Snow et al., 2004). In 2D-network devices consisting a large number of intersecting SWNTs confirmed the V^2/f scaling

of the LF noise. This behavior contrasts the scaling observed between two crossed MWNTs that deviate significantly from the V^2/f behavior (Ouacha et al., 2002). Using the $f = 10$ Hz noise it is plotted the scaled noise, $A = fS_V/V^2$ versus device resistance (Fig. 9). The solid line in the Fig. 9 is a plot of $A = 10^{-11}R$. Note that the level of noise in these devices and the noise levels observed in (Collins et al., 2000) are in good agreement. The measured data indicate that the resistance value alone is insufficient to predict the level of 1/f-noise. Note that the 1/f -noise magnitude in devices discussed in (Snow et al., 2004) also does not correlate well with the resistance. So, the device size is an important additional component in predicting the magnitude of 1/f-noise. In order to observe this size dependence in (Snow et al., 2004) plot this same data set as A/R versus the electrode spacing L (see Fig. 10).

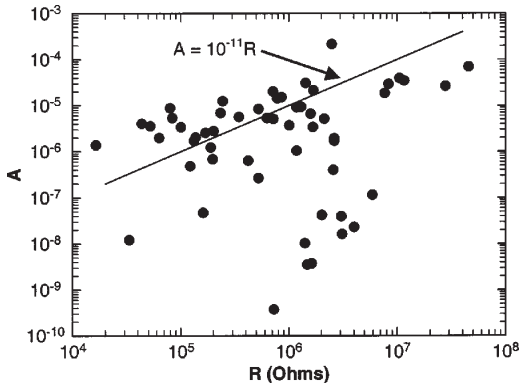

Fig. 9. Plot of the scaled noise, $A = fS_V/V^2$, measured in 2D networks versus the device resistance. The solid line corresponds to the empirical relationship established in (Collins et al., 2000) (Snow et al., 2004).

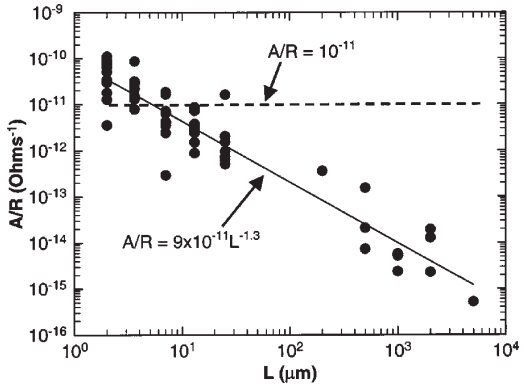

Fig. 10. The same data as in Fig. 9 plotted as A/R versus the electrode spacing L. The dashed line represents $A/R = 10^{-11}$ (Collins et al., 2000) and the solid line is a least-squares power-law fit to the data. A clear relationship between the level of 1/f -noise and the device size is established (Snow et al., 2004).

Power-law fit of the data (solid line) yields:

$$A/R = 9\times10^{-11}/L^{1.3}\,, \tag{18}$$

where L is in units of mm. The resulting empirical formula

$$S_V = 9\times10^{-11}\frac{R}{L^{1.3}}\frac{V^2}{f} \tag{19}$$

is a good predictor of the LF noise in SWNT networks ranging in resistance from $10^4 \div 10^7\,\Omega$ and spanning device areas from 10 to 108 μm2. It is shown that for films, A is inversely proportional to the dimensions of the bulk but remains proportional to $10^{-11}\,\Omega^{-1}$ (Snow et al., 2004).

For comparison, this expression predicts that a 1-mm-sized, 1 MΩ SWNT sensor biased at 10 nA will exhibit 1/f-noise in excess of the background thermal noise ($S_V = 4kTR$) for $f < 70$ Hz. The reduction of the 1/f-noise with device size is consistent with other electronic systems in which the magnitude of the 1/f -noise varies inversely with the number of charge carriers N in the device. According to this behavior the 1/f -noise should scale as R/L^2 (i.e., $R/L^2 = 1/e\mu N$). The R/L^2 behavior assumes a uniform system of uncorrelated noise sources that number in proportion to N.

In contrast, the SWNT network consists of many parallel one dimensional paths formed by intersecting SWNTs. The SWNTs consist of a mixture of both metallic and semiconducting CNTs that have large variations in resistance, which results in nonuniform voltage drops along the conduction paths. Thus, the dominant noise sources will occur at the high-resistance segments of the current paths. The gate field might also produce charge fluctuations in the SiO_2 gate dielectric that increases the level of 1/f -noise. In Fig. 11 presented the normalized resistivity fluctuations $S_\rho/\rho^2\left(=S_V/V^2\right)$ versus resistivity ρ.

On the basis of the statistics of a large number of devices consisting of mixtures of different types of CNTs (i.e., 2D mats and 3D networks), it has been concluded that the 1/f -noise amplitude in these CNT-based devices increases with the sample resistance R with an A/R ratio depending on device dimensions (Snow et al., 2004).

The results of Monte-Carlo LF noise simulations as a function of film thickness, width and length were presented and compared with experimental data (Behnam et al., 2008; 2009). By comparing the simulation results with the experimental data, it is finding that the noise generated by tube-tube junctions dominates the total CNT film 1/f -noise. It is also show that the 1/f -noise amplitude depends strongly on device dimensions, CNT degree of alignment, and the film resistivity, following a power-law relationship with resistivity near the percolation threshold after properly removing the effect of device dimensions. It is find that the critical exponents associated with the noise-resistivity and noise-device dimension relationships are not universal invariants, but rather depend on the specific parameter that causes the change in the resistivity and 1/f -noise, and the values of the device other parameters. Since 1/f -noise is a more sensitive measure of percolation than resistivity, these simulations not only provide important fundamental physical insights into the complex interdependencies associated with percolation transport in CNT networks and films, but also help understand and improve the performance of these nanomaterials in potential device applications, where noise is an important figure of merit.

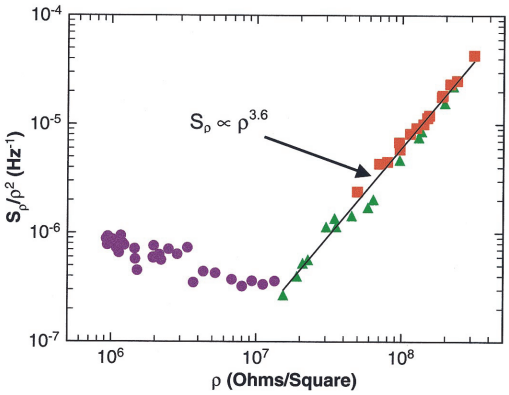

Fig. 11. S_ρ / ρ^2 vs ρ. The circles correspond to $V_g < 0$ V, the triangles to $0 < V_g < 1.6$ V, and the squares to $V_g > 1.6$ V. As the gate bias shuts off the current in the network, the noise increases as a power law of the resistance. This behavior is similar to the 1/f -noise scaling observed in percolating systems (Snow et al., 2004).

To model physical properties of the film, the resistance of an individual CNT is calculated by the expression $R_{CNT} = R_0 L/\lambda$. For computing the 1/f -noise in the CNT film it is used a model which takes into account the noise contributions from both the CNTs themselves and the tube-tube junctions in the film and assumed $\lambda \approx 1$ μm. Assuming independent noise sources the relative 1/f-noise magnitude of the film, A_{eq}, can be written as

$$A_{eq} = \frac{S_I f}{I^2} = \frac{1}{V^2 I^2} \sum_n i_n^4 r_n^2 A_n ,$$

where i_n is the current, A_n is the relative 1/f -current noise amplitude, and r_n is the resistance of the tube or junction associated with the *n*-th individual noise source.
The decrease in the noise amplitude with device length is consistent with Hooge's law, where $A \sim 1/N$. However, since the resistance of the CNT film device is given by $R = \rho L/Wt$, where N scales with the device volume, i.e. $N \sim LWt$, A/R is expected to scale as $A/R \sim L^{-2}$. For $W > 2$ μm A is inversely proportional to W ($\sim W^{-1.1}$). For $W < 1$ μm there is a strong power-law relationship between A and W ($\sim W^{-5.6}$). This shows that the variation of resistivity has a strong effect on the noise. The authors demonstrate that the flicker noise amplitude depends strongly on the resistivity, following a power-law relationship with resistivity near the percolation threshold after properly removing the effect of device dimensions. The data obtained strongly suggest that transport peculiarity in the CNT network due to tube-tube junctions, and not the nanotubes themselves, dominate the overall CNT film 1/f -noise. Thus, the 1/f -noise is very sensitive measure of percolation transport in CNT networks.

4.4 Noise power as a function of the network morphology

The noise analysis can be used for characterization the internal structure of the CNT film. The study of relationship between the noise power of CNT nanowire network and the

network morphology was performed by Zhou et al. (2008). A thin film of a CNT network is mapped into a resistor network containing tunneling junctions that are randomly switched. The junctions can be branching or touching, therefore they have internal structures. The $1/f$ -noise spectra results from the superposition of a large number of Lorentzian spectra corresponding to unstable junctions between CNTs due to random structure of the film. A possible mechanism for instabilities of the junctions is local trapping sites with occupation number affecting the junction resistance. When the junction resistance is small, the fluctuation in current noise is large due to increased influence from switching on a junction. It is shown that the noise power scales with the average current in a power law $S \propto I^{-\omega}$, where ω is a function of the network morphology.

Thus the authors found that the total noise power and its relation to the current and junction resistance are most useful macroscopic quantities that contain information of the microscopic geometric structure of the CNT network.

5. Noise characteristics of the FETs based on parallel aligned CNTs

5.1 Omitting of noise due to crossover and misalignment

Using parallel aligned CNTs it is possible to remove crossover among CNTs and reduce noise level by removing the noise generated by tube-tube junctions**.** In (Lee et al., 2010) developed a wide contact structure for low-noise nanochannel devices based on a CNT network. This low-noise CNT network-based device has a dumbbell-shaped channel, which has wide CNT/electrode contact regions and, in effect, reduces the contact noise. It is established an empirical formula that can explain the noise behavior of arbitrary-shaped CNT network-based devices including the effect of contact regions and CNT alignment. Analysis revealed that the noise amplitude of aligned CNT networks behaves quite differently compared with that of randomly oriented CNT networks. In back-gate FETs where most of the surface area of the nanorod is exposed to the ambient, the surface states could be the major noise source via random walk of electrons for the $1/f$ -noise. In dual gate transistors, the interface states and oxide traps can compete with each other as the main noise source via random walk and tunneling, respectively.

The charge transport and noise properties of three terminal, gated devices containing multiple single-wall metallic and semiconducting CNTs were measured at room temperature and the relative low-frequency excess noise of the metallic tubes was observed to be two orders of magnitude lower than that of the semiconductor tubes (Reza, et al., 2006). The low-frequency current NSD in five arc-discharge-grown MWNTs have been recorded at temperatures of 295K, 77K, and 4.2K, and find that the noise decreases moderately with temperature (Tarkiainen et al., 2005). At 4.2K, instead of the usual $1/f$ -type of spectra, authors observe Lorentzian line shapes resulting from one or a few systems of two-level fluctuations. Analyze of these spectra in terms of resistance fluctuations ΔR and obtain $\Delta R = 1\text{k}\Omega$, most likely caused by changes in the contact resistance. Single CNTs approximately 20 nm in diameter and 1 μm in length, were positioned across a gap between two wide, and pre-patterned gold electrodes. At 295 and 77 K the NSD can be accounted for by the Eq. (5) and the values of exponents β and γ are given in Table 1 for the 5 samples.

Sample	R_{295K} (kΩ)	$S_I(295\text{K})$ (pA²)/Hz	$\gamma_{295\text{K}}$	$\beta_{295\text{K}}$	$R_{77\text{K}}$ (kΩ)	$S_I(77\text{K})$ (pA²)/Hz	$\gamma_{77\text{K}}$	$\beta_{77\text{K}}$	R_{4K} (kΩ)	$S_I(4\text{K})$ (pA²)/Hz
1	33	8	1.07	2.28	53	6	1.03	2.00	55	1
2	390	40×10^3	1.09	1.76	2450	2×10^3	1.09	1.54	620/910a	300
3	133	200	1.15	2.04	801	8	1.16	2.12	275	1
4	-	-	-	-	70	20	0.94	1.87	106	1
5	13	90	1.07	1.93	26	20	b	1.79	49	4

[a]The differential resistance is asymmetric with respect to the current direction.

[b]The experimental value was not determined. $\gamma = 1$ was assumed for extrapolation.

Table 1. Exponents β and γ, and inter-extrapolated NSD at $f_0 = 100$ Hz and $I = 100$ nA (Tarkiainen et al., 2005)

The linear resistance is given for 295 K and 77 K, while the 4 K value is the differential resistance at 100 nA. It is clear that $\beta = 2$ is expected for pure resistance fluctuation in ohmic conductors. The $\beta \neq 2$ behavior is associated with nonlinear characteristics, and the fact that $\beta < 2$ suggests that S_I/I^2 scales proportionally to the resistance. At the temperature 4.2 K found that the 1/f-structure of Eq. (5) cannot account for the data anymore. Instead, the measured noise spectra are composed of a sum of a few Lorentzian line shapes (Tarkiainen et al., 2005):

$$S_I = I^2 \Sigma \frac{S_L^{(i)} \tau_i}{1 + (2\pi\tau_i f)^2}, \tag{20}$$

where each Lorentzian is characterized by a lifetime τ_i and an amplitude $S_L^{(i)}$. Those Lorentzians are found to depend on the bias voltage, which leads to irregular and nonmonotonic current dependence of the noise. According to the generic 1/f-model, the individual fluctuations are thermally activated, and freeze out, as the temperature is lowered. The two parameters characterizing an individual fluctuator, the magnitude S_L and the life time τ, were both found to depend on the bias current. It is found that the level of LF excess noise decreases by a factor of 10–100 when temperature is lowered from 300 to 4 K. At 4.2 K, single fluctuators play a significant role in the noise behavior of NTs. A model with exponentially current-dependent time constants was utilized to explain the measured current noise spectra, reminiscent of findings in tunnel junctions. It is find the metal–CNT contacts are a likely source for these fluctuations. Eventually, so few sources are left that they show up as individual Lorentzians. The noise scales as

$$S_I \propto kD(\tilde{E}) \cdot \tag{21}$$

Here $D(E)$ is the distribution of the activation energies and

$$\tilde{E} = -kT\ln(2\pi f\tau_0), \tag{22}$$

where τ_0^{-1} is the attempt frequency (Dutta & Horn, 1981). Assuming weakly energy-dependent $D(E)$, the examined samples in (Tarkiainen et al., 2005) full quite close to this model. Using value $A = S_I f / I^2$ one can obtain at 295 K $A = 8\times10^{-8} \div 4\times10^{-4}$. This is comparable to $A = 3\times10^{-7}$ reported for a MWNT (Ouacha et al., 2002). Appenzeller with co-workers reported a substantial noise reduction for a tube transistor with multiple carbon nanotubes in parallel (Appenzeller et al., 2007). An intriguing experiment of detection molecules as additional scattering sources using noise properties of CNT-FETs based on aligned in parallel CNTs has been demonstrated in (Xu et al., 2008). The results are important for future sensors developments.

Thus, in this section we discussed how current in a CNT transistor is determined by the injection of carriers at the electrode/CNT interface, while at the same time excess noise is related to the number of carriers inside the CNT channel. It is demonstrated a substantial reduction in noise amplitude for a tube transistor with multiple CNTs in parallel.

5.2 Reduced influence of parasitic conduction channel

Decreasing the Schottky barriers and in the ideal case obtaining ohmic contact at the contact regions will allow the intercontact distances to be reduced simultaneously using the advantages of channel transport phenomena with different surface modified conditions in CNTs. Therefore the study, modification and optimization of conductivity in CNT-FETs has recently become an important research topic. One of the most effective methods for modifying material properties and interface states is gamma radiation treatment. Very interesting effects of treatment are observed after gamma irradiation at small doses for conventional semiconductor devices. During increasing accumulation dose, regions of certain radiation doses can be found, where the structural and electrical parameters of materials can be improved due to radiation-stimulated diffusion process and the structural ordering of native defect structures and strain relaxation effect**.**

We investigated the influence of γ-radiation with several small doses of radiation treatment of single-walled carbon nanotube FETs (Fig. 12) by using a ^{60}Co source (Vitusevich et al., 2009). Noise spectroscopy is used to extract additional important information about the mechanisms of transport formation in the multilayer structure of FETs before and after gamma radiation treatment. In the structures under test typically 500-600 nanotubes were found to be connected in parallel between the contacts using scanning electron microscope. It will be shown below that such a structural design with a sufficiently large length between the contacts allows effective current control through the CNTs of FET structures rather than the contact resistance. A standard isotope ^{60}Co source was used to emit characteristic gamma rays with a flux of 1 Gy/s and energy of 1.2 MeV. Gamma irradiation results in the trapping of holes in the SiO_2 near the Si/SiO_2 interface and the creation of interface states at the Si/SiO_2 boundary. High-quality Si/SiO_2 structures have pre-irradiation interface trap densities in the range of 10^9-10^{10} traps/cm^2. In the bulk of the oxide film, the silicon ionization and the interstitial oxygen donor centers are shown to be responsible for the radiation-generated positive space charge build-up (oxide charge) in thermally grown silicon oxide**.** Usually non-recombined holes remain initially close to their points of creation and cause a negative shift of the flat band voltage and the threshold voltage. Holes created by gamma irradiation result in decreasing summary resistance.

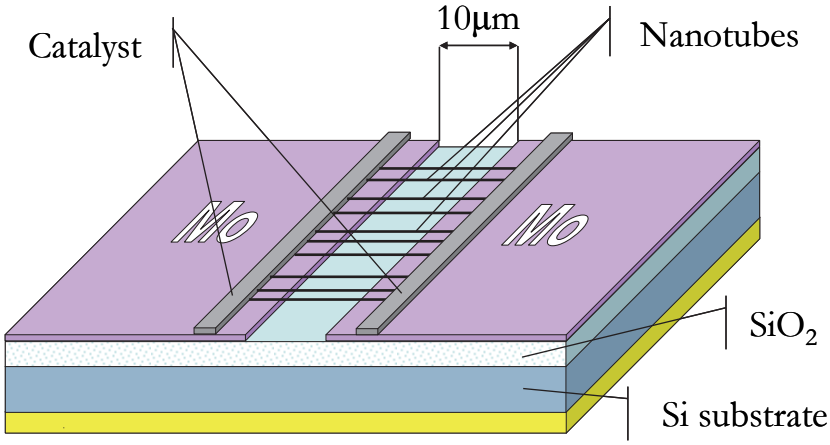

Fig. 12. Schematic of the investigated CNT-based FETs

In the investigated CNT FET structures, it was not observed any shift in threshold voltage or decrease of the summary resistance after a small dose of gamma radiation of 1x10⁴ Gy. Moreover, increasing summary resistance was registered. This fact demonstrates that the main changes in transport properties after gamma radiation treatment are related to channel conductivity determined by CNTs. The origin of this modification can be explained by a slight modification of surface atom ordering in CNT due to the introduction of vacancies and interstitial point defects. In addition, the change in drain current before and after gamma radiation was found to be independent on gate voltage. The fact demonstrates that the radiation treatment removed a resistance parallel to the nanotubes. The results of noise spectroscopy give additional important information about the processes and mechanisms of transport formation in the structure. An analysis of the current noise power spectra allows confirming that the main noise source is caused by transport phenomena in carbon nanotubes.

After gamma irradiation this flicker noise component shifts to the lower frequency range (Fig. 13) and demonstrates decreased changes with V_G. It is known that the relative noise level in different kinds of materials can be estimated according to the Hooge relation as follows:

$$\frac{fS_I}{I^2} = \frac{\alpha_H}{N}. \tag{23}$$

The substitution of the total number of carriers that can be found as $N = \frac{L_{DS}^2}{e\mu R_N}$ into Eq. (23) yields:

$$\alpha_H = \frac{fS_I L_{DS}^2}{I^2 e\mu R_N}, \tag{24}$$

where R_N is the resistance of carbon nanotubes.

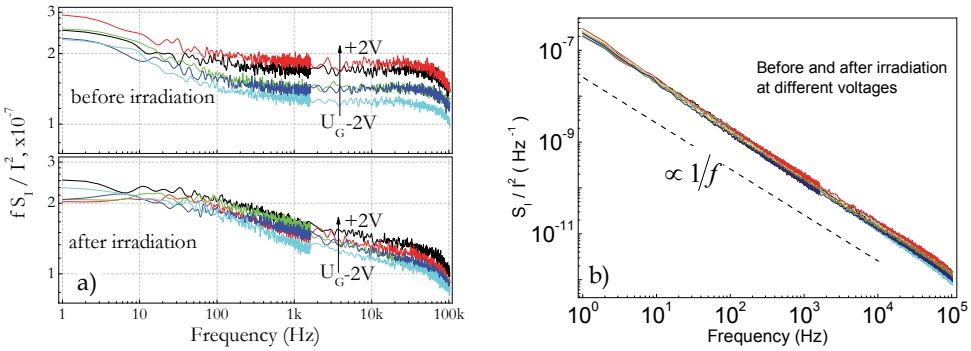

Fig. 13. Normalized current noise power spectra of CNT-FETs (a) measured before and after irradiation with a dose of 1×10^4 Gy at different V_G in the range from -2V to 2V with step 1V and V_{DS} =30 mV; (b) Noise power spectra measured at different V_G and constant V_{DS} and vice versa before and after gamma radiation treatment, demonstrating 1/f-noise dependence.

If the current I drops due to the mobility μ decreasing then value of fS_I/I^2 increases by 1.3 times and this result in the increase of α_H. In the spectra of the low-frequency range, the noise level at $f=1$ Hz also increases by about 1.3 times. This fact confirms the suggestion that the noise in CNT is caused by defects introduced by gamma radiation. Taking into account the measured value of mobility 1.5x10^5 cm^2/Vs and Eq. (24) one can obtain the Hooge parameter as α_H =3.8x10^{-3} before gamma irradiation and 5.3x10^{-3} after irradiation. This low value of the parameter is even better than the values obtained previously for carbon nanotube samples with a long length of the tube without gamma irradiation treatment and is comparable with those of conventional semiconductors such as GaAs, GaN, Si, which indicates the low noise level of the carbon nanotubes themselves. We found for the 1/f -noise component that the dependence on gate voltage at increasing V_G from -2 V to +2 V noise level increases 1.25 times and the current decreases 1.11 times. Such noise behaviour is approximately the same before and after gamma irradiation. According to Eq. (24), the value fS_I/I^2 increased with decreasing current as $1/I$ in 1.11 times. The remaining 1.13 times can be explained by decreasing in $\sqrt{1.13}=1.06$ times the active part of the length of the channel. The latter is usually observed in FETs and confirms that the origin of 1/f -noise is not due to the contact noise.

In addition to the flicker noise component, the generation-recombination noise component can be resolved in the low-frequency range of the spectra. The G-R component of the noise spectra can be described by

$$\frac{fS_I^{GR}}{I^2}=\frac{fS_I^{GR}(0)}{1+(2\pi f\tau)^2}, \tag{25}$$

where S_I^{GR} is the G-R current noise spectral density, and τ is the time constant of the G-R process.

From this part of noise spectra, the numerator increases twofold after gamma irradiation with respect to noise level before irradiation, at the same time the denominator change is caused by decreasing time constant τ as a result of the influence of radiation. It should be noted that the G-R component has weak dependence on gate voltage, but the dependence is nonmonotonous in both cases before as well as after gamma irradiation. The noise spectra after subtracting the 1/f -noise component demonstrate that the main difference between the spectra is the shift of regions with $1/f^2$ -dependence to the higher frequency range. The result indicates that traps with different energy levels were activated as a device was exposed to small doses of gamma radiation. At the same time, the noise level has approximately the same value for both cases and the concentration of the traps does not change very much at this low exposure dose.

In addition, the results of transport and noise measurements obtained after gamma radiation treatment with a dose of $2x10^4$ Gy confirm such a behaviour. The level of normalized current noise power spectra was found to be independent on drain and gate voltages. The experiments rule out any predominant contribution from the contacts and confirm that the main source of noise in the structure is related to the transport phenomena in CNTs.

Thus, the analysis shows that the difference in output characteristics of the FETs before and after small doses of gamma radiation treatment is due to a reduced contribution to the total current parallel to the nanotube resistance. The transconductance of the CNT-FETs and level of noise did not change strongly after γ-irradiation at a dose of $1x10^4$ Gy and $2x10^4$ Gy. The results show that active γ-radiation treatment can improve the transport and noise properties of CNT-FETs at some small optimal dose. The radiation treatment was found to decrease the influence of parasitic conduction channels on DC characteristics of the device. The Hooge parameters obtained are comparable with typical values obtained for conventional semiconductors.

6. Shot noise as a probe of elastic and inelastic transport phenomena

In this section we briefly describe and emphasize an importance of shot noise studies. The shot noise allows analyzing discrete carrier motion with different correlation degree induced by collective phenomena in mesoscopic transport. Poisonnian shot noise $S_I = 2eI$ is usually registered when temperature is decreased and transport is determined by an uncorrelated stochastic process. At the same time if electron –electron process becames correlated due to interactions such as Coulomb repulsion or resulting from Pauli Exclusion Principle, then shot noise can be suppressed. In the case of enelastic scattering process the shot noise can be increased. The degree of correlation process can be described by Fano factor, F, represented the ratio of the measured noise power spectral density S_I to the full shot noise value: $F=S_I/2eI$.

Using shot noise measurement in SWNTs at high bias, Wu and co-workers found strong suppression of noise with increasing voltage and determined the electronic temperature (Wu et al., 2010). The authors show that this temperature is in good agreement with phonon one, obtained by Raman spectroscopy. The fact allows concluding that optical phonons and electrons are nearly at the same temperature and standard heat flow model with typical electron-phonon coupling parameters can be applied for the SWNTs. For electron transport

throught a quantum dot and defect free CNTs shot noise can be either suppressed or enhanced with respect to the Poissonian value (Onac et al., 2006; Betti et al., 2009). If the barriers are symmetric, the resonant charge state is occupied 50% of the time and a $F = 1/2$ shot noise suppression is predicted. Onac with co-workers found, that depending on the tunneling rate through the excited state and the relaxation rate two tunneling regimes can be distinquished (Onac et al., 2006). For inelastic cotunneling super-puassonian noise $F > 1$ (but smaller than the maximum $F = 3$ predicted value) was measured for the first time, while elastic cotunneling leads to Poissonian noise $F = 1$. Shot noise with interaction effect was found in SWNT (Wu et al., 2007; Herrmann et al., 2007) as a result of asymmetric Fabry-Perot resonances. Kim et al., 2007 studied also shot noise in the Fabry-Perot regime in ballistic SWNT and obtained power law dependence at low bias voltages as well as reduced conductance oscillations at larger bias. The measurements constitute the first quantitative investigation of a Tomonage-Luttinger Liquid interaction effects in the shot noise of SWNTs. Roche with co-workers studied noise properties in suspended ropes of single wall CNTs in wide temperature range at different currents (Roche et al., 2002). The effect of strong shot noise reduction was explained by correlation between the current noises in different tubes. The charge and spin transport was theoretically analysed using shot noise in single-walled CNT weakly coupled to metallic leads: ferromagnetic and nonmagnetic (Weymann et al., 2007). It has also been shown that Fano factor in the antiparralel configuration is typically larger that the Fano factor in the parallel one. The spin-dependent rectification of the current caused by asymmetry was registered experimanttally in the CNTs contacted with one ferromagnetic and one normal-metal electrode (Merchant et al., 2008). The authors also observed a significant periodic reduction in the current shot noise, explained by increased spin-flip rates at sertain gate volgates.

7. Conclusion and outlook

Carbon nanotubes represent a novel material for development of field-effect transistors with characteristic sizes considerably smaller compared to conventional down-scaled silicon transistors. Thus, CNTs offer new perspectives due to the high degree of ordering of carbon atoms on the surface of the tube, which serves as very uniform channel for high-speed electron transport. The study of noise properties in CNT materials and CNT-FETs is proved to be expremely sensitive method for basic research. It has been illustrated that noise can be used to investigate transport phenomena and factors determining the transport: influence of contact interfaces, dielectric-nanotube interactions, effect of different surroundings. Noise spectra demonstrate high sensitivity to percolation transport and network morphology, to external gamma radiation treatment, to collective phenomena, like in the case of a Tomonage-Luttinger Liquid interaction effects. Noise-enhanced signal processing at the nanolevel promises applications to signal detection in wideband communication systems, biological and artificial neural networks. Investigations of LF noise provide better understanding of physical processes taking place in the bulk region, on the interfaces and on the surfaces of nanotubes and their role in the low frequency noise origin.

- LF noise spectral density can be described as

$$S_V = A\frac{V^{2+\beta}}{f^{\gamma}}.$$

- Parameter A generally reflects the sample quality and increases with decreasing device size and depends on many parameters of material, its structure, sizes, CNT's bulk and surface physical and chemical conditions, from its fabrication method. The noise amplitude

$$A \propto R, \quad A \propto \frac{1}{N}, \quad A = \frac{\alpha_H}{N}, A \propto \frac{1}{L},$$

  R is the device resistance, N is the number of atoms or carriers in the system, L is the sample length ($N \propto L$). $A = 1.0 \times 10^{-11} R$. Parameter A varies within 10^{-13} up to 4×10^{-4}.
- Parameter $\beta = 0$ is expected for pure resistance fluctuation in ohmic conductors. The $\gamma \neq 1$ behavior is associated with nonlinear characteristics. Usually $|\beta| << 1$, $|\Delta\gamma| << 1$ are material dependent numbers ($\gamma = 1 + \Delta\gamma$).
- Excess noise with a slope different from unity ($\gamma \neq 1$) can be explained by a superposition of a few Lorentzians and of the 1/f-noise. The change in slope with respect to temperature is thus explained by the variation of trap activities. A value of close of 1 for γ indicates that the origin of the measured noise is conductance fluctuations; a value of 1.5 for γ suggests a diffusion process between two different media.
- Tersoff proposed the alternative "charge-noise model", which was successfully proved on the SWNT-FETs affected by random fluctuation of charge in different environments.
- Investigation of noise sources and its behaviour will be source for determination and explanation of physical processes in nanotubes and will help one to suggest noise reduction method nanotube's based devices.

Nanotubes are promising candidates for advanced nanoelectronic devices, and they have great potential in a wide range of applications, such as FETs, elementary logic circuits, bio- and chemical sensors, nanotechnology, biotechnology, electronics, memory devices, optics and other fields of materials science, as well as potential uses in architectural fields.The pronounced noise level observed in CNT devices simply reflects the small number of carriers involved in transport. These results not only provide the basis to quantify the noise behavior in a 1D transport system but also suggest a valuable way to characterize low-dimensional nanostructures based on the 1/f-fluctuation phenomenon. Noise spectra can be applied to several types of challenges:

- Determination of noise parameter A or patterns that characterize the dynamics or structural features of CNTs;
- Transport phenomena of individual CNTs,
- Percolation transport and novel phenomena in CNT-FETs fabricated based on CNT thin films,
- Determination of flow dynamics in distributed systems based on the analysis of dynamic correlations in stochastic signals which are simultaneously measured at different points in space,
- Registration of environmental changes and identification of molecular objects, also at the level of single molecule.

Studies on nanoscale FET sensors reveal the crucial importance of the LF noise for determining the ultimate detection limit. In this respect, the noise results have been

highlighted some future directions for CNT-FETs technology. As a big challenge one has to face the synthesis of parallel aligned CNTs with well defined type of conductivity. This is particularly important for the LF noise suppression and increasing of SNR. Technology and understanding of the contact-CNT interface remains an important issue for further studies. Controlled doping of the contacts may provide one of the methods of the problem solving. It has been shown that CNTs and CNT-FETs are especially promising for sensing applications. Compared to conventional FETs, nanoscaled devices provide a larger surface-to-volume ratio. This results in a high sensitivity of the overall FET channel conductance to changes in the surface potential caused by the adsorption of molecules. In order to reach the detection limit, intense attempts have recently been made to understand the factors determining the SNR. Studies on CNT-FETs showed that the SNR considerably increases in optimal operation regime. Biomolecules and biological object contain as backbone carbon atoms. Therefore interfacing living systems with nanocarbon materials is promising direction for biosensor applications. One may anticipate a broad scope of noise spectroscopy applications in the area of bioanalytic and advanced material research.

8. References

Akabane, H. & Miwa; N. (2009). 1/f resistance fluctuation in carbon nanotubes. *Proceedings of 20th Int. Conf. on Noise and Fluctuations, Pisa, Italy, 14-19 June.* NY 2009, pp. 483-486.

Anantram, M.; Delzeit, L.; Cassell, A.; Han, J. & Meyyappan, M. (2001). Nanotubes on nanoelectronics: Transport, growth and modeling, *Physica E*, Vol. 11, No. 2, pp. 118-125

Appenzeller, J.; Lin, Y.M.; Knoch, J.; Chen, Z. & Avouris, P. (2007). 1/f noise in carbon nanotube devices – On the impact of contacts and device geometry. *IEEE Trans. On Nanotechnology*, Vol. 6, No. 3, pp. 368-373

Asriyan, H.V. & Gasparyan, F.V. (2004). 1/f Noise component conditioned by built-in electric field in semiconductors. *Modern Physics Letters B*, Vol. 18, No. 10, pp. 427-442

Asriyan, H.V.; Gasparyan, F.V.; Aroutiounian, V.M.; Melkonyan, S.V.; Soukiassian, P. (2004). Low-frequency noise in non-homogeneously doped semiconductor. *Sensors and Actuators A,* Vol. 113, No. 3, pp. 338-343

Back, J.H.; Sunkook, K.; Saeed, M.; Moonsub S. (2008). Low-frequency noise in ambipolar carbon nanotube transistors. *Nano letters*, Vol. 8, No. 4, pp. 1090-1094

Bachtold, A.; Hadley, P.; Nakanishi, T.; C. Dekker. (2001). Logic Circuits with Carbon Nanotube Transistors. *Science*, Vol. 294, No. 5545, pp. 1317-1320

Behnam, A.; Bosman, G. and Ural A. (2008). Percolation scaling of 1/f noise in single-walled carbon nanotube films. *Phys. Rev.* B, Vol. 78. No. 8, pp. 085431 (1-9)

Behnam, A.; Ural, A.; & Bosman, G. (2009). Modeling and measurements of low frequency noise in single-walled carbon nanotube films with bulk and percolation configurations. *Proceedings of 20th Int. Conf. on Noise and Fluctuations, Pisa, Italy, 14-19 June*. NY 2009, pp. 79-84

Betti, A.; Flori, G. & Iannaccone, G. (2009). Enhanced shot noise in carbon nanotube field-effect transistors. *Appl. Phys. Lett.,* Vol. 95, No. 25, pp. 252108 (1-3)

Briman, M.; Bradley, K.; Gruner, G. (2006). Source of 1/f noise in carbon nanotube devices. *J. of Appl. Phys.*, Vol. 100, No. 1, pp. 013505 (1-5)

Chan, J.; Burke, B.; Evans, K.; Williams, K.A.; Vasudevan, S.; Liu, M.; Campbell, J. & Ghosh, A.W. (2009). Reversal of current blockade in nanotube-based field effect transistors through multiple trap corrections. *Phys. Rev. B,* Vol. 80, pp. 033402 (1-4)

Chan, J.; Kidd, D.; Burke, B.; Harriott, L.; Williams, K. (2010). Noise analysis of carbon nanotube field-effect transistors irradiated by electron beam. *Journ. Vac. Sci. Techn.B,* Vol. 28, pp. C6P66-C6P69

Charlier, J.-C.; Blasé, X.; Roche, S. (2007). Electronic and transport properties of nanotubes. *Rev. Mod. Phys.,* Vol. 79, No. 2, pp. 677–732

Chico, L.; Crespi, V.H.; Benedict, L.X.; Louie, S.G. & Cohen, M.L. (1996). Pure Carbon Nanoscale Devices: Nanotube Heterojunctions. *Phys. Rev. Letters*, Vol. 76, No. 6, pp. 971-974

Collins, P.G.; Fuhrer, M.S. & Zettl, A. (2000). 1/f noise in carbon nanotubes. Appl. *Phys. Lett.,* Vol. 76, No. 7, pp. 894-896

Dillon, A. C.; Jones, K. J.; Bekkedahl, T. A.; Kiang, C. H.; Bethune, D. S.; Heben, M. J. (1997). Storage of Hydrogen in Single-Walled Carbon Nanotubes. *Nature*, Vol. 386, pp. 377-379

Dutta, P. & Horn, P.M. (1981). Low-frequency fluctuations in solids - 1/f noise. *Rev. Mod. Phys.,* Vol. 53, No. 3, pp. 497-516

Fischer, J.E.; Dai, H.; Thess, A.; Lee, R.; Hanjani, N.M.; Dehaas, D.L. & Smalley, R.E. (1997). Metallic resistivity in crystalline ropes of single-wall carbon nanotubes. *Phys. Rev. B*, Vol. 55, No. 8, pp. R4921-R4924.

Fuhrer, M.S.; Kim, B.M.; Durkop, T. & Brintlinger, T. (2002). High-mobility nanotube transistor memory. *Nano Lett.*, Vol. 2, No. 7, pp. 755-759

Gasparyan, F.V.; Poghossian, A.; Vitusevich, S.A.; Petrychuk, M.V.; Sydoruk, V.A.; Surmalyan, A.V.; Siqueira, J.R. Jr.; Oliveira, O.N.Jr., Offenhäusser, A.; Schöning, M.J. (2009). Low frequency noise in electrolyte-gate field-esffect devices functionalized with dendrimer/carbon-nanotube multilayers. *Proceedings of 20th Int. Conf. Fluctuation and Noise, 14-19 June, Pisa, Italy*. 2009, pp. 133-136

Gasparyan, F.V.; Asriyan, H.V.; Melkonyan, S.V. & Corman, C.E. (2010). "Method of 1/f noise reduction and Noise Level Manipulation in semiconductor based devices" May 7, 2010 as U.S. Patent Application for Letters Patent of the United States No. 61/332, 408.

Gasparyan, F.V.; Poghossian, A.; Vitusevich, S.A.; Petrychuk, M.V.; Sydoruk, V.A.; Siqueira, J.R.; Oliveira, O.N.; Offenhäusser, A.; Schöning, M.J. (2011a). Low-Frequency Noise in Field-Effect Devices Functionalized With Dendrimer/Carbon- Nanotube Multilayers. *IEEE Sensors Journal*, Vol. 11, No. 1, pp. 142-149

Gasparyan F.V., Vitusevich S.A., Offenhäusser, A.; Schöning, M.J. (2011b). Modified charge fluctuation noise model for electrolyte-insulator-semiconductor devices. *Modern Physics Letters B,* Vol. 25, No. 11, pp.831-840

Haspel, H.; Ionescu, R.; Heszler, P.; Kukovecz, A.; Konyal, Z.; Gingl, Z.; Maklin, J.; Mustonen, T.; Kordas, K.; Vajtai, R.; & Ajayan, M. (2008). Fluctuation enhanced gas sensing on functionalized carbon nanotube thin films. *Phys. Stat. Sol. (b),* Vol. 245, pp. 2339-2342

Heinze, S., Radosavljevic, M., Tersoff, J. & Avouris, P. (2003). Unexpected scaling of the performance of carbon nanotube Schottky-barrier transistors. *Phys. Rev. B*, Vol. 68, No. 23, pp. 235418-1-5

Heinze, S., Tersoff, J. & Avouris, P. (2005). Carbon Nanotube Electronics and Optoelectronics, In: Introducing Molecular Electronics, Cuniberti, G. and Richter, K., (Ed.), 381-409, Springer, 978-3-540-27994-5, Netherlands

Heller, I.; Mannik, J.; Lemay, S.G. & Dekker, C. (2009). Optimizing the signal-to-noise ratio for biosensing with carbon nanotube transistors. *Nano Lett*., Vol. 9, No. 1, pp. 377-382

Hermann, L.G.; Delattre, T.; Morfin, P.; Berroir, J.-M.; Placais, B.; Glatti, D.C.; Kontos, T. (2007). Shot noise in Fabry-Perot interferometers based on carbon nanotubes. *Phys. Rev. Lett.,* Vol. 99, No. 15, pp. 156804 (1-4)

Hooge, F.N. (1969). 1/f noise is no surface effect. *Phys. Lett.,* Vol. 29A, No. 3, pp. 139-140

Hooge, F.N.; Kleinpenning, T.G.M.; Vandamme, L.K.J. (1981). Experimental studies on 1/f noise. *Rep. Prog. Phys.,* Vol. 44, No. 5, pp. 479–532

Hooge, F.N. (1994). 1/f noise sources. *IEEE Trans. Electron Devices*, Vol. 41, N. 11, pp. 1926–1935

Hung, K.; Ko, P.; Hu, C. & Cheng, Y. (1990). A unified model for the flicker noise in metal-oxide-semiconductor field-effect transistors. *IEEE Trans. Electron Devices*, Vol. 37, N. 3, pp. 654-665

Ishigami, M.; Chen, J.H. & Williams, E.D. (2006). Hooge's constant for carbon nanotube field effect transistors. *Appl. Phys. Lett.,* Vol. 88, pp. 203116 (1-3)

Javey, A.; Guo, J.; Wang, Q.; Lundstrom, M. & Dai, H. (2003). Ballistic carbon nanotube fieldeffect transistors. *Nature,* Vol. 424, N. 6949, pp. 654-657

Javey, A.; Guo, J.; Farmer, D.B.; Wang, Q.; Yenilmez, E.; Gordon, R.G.; Lundstrom, M. & Dai, H. (2004). Self-aligned ballistic molecular transistors and electrically parallel nanotube arrays. *Nano Letters,* Vol. 4, No. 7, pp. 1319-1322

Jhang, S.H.; Lee, S.W.; Lee, D.S.; Campbell, E.B.; Roth, S.; Park, Y.W. (2005). Random telegraph noise in individual metallic single-walled carbon nanotubes. *MRS Symp. Proc.*, Vol. 858E, pp. HH8.5.1-6

Kamimura, T. & Matsumoto, K. (2005). Electrical Heating Process for p-Type to n-Type Conversion of Carbon Nanotube Field Effect Transistors. *Jpn. J. Appl. Phys*., Vol. 44, No. 4A, pp. 1603-1605

Kamimura, T. & Matsumoto, K. (2010). Chapter 10: Gate controlled Particle-Wave duality in a single walled carbon nanotube hole-transistor. In: Carbon Nanotubes, Ed. by J.M. Marulanda, PH InTech

Kawahara, T.; Yamaguchi, S.; Maehashi, K., Yasuhide, O.; Matsumoto, K.; Kawai, T. (2010). Robust noise modulation of nonlinearity in carbon nanotube field-effect-transistors. *Jap. Journ. Appl. Phys.,* Vol. 49, pp. 02BD11(1-5)

Kim, N.Y.; Recher, P.; Oliver, W.D.; Yamamoto Y.; Kong, J. & Dai, H. (2007). Tomonage-Luttinger liquid features in ballistic single-walled carbon nanotubes: conductance and shot noise. *Phys. Rev. Lett.,* Vol. 99, No. 3, pp. 036802 (1-4)

Kim, K.; Jang, D.; Lee, K.; Kang, H.; Yu, B.Y.; Lee, J.I. & Kim. G.T. (2010). Influence of electrical contact on the 1/f noise in individual multi-walled carbon nanotubes. *Nanotechnology,* Vol. 21, pp. 335702(1-4)

Kim, N.-P.; Heinze, S. & Tersoff, J. (2007). Random-Telegraph-Signal Noise and Device Variability in Ballistic Nanotube Transistors. *Nano Lett*., Vol. 7, No. 4, pp. 910–913

Kim, U.J.; Kim, K.H.; Kim, K.T.; Min, Y.-S. & Park, W. (2008). Noise characteristics of single-walled carbon nanotube network transistors. *Nanotechnology*, Vol. 19, No. 28, pp. 285705(1-4)

Kim, S.; Kim, S.; Janes, D.B.; Mohammadi, S. & Shim, M. (2010). DC modeling and the source of flicker noise in passivated carbon nanotube transistors. *Nanotechnology* , Vol. 21, No. 38, pp. 385203(1-7)

Kingrey, D.; Khatib, O. & Collins, P.G. (2006). Electronic Fluctuations in Nanotube Circuits and Their Sensitivity to gases and Liquids Nano Lett., Vol. 6, No. 7, pp. 1564 – 1568

Kong, J.; Franklin, N.R.; Zhou, C.W.; Chapline, M.G.; Peng, S.; Cho, K.J. & Dai, H.J. (2000). Nanotube molecular wires as chemical sensors. *Science,* Vol. 287, No. 5453, pp. 622-625, 0036-8075

Kordrostami, Z. and Sheikhi, M.H. (2010). Chapter 9: Fundamental Physical Aspects of Carbon Nanotube Transistors. In: Carbon Nanotubes, Ed. by J.M. Marulanda, PH InTech

Ksenevich, V.; Galibert, J. & Samuilov, V. (2010). Chapter 7: Charge Transport in Carbon Nanotube Films and Fibers. In: Carbon Nanotubes, Ed. by J.M. Marulanda, PH InTech

Lee, H.; Lee, M.; Namgung, S. & Hong, S. (2010). Wide contact structures for low-noise nanochannel devices based on a carbon nanotube network. *ACS Nano,* Vol. 4, pp. 7612-7618

Lee, I.; Zhou, C.; & Kosko, B. (2006). Noise-enhansed detection of subthreshold signals with carbon nanotubes. *IEEE Trans.Nanotechnology,* Vol. 5, pp. 613-627

Leonard, F. & Tersoff, J. (1999). Novel Length Scales in Nanotube Devices. *Phys. Rev. Lett.,* Vol. 83, No. 24, pp. 5174–5177

Leonard, F. & Tersoff, J. (2000). Role of Fermi-Level Pining in Nanotube Schottky Diodes. *Phys. Rev. Lett.,* Vol. 84, No. 20, pp. 4693-4696

Lin, Y-M.; Appenzeller, J. & Avouris, Ph. (2004). Ambipolar-to-unipolar conversion of carbon nanotube transistors by gate structure engineering. *Nano Lett.,* Vol. 4, No. 5, pp. 947–950

Lin, Y.-M.; Appenzeller, J.; Knoch, J.; Chen, Z. & Avouris, P. (2006). Low-Frequency Current Fluctuations in Individual Semiconducting Single-Wall Carbon Nanotubes. *Nano Lett.*, Vol. 6, No. 5, pp. 930–936

Lin, Y-M.; Appenzeller, J.; Chen, Z. & Avouris, P. (2007). Electrical transport and 1/f noise in semiconducting carbon nanotubes. *Physica E: Low-dimensional Systems and Nanostructures*, Vol. 37, No. 1-2, pp. 72-77

Lin, Y.-M.; Tsang, J.C.; Freitag, M. & Avouris, P. (2007a). Impact of oxide substrate on electrical and optical properties of carbon nanotube devices. *Nanotechnology*, Vol. 18 pp. 295202(1-6)

Liu, X.; Lee, C.; Zhou, C.; Han, J. (2001). Carbon Nanotube Field-Effect Inverters. Appl. *Phys. Lett.*, Vol. 79, No. 20, pp. 3329-3331

Liu, F.; Bao, M.; Kim, H.; Wang, K.L.; Li, C.; Liu, X. & Zhou, C. (2005). Giant Random Telegraph Signals in the Carbon Nanotubes as a Single defect Probe. *Appl. Phys. Lett.,* Vol. 86, pp. 163102 (1-3)

Liu, F.; Wang, K.L.; Zhang, D. & Zhou, C. (2006a). Random telegraph signals and noise behaviors in carbon nanotube transistors. *Appl. Phys. Lett.,* Vol. 89, pp. 243101(1-3)

Liu, F.; Wang, K.L.; Li, C. & Zhou, C. (2006b). Study of Random Telegraph Signals in Single-Walled Carbon Nanotube Field Effect Transistors. *IEEE Trans. On Nanotechnology*, Vol. 5, No. 5, pp. 441-445

Liu, F.; Wang, L. (2006c). Noise in carbon nanotube field effect transistor. *Appl. Phys. Lett.,* Vol. 89, pp. 063116(1-3)

Liu, F.; Wang,L. (2008). Carrelated random telegraph signal and low-frequency noise in carbon nanotube transistors. *Nano Lett.,* Vol. 8, pp. 147-151

Lu, R; Xu, G; & Wu, J.Z. (2008). Effect of thermal annealing on noise property and temperature coefficient of resistance of single-walled carbon nanotube films. *Appl. Phys. Lett.,* Vol. 93, pp. 213101(1-3)

Mannik, J.; Heller, I.; Janssens, A.M.; Lemay, S.G. & Dekker, C. (2008). Charge noise in liquid-gated single-waal carbon nanotube transistors. *Nano Lett.,* Vol. 8, No. 2, pp. 685-688

Martel, R.; Schmidt, T.; Shea, H.R.; Hertel, T. & Avouris, Ph. (1998). Single- and multi-wall carbon nanotube field-effect transistors. *Appl. Phys. Lett.,* Vol. 73, N. 17, pp. 2447-2449

Martel, R.; Derycke, V.; Lavoie, C.; Appenzeller, J.; Chan, K.K.; Tersoff, J. & Avouris, Ph. (2001). Ambipolar Electrical Transport in Semiconducting Single-Wall Carbon Nanotubes. *Phys. Rev. Lett.,* Vol. 87, N. 25, pp. 256805(1-4)

McWhorter, A.L. (1958). In: Semiconductor surface Physics; R.H.Kingston (Ed.), pp. 207-228, University of Philadelphia Press, Philadelphia, PA

Melkonyan, S.V.; Gasparyan, F.V.; Aroutiounian, V.M.; Korman, C.E. (2003). Current carrier mobility fluctuations in homogeneous semiconductors. *Proceedings of SPIE's 1st Int .Symp on Fluctuation and Noise. 1-4 June 2003, Santa Fe, New Mexico USA,* Vol. 5115, pp. 412-420.

Melkonyan, S.V.; Aroutiounian, V.M.; Gasparyan, F.V.; Korman, C.E. (2005a). Peculiarities of electron distribution function's fluctuations damping in homogeneous semiconductors. *Physica B: Physics of Condensed Matter*, Vol. 357, No. 3-4, pp. 398-407

Melkonyan, S.V.; Gasparyan, F.V.; Aroutiounian, V.M.; Asriyan, H.V. (2005b). 1/f –type noise in view of phonons interface percolation dynamics. *Proceedings of 18th Int. Conf. on Noise and Fluctuations (ICNF 2005) September 19-23, 2005; Salamanca, Spain*, Vol. 780, pp. 87-91

Melkonyan, S.V.; Aroutiounian, V.M.; Gasparyan, F.V.; Asriyan, H.V. (2006). Phonon mechanism of mobility equilibrium fluctuation and properties of 1/f-noise. *Physica, B: Physics of Condensed Matter*, Vol. 382, No.1-2, pp. 65-70

Melkonyan, S.V.; Gasparyan, F.V.; Asriyan, H.V. (2007). Main sources of electron mobility fluctuations in semiconductors. *Proceedings of SPIE 4th Int. Symp. Fluctuation and Noise, ay 2007, Florence, Italy*, Vol. 6600, pp. 6600K (1-8)

Merchant, C.A.; & Marcovic, N. (2009). Current and shot noise measurements in a carbon nanotube-based spin diode. *Journ. Appl. Phys.,* Vol. 105, No. 7, pp. 07C711 (1-4)

Mihaila, M.N. (2002). Chapter 18. In: Noise and Fluctuations Control in Electronic Devices; A. Balandin, (Ed.), pp. 366-385, American Science Publishers: Stevenson Ranch, CA

Mihaila, M.N. (2004). Phonon-induced 1/f noise in MOS transistors. *Fluctuation Noise Lett.,* Vol. 4, No. 2, pp. L329-L343

Nguyen, C.V.; Delzeit, L.; Cassell, A.M.; Li, J.; Han, J.; Meyyappan, M. (2002). Preparation of Nucleic Acid Functionalized Carbon Nanotube Arrays. *Nano Lett.,* Vol. 2, N. 10, pp. 1079-1081

Odom, T.W.; Huang, J.-L. & Lieber, C.M. (2002). STM studies of single-walled carbon nanotubes. *J. Phys.: Condens. Matter*, Vol. 14, No. 6, pp. R145-R167

Onac, E.; Balestro, F.; Trauzettel, B.; Lodewijk, C.F.J. & Kouwenhoven, L.P. (2006). Shot-noise detection in a carbon nanotube quantum dot. *Phys. Rev. Lett.,* Vol. 96, No. 2, pp. 026803 (1-4)

Ouacha, H.; Willander, M.; Yu, H.Y.; Park, Y.W.; Kabir, M.S.; Magnus Persson, S.H.; Kish, L.B. & Ouacha, A. (2002). Noise properties of an individual and two crossing multiwalled carbon nanotubes. *Appl. Phys. Lett.*, Vol. 80, No. 6, pp. 1055-1057

Postma, H.W.Ch.; Teepen, T.F.; Yao, Z.; Dekker, C. (2001). 1/f noise in carbon nanotubes. *Proceedings of XXXVI-th Rencontres de Moriond, EDP Sciences, France,* 2001

Radosalvljevic, M.; Freitag, M.; Thadani, K.V. & Johnson, A.T. (2002). Non-volatile molecular memory elements based on ambipolar nanotube field effect transistors. *Nano Lett.,* Vol. 2, No. 7, pp. 761-764

Raychaudhuri, A.K. (2002). Measurement of 1/f Noise and Its Application in Materials Science. Curr. *Opin. Solid State Mater. Sci*., Vol. 6, No. 1, pp. 67-85

Raychowdhury, A., Keshavarzi, A., Kurtin, J., De, V. and Roy, K. (2006). Carbon Nanotube Field-Effect Transistors for High-Performance Digital Circuits; DC Analysis and Modeling Toward Optimum Transistor Structure. *IEEE Transactions on ElectronDevices*, Vol. 53, No. 11, pp. 2711-2717

Reich, S.; Thomsen, C. & Maultzsch, J. (2004). Carbon Nanotubes. *EILEY-VCH Verlag GmbH& Co. KGaA*, ISBN 3-527-40386-8

Reza, S.; Huynh, Q.T.; Bosman, G.; Sippel-Oakley, J. and Rinzler A.G. (2006). 1/f noise in metallic and semiconducting carbon nanotubes. J. Appl. Phys., Vol. 100, No. 9, pp. 094318 (1-5)

Roche, P.-E.; Kociak, Gueron, M.S.; Kasumov, A.; Reulet, B.; Bouchiat, H. (2002). Very low shot noise in carbon nanotubes. *Eur. Phys. J. B*, Vol. 28, No. 2, pp. 217-222

Roschier, L.; Tarkiainen, R.; Ahlskog, M.; Paalanen, M. & Hakonen, P. (2001). Multiwalled carbon nanotubes as ultrasensitive electrometers. *Appl. Phys. Lett.,* Vol .78, No. 21, pp. 3295-3297

Rossenblatt, S.; Yaish, Y.; Park, J.; Gore, J.; Sazonova, V. & McEuen, P.L. (2002). High performance electrolyte gated carbon nanotube transistors. *Nano Lett*., Vol. 2, No. 8, pp. 869-872

Roumiantsev, S.; Vajtai, R.; Pala, N.; Wei, B.Q.; Shur, M.S.; Kish, L.B. & Ajayan P.M. (2001). Proceedings of the Ninth Int. Symp. on Nanostructure: Physics and Technology, ed. by Z. Alferov, L. Esaki, and L. Solovyova (St. Petersburg, 2001), p. 418.

Sánchez-Pomales, G.; Pagán-Miranda, C.; Santiago-Rodríguez L. & Cabrera, C.R. (2010). Chapter 35: NA-Wrapped Carbon Nanotubes: From Synthesis to Applications. In: Carbon Nanotubes, Ed. by J.M. Marulanda, PH InTech

Sangwan, V.K.; Ballarotto, V.W.; Fuhrer, M.S.; & Williams, E.D. (2008). Facile fabrication of suspended as-grown carbon nanotube devices. *Appl. Phys. Lett.,* Vol. 93, pp. 1131112(1-3)

Service, R. F. (1998). Superstrong Nanotubes Show They are Smart, Too. *Science*, Vol. 281, pp. 940-942

Sheng, P. (1980). Fluctuation-induced tunneling conduction in disordered materials. *Phys. Rev. B*, Vol. 21, No. 6, pp. 2180–2195

Sin, M.L.Yi.; Chow, G.C.T.; Wong, G.M.K.; Li, W.J.; Leong, P.H.W. & Wong, K.W. (2007). Ultralow-power alcohol vapor sensor using chemically functionalized miltiwalled carbon nanotubes. *IEEE Trans. Nanotechnol.,* Vol. 6, pp. 571-577

Snow, E.S.; Novak, J.P.; Lay, M.D. & Perkins, F.K. (2004). 1/f noise in single-walled carbon nanotube devices. *Appl. Phys. Lett.,* Vol. 85, No. 18, pp. 4172-4174

Snow, E.S.; Perkins, F.K.; Houser, E.J.; Badescu, S.C.; Reinacke, T.L. (2005). Chemical detection with a single-walled carbon nanotube capacitor. *Science,* Vol. 307, No. 5717, pp. 1942-1945

Soliveres, S.; Hoffmamm, A.; Pascal, F.; Delseny, C.; Kabir, M.S.; Nur, O.; Salesse, A.; Willander, M. & Deen, J. (2006). Excess low frequency noise in single-wall carbon nanotube. *Fluctuation and Noise Letters*, Vol. 6, No. 1, pp. L45-L55

Soliveres, S.; Martinez, F.; Hoffmann, A.; Pascal; F. (2009). 1/f noise transport and percolation in carbon nanotube film field-effect transistors: simulation and experiment. *Proceedings of 20th Int. Conf. on Noise and Fluctuations, Pisa, Italy, 14-19 June*. NY 2009, pp. 85-88.

Svizenko, A.; Anantram, M.P. & Govindan, T.R. (2005). Ballistic transport and electrostatics in metallic carbon nanotubes. *IEEE Trans. Nanotechnol*., Vol. 4, No. 5, pp. 557-562

Tanaka, T.; Imai, E.S.M. & Akiyama, K. (2010). Low-Frequency Noise in Carbon-Nanotube/Cellulose Composite Paper. *Jpn. J. Appl. Phys*., Vol. 49, pp. 055101(1-3)

Tans, S.J.; Verschueren, A.R.M.; Dekker, C. (1998). Room-temperature transistor based on a single carbon nanotube, *Nature,* Vol. 393, pp. 49-52

Tarkiainen, R.; Roschier, L.; Ahlskog, M.; Paalanen, M.; Hakonen, P. (2005). Low-frequency current noise and resistance fluctuations in multiwalled carbon nanotubes. *Physica E*, Vol. 28, pp. 57-65

Tersoff, J. (1984).Theory of semiconductor heterojunctions: The role of quantum dipoles. Phys.rev.B, Vol. 30, No. 8, pp. 4874–4877

Tersoff, J. (2007). Low-Frequency Noise in Nanoscale Ballistic Transistors. *Nano Lett*., Vol. 7, No. 1, pp. 194–198

Tobias, D.; Ishigami, M.; Tselev, A.; Barbara, P.; Williams, E.D.; Lobb, C.J. & Fuhrer, M.S. (2008). Origins of 1/f noise in individual semiconducting carbon nanotube field-effect transistors. *Phys. Rev*., Vol. B77, No. 3, pp. 033407 (1-4)

Vajtai, R.; Wei, B.Q.; Zhang, Z.J.; Jung, Y.; Ramanath, G.; Ajayan, P.M. (2002). Building carbon nanotubes and their smart architectures. *Smart Mater. Struct*., Vol. 11, N. 5, pp. 691-698

Vandamme, L.K.J.; Li, X. & Rigaud, D. (1994). 1/f Noise in MOS devices, mobility or number fluctuations? *IEEE Trans. Electron Devices*, Vol. 41, N. 11, pp. 1936-1945

Vijayaraghavan, A.; Kar, S.; Rumyantsev, S.; Khanna, A.; Solando, C.; Pala, N.; Vajtai, R.; Kanzaki, K.; Kobayashi, Y.; Nalamasu, O.; Shur, M.S. & Ajayan, P.M. (2006). Effect of ambient pressure on resistance and resisnatnce fluctuations in single-wall carbon nanotube devices. *Journ. Appl. Phys.,* Vol. 100, pp. 024315 (1-4)

Vitusevich, S.A.; Sydoruk, V.A.; Petrychuk, M.V.; Danilchenko, B.A.; Klein, N.; Offenhäusser, A.; Ural, A. & Bosman, G. Transport properties of single-walled carbon nanotube transistors after gamma radiation treatment. *(2010). Journ. Appl. Phys.,* Vol. 107, pp. 063701 (1-6)

Wang, N.-P.; Heinze, S. & Tersoff J. (2007). Random-Telegraph-Signal Noise and Device Variability in Ballistic Nanotube Transistors. *Nano Lett.*, Vol. 7, No. 4, pp. 910–913

Weissman, M.B. (1988). 1/f noise and other slow, nonexponential kinetiks in condensed matter. *Rev. Mod. Phys.*, Vol. 60, No.2, pp. 537-571

Weymann, I.; Barnas, J. & Krompiewski, S. (2007). Theory of shot noise in single-walled meatllic carbon nanotubes weakly coupled to nonmagnetic and feromagnetic leads. *Phys. Rev. B.,* Vol. 76, No. 15, pp. 155408 (1-9)

Wu, F.; Queipo, P.; Nasibulin, A.; Wang, T.H.; Kauppinen, E. & Hakonen, P.J. (2007). Shot noise with interaction effects in single-walled carbon nanotubes. *Phys. Rev. Lett.,* Vol. 99, No. 15, pp. 156803 (1-4)

Wu. F.; Virtanen, S.; Andresen, S.; Placais, B. & Hakonen, P.J. (2010). Electron-phonon coupling in single-walled carbon nanotubes determined by shot noise. *Appl. Phys. Lett.,* Vol. 97, No. 26, pp. 262115 (1-3)

Xu, G.; Liu, F.; Han, S.; Ryu, K.; Badmaev, A.; Lei, B.; Zhou, C. & Wang, K.L. (2008). Low-frequency noise in top-gated ambipolar carbon nanotube field effect transistors. *Appl. Phys. Lett.,* Vol. 92, pp. 223114(1-3)

Yao, Y. (2010). Chapter 28: Hydrogen Storage Using Carbon Nanotubes. In: Carbon Nanotubes, Ed. by J.M. Marulanda, PH InTech

Yao, Z.; Dekker, C. & Avouris, P. (2002). *Carbon Nanotubes: Synthesis, Structure, Properties and Application.* Springer, New York, 2002, p. 147

Zhou, C. & Zhang, X.-G. (2008). Numerical study of the noise power of a carbon nanowire network. *Phys. Rev. B.,* Vol. 78, No. 17, pp. 174307(1-6)

Ziel, A. (1986). Noise in solid state devices and circuits. John Wiley&Sons, New York, 306p.

12

High Frequency Properties of Carbon Nanotubes and Their Electromagnetic Wave Absorption Properties

Mangui Han and Longjiang Deng
State Key Laboratory of Electronic Thin Films & Integrated Devices, University of Electronic Science and Technology of China, China

1. Introduction

Since the discovery of carbon nanotubes (CNT) in 1991 by Iijima (Iijima, 1991), the intensive investigations on CNT have shown that CNT has a series of unique mechanical, electrical, magnetic, optical and thermal properties (Poncharal et al, 1999; Mintmire et al, 1992; Wang, et al, 2005; Xu et al, 2006; Zhao et al, 2006). For a completely pure, defect-free state CNT, it is diamagnetic with a large diamagnetic susceptibility spanning more than two orders of magnitude. Generally, there are two categories of CNTs available for various applications: single wall carbon nanotubes (SWCNT) and multiwalled carbon nanotubes (MWCNT). MWCNT consists of two or more concentric cylindrical shells of graphene sheets coaxially arranged around a central hollow core. SWCNT comprises a single graphene cylinder. Such a tube configuration has a so-called electronic conjugate π-structure which is responsible for its unique electronic transport behaviors. CNTs have been reported to find new applications in bolometers (Lu et al, 2010); gas pressure sensors (Tooski et al, 2011), nanometer resolution optical probes (Nakata et al, 2011), etc. Recently, there is an increasing interest in the developing materials for electromagnetic engineering applications, such as electromagnetic wave absorbers, antennae, circulators, etc. Especially, as telecommunication systems and electronic devices such as wireless local area networks and antenna system are ushered into the GHz arena, electromagnetic interference (EMI) problems that degrade the performance of electric circuits and communication systems are becoming more and more serious. One solution to these problems is to absorb the unwanted electromagnetic wave using microwave absorbing materials (Han et al, 2010a, 2010b, 2009a, 2009b; Xie et al, 2007; Chen et al, 2010). Since the application of conventional microwave absorbers such as spinel ferrites is restricted in the MHz region due to their Snoek's limit (Snoek, 1948), researches are urged to explore new types of microwave absorbers that can meet requirements like light weight and strong absorption in a wide frequency range, such as ferrites, metallic nanostructured magnetic materials (such as Fe, Co, Ni and alloys made from them), magnetic microwire, etc. The significant drawback of these materials is their large density, especially for ferrites, which are the most widely used materials for electromagnetic wave absorbers. For instance, the density of ferrites is usually around 4~5 g/cm^3. A CNT/epoxy resin composite is considered a good candidate material for microwave applications due to its lower density

(for instance 0.14 g/cm^3), large dielectric loss, such as antireflection, electromagnetic interference shielding or microwave absorbing. Wu et al (Wu et al, 2004) found the MWCNT/epoxy resin composites exhibited large relative permittivity over a broad bandwidth, and the permittivity increased with the increase of the MWCNT contents in the composites. Kim et al (Kim et al, 2004) had found that the MWCNT/PMMA (polymethyl methacrylate) composites exhibited excellent EMI shielding performances in GHz range. Recently, the molecular electronics research which aims at combining spintronics with molecular structures has been motivated to study the magnetic proximity effect in carbon nanotubes, where a measurable induced magnetic moment has been observed when CNTs are contacting with magnetic materials, especially with half metal magnetic materials, for instance Fe_3O_4. The induced magnetic moment was believed due to the spin polarized charge transfer between CNTs and magnetic material (Cespedes et al, 2004; Coey et al, 2002). Except for this induced magnetism, there are always some nano-sized residual magnetic metals (Fe, Co or Ni) left on CNT during the CNT manufacture process, and enable the CNT to exhibit a weak ferromagnetism. A magnetoresistance effect also has been found in carbon nanotube (Stamenov et al, 2005). None the less, there are many other unexploited application areas for the carbon nanotube-based system. For instance, whether there is an interaction between the ferrite and the MWCNT; If such an interaction exists between the ferrite and the MWCNT, whether the dynamic magnetic properties (such as resonance frequency) of ferrite can be tuned by doping with the MWCNT; As we know, electromagnetic wave absorbers work by dissipating electromagnetic energy into heat via magnetic loss and dielectric loss. Spinel ferrites are one of the frequently used electromagnetic wave absorbing materials, but they suffer from the lower spin rotation resonance compared with other ferrites, such as hexagonal ferrites. In this chapter, we will firstly discuss the static magnetic properties of MWCNTs and SWCNTs and their origins, then their electromagnetic wave properties. Finally, we will study the doping effect of MWCNTs on the electromagnetic properties of NiCoZn spinel ferrites.

2. Experimental details

The MWCNTs and SWCNTs were purchased from a vendor (TimesNano, Inc.®, Chengdu, China) and the MWCNTs were prepared by a chemical vapor deposition method using Ni as the catalyst. While SWCNTs were prepared using the same technique but Co was used as the catalyst. The average length of MWCNT is about 50 μm. The outer diameter of MWCNTs is about 10~30 nm. The purities of MWCNTs and SWCNTs have been checked by the energy dispersive x-ray (EDX) measurements. The content of Ni impurity in MWCNTs is about 0.5 wt. %. The Co impurity in SWCNTs is about 0.2 wt. %. The images of MWCNTs were taken by a transmission electronic microscope (TEM). Field emission scanning electron microscopy (FE-SEM) images also have been taken for both SWCNTs and MWCNTs. In order to study the high frequency properties of MWCNTs and SWCNTs, toroidal samples with the inner, outer diameter and thickness as 3, 7 and 3.7 mm respectively were prepared by mixing the MWCNTs (SWCNTs) and wax for microwave measurements. The weight ratio of CNTs over wax is 0.2. The dependences of permittivity on frequency were theoretically studied based on the Cole-Cole law. With the obtained permeability and permittivity values, their electromagnetic wave absorption properties were evaluated and compared. To show the effect of CNTs on tuning the electromagnetic properties of ferrites, we have synthesized spinel ferrites $(Ni_{0.4}Co_{0.24}Zn_{0.36})Fe_2O_4$ with average particle size of 2~3

μm by sintering the oxide mixtures of Fe_2O_3, NiO, ZnO, and Co_2O_3 at 1250 °C for 2 h. The crystal structure of prepared ferrite checked by x-ray diffraction shows a typical spinel structure. We have prepared three samples to study the doping effect of MWCNTs on the electromagnetic properties of ferrites. Sample 0 has not been doped with MWCNTs. Sample 1 contains 5.2 wt. % MWCNTs. Sample 2 contains 10.4 wt. % MWCNTs. For these three ferrite samples, the weight percentage of wax is about 16%. The ferrite, MWCNT and wax are carefully mixed to ensure that the samples are homogenous and isotropic. The high frequency properties were also measured. All the high frequency measurements were carried out on an Agilent Vector Network Analyzer 8720 based on the transmission/reflection method. During a high frequency measurement, a sample under study was inserted into a segment of coaxial transmission line. All four scattering parameters can be obtained from the measurements.

$$S_{11} = R_1^2 \frac{\Gamma(1-\mathrm{T}^2)}{1-\Gamma^2 T^2} \tag{1}$$

$$S_{22} = R_2^2 \frac{\Gamma(1-\mathrm{T}^2)}{1-\Gamma^2 T^2} \tag{2}$$

$$S_{21} = S_{12} = R_1 R_2 \frac{\Gamma(1-\mathrm{T}^2)}{1-\Gamma^2 T^2} \tag{3}$$

, where R_1 and R_2 are the reference plane transformations at two ports: $R_i = \exp(-\gamma L_i)$ (i = 1, 2), T is the transmission coefficient: $T = \exp(-\gamma L)$, where L is the thickness of sample under study. The reflection coefficient Γ can be given as:

$$\Gamma = \frac{\sqrt{\mu_r / \varepsilon_r} - 1}{\sqrt{\mu_r / \varepsilon_r} + 1} \tag{4}$$

Employing the Nicolson-Ross-Weir(NRW) algorithm, the complex relative permittivity and permeability can be derived from above equations, which are given as following:

$$\mu_r = \frac{1+\Gamma}{(1-\Gamma)\Lambda\sqrt{(1/\lambda_0^2)-(1/\lambda_c^2)}} \tag{5}$$

$$\varepsilon_r = \frac{\lambda_0^2}{\mu_r[(1/\lambda_c^2)-(1/\Lambda^2)]} \tag{6}$$

, where λ0 is the free-space wavelength, λc is the cutoff wavelength of the transmission line section. For a coaxial line, λc = ∞.

$$\frac{1}{\Lambda^2} = -[\frac{1}{2\pi D}\ln(\frac{1}{T})]^2 \tag{7}$$

More detailed descriptions on this measurement principle can be found in Ref. (Chen et al, 2004).

3. Morphologies of MWCNTs and SWCNTs

TEM images have been taken for both MWCNTs and SWCNTs, as shown in Fig. 1. Tabular structures can be seen in these images. FE-SEM images have also been taken for MWCNTs and SWCNTs, which are shown as Fig. 2(a) and (b). The diameter of SWCNTs is found to be around 18.4 nm. The diameter of MWCNTs is about 23.9 nm.

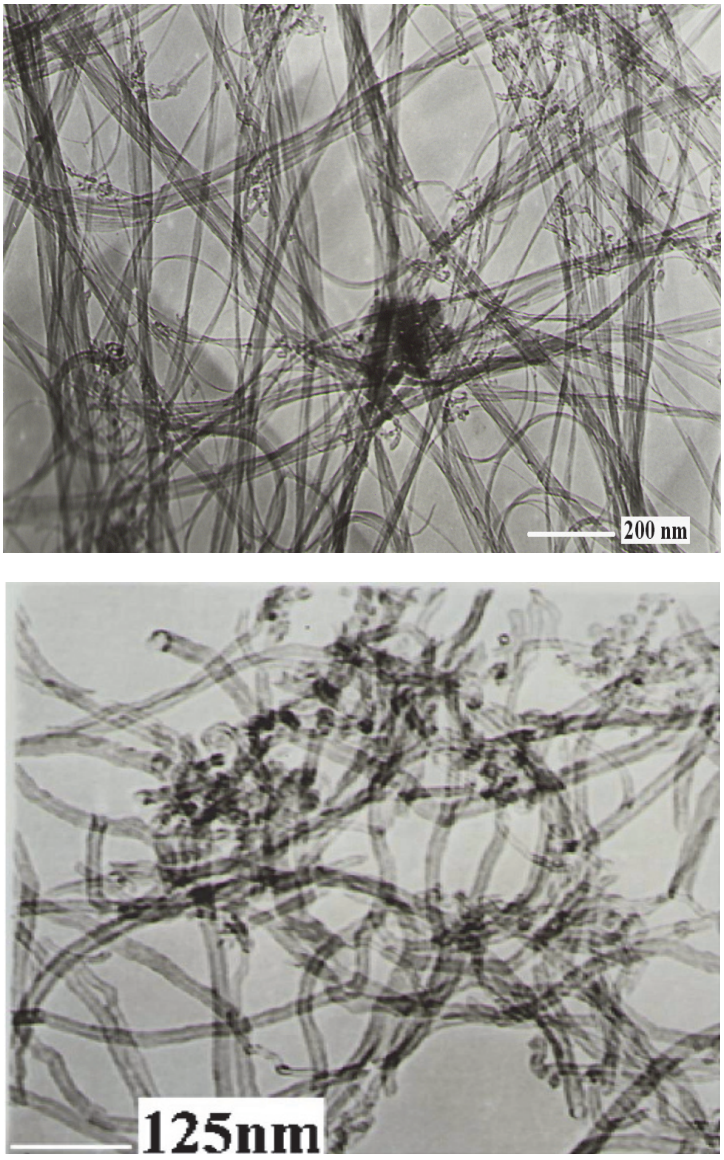

Fig. 1. TEM images of SWCNTs (a) and MWCNTs (b)

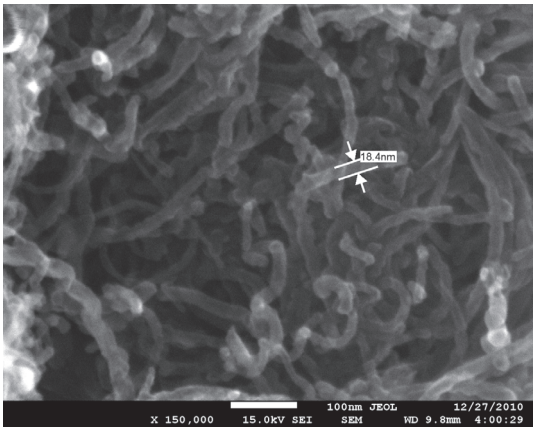

Fig. 2 (a). FE-SEM of SWCNTs

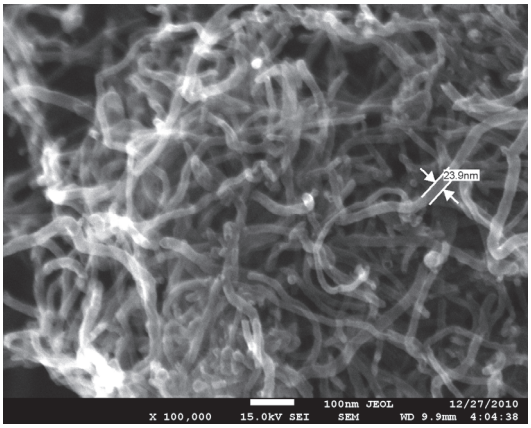

Fig. 2 (b). FE-SEM of MWCNTs

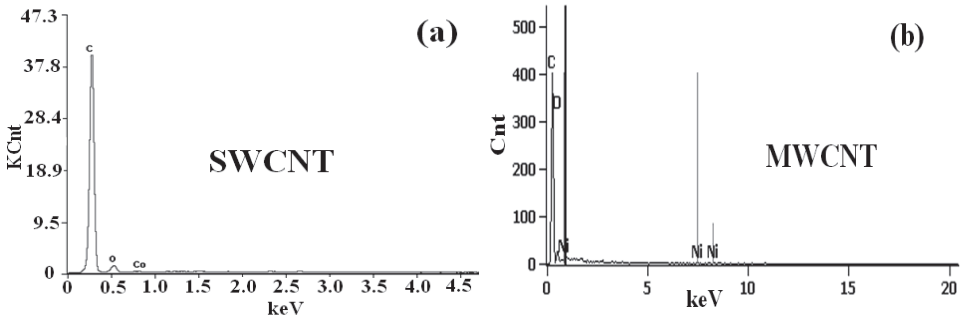

Fig. 3. EDX of SWCNTs in (a) and MWCNTs in (b)

4. The static magnetic properties of MWCNTs and SWCNTs

Usually, pure SWCNTs or MWCNTs should not exhibit ferromagnetic properties. However, many researchers have reported that CNTs exhibit weak ferromagnetic properties (Tang et al, 2008; Zhang et al, 2000; Kudo, et al, 2007).

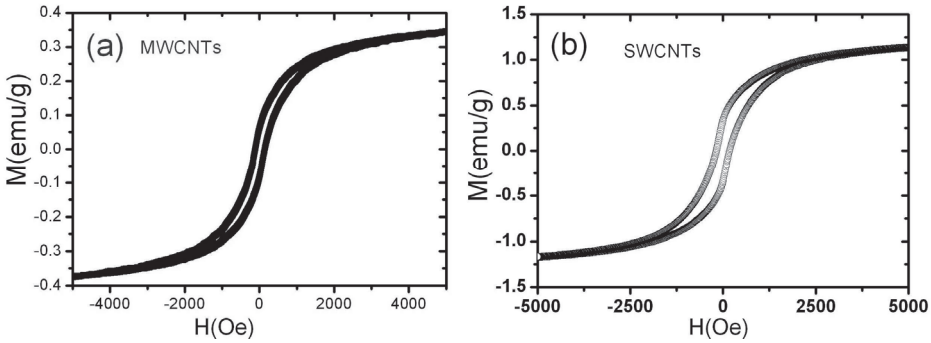

Fig. 4. Magnetic hysteresis loops of MWCNTs (a) and SWCNTs (b)

In this study, we have carried out the measurements of static magnetic properties. The measurement results are shown in Fig. 4(a) and (b). The results show that both MWCNTs and SWCNTs exhibit ferromagnetic properties. Especially, SWCNTs have stronger magnetic response in term of saturation magnetization (Ms). For SWCNTs, *Ms* value is about 1.17 emu/g. For MWCNTs, *Ms* is about 0.35. The coercivity (Hc) of SWCNTs is about 179.7 Oe. For MWCNTs, Hc value is about 127.5 Oe. Our EDS measurements show that there are a tiny amount of ferromagnetic substances can be found in MWCNTs or SWCNTs. For MWCNTs, the ferromagnetic impurity is nickel. For SWCNTs, the ferromagnetic impurity is cobalt. Therefore, we hypothesis that the observed weak ferromagnetic properties arise from the existence of ferromagnetic impurities in CNTs. The different static magnetic properties arise from the differences between Ni and Co.

5. Electromagnetic properties of MWCNTs and SWCNTS

According to Ref. (Watts et al, 2003), there are many factors making contributions to the dielectric properties: dielectric relaxation, resonance, the motion of conduction electrons, defects in the nanotubes, length, diameters, chirality, etc. Therefore, it will be extremely difficult to describe the permittivity dispersion behaviors of CNTs when taking into account of all these factors. Here, we assume that there are only two mechanisms making major contributions to the permittivity dispersion of MWCNTs. One is the general permittivity behaviors of dielectric materials which can be described by the Cole-Cole model (Cole et al 1941; Li, 1990), such as electrons polarization, charges polarization, etc. The other one is due to the motion of conducting electrons (Leon et al, 2001; Wu et al, 2004; Schultz et al, 2003). For instance, the contribution to the permittivity dispersion due to the conductivities has also been considered for carbon nanotubes composites in Ref. (Leon et al, 2001) and Ref. (Wu et al, 2004). In this chapter, we will adopt the following equations to fit the permittivity dispersion spectra. Eqs. 8 and 9 represent the contributions from the polarization of electrons, charges polarization.

$$\varepsilon' = \varepsilon_{r\infty} + (\varepsilon_{rs} - \varepsilon_{r\infty}) \frac{1 + (\omega\tau)^{1-\alpha} \sin(\pi\alpha / 2)}{1 + 2(\omega\tau)^{1-\alpha} \sin(\pi\alpha / 2) + (\omega\tau)^{2(1-\alpha)}} \tag{8}$$

$$\varepsilon'' = (\varepsilon_{rs} - \varepsilon_{r\infty}) \frac{(\omega\tau)^{1-\alpha} \cos(\pi\alpha / 2)}{1 + 2(\omega\tau)^{1-\alpha} \sin(\pi\alpha / 2) + (\omega\tau)^{2(1-\alpha)}} \tag{9}$$

where ε_0 is the permittivity in free space, ω is the angular frequency, $\varepsilon_{r\infty}$ is the permittivity when frequency is infinity, ε_{rs} is the static permittivity, τ is the relaxation time, α is the distribution of relaxation time ($0 \le \alpha \le 1$), and a smaller α value means a narrower distribution of relaxation time. The permittivity dispersion behaviors have been studied based on the Cole-Cole law, and are shown by the dotted line in Fig. 5(a) and Fig. 6(a). The fitting results are given in Table 1.

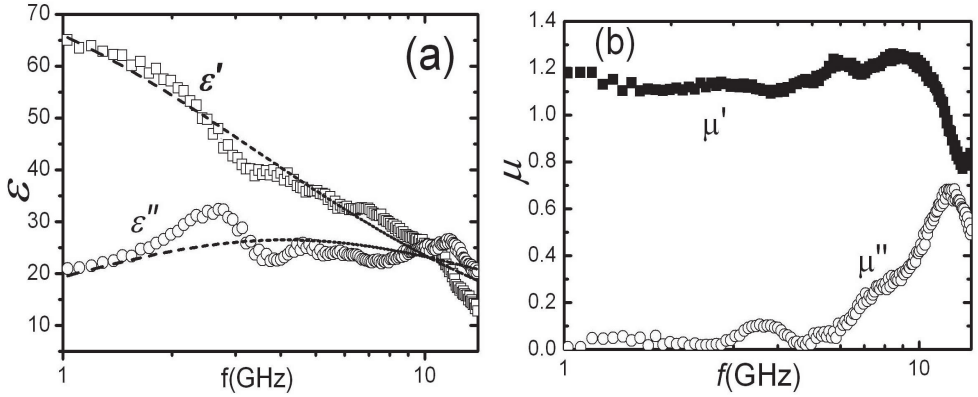

Fig. 5. High frequency permittivity and permeability dispersion spectra of SWCNTs-wax composites (SWCNTs: wax = 1: 5)

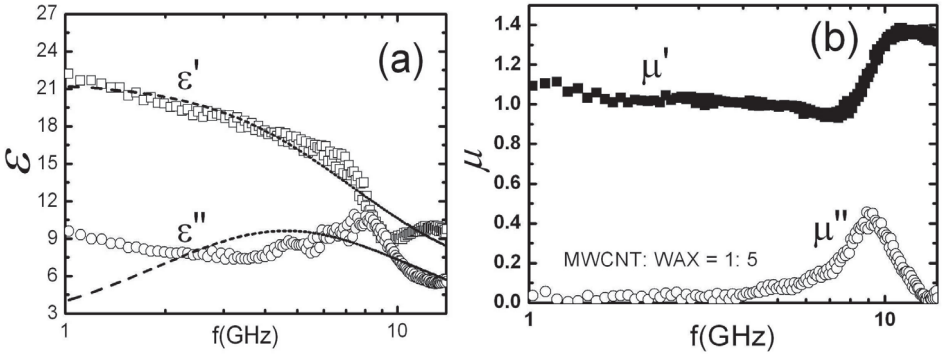

Fig. 6. High frequency permittivity and permeability dispersion spectra of MWCNTs-wax composites

Samples	τ	α	ε_{rs}	$\varepsilon_{r\infty}$
SWCNTs	4.57×10^{-11}	0.31	86.56	1.28×10^{-11}
MWCNTs	2.20×10^{-11}	3.24×10^{-15}	21.52	4.92

Table 1. Fitting results of permittivity spectra of MWCNTs and SWCNTs

As indicated in Table 1, in comparison to SWCNTs, MWCNTs have a smaller static permittivity value and smaller α value which means MWCNTs have a narrower distribution of polarization relaxation time. The dependences of permeability on frequency have been shown in Fig. 5(b) and Fig. 6(b) for SWCNTs and MWCNTs respectively. A major dispersion peak has been seen in each graph, which might be due to the existence of ferromagnetic impurity. For SWCNTs, the major resonance peak is around 12.4 GHz, while the major resonance peak of MWCNTs is found to be about 8.9 GHz. As we mentioned, SWCNTs contain a small quantity of Co. MWCNTs contain a small quantity of Ni, see Fig. 3(a) and (b). According to the Snoek' law (Snoek J. 1948): $(\mu_s\text{-}1)f_r = (2/3)\gamma' 4\pi M_0$, where f_r is proportional to the magnetocrystalline field. Therefore, the observed differences in permeability dispersion behaviors arise from their difference static properties. Such as the magnetocrystalline anisotropy of Co is larger than that of Ni, which will result in SWCNTs will have a larger resonance frequency than MWCNTs. With the obtained values of permittivity and permeability of the material under study, usually we can then evaluate the performance of electromagnetic absorber made from this material. The electromagnetic wave absorbing property of an absorber are dependent on six parameters, such as the thickness (t) of the absorber, ε', ε'', μ', μ'' and frequency (f). The criterion of absorption performance usually is expressed by the reflection loss (RL) in dB unit. Based on the measured complex permittivity and permeability, and we assume that a single layer of carbon nanotubes/paraffin composite is attached on a metal plate, then the electromagnetic wave absorbing properties usually can be evaluated by the following equation(Naito et al, 1971; Maeda et al, 2004):

$$RL = 20\log\left|(Z_{in} - Z_0)/(Z_{in} + Z_0)\right| \tag{10}$$

, where Z_0 is the impedance of free space, Z_{in} is the input impedance of the absorber, which can be expressed as:

$$Z_{in} = Z_0\sqrt{\mu_r/\varepsilon_r}\tanh\{j(2\pi ft/c)\sqrt{\mu_r\varepsilon_r}\} \tag{11}$$

, where c is the speed of light. Fig. 7 is a 3-dimensions graph which clearly shows the electromagnetic wave absorption properties of carbon nanotube/paraffin composite with different thickness within the measurement frequency range of 1-14 GHz. The color bar in Fig. 7 indicates different RL values in dB unit corresponding to different colors. Fig. 7(a) and (b) have shown the electromagnetic wave absorption properties of CNTs absorbers with different thickness (1-10 mm) within 1 – 14 GHz. It is clearly shown that MWCNTs have better electromagnetic wave absorption properties in terms of RL value. The minimum RL value of MWCNTs is about -20 dB. However, the minimum value of RL is -9.5 dB for SWCNTs. For many applications, the RL value smaller than -10 dB is accepted. A two-dimension contour map can be used to clearly show the electromagnetic wave absorption properties of absorbers with different thickness, which are given in Fig. 8(a). Learned from this map, the RL value of MWCNTs is less than -10 dB except for the

frequency range of 6-10 GHz and with the thickness ranging from 2.2 mm -3 mm. Especially, a thin MWCNTs absorber with a thickness of 1.62 mm can have an excellent absorption property (RL = -20 dB). Several examples showing the reflection loss of MWCNTs have been given for thickness of 1.62 mm, 2 mm, 4 mm and 6 mm, please see Fig. 8(b). The bandwidth with the RL value less than -10dB is respectively 0.56 GHz, 0.73 GHz, 1.90 GHz and 2.85 GHz for the thickness (t) as 6 mm, 4 mm, 2 mm and 1.62 mm. Compared with Fig. 8(b), Fig. 8(a) can give a straightforward presentation on the bandwidth of an absorber with different thickness.

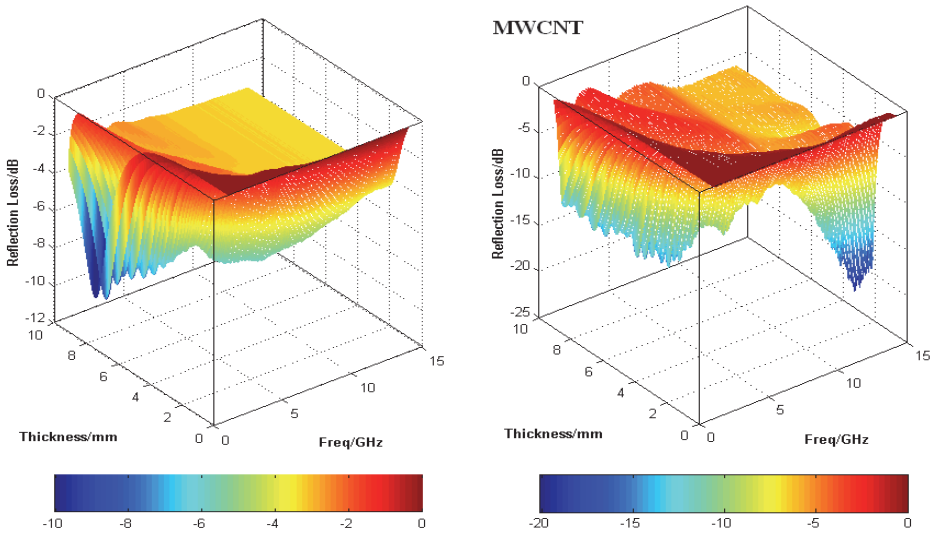

Fig. 7. (a) Reflection loss of SWCNTs (1:5 wax) ; (b) MWCNTs (1:5 wax)

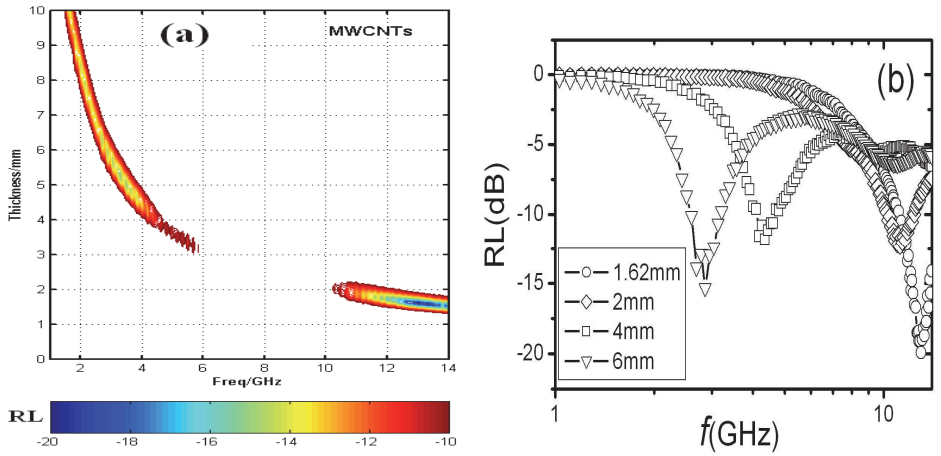

Fig. 8. (a) Contour map indicating the RL values less than -10 dB; (b) the RL~ f spectra of an absorber with different thickness values.

6. Doping effects of CNTs on electromagnetic properties of ferrites

Generally speaking, two well separated peaks are rarely observed in NiZn spinel ferrites in GHz range. However, as shown in Fig. 9(a), two peaks are found in the spectrum of u'' – f for sample 0 (NiCoZn ferrite / wax composite). For these two peaks, one is at 1.76 GHz, the other one is at 6.8 GHz. It is well accepted that there are two mechanisms responsible for the permeability dispersion of power ferrites. One is the domain wall motion, and the other one is the spin rotation. The resonance frequency of domain wall motion (i. e. f_{dw}) is lower than the one for the spin rotation (i. e. f_r). The permeability dispersion curve of pure MWCNT is shown in Fig. 6(b). The observed permeability of MWCNT is believed due to the residual nano-sized Ni particles on MWCNT. For sample 1, 2, the magnetic materials contributing to the permeability spectrum shape include ferrite and Ni. For such hybrid magnetic composites containing two ferromagnetic substances, the dispersion curve is extremely difficult to be expressed by superposing the magnetic spectrum of each magnetic material. Similar situation has been reported in permalloy-NiZn ferrite hybrid composite materials by Kasagi et al (Kasagi et al, 2004). Also, if the permeability dispersion curve is badly distorted, the dispersion curve would be very difficult to be fitted by assuming it comprises two component spectra: one is for domain wall movement; one is for spin resonance.

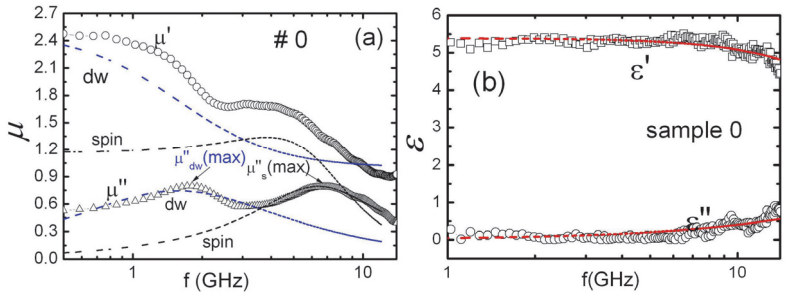

Fig. 9. High frequency properties of sample 0, (a) permeability spectra; (b) permittivity spectra, "*dw*" denotes the domain wall component. "*spin*" denotes the spin rotation component.

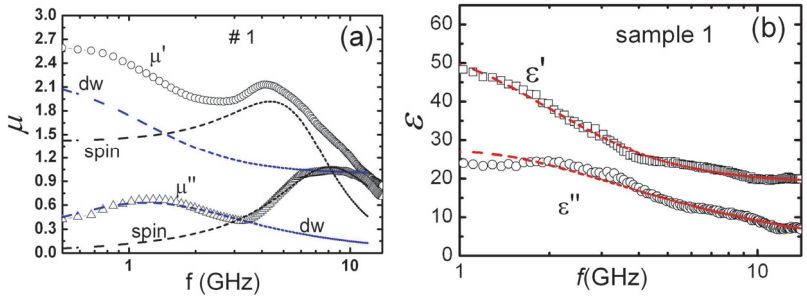

Fig. 10. High frequency properties of sample 1, (a) permeability spectra; (b) permittivity spectra.

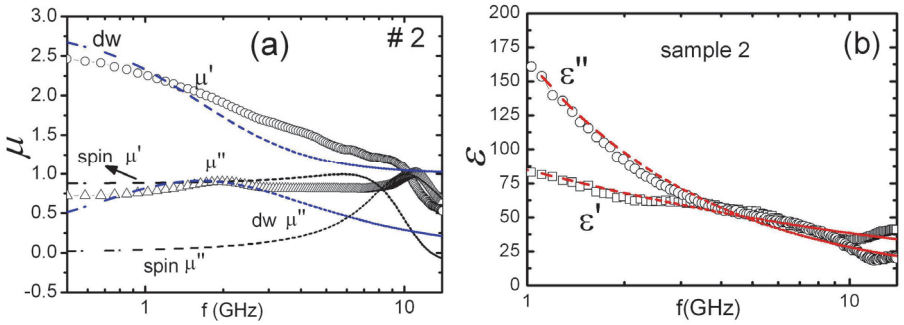

Fig. 11. High frequency properties of sample 2, (a) permeability spectra (b) permittivity spectra

Based on the spectrum shape, we learn that the spectra in Fig. 9(a) are the relaxation type because no negative μ′ values have been observed. Therefore, the resonances at lower frequencies in Fig. 9(a), 10(a) and 11(a) are due to the domain wall movement mechanism. The resonances at higher frequencies are due to the spin rotation mechanism. In Fig. 9(a), f_{dw} and f_s are 1.76 GHz, 6.80 GHz respectively for sample 0 without MWCNT. In Fig. 10 (a), f_{dw} and f_s are 1.28 GHz, 8.03 GHz for sample 1 with 5.2 wt% MWCNT. In Fig. 11 (a), f_{dw} and f_s are 1.98 GHz, 11.08 GHz for sample 2 with 10.4 wt% MWCNT. Clearly, the doping effect of MWCNT on the resonance frequency of spin rotation is much significant than that of domain wall movement. For the domain wall resonance with a relaxation type spectrum, the real part and imaginary part of permeability can be expressed by the Debye's dispersion law (Liao, 1988):

$$\mu_{dw}^{'} = 1 + \chi_{d0} \frac{1}{[1-(f/f_{dw})^2]} \tag{12}$$

$$\mu_{dw}^{''} = \chi_{d0} \frac{f/f_{dw}}{[1-(f/f_{dw})^2]} \tag{13}$$

, where χ_{d0} is the static susceptibility for domain wall movement. The resonance frequency f_{dw} above can be expressed by physical parameters as (Liao, 1988): $f_{dw} = (9\ \pi\ \sigma_{wall}\ \rho) / (8\ a\ \mu_0^2\ Ms^2)$, where σ_{wall} is the density of domain wall energy, a is the average distance of impurities in a ferrite particle which impede the domain wall movements. ρ is the electric resistivity of ferrite. Ms is the saturation magnetization. In our case, the ferrites in different composite samples are same. Hence, σ_{wall} can be considered as a constant. The particle size of ferrites is about 2~3 μm. Multi domains can exist in each ferrite particle, so the parameter a can be assumed as a constant. Then, as shown in this equation, f_{dw} is dependent on ρ and Ms. It is well known that MWCNT is a substance with very low resistivity and weak ferromagnetism. Doped with MWCNT, both ρ and Ms of ferrite-wax composite will drop. Qualitively speaking, for sample 1, we can conjure that the drop in ρ is stronger than the drop in Ms, hence f_{dw} is lower than the one for sample 0.

As for the spin resonance frequency f_s, it depends on (Rado,1953): $f_s = (\gamma/2\pi)\ H_A$, where γ is the gyromagnetic ratio, H_A is the effective magnetic anisotropic field. In our case, the

permeability spectrum due to the spin rotation mechanism is a relaxation type. Accordingly it can be expressed as (Tsutaoka 2003):

$$\mu_s^{'} = 1 + \frac{\chi_{s0}\omega_s^2[(\omega_s^2 - \omega^2) + \omega^2\alpha^2]}{[\omega_s^2 - \omega^2(1+\alpha^2)]^2 + 4\omega^2\omega_s^2\alpha^2} \tag{14}$$

$$\mu_s^{''} = \frac{\chi_{s0}\omega_s\omega\alpha[\omega_s^2 + \omega^2(1+\alpha^2)]}{[\omega_s^2 - \omega^2(1+\alpha^2)]^2 + 4\omega^2\omega_s^2\alpha^2} \tag{15}$$

, where χ_{s0} is the static susceptibility for spin rotation; ω_s is the angular resonance frequency; α is the damping factor for spin rotation. ω is the angular frequency of alternating magnetic field.

Fitting the experimental curves in Fig. 9(a), 10(a) and 11(a) with combined equations for μ′-f (equations (12) + (14)) and μ″-f (equations (13) + (15)) respectively is found extremely difficult. Therefore, we have separately fitted the peaks for spin rotation component (designated as "spin") and domain wall component (designated as "dw") in the spectra: Firstly, we fit each peaks in the μ''-f curves. Secondly, we calculate the μ'-f curves by using the obtained fitting parameters and corresponding μ′ expressions (equation 12 or 14). The fitting results are shown in Fig. 9 (a), 10(a) and 11(a). The fitting parameters are listed in Table 2. f_s (exp) is the frequency at which the μ″ value of the spin rotation component reaches a maximum value on the experimental curve. f_{dw} (exp) has a similar definition for the domain wall component on the experimental curve. As shown clearly in Table 2, the damping factor α of spin rotation mechanism is monotonously decreased with the increase of the MWCNT contents in the composites. For spin rotation resonance, the maximum frequency f_s(max), which is defined as the frequency at which μ″ reaches a maximum value, can be derived from the equation (8) as (Tsutaoka 2003): $f_s(\max) = f_s / \sqrt{\alpha^2 + 1}$. With the obtained fitting parameters, the calculated $f_s(max)$ values are also listed in Table 2. The small difference between the experimental $f_s(exp)$ values and the fitted f_s (max) values indicate that our fitting method makes senses.

Sample	Domain wall motion			Spin rotation				
	f_{dw}	f_{dw}(exp)	χ_{d0}	f_s	f_s(exp)	f_s(max)	χ_{s0}	α
# 0	1.57(GHz)	1.76 (GHz)	1.49	9.42 GHz	6.80(GHz)	6.39(GHz)	1.167	1.08
# 1	1.20(GHz)	1.28 (GHz)	1.26	10.73 GHz	8.03(GHz)	8.12(GHz)	1.411	0.86
# 2	1.63(GHz)	1.98 (GHz)	1.83	11.37 GHz	11.08(GHz)	10.20(GHz)	0.881	0.49

Table 2. Fitting parameters for permeability dispersion curves, where f_{dw}(exp) and f_s (exp) denote the frequencies at which the μ'' values on experimental curves reach maximum for domain wall motion component and spin rotation component respectively. f_s(max) is the calculated value, please see its definition in the text. f_{dw}, f_s, χ_{d0}, χ_{s0} and α are the fitting parameters.

Tsutaoka reported that in ferrite/resin composites, both f_{dw} and f_s increased with the decrease of the volume fraction of Ni-Zn ferrites (Tsutaoka 2003). They ascribed this to the gap parameter (δ/D) in ferrite composites. According to their theory, a sphere ferrite particle (or a particle cluster) with a diameter of D is supposed to be enclosed by a layer of nonmagnetic substance, such as epoxy resin. The thickness of nonmagnetic layer is $\delta/2$. f_{dw} and f_r can be expressed respectively as: $f_{dw} = f_{B-dw}(1+\chi_{B-dw}\frac{\delta}{D})^{1/2}$ and $f_s = f_{B-s}(1+\chi_{B-s}\frac{\delta}{D})$, where $\chi_{B\text{-}dw}$ ($f_{B\text{-}dw}$) and $\chi_{B\text{-}s}$ ($f_{B\text{-}s}$) are the static susceptibility (resonance frequency) of bulk ferrite for domain wall motion and spin rotation mechanisms respectively. As the concentration of nonmagnetic material increases (i.e., the concentration of magnetic material decreases), the δ/D value increases. According to Tsutaoka's theory (Tsutaoka 2003), it is clear that both f_{dw} and f_s increase with the decrease of ferrite content. However, in our case, the f_{dw} value is not monotonously increased with the decrease of the ferrite content (83 wt%, 78 wt%, and 72.9 wt% for sample 0, 1, 2 respectively). For instance, f_{dw} in sample 1 is lower than those in sample 0 and 2, see Table 2. Furthermore, we also found that with more MWCNT (15.6 wt %) added in the composite studied, the dispersion curve will be seriously distorted. In addition, the permeability behaviors of the MWCNT/NiCoZn ferrites/wax hybrid composites are different from the one reported by Tsutaoka (Tsutaoka 2003). Such an unusual behavior is believed due to the interactions between the MWCNTs and the NiCoZn ferrite particles. Interactions maybe occur between the residual nano-sized Ni particles in MWCNT and NiCoZn ferrites particles, or between the MWCNT and NiCoZn particles. Further investigation will be conducted in the future. The variation of permeability peak shapes also indirectly manifests the existence of such an interaction.

The permittivity spectra for NiCoZn/MWCNT/wax hybrid composites are shown in Fig. 9(b), 10(b) and 11(b). For sample without MWCNT (sample 0), the ε values are almost constant within the measurement frequency range: ε' is about 5 and ε″ is about 0, showing a typical feature of ferrite in GHz range. With increasing the MWCNT contents in composites (sample 1 and 2), both ε' and ε'' increase within the frequency range, and both are gradually decreased with increasing frequency. Especially, for sample 2, there is a clear inverse proportion relationship between ε'' and frequency. This is a typical feature of a conducting media and shows that with more MWCNT added into the studied composite, it will become a conducting composite due to the high conductivity of MWCNT. At lower frequency range of 0.5 GHz - 6 GHz, sample 2 shows a significant dielectric loss, please see the ε″/ε′ values in Fig. 12.

Samples	τ(s)	α	ε_{rs}	$\varepsilon_{r\infty}$
#0	3.89×10^{-12}	1.39×10^{-14}	5.38	1.18×10^{-13}
#1	7.94×10^{-11}	1.08×10^{-16}	57.38	18.89
#2	6.70×10^{-10}	0.57	249.00	2.05

Table 3. Fitting results of permittivity spectra of sample 0, 1 and 2.

The permittivity dispersion spectra of these three samples have been studied based on the previous Cole-Cole dispersion law. The fitting spectra shown as the dotted lines are also presented in the above figures. The fitting results are given in Table 3. It is clear that both the static permittivity value (ε_{rs}) and the relaxation time (τ) increase with more MWCNTs added into the ferrites.

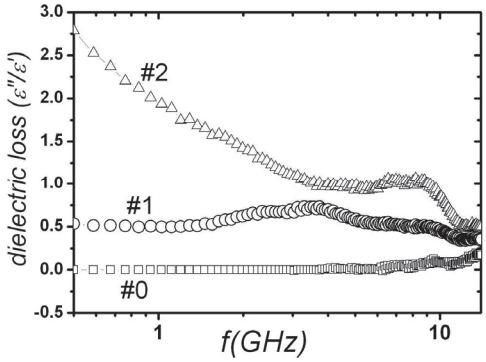

Fig. 12. Dielectric loss of ferrites doped with different amount of MWCNTs

7. Conclusions

In this chapter, we have studied the static properties of MWCNTs and SWCNTs. Our results show that the observed ferromagnetic properties are believed due to the residual ferromagnetic substances from the CNTs fabrication processes. Employing the Cole-Cole permittivity dispersion law, the high frequency permittivity properties have been explained for MWCNTs and SWCNTs. The observed high frequency permeability properties are also thought to be due to the ferromagnetic impurities in MWCNTs and SWCNTs. The microwave absorption properties of MWCNTs are better than those of SWCNTs in terms of reflection loss (RL) and absorption bandwidth. Our experimental results show that the high frequency properties of spinel ferrites can be effectively tuned by doping them with a small amount of MWCNTs. Especially, the permittivity of ferrites can be greatly altered by doping with MWCNTs, for instance, the dielectric loss. Both the resonance peaks of permeability spectra and values are seen to be altered by doping with MWCNTs.

8. Acknowledgments

This work is financially supported by NSFC (No. 60701016), the Prior Research of the State Key Development Program for Basic Research of China (No.2010CB334702), Fundamental Research Funds for the Central Universities (No.ZYGX2009J036), and National Science Foundation for Distinguished Young Scholars of China (No.51025208).

9. References

Cespedes O., Ferreira M. S., Sanvito S., Kociak M., D. Coey J. M., (2004). Contact induced magnetism in carbon nanotubes, *J. Phys.: Condens. Matter,* Vol. 16, L115-L117.

Chen L. F., Ong C. K., Neo C. P., Varadan V. V., Varadan V. K., (2004). *Microwave electronics-Measurement and Material Characterization*, John Wiley & Sons Ltd, ISBN 0-470-84492-2, England.

Chen W. B., Han M., Deng L. J. (2010). High frequency microwave absorbing properties of cobalt nanowires with transverse magnetocrystalline anisotropy, P*hysica B*, Vol. 405, 1484-1488.

Cole K. S., Cole R. H., (1941). Dispersion and Absorption in Dielectrics, *J. Chem. Phys.* Vol. 9, 341-343.

Coey J. M. D., Venkatesan M., Fitzgerald C. B., Douvalis A. P., Sanders I. S. (2002). Ferromagnetism of a graphite nodule from the Canyon Diablo meteorite, *Nature,* Vol. 420, 156-158.

Han M., Lu H. P., and Deng L. J. (2010). Control of gigahertz permeability and permittivity dispersion by means of nanocrystallization in FeCo based nanocrystalline alloy, *Appl. Phys. Lett.* Vol. 97, 1925071-1925073.

Han M., Tang W., Chen W.B., Zhou H., Deng L. J. (2010). Effect of shape of Fe particles on their electromagnetic properties within 1–18 GHz range, *J. Appl. Phys*, Vol. 107, 09A9581-09A9583.

Han M., Ou Y., Deng L. J. (2009). Microwave absorption properties of double-layer absorbers made of NiCoZn ferrites and hollow glass microspheres electroless plated with FeCoNiB , *J. Magn. Magn. Mater.* Vol. 321, 1125-1129.

Han M., Ou Y., Liang D. F., and Deng L. J. (2009). Annealing effects on the microwave permittivity and permeability properties of Fe79Si16B5 microwires and their microwave absorption performances, *Chin. Phys. B*, Vol. 18, No 3, 1261-1265.

Iijima S. (1991). Helical microtubules of graphitic carbon, *Nature*, Vol. 354, 56-58.

Kasagi T., Tsutaoka T., Hatakeyama K. (2004). Complex permeability of permalloy-ferrite hybrid composite materials, J. *Magn. Magn. Mater.* Vol. 272-276, 2224-2226.

Kim H. M., Kim K., Lee C. Y., Joo J., Cho S. J., Pejakovic D. A., Yoo J. W., Epstein A. J. (2004). Electrical conductivity and electromagnetic interference shielding of multiwalled carbon nanotube composites containing Fe catalyst, *Appl Phys. Lett.* Vol. 84, 589-591.

Kudo Y., Hira T., Ishii S., Morisato T., Ohno K. (2007). Interaction between Fe and single-walled carbon nanotube near the entrance, J. *Phys.: Conf. Ser.* Vol. 61, 633-637.

Leon C., Rivera A., Varez A., Sanz J., and Santamaria J., (2001). Origin of constant loss in ionic conductors, *Phys. Rev. Lett. Vol.* 86, 1279-1281.

Liao S. B. (1988). *Ferromagnetism* (in Chinese), Sciences Publishing House, Beijing.

Li H. R. (1990). *Introduction to Physics of Dielectrics*, 1st ed. University of Science and Technology of Chengdu, Chengdu.

Lu R. T., Shi J. J., Baca F. J., Wu J. Z. (2010). High performance multiwall carbon nanotube bolometers, *J. Appl. Phys.* Vol. 108, 084305-084309.

Maeda T., Sugimoto S., Kagotani T., Tezuka N., and Inomata K. (2004). Effect of the soft/hard exchange interaction on natural resonance frequency and electromagnetic wave absorption of the rare earth-iron-boron compounds, *J. Magn. Magn. Mater.* Vol. 281, No. 2-3, 195-205.

Mintmire J. W., Dunlap B. I., White C. T. (1992). Are fullerene tubules metallic? *Phys. Rev. Lett.* Vol. 68, 631-634.

Naito Y. and Suetake K. (1971). Application of ferrite to electromagnetic wave absorber and its characteristics, I*EEE Trans. Microw. Theory Techn.* Vol. 19, No. 1, 65-72.

Nakata T., Watanabe M. (2011). Nanometer-resolution optical probe using a metallic-nanoparticle-intercalated carbon nanotube, *J. Appl. Phys.* Vol.109, 013110-013114.

Poncharal P., Wang Z. L., Ugarte D., de Heer W. A. (1999). Electrostatic deflections and electromechanical resonances of carbon nanotubes, *Science,* Vol. 283, No. 5407, 1513-1516.

Rado G. (1953). Magnetic spectra of ferrites, *Rev. Mod. Phys.* Vol. 25, 81-89.

Schultz J. W. and Moore R. L. (2003). Effective Medium Calculations of the Electromagnetic Behavior of Single Walled Carbon Nanotube Composites, *Mater. Res. Soc. Symp. Proc.* Vol. 739,151-153.

Snoek J. L. (1948). Dispersion and Absorption in Magnetic Ferrites at Frequencies above One Megacycle, *Physica*, Vol. 14, No. 4, 207-217.

Stamenov P., Coey J. M. D. (2005). Magnetic susceptibility of carbon--experiment and theory, *J. Magn. Magn. Mater.* Vol. 290-291, No. 1, 279-285.

Tang N. J., Zhong W., Au C. K., Yang Y., Han M., Lin K, J., Du Y. W. (2008). Synthesis, Microwave Electromagnetic, and Microwave Absorption Properties of Twin Carbon Nanocoils, *J. Phys. Chem. C*, Vol. 112, No. 49, 19316-19323.

Tooski S. B. (2011). Theoretical study of carbon-nanotube-based gas pressure sensors, *J. Appl. Phys.* Vol. 109, 014318-014324.

Tsutaoka T. (2003). Frequency dispersion of complex permeability in Mn–Zn and Ni–Zn spinel ferrites and their composite materials, *J. Appl. Phys.*, Vol. 93, 2789-2796.

Watts P. C. P., Hsu W. K., Barnes A., and Chambers B. (2003). High Permittivity from Defective Multiwalled Carbon Nanotubes in the X–Band, *Adv. Mater.* Vol. 15, No. 7-8, 600-603.

Matitsine S. M., Liu L., Chen L. F., Gan Y. B., and Ong C. K. (2005). Comment on "High microwave permittivity of multiwalled carbon nanotube composites", *Appl. Phys. Lett.* Vol. 87, 0161011-0161013.

Wu J. H., Kong L. B. (2004). High microwave permittivity of multiwalled carbon nanotube composites, *Appl. Phys. Lett.* Vol. 84, 49561-49563.

Wang L., Dang Z. M. (2005). Carbon nanotube composites with high dielectric constant at low percolation threshold, *Appl. Phys. Lett.* Vol. 87, 0429031-0429033.

Xie J. L., Han M., Chen L., Kuang R. X. , Deng L. J. (2007). Microwave-absorbing properties of NiCoZn spinel ferrites, *J. Magn. Magn. Mater.* Vol. 314, 37-42.

Xu Y., Zhang Y., Suhir E. (2006). Thermal properties of carbon nanotube array used for integrated circuit cooling, *J. Appl. Phys.* Vol. 100, 074302-074306.

Zhang Y., Franklin N. W., Chen R. J., and Dai H. (2000). Metal coating on suspended carbon nanotubes and its implication to metal-tube interaction, *Chem. Phys. Lett.* Vol. 331, No. 1, 35-41.

Zhao G. L., Bagayoko D., Yang L.(2006). Optical properties of aligned carbon nanotube mats for photonic applications, *J. Appl. Phys.* 99, 114311-114315.

Part 3

Devices and Applications

13

Application of Carbon Nanotubes to Mirror Actuators for Space Laser Communications

Yoshihisa Takayama and Morio Toyoshima
National Institute of Information and Communications Technology
Japan

1. Introduction

Recently free-space laser communications attract attentions as one of the promising technologies to provide broadband wireless communications. Especially in the inter-satellite communications and the satellite-ground communications, the successful demonstrations showed the possibilities of the laser communications for the practical use (Tolker-Nielsen, 2002; Jono, 2006; Smutny, 2008; Toyoshima, 2009; Perlot, 2007).
Concerning the laser communication equipment used in those demonstrations, the designs are mutually different but some functions are commonly used. The typical example is a function to control the direction of the telescope. Some terminals have a motorized gimbals system to hold a telescope and control the direction of the aperture. The other terminals use a set of mirrors put in front of a fixed telescope aperture, and the direction of the telescope view is changed by using the reflection of the mirrors. These direction steering functions are usually employed for the coarse pointing of a communicating object. In the internal optics of the communication equipment, two sets of moving mirrors are found in most cases. One is a set of fast steering mirrors for the fine pointing mechanisms and the other is a similar set of mirrors to give a point-ahead angle to the emitted laser beam. Since the laser communications require accurate pointing for stable communications, the fine pointing mechanisms are necessary to eliminate the angular errors remained after the coarse tracking by the telescope. Besides, when the laser communications are carried out between moving objects, the fast velocities of satellites and the large distance between communicating terminals require the point-ahead angles (Miller, 1993). So far, in those kinds of functions, the tilt angle of the mirrors is controlled by piezoelectric actuators, voice coils, micro-electro-mechanical systems, diaphragms with electromagnetic torque, spherical motors, and so on (Aoki, 2004; Suhonen, 2001; Bandera, 1999; Langenbach, 2005).
When equipment is mounted in a satellite, we should care that the resources such as the mass, the volume and the consumption power for the equipment are severely restricted. Therefore, devices of light weight, small size and low power consumption are useful for constructing those tracking and pointing mechanisms.
On the other hand, in the field of electro-active polymer actuators, many research activities have been reported to develop materials responding to applied stimuli such as temperature, magnetism and electricity (Baughman, 1999; Jordan, 2007; Lu, 2008). Those materials are aimed to be utilized in biomimetic motions, micro-electro-mechanical-systems, sensors, and precise positioners. The features of the polymer actuators are the low voltage operations, light weight,

large stretching characteristics and mechanically simple structure which conform to the requirements for constructing small, light and low power consumption laser communications equipment. Furthermore the flexibility in the shape design implies the applicability of the actuator in various manners. Therefore, we look at the possibilities of the actuators to be applied to the moving parts in the laser communication terminals (Takayama, 2010).
The polymer actuators require wet for operation because the fundamental is swell due to ionic mobility. Therefore if the actuators are used in the steering mirror functions, especially in space environment, an approach to prevent the evaporation of moisture becomes necessary. As the solution to suppress the evaporation of moisture, the use of the ionic liquid is one of the effective approaches.
In this chapter, we would like to study a potential of the polymer actuators to be used in the optical terminals. First, we show a typical example of a laser communication terminal and introduce the functions that consist of mechanical steering parts. Second, we perform numerical analyses to study the operation requirements on those parts. For the study, a scenario in which an optical ground station and a satellite in a low earth orbit carry out laser communications is assumed. The angular operations of the movable parts to track the communicating counter object are estimated. As the third step, we fabricate a prototype of a carbon nanotube actuator that is employed as a steering function of the reflection angle of a mirror. By using this sample, the angular operation characteristics of the actuator are investigated. Here we employ a perfluorosulfonic acid ionomer, an imidazole tetrafluoroborate for the fabrication processes as the ionic liquid and carbon single-walled nanotube covered with a gold layer for the electrode. With changing the applied voltage to the actuator, the mirror's reflection angle is measured.

2. Space laser communication terminal and requirements on actuators operation characteristics

In this section, we provide a sample structure of a laser communication terminal in order to identify the movable parts discussed here. These are the intended potential targets to be replaced with the carbon actuators. The roles of the steering functions are introduced respectively and the required angular operations of those movable parts are calculated with assuming a scenario in which the optical ground station and a satellite perform the laser communications.

2.1 Optical communication terminal

An example of optical terminals for space laser communications is shown in the figure 1, where the solid bold lines indicate the propagating paths of the received beam and the dashed bold lines show the path of the transmitted beam. In most cases, three mechanically movable parts, the coarse pointing function, the fine pointing function and the point-ahead function, are contained.
The coarse pointing function controls the pointing direction of the telescope to keep looking at the communicating object. If the object moves, the telescope tracks the object. The optical characteristics are dependent on the design of the communication system. But as an example of a terminal successfully operated in space, we have that the field-of-view of the telescope is ±0.2deg and the tracking accuracy is within ±0.01deg (Jono, 2006).
Even if the coarse pointing function controls the direction of the telescope aperture precisely, the arrival angle of the received beam still changes within the tracking accuracy of

the coarse pointing function. Therefore the fine pointing function is employed to eliminate such small but rapid angular changes remaining in the received beam. The continuous elimination of the angular uncertainty in the arrival beam is equivalent to instantaneously find the precise direction of the communicating counter object as well as providing the stable illumination of the optical receiver to detect the signal.
When the communicating object moves fast, angular compensation is required in the pointing direction of the beam transmission. The difference between the arrival angle of the received beam and the pointing direction of the transmission beam is observed when the travel distance of the counter object cannot be ignored during the period of the propagation of light. The point-ahead function gives the compensation angle to the propagation direction of the transmitted light.
These three functions have their own optical sensors as shown in the figure 1. The coarse pointing and the fine pointing functions use the sensors to detect the received light for the closed-loop steering, while the sensor of the point-ahead function detects the transmitted light.

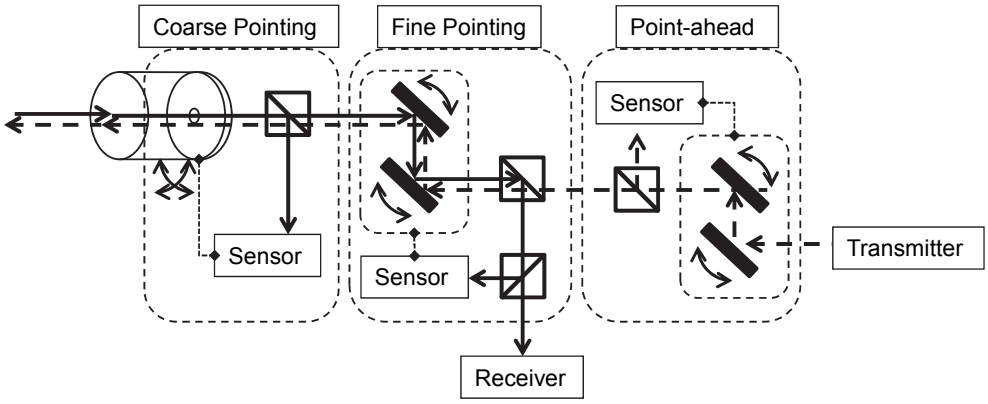

Fig. 1. Schematic drawing of an optical communication terminal. The solid bold lines indicate the optical path of the received beam and the dashed bold lines are the path of the transmitted beam.

2.2 Requirement in angular movement for coarse pointing

To estimate the angular range of the moving parts in the optical terminal, we focus on the satellite-ground laser communications. Here we assume to track the International Space Station (ISS) as the one of the widely recognized satellites by using an optical ground station. The ISS orbits the earth at an altitude of about 400 km which is regarded as a low earth orbit.
The direction of the communicating counter object can be described by the pair of angles of the azimuth and the elevation. In the case of the ground stations, the basis to measure these angles is the horizontal plane and the zenith at the ground station. But in the case of the satellite, the basis depends on the satellite attitude. Since the satellite attitude changes with orbiting the earth, we concentrate on the azimuth angle and the elevation angle at a ground station in the following analysis for the sake of simplicity.
The date of the orbit computation is assumed as 2nd Oct. 2010, for instance. The azimuth angle and the elevation angle measured at the ground stations to track the ISS are shown in

the figures 2(a) and 2(b), respectively. In these figures, the curves labelled with (1) are the calculation results for the optical ground station located in Tokyo, Japan. The latitude and the longitude are given as 35.7deg and 139.5deg, respectively. For the labels of (2)-(5), we keep the latitude of the ground station as the same as 35.7deg but change the longitude as 149.5deg, 159.deg, 169.5deg, and 219.5deg, respectively, in order to obtain the different maximum elevation angles. The corresponding maximum elevation angles are obtained as 34.3deg, 64.2deg, 88.6deg, 87.9deg and 56.3deg for (1)-(5).

The figure 3(a) and 3(b) are the absolute values of the azimuth angle rate and the elevation angle rate obtained from the figures 2(a) and 2(b). Concerning the angular rates for the azimuth and the elevation angles, faster motion is required in the azimuth for the case of high elevation angles. Theoretically the rotation velocity around the azimuth axis is required to be infinite if the ground station tracks the object passing right above the zenith of the ground station.

According to those calculations shown in the figures 2 and 3, the requirement in angular movement is that the angular range of the azimuth should be more than 360deg, and the range of the elevation is from 0 to 90deg. The rate of the angular motion is more than 48deg/s for the azimuth if we intend to track a satellite passing almost right above the ground station, while the rate is less than 1.2deg/s for the elevation.

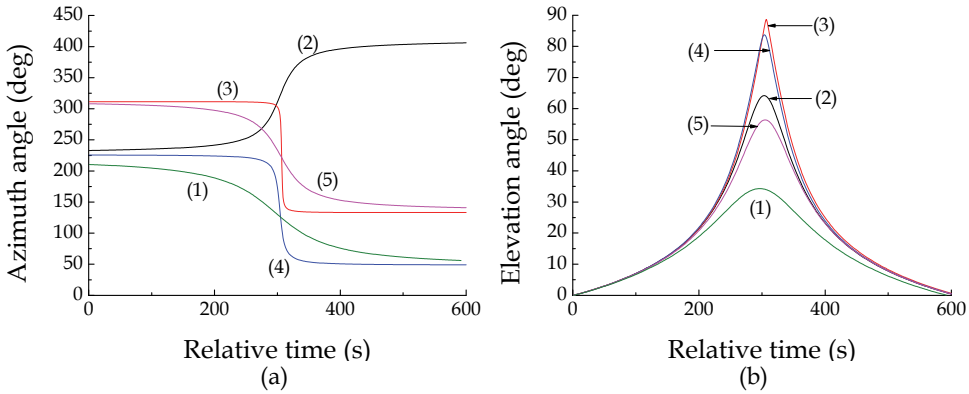

Fig. 2. (a) Azimuth angle and (b) elevation angle at ground station to track the ISS. The labels (1)-(5) indicate the observation points. The longitude is 139.5deg for the label (1), 149.5deg for (2), 159.5deg for (3), 169.5deg for (4) and 219.5deg for (5). The location's latitude is fixed as 35.7deg.

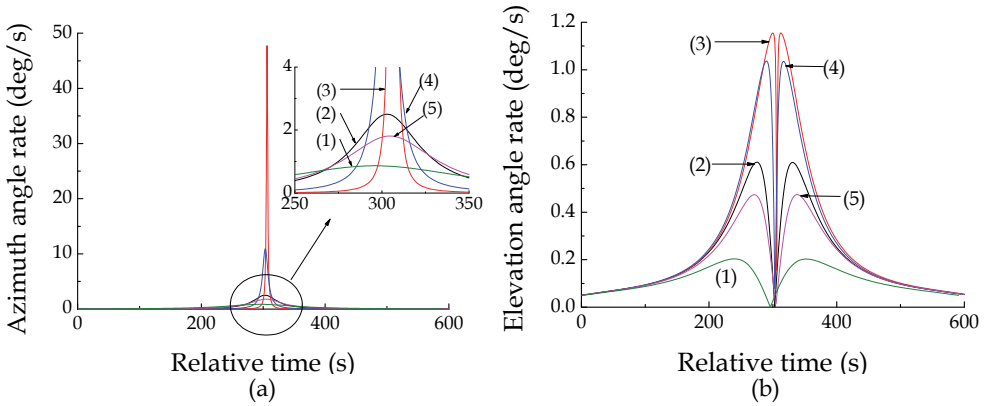

Fig. 3. Absolute values of (a) azimuth angle rate and (b) elevation angle rate to track the ISS.

2.3 Requirement in angular movement for fine pointing and point-ahead functions

The coarse pointing function steers the telescope to track the communicating object and the fine pointing function compensates the remaining propagation angle of the received beam inside the optical terminal as shown in the figure 1. In most cases, the propagation angle of the received beam led to the internal optics is magnified by a certain times. If the tracking accuracy of the coarse pointing function is given as ±0.01deg (Jono, 2006), and if he magnification is 10 times for example, the propagation angle range of the received beam in the internal optics extends to ±0.1deg. This could be regarded as the angular coverage for the fine pointing function.

The required point-ahead angle is dependent on the tangential component of the moving speed of the object. The orbiting velocity of the satellite v_{sat} is given as a function of the altitude as

$$v_{sat} = sqrt\left(g_c / \left(r_e + h_{sat} \right) \right) \tag{1}$$

, where g_c is the gravitational constant times mass of Earth, r_e is the radius of the earth, and h_{sat} is the altitude of a satellite (Miller, 1993). We set that g_c=398600.5km^3/s^2 and r_e=6378.14km and plot the velocity in the figure 4, where the abscissa axis is the altitude of a satellite. In this figure, the velocity is given as the left-hand ordinate axis. The velocity of a satellite is about 3km/s at the altitude of 36000km, and about 7.7km/s at the altitude of 400km.

The point-ahead angle θ_{PA} is given as

$$\theta_{PA} = 2v_{\tan} / c \tag{2}$$

, where v_{tan} is the tangential component of the object velocity and c is the velocity of the light (Miller, 1993). If we assume that the ground station locates in the orbit plane of a satellite and tracks the satellite passing through the zenith of the station, v_{tan} in the equation (2) becomes equivalent to v_{sat} in the equation (1). In this case, the point-ahead angle is proportional to the velocity. Therefore, the computed result is shown in the figure 4 with the right-hand ordinate axis. According to the result, the point-ahead angle is obtained as about 51μrad for the satellite at the altitude of 400km, and about 20μrad for the altitude of 36000km.

When the satellite is in a geostationary orbit, the elevation angle looking at it from the ground station is unchanged. But if the satellite is in a low earth orbit, the elevation angle at the ground station changes to track the satellite. Since the tangential component of a satellite depend on the elevation angle at the ground station, we calculate the point-ahead angle as a function of the elevation angle. The result is shown in the figure 5, where the altitude of a satellite is assumed as 400km, for instance. Besides, the angle rate for the point-ahead is shown in figure 6 as the same case as the label (3) in the figures 2 and 3. As a result, it is found that the angle rate could be less than 0.37μrad.

In the end of this section, it should be noted that among the three steering functions of the coarse pointing, the fine pointing and the point-ahead, only the fine pointing function needs the repeated back and forth motion, because the role of the fine pointing function is the compensation of the angular errors. On the other hand, the control manners of the coarse pointing function and the point-ahead function are monotonically increasing or decreasing as shown in the figures 2 and 5.

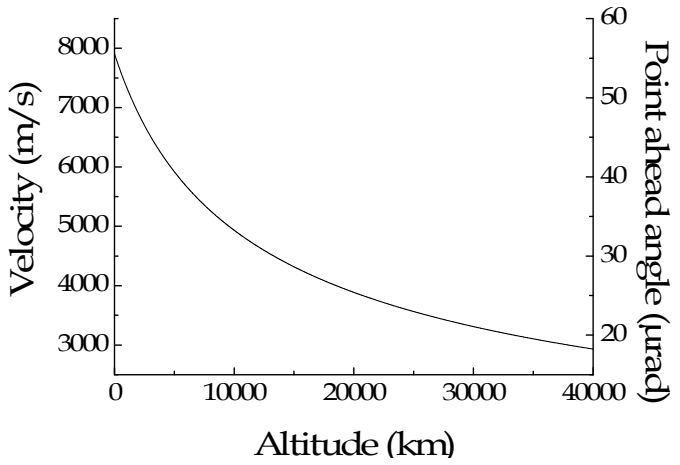

Fig. 4. Velocity of satellite as a function of the orbit altitude (the left-hand ordinate) and the point-ahead angle (the right-hand ordinate) in the case that the satellite passes through the zenith of the ground station.

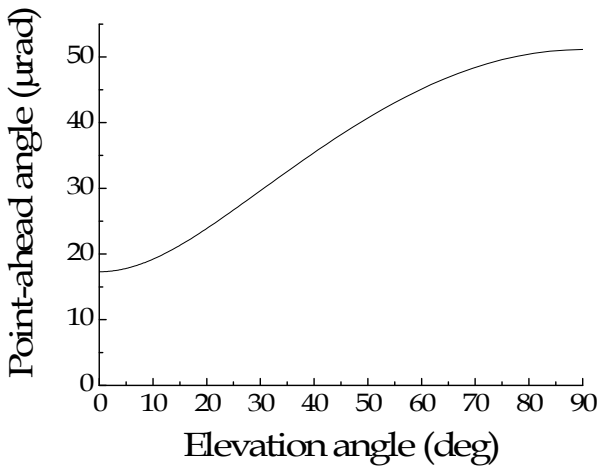

Fig. 5. Point-ahead angle as a function of the elevation angle at the ground station. The altitude of the satellite to be tracked is in a low earth orbit at the altitude of 400km.

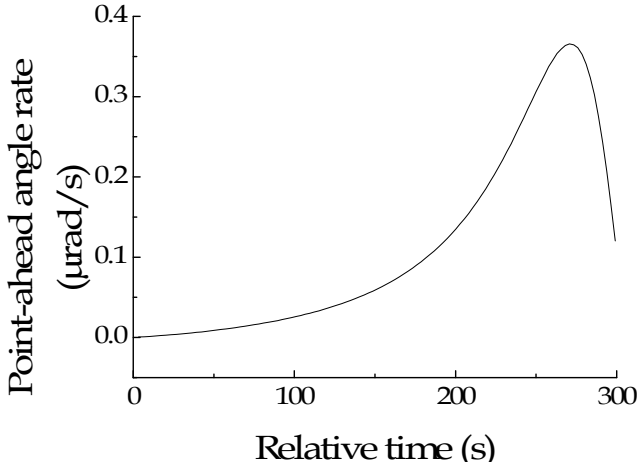

Fig. 6. Point-ahead angle rate when the maximum elevation angle at the ground station reaches 88.6 deg.

3. Trial production of actuator and its operation characteristics

We introduce the structure of the actuator prepared for the estimation of the operation characteristics. The fabricated sample is employed to the tilt mirror actuator. The mirror's reflection angle is changed with the applied voltage and is experimentally measured. With the results, we show the feasibility of the carbon nanotube actuators to be used in the laser communication equipment.

3.1 Preparation of sample

A schematic drawing of the actuator's structure is shown in the figure 7. The polymer layer is an admixture of the carbon nanotube, the ionic liquid of 1-ethyl-3-methyl-1H-imidazole-3-ium tetrafluoroboron(IV) (C6H11N2BF4) and a perfluorosulfonic acid ionomer, Nafion ® . This layer is placed between the carbon single-walled nanotube (SWNT) sheets and covered with the gold electrodes.

The figure 8(a) is a photograph of the SWNT sheets and 8(b) shows the polymer layer. The carbon nanotube is mixed with water by using ultrasonic agitation and dried to make the sheets. The fabrication of the polymer layer also uses the ultrasonic agitation to obtain the admixture paste. The paste is sandwiched between the carbon nanotube sheets and the shape is arranged.

The layered sheet covered with gold electrode is shown in the figure 9. The thickness of the gold is about 30nm. This sheet is cut to make 3 pieces actuators of the size 8mm×12mm×0.4mm. Those pieces are arranged in rotational symmetry by 120deg around the center-axis to support a mirror as shown in the figure 10. The mirror has a diameter of 20mm and is simply put on the actuators.

The actuator piece bends with applied voltage as shown in the figure 11. The bending turns in the opposite direction when the applied electrical polarity is reversed. The cross-section image of the tilt mirror is shown in the figure 12, where the notation θ is the tilt angle of the mirror and the arrows indicates the incident beam and the reflected beam.

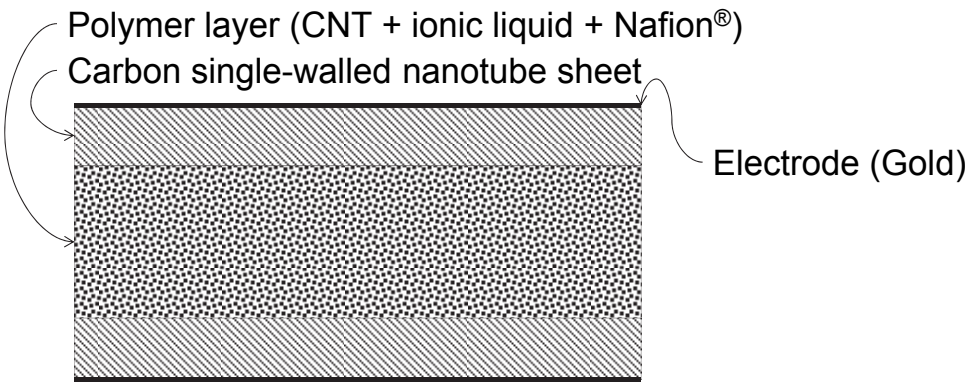

Fig. 7. Structure of the polymer actuator. Polymer layer is an admixture of CNT, ionic liquid and Nafion and is covered with CNT sheet and the gold electrode.

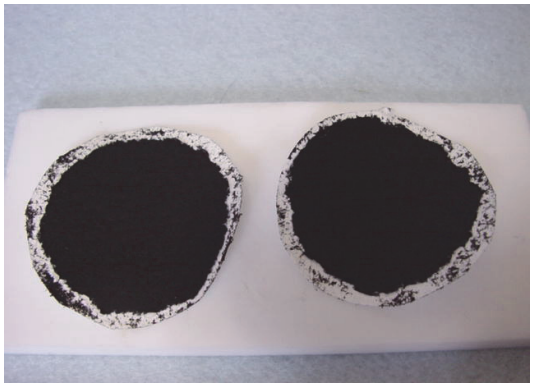

(a)

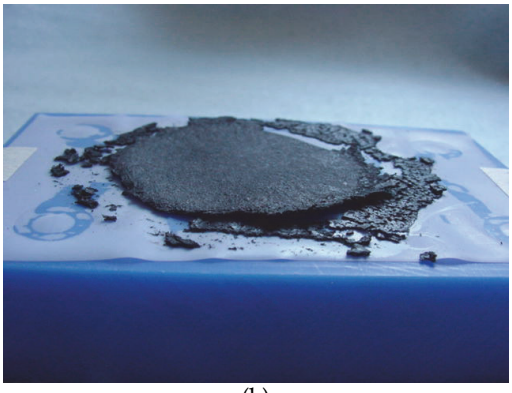

(b)

Fig. 8. (a) Carbon single-walled nanotube sheet, and (b) polymer layer with CNT, ionic liquid and Nafion® .

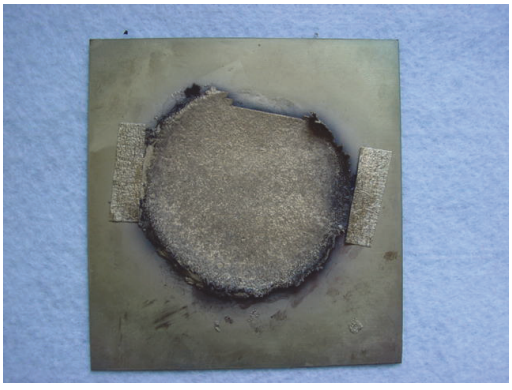

Fig. 9. Carbon nanotube sheet covered with gold.

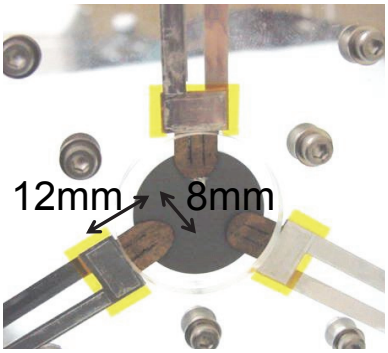

(a)

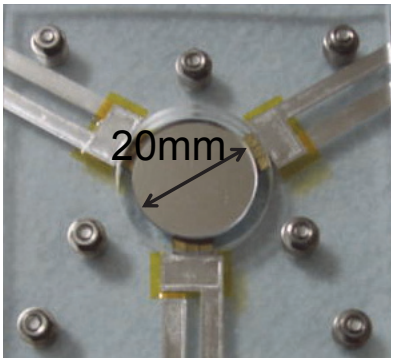

(b)

Fig. 10. Mirror supported with three carbon nanotube pieces arranged in rotational symmetry by 120deg. (a) the back side view and (b) the front side view.

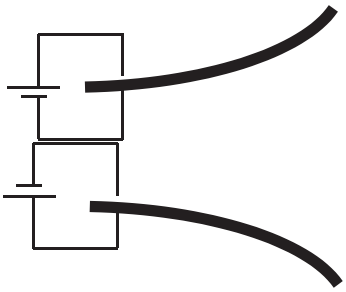

Fig. 11. Bending of actuator. The bending direction is changed with the polarity of the applied voltage.

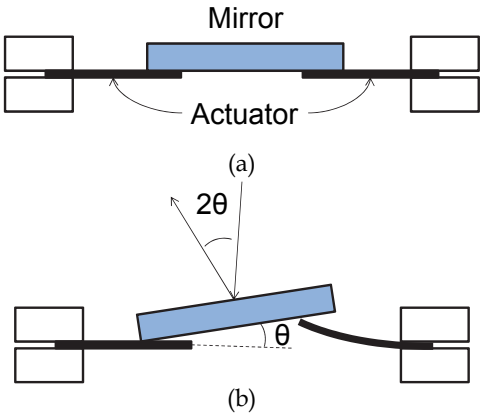

Fig. 12. (a) Cross-section of the tilt mirror, and (b) the reflection angle of light.

3.2 Operation characteristics

The bending angle of the carbon nanotube actuator depends on the applied voltage. First we carry out a long period observation of the tilt angle with the applied voltage of 2V. The measured tilt angle is shown in the figure 13, where a single actuator of the three is activated for the observation. The tilt angle is observed up to 4.4deg. Since the time taken to show such a bending angle is long, the response time should be improved much faster. But when the maximum tilt angle is only focused on, the operation range of the tilt mirror seems to cover the angular range required in the internal optics. The sample estimation for the fine pointing function in the above section indicated that the angular range to be compensated in the internal optics is within 0.1deg if the coarse pointing function steer the telescope within the accuracy of 0.01deg and the magnification factor of the internal optics is 10. That implies that even if the coarse pointing accuracy is degraded to 0.1deg, the angular range to be covered is 1.0deg and is still within the observed tilt angle.

To look at the transient characteristics around the rising period, we plot the curves in the figure 14 with the applied voltages of 1-3V, respectively. For the measurement, one of the actuators notated with the black triangle in the inset image is operated. In this figure, the circle with the solid black line bundles the plotted curves in which the tilt angles are measured along the solid arrow drawn in the inset. The circle with dashed black line means that the angles are measured along the dashed arrow direction. During the observation period, the angle variation reaches the stationary value in the case of applying 1.0V. The rising time from the 10% of the stationary value to the 90% value is estimated to 16.5 sec.

The rates of the tilt angles are calculated from the measured angles and plotted in the figure 15. The maximum rate is about 0.5mrad/s for the applied voltage of 1V, 1mrad/s for 2V and 1.25mrad/s for 3V.

To observe the transient characteristics of the back and forth motion, the voltages of +1V and -1V is applied alternately with 5s intervals. The measured results are shown in the figure 16(a). The upper image is the applied voltage and the bottom one is the measured tilt angle. According to the figure, the bending operation of the actuator seems to immediately respond to the change of the applied voltage. The peak-to-peak value ranges 1.2~1.3mrad which could be about 35% of the required angular range of ±0.1deg in the sample estimation

with the assumption of the 0.01deg accuracy for the coarse pointing and the magnification factor of 10 for the internal optics. When the voltages of ±2V are applied, the peak-to-speak value becomes about 3.3~3.6mrad as shown in the figure 16(b). This is almost the equal to the estimated angular range to be covered.
The angular rates corresponding to the figure 16(a) and 16(b) are plotted in the figure 17(a) and 17(b), respectively. According to these figures, the angular rates show almost the same transient characteristics after the several voltage alternations, which is appropriate for the fine pointing function.

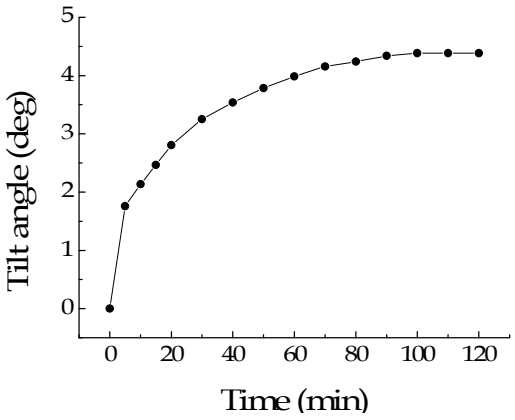

Fig. 13. A long period observation of the tilt angle of the mirror. The voltage of 2V is applied to one of the three actuators.

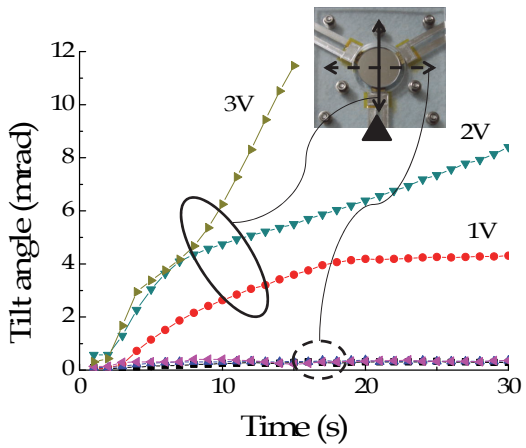

Fig. 14. Transient characteristics of the tilt angle around the rising period. The solid and dashed black circles indicate that the tilt angles are measured along the connected arrows in the inset image.

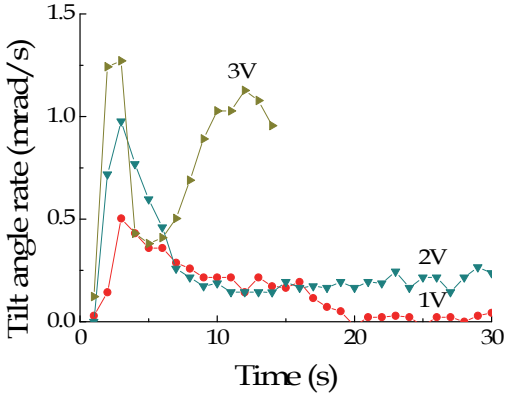

Fig. 15. Tilt angle rate around the rising period.

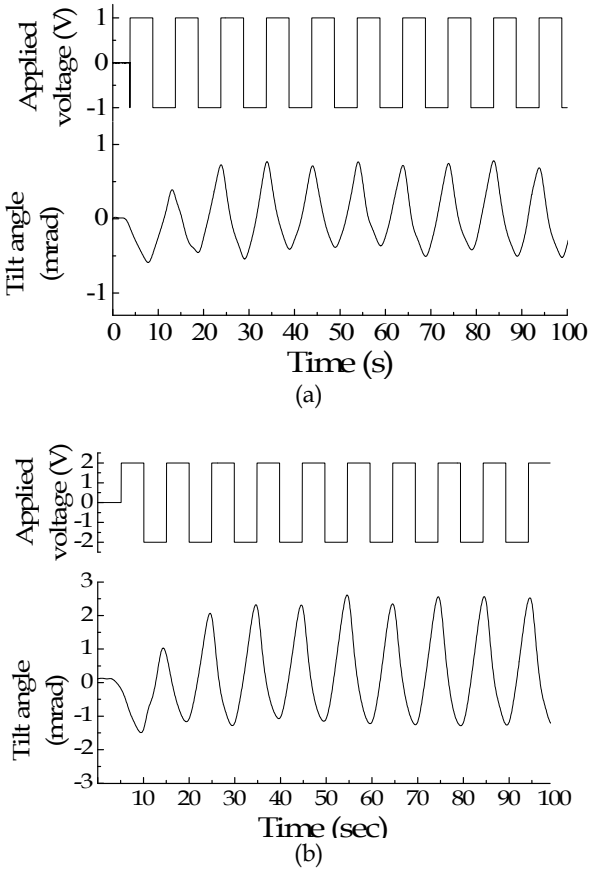

Fig. 16. Tilt angle with alternate change of applied voltage of (a) ±1V, and (b)±2V.

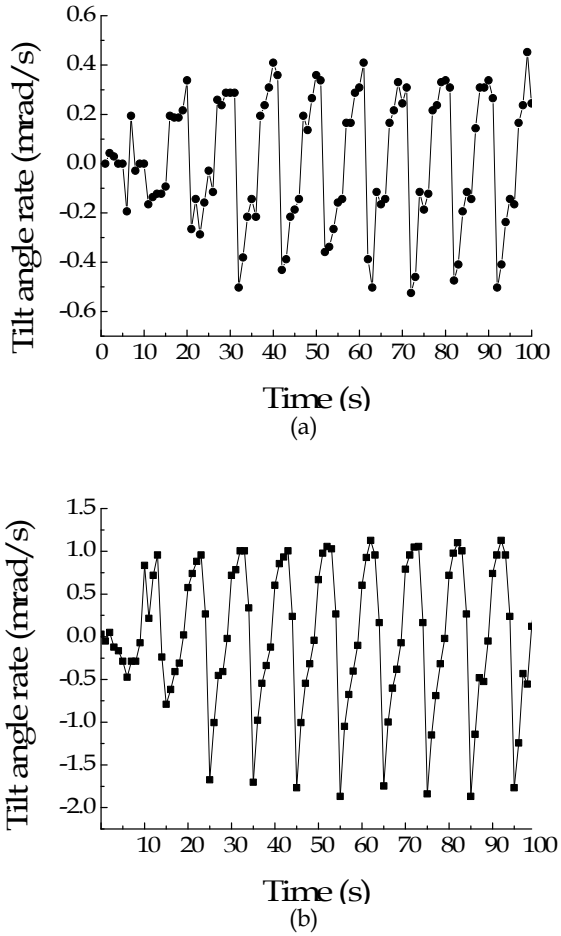

Fig. 17. Tilt angle rate with alternate change of applied voltage of (a) ±1V and (b)±2V.

4. Conclusion

In this chapter, we have carried out a feasibility study of carbon nanotube actuators as the steering functions for the optical communication terminals. We have shown a typical example of a laser communication terminal and introduced the functions of the coarse pointing, the fine pointing and the point-ahead functions as the candidates for the application of the actuators. The required characteristics for those functions are identified with the numerical analysis assuming a scenario in which a ground station tracks a satellite. We have fabricated a trial production of an actuator that is employed to make a steering function of the reflection angle of a mirror. The operation characteristics have been investigated experimentally to find the features adaptable to the laser communication equipment and the features to be improved.

Concerning the angular range, the trial production actuator should be much improved to be used in the coarse pointing function, but almost adaptable to the fine pointing and the point-ahead functions. For the angular rate, the actuator can satisfy the requirement of the point-ahead function, while the operation speed should be improved by 10times faster or more to be used in the coarse pointing function. Still the features of the carbon nanotube actuators such as the low voltage operations, light weight, simple structure, and the flexibility in the shape design are attractive for the steering functions in the optical communication terminal.

5. Acknowledgment

Taking advantage of the opportunity, we, the authors, would like to express the appreciation for the support of the Space link Co. Ltd. Tokyo Japan.

6. References

Aoki, K., Yanagita, Y., Kuroda, H. & Shiratama, K. (2004). Wide-range fine pointing mechanism for free-space laser communications, Free-Space Laser Communication and Active Laser Illumination III, Vol. 5160, pp. 495-503, ISBN 9780819450333, San Diego, CA, USA, Aug. 2003.

Bandera, P. (1999). A fine pointing mechanism for intersatellite laser communication, 8th European Space Mechanisms and Tribology Symposium, ISBN 10 9290927526, Toulouse, France, Sept. 1999.

Baughman, R. H., Cui, C., Zakhidov, A. A., Iqbal, Z., Barisci, J. N., Spinks, G. M., Wallace, G. G., Mazzoldi, A., Rossi, D. D., Rinzler, A. G., Jaschinski, O., Roth, S., Kertesz, M. (1999). Carbon nanotube actuators, Science, Vol. 284, pp. 1340-1344, ISSN 0036-8075.

Jono, T., Takayama, Y., Ohinata, K., Kura, N., Koyama, Y., Arai, K., Shiratama, K., Sodnik, Z., Bird, A. & Demelenne, B. (2006). Demonstrations of ARTEMIS-OICETS Inter-Satellite Laser Communications, 24th AIAA International Communications Satellite Systems Conference, AIAA-2006-5461, 1355, pp. 1-7, ISBN 1-56347-816-1, San Diego, CA, USA, Jun. 2006.

Jordan, G., Lyons, A. M. (2007). Thermomechanically driven polymer actuator for high-precision optical alignment, IEEE Photonics Tech. Lett., Vol. 19, pp. 212-214.

Langenbach, H., Schmid, M. (2005). Fast steering mirror for laser communication, European Space Mechanisms and Tribology Symposium, ISBN 10 9290929022, Lucerne, Switzerland, Sept. 2005.

Lu, J., Kim, S.-G., Lee, S., Oh, I.-K. (2008). Fabrication and actuation of electro-active polymer actuator based on PSMI-incorporated PVDF, Smart Mater. Struct. Vol. 17, pp. 045002-1-10.

Miller, M. J., Vucetic, B., Berry, L. (1993). Satellite Communications Mobile and Fixed Services, Kluwer Academic Publishers, Boston.

Perlot N., Knapek, M., Giggenbach, D. , Horwath, J., Brechtelsbauer M., Takayama, Y. & Jono, T. (2007). Results of the Optical Downlink Experiment KIODO from OICETS Satellite to Optical Ground Station Oberpfaffenhofen (OGS-OP), Proceedings of SPIE, Vol. 6457, pp. 645704-1-8, ISBN 9780819465733, San Jose, CA, USA, Feb. 2007.

Smutny, B., Lange, R., Kampfner, H., Dallmann, D., Muhlnikel, G., Reinhardt, M., Saucke, K., Sterr, U., Wandernoth, B. & Czichy, R. (2008). In-orbit verification of optical

inter-satellite communication links based on homodyne BPSK, Proceedings of SPIE, Vol. 6877, pp. 687702-1-6, ISBN 9780819470522, San Jose, CA, USA, Jan. 2008.

Suhonen, M., Graeffe, J., Sillanpää, T., Sipola, H., Eiden, M. (2001). Scanning micromechanical mirror for fine-pointing units of intersatellite optical links, Smart Materials and Structures, Vol. 10, pp. 1204-1210.

Tolker-Nielsen, T. & Oppenhaeuser, G. (2002). In-orbit test result of an operational optical intersatellite link between ARTEMIS and SPOT4, SILEX, *Proceedings of SPIE*, Vol. 4635, pp. 1-15, ISBN 9780819443748, San Jose, CA, USA, Jan. 2002.

Takayama, Y., Toyoshima, M., Abe, T. (2010). Low voltage actuator using carbon nanotube to tilt mirror angle, Proc. of SPIE Vol. 7587, pp. 75870K-1-6, Feb. 2010.

Toyoshima, M., Takenaka, H., Schaefer, C., Miyashita, N., Shoji, Y., Takayama, Y., Koyama, Y., Kunimori, H., Yamakawa, S. & Okamoto, E. (2009). Results from phase-4 Kirari Optical Communication Demonstration Experiments with the NICT optical ground station (KODEN), 27th AIAA International Communications Satellite Systems Conference, Vol. 13, pp. 1-9, ISBN 1-56347-941-9, Edinburgh, Scotland, Jun. 2009.

14

Sonophysically Exfoliated Individual Multi-Walled Carbon Nanotubes in Water Solution and Their Straightforward Route to Flexible Transparent Conductive Films

Wen-Yin Ko, Jun-Wei Su and Kuan-Jiuh Lin
Department of Chemistry, National Chung-Hsing University, Taiwan (ROC)

1. Introduction

Flexible transparent conducting films (TCFs) with low electric resistance and high optical transmittance have received considerable attention for niche applications such as flexible/foldable displays, touch screens, solar cells, transistors, and transparent electrodes for liquid crystal displays. (Calnan & Tiwari, 2010; Gruner, 2006; Heo et al., 2010; Jo et al., 2010; Takenobu et al., 2006) Deposition of indium tin oxide (ITO) onto plastic substrates to prepare the flexible TCFs has been an attractive strategy owing to its transparency, conductivity, and wide usability. (D. H. Kim et al., 2006; Lin et al., 2008; Na et al., 2008; Sierros et al., 2009; Wang et al., 2008) Nevertheless, the flexible ITO-based TCFs still suffer from several drawbacks. For example, the films are often prepared under vacuum and high temperature conditions, resulting in the limitation of their suitability for many polymer substrates such as polyethylene terephthalate (PET), which are often used in flexible devices and touch screen panels. Also, ITO is expensive owing to the limited supply of indium; it is brittle and will crack under a 2% strain, resulting in loss of conductivity. Furthermore, the film transparency is poor in the near-infrared range. (Feng et al., 2010; Manivannan et al., 2010; Park et al., 2010) Therefore, a substitute for ITO is necessary.

To address this issue, carbon nanotubes (CNTs), because of their high flexibility, specific surface area, low density, and excellent electrical, optical, and mechanical properties, have been regarded as the most promising alternative. CNTs have a preeminent status in nanomaterials and have a huge range of potential applications. (Z. R. Li et al., 2007; Paul & Kim, 2009; Simien et al., 2008) Single-walled CNT (SWCNT)–based conductors and semiconductors were used as the active material in the fabrication of flexible CNT-TCFs. Recent efforts towards the fabrication of SWCNTs on several substrates of glass, UV-ozone (UV-O3) treated glass, poly(styrenesulfonate) (PEDOT:PSS) coated glass, flexible PET films, and other substrates to form transparent conducting SWCNT films with sheet resistance and transparency equivalent to ITO have been attempted. These attempts used various approaches such as spin coating, spray coating, solution dipping where the SWCNTs were pre-formulated in combination with surfactants and polymers. (Chen et al.; Dan et al., 2009; Manivannan et al., 2010; Paul & Kim, 2009; Saran et al., 2004; Xiao et al., 2010) However, the

performance of SWCNT-based TCFs does not yet meet the industrial requirements because of their high cost and limited scalability. Furthermore, it is still difficult to purify and disperse SWCNTs in gas or liquid. To overcome these limitations, inexpensive multi-walled CNTs (MWCNTs) are required. A few methods for the fabrication of flexible TCFs using MWCNTs have been developed. (Feng et al., 2010; Kaempgen et al., 2005; Xu et al., 2008; Zhang et al., 2005) However, there are still only a few documented examples of the use of MWCNTs in the fabrication of flexible TCFs. This is because of the fact that MWCNTs self-aggregate into large bundles and ropes in aqueous solutions resulting from strong intertube van der Waals attractions (ca. 500 eV/μm) (Girifalco et al., 2000). Such aggregation results in a decrease of their unique physical properties, especially in their optical transparency in the visible spectrum. (O. K. Kim et al., 2003; Paloniemi et al., 2005)

Currently two approaches are widely applied to promote dispersion of the MWCNTs—the mechanical approach and the functionalization approach. Unfortunately, both methods have significant drawbacks. The mechanical approach including ultrasonication and high-shear mixing is a time-consuming, low-efficiency synthetic process and the stability of the resulting dispersion is poor. (Lu et al., 1996) The functionalization process involves the modification of the MWCNT surface with various surfactants and polymers by covalent and noncovalent methods. The covalent method, which involves the bonding of different chemical functional groups on the sidewalls of CNTs, can damage the structure of pristine nanotubes and alter their intrinsic properties. The noncovalent method, which involves adsorption of chemical moieties onto the surface of nanotubes via π–π stacking interaction or coulomb attraction results in a suspension with poor long-term because of the weak interactions between the chemical moieties and the surface of CNTs. (D. Li et al., 2003; Madni et al., 2010; Marsh et al., 2007; Rastogi et al., 2008) To overcome the above mentioned problems, the main object of the present invention is to provide a method for the rapid dispersion of MWCNTs in solvents such that the desirable properties of carbon nanotubes are retained and the resulting suspension is stable and uniform for a long time. Another objective of the present invention is to provide an agent that can calibrate the concentration of the carbon nanotubes. Thus, in this chapter, we first propose a sonophysically exfoliated method with the aid of surfactants or polymers that produces a homogeneous MWCNTs–water solution. Significantly, the resulting suspensions of water-soluble MWCNTs were homogeneous and the MWCNTs were uniformly dispersed for at least two years; neither sedimentation nor aggregation of nanotubes was observed. Furthermore, our sonophysically exfoliated method does not alter the crystalline and metallic electric properties; importantly, this dispersion is suitable for the determination of solubility and dispersion limits using concentration-dependent optical absorption spectrum. Next, porous MWCNT structures generated by ultrasonic atomization from a well-dispersed aqueous solution are spin-cast onto a poly(ethylene terephthalate) (PET) substrate to form a flexible conducting film (MWCNT-PET). Remarkably, the as-prepared film exhibits excellent sheet resistance, competitive transparency at 550 nm, and remarkable flexibility compared to other related transparent conducting materials such as ITO and SWCNTs.

2. Experimental detail

2.1 Synthesis and purification of MWCNTs

MWCNTs, with average diameters of 10-30 nm and lengths of 5-15 μm were prepared from a mixture of ethylene (C_2H_4) and methane (CH_4) by a high-temperature chemical vapor

deposition (CVD) process using the First Nano-EasyTube 2000 system and iron oxide powder as a catalyst (Figure 1a). The produced MWCNTs were further purified by treatment with concentrated hydrochloric acid, followed by washing with water and precipitation, and then were dried under vacuum. The dried MWCNTS were subsequently heat treated in air at 400 °C to remove amorphous carbons. The purity thus achieved > 99 wt%, as indicated by thermogravimetry analysis measurements (TGA, PERKIN ELMER TGA7792), shown in Figure 1b. Figure 1c represents the typical Raman spectrum of the as-prepared MWCNTs before and after purification. These peaks appeared at approximately the same position for all samples in which three significant Raman fingerprints were determined: *D*-band at ca. 1323 cm^{-1}, *G*-band at ca. 1578 cm^{-1}, and *G'*-band at ca. 2648 cm^{-1}. A decrease in the I_D/I_G ratio and an increase in the $I_{G'}/I_G$ ratio for purified MWCNTs relative to the as-prepared ones were noticed, which is indicative of the decrease of impurities and enhancement of MWCNT quality. Besides, the extremely high intensity of the G'-band and the narrow FWHM of the G-band and G'-band in our result reflect the purified MWCNTs are pure with a high degree of crystalline perfection and retain their metallic property.

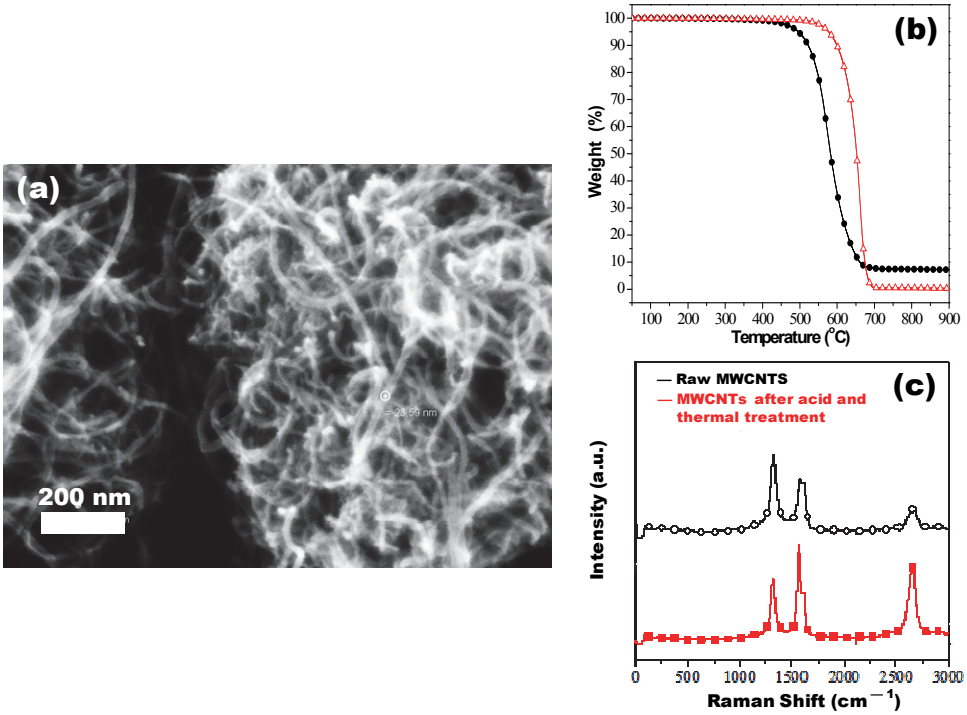

Fig. 1. (a) FESEM images of as-prepared MWCNTs by CVD, (b) TGA profiles, and (c) Raman spectra of MWCNTs with (red) and without (black) purification.

2.2 Dispersion of MWCNTs

In order to obtain a well-dispersed and homogeneous MWCNT-solution, we mixed 250 mg/L MWCNTs into 500 mg/L aqueous solution in the presence of sodium dodecyl sulfate

(SDS) surfactant and then sonicated the suspension using a probe type sonicator (SONICS® VCX750, supplied by Sonics & Materials, Inc.) at 20% of the maximum power (750 W) for 5 minutes as well as at 39% of the maximum power for 5 min so as to prevent the aggregation of the MWCNTs. Initially, the processes of formation, growth, and implosive collapse of acoustic cavitation bubbles induced by the probe-type sonicator would generate the requisite energy at the CNT-CNT interface to cause individual CNTs exfoliation. (Su et al., 2009; Thiruvengadathan et al., 2007) Then, the SDS micelles wrap around the individual MWCNTs and prohibit the aggregation of the nanotubes thereby resulting in a stable and homogenous MWCNT aqueous suspension.

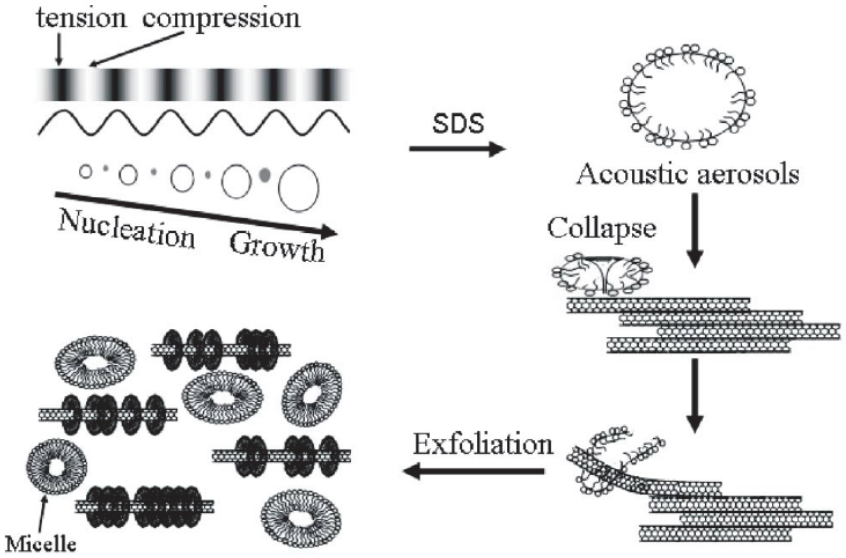

Fig. 2. Schematic of surfactant-assisted ultrasonication routes to carbon nanotube dispersion in aqueous solution.

2.3 Fabrication of MWCNT-PET transparent thin films

Polyethylene terephthalate (PET) substrates (3M, Transparency Film, Made in E.U. 0.10 mm, KB-9997-4219-4, 4 × 4 cm) were used in the present experiments. Ultrasonic atomization, a technique of producing a fine spray from a liquid, is a relatively inexpensive technique for the continuous production of micro- and nano-sized materials to assist the production of large-sized films by spin coating. It involves the generation and subsequent deposition of a mist of micron-sized droplets from a humidifier onto the surface of a substrate. Next, the water evaporated and the solute precipitated to form products. (Su et al., 2008) All the steps in the preparation of CNT-based TCFs were carried out using our designed ultrasonic atomization-spin coating equipment, as shown in Figure 3. For the fabrication of the MWCNT-PET conducting films, first, isolation of the MWCNTs is needed. This involves the formation of atomized particles ranging from 1 to 50 μm in size including carbon nanotubes, prepared by the atomization of the homogeneous carbon nanotube solution (10 mg/L), which has a viscosity ranging from 1 to 50 c.p. The atomization was controlled by tuning the

amount of SDS surfactants at room temperature at a supersonic atomizing frequency of 20 KHz-2.45 MHz and atomizing rate of 25-30 mL/h in an ultrasonic atomizer (Pro-Wave Electronic Corp M165D25). The frequency of the supersonic atomizing member for producing the atomized particles with desirable size can be determined from the following formula: (Miller, 1984)

$$D=\alpha\left(\frac{8\pi T}{\rho f^2}\right)^{\frac{1}{3}}$$

wherein:
D is the particle size of the atomized particles;
T is a surface tension coefficient (N/cm);
ρ is the density of the carbon nanotube solution;
f is the supersonic atomizing frequency; and
α is a constant of 0.34.

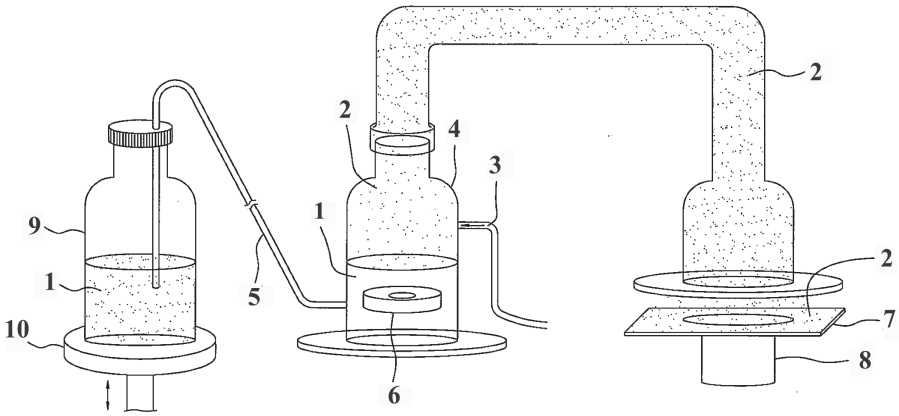

Fig. 3. Schematic view of our designed equipment that combines ultrasonic atomizer with spin-coating apparatus for fabricating conducting thin films. The CNT solution (1) is atomized at a supersonic atomizing frequency to form atomized particles of various sizes (2) including the CNTs. Specifically, (1) is contained in an atomizing container (4) and is maintained at a constant level using a siphon (5) that connects (4) with a reservoir (9). Thus, a supersonic atomizing member (6) that generates the supersonic atomizing frequency is maintained at a constant depth below the level of (1) to produce the atomized particles (2) of desirable particle size. (9) is placed on an elevating device (10). The level (1) in (4) can be controlled by adjusting the height of (10). Preferably, (9) can be provided with a probe type sonicator (not shown) to maintain a homogeneous dispersion of (1) in (9.) A carrier gas (3) is provided to carry (2) to a substrate (7) placed on spin coating equipment (8) for the formation of the conductive thin CNT films.

These atomized particles are transferred to spin-coating equipment with a carrier gas stream of nitrogen at a flow rate of 22 L/min and then spin-coated onto PET films at a speed of 6000 rpm (SP-03, Taiwan), followed by rinsing with water several times to remove the remaining

SDS. The optical transmittance of the MWCNT-PET film was controlled by the deposition time of ultrasonic atomization. Then, to enhance the electric flexibility and reinforce the mechanical properties of the film, 1.25 mL of the PVA water solution (0.1 %) was spun cast on top of the as-produced MWCNT-PET substrate. Finally, the PVA-coated MWCNT-PET film was hot pressed at a temperature of 80 °C under a pressure of 100 kg/cm^2 for 30 min using a thermo-compression method (BM-HP-6000K, Taiwan). The resulting film possessed not only good mechanical flexibility but also excellent conductivity owing to its dense, compact structure.

3. Results and discussions

3.1 Characterization of MWCNT dispersion

For broad applications of MWCNTs, it is necessary that the MWCNT bundles are processed to form individually dispersed nanotubes prior to their use. SDS is extensively used for carbon nanotube dispersion by adsorbing onto nanotube surface via a noncovalent approach in which the higher charge in the head groups strengthens the electrostatic repulsion among surface-covered nanotubes, rendering them disaggregate thereby resulting in a more stable suspension. Figure 4 shows the solubility of the MWCNTs in a SDS aqueous solution with low concentration of 0.25 wt%. It is clear that MWCNTs were not completely soluble in the SDS solution even after 8 h of sonication using the bath sonicator because sedimentation of the MWCNTs at the bottom of the bottle was observed (Figure 4a). Notably, by using high-energy probe type ultrasonication, the MWCNTs were entirely dispersed in the aqueous solution in the presence of SDS, forming a homogeneous-free solution (Figure 4b). Significantly, the observed MWCNT dispersions were stable without any sedimentation or aggregation of nanotubes bundles for at least two years. These results indicate that the high-energy probe type ultrasonication process combined with the assistance of SDS surfactant could be successfully used to obtain a stable and homogeneous MWCNT aqueous solution, even with a low SDS concentration.

In addition to the obvious difficulty in obtaining a stable and homogeneous solution of individual carbon nanotube suspensions, another complication is to find a valid method to evaluate their state and concentration in the solution, which is usually necessary for qualitative and quantitative analysis of the data. The optical absorption measurement has been employed for the determination of individual CNT solubility and dispersion limits, in which the absorption was strongly dependent on the amount of CNT dissolved in the solution. (Priya & Byrne, 2008) Importantly, a linear fit between the absorption and CNT concentration was present, in accordance with Beer's law, and intersected at zero, indicating that the region consisted of significantly debundled CNTs. (Jeong et al., 2007; Priya & Byrne, 2008; Rastogi et al., 2008) In Figure 5a, we present a series of black, macroscopically homogeneous MWCNT dispersions at different concentrations of 25, 12.5, 8.33, 6.25, 5.00, and 2.5 mg/L obtained by diluting the starting MWCNT dispersions, which were also applied to calibrate the solubility of MWCNTs by measuring the intensity of the absorption. Figure 5b depicts the UV–vis spectra of MWCNTs with varying concentrations of nanotubes in SDS surfactant solutions. The absorption decreased with the decreasing concentration of MWCNT aqueous solutions and a linear relationship between them, following Beer's law, could be observed between 200 to 1200 nm (Figure 5c). This result indicates that the as-prepared MWCNT aqueous solution had significantly individual SWCNTs and no effect could be associated with the concentration-dependent carbon nanotube aggregation. Thus,

the concentration-dependent absorption spectroscopy can be used as an effective probe for the monitoring the aggregation state of CNTs in suspension. The suspension of individual MWCNTs was further confirmed by tapping-mode atomic force microscopy (AFM, Veeco DI-3100) and high-resolution transmission electron microscopy (HRTEM, JEOL JEM-2100F). AFM images (Figure 6a) show that the MWCNTs are almost present in the dispersions as single tubes with no bundles. The average diameter of these tubes measured by AFM was approximately 40 nm, which is larger than that of the original synthetic MWCNTs. This was a result of the SDS surfactants wrapping around the nanotubes, resulting in them remaining well dispersed in water. HRTEM images (Figure 6b) also show that the probe ultrasonication-treated MWCNTs do not contain any metal/oxide catalyst. The images also showed that the bundled architectures of the suspended MWCNTs consisted of 10-15 concentric shells with inner and outer diameters of the nanotubes of 5 and 15 nm, respectively, and the layers were separated by the graphitic distance. The selected-area electron diffraction (SAED) pattern of the debundled carbon nanotubes, which are inserted in Figure 6b, illustrates the degree of crystallinity.

Fig. 4. Optical micrographs of MWCNTs dispersions in water in the presence of SDS surfactants prepared by means of (a) a bath sonication process for 8 h and (b) a high-energy probe type sonication process for 3 min, respectively.

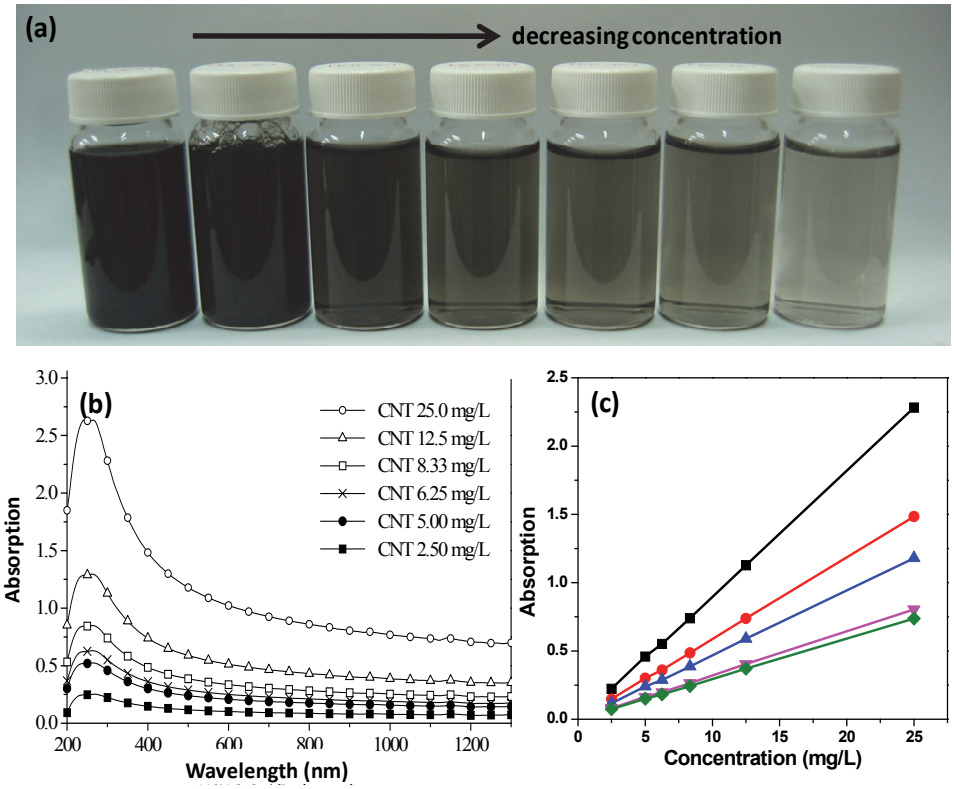

Fig. 5. (a) Optical micrograph of the MWCNT aqueous suspensions at different concentrations: 250 mg/L (starting MWCNT solution), 25.0 mg/L, 12.5 mg/L, 8.33 mg/L, 6.25 mg/L, 5.00 mg/L, and 2.50 mg/L in the presence of 0.25 wt% SDS surfactant. (b) UV-vis spectra recorded from an UV/Vis/NIR spectrometer (Perkin-Elmer Lamda 900) of the MWCNT aqueous solution at different concentrations in the presence of 0.25% SDS surfactant. (c) Absorption as a function of the concentration of the MWCNT aqueous solutions conducted at the wavelength of (■) 300 nm, (●) 400 nm, (▲) 500 nm, (▼) 900 nm, and (◆) 1100 nm. The linear fits are forced through zero.

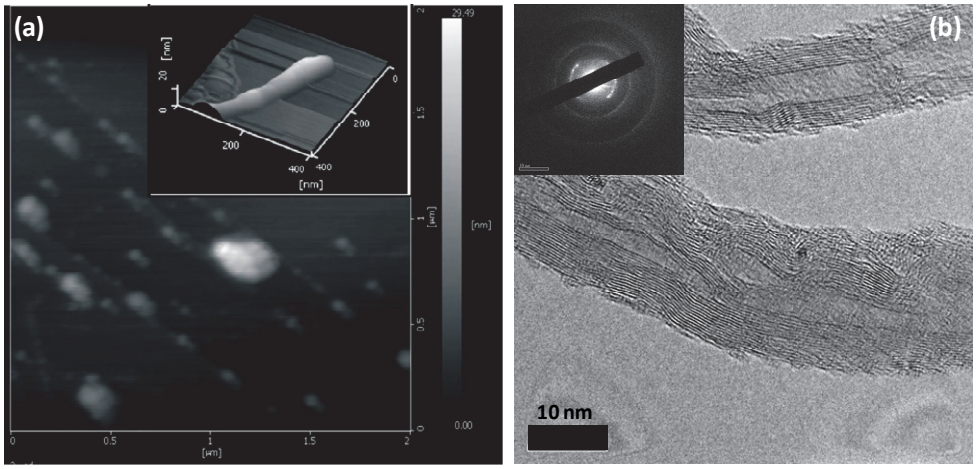

Fig. 6. (a) AFM images of the MWCNT aqueous solution with SDS surfactants. (b) HRTEM image of a MWCNT, which consisted of lattice finger walls. Inset shows the electron diffraction pattern of the carbon nanotube.

3.2 MWCNT-based flexible transparent conducting thin film

CNT-related films that possess porous geometries are of great interest as a class of structures owing to their unique intrinsic properties and potential scientific and technical applications in optoelectronic devices. (Motavas et al., 2009; Skrabalak & Suslick, 2006; Ulbricht et al., 2007) The open porosity structure has great benefits in the fabrication of CNT-related films with both high transparency and good electrical conductivity as a result of the porosity cavities and intersecting nanotube networks. Herein, we report for the first time the successful formation of MWCNT TCFs with porous structures constructed from two different architectures, i.e., unusual open rings and a honeycomb network, through the use of the ultrasonic atomizer technique from the dispersing MWCNT aqueous solution.

3.2.1 Open rings network-based MWCNT TCFs

Open-rings of MWCNTs stacked to form porous networks onto a poly(ethylene terephthalate) (PET) substrate in the formation of a flexible conducting film with great electrical conductivity and transparency were generated by ultrasonic atomization combined with a spin-coating technique.

Large-scale, transparent and flexible PVA-coated MWCNT-PET thin films prepared at different ultrasonic atomization time were successfully obtained as shown in Figure 7, in which the PVA film provided an additional advantage for mechanical reinforcement of the MWCNT thin film. It is notable that the ultrasonic atomization time plays an important role in the optical transparency of the films. As the ultrasonic atomization proceeded, the transmittance of the films decreased, which is ascribed to the increasing amount of the MWCNTs deposited on the PET film. The effect of ultrasonic atomization time on the transmittance and electrical conductivity of the as-prepared films was further studied by a UV/Vis/NIR spectrometer (Perkin-Elmer Lamda 900) and four probe point system (SR-4, Everbeing), as shown in Figure 8. From Figure 8a, we could observe that the transmittance and electrical resistance of the films decreased with the increase of the reaction time. At

early reaction times of approximately 5 min, the MWCNT film exhibited the highest resistance of around 4 M Ω/sq when the optical transmittance reached 93% at 550 nm. After the deposition time of 15 min, the sheet resistance dramatically decreased to 460 Ω/sq with the optical transmittance of 89%. The substantial decrease in sheet resistance is due to the efficient percolation paths for charge transport through the well-interconnected networks. (Hu et al., 2004) Subsequently, the sheet resistance dropped off to ~200 Ω/sq at 120 min, while the corresponding transmittance was observed to decreased to 69%. The relationship of the optical transmittance at 550 nm and sheet resistance was plotted in Figure 8b.

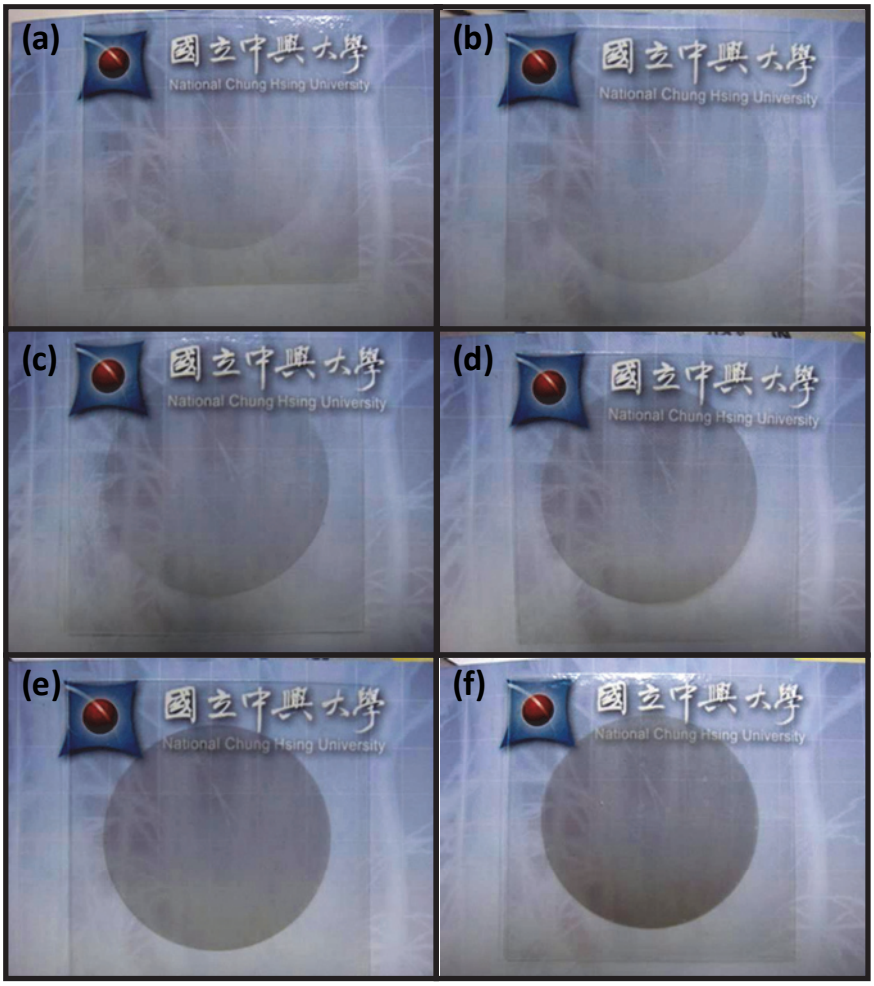

Fig. 7. (a) Photographs of the PVA-coated MWCNT-PET film prepared by ultrasonic atomization combined with the spin-coating technique with the aid of a thermo-compression method. The ultrasonic atomization time used for the preparation of the MWCNT-PET film was controlled at (a) 5 min, (b) 15 min, (c) 30 min, (d) 45 min, (e) 60 min, and (e) 120 min.

With such excellent transparency and electrical conductivity properties, it is interesting to investigate the architecture stacked by MWCNTs onto the surface of PET films. Therefore, FESEM analysis was used to further study the architecture using a Zeiss URTRA 55 and JEOL JEM-7500F. Figure 9a and 9b show the FESEM images of the MWCNT-PET film prepared at the initial ultrasonic atomization time of 30 s, which illustrates that the porous network structure of MWCNTs are randomly stacking by the overlapping and crossing the open rings which are with 80 - 100 μm in diameter and 800 nm in wall width. This ring structure, constructed by the interaction of the droplet gravity, liquid surface tension, and centrifuge force during the atomization process, was quite suitable for making transparent conducting films. (Qiao & Chandra, 1996) It is important to note that the wall of the open rings was constructed from individual MWCNTs (Figure 9c), which have long persistence lengths and are naturally interconnected and entangled with each other by van der Waals forces to form intersecting points and a spider web-like structure within the wall structure, leading to a robust conducting open-ring. They were further interconnected in the assembly to make a porous network that can permit fast charge transport between the inter-connection conducting paths of wall structures and achieve high optical transparency because of the well-developed porous structures.

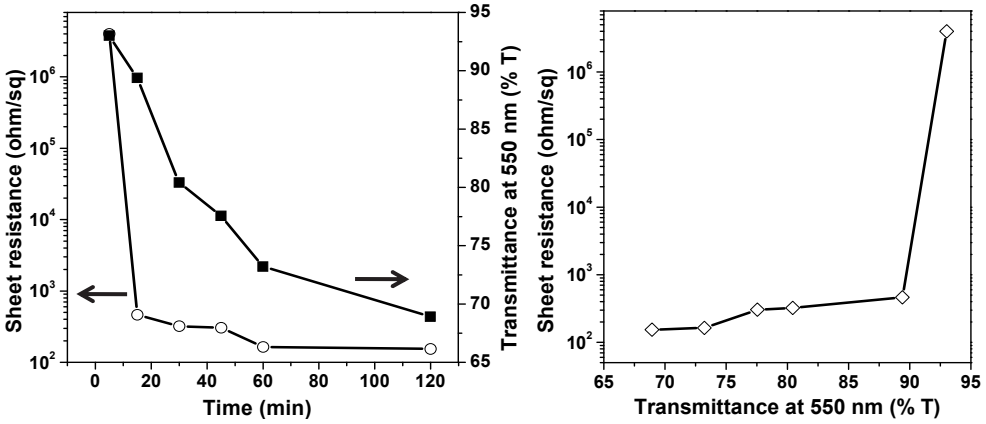

Fig. 8. (a) Optical transmittance (at 550 nm, ■) and sheet resistance (o) of the MWCNT-PET thin film, as a function of the time of ultrasonic atomization. (b) Transmittance vs. resistance of the as-produced MWCNT-PET at the ultrasonic atomization time of 120 min, 60 min, 45min, 30 min, 15 min, and 5 min (from left to right).

To further explore the feasibility of these open ring network-based MWCNT TCFs, we analyzed the strain-dependent electrical resistance characteristics of the films with and without the incorporation of PVA thin films by a two-point bending test. Representative results are presented in Figure 10. Figure 10b reveals the sheet resistance versus the flexing cycles for the representative MWCNT-PET without coating the PVA film. It was found that the sheet resistance dramatically increased by more than 30 times after bending and then gradually recovered after relaxation, which is due to the fact that the van der Waals interactions are strong enough to maintain the porous network structure. In addition, small changes could be observed after 3 bending cycles. The sheet resistances are maintained at ca.

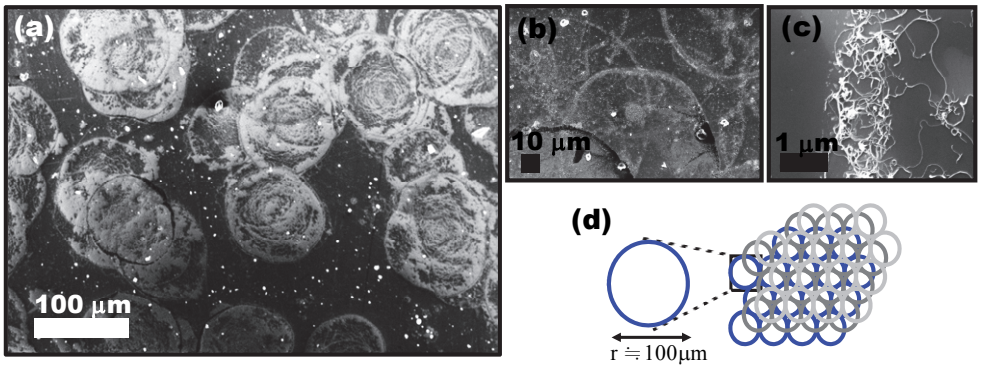

Fig. 9. FESEM images of open-rings of MWCNTs on a PET substrate (a) before and (b) after the removal of SDS. The time of ultrasonic atomization was 30 s. (c) One part of wall of the selected ring. (d) Schematic formation of the porous MWCNT network by the open-rings structure.

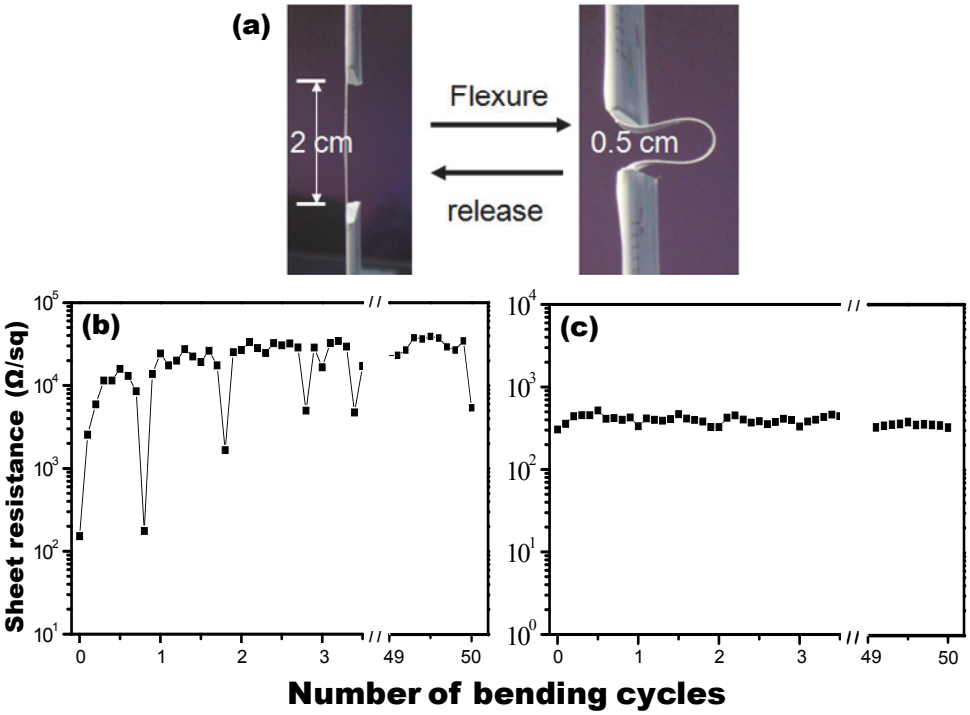

Fig. 10. (a) Schematic graph of the two-point bending test for the generated MWCNT-based thin film. Changes in sheer resistance of the (a) as-produced MWCNT-PET thin film and (b) the PVA-enhanced film during repeated bending.

3700 (±1%) ohm/sq with complete recovery after bending. This observation illustrates that the flexibility of MWCNT films is quite reliable, but the electric conductivity does not meet the criteria necessary for practical touch screen application (sheet resistance < 500 ohm/sq). The increased resistance of the MWCNT thin films can be attributed to the change of contact resistance among carbon nanotubes and pressure-induced changes in the band gap of carbon nanotubes, even though as a whole it remains conductive. (Cao et al., 2007) Interestingly, relatively small changes were observed in sheet resistance during the bending of the PVA-coated MWCNT-PET thin film, which possessed around 360 ohm/sq after bending 50 times (Figure 10c). Most importantly, there is no significant degradation in conductivity even after 500 bending cycles where the sheet resistances remained approximately 370 (±3 %) ohm/sq. Besides, a splendid transparency remained with the transmittance of around 77% at 550 nm (not shown). The result illustrates that the produced thin films have a robust flexibility and do not break/crack upon bending and relaxing, meaning they can be rolled and unrolled repeatedly with no impact to their transparency and conductivity. This result indicates the PVA-coated open-rings MWCNT thin film could be considered as an alternative for optoelectronic device applications such as FETs, sensors, and touch screens.

3.2.2 Two-dimensional honeycomb network-based MWCNT TCFs

Another porous carbon materials film constructed with a quasi-honeycomb network was also generated by our continuous and one-step spin-coating method combined with ultrasonic atomization to the as-prepared MWCNT-SDS supernatant solution by tuning some experimental parameters.(Su et al., 2008) A quasi-honeycomb framework built up through carbon nanotube wires was observed after the removal of the surfactant of SDS, as shown in Figure 11a. The individual CNT "sticks" are connected with each other through van der Waals interactions to form one-dimensional conducting wires, which have long persistence lengths and tend to entangle to form intersecting points in the networks. These conducting sticks play an important role in the electric properties of CNT networks, where the larger the nanowire conductivity, the better the network conductance. With such a unique honeycomb network formed by interconnected individual CNT sticks, we could expect that the two-dimensional honeycomb network-based MWCNT TCFs have good transparency and electrical conductivity. Figure 11b shows that this level of porosity of the honeycomb network-based MWCNT TCFs is consistent with its optical properties, with ultra-high film transmittance >85% over the visible part of the spectrum. Moreover, there is no difference in the analysis of optical transmittance for this representative CNT film, indicating that the size of homogeneous honeycomb structure is up to 4 × 4 cm^2. The corresponding sheet resistance can reach 500 ohm/sq (using a four probe point stand equipment), which is comparable to that of SWCNTS and ITO materials on PET substrates. (Dettlaff-Weglikowska et al., 2005; Geng et al., 2007; Hu et al., 2004) According to the excellent optical and electrical properties, the conducting honeycomb CNT films should present new opportunities for the development of next-generation flexible touch screens.

4. Conclusion

The present invention provides a method for the rapid dispersion of CNTs in an aqueous solution with the aid of nontoxic surfactants through a novel, simple, fast, and inexpensive sonophysically exfoliated method. In this method, the carbon nanotubes are added to an aqueous solution of a nontoxic surfactant, and then dispersed therein through ultrasonic

oscillation. Importantly, this uniform dispersion can last stably for at least two years without aggregation, suspension, or precipitation. This dispersion is suitable for calibrating the concentration of the carbon nanotubes. Further, the as-prepared dispersed MWCNT aqueous solution could be successfully further used for making MWCNT TCFs with porous carbon nanotubes frameworks onto the surface of PET films through the spin-coating method combined with ultrasonic atomization. Two types of the porous structures were achieved: open rings and a honeycomb network. This approach is straightforward for a large-sized film. Importantly, compared with other MWCNT-based transparent thin films, (Castro & Schmidt, 2008; de Andrade et al., 2007; Havel et al., 2008; Kaempgen et al., 2005) this process dramatically improved the electrical conductivity for transmittance in the range of ~65%-85% in both of these systems, as shown in Figure 12. Furthermore, we find that the coating of the ultrathin PVA film provides an additional advantage for the enhancement of the electric flexibility and reinforcement of the mechanical property of the film. Thus, because of the ease of use and low implementation cost of the ultrasonic atomization-spin coating process, our approach could provide a straightforward technique for large-sized transparent conducting film production and open new opportunities for the development of next-generation flexible touch screens and porous carbon nanotube-based electrodes.

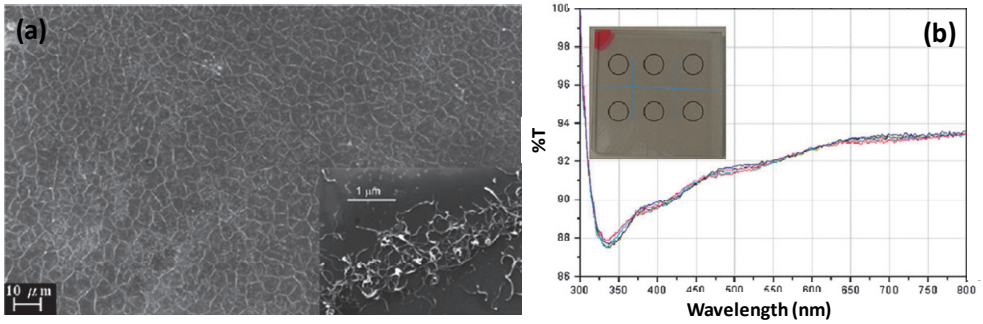

Fig. 11. (a) FE-SEM image of the morphology of honeycomb networks constructed from pure CNT wires. Inset: one selected wall of the CNT network. (b) UV-Vis spectra for the honeycomb CNT film, showing good transparency on the homogenous uniform film (4 × 4 cm^2). Six selected optical spectra on the circles were taken (Inset).

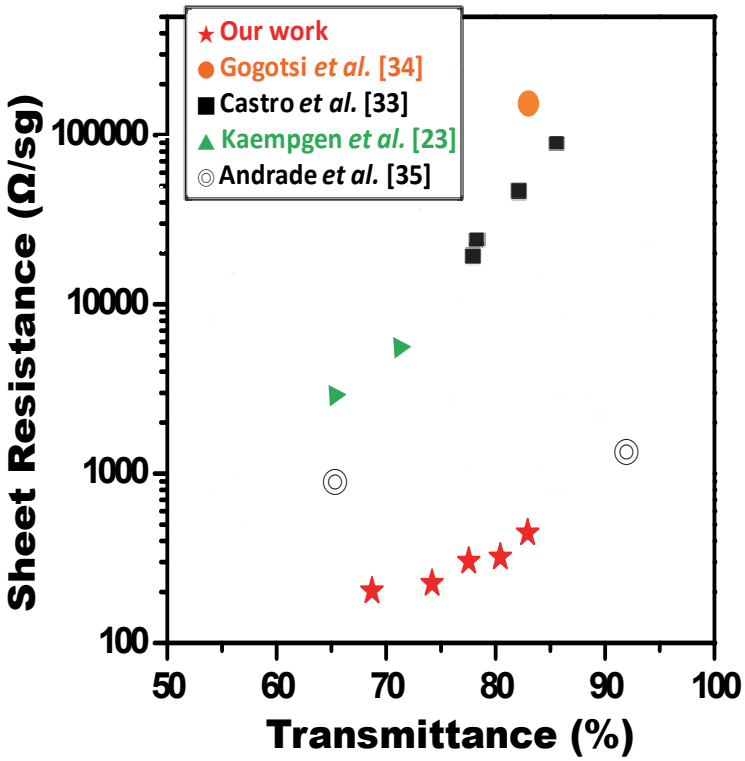

Fig. 12. Comparison of the sheet resistance of our open-ring MWCNT-PET thin films with other MWCNT-based thin films reported in the literature, as a function of transmittance at 550 nm.

5. Acknowledgement

We gratefully acknowledge the support through the National Science Council of Taiwan, Republic of China, under project NSC-98-2113-M-005-004-MY3 and NSC-98-2120-M-007-009.

6. References

Calnan, S. & Tiwari, A. N. (2010). High mobility transparent conducting oxides for thin film solar cells. *Thin Solid Films, 518*(7), 1839-1849.

Cao, C. L.; Hu, C. G.; Xiong, Y. F.; Han, X. Y.; Xi, Y. & Miao, J. (2007). Temperature dependent piezoresistive effect of multi-walled carbon nanotube films. *Diam. Relat. Mat., 16*(2), 388-392.

Castro, M. R. S. & Schmidt, H. K. (2008). Preparation and characterization of low- and high-adherent transparent multi-walled carbon nanotube thin films. *Mater. Chem. Phys., 111*(2-3), 317-321.

Chen, P. C.; Chen, H. T.; Qiu, J. & Zhou, C. W. Inkjet Printing of Single-Walled Carbon Nanotube/RuO2 Nanowire Supercapacitors on Cloth Fabrics and Flexible Substrates. *Nano Research, 3*(8), 594-603.

Dan, B.; Irvin, G. C. & Pasquali, M. (2009). Continuous and Scalable Fabrication of Transparent Conducting Carbon Nanotube Films. *Acs Nano, 3*(4), 835-843.

de Andrade, M. J.; Lima, M. D.; Skakalova, V.; Bergmann, C. P. & Roth, S. (2007). Electrical properties of transparent carbon nanotube networks prepared through different techniques. *Phys. Stat. Sol. (RRL), 1*, 178-180.

Dettlaff-Weglikowska, U.; Skakalova, V.; Graupner, R.; Jhang, S. H.; Kim, B. H.; Lee, H. J., et al. (2005). Effect of SOCl2 treatment on electrical and mechanical properties of single-wall carbon nanotube networks. *Journal of the American Chemical Society, 127*, 5125-5131.

Feng, C.; Liu, K.; Wu, J. S.; Liu, L.; Cheng, J. S.; Zhang, Y. Y., et al. (2010). Flexible, Stretchable, Transparent Conducting Films Made from Superaligned Carbon Nanotubes. *Advanced Functional Materials, 20*(6), 885-891.

Geng, H. Z.; Kim, K. K.; So, K. P.; Lee, Y. S.; Chang, Y. & Lee, Y. H. (2007). Effect of acid treatment on carbon nanotube-based flexible transparent conducting films. *Journal of the American Chemical Society, 129*(25), 7758-+.

Girifalco, L. A.; Hodak, M. & Lee, R. S. (2000). Carbon nanotubes, buckyballs, ropes, and a universal graphitic potential. *Physical Review B, 62*(19), 13104-13110.

Gruner, G. (2006). Carbon nanotube films for transparent and plastic electronics. *Journal of Materials Chemistry, 16*(35), 3533-3539.

Havel, M.; Behler, K.; Korneva, G. & Gogotsi, Y. (2008). Transparent thin films of multiwalled carbon nanotubes self-assembled on polyamide 11 nanofibers. *Advanced Functional Materials, 18*(16), 2322-2327.

Heo, G. S.; Matsumoto, Y.; Gim, I. G.; Lee, H. K.; Park, J. W. & Kim, T. W. (2010). Transparent conducting amorphous Zn-In-Sn-O anode for flexible organic light-emitting diodes. *Solid State Communications, 150*(3-4), 223-226.

Hu, L.; Hecht, D. S. & Gruner, G. (2004). Percolation in transparent and conducting carbon nanotube networks. *Nano Letters, 4*(12), 2513-2517.

Jeong, S. H.; Kim, K. K.; Jeong, S. J.; An, K. H.; Lee, S. H. & Lee, Y. H. (2007). Optical absorption spectroscopy for determining carbon nanotube concentration in solution. *Synthetic Metals, 157*, 570-574.

Jo, G.; Choe, M.; Cho, C. Y.; Kim, J. H.; Park, W.; Lee, S., et al. (2010). Large-scale patterned multi-layer graphene films as transparent conducting electrodes for GaN light-emitting diodes. *Nanotechnology, 21*(17), 175201.

Kaempgen, M.; Duesberg, G. S. & Roth, S. (2005). Transparent carbon nanotube coatings. *Applied Surface Science, 252*(2), 425-429.

Kim, D. H.; Park, M. R.; Lee, H. J. & Lee, G. H. (2006). Thickness dependence of electrical properties of ITO film deposited on a plastic substrate by RF magnetron sputtering. *Applied Surface Science, 253*(2), 409-411.

Kim, O. K.; Je, J. T.; Baldwin, J. W.; Kooi, S.; Pehrsson, P. E. & Buckley, L. J. (2003). Solubilization of single-wall carbon nanotubes by supramolecular encapsulation of helical amylose. *Journal of the American Chemical Society, 125*(15), 4426-4427.

Li, D.; Wang, H. Z.; Zhu, J. W.; Wang, X.; Lu, L. D. & Yang, X. J. (2003). Dispersion of carbon nanotubes in aqueous solutions containing poly(diallyldimethylammonium chloride). *Journal of Materials Science Letters, 22*(4), 253-255.

Li, Z. R.; Kandel, H. R.; Dervishi, E.; Saini, V.; Biris, A. S.; Biris, A. R., et al. (2007). Does the wall number of carbon nanotubes matter as conductive transparent material? *Applied Physics Letters, 91*(5), 053115.

Lin, Y. C.; Li, J. Y. & Yen, W. T. (2008). Low temperature ITO thin film deposition on PES substrate using pulse magnetron sputtering. *Applied Surface Science, 254*(11), 3262-3268.

Lu, K. L.; Lago, R. M.; Chen, Y. K.; Green, M. L. H.; Harris, P. J. F. & Tsang, S. C. (1996). Mechanical damage of carbon nanotubes by ultrasound. *Carbon, 34*(6), 814-816.

Madni, I.; Hwang, C. Y.; Park, S. D.; Choa, Y. H. & Kim, H. T. (2010). Mixed surfactant system for stable suspension of multiwalled carbon nanotubes. *Colloids and Surfaces a-Physicochemical and Engineering Aspects, 358*(1-3), 101-107.

Manivannan, S.; Ryu, J. H.; Lim, H. E.; Nakamoto, M.; Jang, J. & Park, K. C. (2010). Properties of surface treated transparent conducting single walled carbon nanotube films. *Journal of Materials Science-Materials in Electronics, 21*(1), 72-77.

Marsh, D. H.; Rance, G. A.; Zaka, M. H.; Whitby, R. J. & Khlobystov, A. N. (2007). Comparison of the stability of multiwalled carbon nanotube dispersions in water. *Physical Chemistry Chemical Physics, 9*, 5490-5496.

Miller, D. L. (1984). Gas body activation. *Ultrasonics, 22*(6), 259-260.

Motavas, S.; Omrane, B. & Papadopoulos, C. (2009). Large-Area Patterning of Carbon Nanotube Ring Arrays. *Langmuir, 25*(8), 4655-4658.

Na, S. I.; Kim, S. S.; Jo, J. & Kim, D. Y. (2008). Efficient and Flexible ITO-Free Organic Solar Cells Using Highly Conductive Polymer Anodes. *Advanced Materials, 20*(21), 4061-4017.

Paloniemi, H.; Aaritalo, T.; Laiho, T.; Liuke, H.; Kocharova, N.; Haapakka, K., et al. (2005). Water-soluble full-length single-wall carbon nanotube polyelectrolytes: Preparation and characterization. *Journal of Physical Chemistry B, 109*(18), 8634-8642.

Park, H.; Kim, J. S.; Choi, B. G.; Jo, S. M.; Kim, D. Y.; Hong, W. H., et al. (2010). Sonochemical hybridization of carbon nanotubes with gold nanoparticles for the production of flexible transparent conducing films. *Carbon, 48*(5), 1325-1330.

Paul, S. & Kim, D. W. (2009). Preparation and characterization of highly conductive transparent films with single-walled carbon nanotubes for flexible display applications. *Carbon, 47*(10), 2436-2441.

Priya, B. R. & Byrne, H. J. (2008). Investigation of sodium dodecyl benzene sulfonate assisted dispersion and debundling of single-wall carbon nanotubes. *Journal of Physical Chemistry C, 112*(2), 332-337.

Qiao, Y. M. & Chandra, S. (1996). Boiliing of droplets on a hot surface in low gravity. *lnt. J. Heat Mass Transfer, 39*(7), 1379-1393.

Rastogi, R.; Kaushal, R.; Tripathi, S. K.; Sharma, A. L.; Kaur, I. & Bharadwaj, L. M. (2008). Comparative study of carbon nanotube dispersion using surfactants. *Journal of Colloid and Interface Science, 328*(2), 421-428.

Saran, N.; Parikh, K.; Suh, D. S.; Munoz, E.; Kolla, H. & Manohar, S. K. (2004). Fabrication and characterization of thin films of single-walled carbon nanotube bundles on

flexible plastic substrates. *Journal of the American Chemical Society, 126*(14), 4462-4463.

Sierros, K. A.; Morris, N. J.; Kukureka, S. N. & Cairns, D. R. (2009). Dry and wet sliding wear of ITO-coated PET components used in flexible optoelectronic applications. *Wear, 267*(1-4), 625-631.

Simien, D.; Fagan, J. A.; Luo, W.; Douglas, J. F.; Migler, K. & Obrzut, J. (2008). Influence of nanotube length on the optical and conductivity properties of thin single-wall carbon nanotube networks. *Acs Nano, 2*(9), 1879-1884.

Skrabalak, S. E. & Suslick, K. S. (2006). Porous carbon powders prepared by ultrasonic spray pyrolysis. *Journal of the American Chemical Society, 128*(39), 12642-12643.

Su, J. W.; Fu, S. J.; Gwo, S. & Lin, K. J. (2008). Fabrication of porous carbon nanotube network. *Chemical Communications*(43), 5631-5632.

Su, J. W.; Hsu, C. Y.; Fu, S. J.; Guo, C. H. & Lin, K. J. (2009). Sonophysically-Exfoliated Individual Multi-Walled Carbon Nanotubes in Water Solution. *J. Chin. Chem. Soc., 56*(5), 935-939.

Takenobu, T.; Takahashi, T.; Kanbara, T.; Tsukagoshi, K.; Aoyagi, Y. & Iwasa, Y. (2006). High-performance transparent flexible transistors using carbon nanotube films. *Applied Physics Letters, 88*(3), 033511.

Thiruvengadathan, R.; Levi-Kalisman, Y. & Regev, O. (2007). Synergetic effect of ultrasound and sodium dodecyl sulphate in the formation of CdS nanostructures in aqueous solution. *Ultrasonics Sonochemistry, 14*(3), 398-404.

Ulbricht, R.; Lee, S. B.; Jiang, X. M.; Inoue, K.; Zhang, M.; Fang, S. L., et al. (2007). Transparent carbon nanotube sheets as 3-D charge collectors in organic solar cells. *Sol. Energy Mater. Sol. Cells, 91*(5), 416-419.

Wang, L. M.; Chen, Y. J. & Liao, J. W. (2008). Characteristics of indium-tin oxide thin films grown on flexible plastic substrates at room temperature. *Journal of Physics and Chemistry of Solids, 69*(2-3), 527-530.

Xiao, G. Z.; Tao, Y.; Lu, J. P. & Zhang, Z. Y. (2010). Highly conductive and transparent carbon nanotube composite thin films deposited on polyethylene terephthalate solution dipping. *Thin Solid Films, 518*(10), 2822-2824.

Xu, G. H.; Zhang, Q.; Zhou, W. P.; Huang, J. Q. & Wei, F. (2008). The feasibility of producing MWCNT paper and strong MWCNT film from VACNT array. *Applied Physics a-Materials Science & Processing, 92*(3), 531-539.

Zhang, M.; Fang, S. L.; Zakhidov, A. A.; Lee, S. B.; Aliev, A. E.; Williams, C. D., et al. (2005). Strong, transparent, multifunctional, carbon nanotube sheets. *Science, 309*(5738), 1215-1219.

15

Application of Multi-Walled Carbon Nanotubes for Innovation in Advanced Refractories

Yawei Li[1], C.G. Aneziris[2], Shengli Jin[1], Shaobai Sang[1] and Xilai Chen[1]
[1]*Wuhan University of Science and Technology*
[2]*Technische Universität Bergakademie Freiberg*
[1]*P. R. China*
[2]*Germany*

1. Introduction

Carbon nanotubes (CNTs) have attracted extensively interest of scientists and engineers due to their outstanding physical properties such as low density, high aspect ratio, Young's modulus, electrical and thermal conductivities. When single-wall carbon nanotubes (SWCNTs) or multi-wall carbon nanotubes (MWCNTs) are introduced into ceramics, metals and polymers as matrices, ultra-high strength and/or multifunctional composites can be developed as expected. Recently, CNT composite refractories have been the subject of intense research activities. In this chapter, MWCNTs (hereafter named as CNTs) were introduced into refractories to improve their mechanical properties and thermal conductivity, such as Al_2O_3-C refractories for slide gates and carbon blocks for blast furnaces in iron and steel making industry.

2. Application of CNTs in Al_2O_3-C refractories

2.1 Experimental procedure

Tabular alumina (8-14 mesh, -14 mesh and –325 mesh, 99.5 -wt%Al_2O_3, Almatis), reactive alumina (d_{50} = 5 μm, CT9FG, 99.5 -wt% Al_2O_3, Almatis), silicon powder (-325 mesh, 99.5 -wt%Si, Welsch), Aluminium powder (45-75 μm, 99.7 -wt%Al, TLS Technik), Microsilica fume (98.3 -wt%SiO_2, Elkerm), multi-walled CNTs (~50nm, 95 -wt%C, Chengdu Organic Chemicals), Graphite (-200 mesh, 93.0 -wt%C, Fuchs Lubirtech), Phenol Novolak Resin PF6446FL (Co. Hexion) and Carbores^P powder (high melting coal-tar resin, Co. Rütgers) were used as starting materials. The batch composition consisted of 43-wt% 8-14 mesh tabular alumina, 17 -wt% -14 mesh tabular alumina, and 5.0 -wt% calcined alumina. Rest 35 -wt% starting materials consisted of –325 mesh tabular alumina, flake graphite, Al (Si, SiO_2, CNTs) additives. –325 mesh tabular alumina and Al (Si, SiO_2, CNTs) were first hand-mixed for a certain time in a corundum mortar till the colour of mixture looked homogeneous. An extra mixture of 4.0-wt% liquid novolak resin with 0.4-wt% hardener hexa and 2.0-wt% Carbores^P powder was used as bonding system. The whole residual carbon of the sample was set at around 5.0-wt%.

All batches were mixed following the same procedure by Toni mixer and then pressed to bars (25 mm in height, 25 mm in width and 150 mm in length) with the aid of a hydraulic press at a pressure of 150 MPa. Consequently, all the samples were hardened following the

standard temperature-time curve up to 180 °C. Then, the samples were treated at 1200 or 1400 °C in coke grit bed for 3h. The apparent porosity was measured according to EN 933-1. The cold modulus of rupture (CMOR) was measured due to three-point bending test with respect to EN 933-6, and Young's modulus by impulse method according to DIN 51942. The thermal shock resistance was tested according to EN 993-11. Namely, after the temperature has reached 950 °C, bar samples were put into the carbon grit bed and soaked for 30 minutes then cooled down to room temperature in five minutes by compressed air (P=1.0 bar, 100 mm distance between sample surface and spraying nozzle).
The microstructure of the samples was observed via scanning electron microscope (SEM, Philips, XL30ESEM) linked with energy dispersive spectrometer (EDS, EDAX, PHOENIX). Calorimetric signals from phase transformations of coked powder resin, coked Carbores^{P} powder and CNTs were monitored by differential thermal analyzer (DTA) using SHIMADZU DTA-50 system. Continuous-heating regimes from room temperature to 1173 K with a heating rate of 10 K/min, samples of 30 mg, open wide Al_2O_3 pans in static dried air. For the DTA measurements, powder resin with 10 -wt% hexa was hardened following the standard temperature-time curve up to 180 °C and then coked at 1000 °C for 3 h in coke grit bed. Also Carbores^{P} powder was coked at 1000 °C for 3 h in coke grit bed. The fracture behaviour was recorded by high speed camera (SpeedCam MacroVis, High Speed Vision Co.) with a CCD resolution of 1280×386 pixels at the speed of 3000 fps.

2.2 Mechanical properties and microstructure

Table 1 shows the main variable compositions, the apparent porosity, CMOR, Young's modulus, and σ/E of different batches. In comparison of Al (AT), Si (BT), and SiO_2 (CT) respectively playing with CNTs after coked at 1200°C, the apparent porosity of all the batches almost was the same. However, CMOR of batch BT was higher than the other two batches, and then batch CT followed. By increasing the treating temperature, the apparent porosity remained almost the same; in contradiction CMOR of BT and CT batches decreased a lot, and only CMOR of batch AT increased. Among these three batches, Young's modulus of batch CT was the lowest, and its ratio of σ/E reached a value of 0.5×10^{-3} after coking at 1200°C. Using combination of Al, Si and CNTs as additives, the apparent porosity of samples was slightly lower than batches AT, BT and CT after coking at 1200°C and 1400°C, respectively; their CMOR and young's modulus were a little higher than those of other batches. Based on the composition of industrial products, a reference batch D was created. Its CMOR and Young's modulus were quite higher than the former batches after coking at 1200°C. Whereas, after coking at 1400°C, the apparent porosity of batch D increased and their CMOR decreased sharply with a high young's modulus.
Our previous research shows that the CMOR of samples with liquid novolak resin binder is lower than that of corresponding samples with Carbores^{P} (Aneziris et al., 2009). The previous results also show that by using the combination of Al, Si, SiO_2 and CNTs additives, Al_2O_3-C refractories can achieve better mechanical and thermo mechanical properties. Hence this combination was introduced into Al_2O_3-C refractories with carbonaceous resin powder, referred as E series. With the increase of CNTs from zero to 0.5 -wt%, CMOR of the samples after coking at 1200°C reached its maximum as CNTs content was 0.05 -wt%. However, after coked at 1400°C, CMOR of the samples kept close to each other. It is worth noting that Young's modulus of batch E-0.05 was quite close to that of batch E, although CMOR of batch E-0.05 was higher than the latter. σ/E of batch E-0.05 was higher than that of

E, which indicates the samples with all the additives will possess better thermo mechanical properties in terms of thermal shock performance.
Fig.1 shows SEM images of samples with Al and CNT additives, there were a lot of whiskers in the matrix, which were seldom found in the matrix of samples with same additives and powder resin as bonding system (Aneziris et al., 2009). As demonstrating in Fig.2, these whiskers were nanotubes or of submicron size. Al_4C_3 granules were deposited on the surface of whiskers obviously, some of which grew as branches out from the surface of the whiskers. In case of the samples with Si and CNTs additives, nano-sized SiC whiskers were found easily (Fig.3). Compared to the original shape and dimension of CNTs in the samples (Fig.4), it is evident that whiskers in batch AT were much thicker in diameter and in contradiction those in batch BT were thinner. In addition, the surface of all the whiskers in batch AT and BT was quite rough. When SiO_2 was added into Al_2O_3-C materials with CNTs, only SiO_2 balls coated with SiC layer and honeycomb microstructure were identified in Fig.5, which is similar to the achieved results in the samples with liquid and powder resin binder.

		AT	BT	CT	DT	D	E	ET-0.05	ET-0.1	ET-0.3	ET-0.5
-325mesh tabular alumina		32.6	32.6	32.6	31.1	31.1	29.6	29.6	29.6	29.6	29.6
Al		1.5	-	-	1.5	1.5	1.5	1.5	1.5	1.5	1.5
Si		-	1.5	-	1.5	1.5	1.5	1.5	1.5	1.5	1.5
SiO_2		-	-	1.5	-	-	1.5	1.5	1.5	1.5	1.5
CNTs		0.3	0.3	0.3	0.3	-	-	0.05	0.1	0.3	0.5
Graphite		0.6	0.6	0.6	0.6	0.9	0.9	0.85	0.8	0.6	0.4
1200 °C	Apparent porosity (%)	18	18	19	17	16	15	15	15	16	17
	Cold modulus of rupture (MPa)	6.27	9.30	7.79	9.78	13.40	18.42	19.40	17.66	15.10	11.54
	Young's modulus (GPa)	21.3	23.9	15.8	26.0	33.6	41.0	40.9	37.7	32.8	27.6
	σ/E (10^{-3})	0.3	0.4	0.5	0.4	0.4	0.4	0.5	0.5	0.5	0.4
1400 °C	Apparent porosity (%)	18	17	18	17	19	17	16	16	16	17
	Cold modulus of rupture (MPa)	7.71	7.16	6.97	8.94	8.89	13.30	13.11	13.75	14.41	13.49
	Young's modulus (GPa)	24.8	21.6	20.3	24.7	30.6	39.0	39.7	37.3	33.1	28.4
	σ/E (10^{-3})	0.3	0.3	0.3	0.4	0.3	0.3	0.3	0.4	0.4	0.5

Table 1. Properties among different recipes of Al_2O_3-C materials prepared by premixing CNTs with fine powders.

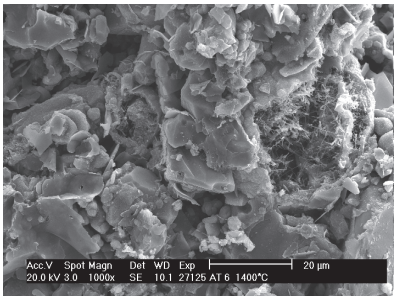

Fig. 1. Microstructure of the sample with Al and CNTs additives, magnification 1000x, coked at 1400°C for 3h.

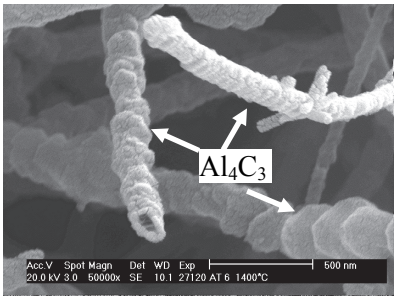

Fig. 2. Microstructure of the sample with Al and CNTs additives, magnification 50000x, coked at 1400°C for 3h.

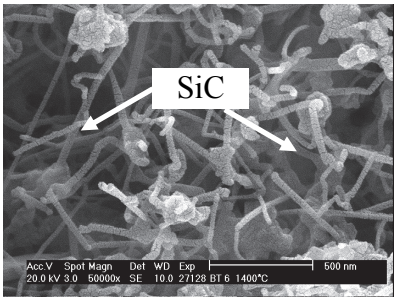

Fig. 3. Microstructure of the sample with Si and CNTs additives, magnification 50000x, coked at 1400°C for 3h.

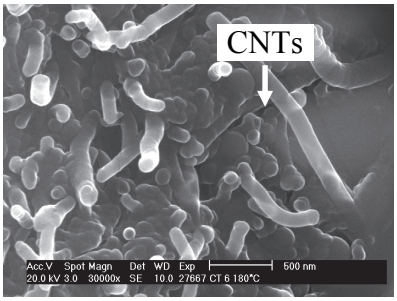

Fig. 4. Microstructure of the sample with SiO_2 and CNTs additives, magnification 30000x, cured at 180°C.

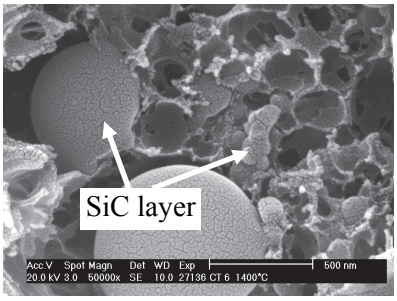

Fig. 5. Microstructure of the sample with SiO_2 and CNTs additives, magnification 50000x, coked at 1400°C for 3h.

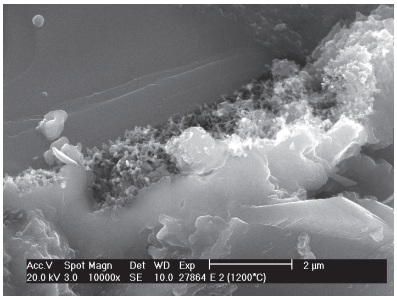

Fig. 6. Microstructure of the sample with Al, Si, and SiO_2 additives, magnification 10000x, coked at 1400°C for 3h.

The samples with Al, Si and SiO_2 additives, fewer amounts of short whiskers were registered between coarse particles and matrix (Fig. 6), compared with the samples with Al and Si additives (Fig.7). In case of the samples with Al, Si, SiO_2 and 0.05-wt%CNTs additives coked at 1200°C, a lot of smoothly nano-sized whiskers were observed, which diameters were less than those of original CNTs (Fig.8). With further enhance of treating temperature, the whiskers became

aggregated and looked inhomogeneous (Fig.9). In addition, an increase of CNTs content in the samples promoted whiskers growth into submicron diameters (Fig.10). It is interesting to observe a lot of CNT-shaped materials still buried in the matrix even after coked at 1400°C (Fig.11), and this phenomenon is hardly seen in the samples with liquid resin and powder resin as binders. Definitely, Carbores^{P} powder has exerted a particular influence on the microstructure evolution and as a result on the achieved mechanical properties of Al_2O_3-C refractories.

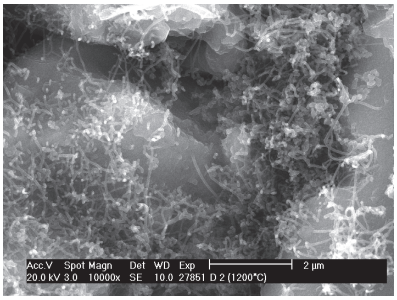

Fig. 7. Microstructure of the sample with Al, Si additives, magnification 10000x, coked at 1400°C for 3h.

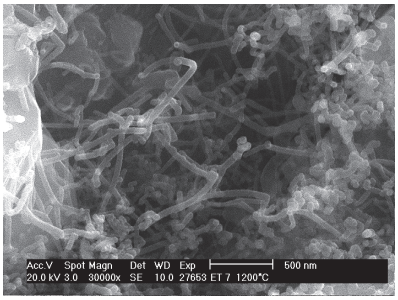

Fig. 8. Microstructure of the sample with Al, Si, SiO_2 and 0.05-wt% CNTs additives, magnification 30000x, coked at 1200°C for 3h.

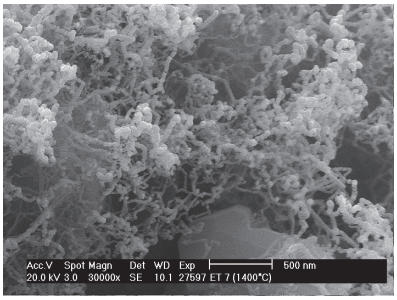

Fig. 9. Microstructure of the sample with Al, Si, SiO_2 and 0.05-wt% CNTs additives, magnification 30000x, coked at 1400°C for 3h.

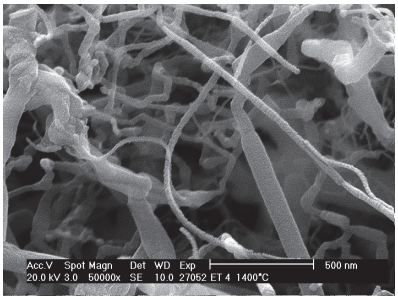

Fig. 10. Microstructure of the sample with Al, Si, SiO_2 and 0.5-wt% CNTs additives, magnification 50000x, coked at 1400°C for 3h.

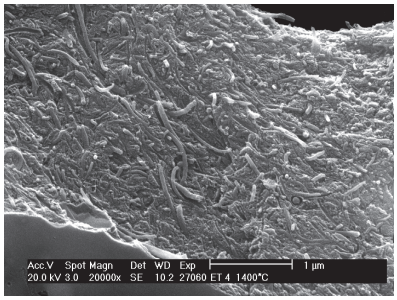

Fig. 11. Microstructure of the sample with Al, Si, SiO_2 and 0.5-wt% CNTs additives, magnification 20000x, coked at 1400°C for 3h.

2.3 Thermal shock resistance and fracture behaviour

Usually, Al and Si are employed in commercial Al_2O_3-C slide gates to improve their mechanical and thermo mechanical properties. Therefore, batch D was chosen as reference to compare its thermal shock performance with those of batch E and E-0.05 (Table 2). After 5 thermal shock cycles, Batch D performed the worst resistance to thermal shock with 48% loss of the CMOR down to 6.95MPa. Batch E and E-0.05 achieved 26% loss in CMOR value. After 5 times thermal shock cycles, E-0.05 still presented a higher CMOR value than E as before thermal shock attack. It is too early to conclude that Batch E is more attractable according to this thermal shock test with the aid of blowing air, due to its low cost without CNTs additive.

After coked at 1200°C	D*	E	E-0.05
CMOR/MPa	6.95	13.60	14.28
Loss in CMOR / %	48	26	26

Table 2. Results of batch D, E and E-0.05 after 5th thermal shock cycles

Three-point bending tests were further performed accompanied by high speed camera records. During the bending test, the initiation of cracks started from the defective places such as scratches, holes or weak bonding positions at the edges of the samples, as shown in Fig.12-14. It is difficult to calculate the propagation length of crack as a function of time step, due to the fact, that the first crack line propagated very fast into the centre. Furthermore, the crack was hardly distinguished due to pictures obtained with the aid of the high speed camera because the surface of samples was rough and relatively dark..

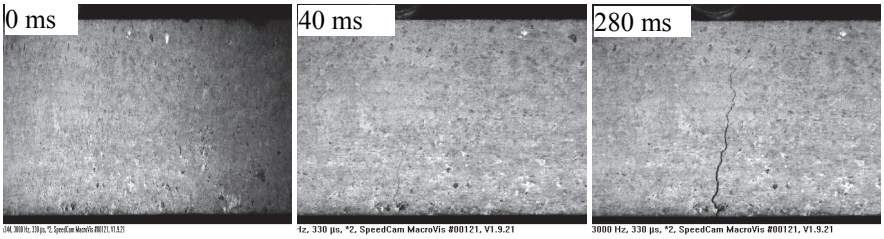

Fig. 12. Fracture evolution of the sample with Al and Si additives after coked at 1200°C for 3h.

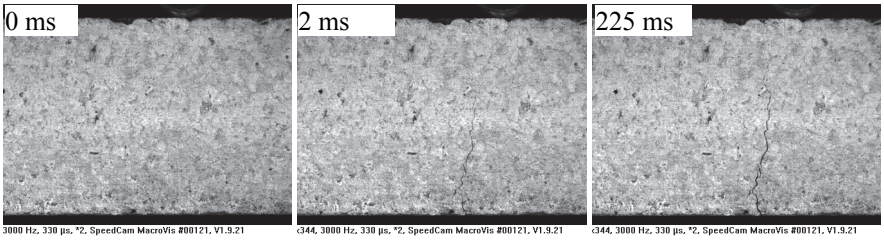

Fig. 13. Fracture evolution of the sample with Al, Si and SiO_2 additives after coked at 1200°C for 3h.

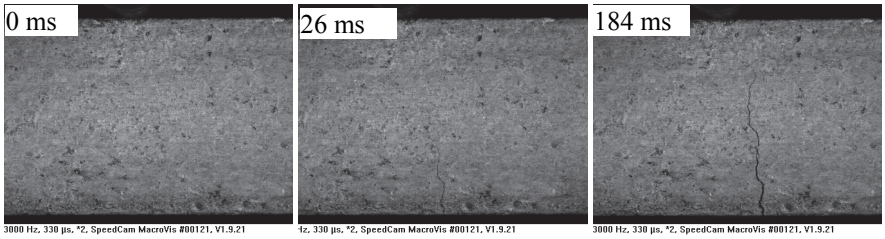

Fig. 14. Fracture evolution of the sample with Al, Si, SiO_2 and CNTs additives after coked at 1200°C for 3h.

According to these observing conditions only two time dependent stages of the crack propagation could be defined. The first stage is before the crack is reaching half of the thickness of the sample, and the second stage before the crack is reaching 3/4 of the thickness of the sample. Correlating the propagation time of the cracks to the real thickness of the samples, propagation velocities were calculated, Table.3. For all samples, the propagation velocities of the first stage were quite higher than these of the second stage. . This phenomenon suggests that propagation of crack in the first stage is very important for understanding and describing the fracture behaviour. During the first stage, batch E presented the highest propagation velocity up to 7.42 m/s. The crack propagating velocity of batch E seems to be related with its microstructure, where whiskers were not contributing to the main bonding reinforcement. In contrast, batch D presented the lowest propagation velocity of crack and batch E-0.05 was in the same order of magnitude to batch D, where a lot of whiskers interlocked the particles and the matrix. Al_2O_3-C refractories working at high temperature as slide gate, endures not only the thermal shock but also the strength from exterior. After service in a certain time, a lot of cracks will be generated. If the resistance to crack propagation is weak, the working safety will lead to total failure of the component.. On the other hand, thermal shock tests of carbon bonded refractories with the aid of blowing air gives insufficient information about crack propagation. Taking into account the propagation velocity and with respect to the CMOR value as coked and after thermal shock, we can assume that batch E presents insufficient service properties during long loading time, and batch E-0.05 achieves excellent mechanical properties.

Coked after 1200°C	Propagation velocity of cracks	
	First stage	Second stage
D	0.32m/s	0.03m/s
E	7.42m/s	0.03m/s
ET-0.05	0.50m/s	0.03m/s

Table 3. Propagation velocities of cracks during bending tests

In order to illustrate the contribution of Carbores^P in Al_2O_3-C materials, the oxidation behaviour of three carbon resources was compared via DTA. Both powder resin with curing agent of hexa and Carbores^P were coked in 1000°C for 3 h before measurement. According to the patterns in Fig.15, the oxidation of the coked powder resin and CNTs were initiated at the temperature around 470°C. However, the slope of DTA curve from CNTs was higher than that of coked powder resin. In addition, the maximum height of DTA curve from CNTs

was larger than that of coke powder resin, which demonstrates the oxidation of CNTs is more intensive than powder resin. In the case of coked powder resin, the oxidation trace was significantly prolonged from 633.34°C to 700.97°C. As for CNTs, except the calometric peak in 662.13°C responsible to the oxidation, another peak in 862.85°C represents the oxidation of the remaining metallic dopant (Illeková & Csomorová, 2005). When coked Carbores^P powder was measured, one endothermic peak was identified at 528.82°C corresponding to softening of Carbores^P; this peak was even registered if Carbores^P powder had been pre-coked at 1000°C for 3h. The oxidation of Carbores^P took place obviously at 672.38°C, and then presented slow oxidation behaviour over 950°C. Carbores^P powder performed the best oxidation resistance among the three carbon resources.

As described by Aneziris et al., Carbores is an environmental friendly artificial tar resin, with a softening point over 200°C (Aneziris et al., 2009; Boenigk et al., 2004). It preserves the characteristic of pitch, which is softening and pyrolyzes in liquid state at higher temperature during heating process, while powder resin pyrolyzes in solid state. This liquid state decreases the oxidation of antioxidants, as well as the oxidation of CNTs wrapped by the liquid, since the oxidation in carbon containing materials is controlled by oxygen diffusion in the decarbonised layer (Simmat et al., 2003). This is the reason that a lot of CNTs still can be found after coked at 1400°C as shown in Fig.9. On the contrary, CNTs can not be observed in the matrix of the samples with liquid and powder resin as binder systems. In one hand, Carbores^P powder improves the mechanical properties by promoting the formation of carbides or nitrides from antioxidants as Al, Si in the Al_2O_3-C refractories due to the liquid state of Carbores^P at elevated temperature. On the other hand, ceramic bonding makes Al_2O_3-C materials much brittle to resist the thermal shock and crack propagation under load, as revealed by batch E in Table 3. Thus the flexible phases such as CNTs are necessary to enhance the integrated service properties of Al_2O_3-C refractories.

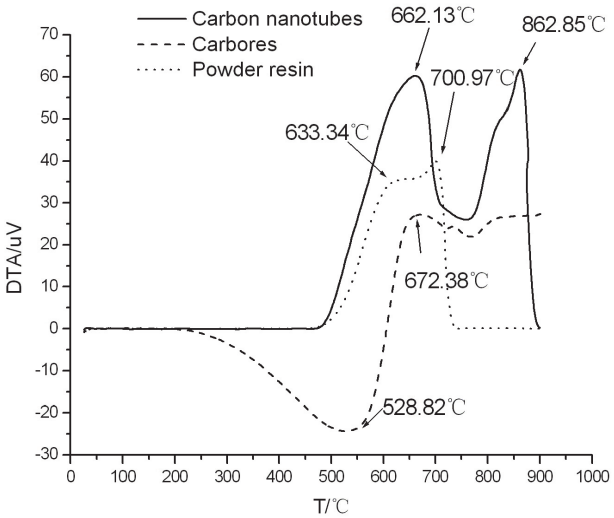

Fig. 15. DTA traces of high temperature oxidation of coked powder resin, coked Carbores and carbon nanotubes at 10K min^{-1}

2.4 Conclusion

Carbonaceous resin powder (Carbores) is well known in carbon containing materials due to not only its environmental friendly but also its improvement on the oxidation resistance and mechanical properties of refractories, compared to liquid and powder resin. Due to the protection based on the Carbores^{P} –binder system during the heating process, antioxidant Al reacts with CNTs into thicker Al_4C_3 nano or submicron tubes before Al or CNTs are oxidised. Whiskers formed by Si with carbon nanotubes are much thinner than original CNTs, and microsilica fume with a SiC layer is generating anchors and honeycomb microstructures. The combination of additives such as Al, Si, SiO_2 and CNTs enhance the mechanical and thermo mechanical properties, whereby the propagation velocity of the crack is decreased due to the flexibility enforcement by CNTs.

3. Application of CNTs in carbon block for blast furnace

The lifetime of a blast furnace (BF) is decided mainly by the rate of erosion and corrosion of the carbon block in the hearth and bottom area. Currently, carbon block for a BF are being developed with high thermal conductivity and a highly microporous structure. Here, the effect of CNTs addition on the thermal conductivity and porosity characteristics of carbon block for BF is demonstrated. Further considering the cost and dispersion of CNTs, in-situ formation of CNTs in the carbon specimens may be a better choice. In our work, CNTs can be derived from the modified resin containing Ni element, and resin is also one of binders of carbon block. So the effect of the modified resin containing Ni element on the thermal conductivity and porosity characteristics of carbon block is investigated.

3.1 Experimental procedure

Electric-calcined anthracite granules and fine powder (3–5 mm, 1–3 mm, 0–1 mm, and <0.088 mm; Fangda Carbon Co., Ltd., Beijing, China), flaky graphite (<0.075 mm; Qingdao Hengsheng Graphite Co., Ltd., Qingdao, China), brown corundum (<0.075 mm; Zhengzhou Zhenjin Refractory Co., Ltd., Zhengzhou, China), metallic silicon (<0.045 mm; Zhejiang Kaiyuantong Silicon Co., Ltd., Kaiyuan, China), and CNTs (Alpha Nano Tech. Inc., Chengdu, China; diameter: >50 nm, length: ~20 lm, purity: >95 wt%, ash:<1.5 wt%, electrical conductivity:>104 S/m) were used as starting materials. Thermosetting phenolic resin (50 wt% of carbon yield; Yongli Refractory Co., Ltd., Zibo, China) was used as a binder. The chemical composition of all the starting materials is shown in Table 4. The basic recipe contains 66 wt% electric-calcined anthracite, 20 wt% graphite, 6 wt% brown corundum, and 8 wt% Si. CNTs content in the carbon block various from0.5, 1, 2, 3, 4, to 5 wt%. 11 wt% resin was used as a binder with 5 wt% absolute alcohol. For the homogeneous dispersion of CNTs in the mixture, CNTs were first mixed with resin for 30 minutes with the aid of absolute alcohol. In another experiments, the modified resin containing Ni element as binder was added into the carbon block(2%, 4%, 6%, 8% and 11% respectively). The starting materials were mixed for 30 minutes in a mixer with the rotating speed of 80–100 revolutions per minute. After kneading, cylindrical specimens with 50 mm in diameter and 50 mm in height were pressed under the pressure of 100 MPa. Afterwards the specimens were cured at 110°C and 200°C for 10 hours, respectively, in a muffle furnace. The coking of as-prepared specimens was carried out at 1200°C and 1400°C for 3 hours, respectively, in a crucible filled with industrial carbon grit.

	C	Al_2O_3	SiO_2	Si	Ash	Volatile	Fe	TiO_2
electric-calcined anthracite	93	3.87	3.96		7.34	1.35		
Flaky graphite	≥97					1.4		
Brown corundum		≥96	≤0.9				≤0.15	2.5
Metallic silicon				≥98			0.5	

Table 4. Chemical compositions of the raw materials (mass percent)

The bulk density and apparent porosity of the fired specimens were measured. The cold crushing strength was determined in terms of GB/T 2997–85. The micropore size distribution was examined by a mercury porosimeter (Autopore IV9500; Micromeritics Instrument Corp., Norcross, GA). The thermal conductivity was calculated from the product of thermal diffusivity measured using the flash diffusivity technique (Flashline 5000; Anter Corp., Pittsburgh, PA); and heat capacity were also measured. The diffusivity was measured in a direction parallel to the forming direction of the initial carbon block. The samples for cross-sectional analysis were prepared from the fractured specimens and were observed by a field-emission SEM (Nova400 Nano FESEM; FEI Co., Philips', Hillsboro, OR).

3.2 Results and discussion

3.3.1 Effect of CNTs on pore structure and thermal conductivity

A. Pore characteristic and microstructure

Fig. 16 and 17 show the apparent porosity and bulk density of specimens with different CNTs content treated at 1200 °C and 1400 °C in coke bed. The apparent porosities increase and bulk densities decrease with increasing CNTs content. Fig. 18 shows the variations of porosity characteristics. The mean pore diameter for the coked specimens decreases by the addition of 0.5 wt% CNTs, but increases gradually again by subsequent addition of CNTs, e.g., at 1400 °C, from 0.18 μm for 0.5 wt% CNTs to 0.44 μm for 5 wt% CNTs. Meanwhile, the trend of<1 μm pore volume was opposite to that of mean pore diameter, e.g., at 1400 °C, from 80.8 pct for 0.5 wt% CNTs to 66.7 pct for 5 wt% CNTs. As 0.5 wt% CNTs were added, a less amount of CNTs can be dispersed in the matrix easily as filler and can result in an increased particle packing density. The degradation of porosity characteristics by adding CNTs of more than 0.5 wt% may be due to high surface area ratio of CNTs and difficulties in getting a homogeneous dispersion.

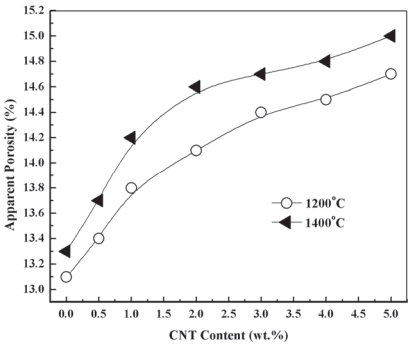

Fig. 16. The variations of apparent porosity as a function of CNT content.

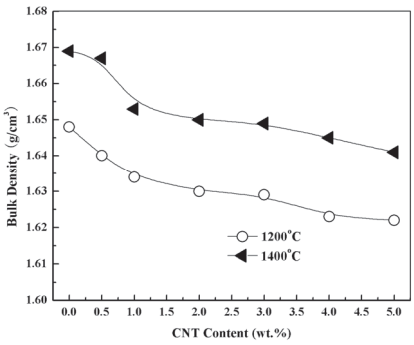

Fig. 17. The variations of bulk density as a function of CNT content.

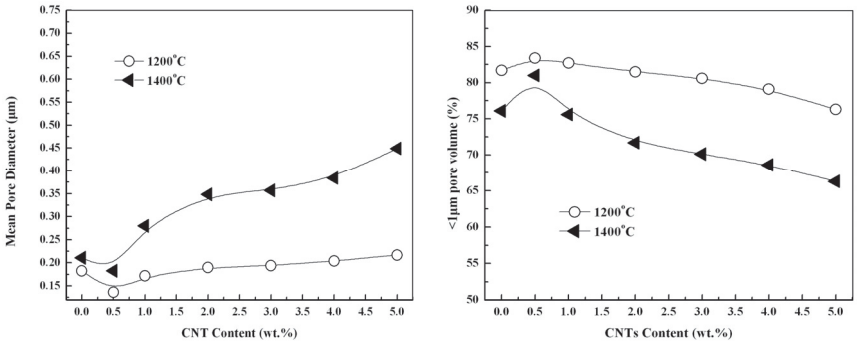

(a) Mean pore diameter (b) < 1μm pore volume

Fig. 18. The variations of porosity characteristics as a function of CNT content. (a) Mean pore diameter and (b) <1μm pore volume.

Fig. 19 shows SEM images of fractured specimens with different CNT contents after coking at 1200 °C. For the specimen without CNTs, large amounts of cristobalite particles and SiC whiskers are observed in the matrix with pores (Fig. 19(a)). The amount of cristobalite decreased and SiC increased with the addition of CNT (Fig. 19(b) and (c)), which was attributed to the oxygen partial pressure reduction by adding CNTs. Another notable phenomenon is that the aspect ratio of SiC whiskers became larger with the increased amount of CNTs. From previous work, it was deduced that the pore structures of specimens became worse (Li et al., 2009). Temperature played an important role in the evolutions of cristobalite and SiC whiskers. For the specimens prepared by coking at 1400 °C, the amount of cristobalite decreased and that of SiC increased (Fig. 20), which reveals that the elevated temperature can be favourable for the formation of SiC.

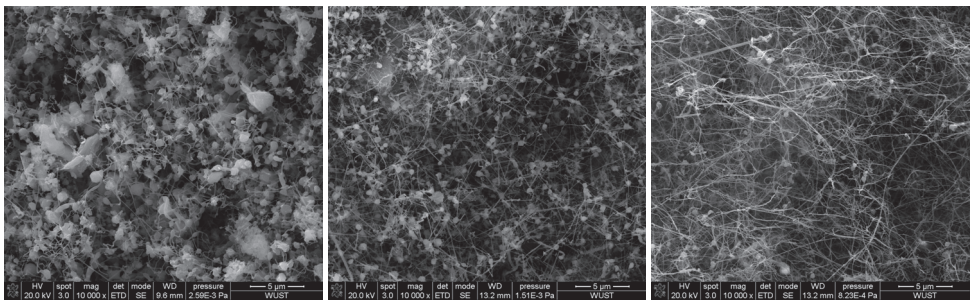

(a) (b) (c)

Fig. 19. SEM images of fractured specimens with different CNT contents after coking at 1200°C: (a) 0, (b) 2 wt%, and (c) 5 wt%..

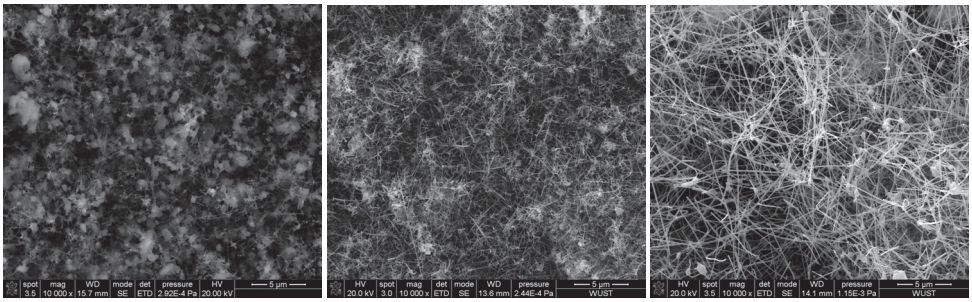

(a) (b) (c)

Fig. 20. SEM images of fractured specimens with different CNT contents after coking at 1400 °C: (a) 0, (b) 2 wt%, and (c) 5 wt%.

It was difficult to detect CNTs in the coked specimens. High-magnification SEM indicates that some CNTs were aggregated in the resin locally and were surrounded by graphite flake (Fig.19). Agglomeration observed in coked body resulted from poor dispersion of CNTs during mixing process, which hardly can be avoided because of the high specific surface area of CNTs. It is difficult to achieve a tight interface bonding between the CNTs and the surrounding matrix (Indra et al., 2007; Tsuyohiko et al., 2009), and thus, some CNTs were surrounded by the presence of oxygen. Combined with the previous observations, it can be deduced that the CNTs act as carbon source based on their high reactivity (Emilia & Katarina, 2005) and were consumed by the following reaction during heating process:

$$3C\ (s)+O_2(g)+Si\ (s)=SiC\ (s)+2CO\ (g) \quad (1)$$

It seems that the surrounding atmosphere can produce a significant effect on the survival of CNTs. Under the N_2 (Lim et al., 2005) or vacuum atmosphere (Yeh et al., 2006), CNTs remained intact after the heating treatment. In this work, although the main atmosphere consists of CO and N_2 in theory (Chen, et al., 2008), in fact, locally the oxygen partial pressure is high, especially in the pores and interfaces, plus the high activation of CNTs, and thus CNTs can be consumed easily in increased temperature.

B. Thermal conductivity

The variations of thermal conductivity (25°C) are shown in Fig. 22. The thermal conductivity of the specimens coked at two different temperatures was increased with the increased amount of CNTs up to 4 wt%. For example, at 1400 °C, the thermal conductivity was enhanced from 16.5W/(m·K) for the no CNT specimen to 20.8 W/(m·K) for the 4 wt% CNT specimen, but it decreased slightly again by adding more CNTs. For each carbon specimen, the thermal conductivity of specimens coked at 1400°C was higher than that at 1200°C. The enhancement of thermal conductivity with the addition of CNTs was explained by the increased formation of SiC and the presence of more residual CNTs. The degradation of thermal conductivity by adding CNTs of more than 4 wt% may be attributed to the matrix structure deterioration of coked specimens, which can be shown from the variations in apparent porosity and bulk density. The apparent porosity increased and the bulk density decreased with increasing CNT content. The formation of more interfaces and difficulties in getting a homogeneous CNT dispersion can be responsible for such variations. Indra et al. reported that the interface has a negative effect on thermal conductivity of the composites (Indra et al., 2007). Jiang and

Tsuyohiko et al. found that the homogeneous dispersion of CNTs can increase in the thermal conductivity (Jiang et al., 2008; Tsuyohiko et al., 2009). In our previous work, we found that the high thermal conductivity SiC phase content increased with the coking temperature (Chen et al., 2009), which resulted in the increase of thermal conductivity.

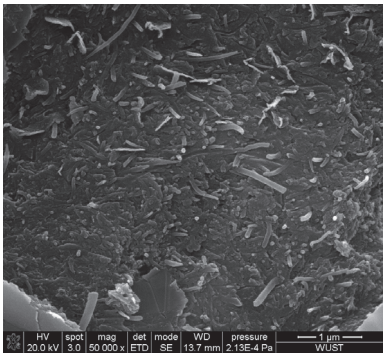

Fig. 21. CNTs in the matrix of specimen with 5% CNTs cocked at 1400 °C.

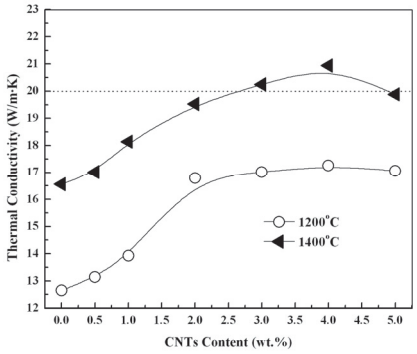

Fig. 22. The variations of thermal conductivity (25 °C) as a function of CNT content.

Theoretically, CNTs can improve the thermal conductivity of coked specimens considerably because of their high thermal conductivity. However, most CNTs were consumed and thus unused, which was contrary to the original expectation. So, how to retain the CNTs intact in the coked specimens is a big challenge. Morisada et al. reported that CNTs can be coated with a SiC layer using SiO vapor in vacuum, thereby enhancing the oxidation resistance of CNTs (Morisola et al., 2004). Liang et al. found that uniform and compact SiC coatings on the surfaces of CNTs can be synthesized in the initial polycarbonsilane/xylene concentration section of 10–15 pct (Liang et al., 2008). Incorporating or in situ forming such CNTs coated with SiC in carbon block may result in the retention of CNTs.

3.3.2 Effect of modified resin on pore structure and thermal conductivity

A. Pore characteristic and microstructure

Fig. 23 shows the mean pore diameter and < 1μm pore volume of specimens with different modified resin content. The mean pore diameters of specimens treated at 1200 °C have no obvious change, but they increased markedly with increasing of modified resin content at 1400 °C, accordingly, < 1μm pore volume of specimens decrease evidently.

Fig. 24 shows SEM images of fractured specimens with different modified resin contents. At 1200 °C, there are a great deal of cristobalite particles and SiC whiskers in the specimens; the amount of cristobalite particles also decreased and SiC whiskers increased with the addition of modified resin. Compared with the addition of CNTs, the amount of SiC whiskers are more, and the length/diameter ratio of the whiskers increases. Further observation at high magnification , CNTs are not detected, but a great deal of one dimension of nanoscale fibres/whiskers are easily found in the matrix, just about 10-30 nm in diameter, and mostly composed of carbon with a little Si element. In our previous work, CNTs can be derived by the catalysis of Ni during the process of pyrolysis of modified resin. However, new CNTs have high reaction activity; it is easily oxidised under high oxygen partial pressure conditions in coke bed. In addition, there are 8% silicon in our system, and gaseous substances such as Si(g)

or SiO(g) will occur at high temperature. So the addition of modified resin benefits the formation of SiC whiskers. When the treated temperature is up to 1400 °C, more cristobalite particles occur and just a few SiC whiskers exist in the specimens. At elevated temperature, more gaseous substances are generated, and a part of gaseous substance escape from the inner of specimen, which leads to the apparent porosity increase and the accelerated oxidation of CNTs. This may be the reason for the reduction of whiskers and increase of cristobalite particles obviously.

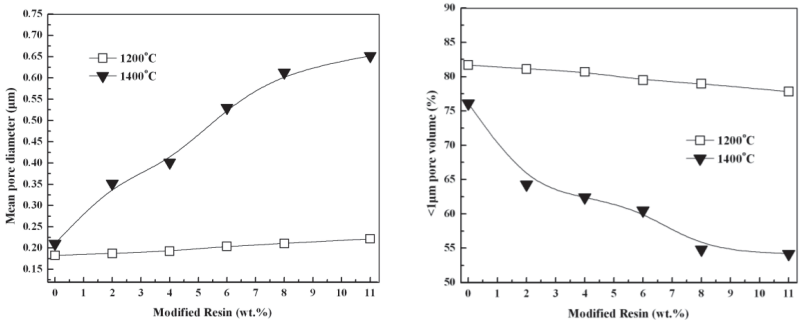

(a) Mean pore diameter (b) < 1μm pore volume

Fig. 23. Mean pore diameter and < 1μm pore volume as a function of modified resin content

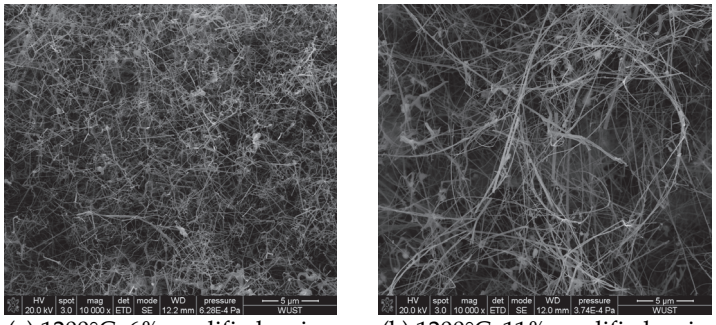

(a) 1200°C, 6% modified resin (b) 1200°C, 11% modified resin

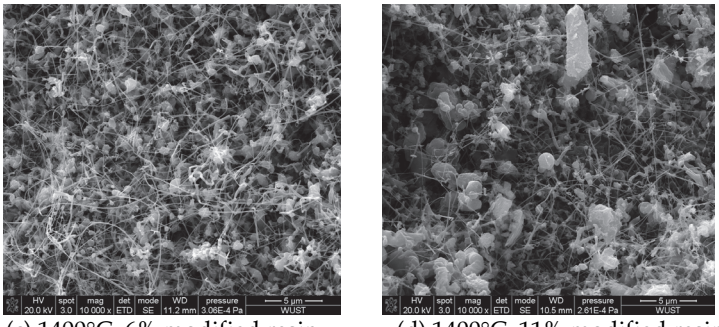

(c) 1400°C, 6% modified resin (d) 1400°C, 11% modified resin

Fig. 24. SEM images of fractured specimens with different modified resin content after coking

B. Thermal conductivity

Fig. 25 shows the thermal conductivity of the carbon specimens coked at 1200°C and 1400°C when the modified resin was used. The thermal conductivities at room temperature increased with the addition of modified resin and decreased when the amount of modified resin is bigger than 8%. The thermal conductivity of the specimen with 8 wt% modified resin coked at 1400°C is the largest, approaching to22.2 W/m·K; compared with no modified resin specimen, it increases by about 30%. From the fracture microstructure of specimens, some fine SiC whiskers or one dimension carbon materials can be easily found in the matrix, and the quantity of SiC whiskers increases with the addition of modified resin. Whether modified resin transforms into CNTs or SiC whiskers, they all enhance thermal conductivity of the specimens. Compared with the direct addition of CNTs, the addition of modified resin is more effective to enhance thermal conductivity. So it is feasible to use modified resin as the binder for improving the thermal conductivity of carbon block.

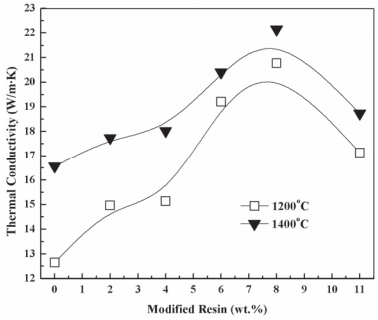

Fig. 25. Thermal conductivity at room temperature changing with addition of modified resin

3.3 Conclusions

The direct addition of CNTs benefits the enhance of the thermal conductivity of carbon block for blast furnace, although just a few CNTs are remaining in the specimens. At high temperature, most of CNTs act as carbon source, react with Si to form SiC whiskers. With the increase of CNTs content, the formation amount of SiC whiskers is increased and their aspect ratio becomes larger, and the SiC whiskers tend to be nonhomogeneously distributed. The thermal conductivity of the carbon specimen containing 4 wt% CNTs is the highest, which can be attributed to the contribution of the SiC whiskers and residual CNTs. However, the excessive addition of CNTs degrades the porosity characteristics. The addition of modified resin also benefits the formation of SiC whiskers, and enhances thermal conductivity more effectively. Considering the cost and dispersion of CNTs, it is feasible to use modified resin as a binder system for improving the thermal conductivity of carbon block.

4. References

Aneziris, C; Borzov, D. & Ulbricht J. (2003). Magnesia-Carbon bricks-a high duty refractory material, *Interceram- Refractories Manual*, 22-27, ISSN 0020-5214.

Aneziris, C; Jin, S. & Li, Y. (2009). Interactions of carbon nanotubes in Al_2O_3-C refractories for sliding gate application. *UNITECR'09*, 2009, Brazil.

Boenigk, W.; Stiegert, J. & Jacob, C. (2004). MgO-C-bricks produced in a cold-mixing process using a graphite forming binder system, *47th Intern. Colloquium on Refractories*, Aachen, 46-51, ISSN 1004-4493.

Chen, X.; Li, Y. & Li, Y. (2008). Carbothermic reduction synthesis of Ti(C, N) powder in the presence of molten salt. *Ceramics International*, 34: 1253-1259, ISSN 0272-8842.

Chen, X.; Li, Y. & Li, Y. (2009). Effect of temperature on the properties and microstructures of carbon refractories for blast furnace (BF). *Metallurgical and Materials Transactions A*, 40A, 1675-1683, ISSN 1073-5623.

Emilia, I. & Katarina, C. (2005). Kinetics of oxidation in various forms of carbon. *Journal of Thermal Analysis and Calorimetry*, 80:103-108, ISSN 1572-8943.

Illeková, E. & Csomorová, K. (2005). Kinetics of oxidation in various forms of carbon, *J. Thermal Analysis and Calorimetry*, 80: 103-108, ISSN 1418-2874.

Indra, S.; Masataka, T. & Morinobu, E. (2007). Effect of interface on the thermal conductivity of carbon nanotube composites. *International Journal of Thermal Sciences*, 46: 842-847, ISSN 1290-0729.

Lim, D.; You, D. & Choi, H. (2005). Effect of carbon nanotube addition on the tribological behavior of carbon/carbon composites. *Wear*, 259: 539-544, ISSN 0043-1648.

Jiang, L. & Gao, L. (2008). Densified multiwalled carbon nanotubes–titanium nitride composites with enhanced thermal properties. *Ceramics International*, 34: 231-235, ISSN 0272-8842.

Li, Y.; Chen, X. & Sang, S. (2010). Microstructure and Properties of Carbon Refractories for Blast Furnace with SiO_2- and Al-additions. *Metallurgical and Materials Transactions A*, 41A: 2085-2092, ISSN 1073-5623

Liang, T.; Zhao, H. & Zhang, Y. (2006). Electromagnetic Wave Absorption Properties of SiC Coated CNTs Nano-composites, *J. Inorg. Mater.*, 21(3): 659–63, ISSN 1000-324X.

Tsuyohiko, F.; Takahiro, F. & Naotoshi, N. (2009). Evaluation of dispersion state and thermal conductivity measurement of carbon nanotubes/UV-curable resin nanocomposites. *Synthetic Metals*, 159: 827–830, ISSN 0379-6779.

Morisada, Y.; Maeda, M. & Shibayanagi, T. (2004). Oxidation resistance of multiwalled carbon nanotubes coated with Silicon Carbide. *Journal of the American Ceramic Society*, 87(5): 804 -808, ISSN 0002-7820.

Simmat, R. & Pötschke, J. (2003). Oxidation experiments on different types of carbon bond of refractories, *Stahl und Eisen Special*, 11-12, ISSN 0340-4803.

Shadab, S.; Khalid, L. & Edward, S. (2007). The effect of a CNT interface on the thermal resistance of contacting surfaces. *Carbon*, 45: 695-703, ISSN 0008-6223.

Yeh, K.; Tai, H. & Liu, H. (2006). Mechanical behavior of phenolic-based composites reinforced with multi-walled carbon nanotubes. *Carbon*, 44: 1-9, ISSN 0008-6223.

16

Carbon Nanotube-Based Photonic Devices: Applications in Nonlinear Optics

Amos Martinez and Shinji Yamashita
The University of Tokyo
Japan

1. Introduction

Carbon Nanotubes (CNTs) were first discovered by Sumio Ijima in the early 90s (Ijima et al., 1991). CNTs have since become a prominent material for an amazing breath of scientific and technological disciplines ranging from structural and material science to chemistry, biology and electronics (Dresselhaus et al., 2001). Compared to other areas of science, the study and exploitation of the optical properties of CNTs is still in its early years. In the late 1990s, various theoretical and experimental studies reported the remarkable optical properties of Carbon nanotubes (CNTs) (Kataura et al., 1999; Margulis & Sizikova, 1998). Since then, the potential applications of CNTs have been attracting increasing attention from the photonics research community. CNTs exhibit an exceptionally high third-order optical nonlinearity and nonlinear saturable absorption with ultrafast recovery time and broad bandwidth operation. Thus, CNTs are becoming a key component towards the development of fibre lasers and nonlinear photonic devices. Despite the relative late start, photonics is now one of the research fields where CNTs are making a more significant contribution towards the development of next generation devices both from an academic and an a commercial point of view.

CNTs are structures from the fullerene family consisting of a honeycomb sheet of sp^2 bonded carbon atoms rolled seamlessly into itself to form a cylinder. Single-walled CNT are nearly one-dimensional (1D) materials with a diameter ranging from 1nm to 3 nm, and a length that can go from 100s of nanometers to centimetres. The electronic properties of single-wall CNTs are governed by a single parameter named the chiral vector, which indicates the orientation of the tube axes with respect to the orientation of the honeycomb. Depending on this parameter, single-wall CNTs may behave as semiconductors or as metals. Those CNTs that behave as semiconductors exhibit a direct electronic bandgap which is directly proportional to the diameter of the nanotube. The optical absorption of CNT is determined by their electronic bandgap and broadband operation is a result of a large distribution of diameters formed during the CNT fabrication (Kataura et al. 1999). This discovery led to the now widespread use of CNTs in saturable absorption applications. Previous to that work, Margulis and Sizikoba had estimated theoretically that CNT presents a very high third order susceptibility $\chi^{(3)}$ in the order of $10^{-8} m^2/W$. Third order susceptibility is responsible for processes such as third harmonic generation (THG), optical Kerr effect, self-focusing and phase conjugation (Margulis and Sizikoba, 1998). Materials with a high nonlinearity combined with a fast response time are desired for roles areas such as optical

communications and information technology, where they can perform optical functions such as optical switching, routing and wavelength conversion.
CNTs have also found several other applications in photonics including nanometre-scale light sources, photodetectors and photovoltaic devices (Avouris et al., 2008). These applications rely on the properties of a single CNT and their potential applications in a field-effect-transistor (CNT-FET) configuration. Such CNT-FETs not only have great potential towards the development of future optoelectronic applications, but also offer an excellent platform to study optical phenomena in one-dimension. The focus of this chapter however, lays in the CNT applications in the areas of fibre lasers and optical communications. Those applications are based on the CNTs nonlinear optical absorption which is useful for noise suppression and passive mode-locked lasing (Set et al., 2004) and their high nonlinearity which has a great potential towards the implementation of optical switches (Liu et al., 1999; Chen et al., 2002). These applications rely on using a large number of CNTs and their combined optical properties. During their bulk fabrication, a large number of single-walled CNT with different tube diameters and different electrical properties are created. For most applications, the lack of ability to fully control the diameter and chiral vector of the CNTs during fabrication is a drawback. For optical fiber devices on the contrary, it is auspicious that the current fabrication processes produces a distribution of single-wall CNTs with different diameters, some behaving as a semiconductor and some as metals. The role of the semiconducting CNT is to provide the saturable optical absorption, which is proportional to the diameter of each individual CNT. The wide distribution of CNT's diameters provides broadband operation and the metallic CNTs also play an important role towards reducing the recovery time.
This chapter is structured as follows; in section 2, the physical mechanisms that are accountable for the exceptional optical properties of carbon nanotubes (CNTs) will be described. In section 3, we will describe the various methods that have been proposed for the fabrication of CNT-based photonic devices and introduce the relevant parameters that must be taken into account while preparing a CNT-based device for different applications. In section 4 we will review the most significant advances reported to date regarding passive mode-locked lasing, which is arguably the application were CNTs have made their most significant contribution so far. In section 5, we will investigate the potential applications of CNTs in optical switching devices by four-wave mixing and polarization rotation and discuss the requirements that would need to be met before such devices can be considered for commercial applications. Finally, in section 6, we will discuss the future of CNT-based photonic devices in the context of becoming an integral part in the fast developing fiber laser technology and the challenges ahead, such as the advent of graphene as an alternative to CNTs and semiconductor saturable absorbers (SESAMs) for many applications and the needs for improved robustness and long term stability of CNT-based photonic devices.

2. Optical properties of CNT

The original interest to apply CNTs in photonics started in the late 1990s soon after Margulis et al. reported the first theoretical study on the very high third order nonlinearity of CNT and Kataura et al. reported for the first time the nonlinear optical properties of single-wall CNT. Most applications in photonics require single-wall CNT, hence from here on we will refer to those single-wall CNTs simply as CNTs. The optical properties of CNTs are linked closely to their structural and electronic properties and are fully governed by one parameter, its chiral vector, which describes how the carbon-atom honeycomb is organized with respect

to the CNT axis. Depending solely on this parameter, CNTs may behave as a direct band-gap semiconductor or as a metal.

2.1 Electronic structure

The electronic properties of a CNT are determined by its chiral vector. This vector describes how the graphene sheet is rolled when forming the nanotube. The chiral vector, C_h is expressed by two real space unit vectors a_1 and a_2 and two integers n and m as shown in equation 1:

$$C_h = n\bar{a}_1 + m\bar{a}_2 \tag{1}$$

Graphene is a semimetal, when the single-layer graphene is rolled to form a tube an extra level of confinement into a quasi-1D structure is added. CNTs behave as metals if the subtraction of the integer values n and m is an integer multiple of 3 (n-m=3k) otherwise it is a semiconductor (n-m≠3). Hence, statistically we can conclude that 2/3 of CNTs will be semiconductors, while 1/3 will be metallic CNTs. Saturable absorption is a result of the excitonic absorption in semiconductor nanotubes (Saito et al., 1992).

The density of states of a semiconducting CNT can be numerically calculated. In figure 1, the density of state of two semiconducting CNTs with different diameters is shown. In fact, the electronic density of states of CNT, originates from the "slicing of the graphene density of states due to the quasi-1D confinement of the electrons, which leads to the presence of the characteristic Van Hove singularities observed in their electronic densities of state (DOS) of the two CNTs shown in figure 1 (from Yamashita et al., 2007). Semiconducting CNTs absorb photons in the same way an ordinary direct bandgap semiconductor would do when the energy of the photon is equal to the bandgap of the CNT. The CNT's bandgap is inversely proportional to the diameter of the tube. It is particularly fortunate that the diameter of a CNT typically ranges from 1nm to 2nm, which leads to an optical absorption that overlaps the 1550nm window commonly used for fiber optic technologies.

Figure 1(c) shows the characteristic relation of the energy bandgap as a function of the diameter of the semiconductor CNT. This figure is known as the Kataura plots and indicates the allowed band transmissions based on the diameter of the tube.

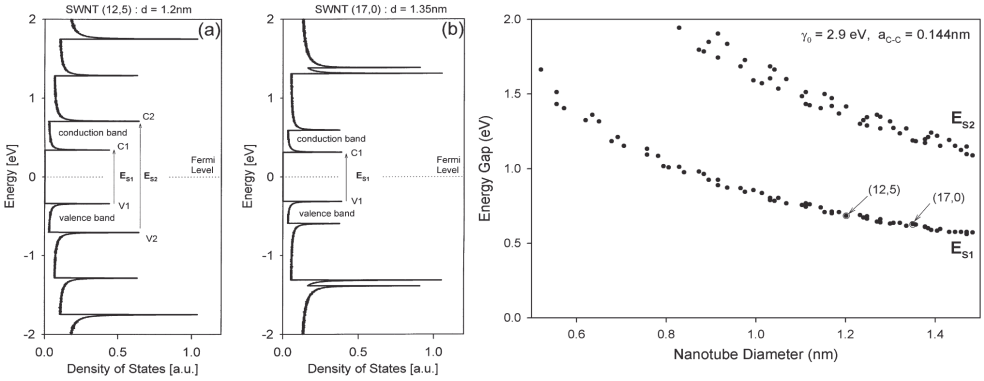

Fig. 1. (a) and (b) show the calculated electronic density of states (DOS) of two CNTs with tube diameters 1.2nm and 1.35, respectively. Both DOS exhibit sharp singularities caused by the characteristic 1D structure of CNT (c) shows the relation between the nanotube's diameter and the allowed electron transitions. Figure taken from (Yamashita et al., 2007)

2.2 Saturable absorption

The optical absorption of CNTs is of saturable, intensity-dependent nature, it is, therefore, a suitable material to employ for passively mode-locked laser operation. Passive mode-locking is achieved by incorporating an intensity-dependent component into the optical system, this is generally a saturable absorber which absorbs the incoming light linear up to a given threshold intensity, after which it saturates and becomes transparent. Such saturable absorbers discriminate in favor of pulse formation over continuous wave lasing.

Current processes for the bulk fabrication of CNTs do not allow complete control over the chirality and diameter of the fabricated CNTs. Instead, a combination of metal and semiconductor CNTs and multi-wall CNTs are produced during fabrication. Nevertheless, researchers are now able to separate CNTs according to their chiral vector through post-fabrication processes. In actual fact, depending on the application, a wide distribution of CNT diameters or a very narrow distribution may be beneficial. Hence, the ability to control the mean diameter and diameter distribution through the fabrication, purification and separation processes is likely to further extend the applications of CNTs in photonics. Figure 2(a) shows the typical absorption of a suspension of CNT fabricated by the high pressure carbon monoxide method (HiPCO) and measured by a spectrometer, Absorption peaks rise from the inter Van Hove transitions between the different semiconductor and metal transitions and can be clearly identified in the spectrometer measurements.

For ultrashort pulse generation, a saturable absorber with a fast recovery time is required for stabilizing laser mode locking, while a slower recovery time could facilitate laser self-starting. Ultrafast recovery times of few 100s of femtoseconds have been reported making CNTs a suitable material for ultrashort pulse generation. But it is worth noting that, the recovery time is not so fast if we consider only isolated semiconducting CNTs, in this case, the recovery time is in the order of 30ps (Reich et al., 2004). The ultrafast response time of CNTs is based on bundle and entanglement of semiconducting and metallic CNTs because electrons which are excited by photons in semiconducting CNTs tunnel and couple to metallic CNTs, resulting in ultrafast recovery time of semiconducting CNTs. The combination of fast and slow processes within the CNT distribution, allows CNT to be a very efficient saturable absorber both to self-start the mode-locking operation and to produce ultrashort pulses. In addition, the inability to fully control the diameter of the CNTs during their growth is advantageous for the implementation of fiber lasers. In fact, the wide distribution of CNT diameters is responsible for the very broadband operation of CNT-based saturable absorbers. This is one of the key advantages of CNT-based devices, as has been demonstrated by Kivistö et al. achieving passive mode-locked operation not only in the C and L band but covering also the wavelength range from 1μm to 2μm using a single CNT saturable absorber (Kivistö et al., 2009).

In figure 2, the absorption characteristics of CNT-devices are summarized. Figure 2(a) shows the characteristic optical absorption properties of a CNT dispersion, the characteristic absorption peaks generated by the Van Hove transitions can be clearly observed. Figure 2(b), depicts the normalized saturable absorption, from the data in Figure 2(b) we can determine three parameters that together with the response time give us an indication of the applicability of CNTs for passive mode-locking applications. Those parameters are the non-saturable losses (α_{ns}), the modulation depth (α_0) and the saturation intensity (I_{sat}) fitted using a saturable absorber model, based on equation 2 (Wang et al., 2008).

$$\alpha(I)=\frac{\alpha_0}{1+I/I_{Sat}}+\alpha_{ns} \quad (2)$$

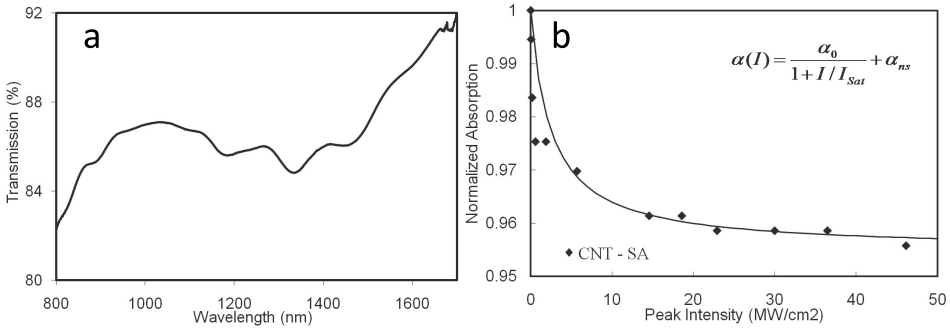

Fig. 2. Characterization of the optical absorption of CNT. (a) Characteristic broad optical absorption of a CNT solution measuredby an spectrometer. (b) Normalized absorption, the modulation depth and saturation fluence are in this case, 5% and 3MW/cm^2.

2.3 Third order nonlinearity

The first theoretical studies on the third order nonlinearity of CNTs appeared in 1998 when Margulis and Sizikova reported an estimated nonlinear refractive index coefficient, n_2 as high as $2x10^{-8}$ (m^2/W). To put this theoretical value into context, n_2 for the silica glass is $3x10^{-20}$(m^2/W) and chalcogenide glass, which is recently receiving much attention as a suitable material for the fabrication of highly nonlinear fibers has a n_2 value of $2x10^{-18}$m^2/W. Table 1 shows typical third order susceptibility values for various materials used in nonlinear optics.

	Silica glass	Chalcogenide glass	Poly-diacetylene (PDA)	GaAs	Si	CNT
n_2 (m^2/W)	3×10^{-20}	2×10^{-18}	1×10^{-15}	1×10^{-10}	4×10^{-18}	2×10^{-12}
Response time (ps)	~0.01	~0.01	~0.01	~100	0.01	<1
Absorption	small	small	small	large	small	large

Table 1. Comparison for the nonlinear refractive coefficient (n_2), the response time and the optical absorption for various materials commonly used for nonlinear optics.

The optical nonlinearity of CNT comes from the 1D motion of the delocalized π-band electrons at a fixed lattice ion configuration. These estimations attracted a great deal of attention since third order nonlinearity is responsible for phenomena such as third harmonic generation (THG), optical Kerr effect, self-focusing and phase conjugation. As a result, third

order nonlinear materials can be considered for optical functions such as optical switching, routing and wavelength conversion. The difficulty is that for most third order nonlinear optical materials, the third order susceptibility was too low for practical applications; the extremely high n_2 of CNT opened a new potential application for CNT.
Optical nonlinearity is due to optical intensity dependent nonlinear response of dielectric materials. When the optical intensity of propagating light in a dielectric material is low, stimulated polarization is linearly proportional to the optical intensity. However, at high optical intensities, the stimulated polarization, P, exhibits a nonlinear response to the optical electric field, E, as described by equation 3 (Agrawal, 1995);

$$P = \varepsilon_0 \left(\chi^{(1)} \cdot E + \chi^{(2)} : EE + \chi^{(3)} \vdots EEE + \ldots \right) \tag{3}$$

Where $\chi^{(1)}$, $\chi^{(2)}$ and $\chi^{(3)}$ correspond to the linear, second and third order susceptibility. It has been reported that some types of CNTs present a high $\chi^{(2)}$, however there is not much active research on exploiting this property. On the other hand, the high values of $\chi^{(3)}$ calculated theoretically and experimentally are of great interest. In most cases there is a trade-off between high optical nonlinearity and recovery. For instance, optical fibers generally exhibit low nonlinearity and a fast response time while semiconductor based devices generally operate with a high nonlinear coefficient and low response time. Remarkably, CNT devices offer a very high nonlinear coefficient combined with a fast response time due to their nanostructures and the Van der Waals induced bundling. In CNTs, there are two main contributions to their relaxation processes; a non-radiative relaxation such as multi-phonon emission through electron-phonon coupling and an excited electron tunneling to neighbouring CNTs. Since the CNTs whose electrons are excited and those whose electrons are relaxed are different, fast relaxation process in the order of 100s of femtoseconds combined with an extremely high nonlinear coefficient can be obserbed in real CNT devices. Of course, the technological implications of using such material would be enormous since it opens the door for the fabrication of nonlinear devices with miniature size and lower power consumption leading to further integration and compactness of CNT-based nonlinear devices. However, their implementation presents numerous challenges; in particular in order to exploit the third order nonlinearity of such devices CNT, the interaction length between the CNT and the optical field must be increased. Unlike silica and chalcogenide glasses, CNTs absorption of the incident light is very high, this combined with the high scattering of CNT bundles complicates the fabrication of nonlinear devices with longer interaction lengths required to increase the nonlinearity of the device. In section 3.3, the current efforts towards fabrication CNT-fiber devices with increased interaction length suitable for the exploitation of the nonlinear susceptibility of CNT for optical switching applications is described. Section 5, describe the few experimental demonstrations of optical switching by polarization rotation and four wave mixing (FWM) using CNT-based devices with long interaction lengths.

3. Fabrication of CNT-based photonic devices

Since 2003, several laser configurations and methods in which to integrate the CNTs into the fiber have been considered, each to suit different requirements. Initial devices were fabricated by spraying a solution of CNT in a substrate, mirror or fiber ferrule (Set et al., 2004; Yamashita et al., 2005) or by direct growth of the CNT in a substrate using chemical

vapor deposition (CVD) (Song et al., 2007). In order to spray the CNTs, they are first independently dispersed into a solvent, such as Dimethylformamide (DMF) solvent by ultrasonification. This is necessary in order to separate individual CNTs and breaking of bundles of CNT that are formed due to van der Waal forces. Once efficient dispersion is achieved the solution is subjected to centrifugation so the remaining agglomerated CNTs can be separated and discarded. The CNTs can then be sprayed into the substrate surface, using a set-up such as shown in figure 3(a).

While the spray method is suitable to fabricate CNT-Saturable absorbers, the usage of CNT in order to coat the fiber is very high. Kashiwagi et al. and Nicholson et al. developed a method where by using an optical deposition technique CNTs could be deposited efficiently only in the core area of the fiber, reducing the CNT solution usage dramatically (Kashiwagi et al., 2007; Nicholson et al., 2007). The experimental set-up used for the optical deposition of the samples is shown in Fig.3 (b). Deposition is achieved by immersing a flat fiber connector into the solution of CNT on DMF and launching a high-power light into the fiber. The optical power required to achieve optical deposition is dependent on a number of parameters, including the concentration levels of the solution, and how well the CNTs have been dispersed on the solvent.

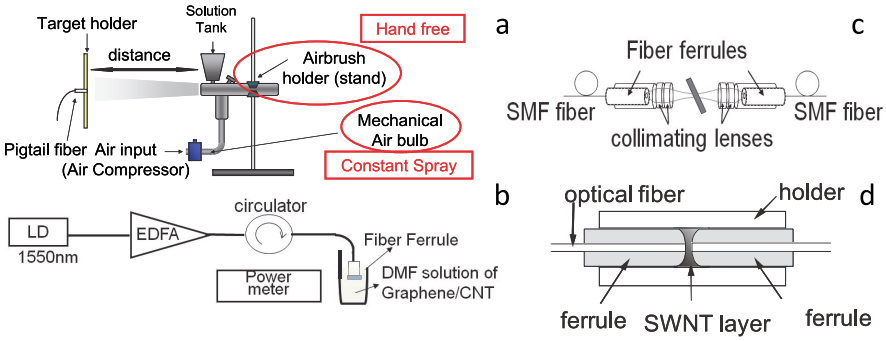

Fig. 3. Experimental set-up for the fabrication of CNT saturable absorbers (a) using the spray method (b) using the optical deposition method. (c) and (d) show original configurations used to integrate the CNT into the optical system.

The physical mechanisms responsible for the optical deposition consist of a combination of optical trapping and heat convention effects. The first demonstrated saturable absorber incorporating CNT consisted of a glass plate with sprayed CNT on its surface such as the one shown if figure 3(c) however this approach required free space alignment and this led to increased insertion losses and lower stability. It was soon recognized that saturable absorbers fabricated directly into the fiber-end by either the spray method or the optical deposition method would benefit from more stable operation in a simpler and highly integrated configuration (Fig.3.(d)). Using these two simple methods a great diversity of devices have been fabricated. The saturable absorber consists on the CNT-coated fiber ferrule butt-coupled between two fiber ferrules and inserted into an all fiber ring cavity laser. Using this configuration, short pulse operation can be achieved, with pulse durations in the order of 100s of femtoseconds. Figure. 4 shows the microscope picture and scanning electron microscope picture of a CNT-coated fiber-end by optical deposition.

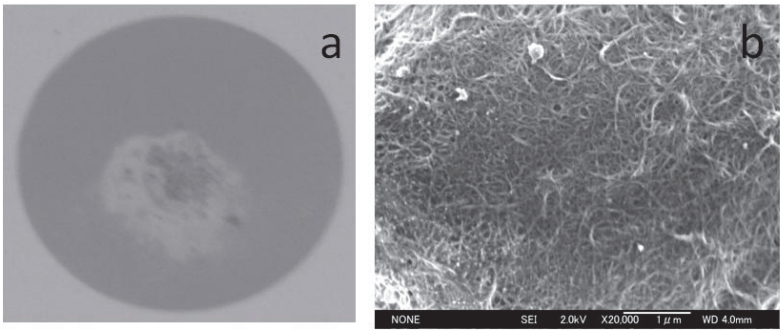

Fig. 4. (a) Microscopic picture of a fiber with optically deposited CNT, (b) Scanning electron microscope image of the same sample.

3.1 Fabrication of CNT-polymer composites

The first demonstrations of CNT-based photonic devices were fabricated by spray-coating a substrate with CNTs suspended in a solvent or by directly synthesizing a CNT film on a substrate. While those reports confirm the feasibility and great potential of this novel technology, they also showed the stringent limitations of those fabrication techniques. CNT-based devices could only be formed as thin films, and that limited the interaction length between the propagating light and the CNTs therefore, hindering the efficient exploitation of their nonlinear properties. In addition, those devices suffer degradation owing to the permanent contact with the external environment. In order to fully utilize the nonlinear optical properties of CNT, these shortcomings needed to be addressed. Researchers concentrated their efforts on finding an optimum host material in which to disperse and embed the individual CNTs. Polymers were identified as such suitable host material since they are transparent at optical communications wavelengths and have a structural composition that allows uniform dispersion of the CNTs. There have been numerous reports of composites consisting of CNT embedded in polymers such as polyvinylalcohol (Rozhin et al., 2006), polyamide (Schibli et al., 2005), carboxymethyl cellulose (CMC) (Tausenev et al., 2007) or polymethyl-methacrylate and polysterene (Nakazawa et al., 2006). Those devices were used as saturable absorbers in various passively mode-locked laser configurations. The main challenge initially was to disperse efficiently the CNT in the polymer. CNTs tend to agglomerate together forming bundles of tens to hundreds of individual carbon nanotubes, the dispersion of such bundles is a key factor to fabricate efficient devices. The bundle breaking process is generally carried out by subjecting the CNTs to an ultrasonic bath in the presence of a solvent. Most approaches to fabricate CNT-doped polymers consist on dispersing the CNTs in a solution of polymer. As a result, the process of solvent evaporation is inevitable which limits the composite dimensions. Furthermore, the dispersion takes place in a rather viscous solution complicating the breaking up of bundles and efficient dispersion of the CNT. Creating bulk CNT-polymer compounds is important since it provides a platform to fabricate complex photonic structures such as CNT-doped fibers, and such structures would allow the efficient exploitation of the nonlinear saturable absorption and third order nonlinearity of CNTs. An alternative method developed by S. Uchida consists on adding the CNT to a solution of methyl-methacrylate (MMA) monomer with a polymerization initiator. CNTs are mixed and dispersed by ultrasonication in methyl-

methacrylate (MMA) monomer prior to and during the polymerization process, thus it does not require the use of solvents (Uchida et al., 2009). The CNTs are dispersed in a low viscosity liquid (MMA) rather than a dissolved polymer, hence CNT bundle separation is facilitated. After the thermally-aided polymerization we obtain a bulk state of evenly dispersed CNT-doped PMMA. Using this method, bulk CNT-embedded PMMA with a tangible improvement in the dispersibility of the CNTs and with added flexibility on device design can be produced. In Figure. 5, polished disks from bulk CNT-PPMA composites are shown, the effect of adding dopants such as DPS and BEN was also investigated with results indicate that these dopants play the role of CNT dispersion stabilizer and thus improving the optical properties of the CNT-PMMA composite. Nowadays, the fabrication of CNT-polymer composites has advanced greatly and the evolution an current state of CNT-polymer composites has been reviewed in detail by T. Hasam (Hasam et al. 2009).

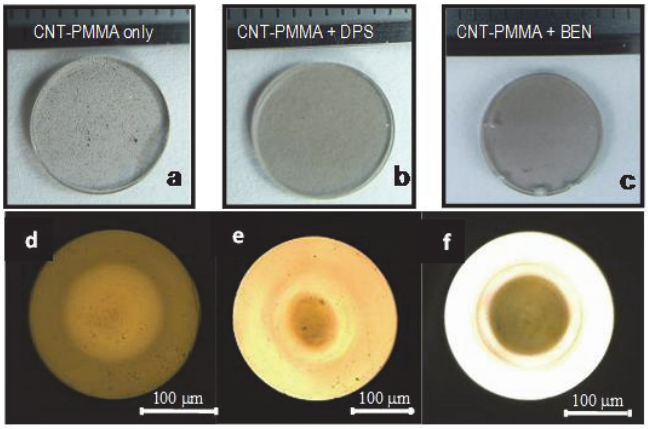

Fig. 5. Bulk fabrication of polymethyl-methacrylate (PMMA) doped with CNT under the presence of different dopants (a) no dopant, (b) diphenyl sulfide (DPS) and (c) benzyl benzoate (BEN). (d), (e) and (f) correspond to CNT-doped polymer optical fibers fabricated using PMMA (Uchida et al., 2009)

3.2 CNT based devices for enhanced nonlinear applications

The nonlinearity in an optical material is proportional to the interaction length between the nonlinear material (i.e. carbon nanotubes) and the propagating optical field. Hence, such nonlinearity can be enhanced by increasing the length of interaction between the CNTs and the propagating optical field. Numerous approaches have been considered for this purpose by employing devices such as D-Shape fibers (Song et al., 2007) tapered fibers (Kieu et al., 2009), hollow core fibers (Choi et al, 2009), micro-slot fiber devices (Martinez et al., 2010) and planar waveguides (Kashiwagi et al., 2007). These approaches involve evanescent coupling, where the CNTs are placed adjacent to the optical waveguide. Using these approaches the interaction length can be significantly increased and only the tail of the pulse propagating outside of the core interacts with the CNT. This means that the CNT are subjected only to a small fraction of the peak power propagating through the device. Thus, the device can operate at higher powers before damage is observed. Using such approach the nonlinear response increases due to the longer interaction, this increase in nonlinearity is somehow hampered by the lower intensity of

the light that effectively interacts with the CNT (note that the nonlinearity is also dependent on the light intensity). Other approaches based on evanescent and direct interaction have been demonstrated that provide increased interaction length with the CNTs. Recently, the fabrication of CNT-doped polymer optical fibers (POF) has been demonstrated. By doping the POFs core with CNTs, highly integrated devices can be in principle integrated, which will allow the efficient utilization of the optical properties of the CNTs (Uchida et al., 2009). However, this CNT-doped POF suffers from high insertion and coupling losses due to been multimode, large core area fibers (150μm core diameter) as well as experiencing further losses when launching the light into the fiber. An alternative approach based on directly injecting a solution of CNT into a micro-channel fabricated into a standard optical power has been proposed (Martinez et al., 2010). This method offers the means to achieve a highly integrated and compact configuration, while ensuring the stability and low insertion losses by directly fabricating the saturable absorber within the optical fiber. In Figure 6, various device configurations designed to increase the interaction length and nonlinearity of CNT devices are depicted.

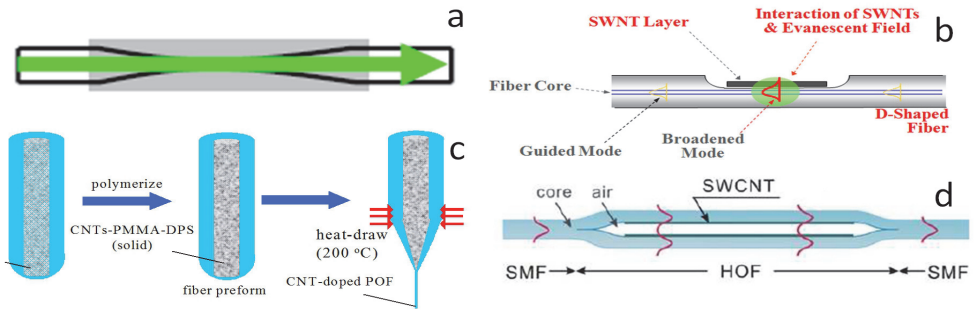

Fig. 6. (a) CNT-polymer coated taper fiber (Kieu et al., 2007), (b) D-shape coated with CNT (Song et al., 2007), (c) Polymer optical fiber doped with CNT (Uchida et al, 2009), (d) Hollow optical fiber filled with CNT (Choi et al., 2009)

In addition, to the length of interaction, the spray method and the optical deposition method present some drawbacks associated to them. In general, after spray or optical deposition, the CNTs are randomly oriented and entangled. The CNT optical absorption is highly anisotropic, and hence the direction of the propagating field with respect to the CNT axis strongly affects the nature of the interaction. Since the CNTs are randomly dispersed, only a fraction of them would contribute to the device operation. There is however a fabrication technique based on low-temperature alcohol catalytic chemical vapor deposition (CVD) method which not only can directly synthesize high-quality SWNTs onto the substrates, but also enables the fabrication of vertically aligned CNTs. This fabrication technique in conjunction with a D-shape fiber configuration has been used for the fabrication of high-pulse energy, high efficiency fiber lasers (Song et al., 2007)

4. Passive mode-locked lasers using CNT saturable absorbers

Passive mode-locked lasers are, nowadays, present in many industrial and scientific applications that range from micromachining and microscopy to optical communications. Passive mode-locking is achieved by incorporating an intensity-dependent component,

generally a saturable absorber, into the optical system. Broadly speaking, this component absorbs the incoming light linearly up to a certain threshold intensity. Once this intensity is reached, the saturable absorber saturates and becomes transparent. Such saturable absorbers discriminate in favor of pulse formation over continuous wave lasing. Passive mode-locking is generally preferred to active mode-locking techniques due to its simplicity and the ability to produce transform-limited pulses without the need for any external active devices such as modulators. The optical absorption of CNTs is of saturable, intensity-dependent nature and hence it is a suitable material to employ for passively mode-locked laser operation with CNT-based saturable absorbers rapidly gaining ground on more conventional approaches to achieve saturable absorption such as the semiconductor-based saturable absorbers mirrors (SESAM) and Nonlinear Optical Loop Mirrors (NOLM). At this moment, SESAMs are still the prevalent device in commercial passively mode-locked lasers, however their fabrication process is complex requiring clean room facilities and specific fabrication for each operational wavelength. The recovery time of a saturable absorber limits the laser repetition rate, SESAMs require an additional ion implantation fabrication step to reduce the recovery time from the nanosecond regime into the picosecond regime. On the other hand, CNTs exhibit a sub-picosecond recovery time, broadband operation, compatibility with fiber, a small foot-print and simple fabrication. In addition, CNT-based saturable absorbers can operate in either a transmission-mode or reflection-mode. Hence, there are several reasons why researchers are starting to favor CNT-based devices over the more established SESAMs for commercial applications.

4.1 Passively mode-locked fiber lasers

Passively mode-locked fiber lasers are nowadays capable of producing ultrashort, high power pulses with high beam quality, efficient heat dissipation and very robust operation in a compact configuration. Hence fiber laser devices are sought for material processing, supercontinuum generation, optical frequency metrology and biomedical applications where they are a more cost-effective and viable solution than their bulkier solid state laser counterparts (Fermann and Hartl, 2009). For fiber laser technology, however, there are still challenges to be met in order to compete in a level field with solid state lasers in particular in terms of the shortest available pulse durations and highest available pulse energies. In order to meet these demands, passively mode-locked laser technology is in the midst of a fascinating evolution striving towards higher powers, shorter pulses and improved stability. This evolution is been fueled by the development of novel fiber designs and model-locking mechanisms such as stretched-pulse mode-locking (Tamura et al., 1993), and the dissipative soliton regimes (Chong et al., 2006). CNTs are becoming an integral building block for many of those advances.

Since 2003, when the first demonstration of a fiber laser passively mode-locked by CNTs was reported, CNT-based devices have been demonstrated in multiple configurations and for all the relevant operational wavelengths ranging from 1μm to 2μm (Kivistö et al., 2009). Initially, all the fiber laser reports employing CNTs operated in the slightly anomalous dispersion regime. Thus, these lasers operated in the robust and highly stable soliton-regime. Soliton-like fiber laser operation is capable of producing highly stable, close to transform limited (with a very low chirp), hyperbolic-secant pulse shapes with a sub-picosecond pulse duration, by balancing out the chromatic dispersion of the cavity with the accumulated Kerr-nonlinearity in the fiber. Soliton-like pulses are very robust, but the pulse

energy can hardly be scaled up, since increasing the intra-cavity power leads to increased nonlinearity consequently the dispersion and nonlinearity balance cannot be maintained. Furthermore, with this mode-locking regime pulse duration as short as a few hundreds of femtoseconds can be produced but it is difficult to further reduce the pulse duration. Figure 7, shows the typical configuration of a fiber laser operating in the soliton regime, and its characterization in terms of optical spectrum, pulse duration and rf signal. The narrow peaks observed in the optical spectrum trace are known as Kelly sidebands, they are common features of fiber lasers operating in the soliton regime and originate from resonant coupling between the soliton and weak co-propagating dispersive waves.

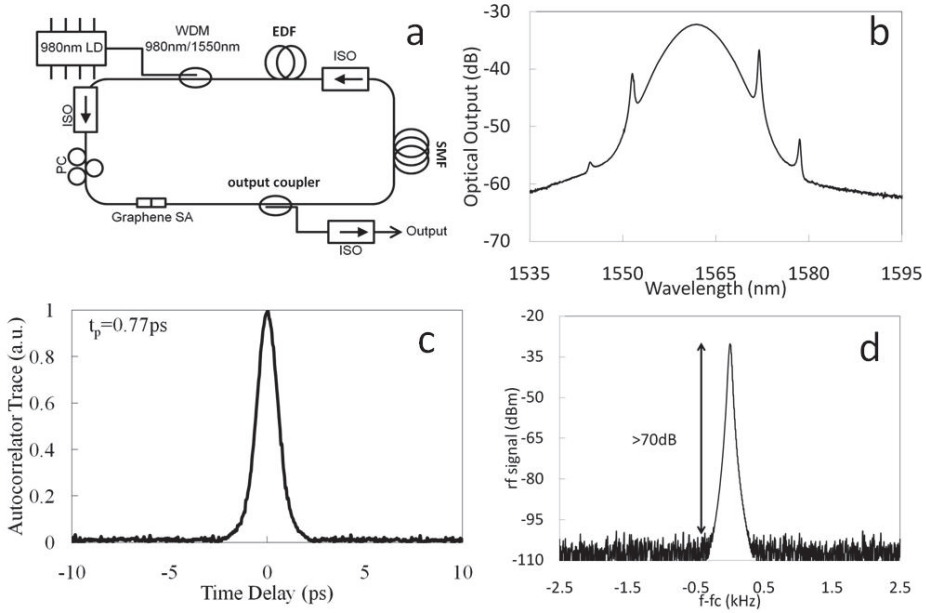

Fig. 7. Ring cavity fiber laser: (a) set-up (b) optical spectrum (c) autocorrelator trace (d) rf signal.

In recent years, researchers have also demonstrated other mode-locking regimes employing CNT saturable absorbers. For instance, stretch-pulse mode-locking, combines a section of fiber with positive dispersion and a section with negative dispersion, as a result the pulse "breaths" within the cavity, and it is chirped in certain sections of the fiber and then recompressed. The laser output in this regime is Gaussian and the operation in this regime, has several advantages with respect to soliton regime since shorter pulses and higher powers can be achieved and the Kelly sidebands can be suppressed (Kieu et al., 2009; Sun et al., 2010). Another laser regime is the dissipative soliton regime. In this case, the fiber in the cavity has positive dispersion (often used for Yb-fiber Lasers), chirp grows continuous through the fiber leaving the gain filtering mechanism and the saturable absorber to limit the spectral broadening of the pulse. Evidently, the output is strongly chirp, but this chirp is linear so it can be easily compensated outside the cavity (Kelleher et al., 2009; Sun et al., 2009).

4.2 Other laser configurations

CNTs can be used to coat a mirror. Such mirror can then be used to operate in a laser in a reflection-mode. This can be applied to the fabrication of solid state lasers, where by using spin coating a CNT-polymer can be deposited over the solid state laser mirror (Schmidt et al., 2008). It is also useful to achieve short cavity lasers with multi-gigahertz repetition rates. In fact, the highest ever reported fundamental repetition rates for a fiber laser employed a phosphosilicate fiber codoped with erbium and ytterbium with a CNT-coated fiber ferrule mirror and reached a repetition rate as high as 20GHz (Martinez et al., 2011). The laser set-up and output characteristics are summarized in Figure 8. Similarly, High repetition rate, passively mode-locked lasing by using an ultrashort cavity with a gain media consisting of a semiconductor optical amplifier (SOA) has been demonstrated, the repetition rate in this case was 17.2GHz (Song et al., 2007). In ring cavity fiber lasers, the long gain fibers can compensate for the insertion losses of the saturable absorber. However, for this type of applications, the requirements for the saturable absorber are much more stringent, with excessive non-saturable losses truncating the modelocked operation and were optical power and heat damage must be carefully taken into account in the design of the saturable absorber.

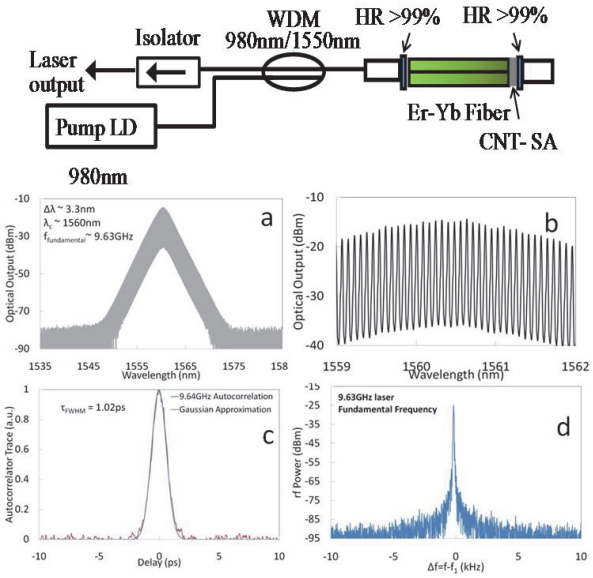

Fig. 8. (a) Set-up for the multi-gigahertz repetition rate laser. (b) Optical output, (c) close up to the longitudinal mode spacing (d) autocorrelator trace (e) rf spectrum.

5. Ultrafast optical switching using CNT's third order susceptibility

Considering the vast amount of theoretical and experimental studies on the high third order nonlinearity of CNT now available in literature and the extraordinary evolution of the CNT-based fiber laser technology, the number of reports demonstrating functional CNT devices that exploit the third order susceptibility of CNT is subdued. In this section, we describe some of the most significant advances in the implementation of CNT-based devices

demonstrating optical switching by wavelength rotation and by four-wave mixing (FWM). This work was pioneered by Y.W. Song et al. and K. Kashiwagi et al., who used CNT-coated D-shape fiber (Song et al., 2007) and a CNT-coated planar lightwave circuit (Kashiwagi et al., 2007) respectively in order to increase the nonlinearity of the devices.

5.1 Wavelength conversion by polarization rotation

Tunable wavelength conversion by polarization rotation has been demonstrated using two types of fiber devices, namely a D-shape fiber and a standard SMF fiber with a micro-slot fiber devices inscribed through the core. In this case, the nonlinear process responsible for the polarization rotation is cross-phase modulation (XPM). The concept of optical switching by polarization rotation is described in Figure 9.

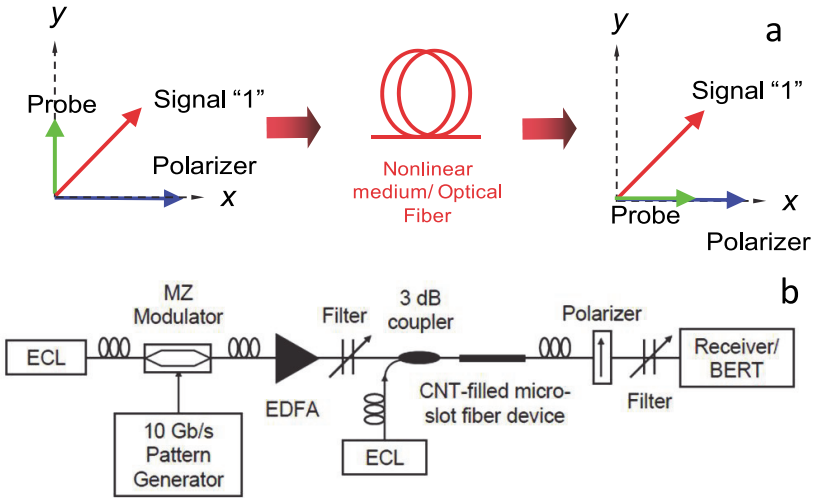

Fig. 9. (a) Depiction of the process of optical switching by polarization rotation. (b) Experimental set-up used for polarization rotation by a micro-slot fiber device (Chow et al., 2009).

Here, we will describe a characteristic polarization rotation experiment by XPM using a CNT filled micro-slot fiber device. Conceptually, the process is the same for similar devices using D-shape or taper fibers. The set up used for this experiment is shown in figure 9, the pump light polarization is set so in absence of probe light its state of polarization is 45º with respect to the polarizer, and the probe is set so its state of polarization is 90º with respect to the polarizer (hence in the absence of pump light the output from the source would be fully suppressed). When both pump and probe co-exist in the nonlinear media (in this case the CNT) the state of polarization of the probe light rotates hence the probe light is received in the detector. In principle, by adjusting the pump light power, it should be possible to transmit through the polarizer 100% of the probe light. In this particular case, The input signal was a 2^{31}-1 bits pseudorandom NRZ signal at 10 Gb/s amplified by an erbium-doped fiber amplifier (EDFA), an optical bandpass filter was used to eliminate the ASE from the EDFA. The pump and probe were combined through a coupler and launched into the nonlinear fiber device component, which in this case is a 50μm-long CNT-filled micro-slot fiber device. For this set-up, the launched signal power and cw light are estimated to be 17 dBm and -3 dBm, respectively.

The spectrum obtained at the output of the polarizer is shown in Figure 10. In our experiment the input and converted signals are set at 1555.0 nm and 1545.0 nm, respectively. Fig. 10(b) and 10(c) depicts the close-up spectra with a resolution of 0.01 nm of the input signal and converted signal, respectively. Note that the converted wavelength is modulated with obvious spectral broadening, showing that wavelength conversion is successfully obtained. In a previous experiment with cw light only without signal modulation, an on off extinction ratio of 13 dB of the converted wavelength is obtained. Also, it is worth noting that the converted signal is tunable with similar switching properties. In order to investigate the system performance of the wavelength converter, 10 Gb/s bit-error-rate (BER) measurements were performed. Fig. 10(d) plots the output BER against the received optical power. The wavelengths used for input and converted signal are the same with those shown in Fig. 10(a). Fig. 10(e) shows the 10 Gb/s eye diagrams of the input signal and the converted signal. The figure shows the results of a 10-nm down-conversion and the power penalty is measured to be 3 dB at 10^{-9} BER level. It is believed that one possible source of the power penalty is originated from the insufficient extinction ratio of the converted signal. If the length of the micro-slot and the CNT concentration inside are further increased, higher extinction ratio and lower power penalty are expected.

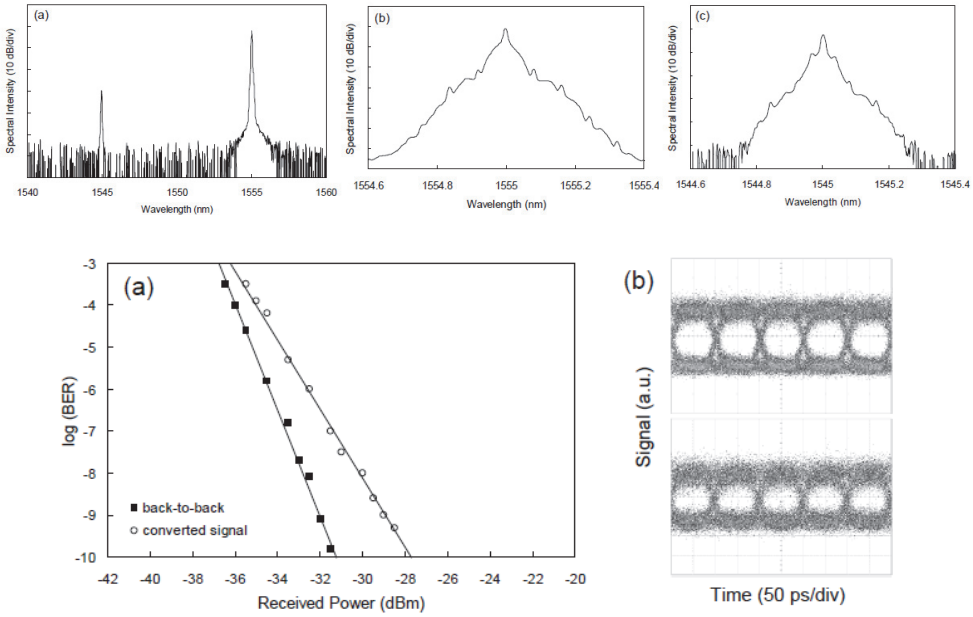

Fig. 10. Experimental results (a) pump and probe signals. Close up of the modulated (b) pump and (c) probe. (d) Bit-error-rate as a function of the received power and (e) eye diagram of the input and received signal.

Similar experiments have been carried out using a 5cm-long D-shape fiber coated with CNT. In this case the interaction length was three orders of magnitude longer than for the micro-slots here described, furthermore, the launched pump power was 21dBm (higher than the 17dBm used for the micro-slots). However, the power penalty was approximately the same

(2.5dB). These results can be understood considering that the D-shape fiber method in actual fact makes use of evanescent field interaction and therefore the light intensity interacting with the CNT is significantly lower than in the case of the micro-slot fiber devices. Furthermore, it is difficult to fabricate a D-shape with a smooth surface and accurate control of the distance between the fiber and the core. Roughness in the surface leads to increases in the scattering losses.

5.2 Four-wave-mixing by wavelength conversion

Four-wave mixing as well as the nonlinear polarization rotation is caused by a propagating media with a high third-order optical nonlinear susceptibility, $\chi^{(3)}$. In this case, when two frequency components propagate through the CNT-device, and additional frequency component is created. An graphic illustration of the process employed is depicted in figure 11(a), two photons of frequency ω_1 (pump) interact with a single photon of frequency ω_2 (signal) to create an additional component with a frequency of $2\omega_1 - \omega_2$. FWM is a phase-sensitive process and the effect can accumulate over distance if the phase matching conditions are met. In a fiber configuration, phase matching conditions are satisfied if the components' frequencies are close to each other, or nonlinear propagating media exhibits the required chromatic dispersion. FWM is caused by self-phase and cross phase modulation.

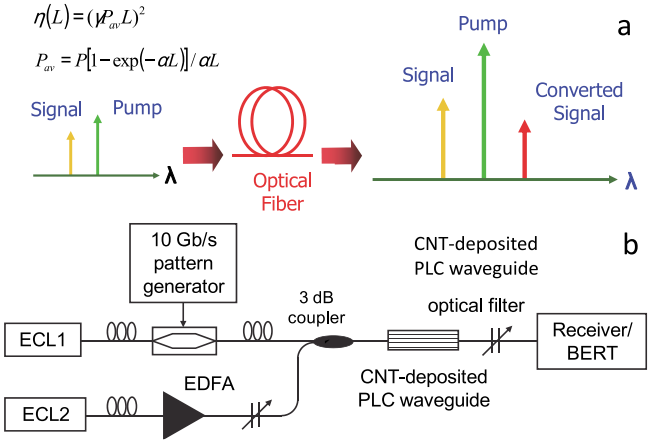

Fig. 11. (a) Depiction of the process of optical switching by four wave mixing FWM). (b) Experimental set-up used for the FWM experiments using a planar lightwave circuit (PLC) (Chow et al., 2010).

FWM employing CNT has been achieved by using a CNT-coated taper fiber and a planar lightwave circuit (PLC). The set-up described in figure 11 corresponds to experiments employing the PLC device. The probe light is combined with a cw pump light from ECL2 through a 3 dB coupler. The combined light is then launched on a high power EDFA followed by the prepared CNT-deposited tapered fiber. The launched pump power into the fiber is estimated to be around +27 dBm. The amplified light then undergoes FWM effect and idlers with new wavelengths are generated. Figure 12 shows the FWM spectrum obtained after the CNT-deposited tapered fiber. In this experiment, the pump is fixed at 1550.0 nm and different

idler wavelengths are obtained by tuning the probe wavelength. FWM conversion efficiency can be defined as the ratio of the idler power to the probe power inside the CNT-deposited tapered fiber. The FWM conversion efficiency can be approximately as shown in equation 4;

$$\eta(L) = (\gamma P_{av} L)^2 \tag{4}$$

where L is the propagation distance through the CNT-deposited region, γ is the effective nonlinear coefficient, and P is the pump power. The effective nonlinear coefficient of the CNT-deposited PLC in our experiment is calculated to be 5.64×10^5 W^{-1} km^{-1}.

The nonlinear properties of the CNT-deposited PLC are used for FWM-based wavelength conversion experiment by modulating the probe light to be a 2^{31}-1 bits pseudorandom NRZ signal at 10 Gb/s. The signal is then amplified by a low noise EDFA with amplified spontaneous emissions ASE filtering in order to compensate the insertion loss of the modulator. The signal and the cw pump are then combined and launched into the CNT-coated PLC. As shown in Figure 12, FWM is achieved and the relationship between the conversion efficiency and the input signal wavelength detuning against the fixed pump is shown in Fig. 12 (d). A 3 dB tunning range of 8nm is obtained. However, since the length of the device is very short, it is in principle relatively easy to maintain the FWM phase matching condition. Fig. 12(e) shows the bit error rate (BER) as a function of the received optical power with the inset showing the 10 Gb/s eye diagrams of the input signal and the converted signal. The figure shows the results of a 3 nm down-conversion of the input signal with a power penalty of 3dB at 10^{-9} BER level.

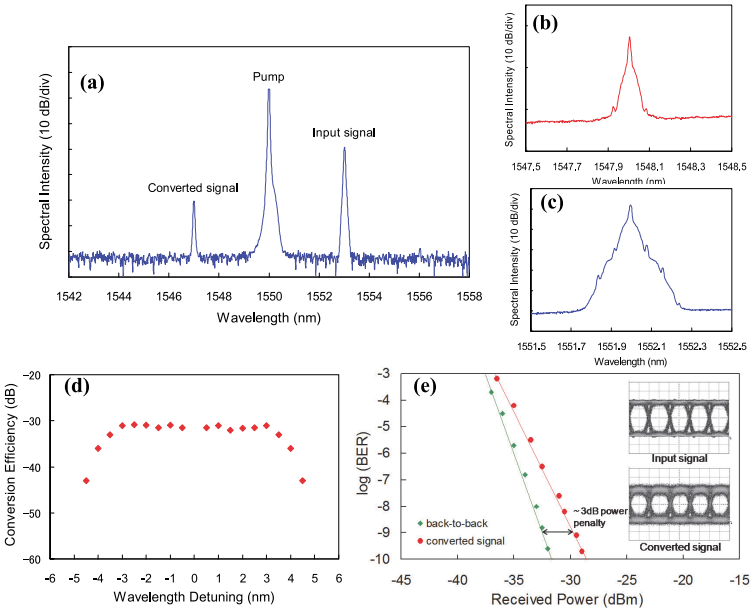

Fig. 12. (a) Optical output showing the pump and converted and input signal, close up of the (b) converted and (c) input signal. (d) Detuning range and (e) Bit error rate as a function of the received power. Inset shows the input and received eye diagrams.

6. Current trends and outlook

Carbon nanotube photonic technology is already a reality with various commercial photonics solution employing CNT-based devices. it has been remarkable the transformation of CNT-based fiber lasers from a scientific curiosity into a fundamental building block in laying the foundations of the next generation fiber laser devices. Recently, graphene has also been considered for saturable absorption applications. Graphene in itself is also a very interesting material with extraordinary potential in several photonic applications, and it is gaining ground over CNT and SESAM devices in part thanks to the knowledge acquired over the years studying CNTs to implement efficient devices. It is still early to say whether these three technologies will over time coexist and be applied depending on the application or one of the three will overtake the others. In the last few years, CNT have been making the transition from a material with very interesting optical properties and potential from a scientific point of view to a position where CNT-SA are an important device in the development of real technological applications and their advantages over competing techniques are utilized. In addition to the results reported in this paper, a number of reports apply CNT to the development of optical sampling systems (Set et al, 2008), frequency combs (Lim et al., 2009), octave spanning supercontinuum generation Kieu et al., 2010), few-cycle pulses fiber lasers (Kieu et al., 2010) and tunable, ultra-broadband fiber laser operation (Wang et al. 2008). CNT-based optical switching on the other hand is still in its infancy, current demonstrations only show modest results and while the very high third order susceptibility combined with the fast optical response is promising, significant developments will need to be made before optical switching by CNT can become a reality in a realistic commercial application.

7. Conclusion

In this chapter we described the optical properties of CNT and their most relevant applications, including saturable absorption for the passive mode-locking of fiber lasers, and optical switching for wavelength conversion have been reviewed.

8. References

H. Kataura, Y. Kumazawa, Y. Maniwa, I. Umezu, S. Suzuki, Y. Ohtsuka, and Y. Achiba "Optical properties of single-wall carbon nanotubes," Synth. Met. 103, 2555-2558 (1999)

Margulis, AV, Sizikova, TA: Theoretical study of third order nonlinear optical response of semiconductor carbon nanotube. Physica B, 245, 173–189 (1998)

S. Ijima "Helical microtubules of graphitic carbon", Nature, 354 56-58 (1991)

M. S. Dresselhaus, G. Dresselhaus, and P. Avouris, Eds., Carbon Nanotubes: Synthesis, Structure, Properties, and Application. New York: Springer-Verlag, Berlin, 2001)

P. Avouris, M. Freitag and V. Perebeinos, "Carbon-nanotube Photonics and Optoelectronics", Nature Photonics 2, 341-350 (2008)

S. Y. Set, H. Yaguchi, Y. Tanaka and M. Jablonski, "Ultrafast Fiber Pulsed Lasers Incorporating Carbon Nanotubes," IEEE J. Sel. Top. Quantum Electron. 10, 137 (2004)

Y.-C. Chen, N.R. Raravikar, L.S. Schadler, P.M. Ajayan, Y.-P. Zhao, T.-M. Lu, G.-C. Wang and X.-C. Zhang, "Ultrafast optical switching properties of single-wall carbon nanotube polymer composites at 1.55 mu m," Appl. Phys. Lett. 81, 975-977 (2002)

X. Liu et al. "Third-order optical nonlinearity of the carbon nanotubes", Appl. Phys. Lett. 74, 164-166, (1999)

R. Saito, M. Fujita, G. Dresselhaus, and M. S Dresselhaus "Electronic structure of chiral graphene tubules"Appl. Phys. Lett. 60, 2204 (1992)

S. Yamashita et al. "Saturable absorbers incorporating carbon nanotubes directly synthesized onto substrates and fibers and their application to mode-locked fiber lasers," Opt. Lett. 29, 1581-1583 (2004)

S. Reich et al., Carbon Nanotubes, Wiley-VCH,2004

Samuli Kivistö, Tommi Hakulinen, Antti Kaskela, Brad Aitchison, David P. Brown, Albert G. Nasibulin, Esko I. Kauppinen, Antti Härkönen, and Oleg G. Okhotnikov, "Carbon nanotube films for ultrafast broadband technology," Opt. Express 17, 2358-2363 (2009)

F. Wang, A.G. Rozhin, V. Scardaci, Z. Sun, F. Hennrich, I.H. White, W.I. Milne, A.C. Ferrari, "Wideband-tuneable, nanotube mode-locked, fibre laser," Nature Nanotechnology, 3, 738-742 (2008)

Agrawal G.P. "Nolinear Fiber Optics", Academic Press, 2nd edition 1995

Y. W. Song, S. Yamashita, E. Einarsson, S. Maruyama, "All-fiber pulsed lasers passively mode-locked by transferable vertically aligned Carbon nanotube film," Optics Letters, 32, pp.1399-1401, (2007).

K. Kashiwagi, S. Yamashita, and S. Y. Set, "Optical reflectometry for in-situ monitoring of carbon nanotubes deposition by optical tweezers," Conference on Lasers and Electro Optics (CLEO 2007), no.JThD82, May 2007.

J. W. Nicholson, R. S. Windeler, and D. J. DiGiovanni, "Optically driven deposition of single-walled carbon-nanotube saturable absorbers on optical fiber end-faces," Opt. Express 15, 9176-9183 (2007).

A.G. Rozhin, Y. Sakakibara, S. Namiki, M. Tokumoto, H. Kataura, "Sub-200-fs pulsed erbium-doped fiber laser using a carbon nanotube-polyvinylalcohol mode-locker," Appl. Phys. Lett. 88, 051118 (2006)

T.R. Schibli, K. Minoshima, H. Kataura, E. Itoga, N. Minami, S. Kazaoui, K. Miyashita, M. Tokumoto and Y. Sakakibara, "Ultrashort pulse-generation by saturable absorber mirrors based on polymer-embedded carbon nanotubes," Opt. Express 13, 8025-8031 (2005)

A.E. Tausenev, E.D. Obraztsova, A.S. Lobach, A.I. Chernov, V.I. Konov, A.V. Konyashchenko, P.G. Kryukov and E.M. Dianov, "Self-mode-locking in erbium-doped fibre lasers with saturable polymer film absorbers containing single-wall Carbon nanotubes synthesized by the arc discharge method," Quantum Electron. 37 205-208 (2007).

M. Nakazawa, S. Nakahara, T. Hirooka, M. Yoshida, T. Kaino and K. Komatsu, "Polymer saturable absorber materials in the 1.5 μm band using polymethyl-methacrylate and polysterene with single-wall carbon nanotubes and their application to a femtosecond laser," Opt. Lett. 31, 915-917 (2006).

S. Uchida, A. Martinez, Y.-W. Song, T. Ishigure, and S. Yamashita, "Carbon nanotube-doped polymer optical fiber," Opt. Lett. 34, 3077-3079 (2009)

Hasan, T., Sun, Z., Wang, F., Bonaccorso, F., Tan, P. H., Rozhin, A. G. and Ferrari, A. C., "Nanotube–Polymer Composites for Ultrafast Photonics", Advanced Materials, 21, 3874–3899 (2009)

S. Y. Choi, F. Rotermund, H. Jung, K. Oh, and D-I Yeom, "Femtosecond mode-locked fiber laser employing a hollow optical fiber filled with carbon nanotube dispersion as saturable absorber," Opt. Express 17, 21788-21793 (2009)

K. Kieu, M. Mansuripur "Femtosecond laser pulse generation with a fiber taper embedded in carbon nanotube/polymer composite," Opt. Lett. 32, 2242-2244 (2007)

A. Martinez, K. Zhou, I. Bennion and S. Yamashita "In-fiber microchannel device filled with a carbon nanotube dispersion for passive mode-lock lasing" Optics Express, 16, 15425-15430 (2008)

M. E. Fermann and I. Hartl, "Ultrafast fiber laser technology", IEEE J. Sel. Top. Quantum Electron. 15 , 191-206 (2009).

K. Tamura, E. P. Ippen, H. A. Haus, and L. E. Nelson, "77-fs pulse generation from a stretched-pulse mode-locked all-fiber ring laser," Opt. Lett. 18, 1080-1082 (1993)

Z. Sun, T. Hasan, F. Wang, A. G. Rozhin, I. H. White, and A. C. Ferrari, "Ultrafast Stretched-Pulse Fiber Laser Mode-Locked by Carbon Nanotubes" Nano Res, 3, 404 (2010)

A. Chong, J. Buckley, W. Renninger, and F. Wise, "All-normal-dispersion femtosecond fiber laser," Opt. Express 14, 10095-10100 (2006)

K. Kieu and F. W. Wise, "All-fiber normal-dispersion femtosecond laser," Opt. Express 16, 11453-11458 (2008)

E. J. R. Kelleher, J. Travers, Z. Sun, A. Rozhin, A. Ferrari, S. Popov, and J. Taylor, "Nanosecond-pulse fiber lasers mode-locked with nanotubes," Appl. Phys. Lett. 95, 111108 (2009).

Andreas Schmidt, Simon Rivier, Günter Steinmeyer, Jong Hyuk Yim, Won Bae Cho, Soonil Lee, Fabian Rotermund, Maria C. Pujol, Xavier Mateos, Magdalena Aguiló, Francesc Díaz, Valentin Petrov, and Uwe Griebner, "Passive mode locking of Yb:KLuW using a single-walled carbon nanotube saturable absorber," Opt. Lett. 33, 729-731 (2008)

Amos Martinez and Shinji Yamashita, "Multi-gigahertz repetition rate passively modelocked fiber lasers using carbon nanotubes," Opt. Express 19, 6155-6163 (2011)

Y. W. Song, S. Yamashita, C. S. Goh, S. Y. Set, "Passively mode-locked lasers with 17.2-GHz fundamental-mode repetition rate pulsed by Carbon nanotubes," Optics Letters, .32, 430-432, (2007)

K. K. Chow, S. Yamashita, and Y. W. Song, "A widely tunable wavelength converter based on nonlinear polarization rotation in a carbon-nanotube-deposited D-shaped fiber," Opt. Express 17, 7664-7669 (2009)

K. K. Chow, S. Yamashita, and S. Y. Set, "Four-wave-mixing-based wavelength conversion using a single-walled carbon-nanotube-deposited planar lightwave circuit waveguide," Opt. Lett. 35, 2070-2072 (2010)

17

Carbon Nanotube Industrial Applications

Fang-Chang Tsai et al*
Ministry-of-Education Key Laboratory for the Green Preparation and Application of Functional Materials, Faculty of Materials Science and Engineering, Hubei University China

1. Introduction

Since carbon nanotube was discovered by S. Ijima in 1991, it has become one of the main academic research subjects. Carbon nanotube is the thinnest tube human can make presently. It has advantages in lightweight, high strength, high toughness, flexibility, high surface area, high thermal conductivity, good electric conductivity and chemical stability. Carbon nanotube can be applied to manufacture smaller transistors or electronic devices. Samsung Korea has made carbon nanotube into Field Emission Display. When the technology is matured and the cost is reduced, it will replace traditional bulky cathode ray tube (CRT) screen. Carbon nanotube has high toughness, so it can be made into high-strength composite with other materials. Thus, carbon nanotube is a material with high economic value and very worth researching. Besides, carbon nanotube has both conductor and semiconductor properties. Therefore, for electronic circuit, the semiconductor property of carbon nanotube enables its application to field emission transistor (FET) gate electrode, which has 100 times higher electric conductivity than silicon semiconductor when voltage is applied and 1000 times higher operational frequency than current Complementary Metal-Oxide Semiconductor (CMOS). The conductor property makes carbon nanotube have similar thermal conductivity to diamond and superior current carrying capacity to copper and gold. For the application of display, its long-term reliability is very excellent [Iijima, 1991, Lee et. al., 1977]. In order to create new material systems with superior properties, various nanoparticle morphologies have been used as reinforcing fillers in elastomeric matrices. These nanometerscale reinforcing particles include spherical particles such as silica or titania [McCarthy et. al., 1997, Kohjiya et. al., 2005], platelets such as layered silicates [Osman et. al., 2001, Joly et. al., 2002, Varghese & Karger-Kocsis, 2003, Kim et. al., 2004, Arroyo et. al., 2003, Bala et. al., 2004, Jeon et. al., 2004], carbon [Gauthier et. al., 2005] or clay fibers [Bokobza & Chauvin, 2005] and multiwall or singlewall carbon nanotubes[Barraza et.

* Chi-Min Shu[2], Lung-Chang Tsai[2], Ning Ma[1], Yi Wen[1], Sheng Wen[3],Ying-Kui Yang[1], Wei Zhou[1], Han-Wen Xiao[1], Yao-Chi Shu[4] and Tao Jiang[1]
[1]*Ministry-of-Education Key Laboratory for the Green Preparation and Application of Functional Materials, Faculty of Materials Science and Engineering, Hubei University, China*
[2]*Process Safety and Disaster Prevention Laboratory, Department of Safety, Health, and Environmental Engineering, National Yunlin University of Science and Technology, Republic of China*
[3]*Faculty of Chemistry and Material Science, Xiaogan University, China*
[4]*Department of Polymer Materials, Vanung University, Republic of China*

al., 2002, López-Manchado et. al., 2004, Hirsch, 2002]. Modified CNTs can enhance the adhesion between CNTs and polymer matrix. Acid modification is one of the most common methods of CNT modification. CNT can be modified by refluxing with nitric acid or a mixture of nitric acid and sulfuric acid. Carboxyl and hydroxyl functional groups are formed on the CNT surface during acid modification [Liu et. al., 2005]. Acid-modified MWCNT can be modified with silane coupling agent [Lee et. al., 2006, Liu et. al., 2005]. The silane will react with the hydroxyl groups (–OH) on the surface of MWCNTs. The oxidation of MWCNT may generate carboxylic groups (–COOH) rather than hydroxyl groups. Ma et. al. and Vast et. al. suggested that the acid modified MWCNT can generate more hydroxyl groups by reduction process [Ma et. al., 2006 and Vast et. al., 2004]. The development and addition of inorganic and organic moieties into polymer matrix resulted in increasing properties has attracted much interest in the past few years [Liu et. al., 2005, Lee et. al., 2006, Liu et. al., 2005]. Exfoliation is a thermodynamic event that requires compatibility between resin and clay [Vaia & Gianneli, 1977]. Compatibility can be achieved by modifying natural clay using an ion exchange process to replace naturally occurring sodium ions in the gallery between silicate layers with quaternary ammonium ions having organic functionality that render the clay surface hydrophobic [Wen et. al., 2009, Tsai et. al., 2010].

Polyvinyl alcohol (PVA) is low cost, non-toxic, non-polluting, highly transparent, static-interference-free in packaging process, UV resistant and completely biocompatible. Under a dry condition which relative humidity is lower than 50%, PVA and Ethylene Vinyl Alcohol (EVOH) have very good barrier property to effectively block gases and water penetration [Yeh et. al., 2004, Cui et. al., 2009, Okaya et. al., 1992], wear resistance and emulsification ability, and excellent chemical and solvent resistance [Yan, 1998]. However, when the environmental relative humidity is higher than 50% the barrier property for PVA is significantly reduced. Besides, PVA is usually not made into film by hot melt process but by solution process. To improve high-humidity barrier property, PVA is usually treated by capping or crosslinking hydroxyl groups to be less water-absorbing. In recent years, PVA barrier composite film has found applications in food packaging by modifying PVA hydrophobicity and retaining high barrier property. Besides being used as fiber raw material, PVA is largely used in producing coatings, adhesives, paper additives, emulsifiers, dispersants and membranes etc. Its applications spread over textile, food, medicine, construction, wood processing, papermaking, printing, agriculture, steel making and polymer chemicals etc.

In this study, PVA is selected as substrate and mixed-acid and hydrogen peroxide modified carbon nanotube as filler. Mixed acid [Liu et al., 1988] and hydrogen peroxide are first used to treat carbon nanotube by carboxylation to improve its dispersibility. Here, different groups according to different reaction times are investigated to compare among different carboxylation times and carboxylation methods. Then, the carboxylation products are subject to characteristic analysis to learn the effect of reaction condition on the carboxylation degree of CNTs. The modified carbon nanotubes are added to PVA substrate in different mass compositions. The study provides investigation for the first time into the effect of carboxylation method on carbon nanotube structure and property. The result can be used as references for selecting carboxylation method. In the composite aspect, the product comprises water-soluble barrier plastic and conductive filler. The composite retains the performance advantages from both types of materials, such as mechanical properties and electric properties etc. The potential applications for this composite are very versatile, for examples, circuit board with conductive coating, conductive coating on color CRT,

conductive adhesive, nanocarbon conductive coating on electrical grounding network, nanocapacitor, photoelectric conversion device, conductive membrane, antistatic coating, antistatic fiber product and conductive coating plated on non-metal material etc. Better carbon-based electrodes are needed for fuel cells, photocatalyzed water splitting, hydrogen pumps, batteries and other electrocatalytic devices. The requirements for the bulk of fuel cell membranes are mainly high proton conduction, chemical stability and electron insulation. We review the present state of polymer nanocomposites research in which the fillers are carbon nanotubes. In this review, an extended account of the various chemical strategies for grafting polymers onto carbon nanotubes and the manufacturing of carbon nanotube/polymer nanocomposites are given. The thermal analysis and electrical properties to date of a whole range of nanocomposites of various carbon nanotube contents are also reviewed in an attempt to facilitate progress in this emerging area.

2. Modification of carbon nanotubes with polymers

2.1 Materials and sample preparation

The PVA resin and multi-wall carbon nanotube (CNTs) used in this study were obtained from Chang Chun Plastics Co., LTD and Nanotechnologies Port Co., Ltd, Shenzhen, China wherein PVA resin and CNTS had a trade name of 101 L and CNTS is a S.MWNTs-4060. The CCNTs was prepared by sulfuric and nitric mixed acid under ultrasonic vibration. The compositions of the CNTs, CCNTs and PVA / CNTs series specimens prepared in this study are summarized in Table 1, 2 and 3, respectively. According to A series reaction time in Table 1, a proper amount of carbon nanotube is added to mixed acid (concentrated sulfuric acid: concentrated nitric acid = 3: 1).

A series Reaction group	Mixed-acid treatment time (hour)	Hydrogen peroxide treatment time (hour)	B series Reaction group	Mixed-acid treatment time (hour)	Hydrogen peroxide treatment time (hour)
A0	0	0	B0	0	0
A1	1	0	B1	1	0.5
A2	2	0	B2	2	1
A3	4	0	B3	4	2
A4	6	0	B4	6	3
A5	8	0	B5	8	4

Table 1. Formulation for carbon nanotube carboxylation

Ultrasonic vibration is applied according to reaction time. Filtration is conducted with micropore filter and sand core filter. D. I. water is used to rinse the filtrate until it is neutral. The carbon nanotubes from filter are dried in drying oven to obtain a series of mixed-acid modified carbon nanotubes, which are labeled $CCNT^{a0}$ (CNTs), $CCNT^{a1}$, $CCNT^{a2}$, $CCNT^{a3}$, $CCNT^{a4}$ and $CCNT^{a5}$. Again, according to B series reaction time in Table 1, carbon nanotubes and mixed-acid are treated with ultrasonic vibration and rinsed until it becomes neutral. Then carbon nanotubes are dried in drying oven. The difference with A-series is that hydrogen peroxide ultrasonic vibration treatment is applied to dried carbon nanotube and then the filtrate is rinsed until it becomes neutral. The obtained B series carbon nanotubes are labeled $CCNT^{b0}$ (CNTs), $CCNT^{b1}$, $CCNT^{b2}$, $CCNT^{b3}$, $CCNT^{b4}$ and $CCNT^{b5}$.

2.2 Observation of carbon nanotube dispersed polarity before and after modification

Six small reagent bottles are added with approximately 6 mL D. I. water and 4 mL toluene and a small amount of carbon nanotubes derived from Table 1. After they are placed in ultrasonic vibrator for 0.5 hours and then, the solution standing storage for 12 hours, they are covered and observed.

2.3 Selection of PVA substrate

Four PVA types are made into solutions of different composition. According to the material property requirements, their electric conductivity and film formation are measured and compared. Then, the one with the highest overall performance is selected as the substrate. After PVA type is decided, eight PVA aqueous solutions are prepared in 1%, 2%, 5%, 6%, 8%, 10%, 12% and 15%. Electric conductivity and aqueous solution stability are used to determine the concentration of PVA aqueous solution as the composite film substrate.

2.4 Preparation of PVA / carbon nanotube composite film

According to the formulations in Table 2 and Table 3, composite film solutions of series-I and series-II are prepared. For series I, 5 groups of CNTs with different carboxylation degree and one unmodified CNTs are used as fillers.

Compositions	PVA (wt%)	CNTs (wt%)
PVA	100.0	0.0
$PVA^{8\%}{}_{99.5}/CCNT^{b1}{}_{0.5}$	99.5	0.5
$PVA^{8\%}{}_{99.5}/CCNT^{b2}{}_{0.5}$	99.5	0.5
$PVA^{8\%}{}_{99.5}/CCNT^{b3}{}_{0.5}$	99.5	0.5
$PVA^{8\%}{}_{99.5}/CCNT^{b4}{}_{0.5}$	99.5	0.5
$PVA^{8\%}{}_{99.5}/CCNT^{b5}{}_{0.5}$	99.5	0.5
$PVA^{8\%}{}_{99.5}/CCNTs_{0.5}$	99.5	0.5
CNTs	0.0	100.0

Table 2. Compositions of PVA / CNTs film specimens

They are added in an equal amount into 8% PVA aqueous solutions respectively. By solution blending, they are made into 6 different series I solutions. For series II, CNT^{b5} is used as filler and added 8% PVA aqueous solutions respectively according to formulations in Table 3. Similarly, by solution blending, they are made into 5 different series II solutions. First, weigh the corresponding amount of carbon nanotube into a beaker, add a proper amount of D. I. water, and conduct ultrasonic vibration for 2.5 hours to break apart the agglomerated carbon nanotubes. Weigh the corresponding amount of PVA into the beaker. Place the beaker into a water bath at 80 ^{o}C. Agitation is applied by magnetic stirrer for 12 hours to evenly mix carbon nanotubes and PVA. After mixing, transfer the beaker into a heating mantel at about 80 ^{o}C to remove excessive solvent – water. In the process, continuous agitation with a glass rod is necessary to prevent formation of a thin layer due to uneven heating. Continue heating and agitation until excessive solvent is removed. Stop when the desired concentration is reached. Keep it still and covered for defoaming. Then, pour the solution into a specially designed mold. Let it dry at room temperature for 12 hours and transfer it to vacuum drier for drying 12 hours. After complete drying, demold to obtain the composite film sample.

Compositions	PVA (wt%)	CNTs (wt%)
PVA	100.0	0.0
$PVA^{8\%}{}_{99.9}/CNT^{b5}{}_{0.1}$	99.9	0.1
$PVA^{8\%}{}_{99.8}/CNT^{b5}{}_{0.2}$	99.8	0.2
$PVA^{8\%}{}_{99.5}/CNT^{b5}{}_{0.5}$	99.5	0.5
$PVA^{8\%}{}_{99.0}/CNT^{b5}{}_{1}$	99.0	1
$PVA^{8\%}{}_{98.0}/CNT^{b5}{}_{2}$	98.0	2
CNTs	0.0	100.0

Table 3. Compositions of PVA / CNTs film specimens

2.5 Fourier transform infrared spectroscopy (FT–IR)

Fourier transform infrared spectroscopic measurements of PVA and PVA/CNTs series specimens were recorded on a Nicolet Avatar 320 FT-IR spectrophotometer at 25°C, wherein 32 scans with a spectral resolution 1 cm^{-1} were collected during each spectroscopic measurement. Infrared spectra of the film specimens were determined by using the conventional KBr pellet technic.

2.6 Particle size analysis

The particle size analysis measurements of CNTs and CCNTs series specimens were recorded on a Dandong Bettersize Instruments Ltd. BT-9300H at 25 °C and 50 % relative humidity, wherein 6 scans with a 0.1-340 μm were collected during each data measurement. Particle size analysis of powder specimens was determined by using the approximately 15 mL D. I. water and a small amount of carbon nanotubes derived from Table 1.

2.7 Thermal and wide angle X-ray diffraction properties

The thermal properties of PVA and PVA/CNTs series specimens were determined at 25 °C and 50 % relative humidity using a TA Q100 differential scanning calorimetry (DSC), respectively. All scans were carried out at a heating rate of 10°C/min and under flowing nitrogen of a flow rate of 50 mL/min. The instrument was calibrated using pure indium. Samples weighing about 10mg were placed in standard aluminum sample pans for each DSC experiment. The samples were rapidly heated at a heating rate of 40 °C/min and kept at 250 °C for 3 minutes in order to eliminate any residual crystals. The fully melted samples were then cooled at a rate of 10 °C/min, until the crystallization was completed. The melting temperatures of the samples were determined by heating the specimens to 250 °C at a rate of 10 °C/min. The wide angle X-ray diffraction (WAXRD) properties of PVA and PVA/CNTs series specimen diffractometer equipped with a Ni-filtered CuKα radiation operated at 40 kV and 100 mA. Each specimen with 2 mm thickness was maintained stationary and scanned in the reflection mode from 5 to 50˚ at a scanning rate of 5˚ /min.

2.8 Measurement of composite film solution conductivity

Use the DJS-1C type platinum black electrode included with the equipment. Prior to measurement, use D. I. water to soak for 24 hours to activate the electrode. Use a thermometer to measure the solution temperature, which is around 23 °C. Switch to CAL and set temperature at 23 °C. According to the electrode constant K=0.952 indicated on electrode cap, adjust the equipment constant to display 952. Now, the equipment set-up is

completed. Use D. I. water to clean the electrode and dry the electrode. Place the electrode into the solution and set the range to 2 ms/cm. Take the reading when it becomes stable. The reading is the electric conductivity for the film solution at 25 °C. After measurement, use D. I. water to clean the electrode and switch the range back to 2 us/cm. When the equipment displays 0, it is ready to measure the next sample. After measurement work is completed, shut off the power, clean the electrode and soak the electrode into D. I. water for next use.

3. Results and discussion

3.1 FT-IR spectral analysis

Figure 1 and Figure 2 summarize FT-IR spectra for all CNTs samples. From the figures, it can be found that absorption band centers for characteristic absorption peaks of CNTs samples are located at 960 and 1645 respectively, referring to bending vibration of hydroxyl group (O-H) of CNTs molecule on different planes and stretching vibration of carboxylate anion. Except that the absorption peak for CNT_{a1} sample is not clear, all other CNTs samples have clear peaks on their spectra.

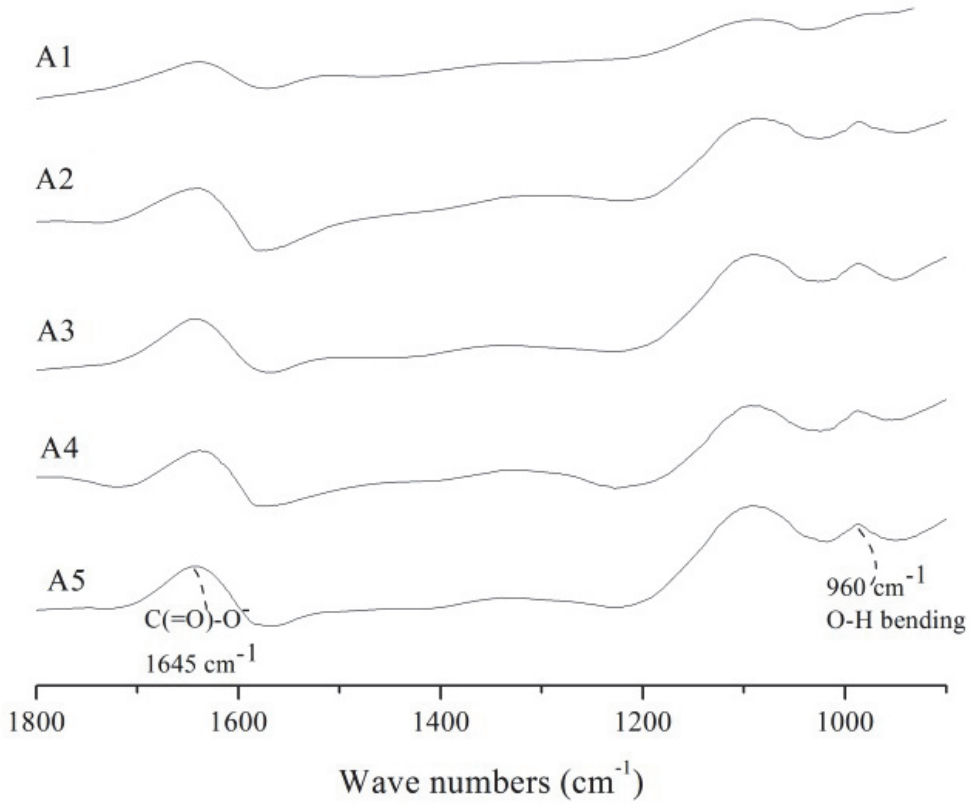

Fig. 1. FT-IR spectra of CCNTs specimens of A-series determined at 25 °C

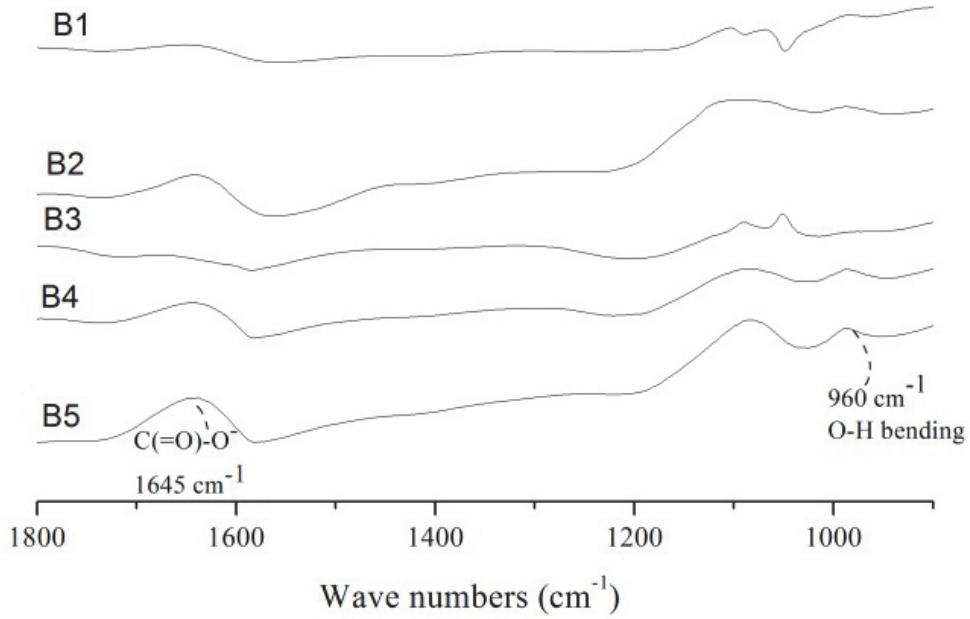

Fig. 2. FT-IR spectra of CCNTs specimens of B-series determined at 25 °C

This proves that in Table 1 except A1 all other reaction groups can effectively add carboxyl groups to the carbon nanotubes. After further comparison of the spectra of A series and B series CNTs, it can be found that B series CNTs have stronger absorption peaks than A series CNTs, indicating that the carbon nanotubes treated with mixed-acid, hydrogen peroxide and ultrasonic vibration have more carboxyl groups than the carbon nanotubes treated only with mixed-acid and ultrasonic vibration. The possible carboxylation mechanism on carbon nanotube：mixing concentrated sulfuric acid and concentrated nitric acid generates a large amount of heat; ultrasonic vibration also generates a large amount of heat; the heat facilitates decomposition of concentrated sulfuric acid and release of NO_2 and free oxygen; when two free oxygen atoms and a carbon atom on carbon nanotube combine, it is possible to form a CO_2 and cause carbon nanotube breakage or rupture; the high acidity of the mixed-acid and the strong ultrasonic vibration can also damage and break carbon nanotube; while carbon nanotube becomes thinner, the activity of the carbon atoms on carbon nanotube fracture site increases due to unsaturation; the combination of one oxygen atom and one carbon atom could form a C=O on carbon nanotube and further interact with aqueous H^+ and OH^- and free oxygen to form -COOH or -C-OH to generate hydroxyl group; .in the oxidation process,-COOH and –OH are usually produced at carbon nanotube end or fracture site, but their quantity is not much.

3.2 Particle size analysis

Particle size analysis is conducted on A-series and B series of carboxylated carbon nanotubes. From Figure 3 and Figure 4, it can be found that with increasing carboxylation reaction time, the extent of carbon nanotube shortening also increases.

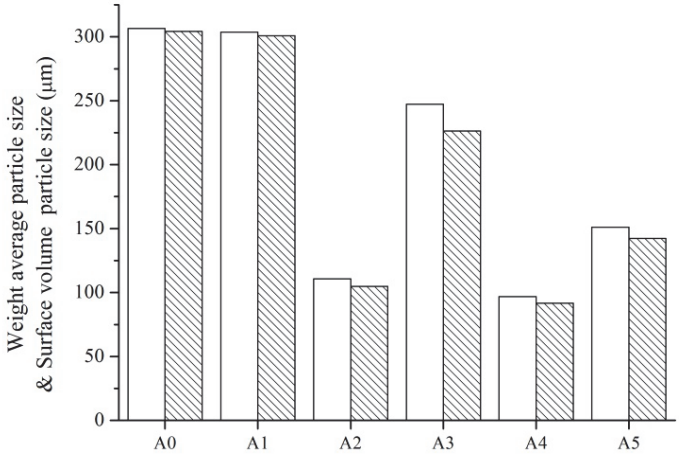

Fig. 3. The A-series of CNTs specimens on weight average particle size (white column) and surface volume particle size (slash column) determined at 25 °C

Particularly in B series, the carbon nanotubes treated with mixed-acid, hydrogen peroxide and ultrasonic vibration basically are all shortened. They are apparently much shorter than A-series of carbon nanotubes treated only with mixed-acid and ultrasonic vibration. This also supports the FT-IR result from a different perspective. The longer the carboxylation reaction time is, the more severe the carbon nanotube is damaged, and the more the rupture on C-C bond the carbon nanotube has. The higher activity at carbon nanotube opening facilitates the bonding with free O and H in water or solution and formation of carboxyl group on fracture site. This can increase the carboxyl functional groups on carbon nanotube and the carboxylation extent for carbon nanotube.

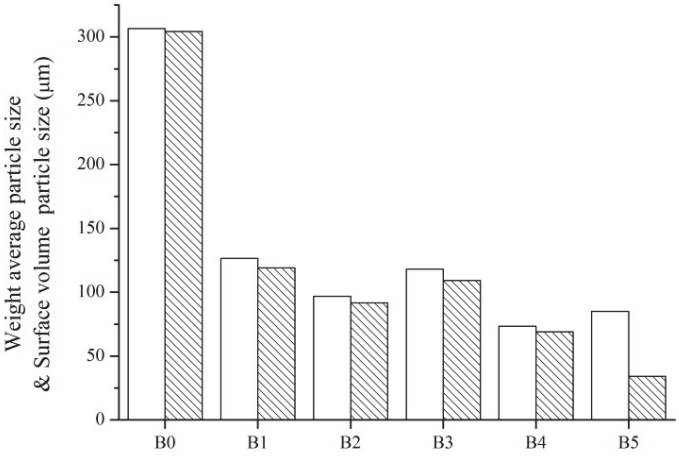

Fig. 4. The B-series of CNTs specimens on weight average particle size (white column) and surface volume particle size (slash column) determined at 25 °C

3.3 Dispersed polarity analysis

Typical photograph of the polarity of CNTs and CCNTs specimens are summarized in Fig. 5. As a result of involves the dispersion state and stability for modified carbon nanotubes in aqueous solution and organic solvent solution. Figure 5 shows the dispersion state for the modified carbon nanotubes in a medium after the treatment in Table1 and being kept still for 12 hours. It can be found from the figure that in the six groups of carbon nanotubes except the unmodified carbon nanotube always existing in the interface of two phases and undissolvable in both phases, all other five groups show different extent of dispersion. Especially, $CCNT^{b3}$ has the most even and stable dispersion in aqueous phase and after being kept still for a week it still maintains the state as in the figure.

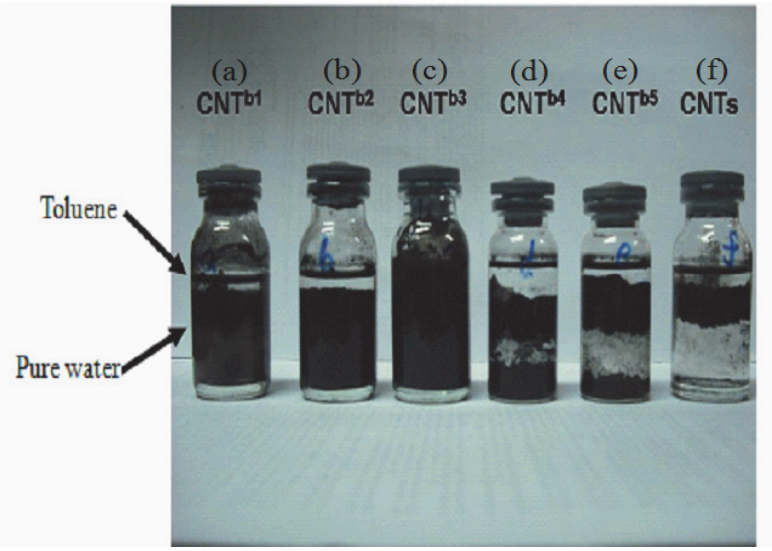

Fig. 5. The photograph of the polarity of pure CNTs specimens

3.4 Selection of PVA type and concentration

The electric conductivities for 3 %, 5 %, 10 % aqueous solutions from A, B, C, D types of PVA are measured and shown in Figure 6. At the same concentration, PVA^{C} has much higher conductivity than the other three. The figure also suggests that the conductivity of PVA solution increases with concentration. The result shown in Figure 7 proves the hypothesis. It shows the conductivities of PVA-C solutions in different concentrations. It can be found that for the aqueous solutions of 1 % - 15 % the conductivity increases with solution concentration. It is worth mentioning that when the concentration reaches above 10 % PVA^{C} solution shows more noticeable gelation and the gel will break up when the temperature increases and show up again when the temperature is back to room temperature. The 8 % PVA aqueous solution is stable without gelation. There is also a reference to indicate 8 % PVA aqueous solution has the most stable viscosity [13] and does not have gelation at room temperature. Gelation will affect significantly product performance. Thus, with consideration of the desired properties for target product, 8 % is the optimal concentration for PVA aqueous solution.

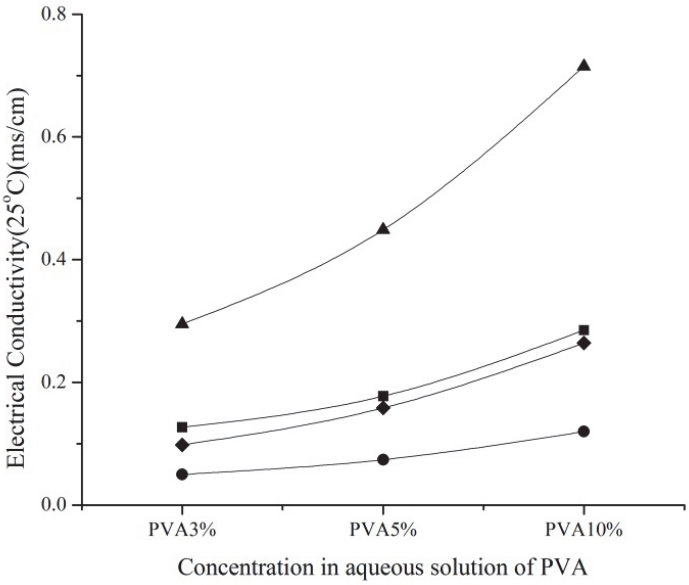

Fig. 6. The electrical conductivities for 3 %, 5 % and 10 % aqueous solutions from A(■), B(●), C(▲), D(♦) types of PVA

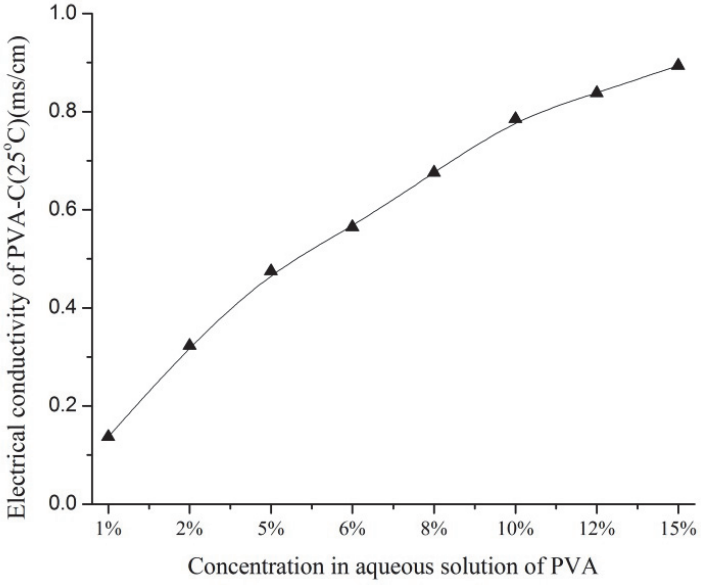

Fig. 7. The electrical conductivities measured at varying concentration in aqueous solutions and 25 °C of PVA[c]

The author also conducts draw down to investigate the film forming ability for the four types of PVA. It is conducted on smooth and cleaned glass (by anhydrous ethanol: ether =1: 1) with the PVA solutions of the same concentration. The sample is dried at room temperature and transferred to drying oven at 50 °C for drying until it is completely dried. After the film formation study with 3 % and 5 % PVA aqueous solutions, it is very clear that PVA^C has the best film forming ability and its film has the best stretching property, the best tensile strength and the best demoldability; PVA^D is the second best, and PVA^B and PVA^A perform similarly and not as good as the other two. Based on the consideration of the above two aspects, the final decision is to use 8 % PVA^C aqueous solution as polymer substrate.

3.5 Measurement of electric conductivity for composite films from PVA blended with CNTs of different carboxylation degree

The conductivities for series I films in Table 2 are shown in Figure 8. B0 in the figure represents unmodified CNTs as the control. As shown in the figure, after addition of carbon nanotube the conductivity for composite film solution increases drastically with the carboxylation degree of carbon nanotube. The composite film with carboxylated carbon nanotube has clearly higher electric conductivity than the composite film with unmodified carbon nanotube. Among carboxylated carbon nanotubes, the electric conductivity for the composite films from B1, B2, B3 groups of carbon nanotubes increases with carboxylation degree, but still looks flat without much distinction. It only shows a tendency of increase. However, the composite films from B4, B5 have much higher electric conductivity than the above four groups. Particularly, the carbon nanotube in B5 can achieve the highest electric

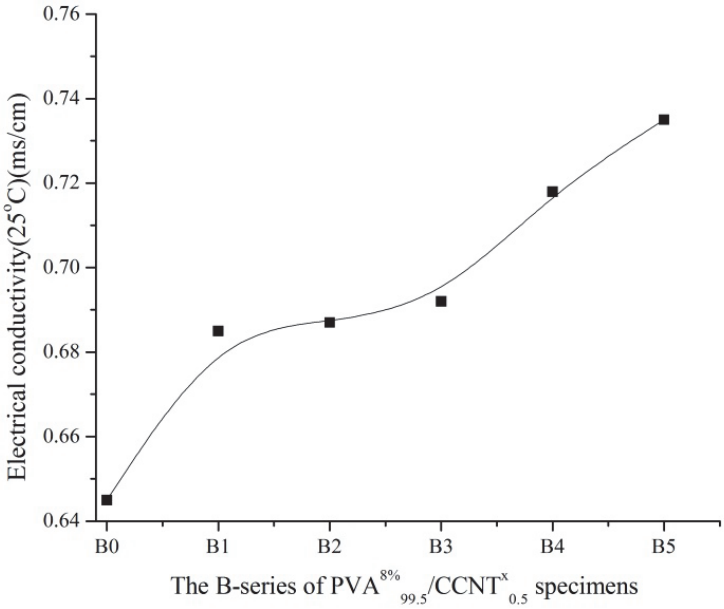

Fig. 8. The B-series of $PVA^{8\%}{}_{99.5}/CCNT^{x}{}_{0.5}$ specimens on electrical conductivities determined at 25 °C

conductivity in PVA film solution among all types of carbon nanotubes. From here it can be inferred that the higher the carboxylation degree for carbon nanotube, particularly in this study, the higher the electric conductivity for the composite film is. The hypothesis is that when the carboxylation degree for carbon nanotube is higher, more carbon nanotubes break. The same conclusion can be derived from the particle size analysis result. When the surface hydroxyl groups are more, the carbon nanotube becomes smaller. Since hydroxyl group is hydrophilic and PVA is a water-soluble polymer, in water the more carboxyl groups on carbon nanotube the better affinity with water and the better bonding with PVA. In other words, carbon nanotube will have better dispersibility in PVA substrate. When carbon nanotubes are highly dispersed in every part of PVA molecular framework, it is like adding many conductors to the framework. When carbon nanotubes are added to a certain quantity level, they will form a pseudo conductive network and the composite material will achieve a desirable electric conductivity level.

3.6 Measurement of electric conductivity for composite films from PVA blended with different amount of CNT^{b5}

Figure 9 shows the electric conductivities for PVA film solutions blended with different amount of $CCNT^{b5}$. It can be found from the figure that in the $CCNT^{b5}$ addition range of 0.1 % - 0.5 % the electric conductivity for composite film increases with increasing addition amount; and in the $CCNT^{b5}$ addition range of 1 % - 2 % the electric conductivity for composite film also increases with increasing addition amount, but less than that in the range of 0.1 % - 0.5 %. Interestingly, in the range of 0.5 % - 1 % the conductivity for composite film solution decreases greatly. Possibly because of insufficient number of composition ratios the trend is not very clear. But it can be anticipated that in the range of 0.5 % - 1 % there will be a composition % for the composite film solution to have the maximum electric conductivity.

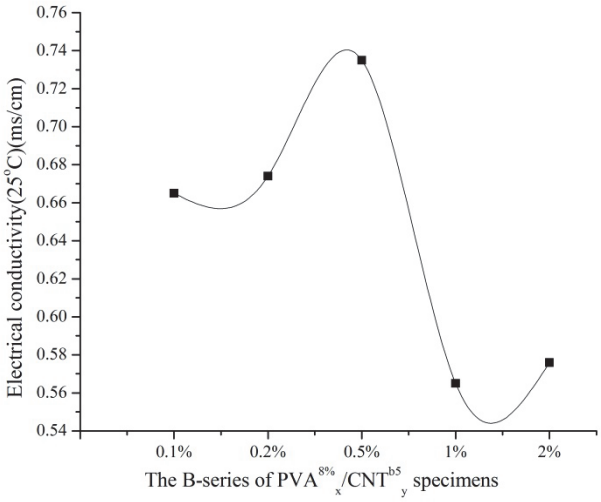

Fig. 9. The B-series of $PVA^{8\%}{}_x/CCNT^{b5}{}_y$ specimens blended with varying amounts CCNT on electrical conductivities determined at 25 °C

3.7 DSC analysis on composite films from PVA blended with different carboxylated CNTs

Figure 10 shows the DSC crystallization curve for the composite films from PVA blended with different carboxylated carbon nanotubes at 0.5 % by weight. It can be found from Figure 10 that addition of carbon nanotube can raise PVA crystallization temperature. Pure PVA has crystallization peak at 193.68 ^{o}C. After addition of carbon nanotube, the crystallization peak for all composite films rises to around 203.66 ^{o}C of PVA/CNTs and 203.66^{o}C of PVA/CCNTs, respectively. With increasing carboxylation degree for carbon nanotube or increasing damage degree for carbon nanotube, the crystallization peak area for the obtained composite films tends to increase only. It can be inferred that the dispersed carbon nanotubes cause heterogeneous nucleation to PVA crystallization and increase crystallization degree. Due to more perfect crystal, the crystallization temperature for the composite film also increases.

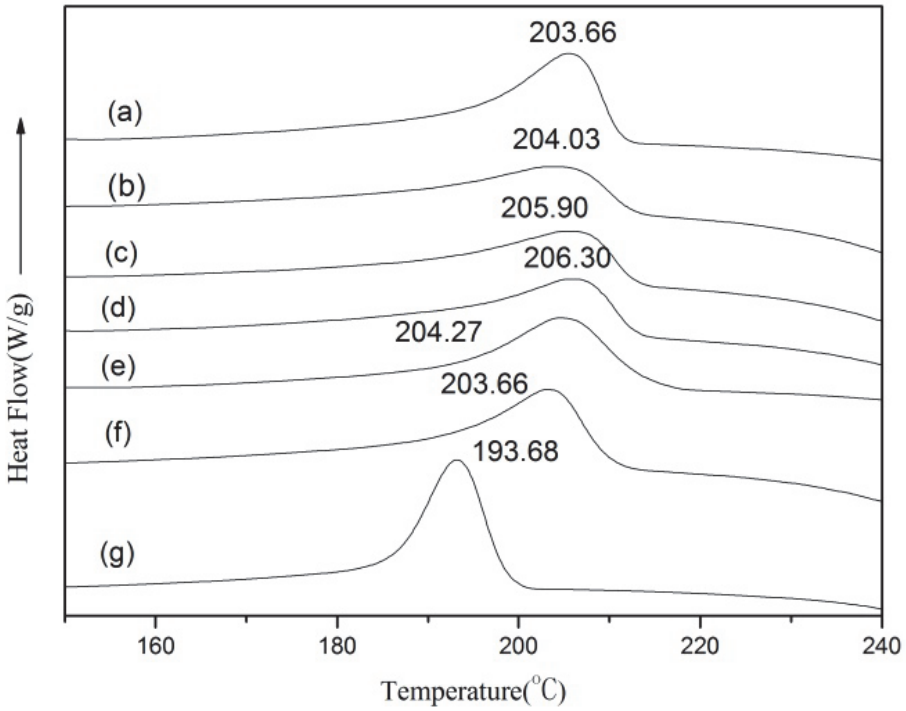

Fig. 10. DSC thermograms of non-isothermal crystallization of (a)PVA$^{8\%}{}_{99.5}$/CCNT$^{b5}{}_{0.5}$, (b) PVA$^{8\%}{}_{99.5}$/CCNT$^{b4}{}_{0.5}$, (c) PVA$^{8\%}{}_{99.5}$/CCNT$^{b3}{}_{0.5}$, (d) PVA$^{8\%}{}_{99.5}$/CCNT$^{b2}{}_{0.5}$, (e) PVA$^{8\%}{}_{99.5}$/CCNT$^{b1}{}_{0.5}$, (f) PVA$^{8\%}{}_{99.5}$/CCNTs$_{0.5}$ and (g) PVA

Figure 11 shows the melting curve for the composite films from PVA blended with different carboxylation degree of CCNT at 0.5 wt%. Increasing addition of carbon nanotube increases melting temperature for the composite film. For instance, addition of carbon nanotube, the melting temperature for the composite film increases from 218.79 ^{o}C for pure PVA to above 224.42 ^{o}C of PVA/CNTs and 228.43^{o}C of PVA/CCNTs, respectively.

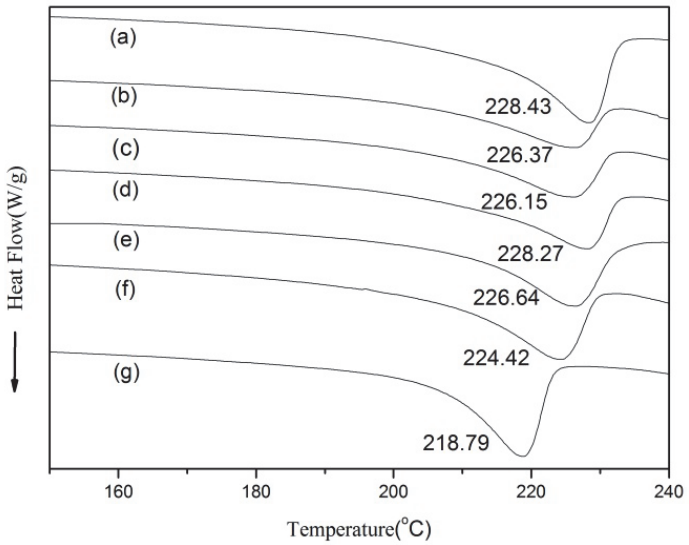

Fig. 11. DSC thermograms of non-isothermal melting of (a)$PVA^{8\%}{}_{99.5}/CCNT^{b5}{}_{0.5}$, (b) $PVA^{8\%}{}_{99.5}/CCNT^{b4}{}_{0.5}$, (c) $PVA^{8\%}{}_{99.5}/CCNT^{b3}{}_{0.5}$, (d) $PVA^{8\%}{}_{99.5}/CCNT^{b2}{}_{0.5}$, (e) $PVA^{8\%}{}_{99.5}/CCNT^{b1}{}_{0.5}$, (f) $PVA^{8\%}{}_{99.5}/CCNTs_{0.5}$ and (g) PVA

Figure 12 shows the DSC crystallization curve for the composite films from PVA aqueous solutions blended with different amount of $CCNT^{b5}$, 0.1 %, 0.2 %, 0.5 %, 1 %, 2 %.

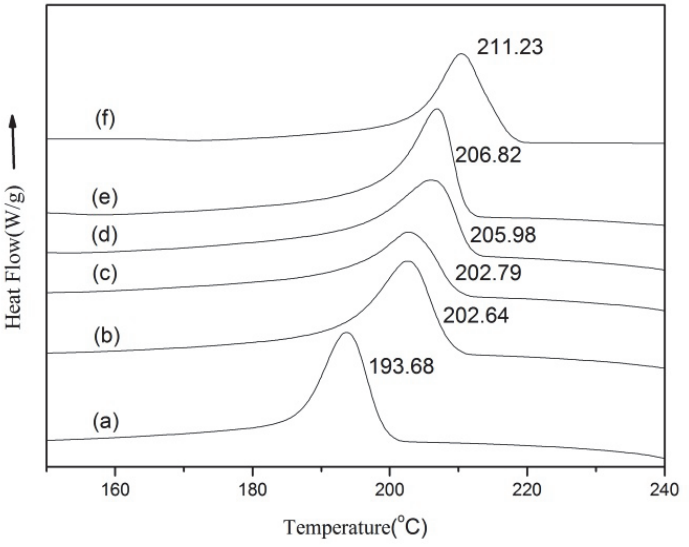

Fig. 12. DSC thermograms of non-isothermal crystallization of (a) PVA, (b) $PVA^{8\%}{}_{99.9}/CCNT^{b5}{}_{0.1}$, (c) $PVA^{8\%}{}_{99.8}/CCNT^{b5}{}_{0.2}$, (d) $PVA^{8\%}{}_{99.5}/CCNT^{b5}{}_{0.5}$, (e) $PVA^{8\%}{}_{99.0}/CCNT^{b5}{}_{1}$ and (f) $PVA^{8\%}{}_{98.0}/CCNT^{b5}{}_{2}$

Compared to pure PVA, i.e. curve a，the PVA blended with carbon nanotube shows higher crystallization temperature, which supports the hypothesis in previous Section. It can also be found from this figure that the crystallization temperature for the composite film increases with increasing addition of carbon nanotube. In the figure when the composition is $PVA^{8\%}{}_{98.0}/CCNT^{b5}{}_2$, the crystallization temperature reaches 211.23 °C and the peak area is the largest. It can be inferred that increasing addition of carbon nanotube can prolong crystallization for PVA composite film and increase crystallization degree. This also means more complete crystallization and more significant heterogeneous nucleation.
Figure 13 shows the melting curve for the composite films from PVA blended with different amount of $CCNT^{b5}$.

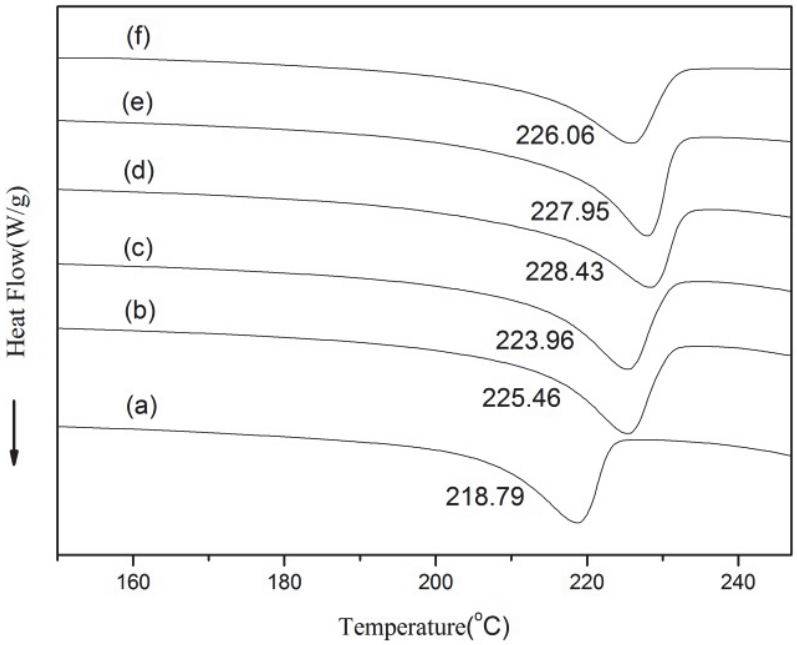

Fig. 13. DSC thermograms of non-isothermal melting of (a) PVA, (b) $PVA^{8\%}{}_{99.9}/CCNT^{b5}{}_{0.1}$, (c) $PVA^{8\%}{}_{99.8}/CCNT^{b5}{}_{0.2}$, (d) $PVA^{8\%}{}_{99.5}/CCNT^{b5}{}_{0.5}$, (e) $PVA^{8\%}{}_{99.0}/CCNT^{b5}{}_1$ and (f) $PVA^{8\%}{}_{98.0}/CCNT^{b5}{}_2$

Increasing addition of carbon nanotube increases melting temperature for the composite film. With increasing addition of carbon nanotube, the melting temperature for the composite film increases from 218.79 °C for pure PVA to above 228.43°C of $PVA^{8\%}{}_{99.5}/CCNT^{b5}{}_{0.5}$. The composite film with more than 0.5% $CCNT^{b5}$ has melting point around 226.06 °C of $PVA^{8\%}{}_{98.0}/CCNT^{b5}{}_2$. It can be inferred that with the similar reasoning for Figure 12 the crystallization degree is more complete and the melting point is higher.

3.8 WAXRD analysis

Figure 14 and Figure 15 show the composite films from PVA blended with different carboxylated carbon nanotubes and different amount of $CCNT^{b5}$.

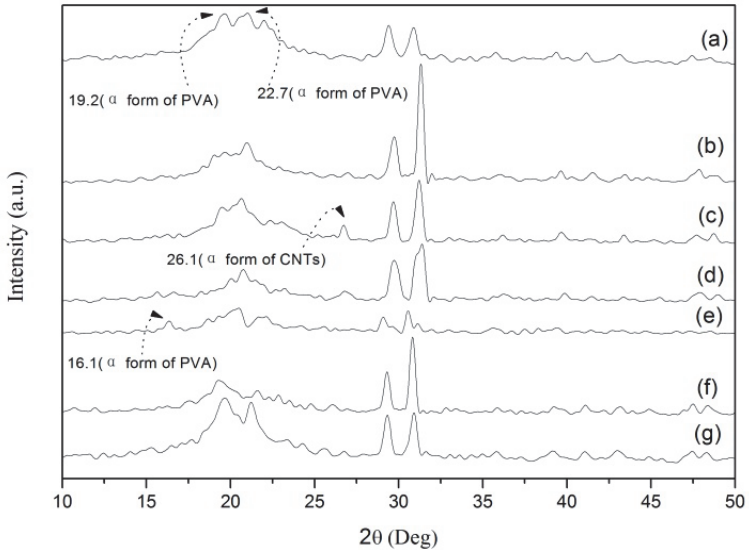

Fig. 14. WAXS diffraction patterns of (a) PVA, (b) $PVA^{8\%}{}_{99.5}/CCNT^{b1}{}_{0.5}$, (c) $PVA^{8\%}{}_{99.5}/CCNT^{b2}{}_{0.5}$, (d) $PVA^{8\%}{}_{99.5}/CCNT^{b3}{}_{0.5}$, (e) $PVA^{8\%}{}_{99.5}/CCNT^{b4}{}_{0.5}$, (f) $PVA^{8\%}{}_{99.5}/CCNT^{b5}{}_{0.5}$ and (g) $PVA^{8\%}{}_{99.5}/CNTs_{0.5}$

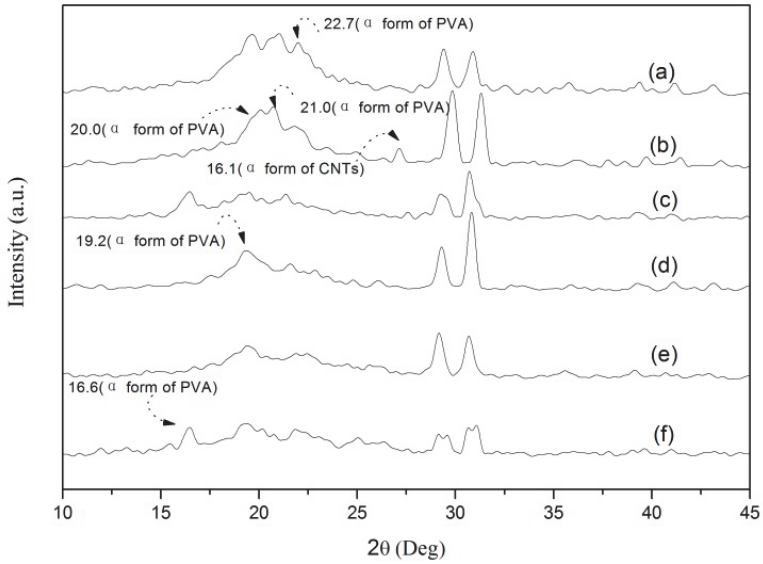

Fig. 15. WAXS diffraction patterns of (a) PVA, (b) $PVA^{8\%}{}_{99.9}/CCNT^{b5}{}_{0.1}$, (c) $PVA^{8\%}{}_{99.8}/CCNT^{b5}{}_{0.2}$, (d) $PVA^{8\%}{}_{99.5}/CCNT^{b5}{}_{0.5}$, (e) $PVA^{8\%}{}_{99.0}/CCNT^{b5}{}_{1}$ and (f) $PVA^{8\%}{}_{98.0}/CCNT^{b5}{}_{2}$

It is consistent with literature values that in the study the X ray diffraction peak angles for the α crystals from PVA samples crystallized from cooling at 25 °C mainly show up at 16.1°、19.2°、20.0°、21.0° and 22.7°; the XRD peak angle for CNTs sample appears at 2θ=26.7° because the characteristic diffraction peak [14][15] for crystal plane (002) increases with carboxylation degree. Although the WAXRD diffraction peak for CNTs gradually decreases, their existence is still visible. PVA's diffraction peak levels off. Increasing addition of carbon nanotube decreases the WAXRD diffraction peak for $CCNT^{b5}$ for the composite film. When carbon nanotube is added more than 1 % by weight, $CCNT^{b5}$ peak almost disappears. PVA diffraction peak intensity tends to decrease with increasing addition of carbon nanotube. This proves that carbon nanotube has successfully been blended into PVA substrate and changed PVA crystal morphology. This also supports the projection by DSC that carbon nanotube cause's heterogeneous nucleation in PVA substrate.

4. Conclusion

In summary, carboxylation for carbon nanotube is an effective solution to improve the dispersibility of carbon nanotubes in polymer. Addition of carbon nanotube into substrate, like PVA, can improve electric property, thermal property and crystal morphology. Carbon nanotube is certainly excellent electrically-conductive and thermally-conductive nano filler for polymers.

5. References

Iijima, S. (1991). Nature, 354, pp. 56.

Lee, R.S.; Kim, H.J. & Fischer, J.E. (1997). Nature, 388, pp. 255.

McCarthy, D.W.; Mark, J.E. & Schaffer, D.W. (1998). Journal of Polymer Science, Part B: Polymer Physics, 36, pp. 1167.

McCarthy, D.W.; Mark, J.E.; Clarson, S.J. & Schaffer, D.W. (1998). Journal of Polymer Science, Part B: Polymer Physics, 36, pp. 1191.

Kohjiya, S.; Murakami, K.; Iio, S.; Tanahashi, T.; Ikeda, Y.; (2005). Rubber Chemistry and Technology 2001, 74, pp. 16.

Osman, M.A.; Atallah, A. Muller, M. & Suter, U.W. (2001). Polymer, 42, pp. 6545.

Joly, S.; Garnaud, G.; Ollitrault, R. & Bokobza, L. (2002). Chemistry of Materials, 14, pp. 4202.

Varghese, S. & Karger-Kocsis J. (2003). Polymer, 44, pp. 4921; (2004). Rubber World, 230, pp. 32.

Kim, J.T.; Oh, T.S. & Lee, D.H. (2004). Polymer International, 53, pp. 406.

Arroyo, M.; Lo´pez-Manchado, M.A. & Herrero, B. (2003). Polymer, 44, pp. 2447.

Bala, P.; Samantaray, B.K.; Srivastava, S.K. & Nando, G.B. (2004). Journal of Applied Polymer Science 92, pp.3583.

Jeon, H.S.; Rameshwaram, J.K. & Kim, G. (2004). Journal of Polymer Science, Part B: Polymer Physics, 42, pp. 1000.

Gauthier, C.; Chazeau, L.; Prasse, T. & Cavaille´, J.Y.; (2005). Composites Science and Technology, 65, pp. 335.

Bokobza, L. & Chauvin, J.-P. (2005). Polymer, 46, pp. 4144.

Barraza, H.J.; Pompeo, F.; O'rear, E.A. & Resasco, D.E. (2002). Nano Letters, 2, pp. 797.

Frogley, M.D.; Ravich, D. & Wagner, H.D. (2003). Composites Science and Technology, 63, pp. 1647.

Lo´pez-Manchado, M.A.; Biagiotti, J.; Valentini, L. & Kenny, J.M. (2004). Journal of Applied Polymer Science, 92, pp. 3394.

Hirsch, A. (2002). Angewandte Chemie International Edition, 41, pp. 1853-1859

Ma, P.C.; Kim, J.K. & Tang, B.Z. (2006). Carbon, 44, pp. 3232-3238

Vast, L.; Philippin, G.; Destree, A.; Moreau, N.; Fonseca, A. & Nagy, J.B. (2004). Nanotechnology, 15, pp. 781-785.

Liu, H.; Zhang, W. & Zheng, S. (2005). J Polym, 46, pp. 157-165.

Lee, Y.J.; Kuo, S.W.; Huang, C.F. & Chang, F.C. (2006). J Polym, 47, pp. 4378-4386.

Liu, Y.; Zheng, S. & Nie, K. (2005). J Polym, 46, pp. 12016-12025.

Vaia, R.A. & Giannelis, E.P. (1997). Macromolecules, 30, pp. 7990–7999.

Vaia, R.A & Giannelis, E.P. (1997). Macromolecules, 30, pp. 8000–8009.

Wen, Y.; Liu, K.; Shang, X.-P.; Tsai, L.-C. & Tsai, F.-C. (2009) "Fabrication and conduction properties of poly(vinyl alcohol) and modified carbon nanotubes blends", 2009 International Workshop on Processing and Properties of Reinforced Polymer Composites, p45.

Tsai, F.C.; Li, P.; Shang, X.P.; Ma, N.; Tsai, L.C. & Yeh, J.T. (2010). Advanced Materials Research, 87-88, pp. 363-368

Yeh, J. T.; Xu, P. & Tsai, F. C. (2007). J. Material Sci., 42, pp. 6590.

Cui, L.; Yeh, J.T.; Wang, K.; Tsai, F. C. & Fu, Q. (2009). J. Memb. Sci. 327, pp. 226.

Okaya, T. & Ikari, K. (1992). in Polyvinyl Alcohol-Developments[C], C.A. Finch Ed, at Chapter 8, John Wiley & Sons, New York

Yan, R. X. (1998). Water-soluble polymer, Chemical industry press, Beijing,

Liu, J.; Rinzler, A. G.; Dai, H.; Hafner, J. H.; Kelley Bradley, R.; Boul, P. J.; Lu, A.; Iverson, T.; Shelimov, K.; Huffman, C. B.; Macias, F. R.; Shon, Y.S.; Lee, T. R.; Colbert, D. T. & Smalley, R. E. (1998). Science, 280 , pp. 1253.

18

Carbon Nanotube Nanofluidics

Jong Won Choi, Maria A. Alexandrova and Hyung Gyu Park*
Swiss Federal Institute of Technology Zurich (ETH Zürich), Zürich, Switzerland

1. Introduction

Carbon nanotubes (CNT), with diameters in the nanometer range and atomically smooth surfaces, offer a unique system for studying molecular transport and nanofluidics. Although the idea that water can occupy such confined hydrophobic channels is somewhat counter-intuitive, experimental evidence has confirmed that water can indeed occupy these channels (Naguib, Ye et al. 2004; Kolesnikov, Loong et al. 2006). Water transport through molecular-scale hydrophobic channels is also important because of the similarity of this system to transmembrane protein pores such as aquaporins (Agre, Borgnia et al. 2001; Agre 2004; Agre 2006). In recent years, numerous simulations (Hummer, Rasaiah et al. 2001; Kalra 2003) of water transport through single-walled carbon nanotubes (SWNT) have suggested not only that water occupies these channels, but also that fast molecular transport takes place, far in excess of what continuum hydrodynamic theories would predict if applied on this length scale. Molecular dynamics (MD) simulations attribute this enhancement to the molecular-level smoothness of the nanotube interior surface and to molecular ordering phenomena that may occur on confined length scales in the 1- to 2-nm range (Hummer, Rasaiah et al. 2001; Skoulidas, Ackerman et al. 2002; Kalra 2003). For similar reasons, simulations of gas transport through SWNTs (Lai, Bonilla et al. 2003) predict flux enhancements of several orders of magnitude relative to other similarly sized nanoporous materials. Membrane-based gas separations, such as those using zeolites (Hinds, Chopra et al. 2004), provide precise separation and size exclusion, although often at the expense of throughput or flux. It may be possible to use SWNT to create a membrane that offers both high selectivity and high flux.

To investigate molecular transport on this length scale, we need to fabricate a carbon nanotube membrane that has a pore size of the order of 1 nm. Researchers have recently fabricated multi-walled carbon nanotube (MWNT) membranes with larger pore diameters (6 to 7 nm) by encapsulation of vertically aligned arrays of MWNTs (Hinds, Chopra et al. 2004; Holt, Noy et al. 2004) and by templated growth within nanochannel alumina (Li, Papadopoulos et al. 1999). Enhanced water transport through these larger MWNTs has recently been reported (MajumderMainak, ChopraNitin et al. 2005). Quantifying transport through an individual tube in a MWNT membrane is difficult, however, because MWNTs are prone to blockages, in particular by "bamboo" structures and catalyst particles that can migrate to and obstruct the nanotube interior (Cui, Zhou et al. 2000; Maruyama, Einarsson et al. 2005; Wang, Gupta et al. 2005). The consequence of such blockages is a marked reduction

*parkh@ethz.ch

of the active membrane pore density. In contrast, there are few, if any, reports of "bamboo" structure formation or catalyst migration in SWNTs or double-walled carbon nanotubes (DWNTs). However, it has been difficult to produce vertically aligned carbon nanotubes of this size uniformly and at large scale (Kalra 2003; Hata, Futaba et al. 2004). The major challenges also lie in finding a conformal deposition process to fill the gaps in this nanotube array, as well as in designing a selective etching process to open up the nanotube channels without producing voids in the membrane. These challenges in nanomanufacturing are one of the major reasons for the imbalance between the number of reports from computational and experimental studies, offering great research opportunities in the area of experimental *Carbon Nanotube Nanofluidics*.

This book chapter is intended to provide an intermediate level overview of *Carbon Nanotube Nanofluidics* to the beginners and scientists who are interested in this emerging research field. For that purpose, we write discussions of *Carbon Nanotube Nanofluidics* with respect to transporting entities. In section 2, we discuss water transport under the CNT nanoconfinement in view of the unique transport phenomena including spontaneous water filling, fast water transport and mechanisms behind it. In section 3, we discuss the various aspects of gas transport in CNT. We present fundamental findings of *Carbon Nanotube Nanofluidics* for the gas transport, followed by a perspective of gas separation using CNT membranes. In section 4, we introduce recent achievements made by theoretical and experimental studies focusing on the behavior of ions in CNT including transport of ions under the CNT nanoconfinement, and ion exclusion and selectivity in association with CNT membrane technology. Finally, we will conclude several aspects of *Carbon Nanotube Nanofluidics* in section 5.

2. Water transport

2.1 Introduction and overview

Nanoscale confinement carbon nanotube (CNT) provides can lead to transport phenomena unique at this length scale featured by spontaneous water filling and fast water transport. It is the graphitic curvature of the internal space of CNT that effectively smoothes the potential energy landscape to cause minimal friction to water flows. The last decade saw growing attention on the flow enhancement of pressure-driven water through CNT membranes that exceeds the continuum theory prediction by three to four orders of magnitude. This phenomenon renders CNT an attractive building block for various nanofluidic applications such as molecular sensors, nanopipettes, hydrogen storage, membrane filtration, drug delivery, energy conversion and dissipation, in which the hydrophobicity, atomic-level smoothness and nanoscale pore size interplay to result in considerable improvement of energy efficiency.

Conduits of CNT consist of rolled sheets of graphene with sp^2-hybridized carbon atoms that are not generally known to be wetted by water. In view of continuum models, it seems incredible that polar liquids, especially water, may fill in such narrow hydrophobic CNT conduits. However, at nanometer scales where surmises of those continuum models no longer hold, water molecules can behave somewhat differently from macroscopic predictions, mostly characterized by ordered configuration of the hydrogen bond network. Hummer *et al*. (Hummer, Rasaiah et al. 2001) used equilibrium molecular dynamics (MD) simulation about

an 8 Å wide (6, 6) CNT in a water bath to argue that water molecules do not only enter the narrow hydrophobic channel spontaneously, but can also move very fast through it. They supported the argument of spontaneous filling by comparison of water binding energy distributions between bulk and nanoconfinement states. Unlike Gaussian distribution of bulk water binding energies centered around a value corresponding to ca. four hydrogen bonds, the binding energy distribution under the nanoconfinement showed degeneracy featured by population inversion at lower binding energies. In other words, lower binding energies are less populated by water under the nanoconfinement of CNT, leading to tight hydrogen bonding network of a single file and a decrease in chemical potential, a thermodynamic explanation of the spontaneous filling of CNT conduits with water molecules.

To support the next part of the argument (rapid water conduction), Hummer et al. (Hummer, Rasaiah et al. 2001) counted water molecules passing through CNT on a computational domain. Even though average flow rate estimate was zero because their simulation was equilibrium molecular dynamics, most of the constituent microstates involved burst-like motions of the single-file water molecules as fast as 17 ns^{-1}. Another simulation on the water transport through a membrane that consists of open-ended (6, 6) CNTs was performed under an osmotic pressure gradient by Kalra *et al*. (Kalra 2003). They obtained the motion of about 5 ns^{-1} and found that single-file water molecules are governed by microscopic fluctuations and nearly independent of the tube length due to very low friction coefficient. These theoretical predictions were verified with experimental studies of Holt, Park *et al*. (Holt 2006), in which the water flow was measured through microfabricated CNT membranes with pores less than 2 nm. The measured water flow rates exceeded the prediction of a continuum hydrodynamics model by more than three orders of magnitude. Majumder *et al.* (Majumder, Chopra et al. 2005) also made an investigation of the water transport through CNT membrane with large pores of around 7 nm. In this experiment, the measured flow rates were four to five orders of magnitude larger than a continuum hydrodynamics model. Joseph and Aluru (Joseph and Aluru 2008) simulated the pressure-driven flow in a (16, 16) CNT to reveal that the enhanced flow rate over Hagen-Poiseuille formalism is primarily caused by a velocity "jump" in a depletion region between the nearest water layer and the carbon wall. They concluded that a slightly modified water-carbon interaction potential to make the CNT wall surface more hydrophilic could greatly reduce the enhancement in the water transport because it would lower down the number of hydrogen atoms pointing toward the carbon wall in the depletion layer. Nanoscale roughness in the tube walls caused no significant flow enhancement. Additional phenomena and effects of nanoconfinement in CNTs on the water structure, density profile, hydrogen bonds, and some suggestions about the fast water transport are illustrated in detail in the following sections. This chapter begins with explaining the classical theory of fluid mechanics briefly, limit of the application of the theories, and hydrophobic Interaction between the water molecules and CNT. Subsequently, using several literatures for water transport under nanoconfinement of CNT, we will summarize water structure in CNTs, water density profile in CNTs, and hydrogen bonds of water inside CNTs. In the next, we will enlist some theoretical descriptions about the main principles and mechanisms of infiltration and transport of water in CNT. Finally, we will discuss nanofluidic applications and some perspectives the ultrafast water transport poses potential of.

2.2 Continuum limit of water

Continuum model of water hypothesizes that the spatial and temporal derivatives of all the macroscopic dependent variables such as density, velocity, stress, and heat flux exist in a continuous and differentiable manner. Navier-Stokes equation derived from the force balance has been representatively used for explaining the dynamic behavior of fluids such as diffusion, conduction, and momentum transport in the macro scale, where the physical properties such as density and velocity profiles can vary appreciably over the molecular length and relaxation time scales regardless of the nature of the molecular structure and configuration of a fluid under consideration. However, in nanoscale conduits of CNT, much larger flow rates are observed for the fluid transport that cannot be explained by the continuum theory. Derived from these phenomena, one may raise several questions: How does the Navier–Stokes equation break down at the nanoscales? Can we still use the continuum-based theories to predict the behavior such as diffusion, heat transfer, or momentum transport? Why would the water inside CNT have anything specific for the transport? Indeed, there have been many efforts to define the boundary between bulk water and confined water transport. A liquid fluid particle can be heuristically defined as a volume containing more than 10,000 molecules because we need at least 10,000 molecules for obtaining less than 1% statistical fluctuation in measuring physical properties. Thus, one may reasonably consider the liquid particle of 10,000 molecules as a continuum limit. Since a sphere containing an aggregate of 10,000 equidistant molecules has an equivalent diameter of about 25 molecules and the size of a water molecule is estimated as ca. 0.3 nm, the diameter of the 10,000 water molecules will be calculated as about 7.5 nm. A tube with the diameter of much larger than 7.5 nm can allow the fundamental hypothesis of hydrodynamics. Hence, it would be sensible to set a threshold for the continuum treatment of liquid as around 7.5 nm.

In the non-continuum regime, there exists another threshold associated with variation in fluid properties. Raviv and Klein (Raviv 2002) asserted that water loses its bulk viscosity below 1–2 nm, with a drastic change for stronger confinements. They presented the wettability of confining surface plays a dominant role for the viscosity below 1-2 nm. This threshold was emphasized again by other researchers (Lei and Leng 2010; Thomas, Iutzi et al. 2010). These two threshold values could impart guideline values in the analysis of nanoscale molecular transport phenomena.

2.3 Slip length theory

A no slip boundary condition is typically used in continuum fluid dynamics. It constrains a fluid closest to a solid boundary to obtain the same tangential velocity as the solid. When the tangential velocity of fluid differs from that of solid, we usually say the surface imposes a slip boundary condition as depicted in **Fig. 2.1**. One may wonder whether the slippery motion of water in a nanoscale hydrophobic tube of CNT can be well described using continuum equations. Nevertheless, the slip boundary condition helps us describe non continuum behavior of water transport inside CNT in the framework of continuum dynamics. For example, slip length, L_s, may serve as a good indicator for the molecular interaction between water molecules and CNT via provision of information about the degree of departure the transport innately has from the hydrodynamic Hagen-Poiseuille flow. Also, the slip length indicator can compare with results of MD simulations often used for the exact prediction of water flow under the CNT nanoconfinement.

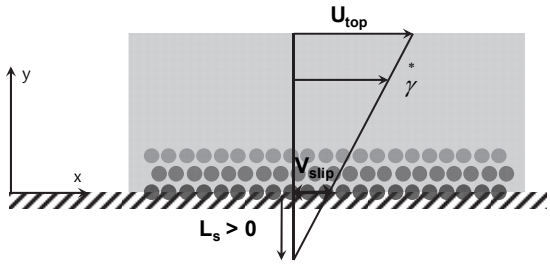

Fig. 2.1. Hydrodynamic slip flow profile characterized by slip length, L_s.

Unfortunately, there exists no definite criterion or nondimensional number that categorizes liquid flow regimes. In this situation, the Knudsen number used for distinguishing the gas flow regimes may serve as an indirect gauge that could tell us about the liquid flow regime. It is defined as the ratio of mean free path to characteristic length. Well accepted criteria for gas flows are given as follows (Steckelmacher 1986).

$$\mathrm{Kn} < 0.001 \qquad \text{(Continuum flow)}$$

$$0.001 < \mathrm{Kn} < 0.1 \qquad \text{(Slip flow)}$$

$$0.1 < \mathrm{Kn} < 10 \qquad \text{(Transition flow)}$$

$$10 < \mathrm{Kn} \qquad \text{(Free molecular flow)}$$

In liquid, molecules are rather densely aggregated and they interact one another within the length scale of the molecule's own size. If one would define a pseudo mean free path of liquid water as the molecular size, the Knudsen number for the tube having diameter of 1 nm is calculated to be 0.15, placing the transport between slip flow and transition flow regimes. Hence, continuum hydrodynamics may not be allowed to define the velocity profile in narrow CNT. Slip length, L_s, is convenient to explain the hydrodynamic boundary condition at the interface of fluid and wall, which is defined according to the Navier boundary condition in equation (2.1).

$$L_s \left.\frac{\partial v_t}{\partial n}\right|_{\text{wall}} = v_{t,\text{wall}} - v_{\text{wall}}, \tag{2.1}$$

where n and t denote normal and tangential directions of the wall, v_t is the velocity of a fluid tangential to the wall, and v_{wall} is the velocity of the wall. $v_{t,\text{wall}} - v_{\text{wall}}$ is denoted as a slip velocity. In some sense, the slip length is related to the surface friction at the fluid-wall interface. Larger slip lengths can be related with lower liquid–solid friction. For example, the slip length at solid surfaces depends on the wettability of the surface: easily wetted surface may exert larger friction. Therefore, very large slip lengths of water flows obtained in CNT signify a considerable enhancement in water flow rates (Lee, Choi et al. 2008). As the size of the nanotube decreases, the dynamics at its surface plays an increasingly important role (Willmott and Tallon 2007). For investigating the relationship between the slip length and the interfacial properties, it is useful to understand the slip length in connection of liquid–solid interface friction. The friction force is linearly proportional to slip velocity as in

equation (2.2). By definition, the slip length is related with a friction coefficient: equation (2.3).

$$F_{\text{friction}} = -A_L f\left(v_{\text{t,wall}} - v_{\text{wall}}\right), \tag{2.2}$$

$$L_s = \mu / f, \tag{2.3}$$

where f is the friction coefficient, A_L is the lateral area, and μ is the bulk viscosity.
An approximation of the Green–Kubo relation can give an expression for the friction coefficient f: equation (2.4) (Sendner, Horinek et al. 2009).

$$f \approx \frac{1}{A_L k_B T}\left\langle F_{\text{friction}}{}^2 \right\rangle_{\text{equilibrium}} \times \tau, \tag{2.4}$$

where τ is the relaxation time, $\langle F^2 \rangle_{\text{equilibrium}}$ is the rms friction force, and $k_B T$ is the reference thermal energy. The relaxation time is written by $\tau \approx \sigma^2 / D$ where σ is the scale of molecular diameter and D is the fluid diffusion coefficient. From equations (2.3) and (2.4), we can estimate the function of slip length as

$$L_s \approx \frac{A_L k_B T \mu D}{\sigma^2 \left\langle F_{\text{friction}}{}^2 \right\rangle_{\text{equilibrium}}}, \tag{2.5}$$

According to equation (2.5), a large degree of flow slippage implying a weak liquid–solid interaction is expected to occur at high temperatures or on very smooth surfaces (low friction force). The solutions for the velocity and the corresponding volume flow rate in the flow direction, z, with respect to the distance from the center, r, have a parabolic profile given by:

$$U_{\text{s}} = -\frac{dp}{dz}\frac{R^2}{4\mu}\left(1 - \frac{r^2}{R^2} + \frac{2L_{\text{s}}}{R}\right), \tag{2.6}$$

$$Q_{\text{Hagen-Poiseuille}} = -\frac{dp}{dz}\frac{\pi R^4}{8\mu}, \tag{2.7}$$

$$Q_{\text{s}} = Q_{\text{Hagen-Poiseuille}}\left(1 + \frac{4L_{\text{s}}}{R}\right), \tag{2.8}$$

where μ, p, and R represent viscosity, pressure, and tube radius, respectively.
There are two primary reasons to investigate a continuum theory of a molecular scale slip behavior in this section. On the one hand, it helps to understand the behavior of a flow in nanoscale tube, thereby predicting what kinds of factors or physical mechanisms are responsible for the flow enhancement. On the other hand, the slip length theory can serve as a reference to explain large water flow enhancements, compared with no-slip Hagen-Poiseuille formalism, observed by several experimental studies using CNT membranes.

Researchers used the slip length theory to discuss their experimental results with CNT membranes (Majumder, Chopra et al. 2005; Holt 2006; Whitby, Cagnon et al. 2008). By use of a MWNT membrane with a pore diameter of 7 nm, Hinds and colleagues reported largely enhanced flow rate per pore, beyond any theoretical expectation. Bakajin and colleagues also measured water flow enhancement through a DWNT membrane based on nanocomposite out of vertically aligned CNTs having a pore size of 1.3–2 nm and silicon nitride. They all quoted corresponding slip lengths of 53,728 nm (enhancement factor of 61,404 (Majumder, Chopra et al. 2005)) and 140 to 1,400 nm (enhancement factor of 560-8,400 (Holt 2006)). Later experiments performed through carbon nanopipes with diameters of 44 nm suggested a slip length of 32-38 nm (enhancement factor of 22-24 (Whitby, Cagnon et al. 2008)). In the absence of enough experimental data to judge, it is still a question which results are more acceptable yet or how the enhancement factor is related with the tube size, creating a need of more experimental verifications out of various degrees of CNT nanoconfinements for obtaining reasonable enhancement values and relationship between the enhancement value and nanotube geometry. Although a challenge in manufacturing remains, additional experimental efforts will provide the answers to the questions such as when the continuum theory breaks down and what kinds of theory would explain the fluidics inside CNT better.

2.4 Water structure and hydrogen bonds

Although the ultrafast water transport in the CNT could, in part, be explained by the slip length model, it is indeed well reported that the water flow rate depends not on bulk properties such as density and viscosity but rather on the interaction between water molecules and carbon atoms in the CNT wall. Accordingly, one can model the relation between the surface friction and structure of water molecules inside CNT. In this section, instead of slip flow theory, results of MD simulations, especially on the water configuration, are introduced and compared since it is a stronger and effective way to investigate many fundamental nanofluidic characteristics. While water molecules inside CNT conduct in a single file configuration when the tube becomes narrow down to a few water molecular size (i.e. sub 1 nm), the structure of water in wider CNTs seems to take a layered configuration especially near the internal walls.

A hydrogen bond found in water is an attractive interaction between a hydrogen atom of one water molecule and an electronegative atom, oxygen of another water molecule. It is stronger than a van der Waals interaction, but weaker than covalent or ionic bonds. Actually, lots of physical properties of water depend on the coherence and the number of the hydrogen bonds. The hydrogen bond is useful in explaining water configuration or properties inside CNT, since water has a dipole and an electrostatic interaction via hydrogen bonding. It is well known that each water molecule can have approximately 3.6 of hydrogen bonded neighbor molecules in bulk water. Many results of MD simulations support that the average hydrogen bond between water molecules decreases in confined tube and the confined water molecules lose two hydrogen bonds on average from the bulk configuration, since there is a lack of space to retain the bulk state in such a narrow nanotube, and therefore this value reaches approximately 1.6 bonds in narrow CNTs, where only a single file of water is allowed as shown in **Fig. 2.2** (Hummer, Rasaiah et al. 2001; Eschermann, Li et al. 2006; Banerjee, Murad et al. 2007; Hanasaki, Nakamura et al. 2008).

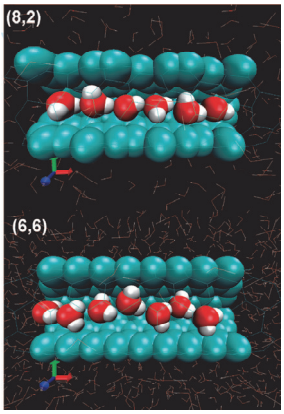

Fig. 2.2. Single-file configuration of water molecules in (8,2) and (6,6) carbon nanotubes (Alexiadis and Kassinos 2008).

Byl *et al.* (Byl, Liu et al. 2006) assessed that water molecules are highly oriented and aligned hand in hand along the axis of a single-file chain, thereby allowing water molecules to rotate freely around the aligned hydrogen bonds. Study on the single file was introduced by Hummer and colleagues (Hummer, Rasaiah et al. 2001) using water molecules in 8 Å-wide (6,6) SWNT at the pressure of 1 bar. They found counter intuitively that water molecules may configure themselves in a single file, allowing only two hydrogen bonds per molecule, and occupy the CNT spontaneously during the entire simulation period of 66 ns. This occupancy, nevertheless, can degrade into fluctuation between filled- and empty states when the water-to-carbon interaction potential is slightly rendered more hydrophobic. They explained that it is not because of the average water binding energy in CNT (enthalpic contribution) but because of the local excess chemical potential (enthalpo-entropic contribution) that determines the water occupancy of narrow CNTs. Kolesnikov and his group (Kolesnikov, Loong et al. 2006) provided evidence that water can indeed fill inside narrow (10,10) CNT and pose a configuration of a single file inside an octagonal water nanotube. Mashl *et al*. (Mashl, Joseph et al. 2003) simulated the similar situation to predict a hexagonal water inside (9,9) SWNT at 1 bar, but they did not find any similar structure among (7,7), (8,8), or (10,10) CNTs. However, MD simulation by Byl *et al.* (Byl, Liu et al. 2006) did not find any distinguishable water structure inside CNTs from (7,7) to (10,10), while they found a single file formation in (5,5) SWNTs by using different potential parameter. Even with a large number of efforts to determine the water layer structure in CNTs with various diameters, the results are still different from one another. This discrepancy can be explained by diverse water models and water-to-carbon interaction potentials. For example, a lower interaction potential value is likely to allow confined water to form n-gonal structures easily, while a higher value tends to keep water molecules disordered. However, it is certain that all the simulations show that water confined in CNTs shows characteristics that considerably differ from those of bulk water, regardless of selected water models. Recent study on the water structure on temperature and pressure was carried out by Koga *et al.* (Koga, Gao et al. 2001). They found that water took an n-gonal configuration between 500 and 5,000 bars, and lifetime of defect (break and reunion) was longer for wider CNTs. They concluded that the number of concentric water nanotubes could be determined by the nanotube chirality (i.e. with n = 4, 5,

and 6 for (14,14), (15,15), and (16,16) CNTs, respectively.) Likewise, Lin *et al.* (Lin, Shiomi et al. 2009) showed the radial density profile and water structure using different density values inside SWNTs of (6,6), (8,8), (10,10), and (14,14). They presented the water could fill into the tube for the density of 1.4 g/cm^3 among the water densities of 1.0, 1.2, and 1.4 g/cm^3 at least except for (6,6) SWNT, which was partially filled spontaneously for all the given densities. The maximum water peaks are slightly increased as the diameters increase due to the flexibility of the SWNTs. The water configurations for different diameters of CNT are shown in **Fig. 2.3**. As the tube diameters increase from (6,6) to (14,14), water configuration in CNT evolved from a single-file chain to a single wall water nanotube, to a single file in a single wall water nanotube, and finally to a single file in a multi-walled water nanotube. Using these simulation results, Alexiadis and Kassinos (Alexiadis and Kassinos 2008) calculated diameter dependence of an average number of the hydrogen bonds, determined based on the criteria of oxygen-to-oxygen distance of 3.3 Å, oxygen-to-hydrogen distance of 2.4 Å, and bonding angle between O-O direction and H-O direction of less than 30°: **Fig. 2.4**. The diagram of H-bond number vs. CNT diameter allowed them to identify distinctive water structures such as "single-file water", "water layers", and "bulk mode." However, more recent experimental work carried by Kyakuno *et al.* (Kyakuno, Matsuda et al. 2010) did not support this finding. They constructed a phase diagram of water inside SWNT as shown in **Fig. 2.5,** based on the XRD (green squares), NMR (red circles), and two MD simulation sources from Shiomi *et al.* (Shiomi, Kimura et al. 2007) (black squares) and Takaiwa *et al.* (Takaiwa, Koga et al. 2007) (blue triangles). The approximate diameter near the boundary between liquid and ice is around 1.5 nm, in which they proposed that there exist double or triple shell geometries. In narrower CNTs, $1.17 < d < 1.45$ nm, a new water configuration named ice nanotubes has the transition freezing points similar with ice. As inferable from these results, it would be meaningful to establish the phase of water for $1.17 < d < 1.45$ nm and at near room temperature.

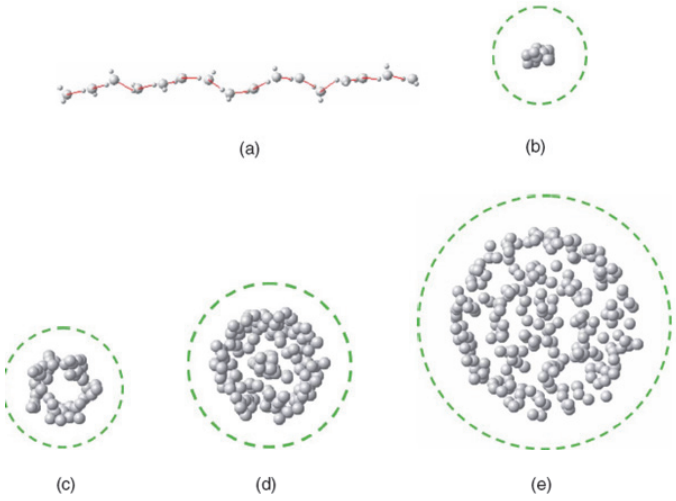

Fig. 2.3. Water inside SWNTs with different diameters. (a) side view of water inside (6,6) SWNT (b) cross section in (6,6) SWNT, (c) (8,8) SWNT, (d) (10,10) SWNT, (e) (14,14) SWNT. Only oxygen atoms are shown for clarity (Lin, Shiomi et al. 2009).

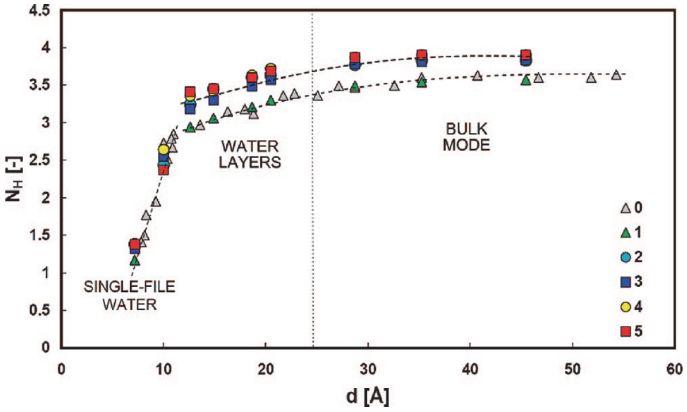

Fig. 2.4. Hydrogen bonding (calculated with R_{OO} = 3.3 Å, R_{HO} = 2.4 Å, and φ = 30°) versus diameter. The data are divided into six different groups: (0) TIP3P water model/rigid CNT; (1) TIP3P water model/flexible CNT; (2) SPC/E water model/rigid CNT; (3) flexible TIP3P water model/rigid CNT; (4) flexible SPC water model/rigid CNT; and (5) flexible SPC water model/flexible CNT (Alexiadis and Kassinos 2008).

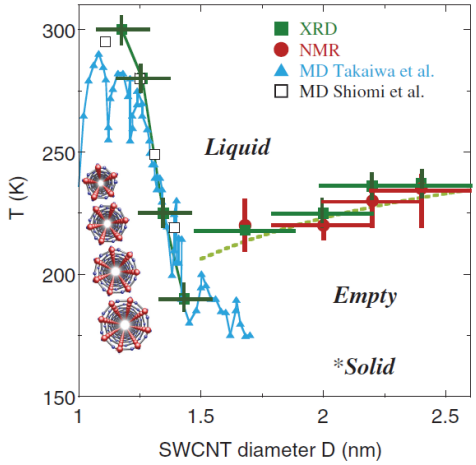

Fig. 2.5. Global temperature–diameter (T–D) phase diagram of water inside SWNT (Kyakuno, Matsuda et al. 2010).

2.5 Radial and axial water density distribution

Probing of water density distribution is probably a promising way to understand the confinement effect because it can give intuition about a possible water layer existing in CNT. Pozhar (Pozhar 2000) pointed out that the dynamics of liquid flows such as a radial density distribution is not influenced by fluid but only by intermolecular potentials such as van der Waals interaction potential through investigation of simple Lennard-Jones fluids. Hanasaki and Nakatami (Hanasaki and Nakatani 2006) carried out an MD simulation on radial

density distribution of water confined under SWNTs of different sizes from (6,6) to (20,20) to confirm that water configuration depends primarily on the tube diameter. **Fig. 2.6** shows relative local radial density profiles (local density/bulk density) of water with respect to various diameters of CNTs (Alexiadis and Kassinos 2008). In a very narrow tube like (6,6) SWNT, only one water peak could be observed because there is no more space between a single-file water wire and the graphitic wall except a depletion region. As CNT diameter increases, it is sensible to expect the second peak and a maximum water peak sifted toward the carbon wall, which means that the center line is less favored energetically. The number of water layers, n, with a given tube radius also depends on both σ_{OO} and σ_{CO}, and can be calculated by the following equation (Wang, Zhu et al. 2004).

$$n = 1 + \frac{r - \sigma_{CO}}{\sigma_{OO}}, \tag{2.9}$$

Wang *et al*. (Wang, Zhu et al. 2004) presented that the water in CNT tends gradually to behave as bulk water when the molecules are placed beyond three or four water layers away from the wall because the confinement effect on density weakens so that the radial density distribution may converge to that of water on a graphite slab. While the radial density distribution represents water layering across the diameter of CNT, it is the axial density distribution that explains how much the water molecule is affected by hexagonal cells of carbon. Therefore, if the radial and axial density distributions are obtained, the overall water density in CNTs can be calculated by integrating these two profiles in the nanotube. Thomas and McGaughey (Thomas and McGaughey 2008) investigated the confinement effects on the radial density profile inside and outside tubes for SWNT diameters of 1.1, 2.8, 6.9, and 10.4 nm to suggest a criterion for the CNT radius to distinguish confined water from unconfined water. For example, both inside and outside the 10.4 nm-CNT, the water density distribution looks exactly the same as that on a flat graphene sheet. The unconfined water density outside the CNT showed the first local maximum at $r = R_c$+0.3 nm, the local minimum at $r = R_c$+0.5 nm, and the second local maximum at $r = R_c$+0.7 nm, where R_c is the radius measured between the centerline and the center of carbon atoms of CNT. As the CNT diameter decreases, however, the density profiles took different shapes between inside and outside of CNT because surface curvature of narrow tubes could effectively reduce the water density by pulling water molecules away from the surface. As a result, the maximum density was located at $r = R_c$−0.3 nm and $r = R_c$−1.3 nm for tubes with diameters of 1.1 and 2.8 nm, respectively. Zhou *et al*. (Zhou and Lu 2007) investigated the axial density distributions for (6,6), (8,8) and (9,9) SWNTs, which looks like periodic corrugation along the axis regardless of the radius. The distance between two water peaks was about 2.5 Å, almost same as the distance between two carbon atoms of a hexagonal cell. Alexiadis and Kassinos (Alexiadis and Kassinos 2008) studied the water density profiles using several water models and flexible/rigid nanotubes to suggest that the water molecules should exist in the form of a "single-file" or "layered" structure inside CNT with diameter below 24.8 Å. They also examined how water density distribution can vary with respect to the tube diameter. If the nanotube diameter decreases from (8, 2) to (6, 6), the density increases since the volume of the nanotube decreases although the number of molecules per nanotube length does not change. On the other hand, as the tube diameter increased from about 1 nm to 24.8 nm, the water density decreased because CNT could allow more than one water layers. As a consequence, water molecules located at the centerline of CNT can behave as bulk water if

the diameter further increases. The following correlation was derived from **Fig. 2.6**, which can be used to approximate the water density in nanotubes with different diameters.

$$\begin{aligned}
&\frac{\rho}{\rho_0} = 1 - \frac{\rho_1^*}{(d/d_1^* + 1)^2}, \text{ with } d_1^* = 20.6\,\text{Å}, \\
&\qquad \rho_1^* = 1.4\,\text{g/cm}^3 \text{ for } d < 24.8\,\text{Å} \\
&\frac{\rho}{\rho_0} = 1 - \frac{\rho_2^*}{(d/d_2^* + 1)^2}, \text{ with } d_2^* = 55.0\,\text{Å}, \\
&\qquad \rho_2^* = 0.6\,\text{g/cm}^3 \text{ for } d \geq 24.8\,\text{Å}
\end{aligned} \tag{2.10}$$

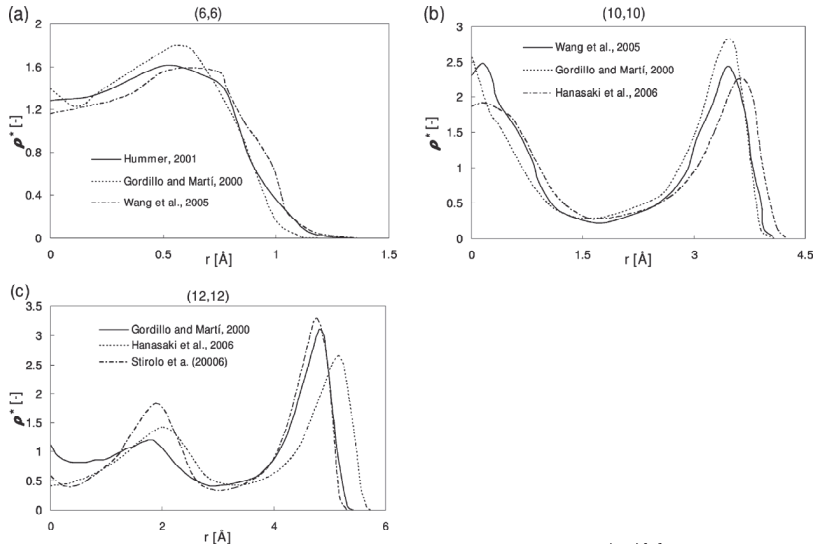

Fig. 2.6. Dimensionless local water density (ρ^*) $\rho/\langle\rho\rangle$, where ρ is the actual and ⟨ρ⟩ the total density) inside different nanotubes (Alexiadis and Kassinos 2008): (a) (6,6), (b) (8,8), (c) (10,10). Note that, in (a, b, c) the abscissas represent the distance from the centerline of CNT. The tube is open to a water reservoir as in Hummer *et al*. (Hummer, Rasaiah et al. 2001) and Hanasaki and Nakatami (Hanasaki and Nakatani 2006), and closed in all the other cases.

2.6 Water infiltration and fast transport in CNT

Many researchers have raised a question whether it is possible that the hydrophilic liquids, especially water, can fill in such a narrow hydrophobic channel of CNT and whether there exists a minimum diameter of a CNT to allow spontaneous filling. Aluru and his group (Aluru, Won et al. 2006) carried out MD simulations to point out that the van der Waals interactions between water molecules and carbon atoms are primarily responsible for water filling. Through this process, they could put a limiting size of CNT for water infiltration. For example, water cannot go into a (5,5) SWNT with diameter of 6.9 Å. In addition, Wang *et al*. (Wang, Zhu et al. 2004) suggested a minimum diameter that allows to form a certain number of water layers (n) is approximately $2(\sigma_{CO} + (n-1)\sigma_{OO})$ by employing different sets of

C-O interaction potentials in their simulation. Washburn (Washburn 1921) provided an explanation of the capillary filling and liquid meniscus dynamics by use of Hagen-Poiseuille equation and Young-Laplace equation. The imbibing length L at time t of a capillary of radius R is given by:

$$L^2 = (R\gamma / 2\mu)t, \tag{2.11}$$

where γ is a liquid/vapor surface tension and μ is the viscosity of liquid. The Washburn equation (Equation (2.11)) is very useful in describing the marching front of a viscous liquid in capillary tubes as time goes by, while less powerful in explaining the marching motion for non-slip boundary or very short period of time. Indeed, filling narrow CNTs like (6,6) with water molecules is not an ordinary phenomenon because water molecules would have no reason to fill in such a narrow hydrophobic channel of CNT at the first glance. However, both MD simulation and experiments support that water can gain access to narrow nanotubes even though a water molecule may have to lose around two hydrogen bonds, corresponding to ca. 10 kcal/mol. One way of explaining this counterintuitive phenomenon is to compare binding energy distributions of hydrogen bonds among water molecules at bulk and under the CNT nanoconfinement. According to MD simulation (Hummer, Rasaiah et al. 2001), the probability distribution of the hydrogen bonding energy between water molecules becomes narrower under the nanoconfinement than in bulk state as shown in **Fig. 2.7**.

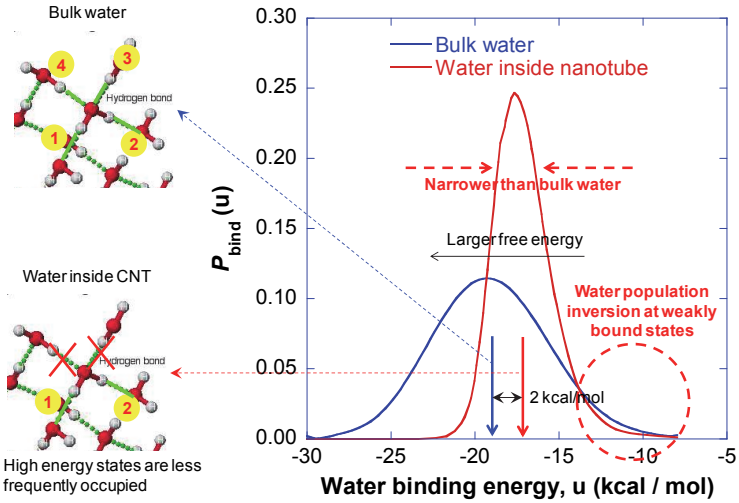

Fig. 2.7. Probability distribution over water binding energy for bulk water (blue) and water inside CNT (red). Two vertical arrows indicate average binding energies. Dotted circle emphasizes the population inversion region, in which weakly bound states are more populated in bulk water. Reconstructed from Hummer *et al.* (Hummer, Rasaiah et al. 2001).

For water in CNT, this change can shift the mean binding energy value toward a higher one, energetically unfavorable. Even energetic compensation given by van der Waals attraction between water and CNT (ca. 4 kcal/mol) is not found sufficient to cover the 10-kcal/mol

enthalpic loss. The degeneration in water binding energy distribution, however, can result in a lower population in the high energy region, which can effectively lower down a local excess chemical potential, enthalpo-entropic gain. This finding implies that water molecules can overcome enthalpic penalty and obtain enthalpo-entropic gain to be thermodynamically stable under the CNT nanoconfinement as predicted by Hummer *et al.* (Hummer, Rasaiah et al. 2001). Subsequently, they pointed out that the water occupancy in CNTs (hydration) is dominated not by how strongly bound the hydrogen bonds are on average but rather by how weakly these bound states are populated. Also, by tuning the water-to-carbon interaction potential, they demonstrated that it is possible to create a transition state in which CNT may be either filled or empty. This intermittent permeation can be described as bi-stability. Zhao et al. (Zhao, Liu et al. 2009) explored a critical pressure barrier associated with infiltration of SWNT employing nonequilibrium molecular dynamics for various temperatures, diameters, and surrounding pressures, assuming that the hydrogen bond is associated with the surface tension of the confined water. Reduced critical pressure barrier makes it easier for water molecules to fill in the tube, which indicates that a small pressure barrier could enlarge the accessible entry area of the nanotube, thereby weakening the hydrogen bond interaction. Their results showed that the magnitude of the critical pressure barrier could become smaller as the temperature increases, the diameter decreases, and loading rate gets higher. Waghe *et al.* (Waghe, Rasaiah et al. 2002) who carried out the first study on the filling and emptying kinetics of water inside SWNT, calculated the free energy of water molecules transporting inside a 27 Å long (6,6) CNT. They took into account that filling thermodynamics and kinetics depend on sensitivity of the attractive interactions between the nanotube and water molecules which increases with the length of the tubes, and the Gibbs free energy increases until the nanotube is filled completely. After then, additional entry of water molecule makes another hydrogen-bond chain with the initial orientation. If one water molecule would go into CNT, the movement of an additional molecule costs less Gibbs free energy. Finally, this behavior makes water molecules filled completely in CNT and reach the Gibbs free energy minimum. However, filling motion cannot be happened simultaneously from both ends because of the dipolar orientation incompatibility. The water chain can be broken up especially at the end of tube where the direction of the hydrogen bond points outward, which can explain water behaves burst-like motion. The water filling mechanism can be summarized using the Gibbs free energy.

$$G_N = -\ln p(N) / k_B T, \tag{2.12}$$

where G_N is the Gibbs free energy of N water molecules occupying a nanotube. G_N is associated with the probability function p (N) that N molecules can be found inside CNT.
First, water filling occurs at the end of a nanotube, with hydrogen entering first and dipoles orientation pointing inward CNT

$$G_0 = 0\,,\ G_1 = \Delta G_0, \tag{2.13}$$

Second, successive entry of water molecules grows the hydrogen-bonded chain with the initial orientation and the chain progresses with all dipoles pointing inward. The Gibbs free energy of introducing one additional molecule to the chain, ΔG, linearly depends on an attraction potential control parameter (λ) to be taken account into below

$$G_N = \Delta G_0(\lambda) + (N-1)\Delta G(\lambda),\ \Delta G \propto -\lambda, \tag{2.14}$$

Finally, the last water molecule going into CNT may enter from either side of the tube. If M is defined as the maximum available number of molecules in a single-file chain,

$$G_M = G_{M-1} + \Delta G_1(\lambda), \tag{2.15}$$

In the meantime, if water indeed enters CNTs spontaneously, what can affect the water transport according to confinements? There still exist different assertions on why carbon nanotubes are fast transporter of water because simulation results are very sensitive to the choice of water models and potential properties and few experimental studies are provided to verify only the fact that the water indeed flows with much larger flow rate than expectations in macro- or micro- scale. However, it is no doubt that the reasons should be classified into water structure that minimizes the energy to move or hydrophobicity that indicates smoothness of the channels. Up to now, it is commonly explained that the fast water transport in CNTs is caused by the hydrophobicity to make a depletion region at the interface occurred. In recent work, Thomas and McGaughey (Thomas and McGaughey 2008) reassessed the fast water transport in CNT by deriving an equation of flow enhancement in CNT from a continuum based, pressure-driven flow model that incorporates the variation of water viscosity and slip length with respect to the CNT diameter.

$$\varepsilon = \left[1 + 8\frac{L_s(d)}{d}\right]\frac{\mu_{bulk}}{\mu(d)}, \tag{2.16}$$

$$\mu = \mu_i \frac{A_{\text{interface}}}{A_{\text{total cross section}}} + \mu_{\text{bulk}}\left(1 - \frac{A_{\text{interface}}}{A_{\text{total cross section}}}\right)[mPa.s], \tag{2.17}$$

$$L_s = 30 + \frac{352}{d^3}[nm], \tag{2.18}$$

Equation (2.16) shows good agreement with MD simulations, also valid in CNTs with larger diameters than 1.66 nm. The enhancement factor obtained by Holt, Park *et al.* (Holt 2006) is in proximity to the range this equation can predict. Kalra *et al.* (Kalra 2003) proposed the single-file water transport in CNTs can be modeled with a one-dimensional random walk theory. From their work, water transport in CNTs should be fast due to nearly frictionless surface and microscopic fluctuations. One-dimensional random walk model is limited to a single-file conduction of water. Joseph and Aluru (Joseph and Aluru 2008) investigated hydrogen bonding configuration of water under different degrees of CNT nanoconfinement via comparison of effects of diverse interatomic potentials by holding nanochannel geometry of 1.6-nm-wide CNT. In this study, they compared four distinct nanoconfinements of water: (1) hydrophobicity and atomic-level smoothness (CNT); (2) hydrophobic and non-atomic-level smoothness (BNNT); (3) hydrophilic and atomic-level smoothness (CNT with interatomic potential of Si); (4) hydrophobic and nanoscale roughness (CNT with a several angstrom of step). For the CNT nanoconfinement that is hydrophobic and smooth on the atomic level, water transport showed an enhancement by 3 orders of magnitude compared with Hagen-Poiseuille formalism. The hydrophobic but less smooth nanoconfinement of BNNT also enhanced the flow, but the enhancement was slightly smaller. The hydrophilic and atomic-level smooth nanoconfinement, however, lost a significant amount of flow enhancement. Lastly, the nanoscale roughness provided by connecting two CNTs having

different diameters negated the flow enhancement effect almost completely. They described that the fast water transport depends primarily on the water configuration caused by the hydrogen bonding nature because the enhancement factor even in a silicon nanotube that has larger friction is still larger than predictions calculated by slip length theory as a number of hydrogen bonds decrease. They also identified a hydrogen-bonding depletion layer near the hydrophobic wall, which is in part responsible for the ultrafast water transport.

Hummer *et al.* (Hummer, Rasaiah et al. 2001) have presented a single-file water wire that showed the burst-like motion along the nanotube axis because, in their equilibrium MD simulation, rapid conduction of water was driven by thermal fluctuation of water molecules at either open end of CNT. Beckstein and Sansom (Beckstein 2003) have also pointed out that it is not a single-file chain but one-dimensional nanoconfinement that increases the self-diffusivity of water, thereby supporting bursting motion of water molecules along the tube although water molecules retain the three-dimensional molecular thermal velocity distribution under this confinement. Up to now, there have been several efforts to suggest reasonable equations for comparing and understanding the fast water transport in CNT. Thomas and McGaughey (Thomas and McGaughey 2008) suggested the pressure-driven water transport equation (Equation (2.16)) based on the slip length theory for CNT diameters between 1.7 and 5.0 nm, assuming that the large flow velocity though CNT is mainly caused by the nearly frictionless surface. Their flow enhancement calculation partially overlapped the range of enhancement given by Holt, Park *et al.* (Holt 2006), and yet did not agree well with Majumder *et al.* (MajumderMainak, ChopraNitin et al. 2005). This assessment led Thomas and McGaughey to an argument that the flow enhancement measurements should have been smaller, although their model equation has parameters that has not been determined either by experiment or by exact theory, but has rather been determined from their own simulation result. Therefore, the validity of their argument awaits further experimental and theoretical verification. Recently, Falk *et al.* (Falk, Sedlmeier et al. 2010) reported a strong curvature dependence of the friction of water inside CNT. According to their MD simulation analysis, the friction decreased when water is placed inside narrower CNTs, leading to super lubricity for sub-1-nm CNT and single-file water wiring. When water is placed outside CNT, the friction increased as the curvature gets larger. In a reference case of water on a flat graphene surface, they did not predict any change in friction. The predicted flow enhancement is on the order 10^3-10^4 for CNTs with diameters in the range of 1-2 nm and 10^1 for diameters of the order of 50 nm. Actually, water molecules in CNT is so tightly confined and stratified in the radial direction that they may experience less thermal fluctuation in the radial direction, thereby allowing thermal fluctuation in the axial direction to have a major effect.

Based on the aforementioned results, here we present a summary of the water filling mechanism in **Fig. 2.8.**

2.7 Summary

Up to now, a large number of studies have been carried out on the phenomena and properties of water confined inside CNT. We focused in this chapter on the simulation results of water infiltration of and transport through CNT, and the experimental works for the verification of theories. It is very interesting that water can enter and flow so rapidly in narrow and hydrophobic CNTs. Since 2001, MD simulations have started providing the first answer about these nanoscale phenomena. Researchers pointed out that the water infiltration of narrow CNTs is related to the degeneration of hydrogen bonding energy

distribution that lowers chemical potential in effect. When water is placed in the CNTs, hydrophobic interaction takes an action to create a depletion region between water and the graphitic wall of CNT, thereby smoothening a potential landscape that water experiences during the transport. Hence, we need to note how the water can enter and fill inside CNTs with thermodynamic equilibrium state. According to several simulation results, one may make a summary of water infiltration, water structure and fast water transport.

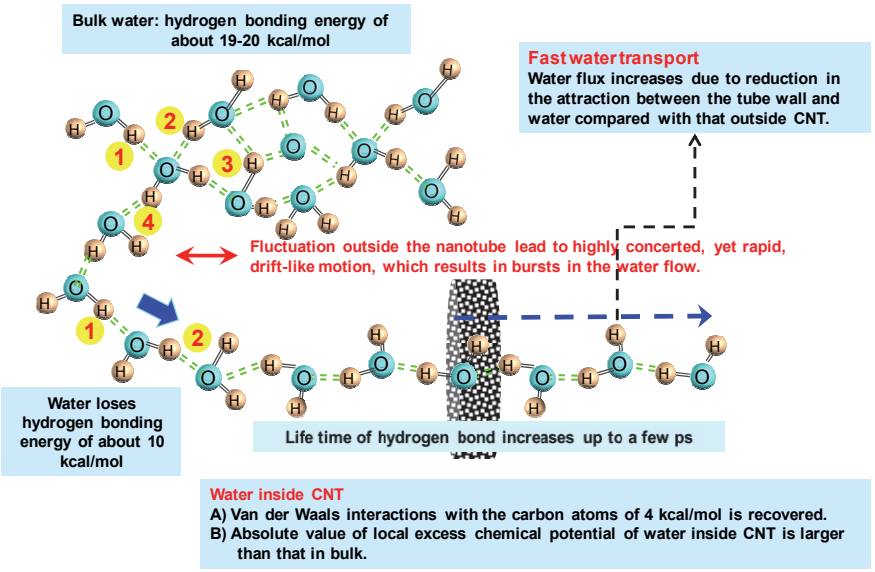

Fig. 2.8. Schematic explaining briefly how water can fill in CNT and water transports fast along CNT.

1. As the CNT diameter increases up to a certain minimum value for hydration, water molecules fill the narrow space rather homogeneously, yet not hydrogen-bonded, as expected for vapor.
2. While the configuration becomes a single-file chain in CNTs with diameter of sub 1 nm, hydrogen bonds form distinct layers as well as a single-file chain in wider carbon nanotubes. In addition, the number of water layers inside CNTs increases from one to two and from two to three sequentially, with the central water column being the preferred position.
3. As the CNT diameter further increases, the maximum radial density shifts slightly from the center toward the wall, and thus the center line is not favored energetically. Moreover, the curvature effect on density weakens so that the radial density distribution seems almost identical to the situation near a planar hydrophobic slab such as grapheme layer, with most of the density near the center line being close to that of bulk water.
4. Once water molecules fill in CNT, the flow velocity profile is far from parabolic derived from the momentum transport mechanism in the continuum based fluid mechanics theory, rather it is more plug-like than parabolic because hydrophobicity weakens the friction and confines its effects to the outermost layer.

Carbon Nanotube Nanofluidics of water still raises unanswered fundamental questions in comparison with conventional theories even though there are a number of literatures that predict water configuration and flow in CNTs. How can one observe the relationship between the hydrogen bonding (or water configuration) and fluidic properties such as viscosity, density and phase change? Would it be possible to explain the infiltration and transport phenomena in view of an enthalpo-entropic picture?, Can one suggest a new dimensionless number that can well characterize the water transport inside CNT? How can one predict the dependence of CNT hydration on other inherent CNT properties such as nanotube charge and length? Finally, can one make some sorts of validation mapping of simulation results by implementing more experiments in near future before we apply *Carbon Nanotube Nanofluidics* to any useful engineering technologies?

Taking a look deeper, it would be an interesting and promising work to offer new viewpoints tangential to conventional theory, from which new applications with high efficiency and portability could be developed. Accordingly, if answers about the above questions are found and validated by experiments in the foreseeable future, we may also make one step closer to the description of biological translocation processes such as a biomolecular (DNA, RNA) transport through biological pores that share their dimensions with CNT.

3. Gas transport

3.1 Introduction and overview

The use of CNT as a membrane pore wall material for gas transport gives an additional and possibly the most significant advantage because the bottom-up process of CNT array synthesis can provide molecularly smooth wall for the gas flows, notwithstanding the fact that the nanochannel size becomes commensurable with the size of the fluid molecules flowing through it. Thus, one may raise a question about the way in which properties of gas inside CNT are affected by diameters, lengths, and tube shapes. Perhaps one may be more concerned about pumping power required for transporting a certain amount of gases (Wang, Gupta et al. 2005). Many fundamental studies in the past several years revealed that the infiltration and emptying mechanisms of water, gases, and ionic liquids possess distinct characteristics from those of bulk phase. Among these discrepancies, gases inside CNT of only a few molecular diameters are well known to diffuse rapidly due to the unique CNT properties such as molecular smoothness and nanoconfinement effect (Skoulidas, Ackerman et al. 2002). Gas molecules can pass nanotube pores by orders of magnitude faster than they pass pores out of other materials of comparable sizes. When gases are confined inside CNT, their properties are quite different from those seen for the bulk fluid. This phenomena is often characterized by the Knudsen number defined as the ratio between the gas mean free path and the characteristic length given by the confinement (Cannon and Hess 2009). Simply speaking, the former length scale represents intermolecular collision-based, momentum and energy exchanges, whereas the latter does momentum and energy exchanges between transporting gas molecules and the substance comprising the confining wall. Indeed, it is very important to understand the diffusive behaviors of gas molecules in CNT because of possible applications such as drug delivery and selective transport (single- or mixed gas separation). Skoulidas *et al*. (Skoulidas, Ackerman et al. 2002), for the first time, reported that diffusion of light gases through SWNT can excel diffusion through zeolites by orders of magnitude, implying energy efficiency in using CNT as a gas separation medium. Current

studies of gas transport inside CNT are focusing on large liquid-solid interfaces for a flow boundary condition analysis (Steitz, Gutberlet et al. 2003) and surface force measurements (Meyer 2005), as evidenced by grazing incidence X-ray scattering by Daillant (Daillant 2009). Nevertheless, both theoretical and experimental studies on the kinetics of gas-liquid-solid interactions with respect to confinement are still missing. One of the primary objectives of this chapter is to explore gas transport under the nanoconfinement. In general, different transport types or flow regimes can be categorized via Knudsen number as shown in **Fig. 3.1**. In terms of CNT diameter, a Knudsen number larger than 10 from which gas transport in CNT enters a free molecular flow regime can be obtained CNT interior diameters below 6.5 nm. However, one may raise a question whether gas in CNT with diameter of 6.5 nm has characteristics of transition flow or those of free molecular flow since the classification of flow regimes is not too strict. Therefore, it would be necessary to carry out case studies with respect to CNT diameter.

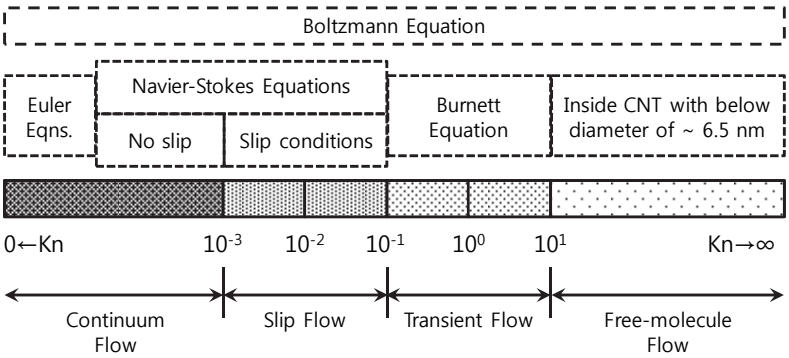

Fig. 3.1. Flow regimes categorized by Knudsen numbers (Roy, Cooper et al. 2005). It should be noted that the classification is not strict and the categorizing Knudsen number between flow regimes may vary, depending on the flow situation.

Meanwhile, Holt, Park *et al.* (Holt 2006) reported molecular weight selectivity referenced to helium flows, with measuring five hydrocarbon and eight non-hydrocarbon gas flows through the pores of sub-2-nm DWNT, or Knudsen number of ca. 30. They measured gas flow rates of 16 – 120 times larger than a Knudsen diffusion prediction that models free molecular gas transports. Generally, it is collisions between gas molecule and tube wall that may significantly alter the way of describing the micro-nanoscale flows. Two types of collisions are generally classified. One is called a "diffuse collision," or "Knudsen diffusive collision" or "ballistic diffusive collision," wherein a colliding gas molecule thermalizes itself with a wall and randomizes its bouncing velocity whenever it collides with the wall. The source of the velocity randomization may include wall roughness on atomic to mean free path levels and chemical inhomogeneity (Malek and Coppens 2003). The other is a "specular collision," in which a reflecting gas molecule will conserve its incident tangential velocity (momentum) component along a colliding surface. Specular reflection on the wall is sometimes referred to as slippery collision. Generally, rarefied gas collisions may have both diffusive and specular components. One way of incorporating the component of specular collision in transport theories is to introduce as a correction factor a parameter called tangential momentum accommodation coefficient (TMAC or σ_v) as a measure of a portion of

molecules that undergo diffuse reflections. A detailed interpretation of TMAC is well reviewed by Sokhan *et al.* (Sokhan, Nicholson et al. 2004). Considering the influence of slippery collisions between gas molecules and the pore wall, the Knudsen-Smoluchowski correction model was introduced to experiments for argon and oxygen flows through 10-nm polycarbonate nanopores by Roy *et al.* (Roy, Cooper et al. 2005). According to the model, the effective transport diffusivity is given by $D = D_{Kn}(2-\sigma_v) / \sigma_v$, where D_{Kn} and σ_v represent the original Knudsen diffusivity assuming a 100% diffuse collision and tangential momentum accommodation coefficient, respectively. For 10 nm polycarbonate membranes, their experiment resulted in TMAC to be 0.28. In a slip flow or an early transition regime (Kn ≈ 0.4), Arkilic *et al.* (ARKILIC, BREUER et al. 2001) reported a value of 0.8 for a nitrogen gas on a prime silicon wafer surface. The Knudsen-Smoluchowski diffusion model is a correction model of the Knudsen diffusion model, and in an isothermal free molecular flow regime, the Smoluchowski-corrected flow rate is obtained by multiplying $(2-\sigma_v) / \sigma_v$ to the original Knudsen flow formula. More detailed explanation of TMAC will follow in next section. Finally, experimentally measured gas flow through the nanopores can be compared with theoretical predictions useful in the nanometer size regime, e.g. Knudsen diffusion model, the unified flow models, or MD simulations. In this section, we introduce three flow models that describe the behavior of gas species under nanoconfinement, and discuss possibilities and perspectives of the CNT gas transport paths as a passive gas separator.

3.2 Investigation of transport theories

3.2.1 Consideration of two length scales

If air molecules distribute themselves evenly in a three-dimensional box, an estimate of their intermolecular spacing can be $n^{-1/3}$, where n is a molecular number density at the corresponding thermodynamic conditions. Treating air as an ideal gas, $n = P / k_B T$, where P, T and k_B are pressure, temperature and Boltzmann constant, respectively, results in average intermolecular spacing of about 3.4 nm at room temperature and 1 atm. This spacing is about 10 times larger than molecular sizes of nitrogen and oxygen. In such a dilute medium, most of the momentum and energy transfers occur via intermolecular collisions. In random collisions, the most probable situation is the collision between two molecules possessing distinct thermal velocities. It is not the average gas spacing, but the mean free path that will determine the momentum and energy transfers in gas phase collisions. Estimation of the mean free path at 1 atm and 300 K gives a mean free path of 70 nm for air, which is about 20 times larger than the average molecular spacing and more than 200 times larger than the size of a molecule. If a carbon nanotube of 2 nm in diameter is placed in the box, air molecules will primarily collide on the external surface. Sometimes a portion of molecules will get into the open ends. Some of the incident molecules will bounce back at the mouth and some will go through and emerge from the other open end. Since the nanotube diameter is much smaller than the air mean free path, molecules inside the nanotube will collide exclusively with the wall, instead of exchanging momentum and energy through intermolecular collisions.

Since collisions induce momentum exchange, the nature of the collisions is important in describing mass transport or flow through a nanoscale channel. Two length scales become important: the mean free path and the channel size. If the mean free path is much smaller than the transverse channel size, momentum transfer will take place most likely through intermolecular collisions and gas kinetic theory may determine the fluid property. This

type of flow is called macroscale flow. If, on the other hand, the mean free path becomes much larger than the lateral channel size, most of the transport will occur through molecule-to-wall collisions, in which case the dynamics of the transport will be undoubtedly different. Therefore, a comparison between those two length scales enables determination of transport types. Knudsen number (Kn), defined as a ratio of the mean free path to the channel characteristic length is an important parameter considered in this comparison.

3.2.2 Knudsen diffusion model

The Knudsen diffusion model is widely used to describe mass transport in the free molecular flow regime. The regime where the diffusion process is dominated by fluid-interface collisions (large Knudsen number) is called the "Knudsen regime" or "rarefied gas state." Knudsen (Steckelmacher 1986) developed a free molecular flow model based on kinetic theory and his experiment of long tubes in vacuum. He proposed a formula which can be used in all flow regimes by combining the Poiseuille flow equation for viscous flow, his model for the free molecular flow and an interpolating function determined by a fit to his experimental data for transition flow, which is called "Knudsen flow model" because the difference between molecular flow and diffusion is not definite at the microscopic level in the free molecular regime. There are two types of diffusion coefficients that are related to mass transfer within the pore: Maxwellian and Knudsen. Knudsen diffusion occurs when the molecules in the fluid collide with the pore walls, while Maxwellian diffusion is also known as bulk diffusion caused by intermolecular collisions. Knudsen diffusion is prominent when the mean free path of the molecules is much larger than the diameter of the pore. The formula in the free molecular gas flow regime is as follows.

$$J = D_{\mathrm{Kn}} \frac{\Delta P}{RTL},\ D_{\mathrm{Kn}} = \frac{d}{3}\sqrt{\frac{8RT}{\pi M}}, \tag{3.1}$$

where J, D_{Kn}, P, R, T, L, d and M represent a molar flux, Knudsen diffusivity, pressure, universal gas constant, temperature, channel length and diameter, and molecular weight, respectively. The original Knudsen diffusion model, thus Knudsen diffusivity, hypothesizes diffuse reflection as a boundary condition between molecules and channel (pore) wall. The other type is specular collisions, where a reflecting gas molecule will conserve its incident tangential velocity component along a colliding surface, a concept of slippery collision. The rarefied or nanoscale gas collisions may generally have both diffuse and specular components. For instance, The Knudsen number of 0.17 for a nanotube with a diameter of O(1 nm) means that the mean free path in the nanotube is less than 0.5 nm. Since the mean free path is inversely proportional to the molecular number density or the gas pressure in the nanotube, this small value of the mean free path may mean that the local average number density can be over two orders of magnitude larger than in the STP condition; the mean free path in the STP state gives ~ 65 nm for air. In terms of pressure, Kn of 0.17 for air in sub-2-nm diameter nanotube may be established at about 200 atm at room temperature. **Fig. 3.2** shows the dense molecular packing inside the carbon nanotube Sokhan *et al.* (Sokhan, Nicholson et al. 2002) have simulated. As stated above, one way of incorporating the component of specular collision in transport theories is to introduce a parameter called tangential momentum accommodation coefficient (TMAC, σ_v) as a measure of a portion of molecules that undergo diffuse reflections.

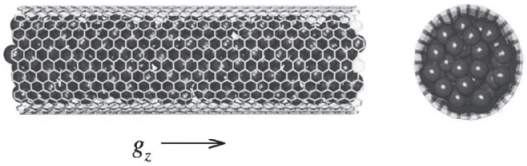

Fig. 3.2. Sketch of the system for MD simulations to investigate gas transport in CNT. An external force is applied along the long axis of CNT. Owing to issues with computational cost, most of today's molecular dynamics simulations of gas transport under CNT nanoconfinement investigate densely packed gas molecules at high pressures (Sokhan, Nicholson et al. 2002).

As the dimensions of the pore diminish, the mean free path (λ) becomes larger than the channel dimensions (d) and the transport enters the molecular flow regime. In such situations, where particle-surface collisions dominate over particle-particle collisions, the Knudsen diffusion model is frequently applied. The Knudsen-Smoluchowski diffusion model is a correction model of the Knudsen diffusion model, and in an isothermal free molecular flow regime, the Smoluchowski-corrected flow rate is obtained by multiplying $(2 - \sigma_v) / \sigma_v$ to the original Knudsen formula. The multiplication factor may contribute to the enhancement factor measurement (Porodnov, Suetin et al. 1974). Maxwell coefficients or TMACs can be estimated from the enhancement factor in by the following relation, where Q and V_m stand for volumetric flow rate and molar volume of a gas species, respectively.

$$\sigma_v = \frac{2}{1+\frac{Q_{\text{experiment}}}{Q_{\text{Kn}}}} = \frac{2}{1+\frac{Q_{\text{experiment}}}{\frac{2}{3}\sqrt{\frac{8\pi}{MRT}}\left(\frac{d}{2}\right)^3 V_m \frac{\Delta P}{L}}}, \tag{3.2}$$

The Knudsen diffusion mechanism states that each particle-to-wall collision accompanies complete thermalization in a way that the angle of reflection randomizes fully with respect to the angle of incidence. In that sense, the Knudsen transport mechanism doesn't seem to be somewhat feasible in CNTs as demonstrated by Holt, Park *et al.* (Holt 2006) because of specular collision that gas molecules are believed to undergo on the molecularly smooth wall of a CNT interior (Maxwell coefficient < 1) (Holt, Noy et al. 2004). The Knudsen diffusion model can still suggest one criterion to compare the flow enhancement of gas molecules through CNT. Roy *et al*. (Roy, Cooper et al. 2005) reported argon and oxygen flows through a 10 nm polycarbonate membrane whose rates are an order of magnitude higher than would be predicted by Knudsen diffusion alone. They ascribed the flow enhancement to the rarefied diffusion with slip (Knudsen-Smoluchowski diffusion) and obtained the TMAC as small as 0.21. Through a finite element method modeling with a first-order slip boundary condition, they claimed that the hydrodynamic model may predict Knudsen-like diffusion for Kn up to 10. However, Karniadakis *et al*. (Karniadakis, Beskok et al. 2005) pointed out that the use of the slip boundary condition to explain the flow enhancement by increasing the total flow rate works well only at the expense of accuracy in the velocity profile. Therefore, the success of the modified hydrodynamic model with appropriate slip boundary condition in high Kn

numbers corresponding to transition and free molecular flows needs further investigation with respect to both the total flow rate and the local velocity profile. With a carbon pore membrane with 170 - 235 nm pores obtained by the chemical vapor deposition of carbon films on the alumina membrane (Miller, Young et al. 2001), Cooper *et al*. (Cooper, Cruden et al. 2003) saw evidence of modification of the pore surface characteristic from diffuse to diffuse-specular one. They observed gas flow enhancement compared to diffuse Knudsen model and determined TMAC to be 0.52. Considering the large pore diameter and the fact that the pore became partially oxidized, it is questionable whether the pore may represent fully graphitic carbon nanotube surfaces. Nitrogen flow through fully graphitic MWNTs was first measured by Hinds *et al*. (Hinds, Chopra et al. 2004). In characterizing their MWNT membranes, they measured nitrogen permeability as 2.6 μmol/m^2-s-Pa, corresponding to 0.59 cc/cm^2-s-atm. The Knudsen number for the nitrogen flow in their experiment was 9.3, a value that places the gas flow regime on the verge of transition and free molecular flows. They reported that the measured permeability for their membrane was as expected by the Knudsen flow model, implying the TMAC close to 1 for this kind of MWNT. This large value of TMAC of MWNT is somehow unseen in most of the engineered surfaces.

It is the pore number estimation that imparts the single largest uncertainty to the precise determination of TMAC for CNT. As pointed out by Skoulidas *et al*. (Skoulidas, Sholl et al. 2006), however, the pore density estimation of the MWNT pores shows a certain degree of uncertainty in the later reports: 6×10^{10} cm^{-2} (Hinds, Chopra et al. 2004), 5×10^{10} cm^{-2} (Majumder, Chopra et al. 2005), and $1.0 - 3.4 \times 10^{9}$ cm^{-2} as in the supplementary information of (MajumderMainak, ChopraNitin et al. 2005). This order-of-magnitude fluctuation in the number of open pores of MWNT obscures concluding whether carbon nanotubes can enhance gas flows through them or not, which means that the uncertainty on the pore density quantification may also cause a difficulty in comparing the gas flux through a MWNT membrane with the Knudsen model prediction. This uncertainty has its root in part to the nature of "bambooing" or self-blocking of a tube during MWNT synthesis. On the other hand, SWNT and DWNT having smaller inner diameters have not been reported about self-blocking so far.

3.2.3 Unified flow model

The Knudsen diffusivities are always lower than experimental results because it is assumed that every collision leads to diffusion itself, therefore it only holds when the TMAC becomes closer to untity. While, the unified gas flow model may successfully predict the flow regime with high Knudsen numbers in association with nanoscale conduits. The unified gas flow model, considering wall slip and rarefaction effects, can predict higher volumetric flow rates than the free molecular flow theory of Knudsen diffusion. Beskok *et al*. (Beskok and Karniadakis 1999) proposed a theoretical model called the unified gas flow model that is useful in both the transitional and free molecular regimes. The model assumes that the velocity profile is a shifted parabola towards the main flow direction. For rarefied flow, they compared their model with a solution obtained from the linearized Boltzmann equations (Loyalka and Hamoodi 1990) in order to verify agreement with the linear Boltzmann solution in the Knudsen number range between 0.1 and 10 and to determine the general slip coefficient of their model, b, to be -1. In the unified gas flow model, the flow velocity profile is given as follows.

$$U^*(r,\mathrm{Kn}) = \frac{U(z,r)}{\bar{U}(z)} = \frac{-\left(\frac{r}{d/2}\right)^2 + 2\frac{\mathrm{Kn}}{1+\mathrm{Kn}} + 1}{\frac{1}{2} + 2\frac{\mathrm{Kn}}{1+\mathrm{Kn}}}, \tag{3.3}$$

where r and z are the radial and axial coordinates, respectively. In the limit of macroscale continuum flow (Kn→0), the model converges to a Poiseuille flow profile, or $U^* = 2\left[1-(r/(d/2))\right]^2$. The shape of the profile is a parabola shifted in the axial direction by 2Kn / (1+Kn), with a shrinkage of the maximum velocity in order to meet the mass continuity requirement. In Equation (3.3), Kn is a local Knudsen number. Meanwhile, the volumetric flow in a pipe can also be obtained by integrating the velocity equation derived from Navier-Stokes equation with Maxwell's slip boundary condition over the tube cross section.

$$Q = -\frac{\pi(d/2)^4}{8\mu_o}\frac{dP}{dx}(1+\alpha\mathrm{Kn})\left[1+\frac{4\mathrm{Kn}}{1+\mathrm{Kn}}\right], \tag{3.4}$$

In Equation (3.4), μ_o is a bulk dynamic viscosity and α is the only model parameter accounting for the rarefaction or confinement effect.

$$\alpha = \alpha_o\frac{2}{\pi}\tan^{-1}(\alpha_1\mathrm{Kn}^{\beta}),\ \alpha_o = \left.\frac{64}{3\pi\left(1-\frac{b}{4}\right)}\right|_{b=-1} = 1.358, \tag{3.5}$$

where α_1 and β are 4.0 and 0.4, respectively. In Equations (3.4) and (3.5), Kn is a global Knudsen number and usually determined at the average pressure between upstream and downstream. The rarefaction coefficient (1+aKn) in Equation (3.4) accounts for a hybrid length scale combining the tube diameter and the mean free path, giving variation to the dynamic viscosity. The concept of the variable diffusion coefficient model (Beskok, Karniadakis et al. 1996) is shown below.

$$\mu \approx \rho\bar{v}_{th}\left[\frac{1}{\frac{1}{d}+\frac{1}{\lambda}}\right] = \rho\bar{v}_{th}\lambda\left[\frac{1}{1+\mathrm{Kn}}\right], \tag{3.6}$$

The length scale used in determining the dynamic viscosity in kinetic theory is the mean free path. As Kn increases and the flow enters the transition regime, both the channel dimension and the mean free path become comparable. According to Equation (3.6), the fluid viscosity is determined by the combination of these two lengths. In the molecular viewpoint, as Kn increases the entity a gas molecule collides with will change from other molecules to either the wall surface or other molecules. Thus, the modified viscosity, called the generalized diffusion coefficient, is expressed as follows.

$$\mu(\mathrm{Kn}) = \mu_o\left[\frac{1}{1+\mathrm{Kn}}\right], \tag{3.7}$$

Equations (3.6) and (3.7) were proposed by intuition (Beskok, Karniadakis et al. 1996; Beskok and Karniadakis 1999). Further study revealed that the rarefaction coefficient further generalizes the variable diffusion coefficient by dividing the bulk dynamic viscosity by (1+aKn) instead of (1+Kn). Park (Park 2007) reported that the air flow rates through all three DWNT membranes are higher than the unified model prediction by an order of magnitude, while the flow rates through MWNT and PC membranes are within the order of magnitude of the unified flow model prediction. However, they also had a question whether the unified gas flow model applies in the MWNT case or not due to the uncertainty in the open pore density of MWNT membranes, although relatively higher gas flux than predictions was measured.

3.2.4 Molecular dynamics simulations

Molecular dynamics (MD) simulations have also found that the gas molecular flux may be more than three orders of magnitude faster in carbon nanotubes than in zeolites. According to their MD simulations, transport diffusivities of light gases such as hydrogen and methane are much higher through SWNTs than in zeolites. The diffusivity reached almost the same level as that of the bulk diffusivity of a gas ($O(10^{-1}$ cm^2/s)) although the transport diffusivity of gases through zeolites are on the order of 10^{-9} - 10^{-10} cm^2/s. Depending on the nanotube diameter, the diffusivity was as large as 10 cm^2/s for hydrogen. Skoulidas *et al.* asserted that the large transport diffusivities is caused by intrinsic smoothness of the rolled graphene wall, instead of the details of the molecule-nanotube interaction potentials, thereby the chirality of nanotube doesn't influence on the diffusivity (Skoulidas, Ackerman et al. 2002). In the later analysis (Skoulidas, Sholl et al. 2006), they presented a detailed picture on the behavior of gas molecules inside a SWNT by displaying a density profile and molecular trajectories as shown in **Fig. 3.3**. At atmospheric pressure, most gas molecules adsorb on the tube wall and make a tubular structure, or a gas nanotube. Unlike water molecules, the gases do not have strong hydrogen bonds among one another, and thus the gas nanotube does not move collectively. Perhaps the right picture is that the gas molecules diffuse downstream, or in the direction toward a lower potential, following the surface of this gas nanotube. The pressure-dependent adsorption gradient, determined by the gas adsorption isotherm assuming local equilibrium, will drive surface diffusion. At the same time, as shown in **Fig. 3.3(b)**, there exist collisions between the wall and traveling gas molecules in the span-wise direction, in which wall smoothness at a molecular level may augment the contribution of specular reflections to the gas transport. The combination of surface diffusion and Knudsen-Smoluchowski diffusion denoted as a configurational diffusion by Skoulidas *et al*. (Skoulidas, Ackerman et al. 2002) could describe the molecular level gas transport at pressures of the order of 1 bar. Therefore, two different length scales may be considered, one is the surface interaction length scale and the other the tube diameter. The former will describe the trapping of a gas molecule in a gas nanotube near the inner surface of CNT, thereby making this length scale closer to the van der Waals potential well width which is usually between 0.3 and 0.4 nm for gas species and carbon atoms. The latter will explain the motion of a free molecule traveling across the tube diameter and will be related to the Knudsen-Smoluchowski diffusion. As the pressure increases and more gas molecules can enter the CNT, another gas nanotube could form on top of the first layer. It is the long range van der Waals attraction potential that could enable the formation of these gas nanotubes. The more gas nanotubes form, the more they shield the attraction from the wall. At much higher pressure, gas molecules in the middle of CNT would rather flow with a

form of chunk than with additional layers as shown in **Fig. 3.3(A)**. According to Skoulidas *et al*. (Skoulidas, Ackerman et al. 2002; Skoulidas, Sholl et al. 2006), the transport diffusivities are nearly inversely proportional to the CNT diameters. As the radius of a CNT decreases, the gas nanotubes will dominate the configuration of the gas molecules. The layering effect of gas nanotubes seems to play a significant role in gas transport in small-diameter CNTs. They also pointed out that any source on the surface: i.e. a defect that breaks the molecular smoothness of the molecule-CNT potential energy surface may have an adverse influence on the otherwise large transport diffusivity. Sokhan *et al*. (Sokhan, Nicholson et al. 2001; Sokhan, Nicholson et al. 2002; Sokhan, Nicholson et al. 2004), through a series of MD simulations, have agreed to Skoulidas *et al*. (Skoulidas, Sholl et al. 2006). They simulated both an atomic network of carbons and a smooth imaginary surface with a given slip boundary condition. Through the simulations, they determined Maxwell's coefficient or tangential momentum accommodation coefficient (TMAC) of the order of 10^{-3} (Sokhan, Nicholson et al. 2004). This TMAC value means that statistically only 0.1% of gas molecules in the nanotube are thermalized by the wall and randomize their reflection velocities. In other words, the wall may thermalize a colliding gas molecule with 0.1% of probability, on average. Based on the high loading and low TMAC values, one can imagine a collective motion of the chunk of molecules, similar to the motion of a liquid plug on a slippery wall. Since a large number of gas molecules were loaded in their simulation domain, their nanotubes were densely packed as seen in **Fig. 3.2**. The reported Knudsen number is, therefore, less than 0.17, which places the gas flow in the slip flow regime. They mentioned that, when the fluid density decreases, the fluid-solid collisions begin to dominate molecular collisions.

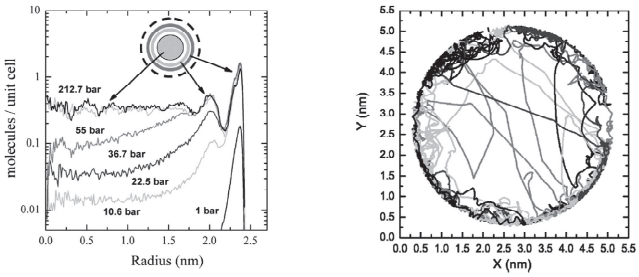

(a) (b)

Fig. 3.3. (a) Density profiles for CO_2 adsorbed in a (40,40) CNT as a function of the bulk gas pressure. (b) Trajectories of CO_2 in a (40,40) CNT at 298 K and 1 bar (Skoulidas, Sholl et al. 2006).

3.3 Flow enhancement of single component

Similar to water transport inside CNT, the gas is known to flow faster than the prediction of the Knudsen diffusion flow through CNT, which can make CNT membranes a potentially high flux and high selectivity medium. Skoulidas *et al.* (Skoulidas, Ackerman et al. 2002) showed that the potential energy barrier for axial translation of CH_4 inside a (10, 10) SWNT ($0.02\ k_BT_{room}$) is much less than that in zeolite ZSM-12 ($1.7k_BT_{room}$). The difference in energy barrier can lead to provision of a much smoother energy landscape to the transporting gas molecules under the CNT nanoconfinement. Additionally, many results from MD

simulations claim that the smoothness of the graphitic wall and relatively weak interaction between gas molecules and inner surface can allow for the fast gas transport. The most common diffusion mechanisms known as activation diffusion, surface diffusion, and Knudsen diffusion, usually dominate in small pores (d < 3 Å), medium pores (3 Å < d < 10 Å) and large pores (10 Å < d < 500 Å) for light gases, respectively (Washburn 1921; Sokhan, Nicholson et al. 2004).

Sholl and Johnson (Sholl and Johnson 2006) reported three orders of magnitude higher gas flux per a pore in CNTs than in zeolites with equivalent pore sizes. In this study, especially, light gases such as hydrogen and methane have almost same diffusivities as that of bulk state. They also showed a motion of gas molecules over the cross section of a SWNT by use of a molecular density and trajectories. According to their result, gas transport through CNTs takes place through predominantly specular collisions between molecule and tube wall, and therefore most of gas molecules flow fast along the CNT. Also, they suggested another transport mechanism that the gas molecules move through CNT with the surface diffusion since some molecules can be adsorbed on the tube walls. Other transport mechanisms were also proposed that emphasize transfer limitations at the tube entrance by Verweij *et al.* (Verweij, Schillo et al. 2007). They found the efficient transport in the tubes makes the kinetics of surface diffusion becomes more important. Miranda *et al*. (Miranda, Short et al. 2009) argued that conductance of gas molecules can counter-intuitively decrease as the inlet pressure increases due to the flow impedance given by the tube wall, and asserted that the decreasing sensitivity becomes smaller by showing the experimental results using a direct coupled CNT membrane to a mass spectroscopy. In a CNT membrane, conductance of all the gases used for experiments decreased with increasing total pressure as shown in **Fig. 3.4**. In other words, the gas flow resistance through CNT grows generally with increasing pressure but at different degrees among gases in terms of the pressure sensitivity of flow resistance. For several gas species, the slope of an increase in the gas flow resistance with respect to pressure, called pressure sensitivity, lies in a descending order: N_2 > CH_4 > O_2 > Ar > CO_2. According to Miranda *et al.*'s explanation, flow conductance of a CNT membrane decreases with increasing pressure because of interfacial resistance as well as molecular weight. This result was supported and explained in detail by Cannon and Hess (Cannon and Hess 2009). Through a non-equilibrium MD simulation, they reported that the gas flux can be highly influenced by the potential depth at the center of the nanotube as well as by the pore size, and therefore a structure without any defects attributes to higher flow rates. Moreover, the highest gas flux was obtained in the largest nanotubes above a certain back pressure, since the average kinetic energy of a gas molecule exceeds threshold energy for overcoming the interaction between molecules and tube wall. According to their finding, a higher back-pressure can cause a lower flux, and carbon interaction strength can play an important role in separation of gas molecules.

Holt, Park *et al*. (Holt 2006) have measured the bulk flow rate of air through a DWNT membrane under a pressure gradient of one bar. With observing and estimating the number of pore of the tube by using TEM, they compared the experimental results with other simulations. They concluded that the measured gas flow rates are about one hundred times larger than predictions of the Knudsen diffusion model **(see Fig. 3.5(a))**. Although their experiment could not reveal the definite reason of the ultrafast flow, the agreement between MD simulations supports that collisions between gas molecules and tube wall shift from diffusive to specular collision under the sub-2-nm CNT nanoconfinement (Skoulidas,

Ackerman et al. 2002). They also found out that non hydrocarbon gas species follow Knudsen scaling in which enhanced permeabilities of different gas species scale one another to the inverse square root of molecular weight. In addition, they demonstrated one possible route to hydrocarbon gas separation by use of hydrocarbon's deviation from the Knudsen scaling in sub-2-nm DWNT membranes, perhaps caused by additional surface adsorption and diffusion along the surface as shown in **Fig. 3.5(b)**. Mi *et al*. (Mi, Lin et al. 2007) also fabricated vertically aligned MWNT membranes using CNTs on the R-Al_2O_3 disk. Although this membrane shows a lower value of areal pore density as compared to SWNT or DWNT membranes, their gas permeability is also inversely proportional to the squared root of the molecular weight. Diffusivities of gases in their study are about four times larger than the Knudsen model prediction. Fedorov and Sadreev (Fedorov and Sadreev 2009) investigated the influence of tube diameter and temperature on the self-diffusion of the hydrogen thermo-activated inside three kinds of narrow nanotubes using DFT calculation. They presented that the potential profile is different between (3, 3) and (6, 0) nanotubes although the diameters are comparable to each other, indicating that hydrogen transport can vary with respect to a CNT chirality because CNTs with different chiralities could induce distinct phonon interaction, or thermal fluctuation, on the tube walls. In addition, the hydrogen density inside CNT was observed to shift in the direction of descending temperature as shown in **Fig. 3.6**. Accordingly, the authors proposed that it is possible to realize the molecular pump driven by a thermal gradient.

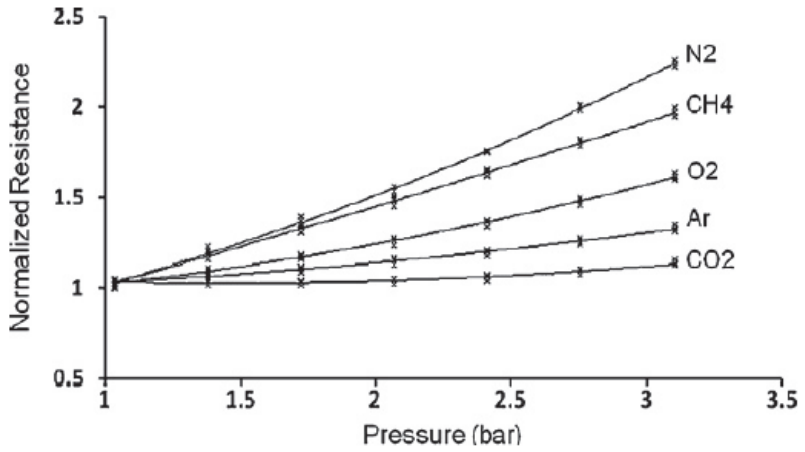

Fig. 3.4. Normalized transport resistance of each gas component in CNT with increasing pressure (Miranda, Short et al. 2009).

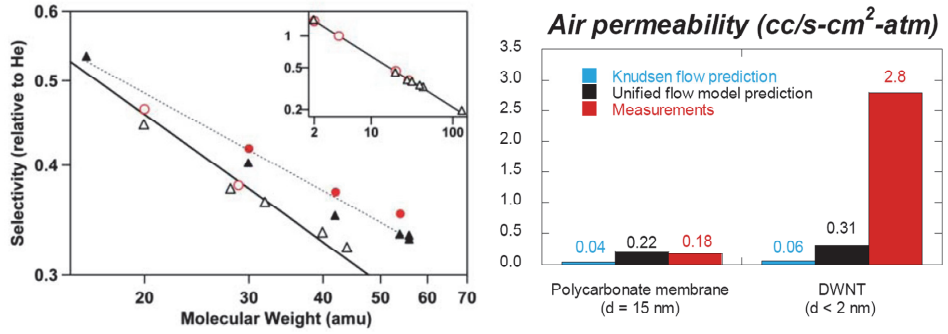

(a) (b)

Fig. 3.5. (a) Gas selectivity (defined as permeability relative to that of He) for sub-2-nm DWNT (triangle) and MWNT (circules) membranes. (b) Comparison of air permeabilities between DWNT and polycarbonate membranes. The average DWNT-membrane permeability is compared with theoretical predictions by Knudsen diffusion model and the unified flow model. DWNT-membrane shows an order of magnitude higher permeability compared to the model predictions, while polycarbonate membrane lies at the same level as them (Holt 2006).

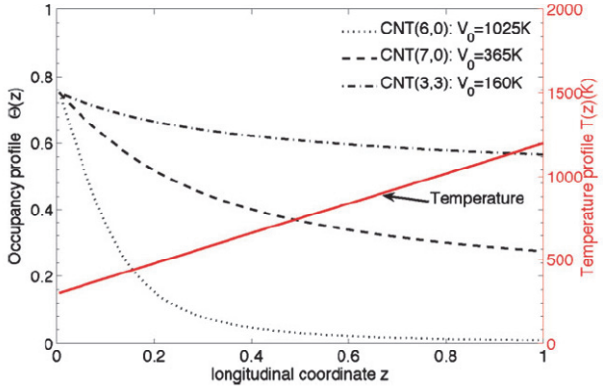

Fig. 3.6. Equilibrium distribution of H_2 molecule occupancies Θ(z) along SWNT and temperature profile T(z) (Fedorov and Sadreev 2009).

Another interesting effect on the gas diffusion is the tube flexibility. Chen *et al.* (Wu, Sou et al. 2006) observed a distinct influence of tube flexibility on the transport diffusion of single gases and claimed that the influence of tube flexibility on diffusion in the wall-fluid collision dominated the Knudsen regime. The following work done by Jakobtorweihen *et al.* (Jakobtorweihen, Lowe et al. 2007) showed that CNT flexibility can be very important for the diffusion of rarefied gases. They concluded that the influence of tube flexibility on transport diffusion is stronger for the gas molecule with longer chains. The influence of tube flexibility on the diffusivity of chain-molecules such as methane, ethane, propane, butane, pentane and hexane increases as the chain length of a molecule gets longer, since the longer

chain molecules have a higher probability to collide with the wall whereas the shorter chain molecules hardly collide. For example, CNT flexibility has a limited influence on the rotational motion for butane whereas the hexane rotational motion is merely influenced by it. Additionally, it has been suggested early to tailor the pore size of membrane by tuning the transport properties (Walther, Jaffe et al. 2001). Thorntona *et al.* (Thornton, Hilder et al. 2009) suggested a way to distinguish the gas diffusion regime occurring in CNT for different diameters, shapes, and compositions by using a mathematical modeling employing the Lennard-Jones interactions between the gas molecule and the pore wall, which is well matched with the transport of light gases such as He, H_2, CO_2, O_2, N_2 and CH_4. They also showed a minimum diameter for barrier-free transport, a minimum diameter for Knudsen diffusion, and an intermediate region in which an accelerated entering velocity is influenced by the attractive van der Waals forces, in order to provide a theoretical determination of membrane pore sizes, new guidelines to design a CNT membrane for desired separation.

3.4 Transport in separation applications

The last decade has seen many efforts to mitigate carbon dioxide emission and reduce the aftermath of global warming by applying lots of chemical reactions to an exhaust gas. Nowadays, the major production cycles consume as much as 40-50% of the total energy use only for separations, often carried out by inefficient thermally driven separation processes, therefore it became more important to find a new technology that can increase the efficiency and reduce the operating expenditure. Recently, separation of a single species or mixture gases such as oxygen or nitrogen from air using unique characteristics of CNT has attracted much attention. Molecular dynamics (MD) simulations are investigating the idea of gas transport inside SWNT. These simulations reported that the gas transport inside CNT is orders of magnitude faster than inside any other materials with the same pore dimension because the CNT walls have much smoother surface. Indeed, Holt, Park *et al.* (Holt 2006) who have fabricated the first membranes from aligned SWNT and DWNT showed that CNT membranes do not only possess ultrahigh fluxes but a certain level of single-component selectivity as well. It is noteworthy that the hydrocarbon selectivity among the single components would be more pronounced for practical gas separation problems where mixtures are involved. Since this pioneering work, a number of simulations have noted that CNT may have such amazing characteristics when the CNT membranes are used for gas separations. For example, SWNTs having diameters of 4-12 Å as membrane pores can promise not only fast transport rates but also size-selectivity for a gas mixture (Wu, Sou et al. 2006). Jakobtorweihen *et al.*'s study on the relationship between SWNT flexibility and n-alkane diffusion (Jakobtorweihen, Lowe et al. 2007) has found out that Knudsen diffusivities can predict slower transport for molecules with chain (n-alkanes) or mixtures, since Knudsen diffusion assumes all collisions are diffuse.

Kim and colleagues produced mixed matrix SWNT membranes based on polysulfone (Kim, Jinschek et al. 2007). The authors investigated transport of CO_2/CH_4 mixtures experimentally through CNT membranes, and reported that mixed diffusion seems to indicate the presence of transport resistances for molecules entering and leaving the nanotube ends. Following a study on the separation of a gas mixture through CNT carried out by Chen and Sholl (Chen and Sholl 2006), they showed that the selectivity through the SWNT membranes for CH_4/H_2 mixture gas is dominated by the preferential adsorption of CH_4 relative to H_2 in the nanotubes. This preferential adsorption can induce partial filtration of CH_4 from the gas mixture to

present (adsorption) CH_4 selectivity ranging from 10 to 35, depending on the gas pressure. The surface diffusion resistance of molecules moving along the pores increases as the temperature becomes lower or the adsorption strength of the gas molecules inside CNT increases. CH_4 in SWNT could also diffuse faster than other light gases such as Ar, Ne, N_2, or CO_2, and the transport mechanism depends weakly on CNT diameter (Wu, Sou et al. 2006), later supported by the work of Newsome and Sholl (Newsome and Sholl 2006). Calculation of surface diffusion resistances for CH_4 in a (20,0) SWNT at room temperature revealed that surface diffusion resistances accounting for pore entrance and exit of molecules would be larger for strongly adsorbing species such as n-alkanes than for CH_4. This result presents one possibility of separation between CH_4 and n-alkanes because stronger adsorption of n-alkanes would expectedly undergo more difficulties in permeating a CNT membrane via the surface diffusion mechanism. Importantly, it is pointed out that surface resistances could be negligible for long CNTs as 5–10 mm but can become significant for sub-micrometer long CNTs.

Separation of a nitrogen-oxygen gas mixture by SWNT was also examined by Arora and Sandler (Arora and Sandler 2006) for various nanotube diameters, temperatures, and pressures, after Wang *et al.* (Wang, Kim et al. 2005) reported that the nitrogen adsorption energy can increase as the nanotube diameter narrows toward a molecular length scale. They found out that the selectivity of a nitrogen-oxygen gas mixture depends strongly on the nanotube diameters, temperature, and molecular structure. They also reported that the large gas permeability in SWNT has not been merely observed for pure components such as individual nitrogen and oxygen but also for the gas mixture, adding that SWNT has a benign kinetic selectivity for separating of air and the kinks of SWNT could be used for a molecular sieve (Wei, Vajtai et al. 2002). Recently, Kowalczyk *et al*. (Kowalczyk, Brualla et al. 2007) reported a possibility of storing and separating hydrogen/methane mixtures at room temperatures for SWNT with pore diameters ranging between 0.6 and 2.4 nm. Neither of hydrogen nor methane could enter CNT as narrow as 0.6 nm. When the diameter grows to 0.8 nm, methane could adsorb on the CNT interior. Hydrogen showed selective adsorption and storage capability by forming a bulk gas in a 0.7-nm-wide CNT. Although all of these predictions could not be verified experimentally in the extreme conditions of the simulations owing to the difficulty in fabrication, they provide an understanding of the mechanism responsible for the separation of homogenous or mixture gases by CNT pores, rendering the CNT membrane an option for a molecular sieve with improved selectivity and permeability. However, far more experiments should be carried out to gain better insights about static and dynamic mechanisms of gas separation that keeps fast transport and high selectivity. Qiao *et al.* (Qiao, Cao et al. 2007) investigated the role of dissolved gases by simulating CNTs of diameters between 1.4 nm and 5.4 nm. As shown in **Fig. 3.7**, CO_2 gas molecules form a cluster trapped in between water layers of a narrow CNT, while they stay dissolved in water in a wide CNT. They also observed that a single gas molecule can help infiltration and emptying of liquid only in the narrow CNT under pulsating pressures of 200–1000 atm. From this result, it is inferable that gas molecules inside narrow, hydrated CNT could be a driving force for wetting or dewetting of the CNT. Accordingly, further efforts to obtain the high flux and selectivity of CNT membranes by combinational use of gas and liquid can serve as one of the interesting options for gas separation. Finally, breakthroughs in gas separation technology would be made in an accelerating fashion by a hybrid merge of CNT membrane technology enabled by the *Carbon Nanotube Nanofluidics*' preliminary achievements to industrial techniques already used and under development.

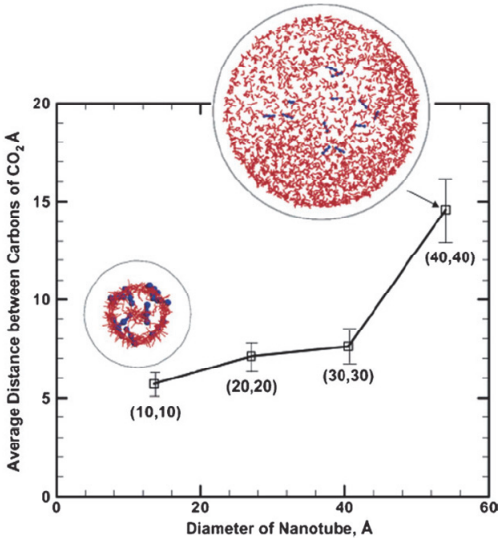

Fig. 3.7. Average distance between carbon atoms of CO_2 molecules within hydrated CNTs of different diameters (Qiao, Cao et al. 2007).

3.5 Summary

Gas transport in CNT can undergo specular collisions with the interior CNT wall to maintain their forward momentum in a different way from Knudsen diffusion. This mechanism is particularly useful for separation of single- or mixture gas molecules. Recent years after Holt, Park *et al*. (Holt 2006) have seen lots of experimental studies carried out to investigate somewhat counter-intuitive phenomena about gas transport behavior inside CNT and to validate predictions of MD simulations.

Although the complete fundamental mechanisms of gas transport for various operating conditions are not unveiled until now, it is of no doubt that, in the foreseeable future, a rational design and an improved fabrication scheme of CNT membranes will emerge and lead to the development of a technology of gas separation and purification that focuses on reduction of energy and capital consumptions. We believe it will be possible because of the unique properties of large permeability and of the possibility of high selectivity that CNT membrane can pose. We also stress that the manufacturing efforts of developing large-scale CNT membranes should continue to be exerted, in parallel with the investigation of the fundamental science, in order for the CNT membrane technology to gain economic viability and market acceptance.

4. Ionic solution in CNT

4.1 Introduction and overview

Aqueous solutions of ions partake in many biological processes. Depending on applications, ion-water systems could be assigned three different categories; ion transport system (when ions in CNT are desirable), ion selectivity system (when ions are selectively desirable in CNT) and ion exclusion system (when ions are undesirable in CNT). One of the most

important cases of ion exclusion is water purification for human consumption and for other purposes including medical, chemical, and industrial uses. Most of the modern interests in desalination/demineralization are centered on development of cost-effective ways of providing potable water in which most of the dissolved salts are ionic in nature. Although membrane techniques such as reverse osmosis (RO) (Suk, Raghunathan et al. 2008), electrodialysis (ED) and membrane distillation (MD) for desalination are widely employed all over the world, the development of more efficient membrane materials that can separate salt from water draws critical attention as it has potential of widening fresh water availability by making desalination cheaper.

The fast water transport in CNT discussed in the previous section and pore sizes commensurable with the ions' own dimensions are rendering use of CNTs a very promising option for the removal of undesirable chemicals, materials, and biological contaminants from contaminated water sources. Using molecular dynamics simulations, Corry *et al*. (Corry 2007) reported that CNT membranes with sub-nanometer-wide pores can provide significantly higher performance when used in a reverse osmosis-type desalination. According to the simulation, CNTs of (5,5) and (6,6) chiralities could reject 100% of salt, a 680-to-1100-fold improvement than commercial membranes such as FILMTEC SW30HR-380 used for reverse osmosis. This expected achievement was attributed to the energy barriers at the entrance and exit of such narrow tubes that can control the permeation of ions into CNT pores. The detailed mechanism is related to the energy cost required for removal of water hydration shell surrounding ion. For water entry to the same CNT pore, in turn, it is stability of the remaining hydrogen bonds of water molecules inside CNT that minimizes the energy cost spent for the entry.

Likewise, ion channels can regulate many functions in human body such as transfer of electrical impulses to the nerves, hormones secretion, muscle system control and many others. Diffusion of ions through the bio channels is supposed to be a simple physical process. Characteristics of ionic transport in CNT could be used as simplified theoretical and experimental models for the transmembrane protein studies for inorganic ion flux across cell membranes in a way of improving our understanding of how ions get into and out of cells. This understanding would lead us to bio medical solutions of many human deceases caused primarily by ion channel dysfunction. Selectivity hypothesis of K^+ from Na^+ ions could be built on an idea that removal of K^+ ions from their hydration shells is energetically more favorable than stripping hydration shells from Na^+. This hypothesis could be potentially applied for MD and experimental studies. In addition, application of Donnan membrane principle to the ionic transport under CNT nanoconfinement could assist design and fabrication of devices for efficient separation, product recovery, synthesis of smart materials, and other innovative applications (Fornasiero, Park et al. 2008; Sarkar, SenGupta et al. 2010). These techniques use water as a process mediator and do not require either electricity or pressure gradient for sustained operation. It has potential of recovery of the alum in a high purity in a single-step process and reuse of it in the same plant or elsewhere as a coagulant. Also, the CNT based devises designed for ionic liquid transport and selectivity have potential applications in energy generation such as fuel cells, chemical nanoreactors, nanosensors and unipolar ionic field-effect transistors (Daiguji, Yang et al. 2004; Kang, Byun et al. 2004), since the high surface-to-volume ratio in CNT leads to ion separation via a transport mechanism governed by surface charges. While chapter 2 and 3 have discussed the progress and basic understandings of water and gas transport phenomena inside CNT,

this chapter focuses on introductions of the MD simulation theories associated with ionic liquids inside CNT. In the first section, we will present an introduction to the basic theoretical models and formulas for MD simulations employed to describe the behavior of ionic liquids in nanochannels. Following sections will cover ion exclusion, selectivity and transport. Main aspects of the sections are summarized in the last section.

4.2 MD simulation theories

Today, molecular dynamics sees a widely spread use in the investigation of motion and interaction of biomolecules. Although MD simulation of real objects even at the nanometer scales is limited, success of MD in modeling liquids and gases under CNT nanoconfinement has been motivating researchers to utilize this tool in the analysis of the behavior of ionic solutions under CNT nanoconfinement. Fundamentally, MD combines Newtonian second law and interparticular potential energy.

$$m_i \frac{\partial^2 \vec{r}_i}{\partial t^2} = -\frac{\partial}{\partial \vec{r}_i} U_T(\vec{r}_1, \vec{r}_2, ..., \vec{r}_N), \quad i = 1, 2, ..., N, \tag{4.1}$$

where m_i is mass of a particle (atom or molecule) i, r_i is its position, and U_T is the potential energy that depends on atomic positions. Choice of the potential is the most critical as it can determine interactions between those particles in the simulation domain. To represent electrostatic interactions such as van der Waals attraction and Pauli repulsion, a mathematical function, viz. Lennard-Jones potential, is widely used. Contribution of the electrostatic charges of particles to the potential follows the Coulomb's law (Shao, Zhou et al. 2009).

$$U(r_{ij}) = 4\varepsilon_{ij}\left[\left(\frac{\sigma_{ij}}{r_{ij}}\right)^{12} - \left(\frac{\sigma_{ij}}{r_{ij}}\right)^{6}\right] + \frac{q_i q_j}{r_{ij}}, \tag{4.2}$$

Equation (4.2) represents a typical interaction potential incorporating the electrostatic charge effect, in which r_{ij} is the distance between particles i and j, q_i is the partial charge assigned to the particle i, and ε_{ij} and σ_{ij} are respectively energy and size parameters obtained by the Lorentz-Berthelot combining rule: potential vanishes at the interparticular distance of $\sigma_{ij} = \left(\sigma_i + \sigma_j\right)/2$ and has a minimum well of $\varepsilon_{ij} = \left(\varepsilon_i \varepsilon_j\right)^{1/2}$. Poisson (Equation 4.3) and Nernst-Plank (Equation 4.4) equations are used for mathematical description of those potentials (Daiguji, Yang et al. 2004; Coalson and Kurnikova 2005; Peter and Hummer 2005).

$$\nabla^2 \Phi(r) = -\frac{1}{\varepsilon_0 \varepsilon} \sum_i z_i e n_i, \tag{4.3}$$

$$J_i = -D_i\left(\nabla n_i + \frac{z_i e n_i}{k_B T} \nabla \phi\right), \tag{4.4}$$

In Equations (4.3) and (4.4), ε_0 is the permittivity of vacuum, ε is the solution dielectric constant, n_i is the number density of ions of species i, $z_i e$ is their charge, J_i is an ion flux, and

D_i is an ion diffusivity of species *i*. Equations (4.3) and (4.4) can calculate ionic current along a nanofluidic channel and surface charge density. When the tube surface is charged in a way that Debye length enlarges close to a pore radius, repellence of co-ions imparts ionic selectivity to the nanopore. In this manner, ion transport can be tuned by surface charge modulation (Daiguji, Yang et al. 2004). For ion transport and selectivity, concepts of energy penalty on CNT entry and water coordination shell number can play a major role. That is why analysis of ion hydration configuration in the bulk water and under CNT nanoconfinement is in scope of great interest. MD can determine the probabilities of the ion position $P(z,r)$ out of the radial distribution function. Free energy profile, $G(z)$, e.g. potential of mean force (PMF) for the CNT in one-dimensional case, could be calculated as follows:

$$G(z) = -k_B T \ln \int_0^R P(z,r) dr, \tag{4.5}$$

where *R* is the tube radius, *T* is absolute temperature and k_B is Boltzmann's constant.

Some of ab initio MD (AIMD) take into account the polarizability of CNT in the framework of density functional theory (DFT) (Eschermann, Li et al. 2006; Leung and Marsman 2007; Aluru and Xu 2008). Polarizability of the tubes differs depending on delocalized π-electrons. For example, an infinite polarizability of metallic CNT makes ion permeation less favorable than for the case of semiconducting CNT. The main action of large polarizability in ion permeation remains to be elucidated. Besides, huge computational cost prevents a wide spread use of the ab initio analysis in large structures, rendering it still remain a challenging task to calculate ion free energies compared with classical force fields approaches. Despite the difficulties, differences in polarizability could somehow be used for CNT characterization when proper experimental techniques would emerge. Aluru and Xu (Aluru and Xu 2008) showed that metallic SWNT has much stronger screening effects than semiconducting SWNT does when water molecules and ions permeates the nanotubes. These results imply that it would be possible to identify differently charged ions and to differentiate between metallic and semiconducting nanotubes. Leung and Marsman (Leung and Marsman 2007) carried out AIMD to demonstrate that intrinsic binding energies for metallic (6,6) SWNT are 2.9 and 1.8 eV for Na^+ and Cl^-, respectively, while a much wider (18,18) SWNT exhibit lower binding energies of 2.2 and 1.1 eV. This suggests that the proposed use of vertically aligned CNT in ion rejection membranes may need careful re-examination. They also pointed out that confined environment and molecular configurations can play a dominant role in the transport and selectivity processes. In this sense, ions behave in a similar manner in CNTs with diameters larger than 0.96 nm, regardless of water configuration under nanoconfinements (Dzubiella and Hansen 2005; Peter and Hummer 2005; Corry 2007; Shao, Zhou et al. 2009; Beu 2010). The behavior of ions in larger diameter CNT agrees well with experimental results (Majumder, Chopra et al. 2005; Fornasiero, Park et al. 2008; Lee, Choi et al. 2010; Yu, Funke et al. 2010).

Unique properties not evident at macroscales can appear when liquids lie under nanoconfinement. In a narrow CNT, the size of the tube could become commensurable with the size of the transporting molecules. In this situation, interaction between transporting molecules and CNT wall could emerge as a governing factor for the flow process, thereby nullifying continuum assumption and sometimes resulting in a single file configuration of

water (Levinger 2002; Dong, Zhou et al. 2009). These unique nanoscale phenomena do not only apply to water molecular transport, but also to water as a processing chemical during ion transport and selectivity. The quantum state of the protons in the low temperature phase of water in nanotubes is qualitatively different from that of any phase of water seen so far. A transition temperature between bulk water and ice-like water phases is likely to depend on CNT size and details of the interaction between water molecules and the confining CNT. Should the phase exist at room temperatures for CNTs with different sizes, that would be of great interest in understanding the structure and transport of water in biological pores (Reiter, Burnham et al. 2006).

MD is a very powerful tool that helps us understand transport phenomena in CNT that are difficult or impossible to capture by state-of-the-art experimental techniques. Nevertheless, all models have their own restrictions and applied theories are mostly developed for macro scale. Hence, in applying these models directly to nanoscale, one should critically consider the validity of simulation results. Though, significance of molecular dynamics is arguably no less than experimental studies.

4.3 Ion exclusion, selectivity and transport

When it comes to the behavior of ionic liquids in CNT, it is difficult to draw a distinction among exclusion, selectivity and transport. Dissatisfaction of one process becomes gate conditions for the other. For example, cessation of ion transport means ion exclusion, and selectivity of ions implies exclusion of some of ion species and transport of the other species. Numerous simulations and experimental studies uncovered several possibilities in order to promote desirable processes. These possibilities range from the application of external pressure and electrical forces to the chemical addition of charged functional groups to the CNT opening or to the sidewall. Knowledge on the combination between driving force and chemical implantation per specific case would be crucial, as each combination may result in entirely different applications.

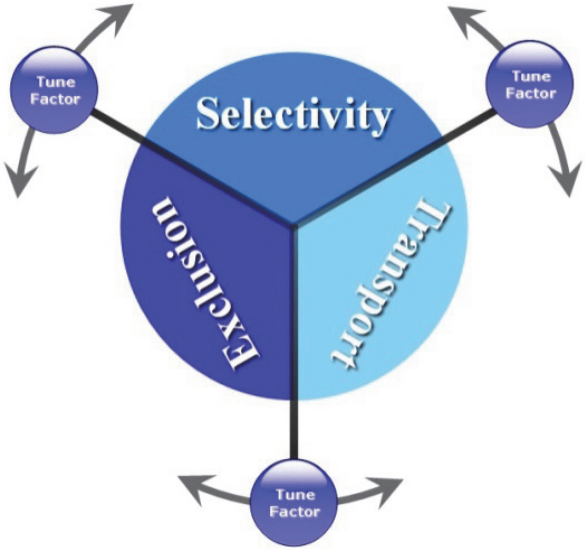

4.3.1 Ion exclusion

Although water is the most abundant liquid in the planet, merely 3% is drinkable. Therefore, desalination and purification of seawater and brackish water are drawing a surge of attention today in association with future water scarcity. Fornasiero *et al*. (Fornasiero, Park et al. 2008) fabricated sub-2-nm CNT membranes and observed the ionic solution transport inside CNT. At the nanotube inlet, hydroxyl (OH), carbonyl (C=O), and carboxylic (COOH) functional groups are chemically added in order to impart a ring of negative charges to the CNT mouth. They examined ion transport and exclusion characteristics of this system, as a function of solution concentration, pH, ion valence, and ion size. For the first time, they demonstrated that hydrophobic, sub-2-nm-wide CNT pores charged with negative moieties on the pore mouth can exclude ions and provide a strong indication that electrostatic interaction is responsible for ion rejections in CNT pores of this size (see **Fig. 4.1**). Their results made a good agreement with the Donnan membrane equilibrium theory, another evidence supporting the action of electrostatic interaction (Sarkar, SenGupta et al. 2010). Later, Banerjee *et al*. (Banerjee, Murad et al. 2007) pointed out that CNTs can be utilized for water and ion separation from a salt solution via three different electrostatic charge distributions on the pore surface (see **Fig. 4.2**). Molecular dynamics simulations showed that when these different charge distribution patterns are applied ion intake into the nanotubes is minimal, and negative charges on SWCNTs reduce the ion permeation to the tube that means it increase the value of the CNTs based devises as a water-purifying system. Goldsmith et al. (Goldsmith and Martens 2009) simulated an idealized model of membranes having surface-modified nanoporous of armchair CNTs of (8,8), (10,10), (12,12), (14,14), and (16,16). Nonequilibrium MD was applied for a pressurized flow of an aqueous NaCl solution for both uncharged CNT and CNT with artificial surface charge patterns (see **Fig. 4.2**). For uncharged CNT, the ionic flow rates showed a linear dependence on the driving pressure and increased with pore diameter. The amount of ion transport was orders of magnitude smaller than that of water, an evidence of salt rejection from the solution. Charged CNT, on the other hand, showed both water and ion transport rates smaller than those for uncharged CNT, and the smallest (8,8) and (10,10) systems exhibited nearly complete ion rejection. CNT surface modification with partial charges (**Fig. 4.3**) led to a decrease in overall flux of water but enhanced the amount of excluded salt from the system. Such enhancement of salt rejection could be achieved for larger pores.

As a membrane based distillation platform, Gethard *et al*. (Gethard, Sae-Khow et al. 2010) suggested a mixed matrix out of a polypropylene membrane embedded with uniformly distributed, PVDF surrounded MWNTs. It was the hydrophobic property of MWNT that augmented removal of the NaCl and $MgSO_4$ salts from the ionic solution. Since water transport takes place in a vapor phase during the distillation process, water did not face any permeation barrier. In this way, permeated water purity was increased. One method of using a sheet network of chemically oxidized CNTs as absorbent of salts in ionic solutions was proposed by Tofighy et al. (Tofighy and Mohammadi 2010), with a decent degree of success. Subsequently, a capability of MWNT in adsorbing toxic heavy metal from water was experimentally described by Kandah et al. (Kandah and Meunier 2007) using oxidized MWNT ranging between 5.5 and 14 nm. Oxidized CNT powders saw a certain degree of efficiency in adsorbing nickel from water solution. For example, negatively charged functional groups on CNT improved cation removal capacity. These oxidized CNT powders have excelled a commercial membrane (MINOTAUR) in the nickel removal capacity from water. However, we suppose that efficiency and efficacy of using CNT for water desalination and purification

could be far more improved by use of CNT as membrane pore material than merely as absorbent or hydrophobic agent. The utilization of CNT as a basis channel for ion exclusion devices marks a promising route toward ion exclusion from aqueous solutions, attributed primarily to the capability of tailoring an entrance penalty of target ions and water. One of the best candidate mechanisms of ion exclusion is the manipulation of electrostatic interactions at the CNT pore, since the required ion exclusion could be achieved via rather simple methods such as functionalization of CNT or controlling pH of the ionic solution.

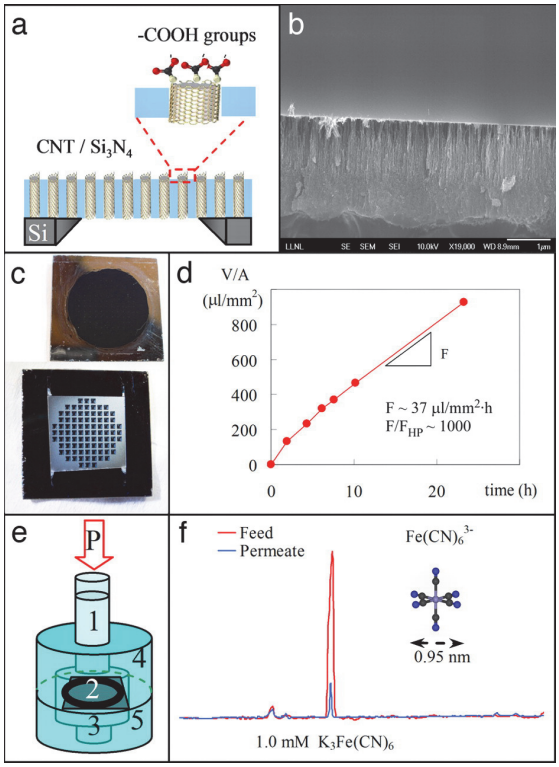

Fig. 4.1. CNT/silicon nitride membrane platform for ultrafast nanofiltration of electrolytes. (a) Cross-section schematic of a CNT membrane constituting a silicon support, aligned CNTs, silicon nitride matrix filling the gap between the CNTs, and the CNT tips functionalized with carboxylic groups. (b) Cross-section SEM image of the CNT/silicon nitride composite showing the gap-free coating of silicon nitride. (c) Photographs of the membrane sides exposed to the feed (upper) and to the permeate (lower). (d) Time variation of permeate volume per unit area of freestanding membrane during the filtration of a 0.6-mM $K_3Fe(CN)_6$ solution. The resulting permeation flux, F, is ca. 1,000 times larger than the value calculated by Hagen–Poiseuille equation, F_{HP}. (e) Schematic of the dead-end nanofiltration cell showing the column of feed solution (1) pressurized at P = 0.69 bar, the CNT membrane (2), the permeate solution (3), and feed (4) and permeate (5) chambers. (f) Capillary electrophoresis chromatogram for feed (red) and permeate (blue) showing a 91% exclusion of the ferricyanide anion after nanofiltration of a 1.0-mM $K_3Fe(CN)_6$ solution (Fornasiero, Park et al. 2008).

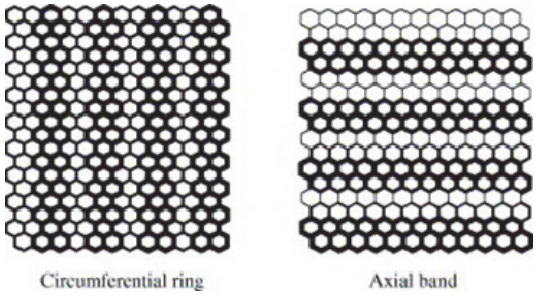

Fig. 4.2. Schematic diagrams of the simulated charge distributions. The darker shade corresponds to a negative charge on a carbon atom while the lighter shade is for a positive charge (Banerjee, Murad et al. 2007).

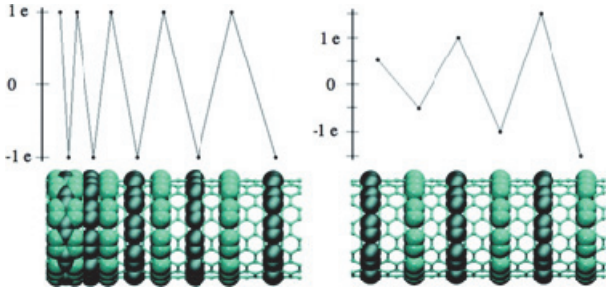

Fig. 4.3. Typical charge patterns employed for the surface-modified model CNTs. Partial charges are added to selected carbon atoms, as indicated in the figure by spheres of large radii in light and dark blue for positive and negative charges, respectively. The graph above each pore diagram indicates the total charge on the corresponding ring of carbon atoms. The left hand case consists of rings of equal amounts of charge, but an unequal spacing along the pore. The right hand case depicts equally spaced rings of charge, but increasing magnitudes along the pore (Goldsmith and Martens 2009).

4.3.2 Ion selectivity

Understanding and explanation of ion selectivity, for example in a potassium channel, are fundamental questions in nature, and therefore an inquiry of how channel can interact differently with K^+ and Na^+ ions have attracted much attention among researchers. Ions in aqueous solutions appear to find more energetically favorable when an ion is hydrated. When pore size is smaller than the dimension of the first hydration shell, the ion needs to get partially stripped of hydrating water molecules in order to gain entry to the pore, at the expense of energy penalty of the partial dehydration. This mechanism could be used for gated ionic transport via tailoring of the entrance energy barrier (Beckstein, Tai et al. 2004; Peter and Hummer 2005; Alexiadis and Kassinos 2008; Rasaiah, Garde et al. 2008).

Peter and Hummer (Peter and Hummer 2005) modeled a hexagonally packed CNT membrane to conclude that nonpolar pores with diameter around 5 Å can block Na^+ ions completely, while they permeate the ions when the pore diameters increase to 10 Å. This finding was attributed to the interaction of hydration shell and pore in a way that an entropic loss equalizes

to the potential barrier for ion penetration. Shao *et al*. (Shao, Zhou et al. 2009) investigated Na^+ and K^+ selectivities inside CNTs with diameters 0.60, 0.73, 1.0, 1.28 and 2.00 nm. Out of the five CNTs of their work, the first two small CNT were found favorable for confining a hydrated K^+. On the contrary, the situation reversed in the wider CNTs with diameters of 0.87, 1.0, and 1.28nm. From this finding, they supposed that the ion selectivity is related to the energy cost of incorporating the hydrated cation under CNT confinement. Gong *et al*. (Gong, Li et al. 2010) also demonstrated how selectivity in (9,9) SWNT could be improved by modification of the inner wall by eighth or sixteen carbonyl oxygen atoms. Their simulation showed a remarkable selectivity, attributed to the hydration structure of Na^+ or K^+ confined in the nanotube, which could further be precisely tuned by different patterns of the carbonyl groups. In the meantime, using MD simulation under equilibrium and nonequilibrium conditions, Dzubiella *et al*. investigated the ionic aqueous solution in a hydrophobic pore by focusing on dependence of ion and water permeations on pore diameter and electric field (Dzubiella and Hansen 2005). They reported that the energy barrier at the CNT pore entry was lower for the K^+ than for the Na^+ ions. Additionally, when the pore radius was smaller than a critical value, water had to be forced by an electric field to gain entry to the pore. The energy barrier that prevents ion penetration into CNT dropped to a few k_BT by increasing the electric field that polarized the channel. Similar results on ion selectivity in charged surroundings were also obtained by Yang *et al*. (Yang and Garde 2007). They studied the partitioning of cations of increasing size (Na^+, K^+, and Cs^+) in negatively charged (5,5) CNT-like nanopore using MD. When the charge density of the pore was low, they found no entrance event of ions into CNT. An increase in the pore charge density, on the other hand, promoted the ion partitioning in the order $K^+ > Cs^+ > Na^+$, and the large K^+ and Cs^+ ions entered the CNT-like pore faster than small Na^+ ions. From this finding, they suggested an existence of a free energy barrier for the pore partitioning that could be adjusted via tailoring of pore charge density as shown in **Table 4.1**.

	Nanopore (-2*e*)			**Nanopore (-5*e*)**			**Nanopore (-8*e*)**		
	$\Delta\mu^{ex}_{LJ}$	$\Delta\mu^{ex}_{ele}$	$\Delta\mu^{ex}_{hyd}$	$\Delta\mu^{ex}_{LJ}$	$\Delta\mu^{ex}_{ele}$	$\Delta\mu^{ex}_{hyd}$	$\Delta\mu^{ex}_{LJ}$	$\Delta\mu^{ex}_{ele}$	$\Delta\mu^{ex}_{hyd}$
Na^+	-7.0	68.8	61.8	-7.1	-92.6	-99.7	-6.9	-276.8	-283.7
K^+	5.9	7.6	13.5	7.4	-147.7	-140.3	9.8	-323.4	-313.6
Cs^+	29.4	-20.4	9.0	32.5	-138.9	-106.4	36.2	-317.2	-281.0

Table 4.1. Free energies of water-to-hydrated-nanopore transfer of cations for three charge states of the nanopore. Contributions from LJ and electrostatic interactions are also listed. Units: kJ/mol (Yang and Garde 2007).

Later, Song *et al.* (Song and Corry 2009) demonstrated pressure controlled ion selectivity in narrow CNTs. For this purpose, they examined SWNTs with diameters of 3.4-6.1 Å to reveal that Na^+, K^+ and Cl^- ions face different energy barriers in entering the pore mouth of CNT. For example, in the (5,5) tube, the order of free energy barriers upon entry is $\Delta G_{Cl^-} > \Delta G_{Na+} > \Delta G_{K+}$, which means that it is easiest for K^+ to enter the SWNT and the PMF barriers are no longer distinguishable. Major contribution to the free energy barrier difference is to bring about energy cost associated with a hydration shell of the ions. Ions in narrow pores could not gain a coordination number close to their bulk value. Selectivity in this case was governed by the ion solvation energy. Probably, this could also be more or less a correct

description about the selectivity in potassium channels. Simulations and experimental studies have recognized the importance of a dimension of hydration shells around an ion in the ion selectivity. This implies a connection between the ions' behavior under CNT nanoconfinement and biological processes of human body and nature. Therefore, those studies could contribute to the discovery of the cure for ailments such as blindness, Alzheimer's disease, heart diseases and many others in the aging societies of the century.

4.3.3 Ionic liquid transport

Ionic flow through the CNT can promote a lot of interests from industry because of energy applications as well as from the academia because of the fundamental impact of the basic transport mechanisms associated with it. Gated ion transport gives a perspective of using CNT as a storage container for the drug delivery systems, nanoreactors, molecular detectors, ionic transistors, rectifier circuits and many others. Insight obtained from ion transports under CNT nanoconfinement can be readily applied to the biological area via parallel CNT channels as a man-made analogy to biological ion channels that are able to generate coherent and oscillatory signals contingent upon physiological endo- and exocellular environments. By appling a simplified model of hydrophobic pores, Dzubiella *et al.* (Dzubiella and Hansen 2005) investigated cation transport in an aqueous solution under equilibrium and nonequilibrium conditions. Their simulation studies showed the intermittent filling of the hydrophobic cylindrical pore by water under equilibrium conditions, provided that the pore radius exceeds a critical value R_c = 5.3 Å. Below this critical radius, R_c, water could still permeate the pore under the action of a strong electric field. In addition, it was demonstrated that the hydrophobic pore has a lower entrance energy barrier for K^+ than that for Na^+, despite the smaller size of the sodium ion. Recently, experiment and MD simulation implemented by Strano *et al.* (Strano, Kim et al. 2009) demonstrated a horizontal nanofluidic device. They used ionic solutions of KCl, NaCl, and LiCl, induced the transport by a standard patch clamp technique, and traced currents for various applied electric fields (600 to 6000 V/m) across two reservoirs connected by up to 45 nanotubes that are 500 mm long as depicted in **Fig. 4.4**. They observed the stochastic pore blocking when individual cations partition into CNT obstructing an otherwise stable proton current. Domination of the proton conductance through the channel could be attributed to accumulation of protons and repulsion of anions from a negatively charged pore mouth etched by oxygen plasma. The measured proton transport is comparable with gramicidin proton channel, which recommends SWNT as an efficient candidate for a proton transport channel. Although stochastic signals in CNT look similar to those in biological channels, the transport and gate mechanisms of hydrated ions for CNT differ from those for biochannels, since the amount of negatively charged moieties CNT had at the pore mouth was not enough and ions had to be externally forced to enter the CNT. Their simulations assumed existence of optimal rate of proton diffusion through the nanopore that increases efficiency of ion transport from 5 ions/min to 480 ions/min. In other words, they observed single molecule ionic resonator. Ions can easily permeate CNT when external forcing is applied. According to MD simulation of electric field driven potassium ion transport in (5,5) CNT (Kang, Byun et al. 2004), K^+ ions can enter CNT much faster when driven by external force field than driven by thermal fluctuations at equilibrium. This finding implies an application of data storage device via controllable gate ion transport in CNT.

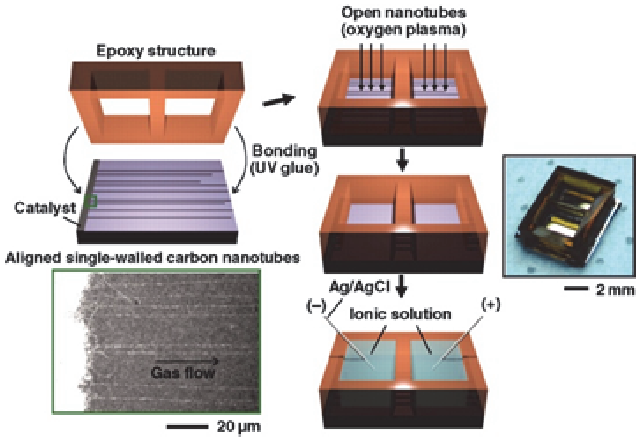

Fig. 4.4. Fabrication of SWNT ion channels. An epoxy structure with two compartments is bonded onto a substrate with ultralong and aligned CVD-grown nanotubes (scanning electron microscope image) (Strano, Kim et al. 2009).

Another MD simulation by Beu *et al.* (Beu 2010) investigated CNT diameter dependence of the ionic current. The simulations showed clearly that the ions in an aqueous solution inside the nanopore face significant energy barriers and can pass only through CNTs larger than (7,7). The (8,8) CNT does not appear to permeable ions very well, evidenced by rather low current measurement of about 0.05 nA under all conditions. A six-fold increase in an ionic current was measured for the (9,9) CNT with 0.68 Å of channel. Qualitatively, the ion current or average number of ion passages through CNT exhibits a quadratic variation with respect to the CNT pore size and vanishes when the CNT diameter becomes about 1.1 nm corresponding to the (8,8) CNT, as seen in **Fig. 4.5**.

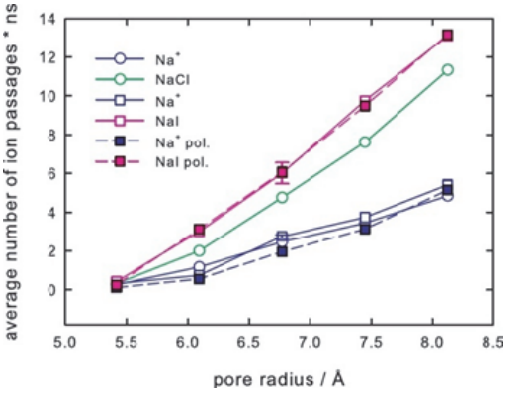

Fig. 4.5. Average total numbers of ion passages per nanosecond for the NaCl and NaI solutions as functions of the CNT radius. The partial currents due to the Na^+ ions only are plotted with blue lines and symbols. Filled symbols and dashed lines indicate the usage of polarizable models. The error bars represent the double difference between the values obtained using the time steps of 1 and 2.5 fs (Beu 2010).

Unlike MD simulations, experimental studies of ion transport through CNT do not abound. Yu *et al*. (Yu, Funke et al. 2010) experimentally investigated ion transport though a dense CNT membranes with both 3 nm CNT and 3 nm interstitial pores. They prepared this membrane with a solvent evaporation process, and used it as a model system for investigating an ion diffusion behavior in CNT. Interestingly, tuning of water wettability could observe a gated behavior of the ion diffusion through the CNT membrane. At the temperature of 298 K, ion diffusion through these dense CNT membranes stopped after a few hours, but ion diffusion dramatically increased when the temperature elevated by 20 K and when the membrane was subjected to ultrasound sonication. Water adsorption isotherms of dense CNT membranes suggested that the adsorbed water may form a discontinuous phase at 293 K, but it can quickly build a continuous layer at higher temperatures. When the temperature increase or ultrasound sonication opened up the ion diffusion channel, ions were found to diffuse through CNT at a rate similar to that of bulk diffusion in an aqueous solution. This finding may also bear implications for use of CNT membrane for desalination and water treatment. MD simulation of water assisted ionic transport in (9,9) and (10,10) CNTs performed by Dong *et al*. (Dong, Zhou et al. 2009) provided direct structural evidence about an anomalous phase behavior of the ionic liquid under CNT nanoconfinement. Although the entering numbers of cations and anions are equal when the CNT was saturated, cations always enter faster into the CNT channel than anions do during the entire filling process. The hydrogen bonding interaction plays a dominant role between cations and anions when an ionic liquid is confined by CNT. Consideration of free energy, which can determine a driving force of ions and ion pairs in entering CNT from its bulk phase, explained that a cation can enter CNT mostly by favorable dispersion of Lennard-Jones interactions. The free energy calculation revealed, however, that it is difficult for an anion to enter the CNT channel spontaneously. A more favorable case would be an ion pair entering CNT, with a cation "pulling" its counter anion by hydrogen bonding.

Water is required as a process mediator for the ion transport in CNT. One of the options to access gated ion transport in CNTs is to control the water flow inside the tube. Ionic current through CNT was found extremely dependent on CNT diameter. This clue offers one way of manipulating ion gating under CNT nanoconfinement. Another opportunity of controlling the ion flow in the nanochannels is to regulate electrostatic interactions between ions and CNT pore. It could be done via merge of concentration gradient, chemical addition of functional groups to CNT, polarization of CNT, application of an external electric field and so on. Quite often, simulations based on highly simplified water potentials tend also to neglect the polarizability effect in the MD modeling. As of a length scale, a discrepancy exists between simulated CNT and CNT used in experimental verification, the former being ca. 1 nm, while the latter being a few micrometers. All of these simplifications originated from a limit in computational cost could dramatically affect the validity of simulated data about ion selectivity and transport, unless care is taken.

4.4 Summary

Molecular dynamics is widely used to study the behavior of ions inside CNT, and yet it is not mature to capture the detailed essence of ionic configuration and transport under CNT nanoconfinement. Therefore, there exist emerging research opportunities. A variety of interatomic interaction potentials have been tested in order to describe water and ionic

behaviors so far, however each potential has seen only a limited success in capturing the entire picture of those behaviors. In addition, computational cost sets a limit to the simulated CNT length scale of about one nanometer, which often forces researchers to ignore one important factor in modeling nanoconfined ions: polarizability. Therefore, the amount of research effort geared toward a description of ions' behavior under CNT nanoconfinement does not abound.

Exclusion, selectivity, and transport of ions are all much related processes. The close interplay between these concepts is based on the same basic mechanisms that govern ions behavior in CNT. In detail, in narrow CNT, it is the interaction between the water hydration shell of an ion and the narrow opening of CNT that plays a crucial role, primarily because of the commensurability in their dimensions. This interaction can especially become important to ion exclusion and selectivity. For CNTs with larger diameters, ion transport takes place more often than other phenomena. External forces applied to CNT can, however, provide a gated ion transport mechanism, imparting the selectivity component to the otherwise unselective ion transport. Functionalization of the CNT mouths and defect sites can strengthen an electrostatic interaction between ions and CNT, giving another selectivity route to the ion transport. Incorporation of an electric current or control of a solution pH in the ion transport can also conjugate the selectivity mechanism. Combined control of different physical mechanisms in association with ions and CNT may enable practical selection among ion exclusion, ion selectivity, and ion transport.

Existing perspectives about the use of CNT as material for water purification and desalination are encouraging researchers to develop new models of simulation and experimental techniques and platforms for studying the ion exclusion phenomenon out of an aqueous solution. Analogy between CNT and biological channels brings a hope to the facilitated understanding of the mechanism of selectivity between potassium and sodium ions in human body. Ion transport under CNT nanoconfinement offers an opportunity for numerous applications such as a storage container for the drug delivery systems, nano-reactors, molecular detectors, ionic transistors and rectifier circuits. Finally, active interaction between simulation and experimental studies will allow us to better understand the fundamental science of ionic species under CNT nanoconfinement and to identify useful areas to apply the basic science to.

5. Conclusion

The recent development in nanotechnology enabled the integration of nanomaterials into conventional micro- and macrostructures, and thereby the probing of the novel nanoscale behaviour of mass transport or fluid dynamics of molecules confined in geometries commensurable with the molecular size.

In this chapter, we introduced and provided an overview of *Carbon Nanotube Nanofluidics* with three focal areas: water transport (section 2); gas transport (section 3); and ionic liquid transport (section 4). *Carbon Nanotube Nanofluidics* can be defined as both a discipline and a research area that pertains to mass transport under nanoscale confinement given by CNT. It studies nanoscale mass transport phenomena uniquely taking place inside CNT.

One common feature of these transports is the importance of molecular interaction under CNT nanoconfinement between transport entity and carbon wall. This interaction becomes dominant as the confinement tightens up. When water is placed in CNT, water molecules will experience a potential landscape provided by the hexagonal network of carbon atoms. It

is hydrophobicity, atomic smoothness and curvature of CNT that are identified as the most important factors that determine water transport. As a result, water transport in large curvature CNTs exceeds any prediction of continuum formalism.

CNT can also transport gas efficiently. Transport mechanism of gas is characterized by a collision process. When gas enters CNT, its momentum transfer mechanism immediately shifts from gas-to-gas collision to gas-to-CNT collision. In this case, the atomic smoothness of CNT plays a primary role by augmenting specular collision between gas molecules and CNT wall, thereby enhancing the transport.

Ions inside CNT can take three pathways, i.e. exclusion, selectivity, and transport, depending on the dimensional comparison between CNT opening and effective hydration shell of ion. On top of the dimensional comparison, other physical mechanisms can also take part in selecting one of the ion transfer pathways. They include electrostatic interaction, electric field, and solution pH.

Ultrafast transport of water and gas under CNT nanoconfinement can act as a major feature for energy efficient filtration, if combined with selectivity generation mechanisms. Noticeable avenues this concept could see a success encompass seawater desalination, water purification, demineralization, gas separation for greenhouse gas emission mitigation, rapid DNA sequencing, biomolecular separation, and so forth. *Carbon Nanotube Nanofluidics* is quickly combining fundamental nanoscience and socio-industrial needs, and poses potential for addressing future sustainability issues of humanity.

6. References

Agre, P. (2004). "Aquaporin water channels (Nobel lecture)." Angewandte Chemie-International Edition 43(33): 4278-4290.

Agre, P. (2006). "Aquaporin water channels: from atomic structure to clinical medicine." Acta Pharmacologica Sinica 27: 27-27.

Agre, P., M. J. Borgnia, et al. (2001). "Discovery of the aquaporins and their impact on basic and clinical physiology." Aquaporins 51: 1-38.

Alexiadis, A. and S. Kassinos (2008). "Influence of water model and nanotube rigidity on the density of water in carbon nanotubes." Chemical Engineering Science 63(10): 2793-2797.

Alexiadis, A. and S. Kassinos (2008). "Molecular Simulation of Water in Carbon Nanotubes." Chemical Reviews 108(12): 5014-5034.

Aluru, N. R., C. Y. Won, et al. (2006). "Effect of quantum partial charges on the structure and dynamics of water in single-walled carbon nanotubes." Journal of Chemical Physics 125(11).

Aluru, N. R. and Y. Xu (2008). "Carbon nanotube screening effects on the water-ion channels." Applied Physics Letters 93(4).

ARKILIC, E. B., K. S. BREUER, et al. (2001). "Mass flow and tangential momentum accommodation in silicon micromachined channels." Journal of Fluid Mechanics 437: 29-43.

Arora, G. and S. I. Sandler (2006). "Air separation by single wall carbon nanotubes: Mass transport and kinetic selectivity." The Journal of Chemical Physics 124(8): 084702.

Banerjee, S., S. Murad, et al. (2007). "Preferential ion and water intake using charged carbon nanotubes." Chemical Physics Letters 434(4-6): 292-296.

Beckstein, O. (2003). "Liquid-vapor oscillations of water in hydrophobic nanopores." Proceedings of the National Academy of Sciences 100(12): 7063-7068.

Beckstein, O., K. Tai, et al. (2004). "Not Ions Alone: Barriers to Ion Permeation in Nanopores and Channels." Journal of the American Chemical Society 126(45): 14694-14695.

Beskok, A. and G. E. Karniadakis (1999). "A model for flows in channels, pipes, and ducts at micro and nano scales." Microscale Thermophysical Engineering 3(1): 43-77.

Beskok, A., G. E. Karniadakis, et al. (1996). "Rarefaction and compressibility effects in gas microflows." Journal of Fluids Engineering-Transactions of the Asme 118(3): 448-456.

Beu, T. A. (2010). "Molecular dynamics simulations of ion transport through carbon nanotubes. I. Influence of geometry, ion specificity, and many-body interactions." Journal of Chemical Physics 132(16).

Byl, O., J.-C. Liu, et al. (2006). "Unusual Hydrogen Bonding in Water-Filled Carbon Nanotubes." Journal of the American Chemical Society 128(37): 12090-12097.

Cannon, J. and O. Hess (2009). "Fundamental dynamics of flow through carbon nanotube membranes." Microfluidics and Nanofluidics 8(1): 21-31.

Chen, H. and D. S. Sholl (2006). "Prediction of selectivity and flux for CH4/H2 separations using single walled carbon nanotubes as membranes." Journal of Membrane Science 269(25): 152-160.

Coalson, R. D. and M. G. Kurnikova (2005). "Poisson-Nernst-Planck theory approach to the calculation of current through biological ion channels." Ieee Transactions on Nanobioscience 4(1): 81-93.

Cooper, S. M., B. A. Cruden, et al. (2003). "Gas Transport Characteristics through a Carbon Nanotubule." Nano Letters 4(2): 377-381.

Corry, B. (2007). "Designing Carbon Nanotube Membranes for Efficient Water Desalination." The Journal of Physical Chemistry B 112(5): 1427-1434.

Cui, H., O. Zhou, et al. (2000). "Deposition of aligned bamboo-like carbon nanotubes via microwave plasma enhanced chemical vapor deposition." Journal of Applied Physics 88(10): 6072-6074.

Daiguji, H., P. D. Yang, et al. (2004). "Ion transport in nanofluidic channels." Nano Letters 4(1): 137-142.

Daillant, J. (2009). "Recent developments and applications of grazing incidence scattering." Current Opinion in Colloid & Interface Science 14(6): 396-401.

Dong, K., G. Zhou, et al. (2009). "Structural Evidence for the Ordered Crystallites of Ionic Liquid in Confined Carbon Nanotubes." The Journal of Physical Chemistry C 113(23): 10013-10020.

Dzubiella, J. and J. P. Hansen (2005). "Electric-field-controlled water and ion permeation of a hydrophobic nanopore." Journal of Chemical Physics 122(23).

Eschermann, J., Y. Li, et al. (2006). "Self-consistent ion transport simulation in carbon nanotube channels." Journal of Computational Electronics 5(4): 455-457.

Falk, K., F. Sedlmeier, et al. (2010). "Molecular Origin of Fast Water Transport in Carbon Nanotube Membranes: Superlubricity versus Curvature Dependent Friction." Nano Letters 10(10): 4067-4073.

Fedorov, A. S. and A. F. Sadreev (2009). "Ab-initio investigation of thermoactivated directional transport of hydrogen molecules inside narrow carbon nanotubes." physica status solidi (b) 246(11-12): 2598-2601.

Fornasiero, F., H. G. Park, et al. (2008). "Ion exclusion by sub-2-nm carbon nanotube pores." Proceedings of the National Academy of Sciences 105(45): 17250-17255.

Gethard, K., O. Sae-Khow, et al. (2010). "Water Desalination Using Carbon-Nanotube-Enhanced Membrane Distillation." ACS Applied Materials & Interfaces 3(2): 110-114.

Goldsmith, J. and C. C. Martens (2009). "Molecular Dynamics Simulation of Salt Rejection in Model Surface-Modified Nanopores." The Journal of Physical Chemistry Letters 1(2): 528-535.

Gong, X., J. Li, et al. (2010). "A Controllable Molecular Sieve for Na+ and K+ Ions." Journal of the American Chemical Society 132(6): 1873-1877.

Hanasaki, I., A. Nakamura, et al. (2008). "Structure and stability of water chain in a carbon nanotube." Journal of Physics: Condensed Matter 20(1): 015213.

Hanasaki, I. and A. Nakatani (2006). "Flow structure of water in carbon nanotubes: Poiseuille type or plug-like?" The Journal of Chemical Physics 124(14): 144708.

Hata, K., D. N. Futaba, et al. (2004). "Water-assisted highly efficient synthesis of impurity-free single-waited carbon nanotubes." Science 306(5700): 1362-1364.

Hinds, B. J., N. Chopra, et al. (2004). "Aligned multiwalled carbon nanotube membranes." Science 303(5654): 62-65.

Holt, J. K. (2006). "Fast Mass Transport Through Sub-2-Nanometer Carbon Nanotubes." Science 312(5776): 1034-1037.

Holt, J. K., A. Noy, et al. (2004). "Fabrication of a carbon nanotube-embedded silicon nitride membrane for studies of nanometer-scale mass transport." Nano Letters 4(11): 2245-2250.

Hummer, G., J. C. Rasaiah, et al. (2001). "Water conduction through the hydrophobic channel of a carbon nanotube." Nature 414(6860): 188-190.

Jakobtorweihen, S., C. P. Lowe, et al. (2007). "Diffusion of chain molecules and mixtures in carbon nanotubes: The effect of host lattice flexibility and theory of diffusion in the Knudsen regime." The Journal of Chemical Physics 127(2): 024904.

Joseph, S. and N. R. Aluru (2008). "Why Are Carbon Nanotubes Fast Transporters of Water?" Nano Letters 8(2): 452-458.

Kalra, A. (2003). "From The Cover: Osmotic water transport through carbon nanotube membranes." Proceedings of the National Academy of Sciences 100(18): 10175-10180.

Kandah, M. I. and J.-L. Meunier (2007). "Removal of nickel ions from water by multi-walled carbon nanotubes." Journal of Hazardous Materials 146(1-2): 283-288.

Kang, J. W., K. R. Byun, et al. (2004). "Molecular dynamics study on the field effect ion transport in carbon nanotube." Physica E-Low-Dimensional Systems & Nanostructures 24(3-4): 349-354.

Karniadakis, G., A. Beskok, et al. (2005). Microflows and Nanoflows: Fundamentals and Simulation (Interdisciplinary Applied Mathematics), Springer.

Kim, S., J. R. Jinschek, et al. (2007). "Scalable Fabrication of Carbon Nanotube/Polymer Nanocomposite Membranes for High Flux Gas Transport." Nano Letters 7(9): 2806-2811.

Koga, K., G. T. Gao, et al. (2001). "Formation of ordered ice nanotubes inside carbon nanotubes." Nature 412(6849): 802-805.

Kolesnikov, A. I., C. K. Loong, et al. (2006). "Anomalously soft dynamics of water in carbon nanotubes." Physica B: Condensed Matter 385-386(Part 1): 272-274.

Kowalczyk, P., L. Brualla, et al. (2007). "Single-Walled Carbon Nanotubes: Efficient Nanomaterials for Separation and On-Board Vehicle Storage of Hydrogen and Methane Mixture at Room Temperature?" The Journal of Physical Chemistry C 111(13): 5250-5257.

Kyakuno, H., K. Matsuda, et al. (2010). "Global Phase Diagram of Water Confined on the Nanometer Scale." Journal of the Physical Society of Japan 79(8): 083802.

Lai, Z. P., G. Bonilla, et al. (2003). "Microstructural optimization of a zeolite membrane for organic vapor separation." Science 300(5618): 456-460.
Lee, C., C.-H. Choi, et al. (2008). "Structured Surfaces for a Giant Liquid Slip." Physical Review Letters 101(6): 064501.
Lee, C. Y., W. Choi, et al. (2010). "Coherence Resonance in a Single-Walled Carbon Nanotube Ion Channel." Science 329(5997): 1320-1324.
Lei, Y. and Y. Leng (2010). "Force oscillation and phase transition of simple fluids under confinement." Physical Review E 82(4).
Leung, K. and M. Marsman (2007). "Energies of ions in water and nanopores within density functional theory." Journal of Chemical Physics 127(15).
Levinger, N. E. (2002). "Water in Confinement." Science 298(5599): 1722-1723.
Li, J., C. Papadopoulos, et al. (1999). "Highly-ordered carbon nanotube arrays for electronics applications." Applied Physics Letters 75(3): 367-369.
Lin, Y., J. Shiomi, et al. (2009). "Dielectric relaxation of water inside a single-walled carbon nanotube." Physical Review B 80(4).
Loyalka, S. K. and S. A. Hamoodi (1990). "Poiseuille Flow of a Rarefied-Gas in a Cylindrical Tube - Solution of Linearized Boltzmann-Equation." Physics of Fluids a-Fluid Dynamics 2(11): 2061-2065.
Majumder, M., N. Chopra, et al. (2005). "Nanoscale hydrodynamics - Enhanced flow in carbon nanotubes." Nature 438(7064): 44-44.
Majumder, M., N. Chopra, et al. (2005). "Nanoscale hydrodynamics: Enhanced flow in carbon nanotubes (vol 438, pg 44, 2005)." Nature 438(7070): 930-930.
Majumder, M., N. Chopra, et al. (2005). "Effect of Tip Functionalization on Transport through Vertically Oriented Carbon Nanotube Membranes." Journal of the American Chemical Society 127(25): 9062-9070.
MajumderMainak, ChopraNitin, et al. (2005). "Erratum: Nanoscale hydrodynamics: Enhanced flow in carbon nanotubes." Nature 438(7070): 930-930.
Malek, K. and M.-O. Coppens (2003). "Knudsen self- and Fickian diffusion in rough nanoporous media." The Journal of Chemical Physics 119(5): 2801-2811.
Maruyama, S., E. Einarsson, et al. (2005). "Growth process of vertically aligned single-walled carbon nanotubes." Chemical Physics Letters 403(4-6): 320-323.
Mashl, R. J., S. Joseph, et al. (2003). "Anomalously Immobilized Water: A New Water Phase Induced by Confinement in Nanotubes." Nano Letters 3(5): 589-592.
Meyer, E. E. (2005). "Origin of the long-range attraction between surfactant-coated surfaces." Proceedings of the National Academy of Sciences 102(19): 6839-6842.
Mi, W., Y. Lin, et al. (2007). "Vertically aligned carbon nanotube membranes on macroporous alumina supports." Journal of Membrane Science 304(1-2): 1-7.
Miller, S. A., V. Y. Young, et al. (2001). "Electroosmotic Flow in Template-Prepared Carbon Nanotube Membranes." Journal of the American Chemical Society 123(49): 12335-12342.
Miranda, L. D., R. T. Short, et al. (2009). "Direct coupling of a carbon nanotube membrane to a mass spectrometer: Contrasting nanotube and capillary tube introduction systems." Journal of Membrane Science 344(1-2): 26-31.
Naguib, N., H. H. Ye, et al. (2004). "Observation of water confined in nanometer channels of closed carbon nanotubes." Nano Letters 4(11): 2237-2243.
Newsome, D. A. and D. S. Sholl (2006). "Influences of Interfacial Resistances on Gas Transport through Carbon Nanotube Membranes." Nano Letters 6(9): 2150-2153.
Park, H. G. (2007). Mass Transport in Carbon Nanotubes. Mechanical Engineering. Berkeley, University of California Berkeley. Ph.D.

Peter, C. and G. Hummer (2005). "Ion transport through membrane-spanning nanopores studied by molecular dynamics simulations and continuum electrostatics calculations." Biophysical Journal 89(4): 2222-2234.
Porodnov, B. T., P. E. Suetin, et al. (1974). "Experimental investigation of rarefied gas flow in different channels." Journal of Fluid Mechanics 64(03): 417-438.
Pozhar, L. A. (2000). "Structure and dynamics of nanofluids: Theory and simulations to calculate viscosity." Physical Review E 61(2): 1432.
Qiao, Y., G. Cao, et al. (2007). "Effects of Gas Molecules on Nanofluidic Behaviors." Journal of the American Chemical Society 129(8): 2355-2359.
Rasaiah, J. C., S. Garde, et al. (2008). "Water in Nonpolar Confinement: From Nanotubes to Proteins and Beyond *." Annual Review of Physical Chemistry 59(1): 713-740.
Raviv, U. (2002). "Fluidity of Bound Hydration Layers." Science 297(5586): 1540-1543.
Reiter, G., C. Burnham, et al. (2006). "Anomalous Behavior of Proton Zero Point Motion in Water Confined in Carbon Nanotubes." Physical Review Letters 97(24): 247801.
Roy, S., S. Cooper, et al. (2005). "Single component gas transport through 10nm pores: Experimental data and hydrodynamic prediction." Journal of Membrane Science 253(1-2): 209-215.
Sarkar, S., A. K. SenGupta, et al. (2010). "The Donnan Membrane Principle: Opportunities for Sustainable Engineered Processes and Materials." Environmental Science & Technology 44(4): 1161-1166.
Sendner, C., D. Horinek, et al. (2009). "Interfacial Water at Hydrophobic and Hydrophilic Surfaces: Slip, Viscosity, and Diffusion." Langmuir 25(18): 10768-10781.
Shao, Q., J. Zhou, et al. (2009). "Anomalous Hydration Shell Order of Na+ and K+ inside Carbon Nanotubes." Nano Letters 9(3): 989-994.
Shiomi, J., T. Kimura, et al. (2007). "Molecular Dynamics of Ice-Nanotube Formation Inside Carbon Nanotubes." The Journal of Physical Chemistry C 111(33): 12188-12193.
Sholl, D. S. and J. K. Johnson (2006). "Making high-flux membranes with carbon nanotubes." Science 312(5776): 1003-1004.
Skoulidas, A., D. Ackerman, et al. (2002). "Rapid Transport of Gases in Carbon Nanotubes." Physical Review Letters 89(18).
Skoulidas, A. I., D. M. Ackerman, et al. (2002). "Rapid transport of gases in carbon nanotubes." Physical Review Letters 89(18).
Skoulidas, A. I., D. S. Sholl, et al. (2006). "Adsorption and diffusion of carbon dioxide and nitrogen through single-walled carbon nanotube membranes." Journal of Chemical Physics 124(5): -.
Sokhan, V. P., D. Nicholson, et al. (2001). "Fluid flow in nanopores: An examination of hydrodynamic boundary conditions." Journal of Chemical Physics 115(8): 3878-3887.
Sokhan, V. P., D. Nicholson, et al. (2002). "Fluid flow in nanopores: Accurate boundary conditions for carbon nanotubes." The Journal of Chemical Physics 117(18): 8531.
Sokhan, V. P., D. Nicholson, et al. (2004). "Transport properties of nitrogen in single walled carbon nanotubes." The Journal of Chemical Physics 120(8): 3855.
Song, C. and B. Corry (2009). "Intrinsic Ion Selectivity of Narrow Hydrophobic Pores." The Journal of Physical Chemistry B 113(21): 7642-7649.
Steckelmacher, W. (1986). "Knudsen flow 75 years on: the current state of the art for flow of rarefied gases in tubes and systems." Reports on Progress in Physics 49(10): 1083.
Steitz, R., T. Gutberlet, et al. (2003). "Nanobubbles and Their Precursor Layer at the Interface of Water Against a Hydrophobic Substrate." Langmuir 19(6): 2409-2418.

Strano, M. S., W. J. Kim, et al. (2009). "Connecting Single Molecule Electrical Measurements to Ensemble Spectroscopic Properties for Quantification of Single-Walled Carbon Nanotube Separation." Journal of the American Chemical Society 131(9): 3128-+.

Suk, M. E., A. V. Raghunathan, et al. (2008). "Fast reverse osmosis using boron nitride and carbon nanotubes." Applied Physics Letters 92(13).

Takaiwa, D., K. Koga, et al. (2007). "Structures of filled ice nanotubes inside carbon nanotubes." Molecular Simulation 33(1): 127-132.

Thomas, J. A., R. M. Iutzi, et al. (2010). "Thermal conductivity and phonon transport in empty and water-filled carbon nanotubes." Physical Review B 81(4).

Thomas, J. A. and A. J. H. McGaughey (2008). "Reassessing Fast Water Transport Through Carbon Nanotubes." Nano Letters 8(9): 2788-2793.

Thornton, A. W., T. Hilder, et al. (2009). "Predicting gas diffusion regime within pores of different size, shape and composition." Journal of Membrane Science 336(1-2): 101-108.

Tofighy, M. A. and T. Mohammadi (2010). "Salty water desalination using carbon nanotube sheets." Desalination 258(1-3): 182-186.

Verweij, H., M. C. Schillo, et al. (2007). "Fast Mass Transport Through Carbon Nanotube Membranes." Small 3(12): 1996-2004.

Waghe, A., J. C. Rasaiah, et al. (2002). "Filling and emptying kinetics of carbon nanotubes in water." The Journal of Chemical Physics 117(23): 10789.

Walther, J. H., R. Jaffe, et al. (2001). "Carbon Nanotubes in Water: Structural Characteristics and Energetics." The Journal of Physical Chemistry B 105(41): 9980-9987.

Wang, J., Y. Zhu, et al. (2004). "Diameter and helicity effects on static properties of water molecules confined in carbon nanotubes." Physical Chemistry Chemical Physics 6(4): 829-835.

Wang, Y., M. J. Kim, et al. (2005). "Continued Growth of Single-Walled Carbon Nanotubes." Nano Letters 5(6): 997-1002.

Wang, Y. Y., S. Gupta, et al. (2005). "Hollow to bamboolike internal structure transition observed in carbon nanotube films." Journal of Applied Physics 98(1).

Washburn, E. W. (1921). "The dynamics of capillary flow." Physical Review 17(3): 273-283.

Wei, B. Q., R. Vajtai, et al. (2002). "Microfabrication technology: Organized assembly of carbon nanotubes." Nature 416(6880): 495-496.

Whitby, M., L. Cagnon, et al. (2008). "Enhanced Fluid Flow through Nanoscale Carbon Pipes." Nano Letters 8(9): 2632-2637.

Willmott, G. R. and J. L. Tallon (2007). "Measurement of Newtonian fluid slip using a torsional ultrasonic oscillator." Physical Review E 76(6): 066306.

Wu, C. H., U. C. Sou, et al. (2006). "Influence of bicrystal microstructural defects on high-transition-temperature direct-current superconducting quantum interference device." Applied Physics Letters 88(10).

Yang, L. and S. Garde (2007). "Modeling the selective partitioning of cations into negatively charged nanopores in water." The Journal of Chemical Physics 126(8): 084706-084708.

Yu, M., H. H. Funke, et al. (2010). "Gated Ion Transport through Dense Carbon Nanotube Membranes." Journal of the American Chemical Society 132(24): 8285-8290.

Zhao, J., L. Liu, et al. (2009). "Thermal effect on the dynamic infiltration of water into single-walled carbon nanotubes." Physical Review E 80(6).

Zhou, X.-Y. and H.-J. Lu (2007). "The structure and dynamics of water inside armchair carbon nanotube." Chinese Physics 16(2): 335.

19

Carbon Nanotubes-Based Radiation Detectors

Antonio Ambrosio[1] and Carla Aramo[2]
[1]*CNR-SPIN U.O.S. Napoli*
[2]*I.N.F.N., Sezione di Napoli*
Dipartimento di Scienze Fisiche, Università degli Studi di Napoli Federico II
Italy

1. Introduction

Since lots of events in nature are followed by the emission of electromagnetic (e.m.) radiation in certain wavelengths regions, the necessity to observe, measure and analyze such events have driven the development of suitable radiation detectors. Electromagnetic radiation in the visible spectral region and its spectroscopical neighbourhood, Ultraviolet as well as Infrared, are of major interest since produced into a wide range of observable phenomena, from Sun emission to molecules fluorescence. In this field of investigation, for decades, the main detectors have been photomultipliers and silicon based photo-detectors. The firsts are based on the emission of electrons from the photocathode whereas the latter work by exploiting the generation of an electron-hole pair inside silicon junctions.
Today the trend in photo-detectors research is twofold. On one hand the increase of sensitivity is constant in the development process. On the other hand, the extension of the photo-detector sensitivity to other spectral regions different from visible has gained increasing interest. The latter is mainly driven by new finding in the space observations of UV (300-400 nm) fluorescence tracks and the Cherenkov reflected bump of the extensive air shower induced by ultrahigh-energy particles traversing the atmosphere (Ebisuzaki et al., 2009).
For space physics and for astroparticle physics envisaged for the next decade it will be indispensable to develop UV sensitive detectors, high pixelled and with high quantum efficiency, as described in the Cosmic Vision 2015-2025 plan for the ESA science program that cites*: "The proposed mission will be based on large openings and large field-of-view optics with high throughput, as well as on large area, highly pixelled, fast and high detection efficiency near-UV camera*". It is necessary therefore to start the job of developing matrices of detectors, suitable for single photon counting, finely pixelled on great surfaces, with great quantum efficiency and obviously low cost. Detectors that at the moment do not exist.
In accelerators and space physics it is acquiring great importance the identification of particles through Cerenkov detectors like the RICH used in the ALICE experiment at CERN and AMS2 in the space station. Also in this case the Cerenkov light to detect is ultraviolet. In order to reconstruct the intersection ring of the emitted light cone with the sensitive surface of the detector it is necessary a finely pixelled UV detector with high quantum efficiency. Actually the most promising detectors are the SiPM for their fine structure and the ability to achieve amplification factors up to 10^6. However they introduce severe limitations: the

intrinsic noise due to thermal noise that makes problematic their use above 24 °C; the lowest efficiency in the UV because at such wavelengths the photons are not able to penetrate in the deeper part of the silicon structure; the difficulty to realize matrices with dimensions larger than 5 x 5 mm^2; the elevated cost of the device.

Therefore, watching the scenario of the experiments presently discussed for the next quinquennium, the availability of a cheap, wide area, finely pixelled and UV sensitive radiation detector represents a goal of primary importance.

It is a matter of fact, indeed, that recent progress in light detection and photo-generation has been possible thanks to the improvements in nanotechnology. Nano-inprint technology, for example, is already used to produce new generation compact spectrometers and light-sensors.

Among all the new materials employed in nanotechnology applications, in the last twenty years, Carbon Nanotubes has been largely studied due to their characteristics. One of the key features of such nanostructures for electronic and optoelectronic applications is that their metallic or semiconductive character depends on the chirality (for a review about this specific topic, we suggest one of the numerous papers and books available in literature, for example (Saito et al., 1998; Dresselhaus et al., 2001; Jorio at al., 2008)). Furthermore, the presence of a defect in the nanotube walls, e.g. a single atom missing, can result, locally, in the change of the chirality, thus into the variation of the nanotube electronic chracteristics (semiconductor-metal junction) within a structure that is only a few nanometers wide (Hartschuh et al., 2003; Anderson et al., 2007). Handling such defects and structures would open the way to a new, unprecedented miniaturization degree.

Recently, a new technique called Density Gradient Ultracentrifugation DGU have allowed sorting nanotubes with respect to their metallic or semiconductive character, opening the way to new experiments and combinations (Arnold et al., 2006; Hersam, 2008). In the same time, high-resolution microscopy techniques have allowed the characterization of nanotubes down to the investigation of a single one (Odom et al., 2002; Lin et al., 2006). Owing to these considerations, it is reasonable that the CNTs exploitation in nano-electronic devices is going to become real.

So far, Carbon Nanotubes have already been studied as components for nano-structured gas sensors (Salehi-Khojin, 2010) thanks to their gas absorption-desorption characteristics. A couple of experiments have investigated the possibility to exploit CNTs for the realization of light-sensitive devices (Wei et al., 2006; Itkis et al., 2006; Gabor et al., 2009). However, most of the ligh-sensitive applications have been proposed in the photovoltaic research field where nanotubes are used together with other molecules or polymers in different steps of the charge carriers production and collection (Peumans et al. , 2001; Kymakis et al., 2002; Kymakis et al., 2003; Kymakis et al., 2003; Balasubramanian at al. 2004; Battacharyya et al. 2004; Lee, 2005).

In this chapter, the possibility to use carbon nanotubes in designing new radiation detectors will be discussed. First a proof of the possibility to employ electronic signals produced inside CNTs will be given by discussing the condition where nanotubes are deposited on sapphire that is passive both from the optical and the electronic point of view. Then, the possibility to exploit carbon nanotubes in combination with other materials like silicon, will be presented. In this case, the signals obtained are similar to those obtained with commercially available detectors.

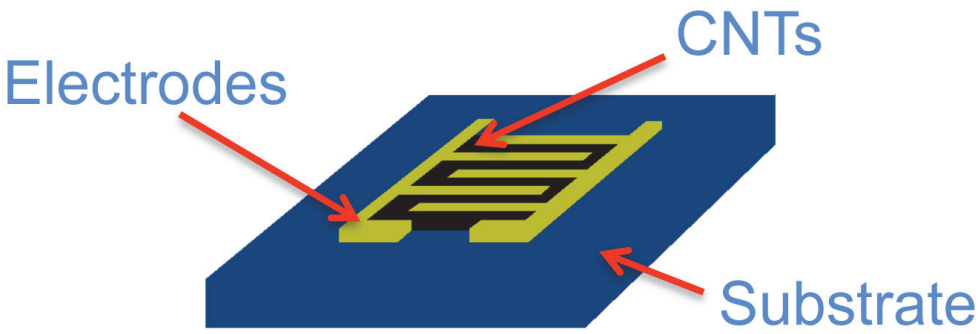

Fig. 1. Sketch of a typical prototype of CNTs-based radiation detector where the nanotubes are grown in between two interdigitated electrodes.

2. Carbon nanotubes detectors

As skectched in figure 1, a possible layout for a CNTs-based prototype detector is that obtained by starting from a suitable substrate (silicon, sapphire or others) whose surface is covered with electrodes. Those electrodes are usually a few microns interdigitated in order to take high the ratio in between the eletrodes distance and the electrodes area. This is a well known configuration, also used in other „sensors", like gas sensors. The electrodes, that are usually made of gold or platinum, are sputtered on the sample surface using masks for area selection.

The substrate with electrodes is then covered with nanotubes. At this step, Carbon nanotubes can be deposited from a solution by drop casting or they can be grown by chemical methods directly on the sample surface. In the first configuration, a web of nanotubes cover the electrodes. This simple preparation allows to use any available CNTs type, commercial, single walled, multi-walled, etc. Instead, in prtotypes resulting from the direct growth of CNTs on the sample surface, nanotubes are usually in between the electrodes only. In fact, in this prototype the deposition technique is the Chemical Vapour Deposition (CVD), a procedure where the nanotubes grow from a catalyst partycle (a few nanometers in size), usually Nichel or Iron, by explulsion of carbon atoms from the saturated particle. In this process, carbon atoms explelled from the particle come from an hydrocarbon gas that fill the atmosphere of the process. The whole process is ussually assisted by substrate heating. The temperature of the substrate can also influence the final CNTs type and distribution. The diffusion of catalyst particles on the metallic electrodes, guarantees the growth of nanotubes in between the electrodes only.

In other configurations instead, CNTs are grown before the electrodes that are then deposited by sputtering on the sample (Coscia, 2009).

Indeed the linear dimensions of this prototypes are usually a few millimeters in size with micro-strip electrodes (about 100 μm wide and 100 μm interspaced). Carbon Nanotubes are then grown by CVD or by solution casting.

About the detectors charatcterization, usually a light beam (often from a laser) shine light onto the sample.

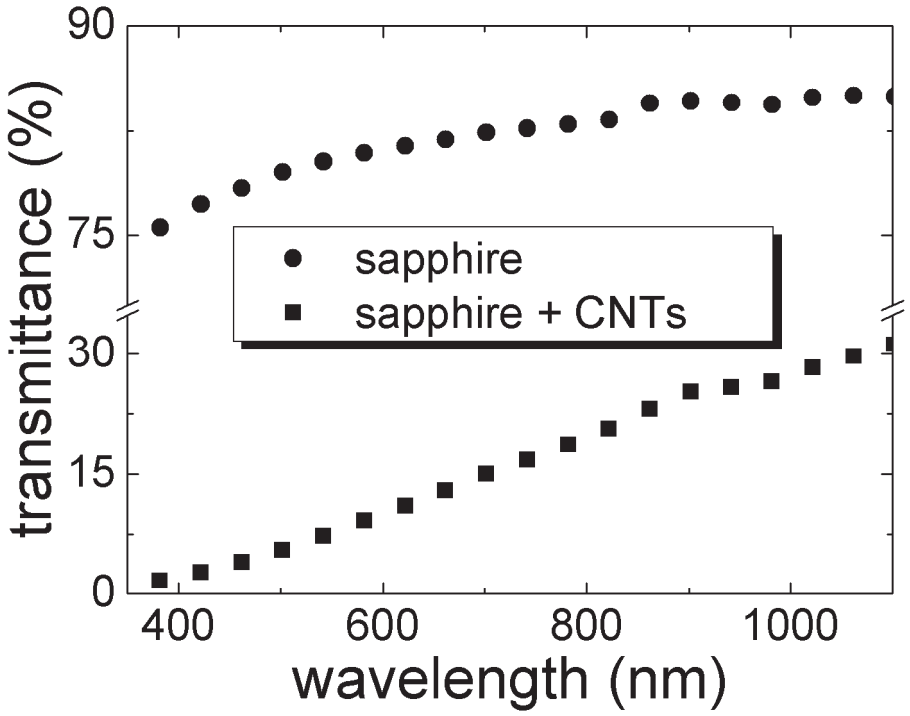

Fig. 2. Optical transmittance of a sapphire substrate and of CNTs grown on a sapphire substrate by means of Chemical Vapour Deposition

In order to collect the charges generated in the CNTs layer, a drain voltage (V_{drain}) is applied to one of the electrodes. The signal from the sample (V_{out}) is then picked up from the other electrode and measured by means of a digital oscilloscope and its internal 50 Ω load resistance (R_{osc}). By naming $I = (V_{out} / R_{osc})$, the current in the equivalent circuit, an equivalent impedance (R_{cnt}) for the sample can be obtained using the relation $V_{drain}/(R_{cnt} + R_{osc}) = V_{out}/R_{osc} = I$.

The possibility to obtain signals from a CNTs carpet is not obvious. For this reason it is worth separating the problem by discussing two configurations. A first one where nanotubes are investigated on a light unsensitive material like sapphire and a second one in which light is used in combination with a light sensitive material, like silicon.

2.1 CNTs on sapphire substrates

The advantage of using substrates like sapphire, that are inactive both from the electrical and optical point of view, allows one to exclude any possible contribution to the collected signals from other than the carbon nanotubes layer.

Figure 2 shows the transmittance, in the visible and near-infrared spectral region, of a Multi-Walled CNTs carpet grown by CVD at 500 °C on a sapphire substrate. The same figure also shows the transmittance of the sapphire substrate only. In accordance with what expected, the contribution to the light absorption from the substrate is negligible with respect to that

from the CNTs. It is evident that the values and shape of the two curves plotted in fugure 2 are quite different especially towards small wavelengths where the spectrum of MWCNTs goes approximately to zero. Sapphire instead appears to be mostly transparent in the wide range investigated, according to reference literature and commercial data sheets. Absorbance values can then be calculated, by definition, as the logarithm of the inverse transmittance. The absorbance spectrum of MWCNTs obtained by subtracting the sapphire absorbance values from the total absorbance values of the sample is shown in Figure 3. The trend of the curve clearly shows higher absorbance for shorter wavelengths, thus for higher photons energy. If the light absorption is thought to be due to charges photo-generation, a similar trend should result also for the dependence of the collected electrical signal from the light wavelength.

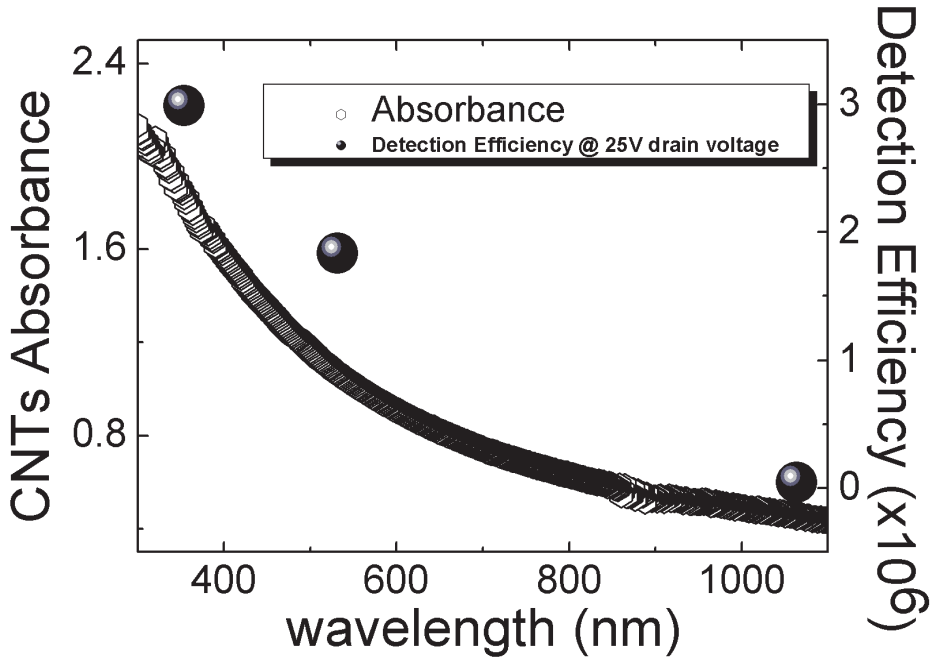

Fig. 3. Absorbance of a CNTs layer, grown by means of CVD technique, together with the detection efficiency of the same layer under a 25V drain voltage.

In the case of reference (Ambrosio A., et al., 2008), for exsample, a pulsed laser beam is generated by means of a Nd:YAG laser, > 10 ns pulse duration, 10 Hz repetition rate. For their study, authors use optical harmonic separators and dielectric mirrors mounted outside of the laser in order to have, time by time, three different beams of adjustable energy and at three different wavelengths, 1064 nm (1.6 mJ energy[1]), 532 nm (0.46 energy[1]) and 355 nm (0.19 mJ energy[1]) (respectively fundamental, second and third harmonic of the neodymium laser). The light pulses hit the sample into a central circular area of about 3 mm in diameter.

[1] average energy per light pulse

This area is selected by means of an adjustable iris so that the exposed sample area is fixed for all the three light wavelengths employed. When laser light is sent onto the sample, a part of the laser beam is also sent to an amplified photodiode producing a trigger signal for the measurement. By integrating the signals, as visualized on the oscilloscope, on the time interval monitored and dividing by the value of the load resistsance, it is possible to estimate the amount of charge involved in the photo-generation process.
By measuring the photo-generated charge amount in experimental configurations like those described above and knowing the energy of the light used to illuminate the sample, it is possible to calculate the detection efficiency as the ratio between the number of collected charges divided by the number of incident photons. In Figure 3 the detection efficiency of the device in the case of drain voltage of 25V in between the electrodse are reported. As it is easy to see, illumination at 355 nm, thus towards UV light, results into higher efficiency values, with respect to other wavelengths.
This result is largely desirable due to the low efficiency of commercial detectors to the UV electromagnetic radiation. Furthermore, as it is evident from what reported in figure 3, the trend of the device efficiency is in agreement with the absorbance characteristics of MWCNTs constituting the sensitive material in the device. Other experiments have confirmed this behaviour by employing both coherent and non-coherent light sources in pulsed as well as continuous illumination regimes (Passacantando et al., 2008; Coscia et al., 2009).
In these experiments, the absence of any photo-electrical response from the substrate guarantees that the signals observed are only due to the nanotube layer.

2.2 CNTs on silicon substrates

The previous device cannot be used as radiation detector due to the dark current of the order of milliamperes. In order to minimize the dark current a different readout configuration has been tested. A sketch of the device is reported in Figure 4a (Ambrosio M., et al., 2010). Both the surfaces of a Si wafer (resistivity 4Ωcm) were covered with a few nanometers thick silicon nitride (Si_3N_4). Two platinum/gold squared electrodes and an extensive Pt/Au back contact were sputtered on the front and rear side of the sample, respectively. Then, carbon nanostructures were grown directly on the front surface by CVD. A 3 nm nickel (Ni) film was thermally evaporated on the substrate. Ni-deposited substrates were introduced into a CVD reactor (base pressure: 10^{-6} Torr) and heated at either 500 or 750°C for 20 min in NH_3 gas at a flow rate of 100sccm. During this period, Si_3N_4 layer prevented nickel diffusion into the silicon wafer so avoiding nickel silicides formation. CNTs were obtained by adding C_2H_2 at a flow rate of
20sccm for 10min at the same temperature of the NH_3 thermal treatment (500 or 750°C). During both the annealing and the CNTs growth, the pressure inside the CVD reactor was kept fixed at 5.5 Torr. [17] Figure 4b and Figure 4c show scanning electron microscopy (SEM) images of the samples synthesized at 500°C and 750°C, respectively. Figure 4b exhibits CNTs very short, bended and characterized by different diameter along the structure.
The average diameter of these nanostructures was of 48±9nm. In Figure 4c, entangled carbon nanotubes (18±7nm in mean diameter), grown as a vertical carpet (Figure 4c, inset), are easily recognizable. High resolution TEM images, not reported here, were also recorded confirming for the former sample the presence of carbon nanofibers and for the latter the formation of MWCNTs.

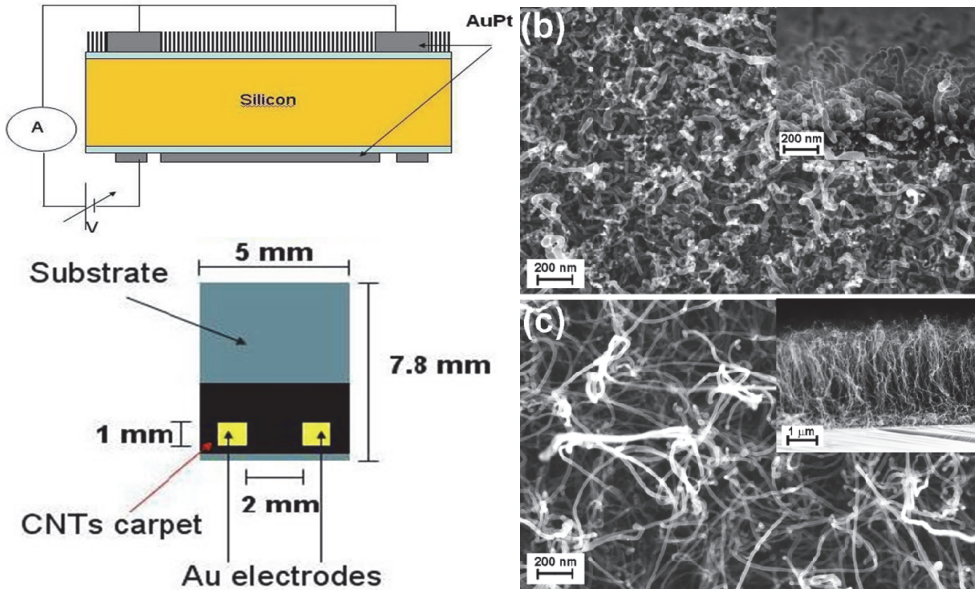

Fig. 4. (a) Section and top view of the multilayer structure constituting the samples. Measurement layout is also depicted. Top and side (inset) SEM view of a CNS sample grown at either 500 (b) or 700°C (c).

Current-voltage measurements were performed at room temperature for the sample at 500 °C. The back contact was grounded, while a potential sweep from negative to positive values of the voltage was applied to one of the Au/Pt front electrodes (see Figure 4a). If the drain voltage is applied to one electrode, and the signal is read on the other a large amount of dark current is drained. When the drain voltage is applied in between the two electrodes in the top side and the electrode on the back of substrate (Figure 4a), no current is expected to be drained due to the insulator layer of Si3N4. The I-V characteristic measured in absence of light (dark current) is reported in Figure 5. Instead the I-V plot, reported in Figure 6, appears similar to that obtained in a metallic-semiconductor junction. Moreover in this configuration the device becomes photosensitive: illuminating CNTs between electrodes, a photocurrent is drained through the silicon substrate proportionally to the intensity of light, and as reported in Figure 7, the photodetection efficiency is about 50% at any beam intensity increasing at lower wavelengths.

The light source is a continuous laser beam, 650 nm wavelength, at different power. It can be seen as the generated signal is typical of a detector: the drained current increases with the drain voltage, up to a voltage value from which the current becomes constant.

This nearly constant current means that all photo-generated carriers have been collected at the electrodes. In the saturation region our device works as an ideal photodetector, in which the output signal depends only on the radiation intensity. Moreover, the proportionality between photocurrent (averaged in the plateau) and light power is linear.

This means that the responsivity of our system, i.e. the slope of the straight fitting lines, is a constant quantity and does not depend on any other parameter, not even the intensity of the incident light. The active role of CNT in the creation of the junction is demonstrated

by the complete absence of signals lighting areas where no CNTs have been grown. Moreover complete absence of photo-signals has been observed in substrates without CNTs. The junction effect becomes evident only after the growth of nanotubes on the silicon substrate.

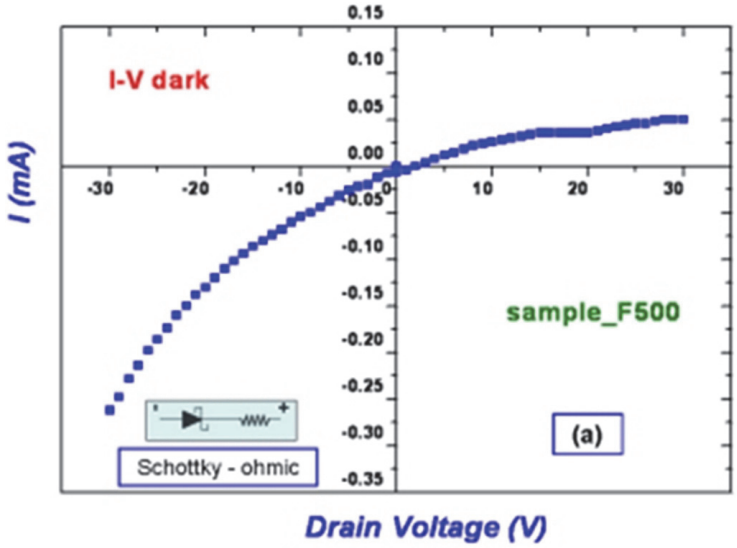

Fig. 5. The I-V dark current in the configuration reported in Fig. 4a.

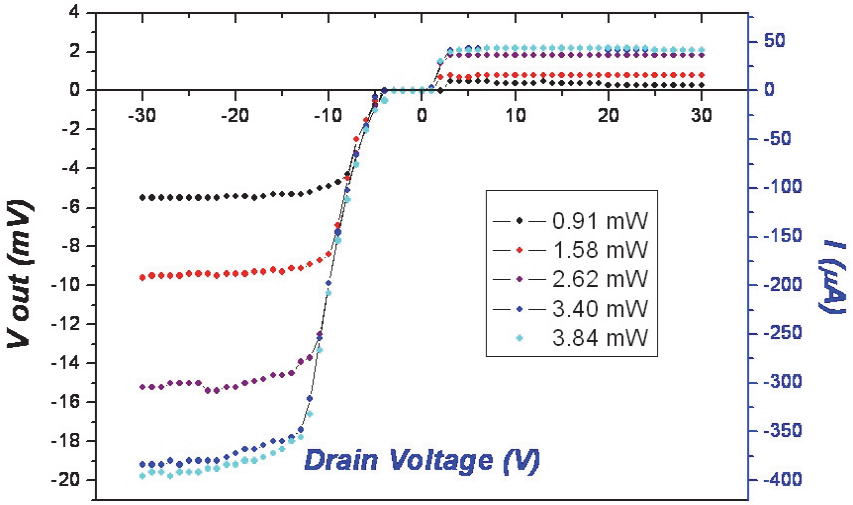

Fig. 6. The I-V plot related a continuous laser beam, 650 nm wavelength, at different power.

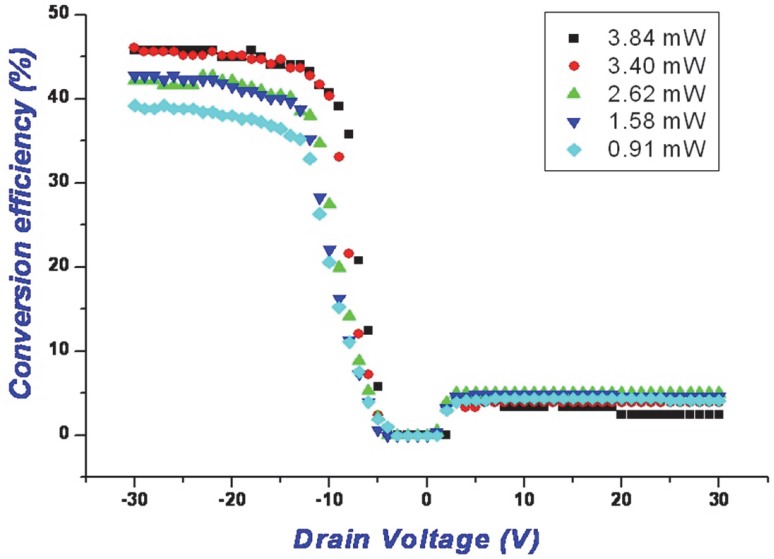

Fig. 7. Convertion efficiency for different illumination intensities.

2.3 Nanolithography and patternization

In order to grow the carbon-nanotubes with a definite pattern, a procedure based on a lift-off process has been developed (Ambrosio M., et al., 2009). "Lift-off" is a method for making metallic patterns on a substrate, especially for those noble metal thin films such as platinum, tantalum, nickel or iron which are difficult to be etched by conventional methods. The general lift-off process is as follow: first a pattern is defined on a substrate using photoresist. A film, usually metallic, is deposited all over the substrate, covering the photoresist and areas in which the photoresist has been cleared. During the actual lifting-off, the photoresist under the film is removed with a solvent, taking the film with it, and leaving only the film which was deposited directly on the substrate. In this way the assisting material layer is exposed (Figure 8a). This layer is then wet-etched so as to undercut the resist (Figure 8b). The metal is subsequently deposited on the wafer, by a thermal evaporation process (Figure 8c). The resist is removed taking away the unwanted metal with it. The assisting layer is then stripped off too, leaving the metal pattern alone (Figure 6d). The dimension of the pattern spread from 10 μm down to 100 nm . This is obtained with an Electron Beam Lithography system.

Figure 9 reports some results obtained with the combined use of nanolithography and Lift-off process. A square matrix of 10x10 pixels 4x4 μm^2 each is shown in Figure 9a; pixels are made of a dense layer of nanotubes, as shown in Figure 9b, and can assume the desired form, for example the INFN logo shown in Figure 9c. The nanotubes grow only where the Lift-off process left the cathalyst: no carbon compounds appear to be present outside the pixel, as shown in Figure 9c.

The possibility to grow CNTs on Silicon substrate according to a defined geometry is very important. As discuss in the previous paragraph, the simple in figure 4a is sensitive to light only where Silicon is covered by CNTs. Outside this area no signal can be detected. This

means that the sample in figure 9a can be considered as a 10 x 10 pixels array. Each pixel is 4 x 4 μm². I this structure is similar to a SiPM, in which pixel cab be at minimum 40 x 40 μm² sized. The pixellization process of CNT on Silicon is very cheap and easy to be obtained, also in complex geometry (figure 9a) permitting the detector to be perfectly coupled with the emitting surface. In particular the CNT distribution can reproduce the complex structure of an optical fibre calorimeter.

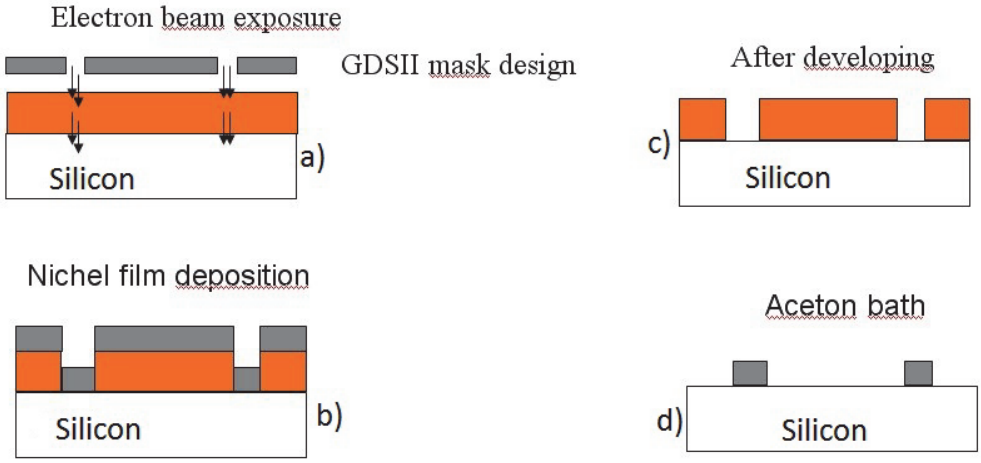

Fig. 8. The Lift-off process used for CNT growth patternization.

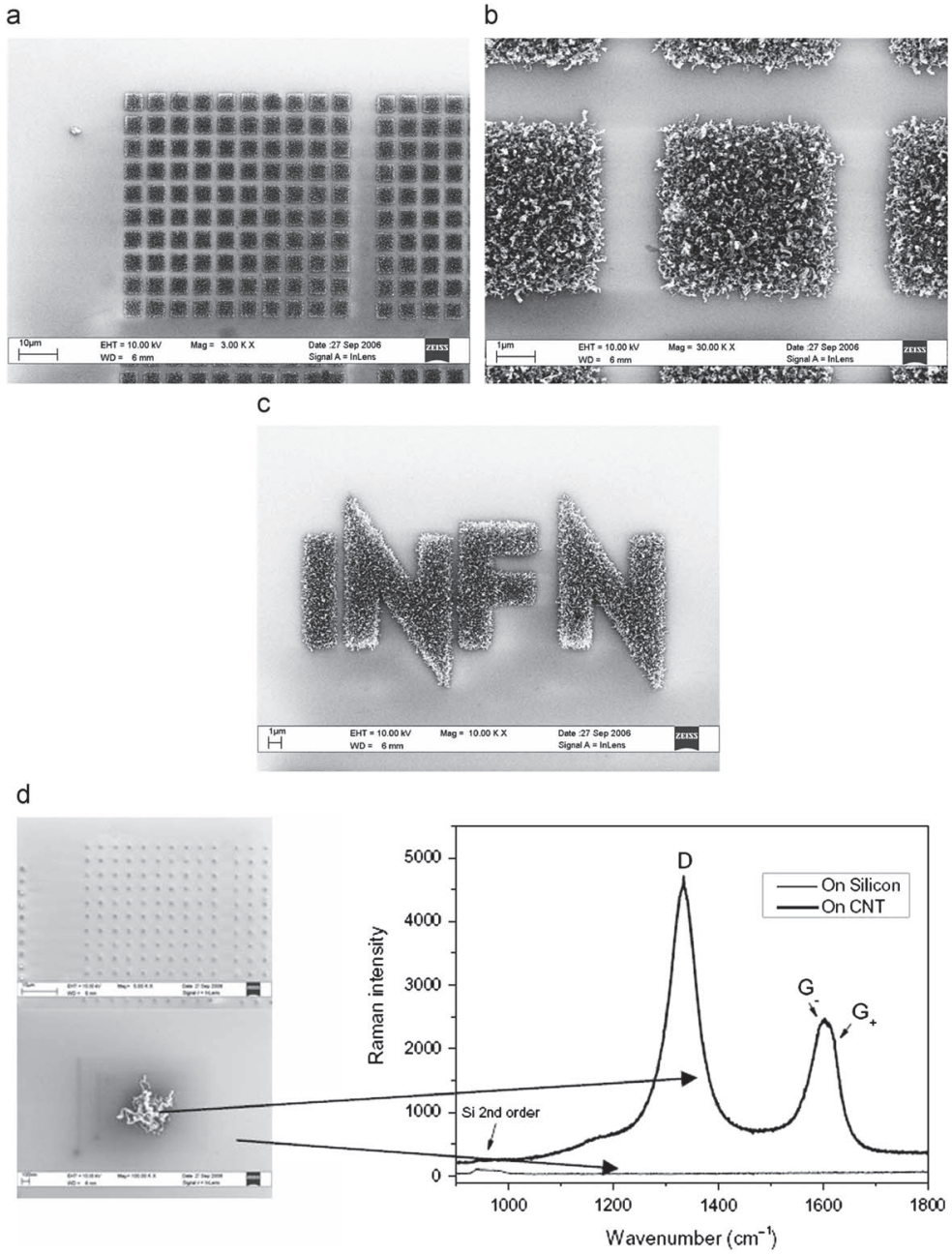

Fig. 9. a) a square CNT matrix of 10x10 pixels 4x4 mm² obtained with a lift-off process on lithographed mask; b) individual 2x2 µm² CNT pixel; c) the INFN logo made of CNT in micrometric scale; d) Raman image of CNT and silicon substrate

3. Electrical analysis of carbon-nanotubes/silicon heterojunctions

A preliminary study of the electrical behavior at varying temperature of the MWCNTs/silicon junctions has been developed (A. Tinti 2010). The device used for this investigation is shown in Fig. 8. The substrate was a 500 μm Si, covered on both its faces by means of a thin silicon nitride (Si_3N_4) layer.
Two platinum/gold squared electrodes were sputtered on the front side of the sample and a similar back contact in the form of a serpentine was realized on the other side. A very thin nickel or iron film was then thermally evaporated on a surface selected area far from the electrodes and turned in cluster by means of thermal heating at two different temperatures of 500 and 740 °C into an ammonia rich chamber. Finally, MWCNTs were deposited by means of the CVD technique.

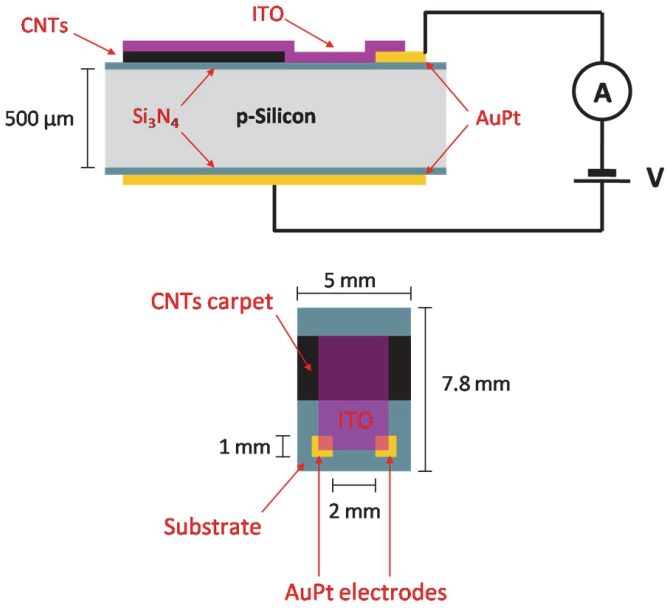

Fig. 10. Section and top views of the multilayer structure constituting the samples. Measurements layout is also depicted.

The last operation in order to make the device suitable to electrical measurements was to accomplish the front contact acting as a bonding among the insulated electrodes and the carpet of CNTs. This was done by sputtering on the sample, through a proper mask, a thin film (100 nm) of indium tin oxide (ITO) which contacted both the Au/Pt pads and the nanotubes (see Fig. 10). ITO is a transparent conductive oxide (TCO) with a direct band gap generally greater than 3.75 eV in energy, depending on the exact composition, and then is an almost completely non-absorbing material in the visible spectral range. An average optical transmittance of 80% was in fact obtained between 400 and 800 nm for such a coating when deposited onto a glass substrate and then analyzed by means of a spectrophotometer. Moreover, Van der Paw technique provided an average electrical resistivity of 8×10^{-4} Ωcm, a sufficiently low value to create a near-ideal ohmic contact at the interface with CNTs.

The experimental layout is also sketched in Fig. 10. A bias voltage ranging from −1 to +1 V in 100 mV steps was applied to the back contact, while the outgoing current signal (in the absence of light) from the sample was picked up from one of the two front electrodes, which are at the same electric potential thanks to the ITO coating, and hence measured. The semi-metallic nature of nanotubes and the p-character of the silicon suggest that the forward polarization of the CNTs/Si heterojunction occurs when a positive voltage is applied to the semiconductor with respect to the tubes. Moreover, by imagining that CNTs grow perpendicular to the substrate with a length in the 10 μm range, we can state that the applied electrical field is parallel to their axis direction. In this way, it can be exploited the ballistic conduction of charge along the tube, a completely quantum-mechanical mechanism rather than a classical electromagnetic one, in order to optimize the drifting process through the junction and then the carrier collection yield by avoiding the signal attenuation. This is also the reason why the Au/Pt electrodes were made externally in respect to the layer of CNTs and a front rather than a lateral contact of ITO was then used as a bridge between them.

During the registration of the dark *I-V* characteristics, the sample was mounted on the cold finger of a closed cycle helium cryostat (CCHC), in order to analyze the device electrical behavior as a function of the temperature, ranging from 150 to 300 K in about 25 K steps and well controlled and measured by a thermistor in contact with the specimen. Figure 11 shows the sets of the current *I* versus voltage *V* plots with varying temperature *T* in dark conditions (no light on the CNTs). The *I-V* characteristics are neither typically ohmic nor semiconductive in shape. They are rather semimetallic curves probably due to the presence of semiconductive tubes and metallic ones at once.

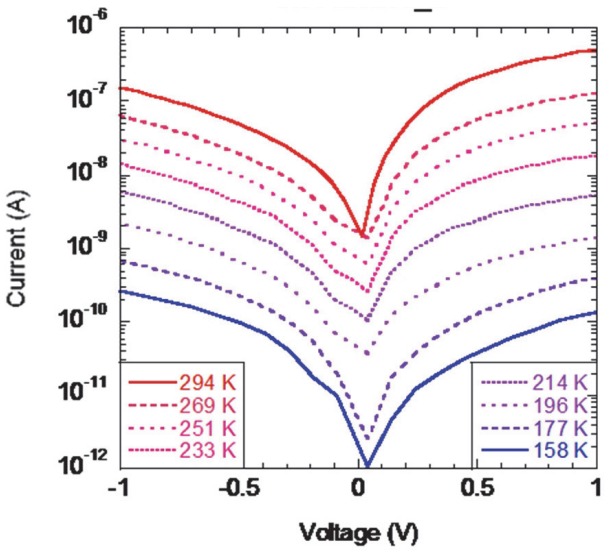

Fig. 11. Set of experimental *I-V* curves as a function of the temperature for the samples investigated. The gradient in the color scale suggests that the higher the temperature (red), the higher the current; on the contrary, the lower the temperature (blue), the lower the current.

The experimental data are not consistent with any activated Arrhenius-type model, in which the current as a function of the temperature for constant voltages would be proportional to the factor $\exp(-E/kT)$, with E the activation energy measured with respect to the valence band. They are instead better fitted by an equation of the form $I_F = I_0\exp(AV_F)$, the subscript F standing for forward, which is typical for currents controlled by tunneling through the energy barrier at the junction. It must be emphasized that different transport processes may be occurring at the barrier of heterojunction, whereas the measured current will usually be dominated by only one of the transport mechanisms. In any case dark current measurements are well explained by assuming that the charge transport is controlled by tunneling at the presumably high defective interface. In particular, among the various tunnel processes, the best results in the fitting of experimental data are obtained by using an equation that describes a multistep crossing of the depletion region by carriers rather than a band-to-band transition. The agreement of the measured values to the theoretical model is very good.

4. Conclusion

Future experiment will impose severe constraints to new detectors for light sensing and photodetection. In particular finely pixelled, large area, cheap and UV sensitive detectors will be necessary for future space and high energy physics experiments. Up to day Silicon detectors play a fundamental role in photodetection, allowing pixellization of the order of ten microns.

The final product is obtained by means of the so called "top-down" process: starting from macroscopic material the matter is manipulated in such a way to obtain many microscopic elements. This process is very critical and expensive, and the final product is a result of a long and sophisticated process.

The modern silicon technology is actually at the border of nanotechnology and quantum effects begin to assume a strong relevance in the new generation of very high integration scale.Nanotechnology instead is based on a reverse approach: nano and micro materials are built by grouping individual atoms and molecules, in a so called "bottom-up" process. The final object dimensions depend on the duration of building process. This new approach is very cheap and relatively easy to do, being mostly a chemical process. This opens a door on the future allowing the extension of the Moore's law in the nanoscale world.

Among the new nanostructured materials, carbon nanotubes appear to be the most promising because of their unique physical and electrical properties. It has been demonstrated that they are characterized by an enhanced sensitivity to the radiation on a wide wavelength range, particularly important in the UV region. This opens the possibility to use this new material to build large area photocathodes sensitive in the fluorescence-Cerenkov light emission region (300 – 400 nm). In addition they can be growth on a surface according to a finely pixelled mask obtained by means of nanolithography processes. Commonly people refer to them claiming to be at the beginning of the post silicon era.

5. Acknowledgment

The authors are grateful to GINT and SINPHONIA Collaboration for the precious help provided . The research leading to these results has received funding from the FP7/ 2007-2013 under grant agreement N. 264098 - MAMA.

6. References

Ambrosio, A. ; Ambrosio, M. ; Ambrosone, G. ; Carillo, V. ; Coscia, U. ; Grossi, V. ; Maddalena, P. ; Passacentando, M. ; Perillo, E. ; Raulo, A. & Santucci, S. (2008). A new radiation detector made of multi-walled carbon nanotubes. *Nuclear Instruments and Methods in Physics Research*, Vol.589, No.3, (March 2008), pp. 398-403, ISSN 0168-9002

Ambrosio, M ; Aramo C.; Ambrosio A. ; Guarino F., Maddalena P. ; Grossi V. ; Passacantando M. ; Santucci S. ; Valentini A. (2009) *Nano-materials and nano-technologies for novel photon detection systems,* Advances in sensors and Interfaces, 2009. IWASI 2009.

Ambrosio, M.; Aramo, C. ;Ambrosio A., ; Guarino F., Maddalena P. ; Grossi V. ; Passacantando M. ; Santucci S. ; Valentini A. (2010) A novel photon detector made of silicon and carbon nanotubes. *Nuclear Instruments and Methods in Physics Research,* Volume 617, Issues 1-3, (May 2010), pp. 378-380, , ISSN 0168-9002

Arnold, M.S.; Green, A.A.; Hulvat, J.F.; Stupp, S.I. & Hersam, M.C. (2006). Sorting carbon nanotubes by electronic structure using density differentiation. *Nature Nanotechnology*, Vol.1, (October 2006), pp. 60-65, ISSN 1748-3387

Anderson, N.; Hartschuh, A. & Novotny, L. (2007). Chirality Changes in Carbon Nanotubes Studied with Near-Field Raman Spectroscopy. *Nano Letters*, Vol.7, No.3, (February 2007), pp. 577-582, ISSN 1530-6984

Balasubramanian, K.; Fan, Y.; Burghard, M.; Kern, K.; Friedrich, M.; Wannek, U. & Mews, A. (2004). Photoelectronic transport imaging of individual semiconducting carbon nanotubes. Applied Physics Letters, Vol.84, No.13, (February 2004), pp. 2400-2402, ISSN 0003-6951

Bhattacharyya, S.; Kymakis, E. & Amaratunga, G.A.J. (2004). Photovoltaic Properties of Dye Functionalized Single-Wall Carbon Nanotube/Conjugated Polymer Devices. *Chemistry of Materials*, Vol.16, No.23, (October 2004), pp. 4819-4823, ISSN 0897-4756

Coscia, U. ; Ambrosone, G. ; Ambrosio, A. ; Ambrosio, M. ; Bussolotti, F. ; Carillo, V. ; Grossi, V. ; Maddalena, P. ; Passacantando, M. ; Perillo, E. ; Raulo, A. & Santucci S. (2009). Photoconductivity of multiwalled CNT deposited by CVD. *Solid State Sciences*, Vol.11, No.10, (October 2009), pp. 1806-1809, ISSN 1293-2558.

Dresselhaus, M.S.; Dresselhaus G & Avouris, P. (2001). *Carbon Nanotubes,* Springer-Verlag, ISBN 978-3-540-41086-7, Berlin

Ebisuzaki T. *et al.* (The JEM-EUSO Collaboration) (2009) Proceedings of the 31th International Cosmic Ray Conference. Lodz, Poland.

Gabor, N.M.; Zhong, Z.; Bosnick, K.; Park, J. & McEuen, P.L. (2009). Extremely Efficient Multiple Electron-Hole Pair Generation in Carbon Nanotube Photodiodes. *Science*, Vol.325, No.5946, (September 1009), pp. 1367-1371, ISSN 1293-2558

Hartschuh, A.; Sanchez, E.J.; Xie, X.S. & Novotny, L. (2003). High-Resolution Near-Field Raman Microscopy of Single-Walled Carbon Nanotubes. *Physical Review Letters*, Vol.90, No.9, (March 2003), pp. 095503-1-3, ISSN 0031-9007

Hersam, M.C. (2008). Progress towards monodisperse single-walled carbon nanotubes. *Nature Nanotechnology*, Vol.3, (July 2008), pp. 387-394, ISSN 1748-3387

Itkis, M.E.; Borondics, F.; Yu, A.; Haddon, R.C.; Bolometric Infrared Photoresponse of Suspended Single-Walled Carbon Nanotube Films. *Science*, Vol.312, No.5772, (April 2006), pp. 413-416, ISSN 0036-8075

Jorio, A.; Dresselhaus, G. & Dresselhaus M.S. (2008). *Carbon Nanotubes, Advanced Topics in the Synthesis, Structure, Properties and Applications,* Springer-Verlag, ISBN 978-3-540-72864-1, Berlin

Kymakis, E. & Amaratunga, G.A.J. (2002). Single-wall carbon nanotube/conjugated polymer photovoltaic devices. *Applied Physics Letters*, Vol.80, No.1, (January 2002), pp. 112-114, ISSN 0003-6951

Kymakis, E.; Alexandrou, I. & Amaratunga, G.A.J. (2003). High open-circuit voltage photovoltaic devices from carbon-nanotube- polymer composites. *Journal of Applied Physics*, Vol.93, No.3, (February 2003), pp. 1764-1768, ISSN 0021-8979

Kymakis, E. & Amaratunga, G.A.J. (2003). Photovoltaic cells based on dye-sensitisation of single-wall carbon nanotubes in a polymer matrix. *Solar Energy Materials & Solar Cells*, Vol.80, No.4, (December 2003), pp. 465-472, ISSN 0927-0248

Lee J.U. (2005). Photovoltaic effect in ideal carbon nanotube diodes. *Applied Physics Letters*, Vol.87, No.7, (August 2005), pp.073101-1-3, ISSN 0003-6951

Lin, M.; Pei, J.; Tan, Y.; Boothroyd, C.; Loh, P.K.; Tok, E.S. & Foo, Y.-L. (2006). Direct Observation of Single-Walled Carbon Nanotube Growth at the Atomistic Scale. *Nano Letters*, Vol.6, No.3, (January 2006), pp. 449-452, ISSN 1530-6984

Odom, T.W.; Huang, J.-L. & Lieber, C.M. (2002). STM studies of single-walled carbon nanotubes. *Journal of Physics: Condensed Matter*, Vol.14, (February 2002), pp. R145-R167, 0953-8984

Passacantando, M. ; Bussolotti, F. ; Grossi, V. ; Snatucci, S. ; Ambrosio, A. ; Ambrosio, M. ; Ambrosone, G. ; Carillo, V. ; Coscia, U. ; Grossi, V. ; Maddalena, P. ; Perillo, E. & Raulo, A. (2008). Photoconductivity in defective carbon nanotubes sheets under ultraviolet-visible-near infrared radiation. *Applied Physics Letters*, Vol.93, No.5, (August 2008), pp. 051911-1-3, ISSN 1077-3118

Peumans, P. & Forrest, S.R. (2001). Very-high-efficiency double-heterostructure copper phthalocyanine/C_{60} photovoltaic cells. *Applied Physics Letters*, Vol.79, No.1, (May 2001), pp. 126-128 , ISSN 0003-6951

Saito, R.; Dresselhaus, G. & Dresselhaus M.S. (1998). *Physical Properties of Carbon Nanotubes,* Imperial College Press, ISBN 978-1-86094-093-4, London

Salehi-Khojin, A.; Lin, K.Y.; Field, C.R.; Masel, R.I. (2010). Nonthermal Current-Stimulated Desorption of Gases from Carbon Nanotubes. Science, Vol.329, No.5997, (September 2010), pp.1327-1330, ISSN 0036-8075

Tinti A.; Righetti F.; Ligonzo T.; Valentini A.; Nappi E.; Ambrosio A.; Ambrosio M.; Aramo C.; Maddalena P.; Castrucci P.; Scarselli M.; De Crescenzi M.; Fiandrini E.; Grossi V.; Santucci S.; Passacantando M. (2010) Electrical analysis of carbon nanostructures/silicon heterojunctions designed for radiation detection, *Nuclear Instruments and Methods in Physics Research Section* A, Vol. 629, Issue 1, (February 2011) pp 377-381, , ISSN 0168-9002

Wei, J.; Sun J.-L.; Zhu J.-L.; Wang, K.; Wang, Z.; Luo, J.; Wu, D. & Cao, A. (2006). Carbon Nanotube Macrobundles for Light Sensing. *Small*, Vol.2, No.8, (August 2006), pp.988-993, ISSN 1613-6829

20

Carbon Nanotubes in Passive RF Applications

Ahmed M. Attiya and Majeed A. Alkanhal
King Saud University, Electrical Engineering Dept
Saudia Arabia

1. Introduction

Carbon nanotubes are characterized by unique electrical properties which make them good candidates for different applications in electronics and electrical engineering. In this chapter we focus mainly on electrical properties of single wall conducting carbon nanotubes in high frequency, electromagnetic waves interaction with carbon nanotubes and the possible passive RF applications. The term "high frequency" here refers to the frequency band from gigahertz to terahertz. This chapter starts from microscopic view by discussing electrodynamics of carbon nanotubes to show the mechanism of time varying electromagnetic field interaction with carbon nanotubes (Slepyan *et al.,* 1999; Slepyan *et al.,* 2008; Mikki & Kishk 2008). Based on these electrodynamics properties, an equivalent dynamic surface conductivity is developed to represent a macroscopic view for the interaction of high frequency electromagnetic fields with carbon nanotubes (Hanson, 2005). This equivalent surface conductivity of carbon nanotube is characterized by complex value with negative imaginary part. This negative imaginary part represents an inductive effect in carbon nanotubes. This inductive effect is due to chiral property of the electric current flow along the carbon nanotube (Slepyan *et al.,* 1998; Miyamoto *et al.* 1999). This inductivity has a significant effect on reducing the wave velocity of electromagnetic wave propagation along carbon nanotube. This wave velocity reduction corresponds to decreasing the wavelength. This property is quite important in passive RF applications like passive circuits and antennas, since the dimensions of these applications depend mainly on the wave length (Slepyan *et al.,* 1999; Slepyan *et al.,* 2008; Attiya, 2009).

Based on the macroscopic surface conductivity of carbon nanotube, the problems of electromagnetic fields interaction with carbon nanotubes can be presented in similar ways to conventional problems related to cylindrical structures with finite surface conductivity. In this way the problem of carbon nanotube antennas can be presented as an electric field integral equation problem which can be treated numerically by method of moments (Hanson, 2005; Hao & Hnason, 2006). Similarly, the problem of surface wave propagation along carbon nanotubes can be presented as a boundary value problem where the difference between the tangential magnetic fields on the two sides of the wall of the carbon nanotube would equal the induced current on the wall of the carbon nanotube. This induced current depends on the tangential electric field along the carbon nanotube and the surface conductivity. This boundary value problem is solved to obtain the field distribution and the complex propagation constants of the surface wave modes propagating along carbon

nanotube (Slepyan *et al.,* 1999; Shuba *et al.* 2007; Slepyan *et al.,* 2008; Attiya, 2009). This surface wave propagation is characterized by highly attenuation coefficient at microwave frequency band. This property makes carbon nanotubes are not suitable for antenna design. However, this high attenuation property is more suitable for other applications which are based on absorbing or attenuating electromagnetic waves like transparent electromagnetic shielding (Xu *et al.,* 2007) and microwave heating in biomedical applications (Mashal *et al.,* 2010). On the other hand, at higher frequency bands in the range above 100 GHz, this attenuation coefficient is decreased and carbon nanotubes can be a good candidate to design low loss antenna structures of much smaller size compared with operating free space wave length (Huang *et al.* 2008 & Attiya, 2009).

Another common approach for simulating electromagnetic wave propagation along carbon nanotube is based on electron fluid model (Burke, 2002; Chiariello *et al.,* 2006a; Miano & Villone 2006). This model is more suitable for simulating transmission line sections of carbon nanotubes. In this case the inductive effect of current flow along the carbon nanotube transmission line is modeled as an additional kinetic inductance in the equivalent circuit model of this transmission line (Burke, 2002; Chiariello *et al.,* 2006b; Miano & Villone 2006; Maffuci *et al.* 2008; Maffuci *et al.* 2009). This kinetic inductance has much greater value than the conventional magnetic inductance of conventional transmission lines. This increase in the total inductance introduces two main effects; decreasing the wave velocity along the line and increasing the characteristic impedance of the line. To improve the properties of carbon nanotube transmission lines, bundles of carbon nanotube are used instead of a single carbon nanotube (Plombon *et al.,* 2007; Rutherglen *et al.* 2008). Extensive studies are presented in literature about the possibility of using carbon nanotube bundles as interconnects in high speed integrated circuits (Massoud & Nieuwoudt, 2006; Naeemi & Meindl, 2009).

Recently, another new approach is discussed for solving the interaction between Maxwell's equation and Schrödinger equation numerically by using finite difference method to obtain electromagnetic field interaction with nanodevices like those which are based on carbon nanotubes (Pierantoni *et al.;* 2008, Pierantoni *et al.;* 2009 & Ahmed *et al.*; 2010). This method is based on space-time discretization. The electromagnetic source is modeled by means of time dependent vector and scalar potentials which are added to the quantum potential profile of the carbon nanotube. Then Schrödinger equation is solved by using a finite difference scheme to obtain the wave equation of electron flow along the carbon nanotube.

The aim of the present chapter is to introduce to the reader an updated view for the problems of electromagnetic field interaction with carbon nanotube with emphasis on the possible passive RF applications. Section 2 presents the electrodynamics of carbon nanotube and the concept of equivalent macroscopic surface conductivity. Section 3 presents the electron fluid model of carbon nanotube and how it can be used to obtain equivalent circuit parameters of carbon nanotube transmission lines. Section 4 presents finite difference time domain method as numerical technique for studying electromagnetic interaction with carbon nanotubes. Section 5 presents detailed analysis of surface wave propagation along carbon nanotubes. Section 6 introduces the electric field integral equation formulation of carbon nanotube antenna and presents sample results for this problem. Section 7 discusses the possibility of using carbon nanotubes in some passive RF circuits. Finally, Section 8 introduces some possible applications of carbon nanotubes based on their absorbing properties in microwave frequencies.

2. Dynamic conductivity of carbon nanotubes

Dynamic conductivity of a carbon nanotube represents a macroscopic quantity relating the disturbance of electron flow along the nanotube due to an incremental temporal variation in the applied electric field along it. For conventional carbon nanotube structures, the length of the nanotube is much greater than its circumference. Thus, for most practical cases, it is assumed that the equivalent current along the surface of the nanotube is transversely symmetric and parallel to the axis of the nanotube. In the following analysis the geometry of the nanotube is assumed to be presented in cylindrical coordinate system, where the axis of the nanotube lies along the *z*-axis. Thus, the proposed dynamic conductivity in this case is the relation between the surface current density J_z and the applied electric field E_z.
The applied field is presented as a time harmonic propagating wave along the axis of the nanotube as follows:

$$E_z(z,t) = \mathrm{Re}\left(E_z^0 e^{j\omega t - \gamma z}\right) \tag{1}$$

where E_z^0 is the amplitude of the incident field, ω is the angular frequency and γ is the complex propagation constant along the nanotube. This complex propagation constant is discussed in detail in Section 5. However, in the present case, the dependence of the electric field on *z* can be assumed to be constant by taking the limit where an incremental length of the nanotube is considered. Thus, for a very small part of the nanotube, the incident field is assumed to be $E_z(t) = \mathrm{Re}\left(E_z^0 e^{j\omega t}\right)$.
This applied electric field introduces a disturbance in the electron distribution function along the nanotube. At equilibrium, the electron distribution function is given by:

$$F(\mathbf{p}) = 1/\left[1 + \exp\left(\mathrm{E}(\mathbf{p})/k_B T\right)\right] \tag{2}$$

where $\mathbf{p} = p_z \mathbf{a}_z + p_\varphi \mathbf{a}_\varphi$ is the electron's two-dimensional quasi-momentum, k_B is Boltzman constant, T is the absolute temperature and $\mathrm{E}(\mathbf{p})$ is the electron energy with respect to the Fermi level in the lattice of the carbon nanotube. By applying an axial time harmonic electric field on the nanotube, this distribution function along an incremental length is modified as follows:

$$f(\mathbf{p},t) = F(\mathbf{p}) + \mathrm{Re}\left(\delta f\, e^{j\omega t}\right) \tag{3}$$

This dynamic distribution function is governed by Boltzman kinetic equation (Dressel & Grüner, 2003). By taking into consideration that the problem is transversely symmetric, the applied field is only along the axis of the nanotube one can obtain Boltzman kinetic equation for the carbon nanotube as follows:

$$\frac{\partial f}{\partial t} + eE_z \frac{\partial f}{\partial p_z} + \mathrm{v}_z \frac{\partial f}{\partial z} = \frac{1}{\tau}\left(F - f\right) \tag{4}$$

where τ is the electron relaxation time in the lattice of the carbon nanotube, $\mathrm{v}_z = \partial \mathrm{E}(\mathbf{p})/\partial p_z$ is axial electron velocity and $\mathrm{E}(\mathbf{p})$ is the electron energy function. This relaxation time is nearly 3 ps in carbon nanotube (Hanson 2006). By applying the time harmonic electric field

and the dynamic distribution function of Equation (3) into Equation (4), one can obtain the incremental disturbance in the distribution function as

$$\delta f = \frac{jeE_z^0}{\omega - j\nu}\frac{\partial F}{\partial p_z} \tag{5}$$

where $v = 1/\tau$ is the relaxation frequency and e is the electron charge. The amplitude of the time harmonic current density along the surface of the nanotube can be obtained by using this disturbance function in the electron distribution function as follows:

$$J_z^0 = \frac{2e}{h^2}\iint_{1^{st}\mathrm{BZ}} \mathrm{v}_z \delta f \, dp_z dp_\phi \tag{6}$$

where h is Planck's constant. The range of integration in Equation (6) refers to the first Brillouion zone of the carbon nanotube lattice. By inserting Equation (5) into Equation (6), one can obtain a linear relation between the amplitude of the incident time harmonic electric field and the resulting surface current density as follows:

$$J_z^0 = \sigma_{zz} E_z^0 \tag{7}$$

where the equivalent axial conductivity σ_{zz} is given by

$$\sigma_{zz} = \frac{2e^2}{h^2}\frac{j}{\omega - j\nu}\iint_{1^{st}\mathrm{BZ}} \frac{\partial F(\mathbf{p})}{\partial p_z}\frac{\partial \mathrm{E}(\mathbf{p})}{\partial p_z} dp_z dp_\phi = \frac{2e^2}{h^2}\frac{j}{\omega - j\nu}\iint_{1^{st}\mathrm{BZ}} \frac{\partial F}{\partial \mathrm{E}}\left(\frac{\partial \mathrm{E}(\mathbf{p})}{\partial p_z}\right)^2 dp_z dp_\phi \tag{8}$$

It should be noted that the azimuth momentum p_ϕ has discrete values in nanotube since electron energy in this case is a periodic function of ϕ. Thus, the double integration in Equation (8) is converted into a finite series of single finite integration.

The key difference between the conductivities of the different types of the carbon nanotube lies in the corresponding electron energy function E(**p**). This electron energy function depends mainly on the chiral vector of the carbon nanotube. Each chiral vector is a combination of integer multiplications factors, *m* and *n*, of the two basis lattice vector for a graphite sheet. For a zigzag carbon nanotube, where the indices of the chiral vector of the carbon nanotube lattice are $m \neq 0$ and $n = 0$ and, The electron energy function is given by:

$$\mathrm{E}_{zigzag}(\mathbf{p}) = \pm\gamma_0\sqrt{1 + 4\cos\left(\frac{3bp_z}{h/\pi}\right)\cos\left(\frac{\sqrt{3}bp_\phi}{h/\pi}\right) + 4\cos^2\left(\frac{\sqrt{3}bp_\phi}{h/\pi}\right)} \tag{9-a}$$

where $b = 1.42\,\mathring{\mathrm{A}}$ is the interatomic distance in a graphite sheet, $\gamma_0 \approx 2.7 - 3.0\,\mathrm{eV}$ is the characteristic energy of the graphene lattice and the azimuth momentum in this case is given by:

$$p_\phi = hs/\left(\sqrt{3}mb\right), \qquad s = 1,2,3,.....,m \tag{9-b}$$

For the case of an armchair carbon nanotube where the indices of the chiral vector are equal, m=n, the electron energy function is given by:

$$E_{armchair}(\mathbf{p}) = \pm\gamma_0\sqrt{1+4\cos\left(\frac{3bp_\phi}{h/\pi}\right)\cos\left(\frac{\sqrt{3}bp_z}{h/\pi}\right)+4\cos^2\left(\frac{\sqrt{3}bp_z}{h/\pi}\right)} \tag{10-a}$$

where the azimuth momentum in this case is given by:

$$p_\phi = hs/(3mb), \qquad s = 1,2,3,.....,m \tag{10-b}$$

By inserting Equations (9) and (10) into Equation (8) and evaluating the required integration one can obtain the axial conductivity for both zigzag and armchair carbon nanotubes. For the cases of small values of m (where m<60), these integrals can be evaluated approximately in closed forms. Zigzag carbon nanotubes have conducting properties for values of m which are integer multiple of three. In this case, the dynamic conductivity of zigzag carbon nanotube is given by:

$$\sigma_{zz\_zigzag} \approx -j\frac{8\pi\sqrt{3}e^2\gamma_0}{mh^2(\omega - j\nu)}, \qquad m = 3N, n = 0 \tag{11-a}$$

On the other hand, armchair carbon nanotubes are always conductor for all values of m. The dynamic conductivity of armchair carbon nanotube is given by:

$$\sigma_{zz\_armchair} \approx -j\frac{8\pi e^2\gamma_0}{mh^2(\omega - j\nu)}, \quad m = n \tag{11-b}$$

For a chiral carbon nanotube where $m \neq n$ and $n \neq 0$, the carbon nanotube is conducting if $2m + n = 3N$ where N is an integer value. In this case the dynamic conductivity of the carbon nanotube is given by:

$$\sigma_{zz\_chiral} \approx -j\frac{8\pi\sqrt{3}e^2\gamma_0}{h^2\sqrt{m^2+mn+n^2}(\omega - j\nu)}, \qquad 2m + n = 3N \tag{11-c}$$

Equation (11) represents the dynamic conductivity for the different types of conducting carbon nanotubes. It should be noted that this conductivity corresponds to a surface conductivity. Thus the unit here is Siemens. It can be noted that these dynamic conductivities are complex values of negative imaginary part while for conventional conductor the conductivity is usually a real part. This negative imaginary part in the conductivity of carbon nanotube corresponds to an additional inductive effect in the mechanism of the electron current flow along it. This inductive effect introduces slow wave propagation along the carbon nanotube as it is discussed in the following section. This slow wave property corresponds to a decrease in the wavelength along the carbon nanotube. Since the dimensions of RF circuits and antennas depend on the electrical length, this reduction in wave velocity along the carbon nanotube is expected to be quite useful for size reductions of RF circuits and antennas.

For the sake of comparison (Hanson 2005) introduced the equivalent surface conductivity of a hollow copper nanotube as:

$$\sigma_{2d\_cu}(\omega) = -j\frac{e^2 N_{e\_cu}^{2d}}{m_e(\omega - jv_{cu})} \tag{12}$$

where $N_{e\_cu}^{2d} \approx 1.9271\times10^{19}\,\text{electrons/m}^2$ is the surface electron density and $m_e = 9.1\times10^{-31}$ kg is the mass of the electron and $v_{cu} = 41.667$ THz is the electron relaxation frequency of copper. Figure 1 shows a comparison between the dynamic conductivity of armchair carbon nanotubes for different values of *m*. It can be noted that the conductivity of the carbon nanotube decrease by increasing *m*. The imaginary part of the conductivity is zero at dc and it has a beak value around 50 GHz. The real part of the conductivity is decreasing by increasing the operating frequency.

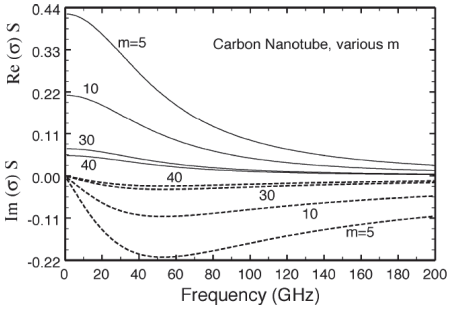

Fig. 1. Dynamic conductivity of armchair carbon nanotube for various *m* values. Solid lines are $\text{Re}(\sigma)$; dashed lines are $\text{Im}(\sigma)$. (Hanson 2005).

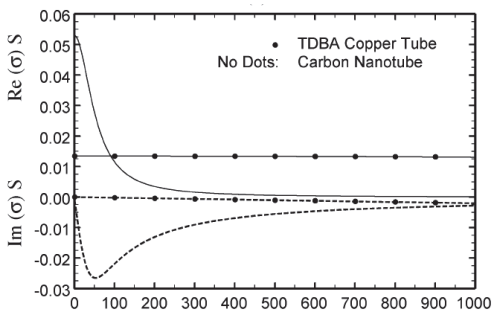

Fig. 2. Comparison between the conductivity of an armchair carbon nanotube of *m* = 40 and the conductivity of an infinitely thin copper tube of the same radius (2.712 nm) (Hanson 2005)

Figure 2 shows a comparison between the conductivity of an armchair carbon nanotube of *m* = 40 with the surface conductivity of a hollow copper tube of the same radius. It can be noted that the imaginary part of the copper conductivity is negligible from dc up to 1 THz. Below 100 GHz, the real part of the conductivity of carbon nanotube is greater the conductivity of copper. However, at higher frequencies both the real and imaginary parts of the conductivity saturate at much smaller values.

3. Electron fluid model of carbon nanotube transmission line

In this section electron fluid model is presented as an alternative representation to describe the linear response of a single wall metallic carbon nanotube to an applied electromagnetic field. This method is based on presenting the problem in the classical form of moving point charges in electric field with using appropriate effective mass for the moving electrons to include the effect of the carbon nanotube lattice. The nanotube is modeled as a continuous infinitesimally thin cylinder shell S of radius r_c and length l. The cylinder is oriented along the z-axis as shown in Figure 3. In thermodynamic equilibrium the π-electrons are distributed uniformly where the applied electromagnetic field perturbs this equilibrium distribution of the π-electrons.

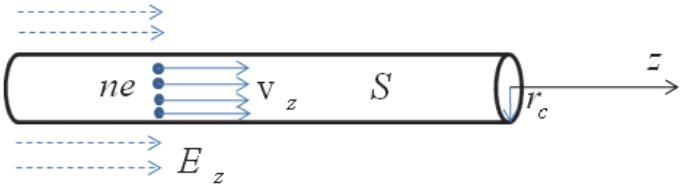

Fig. 3. Carbon nanotube geometry

The collective motion of the perturbed π -electrons is modeled by considering them as a charged fluid. Assuming that $\mathrm{v}_z(\mathbf{r}_s,t)$ is the mean velocity of the electron fluid, where $\mathbf{r}_s$ is the position vector of an arbitrary point on the surface S; $n = n_0 + \delta n(\mathbf{r}_s;t)$ is the surface number density of the electron fluid, where n_0 is the equilibrium value; $p = p_0 + \delta p(\mathbf{r}_s;t)$ *is* the "two-dimensional" pressure of the electron fluid, where p_0 is the equilibrium value. The incremental pressure perturbation is related to the incremental electron density perturbation by the relation $\delta p = m_{eff} c_s^2 \delta n$ where c_s is the thermodynamic speed of sound of the electron fluid if it is neutral and m_{eff} is the mean effective mass of the π -electrons. This thermodynamic speed equals nearly electron Fermi velocity $c_s \approx v_F = 3\pi\gamma_0 b / h \approx 8\times 10^5 m/s$ The motion of π -electron fluid follows the law of momentum conservation which can be presented in the present case as

$$n_0 m_{eff} \frac{\partial \mathrm{v}_z}{\partial t} + v n_0 m_{eff} \mathrm{v}_z + \frac{\partial \delta p}{\partial z} = n_0 e E_z \tag{13}$$

This momentum conservation equation can be presented in terms of the longitudinal current $I_z = 2\pi r_c e n \mathrm{v}_z$ and the surface charge density $q = 2\pi r_c e n$ as follows

$$\frac{\partial I_z}{\partial t} + v I_z + c_s^2 \frac{\partial q}{\partial z} = \frac{2\pi r_c n_0 e^2}{m_{eff}} E_z \tag{14}$$

The parameter n_0 / m_{eff} takes into account the influence of the atomic crystal field. This parameter is obtained for the case of a conducting armchair carbon nanotube by using semiclassical model based on Boltzmann equation as $n_0 / m_{eff} \approx 4 v_F / \pi h r_c$.
This representation corresponds to an equivalent distributed series RL per unit length with shunt quantum capacitance per unite length as shown in Figure 4, where

$$E_z = L_k \frac{\partial I_z}{\partial t} + RI_z + \frac{1}{C_q}\frac{\partial q}{\partial z} \tag{15}$$

The elements of this equivalent circuit are the kinetic inductance per unit length $L_k = h/8e^2 v_F$, the quantum capacitance per unit length $C_q = 8e^2/hv_F$ and the ohmic resistance per unit length $R = vh/8e^2 v_F$ respectively. Typical values of kinetic inductance and quantum capacitance are $L_K = 4\text{nH}/\mu\text{m}$ and $C_Q = 400a\text{F}/\mu\text{m}$ respectively.

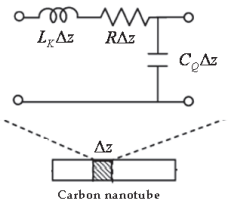

Fig. 4. Circuit model for electron flow along carbon nanotube

It is interesting to note that the series elements of this equivalent distributed circuit of carbon nanotube can be directly obtained by using the equivalent surface conductivity of armchair carbon nanotube which is discussed in the previous section as follows:

$$Z_s = \frac{1}{2\pi r_c \sigma_{zz}} = R + j\omega L_k \tag{16}$$

However, the parallel quantum capacitance element cannot be obtained directly from this surface impedance since we neglected the longitudinal derivative of the electron distribution function in the derivation of the equivalent surface conductance. It would be shown in the following discussion that the wave propagation on carbon nanotube is mainly dominated by the kinetic inductance and the loss resistance. Thus, the approximation used in deriving surface conductance does not have a significant effect on studying electromagnetic wave propagation along carbon nanotube.

For the case of a carbon nanotube transmission line above a PEC ground plane as shown in Figure 5, the equivalent distributed circuit would be a combination of the equivalent circuit for electron current flow along the carbon nanotube and the conventional distributed transmission line circuit which is based on electrostatic capacitance and magnetostatic inductance of the transmission line structure. In the present case the distributed elements of the equivalent circuit of the transmission line per unit length are

$$L_M = (\mu_0/2\pi)\ln(2d/r_c) \tag{17-a}$$

$$C_E = 2\pi\varepsilon_0\varepsilon_r / \ln(2d/r_c) \tag{17-b}$$

where d is the separation distance between the carbon nanotube line and the ground plane and ε_r is the relative permittivity of the supporting substrate. A typical value of substrate thickness is between $100\,\text{Å}$ and $1\,\mu m$ (Burke 2002) and Silicon dioxide substrate has a dielectric constant $\varepsilon_r = 4$. For a Silicon dioxide substrate of $0.2\ \mu m$ thickness, typical values

of single wall carbon nanotube transmission line equivalent circuit parameters would be $C_{ES} \approx 50a\text{F}/\mu\text{m}$, and $L_M \approx 1\text{pH}/\mu\text{m}$.

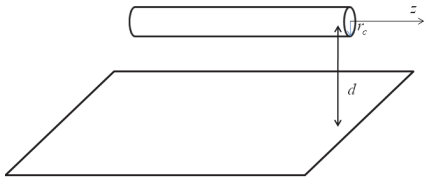

Fig. 5. Carbon nanotube transmission line above a PEC ground plane

In this case the effective inductance and resistance of the equivalent distributed circuit of the carbon nanotube transmission line above a ground plane are given by

$$L_{eff} = \left(L_M + L_k\right) / \left(1 + C_E / C_Q\right) \tag{18-a}$$

$$R_{eff} = R / \left(1 + C_E / C_Q\right) \tag{18-b}$$

while the effective capacitance in this case is the conventional electrostatic capacitance C_E . In addition to this equivalent distributed circuit, two additional contact resistances should be included at the two ends of the equivalent circuit of the carbon nanotube transmission line. The value of this contact resistance is given by $R_c = h / 8e^2$.

By comparing these values, it can be noted that the kinetic inductance is much larger than the magnetostatic inductance of transmission line section where the ratio of $L_k / L_M \approx 4 \times 10^3$. This means that the kinetic inductance has the dominant inductive effect on the equivalent distributed circuit. On the other hand, the quantum capacitance is nearly of the same order of the electrostatic capacitance of the transmission line section. This property has two main effects on electromagnetic wave propagation along the carbon nanotube transmission line; slow wave propagation and high characteristic impedance. The complex propagation constant, phase velocity and characteristic impedance in this case are given by:

$$\gamma = \alpha + j\beta = \sqrt{j\omega C_E \left(R_{eff} + j\omega L_{eff}\right)} \tag{19-a}$$

$$\lim_{R_{eff} << \omega L_{eff}} v_p = \lim_{R_{eff} << \omega L_{eff}} \frac{\omega}{\sqrt{\frac{1}{2}\left(\omega^2 C_E L_{eff} + \sqrt{\omega^4 C_E^2 L_{eff}^2 + \omega^2 C_E^2 R_{eff}^2}\right)}} \approx \sqrt{1 / L_{eff} C_E} \tag{19-2}$$

$$Z_c = \sqrt{\left(R_{eff} + j\omega L_{eff}\right) / \; j\omega C_E} \tag{19-c}$$

The phase velocity in this case is nearly of the same order of Fermi velocity v_F which is nearly two-order less than free space light speed. This means that the wavelength along carbon nanotube transmission line is nearly two-order less than conventional transmission

lines. This property has a significant importance in RF applications since the dimensions of passive circuits like filters, couplers and power dividers are comparable with operating wave length. However, these additional inductance and capacitance introduce high characteristic impedance of order 12.5 k Ω. Recently, parallel carbon nanotubes and carbon nanotube bundle have been introduced to overcome this disadvantage. The effective distributed elements of the equivalent circuit for a carbon nanotube bundle are simply the parallel combination of the circuit for a single carbon nanotube. Thus, both the effective inductance and resistance are divided by N and the effective quantum capacitance is multiplied by a factor N where N is the number of the nanotubes in the bundle. Different experimental results have shown that using parallel carbon nanotube decreases both the DC and RF impedance. However, it increases the wave velocity and subsequently the wave length. Thus, a compromise between the required wave velocity and characteristic impedance should be considered to select the appropriate number of carbon nanotubes in the bundle. On the other hand, the attenuation coefficient has a significant effect at the operating frequencies less than electron relaxation frequency where $\omega < R_{eff} / L_{eff} = \nu$. Thus at lower frequency band below relaxation frequency, carbon nanotube presents a good candidate for an absorbing structure more than a guiding structure.

4. Finite difference analysis of coupled Maxwell-Schrödinger equations

In this section we present another approach which is useful to study electromagnetic interaction with nanodevices like carbon nanotubes. This approach is based on coupling Schrödinger equation which describes the motion of charged particles along the nanodevice with Maxwell's equations which describe the electromagnetic waves in the region of the nanodevice. Both Schrödinger and Maxwell's equations can be presented as partial differential equations which can be solved numerically by using finite difference scheme based on specific sources and boundary conditions. This approach is quite useful to study electromagnetic field interaction with short nanotubes of length less than 100 nm where the electron transport is nearly ballistic.

The quantum motion of electrons along a nanodevice can be presented by Schrödinger equation as follows:

$$j\frac{h}{2\pi}\frac{\partial\psi(\mathbf{r},t)}{\partial t}=\left(-\frac{h^2}{8\pi^2 m}\nabla^2+V(\mathbf{r})\right)\psi(\mathbf{r},t) \tag{20}$$

where $\psi(\mathbf{r},t)$ is the complex state variable of the electron on the nanodevice and $V(\mathbf{r})$ is the static potential along this nanodevice. The key difference between different nanodevices lies in this static potential. In the presence of time-varying electromagnetic fields, Schrödinger equation is modified as follows:

$$\begin{aligned} j\frac{h}{2\pi}\frac{\partial\psi(\mathbf{r},t)}{\partial t}=\frac{1}{2m}\Bigg(&-\frac{h^2}{4\pi^2}\nabla^2\psi(\mathbf{r},t)-j\frac{he}{2\pi}\nabla\cdot\left(\mathbf{A}(\mathbf{r},t)\psi(\mathbf{r},t)\right)\\ &-j\frac{he}{2\pi}\mathbf{A}(\mathbf{r},t)\cdot\nabla\psi(\mathbf{r},t)+e^2\,|\,\mathbf{A}(\mathbf{r},t)|^2\,\psi(\mathbf{r},t)\Bigg)\\ &+\left(e\phi(\mathbf{r},t)\psi(\mathbf{r},t)+V(\mathbf{r})\psi(\mathbf{r},t)\right)\end{aligned} \tag{21}$$

where $\mathbf{A}(\mathbf{r},t)$ is the applied magnetic vector potential, $\phi(\mathbf{r},t)$ is the applied scalar electric potential and e here represents the absolute value of the electron charge. The resulting quantum current density along the nanodevice can be presented in terms of this electron state variable as follows:

$$\mathbf{J}(\mathbf{r},t)=\frac{e^2}{m}|\psi(\mathbf{r},t)|^2\,\mathbf{A}-j\frac{he}{4\pi m}\left(\psi^*(\mathbf{r},t)\nabla\psi(\mathbf{r},t)-\psi(\mathbf{r},t)\nabla\psi^*(\mathbf{r},t)\right) \tag{22}$$

On the other hand, electromagnetic fields are related by Maxwell's equations as follows:

$$\nabla\times\mathbf{H}(\mathbf{r},t)=\varepsilon\frac{\partial\mathbf{E}(\mathbf{r},t)}{\partial t}+\mathbf{J}(\mathbf{r},t) \tag{23-a}$$

$$\nabla\times\mathbf{E}(\mathbf{r},t)=-\mu\frac{\partial\mathbf{H}(\mathbf{r},t)}{\partial t} \tag{23-b}$$

where the electric and magnetic field components can be presented in terms of the scalar electric potential and vector magnetic potential as:

$$\mathbf{E}(\mathbf{r},t)=-\nabla\phi(\mathbf{r},t)-\frac{\partial\mathbf{A}(\mathbf{r},t)}{\partial t} \tag{24-a}$$

$$\mathbf{H}(\mathbf{r},t)=\frac{1}{\mu}\nabla\times\mathbf{A}(\mathbf{r},t) \tag{24-b}$$

The scalar electric potential and the magnetic vector potential are related by Lorentz condition:

$$\frac{\partial\phi(\mathbf{r},t)}{\partial t}=-\frac{1}{\mu\varepsilon}\nabla\cdot\mathbf{A}(\mathbf{r},t) \tag{25-a}$$

and the magnetic vector potential is related to the current density by non-homogenous wave equation:

$$\frac{\partial^2\mathbf{A}(\mathbf{r},t)}{\partial t^2}=\frac{1}{\mu\varepsilon}\nabla^2\mathbf{A}(\mathbf{r},t)-\frac{1}{\varepsilon}\mathbf{J}(\mathbf{r},t) \tag{25-b}$$

By solving Equations (21)-(25), one can obtain electromagnetic interaction with the proposed nanodevice. Numerical solution of these coupled partial differential equations can be obtained by using finite difference method. This method is based on approximating the differential operator by a difference operator to obtain the required quantities on the nodes of a discrete mesh in the space $(i\Delta x, j\Delta y, k\Delta z)$ at discrete steps in time $(n\Delta t)$. To simplify the problem, the complex state variable of Equation (21) is divided into real and imaginary parts as follows:

$$\psi(\mathbf{r},t)=\psi_R(\mathbf{r},t)+j\psi_I(\mathbf{r},t) \tag{26}$$

Thus, Equation (21) can be reformulated as two coupled partial differential equations of pure real variables:

$$\frac{\partial \psi_R(\mathbf{r},t)}{\partial t} = \frac{1}{2m}\left(-\frac{h}{2\pi}\nabla^2\psi_I(\mathbf{r},t) - e\nabla\cdot\mathbf{A}(\mathbf{r},t)\psi_R(\mathbf{r},t) \right.$$
$$\left. - 2e\mathbf{A}(\mathbf{r},t)\cdot\nabla\psi_R(\mathbf{r},t) + \frac{2\pi}{h}e^2 \mid \mathbf{A}(\mathbf{r},t)\mid^2 \psi_I(\mathbf{r},t) \right) \qquad (27\text{-a})$$
$$+\left(\frac{2\pi}{h}e\phi(\mathbf{r},t)\psi_I(\mathbf{r},t) + \frac{2\pi}{h}V(\mathbf{r})\psi_I(\mathbf{r},t) \right)$$

$$\frac{\partial \psi_I(\mathbf{r},t)}{\partial t} = \frac{1}{2m}\left(\frac{h}{2\pi}\nabla^2\psi_R(\mathbf{r},t) - e\nabla\cdot\mathbf{A}(\mathbf{r},t)\psi_I(\mathbf{r},t) \right.$$
$$\left. - 2e\mathbf{A}(\mathbf{r},t)\cdot\nabla\psi_I(\mathbf{r},t) - \frac{2\pi}{h}e^2 \mid \mathbf{A}(\mathbf{r},t)\mid^2 \psi_R(\mathbf{r},t) \right) \qquad (27\text{-b})$$
$$-\left(\frac{2\pi}{h}e\phi(\mathbf{r},t)\psi_R(\mathbf{r},t) + \frac{2\pi}{h}V(\mathbf{r})\psi_R(\mathbf{r},t) \right)$$

For the case of a carbon nanotube where the length of the nanotube is usually much larger than its diameter, the problem can be presented as 1-D problem along the length of the nanotube. In this case the ∇ operator in the above equation can be simply replaced by $\partial / \partial z\, \mathbf{a}_z$.

The scalar electric potential and magnetic vector potentials are assumed to be known at the time steps n and $n+1/2$. Thus by discretizing Equation (25-b) one can obtain the update equation of the magnetic vector potential at time step $n+1$ as follows:

$$A_z^{n+1}(k) = 2A_z^{n+1/2}(k) - A_z^n(k)$$
$$+\frac{(\Delta t/2)^2}{\mu\varepsilon(\Delta z)^2}\left(A_z^{n+1/2}(k+1) - 2A_z^{n+1/2}(k) + A_z^{n+1/2}(k-1) \right) - \frac{(\Delta t/2)^2}{\varepsilon} J_z^{n+1/2}(k) \qquad (28)$$

Based on the result of Equation (28) and the previously stored electric potential and vector potentials, one can obtain the update equation for the electric field along the nanotube at the time step $n+1/2$ by discretizing Equation (24-a)

$$E_z^{n+1/2}(k) = -\frac{\phi^{n+1/2}(k+1) - \phi^{n+1/2}(k-1)}{2\Delta z} - \frac{A_z^{n+1}(k) - A_z^n(k)}{\Delta t} \qquad (29)$$

The update equations of the electric fields at the time step $n + 1/2$ in the remaining domain outside the nanotube can be obtained by using conventional FDTD formulation for the differential form of Ampere's law, Equation (23-a),

$$\mathbf{E}^{n+1/2}(\mathbf{r},t) = \mathbf{E}^{n-1/2}(\mathbf{r},t) + \frac{\Delta t}{\varepsilon}\nabla\times\mathbf{H}^n(\mathbf{r},t) \qquad (30)$$

It should be noted that we assumed here the present current density is limited to the nanotube structure only which is already included in Equation (29). Thus Equation (30) does not include an electric current term. Similarly, the update equations of the magnetic fields at the time step $n + 1$ are obtained by using conventional FDTD formulation for the differential form of Faraday's law, Equation (23-b),

$$\mathbf{H}^{n+1}(\mathbf{r},t)=\mathbf{H}^{n}(\mathbf{r},t)-\frac{\Delta t}{\mu}\nabla\times\mathbf{E}^{n+1/2}(\mathbf{r},t) \tag{31}$$

The update equations of the scalar electric potential function at the time step n+1 can be obtained by discretizing Equation (25-a) as follows:

$$\phi^{n+1}(k)=\phi^{n}(k)-\frac{1}{\mu\varepsilon}\frac{\Delta t}{2\Delta z}\left(A_z^{n+1/2}(k+1)-A_z^{n+1/2}(k-1)\right) \tag{32}$$

To obtain the above quantities at the following time step, it is required to update the potential functions and the current density to the time step n+3/2. To do this it is required to use Schrödinger equation to update the state variable and consequently the current density and the potential functions. Assuming that the state variables are known at time steps n and n+1/2, one can obtain the temporal update equation of the real and imaginary parts of the complex state function at the time step n+1 in the following forms:

$$\begin{aligned}\psi_R^{n+1}(k)=\psi_R^{n}(k)&-\frac{h\Delta t}{4m\pi}\frac{\psi_I^{n+1/2}(k+1)-2\psi_I^{n+1/2}(k)+\psi_I^{n+1/2}(k-1)}{(\Delta z)^2}\\&-\frac{e\Delta t}{2m}\frac{A_z^{n+1/2}(k+1)-A_z^{n+1/2}(k-1)}{2\Delta z}\psi_R^{n+1/2}(k)\\&-\frac{e\Delta t}{m}A_z^{n+1/2}(k)\frac{\psi_R^{n+1/2}(k+1)-\psi_R^{n+1/2}(k-1)}{2\Delta z}+\frac{\pi\Delta t}{mh}e^2\left(A_z^{n+1/2}(k)\right)^2\psi_I^{n+1/2}(k)\\&+\left(\frac{2\pi\Delta t}{h}e\phi^{n+1/2}(k)\psi_I^{n+1/2}(k)+\frac{2\pi\Delta t}{h}V(k)\psi_I^{n+1/2}(k)\right)\end{aligned} \tag{33-a}$$

$$\begin{aligned}\psi_I^{n+1}(k)=\psi_I^{n}(k)&+\frac{h\Delta t}{4m\pi}\frac{\psi_R^{n+1/2}(k+1)-2\psi_R^{n+1/2}(k)+\psi_R^{n+1/2}(k-1)}{(\Delta z)^2}\\&-\frac{e\Delta t}{2m}\frac{A_z^{n+1/2}(k+1)-A_z^{n+1/2}(k-1)}{2\Delta z}\psi_I^{n+1/2}(k)\\&-\frac{e\Delta t}{m}A_z^{n+1/2}(k)\frac{\psi_I^{n+1/2}(k+1)-\psi_I^{n+1/2}(k-1)}{2\Delta z}-\frac{\pi\Delta t}{mh}e^2\left(A_z^{n+1/2}(k)\right)^2\psi_R^{n+1/2}(k)\\&-\left(\frac{2\pi\Delta t}{h}e\phi^{n+1/2}(k)\psi_R^{n+1/2}(k)+\frac{2\pi\Delta t}{h}V(k)\psi_R^{n+1/2}(k)\right)\end{aligned} \tag{33-b}$$

Based on this complex state variable, one can obtain the current density at the time step n+1by discretizing Equation (22) as follows:

$$\begin{aligned}J_z^{n+1}(k)=&\frac{e^2}{m}\left(\left[\psi_R^{n+1}(k)\right]^2+\left[\psi_I^{n+1}(k)\right]^2\right)A_z^{n+1}-\frac{he}{2\pi m}\left(\psi_I^{n+1}(k)\frac{\psi_R^{n+1}(k+1)-\psi_R^{n+1}(k-1)}{2\Delta z}\right)\\&+\frac{he}{2\pi m}\left(\psi_R^{n+1}(k)\frac{\psi_I^{n+1}(k+1)-\psi_I^{n+1}(k-1)}{2\Delta z}\right)\end{aligned} \tag{34}$$

At this point we have $\phi^{n+1}(k)$, $A_z^{n+1}(k)$, $\psi_R^{n+1}(k)$, $\psi_I^{n+1}(k)$ and $J_z^{n+1}(k)$ in addition to the previously calculated quantities. By repeating the same steps from Equations (32) to (34) and

Equation (28), one can obtain state parameters, current density and potential functions at n+3/2 time step. Thus we obtain scalar electric potential and magnetic vector potentials at the time steps n+1 and n+3/2. Then by repeating the same steps of Equations (28) to (31) one can obtain the electric and magnetic fields in the following time step.
The above analysis represents the core of the finite difference time domain formulation of the coupled Maxwell-Schrödinger equations for solving electromagnetic coupling with nanodevice with emphasis on simple linear nanodevices like carbon nanotube. It should be noted that there are many other problems in this method which require more investigation like absorbing boundary conditions for Schrödinger equation, stability and dispersion. (Pierantoni *et al.;* 2008, Pierantoni *et al.;* 2008 & Ahmed *et al.* 2010)

5. Surface wave propagation along carbon nanotubes

Carbon nanotubes can also be considered as cylindrical guiding structures of finite conductivity. This section shows how to determine the complex propagation constant of this guiding structure based on its macroscopic conducting properties. Since we are mainly concerned with the longitudinal conductivity, the propagating wave along the nanotube would be mainly TM wave. In this case the total field can be represented in terms of the axial TM Hetezian potential Π_e as follows:

$$\vec{E} = \nabla\left(\nabla \cdot \Pi_e\right) + k_0^2 \Pi_e \tag{35-a}$$

$$\vec{H} = j\omega\varepsilon_o \nabla \times \Pi_e \tag{35-b}$$

where the TM Hertezian potential is determined by solving the wave equation

$$\nabla^2 \Pi_e + k_0^2 \Pi_e = 0 \tag{36}$$

For a cylindrical configuration, the general solution of wave equation can be presented as Bessel functions. The field inside the cylinder is finite in the range $0 \le \rho \le r$ where r is the radius of the proposed cylinder. Thus the field in this region is represented by Bessel function of first kind. On the other hand, the field outside the cylinder is finite at $\rho = r$ and is exponentially decaying for $\rho = r$. Thus, the field in this region is represented by Hankel function of second kind. Hence, the general solution of the TM Hertizian potential in carbon nanotube (single or a circular bundle) can be represented as:

$$\Pi_e = A\vec{a}_z \begin{Bmatrix} \mathrm{J}_n(\kappa\rho)\mathrm{H}_n^{(2)}(\kappa r) \\ \mathrm{J}_n(\kappa r)\mathrm{H}_n^{(2)}(\kappa\rho) \end{Bmatrix} e^{-j\gamma z} e^{-jn\varphi} \quad \begin{matrix} \rho \le r \\ \rho \ge r \end{matrix} \tag{37}$$

By using this Hertezian potential in Equation (35) and applying the boundary condition

$$J_z = \sigma_{zz} E_z(r) = -\lim_{\delta \to 0}\left[H_\phi(r+\delta) - H_\phi(r-\delta) \right] \tag{38}$$

one can obtain the dispersion equation for surface wave propagation as follows:

$$\left(\frac{\kappa}{k_0}\right)^2 \mathrm{J}_n(\kappa r)\mathrm{H}_n^{(2)}(\kappa r) = \frac{2}{\pi\sigma_{zz}Z_0 k_0 r} \text{ where } \mathrm{Im}(\kappa) \le 0 \tag{39}$$

The longitudinal propagation constant is given by:

$$\gamma = \sqrt{k_0^2 - \kappa^2} \text{ where } \mathrm{Im}(\gamma) \le 0 \tag{40}$$

It would be useful here to study the limit of the above dispersion equation for the zero-order mode at small argument limit. In this case the Bessel function combination of the right hand side can be approximated as:

$$\mathrm{J}_0(\kappa r)\mathrm{H}_0^{(2)}(\kappa r) \approx \left(1 - j\frac{2}{\pi}\left[\ln(\kappa r/2) + 0.577215\right]\right) \tag{41}$$

Unlike Bessel function, the logarithmic function in the right hand side of Equation (41) can be represented by a slowly convergent series for small argument. However, for gigahertz frequency band, the average value of this logarithmic function is nearly around minus ten. Thus, an approximate value of the zero order mode complex surface wave propagation coefficient along a carbon nanotube is given by:

$$\gamma \approx k_0\sqrt{1 - \frac{1}{\sigma_{zz}Z_0 k_0 r(\pi/2 + j10)}} \tag{42}$$

It can be noted that, by increasing the longitudinal conductivity of the tube the surface wave propagation constant approaches the free space propagation constant.

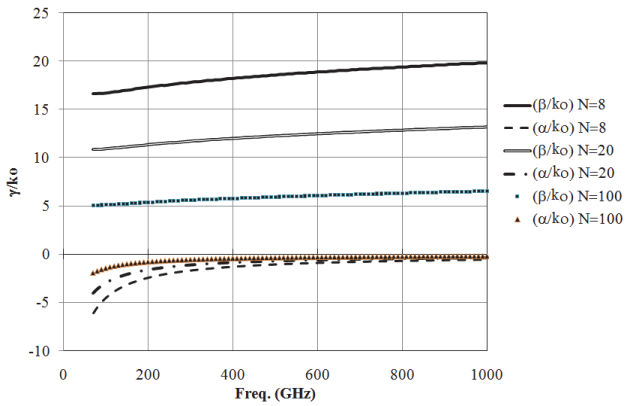

Fig. 6. Surface wave propagation on carbon nanotube bundles of different values of *N*. The bundle is composed of armchair carbon nanotubes with lattice parameters $m = n = 40$. (Attiya 2009)

Figure 6 shows complex wave propagation constant of TM surface waves along a carbon nanotube circular bundle for different values of *N* where *N* is the number of carbon nanotubes in the bundle. The present results are based on armchair carbon nanotubes of $m = n = 40$. For

this configuration, the radius of the nanotube is r_c = 2.7nm. For a closely backed bundle composed of *N* carbon nanotubes arranged in a single circular shell the radius of the bundle is

$$r = 2Nr_c / \pi \tag{43-a}$$

In this case the effective axial surface conductivity of this shell can be approximated by

$$\sigma_{zz}^{b} \approx N\sigma_{zz}^{cn} r_c / r \tag{43-b}$$

It can be noted that the attenuation coefficient increases by decreasing the operating frequency as shown in Figure 6. The effect of this attenuation coefficient is negligible in the frequency range from 100 to 1000 GHz. On the other hand, this attenuation coefficient has a significant effect in the frequency band below 100 GHz.

6. Carbon nanotube antenna

Carbon nanotube can also be a good candidate for antenna structures. Slow wave property of electromagnetic propagation along carbon nanotube is expected to play an important role in reducing the size of resonant carbon nanotube antenna. From the mathematical point of view, carbon nanotube antennas can be treated as an antenna composed of finite-conducting cylinders. In this case the dynamic conductivity derived in Section 2 is used to include the electrical properties of carbon nanotube in the mathematical modeling of the corresponding antenna structure. This electromagnetic formulation can be presented in any form like integral equation, finite difference or finite element. However, for simple wire antenna configuration, electric field integral equation method may be the most appropriate method. Thus we would focus on this method in the following part of this section.

For the case of a simple dipole antenna oriented along the z axis, the relation between the excitation field and the current distribution can be presented by Hallen's integral equation as follows:

$$\int_{-L}^{L} \left(\frac{e^{-jk_0\sqrt{(z-z')^2+r^2}}}{\sqrt{(z-z')^2+r^2}} + \frac{1}{Z_0\sigma_{zz}r} e^{-jk_0|z-z'|} \right) I(z')dz' = C\cos k_0 z - j\frac{4\pi\omega\varepsilon_0}{2k_0}\sin k_0 \,|\, z - z_0 \,| \tag{44}$$

where r is the radius of the dipole ($r = r_c$ for single nanotube) and σ_{zz} is the effective surface conductivity of the dipole, z_0 is the location of the feeding point, *C* is a constant that would be determined to satisfy the current vanishing at the edges of the dipole and *L* is the half length of the dipole. The effect of the carbon nanotube in this integral equation lies in surface conductivity and the radius of the nanotube. This formulation can be used to simulate a dipole antenna composed of single carbon nanotube or a bundle of carbon nanotubes. In the case of a carbon nanotube bundle, the corresponding radius and surface conductivity are obtained by Equation (43).

This integral equation can be solved numerically by using method of moments to find out the current distribution and subsequently the input impedance, radiation pattern, radiation efficiency and other antenna parameters. This method is based on expanding the unknown current distribution as a finite series of known basis functions of unknown amplitudes. To determine these amplitudes, Equation (44) is weighted by a set of weighting functions

which equals the number of the unknown amplitudes. Thus, Equation (44) is converted into a system of equations which is solved to obtain the unknown amplitudes of the current distribution functions. Details of solving this integral equation numerically by using method of moments can be found in (Elliot 2003).

Figure 7 shows the complex input impedance of a dipole of a carbon nanotube for two cases as functions of the operating frequency. The present results are based on conducting armchair carbon nanotubes of $m = n = 40$. The length of the dipole is assumed to be 30 μm and 1 mm for the first and second case respectively. It can be noted that the first case has a first resonance at nearly 160 GHz. However, the second case does not have any resonance. Figure 8-a shows the current distribution along the 10 μmdipole antenna at its first resonance frequency due to a unity voltage source at its feeding point. It can be quite clear that the dipole in this case corresponds to a half-guided-wave length dipole. It can also be noted that the length of the first resonant carbon nanotube antenna is nearly 0.0107 times the length of conventional half-wave length dipole at this frequency. This represents an important feature of carbon nanotube antenna. It can also be noted the corresponding input impedance in this case is nearly 11 kΩ which is much greater than the conventional input impedance of a half-wave dipole which is nearly of order 75Ω. On the other hand, the current distribution along the 1 mm dipole antenna has different properties as shown in Figure 8-b, where the real and imaginary parts of the current are concentrated around the center of the dipole and highly damped at its ends. It can be concluded from this result that the problem of carbon nanotube antenna at different frequency ranges cannot be directly obtained by simple scaling as the case in perfect electric conductor.

Figure 9 shows the input impedance of a dipole of a carbon nanotube bundle for different values of N. The length of the dipole is taken to be 30 μm and 3000 μm. It can be noted that the 30 μm dipole has a first resonance, that corresponds to a half-guided-wave length dipole for N = 8, at 280 GHz. The resonance impedance in this case is nearly 2100 Ohms. By

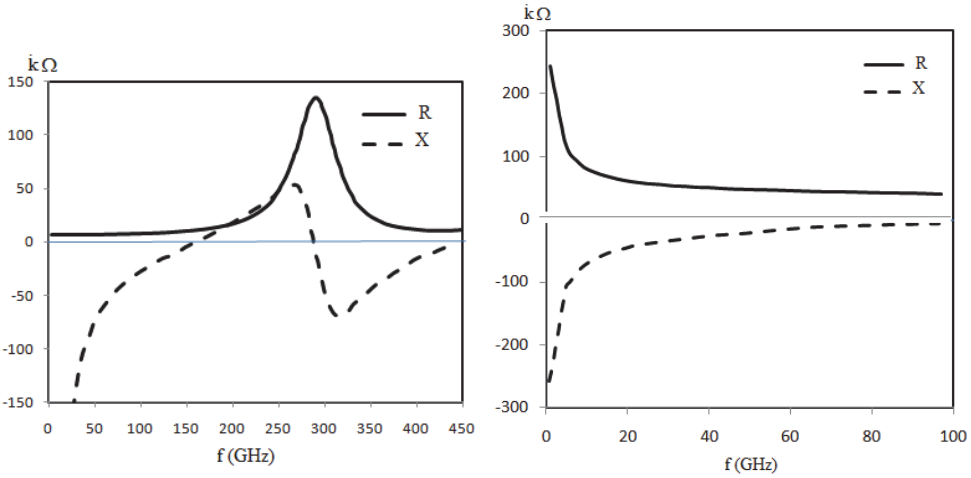

(a) The length of the dipole is 10 μm (b) The length of the dipole is 1 mm

Fig. 7. Input impedance for a carbon nanotube antenna. The carbon nanotube is armchair of lattice parameters m=n=40.

comparing this length with free space half-wave at this frequency it can be noted that this carbon nanotube antenna has a reduction scale factor of nearly 0.056 compared with conventional half-wave length dipole. Increasing the number of nanotubes in the bundle decreases the total surface impedance of the dipole. This has two effects, increasing the resonance frequency for a specific length and decreasing the resonance impedance as shown in the case where N is increased to twenty. In this case the first resonance frequency is 404 GHz and the resonance impedance is 840 Ohms. The scale reduction factor in this case is nearly 0.081. For a hundred nanotube bundle of the same length, the resonance frequency would be 740 GHz and the resonance impedance would be 174 Ohms. In this case the scale reduction factor is nearly 0.15. It can be noted that by increasing the number of carbon nanotubes in the bundle, both resonance frequency and reduction factor are increased while the input impedance is decreased. On the other hand, the 3000 μm dipole does not introduce resonance behavior for any value of N as it is shown in Figure 9-b. This result is quite similar to the results of a single carbon nanotube antenna shown in Figure 7.

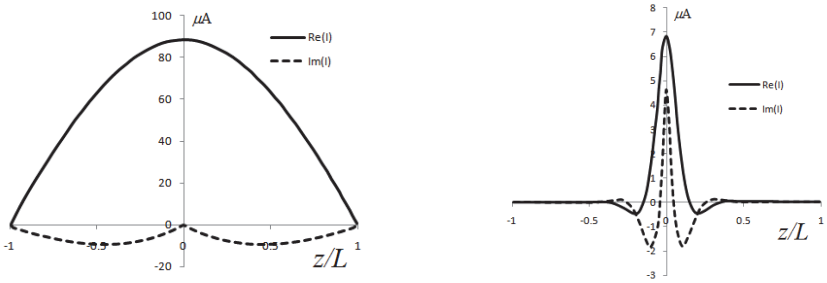

(a) The length of the dipole is 10 μm and the operating frequency is 160 GHz

(b) The length of the dipole is 1 mm and the operating frequency is 10 GHz

Fig. 8. Current distributions along carbon nanotube dipole antennas due to a unity voltage source.

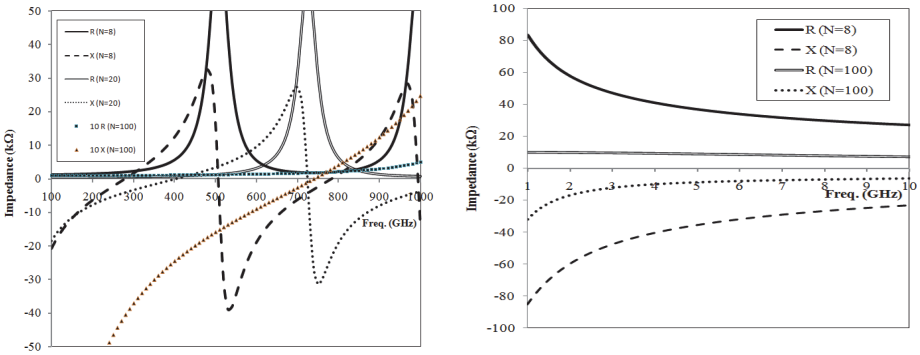

(a) L = 30 μm

(b) L = 3000μm

Fig. 9. Input impedance of bundle dipole. The bundle is composed of armchair carbon nanotubes with lattice parameters $m = n = 40$. Numbers of nanotubes in the bundles are N=8, N=20 and N=100 (Attiya 2009)

It is noted that the inverse reduction factors of the resonant bundle dipoles equals nearly the ratio of the surface wave propagation constant with respect to the free space wave number shown in Figure 6 for the same bundles. These results show the relation between the resonant dipole length and the surface wave velocity on its arms. On the other hand, by studying the surface wave complex wave propagation constant, it can be noted that the attenuation coefficient increases by decreasing the operating frequency as shown in Figure 6. The effect of this attenuation coefficient is negligible in the frequency range from 100 to 1000 GHz. Thus, the main behavior of the input impedance of the dipole antenna is nearly the same of traditional dipole antenna with taking into account scaling reduction factor due to the slow surface wave velocity. However, in the band from 1 to 10 GHz, the wave propagating on the arms of the dipole is attenuated. Thus, the reflected wave does not add completely at the feeding point which means the inductive effect due to the delayed reflected signal does not compensate completely the capacitive effect of the dipole arms. This explains the capacitive behavior of CNT dipoles in Figures 7-b and 9-b. In this case, the wave propagating on the arms of the dipole is highly attenuated, such that the active part of the dipole is much smaller than the physical length of the dipole itself. Thus, the dipole would always be a short dipole in this case and it is not resonant in any case. This result shows that the advantage of size reduction combined with surface wave propagation can be used only in high frequency bands above 100 GHz.

7. Carbon nanotubes in passive RF circuits

Recent advances in carbon nanotubes make them competitive elements in many RF applications. New fabrication techniques can be used to synthesize and electrically contact single carbon nanotube up to nearly 1 cm (Li *et al.* 2007). In addition using solubilized carbon nanotube and dielectrophoresis can be used to accumulate hundreds to thousands of carbon nanotubes in parallel (Rutherglen *et* al. 2008). These advances in fabrication techniques open the door for more research on different configurations of carbon nanotubes which are believed to be visible in near future.

On the other hand, metallic single-wall carbon nanotube transmission line shows an important advantage of slow electromagnetic wave propagation compared with free space wave velocity. This wave velocity reduction is due to the additional kinetic inductance and quantum capacitance in the equivalent circuit model of the nanotube transmission line circuit. In this case the wave velocity along the single-wall carbon nanotube transmission line has the same order of Fermi velocity which is nearly 8×10^5 m/s. This means that the wave velocity in this case is nearly two-order less than free space wave velocity. Thus the wavelength along the single-wall carbon nanotube transmission line is nearly two-order smaller than free space wave length. This property is quite useful to reduce the physical dimensions of microwave circuits to be in hundred-micrometer scale instead of centimeter scale. However, these additional inductance and capacitance introduce high characteristic impedance of order 12.5 k Ω. In addition, the single-wall carbon nanotube transmission line has an intrinsic resistance of 6.5 kΩ and Ohmic contact resistance of order 20 kΩ which introduce high attenuation coefficient. These parameters make carbon nanotube transmission line is not suitable for microwave applications from the point of view of characteristic impedance and attenuation.

Recently, parallel carbon nanotube and carbon nanotube bundle have been introduced to overcome these disadvantage (Attiya & Kanhal, 2009). Different experiments introduced by

different authors have shown that using parallel carbon nanotube decreases both the DC and RF impedance; for example a bundle composed of ten parallel single wall carbon nanotube shows a DC impedance around 750Ω while hundreds of parallel single wall carbon nanotubes show an AC impedance from 60 to 40Ω in the frequency range from few MHz to 20 GHz (Rutherglen *et al.* 2008). These experimental results introduced the possibility of using parallel single wall carbon nanotubes to obtain nearly matched transmission line sections with low wave velocity. Parallel carbon nanotube transmission line sections can be used to replace traditional printed transmission line sections in microwave circuits to have a significant reduction in the total size of these circuits. However, one should consider the lossy and mismatch effects of parallel carbon nanotube transmission line. Further theoretical and experimental investigations are still required to study the possibility of using parallel carbon nanotube transmission lines in passive microwave circuits like hybrid couples, power dividers, filters… etc.

Other RF and microwave applications like switches, filters and resonators can also be obtained by using electromechanical propertied of carbon nanotubes. (Demoustier *et al.* 2008) introduced an RF nanoswitch based on vertically aligned carbon nanotubes. It consists of carbon nanotube perpendicular to the substrate. Two different architectures are proposed for this carbon nanotube switch; series-based switch using ohmic contact between carbon nanotubes and a capacitive-based switch implemented in shunt configuration. RF ohmic switch is designed by implementing carbon nanotubes in two sides of a coplanar waveguide discontinuity as shown on Figure 10-a. By applying dc voltage on the two sides of the coplanar waveguide discontinuity, an electrostatic force is introduced between the two arms of the carbon nanotube switch. This electrostatic closes the switch and the RF signal is transmitted across the coplanar waveguide as shown in Figure 10-b. On the other hand, shunt switch is based on two nanotube capacitive contacts between the inner line and the two sides of the ground planes of the coplanar waveguide as shown in Figure 11-a. By applying dc voltage between the inner and outer sides of the coplanar waveguide, the electrostatic field introduces a short circuit between the inner and the outer sides as shown in Figure 11-b. This short circuit reflects the propagating wave along the coplanar waveguide which corresponds to switching off the RF signal. To achieve the expected performance in the required operating frequency band, two inductive sections are added along the coplanar waveguide in series with nanotube to perform a series LC resonance at the center of operating frequency band. This resonant LC circuit introduces higher isolation level in the switch isolation state.

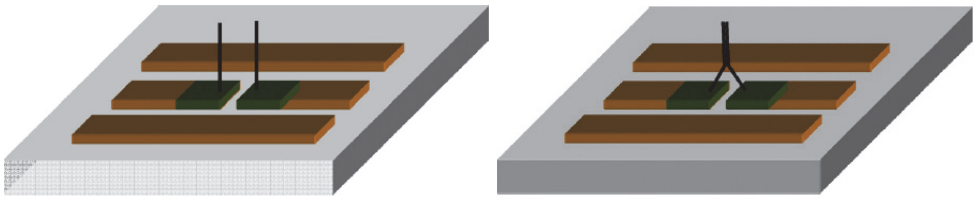

(a) Isolation state (b) Transmission state

Fig. 10. Architecture of Carbon nanotube ohmic switch (Demoustier 2008)

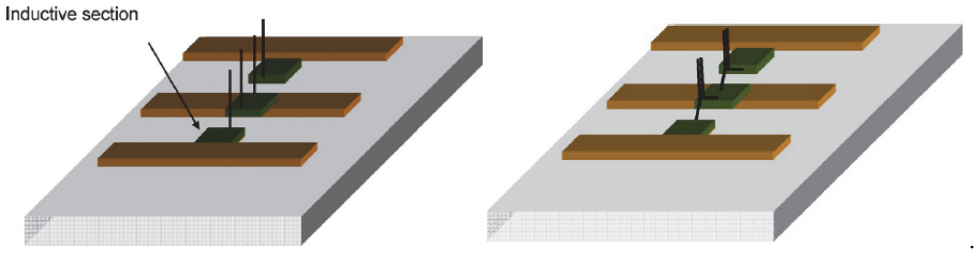

(a) Transmission state (b) Isolation state

Fig. 11. Architecture of Carbon nanotube shunt capacitive switch (Demoustier 2008)

Another application for carbon nanotubes in passive RF circuits based on their electromechanical properties is the microwave resonator and filter (Dragoman 2005). It is found that carbon nanotube has a mechanical resonance in the frequency range from 1 to 3 GHz with quality factor of 1000. The basic theory of carbon nanotube filter is based on coupling the electromagnetic fields of the incident signal to a perpendicular array of carbon nanotubes. This can be obtained by inserting this array of carbon nanotubes inside a coplanar waveguide as shown in Figure 13. In this case the coplanar waveguide transmits only the signals which are resonant with carbon nanotube array. To introduce the coupling between the incident electromagnetic wave and the carbon nanotube array, it is required to produce electric charges on the carbon nanotube. These electric charges are obtained by applying a dc electric field parallel to the direction of electromagnetic wave propagation and orthogonal on carbon nanotubes as shown in Figure 13. The presence of these electric charges introduces Coulomb forces between the carbon nanotubes and the electric field of the incident wave. The resonance of this filter is controlled by the value of the applied dc voltage. The vibration of the excited tubes located near the input electrode is propagating along the entire array like an acoustic excitation.

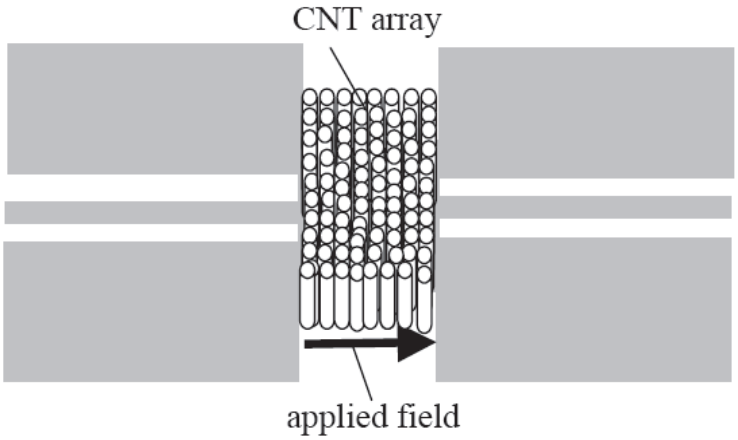

Fig. 13. Architecture of an RF bandpass filter based on a carbon nanotube array.

8. Carbon nanotubes composites for RF absorbing and shielding applications

From the above discussions about the possibility of using carbon nanotubes in microwave circuits it can be concluded that the high attenuation coefficient of wave propagation along carbon nanotube represents a main limiting factor in these application which may be overcome by using bundle of carbon nanotubes. However, this attenuation property is quite important in other microwave applications like absorbing and shielding. For these applications it is not required to arrange the carbon nanotubes in a bundle like the cases of antennas, transmission lines and interconnects. However, carbon nanotubes in these cases are mixed with other materials in a random form.

The effective dielectric constant of a dielectric mixture including conducting particles can be formulated by using Maxwell-Granett mixing rule as follows (Koledintseva 2009):

$$\varepsilon_{eff} = \varepsilon_b + \frac{\frac{1}{3} f_i (\varepsilon_i - \varepsilon_b) \sum_{k=1}^{3} \frac{\varepsilon_b}{\varepsilon_b + N_{ik}(\varepsilon_i - \varepsilon_b)}}{1 - \frac{1}{3} f_i (\varepsilon_i - \varepsilon_b) \sum_{k=1}^{3} \frac{N_{ik}}{\varepsilon_b + N_{ik}(\varepsilon_i - \varepsilon_b)}} \tag{45}$$

where ε_b is the relative permittivity of the base dielectric, ε_i is the permittivity of the inclusion particles, f_i is the volume fraction occupied by the inclusion, N_{ik} is the depolarization factor of the inclusions and the index $k = 1,2,3$ corresponds to x, y and z in Cartesian coordinates. The depolarization factors for an ellipsoid inclusion of radii *a,b* and *c* in x, y and z directions are given by:

$$N_{i1} = \frac{abc}{2} \int_0^\infty \frac{1}{(s+a)\sqrt{(s+a)(s+b)(s+c)}} ds \tag{46-a}$$

$$N_{i2} = \frac{abc}{2} \int_0^\infty \frac{1}{(s+b)\sqrt{(s+a)(s+b)(s+c)}} ds \tag{46-b}$$

$$N_{i3} = \frac{abc}{2} \int_0^\infty \frac{1}{(s+c)\sqrt{(s+a)(s+b)(s+c)}} ds \tag{46-c}$$

For the case of a carbon nanotube inclusion $a = b = r_c$ and c corresponds to the half-length of the carbon nanotube. To simplify the formulation it is assumed that all nanotube inclusions are directed parallel to the z axis. In this case the depolarization effect of the inclusions would be mainly dominating in the z direction while the dielectric constant in transverse directions would be the same as the base dielectric. In this case the dielectric constant of the carbon nanotube inclusion is defined as $\varepsilon_i = j\sigma_{3D} / \omega$ where the equivalent 3D conductivity of carbon nanotube is related to the surface dynamic conductivity of carbon nanotube as $\sigma_{3D} = \pi\sigma_{zz} / 2r_c$ (Mikki & Kishk 2009). Different experimental researches have been introduced to study the electrical prosperities of carbon nanotube composites. We demonstrate two specific cases in this following part of this section as examples for these carbon nanotube composites.

In microwave hyperthermia applications, it is required to an increase electromagnetic power dissipation in the specific region that is required to be more heated than other regions. Carbon nanotubes are found to be a good candidate for this application. To verify the applicability of carbon nanotube in this application (Mashal *et al.* 2010) demonstrated an experiment based on mixing tissue mimicking materials with carbon nanotubes and measuring their electrical properties and their heating response to incident electromagnetic wave. These tissue mimicking materials are constructed from oil-in-gelatin dispersions. The dielectric properties of these materials are customized to mimic the properties of a variety of human soft tissues by controlling the concentrations of gelatin, safflower oil, kerosene, and preservatives. The carbon nanotubes used in their experiments were 1-2 nm in diameter and 5-30 μm in length, and were composed of mainly single wall carbon nanotubes. Figure 14 shows the measured relative permittivity and effective conductivity of the corresponding composite for different concentrations of carbon nanotubes. It can be noted that both the permittivity and effective conductivity of the tissue mimic materials increase by increasing concentration of the carbon nanotubes.

The electromagnetic heating responses of this tissue mimic composites with carbon nanotube were examined by inserting a sample inside a WR-284 rectangular wave guide of an inner cross section 72 mm × 34 mm and applying a 3-GHz CW signal of power 1 Wt. The source generator is turned on for 3 minutes to heat the sample and turned off for 5 minutes to cool the sample. Figure 15 shows the measured heating responses for different values of carbon nanotube concentrations. It can be noted that the maximum temperature of the tissue mimic mixture increases by increasing the concentration of carbon nanotubes.

It can be concluded from these results that low concentrations of carbon nanotubes significantly impact the dielectric properties and heating response of tissue mimicking materials. For example, at 3 GHz, carbon nanotubes concentrations as small as 0.22% by weight increased the relative permittivity of the tissue mimicking material by 37% and the effective conductivity by 81%. This concentration of carbon nanotubes led to an average steady-state temperature rise that was 6 °C higher than the rise observed in the tissue mimicking material without carbon nanotubes. These results suggest that carbon nanotubes may enhance contrast for microwave imaging and facilitate selective microwave heating for treatment of breast cancer (Mashal *et al.* 2010).

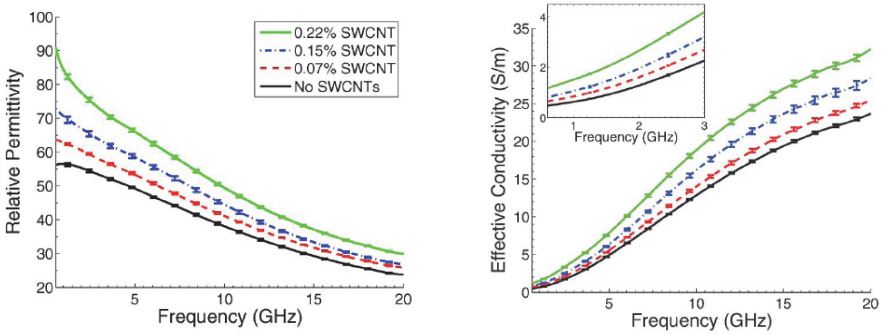

(a) Relative permittivity (b) effective conductivity

Fig. 14. Electrical properties of tissue-mimicking mixtures with varying concentrations of single wall carbon nanotubes measured from 0.6 to 20 GHz. (Mashal *et al.* 2010)

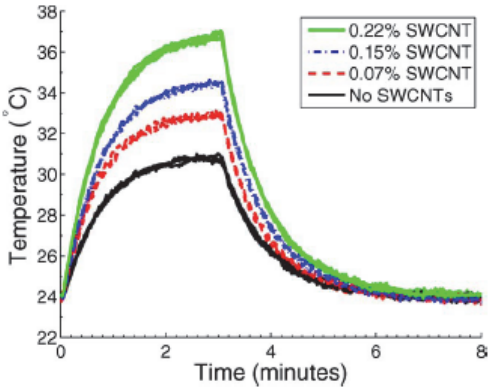

Fig. 15. Microwave heating response of tissue mimic materials with various concentrations of carbon nanotubes. Each curve shows the temperature profile of a sample that was heated via 3-GHz microwave illumination for 3 min and allowed to cool for 5 min. (Mashal *et al.* 2010)

Another important application of carbon nanotube composites is optical-transparent electromagnetic shielding composite film. Thin films of conducting single wall carbon nanotube of a thicknesses less than 300 nm on polyethylene terephthalate substrates are good candidate for this application. (Xu *et al.* 2007) introduced an experimental study to characterize the shielding properties of these composite films. Their study is based on measuring the reflection coefficient of a coaxial annular ring resonator placed above the carbon nanotube layer by using a vector network analyzer. Based on this reflection coefficient they obtained the equivalent impedance of the composite film. This impedance includes the impedance of the carbon nanotube film and the impedance of the holding substrate. To extract the impedance of the substrate, they measured the reflection coefficient of the coaxial annular resonator on the substrate only. After extracting the impedance of the substrate, they obtained the impedance of the carbon nanotube layer. This impedance is used to determine the equivalent complex conductivity of the carbon nanotube layer. Then the problem is treated as a two-layered structure of specific values of permitivities and conductivities to determine the transmission coefficient of this structure.

Figure 16 shows the shielding effectiveness in dB as a function of frequency for different thicknesses of carbon nanotube films. It is noted that this shielding effectiveness is proportional to log $(1/f)$. For the 10 nm film, the shielding effectiveness varies from 43 to 28 dB in the range of 10 MHz–30 GHz. The dependence of the shielding effectiveness on the thickness of the carbon nanotube layer t_0 is nearly proportional to log (t_0). On the other hand, Figure 17 shows the optical transmission coefficient at wavelength of 550 nm as a function of the thickness of the carbon nanotube film. For a 30 nm thickness film, the optical transmittance is about 80% and the shielding effectiveness are 33 dB at 10 GHz, 36 dB at 1 GHz, and 46 dB at 10 MHz. This shielding effectiveness of carbon nanotube films satisfies requirements for commercial applications like cell phones which require approximately 20 dB shielding effect. For high shielding requirements such as for magnetic resonant imaging window where 60 dB shielding effectiveness is required, carbon nanotube films still need to be improved.

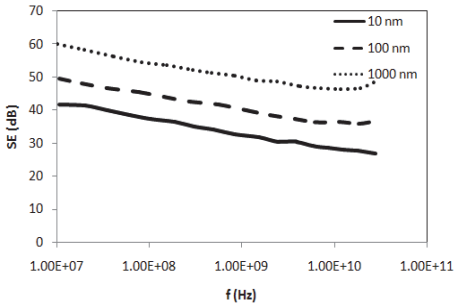

Fig. 16. Microwave shielding effectiveness of a carbon nanotube film for different values of thicknesses. (Xu *et al.* 2007)

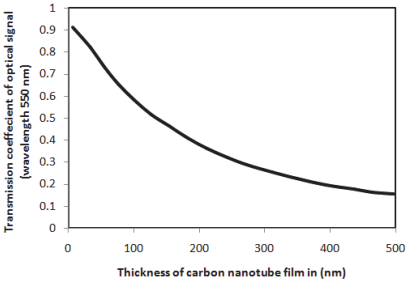

Fig. 17. Optical transmission coefficient at wavelength of 550 nm as a function of the thickness of carbon nanotube film. (Xu *et al.* 2007)

9. Conclusion

This chapter introduced different techniques for studying interaction of high frequency electromagnetic fields with carbon nanotubes. Boltzman kinetic equation is used to introduce an equivalent surface conductivity and electron fluid model is used to introduce an equivalent circuit model for carbon nanotube transmission line. Another model is introduced based on coupling Maxwell's equation with Schrodinger equation. Finite difference time domain is discussed as an efficient numerical technique for solving coupled Maxwell-Schrodinger equations to obtain a full wave analysis for electromagnetic interaction with carbon nanotubes.

These models show that carbon nanotubes are characterized by high inductive effect due to the additional kinetic inductance. This high inductive effect reduces wave velocity along carbon nanotubes and increases its corresponding characteristic impedance. Reduction of wave velocity has a significant importance in reducing the size of RF components, passive circuits and antenna structures. On the other hand, parallel carbon nanotubes can be used to reduce the characteristic impedance. Analytical analysis of surface wave propagation along circular carbon nanotube bundle is discussed based on the equivalent surface conductivity. Resulting complex wave propagation constant along carbon nanotube bundles shows slow wave propagation which is consistent with the transmission line model introduced by

electron fluid model. In addition, attenuation coefficient is found to be increased by decreasing the operating frequency. Carbon nanotubes are also found to be a good candidate for dipole antennas at operating frequencies above 100 GHz. At lower frequencies the high attenuation coefficient of wave propagation along the carbon nanotube structure makes it not suitable to obtain resonant antenna. Further theoretical and experimental studies are still required to investigate the possibility of using parallel carbon nanotubes in RF circuits and antennas. In addition electro-mechanical properties of carbon nanotubes can be also be useful in RF applications like filtering and switching. On the other hand, the high attenuation at lower frequencies below 100 GHz makes carbon nanotubes good candidate for absorbing and shielding applications. Absorbing properties of carbon nanotubes can be quite useful in medical applications such as microwave imaging and selective microwave heating for cancer treatment. Thin film of carbon nanotubes above a polyethylene substrate is also found to good candidate for transparent shielding surface up to 20dB. Higher shielding effectiveness combined with high transparence is still under investigation.

10. Acknowledgement

The authors would like to acknowledge the assistance and the financial support provided by the Research Center at the College of Engineering at King Saud University for this chapter.

11. References

Ahmed, I.; Khoo, E. H.; Li, E. & Mittra, R. (2010). A hybrid approach for solving coupled Maxwell and Schrödinger equations arising in the simulation of nano-devices. *IEEE Antenna and Wireless Propagations Letters,* Vol. 9, (2010), pp. 914-917

Attiya, A.M. (2009). Lower frequency limit of carbon nanotube antenna. *Progress In Electromagnetics Research*, Vol. 94, 419-433, 2009.

Attiya, A.M.; Alkanhal, M.A. (2009). Parallel single wall carbon nanotubes for microwave applications. *Microwave Conference, 2009. APMC 2009. Asia Pacific,* 7-10 Dec. 2009, pp.2459-2462

Burke, P. J. (2002). Lüttinger Liquid Theory as a Model of Gigahertz Electrical Properties of Carbon Nanotubes. *IEEE Trans. Nanotechnology*, Vol. 1, No.3, (Sept. 2002), pp. 129-144

Chiariello, A.G.; Maffucci, A.; Miano, G.; Villone, F.; Zamboni, W. (2006a). Metallic Carbon Nanotube Interconnects, Part I: a Fluid Model and a 3D Integral Formulation," *IEEE Workshop on Signal Propagation on Interconnects*, 9-12 May 2006, pp.181-184

Chiariello, A.G.; Maffucci, A.; Miano, G.; Villone, F. & Zamboni, W. (2006b). Metallic Carbon Nanotube Interconnects, Part II: a Transmission Line Model. *IEEE Workshop on Signal Propagation on Interconnects*, 9-12 May 2006, pp.185-188

Demoustier, S.; Minoux, E.; Baillif,M. L.; Charles,M.; and Ziaei,A. (2008), Review of two microwave applications of carbon nanotubes: nano-antennas and nano-switches, *Comptes Rendus Physique*, Vol. 9, No. 1, *New concepts for nanophotonics and nano-electronics*, (Jan. 2008), pp. 53-66

Dragoman, M., Hartnagel, H. L.; Tuovinen, J; and Plana, R. (2005), Microwave applications of carbon nanotubes, *Frequenz*, Vol. 59 No. 11-12, (2005) pp. 251-263

Dressel, M. & Grüner, G. (2003). *Electrodynamics of Solids: Optical Properties of Electrons in Matter*, Cambridge University Press, ISBN 0 521 59253 4, Australia

Elliot, R. S. (2003). *Antenna theory and design*, IEEE press, ISBN 0471449962.

Hanson, G. W. (2005). Fundamental Transmitting Properties of Carbon Nanotube Antennas. *IEEE Trans. Antennas Propag.*, Vol. 53, No. 11, (Nov. 2005), pp. 3426-3435

Hanson, G. W. (2006). Current on an infinitely-long carbon nanotube antenna excited by a gap generator. *IEEE Trans. Antennas Propag.*, Vol. 54, No. 1, (Jan. 2006), pp. 76-81

Hao, J. & Hanson, G. W. (2006). Infrared and Optical Properties of Carbon Nanotube Dipole Antennas. . *IEEE Trans. Nanotechnolgy*, Vol. 5, No.6, (Nov. 2006), pp. 766-775

Huang, Y.; Wen-Yan, Y. & Liu; Q. H. (2008). Performance Prediction of Carbon Nanotube Bundle Dipole Antennas. *IEEE Trans. Nanotechnology*, Vol. 3, No.3, (May 2008), pp. 331-337

Koledintseva, M. Y.; Drewniak, J. L.; DuBroff, R. E.; Rozanov, K. N.; & Archambeault, B. (2009), Modeling of shielding composite materials and structures for microwave frequencies, *Progress In Electromagnetics Research B*, Vol. 15,(2009) pp. 197-215

Li, S.; Yu, Z.; Rutherglen, C.; & Burke, P. (2007). Electrical properties of 0.4 cm long single walled carbon nanotubes. *Nano Lett.*, Vol. 4, No. 10, (2007), pp. 2003-2007

Maffucci, A.; Miano, G. & Villone, F. (2009). A New Circuit Model for Carbon Nanotube Interconnects With Diameter-Dependent Parameters. *IEEE Trans. Nanotechnology,* Vol.8, No.3, (May 2009), pp.345-354

Maffucci, A.; Miano, G.; Villone, F. (2008). Electromagnetic and circuital modeling of carbon nanotube interconnects. *Electronics System-Integration Technology Conference, 2008. ESTC 2008. 2nd* , pp.1051-1056, 1-4 Sept. 2008

Mashal, A.; Sitharaman, B.; Xu Li; Avti, P.K.; Sahakian, A.V.; Booske, J.H. & Hagness, S.C. (2010). Toward Carbon-Nanotube-Based Theranostic Agents for Microwave Detection and Treatment of Breast Cancer: Enhanced Dielectric and Heating Response of Tissue-Mimicking Materials. *IEEE Transactions on Biomedical Engineering,* Vol.57, No.8,(Aug. 2010), pp.1831-1834

Massoud, Y. ; & Nieuwoudt, A. (2006). Modeling and Design Challenges and Solutions for Carbon Nanotube-based Interconnect in Future HighPerformance Integrated Circuits. *ACM Journal on Engineering Technologies in Computing Systems*, Vol. 2, No. 3, (July 2006), pp. 155-196

Miano, G. &Villone, F.; (2006). An Integral Formulation for the Electrodynamics of Metallic Carbon Nanotubes Based on a Fluid Model. *IEEE Trans. Antennas Propag.*, Vol.54, No.10, (Oct. 2006), pp.2713-2724,

Mikki, S.M. & Kishk, A.A. (2009). Mean-Field Electrodynamic Theory of Aligned Carbon Nanotube Composites. *IEEE Trans. Antennas Propag.*, Vol.57, No.5,(May 2009), pp.1412-1419

Miyamoto, Y.;Rubio, A.; Louie, S. G.; & Cohen, M. L. (1999). Self-inductance of chiral conducting nanotubes. *Phys. Rev. B*, Vol. 60, No. 19, (Nov. 1999), pp. 13885-11889

Naeemi, A. & Meindl, J. D., (2009). Performance Modeling for Carbon Nanotube Interconnects, In : *Carbon Nanotube Electronics*, Javey, A. ; & Kong, J. (Eds.) 163-189, Springer, ISBN 978-0-387-36833-7

Pierantoni, L.; Mencarelli, D.; Rozzi, T. (2008). A New 3-D Transmission Line Matrix Scheme for the Combined SchrÖdinger–Maxwell Problem in the Electronic/ Electromagnetic Characterization of Nanodevices. *IEEE Transactions Microwave Theory and Techniques*, Vol.56, No.3,(March 2008), pp.654-662

Pierantoni, L.; Mencarelli, D. & Rozzi, T. (2009). Boundary Immittance Operators for the SchrÖdinger–Maxwell Problem of Carrier Dynamics in Nanodevices. *IEEE Transactions Microwave Theory and Techniques*, Vol.57, No.5, (May 2009). pp.1147-1155

Plombon, J. J.; O'Brien, K. P.; Gstrein, F.; Dubin, V. M. & Jiao, Y. (2007). High-frequency electrical properties of individual and bundled carbon nanotubes. *Phys. Lett.* Vol. 90, (2007), pp. 063106

Rutherglen, C.; Jain, D. & Burke, P. (2008). RF resistance and inductance of massively parallel single walled carbon nanotubes: Direct, broadband measurements and near perfect 50 Ω impedance matching. *Appl. Phys. Lett.* Vol .93,(2008), pp. 083119

Shuba, M. V.; Maksimenko, S. A. & Lakhtakia, A. (2007). Electromagnetic wave propagation in an almost circular bundle of closely packed metallic carbon nanotubes. *Physical Review B*, Vol. 76, (2007), 155407

Slepyan, G. Y.; Maksimenko, S.A.; Lakhtakia, A.; Yevtushenko, O. M. & Gusakov, A. V. (1998) Electronic and electromagnetic properties of nanotubes, *Physical Review B*, Vol 57, No. 16 (April 1998), pp. 9485-9497

Slepyan, G. Y.; Maksimenko, S. A.; Lakhtakia, A.; Yevtushenko, O. & Gusakov, A. V. (1999). Electrodynamics of carbon nanotubes: Dynamic conductivity, impedance boundary conditions, and surface wave propagation. *Physical Review B*, vol. 60, Issue 24, (1999), pp. 17136-17149

Slepyan, G. Ya.; Nemilentsau, A. M. & Maksimenko, S. A. (2008). Electromagnetic Theory of Nanodimensional Antenna for Terahertz, Infrared and Optics Regiems. *2008 12th International Conference on Mathematical Methods in Electromagnetic Theory*, June 29-July 02, pp. 118-123, Odesa, Ukraine

Xu, H.; Anlage, S. M.; Hu, L. & Gruner, G. (2007). Microwave shielding of transparent conducting single-walled carbon nanotube films. *Applied Pysics Letters*, Vol. 90, (2007), 183119

21

Chemically Modified Carbon Nanotubes: Derivatization and Their Applications

Malingappa Pandurangappa and Gunigollahalli Kempegowda Raghu
Department of Chemistry, Bangalore University,
Central College Campus, Bangalore
India

1. Introduction

Nanotechnology and Nanoscience is the fastest emerging and developing field of science, which find technological importance and intense interest to many researchers. The unique chemical, physical, electronic (metallic or semiconducting) and high thermal properties of carbon nanotubes (CNTs) made them interesting materials for widespread application in the fields such as electrochemical sensors, biosensors, supports for heterogeneous metal catalysts in organic synthesis, fuel cells, semiconductors, batteries, random access memory cells, field effect transistor, field emission display, atomic force microscopy probes, microelectrodes, specific adsorbents to remove organic pollutants from water and waste water and as a potential drug carriers in cancer therapy. The poor solubility of carbon nanotubes in organic solvents restricts them to be used as drug delivery agents into living systems in drug therapy. Hence many modification approaches like physical, chemical or combined have been exploited for their homogeneous dispersion in common solvents to improve their solubility [1-4]. The reports appeared till now in the literature reveals that the modification is required to control the dispersion and such modification introduces specific functionalities as molecular wedges onto the surface of the carbon nanotubes. Thus the functional groups present on the surface control the lateral interactions between the bundles and separate indivisual tubes. Hence homogeneous dispersion can be achieved by breaking the close lateral contact between them which enhances the affinity towards solvents and other related matrices [2]. Due to these specific properties, many research groups explored the development of novel methods for the modification of nanotubes and investigated the mechanistic aspects of these new class of novel materials called chemically modified carbon nanotubes (CMCNTs).

Many applications require covalent modification to meet specific requirements i.e. in case of biosensors the biomolecules require electron mediators to promote electron transfer [5]. Similarly electrochemical metal ion sensors require specific functional groups which show potential affinity towards particular metal ion [6]. The chemical modification of a carbon substrate material was first reported by Murray et. al. in 1970s [7]. The modification protocol was generally achieved by attaching specific molecule or entity which imparts chemical specificity to the substrate material [8]. These chemical modifications can be easily achieved in many ways but in this chapter the modification routes are mainly classified into two

types namely surface modification and bulk modification. The surface modification includes electrochemical induced method, polymer grafting and metal nanoparticle deposition. The later includes chemical reduction of diazonium salts using hypophosphorous acid as a reducing agent, thermally activated covalent modification, microwave assisted modification and ball milling modification.

2. Derivatization methodologies

2.1 Electrochemically assisted covalent modification

Electrochemically assisted covalent modification of carbon substrate material has become a new era in the field of chemically modified electrodes which involves the formation of covalent bond between the substrate and the modifier molecule which had been reviewed by Alison J Downard [9]. Two strategies have been reported in the literature, one is the reductive strategy which involves the electrochemical reduction of aromatic diazonium salts and the other includes the oxidation of aromatic amines [10] which have been discussed elaborately in reviews appeared recently [9,11].

The reductive strategy was initially developed by Jean Pinson and co-workers in 1990 [12] and later developed by a number of workers including McCreery [13] and Downard group [9]. The basic mechanism involved in this modification is the generation of aryl radical at the solution/electrode interface by one electron electroreduction of corresponding diazonium salt and its subsequent attachment on the surface of carbon nanotubes which results in the formation of covalent bond between carbon atom of substrate and carbon atom of the modifier molecule. The schematic modification of the carbon surface has been shown in the figure 1[12].

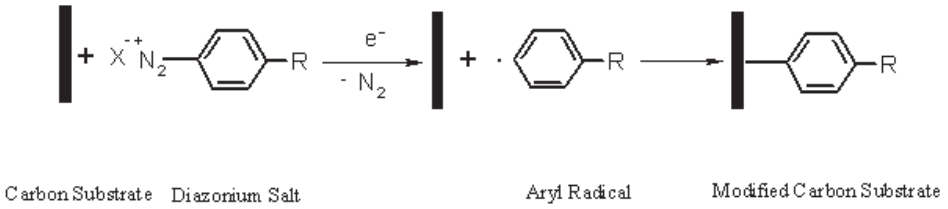

Fig. 1. Schematic representation of electrochemical reduction of aromatic diazonium salt [12]

Electrochemical modification can be achieved easily using techniques like cyclic voltammetry [14] or controlled potential electrolysis [15] either in non aqueous or in aqueous solutions of pH less than 3 [16]. The thickness of the modifying molecule on the surface of CNTs can be controlled by varying the experimental variables like applied potential or current, length of modifier molecule, concentration and scan rate. McCreery et.al. have predicted that the concentration less than 1 mM of modifier forms monolayer and greater than 1 mM concentration results multilayer formation [10, 17]. Very low reduction potentials have to be applied typically around 0 V vs SCE, to generate radical because of electron withdrawing nature of diazonium group. The C - C bond formed in this strategy is significantly stronger than the gold - thiol bond and they can withstand temperature upto 700 K without being lost from the surface [18]. It is quite stable over wide potential window in the range 2.6 - 5.6 V depending on the substituents on the para position [19]. In contrast to

the enhanced stability, formation of these layers on electrode surfaces are less controlled than for the alkane-thiol system. The aryl radicals generated electrochemically are captured by the carbon surface, a fraction of aryl radicals generated in the reaction may bound on the carbon surface, rest of them goes into solution. Allongue et.al. have reported that 84% of radicals form bonds with a glassy carbon surface while only 56% form bonds with the basal planes of highly oriented pyrolytic graphite (HOPG) [18]. The order and coverage of the modifier molecules in the modification layer also depends on the type of modifier as well as the substrate surface. This has been illustrated by McCreery and co-workers [20] where the diazonium salt of nitroazobenzene gave well ordered monolayers on glassy carbon but not on the basal planes of HOPG or diamond where the coverage was only between 50 - 70% of a monolayer [21].

Steven et.al. has modified the indivisual single walled carbon nanotubes(SWCNTs) by the electrochemical reduction of diazonium salt of p-nitro phenol in a home built miniaturized electrochemical cell equipped with platinum wire as counter electrode and pseudo-reference electrodes. Based on experimental results they concluded that the covalent bond formation occurs between the lattice of carbon nanotubes and carbon atom of substituted phenyl groups. The detailed investigations revealed that the degree of functionalization of the carbon nanotubes was as high as 5% of carbon atoms bearing a functionalized moiety, implying that it is not only the ends but also the sidewalls of the SWCNTs that were susceptible to radical attack [10]. Another way of electrochemical modification involves the oxidation of amines. The carbon substrate surfaces like CNTs, graphitic carbon, carbon fibers and glassy carbon spheres were functionalized with amines by their oxidation which forms surface attached layers on the electrode surface. Several mechanisms pertaining to the modification of carbon surfaces by the oxidation of amines have been reported in the literature. One such modification proceeds through stepwise manner wherein the proton loss occur after amine gets attached to the surface (Fig. 2A) and the other way involves the formation of amine cation radical with a loss of proton before the amine gets attached on the surface (Fig. 2B) [12].

A variety of primary amines such as 6-aminohexanol, 4-aminobenzoic acid, 4-aminoethyl pyridine, β-alanine, 2-amino-2-methylpropane, butylamine, octylamine, decylamine, dodecylamine, cysteine, dopamine, aspartic acid, 4-aminomethyl phenylboronic acid, 3-nitro benzylamine, octadecylamine, triethylene tetramine, hexamethylene tetramine, 2-amino anthraquinone, 2-amino-4-methyl thiazole, 1,7-diaminoheptane, 1,10-diaminodecane and 4-amino butyl-H_3PO_4 have been covalently attached onto the rigid surfaces of glassy carbon, carbon fiber and graphitic carbon based electrodes respectively. This kind of modification can also be carried out with secondary and tertiary amines also. Comparing the oxidation of primary, secondary and tertiary amines, the tertiary amines undergo oxidation easily compared to primary and secondary amines which were confirmed by the strong, sharp, irreversible oxidation peaks appear at least positive potentials. This kind of observed behavior might be due to the stabilization of amine cation radical by the presence of alkyl substituents [22,23]. The lifetimes of the radical cation formed increases from primary, secondary to tertiary amines. Although the ease of amine oxidation decreased from tertiary, secondary and primary, primary amines were found to give the highest modifier surface concentration when compared to secondary amines. However in case of tertiary amines the attachment was very poor and sometimes not detectable due to stearic hindrance of bulky substituents at the nitrogen atom which prevents the tertiary amine to undergo oxidation and get attached to the carbon surface. Attachment of primary amines on the electrode

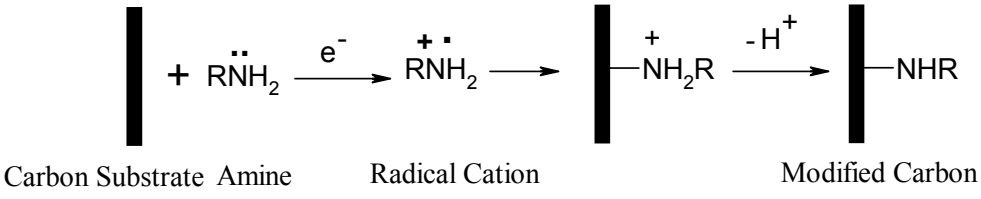

2A)

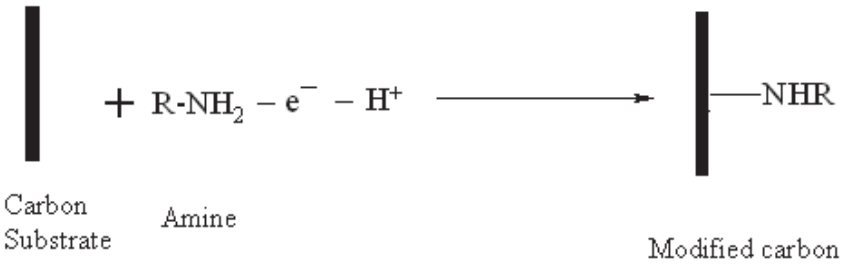

2B)

Fig. 2. Schematic representation of carbon modification through amine oxidation.

surface was supported by an observation that the irreversible oxidation peak disappears and the currents decreased significantly with the increase of number of cycles in cyclic voltammetry (CV), whereas for secondary and tertiary amines the height of the oxidation peak remained relatively unchanged. The attachment of amine to carbon surface through its oxidation preferably requires either primary or secondary amines but not tertiary amines. The amine oxidation mechanism has an H group eliminated during the oxidation process, which is not possible with tertiary amines. The reaction occurs with a monoamine modifier however in case of diamine modifiers it is possible that both amines attach to the surface. In one study that investigated the attachment of ethylene diamines to carbon fibers, it was proposed that the single oxidation peak observed accounted for two single electron processes. The two identical and electronically independent amines were oxidized at closely spaced potentials [24, 12]. The coupling of 4-fluorobenzoyl chloride, the conformation of the ethylene diamines monolayer attached to carbon fibers was suggested to be 75% coverage in the looped arrangement where both amines were surface bound and the remaining 25% were attached via one amine [12]. In another study two irreversible oxidation peaks were observed for modification of carbon fibers with ethylene diamines. The peaks were attributed to the corresponding mono and dication radicals respectively. The potentiometric titrations of modified carbon fibers with HCl has revealed that the majority of the ethylene diamines modifiers were attached to the carbon fibers by oxidation of the two amines which subsequently led to form a polymeric multilayer chain and also a looped configuration. The longer diamines like 1, 7-diaminoheptane 1, 10-diaminodecane and 1, 12-diaminododecane has resulted that only one amine of the diamines was covalently attached to the glassy carbon surface where as the other amine is not surface bound [25]. Steven et.al. modified the indivisiual SWCNTs by the electrochemical oxidation of substituted amino phenol [10].

2.2 Polymer grafting

Polymers with its inherent tunable chemical properties like good stability, number of active sites, strong adherence, homogeneity, electronic properties makes these materials interesting. In addition to these properties, polymers reduces the adsorption phenomena by the selective exclusion of interfering species and also due to the presence of large number of active sites which can preconcentrate the analyte molecules. They are also semipermiable hence only selective analytes can diffuse towards it hence high specificity towards particular analyte can be achieved. The combination of all these properties of polymers and the properties of nanotubes make them a very important class of synthetic materials which mimic the molecular recognition by natural receptors. CNTs modification with polymers can be achieved mainly in three ways, the first one involves simple soaking of the electrode material in a polymer solution the other involves chemical approach which inherently requires an oxidant further it gets converted into a reducing product and the last approach involves electrochemical approach i.e. electropolymerization either by potential cycling or under galvonostatic conditions. Electropolymerization on rigid electrode has got considerable attention in recent years due to the possibility of having great control over the thickness of the polymer layer on the surface of CNTs [26-28]. In this way MWCNTs were modified with polydiphenylamine(PDPA), Poly(acrylic acid), Quinone - o – phenylenediamine, Osmium (4,4 – dimethyl – 2, 2 – bipyridine) chloride and also with most popular electron-conducting polymers like polyaniline(PANI), polypyrrole (PPy) and the derivatives of polythiophene(PTh). Similarly SWCNTs were modified with poly(styrene sulphonic acid) sodium salt, poly(1, 2-diamino benzene) (PABA) [29,30]. These modified materials have been designed as sensing surfaces that are capable of interacting with simple anions, metal ions and small organic molecules.

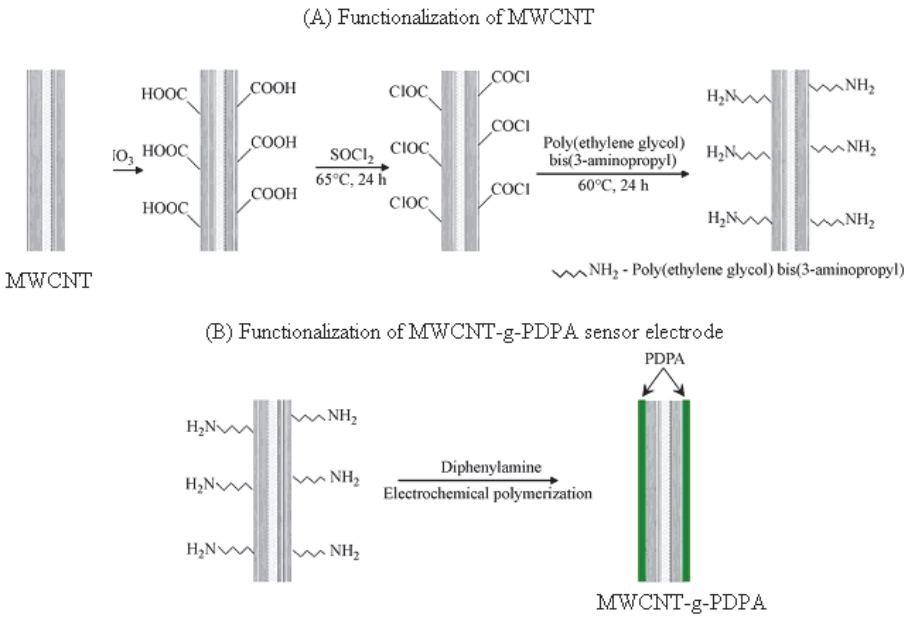

Fig. 3. Modification of MWCNTs-Polydiphenylamine A) amine functionalization of MWCNTs B) fabrication of MWCNTs-PDDA sensor [30]

2.3 Nanoparticle modified carbon nanotubes

Nanoparticles (NPs) in particular metal and semiconductor NPs are the building blocks of nanodevices since from the time of Faraday who proposed that the ruby red color of gold colloid has been the consequence of its small particle size [31]. The size dependent properties have given rise to enormous applications that have emerged in the last few decades [32]. Data storage, sensing devices, catalysis, biological interfaces, quantum dots, nanoelectromechanical devices and nanotribology are some of the areas where the impact has been very substantial and also in several areas from chemistry to physics to material science to biology and medicine [33].

On the other hand, owing to the excellent thermal, electrical, chemical and mechanical properties of CNTs (both SWCNT and MWCNT) they have been intensively studied and gained great deal of attention for their applications in various areas like sensing, biosensing, catalysis due to their inherent properties like high surface area, high electronic conductivity, outstanding chemical and electrochemical stability [34]. The modification of CNTs with nanoparticles for the construction and designing of nanoarchitectures would enhance the electrocatalytic efficiency of many electrochemical processes giving rise to several significant applications like sensors, biosensors, heterogeneous catalysts for fuel cells and nanotechnology [29].

Many methods are reported in the literature for the modification of CNTs with NPs which are associated with their own advantages and disadvantages. As a result of this, here we have focused selective and advanced methods such as electrochemical modification or electrodeposition, electroless deposition and modification through covalent attachment[35].

2.4 Electrodeposition

Electrochemical method is a powerful tool for the modification of nanotubes with NPs through electrodeposition because the method has great control over the nucleation and growth of NPs by varying nucleation potential, deposition time and the concentration of noble metal complexes.

Electrochemical deposition of NPs onto the CNTs is generally performed by the reduction of noble metal salts like $H[AuCl_4]$, $H_2[PtCl_4]$ and $(NH_4)_2[PdCl_4]$ mostly through van der walls interactions which is sufficient enough to provide good adhesion with the tubes [36].

He et.al. modified the nanotubes with Pt-Ru bimetallic nanoparticles with diameter 60-80 nm potentiostatically followed by the electrochemical oxidation in a solution containing various ratios of Pt to Ru in 0.5M H_2SO_4 [37].The developed composite showed a significant electrocatalytic activity towards methanol oxidation and the process is free from commonly interfering problem like CO adsorption which blocks the catalytic sites and it follows bifunctional mechanism as shown below.

$$Pt + CH_3OH \rightarrow Pt\text{-}CO_{ads} + 4H^+ + 4e^-$$

$$Ru + H_2O \rightarrow Ru\text{-}OH + H^+ + e^-$$

$$Ru\text{-}OH + Pt\text{-}CO_{ads} \rightarrow Ru + Pt + CO_2 + H^+ + e^-$$

Day et.al. electrochemically deposited the Pt and Pd NPs onto the surface of tubes at various potentials with different times and from the experimental results they found the strong dependence of deposition potential and time on the size, density and distribution of NPs on the surface of carbon nanotubes [38]. Afterwards they have further extended the

methodology for the electrodeposition of Ag and Pt on high density SWCNT networks and determined the complete dependence of dispersion of NPs in the form of nanowires or in the form of individual nano particles. The driving potential required for the deposition of metal nanoparticles varies with respect to the distance from the metal contact electrode. The potential for deposition decreases with increase of distance from the metal contact electrode therefore the rate of nanoparticles nucleation and growth increased at close proximity to the contact electrode, resulting in continuous nanowires, rather than separate NPs, near the contact electrode.

Chen et.al. have investigated the control on the size of Pt nanoparticles to 2-3 nm by varying the viscosity of the electrolyte and adjusting the potential pulses during course of deposition. Aqueous solutions of $H_2[PtCl_6]$ were used as working solution and its viscosity was varied by adding different quantities of glycerol then it is easily removed simply by rinsing with hot water. The results showed that the particle size of Pt NPs could be easily controlled by adjusting the diffusion of electrolyte and number of potential pulses [39]. Arai et.al.have reported electrodeposition of Cu and Ni nanoparticles on carbon nanotubes [40]. They demonstrated the selective deposition of Ni at ends and defect sites of MWCNTs which can be attributed to their high electrical conductivity in the axial direction and fast electron transfer kinetics at defect sites. Ni coated SWCNT nanowires were also prepared by electrodeposition on SWCNTs supported on alumina membranes. Lee et.al. have used drop coating method using acid treated tubes on a Ni working electrode using Pt wire & saturated calomel as counter and reference electrodes respectively [41]. Under potentiostatic condition at 0.4 V, they have deposited $MnSO_4$ at pH 5.6 as larger aggregates preferentially at the tips of nanotubes. Frank et.al. galvonostatically deposited the Ti from $TiCl_3$ precursor on the pristine SWCNT working electrode at pH 2.5. Similar modifications were also carried out to deposit NiO or RuO_2 via potential cycling by Kim et.al. They have found that the gas atmosphere during post annealing process had a significant effect on the morphology loss of the RuO_2. Further heating in argon atmosphere produced more uniform, spherical nanoparticles while annealing in O_2 atmosphere resulted in elliptical RuO_2 nanoparticles [42,43]. Qu et.al. reported the modification of nanotubes with Pt nanoparticles and [tetrakis (N methylpyridyl) porphyrinato] cobalt as a hybrid thin film electrode. In this case the platinum nanoparticles were generated by chloroplatinic acid in 0.5 M H_2SO_4, then adsorbed onto [tetrakis(N-methylpyridyl)porphyrinato]cobalt modified nanotubes through electrostatic interaction and then the platinate complex was reduced potentiostatically at -0.7V [44]. Tsai et.al. synthesized Pt (Pt-Ru) NPs/CNTs monohybrids by electrochemical deposition in ethylene glycol in presence of H_2SO_4 as supporting electrolyte. They have successfully obtained Pt (Pt-Ru) nanoparticles with 4.5 nm for Pt and 4.8-5.2 nm for Pt-Ru with uniform distribution on the surface of the tubes. Ethylene glycol not only enhanced the dechlorination of Pt and Ru precursor salts but also acts as stabilizing agent preventing the agglomeration of nanoparticles during electro deposition process which results in the better dispersion of small diameter Pt or Pt-Ru NPs [45,46]. Xia et.al. have used a novel methodology by using ultrasonic energy which involves the usual electrodeposition strategy to synthesize bimetallic Au-Pt NPs on the surface of MWCNTs in ionic liquids [47].

2.5 Electroless deposition (ELD)

This method involves the incorporation of NPs onto the surface of nanotubes without any external aid like reducing agent or applied potential for the reduction of metal ions as opposed

to that of electrochemical deposition or chemical reduction methods. The driving force beyond the modification involves the direct redox reaction between the tubes and NPs. For the first time Dai et.al. modified the nanotubes with Pt and Au NPs using this method [48]. ELD can be carried out only when the metal ions having higher redox potentials than nanotubes, hence Au, Pt, Pd metal ions can be used to modify tubes through this method but not metal ions like Ag, Ni and Cu because of their lower redox potentials than that of the nanotubes. The atomic force microscopy (AFM) and Fermi level diagram of SWCNTs is shown in the following figure 4 [48]. In order to overcome the above limitations, Qu and Dai further developed a novel process known as substrate enhanced electroless deposition (SEED) [49]. In this strategy CNTs were supported by a metal substrate having lower redox potential than that of NPs and the deposition of metal NPs was achieved through the redox reaction of a galvanic cell wherein the carbon nanotubes acts as a cathode for metal deposition by the reduction of metal ions in solution and the metal substrate serves as an anode where the metal atoms are oxidized to the corresponding ions and dissolved in solution. The schematic representation of the reaction pathway is shown in the following figure 5 [49].

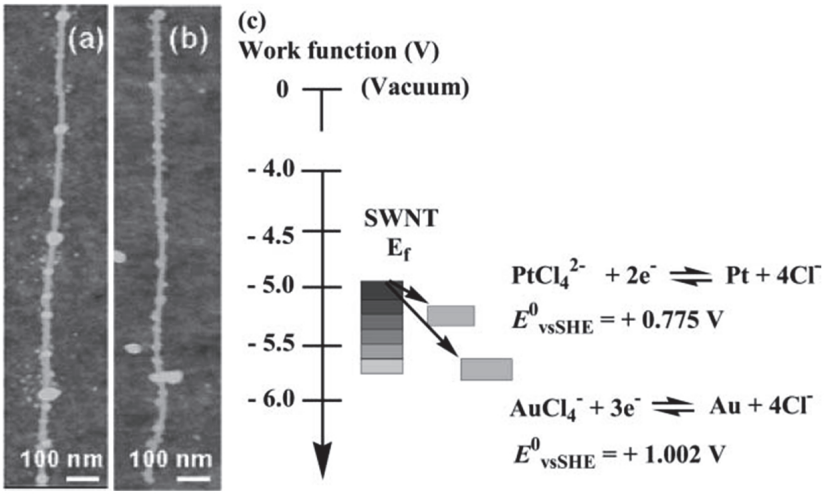

Fig. 4. AFM images of (a) Au and (b) Pt NPs on SWCNTs. (c) Diagram of the Fermi energy (EF) of a SWCNT, and the reduction potentials of Au^{3+} and Pt^{2+} vs. SHE respectively [48].

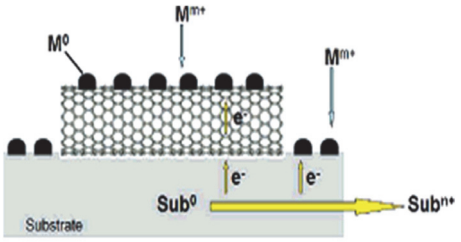

Fig. 5. Schematic illustration of metal nanoparticles deposition on carbon nanotubes through electroless deposition process [49].

2.6 Modification through covalent attachment

Heterogeneous catalytic reactions encounter completely on the surface of supporting substrates, hence surface structure play a very important role in heterogeneous catalysis. In recent years NPs decorated carbon nanotubes are used as catalytic supports but simple deposition of metal NPs results in a poor dispersion and hence least stability due to insufficient binding sites present on the surface of carbon nanotubes. Hence in order to achieve highly stable and uniformly dispersed nanoparticles, the surface of nanotubes must be modified via a proper functionalization procedure which involves the formation of covalent bond with the use of linker. The strength of the modification determines the distribution and concentration of the metal nanoparticles on the surface of carbon nanotubes [50].

Covalent modification of nanotubes can be achieved by many ways which has been reviewed in the literature [51]. The main perspective of this modification involves the generation of oxygen containing functionalities more specifically, carboxylic groups commonly called as surface oxides by the aggressive oxidation treatment using strong acids. The resulting carboxylic acid groups are used to anchor and disperse the NPs on the surface of tubes but it is hard to achieve smaller particle size and high degree of loadings [52]. In order to overcome this drawback, the carboxyl functionalized carbon nanotubes could be further grafted with functional moieties with terminal amine or thiol groups which can effectively control the particle size and dispersion of noble metal NPs on the surface of tubes. Niu and co-workers have proposed the above modification procedure recently [53]. They modified the carboxylated nanotubes with amine terminated ionic liquids through amide bond formation and subsequently attached the gold NPs through electrostatic interaction and ion exchange. The resulting modified CNTs showed nano sized and uniform distribution of NPs. Similarly Guo et.al. have modified the nanotubes using imidazolium salt based ionic liquids (IS-ILs) as linkers. Further they found the enrichment of $PtCl_6^{2-}$ by coupling effect which promotes the nucleation of Pt NPs due to low interface energy [54]. Lu and Imae et.al. have modified the MWCNTs covalently with fourth generation NH_2-terminated poly(amidoamine) (G4-PAMAM) dendrimers (CNT/DEN) and used as support for Au NPs. The particle size of Au NPs could be concisely controlled by tuning the ratio of $H[AuCl_4]$ to the covalently bonded dendrimers on the surface of CNTs (Fig.6) [55].

These results revealed that the Au NPs interacts with the dendrimers in two possible ways. One is the coordination of NPs at outside the dendrimers and the other is the encapsulation of NPs inside the dendrimers [55]. Further, Ag, Cu, Pt and Ag@Au NPs were also successfully synthesized in situ on the surface of CNT/DEN with a great control on its particle size. The Pd NPs were also deposited on the surface of MWCNTs which were initially functionalized with thiol [56], benzenesulfonic [57] and ionic liquid functionalized MWCNTs [58]. Banerjee et.al. have functionalized the CNTs with CdSe QDs through p-mercaptobenzoic acid using ethylenediamine as linker between oxidized CNTs and p-mercaptobenzoic acid. In a similar way, thiol stabilized ZnS capped CdSe QDs were protected with 2-aminoethanethiol and linked to the acid terminated carbon nanotubes in presence of a coupling agent like EDC (Fig. 7) [59]

In contrast to this, metal oxides can be attached to the carboxyl groups without any linker due to their hydrophilic nature as recently demonstrated for MnO_2, MgO, TiO_2 and $Zr(SO_4)_2$. However, the authors observed only weak interactions between the oxides and the acid-terminated nanotubes resulting in rather nonuniform distributions of the NPs. Better adhesion was observed when capping agents were used. Sainsbury and Fitzmaurice produced capped TiO_2 and SiO_2 nanoparticles ($d \approx$ 4-5 nm) via a standard sol-gel process using titanium tetraisopropoxide (TTIP) and tetraethyl orthosilicate (TEOS) as precursors with cetyltrimethyl ammonium bromide (CTAB) as the capping agent (Fig. 8) [60].

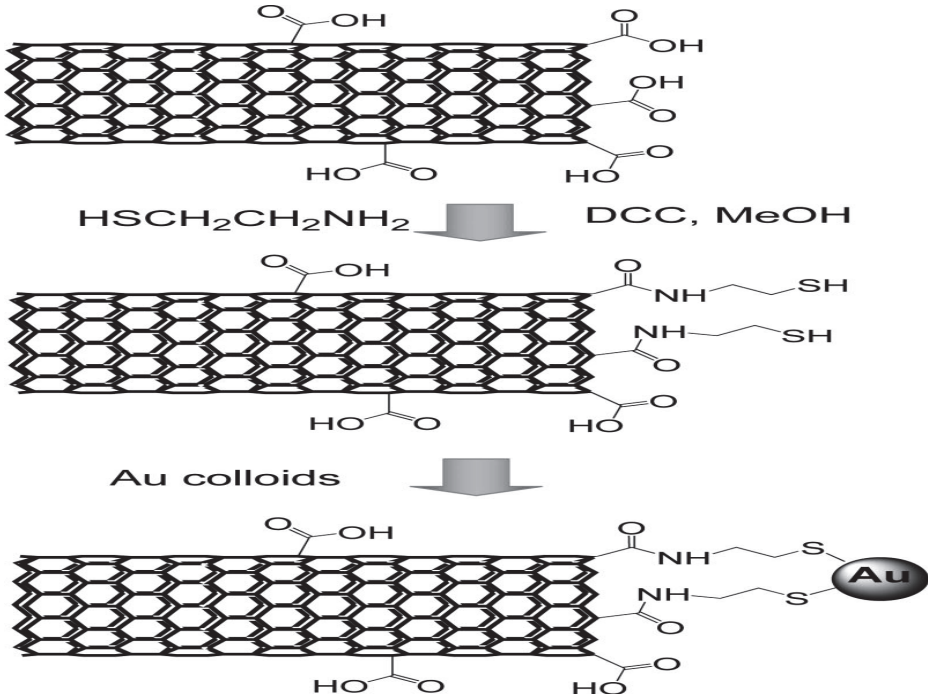

Fig. 6. Covalent attachment of Au nanoparticles to amino or mercapto terminated CNTs [55].

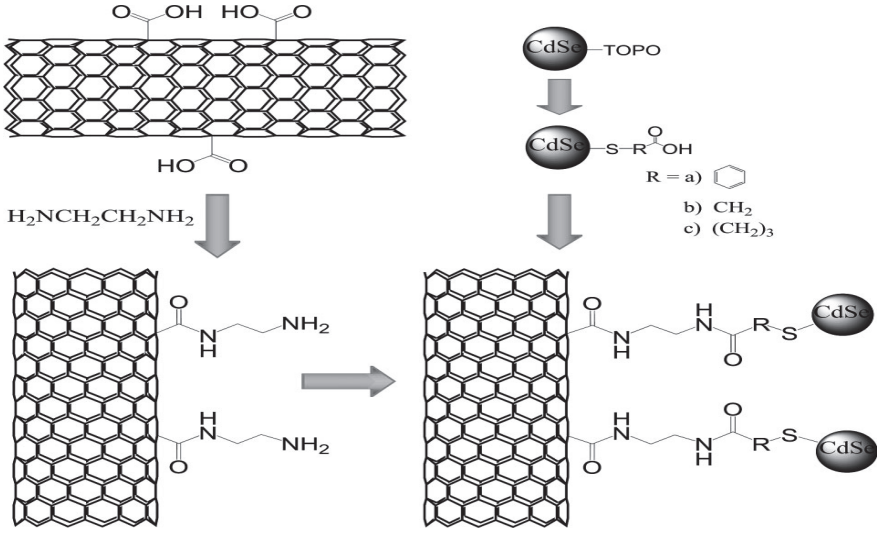

Fig. 7. Multistep process for linking modified CdSe QDs to CNTs via amide bonds, involving oxidation of CNTs and functionalization with ethylenediamine and thiolization of CdSe and termination with acid groups [59].

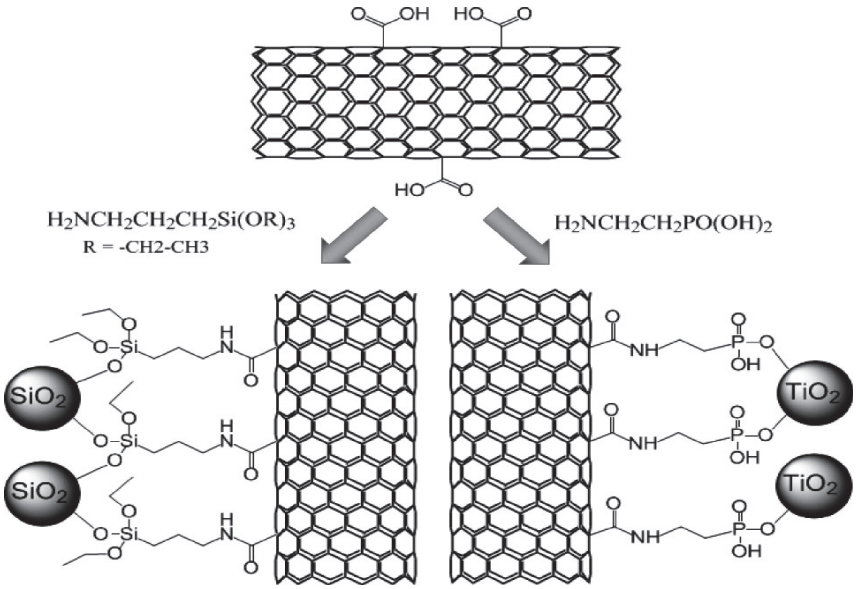

Fig. 8. Modification of carbon nanotubes with SiO_2 and TiO_2 nanoparticles via silane and phosphonic acid bonds [60].

2.7 Modification through chemical reduction of diazonium salts

This class of modification involves one electron chemical reduction of aromatic diazonium salts in presence of hyphophosphrous acid as a reducing agent. The reduction yields molecular nitrogen and a highly reactive aryl radical which subsequently attached to the carbon surface and forms covalent bond between carbon and the modifier molecule. General scheme and modification mechanism has been shown in the figure 9 [61].

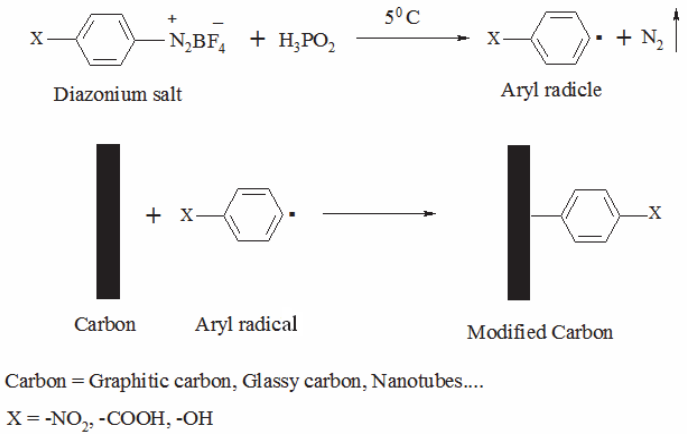

Fig. 9. General scheme of modification of carbon substrates using hypophosphorous acid as a reducing agent.

This method of modification is a simple and convenient for the preparation of gram quantities of modified carbon nanotubes and offers high degree of functionalization which results in bulk modified carbon substrate material. This bulk modified carbon substrate material can be utilized as a thin film to fabricate chemically modified electrodes or it can be compressed into pellets before using as electrode material for various applications [61].
The general procedure of this modification involves the addition of H_3PO_2 into a mixture of carbon substrate material and diazonium salt solution with occasional stirring at 0-5^{0}C for about 30 minutes. Then the resulting mixture is filtered, washed thoroughly with acetonitrile to remove any unreacted diazonium salt and with ample quantities' of water to remove the excess of acid. Finally the modified carbon has been dried by placing in a fuming hood for 12 hours and stored in an air tight container [61]. Using this strategy, Heald et.al. have prepared 1-anthraquinone functionalized MWCNTs and studied their electrochemical behaviour. These electrochemical studies revealed that the modified MWCNTs undergoes two electron, two proton transfer which results in a quasi reversible cyclic voltammograms corresponding to quinine/hydroquinone redox couple which has been confirmed by the pH study (Fig. 10).

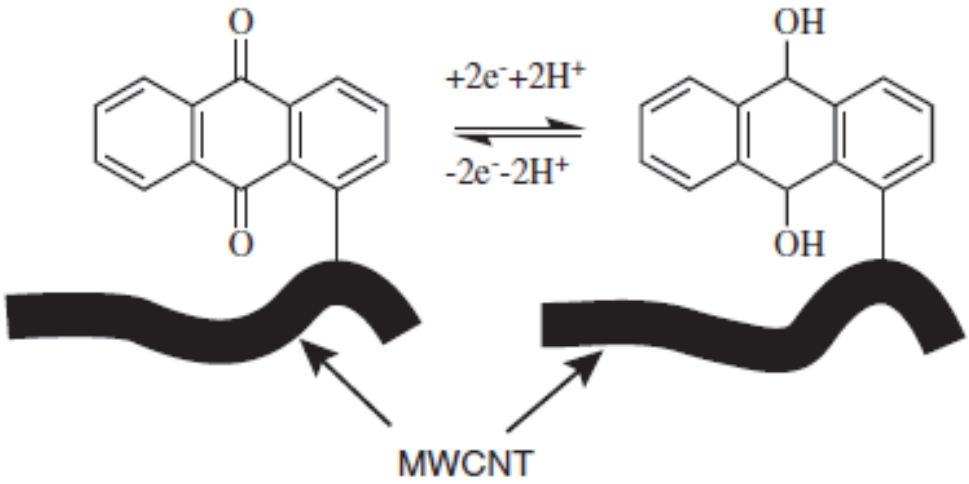

Fig. 10. Two-electron, two-proton redox couple of the anthraquinone/anthrahydroquinone modified MWCNTs [62]

Masheter et.al. have extended the derivatization method of Heald et.al. using nanotubes of different morphologies like b-MWCNTs, h-MWCNTs and SWCNTs and proposed the following modification strategy[63]. In case of MWCNTs, the majority of anthraquinonyl radicals modify the edge-plane like sites at the tube ends than that of the basal planes, whereas a greater degree of sidewall functionalization occurs for the SWCNTs, which reflect their greater reactivity. Masheter et.al. have attached the anthraquinone species covalently onto the surface of graphitic powder after attaching nitrophenyl groups and reducing it to aniline species then coupling with anthraquinone-2-carboxylic acid which results AQ-AN modified CNTs (Fig. 11) [63].

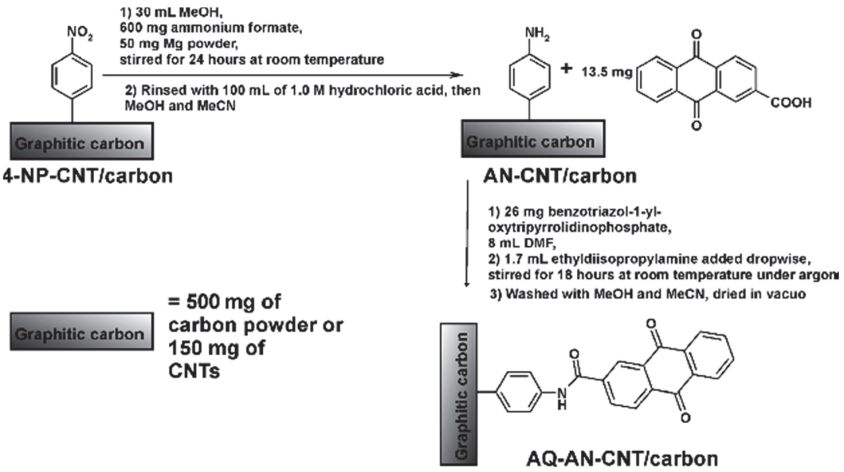

Fig. 11. Derivatization of graphitic carbon using anthraquinone-2-carboxylic acid [63]

This coupling method has the effect of attaching the anthraquinone center to the graphitic surface through a ''spacer'' molecule extending the anthraquinone group farther from the surface of the carbon material into the solution phase. Similar modification was also carried out by Abiman et.al. using MWCNTs of different morphologies in order to study the detailed mechanistic path way of chemical modification [64]. In this regard MWCNTs were derivatized in presence and absence of hypophosphorous acid as a mild reducing agent and the resulting materials were characterized using cyclic voltammetry. The observed peak potentials for the modified materials were found to differ depending on the derivatization conditions (presence/absence of hypophosphorous acid, diazonium salt concentration and temperature) and these differences were interpreted mechanically. The experimental results suggest that in the absence of hypophosphorous acid, the derivatization mechanism likely to proceed through a cationic intermediate, where as in the presence of the hypophosphorous acid the mechanism probably involves either a purely radical intermediate or a mixture of radical and cationic species depending on the concentration of a reducing agent and the reaction temperature (Fig. 12) [64].

Polymerization of the nitro phenyl groups on the surface of nanotubes was studied using different concentrations of 4-nitrobenzenediazonium tetraflouroborate and was found to increase with increasing concentration of cationic intermediates. The effect of the reaction temperature on the derivatization procedure was explored over a range of temperatures from 5 to 50^0C and the optimum derivatization temperature was determined in the presence and absence of hypophosphorous acid. It was found to be 20^0C and 35^0C in presence and absence of hypophosphorous acid respectively. The modified tubes both in presence and in absence of hyphophosphrous acid were physically immobilized onto the surface of MWCNTs and were electrochemically characterized using cyclic voltammetry in order to confirm the modification by utilizing the electroactivity of nitro groups. The cyclic voltammogram clearly shows an irreversible reduction wave of reduction of nitrophenol to hydroxy phenyl amine which corresponds to a four electron and four protons transfer and a quasireversible wave of oxidation of hydroxy phenyl amine to nitroso phenyl groups corresponds to the two protons and two electron processes. The possible mechanism along with cyclic voltammogram has been shown in the figure 13 [64].

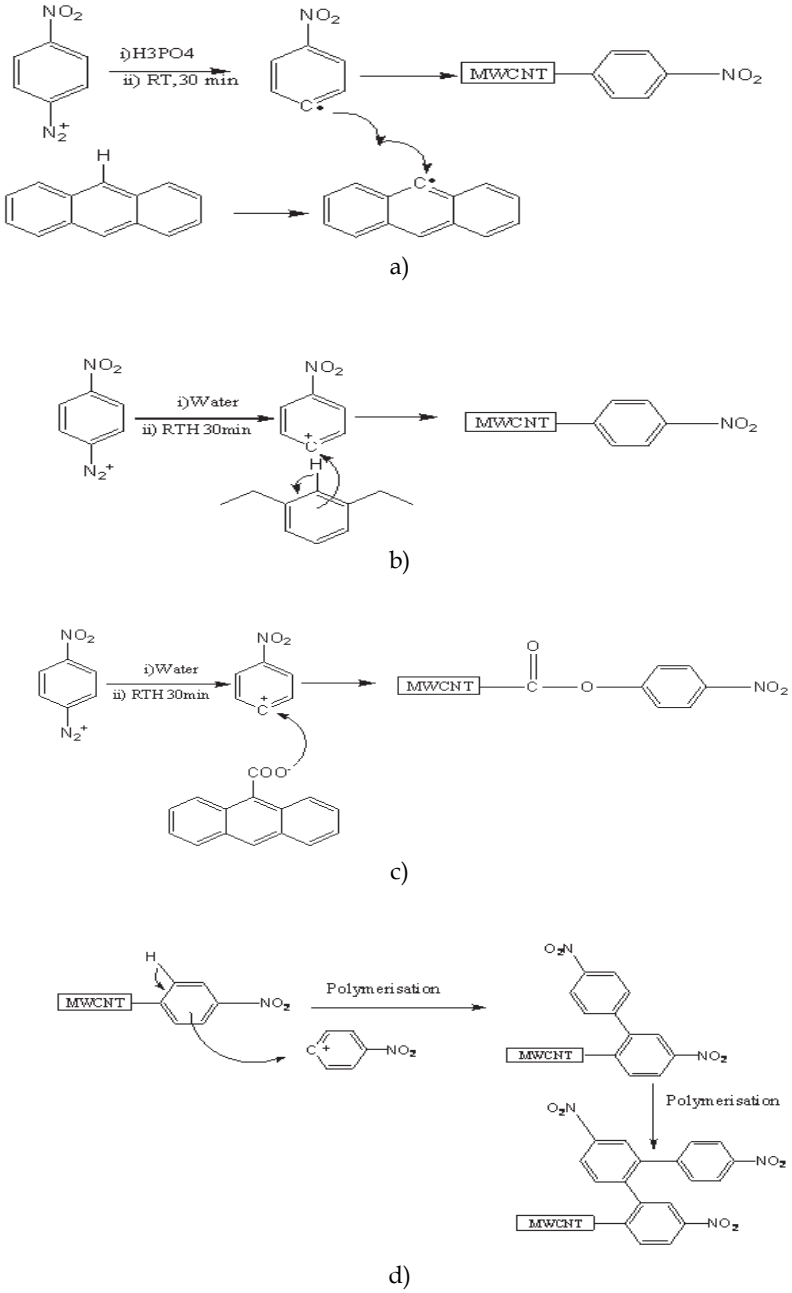

Fig. 12. Proposed mechanistic pathways for the derivatization of MWCNTs through a) radical intermediate; b) cationic intermediate; c) reaction of cationic intermediate with carboxylic group; d) polymerization of cationic intermediates [64].

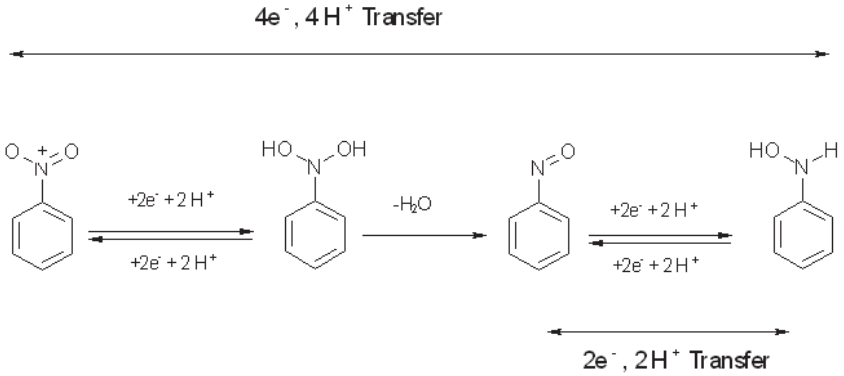

Fig. 13. Mechanistic pathway of electrochemical reduction of aryl nitro group under aqueous condition.

Recently Pandurangappa et.al. have modified SWCNTs using H_3PO_4 as a reducing agent and studied the stability of the modified substrate material by examining the electrochemical behaviour of indicator species for a period of one year [65]. In order to understand the stability of the modifier molecule on the substrate material, it has been examined the cyclic voltametric behaviour at different time intervals. Even after one year the electrochemical behavior of the functionalized CNTs remains more or the less same and the wave shapes are symmetrical with a slight variation in peak currents which might be due to the difference in the quantity of immobilized species drawn on the surface of the electrode during electrochemical study (Fig. 14) [65].

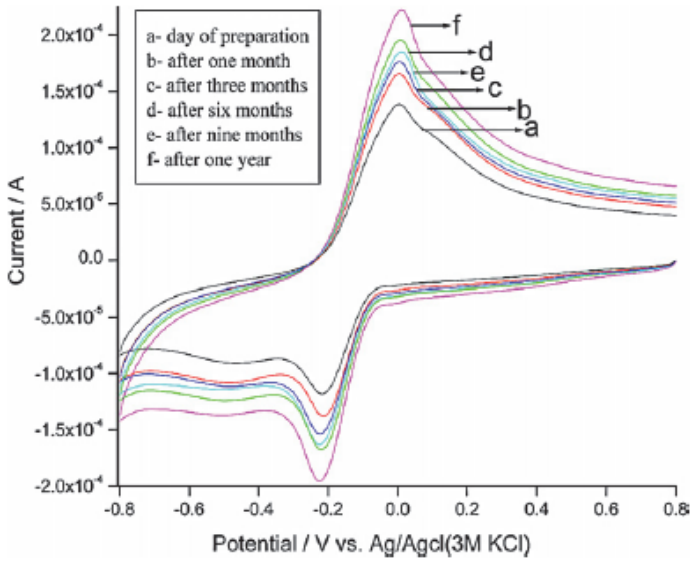

Fig. 14. Overlaid voltammograms of the covalently modified CNTs with anthraquinone species at different time intervals [65].

2.8 Thermally activated chemical covalent functionalization

This type of modification proceeds through three steps that are chemical oxidation, activation and amidation reactions. This multi step process results in highly stable modification with high surface coverage. Following this methodology Hsieh et.al. have reported the amino functionalized carbon nanotubes/carbon paper electrodes which have showed not only hydrophilic coverage for the formation of double layer (double layer capacitance) but also active sites for redox reaction. These materials pocesses higher capacitance, high rate capability and capacitance stability with high columbic efficiency compared to fresh and oxidized carbon nanotube/carbon paper capacitor materials [66,67]. Bifeng Pan et.al. have prepared the MWCNT nano hybrids initially by the oxidative pretreatment of CNTs with 3:1 H_2SO_4/HNO_3 mixture then they were activated using $SOCl_2$ and finally acyl chloride was coupled with ethylene diamine. The resulted MWCNTs were again modified with mercaptoacetic acid coated QDs [68]. Gabriel et.al. modifed the single walled carbon nanotubes similarly with different amines and explored two types of modification schemes. The first scheme involves the usage of $SOCl_2$ and in the second scheme without $SOCl_2$. From the experimental evidences they have concluded that the first scheme is the most efficient method for the functionalization of carbon based substrates which might be due to the increased degree of formation of carboxylic groups. The following scheme illustrates the two different modification strategies [69].

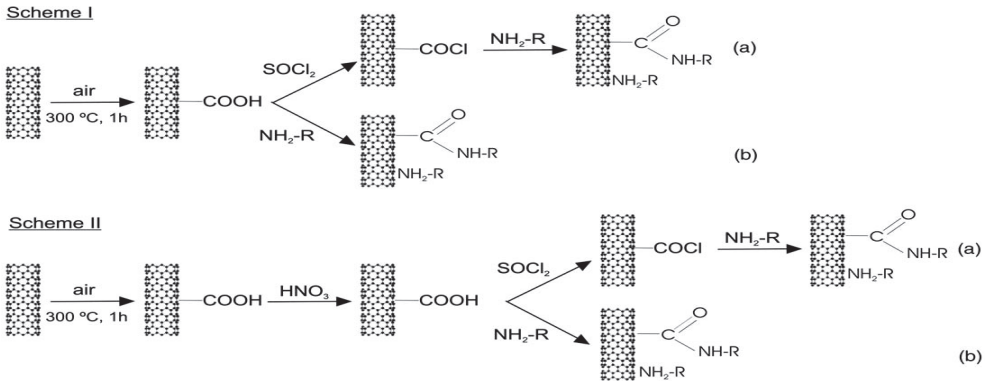

Fig. 15. Schemes illustrating the different strategies used to functionalize SWCNTs [69].

Kai et.al. have modified the MWCNTs with triethylenetetramine with three methods of acid treatments in order to determine the extent of carboxylic groups onto the surface of CNTs [70]. The first method involves the treatment of MWCNTs with 3:1 mixture of concentrated H_2SO_4/HNO_3 under sonication at 40^0C for 10 h. After acid treatment the CNTs were washed with ample quantities of water until the pH value of the washings reaches pH 7, then dried at 80^0C for 24 h. The second method was carried out as that of first method but without H_2SO_4. Similarly the third method was carried out as that of second but at a temperature of 90^0C. Then the acid activated MWCNTs were stirred for about 24 hours at 70^0C in presence of $SOCl_2$. The resulted acyl chlorides were further reacted with TETA at 12^0C under magnetic stirring for 96 h (Fig. 16) [70].

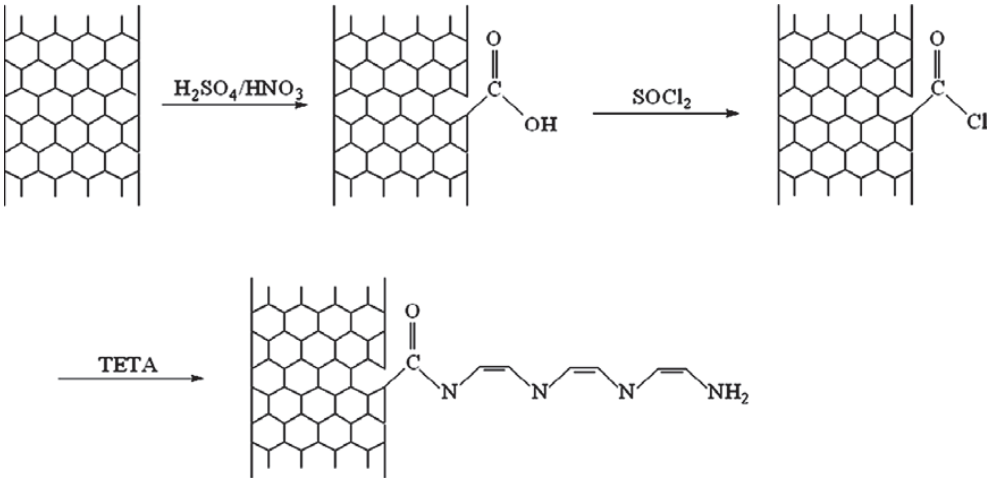

Fig. 16. Schematic representation of TETA grafting on the MWCNTs surface [70].

2.9 Microwave induced modification

Application of Microwave technology is relatively a new area in the field of chemical synthesis as evidenced by number of papers and reviews appearing in the literature in recent years. The chemistry under microwave radiation is known to be faster and more efficient than the conventional methods. Microwave assisted synthesis has been exploited in various fields of organic synthesis including heterocyclic, organometallic, combinatorial chemistry, synthetic transformations, radical reactions, organocatalysis, cycloaddition, metathesis and metal mediated transformations etc. due to the possibility of controlling the reaction by tuning pressure and temperature. These reactions have become significant ones in recent years as it reduces time, volume of solvents, quantity of reactants required for the completion of reaction and results in high purity, good selectivity and yield. The basic principle lying in this method is that when the molecules with permanent dipole moment are subjected into the electric field, the molecules get aligned with respect to the field. Molecular oscillations results as soon as the field oscillations begins and the molecules align and realign continuously giving rise to an intense internal heat energy which in turn agitates the molecules leading in the formation of product molecules [71,72].

Prato et.al. have described a new strategy for the multifunctionalization of nanotubes by the combination of two different addition reactions, 1, 3-dipolar cycloaddition of azomethine ylides and the addition of diazonium salts [73]. Then Ramanath and co-workers have demonstrated a novel strategy in combination with the polyol reduction of a metal salt to derivatize nanotubes with Au NPs in a single step [74]. Y. Wang et.al. have functionalized the SWCNTs with 2, 6-dinitroaniline through 1,3-dipolar cycloaddition initially through microwave irradiation in presence of conc. HNO_3 to produce carboxylic groups and coupling with 2, 6-dinitroaniline using DMF as solvent. Based on these facts they concluded that microwave assisted covalent functionalization can minimize the number of steps and the reaction could be completed within 15 minutes when compared to conventional methods which require long duration [75,76]. Jie Liu had showed the possibility of modifying the nanotubes through radical addition under microwave method using 4-methoxy phenylhydrazine hydrochloride as modifier molecule (Fig. 17) [77].

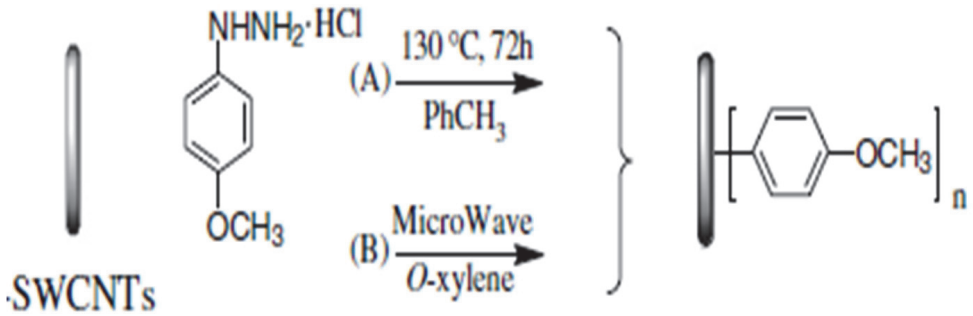

Fig. 17. Functionalization of SWCNTs by 4-methoxy phenylhydrazine through a classical thermal reaction (A) and a microwave assisted reaction (B) [77].

Raghuveer et.al. have demonstrated a novel strategy of combining microwave radiation with polyol reduction of a metal salt to derivatized tubes with Au nanoparticles in a single processing step. It is believed that exposing carbon nanotubes to microwave irradiation results in the formation of defects and functional groups on the tubes surface. These functional groups serve as preferred nucleation points for reducing metal ions from solution by a microwave reduction reaction yielding uniformly gold nanoparticles decorated nanotubes [74]. Nikolaos Karousis et.al. have modified the external wall of C_{60} encapsulated SWCNT peapods by insitu generated aryl diazonium salts using microwave irradiation [78]. Recently Jun Liu et.al. have reported the scalable and economical strategy for the effective transformation of Cu-complex to fabricate CuS CNTs based on the preferential chemical transformation and crystalline process and they have controlled the diameter of CuS/CNT composite by tuning the chemical reaction parameters [79]. This simple and convenient approach opens up a new way to synthesize CNT hetero structures that could be used in developing device concepts, novel catalysts and composites.

2.10 Modification through ball milling

Ball milling is a methodology in which solvent usage is very minimum or almost nil in the organic synthesis as well as in the surface modification reactions. Ball milling methods make the synthesis simple and very efficient phenomenon under green protocols. It is an established method for the generation of active centers on the substrate material surface during functionalization process under solvent free conditions. Simple ball mill grinding facilitates the activation of substrate material and subsequent modification with suitable indicator species often used in inorganic and material chemistry. This kind of modification has been extensively used in the preparation and modification of solids at laboratory and industrial scale levels [80]. The basic principle involved in this process is the generation of frictional forces by the collision between the surfaces of the reactants which results in the increased internal energy, temperature and pressure. In chemical synthesis, ball milling approach provides the required conditions very efficiently thereby the chemical reactions takes place in a very shortest time intervals. The mechanism of modification takes place either by changing the reactivity of the reagents or by breaking the molecular bonds [80]. Pierard et.al. have evaluated the effect of grinding on the structure of single walled carbon nanotubes using a ball mill and found the decreased length of CNTs and increased surface area which is a primary and necessary

condition for heterogeneous catalytic supports [81]. Welham et.al. have examined the effect of extended ball milling on the chemisorption of gases and its dependence on the extent of milling. Similarly Yu Feng Sun reported the adsorptive behavior of aniline in aqueous solution using milled nanotubes compared to unmilled nanotubes [82, 82a]. Li et.al. have reported the functionalization of SWCNTs with alkyl and aryl groups using the high speed vibration mill which have showed that the modified carbon surfaces with long alkyl chains are remarkably soluble in common organic solvents [83]. Peng et.al. have proposed a chemomechanical method for the insitu functionalization of nanotubes in presence of ammonium bicarbonate to introduce amine and amide groups. They have also observed that the conversion of semiconducting behaviour of tubes takes place from p-type to n-type [84]. Konya et.al. have shortened the MWCNTs using ball milling under ambient conditions and proposed different mechanisms for the cleavage of tubes based on the morphology of broken ends [85]. They have modified the MWCNTs with thiol, amine, amide, carbonyl and chlorine in presence of specific atmosphere through milling. The SWCNTs were modified with hydroxyl groups using a simple solid phase mechanochemical reaction at room temperature in presence of potassium hydroxide (Fig. 18) [86]. Recently Yi Liu et.al. have deposited the metal NPs onto the surface of carbon nanotubes by simple mechanochemical process within 10 minutes [87].

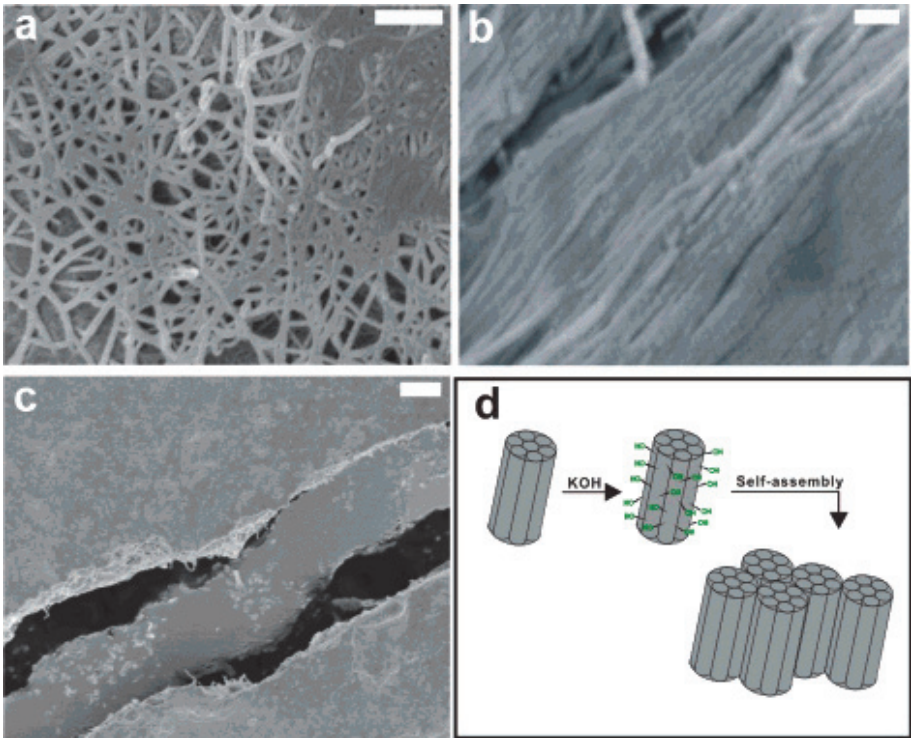

Fig. 18. SEM images of a) native SWCNTs (scale bar, 100nm) b) cross-sectional view of the self assembled SWCNTol sample shown in c) (scale bar, 100nm) c) top view of the self assembled SWCNTol sample (scale bar, 1000 nm) d) schematic representation of the self-assembled process [86].

3. Applications

3.1 Biosensors

Biosensors are the simple analytical devices composed of a sensing element, transducer and a detector which results a biological response in the form of a detectable and quantifiable analytical signal [88]. Several comprehensive reviews and articles have appeared over past few decades on the biosensors. Here only few emerging trends in the design of biosensors appeared in the literature have been discussed.

Since from their discovery, CNTs have been extensively studied and successfully used in fabricating biosensor because of the fact that they play a dual role as a substrate to immobilize the suitable matrix for biomolecules and also acts as a transducer. In addition to these, CNT based electrode materials allows efficient electron shuttling between electrodes and redox centers of the enzymes [89]. The land mark paper using carbon nanotubes as an electrode material in the field of biosensors began with the pioneering work of Britto and co-workers in 1996 by exploring the possibility of electrochemical oxidation of dopamine [90]. Then Joseph Wang has modified the glassy carbon with the suspension of CNT in suitable organic solvent and successfully determined NADH molecule [91]. This concept was extended by several research groups to sense many biomolecules like insulin, uric acid, catechol, morphine, brucine, cytochrome C, galactose, glucose, nitric oxide and horseradish peroxidase as well as hydrogen peroxide[92]. The enzymes like horseradish peroxidase and glucose oxidase (GOx) were immobilized on the surface of nanotube modified GCE which allowed direct electron transfer between them and has resulted symmetrical redox peaks [93]. Similar to that GCE modified with microperoxidase has also showed an enhanced electrocatalytic activity towards the reduction of H_2O_2 and O_2 molecules. This kind of behaviour was also noticed with catalase[94]. The GOx modified MWCNTs composite electrode exhibited high catalytic activity towards glucose molecule with a long term stability [95]. The conjugated monolayer of nanotube cyctochrome C (Cyt C) were prepared and stabilized at air-water interface. The electrochemical measurements showed well resolved redox peaks for modified Cyt C when compared to pure Cyt C due to the fact that the fast electron transfer takes place at the nanotube supports [96]. An amperometric third generation H_2O_2 biosensor based on the immobilization of hemoglobin on MWCNTs and gold colloidal nanoparticles has been reported [97]. The hemoglobin/gold nanoparticles multilayer films were assembled onto hemoglobin/MWCNT film through layer-by-layer assembly technique. The unmodified electrode substrate requires high overvoltage and suffers from electrode fouling due to the formation of radical intermediates [98]. In order to overcome the problem of high over voltage and electrode fouling, mediator modified electrodes have been prepared and applied for different analyte molecules [99]. Rutin modified MWCNTs on the surface of GCE were prepared and used towards the electrooxidation of hydroxylamine [100]. SAMs of SWCNTs with cobalt (II) tetraminophthalocyanine on gold electrode have been prepared and applied in the determination of dopamine and epinephrine [101,102]. Phenothiazine derivatives, Azure C and MWCNTs co-immobilized in the chitosan matrix were used to develop amperometric sensor for the determination of NADH [103]. Similar sensors were also developed using toludine blue, thin layer of 4-aminobenzene sulphonic acid on the substrate of MWCNTs in the determination of tyrosine [104]. MWCNTS/Co-Salophene carbon composites were used in the determination of tryptophan in serum, uric acid and ascorbic acid [105,106,107].

Next type of biosensors involves the use of NPs modified CNTs. The attractive physical and chemical properties of metal NPs have been widely used in exploring the possibility of various sensing applications [108]. NPs in conjunction with nanotubes have been found to enhance the electrocatalytic activity towards many electrochemical processes. Pt-nanoclusters/MWCNTs-GCE were used in the determination of estrogens and also in the oxidation of estradiol, estrone and estriol [109]. The dispersed Pt nanoparticles on 4-aminobenzene functionalized MWCNTs showed a good electrocatalytic activity towards methanol oxidation [110]. A novel nano-silver coated MWCNT composite was prepared on a GCE and applied in the determination trace level of thiocyanate in urine and saliva samples from smokers and nonsmokers [111]. Tri-metallic (Gold, silver and palladium) NPs/MWCNTs composites on GCE were prepared and explored their sensing ability using the model systems like hydrazine, bromide and Tl(I). Metal nanoparticles (Pt, Au or Cu) together with MWCNTs or SWCNTs solubilized in Nafion have been used to form nanocomposite for electrochemical detection of trinitrotoluene (TNT) and several other nitro aromatics. Similarly Cu modified CNTs were used to detect TNT in ppb levels [112]. An amperometric biosensor based on self-assembling of glutamate dehydrogenase and poly(amidoamine) dendrimer encapsulated platinum nanoparticles onto MWCNTs has been developed for the determination of glutamate [113]. Pt nanoparticles encapsulation scheme has been employed to construct an amperometric glucose biosensor based on layer-by-layer electrostatic adsorption of GOx and the dendrimers-encapsulated nanoparticles on MWCNTs. Composites prepared with CNTs and gold nanoparticles (Au-NPs) have demonstrated to possess special properties for biosensors detection due to the coupling of Au-NPs which are having capability to adsorb proteins with no loss of bioactivity, with the electrocatalytic ability of CNTs towards molecules of biochemical interest. A multilayer gold nanoparticles/MWCNTs/GOx membrane was prepared by electrostatic assembly using positively charged poly(dimethylallylammonium chloride) to connect them layer-by-layer and the membrane showed excellent electrocatalytic ability for glucose biosensing at a relatively low potential (−0.2 V) [113]. Polypyrrole modified CNTs were used in the determination of glutamate with high sensitivity, rapid response and low detection limit at 0.2 V [115]. A biosensor with improved performance was also developed through the immobilization of HRP onto electropolymerized PANI films doped with nanotubes [116]. It was found that the use of CNTs in the biosensor system could increase the amount and stability of the immobilized enzyme and greatly enhanced the biosensor response when compared with the biosensor without tubes. A mediator glucose biosensor has been constructed by immobilizing GOx at electropolymerized poly(toludine blue O) film on a CNTs-modified GCE. The toludine blue O moieties served as redox mediators for enzymatic glucose oxidation and as polymeric network to maintain the biosensor activity. Great enhancement in current response was observed for the glucose biosensor and the detection potential could be decreased to −0.1V (vs Ag/AgCl), where common interferences such as ascorbic acid, uric acid and acetamidophenol were not oxidized [117]. Nanofibrous glucose bioelectrodes were fabricated by the immobilization of GOx into an electrospun composite, membrane consisting of polymethylmethacrylatedispersed with MWCNTs wrapped by a cationic polymer (poly (diallyldimethylammonium chloride)). Nanofibrous electrode exhibited excellent electrocatalytic activity towards hydrogen peroxide with a pronounced oxidation current at +0.1 V [118]. Glucose biosensors were also prepared with electropolymerized polyphenylendiamine films, CNTs and GOx [119]. Glucose dehydrogenase(GDH) and its cofactor NAD^+ were covalently attached to polyamino-

saccharide chains of chitosan. Electron conducting films of such macro complexes were prepared on GCE by adding tubes and evaporating the water. These bioelectrodes acted as oxygen independent reagentless biosensors in contrast to the oxidase based electrodes [120]. MWCNTs/polysulfone biocomposite membrane modified thick-film screen-printed electrochemical biosensors have been constructed by the incorporation of HRP by phase inversion technique which facilitated into fabrication of disposable biosensors [121]. The ability of poly(vinyl alcohol) to solubilize the tubes provides a useful way for preparing CNTs binder composite modified electrodes for a wide range of sensing applications. Using this approach a novel amperometric ethanol biosensor was constructed with NADH physically immobilizing within a PVA-MWCNTs composite obtained by a freezing thawing process [122].

3.2 Electrochemical metal ion sensors

Metal ion sensors require specific functionalities on the surface of carbon substrates which showed potential affinity towards particular metal ions. This can be achieved by modifying the electrode surface with suitable indicator species [6,7]. Many electrode materials have been used in the detection and quantification of metal ions but in this chapter the focus has been on the use of CNT as an electrode material. Modified MWCNTs/Nafion films on GCE provided suitable stripping responses for Cd (II) and Pb (II) ions [123]. A similar approach was followed to determine Europium (III) [124]. A SWCNT modified GCE was also employed to determine Cd (II) in water samples [125]. A thiol-tethered-MWCNTs chemically modified gold electrode has been prepared for As (III) speciation and Bi (III) determination at trace levels in natural and high salinity waters [126]. Gold NPs modified nanotubes were used to determine As (III) via anodic stripping voltammetry [127].

3.3 Heterogeneous catalysis

One of the most significant applications of SWCNT/NPs materials is in the area of catalysis [128]. The nanometer scale dimensions of metal nanoparticles facilitate enhanced diffusion rates and fast electron transfer kinetics. Therefore various research groups have done extensive studies on the effect of using carbon nanotube as catalyst. Pt nanoparticles supported on SWCNT electrodes have shown improved catalytic properties for both methanol oxidation and oxygen reduction reactions [129]. SWCNTs deposited on optically transparent electrodes (OTEs) were used as substrates and Pt nanoparticles were electrodeposited on these SWCNTs and used in the oxidation of methanol [129]. Cui et.al. have studied the electrocatalytic oxygen reduction reaction by Pt nanoparticles electrodeposited on MWNTs and found the positive shift in reduction potential and increased current and also showed high electron transfer rate towards methanol oxidation [130]. Use of bimetallic catalysts such as Pt-Ru has been commonly accepted in order to improve the poisoning effects of CO and also to increase the catalytic efficiency. In this direction, He et.al. first studied the electrodeposition of Pt-Ru on SWCNTs and carried out the methanol oxidation with maximum current density [131]. Highly dispersed Pd nanoparticles prepared by electrodeposition on SWCNT bundles have exhibited high catalytic activity for hydrazine oxidation and indicated that if SWCNTs are used as a support, the loading of precious metal catalysts could be minimized [132]. Use of MWCNT as a Pt catalyst supports were investigated by Wang et.al. [133]. Based on their investigations, they have concluded that with smaller sized Pt particles (2.5 nm), the performance of fuel cells could be improved. Most of the studies involved in the use of

random networks, bundles or SWCNT paste electrodes. Aligned networks of SWCNTs will enable better control over the density and distribution of NPs. An interesting liquid phase lamellar flow deposition technique to align carbon nanotubes has been demonstrated by Lay et.al. [134]. For instance one of the current highest values of anodic currents for Pt-C has been reported by Motorola with 40 mA/cm^2 for 2.5 mg Pt/cm^2, while Pt-CNT catalysts exhibited currents as high as 54 mA/cm^2 for 0.43 mg Pt/cm^2 and 25 mA/cm^2 for 10 μg Pt/cm^2. Fu et.al. synthesized hydrous RuO_2 nanoparticles supported on CNTs via a homogeneous oxidation-precipitation method using H_2O_2 as both the oxidant and precipitant at room temperature [135]. The hybrid was very active in the aerobic oxidation of various aromatic, saturated and cyclic alcohols and quite selective towards the corresponding aldehydes/ketones in liquid phase under mild conditions. The CNT-RuO_2 hybrid showed the lowest onset peak potentials of all tested catalysts, indicating the highest activity for the electrooxidation of methanol [136]. Huang et.al. Investigated the activity of V_2O_5 catalysts towards the selective catalytic reduction of NO with NH_3 in the presence of excess oxygen and also for skeletal isomarization reactions [137]. Further, the CNT-WO_3 hybrids exhibited very high skeletal isomerization selectivity exclusively toward olefin reactions. In this example, the improved performance of the CNT-WO_3 hybrid was not only attributed to a more uniform dispersion of WO_3 but also to CNTs due to the fact that the CNTs prevent the complete reduction of WO_3 to metallic tungsten (W) [137]. Another example of a successful application of CNT hybrids has been demonstrated by Chen et.al. who has investigated the catalytic performance of CNT-VO_x in the partial oxidation of *n*-butane. Such dehydrogenation reactions are often highly exothermic and the heat is typically released to the catalyst surface causing sintering of the particles and decreased catalytic activities. Because of their high thermal conductivity, the CNTs can act as a heat sink thus keeping the crystal size small [138].

3.4 Batteries and fuel cells

Fuel cells generate electricity through an electrochemical process in which the energy stored in a fuel is converted directly into electricity. Fuel cells combine the molecules of a fuel and oxidant chemically without burning, dispensing with the inefficiencies and pollution of traditional combustion. Unlike a battery, a fuel cell does not run down or require recharging. It will produce electricity as long as fuel and oxidants are supplied. Pt-based NPs/CNTs nanohybrids showed higher electrocatalytic activity for the methanol oxidation and oxygen reduction reaction than the commercial Pt-based NPs/C catalysts due to its one dimensional structure, excellent electronic conductivity and good electrochemical properties of CNTs [139,140]. Wei et.al. have prepared 1-Pt/FMCNTs and 2-Pt/FMCNTs nanohybrids by spontaneous reduction deposition of Pt NPs on the FMCNTs after or before film membrane CNTs(FMCNTs) coated on the teflon boned carbon electrodes [141]. The two types of nanohybrids exhibited higher electrochemical activity than commercial Pt/C catalyst. They found that the utilization of Pt in electrodes of 1-Pt/FMCNTs, 2-Pt/FMCNTs, and Pt/C were 75.6%, 44.6%, and 39.2% respectively. Electrodes of 2-Pt/FMCNTs and Pt/C were fabricated by the same procedure, but the former has a 5.4% Pt utilization higher than the later, which can be ascribed to a much better connected electron path contributed by FMCNTs in 2-Pt/FMCNTs than that in Pt/C electrode. It is well known that oxygen reduction in cathode of proton exchange membrane fuel cell (PEMFCs) must be able to easily access the surface of the catalyst particles, a pathway for proton diffusion must exist in the proximity of the active sites on catalysts and an electronic conducting pathway from

the catalyst to the electrode is required for electron transport. Yin et.al. have synthesized two kinds of Pt-Au/CNTs nanohybrids with different structures, one contained the separated Pt and Au NPs (Pt/Au/CNTs) and another composed with alloy-like Pt-Au NPs (PtAu/CNTs). Compared with the Pt/CNTs nanohybrids, the two Pt-Au/CNTs nanohybrids showed a lower overpotential for O_2 reduction in the presence of methanol. The Pt/Au/CNTs catalyst with separated Au and Pt NPs exhibited significantly higher methanol tolerance than the alloy like PtAu/CNTs nanohybrids, which should be ascribed to the less methanol absorption on Pt surface due to the effect of Au NPs [142]. In recent years the durability of PEMFCs has also been recognized as one of the most important issues to be addressed before the commercialization of the PEMFCs. Li et.al. have developed a route to stabilize Pt NPs supported on CNTs by anchoring Pt NPs on hydrofluoric acid treated CNTs [143]. Matsumori et.al. have used silica protection layer to improve the stability of Pt NPs supported on CNTs [144]. However the former method involves the use of a nonenvironmental friendly chemical (hydrofluoric acid), which has resulted in some structural damage and loses its conductivity [145,146]. The latter one would reduce the active surface area of the catalysts, resulting in the decrease of the catalytic activity of the catalysts. Chen et.al. have overcome this by developing a novel method to stabilize the CNTs supported Pt NPs by ionic liquid polymer thin film and the long-term operation stability of the obtained nanohybrids (PIL/PtNPs/AP-CNTs) for methanol electrooxidation. This modification has improved the stability of the electrode due to the mechanical isolation of PIL thin layer between PtNPs [147].

4. Conclusions

Carbon nanotubes have been the subject of discussion in recent years due to their diversified structures, properties and variety of applications. Chemically modified carbon nanotubes not only provide selectivity but also specificity for the detection of a wide variety of analyte molecules from all domains. They find widespread application in sensor technology, catalysis, drug delivery agents and as a composite material in high engineering applications.

5. Acknowledgement

The authors acknowledge the financial support and award of fellowship to GKR from the Department of Science and Technology (DST), New Delhi, India.

6. References

[1] S.I. Cha, K.T. Kim, K.H. Lee, C.B. Mo, Y.J. Jeong, S.H. Hong. Carbon 46 (2008) 482.
[2] H.J. Lee, S.W. Han, Y.D. Kwon, L.S. Tan, J.B. Baek. Carbon 46 (2008) 1850.
[3] W. Lu, N. Li, W. Chen, Y.Yao. Carbon 47 (2009) 3337.
[4] L. Wang, D. Zhu, L. Duan, W. Chen. Carbon 48 (2010) 3906.
[5] S. Sampath, O. Lev. J. Electroanal. Chem. 446 (1998) 57.
[6] E. Rico E. Mojica, M. Vidal, A.B. Pelegrina J. R. L. Micor. J.App. Sci. 9 (2007) 1286.
[7] R.W. Murray, A.G. Ewlng, R.A. Dust. Anal. Chem. 59 (1987) 379.
[8] J. Oni, N. Diab, S. Reiter. Sens. Actuators B Chemical 105 (2005) 208.
[9] A. J. Downard. Electroanalysis 12 (2000) 1085.
[10] S. E. Kooi, U. Schlecht, K.Kern. Angew. Chem. 41 (2002) 1353.

[11] J. Pinson and F. Podvorica. Chem. Soc. Rev. 34 (2005) 429.
[12] B. Barbier, j. Pinson, G. Desarmot, M. Sanchez. J. electrochem. Soc. 137 (1990) 1757.
[13] Y. C. Liu, R. L. McCreery. J. Am. Chem. Soc. 117(1995) 11254.
[14] M. Khoshroo, A.A. Rostami. J. Electroanal. Chem. 624 (2008) 205.
[15] S. M. Chergui, N. Abbas, T. Matrab, M.Turmine, E.N. Guyen, R. Losno, J. Pinson, M. Chehimi. Carbon 48 (2010) 2106.
[16] M. Delamar, G. Desarmot, R. Hitmi, J. Pinson J.M. Saveant. Carbon 35 (1997) 801.
[17] A. Solak, L.R. Eichorst, W. J. Clark, R. L. McCreery. Anal. Chem. 75 (2003) 296.
[18] P. Allongue, M. Delamer, B. Desbat, O. Fagebaume, R. Hitmi, J. Pinson, J. M. Saveant. J. Am. Chem. Soc. 119 (1997) 201.
[19] M. D. Amours, D. Belanger. J. Phys. Chem. B 107 (2003) 4811.
[20] K. Ray, R. L. McCreery. Anal. Chem. 69 (1997) 4680.
[21] T. C. Kuo, R. L. McCreery, G. M. Swain. Electrochem. Solid State Lett. 2 (1999) 288.
[22] C. P. Andrieux, F. Gonzalez, J. M. Savent. J. Am. Chem. Soc. 119 (1997) 4292.
[23] S. Senyange, F. Anariba, D. F. Bocian, R. L. McCreery. Langmuir 21 (2005) 11105.
[24] H. Tanaka, A. Aramata. J. Electroanal. Chem. 29 (1997) 437.
[25] J. Liu, S. Dong. Electro. Comm. 2 (2000) 707.
[26] G.G. Wallace, G.M. Spiks, L.A.P. Kane-Maguire, P.R. Teasdale, Conductive electroactive polymers, CRC Press, Second edition 2003.
[27] M.A. Rahman, D. S. Park, M. S. Won, S. M.Park, Y.B. Shim. Electroanalysis 16 (2004) 1336
[28] M.C. Blanco-Lo pez, M.J. Lobo-Castan, A.J. Miranda Ordieres, P. Tunn Blanco. Tren.Anal. Chem. 23(2004) 36
[29] A. Lourdes , Paloma, J. M. Pingarron. Anal. Chim. acta 622 (2008) 11.
[30] P. Santhosh, K.M. Manesh, A. Gopalan, K.-P. Lee, Sens. Actuators B. 125 (2007) 92.
[31] M. Faraday, Philos. Trans. R. Soc., London. 145 (1857) 147.
[32] C. N. R. Rao, A. Muller, A. K. Cheetham. The Chemistry of Nanomaterials. 646 (2004).
[33] V. Georgakilas, D. Gournis, V. Tzitzios, L. Pasquato, D.M. Guldi and M.Prato. J. Mat. Chem. 17 (2007) 2679.
[34] X. Luo, A. Morrin, J. Killard, M.R. Smyth. Electroanalysis 18 (2006) 319.
[35] B. Wu, Y. Kuang, X. Zhang, J. Chen. Nano Today 6 (2011) 75.
[36] G.G. Wildgoose, C. E. Banks, R.G. Compton. Small 2 (2006) 182.
[37] Z.B. He, J.H. Chen, H.H. Zhou, Y.F. Kuang. Diamond Relat. Mater. 13 (2004) 1764.
[38] T. M. Day, P. R. Unwin, N. R. Wilson, J. V. Macpherson. J. Am. Chem. Soc. 127 (2005) 10639.
[39] X.X. Chen, N. Li, K. Eckhard, L. Stoica, W. Xia, J. Assmann, M. Muhler, W. Schuhmann. Electr. Commun. 9 (2007) 1348.
[40] S. Arai, M. Endo. Electro. Commun. 5 (2003) 797.
[41] C. Y.Tsai, H.M. Chuang, S.Y. Lin, P. Tseng, T.Y. J. Electrochem. Soc. 152 (2005) 716.
[42] I.H. Kim, J.H. Lee, Y.H. Kim, K.B. J. Electrochem. Soc. 152 (2005)2170.
[43] Kim, J. D. Kang, B. S. Noh, T. W. Yoon, J.G. Baik, S. I. Kim, Y.W. J. Electrochem. Soc. 152 (2005) 23.
[44] J. Qu, Y. Shen, X. Qu, S. Dong. Chem. Commun. 34 (2004).
[45] M.C. Tsai, T.K. Yeh, C.H. Tsai. Electro. Commun. 8 (2006) 1445.
[46] M.C. Tsai, T.K. Yeh, C.H. Tsai. Mater. Chem. Phys. 109 (2008) 422.
[47] F. Xiao, Z.R. Mo, F.Q. Zhao, B.Z. Zeng. Electro.Commun. 10 (2008) 1740.

[48] H.C. Choi, M. Shim, S. Bangsaruntip, H.J. Dai, J. Am. Chem. Soc. 124 (2002) 9058.
[49] L.T. Qu, L.M. Dai. J. Am. Chem. Soc. 127 (2005) 10806.
[50] X.H. Peng, J.Y. Chen, J.A. Misewich, S.S. Wong. Chem. Soc. Rev. 38 (2009) 1076.
[51] J. Myng Zen, A. Senthil Kumar, D.Tsai. Electroanalysis 15 (2003) 1073
[52] X.M. Hou, L.X. Wang, F. Zhou, L.Q. Li, Z. Li. Mater. Lett. 63 (2009) 697.
[53] Z.J. Wang, Q.X. Zhang, D. Kuehner, X.Y. Xu, A. Ivaska, L. Niu. Carbon 46 (2008) 1687.
[54] S.J. Guo, S.J. Dong, E.K. Wang. Adv. Mater. 22 (2010) 1269.
[55] X. Lu, T. Imae. J. Phys. Chem. C. 111 (2007) 2416.
[56] J.Y. Kim, Y. Jo, S. Kook, S. Lee, H.C. Choi. J. Mol. Catal. A. 323 (2010) 28.
[57] S.D. Yang, X.G. Zhang, H.Y. Mi, X.G. Ye. J. Power Sources 175 (2008) 26.
[58] Y.S. Chun, J.Y. Shin, C.E. Song, S. Lee. Chem. Commun. (2008) 942.
[59] S. Banerjee, S.S. Wong. Nano Lett. 2 (2002) 195.
[60] N. Karousis and N. Tagmatarchis. Chem. Rev. 110 (2010) 5366.
[61] M. Pandurangappa, N. S. Lawrence, R. G. Compton. Analyst 127 (2002) 1568.
[62] G.G. Wildgoose, J. L. Jones , R.G. Compton. Chem. Phys. Chem. 11 (2004) 1794.
[63] Masheter, P. Abiman, G. G. Wildgoose . Mater. Chem. 17 (2007) 2616.
[64] P. Abiman, G.G Wildgoose, R.G. Compton. Int. J. Electrochem. Sci. 3 (2008) 104.
[65] M. Pandurangappa, T. Ramakrishnappa. Mat. Chem and Physics. 122 (2010) 567.
[66] C. Hsieh, H.Teng, W. Y. Chen, Y. S. Cheng. Carbon 48 (2010) 4219.
[67] S. Banerjee, T. H. Benny, S. S. Wang. Adv. Mat. 1 (2005) 17.
[68] B. Pan, D. Cui, R. He, F. Gao, Y. Zhang. Chem. Phy. Letters. 417 (2006) 419.
[69] G. abrial, G. Sauthier, J. Fraxedas, M. Moreno-Manas, M. T. Martinez, C. Miravitlles, J. Casabo. Carbon 44 (2006) 1891.
[70] K.Yang, M. Gu, Y. Guo, X. Pan, G. Mu. Carbon 47 (2009) 1723.
[71] S. Caddick, R.Fitzmaurice. Tetrahedron 65 (2009) 3325.
[72] I.J. Cutress, F. Marken, R. G. Compton. Electroanalysis 21 (2009) 113.
[73] F. G. Brunetti, M. A. Herrero, J. M. Munoz, A.D. Ortiz, J. Alfonsi, M. Meneghetti, M. Proto. J. Am. Chem. Soc. 129 (2007) 14580.
[74] M. S. Raghuveer, S. Agrawal, N. Bishop, and G. Ramanath. Chem. Mater. 18 (2006) 1390.
[75] Y. Wang, Z. Iqbal, S. Mitra. Carbon 43 (2005) 1015.
[76] Y. Chen and S. Mitra. Journal of Nanoscience and Nanotechnology 8 (2008) 1.
[77] J. Liu, M. R. Zubiri, B. Vigolo, M. Dossot, Yves Fort, J.J. Ehrhardt, E. McRae. Carbon 45 (2007) 885.
[78] N. Karousis, S.P. Economopoulos, Y. Iizumi, T. Okazaki, Z. Liu, K. Suenaga and N. Tagmatarchis. Chem. Comm. 46 (2010) 9110.
[79] J. Liu and D. Xue. J. Mat. Chem. 21 (2011) 223.
[80] B. Rodrguez, A. Bruckmann, T. Rantanen, C. Bolm, Advanced Syn. Cat. 314 (2007) 2213.
[81] N. Pierard, A. onseca, J. F. Colomer, C. Bossuot, J. M. Benoit, G. Van Tendeloo, J. P. Pirard, J. B. Nagy. Carbon 42 (2004) 1691.
[82] N. J. Welham, V. Berbenni, P. G. Chapman. Carbon 40(2002) 2307.
[82a] Y.F. Sun, A.M. Zhang, Y. Yin, Y.M. Dong, Y.C. Cui, X. Zhang, J.M. Hong. Materials Chemistry And Physics 101 (2007) 30.
[83] X. Li, J. Shi, Y. Qin, Wang, H. Luo, Zhang, Z.X. Guo, H.S. Woo, D. K. Park. Chem. Phy. Lett. 44(2007) 258.

[84] P. C. Ma, B. Z. Tang, J.K. Kim. Chem. Phy. Lett. 458 (2008) 166.
[85] Z. Konya, J. Zhu, K. Niesz, D. Mehn, I. Kiricsi. Carbon 42 (2004) 2001.
[86] H. Pan, L. Liu, Z.X. Guo, L. Dai, F. Zhang, D. Zhu, R. Czerw, D. L. Carroll. Nano Lett. 3 (2003) 220.
[87] Y. Lin, K. A. Watson, S. Ghose. J. Phy. Chem 33 (113) 14858.
[88] J. Wang. Analytical Electrochemistry, 3.rd Edition, Wiley Publications 2006.
[89] J. Wang. Electroanalysis 17 (2005) 7.
[90] P.J. Britto, K.S. Santhanam, P.M. Ajayan. Bioelectrochem. Bioenerg. 41 (1996) 121.
[91] M. Musameh, J. Wang, A. Merkoci, Y. Lin. Electro.Commun. (2002) 743.
[92] R.G. Compton, G.G. Wildgoose, and E.S. Wong. Biosensing Using Nanomaterials, John Wiley & Sons, Inc 2009.
[93] Y. Yin, Y. Lu, P. Wu, C. Cai. Sensors 5 (2005) 220.
[94] M. Wang, Y. Shen, Y. Liu, T. Wang, F. Zhao, B. Liu, S. Dong. J. Electroanal. Chem. 578 (2005) 121.
[95] H. Zhou, T.H. Lu, H.X. Shi, Z.H. Dai, X.H. Huang. J. Electroanal. Chem. 612 (2008) 173.
[96] J. Li, Y.B. Wang, J.D. Qiu, D.C. Sun, X.H. Xia. Anal. Bioanal. Chem. 383 (2005) 918.
[97] S. Chan, R. Yuan, Y. Chai, L. Zhang, N. Wang, X. Li. Biosensors and bioelectronics 22 (2007) 1268.
[98] S. Sampath, O. Lev. J. Electro. Chem.446 (1998) 57.
[99] C. Xiang, Y. Zuo, j. Xie, X. Fei. Anal. Lett. 39 (2006) 2569.
[100] H.R. Zare, Z. Sobhani, M. Mazloum Ardakani. Sens. Actuators B. 126 (2007) 641.
[101] K.I. Ozoemena, T. Nyokong, D. Nkosi, I. Chambrier, M.J. Cook. Electro.chim.Acta 52 (2007) 4132.
[102] K.I. Ozoemena, D. Nkosi, J. Pillay. electrochim. Acta. 53 (2008) 2844
[103] M. Zhang, W. Gorski. Anal. Chem. 77 (2005) 3960.
[104] K.J. Huang, D.F. Luo, W.Z. Xie, Y.S. Yu. Coll. Surf. B. 61 (2008) 176.
[105] S. Shahrokhian, I. Fotouchi. Sens. Actuators B. 123 (2007) 942.
[106] S. Shahrokhian, H.R. Zare-Mehrjardi. Electroanalysis 19 (2007) 2234.
[107] S. Shahrokhian, H.R. Zare-Mehrjardi. Electrochim. Acta. 52 (2007) 6310.
[108] S. Hrapovic, E.Y. Liu, K. Male, J.H.T. Luong. Anal. Chem. 78 (2006) 5504.
[109] X. Lin, Y. Li. Biosens. Bioelectron. 22 (2006) 253.
[110] D.J. Guo, H. L. Li. Electroanalysis 17 (2005) 869.
[111] P. Yang, W. Wei, C. Tao. Anal. Chim. Acta. 585 (2007) 331.
[112] S. Hrapovic, E.Y. Liu, K. Male, J.H.T. Luong. Anal. Chem. 78 (2006) 5504.
[113] L. Tang, Y. Zhu, L. Xu, X. Yang, C. Li. Talanta 73 (2007) 438.
[114] Y. Liu, S. Wu, H. Ju, L. Xu. Electroanalysis. 19 (2007) 986.
[115] L. Tang, Y. Zhu, L. Xu, X. Yang, C. Li. Talanta 72 (2007) 438.
[116] X. Luo, A.J. Killard, A. Morrin, M.R. Smyth. Anal. Chim. Acta. 575 (2006) 39.
[117] Y.L. Yao, K.K. Shiu. Electrochim. Acta. 53 (2007) 28.
[118] K.M. Manesh, H.T. Kim, P. Santhosh, K.P. Lee. Biosens. Bioelectron. 23 (2008) 771.
[119] L. Tang, Y. Zhu, L. Xu, X. Yang, C. Li. Talanta 72 (2007) 438.
[120] Y. Yao, K.K. Shiu. Anal. Bioanal. Chem. 387 (2007) 2446.
[121] M. Zhang, C. Mullens, W. Gorski. Anal. Chem. 79 (2007) 2446.
[122] S. Sanchez, M. Pumera, E. Cabruja, E. F abregas. Analyst 132 (2007) 142.
[123] Y.C. Tsai, J.M. Chen, F. Marken. Microchim. Acta 269 (2005) 269.
[124] S. Yuan, Q. He, S. Yao, S. Hu. Anal. Lett. 39 (2006) 373.

[125] D. Sun, X. Xie, Y. Cai, H. Zhang, K. Wu. Anal. Chim. Acta 581 (2007) 27.
[126] A. Profumo, M. Fagnoni, D. Merli, E. Quartarone, S. Protti, D. Dondi, A. Albini. Anal. Chem. 78 (2006) 4194.
[127] L. Xiao, G. G. Wildgoose, R.G. Compton. Anal. Chim. Acta. 620 (2008) 44.
[128] J.M. Planeix, N. Coustel, B. Coq, V. Brotons, P.S. Kumbhar, R. Dutartre, P. Geneste, P. ernier, P.M. Ajayan. J. Am. Chem. Soc. 116 (1994) 7935.
[129] G. Girishkumar, K. Vinodgopal, P.V. Kamat. J. Phys. Chem. B. 108 (2004) 19960.
[130] J.S. Ye, H.F. Cui, Y. Wen, W.D. Zhang, F.S. Sheu. Microchim. Acta. 152 (2006) 267.
[131] Z.B. He, J.H. Chen, D.Y. Liu,Y.F. Kuang. Diamond Relat. Mater. 13 (2004) 1764.
[132] D.J. Guo, H.L. Li. J. Colloid Interface Sci. 286 (2005) 274.
[133] C. Wang, M. Waje, X. Wang, J.M. Tang, R.C. Haddon, Y.S. Yan. Nano Lett. 4 (2004) 345.
[134] M.D. Lay, J.P. Novak, E.S. Snow. Nano Lett. 4 (2004) 603.
[135] X. Yu, H. Peng, F. Wang, H. Applied Catalysis A 321 (2007) 190.
[136] B.Huang, R. Huang, D. Jin, D. Ye. Catal. Today. 126 (2007) 279.
[137] B. Pietruszka, G.F. Killer, N. Keller. Catal. Today. 94 (2005) 102.
[138] X.W. Chen, Z. Zhu, M. Havecker, D.S. Su, R. Schlol. Mater. Res. Bull. 42 (2007) 354.
[139] Y.Y. Mu, H.P. Liang, J.S. Hu, L. Jiang, L.J. Wan. J. Phys. Chem. B 109 (2005) 22212.
[140] Y.L. Hsin, K.C. Hwang, C.T. Yeh. J. Am. Chem. Soc. 129 (2007) 9999.
[141] Z.D. Wei, C. Yan, Y. Tan, L. Li, C.X. Sun, Z.G. Shao, P.K. Shen, H.W. Dong. J. Phys. Chem. C 112 (2008) 2671.
[142] J.J. Wang, G.P. Yin, H. Liu, R.Y. Li, R.L. Flemming, X.L. Sun. J. Power sources. 194 (2009) 668.
[143] Y.L. Li, F.P. Hu, X. Wang, P.K. Shen. Electro. Commun. 10 (2008) 1101.
[144] H. Matsumori, S. Takenaka, H. Mastune, M. Kishida. Appl. Catal. A 373 (2010) 176.
[145] Y.L. Hsin, K.C. Hwang, C.T. Yeh. J. Am. Chem. Soc. 129 (2007) 9999.
[146] W.W. Tu, J.P. Lei, H.X. Ju. Electro.Commun. 10 (2008) 766.
[147] B.H. Wu, D. Hu, Y.J. Kuang, X.H. Zhang, J.H. Chen. Chem. Comm. 46 (2010) 7954.

22

Laser Patterning of Carbon-Nanotubes Thin Films and Their Applications

Shiang-Kuo Chang-Jian and Jeng-Rong Ho
Department of Mechanical Engineering
National Chung Cheng University Chia-Yi,
Taiwan

1. Introduction

In 1960 T.H. Maiman successful fabricated the first laser and projected the first laser light. Fifty years later, lasers have found extensive applications in fields including energy, materials, communications, biotechnology and mechanical engineering. In the past several decades, continuous developments have improved the performance of lasers. From an initial wavelength of 694.3 nm, new lasers have been developed achieving wavelengths in the infrared (10.6 μm) and ultraviolet (157 nm) spectra. Laser light has the several features which distinguish it from traditional light sources: directionality, brightness, monochromatity and coherence. These four characteristics have resulted in lasers having a profound influence on industrial development. In the following, the use of laser for material transfer will be briefly introduced.

1.1 Laser transfer techniques

Based on the arrangement of laser, donor thin film and acceptor substrate, laser-induced material transfer can be classified into two groups: laser-induced forward transfer (LIFT) and the laser-induced backward transfer (LIBT), schematically illustrated in Fig. 1(a) and (b), respectively. To date, LIFT is the mainstream technique and has been reported in more applications than LIBT. In LIBT, the accepter substrate needs to be transparent to the laser light, whereas LIFT is not subject to this limitation and can use non-transparent accepter substrates.

1.2 History of the LIFT technique

Bohandy et al.[1] demonstrated the LIFT technique 26 years after the first development of laser light. Using an excimer laser, he successfully deposited copper metal deposition from a supported metal film. The following year Blonder et al.[2] used LIFT to pattern Al for integrated circuit applications, the first application of LIFT in the field of the microelectronics. He showed that LIFT could not only be used for the deposition of metal on a substrate, but could also be applied in many other areas. In the following years, LIFT was successfully used for the deposition of W[3], Cr[4], Au/Sn[5] and Al[6,7].

1.3 Application of the LIFT technique

The LIFT technique quickly showed its potential in the display, biomedical, energy and microelectronic industries. Display researchers successful deposited a layer of emitting

polymer[8] or bilayer emitting polymer/metal[9-11] material on a target substrate, demonstrating that organic light emitting display (OLED) pixels can be manufactured by LIFT. In carbon nanotube field emission displays (CNT-FED) and the plasma display panels (PDP), the carbon nanotube cathodes[12] and the phosphor layers[13] were printed using the LIFT process.
The biomedical industry had long faced problems transferring biological materials. Unlike the deposition of metals, transferring biological materials by laser beam lead to irreversible molecular decomposition. One possible solution was to transfer biological materials in liquid. Using the LIFT technique, researchers successfully transferred DNA[14-15] and several other kinds of biomaterial[16-18]. In the energy industry, the LIFT technique was used to deposit TiO_2 thin film[19] to fabricate the dye solar cell devices with a power conversion efficiency up to 4.3%[20].

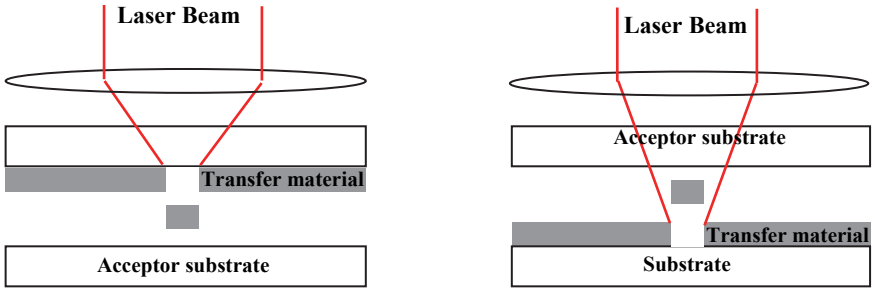

(a) (b)

Fig. 1. Laser transfer techniques: (a) laser-induced forward transfer (LIFT) (b) laser-induced backward transfer (LIBT).

In microelectronics Ag[21], silver[22] and DNNSA-PANI doped with single-walled carbon nanotubes (SWNT)[23] were applied in the deposition of source/drain transistor electrodes, and a line pattern at the sub-10μm level could be achieved over several cm^2. Furthermore, multilayer transfer was successfully used to manufacture organic thin film transistors (OTFT)[24]. The electrodes Ag and the semiconductor layer were simultaneously transferred to the target substrate. The SWNT thin film was also used as the transferring material for the semiconductor layer between the source/drain electrodes to fabricate P- and N-type field effect transistors[25]. In addition, the LIFT technique also could be used to encapsulated organic electronic devices[26], and could be used to repair internal circuit damage.

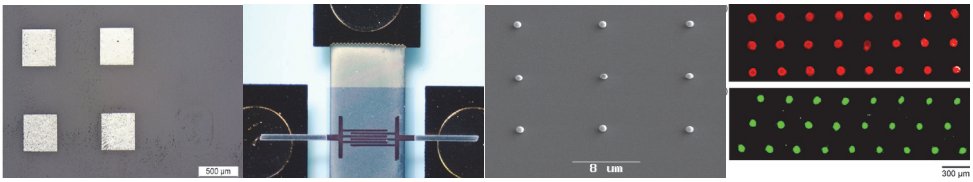

(a) (b) (c) (d)

Fig. 2. (a) (b) LIFT technique used to transfer Al[7] and Ag electrodes of the OTFT[21], (c) (d) LIBT technique used to transfer gold nanodroplets[29] and microarrays of the cDNA[30].

1.4 Application of the LIBT technique

The LIBT technique has been used to transfer Cr[27] on quartz and phahalocyanine solids on PMMA[28]. However, LIBT is used less frequently than LIFT technique due to its need for a transparent acceptor substrate. However, LIBT can be used to transfer spherical gold droplets[29] up to 300 nm to the substrate. Using LIBT technique, the solution material being transferred could have a lower impact force on the acceptor substrate than would be the case using LIFT, thus allowing for the transfer of a smaller amount of solution material to the substrate. cDNA[30] had also been printed with both LIBT and LIFT. Figure 2 shows LIFT transfer of Al film[7] and Ag electrodes to OTFT[21], and LIBT transfer of gold nanodroplets[29] and microarrays to cDNA[30].

1.5 Limitations of laser transfer techniques

Laser transfer techniques had several limitations in material deposition[31]. (1) **Cost**: Transferring metal film requires the metal film to be deposited on the substrate in a vacuum chamber. This process is expensive and increases the cost of the fabrication. (2) **Size**: To date, the minimum reported size is a 300 nm droplet[29], it could reach several micrometers for metal thin film[22]. The laser transfer method has a limitation on the size of line patterns and does not work well when the line width is below 75 nm. The suitable range for this method is from the several hundred micrometers to several hundred nanometers. (3) **Oxidation**: In atmospheric conditions, the metal pattern is easily oxidized, which will affect its conductivity and reduce device performance. (4) **Irreversible phase transition**: Some materials are not easily transferred, and materials undergoing vaporization will be damaged, leading to irreversible phase change in biomaterials, in particular.

1.6 Laser transfer mechanism

In 1970, Levene's group[32] reported their work of material transfer and described the mechanism for the laser transferring of the material as follows: (1) the material to be transferred was heated by a laser beam; (2) the material was superheated and vaporized at the interface; (3) the vaporized material closest to the interface pushes the non-vaporized material away from the substrate to the acceptor substrate; (4) the transfer material is collected on the accepted substrate. Figure 3 shows the mechanism of the laser transfer technique.

During the process of laser transfer, the material is evaporated or melted. This process affects the properties of the transfer material as described above and the researchers have developed several methods[33] to regulate the state of the transfer material: (1) **Use a laser-absorbing layer or a dynamic release layer.** A sacrificial layer is added between the substrate and the transferring material to absorb heat from the laser and repel the transfer material. This layer keeps the transfer material from superheating and will evaporate. (2) **Use composite or matrix-based materials.** This technique was used to transfer various powder mixed with an organic or polymer binder. The binder is photo-sensitive[34] and can decompose at lower laser intensities. When the laser irradiates the binder, it decomposes and pushes the powder to the acceptor substrate. It can transfer thicker films with lower substrate temperatures. (3) **Use liquid buffer layer**: This technique transfers liquid phase material as gel ink or biomaterials. The role of the liquid is to absorb laser intensity and vaporize. The biomaterial is then ejected from the substrate to the acceptor substrate. If the liquid can not adequately absorb the laser intensity, the biomaterial will be damaged.

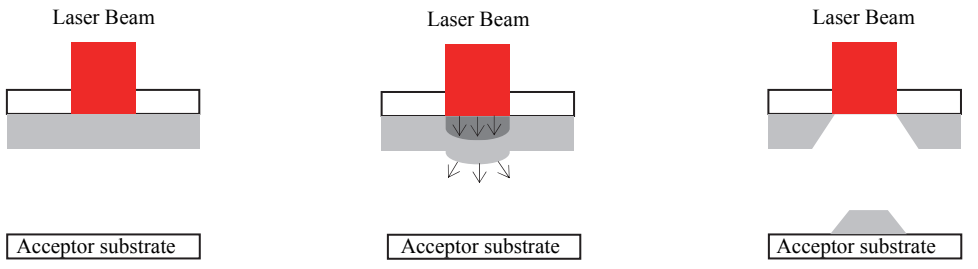

Fig. 3. The laser transfer technique mechanism. (a) The transfer material is heated by a laser beam. (b) The transfer material is superheated and vaporized at the interface. The vaporized material closest to the interface pushes the non-vaporized material away from the substrate to the acceptor substrate. (c) The transfer material is collected on the accepted substrate.

2. Development of carbon nanotubes

In 1959 Richard P. Feynman said, "If we can control miniature bodies in order, we can get a great quantity characteristic out of the ordinary". This was a surprising insight into the nanotechnology which would be developed in the 21st century. The term "Nanotechnology" was coined by N. Taniguchi in 1974, and the preface "nano" has already entered into popular usage. The development of nanotechnology is already starting to be felt in of our daily lives and, as advances in biological and information technology defined the 20th century, nanotechnology is shaping up to define the 21st century.

The 1991 discovery of carbon nanotubes (CNT) by Dr. Sumio Iijima at NEC Corporation opened the possibility of nanotechnology to almost an unlimited extent. CNTs possess many special characteristics including a high aspect ratio, high thermal conductivity and high electrical conductivity. In addition their mechanical strength is one hundred times greater than that of steel. These characteristics present potentially revolutionary applications in fields as diverse as energy, biomedicine, information, electronics, and optoelectronics.

Generally, graphite is composed of planes of carbon atoms in a hexagonal arrangement. In 1985, Sir Harold W. Kroto in the UK, and Robert F. Curl and Richard E. Smalley in the US used lasers to irradiate, and thus completely change the structure of, graphite. After laser irradiation, the carbon atoms in the planar layer in graphite formed three-dimensional hollow spheres composed of pentagonal and hexagonal arrangements of carbon atoms. These hollow spheres were called "buckyballs" (C_{60}), and the discovery merited the 1996 Nobel Prize in Chemistry. In 1991, Iijima was fabricating buckyballs when he discovered a new hollow tube structure of multi-walled carbon nanotubes (MWNTs). In 1993, he also successfully fabricated another type of carbon nanotube – single-walled carbon nanotubes (SWNTs). As their name implies, carbon nanotubes are hollow tubes enclosed by a half buckyball at either end. The tube is laterally composed of planar carbon atoms in pentagonal or hexagonal arrangements. A SWNT can be conceptualized by wrapping a layer of graphite, called graphene, into a seamless cylinder while a MWNT consists of multiple rolled layers (concentric tubes) of graphite. The diameter of a SWNT is about 1.4 nm while the diameter of MWNTs ranges from 20 to 40 nm. The interlayer interactions for MWNTs

occur through van der Waals' forces and CNTs are usually less than 100 μm in length. SWNTs are generally believed to have greater applications than MWNTs due to their superior performance in a wide range of material properties. More recently, double-walled carbon nanotubes have also been successfully fabricated though the properties of these new structures are still largely unknown.

Several methods have been reported for fabricating CNTs including (a) the arc charging method, (b) the laser vaporization/ablation method, and (c) the chemical vapor deposition (CVD) method. In the arc charging method, an inert gas is infused into a vacuum chamber with two graphite electrodes. When a high voltage bias is applied between the two electrodes, the charge of the generated arc can induce the carbon to form a tube structure around the negative electrode. The laser vaporization/ablation method uses a high energy laser beam to vaporize the target graphite, and carbon tubes can then be formed from high-temperature quartz tubes. Generating CNTs using the CVD method typically involves placing substrates pre-coated with suitable catalysts in a high-temperature chamber. Hydrocarbon gas is pumped into the chamber where it decomposes and forms CNTs on the catalysts. The catalyst is usually made of alloys of Fe, Co and Ni.

Due to their extraordinary properties, CNTs can be potentially applied in areas including displays, CPUs, sensors, batteries, electrical and thermal conductors, coelectromagnetic wave shielding, aircraft, bullet proof vests, space elevators, fireproof materials, etc. It is believed that many of their potential applications will be commercialized in the future. On the other hand, like other nanomaterials, CNTs are potentially hazardous. Recent findings have demonstrated that animal DNA can absorb nanoparticles and CNTs, resulting in modifications to cell functions and influencing growth patterns. Nanoparticles in groundwater can interfere with the development of plant roots. Thus, prior to widespread use, the impact of CNTs on the environment, ecological systems and human health, must be systematically evaluated.

2.1 CNT thin film

Many applications of CNTs are in the form of thin film. For example, the transparent CNT film is seen as having great potential to replace the indium tin oxide (ITO) film as transparent electrodes in the future because the price of indium is keeping increase. Thus, fabrication of CNT thin film draws much research attention.

There are several methods for fabricating a CNT thin film: (1) **CVD:** This method[35-39] is suitable for the fabrication large area CNT films. A catalyst of alloys of Fe, Co and Ni is coated on the substrate which is then placed into a high-temperature chamber, to which hydrocarbon gas is added. Figure 4(a) shows the SEM image of the CNT film created by CVD. (2) **Spray coating:** The CNT solution is sprayed on the substrate with an airbrush and heated to dry the CNT droplets. This simple, low-cost method[40-41] is also suitable for the fabrication large area CNT films. Figure 4(b) shows the schematic of the spray coating method and the SEM image of the CNT film spray coating on the substrate. (3) **Dip-coating:** The substrate is immersed into a uniform CNT solution. When removed from the substrate, the CNT solution is adhered to the substrate. As the adsorption CNT solution dries, the CNT network is formed on the substrate. This method[42-44] has advantages in the fabrication of large area CNT films, but high conductivity requires the substrate to be dipped several times and the film thickness does not correlate linearly with the dipping times. Figure 4(c) is the schematic of the dip-coating method and the SEM image of the CNT film dip-coating on the substrate. (4) **Filtration:** The uniform CNT solution is prepared and passed through a

nanoporous filter, leaving a uniform CNT film which can then be transferred to the desired substrate. This method[45-49] has the advantages in the homogeneity of the resulting CNT film but the size of the CNT film has limited by the size of the filter. Figure 4(d) shows the schematic of the filtration method and the SEM image of CNT film filtration on the nano-filter. (5) **Imprint:** This method involves printing CNT film with a standard office laser printer[50], inkjet printer[51-52] or contact printer[53-55]. In a laser printer, CNT powder replaces the toner. The CNTs could be patterned on polymer film. Figure 4(e) shows the schematic of the laser-printer method and the CNT film laser-printed on the substrate. In inkjet printing, the CNT solution replaces the ink. Figure 4(f) shows the CNT film inkjet on the substrate. This method has an advantage in that the patterns are easily edited by a graphic or word-processing software on a computer. The contact printing method is popular for transferring CNT film. The growth or network CNT film is laid on the target substrate, and the transfer takes place during the contact printing process. Figure 4(g) shows the schematic of the contact printing method and the SEM image of the CNT film contact printing on the substrate. (6) **Electrophoretic deposition:** A uniform CNT solution is prepared in the sink. Two metals are connected to direct current (DC) and are used as the anode and the cathode. The CNT film is then deposited on the anode surface. This method[56-58] is well-suited to the fabrication of large-size CNT films, and produces films with high homogeneity and proper surface roughness. However, the substrate needs a conductive anode and must be immersed in the solution. Figure 4(h) shows the schematic of the electrophoretic deposition method and the SEM image of CNT film electrophoretic deposition on the substrate. (7) **Laser transfer:** This method can produce large CNTs films[59] and transfer the film to a selected position [12,25,60-62]. A uniform CNTs solution is placed on a transparent substrate. After the CNTs self-assemble on the transparent substrate, the mask is placed in front of the substrate. High intensity irradiation forms a thick CNT film. The mask is removed and we apply a low laser intensity to irradiate the thick pattern of CNTs. The transparent substrate has a thin residual CNTs film. Figure 4(i) shows the schematic of the laser transfer method and an image of the CNT film deposition on the substrate.

3. Patterning of CNT thin films by laser transfer and their applications

3.1 Carbon nanotube field emission display (CNT-FED)

3.1.1 Development of the field emission display (FED)

The development of the cathode ray tube (CRT) in 1879 led to the invention of the CRT-based television. Continuous improvements, including the development of color and new techniques for mass production led to this device becoming an indispensable home appliance up until the early 1990s. Although high quality CRT displays can be manufactured at low cost, conventional CRT displays cannot be scaled up in size without incurring a proportional increase in depth and weight.

Field emission displays involve an electron hitting a screen and thus inducing a light spot to appear on the screen. This principle is used extensively in displays. Generally, metal surfaces cannot easily be induced to emit electrons and doing so requires overcoming the energy barrier of the metal. The work functions for metals ranging from 2 to 5 eV. Raising the temperature of the metal provides the electron with enough energy to be emitted from the metal, a process known as heated cathode emission. On the other hand, by applying an external electric field with a magnitude large enough to overcome the work function, the electron can be emitted from the metal. This approach does not require heat and is therefore referred to as cold cathode emission.

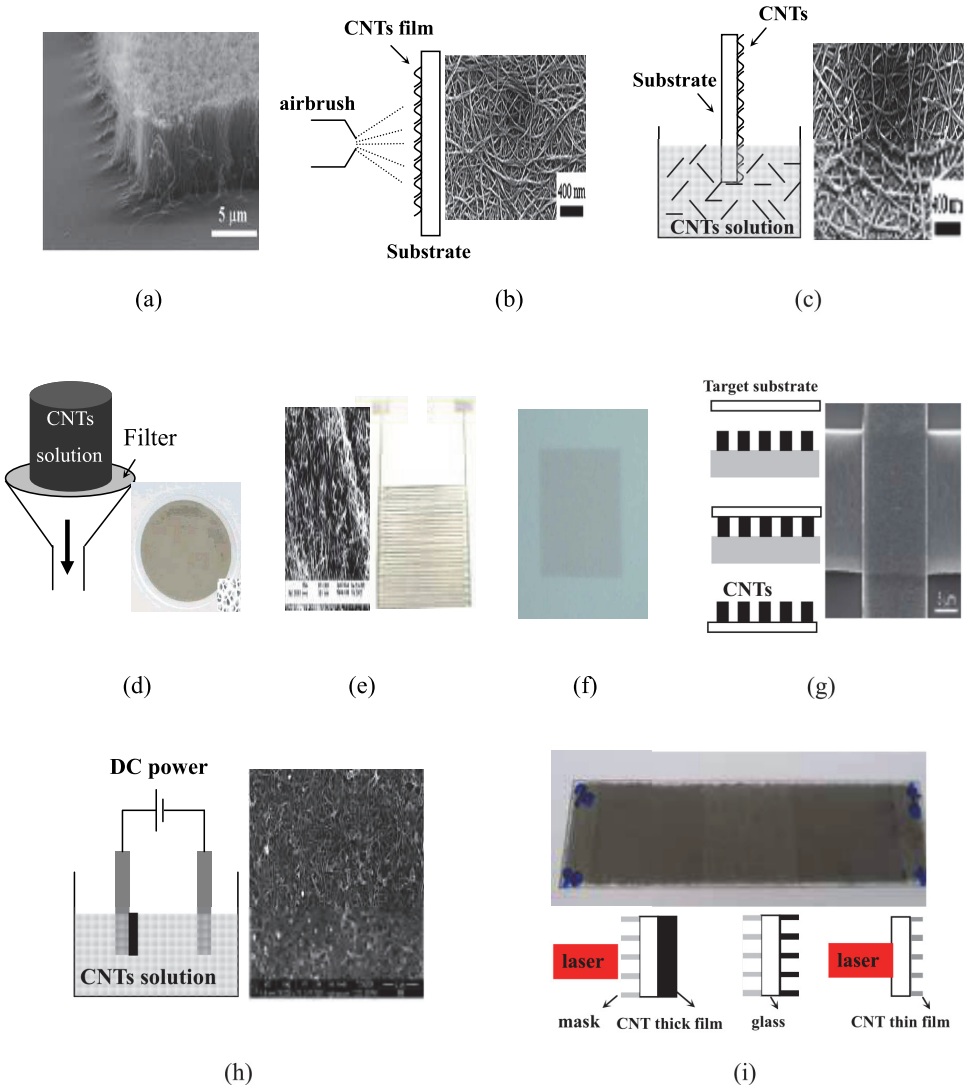

Fig. 4. Schematics for and CNT films resulting from (a) CVD[37] (b) spray coating[40] (c) dip-coating[40] (d) filtration[47] (e) laser-printer[50] (f) ink-jet[51] (g) contact printing[55] (h) electrophoretic deposition[57] (i) laser transfer[59].

In 1968, Spindt et al.[63] at the Stanford Research Institute used a semiconductor manufacturing process to fabricate a Mo tips array as seen in Fig .5(a). The field emission effect is generated by applying a high voltage bias to draw the electrons from the Mo tips to impact the phosphor where it generates a spot of light. Figure 5(b) shows the schematic of the field emission effect. The Mo tips array has a diameter of about several hundred nanometers. However, Mo-based FEDs are still not widely used because the fabrication process is still complicated and the Mo tips are easily damaged.

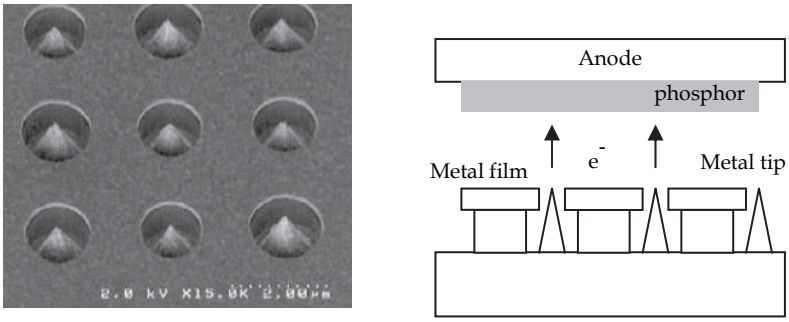

(a) (b)

Fig. 5. Mo field emission display: (a) SEM image for Mo tip array. (b) Schematic of the field emission effect.

Development of CNT-FED began after Iijima's invention of CNTs in 1991. Due to their excellent emission properties, CNTs had been seen as a very promising candidate as an emitter for Flat Panel Displays (FPD). Traditionally, emitters made of Si, W and Mo suffer quick performance degradation, especially under high-voltage conditions, and researchers were searching for a substitute which could maintain a high emission current density even at low operation voltages.

Table 1 shows the electron field emission characteristics of typical emissive materials[64]. The nano-diamond and the carbon nanotubes have had lowest turned on voltages in the range of 2~5 V/μm. The threshold emission voltages for Si and Mo emitters are within 50 and 100 V/μm. For diamonds grown by CVD this value can range from 30 to 120 V/μm. Reports show that nano-diamond can have turn-on voltages as low as those for CNTs (i.e., 3~5 V/μm). However, processing nano-diamonds as cathode emitters requires higher temperatures and is rather more complicated than fabricating CNT emitters. Fabricating CNT-FED devices involves coating and patterning CNT thin films upon an ITO glass, applying a bias voltage between the ITO glass and a positive pole with a pre-coated phosphor. The voltage bias draws electrons from the CNT tips to the phosphor plate to generate a light spot.

Cathode material	**Threshold field (V/μm) for a current density of 10 mA/cm²**
Mo tips	50-100
Si tips	50-100
p-type diamond	160
Defective CVD diamond	30-120
Amorphous diamond	20-40
Cesium-coated diamond	20-30
Graphite powders	10-20
Nano-diamond	3-5 (unstable >30 mA/cm²)
Carbon nanotubes	2-5 (stable >1 μA/tube)

Table 1. Electron Field Emission Characteristics of Typical Emissive Materials [64]

3.1.2 Development of CNT field emission displays

CNT-FED has many advantages over other currently available monitor products. They can be used as light sources for various purposes including street lights, table lamps, back lights for liquid crystal panels and x-ray generators. In 1995, Heer et al.[65] first measured the field-emission current density of CNTs and demonstrated them as a source for generating electrons. Many methods have been proposed to use patterned CNT thin films as cathode emitters. The most commonly-used methods include CVD, electrophoresis deposition and screen printing, and each method has its advantages and disadvantages. CNT films produced by CVD[35-38,66] and electrophoresis deposition[67-69] have been described previously in Section 3. The screen printing method has CNTs mixed with paste and squeezed onto metal meshes to pattern on the substrate[70-74]. The paste can firmly absorb the CNTs on the substrate. However, a weakness of the screen printing method is that the CNT tips are covered by the paste, which will affect the turn on voltage and the emission current density of the CNT film. Several post-production methods can remove the paste from the CNT tip, including the use of adhesive tape[75], mechanical crushing, high speed airflow cleaning[76], atmospheric pressure plasma[77], laser surface treatment[78] and polydimethylsiloxane elastomer[79]. Figure 6(a) shows SEM images of a microcathode produced by CVD and Fig. 6(b) shows the emission image of the CNTs deposited by electrophoresis. Figure 6(c) shows the emission of fully-sealed SWNT-FEDs in color mode with red, green, and blue phosphor columns (left) and the SEM image of a screen-printed CNT cathode (right).

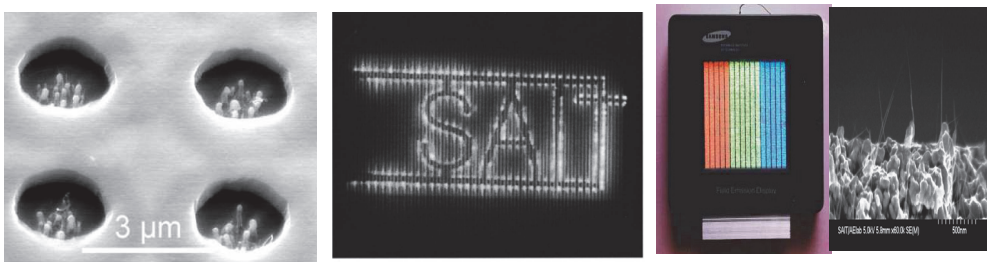

(a) (b) (c)

Fig. 6. (a) SEM images of a microcathode by the CVD; (b) emission image of CNTs deposited by electrophoresis (c) emission image of fully sealed SWNT-FED in color mode with red, green, and blue phosphor columns (left) and SEM image of screen printed CNT cathode (right)

3.1.3 Fabrication of carbon nanotube field emission cathodes by LIFT

Screen printing of large scale CNT displays is made difficult by insufficient CNT outcrops and non-uniform surface emission densities. The LIFT technique is proposed to address this problem. By this method CNT film can be printed on various substrates at room temperature with a CNT outcrop silver paste surface. It also has the advantage of sticking the CNTs firmly in the paste, thus preventing the CNTs from escaping when the substrate temperature is raised during illumination. Chang-Jian et al.,[12] demonstrated the feasibility of using the LIFT technique to print CNTs on silver paste with the steps as follows: (1) the CNT solution is dropped on transparent glass and allowed to self-assemble as in Fig. 7(a); (2) the silver paste is dissolved in alcohol and spun on the ITO substrate; (3) a uniform Nd-YAG pulse laser (1064 nm) is used to irradiate the MWNT film, with alcohol applied to the transparent side; (4) the laser light passes through the mask to the pre-coated CNT film

which absorbs the laser energy, evaporates and is deposited on the silver paste as in Fig. 7(b); (5) the desired pattern is obtained on the silver paste which is heated in an oven for 1.5 hour at 100℃ as in Fig. 7(c). Figure 7(d) shows the lighting image captured by CCD camera, emitting from a 12 × 12 dot array of MWNTs emitters, deposited in a 3 mm by 3 mm area on the ITO surface. Each dot MWNTs emitter has a diameter of 100 μm. Fig. 7(e) shows a partial SEM image of a MWNTs dot array deposited on an ITO glass by laser transfer. Figure 7(f) shows the enlarged SEM image from Fig. 7(e). With a higher magnifying power, the inset shows that the feature size of the patterned emitter as small as 12 μm.

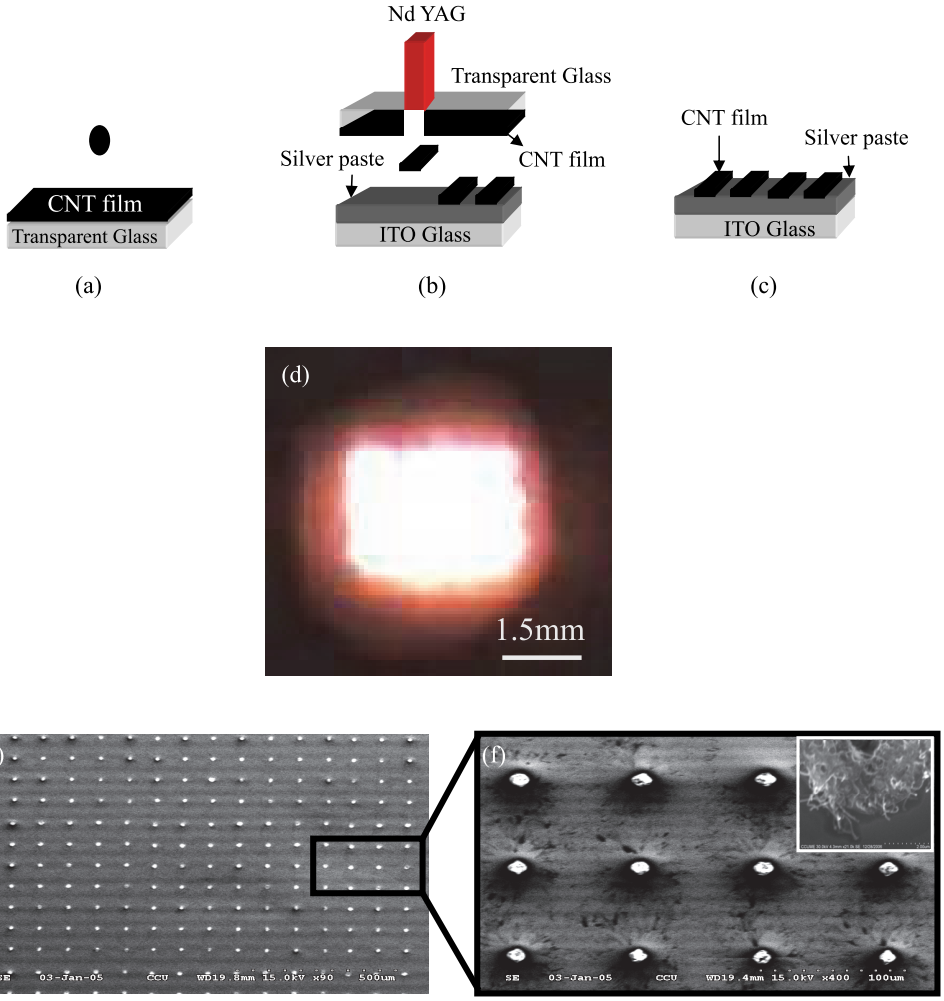

Fig. 7. (a)-(c) CNTs film transfer on the substrate by LIFT[12]; (d) The lighting image emitting from 12 × 12 dot arrayed MWNTs emitters that were deposited within a square, with the dimensions of 3 mm by 3 mm, and on an ITO glass substrate. (e) SEM images showing the patterned CNT spots on ITO glass; (f) corresponding enlarged surface image of (e) with the inset SEM image enlarged from (f).

3.2 CNT field effect transistors (CNT-FETs)

3.2.1 Development of CNT-FETs

The structure of SWNTs reveals both metal and semiconductor-like characteristics that enable their application to CNT field-effect transistors. The diameter of a SWNT is about 1.4 nm, which allows for the scale of electronic devices to be greatly reduced. SWNTs have high heat conductivity that aids in the cooling in electronics, and more research is ongoing into finding applications of SWNT properties in electronic devices.

Two studies on SWNT field-effect transistors found that SWNTs can transfer both types of carriers, electrons and holes, at room temperature and that they have excellent semiconducting characteristics[80-81]. The researchers deposited a catalyst at the source and drain of the electrodes to grow a single SWNT that spanned the two electrodes by CVD with the aim to replace the traditional semiconductor layer with a single SWNT which not only functioned as a traditional transistor, but also permitted a higher mobility and on/off ratio. However, synthesizing a 100% semiconducting SWNT is still a challenge, and current techniques usually max out at 70%.

In 2000, a researcher analyzed the relationship among metal and metal characteristic SWNTs, semiconductor and semiconductor characteristic SWNTs, and metal and semiconductor characteristic SWNTs. The only the connection found was that metal and semiconductor characteristic SWNTs would transfer the hole and electron at room temperature[82], a finding which prompted research into CNT-FETs using non-individual SWNTs as a semiconductor. The dropped[83] and printing[84-85] methods were used to place networked SWNTs between the two electrodes. The SWNTs reveal *p*-type characteristics when they are exposed to air and absorb oxygen. Given that logic circuits are composed of both types of transistors, *n*-type CNT-FETs should be developed as well, and there are several methods to do this using SWNTs including deposition of potassium[86], desorbing oxygen by vacuum annealing[87], covering with polymer[88-89], or contacting with metals[90-91].

3.2.2 Fabrication of CNT-FETs

There are several methods for fabricating CNT-FETs. The more common methods include CVD[80,82, 86-88, 89-91], spin coating[81], dropping[83] and printing[84-85,93,94], each with its own advantages and disadvantages. In the CVD method the catalyst is deposited on the source/drain electrode. The SWNT is grown from the catalyst in the high temperature chamber with gas input, with the SWNT bridging the source and drain electrodes. In spin coating the SWNT solution is spread on a substrate with predefined source/drain electrodes and the SWNT network is placed between them. In the dropping method the SWNT solution is dropped on a substrate with predefined source/drain electrodes. After the SWNT solution dries, the SWNT network is placed between the electrodes. In the printing method the CVD growth SWNT pattern contacts the PDMS (dimethylsioxane). The SWNT pattern is removed from the substrate and then the PDMS contacts the receiving substrate. The SWNT pattern is then transferred to the predefined source/drain electrodes and the SWNT network is placed between them. Figure 8(a) shows the schematic of the CNT-FETs. Figures 8(b)-(e) show the SWNT positioned between the source and drain in the CVD, spin coating, dropped, and printing methods.

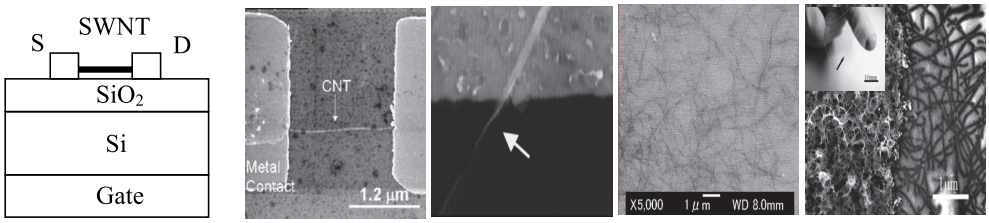

(a) (b) (c) (d) (e)

Fig. 8. (a) CNT FETs schematic; (b)-(e) SEM images of the SWNT between the source and drain by CVD[90], spin coating[81], dropped[83], and printing methods[93].

3.2.3 Fabrication of CNT-FETs by LIFT

Figures 9(a)-(d) show the fabrication processes of *p*-type CNT FETs devices with MWNT electrodes. First, a uniform MWNT film is formed on a transparent glass support. The substrate is a Si wafer pre-coated with a 100 nm thick SiO_2 dielectric layer. The gate electrode is gold. As shown in Fig. 9(a), a metal mask in the desired pattern with through holes is placed between the transparent glass support and the Si substrate. The glass support, mask and the substrate are then clamped together. A pulsed Nd:YAG laser (λ = 1064 nm) irradiates the transparent glass support to transfer the MWNTs through the hole patterns in the mask and deposit the transferred MWNTs onto the SiO_2 surface. After removing the mask, the patterned MWNT electrodes are printed on the SiO_2 layer, as in Fig. 9(b).

For the *p*-type CNT FETs, the SWNTs are used as the semiconducting layer, requiring the fabrication of another transparent glass support coated with SWNT networks following the same procedures as those for the MWNT glass support. However, an additional laser irradiation step is required to regulate the amount of SWNTs on the substrate, which can be accomplished through direct laser illumination on the uniform SWNT film. Laser illumination evaporates most SWNTs on the glass leaving only a small portion on the substrate. Another mask is prepared and placed on the reverse side of the glass support. Here, however, a microscope is required for the mask alignment, as shown in Fig. 9(c).

The same procedures as those for the laser transfer of MWNTs as electrodes are used to transfer the networked SWNTs as the semi-conducting layer. Through the 2nd mask, the SWNT networks can be printed on the SiO_2 layer and between two MWNT electrodes, as shown in Fig. 9(d), thus producing *p*-type CNT FETs. Figure 9(e) shows an SEM image of the MWNT electrodes on the SiO_2 dielectric layer[62]. The patterns assume square and "L" shapes. The distance between the two "L" shapes is 200 μm. The inset shows a close-up of the circled section where the individual MWNT can be easily identified. We find that the transferred MWNTs are compactly interconnected, resulting in excellent electrical conductivity for use as electrodes.

Figure 9(f) shows the I-V characteristics of the fabricated *p*-type CNT FETs after laser transfer of the SWNTs between the MWNT electrodes. The I_{SD}-V_{SD} curves are V_{SD} sweeping from 0 to 7 V as V_G varied from -15 to +15 V at an incremental step of 15 V. The inset shows I_{SD}-V_G curve as V_G sweeping from -15 to 15 V under a constant S/D bias at V_{SD} = 10 V. The current of I_{SD} decreases with the increase of V_G, revealing the characteristics of *p*-type CNT FETs, and mobility is 0.019 cm^2/V s. Figure 9(g) presents an SEM image showing the formed

SWNT networks following laser transfer printing. It shows that the printed SWNTs were well interconnected between the Au source and drain electrodes[25]. The inset is a CNT FET with the SWNT positioned between the Au source and drain electrodes. Figure 9(g) is a close-up of the circled section.

Figure 9(h) shows the transfer characteristics of the fabricated *p*-CNT FETs. The reported device had an R_{SD} = 58 kΩ. The I_{SD}-V_G curve were obtained as V_G first sweeping from -15 V to 15 V and then back to -15 V at a sweeping rate of 1 V/s and under a constant S/D bias of V_{SD} = 0.5 V. The arrows indicate the sweeping direction of the V_G. The inset depicts a family of I_{SD}-V_{SD} curves with V_G varying from 15 V to - 15 V at an incremental step of -7.5 V. The I-V characteristics of the device also exhibited an obvious hysteresis. These I-V characteristics reveal that the fabricated device was a *p*-type CNT-FET, and confirms the efficiency of the laser transfer printing method for fabricating networked and interconnected CNT-FETs.

3.3 CNT buckypaper

3.3.1 Development of CNT buckypaper

Buckypaper is a free-standing CNT film composed of several billion individual CNTs yet retaining the fundamental property of individual CNTs. It is lightweight, stronger than steel, thinner than paper, highly electrically and thermally conductive. Many researchers hope that buckypaper can find applications in aerospace, communications, textiles and displays. Buckypaper has been demonstrated to be 500 times stronger than the steel at only one-tenth the weight and is thus expected to contribute to stronger[95-96] and lighter aircraft which would also be immune to lighting strikes. The relative lightness of such an aircraft would not only save on fuel consumption, but would also have reduced pollution output.

In textiles CNTs can be mixed with other fibers to make clothing resistant to electromagnetism or bullets. A buckypaper bulletproof vest would be much lighter and tougher than a traditional one, and the high thermal conductivity of the CNTs would provide additional comfort to the wearer[97].

The popularity of mobile phones is somewhat offset by concerns about the effect of electromagnetic waves on human health. A buckypaper covering for mobile phones could effectively shield callers from electromagnetic energy emanating from the phone[98], and this application could be extended to equipment which requires electromagnetic shielding.

Buckypaper can also be employed in the field emission displays[99], and can be used to easily create for large-sized displays at low cost. Buckypaper with two-faced CNT tips could be used to fabricate a "double-emission" display, simultaneously showing different images on a single piece of buckypaper, thus displaying messages more economically and effectively.

3.3.2 Fabricating CNT buckypaper

Commonly used methods for fabricating buckypaper included CVD[95,100-103], electrophoretic deposition[96] and filtration[98-99,97,104-107], with each method subject to advantages and disadvantages. CVD and electrophoretic deposition of CNT film had been described above in section 3.1. In the filtration method, the CNTs are suspended in a solution and deposited on the surface of a filter. After the CNTs are dry, the film is removed from the supporting filter membrane. This low cost method is fast and convenient, and can cover a large area. However, the most significant drawback is that buckypaper breaks easily while being separated from the membrane, especially in large and thin sheets. Therefore, the yield rate is low.

Buckypaper is now commercially available, but it is relatively expensive, with a disc-shaped piece of filtration fabricated buckypaper 125 mm in diameter and 0.1 mm thick selling for

$1000. Until this price falls, buckypaper can not be used in everyday applications. Figures 10(a)-(c) show buckypaper fabricated by CVD, electrophoretic deposition and filtration.

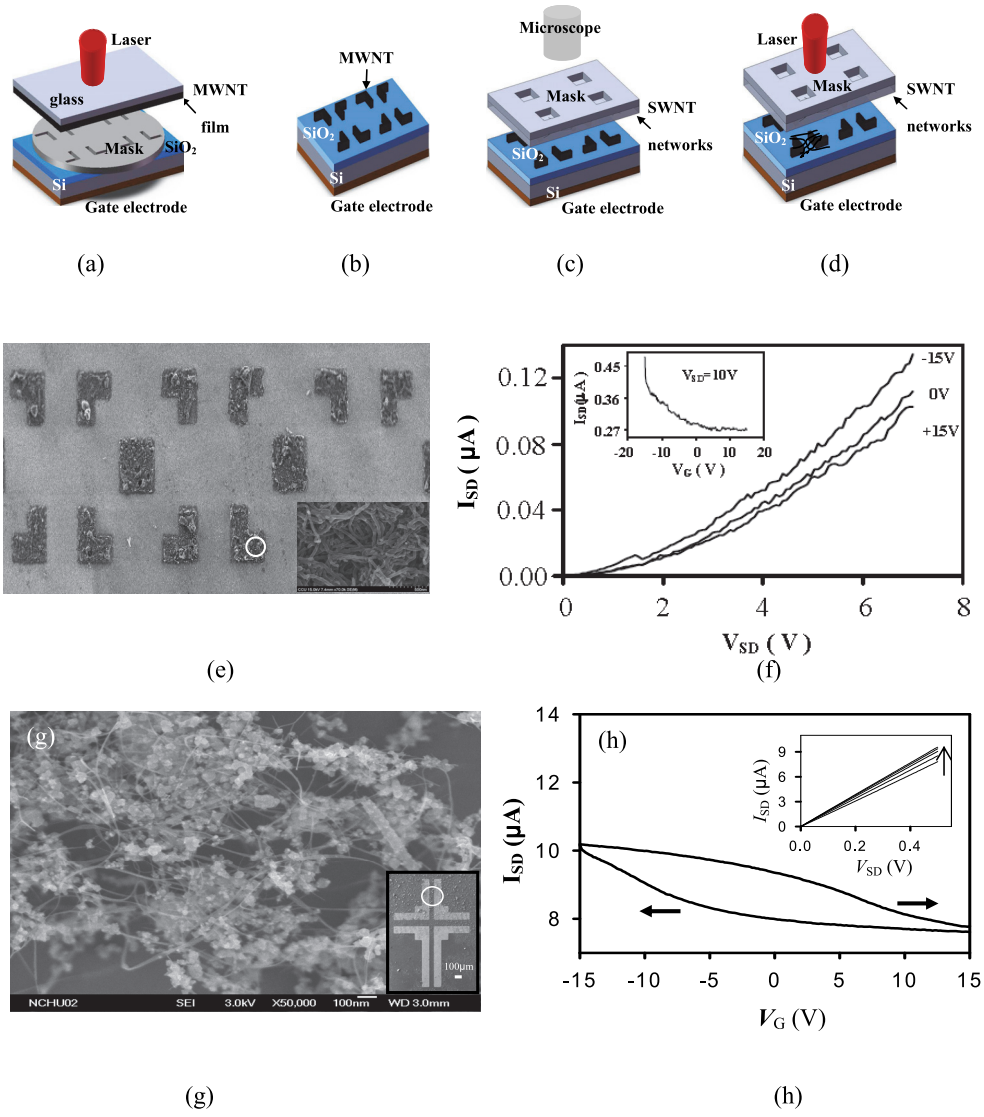

Fig. 9. (a)-(d) schematic of CNT FET fabrication by laser transfer; (e) SEM image showing the transferred MWNT electrodes on the SiO_2 layer[62], the inset is close-up of the circled section; (f) *p*-type CNT FETs characteristics with MWNT electrodes; (g) SEM image of SWNT networks – the inset is a CNT FET in which the SWNTs lie between the Au source and drain electrodes and the circled section is a close-up of (g); (h) p-CNT FETs characteristics of (g) inset[25].

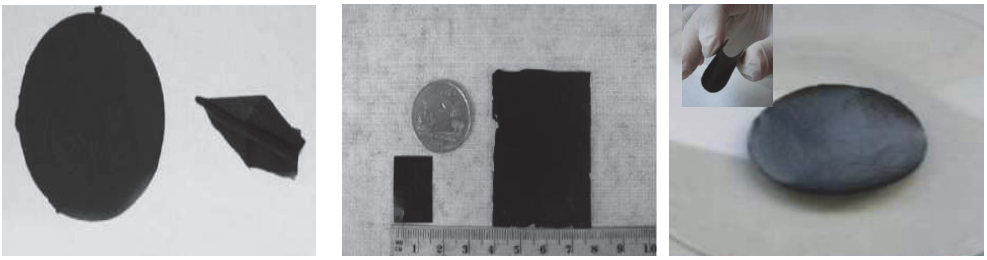

(a) (b) (c)

Fig. 10. (a)-(c) buckypaper fabricated by CVD[100], electrophoretic deposition[96] , and filtration[105].

3.3.3 Fabricating CNT buckypaper by laser irradiation

Recently, we propose a new laser transfer technique to manufacture buckypaper. The proposed technique has many advantages. It can avoid film rupture when separating from a thin and large MWNT film, thus resulting in a higher yield rate for the fabrication of thinner and larger buckypaper than can be obtained through compression. This method is also less expensive than CVD which requires fabrication in a vacuum.

Figures 11(a)-(c) illustrate the processes of fabricating MWNT buckypaper by pulsed laser separation: 1) a pipette is used to drop the MWNT solution on a transparent glass support until the whole surface is covered with a thin liquid film. The alcohol evaporated after about 20 minutes, leaving a thin uniform MWNT film on the front side of the glass, as shown in Fig. 11(a); 2) a patterned mask is placed on the glass support and a uniform laser pulse (Nd:YAG: 1064 nm, pulse width 7 ns) with a 123 mJ/cm^2 laser intensity irradiated the glass from the mask side, as show in Fig. 11(b); 3) scanning the entire MWNT file with a pulsed laser produces a free-standing buckypaper in the designated pattern, as shown in Fig. 11(c).

Depending on the degree of transparency set in the mask pattern, a special contrast in the height difference between the patterned and unpatterned regions was generated on the surface of the resulting buckypaper. Here a commercial PC (polycarbonate) slide was employed as the mask. The designated pattern was printed on the mask by a commercial black-and-white laser printer using HP carbon cartridges while the degrees of transparency for the mask pattern were arranged by tuning the pattern's grey levels in Microsoft Word, as shown in Fig. 11(d). Figure 11(e) shows the resulting patterned buckypaper deposited by the proposed laser-separation method. The "CCU ME" is clearly patterned on the buckypaper. The film thickness was about 40 μm and was placed on a transparent glass slide. Figure 11(f) shows the glass support which separates the pattern from the buckypaper, as shown in Fig. 11(e). Figure 11(f) presents a photographic image showing that the MWNTs have remained on the glass support and the "CCU ME" is patterned on the glass support.

Buckypaper is able to emit electrons from both sides, which is physically appropriate for a double-sided field emitter and, thus, has potentially applications for a double-sided flat panel display or lighting source. Figure 11(g) shows the results of the field-emission characterizations obtained in a vacuum chamber at 2×10^{-5} torr base pressure. The results show the turn-on field was 1.4 V/μm at a current density of 2 μA/cm^2. The corresponding Fowler-Nordheim plots are shown in the inset, presenting the linear relationship between $\ln(J/V^2)$ and $1/V$.

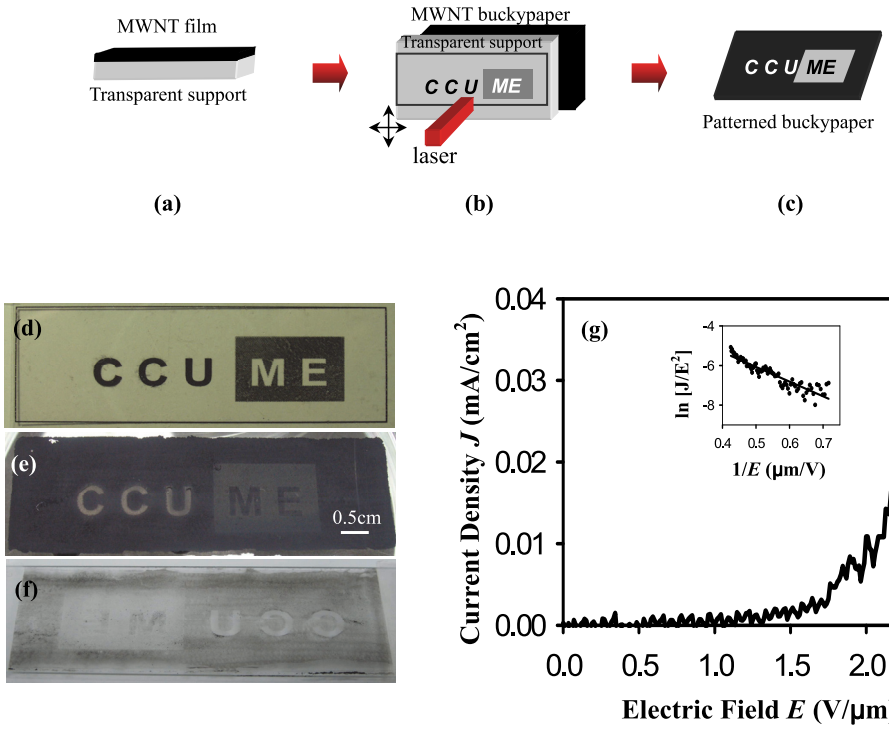

Fig. 11. (a)-(c) fabrication of CNT buckypaper by pulsed laser separation; (d) PC mask; (e) buckypaper patterned by laser-separation; (f) glass support separating the pattern from the buckypaper; (g) field-emission characterizations of double-sided buckypaper; (h) buckypaper ship on water; and (i) MWNT net on paper

The proposed approach also allows for the straightforward fabrication of buckypaper with a curved surface. Figure 11(h) shows a buckypaper presented in the shape of a ship floating on water. This was accomplished by dropping the MWNT solution on the inside of a PMMA spoon, allowing the MWNTs to coat the inside surface of the spoon. We irradiated the MWNT film from the outer surface of the spoon, after which a convex MWNT film separated from the spoon's inside surface. Due to the lightweight and hydrophobic nature of the MWNTs, this buckypaper ship floated very well on water. Thus, shaped buckypaper can be fabricated directly from curved MWNT film, rather than being folded from flat buckypaper, but the process requires a transparent mold in the desired shape as a support.

Figure 11(i) shows a fabricated MWNT net placed on a dollar bill. The net is composed of square grids of different sizes. The inset shows a magnified SEM image demonstrating the line interconnection of a grid point. The line width was about 189 μm. To achieve this effect, we dropped the MWNTs solution on the transparent glass support and waited about twenty minutes for the alcohol to evaporate, leaving the transparent glass support coated with the MWNT film. We then wet the MWNT film with alcohol and placed a mask in the shape of square grids on top of the transparent glass support. A high fluence laser (187.5 mJ/cm^2) passed through the square grid mask and transparent glass support. The sections of the MWNT film unprotected by the mask were separated from the transparent glass support, leaving only the protected square grid shape. We removed the mask and used a low fluence laser (123 mJ/cm^2) to scan the transparent glass support. The MWNT film separated from transparent glass support and forming a square grid free-standing MWNT net about 100~200 μm wide. An MWNT net fabricated by laser separation must be line-limited. If the mask's line pattern is too narrow, it will be broken by the irradiation energy of the laser.

3.4 CNT thin films

3.4.1 Development and fabrication of CNT thin film

In section 3.1 we described several methods for fabricating CNT thin film. At present, CNT thin film could be fabricated in the random networks, vertically alignment and horizontal alignment. Research interest into transparent CNTs thin films has increased with the price of indium tin oxide (ITO) film. ITO film has been used as a universal electrode in various optoelectronic devices such as organic light emitting diodes, solar cells and liquid-crystal displays because of their high transmittance in the visible region and good electrical conductivity. However, not only are ITO films expensive, but their electric conductivity changes when they bend[43,48,50]. Transparent carbon nanotube thin film is highly conductive, it does not change when bent and its low cost make it very suitable for replacing ITO film in next generation products. SWNT/PET sheet resistance was ~80 Ω/sq, with ~80% transparency. It has been extensively used in the optical applications[45], organic light-emitting diodes[47], transistors[52], gas sensors[46], solar cells[41] and field emission devices.[51,59].

3.4.2 CNT thin film fabrication by laser irradiation

Recently, we proposed a practical method for using laser separation to form an MWNT thin film on a flexible transparent substrate[59]. The fabricated MWNT thin film can be sparsely networked and, given sufficient outcrop tube tips, the film surface demonstrates good field-emission characteristics. The laser-based method is less vulnerable to the problem of insufficient outcrops found in the filtration method. By contrast, CVD fabrication must be

executed in a high vacuum and at high temperatures, which raises the cost and is not suitable for flexible substrates. In addition to its ability to form MWNT thin films directly on a curved surface, our proposed method can also be used to fabricate a MWNT thin film with precision patterns and with varying spatial concentrations.

Figures 12(a)-(d) show the processes of fabricating a patterned MWNT thin film with extrusive and vertically aligned surface MWNTs by laser separation. (1) The designated amount of MWNTs is dispersed uniformly in alcohol. (2) A pipette is used to drop the MWNT solution on a polycarbonate (PC) substrate until the whole surface is covered with a thin liquid film which, once the alcohol evaporates, leaves a thin uniform MWNT film on the flexible substrate. (3) A mask with the desired pattern is placed in contact with the back surface of the substrate, i.e., without the pre-coated MWNT film. (4) The pre-coated MWNTs film is wetted with alcohol and then irradiated by a high fluence laser as shown in Fig. 12(a). (5) A small portion of the laser energy is dissipated by reflection by the mask and absorption by the substrate. The penetrating energy is mainly absorbed by the MWNTs around the substrate and the MWNT film interface, causing the MWNTs to evaporate and providing a thrust to separate the unprotected MWNTs from the substrate. Following laser irradiation, the protected part of the MWNT film remains on the substrate, as shown in Fig. 12(b). (6) The mask is removed, and a second stage of laser irradiation is executed with a low fluence laser scanning the substrate from the back, as shown in Fig. 12(c). (7) The second stage of laser irradiation leaves a thinner, more transparent patterned MWNT film on the substrate. At the same time, a free-standing CNT sheet (buckypaper) is formed with the same pattern, as shown in Fig. 12(d). This second-stage laser irradiation reduces the thickness of the patterned CNT film and reinforces the CNTs' vertical alignment. The light source was a pulsed Nd:YAG laser with a wavelength of 1064 nm, a repetition rate of 10 Hz, a pulse width around 7 ns, a maximum output energy of 28 mJ, and a raw beam diameter of 2.75 mm. The fluences for the first-stage and second-stage laser irradiations were set at 187.5 and 123 mJ/cm^2, respectively.

Figure. 12 (e) shows a bent PC substrate used to fabricate the MWNT film with line, grid and square patterns. The substrate was placed on a captioned paper and the caption can be clearly identified through the fabricated transparent MWNT film. Figure 12(f) shows a MWNT thin film on a curved surface, demonstrating the feasibility of direct film fabrication on a curved surface. Figure 12(g) and its inset show a side view SEM image of a fabricated MWNT film surface, showing numerous tube tips protruding from the film's surface, sufficiently dense for field-emitter applications. Figure 12(h) shows the current density as a function of the electric field for a fabricated MWNT thin film on a PC substrate. The turn-on voltage is around 1 V/μm and the inset shows the Fowler–Nordheim plot of the same data.

Widely-used methods for fabricating CNT field emitters include screen-printing, *in situ* growth of CNT tips, and melt mixing of CNT composites. The reported turn-on voltage was in the range 1 to 6 V/μm. Without any parameter optimization in the fabrication process and thin film configuration, the present approach produces excellent field-emission properties even on a plastic substrate. The low turn-on voltage was due to the CNT playing the roles of both the electrode conductor and the field emitter. In terms of supporting electron conduction, this type of configuration can avoid possible non-Ohmic contacts or interface barriers caused by different work functions between the conductor electrode (e.g., silver paste or indium tin oxide) and the CNT emitter. CNTs with good vertical alignment have been demonstrated to exhibit better field-emission characteristics which facilitate electron transport and reduce the turn-on voltage.

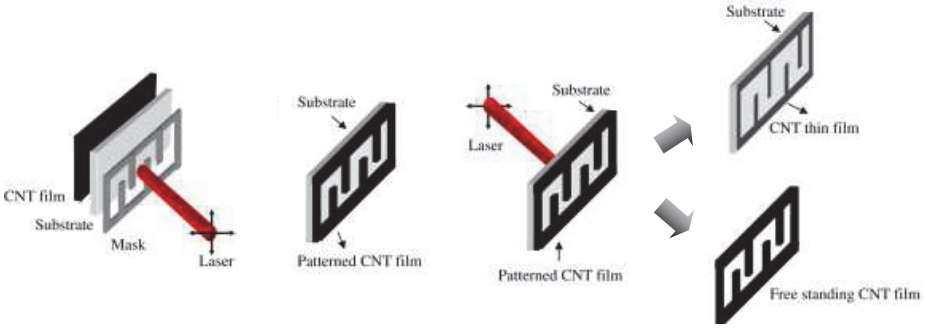

(a) (b) (c) (d)

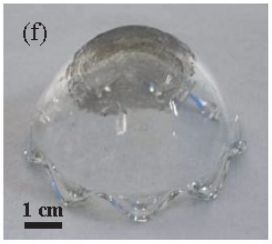

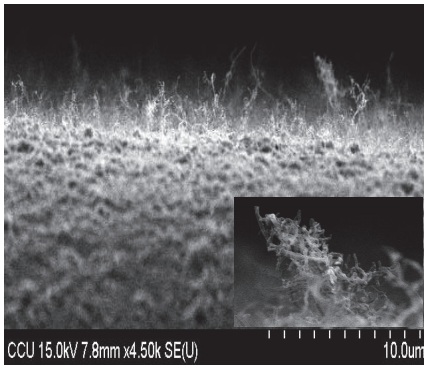

(g)

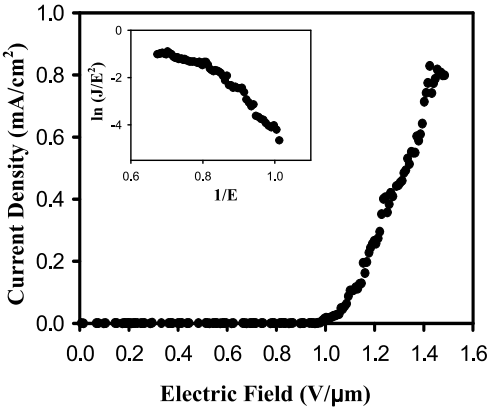

(h)

Fig. 12. (a)-(d) Fabrication of a patterned MWNT thin film by laser separation;[59]. (e) MWNT pattern on the PC substrate; (f) MWNT film on the curved surface; (g) side view of the SEM image showing numerous protruding tube tips on the film surface; And (h) characteristics of MWNT field emitter on PC substrate.

3.4.3 Pattern DWNT thin films by laser ablation

A transparent DWNT flexible thin film was used to fabricate a flexible matrix touch panel by laser ablation, achieving several advantages: the transparent DWNT thin film is considerably less expensive than the ITO film it replaced, and the manufacturing process is less environmentally damaging. In addition, the process is faster while produces larger outputs and higher yield rates than other methods.

Figures 13(a)(b) show the steps for fabricating patterns on transparent DWNT flexible thin film. First, we placed a metal mask on a polyester (PET) substrate which had been pre-loaded with a transparent DWNT flexible thin film (XinNano materials, Inc). The DWNT thin film had the thickness of 20–40 nm, with a sheet resistance of 10^2-10^3 Ω/sq and visible light transmittance of 75-88%. The metal mask with line patterns is laid in contact with the PET substrate on the side without the DWNT thin film. Laser light then passes through the mask openings to irradiate the DWNT thin film below. By simultaneously moving the mask and the PET substrate, the designated area on the PET substrate can completely be exposed to laser light, as shown in Fig. 1(a). The laser used is a pulsed Nd:YAG laser (Continuum) which operates at a wavelength of 1064 nm with a pulse duration between 5 and 7 ns. The size of the laser spot is about 6 mm in diameter and it has a maximum output power of 485 mJ which corresponds to 1716 mJ/cm² in intensity.

As the laser light passes through the mask openings and the transparent PET film, its energy is mainly absorbed by the DWNT thin film on the other side of the PET, causing the DWNTs to evaporate from the PET substrate. Finally, the non-irradiated portion of the DWNT thin film, protected by the mask, remains on the PET substrate to complete the DWNT thin film through laser ablation. Figure 13(b) shows the patterned DWNT thin film on the PET substrate after the mask is removed. Figure 13(c) presents a photographic image of a substrate with a patterned DWNT thin film. The patterned area is 7 cm × 7 cm and contains 100 DWNT line patterns. The caption printed on the paper behind the PET with the patterned DWNT thin film is clearly visible.

Figure 13(d) is an SEM image showing the DWNT line patterns on the PET substrate. The brighter regions are the DWNTs which remain on the PET substrate, while the darker areas are the PET substrate where the pre-coated DWNTs have been ablated by laser. The width of the DWNT lines is 200 μm and the distance between the lines is 150 μm. The inset is an SEM image enlarged from the marked square part of Fig. 13(d), showing that the DWNTs tangle together and the tube diameter ranges from 10 to 20 nm. With the laser ablation technology, we can easily make more complicated patterns. Figure 13(e) is an SEM image showing curved DWNT patterns with a line width of 223 μm. Again, the darker region is the PET surface where the DWNT thin film was ablated.

Figures 13(f)(g) demonstrate the feasibility of fabricating a transparent matrix touch panel by laser patterning of the DWNT thin film. Figure 13(f) schematically shows the exploded diagrams of this matrix touch panel. A spacer is placed between two PET substrates where patterned DWNT thin films are formed by the proposed laser ablation method. The spacer is a commercially-available overhead transparency with a thickness of 100 μm. We use a CO_2 laser to fabricate nine through holes. Each hole is a 1.5 cm ×1.5 cm square, and the distance between any two holes is 2 mm. On each of the PET substrates three pieces of 60 μm-thick aluminum foil are placed in contact and aligned in parallel with the patterned DWNT lines, as shown in Fig. 13(f).

The aluminum foil serves as an electrode. The PET substrates, spacer, and aluminum foil pieces are clamped together using metal clips. The two PET substrates are arranged in such way that their patterned DWNT lines are perpendicular to each other. Figure 13(g) demonstrates the function of this transparent matrix touch panel under bending. The curved

surface of the panel is created by sticking it to the convex surface of a cylindrical glass cup using adhesive tape. The radius of the cup cylinder is 6.5 cm. The top-right corner of Fig. 13(g) presents a schematic showing the top view of the glass cup with the matrix touch panel above a schematic showing the arrangement of the testing circuit. We used a 9 V battery to power a blue LED. When the location on the panel surface is pressed, the patterned DWNT lines on the two separated PET substrates can be well connected and the LED is activated successfully.

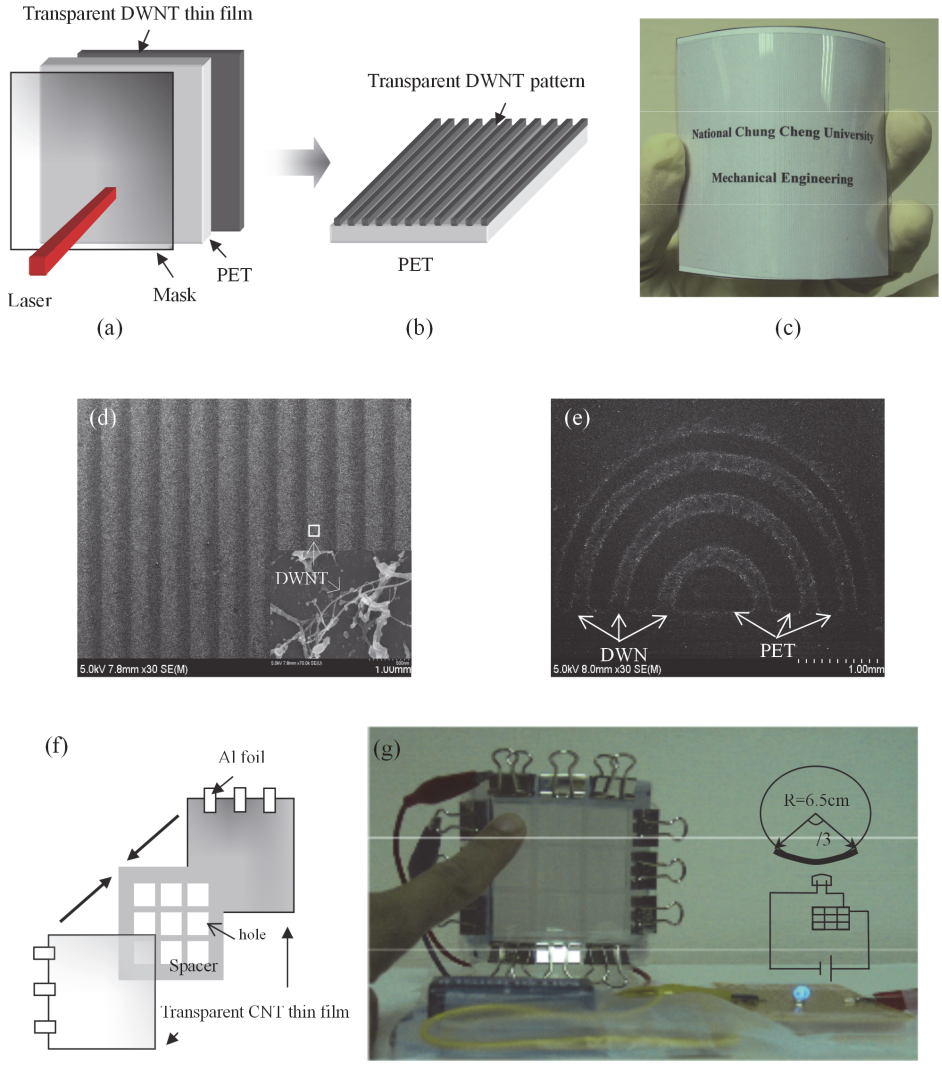

Fig. 13. (a)(b) DWNT film patterning process; (c) DWNT pattern; (d) SEM image of (c), with the inset showing the enlarged SEM image; (e) SEM image of the DWNT pattern; (f) combined schematic of the matrix touch panel; (g) function of the flexible transparent matrix touch panel. The blue color LED is driven by a 9V battery.

4. Summary

We report on the employment of the Nd:YAG laser (1064 nm) to pattern the CNT thin films and fabricate the CNT-based devices in this article. We demonstrate fabrications of carbon nanotubes field emission display (CNT-FED), carbon nanotubes field transistor (CNT-FETs), CNT buckypaper, CNT thin film and transparent DWNT flexible matrix touch panel.

In the CNT-FED, we patterned the CNT field emission cathodes on the substrate by the LIFT technique. The emission test revealed favorable emission characteristics, such as high emission current density, low threshold electrical field, good emission stability and good emission focusing. This method can also afford high pattern resolution, with a feature size down to 10 μm, high feasibility of using various substrates, good MWNTs adhesion and fast deposition rate. Furthermore, all steps can be executed in an ambient environment and at low temperature, consequently offering the benefit of potential low cost fabrication of precision pattern deposition.

As for the CNT-FETs, we report the SWNT printing between the Au electrode and reveal the p-type CNTFETs by LIFT technique. We also successfully demonstrated patterning MWNTs electrodes on SiO_2 substrate and SWNTs between the MWNTs electrode by the LIFT technique. It revealed the p-type CNTFETs characteristics. By introducing a X-Y stage, this method can easily be extended to fabricate large area CNT circuits.

In regard to the CNT buckypaper, we simply accomplished it through employing a pulsed laser to irradiate a transparent support and separate the precoated MWNTs film. Based on this approach, buckypapers with surface patterns and with three-dimensional surfaces were fabricated and demonstrated. The film thickness of the resulting buckypaper could be regulated through adjusting the film thickness precoated on the support. The flexibility of the formation of complicated surface patterns and feasibility in fabrication of thin papers makes the proposed approach a prospective method forbuckypaper fabrication.

Regarding the transparent CNT thin film, we report a new low-temperature method for fabricating thin film MWNTs on a polycarbonate substrate based on the laser peeling method. This method can fabricate a film with varying MWNTs concentrations straightforwardly. The fabricated sparsely networked MWNTs thin film exhibits the feature of sufficient outcrop tube tips on the film surface. It is a favorable arrangement for the field-emission application. The emission test reveals that a low turn-on of 1 V/μm is obtained without any optimization in process and device configuration. Furthermore, all steps can be executed in an ambient environment and at low temperature, consequently offering the benefit of potential low cost fabrication for patterned MWNTs films on flexible substrates.

Regarding the transparent DWNT flexible matrix touch panel, we again use the laser to pattern the DWNT thin film on a plastic substrate and successfully fabricated a flexible matrix touch panel. By increasing the laser energy, the ablation depth of transparent DWNT thin film is increased but sheet resistance is decreased. When laser energy intensity reaches 117 mJ/cm^2, the DWNT can be ablated completely from transparent DWNT flexible thin film. The method is rapid, simple, applicable to large area processing and very suitable for mass production.

5. References

[1] J. Bohandy, B. F. Kim and F. J. Adrian, ”Metal deposition from a supported metal film using an excimer laser,” J. Appl. Phys. 60, 1538-1539 (1986).

[2] G. E. Blonder, G. S. Higashi, C. G. Fleming, "Laser projection patterned aluminum metallization for integrated circuit applications," Appl. Phys. Lett. 50, 766-768 (1987).
[3] Z. Kántor, Z. Tóth and T. Szörényi, "Deposition of micrometer-sized tungsten patterns by laser transfer technique," Appl. Phys. Lett. 64, 3506-3508 (1994).
[4] I. Zergioti, S. Mailis, N.A. Vainos, C. Fotakis, S. Chen and C.P. Grigoropoulos, "Microdeposition of metals by femtosecond excimer laser," Appl. Surf. Sci. 127-129, 601-605 (1998).
[5] R. Ba¨hnisch, W. Groß and A. Menschig, "Single-shot, high repetition rate metallic pattern transfer," Microelectronic Engineering 50, 541–546 (2000).
[6] Sudipta Bera, A. J. Sabbah, J. M. Yarbrough, C. G. Allen, Beau Winters, Charles G. Durfee, and Jeff A. Squier, "Optimization study of the femtosecond laser-induced forward-transfer process with thin aluminum films," Applied Optics 46, 4650-4659 (2007).
[7] Romain Fardel, Matthias Nagel, Frank N esch, Thomas Lippert and Alexander Wokaun, "Laser forward transfer using a sacrificial layer: Influence of the material properties," Appl. Surf. Sci. 254, 1322-1326 (2007).
[8] Michael Kroeger, Thomas Dobbertin, Jens Meyer, Henning Krautwald, Thomas Riedl, Hans-Hermann Johannes, and Wolfgang Kowalsky, "A laser induced local transfer for patterning of RGB-OLED-displays," Proc. of SPIE 5840, 177-184 (2005).
[9] Romain Fardel, Matthias Nagel and Frank Nuesch," Fabrication of organic light-emitting diode pixels by laser-assisted forward transfer,"Appl. Phys. Lett. 91,061103 (2007).
[10] Seung H. Ko, Heng Pan, Sang G. Ryu, Nipun Misra, Costas. P. Grigoropoulos and Hee K. Park," Nanomaterial enabled laser transfer for organic light emitting material direct writing," Appl. Phys. Lett. 93, 151110 (2008).
[11] Romain Fardel, Matthias Nagel, Frank Nuesch, Thomas Lippert and Alexander Wokaun," Laser-Induced Forward Transfer of Organic LED Building Blocks Studied byTime-Resolved Shadowgraphy," J. Phys. Chem.C 114, 5617–5636 (2010).
[12] Shiang-Kuo Chang-Jian, Jeng-Rong Ho, J-W John Cheng and Cheng-Kuo Sung," Fabrication of carbon nanotube field emission cathodes in patterns by a laser transfer method," Nanotechnology 17, 1184–1187 (2006).
[13] Jae Hak Lee, Choong Don Yoo and Yong-Seok Kim, "A laser-induced thermal spray printing process for phosphor layer deposition of PDP," J. Micromech. Microeng. 17, 258-264 (2007).
[14] A. Karaiskou, I. Zergioti, C. Fotakis, M. Kapsetaki and D. Kafetzopoulos, "Microfabrication of biomaterials by the sub-ps laser-induced forward transfer process," Appl. Surf. Sci. 208-209, 245-249 (2003).
[15] M Colina, P Serra, JM Fernández-Pradas, L. Sevillab and J.L. Morenza ,"DNA deposition through laser induced forward transfer," Biosensors and Bioelectronics 20, 1638–1642 (2005).
[16] P.K. Wu, B.R. Ringeisen, J. Callahan, M. Brooks, D.M. Bubb, H.D. Wu, A. Pique', B. Spargo, R.A. McGill and D.B. Chrisey, "The deposition, structure, pattern deposition, and activity of biomaterial thin-films by matrix-assisted pulsed-laser evaporation (MAPLE) and (MAPLE) direct write," Thin Solid Films 398 –399, 607–614 (2001).

[17] J.A. Barron, R. Rosen, J. Jones-Meehan, B.J. Spargo, S. Belkin and B.R. Ringeisen, "Biological laser printing of genetically modified Escherichia coli for biosensor applications," Biosensors and Bioelectronics 20, 246–252 (2004).

[18] T.V. Kononenko, I.A. Nagovitsyn, G.K. Chudinova and I.N. Mihailescu, "Application of clean laser transfer for porphyrin micropatterning," Appl. Surf. Sci, 256, 2803-2808 (2010).

[19] M. Sanz, M. Walczak, M. Oujja, C. Domingo, A. Klini, E.L. Papadopoulou, C. Fotakis and M. Castillejo, "Femtosecond laser deposition of TiO_2 by laser induced forward transfer," Thin Solid Films 518, 5525-5529 (2010).

[20] H. Kim, G. P. Kushto, C. B. Arnold, Z. H. Kafafi and A. Piqué, "Laser processing of nanocrystalline TiO2 films for dye-sensitizedsolar cells," Appl. Phys. Lett. 85, 464-468 (2004).

[21] H Kim, R C Y Auyeung, S H Lee, A L Huston and A Piqu´, "Laser-printed interdigitated Ag electrodes for organic thin film transistors," J. Phys. D: Appl. Phys. 43, 085101(2010).

[22] Hyunkwon Shin, Hyeongjae Lee, Jinwoo Sung, and Myeongkyu Lee," Parallel laser printing of nanoparticulate silver thin film patterns for Electronics," Appl. Phys. Lett. 92, 233107 (2008).

[23] M. Lefenfeld, G. Blanchet and J.A. Rogers, "High-Performance Contacts in Plastic Transistors and Logic Gates That Use Printed Electrodes of DNNSA-PANI Doped with Single-Walled Carbon Nanotubes," Adv. Mater. 15, 1188-1191 (2003).

[24] L. Rappa, S. Nénonb, A P. Allonclea, C. Videlot-Ackermannb, F. Fagesb and P. Delaporte, "Multilayer laser printing for Organic Thin Film Transistors," Appl. Surf. Sci, (2010).

[25] Shiang-Kuo Chang-Jian, Jeng-Rong Ho and J.-W. John Cheng, "Characterization of developing source/drain current of carbon nanotube field-effect transistors with n-doping by polyethylene imine," Microelectronic Engineering 87, 1973–1977 (2010).

[26] Kun-Tso Chen, Yu-Hsuan Lin, Jeng-Rong Ho, J.-W. John Cheng, Sung-Ho Liu, Jin-Long Liao and Jing-Yi Yan, "Laser-induced implantation of silver particles into poly(vinyl alcohol) films and its application to electronic-circuit fabrication on encapsulated organic electronics," Microelectronic Engineering 87, 543–547 (2010).

[27] P. Papakonstantinou, N. A. Vainos and C. Fotakis ,"Microfabrication by UV femtosecond laser ablation of Pt, Cr and indium oxide thin films," Appl. Surf. Sci. 151, 159-170 (1999).

[28] Tsuyoshi Asahi, Hiroshi Y. Yoshikawa, Masaki Yashiro and Hiroshi Masuhara, "Femtosecond laser ablation transfer and phase transition of phthalocyanine solids," Appl. Surf. Sci. 197-198, 777-781 (2002).

[29] A.I. Kuznetsov, J. Koch, and B.N. Chichkov, "Laser-induced backward transfer of gold nanodroplets," Optics Express 17, 8820-18825 (2009).

[30] M. Duocastella, J.M. Fernandez-Pradas, J.L. Morenza, D. Zafra and P. Serra, "Novel laser printing technique for miniaturized biosensors preparation," Sensors and Actuators B 145, 596–600 (2010).

[31] Alberto Piqué, "Laser Transfer Techniques for Digital Microfabrication," Springer Series in Mater. Sci. 135, 259-291 (2010).

[32] M. L. Levene, R. D. Scott and B. W. Siryj, "Material Transfer Recording," applied optics 9-10 (1970).

[33] Craig B. Arnold, Pere Serra, and Alberto Pique, "Laser Direct-Write Techniques for Printing of Complex Materials," MRS BULLETIN 32, 23-31 (2007).

[34] K.K.B. Hon, L. Li and I.M. Hutchings, "Direct writing technology—Advances and developments," CIRP Annals - Manufacturing Technology 57, 601–620 (2008).

[35] J. I. Sohn, S. Lee, Y. H. Song, S. Y. Choi, K. I. Cho, and K. S. Nam, ''Patterned selective growth of carbon nanotubes and large field emission from vertically well-aligned carbon nanotube field emitter arrays," Appl. Phys. Lett. 78, 901 (2001).

[36] G. Pirio, P. Legagneux, D. Pribat, K. B. K. Teo, M. Chhowalla, G. A. J. Amaratunga and W. I. Milne," Fabrication and electrical characteristics of carbon nanotube field emission microcathodes with an integrated gate electrode, " Nanotechnology 13, 1–4 (2002).

[37] T. Y. Tsai, C. Y. Lee, N. H. Tai, and W. H. Tuan, "Transfer of patterned vertically aligned carbon nanotubes onto plastic substrates for flexible electronics and field emission devices," Appl. Phys. Lett. 95, 013107 (2009).

[38] A. Mathur, S.S. Roy, Kiran S. Hazra, D.S. Misra and J.A. McLaughlin, "Growth of carbon nanotube arrays using nanosphere lithography and their application in field emission devices," Diamond & Related Materials 19, (2010) 914–917.

[39] M. Mann, Y. Zhang, K.B.K. Teo, T. Wells, M.M. El Gomati, W.I. Milne, " Controlling the growth of carbon nanotubes for electronic devices, " Microelectronic Engineering 87, 1491–1493 (2010).

[40] Y. Il Song, C. M. Yang, D. Y. Kim, H. Kanoh, K. Kaneko, "Flexible transparent conducting single-wall carbon nanotube film with network bridging method," Journal of Colloid and interface Science 318, 365–371(2008).

[41] S. Kim, J. Yim, X. Wang, D. D.C. Bradley, S. Lee, and J. C. deMello, "Spin- and Spray-Deposited Single-Walled Carbon-Nanotube Electrodes for Organic Solar Cells," Adv. Funct. Mater. 20, 2310–2316 (2010).

[42] Y. Il Song, G. Y. Kim, H. K. Choi, H. J. Jeong, K. K. Kim, C. M. Yang, S. C. Lim, K. H. An, K. T. Jung, and Y. H. Lee, "Fabrication of Carbon Nanotube Field Emitters Using a Dip-Coating Method," Chem. Vap. Deposition 12, 375–379 (2006).

[43] A. Rahy, P. Bajaj, I. H. Musselman, S. H. Hong, Y. P. Sun, D. J. Yang, " Coating of carbon nanotubes on flexible substrate and its adhesion study," Appl Surf. Sci. 255, 7084–7089 (2009).

[44] Y. M. Liu, Y. C. Fan, Y. C. Chen, Y. Sung and M. D. Ger, "Carbon nanotube field emission cathodes fabricated with trivalent chromium conversion coated substrates," Appl. Surf. Sci. 256, 1731–1734 (2010).

[45] Z. Wu, Z. Chen, X. Du, J. M. L., J. Sippel, M. Nikolou, K. Kamaras, J. R. Reynolds, D. B. Tanner, A. F. H., A. G. Rinzler, "Transparent, Conductive Carbon Nanotube Films," Science 305, 1273-1276 (2004).

[46] C. S. Woo, C. H. Lim, C. W. Cho, B. Park, H. Ju, D. H. Min, C. J. Lee and S. B. Lee, "Fabrication of flexible and transparent single-wall carbon nanotube gas sensors by vacuum filtration and poly(dimethyl siloxane) mold transfer," Microelectronic Engineering 84, 1610–1613 (2007).

[47] D. Zhang, K. Ryu, X. Liu, E. Polikarpov, J. L., Mark E. Tompson, and C. Zhou, " Transparent, Conductive, and Flexible Carbon Nanotube Films and Their Application in Organic Light-Emitting Diodes," Nano Lett. 6, 1880-1886 (2006).

[48] J. H. Shin, D. W. Shin, S. P. Patole, J. H. Lee, S. M. Park and J. B. Yoo, " Smooth, transparent, conducting and flexible SWCNT films by filtration–wet transfer processes," J. Phys. D: Appl. Phys. 42, 045305 (2009).

[49] M. Qian, T. Feng, K. Wang,H. Ding, Y. Chen,Q. Li,Z. Sun, "Field emission of carbon nanotube films fabricated by vacuum filtration," Physica E 43, 462–465 (2010)

[50] N. Saran, K. Parikh, D. S. Suh, E. Mun˜oz, H. Kolla, and S. K. Manohar, " Fabrication and Characterization of Thin Films of Single-Walled Carbon Nanotube Bundles on Flexible Plastic Substrates," J. Am. Chem. Soc. 126, 4462-4463 (2004).

[51] J. W. Song, Y. S. Kim, Y. H. Yoon, E. S. Lee, C. S. Han, Y. Cho, D. Kim, J. Kim, N. Lee, Y. G. Ko, H. T. Jung and S. H. Kim, "The production of transparent carbon nanotube field emitters using inkjet printing," Physica E 41, 1513–1516 (2009).

[52] H. Okimoto, T. Takenobu, K. Yanagi, Y. Miyata, H. Shimotani, H. Kataura, and Y. Iwasa, "Tunable Carbon Nanotube Thin-Film Transistors Produced Exclusively via Inkjet Printing," Adv. Mater. 22, 3981-3986 (2010).

[53] A. Kumar, V. L. Pushparaj, S. Kar, O. Nalamasu, and P. M. Ajayan, "Contact transfer of aligned carbon nanotube arrays onto conducting substrates," Appl Phys Lett. 89, 163120 (2006).

[54] H. Liu, D. Takagi, S. Chiashi, and Y. Homma, "Transfer and Alignment of Random Single-Walled Carbon Nanotube Films by Contact Printing," American Chemical Society 4, 933–938 (2010).

[55] C. L. Pint, Y. Q. Xu, S. Moghazy,_ T. Cherukuri, N. T. Alvarez, E. H. Haroz, S. Mahzooni, S. K. Doorn, J. Kono, M. Pasquali, and R. H. Hauge, "Dry Contact Transfer Printing of Aligned Carbon Nanotube Patterns and Characterization of Their Optical Properties for Diameter Distribution and Alignment," American Chemical Society 4, 1131–1145 (2010).

[56] L. Valentini, D. Bagnis, R. Cagnoli, F. Meloni, A. Mucci, L. Schenetti and J. Kenny, "Electrodeposition of carbon nanotube semi-transparent thin films: A facile route for preparing photoactive polymeric hybrid materials," Diamond & Related materials 17, 1573–1576 (2008).

[57] S. Pei, J. Du, Y. Zeng, C. Liu and H. M. Cheng, "The fabrication of a carbon nanotube transparent conductive film by electrophoretic deposition and hot-pressing transfer," Nanotechnology 20, 235707 (2009).

[58] S. B. Bon, L. Valentini, J. M. Kenny, L. Peponi, R. Verdejo, and M. A. Lopez-Manchado, "Electrodeposition of transparent and conducting graphene/ carbon nanotube thin films," Phys. Status Solidi A 207, 2461–2466 (2010).

[59] Shiang-Kuo Chang-Jian,, J. R. Ho, J. W. John Cheng, "A flexible carbon nanotube field emitter fabricated on a polymer substrate by a laser separation method," Solid State Communication 150, 666-668 (2010).

[60] A. A. Stramel, M.C. Gupta, H.R. Lee, J. Yu and W.C. Edwards, "Pulsed laser deposition of carbon nanotube and polystyrene–carbon nanotube composite thin films," Optics and lasers in Engineering 48, 1291–1295 (2010).

[61] C. Boutopoulos, C. Pandis, K. Giannakopoulos, P. Pissis, and I. Zergioti, " Polymer/carbon nanotube composite patterns via laser induced forward transfer," Appl. Phys. Lett. 96, 041104 (2010).
[62] Shiang-Kuo Chang-Jian, Jeng-Rong Ho and J.-W. John Cheng, "Fabrication of all-tube p- and n- type carbon nanotube field-effect transistors by laser transfer method," Laser in Engineering (in press).
[63] C. A. Spindt, "A thin-film field-emission cathode", Journal of Applied Physics 39, 3504-3505 (1968).
[64] Otto Zhou, Hideo Shimoda, Bo Gao, Soojin Oh, Les Fleing, and Guozhen Yue, "Materials Science of Carbon Nanotubes: Fabrication, Integration, and Properties of Macroscopic Structures of Carbon Nanotubes," Acc. Chem. Res. 35, 1045-1053 (2002).
[65] W. A. de Heer, A. Chaˆtelain, and D. Ugarte, "A Carbon Nanotube Field-Emission Electron Source," Science 270, 1179-1180 (1995).
[66] Chi Li, Yan Zhang, Mark Mann, David Hasko, Wei Lei, Baoping Wang, Daping Chu, Didier. Pribat, Gehan A. J. Amaratunga, and William I. Milne, "High emission current density, vertically aligned carbon nanotube mesh, field emitter array," Appl. Phys. Lett. 97, 113107-3 (2010).
[67] W. B. Choi, Y. W. Jin, H. Y. Kim, S. J. Lee, M. J. Yun, J. H. Kang, Y. S. Choi, N. S. Park, N. S. Lee, and J. M. Kim, "Electrophoresis Deposition of Carbon Nanotubes for Triode-type Field Emission Display," Appl. Phys. Lett. 78, 1547-1549 (2001).
[68] Wenhui Lu, Hang Song, Yixin Jin, Hui Zhao, Haifeng Zhao, Lianzhen Cao, Zhiming Li, Hong Jiang, Guoqing Miao, "Electrophoresis deposition and field emission characteristics of planar-gate-type electron source with carbon nanotubes," Physica B 403, 1793–1796 (2008).
[69] Yitian Peng, Yuanzhong Hu, Hui Wang, "Fabrication of carbon nanotube field emission film by electrophoresis deposition and sintering," Colloids and Surfaces A: Physicochem. Eng. Aspects 329, 161-164 (2008).
[70] W.B. Choi, D.S. Chung, J.H. Kang, H.Y. Kim, Y.W. Jin, I.T. Han, Y.H. Lee, J.E. Jung, N.S. Lee, G.S. Park and J.M. Kim, "Fully sealed, high-brightness carbon-nanotube field-emission display," Appl. Phys. Lett. 75, 3129-3131 (1999).
[71] Jean-Marc Bonard, Jean-Paul Salvetat, Thomas Sto¨ ckli, Walt A. de Heer, La´szlo´ Forro´ , and Andre´ Chaˆ telain, "Field emission from single-wall carbon nanotube films," Appl. Phys. Lett. 73, 918-920 (1998).
[72] Jae-Hong Park, Gil-Hwan Son, Jin-San Moon, Jae-Hee Han, Alexander S. Berdinsky,
[73] D.G. Kuvshinov, Ji-Beom Yoo, Chong-Yun Park,"Screen printed carbon nanotube field emitter array for lighting source application," J. Vac. Sci. Technol., B 23, 749-753 (2005).
[74] Li Yukui, Zhu Changchun, Liu Xinghui, "Field emission display with carbon nanotubes cathode: prepared by a screen-printing process," Diamond and Related Materials 11, 1845–1847 (2002).
[75] Juntao Li, Wei Lei, Xiaobing Zhang, Xuedong Zhou, Qilong Wang, Yuning Zhang, Baoping Wang, "Field emission characteristic of screen-printed carbon nanotube cathode," Appl. Sur. Sci. 220, 96-104 (2003).

[76] T. J. Vink, M. Gillies, J. C. Kriege, and H. W. J. J. van de Laar, "Enhanced field emission from printed carbon nanotubes by mechanical surface modification," Appl. Phy. Lett, 83, 3552–3554 (2003).

[77] Fan-Guang Zeng, Chang-Chun Zhu, Xinghui, Weihua Liu, YuKui Li, "A novel mechanical approach to improve the field emission characteristics of printed CNT films," Materials Lett. 60, 2399-2402 (2006).

[78] Se-Jin Kyung, Jae-Beom Park, Maksym Voronko, June-Hee Lee, Geun-Young Yeom, "The effect of atmospheric pressure plasma treatment on the field emission characteristics of screen printed carbon nanotubes," Carbon 45, 649–654 (2007).

[79] Chung-Wei Cheng , Chun-Ming Chen, Yung-Chun Lee, "Laser surface treatment of screen-printed carbon nanotube emitters for enhanced field emission," Appl. Sur. Sci. 255, 5770–5774 (2009).

[80] Hui Ding, Tao Feng , Zhejuan Zhang, Kai Wang, Min Qian, Yiwei Chen, Zhuo Sun, " Enhanced field emission properties of screen-printed doubled-walled carbon nanotubes by polydimethylsiloxane elastomer," Appl. Sur. Sci. 256, 6596–6600 (2010).

[81] S. Tans, A. Verschueren, C. Dekker, "Room-temperature transistor based on a single carbon nanotube," Nature 393, 49-52 (1998).

[82] R. Martel, T. Schmidt, H. R. Shea, T. Hertel, P. Avouris, "Single- and multi-wall carbon nanotube field-effect transistors," Appl. Phys. Lett. 73, 2447-2449 (1998).

[83] M. S. Fuhrer, J. Nygard, L. Shih, M. Forero, Y. Yoon, M. S. C. Mazzoni, H. J. Choi, J. Ihm, S. G. Louie, A. Zettl, P. L. McEuen, "Crossed nanotube junctions," Science 288, 494-497 (2000).

[84] Shiraishi, M., Takenobu, T., Iwai, T., Iwasa, Y., Kataura, H., Ata, M., "Single-walled carbon nanotube aggregates for solution-processed field effect transistors," Chem. Phys. Lett. 394, 110-113 (2004).

[85] Hur, S.-H., Park, O. O. & Rogers, J. A. "Extreme bendability of single-walled carbon nanotube networks transferred from high-temperature growth substrates to plastic and their use in thin-film transistors," Appl. Phys. Lett. 86, 243502-3 (2005).

[86] Meitl, M.; Zhou, Y.; Gaur, A.; Jeon, S.; Usrey, M.; Strano, M.; Rogers, J., "Solution casting and transfer printing single-walled carbon nanotube films," Nano Lett. 4, 1643-1647 (2004).

[87] Zhou, C.; Kong, J.; Yenilmez, E.; Dai, H., "Modulated chemical doping of individual carbon nanotubes," Science 290, 1552-1555 (2000).

[88] V. Derycke, R. Martel, J. Appenzeller, Ph. Avouris, "Carbon nanotube inter-and intramolecular logic gates," Nano Letters 1, 453-456 (2001).

[89] Shim, M.; Javey, A.; Kam, N. W. S.; Dai, H., "Polymer functionalization for air-stable n-type carbon nanotube field-effect transistors," J. Am. Chem. Soc. 123, 11512−11513 (2001).

[90] Zhou, Y. et al. "P-channel, n-channel thin film transistors and p-n diodes based on single wall carbon nanotube networks," Nano Lett. 4, 2031–2035 (2004).

[91] M. H. Yang, K. B. K. Teo, W. I. Milne, and D. G. Hasko, "Carbon nanotube Schottky diode and directionally dependent field-effect transistor using asymmetrical contacts," Appl. Phys. Lett. 87, 253116-3 (2005).

[92] Yosuke Nosho, Yutaka Ohno,a! Shigeru Kishimoto, and Takashi Mizutani, "n-type carbon nanotube field-effect transistors fabricated by using Ca contact electrodes," Appl Phys Lett 86, 073105-3 (2005).

[93] Qing Cao, Seung-Hyun Hur, Zheng-Tao Zhu, Yugang Sun, Congjun Wang, Matthew A. Meitl, Moonsub Shim, and John A. Rogers, "Highly Bendable, Transparent Thin-Film Transistors That Use Carbon-Nanotube-Based Conductors and Semiconductors with Elastomeric Dielectrics," Adv. Mater. 18, 304–309 (2006).

[94] Fumiaki N. Ishikawa, Hsiao-kang Chang, Koungmin Ryu, Po-chiang Chen, Alexander Badmaev, Lewis Gomez De Arco, Guozhen Shen, and Chongwu Zhou, "Transparent Electronics Based on Transfer Printed Aligned Carbon Nanotubes on Rigid and Flexible Substrates," ACS Nano 3, 73–79 (2009).

[95] Sukjae Jang, Houk Jang, Youngbin Lee, Daewoo Suh, Seunghyun Baik, Byung Hee Hong and Jong-Hyun Ahn, "Flexible, transparent single-walled carbon nanotube transistors with grapheme electrodes," Nanotechnology 21, 425201-5 (2010).

[96] L. Song, L. Ci, L. Lv, Z. Zhou, X. Yan, D. Liu, H. Yuan, Y. Gao, J. Wang, L. Liu, X. Zhao, Z. Zhang, X. Dou, W. Zhou, G. Wang, C. Wang and S. Xie, "Direct Synthesis of a Macroscale Single-Walled Carbon Nanotube Non-Woven Material," Advanced Materials 16, 1529-1534 (2004).

[97] J. L. Rigueur, S. A. Hasan, S. V. Mahajan and J. H. Dickerson, "Buckypaper fabrication by liberation of electrophoretically deposited carbon nanotubes," Carbon 48, 4090-4099 (2010).

[98] P. Gonnet, Z. Liang, E. S. Choi, R. S. Kadambala, C. Zhang, J. S. Brooks, B. Wang and L. Kramer, "Thermal conductivity of magnetically aligned carbon nanotube buckypapers and nanocomposites," Current Applied Physics 6, 119-122 (2006).

[99] P. Jin Gyu and et al., "Electromagnetic interference shielding properties of carbon nanotube buckypaper composites," Nanotechnology 20, 415702-7 (2009).

[100] C. YiWen and et al., "Emitter spacing effects on field emission properties of laser-treated single-walled carbon nanotube buckypapers," Nanotechnology. 21, 495702-7 (2010).

[101] M. Endo, H. Muramatsu, T. Hayashi, Y. A. Kim, M. Terrones and M. S. Dresselhaus, "Nanotechnology: 'Buckypaper' from coaxial nanotubes," Nature. 433, 476-476 (2005).

[102] Y. A. Kim, H. Muramatsu, T. Hayashi, M. Endo, M. Terrones and M. S. Dresselhaus, "Fabrication of High-Purity, Double-Walled Carbon Nanotube Buckypaper," Chemical Vapor Deposition. 12, 327-330 (2006).

[103] H. Zhu and B. Wei, "Direct fabrication of single-walled carbon nanotube macro-films on flexible substrates," Chemical Communications, 3042-3044 (2007).

[104] W. Ding and et al., "Highly oriented carbon nanotube papers made of aligned carbon nanotubes," Nanotechnology 19, 075609-6 (2008).

[105] D. Simien, J. A. Fagan, W. Luo, J. F. Douglas, K. Migler and J. Obrzut, "Influence of Nanotube Length on the Optical and Conductivity Properties of Thin Single-Wall Carbon Nanotube Networks," ACS Nano 2, 1879-1884 (2008).

[106] A. Ansón-Casaos, J. M. González-Domínguez, E. Terrado and M. T. Martínez, "Surfactant-free assembling of functionalized single-walled carbon nanotube buckypapers, '' Carbon 48, 1480-1488 (2010).

[107] D. N. Ventura, R. A. Stone, K.-S. Chen, H. H. Hariri, K. A. Riddle, T. J. Fellers, C. S. Yun, G. F. Strouse, H. W. Kroto and S. F. A. Acquah, "Assembly of cross-linked multi-walled carbon nanotube mats," Carbon 48, 987-994 (2010).

[108] J. G. Park, N. G. Yun, Y. B. Park, R. Liang, L. Lumata, J. S. Brooks, C. Zhang and B. Wang, "Single-walled carbon nanotube buckypaper and mesophase pitch carbon/carbon composites," Carbon. 48, 4276-4282 (2010).